Gruppo Nazionale di Geofisica della Terra Solida

BOOK OF ABSTRACTS
42nd NATIONAL CONFERENCE

13 - 16 FEBRUARY 2024

FERRARA

OGS
Istituto Nazionale
di Oceanografia
e di Geofisica
Sperimentale

EAGE
EUROPEAN ASSOCIATION OF GEOSCIENTISTS & ENGINEERS
SEG
SOCIETY OF EXPLORATION GEOPHYSICISTS
SEZIONE ITALIANA

23° CONVEGNO NAZIONALE

Gruppo Nazionale di Geofisica della Terra Solida

BOOK OF ABSTRACTS
42nd NATIONAL CONFERENCE

13 - 16 FEBRUARY 2024

FERRARA

OGS
Istituto Nazionale
di Oceanografia
e di Geofisica
Sperimentale

EAGE
EUROPEAN ASSOCIATION OF GEOSCIENTISTS & ENGINEERS
SEG
SOCIETY OF EXPLORATION GEOPHYSICISTS
SEZIONE ITALIANA
23° CONVEGNO NAZIONALE

42nd GNGTS National Conference

42 nd GNGTS TECHNICAL SCIENTIFIC COMMITTEE

Alessandro Rebez, President
National Institute of Oceanography and Applied Geophysics – OGS
arebez@ogs.it

Daniela Di Bucci
Representing the Civil Protection Department
Daniela.DiBucci@protezionecivile.it

Claudia Piromallo
Representing the National Institute of Geophysics and Volcanology - INGV
claudia.piromallo@ingv.it

Massimiliano Moscatelli
Representing the National Research Council - CNR
massimiliano.moscatelli@igag.cnr.it

Paolo Gasperini
Representing the Universities
paolo.gasperini@unibo.it

Andrea Tognarelli
Representing the EAGE-SEG Italian Section
andrea.tognarelli@unipi.it

Angelo Masi
Representing ReLUIS Consortium
angelo.masi@unibas.it

ORGANISING COMMITTEE

National Institute of Oceanography and Applied Geophysics - OGS
William Toson
Alessandro Asta
Giulia Casalena
Oriela Hailaj

Editor: Alessandro Rebez

10.13120/dna7-2n16

The GNGTS 42nd National Conference was organised by

OGS
National Institute of Oceanography and Applied Geophysics

Endorsed by

Università degli Studi di Ferrara

With the contribution of

CODEVINTEC
Tecnologie per le Scienze della Terra e del Mare

TOPIC 1

SEISMICITY, VOLCANOES, DATA AND MODELS

Session 1.1

Recent advances in the study of earthquakes, faults and seismogenic processes in natural and experimental faults

GNGTS 2024

SEISMICITY, VOLCANOES, DATA AND MODELS

Session 1.1

Recent advances in the study of earthquakes, faults and seismogenic processes in natural and experimental faults

Convenors of the session:
Paolo Galli (DPC) – paolo.galli@protezionecivile.it
Massimo Cocco (INGV) – massimo.cocco@ingv.it
Luisa Valoroso (INGV) – luisa.valoroso@ingv.it

The goal of this session is to present and discuss recent advances in earthquake and fault mechanics through observations, multidisciplinary data, and modeling of natural and experimental faults.
We encourage the submission of contributions on the following topics:

- **Investigations of the Quaternary and structural background of active faults**
- **Paleoseismology and archaeoseismology**
- **Insights of the 2023 Kahramanmaraş (Turkey) and High Atlas Mts. (Morocco) earthquakes**
- **Characterization of capable faults for seismic microzonation studies, in tectonic and volcanic settings**
- **Revisions of historical and instrumental earthquakes and catalogues**
- **Case histories of instrumental and historical seismic sequences**
- **Advanced earthquake location methods, both for research and monitoring purposes**
- **GPS and InSAR data for the evaluation of inter-, post- and co-seismic deformation**
- **Source modelling through the inversion of seismic, geodetic and/or other multidisciplinary datasets**
- **Multidisciplinary, multiscale geophysical imaging for seismotectonic studies**
- **3D modelling for seismotectonics**
- **Insights into the mechanics of earthquake and faulting form from numerical modeling and laboratory experiments**
- **Rocks rheology and role of fluids in the seismogenesis: from laboratory experiments to the Earth crust**

Estimate of seismic fracture surface energy from pseudotachylyte-bearing faults

S. Aldrighetti[1], G. Di Toro[1,2], G. Pennacchioni[1]

[1] *Dipartimento di Geoscienze, Università degli Studi di Padova, Padua, Italy*
[2] *Sezione di Roma 1, Istituto Nazionale di Geofisica e Vulcanologia, Rome, Italy*

Earthquakes are the result of propagation (at km s^{-1}) of a rupture and associated slip (at m s^{-1}) along a fault (Scholz, 2019). The total energy involved in a seismic event is unknown, but qualitatively most of the energy is dissipated by rock fracturing and frictional heat. Seismic fracture energy G (J m^{-2}) is the energy dissipated in the rupture propagation and can be estimated by the inversion of seismic waves (Abercrombie and Rice, 2005; Tinti et al., 2005; Cocco et al., 2023). However, the physical significance of G remains elusive. G may include the contributions of both rock fracturing (energy to form new rock surfaces U_S, J m^{-2}) and fault frictional heating (Q, J m^{-2}). Here we determine both U_S and Q in natural and experimental pseudotachylyte-bearing faults following the approach used by Pittarello et al. (2008). Pseudotachylytes are solidified frictional melts produced during seismic slip. In these rocks: (i) U_S is proportional to the surface of the new fragments produced in both the slip zone and in the wall rocks; and (ii) Q is proportional to the volume of frictional melt.

The selected natural pseudotachylytes are from the East-West-striking, dextral, strike-slip Gole Larghe Fault Zone (Adamello, Italy; Di Toro and Pennacchioni, 2004). To estimate U_S we used Electron Back-Scatter Electrons (EBSD), High Resolution Mid Angle Back-Scattered Electrons (HRMABSD) and Cathodoluminescence-Field Emission-Scanning Electron Microscopy (CL-FESEM). In particular, CL-FESEM imaging reveals a microfracture network in the wall rocks that cannot be detected with other techniques used (Fig. 1).

In the pseudotachylyte-bearing fault, the microstructural analysis reveals (i) a high degree of fragmentation of the wall rock adjacent to the pseudotachylyte fault vein (formed along the slip surface), with clast size down to < 90 nm in diameter, and (ii) a systematic difference in fracture density and orientation of the microfractures on the two opposite wall rock sides of the fault (Fig. 1). In fact, in the northern wall rock the fracture density is low and the microfractures are oriented preferentially East-West, while in the southern wall rock the fracture density is high and oriented preferentially North-South (Fig. 1). This asymmetric distribution of microfracture damage is consistent with the stress perturbation at the crack tip associated with the propagation of the seismic rupture (Di Toro et al., 2005). This suggests that the microfractures developed during coseismic slip and, therefore, can be used to estimate U_S.

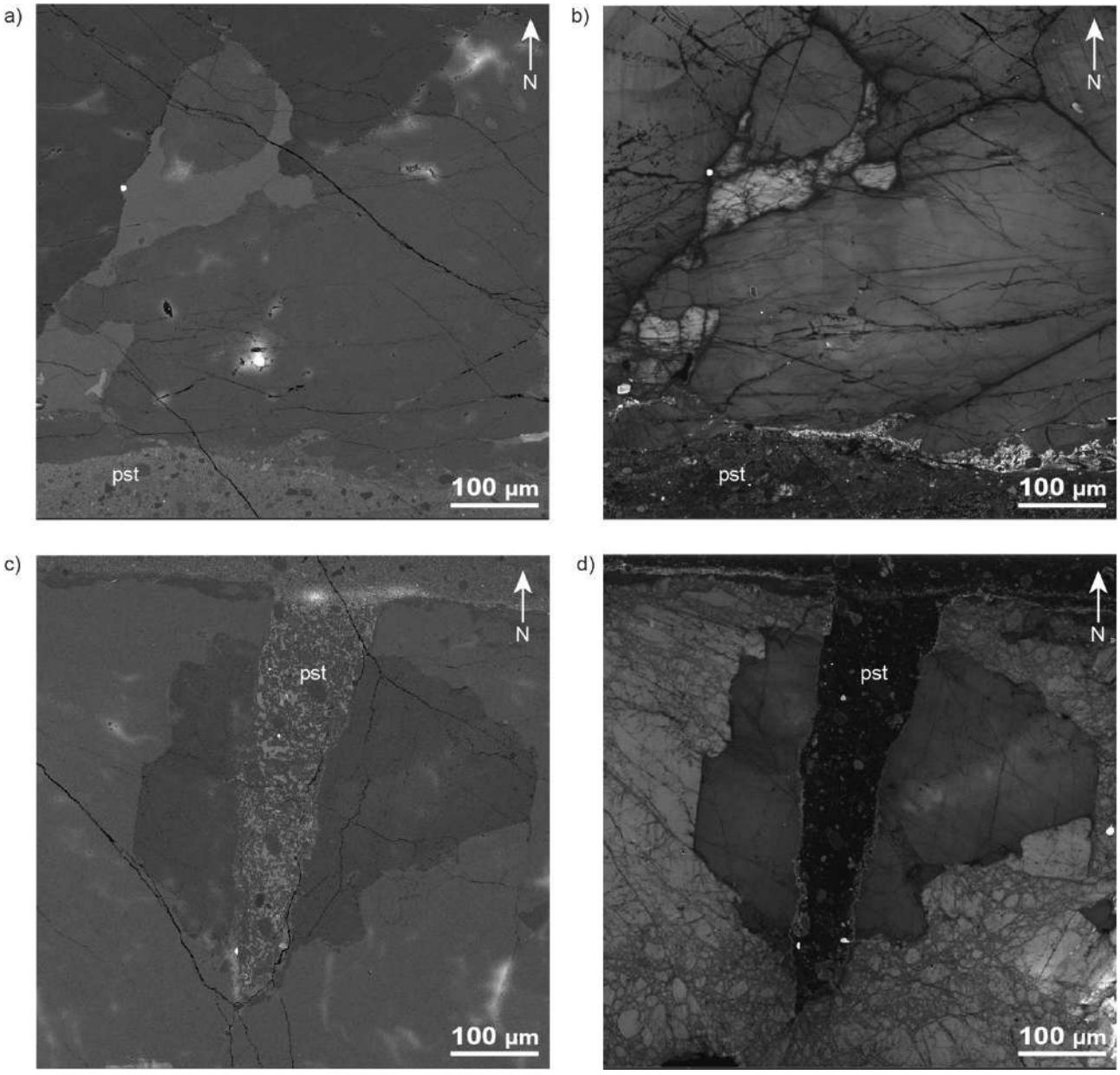

Fig. 1: Microfracture pattern in the two wall rocks of the selected pseudotachylyte-bearing fault. a) BSE-FESEM and b) CL-FESEM microimages of the northern wall rock, displaying low damage and preferential subhorizontal orientation of the microfractures. c) BSE-FESEM and d) CL-FESEM microimages of the southern wall rock, showing instead extreme damage surrounding a pseudotachylyte injection vein, and a preferential subvertical strike of the microfractures. All microimages are taken at the boundary pseudotachylyte-wall rock. Note how in BSE-FESEM microimages the microfracture pattern is extremely underestimated. pst=pseudotachylyte.

Fracture density decreases exponentially from the pseudotachylyte-wall rock contact towards the wall rock. The rock volumes with highest coseismic damage at the contact with the pseudotachylytes are assumed to be representative of the host-rock damage preceding frictional melting along the slip zone (Pittarello et al., 2008). Based on this assumption, U_S is estimated in the range from 0.008 to 1.35 MJ m^{-2}. Q was estimated from the thickness of the pseudotachylyte vein (Pittarello et al., 2008) to be ~32 MJ m^{-2}. In the case of the Gole Larghe Fault, numerical

modelling yield fracture energies G in the range 8-67 MJ m^{-2} (Di Toro et al., 2005) suggesting that U_S is subordinate component of G and that most of the seismological fracture energy is heat.

References

Abercrombie, R. E., and Rice, J. R.; 2005: *Can observations of earthquake scaling constrain slip weakening?* Geophys. J. Int., 162(2), 406–424. https://doi.org/10.1111/j.1365-246X.2005.02579.x.

Cocco, M., Aretusini, S., Cornelio, C., Nielsen, S. B., Spagnuolo, E., Tinti, E., and Di Toro, G.; 2023: *Fracture Energy and Breakdown Work During Earthquakes.* Ann. Rev. Earth Planet. Sci., 51(1), null. https://doi.org/10.1146/annurev-earth-071822-100304.

Di Toro, G., Nielsen, S., and Pennacchioni, G.; 2005: *Earthquake rupture dynamics frozen in exhumed ancient faults.* Nature, 436(7053), Article 7053. https://doi.org/10.1038/nature03910.

Di Toro, G., and Pennacchioni, G.; 2004: *Superheated friction-induced melts in zoned pseudotachylytes within the Adamello tonalites (Italian Southern Alps).* J. Struct. Geol., 26(10), 1783–1801. https://doi.org/10.1016/j.jsg.2004.03.001.

Pittarello, L., Di Toro, G., Bizzarri, A., Pennacchioni, G., Hadizadeh, J., and Cocco, M.; 2008: *Energy partitioning during seismic slip in pseudotachylyte-bearing faults (Gole Larghe Fault, Adamello, Italy).* Earth Planet. Sci. Lett., 269(1), 131–139. https://doi.org/10.1016/j.epsl.2008.01.052.

Scholz, C. H.; 2019: *The Mechanics of Earthquakes and Faulting.* Cambridge University Press.

Tinti, E., Spudich, P., and Cocco, M.; 2005: *Earthquake fracture energy inferred from kinematic rupture models on extended faults.* J. Geophys. Res: Solid Earth, 110(B12). https://doi.org/10.1029/2005JB003644.

Corresponding author: silvia.aldrighetti.1@phd.unipd.it

Offshore fault geometry revealed from earthquake locations using new state-of-art techniques: the case of the 2022 Adriatic Sea earthquake sequence

Like An*[1], Francesco Grigoli[2], Bogdan Enescu[1,3], Mauro Buttinelli[4], Mario Anselmi[4], Irene Molinari[4], and Yoshihiro Ito[5]

[1]Department of Geophysics, Graduate School of Science, Kyoto University, Kyoto, Japan
[2]Department of Earth Sciences, University of Pisa, Pisa, Italy
[3]National Institute for Earth Physics, Magurele, Bucharest, Romania
[4]National Institute of Geophysics and Volcanology, Italy
[5]Disaster Prevention Research Institute, Kyoto University, Uji, Kyoto, Japan

On November 9, 2022, 6:07 AM (UTC), a sequence of two M>5 earthquakes (mainshock of Mw 5.5) occurred 30 km NE off the coast of Fano, Italy. Since locating offshore earthquakes is challenging, we have applied a combined approach to constrain the geometry and depth of the sequence events better. Six M3+ events were first relocated using a travel time stacking method. Next, using the six M3+ earthquakes as reference events, we applied a differential travel-time method to reconstruct the earthquake cluster geometry and locate the remaining events, including the mainshock. The results reveal a 25-35 degree SW dipping cluster. The depth of the mainshock hypocenter obtained using this procedure agrees well with that determined by depth phases. This study's relatively sharp earthquake cluster geometry is consistent with the thrust faults revealed by a local seismic reflection survey and focal mechanism solutions. These approaches are particularly useful for offshore monitoring of industrial operations (e.g., Carbon Dioxide and Methane storage).

Corresponding author:
Like An (like.an.65h@st.kyoto-u.ac.jp),
Mauro Buttinelli (mauro.buttinelli@ingv.it)

Focus on the seismic behavior of the Morrone Fault: the Majella-Morrone experiment

M. Anselmi[1], S. Bagh[1], C. Chiarabba[1], P. De Gori[1], R. Fonzetti[3], A. Govoni[1], I. Menichelli [1,3], G. Pezzo[1], G. Saccorotti[1], F. Silverii[1]

[1] Istituto Nazionale di Geofisica e Vulcanologia, Roma, Italy
[2] Istituto Nazionale di Geofisica e Vulcanologia, Pisa, Italy
[3] Università degli Studi di Roma Tre, Roma, Italy

In the framework of the PON-GRINT project, a working group of INGV researchers, along with some Ph.D. students, carried out a passive seismic experiment, still ongoing. The field activities began in May 2022 in the Abruzzi region (Central Italy). Between May and October 2022, twenty-three (23) temporary seismic stations were deployed in a ~ 250 km^2 area extending from the Sulmona-Pratola Peligna plain to the eastern flank of Monte Morrone.

The location of the study area is in the Central Apennines, southeast of the area struck by the 2009 L'Aquila seismic sequence. The whole Apennine chain consists of thrust and fold systems, the space-time E and NE migration of which are related to the westward subduction of the Adriatic lithosphere and its progressive eastward flexural retreat (Patacca et al. 2008 and references therein). Since the Pliocene, and during the entire Quaternary, the chain was affected by extensional tectonics, contemporaneous to its significant uplift (Galadini et al. 2003a and references therein). The extensional faults have resulted in the formation of several intermontane basins (e.g. the Fucino, Sulmona, L'Aquila) that are filled by continental deposits of Plio-Quaternary age (Bosi et al. 2003; Galadini and Messina 2004).

In particular, the Apennine sector focused in this study, located in the southern-eastern Abruzzi region, has been struck by some large magnitude earthquakes , i.e. the seismic events of 1706 (Maw = 6.6) and 1933 (Maw = 5.7), as well as by the shocks of the 1349 and 1456 seismic sequences (Maw = 6.6 and 7.0, Romano et al. 2013 and references therein). The literature available indicates also the 1456, 1706 and 1933 earthquakes originated in this area (Galadini and Galli 2007; Fracassi and Valensise 2007). Many studies have been carried out to define the seismotectonic characteristics of this Apennine sector. Some probably active faults have been detected along the south-western slopes of Mt. Morrone (Bosi 1975), and in the area located between Mt. Morrone, the Maiella Massif and the Cinque Miglia plain.

Although the last 20 years have been characterised by low-magnitude seismicity, the presence of the Morrone Fault (whose instrumental seismic activity is still debated) motivates the carrying out of the experiment to record the microseismicity occurred in the whole area and also the eventual seismic activity released by the Morrone Fault structure.

The field activity results in building a temporary network, integrated with regional and national seismic networks, with an average station inter-distance of about 7-8 Km. In addition, along with the seismic network, we deployed a subset of seismic stations to make an almost straight transect across the Monte-Morrone, with the goal of defining the fault structure profile by using seismic noise recordings. After almost 12 months of recordings the straight transect was shifted, following the strike of the focused fault, to the north-west, still across the Monte Morrone (Fig.1).

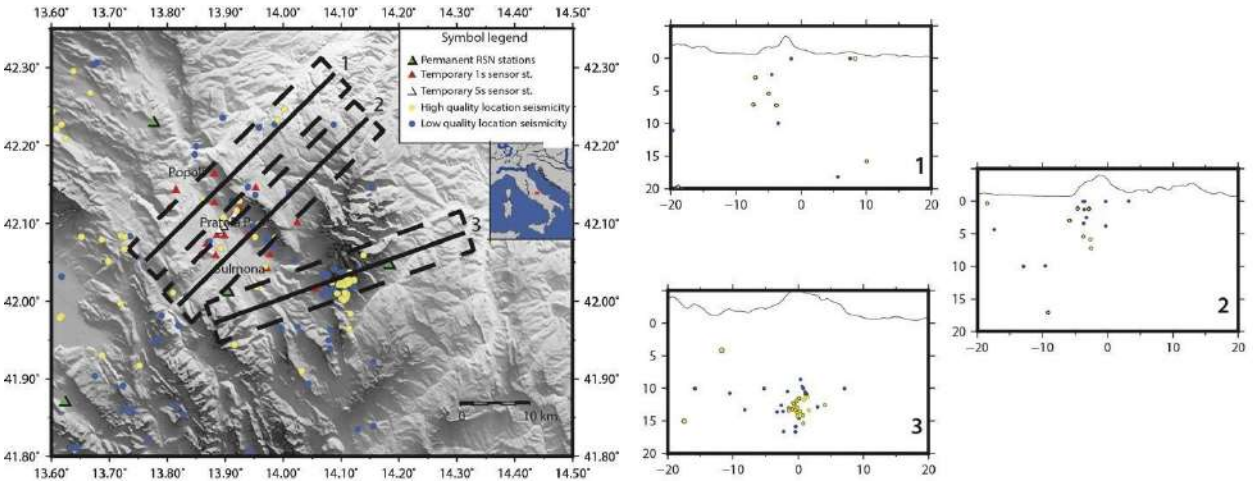

Fig.1 . Map with a temporary network of the experiment: 19 short period + 4 extended period sensors. The seismicity was recorded between November 2022 and January 2023.

The preliminary analysis of the recorded data seems to show a scarce seismicity within the temporary network, mainly clustered in two different areas: one at the north-western side of Monte Morrone and the other between the southeastern part of Monte Morrone and Maiella, probably related to the Caramanico fault that boards the western flank of the Maiella anticline (Fig. 1).

References

Bosi C (1975) Osservazioni preliminare su faglie probabilmente attive nell'Appennino Centrale. Bol Soc Geol Ital 94:827–859

Bosi C, Galadini F, Giaccio B, Messina P, Sposato A (2003). Plio-Quaternary continental deposits in the Latium-Abruzzi Apennines: the correlation of geological events across different intermontane basins. Il Quat (Ital J Quat Sci) 16:55–76

Fracassi U, Valensise G (2007). Unveiling the sources of the catastrophic 1456 multiple earthquake: hints to an unexplored tectonic mechanism in southern Italy. Bull Seism Soc Am 97:725–748

Galadini F, Galli P, Moro M (2003a). Paleoseismology of silent faults in the central Apennines (Italy): the Campo Imperatore fault (Gran Sasso range fault system). Ann Geophys 46:793–813

Galadini F, Messina P (2004). Early-Middle Pleistocene eastward migration of the Abruzzi Apennine (central Italy) extensional domain. J Geodyn 37:57–81

Galadini F, Galli P (2007). Inquadramento sismotettonico della regione interessata dai terremoti del 1703 e 1706. Bullettino della Deputazione di Storia Patria degli Abruzzi. Settecento abruzzese: eventi sismici, mutamenti economico-sociali e ricerca storiografica. In: a cura di Raffaele Colapietra, Giacinto Marinangeli, Colacchi (ed) Atti del convegno L'Aquila 29-30-31 ottobre 2004, Paolo Muzi. L'Aquila 2007, pp 1158

Patacca E, Scandone P, Di Luzio E, Cavinato GP, Parotto M (2008) Structural architecture of the central Apennines: interpretation of the CROP 11 seismic profile from the Adriatic coast to the orographic divide. Tectonics 27:TC3006, 36 pp

Romano, M. A., De Nardis, R., Lavecchia, G., Garbin, M., Peruzza, L., Priolo, E., ... & Ferrarini, F. (2013). Preliminary analysis of the microearthquakes-faults association in the Sulmona basin (central Apennines, Italy). Rendiconti Online della Società Geologica Italiana, 29, 150-153

Corresponding author: mario.anselmi@ingv.it

One Earthquake, Two Scenarios: The Baffling Case of the 1467 Siena Earthquake.

A. Arrighetti[1], B. Gelli[2], V. Castelli[3]

[1] École normale supérieure - Université PSL (AOROC UMR 8546), Paris, France;
[2] Università degli Studi di Siena, Italia; [3] INGV, Bologna/Ancona, Italia

Historical seismology is a work in progress: the overall picture of a given historical earthquake, no matter how long taken for granted, can sometimes change, either thanks to the discovery of "new" (i.e. previously unknown or unheeded) historical sources, or by considering the research output of other disciplines.

Historical seismologists tend to give precedence in their studies to written evidence, derived (when a choice is possible) from the sources 1) most likely to provide information useful to fulfill their main objectives (i.e. assessing macroseismic data points, reconstructing macroseismic fields and damage scenarios), and 2) not requiring long-drawn out, possibly unsuccessful searches that would hardly fit with their generally tight deadlines. Unavoidably, this approach mean to discard interesting but elusive evidence, whose records are buried too deep to make a search cost-effective, or were never written down at all but survive as the marks which past earthquakes left on buildings. It is up to the scholar to find ways and means to interpret these unwritten records, even if the readings taken are not always conclusive.

The archaeoseismological study of historic towns and buildings allows to gain in-depth knowledge of how a given earthquake interacted with architectures and building components and in some cases, it can also provide evidence of the social, economic, or even political consequences of some earthquakes. The project *PROTECT – Knowledge for PReventiON - Technique s for repairing seismic damage from the medieval period to the modern era* (financed by the European Union's Horizon 2020 research and innovation program together with a Marie Skłodowska-Curie Individual Fellowship) applies, on an entirely experimental basis, the methods of archaeoseismological analysis to the historic centre of Siena (Tuscany), to improve the knowledge of its context for purposes of seismic risk reduction. By weaving together the information gathered by different humanistic and scientific disciplines, the PROTECT project aims to define an operational protocol for the archaeoseismological reading of the historic centre of Siena (or part of it). This protocol could be exported to other Italian/European towns, with a view to improve our understanding of their historic heritage and the best ways to protect it from seismic risk.

The PROTECT project started in December 2021 with a first step aimed at a general analysis of the historic city centre with reference to a specific earthquake. After an initial look at the seismic history of Siena, the choice fell on the August-September 1467 seismic sequence (Fig. 1).

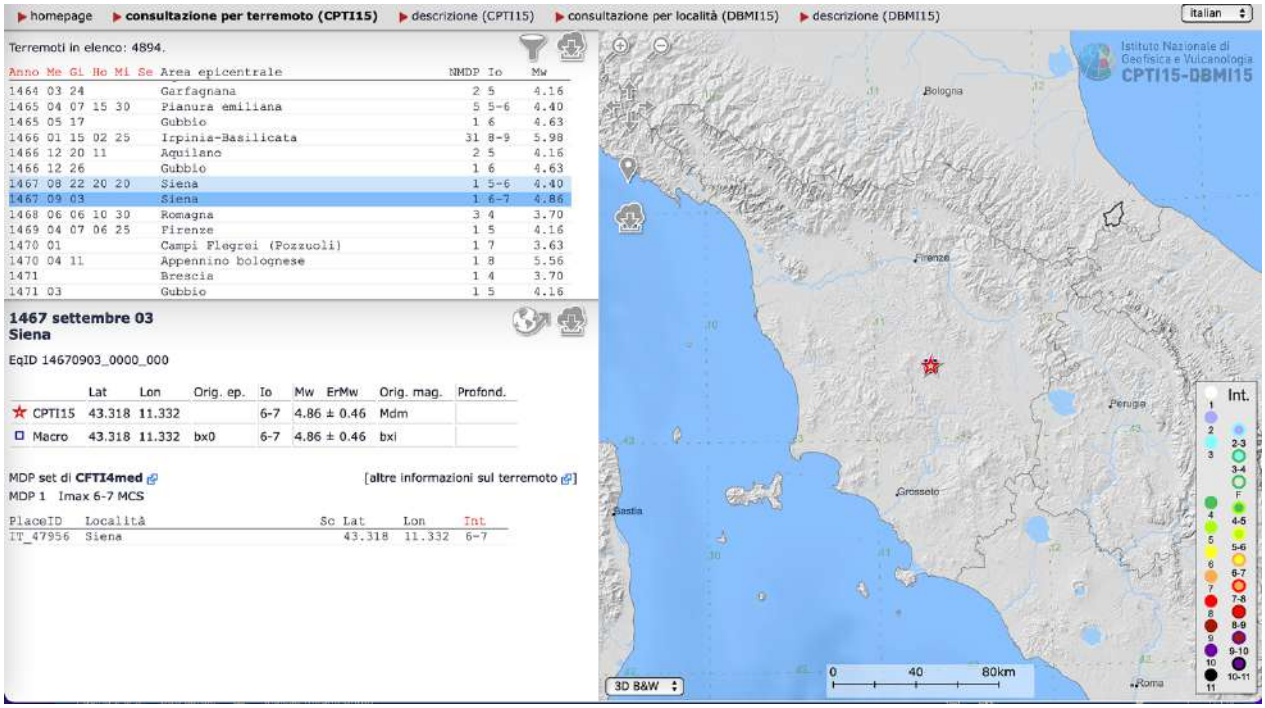

Fig. 1 – The 1467 Siena seismic sequence according to CPTI15 v. 4.0 (Rovida et al., 2022).

What led to the choice of this comparatively “minor” earthquake (Mw 4.8 according to Rovida et al., 2022) was dictated by the awareness that the Archivio di Stato of Siena preserved a a so far unexploited source of exceptional documentary value, the “Lira” of the year 1468. This is a huge collection of tax statements compiled less than a year after the earthquake, by all Sienese citizens and including details on the state of repair of their property. A careful sifting of this “Lira” allows to extract a “snapshot” of the state of conservation of Sienese buildings in 1468. The thematic cartography derived from the collected data was transferred into a GIS environment and the data obtained from this analysis have been used as the basis for undertaking some specific archaeological expeditious analyses of architectural complexes in the historic centre of Siena in order to verify whether the historical source data were legible in the stratigraphy of the buildings.

This paper presents the preliminary results of the analysis carried out within the PROTECT project on the 1467 Siena earthquake. The picture of the seismic sequence – as handed down by the Italian “seismological tradition” and reconstructed by two separate teams of historical seismologists (Castelli et al., 1996; Guidoboni et al., 2007) on the basis of a set of mainly narrative, contemporary or nearly contemporary sources - is challenged by the output of the consultation of the “Lira” of 1468. Was the 1467 earthquake a stronger and more damaging event than contemporary witnesses made it out to have been? Or, perhaps, did its moderate shaking interact with buildings whose vulnerability was already enhanced by some other factor? As it often happens in historical investigation, looking at a “well-known” situation from an unusual point of view makes way for new interpretative perspectives.

Acknowledgments

The project *PROTECT - Knowledge for PReventiOn. Technique for reparing seismic damage from medieval period To modern era* is being funded within the EU program “Horizon 2020 research and innovation” dell’Unione Europea by a Marie Skłodowska-Curie Individual Fellowship (grant agreement No. 101018762) at the Ecole Normale Superiéure of Paris, under the scientific responsibility of Andrea Arrighetti.

References

Castelli V., Monachesi G., Moroni A., Stucchi M. (1996). Revisione dei principali terremoti d'interesse per il territorio toscano, vol. 1: Dall’anno 1000 al 1731, GNDT/CNR, Rapporto interno, Macerata-Milano, https://emidius.mi.ingv.it/ASMI/study/CASAL996

Guidoboni E., Ferrari G., Mariotti D., Comastri A., Tarabusi G., Valensise G. (2007) CFTI4Med, Catalogue of Strong Earthquakes in Italy (461 B.C.-1997) and Mediterranean Area (760 B.C.-1500), INGV-SGA, http://storing.ingv.it/cfti4med/

Rovida A., Locati M., Camassi R., Lolli B., Gasperini P., Antonucci A. (2022). Catalogo Parametrico dei Terremoti Italiani (CPTI15), versione 4.0, Istituto Nazionale di Geofisica e Vulcanologia (INGV), https://doi.org/10.13127/CPTI/CPTI15.4.

Corresponding author: viviana.castelli@ingv.it

A reappraisal of the March 1952 Linera seismic sequence: the case study of the S. Tecla fault (Mt. Etna)

R. Azzaro[1], M.S. Barbano[1,2,3], D. Musumeci[4], G. Orefice[2]

[1] *Istituto Nazionale di Geofisica e Vulcanologia, Osservatorio Etneo, Catania, Italy*
[2] *Dipartimento di Scienze Biologiche, Geologiche e Ambientali, Università di Catania, Italy*
[3] *CRUST - Interuniversity Center for 3D Seismotectonics with Territorial Applications, Chieti, Italy*
[4] *Dipartimento di Scienze Umanistiche, Università di Catania, Italy*

Introduction

The Mt. Etna region is characterised by a very frequent seismic activity, in several cases even destructive, occurring often in form of seismic sequences during both eruptive periods and volcanic quiescence too (Bevilacqua et al., 2022). This volcano-tectonic seismicity has a significant impact particularly in the eastern flank of the volcano where earthquakes, typically featuring very shallow focal depths (h < 3 km) and magnitude rarely exceeding M_L 5, are related to the intense tectonic activity of the Timpe fault system (Azzaro et al., 2017). The short recurrence times for damaging earthquakes, capable of producing macroseismic effects up to degree IX in the European macroseismic scale (hereinafter EMS, see Grünthal, 1998), gives rise to a very high level of seismic hazard in these densely urbanised area of the volcano (Azzaro et al., 2016).

Long-term seismicity at Etna is very well known by the local macroseismic catalogue (hereinafter CMTE, see Azzaro and D'Amico, 2014) which parametrises, starting from a general revision of the historical sources documenting past earthquakes (Azzaro et al., 2000), also fore- and after-shocks and provides indication on the causative faults. This makes it possible to reconstruct the seismic history of each seismogenic structure (Azzaro et al, 2013). In this framework, the S. Tecla fault shows a high seismic potential (Fig. 1a), with a number of strong and minor events rupturing different segments of the structure (Azzaro et al, 2017). The strongest known earthquake is the 1914 event, which entirely ruptured along strike destroying the locality of Linera and surroundings; the maximum intensity was assessed to reach degree IX-X EMS and the equivalent magnitude estimated as M_L 5.2.

An event with similar features is the 19 March 1952 earthquake (Fig. 1b), that almost destroyed again Linera along the central sector of the S. Tecla fault and was preceded by a seismic sequence affecting the northern segment of the fault, south to the town of Zafferana Etnea. The mainshock is reported in the CMTE catalogue according to the intensity dataset by Patanè and Imposa (1995), the only one available, and was not revised in the phase of the catalogue compilation since this study was recent. The maximum intensity was assessed as VII-VIII EMS, corresponding to an equivalent magnitude of M_L 4.0.

In recent years we acquired some sparse information suggesting that this event may be underestimated in the study by Patanè and Imposa (1995). These authors reconstructed the macroseismic field relying on oral testimonies collected more than 30 years after the event, and by very few other sources (two editions of the local newspaper *La Sicilia* of 3 and 20 March 1952, and a technical report). For this reason, we decided to revise it starting from zero with a new historical investigation.

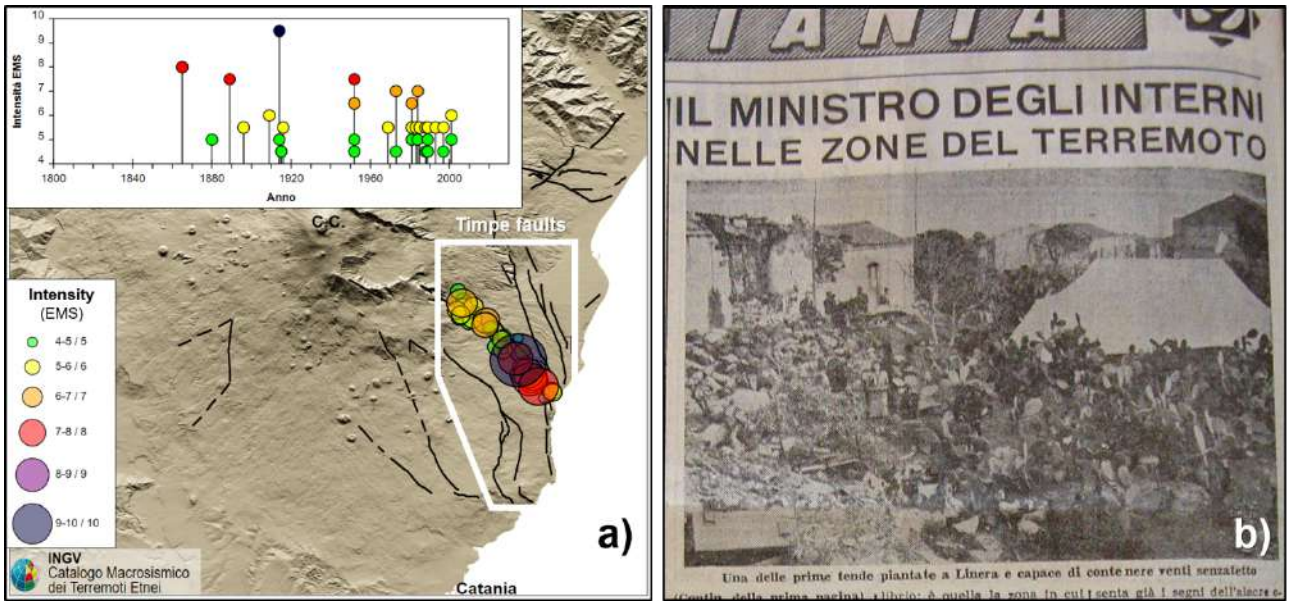

Fig. 1 – a) Main historical earthquakes associated with the S. Tecla fault and related seismic history (from https://doi.org/10.13127/cmte); b) front page of the local newspaper *Corriere di Sicilia* (24-3-1952), reporting the first tent camp set in Linera and the visit of the Minister of the Interior.

The historical sources

In order to revise the 1952 seismic sequence, we followed a strategy tested during the revision of other historical events, particularly the complex sequence of 1968 in western Sicily (see methodological approach in Azzaro et al., 2020). In brief, we performed a search of the contemporaneous sources and classified information as we were simulating, *a-posteriori*, a macroseismic survey carried out day-by-day. In this way we were able to follow in detail the evolution of the sequence and the progression of damage effects on the territory. To this end, we searched the potential sources in different repositories such as local or government archives, municipal libraries, ecclesial archives etc.

As a result, we collected a wide spectrum of sources (Fig. 2): coeval scientific papers, macroseismic questionnaires (seismic postcards or *Cartoline macrosismiche*), archive documents, local diaries and newspapers. As regards the latter, local press is a valuable source of information since news on earthquakes' effects and rescue operations are published daily. In addition, as for other earthquakes of "modern epoch", photographs and two *Istituto Luce* videos were also retrieved.

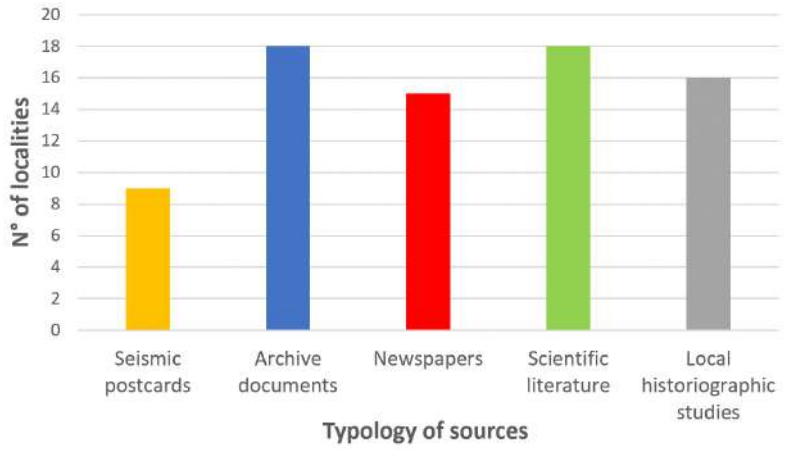

Fig. 2 – Coeval sources reporting information and data on the 1952 seismic sequence along the S. Tecla fault. The number of localities cited in the documents is also indicated.

Analysis and preliminary results

Among the retrieved documents, we found of great interest some tables saved in the State Archive of Catania, compiled by the technicians of the Civil Engineers following the mainshock of 19 March. These tables provide the precise situation of the cumulative damage produced by the seismic sequence in the affected municipalities (Acireale, S. Venerina and Zafferana), classified by ISTAT census sections; the associated number of buildings per sections is also indicated. In particular, the percentages of damaged edifices are divided into three categories: totally unusable, partially unusable, usable even if damaged. This “operative” level of damage was then associated with the grades of damage (D) expected in the EMS, as follows: totally unusable D4-5, partially unusable D3, usable D1-2.

In order to define the vulnerability classes of buildings prevailing in the damage area, we used photos and videos collected in the historical investigation, together with the descriptions on the state of buildings provided in some technical reports. Since we worked at the scale of census sections, the percentage of the different typologies of buildings in the 1950 was estimated according to Pessina et al. (2021) (Tab. 1). In this way, from the analysis of quantity and grade of damage for the different building vulnerability classes in each locality, it has been possible to assess the EMS intensity.

Tab. 1 – Statistical distribution of the EMS vulnerability classes vs buildings’ age (from Pessina et al., 2021).

Age	Vulnerability class [%]		
	A	*B*	*C1*
<1919	74	23	3
’19–‘45	52	40	8
’46–‘60	25	47	28
’61–‘71	4	31	65
’72–‘91	2	19	79

The study allowed to reconstruct in detail the March 1952 seismic sequence and to obtain the intensity data points (IDPs) for the mainshock as well as for two strong foreshocks. The first event occurred on 1 March (12.35 GTM) and had epicenter near Zafferana, where produced diffuse but minor damage (I_0 = VI-VII EMS); it was followed the day after (14.14 GTM) by a stronger shock increasing damage in the same area (I_0 = VII EMS). In the following days there were several other minor shocks of low intensity, locally felt by people; the seismic sequence culminates with the mainshock on 19 March (08.13 GMT, I_0 = VIII-IX EMS), which produced very heavy damage in Linera and other localities nearby, causing two victims and around sixty injured. Aftershocks (not damaging) followed for some days.

Fig. 3 shows the IDPs determined for the mainshock of 19 March: Linera suffered the partial destruction (I = VIII-IX EMS) whereas Bongiardo and Rocca d'Api (I = VIII) had a number of partial/ total collapses especially for the most vulnerable buildings. As usual for the shallow volcano-tectonic earthquakes at Etna (Azzaro et al., 2006), the intensity attenuation is very strong so damage effects disappear quickly at a few kilometers of distance from the causative fault (in Catania the event was only felt). Impressive coseismic faulting phenomena accompanied this earthquake as well as the two strong foreshocks of 1 and 2 March.

This macroseismic field is basically different compared to the one by Patanè and Imposa (1995), both in terms of maximum intensity – I_{max} = VIII-IX vs VII-VIII EMS, respectively – and for the number of IDPs.

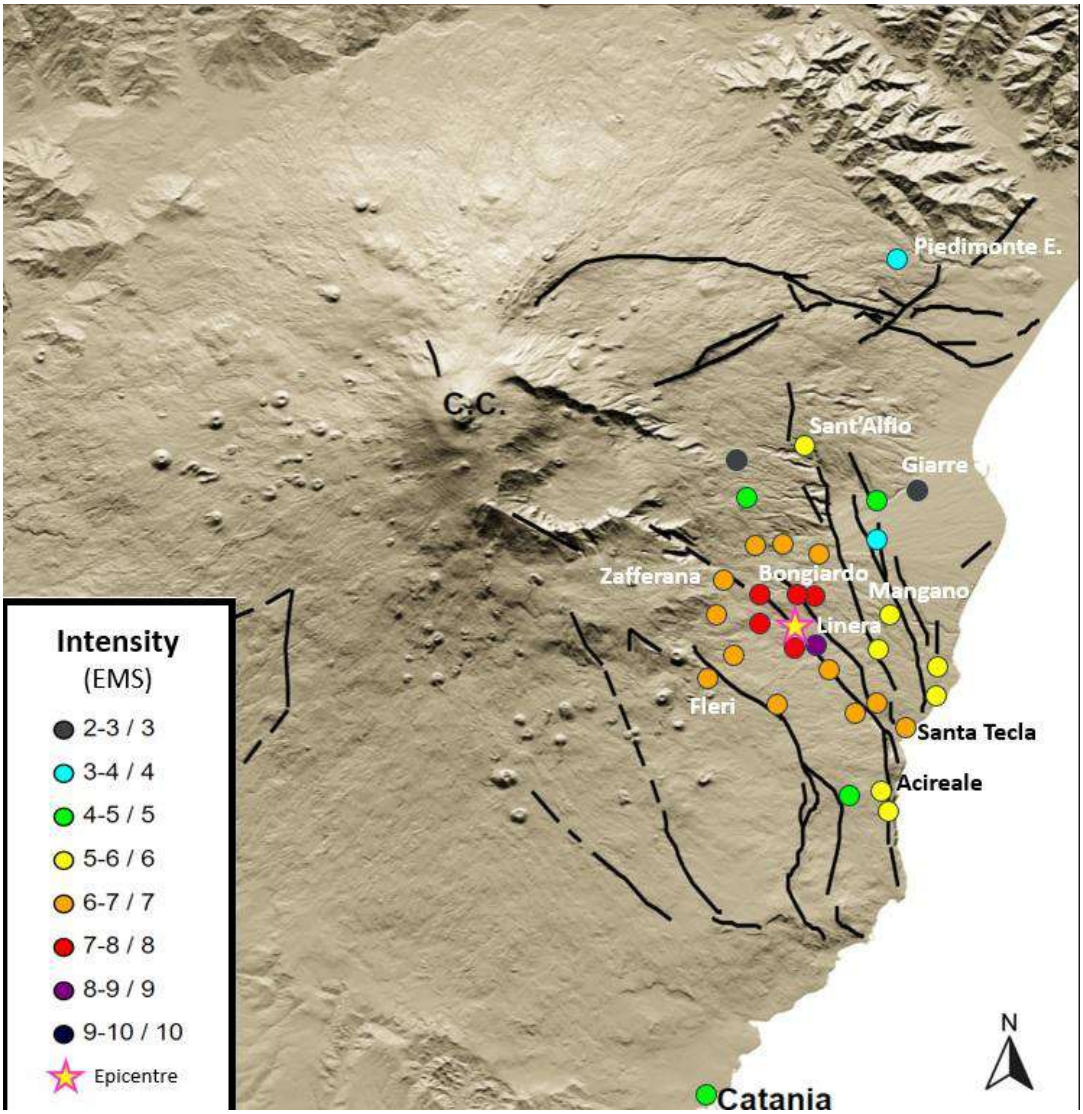

Fig. 3 – Intensity map of the 19 March 1952 earthquake (08.13 GMT) obtained by this study.

In conclusion, the March 1952 seismic sequence ruptured the entire S. Tecla fault, first the northern segment with the foreshocks' activity and then the central-southern part with the mainshock. This determined, from a macroseismic point of view, a cumulative picture of damage not solvable by the analysis of the historical sources. However, the revision produced in this study confirmed that the mainshock was previously underestimated as for the maximum intensity, this determining changes on the earthquake parameters to be reported in the CMTE catalogue: now the epicentral intensity I_0 increases up to VIII-IX EMS, and the corresponding equivalent magnitude up to M_L 4.6. Results also have implications in terms of local hazard assessment, allow a more precise reconstruction of the seismic history of this fault and therefore a more reliable evaluation of its seismic potential.

References

Azzaro R., M.S. Barbano, B. Antichi and R. Rigano; 2000: *Catalogo Macrosismico dei Terremoti Etnei dal 1832 al 1998*. Acta Vulcanologica, 12 (1-2), 3-36 (with CD-ROM).

Azzaro R., Barbano M.S., D'Amico S. and Tuvè T.; 2006: *The attenuation of seismic intensity in the Etna region and comparison with other Italian volcanic districts*. Annals of Geophysics, 49 (4/5), 1003-1020.

Azzaro R., D'Amico S., Peruzza L. and Tuvè, T.; 2013: *Probabilistic seismic hazard at Mt. Etna (Italy): the contribution of local fault activity in mid-term assessment*. Journal of Volcanology and Geothermal Research, 251, 158-169.

Azzaro R. and D'Amico S.; 2014: *Catalogo Macrosismico dei Terremoti Etnei (CMTE), 1633-2023*. Istituto Nazionale di Geofisica e Vulcanologia (INGV), https://doi.org/10.13127/cmte

Azzaro R., D'Amico S. and Tuvè T.; 2016: *Seismic hazard assessment in the volcanic region of Mt. Etna (Italy): a probabilistic approach based on macroseismic data applied to volcano-tectonic seismicity*. Bulletin of Earthquake Engineering, 17 (7), 1813-1825.

Azzaro R., Barberi G., D'Amico S., Pace B., Peruzza L. and Tuvè T.; 2017: *When probabilistic seismic hazard climbs volcanoes: the Mt Etna case, Italy. Part I: model components for sources parametrization*. Natural Hazards Earth System Science, 17, 1981-2017.

Azzaro R., Barbano M.S., Tertulliani A. and Pirrotta C.; 2020: *A reappraisal of the 1968 Valle del Belìce seismic sequence (Western Sicily): a case study of intensity assessment with cumulated damage effects*. Annals of Geophysics, 63 (1), SE105, 1 Appendix, Doi: https://doi.org/10.4401/ag-8308.

Bevilacqua A., Azzaro R., Branca S., D'Amico S., Flandoli F. and Neri A.; 2022: *Quantifying the statistical relationships between flank eruptions and major earthquakes at Mt. Etna volcano (Italy)*. Journal Geophysical Research: Solid Earth, 127, e2022JB024145, https://doi.org/10.1029/2022JB024145.

Grünthal G.; 1998: *European Macroseismic Scale 1998 (EMS-98)*. In: Cahiers du Centre Européen de Géodynamique et de Séismologie. European Seismological Commission, Subcommission on Engineering Seismology, Working Group Macroseismic Scale, 15 (Luxembourg, Conseil de l'Europe).

Patanè G. and Imposa S.; 1995: *Atlante delle isosiste dei terremoti etnei dal 1971 al 1991*. Pubbl. GNGTS-Ist. Geologia e Geofisica Università di Catania, 81 pp.

Pessina V., Meroni F., Azzaro R. and D'Amico S.; 2021: *Applying simulated seismic damage scenarios in the volcanic region of Mount Etna (Sicily): a case-study from the M_W 4.9, 2018 Earthquake*. Front. Earth Sci., Sec. Solid Earth Geophysics 9, https://doi.org/10.3389/feart.2021.629184

Corresponding author: raffaele.azzaro@ingv.it

Three-dimensional magnetotelluric inversion applied in a sector of the Irpinia Fault System (Southern Apennine)

M. Balasco[1], M. De Girolamo[2], D. Di Gennaro[3], G. Romano[3], A. Siniscalchi[3]

[1] Istituto di Metodologie per l'Analisi Ambientale, CNR – Tito Scalo, PZ
[2] Istituto di Geofisica e Vulcanologia INGV, Roma
[3] Università degli Studi di Bari

The magnetotelluric (MT) method is a powerful tool to investigate seismotectonic regions thanks to its capability to image volumetric electrical conductivity variations related to presence of interconnected fluids and partial melt (Bedrosian et al. 2014), especially if correlated with other geophysical observations (Balasco et al. 2022).

In this presentation we show a preliminary 3-D electrical resistivity model obtained sector of the Irpinia Fault System (80x60km) acquiring n. 30 broad band magnetotelluric (MT) soundings at approximately intervals of 5 km, using the inversion code ModEM3DMT (Kelbert et al. 2014).

The study area includes epicentral zones of the two greatest seismic events occurred in the last 100 years in the Southern Italy, 1930 and 1980 earthquakes. Mefite d'Ansanto, the largest source of natural CO2 gas emission measured on the Earth in a non-volcanic environment, also falls in the investigated area (Chiodini et al. 2010).

Many testing were performed building different starting models varying the dimension of horizontal and vertical grid cells, model covariance, and initial damping factors to get the best resultant model for our data. The sea-effect was also taken into account because the coastline is very near to the investigated area.

3-D inversion approach has become fundamental for MT data interpretation with respect to the 2-D inversion that frequently cannot explain important features from geologically complex regions.

Unfortunately, the routine of 3-D codes require high-end workstation or parallel machines, and long computational time. Even if our preliminary MT model of the Irpinia sector is still coarse, the results are promising also take into account a good agreement with other geophysical observations. In particular, the geostructural interpretation of the 3D MT model will also benefit from the seismic data of the ISNET, INGV network and DETECT experiment (DEnse mulTi-paramEtriC observations and 4D high resoluTion imaging, Picozzi et al. 2022).

References

Balasco, M., Cavalcante, F., Romano, G., Serlenga, V., Siniscalchi, A., Stabile, T. A., Lapenna, V. (2021). New insights into the High Agri Valley deep structure revealed by magnetotelluric imaging and seismic tomography (Southern Apennine, Italy), Tectonophysics, 808, Art. n. 228817. doi: 10.1016/j.tecto.2021.228817.

Bedrosian P.A., Feucht D.W. (2014) Structure and tectonics of the northwestern United States from Earthscope USArray magnetotelluric data. Earth Planet Sci Lett 402:275–289.

Chiodini G, Granieri D, Avino R, Caliro S, Costa A, Minopoli C, Vilardo G (2010) Nonvolcanic CO2 Earth degassing: case of Mefite d'Ansanto (southern Apennines), Italy. Geophys Res Lett 37:L11303.

Kelbert A, Meqbel N, Egbert G, Tandon K (2014) ModEM: a modular system for inversion of electromagnetic geophysical data. Computat Geosci 66:40–53.

Picozzi, M., Iaccarino, A. G., Bindi, D., Cotton, F., Festa, G., Strollo, A., Zollo, A., Stabile, T. A., Adinolfi, G. M., Martino, C., Amoroso, O., De Matteis, R., Convertito, V., Spallarossa, D., DESERT, T. (2022): The DEnse mulTi-paramEtriC observations and 4D high resoluTion imaging (DETECT) experiment, a new paradigm for near-fault observations - Abstracts, EGU General Assembly 2022 (Vienna, Austria, Online 2022).

Corresponding author: marianna.balasco@cnr.it

The harsh life of an earthquake in the region that doesn't exist

S. Baranello[1,2], R. Camassi[1], V. Castelli[1]

1 Istituto Nazionale di Geofisica e Vulcanologia, Bologna, Italy
2 Università degli studi di Bologna – Dipartimento di Fisica e Astronomia

The historical research on earthquakes often clashes with harsh reality: if the earthquake is not destructive, if it occurs during a particularly complex historical period, dominated by wars, epidemics, and other misfortunes, there is the possibility of its memory being lost. Sometimes, in addition to the scant production of testimonies about the earthquake and its impact, possible problems arise in the preservation of such testimonies. And finally, the obstacle course of the historical seismologist can find many doors closed today. Literally.
And this happens especially in the region that doesn't exist...
When any of these circumstances (or all of them) occur, research must necessarily pursue not only written testimonies but also simple clues, indirect evidence of the earthquake's occurrence, such as local traditions, the presence of a local earthquake-related cult, etc.
Baratta (1901) devotes only a few very generic lines to the Molise earthquake of May 1712. First of all, he says that an earthquake was felt in early May in Naples, and that it caused panic among the Neapolitans. To this news, Baratta adds that an earthquake was also felt in Campobasso where "some houses and churches were ruined." Finally, he mentions several shocks that were felt in Benevento between May and June 15.
Baratta's sources are respectively a summary of the *Bologna* Gazette published by De Rossi (1889) and a brief mention of Campobasso by Sarnelli (1716).
In the Postpischl (1985) catalogue, these pieces of information are summarized into an event dated generically to May 1712, located in Bojano, with an epicentral intensity of VIII MCS (Tab. 1).

	Year	Mo	Da	Ho	Mi	Lat	Lon	Int	Ref	Epic. Zone
POS85	1712	5		-	-	41 30	14 30	VIII	75	BOIANO
CPTI15	1712	05	08	-	-	41.561	14.660	6-7	AMGNDT995	Campobasso

Tab. 1 – The earthquake of May 1712 in the catalogues by Postpischl (1985) and Rovida et al. (2022)

In the early 1990s, in the frame of the “Hazard Project” - that led to the compilation of various versions of the parametric catalogue, along with the in-depth study of many hundreds of medium-high-energy earthquakes - approximately 250 earthquakes were swiftly reviewed through a simple

verification of seismological compilations. These revisions were then synthesized a few years ago in the data sheets called AMGNDT995 [Macroseismic Archive GNDT, 1995].
The AMGNDT995 data sheet dedicated to the 1712 earthquake considers various information not clearly attributable to a single event and downgrades the earthquake, dated May 8th, locating it in Campobasso with an epicentral intensity uncertain between VI and VII MCS. The study suggests that the assertion that houses and churches were 'ruined' refers to a level of moderate, non-structural damage. This interpretation has been incorporated into the CPTI catalogue in its various versions.
Recently, in the frame of a research project aimed at improving the preliminary AMGNDT995 studies, the case of the 1712 earthquake has been reopened, following the report of the presence of the cult of San Michele in Ripalimosani, connected to the averted danger during an earthquake dated May 1712 [Mascia, 2000].
Along with this reference, attributed to an oral tradition, similar references have been identified respectively in Lucito and Monteodorisio. To verify this information and deepen the research, two avenues were pursued: the first, at the local level, aimed at verifying local historiography and archival evidence. Unfortunately, the research on this front has not progressed as it was hoped. The consultation of materials stored at the State Archive of Campobasso was unsuccessful. It was impossible to examine the documents preserved at the Provincial Library "P. Albino", that has been closed to the public for several years due to technical and structural problems (it is still unclear if and when it will be reopened). The Diocesan Historical Library "V. Fusco" was also consulted, with negative results. Luckily enough, however, additional journalistic sources ([Gazzetta di] Bologna, 1712.05.24; 1712.06.14; [Avvisi di] Napoli, 1712.05.14; 1712.05.17; Il Corriere Ordinario, 1712.06.08) were found, which significantly enriched the information framework (Tab. 2).
Overall, this is certainly a very interesting and complex situation regarding a certainly important earthquake that affected a very large area of central Italy (Fig. 1).

Year	Mo	Da	Ho	Mi	Localities	Lat	Lon	Is
1712	05	08	04	30	Campobasso	41.561	14.660	7
1712	05	08	04	30	Avellino	40.914	14.793	6
1712	05	08	04	30	Benevento	41.131	14.778	6
1712	05	08	04	30	Piedimonte Matese	41.354	14.371	6
1712	05	08	04	30	Alife	41.328	14.331	6
1712	05	08	04	30	Napoli	40.849	14.25	4-5
1712	05	08	04	30	Piedimonte San Germano	41.496	13.749	3
1712	05	08	04	30	Chieti	42.352	14.168	HF
1712	05	08	04	30	Lucito	41.731	14.688	HF?
1712	05	08	04	30	Monteodorisio	42.086	14.652	HF?
1712	05	08	04	30	Ripalimosani	41.613	14.666	HF?

Tab. 2 – Intensity observed for the earthquake of 8 May 1712

This case, certainly not unique, is exemplary of a very broad research space that would require a long-term work plan today. The current Italian parametric catalogue, despite being among the most advanced in the world, contains many hundreds of earthquakes with extremely poor basic data, which should be completely reassessed. At the same time, data losses, informational gaps, and misunderstandings are always possible and would deserve work from a long-term perspective, a condition that today appears entirely illusory.

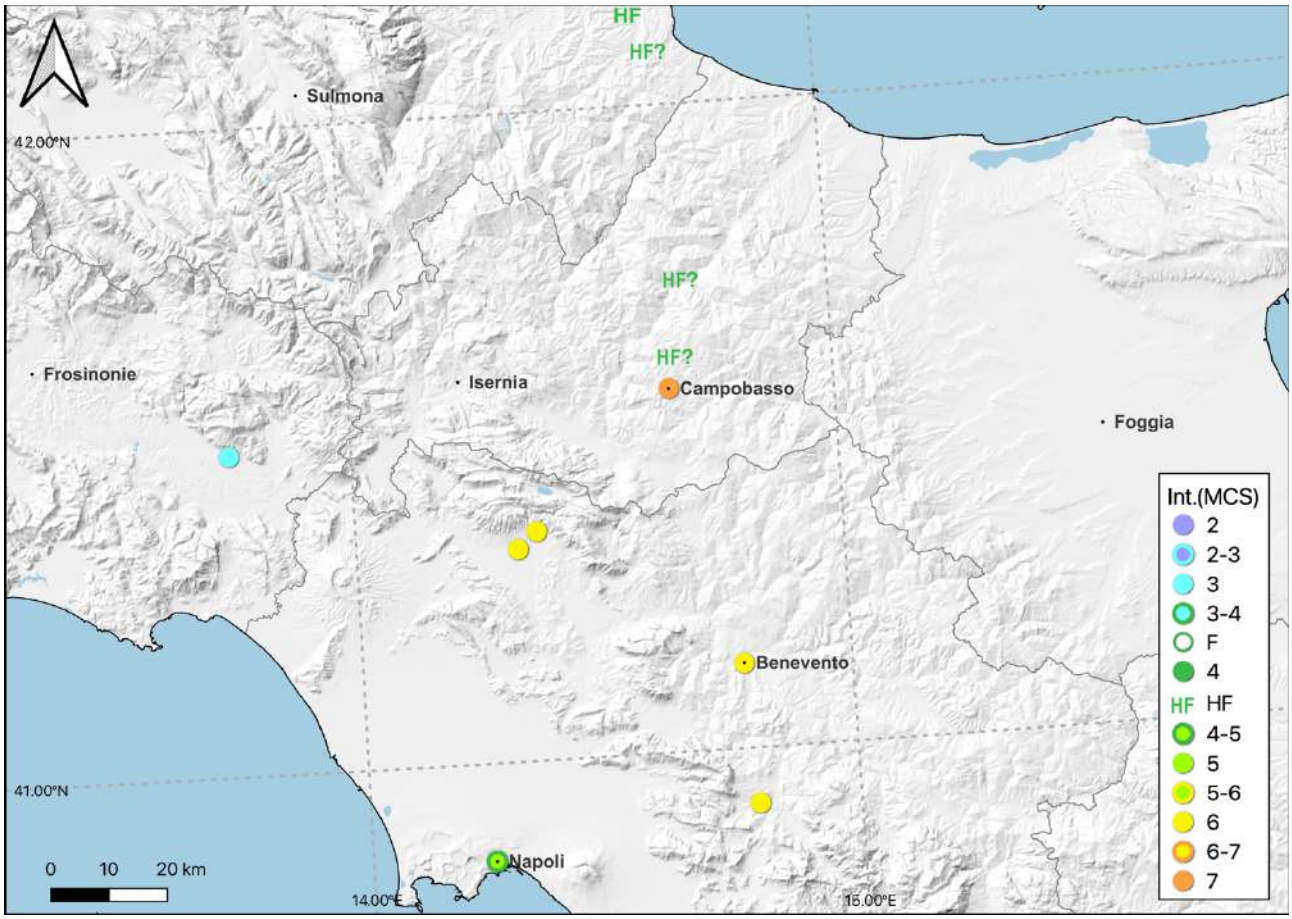

Fig. 1 – Distribution map of the distribution of the effects of the earthquake of 8 May 1712

References

[Gazzetta di] Bologna, 1712.05.24; 1712.06.14.

[Avvisi di] Napoli, 1712.05.14; 1712.05.17.

Il Corriere Ordinario, 1712.06.08.

De Rossi, M.S.; (Ed.) (1889): Documenti raccolti dal defunto conte Antonio Malvasia per la storia dei terremoti ed eruzioni vulcaniche massime d'Italia. Memorie della Pontificia Accademia dei Nuovi Lincei, 5, 169-289.

Mascia G.; (2000): Aspetti del culto popolare di San Michele Arcangelo nel Molise. In: Gioielli M., Madonne, Santi e Pastori. Culti e feste lungo i tratturi del Molise, Palladino Editore, Campobasso,

Postpischl D.; (1985): Catalogo dei terremoti italiani dall'anno 1000 al 1980. Progetto Finalizzato Geodinamica. Quaderni de La Ricerca Scientifica, n. 114, vol.2B

Rovida A., Locati M., Camassi R., Lolli B., Gasperini P., Antonucci A.; (2022): Catalogo Parametrico dei Terremoti Italiani (CPTI15), versione 4.0. Istituto Nazionale di Geofisica e Vulcanologia (INGV). https://doi.org/10.13127/CPTI/CPTI15.4

Sarnelli P.; (1716): Lettere Ecclesiastiche, VII, Appresso Antonio Bortoli, Venezia.

Corresponding author: sofia.baranello@ingv.it

New insights into the seismogenic potential of a low-strain rate region: active faulting in the Siena basin (Cava Capanni quarry, Tuscany)

Andrea Brogi[1,2], Paola Vannoli[3], Martina Zucchi[1], Pierfrancesco Burrato[3], Umberto Fracassi[3], Gianluca Valensise[3], Hsun-Ming Hu[4,5], Chuan-Chou Shen[4,5]

[1] Department of Earth and Geoenvironmental Sciences (University of Bari, Italy)
[2] CNR-IGG, Institute for Geosciences and Georesources (C.N.R., Italy)
[3] Istituto Nazionale di Geofisica e Vulcanologia (Italy)
[4] High-Precision Mass Spectrometry and Environment Change Laboratory (HISPEC), Department of Geosciences, (National Taiwan University, Taiwan, ROC)
[5] Research Center for Future Earth (National Taiwan University, Taiwan, ROC)

We investigate the active tectonics and earthquake potential of a system of active faults located along the eastern Siena Basin, a slowly deforming portion of southern Tuscany falling within the inner Northern Apennines. This region, although classified as a low hazard area (Stucchi et al., 2011; Meletti et al., 2021), has been frequently hit by low magnitude seismic sequences occurring in the uppermost 10 km of the crust, and often concentrated in clusters that appear unrelated to major known seismogenic zones, but also, by rare damaging earthquakes in the Mw range 5.0-6.0. The historical earthquake record includes events such as the 7 August 1414, Mw 5.7, Colline Metallifere; the 13 April 1558, Mw 6.0, Valdarno superiore and the 25 August 1909, Mw 5.3, Crete Senesi, earthquakes (Rovida et al., 2022). As of today, very little is known concerning the geometry of their causative faults, the maximum earthquake potential of such faults and their kinematic characteristics.

The Siena Basin is a Neogene structural depression that developed during the extensional evolution of the inner Northern Apennines along NNW- to NW-striking Plio-Quaternary normal faults, and is filled by an up to 600 m thick sequence of marine terrigenous and continental deposits (e.g. Martini et al., 2021).

Different N-, NE- and WNW-striking fault systems active in Zanclean-latest Quaternary times were described in the eastern Siena Basin (Brogi, 2004; Bambini et al., 2010; Ghinassi et al., 2021). The N-striking faults are Pliocene in age and are associated with the latest evolution of the Siena Basin (Brogi, 2011), whereas the youngest, WNW- and NE-striking faults are Neogene-latest Quaternary in age and appear to control the location of thermal springs and the resulting pattern of travertine deposition. The WNW-striking faults are the youngest structures and still control the ascent of thermal water, gas emissions, and travertine deposition in some areas (e.g., Minissale et al., 2002; Minissale, 2004; Brogi and Capezzuoli, 2009; Bambini et al., 2010). These deposits are especially

useful in active tectonics studies due to (a) the close genetic relationships between active faulting and travertine deposition, (b) the optimal recording and preservation of any brittle deformation events, (c) the quick and permanent sealing of such episodes due to the circulation of pressurized fluids (e.g., Hancock et al., 1999).

We describe in detail and for the first time an active, capable and seismogenic fault system that we identified in the saw-cut walls of Cava Capanni, an active travertine quarry near Serre di Rapolano, few km south-east of the city of Siena. As a matter of fact, the Late Pleistocene-Holocene travertine deposits of the eastern Siena Basin preserved the record of several past earthquakes, in the form of earthquake-induced soft-sediment deformation structures and co-seismic injection of overpressured hydrothermal fluids, in different quarries and archeological sites (e.g. the Campo Muri site near the Serre di Rapolano fissure ridge; Brogi et al., 2017).

To document the geometrical and kinematic characteristics of the active faults, we conducted a detailed geological and structural field survey of the quarry outcrop, collected samples for U-Th dating, and made a virtual outcrop model (VOM) of Cava Capanni using a set of photos taken using an airborne drone.

The active fault system we mapped consists of at least three main WNW-ESE-striking fault segments, rupturing up to the ground surface a sequence of travertine younger than 45 ka. The system has a total vertical displacement of 111 cm, and can be followed in the quarry over a distance of 200+ m. However, its total mapped length is ~700 m, as it continues eastwards for at least 500 m, cutting the Jurassic Tuscan succession and the overlying Zanclean deposits, before disappearing due to the heavy vegetation cover. To the west of the quarry, the fault zone disappears below the Holocene colluvial deposits of the Siena Basin. In addition to the main splays, the fault system exhibits many fractures, collectively defining a several tens of meters-wide damage zone. The fractures are near-parallel to parallel to the main fault segments and locally exhibit anastomosed traces associated with linkage zones (releasing step-overs) and relay ramps, testifying for the transtensive kinematics of the system.

The walls of the faults are covered by cm-thick, well-cemented carbonate siltstone, which often also fills the fractures of the damage zone. Such material derives from sediment liquefaction at the base of the travertine succession, as suggested by the occurrence of fossil remains, forming three generations of clastic dykes that were presumably injected in the fault zone during earthquake-induced shaking. Following this observation, we suggest that the measured displacement is the result of at least three earthquakes.

The Cava Capanni fault system is evidence of a poorly understood but regionally-extensive and potentially seismogenic tectonic mechanism. Based on total displacement and using standard empirical relationships, we estimate that it may generate earthquakes in the Mw range 6.0-6.3 recurring every ~10^4 years. Its orientation and kinematics are compatible with the activity of faults orthogonal to the main chain axis (“anti-Apennines striking”), in contrast with the current tectonic regime of the axial and outer zone of the Northern Apennines, where extension and compression are accommodated by Apennines-parallel faults.

References

Slejko D., Caporali A., Stirling M. and Barba S.; 2010: Occurrence probability of moderate to large earthquakes in Italy based on new geophysical methods. J. Seismol., 14, 27-51, DOI 10.1007/s10950-009-9175-x.

Bambini A.M., Brogi A., Cornamusini G., Costantini A., Foresi L.M. and Lazzarotto A.; 2010: Geologia dell'area di Rapolano Terme in Provincia di Siena (Appennino Settentrionale). Italian Journal of Geosciences 129, 457–95.

Brogi A.; 2004: Miocene low-angle detachments and upper crust megaboudinage in the Mt. Amiata geothermal area (Northern Apennines, Italy). Geodin. Acta 17, 375–387.

Brogi A.; 2011: Bowl-shaped basin related to low-angle detachment during continental extension: the case of the controversial Neogene Siena Basin (central Italy, Northern Apennines). Tectonophysics, 499, 54–76.

Brogi A. and Capezzuoli E.; 2009: Travertine deposition and faulting: The fault-related travertine fissure-ridge at Terme S. Giovanni, Rapolano Terme (Italy). International Journal of Earth Sciences 98 (4), 931–947, DOI 10.1007/s00531-007-0290-z.

Brogi A., Capezzuoli E., Kele S., Baykara M.O. and Shen C-C.; 2017: Key travertine tectofacies for neotectonics and palaeoseismicity reconstruction: Effects of hydrothermal overpressured fluid injection. Journal of the Geological Society 174 (4), 679–699, DOI 10.1144/jgs2016-124.

Ghinassi M., Aldinucci M., Bianchi V., Brogi A., Capezzuoli E., Yu T.-L. and Shen C.-C.; 2021: Lifecycle of an Intermontane Plio-Pleistocene Fluvial Valley of the Northern Apennines: From Marine-Driven Incision to Tectonic Segmentation and Infill. Geosciences, 11, 141, DOI 10.3390/geosciences11030141.

Hancock P. L., Chalmers R.M.L., Altunel E. and Çakir Z.; 1999: Travitonics: using travertines in active fault studies. J. Structural Geology, 21, 903-916.

Martini I., Ambrosetti E., Brogi A., Aldinuicci M., Zwaan F. and Sandrelli F.; 2021: Polyphase extensional basins: interplay between tectonics and sedimentation in the Neogene Siena-Radicofani Basin (Northern Apennines, Italy). International Journal of Earth Sciences, 110, 1,729–1,751, DOI 10.1007/s00531-021-02038-4.

Meletti C., Marzocchi W., D'Amico V., Lanzano G., Luzi L., Martinelli F., Pace B., Rovida A., Taroni M., Visini F. and the MPS19 Working Group; 2021: The new Italian Seismic Hazard Model (MPS19). Annals of Geophysics 64, 1, DOI 10.4401/ag-8579.

Minissale A.; 2004: Origin, transport, and discharge of CO2 in central Italy. Earth-Science Rev., 66, 89-141, DOI 10.1016/j.earscirev.2003.09.001.

Minissale A., Vaselli O., Tassi F., Magro G. and Grechi G.P.; 2002: Fluid mixing in carbonate aquifers near Rapolano (central Italy): chemical and isotopic constraints. Appl. Geochem., 17, 1,329–1,342. DOI 10.4401/ag-3188.

Rovida A., Locati M., Camassi R., Lolli B., Gasperini P. and Antonucci A.; 2022: Catalogo Parametrico dei Terremoti Italiani (CPTI15), versione 4.0. Istituto Nazionale di Geofisica e Vulcanologia (INGV), DOI 10.13127/CPTI/CPTI15.4.

Stucchi M., Meletti C., Montaldo V., Crowley H., Calvi G.M. and Boschi E.; 2011: Seismic hazard assessment (2003-2009) for the Italian building code. Bull. Seism. Soc. Am. 101, 1,885-1,911.

Corresponding author: andrea.brogi@uniba.it

Fluid-rock interaction in eclogite-facies meta-peridotites (Erro-Tobbio Unit, Ligurian Alps)

S. Cacciari[1], G. Pennacchioni[1], M. Scambelluri[2], E. Cannaò[3], G. Toffol[1]

[1] *Università degli Studi di Padova, Italy*
[2] *Università degli Studi di Genova, Italy*
[3] *Università degli Studi di Milano - La Statale, Italy*

The investigation of exhumed blueschist/eclogite-facies ophiolitic serpentinites can provide information on dehydration reactions, fluid activity and, possibly, seismicity occurring at subduction zones intermediate depths. Fluids are progressively released during subduction by breakdown reactions occurring within serpentinites and meta-sediments, leading to periodic fluid pressure build up that may eventually result in brittle failure (dehydration embrittlement mechanism). This mechanism is likely responsible for triggering deep Episodic Tremor and Slow Slip events (deep ETS), composed of correlated tectonic tremor (low-frequency seismic swarms) and aseismic slow-slip events (SSEs). These events are observed along the subduction interface at depth ranges of 25-60 km (*Behr and Bürgmann, 2021*), a rheologically heterogeneous domain characterized by high Vp/Vs ratio, indicating the presence of pressurized fluids. Rheological heterogeneities (i.e. mantle peridotites affected by different degrees of serpentinization) allow for strain partitioning into low-strain domains, developing crack-seal veining and radiating tremor, and high-strain domains accommodating SSEs. These events are geophysically well constrained, however, only a few exhumed geological assemblages have been interpreted as geological records for deep ETS so far.

The Erro-Tobbio meta-peridotite (Voltri Massif, Western Alps) records fluid-rock interactions and associated deformation occurred mostly within the “deep ETS” depth range (Fig.1). The uneven serpentinization experienced by the lherzolite protoliths at the ocean floor and at the forearc region, led to partitioning of the eclogite-facies deformation into high-strain domains of serpentinite mylonites (interpreted as horizons of SSEs), hosting overprinting brittle and ductile structures and low strain domains of undeformed meta-peridotites (interpreted as the asperities reaching failure and triggering tremor), mainly affected by brittle deformation. These rocks, therefore, display association of tens-of-cm-thick mylonitic horizons with a pervasive network of metamorphic olivine (Ol_2) and Ti-clinohumite (*Ti-chu*) veins and reaction bands related to breakdown of brucite (*Brc*) and antigorite (*Atg*) to *Ol* at 350-500 °C (*Hermann et al., 2000*).

At the mesoscale, the *Ol, Ti-chu* reaction bands can be grouped into two main sets: (i) Ol-fabric-1 (OlF1), steeply-dipping around 320°, oriented at high angle (~ 60°) to the mylonites, (ii) Ol-fabric-2 (OlF2) which trends parallel to the mylonitic domains and progressively increases in spatial density towards the mylonites. Locally, the structural arrangement is more complex and includes multiple sets of olivine veins.

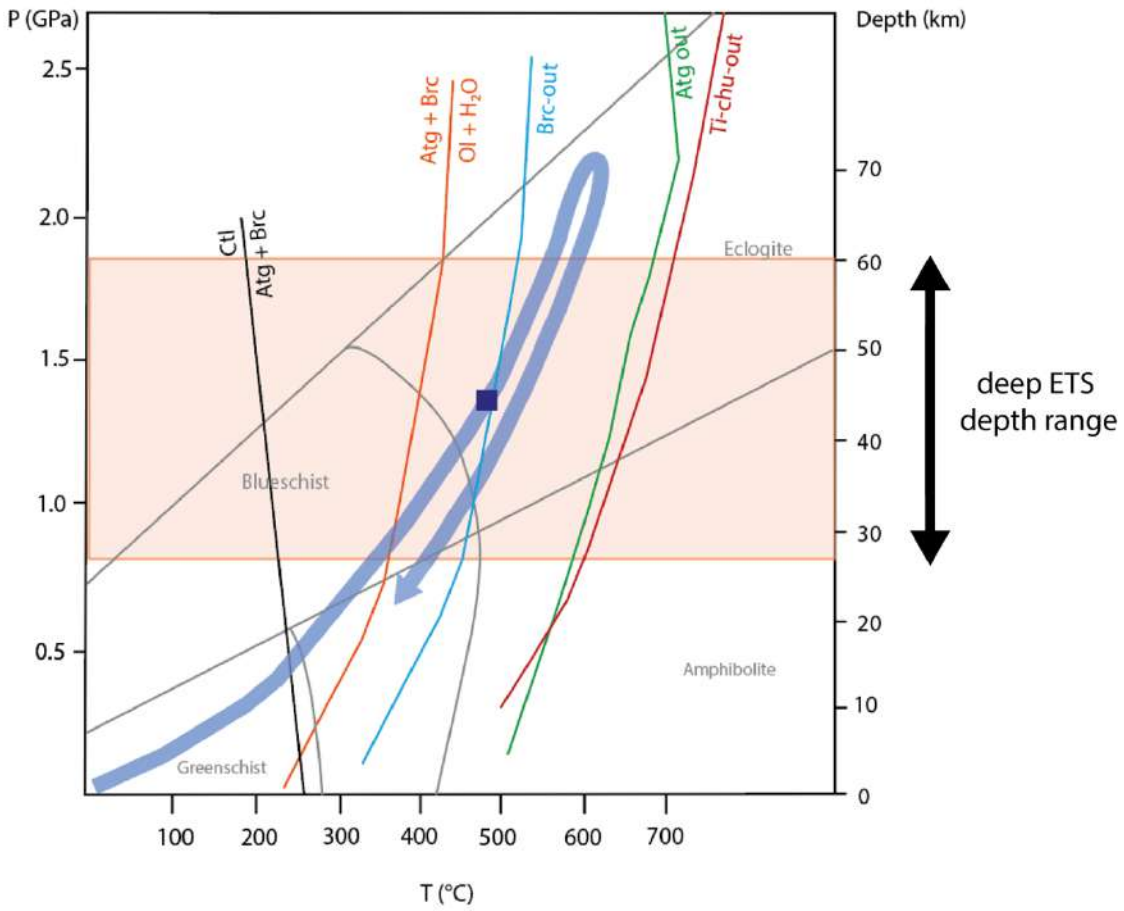

Figure 1. Erro-Tobbio Unit P-T path. The blue rectangle marks the possible conditions of formation of the metamorphic olivine veins and reaction bands

The N-S trending mylonitic horizons include: (i) type 1 mylonites, composed of a planar foliation marked by olivine reaction bands (OlF2), and (ii) type 2 mylonites, displaying a chaotic structure. The southern part of the outcrop contains, in addition, sub-horizontal, cm-thick veins of *Ol + Ti-chu + Chl*, and conjugated right stepping en-echelon arrays of *Ol + Ti-chu* veins.

At the microscale, the meta-peridotite matrix within the undeformed domains consists of coarse *Al-rich Atg* statically replacing mantle olivine (Ol_1) and clinopyroxene (*Cpx*). In these domains, OlF1 is arranged into conjugate *Ol*, *Ti-chu* reaction bands, and radial aggregates, in which *Al-free Atg* replaces Ol_2 along a network of microcracks. These reaction bands include relics of coarse *Al-rich Atg* and *Brc*, suggesting that the formation of Ol_2 localized along *Brc*-rich zones. Coronitic granoblastic olivine grows at the contact between *Brc* and *Atg*, reflecting the dehydration reaction $Atg + Br \rightarrow Ol + H_2O$; a similar mineral phase (Ol_3) was observed within previous Ol_2 sites within the reaction bands. This phase is characterized by a Mg/Si ratio typical of olivine, still, TEM analysis will be performed to unambiguously identify this phase. Ol_1 relics appear structurally linked to the fine-grained Ol_2 that constitutes the reaction-bands. EBSD maps acquired on a reaction band, reveal epitaxial growth of Ol_2 over Atg_1 and Ol_1. Ol_2 grains are iso-oriented with Atg_1 and Ol_1 in areas close to the Ol_1 relics, and the misorientation of the Ol_2 grains increases with the distance from the Ol_1 relics.

Along the mylonitic horizons, the *Al-rich Atg* forming the matrix is affected by ductile deformation, and OlF2 reaction bands mark a foliation parallel to that of *Atg*. Ol_1 relics are also involved in the deformation. Considering Ol_2, EBSD maps revealed the absence of a relationship between the metamorphic olivine (Ol_2), the surrounding *Al-rich Atg* and the Ol_1 relics.

Ol + Ti-chu + Mt + Clinochlore (C-Chl) + Di assemblage was observed within the thicker veins of the southern part of the outcrop and *Ol + Ti-chu* assemblage within the en-echelon veins. The contact between these two sets is sealed by *Mt* and fine-grained *Ol* arranged to form an oblique fabric. From the hand-specimen and the thin sections the following sequence of events was determined: (i) development of horizontal *Atg* veins, hosting µm-sized *Ol* and *Ti-chu* grains, (ii) formation of the *Ol + Ti-chu + Atg + C-chl + Di* vein subparallel to the *Atg* vein, decorated by locally sheared, orthogonal *Atg* lamellae, and of the en-echelon veins (iii) reactivation of the veins through the formation of Atg-bearing microcracks (iv) late veins of calcite and chrysotile crosscutting the previous structures.

In-situ determination of trace elements through LA-ICP-MS allowed the determination of the sources of fluids released during the subduction process and involved in the deformation. The geochemical analyses focused on the distribution of fluid-mobile elements (FMEs: *As, Sb, Ba, W, Li, B*) within the different minerals, as tracers of fluid-rock interactions occurring during dehydration reactions in subducted serpentinites. Enrichment in FMEs detected within the metamorphic olivine and in the Al-free antigorite provide evidence of infiltration of external, sedimentary-derived fluids, indicating an opening of the system during deformation at eclogite-facies conditions, consistently with the results reported by *Scambelluri et al. (2012)* and *Clarke et al. (2020).*

These observations suggest the possible occurrence of two stages of *Atg* dehydration, and an intermediate stage of hydration, occurring within the stability field of *Atg, Brc* and *Ol*. The first extensive dehydration following oceanic serpentinization led to the formation of the metamorphic olivine (Ol_2) arranged along the reaction bands and the veins. The new stage of hydration was localized along *Atg*-bearing microcracks formed especially within the reaction bands, which were, in turn, likely affected by dehydration, leading to growth of granoblastic olivine (Ol_3).

References

Behr W. M., Bürgmann R.; 2021: *What's down there? The structures, materials and environment of deep-seated slow slip and tremor.* Phil. Trans. R. Soc. A 379: 20200218. doi: 10.1098/rsta.2020.0218

Clarke E., De Hoog J. C. M., Kirstein L. A., Harvey J., Debret B.; 2020: *Metamorphic olivine record external fluid infiltration during serpentinite dehydration.* Geochem. Persp. Let. 16, 25–29. doi: 10.7185/geochemlet.2039 25

Hermann J., Müntener O., Scambelluri M.; 2000: *The importance of serpentinite mylonites for subduction and exhumation of oceanic crust.* Tectonophysics 327, 225±238. doi: 10.1016/ S0040-1951(00)00171-2

Scambelluri M., Tonarini S.; 2012: *Boron isotope evidence for shallow fluid transfer across subduction zones by serpentinized mantle.* Geology 40, 10, 907–910. doi: 10.1130/G33233.1

Corresponding author: serena.cacciari@phd.unipd.it

Stress drop scaling is still a very controversial topic: is it real or apparent?

G. Calderoni[1]

[1] *Istituto Nazionale di Geofisica e Vulcanologia (INGV, Italy)*

The stress drop scaling is still an unresolved issue and continues to be controversial in the scientific community. However, knowledge of seismic source scaling parameters plays a fundamental role in assessing the seismic forecasting in a given area and in improving ground motion predictions for seismic hazard mitigation. For this reason, this study compares the Brune stress drop of the earthquake sequence that struck the 2010-2014 Pollino area in the southern Apennines with those estimated for other earthquakes that occurred in different areas of the Apennines during the following seismic sequences: 2009 L'Aquila (Calderoni et al., 2013), 2016-2017 Amatrice (Calderoni & Abercrombie 2023), 2013-2014 Sannio-Matese (Calderoni et al., 2023) and 2019 Northern Edge of the Calabrian Arc Subduction Zone (Calderoni et al., 2020). Three different methods are used, and the results are compared with previous studies.In the first procedure (Calderoni et al. 2019) a two-step approach is used to model the attenuation and then estimate the source parameters from individual earthquake spectra. In the second procedure, an EGF approach is applied. In the third procedure, a modified EGF approach is applied using a scaling law derived by Calderoni et al., (2013) for the L'Aquila 2009 seismic sequence. To gain deeper insights into the interpretation of the result, the structural complexities and tectonic barriers that control seismic activity in the Pollino area are considered (Cirillo et al., 2022).

References

Calderoni, G., & Abercrombie, R. E. (2023). Investigating spectral estimates of stress drop for small to moderate earthquakes with heterogeneous slip distribution: Examples from the 2016– 2017 Amatrice earthquake sequence. Journal of Geophysical Research: Solid Earth, 128, e2022JB025022. https://doi.org/10.1029/2022JB025022

Calderoni, G., L. Improta, and R. Di Giovambattista (2023). Investigating the Role of Fluids in the Source Parameters of the 2013–2014 Mw 5 Matese Seismic Sequence, Southern Italy, Seismol. Res. Lett. XX, 1–21, doi: 10.1785/0220230046.

Calderoni, G., A. Gervasi, M. La Rocca, and G. Ventura (2020). Strike-Slip Earthquakes at the Northern Edge of the Calabrian Arc Subduction Zone, Seismol. Res. Lett. XX, 1–13, doi: 10.1785/0220200251.

Calderoni, G., Rovelli, A., & Singh, S. K. (2013). Stress drop and source scaling of the 2009 April L'Aquila earthquakes. Geophysical Journal International, 192(1), 260–264. https://doi.org/10.1093/gji/ggs011.

Rovelli, A., & Calderoni, G. (2014). Stress drops of the 1997–1998 Colfiorito, central Italy earthquakes: Hints for a common behaviour of normal-faults in the Apennines. Pure and Applied Geophysics, 171(10), 2731–2746. https://doi.org/10.1007/s00024-014-0856-1

Corresponding author: giovanna.calderoni@ingv.it

A “new” Aeolian event in the 20th century: the 19th June 1916 earthquake in Filicudi Island.

C.H. Caracciolo

Istituto Nazionale di Geofisica e Vulcanologia, Sezione di Bologna, Italy

This "work in progress" paper is part of the revision of 20th-century Aeolian seismicity, contributing to the update of the Historical Seismological Database.

In 1916, the second year of the war in Europe and the first in Italy, public opinion was centred on battles, military movements, and news from various fronts, including the sea and the sky. The cost of civil navigation became perilous due to bombardments from ships and attacks with torpedoes from submarines. Against this historical backdrop, Italy experienced intense geological activity, notably the Romagna seismic sequence. Additionally, the Aeolian Islands, particularly Stromboli, witnessed significant lava flows and eruptions, reaching a peak in early July. Two months later, on September 3rd, a moderate earthquake shook Salina island, causing minimal damage to only a few houses, as reported by Molin et al. (2008).

An additional event, absent from recent catalogues (CPTI15, CFTI5med), took place in the archipelago on June 19th. It was likely overshadowed by the news about the war and the eruptions of Stromboli.

However, the PFG catalogue (Postpischl, 1985) records six earthquakes felt in the archipelago between June 12th and 20th, 1916, based on information from De Fiore (1917), Martinelli (1916) and Carrozzo et al. (1975).

Record	Data	Hour	Intensity	Reference	Epicentral Area
25557	1916 06 12	21:00	V - VI	De Fiore (1917)	Basso Tirreno
25558	1916 06 12	21:15	III	Martinelli (1916); Carrozzo et al. (1975)	Basso Tirreno
25560	1916 06 14	21:15	III	De Fiore (1917)	Basso Tirreno
25568	1916 06 17	09:00	V	Carrozzo et. al. (1975)	Basso Tirreno
25575	1916 06 19	21:00	V	Martinelli (1916)	Salina
25578	1916 06 20	02:00	III	Martinelli (1916)	Salina

Tab. 1. Earthquakes in the Aeolian Archipelago during June 1916 according to the catalogue PFG (Postpischl, 1985).

Likely, De Fiore served as the primary source for the other authors, despite the apparent (and likely incorrect) year of the Martinelli publication. Nonetheless, it remains unclear from where Martinelli sourced the data.

In his brief narrative, De Fiore recounts a journey to the Aeolian Islands, just a few months after the events, with the purpose of reporting to the government about the contemporary Stromboli eruption. During this visit, he learned about the earthquakes in Filicudi and decided to investigate further.

Then he visited the island and met local inhabitants, particularly two municipal officials, who shared information about several earthquakes that took place since June. The strongest was said to have occurred on the evening of June 12th. According to De Fiore, there were other two notable earthquakes on July 17th and September 22nd.

While he expressed uncertainty about the precise intensity ("Mercalli V-VI?"), his description suggests a higher degree:

> “It was very strong (V-VI on the Mercalli scale) and caused damage, in some cases significant, to the roofs of houses (constructed, according to local customs, with layers of a kind of beaten concrete forming slightly arched vaults) that appeared in various directions; detachments in the walls, where they formed angles or joined; fractures in the keystones of arches and lintels of doors and windows. There were also rockslides, which I witnessed.” (De Fiore, 1917).

Although De Fiore didn't specify the number of houses damaged, the text implicitly indicates two degrees of damage: "in some cases significant" and less important in others. Therefore, damaged houses were not "exceptions" in the macroseismic scenario, and the uncertainty can be proposed between 6 and 7 degrees on the MCS scale.

De Fiore added that the effects of the earthquake were stronger in the town of Pecorini and that it was also strongly felt in two other islands, Alicudi and Salina, without reporting any damage.

De Fiore's report would be sufficient to update a 20th-century Aeolian earthquake catalogue. However, De Fiore and Martinelli do not align on the sequence of events. Above all, archival documents cast doubt on De Fiore's information regarding the data of the strongest event. According to administrative documentation (Interior Ministry) and seismological records (macroseismic postcards), the earthquake occurred on June 19th, exactly one week after the date indicated by De Fiore. Specifically, on June 20th, Angelo Buganza, the Prefect of Messina province, sent a telegram to the Ministry of the Interior reporting that the previous evening, at 22:00 hours,

a strong earthquake was felt in Filicudi with some damage. He added that a member of the civil engineers would be sent to verify the damage (ACS TUC).

Almost four months later, on October 9th, the Prefect sent a report to Rome with the results of two trips conducted by members of the Civil Engineers Department. According to that document, on Filicudi Island, more than 80% of the buildings were somehow damaged: 60% of the total had light damage, while 17% were heavily damaged, and 4% should be demolished (ACS. MInt.).

This scenario is sufficient for estimating an intensity level of 7 MCS, encompassing the entire island. However, considering Pecorini as the most impacted place (according to De Fiore), allows for the application of the general effects to this locality. On the contrary, for the European Macroseismic Scale (EMS98), the percentage of houses affected and the degree of damage in an urban entity is crucial for estimating the macroseismic intensity. In this case probably the most damaged houses could be situated in Pecorini and the intensity could reach 8 EMS98. Yet, it is only a hypothesis.

In the broader macroseismic scenario, it is noteworthy that the nearby islands of Alicudi and Salina felt the earthquake strongly, though it did not cause any damage. According to the macroseismic postcards (UCMG), in Salina, people fled from their houses, while in Stromboli, individuals felt the earthquake both inside and outside their homes, without experiencing fear. Additionally, the Palermitan newspaper *L'Ora* reported that all residents in Lipari felt a strong earthquake.

The following Table shows the estimated intensities (MCS) for the Aeolian archipelago considering the localities indicated by the sources (Pecorini a Mare, Lipari) or the more important of each island (Santa Marina Salina, San Vincenzo, Alicudi Porto).

Località	**Lat.**	**Lon.**	**Int. MCS**
Pecorini a Mare	38.563	14.567	7
Alicudi Porto	38.535	14.361	5
Santa Marina Salina	38.562	14.873	5
Lipari	38.467	14.955	4-5
Stromboli (San Vincenzo)	38.806	15.235	4

Table 2. Macroseismic Intensities for the Aeolian Earthquake on June 19th, 1916.

Conclusions

This "work in progress" has unveiled a new Aeolian earthquake, pinpointed on June 19th, at 21:00 GMT approximately, in the Filicudi island. At this juncture, it is possible to estimate an Imax of 7 MCS in the town of Pecorini and gauge the perception in the other islands of the Archipelago. However, further research is necessary to establish the entire sequence, considering that various sources indicate additional earthquakes produced further damage, while national and regional authorities were deliberating on how and when to provide financial assistance to the island's residents.

References

Carrozzo, M.T., Cosentino, M., Ferlito, A., Giorgetti, F., Patanè, G., Riuscetti, M.; 1975: Earthquakes Catalogue of Calabria and Sicily (1783-1973).

CFTI5med; 2018: Guidoboni E., Ferrari G., Mariotti D., Comastri A., Tarabusi G., Sgattoni G., Valensise G. - CFTI5Med, Catalogo dei Forti Terremoti in Italia (461 a.C.-1997) e nell'area Mediterranea (760 a.C.-1500). Istituto Nazionale di Geofisica e Vulcanologia (INGV).

CPTI15; 2022: Rovida A., Locati M., Camassi R., Lolli B., Gasperini P., Antonucci A. Catalogo Parametrico dei Terremoti Italiani (CPTI15), versione 4.0. Istituto Nazionale di Geofisica e Vulcanologia (INGV). https://doi.org/10.13127/CPTI/CPTI15.4

De Fiore O.; 1917: I terremoti di Filicudi (isole Eolie) nel 1916. Bollettino della Società Geografica Italiana, v. IV-V. f.2.

Martinelli G.; 1916(!): Macrosismi avvertiti in Italia durante il 1916. Bollettino della Società Sismologica Italiana, v. 20, pp.228-245.

Molin D., Bernardini F., Camassi R., Caracciolo C.H., Castelli V., Ercolani E., Postpischl L.; 2008: *Materiali per un catalogo dei terremoti italiani: revisione della sismicità minore del territorio nazionale*. Quaderni di Geofisica, 57, Istituto Nazionale di Geofisica e Vulcanologia (INGV), Roma, 75 pp.

L'Ora [Palermo], "Terremoto a Lipari", 22-23.06.1916.

Postpischl D.; 1985: (PFG) Catalogo dei terremoti italiani dall'anno 1000 al 1980. Progetto Finalizzato Geodinamica. Quaderni de «La Ricerca Scientifica», n.114, v.2B.

Archival Documents

ACS: MInt. Archivio Centrale dello Stato. Ministero degli Interni. Divisione Servizi Speciali. Servizi in dipendenza dei terremoti. Affari Generali. b. 4 - Filicudi.

ACS: TUC. Archivio Centrale dello Stato. Ministero degli Interni. Telegrammi dell'Ufficio Cifra, "Arrivi", 16.06.1916 - 28.06.1916.

UCGM: Macroseismic Postcards of the *Ufficio Centrale di Meteorologia e Geodinamica*, Macroseismic Archive, Istituto Nazionale di Geofisica e Vulcanologia, Rome, June 1916.

Corresponding author: carlos.caracciolo@ingv.it

A new 3D seismotectonic model of the Pedeapenninic Front between Parma and Bologna (Italy): new perspectives on Seismic Hazard Assessment

G. Carloni[1*] , G. Vignaroli[1], T. Gusmeo[1], L. Martelli[2], G. Viola[1]

[1] Università di Bologna-Dipartimento di Scienze Biologiche, Geologiche e Ambientali
[2] Regione Emilia-Romagna – Area geologia, suoli e sismica
** now at: Provincia di Ferrara – Settore Pianificazione Territoriale e Urbanistica*

Introduction

Understanding how surface brittle deformation patterns of seismic areas relate to their seismogenic source(s) is crucial for seismic hazard assessment protocols and should significantly rely on deterministic geological inputs. Aiming at a better picture of the subsurface along the Pedeapenninic Front of the Northern Apennines (Italy), we built a new 3D seismotectonic model (Fig. 1) of the area between Parma and Bologna incorporating new geological surface constraints with a wealth of subsurface geological and geophysical data, in order to locate, characterise and parametrize the active and seismogenic faults that define the seismotectonic framework of the region. The investigated area extends from the mountainous internal sector of the Northern Apennines, to the south, to the flat Po Plain in the north. Adria-related Tuscan Units crop out in the axial sector and are overthrust by the allochthonous Ligurian and Epiligurian Units. Pliocene and younger units crop out along the Pedeapenninic Front (Boccaletti et al., 1985; DeCelles and Giles, 1996; Boccaletti et al., 2011). Compressive tectonics is currently on-going in the external part of the chain, with the Pedeapenninic Front and the Po Plain blind thrusts striking NW-SE (Jolivet and Faccenna, 2000; Bennet et al., 2012). This thrust system is dissected by transverse normal and transpressive/transtensive faults.

This work provides the scientific community with a 3D seismotectonic model to be used for practical purposes, such as the assessment of seismic hazard in specific areas of interest as well as scientific and educational purposes. The methodological approach used to generate this 3D model, and its associated database, also serves as an inspiring workflow for characterising active and seismogenic faults in other geological settings elsewhere, where seismogenic faults are buried and not directly accessible for field studies.

3D model architecture

The database of the seismotectonic model (Fig. 1) is organized in three levels:

i) The first level consists of folders and subfolders containing 2D input data imported into the software Leapfrog Works, version 2023.2. The georeferenced data are: eight new geological cross-sections deriving from detailed fieldwork carried out along the Pedeapenninic margin; six different cross sections from the two seismotectonic maps of the Emilia-Romagna region (Boccaletti et al., 2004; Martelli et al., 2016); twenty-three geological cross sections from the CARG project (Martelli et al., 2009; Gasperi et al., 2005; Panini et al., 2002; Bettelli et al., 2002; Pizziolo et al., 2002; Cerrina Feroni et al., 2002; Plesi et al., 2002); 113 boreholes and eighteen deep seismic lines from the ViDePi project (https://www.videpi.com/videpi/videpi.asp); hypocenters from > 8000 seismic events extracted from the national catalogs (ISIDe Working Group, 2007; Rovida et al., 2020, 2022) and seventy-nine focal mechanisms from Martelli et al. (2016);

ii) The second level stores 3D geometries created directly within the model from the above input data, such as polylines and meshes;

iii) The third level contains the seismotectonic model with eight reconstructed chronostratigraphic units and fifty-seven mapped active faults.

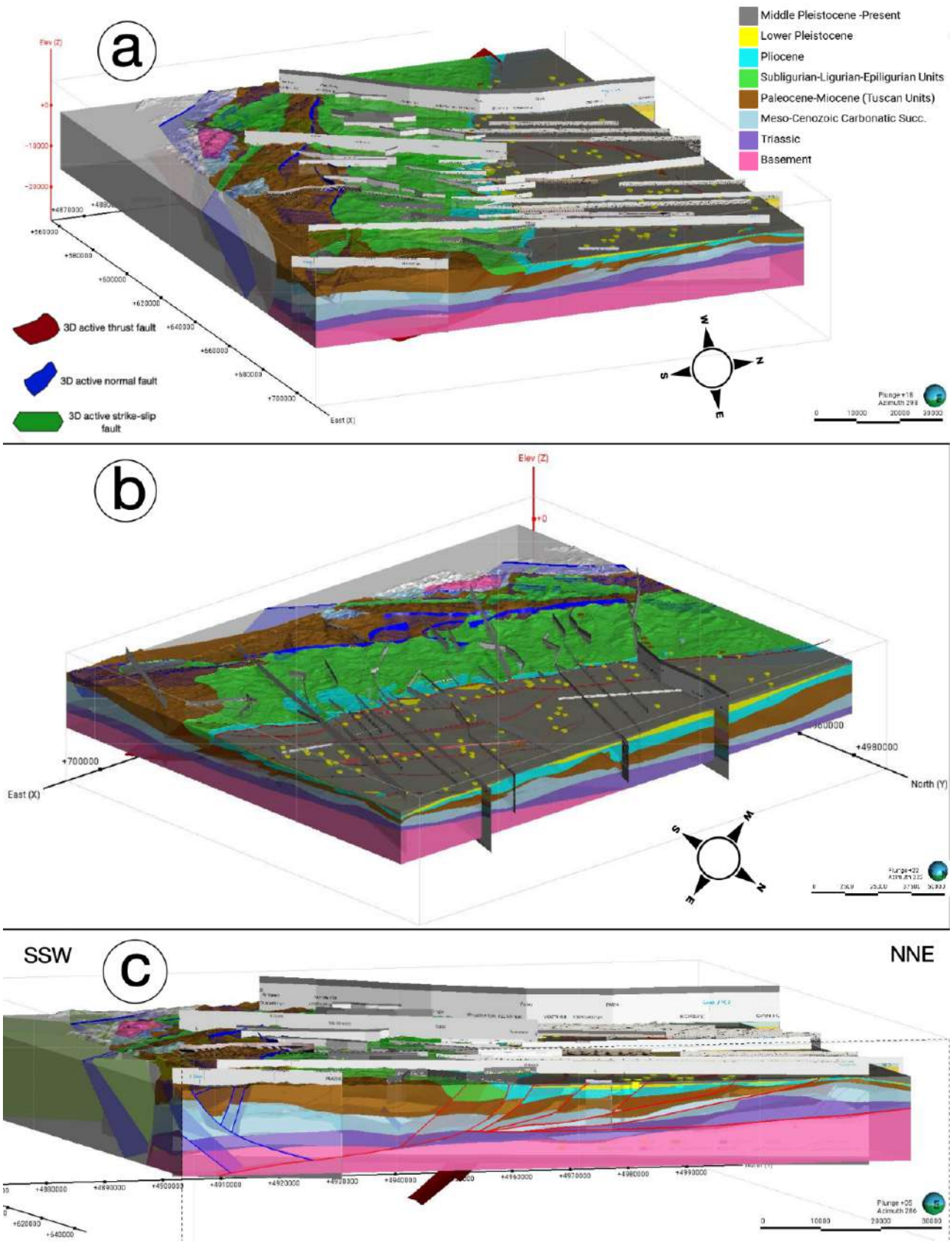

Figure 1: Views from the ESE (a) and the NE (b) of the 3D seismotectonic model, and a NNE-SSW cross-section (c).

Parametrisation of active and seismogenic faults

For each active and/or seismogenic fault populating the 3D database, an attribute table (Fig. 2b) was populated listing their main characteristics, such as:

- geometric parameters directly measured in the model (fault trace length, depth, dip direction, dip angle in Fig. 2a).

- kinematic parameters (Fig. 2a), such as kinematics (estimated based on geological considerations and existing literature), displacement along the fault strike, and slip rate. The displacement was calculated in the 3D model by creating a series of evenly spaced (every 2 km) cross-sections, with the spacing distance chosen based on the size of the analysed structures and the desired level of detail and continuity. On these sections we mapped the position of the intersection points of each chronostratigraphic boundary displaced above and below the fault. The 3D coordinates of these points in the hanging wall and footwall were then extracted and used to seamlessly calculate the three components of displacement and their resultant along the fault strike. To calculate the average slip rate, the previously calculated displacements were sorted according to the age of deposition of the displaced chronostratigraphic limits.

- historical and instrumental seismicity data and available focal mechanisms to obtain the seismological parameters of the studied faults (Fig. 2a). Specific seismic clusters that could be clearly assigned to specific seismogenic faults were analysed to extract the maximum recorded magnitude for a specific fault and to identify the time periods during which the major seismic sequences occurred. For the remaining parameters (slip per event, return period, maximum possible magnitude), we employed well known seismological formulas (e.g., Kanamori & Anderson, 1975; Leonard, 2010).

Active and Seismogenic faults' attribute table ⓐ

Geometric parameters	Applied technique
Fault trace Length (km)	Measured from the 3D model
Depth min. (km)	Measured from the 3D model
Depth max. (km)	Measured from the 3D model
Dip min. (°)	Measured from the 3D model
Dip max. (°)	Measured from the 3D model
Average dip (°)	Measured from the 3D model
Dip Direction (°)	Measured from the 3D model
Kinematic parameters	
Kinematics	From geological constraints and literature data
Average Diplacement calculated for each chronostratigraphic limit	Calculated from serial cross-sections in the 3D model
Average Slip_rate calculated for each chronostratigraphic limit	Average Displacement/age of deposition of the displaced level
Seismological parameters	
Average Slip per Event (Mw>4.5) (yr)	D=M0/μS (Kanamori & Anderson, 1975)
Average Return Period (yr)	Slip per event/ Average Slip Rate
Return Period (Mw>4.5) max.	Slip per event/Slip Rate max.
Return Period (Mw>4.5) min.	Slip per event/Slip Rate min.
Max. registered Mw	Historical/Instrumental seismicity
Max. possible Mw	M_{max}=4.24+1.67 x log(Fault trace length) (Leonard, 2010)
Significant seismic events	Historical/Instrumental seismicity
Quality code of the reconstructed 3D geometry	
References	

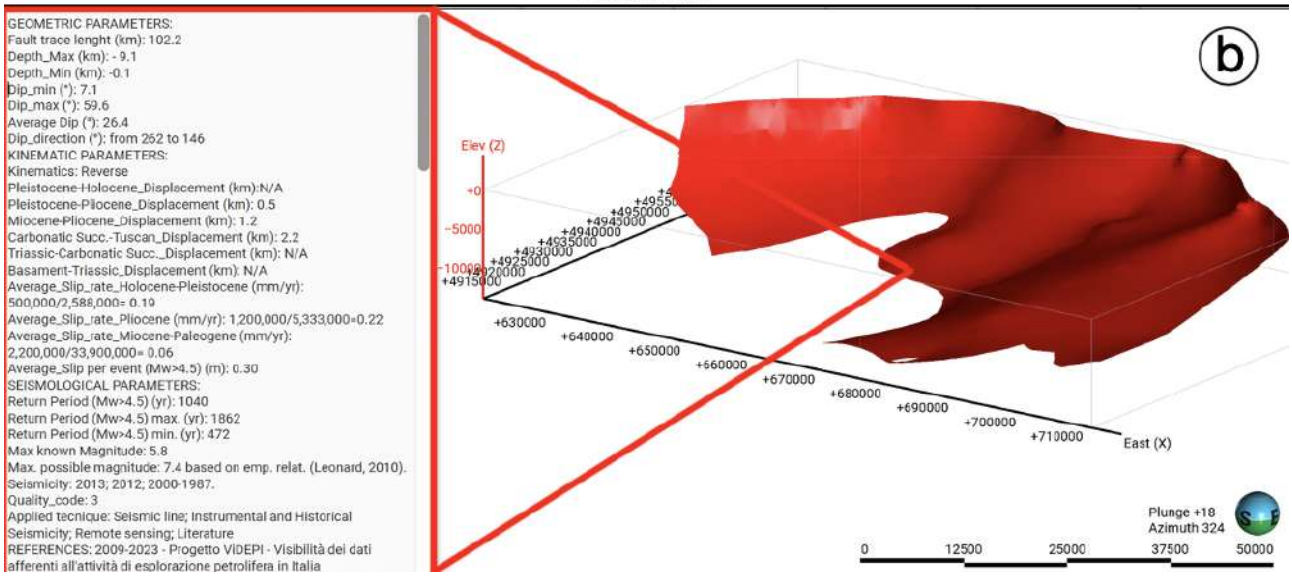

Figure 2: a) List of the main geometric, kinematic, and seismological parameters that have been included in the attribute table of each active and/or seismogenic fault, to the left, and the methodologies by which they have been calculated, to the right. b) An example of what an attribute table looks like when querying a fault within the 3D model.

Model validation

First of all, we validated the assessment procedure of the model through the visual juxtaposition of chronostratigraphic units and faults, as delineated by the input information, against their corresponding 3D modelled geometries. We compared the plan view of the 3D seismotectonic model with the original 2D seismotectonic map of the Emilia-Romagna Region (Martelli et al., 2016; Fig. 3a). Then, we generated six sections from the 3D model using the dedicated *slicer* tool in Leapfrog Work, and we compared them with the real cross-sections used as input (Fig. 3b). This comparison clearly demonstrates the high quality of the model and the correct reproduction of the main mapped geometries. The observed differences are due to the simplification of the geological system and are intentionally overlooked to highlight only the geology of interest. The main horizons and faults that could be easily correlated between different domains were interpolated and created. Therefore, all the lower hierarchical structures are missing in the model sections (to the left in Fig. 3b), because it is impossible to correlate them laterally with the data available in the literature. Another important point to consider when comparing the obtained results with the input data is that, in some model-generated sections, the attitude of the deeper stratigraphic units was inferred beyond the extent of the 2D input sections when the available data allowed for it This type of validation is therefore feasible in areas where 2D input data exist, while the remaining areas of the model are the result of our interpretation.

We further refined the validation of the 3D model by employing data from the existing literature and basic geological knowledge to verify the accuracy of the reconstructed geometries. This evaluation step aimed to determine if the modelled geometries can be considered meaningful and compared with the real geological structures. For the mapped faults, for example, we verified whether their reconstruction is geometrically and kinematically compatible with the thrust-type structures and extensional faults (Anderson, 1951; Fossen, 2016) located in the frontal and in the internal sectors, respectively, of the Northern Apennines fold-and-thrust belt. The geometric, kinematic, and seismological parameters in the attribute table of each fault were compared with the available literature data (ITHACA Working Group, 2019; Basili et al., 2008), thus confirming that the parameters calculated by this model are indeed comparable with those reported in the literature.

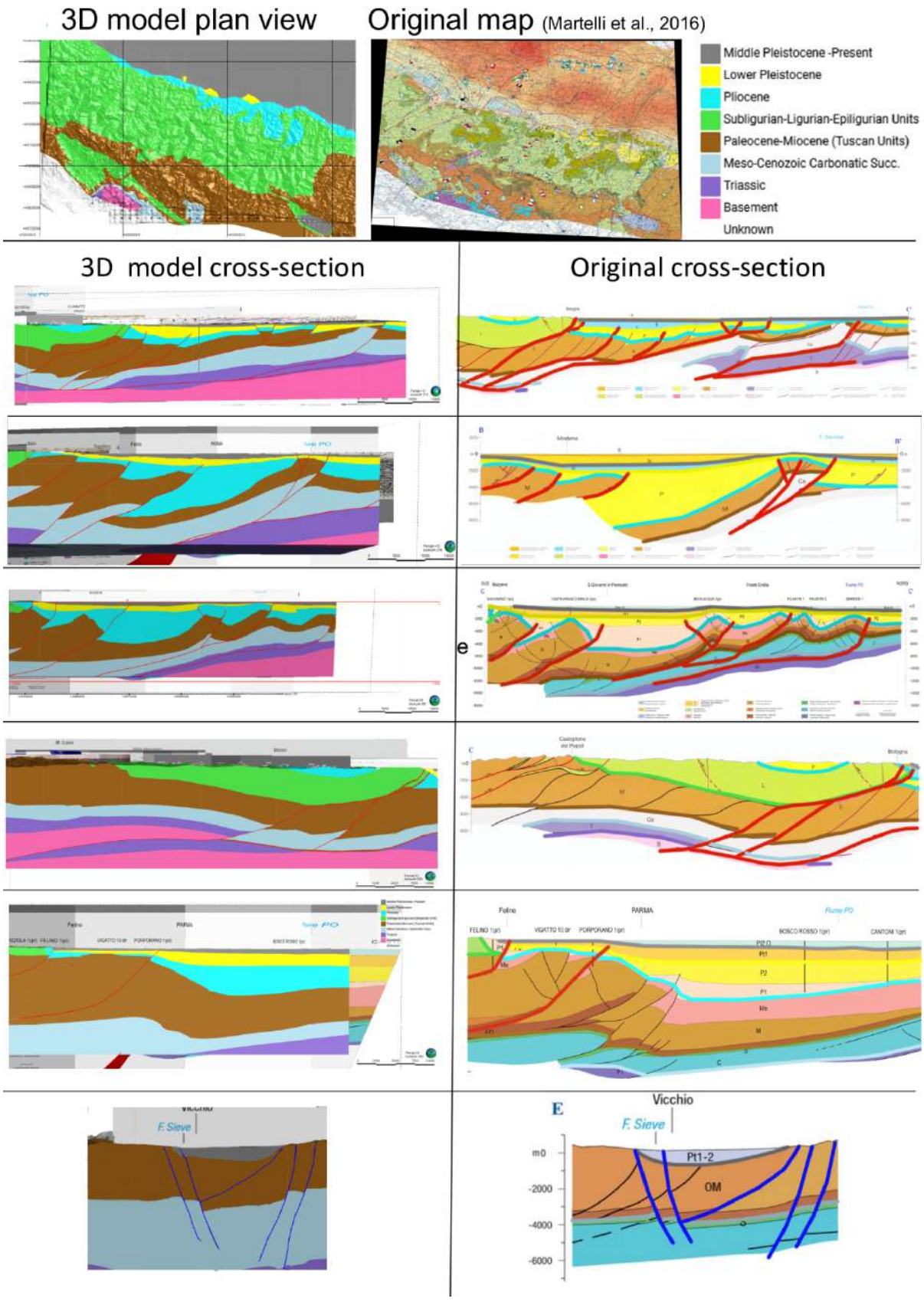

Figure 3: a) Visual comparison between the map view of the 3D seismotectonic model and the real 2D map from Martelli et al., 2016. b) Visual comparison between six slices from the 3D model (to the left) taken in correspondence of the 2D seismotectonic cross-sections (to the right) given as 2D inputs (Boccaletti et al., 2004; Martelli et al., 2016).

References

Anderson E.M., 1951. *The Dynamics of Faulting.* Transactions of the Edinburgh Geological Society, 8, 387-402.

Basili, R., Valensise, G., Vannoli, P., Burrato, P., 2008. T*he Database of Individual Seismogenic Sources (DISS), version 3: Summarizing 20 years of research on Italy's earthquake geology.* Tectonophysics, 453, 20–43.

Bennett, R.A., Serpelloni, E., Hreinsdóttir, S., Brandon, M.T., Buble, G., Basic, T., Casale, G., Cavaliere, A., Anzidei, M., Marjonovic, M., Minelli, G., Molli, G., Montanari, A., 2012. *Syn-convergent extension observed using the RETREAT GPS network, northern Apennines, Italy.* Journal of Geophysical Research: Solid Earth 117. https://doi.org/10.1029/2011JB008744

Bettelli, G., Boccaletti, M., Cibin, U., Panini, F., Poccianti, C., Rosselli, S., Sani, F., 2002. *Note illustrative della Carta Geologica d'Italia alla scala 1:50.000, Foglio 217, Neviano degli Arduini.* Servizio Geologico d'Italia-Regione Emilia-Romagna, p. 112.

Bettelli, G., Panini, F., Cibin, Pizziolo, M., 2002. *Note illustrative della Carta Geologica d'Italia alla scala 1:50.000, Foglio 236, Pavullo nel Frignano.* Servizio Geologico d'Italia-Regione Emilia-Romagna, p. 112.

Boccaletti, M., Coli, M., Eva, C., Ferrari, G., Giglia, G., Lazzarotto, A., Merlanti, F., Nicolich, R., Papani, G., Postpischl, D., 1985. *Considerations on the seismotectonics of the Northern Apennines.* Tectonophyiscs 117, 7–38.

Boccaletti M., Bonini, M., Corti, G., Gasperini, P., Martelli, L., Piccardi L., Tanini, G., Vannucci, G., 2004. *Seismotectonic map of the Emilia-Romagna Region.*

Boccaletti, M., Corti, G., Martelli, L., 2011. *Recent and active tectonics of the external zone of the Northern Apennines (Italy)*. International Journal of Earth Sciences 100, 1331–1348. https://doi.org/10.1007/s00531-010-0545-y

Cerrita Feroni, A., Ottria, G., Vescovi, P., 2002. *Note illustrative della Carta Geologica d'Italia alla scala 1:50.000, Foglio 252, Barberino di Mugello.* Servizio Geologico d'Italia-Regione Emilia-Romagna, p. 130.

DeCelles, P.G., Giles, K.A., 1996. *Foreland basin system*. Basin Research 8, 105–124.

Fossen, H. 2016. *Structural Geology* (Cambridge university press, 2016).

Gasperi, G., Bettelli, G., Panini, F., Pizziolo, M., 2005. *Note illustrative della Carta Geologica d'Italia alla scala 1:50.000, Foglio 219, Sassuolo.* Servizio Geologico d'Italia-Regione Emilia-Romagna, p. 197.

ISIDe Working Group, 2007, *Italian Seismological Instrumental and Parametric Database (ISIDe).* Istituto Nazionale di Geofisica e Vulcanologia (INGV). https://doi.org/10.13127/ISIDe .

ISPRA- Istituto Superiore per la Protezione e la Ricerca Ambientale. *Progetto CARG-Carta Geologica d'Italia alla scala 1:50.000, Regione Emilia-Romagna.* https://www.isprambiente.gov.it/Media/carg/emilia.html

ITHACA Working Group, 2019. *ITHACA (ITaly HAzard from CApable faulting), A database of active capable faults of the Italian territory. Version December 2019*. ISPRA Geological Survey of Italy. Web Portal: http://sgi.isprambiente.it/ithaca/viewer/index.html

Jolivet, L., Faccenna, C., 2000. *Mediterranean extension and the Africa-Eurasia collision*. Tectonics 19, 1095–1106. https://doi.org/10.1029/2000TC900018

Kanamori, H., Anderson, D.L., 1975. *Theoretical basis of some empirical relations in seismology*. Bulletin of the Seismological Society of America; 65 (5), 1073–1095.

Leonard, M., 2010. *Earthquake fault scaling: Self-consistent relating of rupture length, width, average displacement, and moment release*. Bull. Seismol. Soc. Am. 100 (5A), 1971–1988. https://doi.org/10.1785/0120090189

Martelli, L. et al. 2016, *Carta Sismotettonica della Regione Emilia- Romagna e aree limitrofe. Scala 1:250.000* https://ambiente.regione.emilia-romagna.it/it/geologia/pubblicazioni/cartografia-geo-tematica/carta-sismotettonica-della-regione-emilia-romagna-e-aree-limitrofe-edizione-2016

Martelli L., Benini, A., De Nardo, M.T., Severi, P., 2009. *Note illustrative della Carta Geologica d'Italia alla scala 1:50.000, Foglio 220, Casalecchio di Reno*. Servizio Geologico d'Italia-Regione Emilia-Romagna, p.124.

Panini, F., Bettelli, G., Pizziolo, M., 2002. *Note illustrative della Carta Geologica d'Italia alla scala 1:50.000, Foglio 237, Sasso Marconi*. Servizio Geologico d'Italia-Regione Emilia-Romagna, p.176.

Pizziolo, M., Segadelli, S., Vaiani, S.C., 2002. *Note illustrative della Carta Geologica d'Italia alla scala 1:50.000, Foglio 200, Reggio nell'Emilia*. Servizio Geologico d'Italia-Regione Emilia-Romagna, p.110.

Plesi, G., et al., 2002. *Note illustrative della Carta Geologica d'Italia alla scala 1:50.000, Foglio 235, Pievepelago*. Servizio Geologico d'Italia-Regione Emilia-Romagna, p.138.

Progetto ViDEPI. *Visibilità dei dati afferenti all'attività di esplorazione petrolifera in Italia. Ministero dello sviluppo economico DGRME-Società Geologica Italiana-Assomineraria* (cc) BY-Contenuti distribuiti con Licenza Creative Commons Attribuzione 3.0 Italia. https://www.videpi.com/videpi/videpi.asp

Rovida, A., Locati, M., Camassi, R., Lolli, B., Gasperini, P., 2020. *The Italian earthquake catalogue CPTI15.* Bulletin of Earthquake Engineering, 18(7), 2953-2984.

Rovida, A., Locati, M., Camassi, R., Lolli, B., Gasperini, P., Antonucci, A., 2022. Catalogo Parametrico dei Terremoti Italiani (CPTI15), versione 4.0. Istituto Nazionale di Geofisica e Vulcanologia (INGV). https://doi.org/10.13127/CPTI/CPTI15.4

Acknowledgements

We thank Dr. Alberto Martini of the Emilia-Romagna geological survey (RER-SGSS) for providing the high-resolution geological cross-sections and maps of the CARG and seismotectonic sheets. We would also like to express our special thanks to the entire Deformation, Fluids, and Tectonics (DFT) group of the Department of Biological, Geological, and Environmental Sciences in Bologna for their comments and constructive discussions during the development of this project.

Corresponding author: giacomo.carloni@provincia.fe.it

What about the predecessors of the February 2023 earthquakes in Eastern Anatolia?

V. Castelli[1], K. Sesetyan[1,2], A.A. Gomez Capera[3], C. Meletti[4], M. Stucchi[1]

[1]Istituto Nazionale di Geofisica e Vulcanologia - Sezione di Bologna, Bologna/Ancona, Italy;
[2]Bogazici University, Kandilli Observatory and Earthquake Research Institute, Dept. of Earthquake Engineering, Istanbul, Turkey;
[3]Istituto Nazionale di Geofisica e Vulcanologia - Sezione di Milano, Milano, Italy;
[4]Istituto Nazionale di Geofisica e Vulcanologia - Sezione di Pisa, Pisa, Italy.

When large earthquakes occur, it is natural enough to wonder about their likely predecessors (if any). This is why, after the earthquakes of February 2023, we began a review of the historical seismic record of Eastern Anatolia (Fig. 1).

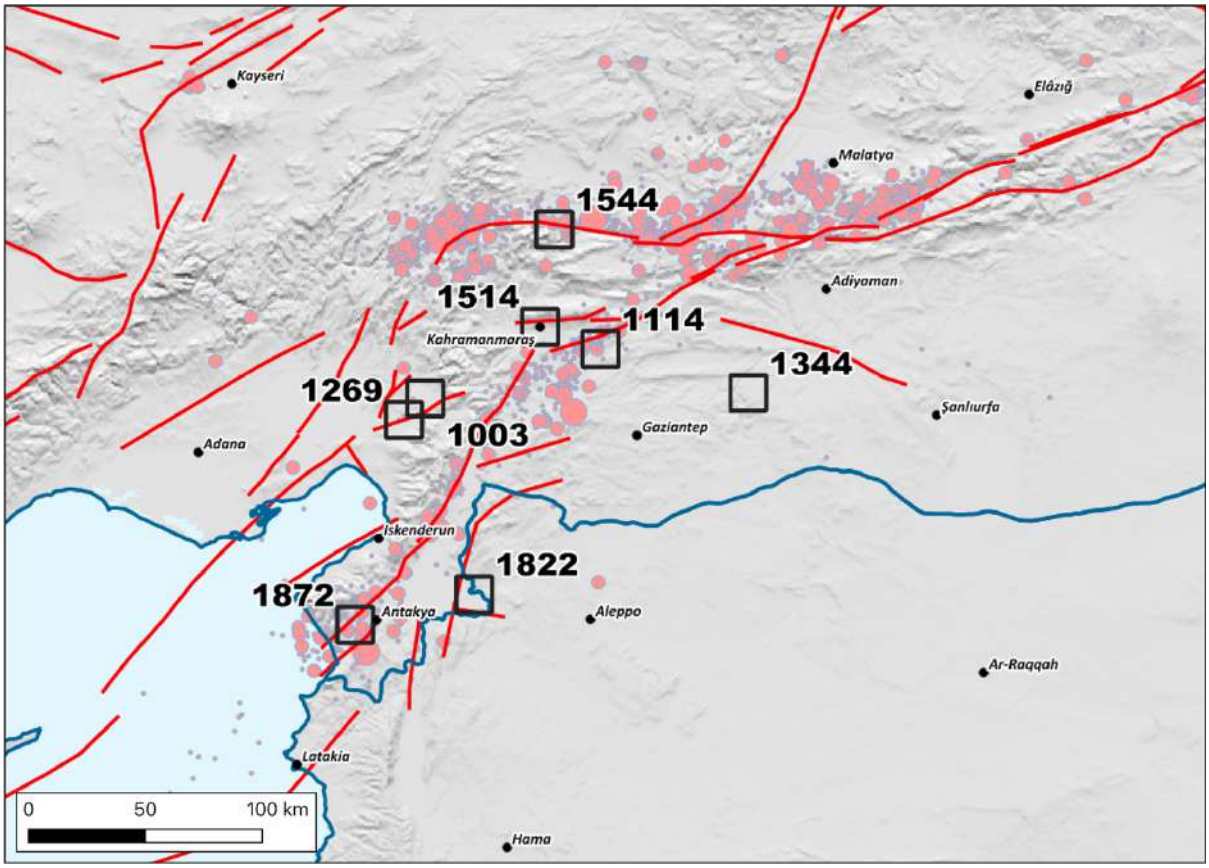

Figure 1. The 2023 seismic sequence superimposed on the major historical earthquakes of the area. Faults traces (in red) from www.seismofaults.eu/. Digital Elevation Model from www.hawaii.edu/its/webservice/

Our investigation concentrated on six major earthquakes/sequences occurred after 1000 AD (1003, 1114/1115, 1269, 1344, 1513/1514 and 1544). The earthquakes of 1822, 1872 and 1893 are better known and do not require priority investigation.

The geopolitical history of this region is very complex, with many changes of rulers along the centuries, but its long-term seismic history is rather well known. Many earthquakes are on record both before and since the date - some 2100 years ago - when the region became a Roman province. Many of its main towns (Aleppo and Antakya for instance) have a long-term history that includes eyewitness observations of many strong earthquakes.

Historical earthquake records for this area were collected and studied several times. The latest studies are Soysal et al. (1981), Ambraseys and Finkel (1995), Guidoboni & Comastri (2005), Sbeinati et al. (2005), Tan et al. (2008). N.N. Ambraseys wrote many papers on this subject and compendiated his work in Ambraseys (2009). However, time, epicentral location and size of many earthquakes are debatable and earthquake catalogues propose contrasting values for the same events.

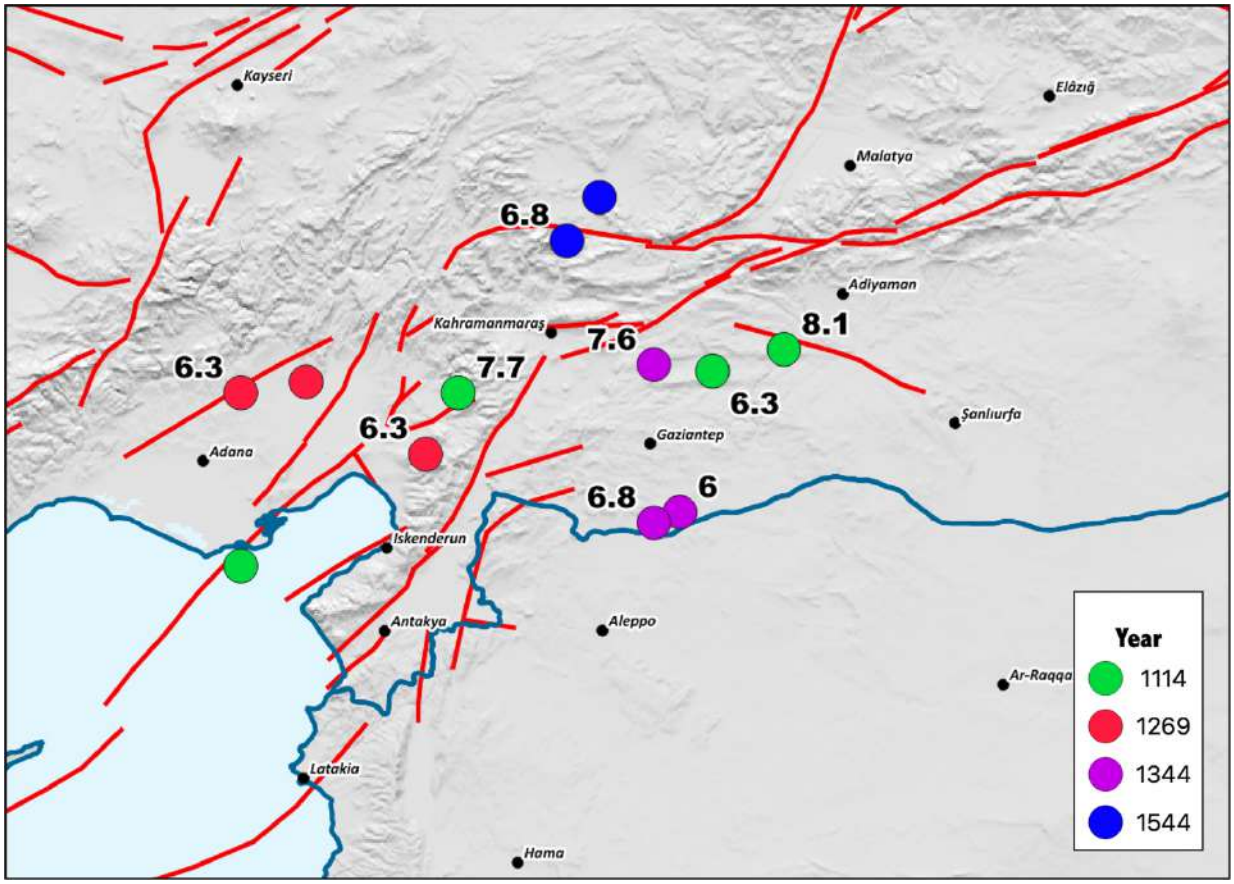

Figure 2. Epicentres and M from Sbeinati et al. (2005), CFTI5Med (2019), Tan et al. (2008). Io from Soysal et al. (1981).

Our work consisted of: a) retrieving and analyzing the main historical sources for each earthquake; b) identifying the localities mentioned in the sources and assessing macroseismic intensities from the original information; c) determining earthquake parameters (Io, Mw and - whenever possible - source azimuth) with the “Boxer” method (Gasperini et al., 1999), after properly calibrating the relevant coefficient by using recent earthquakes of the Anatolian region.

Fig. 3 presents the seismological results of this work: Mw (with uncertainty equal to 0.3) and the "boxes" obtained with the Gasperini et al. (1999) procedure and representing the surface projection of the possible earthquake sources: the epicentre is in the middle of the "box".

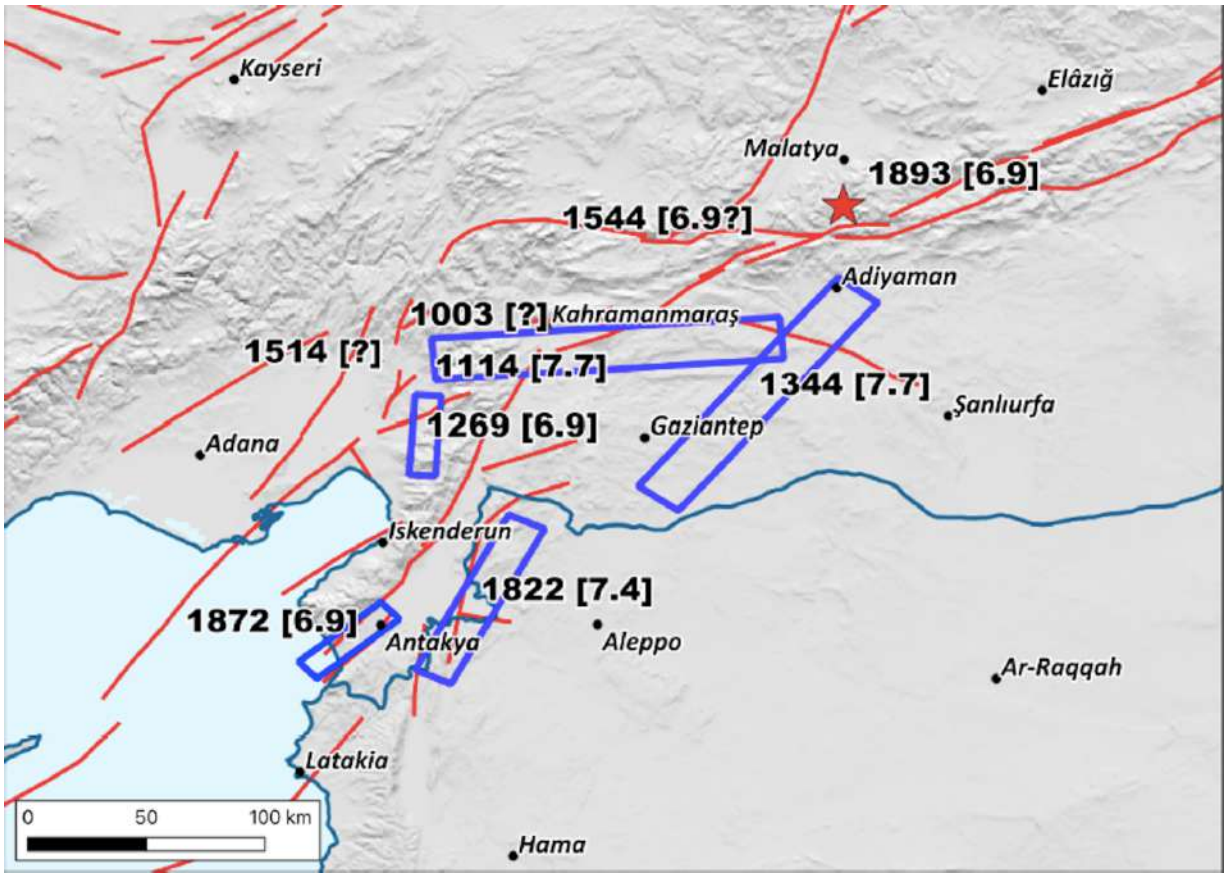

Figure 3. Seismogenic boxes or epicentral areas determined in our study.

The epicentral location and Mw calculated for the main earthquake of 1114 are close to those of the first event of 6 February, 2023. The "box" seems to match the Pazarcik segment of the EAFZ (we refer hereafter to the fault definitions used by Duman and Emre, 2013 and by Duman et al., 2018). The 1269 earthquake was less energetic than the 1114 one, and its parameters are less well constrained. Its "box" suggests the Amanos segment as the likeliest source, with the Toprakkale segment as an alternative candidate. The **1344** earthquake is rather well known and was indeed a very large one. On account of its location it was not considered in the debate on the 2023 earthquake source. However, the identification of its source would be helpful for the understanding of seismicity in this region. As for the **1513/1514** earthquake, the first interpretation by Ambraseys (1988) was -and still is – considered as the absolute truth by literature, leading to a strong connection with the Pazarcık segment. Unfortunately, this interpretation is founded on poor information, as later stated by Ambraseys (2009) and confirmed by us. Though we cannot provide reliable epicentral location and magnitude estimates, we believe that the Toprakkale or Karataş segments could represent a more appropriate option for the source. Similar considerations can be proposed for the **1544** earthquake, whose informative background is

also very weak. It could be located in the area where the recent M7.6 took place (Çardak fault), with Mw around 6.9.

References

Ambraseys N.N.; 1989: Temporary seismic quiescence: SE Turkey. Geophys. J. Int. 96, 311–331.

Ambraseys N.N.; 2009: Earthquakes in the Eastern Mediterranean and the Middle East: a multidisciplinary study of 2000 years of seismicity. Cambridge University Press, 947 p.

Ambraseys N.N., Finkel C.; 1995: The seismicity of Turkey and adjacent areas, a historical review, 1500-1800. Eren, 240 p.

Duman T.Y., Emre Ö.; 2013: The East Anatolian fault: geometry, segmentation and jog characteristics.Geol. Soc. Lond. Spec. Publ. 372, 495–529.

Duman T.Y., Çan T., Emre Ö., Kadirioğlu F.T., Başarır Baştürk N., Kılıç T., Arslan S., Özalp S., Kartal R.F., Kalafat D., Karakaya F.; 2018: Seismotectonic database of Turkey. Bulletin of Earthquake Engineering, 16, 3277-3316.

Gasperini P., Bernardini F., Valensise G., Boschi E.; 1999: Defining seismogenic sources from historical felt reports. Bull. Seismol. Soc. Am. 89, 94–110.

Gasperini P., Vannucci G., Tripone D., Boschi E.; 2010: The location and sizing of historical earthquakes using attenuation of macroseismic intensity with distance. Bull. Seismol. Soc. Am. 100, 2035–2066.

Guidoboni E., Comastri A.; 2005: Catalogue of Earthquakes and Tsunamis in the Mediterranean from the 11th to the 15th Century, Istituto Nazionale di Geofisica e Vulcanologia, 1037 p.

Guidoboni E., Ferrari G., Tarabusi G., Sgattoni G., Comastri A., Mariotti D., Ciuccarelli C., Bianchi M.G., Valensise G.; 2019: CFTI5Med, the new release of the catalogue of strong earthquakes in Italy and in the Mediterranean area, Scientific Data 6, Article number: 80 (2019). doi: https://doi.org/10.1038/s41597-019-0091-9

Sbeinati M.R., Darawcheh R., Mouty M.; 2005: The historical earthquakes of Syria: an analysis of large and moderate earthquakes from 1365 BC to 1900 AD. Ann. Geoph. 48(3), 347–435.

Soysal H., Sipahioğlu S., Kolçak D., Altınok Y.; 1981: Türkiye ve çevresinin tarihsel deprem kataloğu MÖ 2100 – MS 1900, TUBITAK Project, no. TBAG.341, Istanbul.

Tan O., Tapırdamaz M.C., Yörük A.; 2008: The Earthquake Catalogues for Turkey. Turkish J. Earth Sci.17, 405–418.

Corresponding author: viviana.castelli@ingv.it

«Se dice *etiam* per teremoti esser sommerso et ruinato tre terre» (How a large historical earthquake was born).

V. Castelli [1]

[1] *Istituto Nazionale di Geofisica e Vulcanologia-Sezione di Bologna, Bologna/Ancona, Italy*

There was once a physician (called Andrea Alpago or Maestro Andrea da Belluno, from his NE Italy hometown) who went to work for the Venetian consulate in Damascus around 1487, stayed there up to 1517, learned Arabic and was the first European ever to translate Avicenna's works from the original (Levi della Vida, 1960). Thanks to his linguistic skills Maestro Andrea became an expert advisor on the political and commercial situation of the entire East (from Egypt and Turkey to Arabia and India) and in particular on the "Signor Sophi" or "Suffi", i.e. the Shah of Persia Ismāʿīl, founder of the Safawid dynasty (1502-1524), whose alliance Venice was then seeking to obtain against the Turks. Between 1504 and 1514, Maestro Andrea sent to the Venetian government many confidential reports, that were copied by Marino Sanudo in his *Diarii* (De Bertoldi, 1888). In a report dated on 10 March 1514, Mastro Andrea, describes at length the doings of the new Turkish sovereign, Selim I "the Grim", in Anatolia (he was liquidating all his internal enemies – namely his stepbrothers and nephews - before starting a war against Egypt and Persia). The report ends, as an afterthought, with this piece of information: "Se dice *etiam* per teremoti esser sommerso e ruinato tre terre del Soltan a li confini del Turcho, videlicet Malathia et Terso et Adena".

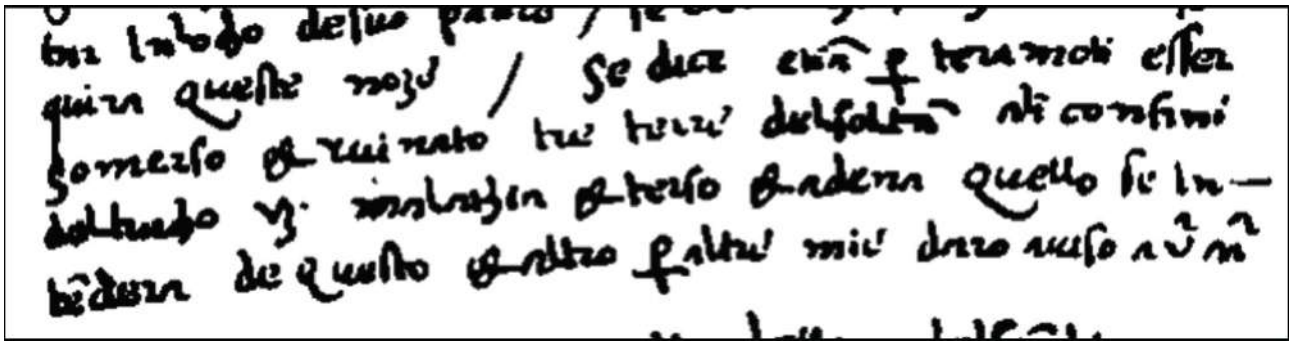

Fig. 1 – Excerpt of the report written Maestro Andrea on 10 March 1514, as transcribed in Venice by Marin Sanudo sometime in the second half of 1514 (Biblioteca Nazionale Marciana, Venice).

This is the earliest, and only contemporary testimony of an earthquake about which very little is known. It must have happened before the letter was written, but was it in late 1513 or early 1514? It heavily damaged (as shown by the verbs "submerged" and "ruined") at least three towns of SE Anatolia, but it seems curious that two of them - Tarsus and Adana - are close to each other, while

the third – Malatya – is more than 300 km away (Fig. 2). What happened in between? Could someone - either Maestro Andrea who wrote by hearsay ("se dice") or Sanudo who copied him - have made a mistake in trascribing one of these names? Could some other place-name have been wrongly transcribed as "Malatya"?

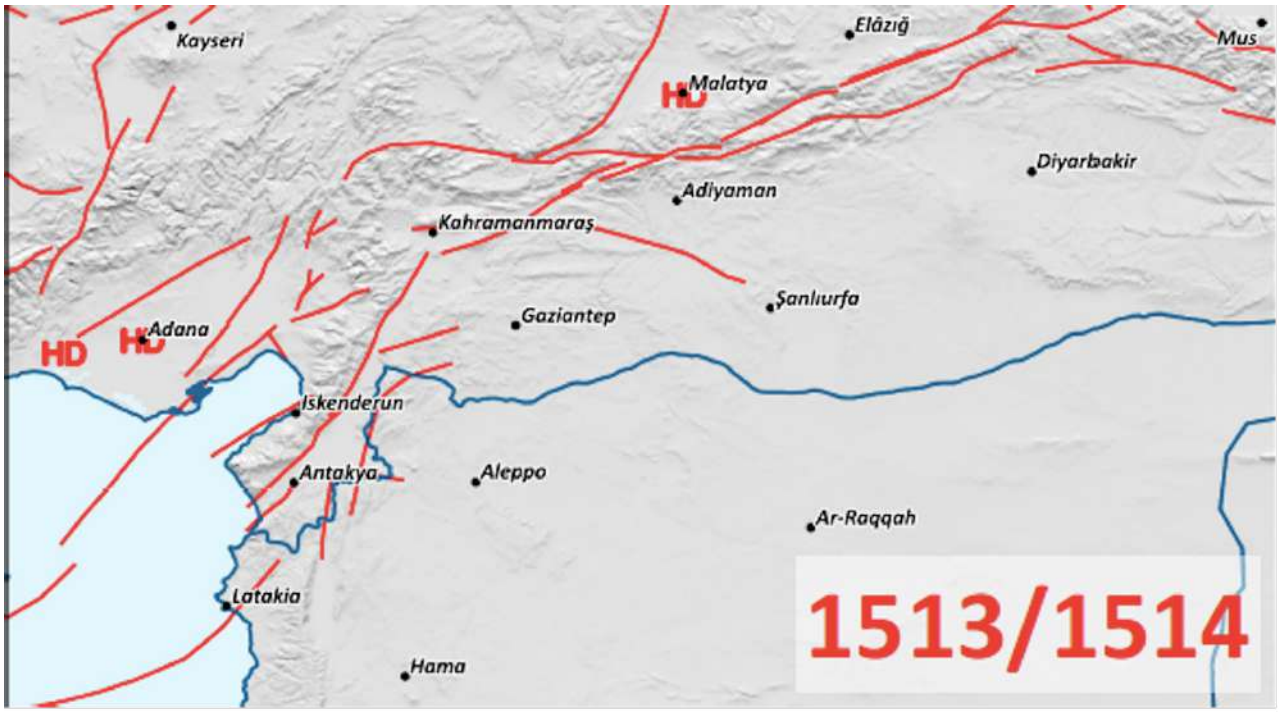

Fig. 2 – Macroseismic data points assessed for the earthquake of the year 1513/1514.

Sanudo copied the information on the earthquake, saving it for future use. It surfaced, with literary flourishes, in a Venetian chronicle of the years 1512-1514 (Barbaro, 16th c.), and after this chronicle was published (1842) in a 19th century geological treatise (Abich, 1882) that in its turn was one of the sources for Calvi (1941). Seismological studies and catalogues then followed in Calvi's wake, locating the earthquake either generically in "Cilicia" (the region to which Tarsus and Adana belong), or in Malatya, with Io 6 (Ergunay et al., 1967) or 7 (Soysal et al., 1981). Them came Ambraseys (1989), that went back to the somewhat romanced narration provided by Barbaro (16th c.), calculating Mw 7.4 and locating the epicentre not far from Maras, on the Pazarcik segment of the Eastern Anatolian Fault with I=IX (maximum intensity observed… but where?).

Subsequent seismological literature on the Eastern Anatolian Fault, both before and since the 2023 earthquake took and still takes the interpretation of the 1513 or 1514 earthquake provided by Ambraseys (1989) as absolute truth: the 1514 earthquake must have been located near Maras, with a M 7 at least and be a most likely predecessor of the February 2023 earthquake. Yet Ambraseys had changed his mind on this account, concluding that "without further details this information is insufficient to indicate the precise date and area over which this earthquake was felt" (Ambraseys, 2009). And, looking back to the original source of information on it, one must surely agree with him.

And how many such “large” earthquakes, based on information as poor as this, could be still taken for granted by overconfident geologists and seismologists, only because they happen to fit with some cherished theory?

References

Abich H.; 1882: Geologie des Armenisches Hochlandes, Wien.

Ambraseys N.N.; 1989: Temporary seismic quiescence. Geophysical Journal, 96, 311-331.

Ambraseys N.N.; 2009: Earthquakes in the Eastern Mediterranean and the Middle East: a multidisciplinary study of 2000 years of seismicity, Cambridge UK..

Barbaro D.; (16th c.): Storia Veneziana di D.B. dall’anno 1512 al 1515, Archivio Storico Italiano, vol. 77, 1842.

Calvi W.; 1941: Erdbebenkatalog der Turkei und Einiger Benaehbarter Gebiete, Yayinlanmamis, Rep. No 276, MTA Enstitüsu; Ankara.

De Bertoldi G.; 1888: Notizie e lettere di Andrea Alpago Medico in Damasco tratte dai Diarii di Marino Sanuto (Nozze Alpago-Novello-Valduga), Belluno.

Levi della Vida G.; 1960: «ALPAGO Andrea». Dizionario Biografico degli Italiani, vol. 2 (online).

Sanudo M.; 16th c.: I Diarii di M.S.(MCCCCXCVI-MDXXXIII) dall' autografo Marciano ital. cl. VII codd. CDXIX-CDLXXVII, vol. XVIII, Venezia, 1877.

Soysal H., Sipahioglu S., Kolcak D., Altinok Y.; 1981: Turkiye ve cevresinin tarihsel deprem katalogu MO” 2100 – MS 1900, TUBITAK Project, no. TBAG.341, Istanbul.

Corresponding author: viviana.castelli@ingv.it

Active Transpressive Faulting Along the High Atlas Mountains: the 8 September 2023, M_W 6.8, Morocco Earthquake

D. Cheloni[1], N. A. Famiglietti[2], R. Caputo[3], C. Tolomei[1], A. Vicari[2]

[1] Istituto Nazionale di Geofisica e Vulcanologia, Rome, Italy
[2] Istituto Nazionale di Geofisica e Vulcanologia, Sezione Irpina, Italy
[3] Department of Physics & Earth Sciences, Ferrara University, Italy

The 2023 Morocco earthquake sequence started on September 8th 2023 with a MW 6.8 event in the western sector of the High Atlas Mountains (Fig. 1), triggering significant aftershocks (including a M4.9 event). The earthquake caused extensive damage, claiming at least 2900 lives and affecting around 320,000 people. The seismicity in Morocco is attributed to the convergent motion between the African and Eurasian plates, with the Atlas region experiencing moderate seismic activity. Morocco's seismic history includes notable events like the 1994, 2014 and 2016 earthquakes in the Rif and Alboran Sea and the 1960 Agadir earthquake. The 2023 event, the strongest recorded in modern times, occurred in the High Atlas region. The seismic regime is characterized by a present-day compressional regime with active deformation along the High Atlas, accommodating about 1.7 mm/yr of WNW-ESE shortening (Serpelloni et al. 2007).

We employed Interferometric Synthetic Aperture Radar (InSAR) data from Sentinel-1 and ALOS-2 satellites to study ground displacement associated with the mainshock of the 2023 seismic sequence. The coseismic deformation field displayed a WSW-ENE elongated ellipse, suggesting a blind rupture. Two fault scenarios were investigated using geodetic modelling: an NNW-dipping fault in agreement with the focal mechanism and an SSW-dipping fault consistent with seismic data. We performed the geodetic modelling using the formulation of Okada (1985), following a standard two-steps procedure (e.g. Atzori et al., 2009; Cheloni et al., 2020). Both models effectively explained the observed data, indicating ambiguity in fault identification. Coulomb stress analysis implicated stress redistribution in aftershock occurrence.

Uncertainties in fault dip direction persisted, with seismic databases showing discrepancies in aftershock distribution. On the other hand, gravity and heat-flow data (Teixell et al., 2005), coupled with geodynamic considerations, favoured the SSW-dipping fault model. The analysis suggests that the high-angle fault model is unrealistic based on rheological arguments and regional geodynamic constraints. Integrating interferometric analyses with geological, tectonic, and seismological data could be crucial for resolving ambiguities in satellite-based models. The study therefore

underscores the complexity of fault identification and the need for a multidisciplinary approach in understanding seismic events.

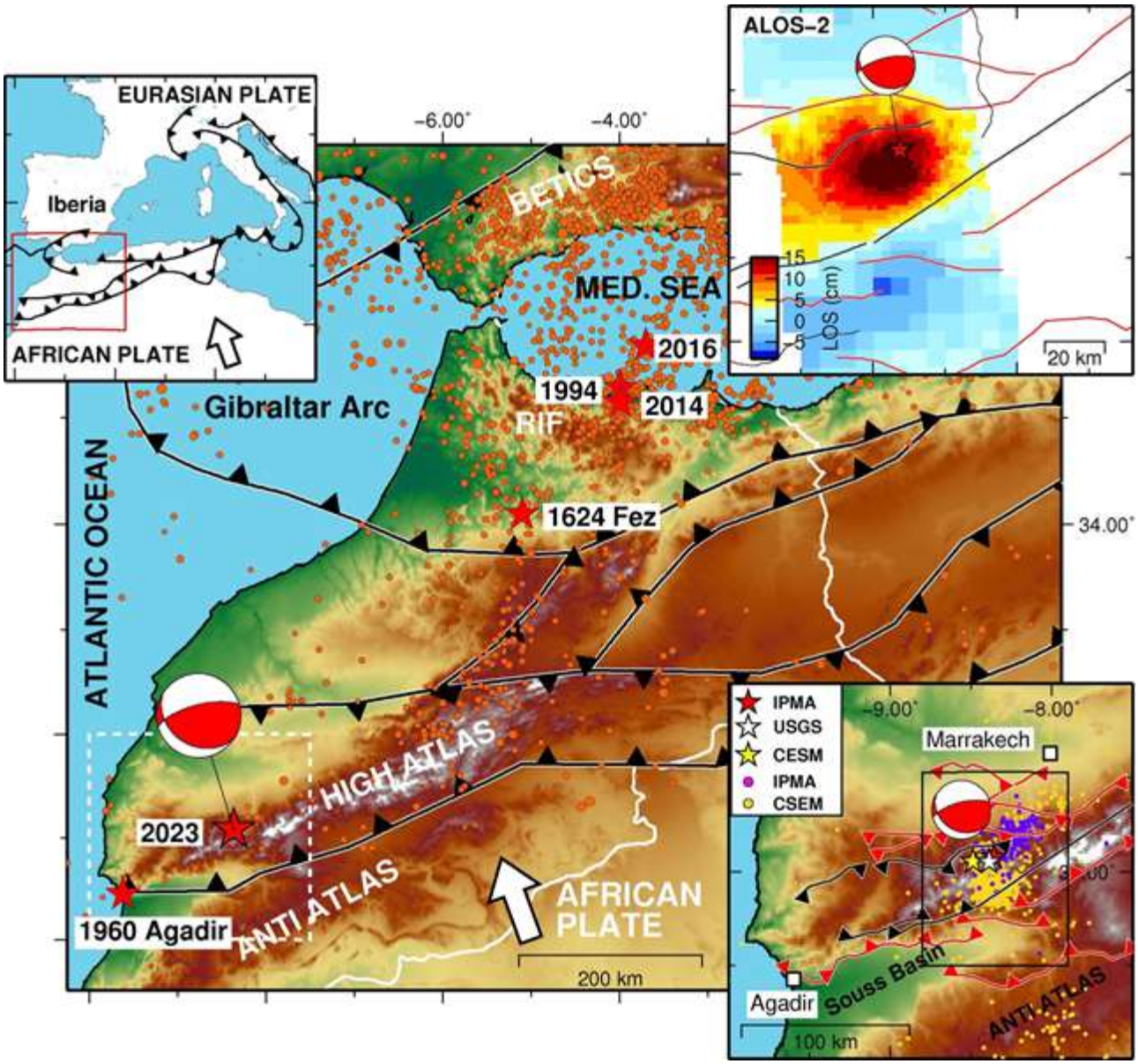

Fig. 1 – Seismotectonic settings of the study area. Solid barbed lines represent the major tectonic lineaments of the area. Orange circles are instrumental seismicity from the ESHM20 catalog (Grunthal and Whalstrom, 2012; Rovida and Antonucci, 2021); red stars are the greatest seismic events (M>6). The bottom inset is a sketch map of the active faults (Sebrier et al., 2016) and of the 2023 seismic sequence in Morocco; the box is the area of the right upper inset showing the ALOS-2 displacement map. The left upper inset is a tectonic sketch of the western Mediterranean region.

References

Atzori S., Hunstad I., Chini M., Salvi S., Tolomei C., Bignami C., Stramondo S., Trasatti E., Antonioli A., Boschi E.; 2009: Finite fault inversion of DInSAR coseismic displacement of the 2009 L'Aquila earthquake (Central Italy). Geophys. Res. Lett., 36(15), doi:10.1029/2009GL039293.

Cheloni D., Akinci A.; 2020: Source modelling and strong ground motion simulations for the 24 January 2020 M_W 6.8 Elazig earthquake, Turkey. Geophys. J. Int., 223, doi:10.1093/gji/ggaa350.

Grunthal G., Whalstrom R.; 2012: The European-Mediterranean Catalogue (EMEC) for the last millennium. Journal of Seismology, 16(3), doi:10.1007/s10950-012-9302-y.

Okada Y.; 1985: Surface deformation due to shear and tensile faults in a half-space. Bull. Seism. Soc. Am., 75(4), doi:10.1785/BSSA0750041135.

Rovida A., Antonucci A.; (2021): EPICA – European PreInstrumental Earthquake CAtalogue, version 1.1 [Data set]. Istituto Nazionale di Geofiscia e Vulcanologia (INGV), doi:10.13127/epica.1.1.

Sebrier M., Siame L., Zouine El M., Winter T., Missenard Y., Laturmy P.; 2006: Active tectonics in the Moroccan high Atlas. Geosciences, 338, doi:10.1016/j.crte.2005.12.001.

Serpelloni E., Vannucci G., Pondrelli S., Argnani A., Casula G., Anzidei M., Baldi P., Gasperini P.; 2007: Kinematics of the Western Africa-Eurasia plate boundary from focal mechanisms and GPS data. Geophys. J. Int., 169(3), doi:10.1111/j.1365-246X.2007.03367.x.

Teixell A., Avarza P., Zeyen H., Fernandez M., Arboleya M.-L.; 2005: Effects of mantle upwelling in a compressional setting: the Atlas Mountains of Morocco. Terra Nova, 17, doi:10.1111/j.1365-3121-2005.00633.x.

Corresponding author: daniele.cheloni@ingv.it

Geodetic Modelling of the 2023 M_W 7.8 and 7.6 Türkiye Earthquake Sequence

D. Cheloni[1], N. A. Famiglietti[2], A. Akinci[1], R. Caputo[3], A. Vicari[2]

[1] Istituto Nazionale di Geofisica e Vulcanologia, Rome, Italy

[2] Istituto Nazionale di Geofisica e Vulcanologia, Sezione Irpina, Italy

[3] Department of Physics & Earth Sciences, Ferrara University, Italy

On 6 February 2023 a M_W 7.8 earthquake occurred at 01:17 UTC in south-eastern Türkiye, near the Pazarcık district in Kahramanmaraş province close to the northern border of Syria (Fig. 1). It was followed 9 hours later by a M_W 7.6 earthquake approximately 90 km to the north, resulting in widespread destruction of buildings and significant loss of life. The largest aftershocks occurred on 6 February and 20 February, and their magnitudes have been assessed as M_W 6.7 and 6.4, respectively. According to the information provided by the Earthquake Department of the Disaster and Emergency Presidency (AFAD) there were over 50,000 reported fatalities and over 100,000 injuries from the devastating seismic sequence. The earthquakes were reported to be on different segments of the well-known left-lateral continental strike-slip East Anatolian Fault Zone (EAFZ), which is one of the two major active strike-slip fault systems in Türkiye, other being the right-lateral North Anatolian Fault Zone (NAFZ). In this study, we analyse the main features of the rupture process during the Kahramanmaras seismic sequence. In this respect, we use Interferometric Synthetic Aperture Radar (InSAR) and Global Navigation Satellite System (GNSS) data to investigate the ground displacement field (inset Fig. 1) and to infer, by using elastic dislocation modelling, the fault geometry and slip distribution of the causative fault segments.

We performed fault slip modelling using rectangular dislocations embedded in an elastic, homogeneous and isotropic half-space (Okada, 1985). We constrain the trace of the rupture surface of the earthquake doublet by examination of the displacements in the near-field InSAR data, extending the fault planes to a depth of 20 km running through the relocated seismicity (Lomax, 2023). The geodetic data is thus inverted for slip magnitude on each fault patch, inferring the optimal geometry iterating over dips and rake angles of the fault planes (Cheloni et al., 2019). In our inversion scheme, we consider 3 main fault segments with variable orientation for the M_W 7.8 main shock (Amanos, Pazarcık and Erkenek segments) and 2 main fault segments for the M_W 7.6 event (the Çardak-Savrun fault and an eastward segment located along the Nurhak complexity). In addition, we also include a segment located in the Narlı Fault Zone, a small splay

fault between the Pazarcık and Erkenek segments, and the Pütürge segment located between the previous 2020 Elaziğ seismic sequence and the north-eastern termination of the 2023 earthquake sequence.

The coseismic slip model on the preferred fault network geometry shows the activation of different fault segments during the 2023 Kahramanmaraş seismic sequence. In particular, the M_W 7.8 earthquake ruptured the Amanos segment to the south and the Pazarcık and Erkenek segment to the north (for a total length of about 300 km), in agreement with previous studies (e.g. Barbot et al., 2023), with little slip resolved along the Narlı segment where the mainshock nucleated (Melgar et al., 2023). The maximum slip is observed along the Pazarcık segment (peak slip of about 10 m). In contrast, the geodetic modelling of the M_W 7.6 earthquake, nucleated in the middle of the E-W trending Çardak-Savrun fault and propagated westward to the Savrun fault and eastward along the Nurhak complexity, indicated a more localized rupture primarily within the Çardak-Savrun segment (for a total length of about 150 km), with up to 15 m of slip. Finally, at the southern termination of the mainshock rupture, our modelling revealed that the 20 February M_W 6.4 aftershock activated the Antakya fault. Including the 2020 Elaziğ and 1971 Bingöl sequences, most of the EAFZ has been recently reactivated; similarly considering the well-known XX century earthquakes succession that reactivated the NAFZ (Stein et al., 1997), within the broader regional scale fault system associated to the lithospheric Arabia indenter, the N-S Dead Sea Trasform fault system could possibly be the focus of future ruptures.

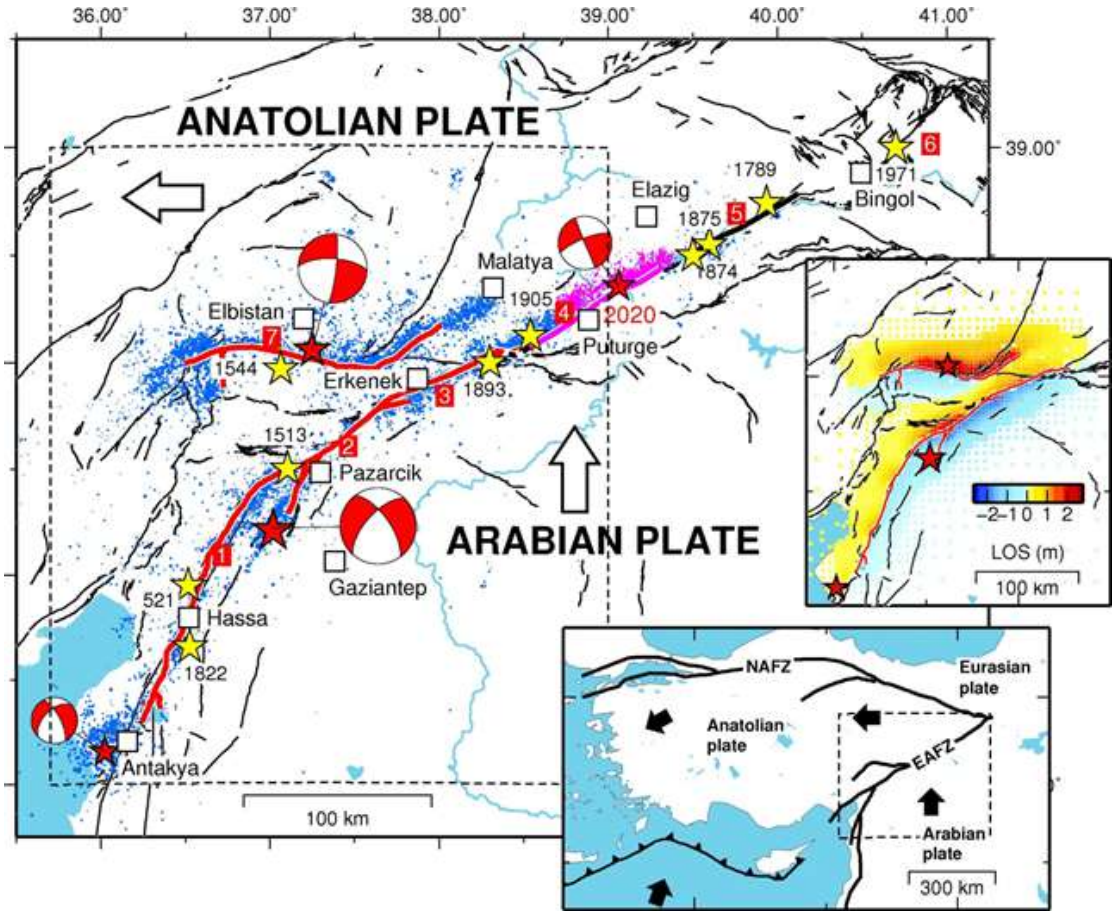

Fig. 1 – Seismotectonic settings of the study area. The solid lines are the main fault segments of the EAFZ (after Duman and Emre, 2013): (1) Amanos, (2) Pazarcık, (3) Erkenek, (4) Pütürge, (5) Palu, (6) Bingöl and (7) Sürgü-Çardak -Savrun segments, respectively. Seismicity: the blue dots are relocated aftershocks of the 2023 sequence (Lomax, 2023); red stars are the location of the main events and their moment tensor solution (KOERI); yellow stars represent the major historical events (Ambraseys 1989). The bottom inset shows a sketch of the main fault systems in and around Turkey, and the dashed box is the area of the main figure. The upper inset shows an example of InSAR data: the unwrapped interferogram showing the cumulative coseismic displacement field from the ALOS-2 ascending track.

References

Ambraseys N.N.; 1989: Temporary seismic quiescence: SE Turkey. Geophys. J. Int., 96(2), doi:10.1111/j.1365-246X.1989.tb04453.x.

Barbot S., Luo H., Want T., Hamiel Y., Piatibratova O., Javed M.T., Braitenberg C., Gurbuz G.; 2023: Slip distribution of the February 6, 2023 Mw 7.8 and Mw 7.6, Kahramanmaras Turkey earthquake sequence in the East Anatolian Fault Zone. Seismica, 2(3), doi:10.26443/seismica.v.2i3.502.

Cheloni D., Falcucci E., Gori S.; 2019: Half-Graben Rupture Geometry of the 30 October 2016 Mw 6.6 Mt. Vettore-Mt. Bove Earthquake. J. Geophys. Res., 124, doi:10.1029/2018JB015851.

Duman T.Y., Emre O.; 2013: The East Anatolian Fault: geometry, segmentation and jog characteristics. Geol. Soc. Lond. Spec. Publ., 372, doi:10.1144/SP372.14.

Okada Y.; 1985: Surface deformation due to shear and tensile faults in a half-space. Bull. Seism. Soc. Am., 75(4), doi:10.1785/BSSA0750041135.

Lomax A.; 2023: Precise, NLL.SSST-coherence hypocenter catalog for the 2023 Mw 7.8 and Mw 7.6 Turkey earthquake sequence, March 2023. https://zenodo.org/record/7699882#.ZAjBfuzMI-Q, doi:10.5281/zenodo.7699882.

Melgar, D., Taymaz T., Ganas A., Crowell B., Ocalan T., Kahraman M., Tsitorni V., Yolsal-Cevikbil S., Valkaniotis S., Irmark T.S., Eken T., Erman C., Ozkan B., Dogan A.H., Altuntas C.; 2023: Sub- and super-shear ruptures during the 2023 Mw 7.8 and Mw 7.6 earthquake doublet in SE Turkiye. Seismica 2(3), doi:10.26443/seismica.v.2i3.387.

Stein, R.S., Barka A.A., Dieterich J.H.; 1997: Progressive failure on the North Anatolian fault since 1939 by earthquake stress triggering. Geophys. J. Int., 128, doi:10.1111/j.1365-246X.1997.tb05321.x.

Corresponding author: daniele.cheloni@ingv.it

Seismic cycle in bituminous dolostones (Central Apennines, Italy)

M. Chinello[1], E. Bersan, M. Fondriest[1], T. Tesei[1], G. Di Toro[1,2]

[1]Dipartimento di Geoscienze, Università degli studi di Padova, Padua, Italy

[2]Istituto Nazionale di Geofisica e Vulcanologia (INGV), Rome, Italy

Central Apennines in Italy is one of the most seismically active areas in the Mediterranean (e.g., L'Aquila 2009, Mw 6.3 earthquake), with mainshocks and aftershocks propagating along extensional faults cutting km-thick sequences of carbonates. As a consequence, fault rock assemblages may record the seismic cycle under a wide range of loading conditions, temperatures, and fluid-rock interactions that activates several mechanical and chemical processes (i.e., fracturing, crystal-plastic deformation, dissolution and precipitation).

We document the interplay between these deformation mechanisms in normal faults cutting through bituminous dolostones in the Central Apennines. We sampled faults with increasing displacement (from 1-2 mm to a few meters) and with ultra-polished slip surfaces ("mirror-like surface").

Microstructural analysis of the slip zones show evidence of cataclasis, pressure solution and smearing of bitumen. Furthermore, the fault surfaces with higher displacement also record multiple slip events with ingression of carbonate-rich fluids and fragments of older slip zones sealed by calcite precipitation. Sometimes, these fragments derive from bitumen-rich slip zones with evidence of viscous flow. We propose that these microstructures preserve the evidence of multiple cycles of: high strain rate coseismic embrittlement (i.e., fragments of previous slip zones associated to fluid ingression), long-term aseismic or post-seismic creep (i.e., bitumen viscous flow and pressure solution) and fault locking/sealing (i.e., calcite precipitation). Since mirror-like surfaces can form both during seismic slip (Fondriest et al., 2013; Siman-Tov et al., 2015; Ohl et al., 2020; Pozzi et al., 2018) and aseismic creep (Tesei et al., 2017; Verbene et al., 2013), this study presents a natural case of different processes acting in the same slip zones throughout the seismic cycle.

References

Fondriest, M. et al.; 2013: Mirror-like faults and power dissipation during earthquakes. Geology 41, 1175–1178.

Ohl, M. et al.; 2020: Mechanisms of fault mirror formation and fault healing in carbonate rocks. Earth Planet. Sci. Lett. 530, 115886.

Pozzi, G., et al; 2018: A new interpretation for the nature and significance of mirror-like surfaces in experimental carbonate-hosted seismic faults. Geology 46, 583–586.

Siman-Tov, S., et al.; 2015: Fault mirrors along carbonate faults: Formation and destruction during shear experiments. Earth Planet. Sci. Lett. 430, 367–376.

Tesei, T. et al.; 2017: Friction and scale-dependent deformation processes of large experimental carbonate faults. J. Struct. Geol. 100, 12–23.

Verberne, B. A. et al.; 2013: Nanocrystalline slip zones in calcite fault gouge show intense crystallographic preferred orientation: Crystal plasticity at subseismic slip rates at 18-150 °C. Geology 41, 863–866.

Corresponding author: miriana.chinello@phd.unipd.it

Diffusivity analysis of clustered seismicity in Central-Southern Apennines

G.M. Cipressi[1], A. Vuan[4,5], M.A. Romano[4], G. Lavecchia[2,3], R. de Nardis[2,3]

[1]Department of Engineering and Geology, University "G. d' Annunzio" of Chieti-Pescara, Italy
[2]DiSPuTer - University of Chieti-Pescara 'G. d'Annunzio', Italy
[3]CRUST- Interuniversity Center for 3D Seismotectonics with Territorial Applications, Italy
[4]National Institute of Oceanography and Applied Geophysics (OGS), Italy
[5] National Institute of Geophysics and Volcanology (INGV), Italy

Seismic swarms are defined as a set of clustered earthquakes with high spatio-temporal variability and with the absence of a main shock. They can originate in different tectonic contexts related to the migration of deep fluids that can alter the stress field (Roland et al., 2009). In particular, the diffusivity parameter, defined by Shapiro et al. (1997) and linked to the migration of the hypocenters over time, allows us to associate the swarms' temporal duration with the rocks' permeability characteristics. Swarms characterized by long durations (years) and low diffusivity values (10^{-3}-10^{-2} m^2/sec) are associated with low permeability fault systems. On the contrary, shorter durations (days) and high diffusivity values (0.5-1 m^2/sec or greater) indicate the presence of highly permeable systems in which seismicity is induced by the rise of fluids at high pressures (Amezawa et al., 2021). We focus on the clustered seismicity in the central-southern Apennines, which extends from the south of L'Aquila to Benevento, to analyze the spatio-temporal characteristics of the swarms and the relationship between their temporal duration and diffusivity.

Compared to the rest of the chain, this sector is characterized by (1) low seismicity rates, which do not allow us to follow the evolution of seismicity and the mechanisms underlying it, and (2) a high seismic risk, as demonstrated by the strongest and most destructive sequences recorded within the historical catalogs which magnitude M ~ 7.

We analyzed the seismicity reported in the catalog of absolute locations CLASS (Latorre et al., 2022), which describes Italian seismic activity over the past 37 years (1981-2018). Additionally, we augmented the catalog within a 7-year time window (2012-2018) using a template matching technique (Vuan et al., 2018). This choice was made based on the optimal distribution and operation of the seismic network. The initial catalog is improved, lowering the completeness magnitude by more than one degree (+ 20,000 events with -1.5<M<5.0). This approach allowed the analysis and comparison of clustered seismicity in two catalogs with different time extensions and resolutions.

Clustered seismicity is defined relative to the background using a nearest-neighbour technique (Zaliapin & Ben-Zion, 2020). Due to the great spatio-temporal variability of the seismic phenomenon, no univocal methods in the literature can establish the spatial dimension and duration of the single cluster. The low seismicity rates of this area require a very detailed analysis

on a small space-time scale and different methodological approaches. For the spatial definition, we used the Kernel Density calculation to determine an event's density probability in each radius. The time duration is defined using the approach described by Roland et al. 2009 based on the evaluation of the percentage of seismicity rate.

We identified 53 polyphasic seismic clusters in the complete catalog (37-year time window), and 30 in the improved catalog (7-year time window). The clusters were subsequently divided into swarms and sequences. The diffusivity was calculated for each cluster using the Shapiro et al. (1997) relationship.

Most of the seismicity is expressed as swarm-type and characterized by high diffusivity values (≥ 1m^2/sec) with short temporal durations (days-months). This result confirms that the clustered seismicity is linked to highly permeable fault zones and the natural injection of fluids under pressure. The swarms present in this sector of the Apennine chain can, therefore, be linked to the deep migration of CO_2-rich fluids (Chiodini et al., 2004), which exploit pre-existing fault zones as a preferential path.

References

Amezawa Y., Taeta T., Kosuga M. (2021) Migration diffusivity as a controlling factor in the duration of earthquake swarms; https://doi.org/10.1186/s40623-021-01480-7

Chiodini, G., C. Cardellini, A. Amato, E. Boschi, S. Caliro, F. Frondini, and G. Ventura (2004). Carbon dioxide Earth degassing and seismogenesis in central and southern Italy, Geophys. Res. Lett., 31, L07615. doi: 10.1029/2004GL019480

Latorre D., Di Stefano R., Castello B., Michele M., Chiaraluce L. (2022) Catalogo delle Localizzazioni ASSolute (CLASS): locations (Version 1). Istituto Nazionale di Geofisica e Vulcanologia (INGV). https://doi.org/10.13127/class.1.0

Roland E., McGuire J.J. (2009) Earthquake swarms on transform faults https://doi.org/10.1111/j.1365-246X.2009.04214.x

Shapiro A.S., Huenges E., Borm G. (1997) Estimating the crust permeability from fluid-injection-induced seismic emission at the KTB site https://doi.org/10.1111/j.1365-246X.1997.tb01215.x

Vuan A., Sugan M., Amati G., Kato A. (2018). Improving the Detection of Low-Magnitude Seismicity Preceding the Mw 6.3 L'Aquila Earthquake: Development of a Scalable Code Based on the Cross Correlation of Template Earthquakes.doi:10.1785/0120170106

Zaliapin, I., & Ben-Zion, Y. (2020). Earthquake declustering using the nearest-neighbor approach in space- time-magnitude domain. Journal of Geophysical Research: Solid Earth, 125, e2018JB017120. https://doi.org/ 10.1029/2018JB017120

Corresponding author: gemmacipressi@gmail.com

Estimating the source parameters of a moderate earthquake using the second seismic moments

A.Cuius[1,2], A. Saraò[3], H. Meng[4], G. Costa[1]

[1] *Department of Mathematics and Geosciences, University of Trieste, Trieste, Italy*
[2] *National Institute of Geophysics and Volcanology, INGV, Roma, Italy*
[3] *National Institute of Geophysics and Applied Geophysics, OGS, Trieste, Italy*
[4] *Department of Earth and Space Sciences, Southern University of Science and Technology, Shenzhen, Guangdong, China*

Introduction

The study of earthquake generation and associated seismic parameters such as seismic moment, rupture size, rupture velocity and direction, and stress drop is crucial for understanding earthquake dynamics and the underlying physics of the seismic process. This information plays an important role in the estimation of ground shaking near the earthquake source and in the assessment of seismic hazard, even for low to moderate magnitude earthquakes.

The kinematic properties of small earthquakes are often difficult to determine, and simple models are often used to represent these events, although improved records show that source complexity is common even for small earthquake ruptures (e.g. Calderoni and Abercrombie, 2023 and reference therein).

A critical task in determining finite source attributes for moderate and low magnitude earthquakes requires good removal of path and site effects. To address this problem, several methods based on empirical Green's function (EGF) deconvolution have been developed in recent decades. Although the EGF offers several advantages, its application is associated with some difficulties, as there are often no focal mechanisms for small earthquakes and source effects have been observed even for low energy events (Calderoni et al. 2023).

The simplest general representation of an earthquake that contains information about the rupture extent and directivity is the point-source representation plus the variances or second-degree moments of the moment-release distribution. The hypocenter and the origin time of the earthquake correspond to the spatial and temporal average (first degree moment) of the release moment distribution. The information about the rupture extent, the characteristic duration and the direction of rupture propagation correspond to the variance of the moment distribution in the spatial, temporal and spatio-temporal domain (second-degree moments). Seismic moments are calculated from apparent durations measured from apparent source time functions (ASTF) for each station after removal of path effects. The ASTF is thus the projection of the rupture process onto the seismic ray path, and its properties also depend on the azimuth and take-off angles (e.g. McGuire, 2004). For a unilateral rupture, the ASTF observed from stations in the direction of propagation would be significantly shorter than the ASTF from stations in the opposite direction.

A major advantage of the second moments method is that it can theoretically be applied to all earthquakes, regardless of their magnitude and complexity, and without requiring the assumptions of an a priori source model (e.g. McGuire 2004; Meng et al., 2020; Cuius et al., 2023). It is also a consistent tool for evaluating scaling relationships between finite source attributes and earthquake magnitudes for large and small earthquakes and for resolving fault plane ambiguity.

However, the elimination of the path effect is crucial, and a biased ASTF calculation would lead to inaccurate calculations of the second seismic moments. However, there may also be other factors that influence the results of the second moments, even if the propagation effects have been correctly removed.

The aim of this study is to implement and test an efficient method for estimating source parameters and rupture directivity in near real-time for medium and small earthquakes. To achieve our goal, we implemented an approach developed by McGuire et al. (2004), which consists of calculating the second-degree seismic moments (Meng et al., 2020; Cuius et al., 2023). In this paper, we first perform a study with some synthetic tests to evaluate the influence of uncertainties related to our prior knowledge and observations on the resulting source parameters (Cuius et al. 2023). We then apply the method to a real earthquake in Italy and present the result.

Analysis of the sensitivity of the second moments tensor resolutions

To evaluate the sensitivity of the second moment solutions, we used synthetic ASTFs computed for a rectangular plane fault discretized by a grid of cells, each assigned a specific slip value. Full details can be found in Cuius et al. 2023. The input parameters used to model the ASTF for a magnitude Mw 4.6 earthquake source are listed in Tab. 1. We assumed that the epicenter was located in central Italy and approximated the fault as a 3.0 km box model (Fig. 1). The rupture area was divided into 12x12 cells, and the slip distribution and rupture time for the unilateral (Fig. 1a; 1b) and bilateral (Fig. 1d; 1e) scenarios were taken from a previous study of a similar magnitude earthquake (SRCMOD database - Mai and Thinbgaijam, 2014), with a focal mechanism of 247° strike, 46° dip and 40° dip. Using the actual station configuration, we calculated the ASTFs with a sampling frequency of 100 Hz and a source time function of 3 seconds. A uniform propagation of the rupture front with a rupture velocity of 2.75 km/s was assumed, which corresponds to 0.9 times the S-wave velocity in the source region. A simplified 1-D velocity model for central Italy was used to model the ASTF (Cuius et al., 2023).

	Unilateral rupture					*Bilateral rupture*				
	(km)	*(km)*	*(sec)*	*| (km/s)*	*Dir*	*(km)*	*(km)*	*(sec)*	*| (km/s)*	*Dir*
Input parameters	1.39	1.21	0.42	2.64	0.80	1.39	1.21	0.31	1.13	0.25

Tab. 1. Input parameters used to model the unilateral and bilateral scenarios for the characteristic rupture size (and), characteristic rupture duration ( ), centroid rupture velocity ( ) and directivity (dir).

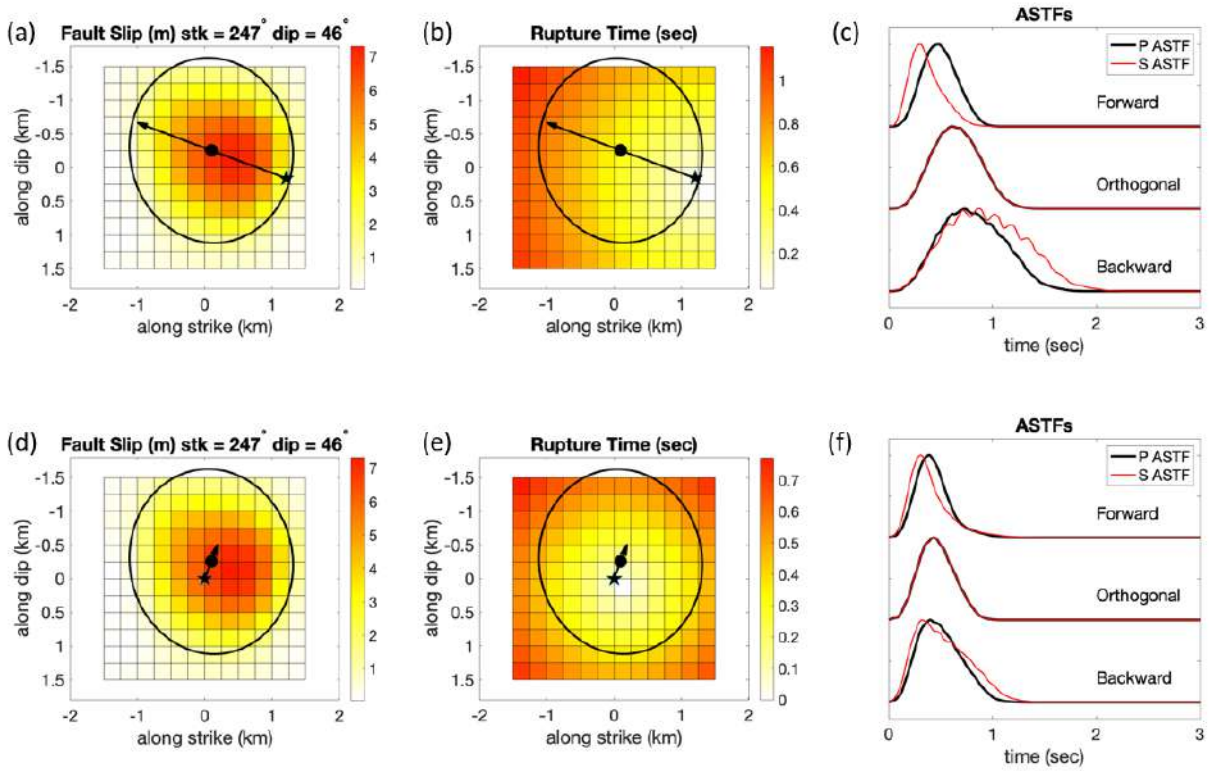

Fig 1. Input source for unilateral (A,B) and bilateral (D,E) scenarios. The star represents the hypocenter, the dot represents the centroid location, and the arrow indicates the rupture direction. Panels (C,F) show the ASTFs calculated from the respective models for three different azimuth directions.

To investigate how the uncertainties introduced by the input data may affect the solutions of the resolved second seismic moments, we used the bootstrap approach. In this technique, perturbations are introduced for each input parameter to be analyzed by generating 1000 variations around the mean value. An inversion is then performed to assess the impact on the mean and standard deviation of the resulting data. The workflow is summarized in Fig. 2.

We investigated the uncertainties associated with the ASTF, the location of the hypocenter, the station distributions around the source, the focal mechanism, and the velocity model used for ray tracing. Some of these tests are interrelated. For example, the uncertainties in the position of the hypocenter and the velocity model affect the calculated ray path, and both the different focal mechanism and station coverage affect the resolution of the fault plane. The uncertainties in the epicenter estimates were not investigated because they have negligible effects on the slowness vectors in the inversion of the second moments.

Results of the synthetic tests

The sensitivity analysis performed in this study shows that the uncertainties in the input data have different effects on the calculation of the source parameters and that an accurate measurement of the ASTF as well as the velocity model play the most important role in influencing the inversion process. The results of our tests (Tab. 2 and Fig. 3) show that the main source parameters, i.e. fracture size, swelling duration and centroid velocity, are generally well reproduced within the standard deviation. The source duration resulting from the inversion process is strongly influenced by the duration of the input ASTF, and even 10 % influences the inversion of the second moment tensor. In the case of dense instrumentation, the horizontal location of the earthquake can be well resolved, but the resolution of the earthquake depth is largely determined by the velocity model, and an inaccurate earthquake location can lead to uncertainties in the resolved second moments. Care must also be taken to avoid artifacts due to the discretization of the velocity model when the hypocenter is located at an interface between two layers with high velocity contrast.

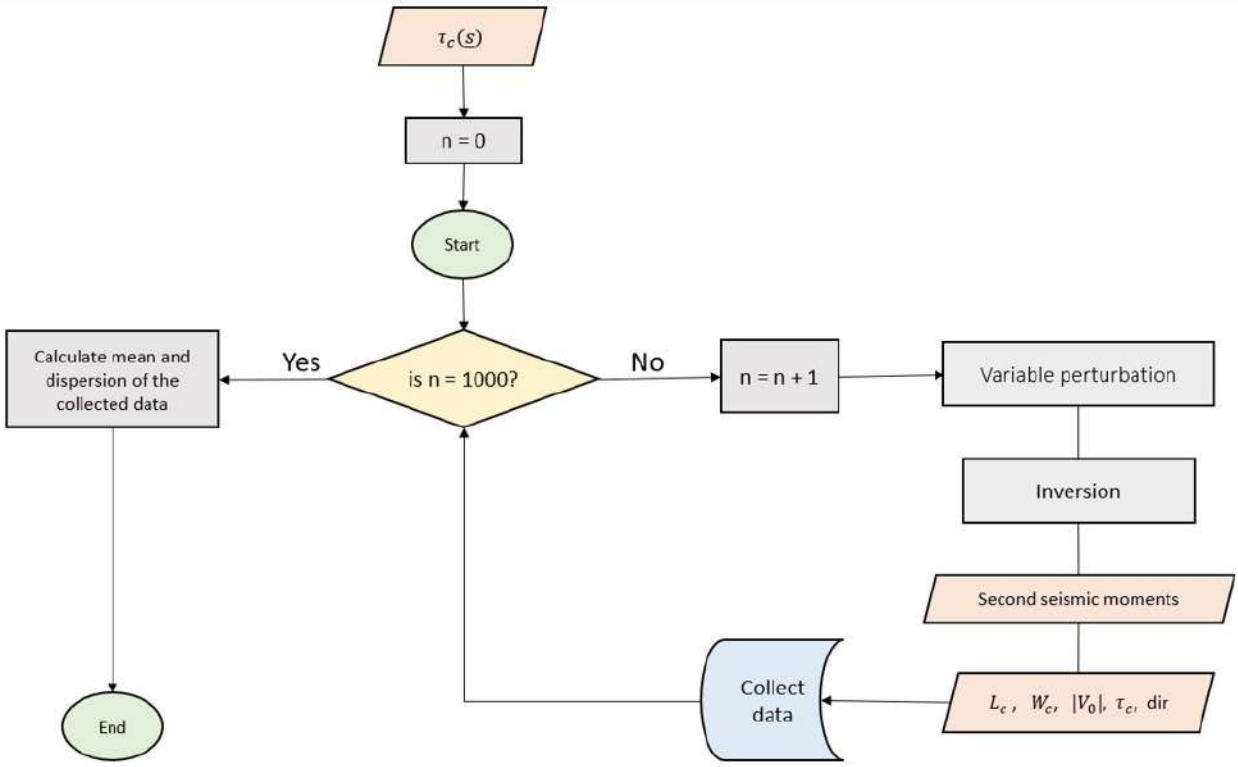

Fig. 2 Flowchart of the perturbation test. For each test, we computed 1000 random station configurations or perturbed input variables (depth, velocity model, focal mechanism, or observed c) with a given standard deviation. Then we performed the inversion and calculated the source parameters and directivity. Finally, we calculated the mean and dispersion of the output variables of the 1000 scenarios.

The values of the directivity depend on the ASTF duration, the choice of velocity model and the focal mechanism (Fig. 3). To ensure good resolution of the fault plane, good coverage of the ray path is critical for both upward and downward waves (McGuire, 2004). The component of rupture directivity along the dip can only be well determined if stations directly above the hypocenter are available, as the seismic rays are nearly horizontal at most other stations.

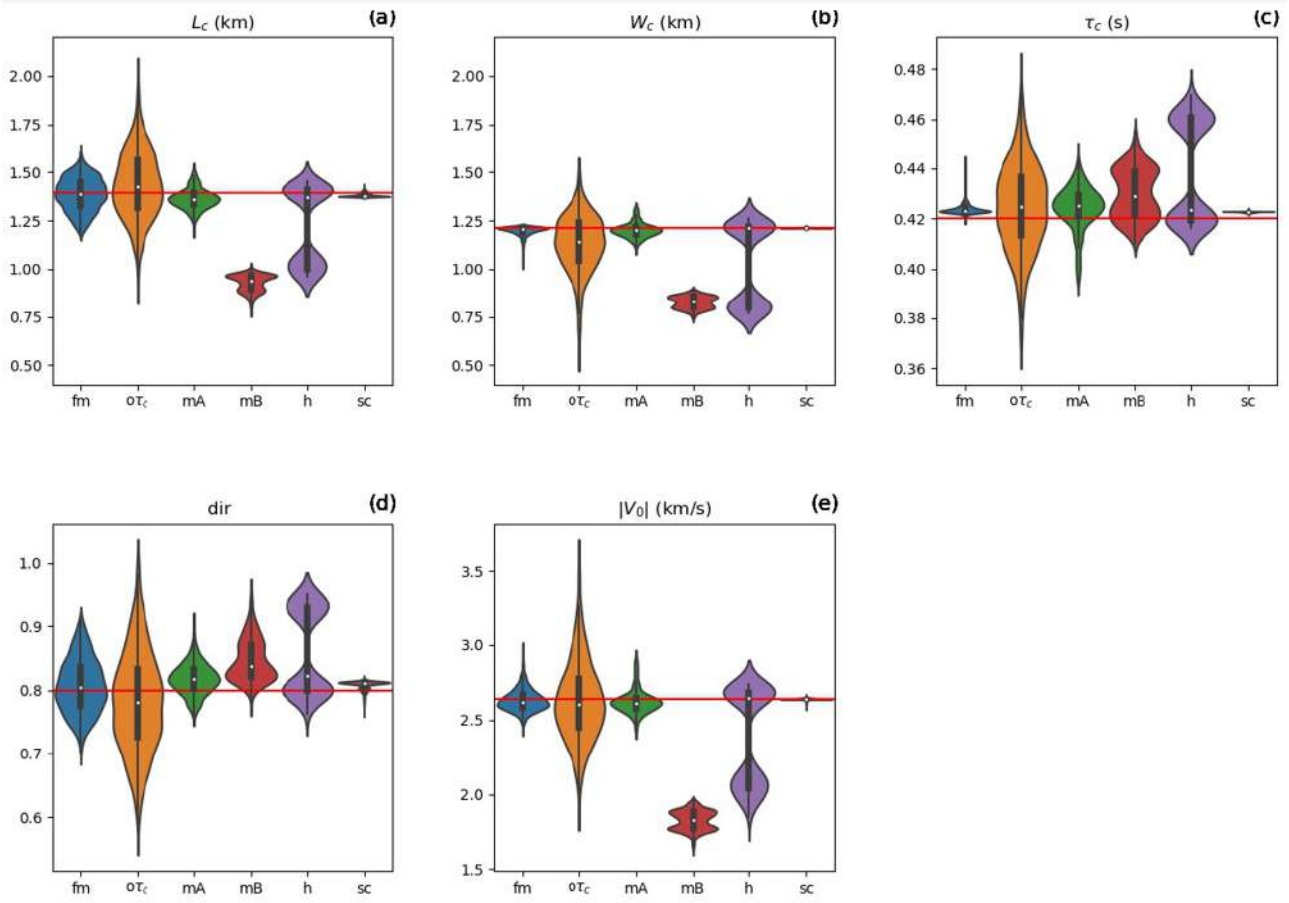

Fig. 3 Violin plots showing the Mean values and dispersions of each output variable resulting from each perturbation test given on the x-axis, i.e., focal mechanism (fm), observed τc (οτc), velocity models (mA and mB, respectively), hypocentral depth (h), and station configuration (sc) for the unilateral scenario. (A–E) represent the solutions for the characteristic length, characteristic width, source duration, directivity and centroid rupture velocity respectively. The y-axis indicates the value of the output variable. The shape of each violin graph reflects the numerical counts of the resulting value. The red line serves as reference, indicating the input value.

	Unilateral rupture					*Bilateral rupture*				
Output variables	*(km)*	*(km)*	*(sec)*	*| (km/s)*	*Dir*	*(km)*	*(km)*	*(sec)*	*| (km/s)*	*Dir*
not perturbed	1.39	1.21	0.42	2.48	0.8	1.38	1.21	0.31	1.13	0.25
Observed (sd = 10%)	1.4	1.13	0.42	2.63	0.78	1.41	1.18	0.31	1.14	0.25
Depth (sd = 1 km)	1.22	1.02	0.44	2.38	0.86	1.20	1.02	0.33	0.81	0.22
Stations' configuration	1.38	1.21	0.4	2.64	0.81	1.39	1.21	0.31	1.12	0.25
Focal Mechanism (sd str = 5°, sd dip = 5°)	1.39	1.20	0.42	2.63	0.81	1.38	1.20	0.31	1.11	0.25
A model (sd = 0.3 km/s)	1.36	1.20	0.42	2.62	0.82	1.37	1.21	0.31	1.10	0.25
B model (sd = 0.3 km/s)	0.93	0.83	0.43	1.83	0.85	0.96	0.84	0.32	0.48	0.15

Tab. 2. Results of the mean of each outcome variable calculated by the perturbation test for the unilateral and bilateral scenarios. For each test case, we report between brackets the standard deviation (sd) applied to the true value.

Application to real case: the Mw 4.6 Central Italy earthquake

The method was then applied to study the Mw 4.6 event of March 2023 in central Italy, using data from the Italian seismic network (RSN (Amato et al., 2008) and the Italian accelerometry network (RAN (Costa et al., 2022)). We compute the ASTFs through the EGF deconvolution using the P and S waves.

We calculated the second seismic moment to obtain information about the directivity and source parameters. The main parameters calculated with this method are the following = 1.16 km, = 0.615, = 0.14 s, = 1.86 m/s, dir = 64, stress drop = 7.37 MPa). The relatively small value of is possibly due to the poor resolution of the vertical component and can be explained by the interaction of two factors: the vertical rupture plane and the small number of stations in the immediate vicinity of the epicenter (< 5 km).

Conclusions

The use of second-moment tensors to determine the source parameters, including directivity, of moderate-magnitude earthquakes could be a valuable tool to improve our understanding of the source dynamics in a given area and to the risk mitigation. One possible application of the second-moments method to small earthquakes would be to identify portions of large faults that produce super-shear ruptures and correlate them with the geology of the fault zone. The second moments method also provides lower constraints on rupture velocity, which can be particularly useful for unilateral ruptures. However, before the results can be interpreted, the resolution limits of the method need to be known due to the possible uncertainties of the parameters used as inputs to the computational procedure.

To overcome the difficulties related to the analysis of noisy signals in the time domain, which can be an important limitation in the calculation of ASTFs and consequently the source duration for low magnitude events, an experimental approach based on the frequency domain is currently being developed. Although the frequency domain deconvolution-based method is currently more time consuming than time domain deconvolution, it can be used in situations where the determination of reliable ASTFs is difficult due to noise, which is often the case for low magnitude earthquakes.

Acknowledgements

We are deeply grateful to the Italian Department of Civil Protection – Presidency of the Council of Ministers for funding this research.

References

Amato, A., & Mele, F. (2008). Performance of the INGV National Seismic Network from 1997 to 2007. Annals of Geophysics.

Calderoni, G., and Abercrombie, R. E. (2023). Investigating spectral estimates of stress drop for small to moderate earthquakes with heterogeneous slip distribution: Examples from the 2016-2017 Amatrice earthquake sequence. J. Geophys. Res.: Solid Earth., 128, e2022JB025022, doi: 10.1029/2022JB025022

Costa, G., Brondi, P., Cataldi, L., Cirilli, S., Ertuncay, D., Falconer, P., ... & Turpaud, P. (2022). Near-Real-Time Strong Motion Acquisition at National Scale and Automatic Analysis. Sensors, 22(15), 5699.

Cuius, A., Meng, H., Saraò, A., & Costa, G. (2023). Sensitivity of the second seismic moments resolution to determine the fault parameters of moderate earthquakes. Frontiers in Earth Science, 11.

Mai, P. M., and Thingbaijam, K. K. S. (2014). SRCMOD: an online database of finite-fault rupture models. Seismol. Res. Lett. 85, 1348–1357. doi:10.1785/0220140077

McGuire, J. J. (2004). Estimating finite source properties of small earthquake ruptures. Bulletin of the Seismological Society of America, 94(2), 377-393.

Meng, H., McGuire, J. J., & Ben-Zion, Y. (2020). Semiautomated estimates of directivity and related source properties of small to moderate Southern California earthquakes using second seismic moments. Journal of Geophysical Research: Solid Earth, 125(4), e2019JB018566.

Corresponding author: arianna.cuius@ingv.it

A natural pump-probe experiment reveals nonlinear elastic properties along the Irpinia Fault, Southern Apennines

N. D'Agostino[1], S. Tarantino[1], P. Poli[2], M. Vassallo[1], G. Ventafridda[3], G. Festa[4], A. Zollo[4]

[1] Istituto Nazionale di Geofisica e Vulcanologia, Italy
[2] Dipartimento di Geoscienze, Università di Padova, Italy
[3] Acquedotto Pugliese SpA, Italy
[4] Dipartimento di Fisica, Università di Napoli Federico II, Italy

The conventional picture of the earthquake cycle implies that rupture is reached by progressive stress buildup until reaching fault's failure strength. Alternatively the failure strength may be altered by changes in pore pressure and/or properties of fault rocks driven by hydrologically-driven strain/stress transients. This scenario may be associated with significant modifications of the elastic properties of the crust potentially detectable with seismological tools. Natural oscillatory stress sources (tides, seasonal and multiannual hydrological stress variations) can thus been exploited to probe the time-dependent response of active fault zones to stress variations at various temporal and spatial scales and investigate time-dependent variations of its elastic properties (Delorey et al., 2021). In the framework of the INGV Pianeta Dinamico project MYBURP (Modulation of hYdrology on stress BUildup on the IRPinia Fault) a multidisciplinary (seismology, geodesy, geochemistry) study is carried out along the Irpinia Fault (Southern Apennines) to investigate the response of the crust to hydrological forcing associated to phases of recharge/discharge of karst aquifers in terms of time-dependent variations of its elastic and hydraulic properties. Charge/discharge phases of the karst aquifers in the Apennines cause significant seasonal and multi-annual strain transients (Silverii et al, 2019), that modulate the secular, tectonic deformation (~3 mm/yr extension across the Apennines). It has been previously observed that these seasonal and multi-annual transients correlate with the seismicity rate (D'Agostino et al, 2018) and seismic velocity variations (Poli et al., 2020). Recent studies (Silverii et al., 2016; D'Agostino et al., 2018) have shown the high sensitivity of the Irpinia Fault System (IFS) volume to hydrological stresses reflected in a complex, time-dependent response of deformation and seismicity. We performed a natural pump-probe experiment to assess the non-linear behavior of the seismogenic volumes in response to non-tectonic deformations. Seasonal horizontal strains associated with discharge and recharge of karst aquifers are used as the "pump". Coda wave interferometry demonstrates to be a powerful tool to probe time-dependent crustal

elastic properties. We computed seismic velocity variations using empirical Green's functions reconstructed by autocorrelation on continuous 14-year-long time series of ambient noise. We analyzed two different sites (co-located GPS and seismic stations), near and afar the IFS. We found that velocity variations are significant (~0.2%) nearby IF (shallow carbonates rocks), rather than far away from it. We compared the velocity variations near IF with the time series of Caposele spring discharge, temperature, horizontal deformation and seismicity rate (computed thanks to dense geodetic and seismic networks). Our observations are coherent at seasonal and multi-annual scales and can be explained with the same mechanism. At the time of the maximum peak of the discharge spring, representing a proxy of the hydraulic head, the seismic wave velocity is minimum, the dilation of crust is maximum and related to the opening of pre-existing cracks' system. The background microseismicity occurrence is favored by the hydrologically-related dilatation, superimposed to the ongoing tectonic extension. From the comparison between hydrological strain variations and velocity changes, we estimate a strain sensitivity of velocity change of ~-10^3 typical of worn crustal material and in good agreement with laboratory experiments. This non-linear elasticity regime suggests the presence of a multi-fractured and damaged crust subject to periodic seasonal phases of weakening/healing, potentially affecting earthquake nucleation processes.

References:

D'Agostino, N. *et al.* Crustal Deformation and Seismicity Modulated by Groundwater Recharge of Karst Aquifers (2018), *Geophys Res Lett* 45, 10.1029/2018GL079794.

Delorey, A. A., Guyer, R. A., Bokelmann, G. H. R. & Johnson, P. A. Probing the Damage Zone at Parkfield (2021), *Geophys Res Lett* 48, 10.1029/2021GL093518.

Poli, P., Marguin, V., Wang, Q., D'Agostino, N. & Johnson, P. Seasonal and Coseismic Velocity Variation in the Region of L'Aquila From Single Station Measurements and Implications for Crustal Rheology (2020), *J Geophys Res Solid Earth* 125, 10.1029/2019JB019316.

Silverii, F., D'Agostino, N., Métois, M., Fiorillo, F. & Ventafridda, G. (2016) Transient deformation of karst aquifers due to seasonal and multiyear groundwater variations observed by GPS in southern Apennines (Italy). *J Geophys Res Solid Earth* 121, 10.1002/2016JB013361.

Corresponding author: nicola.dagostino@ingv.it

Source parameter estimation by using Q tomography: the potentiality of exploiting large sequence of aftershocks

P. De Gori[1], F. P. Lucente[1], C. Chiarabba[1]

[1] *Istituto Nazionale di Geofisica e Vulcanologia (INGV), Rome, Italy*

The determination of seismic source parameters (seismic moment, source dimension, stress drop) play an important role in studying earthquake physics, for example to define fault interaction or to predict the ground shaking. However, the measurement of earthquake source parameters is affected by large uncertainties, and different approaches lead to large variability in results. One crucial aspect is the trade-off between attenuation (Q) and corner frequency (fc) in spectral fitting. Here we describe a method to solve the trade-off based on the fit of displacement spectra to find the source characteristics (corner frequency, fc, and the signal moment, Ω0) and the single-station attenuation operator (t), in addition to the site response. We follow a parametric approach based on the use of 3D Q seismic tomography and a bootstrap-based method for selecting the best spectra fit. The correction of attenuation with synthetic values derived by 3D attenuation tomography efficiently deals with the trade-off between source and path terms, leading to small uncertainties in the determination of source unknowns (fc and signal moment, Ω0), thus yielding constrained estimates of source parameters for low- to medium-magnitude earthquakes. We show an application to the Emilia 2012 seismic sequence, for which we computed the source parameters for 1240 aftershocks (from an initial dataset of 1748) with local magnitude ranging from 2.0 to 4.7 using the spectral fit from P and S waves. This approach gives the opportunity to infer the mechanical state of a complete fault system by taking advantage of the larger number of low-magnitude events (with respect to the largest ones) that always follow a major earthquake.

Corresponding author: pasquale.degori@ingv.it

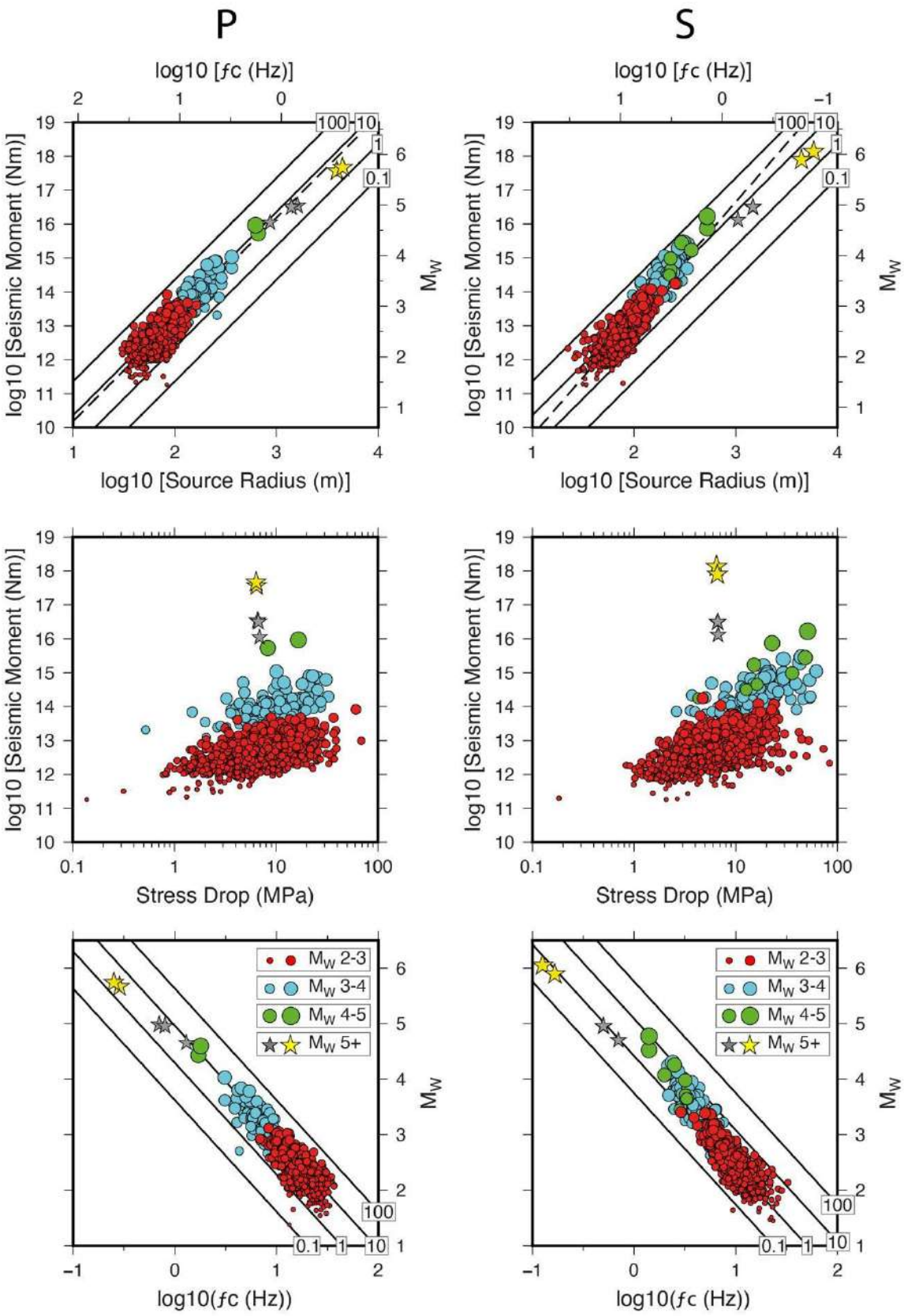

Fig. 1 – Source parameters determined from the fit of (a) P and (b) S spectra. For each phase, the seismic moment versus source radius (top), seismic moment versus stress drop (middle), and moment magnitude versus corner frequency (bottom) are reported. Aftershocks are drawn by circles sized and colored on the basis of their magnitude according to the legend on the bottom panels. Stars are M 5+ events. On the upper and bottom panels, black lines refer to constant stress-drop values expressed in MPa.

Calibration of the local magnitude scale (M_L) for eastern Cuba

E. Diez[1], D. Sandron[2], M. Cutie[1], M. Guidarelli[2]

[1] *Centro Nacional de Investigaciones Sismológicas (CENAIS), Santiago de Cuba, Cuba.*
[2] *Istituto Nazionale di Oceanografia e di Geofisica Sperimentale — OGS, Sgonico, Italy.*

The first attempt to create an international standard for quantifying earthquake energy was made by Richter (1935), who introduced the local magnitude (M_L) as the logarithm of the maximum amplitude from zero to the maximum peak measured with a Wood-Anderson (WA) instrument (with 2800 amplification and a natural period of 0.8 s [Anderson and Wood, 1925]), as follows:

$$M_L = log_{10}A(R) - log_{10} A_0(R)$$

where A(R) is the zero-to-peak amplitude in mm in a WA seismogram; R is the epicentral distance in km, and A_0(R) is the distance correction. The "calibration point" was determined by setting M_L=0 for a displacement amplitude of 1 thousandth of a millimeter at 100 km of epicentral distance. Recently, one hundredth of a millimeter at 17 km was chosen as an alternative anchor point (Hutton and Boore, 1987) and Uhrhammer and Collins (1990) corrected the static gain value for the WA instrument to 2080 (confirmed by Sandron et al. (2015) using data from an original WA instrument still in operation). In 2013, the International Association of Seismology and Physics of the Earth's Interior Magnitude Working Group (IASPEI, 2013) proposed the following general equation:

$$M_L = log_{10}(A) - nlog_{10}(R) - KR - C - S$$

in where A is the maximum amplitude in nanometers recorded by a simulated instrument such as WA with a static gain of 1; R is the hypocentral distance in kilometers; C is a constant; and S is the correction per station due to local conditions (Bormann and Dewey, 2012). The parameters n and K represent the geometric dispersion and the anelastic attenuation, respectively (Bakun and Joyner, 1984).

Several studies have been carried out to calibrate the M_L equation coefficients for different geographical areas around the world. In Cuba, in particular, different approaches have been used to determine local earthquake magnitudes since the establishment of seismological stations in 1964. Álvarez and Bune (1977) and Álvarez et al. (1999, 2000) estimated the parameters for magnitude calculation based on the results obtained from the evaluation of energy class K or K-class, a measure of earthquake strength or magnitude of local and regional earthquakes used in the countries of the former Soviet Union, Cuba and Mongolia. The first equation of M_L,

corresponding to the Richter magnitude scale for the Cuban territory, was proposed by Moreno and González (2001) and was based on the analysis of earthquake records using data from the old short-term stations installed at that time, which were quite limited in quantity and quality. Later, the seismic network was upgraded and converted to digital technology with the installation of broadband stations, which increased the station density in southeastern Cuba and enabled the calculation using digital recordings. With the new database, Moreno (2002) updated the parameters of the M_L considering a new data set. This equation is currently used by the Centro Nacional de Investigaciones Sismológicas (CENAIS). However, in the last 20 years, new stations with new instruments with higher amplification and wider frequency response and dynamic range have been established in the same study region (Diez Zaldívar et al., 2014 and 2022). To date, no comprehensive method has been developed in Cuba to estimate the parameters of the ML equation using many seismic stations and many years of recorded data. For this reason, it was necessary to carry out a study to recalibrate the parameters of the M_L equation with high accuracy and with a focus on the southeastern part of Cuba.

This study covered a geographical area between 19°–22° N and 73°–79° W. In this area, the predominant seismicity is characterized by an "interplate" behavior related to the Oriente fault zone, with a higher frequency of earthquakes that can reach a large magnitude (Mw > 6.0) and a depth of more than 20 km. More than 90% of the earthquakes that strike the country occur in this southeastern area of Cuba (Álvarez and Menendez, 1969; Álvarez and Bune, 1977; Moreno et al., 2002). However, moderate seismicity has also been associated with smaller faults in the interior of Cuba, which have caused some moderate earthquakes with significant damage (Chuy, 1999).

The data comes from the general catalog of the Cuban seismological service CENAIS (2023). Between 2011 and 2021, more than 60,000 earthquakes with fairly well-defined parameters were analyzed by CENAIS seismologists and different signal processing methods were applied, such as filtering, deconvolution with the instrument transfer function and simulation of the WA seismometer by the SEISAN software (Havskov and Ottemoller, 2000). Our selection (M_L in a range between 2 and 5 and at least four triggering stations) includes 7750 seismic events, and the final input dataset contains a total of 33 916 records with: Event ID, date, depth, horizontal component amplitudes, calculated epicentral hypocentral distance, and the number of stations recorded for each seismic event.

We set up the whole procedure of linear regression analysis in the Matlab environment, following Chovanová and Kristek (2018), to obtain the formula for the local order of magnitude in the IASPEI form. In a 3-step procedure, we: 1) removed the outliers; 2) searched for the parameters n, K and Si that minimize the unbiased sample standard deviation of the residuals; c) set the anchor point for the parameter C (1/100 millimeter at 17 km). The new formula for the local parameter M_L is thus defined as follows:

$$M_L = log_{10}(A) - 1log_{10}(R) - 0.003R - 1.963$$

The curve determined is somewhat less attenuated than the curve previously determined by Moreno (2002) for this area and lies between this curve and the curve determined by Hutton and Boore (1987) for California.

The correction values (S) found for the stations are consistent with the local geology, and we can conclude that the M_L scale proposed in this study can replace the local magnitude scale currently used in the routine work of CENAIS.

References

Álvarez, H., and A. Menendez (1969). Sismicidad de Cuba, Izv. Akad. Naukk S.S.S.R. Fizika Zemli 1, 74–78 (in Russian).

Álvarez, J. L., and V. I. Bune (1977). Seismic hazard assessment for southeastern Cuba, Izv. Akad. Naukk S.S.S.R. Fizika Zemli 10, 54–67 (in Russian).

Álvarez, L., T. Chuy, J. García, B. Moreno, H. Álvarez, M. Blanco, O. Expósito, O. González, and A. I. Fernández (1999). An earthquake cata- logue of Cuba and neighbour- ing areas, ICTP Internal Rept. ic/ir/99/1, Miramare, Trieste, Italy, 60, available at http:// iohanis.com/~leoalvar/papers/ ICTPcata.pdf (last accessed November 2023).

Álvarez, L., R. S. Mijailova, E. O. Vorobiova, T. J. Chuy, G. N. Zhakirdzhanova, E. R. Perez, L. M. Rodionova, H. Alvarez, and K. M. Mirzoev (2000). Terremotos de Cuba y áreas aledañas, in Sismicidad de Cuba y estructura de la corteza en el Caribe, J. L. Alvarez (Editor) Editorial Academia, La Habana, Cuba, 7–35 (in Spanish).

Anderson, J. A., and H. O. Wood (1925). Description and theory of the torsion seismometer, Bull. Seismol. Soc. Am. 15, no. 1, 1–72, doi: 10.1785/ BSSA0150010001.

Bakun, W. H., and W. B. Joyner (1984). The ML scale in central California, Bull. Seismol. Soc. Am. 74, 1827–1843.

Bormann, P., and J. W. Dewey (2012). The New IASPEI Standards for Determining Magnitudes from Digital Data and Their Relation to Classical Magnitudes, New Manual of Seismological Observatory Practice 2 (NMSOP-2), Deutsches GeoForschungs Zentrum GFZ, Germany, 1–4.

Chovanová, Z., and J. Kristek (2018). A local magnitude scale for Slovakia, Central Europe, Bull. Seismol. Soc. Am. 108, 5A, 2756–2763, doi: 10.1785/0120180059.

Chuy, T. (1999). Macrosísmica de Cuba y su aplicación en los esti- mados de peligrosidad y microzonación Sísmica, Tesis en opción al Grado de Doctor en Ciencias Geofísicas, Fondos del MES y CENAIS, 150 p. (in Spanish).

Diez Zaldívar, E. R., M. C. Mustelier, C. M. Moracén, R. P. Cláres, V. Poveda Brossard, Z. Yinxing, C. Yang, and W. Fengxia (2014). Modernización de la red sísmica cubana, Instalación, calibración y puesta a punto, Rev. Fac. Ing. UCV 29, 69–78 (in Spanish).

Diez Zaldivar, E. R., E. Priolo, D. Sandron, V. Poveda Brossard, M. Cattaneo, S. Marzorati, and R. Palau Clares (2022). Evaluation of the event detection level of the cuban seismic network, Seismol. Res. Lett. 93, 2048–2062, doi: 10.1785/0220220016.

Havskov, J., and L. Ottemoller (2000). SEISAN Earthquake Analysis Software, Seismol. Res. Lett. 70, 532–534, doi: 10.1785/ gssrl.70.5.532.

Hutton, L. K., and D. M. Boore (1987). The ML scale in southern California, Bull. Seismol. Soc. Am. 77, 2074–2094, doi: 10.1785/ BSSA0770062074.

IASPEI (International Association of Seismology and Physics of the Earth's Interior (2013). Summary of magnitude working group recommendations on standard procedures for determining earthquake magnitudes from digital data, available at http://download .iaspei.org/commissions/CSOI/ Summary_WG_recommendations_ 20130327.pdf (last accessed April 2023).

Moreno, B., and O. González (2001). Local magnitude scale for the eastern region of Cuba, in Sismicidad de Cuba y estructura de la corteza, J. L. Alvarez Gómez (Editor), Editorial Academia, La Habana, Cuba, ISBN: 978-959-02-0242-1 (in Spanish).

Moreno, B., M. Grandison, and K. Atakan (2002). Crustal velocity model along the southern Cuba margin. Implications for the tectonic regime at an active plate boundary. Geophys. J. Int. 151, 632–645.

Richter, C. F. (1935). An instrumental earthquake magnitude scale, Bull. Seismol. Soc. Am. 25, no. 1, 1–32.

Sandron, D., G. F. Gentile, S. Gentili, A. Sarao, A. Rebez, M. Santulin, and D. Slejko (2015). The Wood-Anderson of Trieste (northeast Italy): One of the last operating torsion seismometers, Seismol. Res. Lett. 86, no. 6, 1645–1654, doi: 10.1785/0220150047.

Uhrhammer, R. A., and E. R. Collins (1990). Synthesis of Wood– Anderson seismograms from broadband digital records, Bull. Seismol. Soc. Am. 80, 702–716.

Corresponding author: diez@cenais.cu

Insights on the seismotectonics of the Alps-Apennines transition zone, NW Italy, after the 2022 earthquake sequence near Genoa

E. Eva[1], M.G. Malusà[2] and S. Solarino[1]

[1] Istituto Nazionale di Geofisica e Vulcanologia, Osservatorio Nazionale Terremoti, Genoa, Italy

[2] Department of Earth and Environmental Sciences, University of Milano-Bicocca, Milan, Italy

In the years 2021-2022 three seismic sequences located respectively close to Savignone (August - October 2021), Borzonasca (February – March 2022) and Bargagli (September – October 2022) struck the area ENE of Genoa, in the region classically referred to as the transition between the Alps and the Apennines. According to the instrumental catalogues, seismic events in this sector are infrequent and of low magnitude and even the catalogues of historical seismicity do not report major seismic events. Nevertheless, the earthquake of September 22, 2022 in the Bargagli area (red star in Fig.1), reached a magnitude M_w 4.0. It was felt in a large area and caused minor damages to a cemetery and a church in Bargagli and in a nearby village, respectively. Given the low number of seismic events occurred in the area in the past, the three seismic sequences represent a valuable dataset to shade some light on how the convergence between Africa and Europe is presently accommodated across the Alps-Apennines transition zone. They are thus the topic of this study.

It must be remarked that according to the catalogue CPTI15, only few earthquakes with a magnitude comparable with the event in Bargagli have occurred near Genoa but none in the area of the 2022 earthquake. The first step of this study consisted then in a reappraisal of the events of the last century with an approach profiting from the instrumental data for the events of the last century stored at the Sismos database. In particular, historical seismograms and seismic bulletins provided a new location for the September 21, 1924 earthquake originally located offshore about five kilometres from the Ligurian coast (green star in Fig.1). Based on the results obtained, this earthquake locates near Bargagli (blue star in Fig. 1) and deserves attention in that it can provide insights on the relationship between recent and historical seismicity (Solarino and Eva, 2023). Although the new location has no particular implications for the seismic hazard of the area, however it represents an important information to be taken into account in the calculation of the return period.

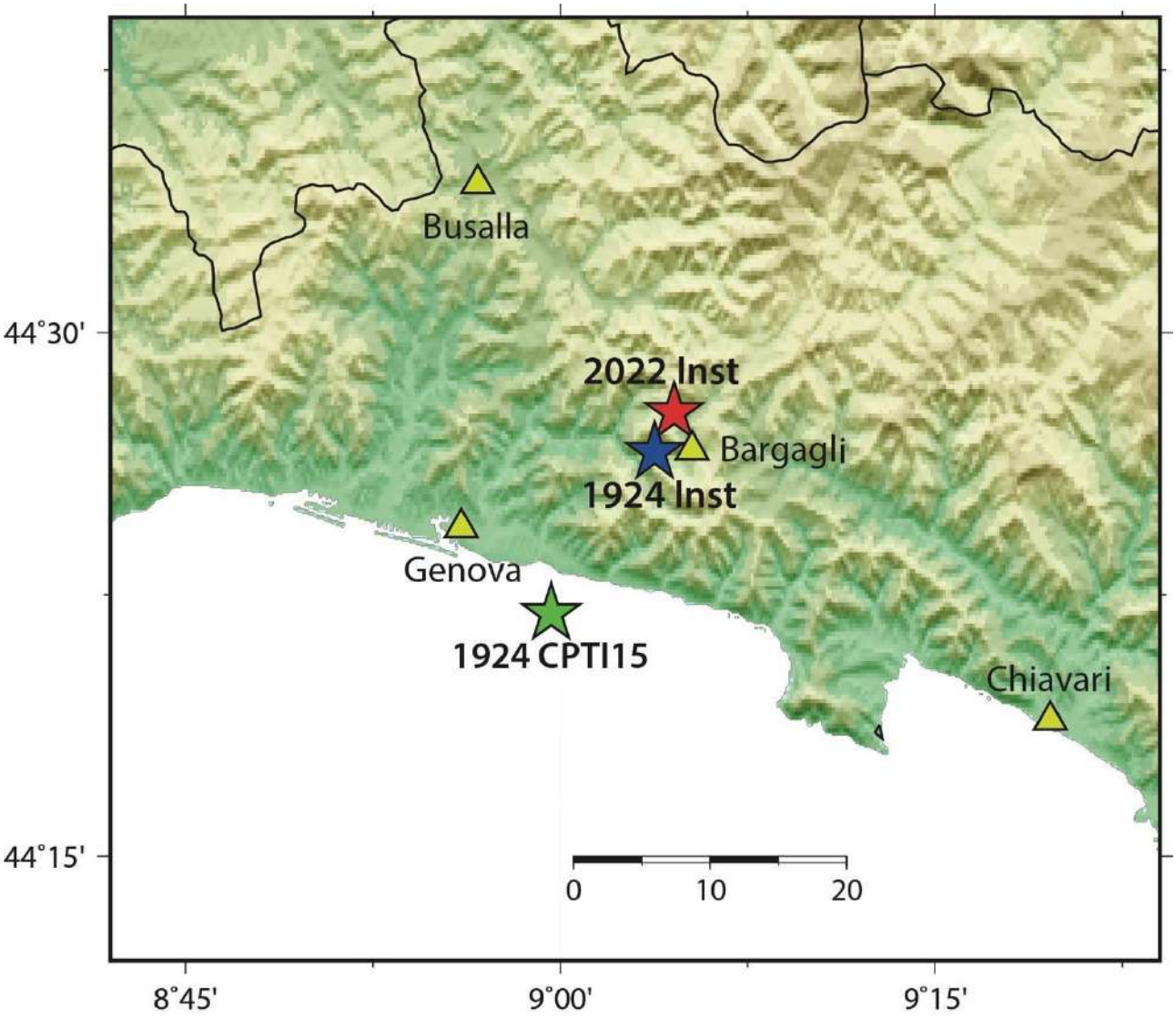

Fig. 1 – Locations of the 2022 and 1924 events. The latter was originally located using macroseismic intensities in the Ligurian Sea, some 5 km from the coast. Instrumental data shifted the event inland, close to Bargagli.

With the double aim of investigating on the seismotectonics of the area and its geodynamic implications, we analysed the events occurred between 1989 and 2022. After relocation using the HypoDD (Waldhauser and Ellsworth, 2000) location code, the events reveal a NE-SW alignment for the Savignone seismic sequence and NNW-SSE alignments for the Borzonasca and Bargagli sequences (Fig. 2). The Borzonasca seismic sequence plots in correspondence of the Villalvernia-Varzi-Ottone Fault, often considered as the transition between the Alps and the Apennines. The seismicity would favour the hypothesis of a kinematic activity in comparison with the Sestri-Voltaggio Fault, along which no seismicity is currently documented. The main-shock focal solutions are invariably strike-slip, with near-vertical NNW-SSE and NE-SW to ENE-WSW nodal planes (Fig. 2). The evident earthquake alignments in the study area mark active, km-scale fault planes in the upper crust, pointing to a scenario of distributed strike-slip deformation in the transition zone between the Alps and the Apennines (Eva et al., 2023). The NE-SW faults are inherited structures that underwent major Neogene rotations and are no longer suitably oriented to accommodate the northward motion of Adria relative to Europe.

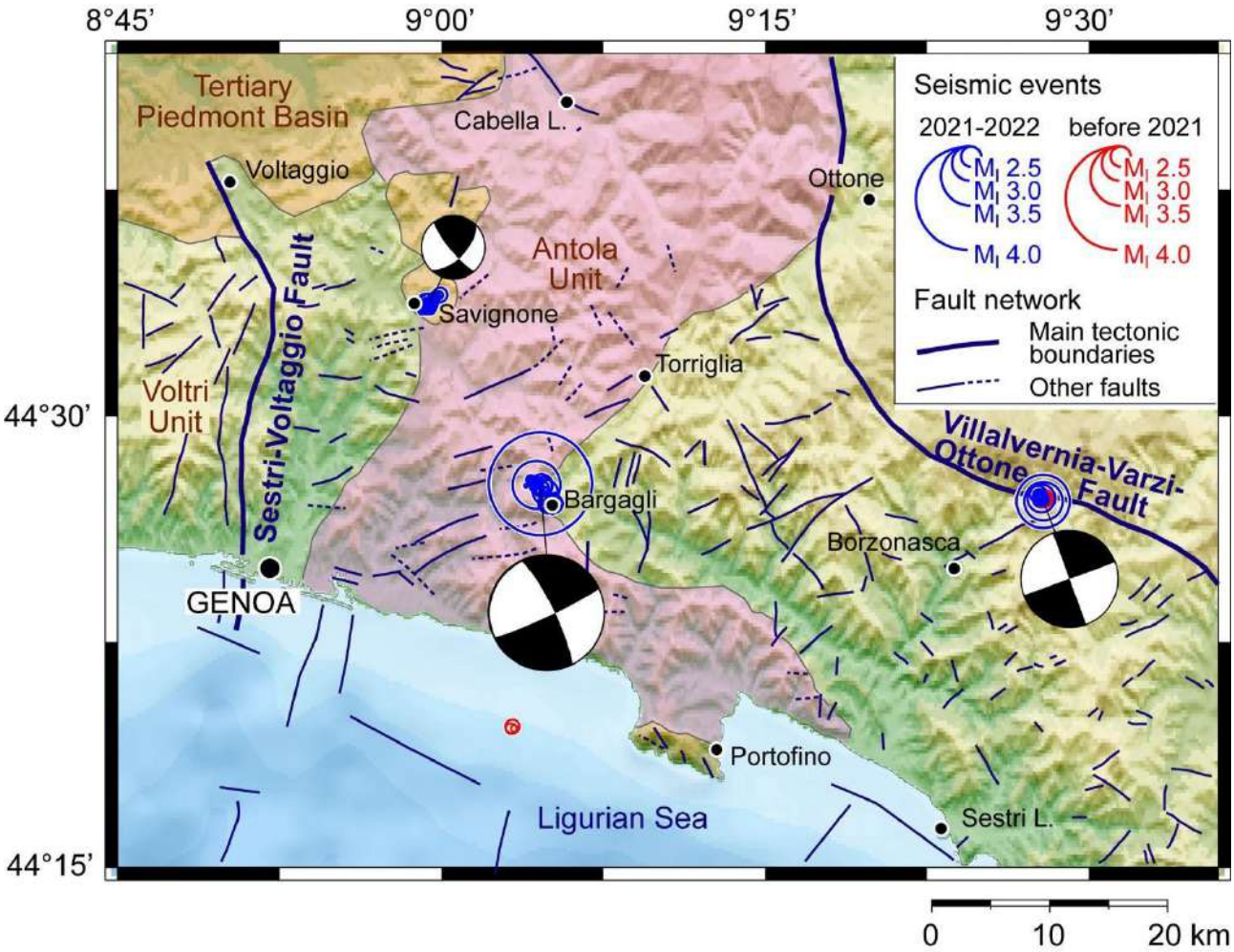

Fig. 2 – Hypo-DD locations of the earthquakes analysed in this study. The focal mechanisms of the main event of the three sequences (Savignone, Borzonasca and Bargagli) are strike-slip. Modified from Eva et al., 2023.

The Bargagli seismic sequence may reflect the formation of new NNW-SSE strike-slip faults in the upper crust that are more suitably oriented to accommodate the present-day stress field, consistent with the seismotectonic framework outlined by recent works in the nearby regions of the Adria-Europe plate-boundary zone (Eva et al., 2020). Our results highlight the important role of strike-slip faulting in the Adria-Europe plate boundary zone not only in the past, but also during its present-day evolution.

Low seismicity areas are often neglected due to the small size of the faults generating low magnitude events. However, our study shows that such areas may contribute to the understanding of the geodynamic evolution putting “a dowel in a larger puzzle”.

References

Eva, E., Malusà, M.G., Solarino, S.; 2020: Seismotectonics at the transition between opposite-dipping slabs (western Alpine region). Tectonics 39. https://doi.org/10.1029/2020TC006086 e2020TC006086.

Eva E., Malusà M.G., Solarino S.; 2023: The 2021–2022 Genoa seismic sequences reveal distributed strike-slip deformation in the Alps-Apennines transition zone, NW Italy Tectonophysics 868. https://doi.org/10.1016/j.tecto.2023.230101.

Solarino, S., Eva, E.; 2023: Il terremoto del settembre 1924 in mar Ligure e la sua relazione con il recente evento sismico a Bargagli (Genova, settembre 2022). Quad. Geofis. 184, 1–24. https://doi.org/10.13127/qdg/184.

Waldhauser, F., Ellsworth, W.L.; 2000: A double-difference earthquake location algorithm: Method and application to the northern Hayward fault, California. Bull. Geol. Soc. Am. 90 (6), 1353–1368. https://doi.org/10.1785/0120000006.

Corresponding author: elena.eva@ingv.it

Single-station ambient noise measurements to detect faults below the ground surface in the Fucino basin.

D. Famiani[1], F. Cara[1], G. Di Giulio[2], M. Vassallo[2], G. Milana[1]

[1] *Istituto Nazionale di Geofisica e Vulcanologia, Rome, Italy.*
[2] *Istituto Nazionale di Geofisica e Vulcanologia, L'Aquila, Italy.*

Microzonation studies generally focus their attention to the characterization of urban areas distinguishing stable zones from those prone to seismic amplification or unstable in general, including also those related to the presence of faults. In order to face this last task, the classical approach in the first-level of microzonation studies is based on geological evidence and information coming from previous studies which allows us to hypothesize the location of the seismic fault line. However, geological evidence or previous studies are often missing but there may be clues of the presence of hidden active faults that it is important to define for urban development or assessment. In all cases, the exact localization of the fault traces is preliminary to perform reflection profiles and seismic trenches to establish whether the faults are active or not.

In this study, we propose and illustrate a procedure that we applied in the Fucino basin (Central Italy) and that has been published in Famiani *et al.* (2022). The procedure is based on single-station microtremor recordings. In particular, in Famiani *et al.* (2022) we performed 88 single-station ambient noise measurements (Fig. 1) and used the horizontal-to-vertical spectral ratio (HVNSR) technique to investigate hidden faults in the Trasacco municipality located in the southern part of the Fucino basin, where microzonation studies pointed out hypothetical fault lines crossing the urban area with the Apennine orientation. The noise survey consisted of two steps: first, the measurement points were set in a regular grid geometry; second, we individuated areas where increasing the spatial density of measurements.

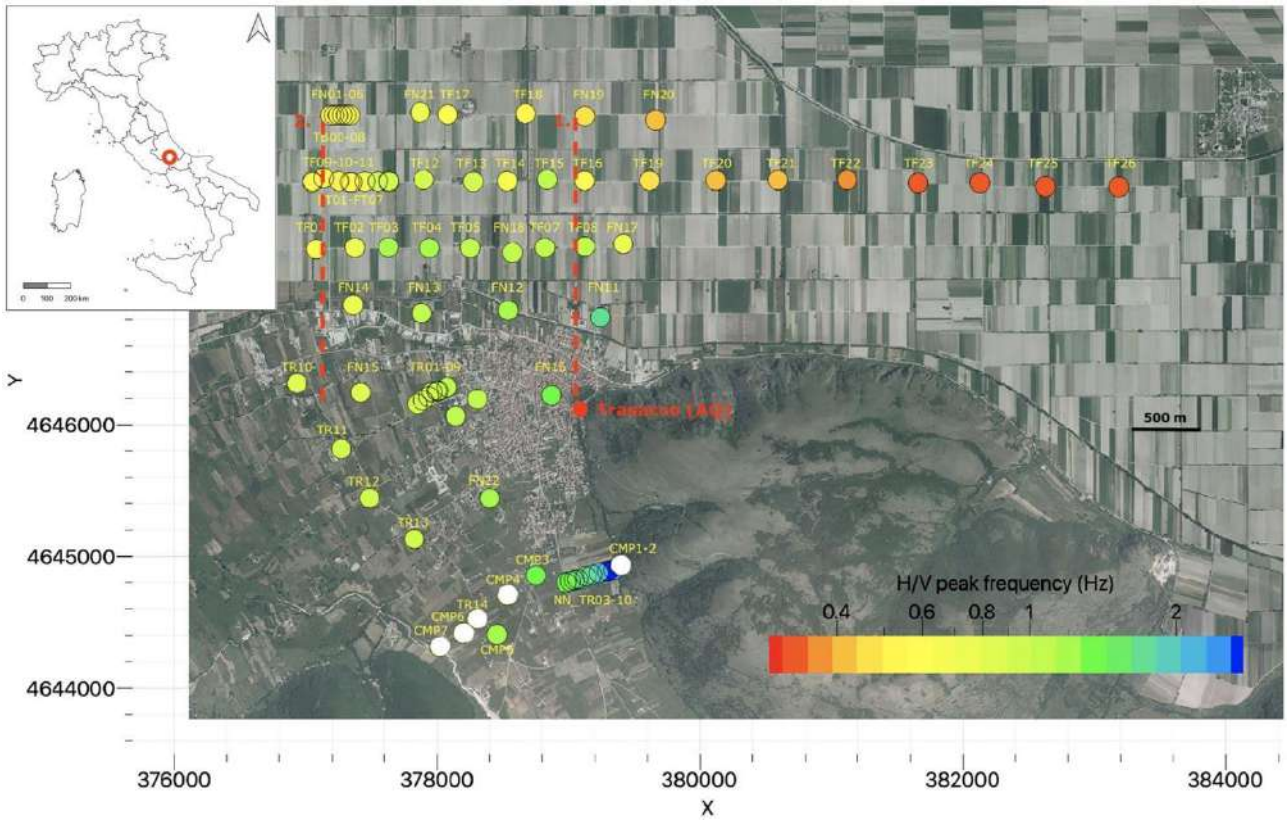

Fig. 1 - f0 results of the 88 HVNSR performed in the Trasacco municipality (modified from Famiani et al. 2022). The trend of the results suggests a deepening of the Quaternary Fucino basin towards east and the presence of a horst structure included between Section 1 and 2 in red dashed lines.

Results of HVNSR for all the measurements highlighted spatial variation of f0 along some transects (Fig. 1) which could also be represented in contour plots (Fig. 2) remarking similar trends of the interpreted seismic lines in Patruno and Scisciani (2021). In consideration of the availability of seismic stations, sometimes it was possible to perform several simultaneous recordings: in these cases the noise surveys acted as seismic arrays. It was then possible also to retrieve the dispersion characteristics of the surface waves, in this case using cross-correlation (CC) and FK analyses.

For some sites with nearby borehole log data availability, the HVNSR curves were inverted around the fundamental resonance (f0) using the aforementioned dispersion curves as constraints. This analysis allowed us to reconstruct some 1D shear wave velocity profiles and interpret results in terms of subsoil setting of geological features. Finally, we performed a rotational analysis of HVNSR for some specific transects of stations, highlighting localized polarization effects that we interpreted as due to the presence of the hidden fault in those positions. This interpretation was supported by available seismic reflection profiles for the area. This case study shows that the low-cost HVNSR technique is able to give preliminary indications of anomalous behaviors when crossing fault lines (Fig. 2).

These results are important for planning specific geophysical surveys, requested to validate the preliminary findings. Therefore, our approach can support microzonation studies, especially in urban areas where fault zones are involved, or in places designated for future developments.

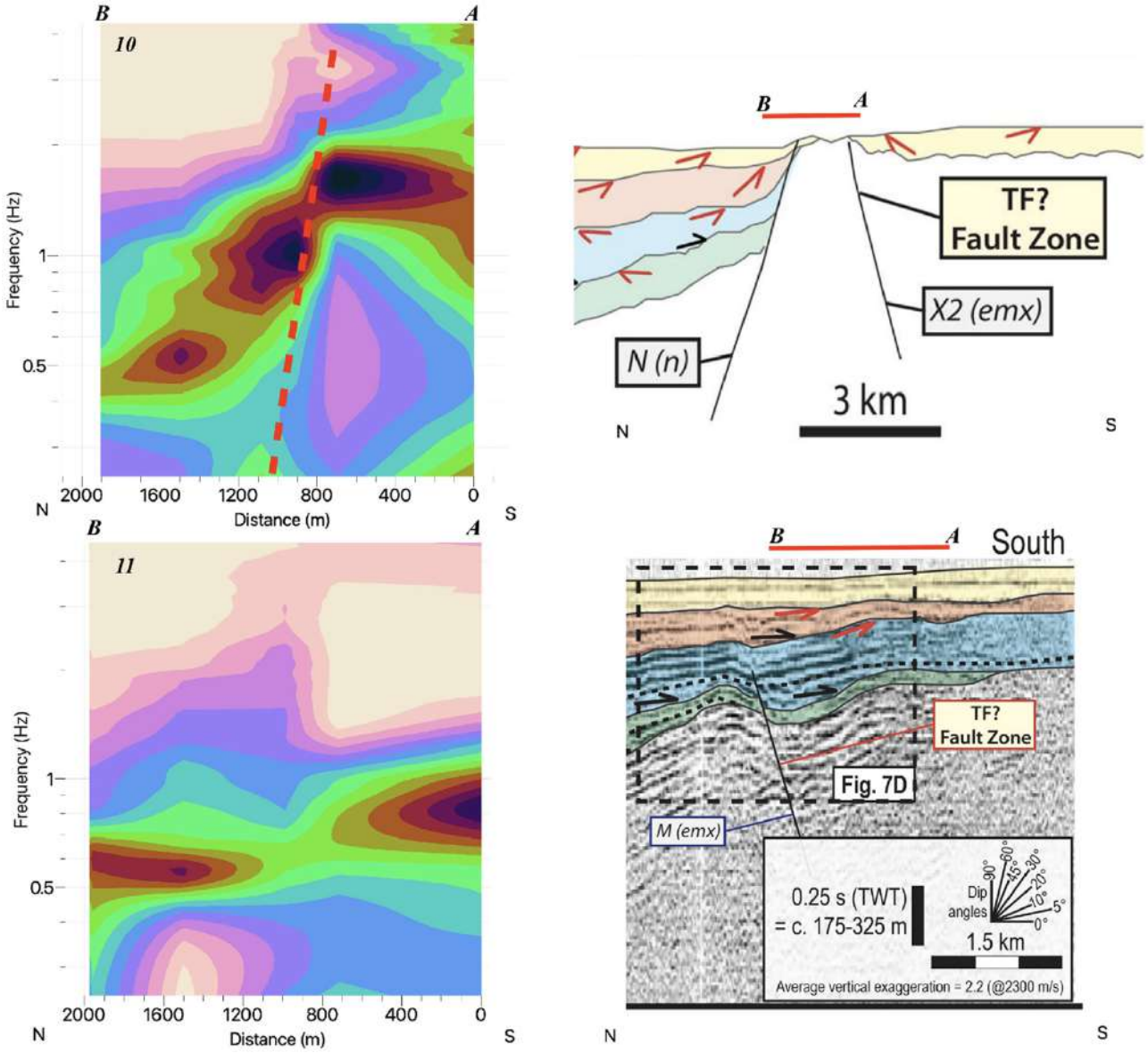

Fig. 2 - Example of HVNSR contour plots of Section 1 and 2 (see Fig. 1 for position) located along seismic lines interpreted in Patruno and Scisciani (2021) (from Famiani et al. 2022).

References

Famiani D., Cara F., Di Giulio G., Vassallo M. and Milana G.; 2022: *Detection of hidden faults within the Fucino basin from single-station ambient noise measurements: The case study of the Trasacco fault system*. Frontiers in Earth Science, 10, p.937848.

Patruno S. and Scisciani V.; 2021: *Testing normal fault growth models by seismic stratigraphic architecture: The case of the Pliocene-Quaternary Fucino Basin (Central Apennines, Italy)*. Basin Research, 33(3), pp.2118-2156.

Corresponding author: daniela.famiani@ingv.it

Early results of a systematic revision of Ferrarese seismicity of the 13th-15th centuries.

A. Faoro[1], R. Camassi[1], V. Castelli[2]

[1] Istituto Nazionale di Geofisica e Vulcanologia - Sezione di Bologna, Bologna, Italy,
[2]Istituto Nazionale di Geofisica e Vulcanologia - Sezione di Bologna, Bologna/Ancona, Italy

Within the PRIN 2020 project NASHA4SHA [Fault segmentation and seismotectonics of active thrust systems: the Northern Apennines and Southern Alps laboratories for new Seismic Hazard Assessments in northern Italy] and in order to improve our general knowledge of the seismic record of the Ferrara area, we are proceeding to examine the ancient local narrative sources, not only to find information on “unknown” or “forgotten" earthquakes, but primarily to improve the understanding of earthquakes already known through a comprehensive study of the original texts which are relied on by the reference studies of the CPTI15 catalogue (Rovida et al., 2022).

Far from limiting ourselves to searching for “earthquake news” and taking them out of context, as we tended to do in the "heroic" days at the dawn of modern historical seismology, we attempted here a more ambitious undertaking. Our aim is to examine original earthquake news in their cultural framework, to check their intrinsic quality and "authoritativeness", and thus to improve the quality of general knowledge on historical earthquake observations. Using data extrapolated from narrative written sources (such as chronicles and annals) to compile earthquake catalogues sometimes risks isolating the data themselves and undermining their evaluation. Indeed, news taken out of the context that reports them, while useful in itself, remain impoverished, like archaeological findings whose site, location and circumstances of discovery are unknown.

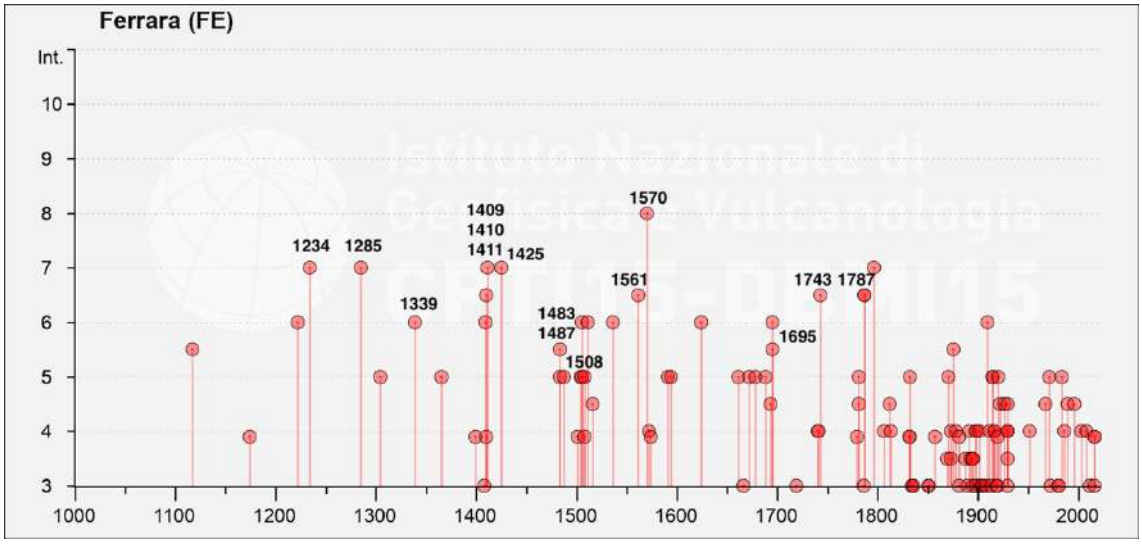

Fig. 1 – Seismic history of Ferrara (1000-2020) from Locati et al. (2022). The dated earthquakes are local ones (i.e. with epicentral location "in" Ferrara or in the "Ferrarese").

Up to now our study has considered some dozen earthquakes with M ≥3.5, dated between 1234 and 1495, of which 11 are located by the CPTI15 catalogue (Rovida et al., 2022) in Ferrara, 3 in Modena, while a couple of cases are unknown to the CPTI15 catalogue. A couple of these earthquakes were never studied at all, in several cases epicentral parameters are derived from reference studies that are almost 20 years old, and in 5 cases even 40 years old. The informative basis for these earthquakes, as summarized in Locati et al. (2022) and Rovida et al. (2022) is rather poor. In many case information on a single locality is available from a single source, whose intrinsic value and reliability are also questionable.

The preliminary results of the revision work are generally an improvement of the intensity estimates. In a few cases, the studied earthquakes turned out to be doubtful or completely fake.

Year	Mo	Da	Ho	Mi	Ax	Ref	**Np**	Imx	Mw	NOTE Prel.
1234	03	20			Ferrara	ENEL85	5	7	5,14	Doubtful
1249	09				Modena	GUAL07	4	7-8	4,93	i.p.
1285	12	13			Ferrara	ENEL85	2	7	5,14	Doubtful
1339	11	16	14	10	Ferrara	GUAL07	1	6	4,72	Doubtful
1346	02	08			Modena	GUAL07	1	5	4,16	i.p.
1379	02	10			Ferrara	-	-	-	-	i.p.
1409	08	17	00	35	Ferrara	GUAL07	1	6	4,72	Pending revision
1410	05	09	22	30	Ferrara	ENEL85	3	6-7	4,93	Doubtful
1411	01	09	02		Ferrara	GUAL07	1	7	5,14	Doubtful
1425	08	10	19		Ferrara	POS85		7	4,72	Pending revision
1474	03	11	20	30	Modena	ENEL85	12	6	4,30	Pending revision
1483	*03*	*03*	*22*		*Ferrara*	*ENEL85*	*1*	*5-6*	*4,51*	Pending revision
1487	01	11	15	40	Ferrara	GUAL07	12	5	3,70	Pending revision
1495	12	5			**Ferrara**	-	-	-	-	Pending revision

Tab. 1 – The list of earthquakes in the Ferrara and Modena currently under revision (time window: 1234-1500; M≥ 3.5).

References

ENEL; 1985: Studi e indagini per l'accertamento della idoneità tecnica delle aree suscettibili di insediamento di impianti nucleari per le Regioni Piemonte, Lombardia e Puglia: indagini di sismica storica. Rapporti tecnici predisposti da ISMES-SGA, Roma.

Guidoboni E., Ferrari G., Mariotti D., Comastri A., Tarabusi G. and Valensise G.; 2007: Catalogo dei forti terremoti 461 a.C.-1997, http://storing.ingv.it/cfti4med/

Locati M., Camassi R., Rovida A., Ercolani E., Bernardini F., Castelli V., Caracciolo C.H., Tertulliani A., Rossi A., Azzaro R., D'Amico S. and Antonucci A.; 2022: Database Macrosismico Italiano (DBMI15), versione 4.0. Istituto Nazionale di Geofisica e Vulcanologia (INGV). https://doi.org/10.13127/DBMI/DBMI15.4

Postpischl D.; 1985: Catalogo dei terremoti italiani dall'anno 1000 al 1980. Progetto Finalizzato Geodinamica. "Quaderni de «La Ricerca Scientifica»", n.114, v.2B.

Rovida A., Locati M., Camassi R., Lolli B., Gasperini P., Antonucci A; 2022: *Catalogo Parametrico dei Terremoti Italiani (CPTI15), versione 4.0*. Istituto Nazionale di Geofisica e Vulcanologia (INGV). https://doi.org/10.13127/CPTI/CPTI15.4

Corresponding author: andrea.faoro@ingv.it

A re-analysis of micro-earthquakes for characterising debated faults in the Esaro valley (Northern Calabria)

H. Fernandez[1,2], G. D. Chiappetta[1], A. Schibuola[1,3], M. La Rocca[4], S. Gentili[1], L. Peruzza[1]

[1] *OGS, Trieste, Italy*
[2] *Università degli Studi "G. d'Annunzio" Chieti - Pescara, Italy*
[3] *Université Gustave Eiffel, Marne-la-vallée, France*
[4] *Università della Calabria, Italy*

The study takes place in the northern part of Calabria, Italy, where a potentially active and capable fault is mapped across the Farneto del Principe's dam, on the Esaro river. A complex set of geological, geophysical and seismological studies performed jointly by the University of Chieti-Pescara (INGEO) and the Istituto Nazionale di Oceanografia e di Geofisica Sperimentale (OGS) are ongoing to estimate the fault seismic activity and its potential surface displacement during major earthquakes.

Our study area lies on the Calabrian Arc that represents the emerging part of the Calabrian accretionary wedge. This region is one of the most seismic-active regions in Italy, with some earthquakes with M ≈ 7.0 (e.g. Feb 1783, *Jacques et al., 2001*). The Esaro valley is located in the Crati Basin in which we find several west-dipping faults with a N-S strike like the Roggiano Fault and the Firmo Fault. As it is reported in the ITHACA database, the Firmo Fault is 16.2 km long, and its surface expression might be crossing the Farneto del Principe's dam but its position, behaviour and activity are debated in the literature. To fill this lack of information and provide more details about the fault, a multidisciplinary study started in 2022, funded by the *Consorzio di Bonifica integrale dei Bacini Settentrionali del Cosentino* .

The historical seismicity around the dam, analysed by mainly 2 historical databases (CPTI15 and ASMI) shows that the 20 km area around the dam seems to be affected only by superficial and moderate earthquakes (M < 5.5); a stronger but more distant earthquake occurred in 1184 earthquake, in the Crati valley, M≈7. Concerning the instrumental seismicity, we collected and compared data from 2 different catalogues: INGV catalogue (1985-2023, 5 events with M > 3.5) and the University of Calabria catalogue (May 2013-Dec 2023, 0 event with M > 3.5). In these 2 datasets, we can notice that events are less frequent in the closest area around the dam; conversely, there is a concentration of shallow events (~10 km deep) in the North (Pollino area) and in the South-East. Furthermore, we find deeper events (> 30 km deep) that are related to the subduction zone, on the west.

As our main goal is to obtain information about the seismicity and the seismic activity of the faults in the surroundings of the Farneto del Principe' dam, we will focus only on events within a constrained area around the dam (Fig. 1). We remove the deep events as they are not related to the same tectonic context of the fault system we are interested in. These criteria give us a list of about 150 events (Fig. 1).

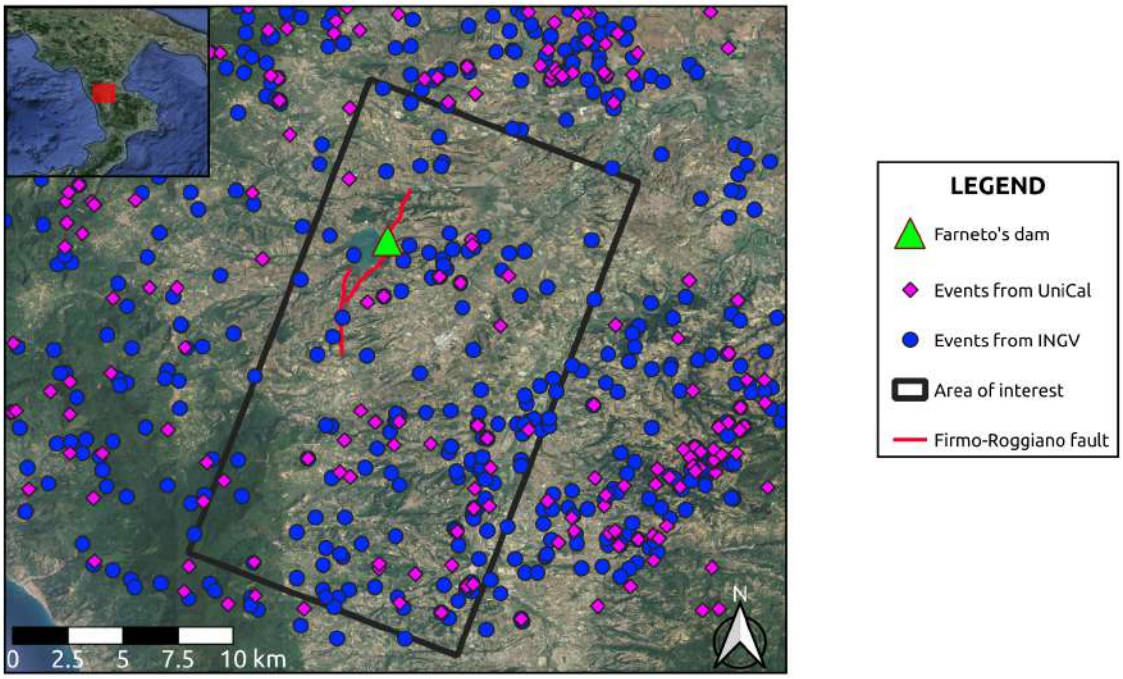

Fig. 1 - Seismic activity on the Esaro valley, Northern Calabria, Italy (1985-2023)

One of the main problems for using different catalogues is that the same event can have a slightly different localisation depending on the catalogue. Since we are studying a very local area, we need to harmonise our list and have the most precise location as possible for each event. Thus, we collect waveforms from the University of Calabria' network, for every event in our new dataset. This will allow us to do, for each station and event, a re-picking of the P- and S- phases, in order to perform a uniform re-localisation of our selected earthquakes.

The re-localisation process is ongoing and is carried out using different codes: Hypo71 (*Lee et al., 1972*), HypoEllipse (*Lahr, 2012*) and Hyposat (*Schweitzer, 2001*). First results show that a small part of the re-localised events has now migrated out of the area of interest, mainly on the west and the northeastern sides. Another interesting feature is a kind of clustering with an E-W trend and 5-20 km deep, just eastwards of the dam.

In our study area, we only have earthquakes with small magnitudes (maximum M≈3) so the focal mechanisms were not released by the national and international agencies. We can now analyse our re-localised events to have indications about the stress regime and the kinematics of the fault.

References

Jacques E.; 2001: Faulting and earthquake triggering during the 1783 Calabria seismic sequence. Geophysical Journal International, Volume 147, Issue 3, December 2001, Pages 499–516.

Lahr J.C.; 1999, revised 2012: HYPOELLIPSE: a computer program for determining local earthquake hypocentral parameters, magnitude, and first-motion pattern: U.S. Geological Survey Open-File Report 99–23, version 1.1, 119 p.

Lee W.H.K., Lahr J.C.; 1972: HYPO71: A computer program for determining hypocenter, magnitude, and first motion pattern of local earthquakes (p. 100). US Department of the Interior, Geological Survey, National Center for Earthquake Research.

Schweitzer J. 2001: HYPOSAT - An enhanced routine to locate seismic events. Pure and Applied Geophysics.

Corresponding author: hfernandez@ogs.it

High-resolution seismic depth imaging challenges across the 1980 (Ms 6.9) Southern Italy earthquake fault scarp at Pantano di S. Gregorio Magno (SA)

G. Ferrara[1], P.P. Bruno[1,2], L. Improta[2]

[1] Dipartimento di Scienze della Terra, dell'Ambiente e delle Risorse, Università degli studi di Napoli 'Federico II', Napoli, Italy
[2] Istituto Nazionale di Geofisica e Vulcanologia, Roma, Italy

In this study, we present initial findings and interpretations derived from an high-resolution seismic dataset, both 3D and 2D, obtained at Pantano di San Gregorio Magno (SA). The data were collected during two field surveys, one in 2005 (the majority of the 2D lines, as detailed in Bruno et al., 2010) and another in 2022, as part of the TESIRA project (i.e., TEst Site IRpinia fAult; Bruno et al., 2023), a collaborative effort involving Istituto Nazionale di Geofisica e Vulcanologia (INGV) and Consiglio Nazionale delle Ricerche (CNR). The seismic surveys focused on the imaging of the basin across a surface scarp resulting from the Ms 6.9, 1980 Irpinia earthquake (Pantosti & Valensise, 1990).

Notably, pre-stack depth migration (PSDM: see Yilmaz, 2001) is crucial for improving the accuracy of shallow seismic reflection images and the measured velocity distribution before stacking, particularly in the presence of complex near-surface conditions (Bradford et al., 2006). However, a comprehensive understanding of the p-wave velocity distribution in the subsurface is crucial for this purpose. In this context, the efficacy of pre-stack migration combined with full-waveform inversion could prove crucial in providing information to iteratively enhance the velocity model and the associated seismic imaging of this complex environment.

We show here the preliminary depth images resulting from pre-stack and post-stack depth migration of the 2D profiles and 3D volume. To enhance PSDM imaging through the refinement of the velocity model, we employed two distinct approaches within SeisSpace ProMAX®: the layer stripping method and the Deregowsky method. Both techniques utilize the Residual Move-Out (RMO) values picked from common image points. In certain instances, PSDM proved effective in enhancing depth image quality compared to post-stack data. Conversely, due to the intricate near-surface conditions characterized by substantial lateral velocity variations, post-stack migration outperformed PSDM in some cases. This implies that our assessment of the background velocity model remains inaccurate.

Even in this early phase of depth imaging, all seismic profiles and the volume clearly depict the intricate splays associated with the 1980 Irpinia fault and its connections to other active segments of the Pantano San Gregorio Magno fault system. The tectonic influence of these faults on basin development and sedimentation is also evident.

References

Bradford, J.H., Liberty, L.M., Lyle, M.W., Clement, W.P., and Hess, S., 2006 Imaging complex structure in shallow seismic-reflection data using prestack depth migration, Geophysics, 71, 6, b175–b181.

Bruno, P.P.G.; Castiello, A.; Improta, L., 2010, Ultrashallow seismic imaging of the causative fault of the 1980, M6. 9, southern Italy earthquake by pre-stack depth migration of dense wide-aperture data. Geophys. Res. Lett., 37.

Bruno, P.P.G., Ferrara, G., Improta, L., Maraio, S., Di Fiore, V., Iacopini, D., Fusco, M., Punzo, M., Paoletti, V., Cavuoto, G., and De Martini, P.M., 2023, High-resolution 3-D geophysical imaging across a seismogenic fault: the TEst Site IRpinia fAult (TESIRA) project, EGU General Assembly 2023, Vienna, Austria, 23–28 Apr 2023, EGU23-11176, https://doi.org/10.5194/egusphere-egu23-11176.

Pantosti, D.; Valensise, G., 1990, Faulting mechanism and complexity of the November 23, 1980, Campania-Lucania earthquake, inferred from surface observations. J. Geophys. Res. Solid Earth, 95, 15319–15341.

Yilmaz, O., 2001, Seismic data analysis (2 volumes), in Investigations in Geophysics; SEG: Tulsa, OK, USA; Volume 10, p. 1000.

Corresponding author: giuseppe.ferrara@unina.it

Linking Seismicity, Geochemical And Environmental Data: The New Frontier Of Multiparametric Networks

E. Ferrari[1], M. Massa[1], A.L. Rizzo[2,1], S. Lovati[1], F. Di Michele[1]

[1] *National Institute of Geophysics and Volcanology (INGV), Milano, Italy*
[2] *Department of Earth and Environmental Sciences, University of Milano-Bicocca, Milano, Italy*

Nowadays increasingly consciousness on the interaction between tectonics and crustal fluids dynamics is lacking simultaneous monitoring of the relative key factors. Changes in water chemistry and levels, spring discharges, soil flux regimes (e.g., CO_2, CH_4, radon) and compositions of dissolved gases in water are well documented in the literature (e.g., Italiano et al., 2001, 2004; Wang and Manga, 2021; Chiodini et al., 2020; Gori and Barberio, 2022 and references therein), as being pre-, co- and post-seismic modifications as well as being markers of the local tectonic stress acting in the crust. However, geological differences among sites require specific knowledge of crustal fluids response to seismicity.

For this purpose, multiparametric stations have been set up starting from the end of 2021 and equipped with: (i) sensors installed in water wells measuring water level, temperature, and electrical conductivity; (ii) meteorological sensors measuring atmospheric pressure, temperature, rain, humidity, wind speed and direction; (iii) seismic sensors providing accelerometric and velocimetric datasets; (iv) radon sensors; (v) CO_2 soil flux chamber. Stations are placed on the major seismogenic structures and are widely distributed among the Alps, Apennines and Pianura Padana. Our new multiparametric network is aimed to address this point and, to the best of our knowledge, it is the first network developed in Italy under this philosophy.

Data are transmitted in near real-time to an *ad hoc* developed dynamic relational database and displayed in a dedicated website. The built-in philosophy is to easily compare distinct parameters from the various sensors and possibly recognize cause-effect relationships among them.

A statistic approach is also applied to the time-series to investigate intra-annual and inter-annual trends and correlations among different parameters. Alternative methods (e.g., signal decomposition, spike detection) will be presented and discussed.

References

Chiodini G., Cardellini C., Di Luccio F., Selva J., Frondini F., Caliro S., Rosiello A., Beddini G., Ventura G., 2020: Correlation between tectonic CO_2 Earth degassing and seismicity is revealed by a 10-year record in the Apennines, Italy. Science Advances, https://www.science.org/doi/10.1126/sciadv.abc2938

Gori F., Barberio M.D., 2022: Hydrogeochemical changes before and during the 2019 Benevento seismic swarm in central-southern Italy. Journal of Hydrology, 604:127250

Italiano F., Martinelli G., Nuccio P.M., 2001: Anomalies of mantle-derived helium during the 1997 – 1998 seismic swarm of Umbria-Marche, Italy. Geophysical Research Letters, 28(5):839-842

Italiano F., Martinelli G., Rizzo A., 2004: Geochemical evidence of seismogenic-induced anomalies in the dissolved gases of thermal waters: A case study of Umbria (Central Apennines, Italy) both during and after the 1997–1998 seismic swarm. Geochemistry, Geophysics, Geosystems, 5:11, doi:10.1029/2004GC000720

Wang C.-Y., Manga M., 2021: Water and Earthquakes. Lecture Notes in Earth System Sciences, Springer Cham, 387 pp., https://doi.org/10.1007/978-3-030-64308-9

Corresponding author: elisa.ferrari@ingv.it

OTRIONS seismic network after ten years of operation: the new seismic catalog

A. Ferreri[1], A. Romeo[2], R. Giannuzzi[1], G. Cecere[2], S. de Lorenzo[1], L. Falco[2], M. Filippucci[1,2], M. Michele[2], G. Selvaggi[2], A. Tallarico[1,2]

[1] Dipartimento di Scienze della Terra e Geoambientali, Università degli Studi di Bari Aldo Moro, Bari, Italy
[2]Istituto Nazionale di Geofisica e Vulcanologia, Italy

The OTRIONS seismic network (FDSN network code OT) is a local network installed in the Apulia region (Southern Italy) with the aim of monitoring the seismicity of the Gargano area (Northern Apulia) and the Salento area (Southern Apulia). The OT network is managed by the University of Bari Aldo Moro (UniBa) and by the National Institute of Geophysics and Volcanology (INGV). It started to operate in 2013 and in 2019 the recording stations migrated to EIDA (all details can be found in Filippucci et al., 2021a). In 2021 a first database was collected, with the event detection achieved both manually and automatically with SeisComP3 (Helmholtz-Centre Potsdam), and was released (Filippucci et al., 2021a; Filippucci et al., 2021b).

After ten years of operations, we focus on the microseismicity of the Gargano area with the aim of collecting a new seismic database for the period from April 2013 to December 2022, by using a recently acquired software, CASP (Complete Automatic Seismic Processor), for the automatic detection, picking and location of seismic events (Scafidi et al., 2019). The CASP software is installed on a remote server implemented by RECAS-Bari, the computational infrastructure of INFN and UniBa.

Through an appropriate parameter setting, we adapted CASP and NonLinLoc (Lomax et al., 2000) to the Gargano area and to the seismic stations available, both OT and INGV permanent seismic networks. We used the 1D velocity model of Gargano developed by de Lorenzo et al., (2017).

The recorded seismic events were organized in two catalogs: the first one is the automatic catalog, obtained from the automatic locations of CASP; the second one is the manual catalog, obtained through a manual revision of P and S waves arrival times. To evaluate the reliability of CASP, a comparison between the automatic and manual catalog was performed.

From a comparison of the manual catalog with the already released catalog of the Gargano seismicity (Filippucci et al., 2021b), the number of events detected by CASP increased a lot. Furthermore, the results show that the choice of the CASP parameters allows us to lower the minimum magnitude threshold of the recorded microseismicity in the Gargano area. Preliminary analysis of the earthquake's foci shows that the seismicity pattern retrace, substantially, the same discussed in the work of Miccolis et al., (2021).

References

de Lorenzo S., Michele M., Emolo A., and Tallarico A.; 2017: *A 1D P-wave velocity model of the Gargano promontory (southeastern Italy)*. J. Seismol., 21 (4), 909–919, doi:10.1007/s10950-017-9643-7

Filippucci M., Miccolis S., Castagnozzi A., Cecere G., de Lorenzo S., Donvito G. and Tallarico A.; 2021a: *Seismicity of the Gargano promontory (Southern Italy) after 7 years of local seismic network operation: Data release of waveforms from 2013 to 2018*. Data in brief, 35, 106783, https://doi.org/10.1016/j.dib.2021.106783

Filippucci M., Miccolis S., Castagnozzi A., Cecere G., de LorenzoS., Donvito G., Falco L., Michele M., Nicotri S., Romeo A., Selvaggi G. and Tallarico A.; 2021b: *Gargano Promontory (Italy) microseismicity (2013-2018): waveform data and earthquake catalogue*. Mendeley Data, V3, doi: 10.17632/7b5mmdjpt3.3

Helmholtz-Centre Potsdam - GFZ German Research Centre for Geosciences and gempa GmbH (2008). The SeisComP seismological software package. GFZ Data Services. doi: 10.5880/GFZ.2.4.2020.003.

Lomax A., Virieux J., Volant P. and Berge-Thierry C.; 2000: *Probabilistic Earthquake Location in 3D and Layered Models*. In: Thurber C.H., Rabinowitz N. (eds) Advances in Seismic Event Location. Modern Approaches in Geophysics, vol 18. Springer, Dordrecht. https://doi.org/10.1007/978-94-015-9536-0_5.

Miccolis S., Filippucci M., de Lorenzo S., Frepoli A., Pierri P., and Tallarico A.; 2021: *Seismogenic Structure Orientation and Stress Field of the Gargano Promontory (Southern Italy) From Microseismicity Analysis*. Front. Earth Sci., Sec. Structural Geology and Tectonics, Volume 9, doi: 10.3389/feart.2021.589332

Scafidi D., Spallarossa D., Ferretti G., Barani S., Castello B., and Margheriti L.; 2019: *A complete automatic procedure to compile reliable seismic catalogs and travel-time and strong-motion parameters datasets.* Seismological Research Letters, 90(3), 1308-1317, doi: 10.1785/0220180257

University of Bari Aldo Moro. (2013). OTRIONS [Data set]. International Federation of Digital Seismograph Networks. https://doi.org/10.7914/SN/OT

Corresponding author: Andrea Pio Ferreri (andrea.ferreri@uniba.it)

Monitoring tectonic environments with DAS: the case study of the Irpinia Near Fault Observatory

G. Festa[1,2], C. Strumia[1], F. Scotto di Uccio[1], A. Trabattoni[3]

[1]Department of Physics 'Ettore Pancini', University of Napoli Federico II, Italy.
[2]Istituto Nazionale di Geofisica e Vulcanologia, Italy.
[3]Université Côte d'Azur, Observatoire de la Côte d'Azur, CNRS, IRD, Géoazur, France.

DAS systems are interrogators connected to a termination of a fiber optic dark cable, that sense the fiber by sending a laser pulse and recovering the back-scattered light. When the fiber is at rest, the pattern of the light is the same after each pulse; during the occurrence of an earthquake, because of the deformation of the cable, the backscattered light changes its pattern and the resulting phase difference can be connected with the strain rate along the direction of the cable (Hartog, 2017). Thus, interferometric analysis provides time series with spatial sampling along the fiber even of few meters, making the DAS recording similar to seismic arrays, with the main advantages of being cheaper, easier to plugin into available dark fibers, and working in harsh environments, such as at the seafloor or in volcanic areas (e.g., Sladen et al., 2019; Currenti et al., 2021). On the other hand, DAS systems collect a huge amount of data that require proper management and advanced processing tools.

We tested the DAS system along a short cable in the Irpinia Near Fault Observatory (INFO), an on-field laboratory of 31 seismic stations that monitors the seismicity along the Campania-Lucania Apennines (Iannaccone et al., 2010; Chiaraluce et al., 2022), across the fault system that generated the 1980, M 6.9 Irpinia earthquake. INFO has been operational in the last 15 years and has recorded more than 3000 earthquakes, with magnitude of completeness of 1.1 (Vassallo et al., 2011). We performed a DAS survey lasting 5 months along a 1.1 km-long fiber, buried in a dry lake at depths ranging from 30 cm to 1.5m, collecting continuous strain rate data at a spatial sampling of 2.4 m and sampling frequency of 200 Hz. The system recorded several earthquakes spanning different magnitude and location, providing an initial dataset to investigate DAS records and related source parameters (Trabattoni et al., 2022). This experiment also provided the basis for the future installation of a long-term monitoring system, grounded on 3 DAS interrogating fibers of different extent across the near-fault observatory.

Seismic phases related to earthquakes were analyzed with the help of seismic refraction experiments and numerical simulations. In this particular context, DAS records appear to be mainly sensitive to waves guided horizontally by the low-velocity structure beneath the site. Because of the near-to-vertical incidence of waves, seismograms appear to be depleted of P waves, and dominated by low velocity S and surface waves. Moreover, the wave pattern is similar for all

earthquakes irrespective of the event azimuth, due to the high velocity contrast between the bedrock and the basin, the main difference being in the P to S differential time owing to the distance between the fiber and the event hypocenter. The high impedance contrast at the base of the dry lake leads to considerable site amplification and allows to detect local microearthquakes without stacking.

We developed an integral approach for converting strain-rate data into kinematic quantities (Trabattoni et al., 2023), based on moving average filters, that allows retrieving the high-pass displacement from DAS records. Using converted data, we performed automatic arrival phase identification using ML based detectors (e.g., EQTransformer, Mousavi et al., 2020; PhaseNet, Zhu et al., 2019). We found phase picking consistent with manual measurements, and an enhanced sensitivity when compared to strain rate data, in terms of number and quality of picks. This approach also enables for event detection when information is integrated across the whole fiber.

We used displacement converted data for local magnitude (ML) computation. The final magnitude was estimated as the median value of the ML distribution at all the usable channels, while uncertainties have been quantified by the standard median absolute deviation (SMAD). Magnitude estimates provided by the DAS are compatible with those computed from the INFO network showing that using DAS recovered velocity enables simple and accurate ML estimation.

We also investigated the correlation between the elastic energy release rate estimated at the fiber and the kinetic energy release rate from the closest station (< 2 km) and we used this scaling to retrieve the energy magnitude from the integral of elastic energy. We found that our observations are compatible with the detection threshold as a function of the distance associated with the signal to noise level of the DAS recordings. Finally, we evaluated seismic moment and source size by inverting the spectral amplitude of DAS records, after removal of site effects, according to the Anderson and Hough (1984) model.

In conclusion, this workflow enables for automatic event detection and characterization from DAS records, even in presence of longer cables and larger bunches of data.

References

Anderson, J. G., Hough, S. E.; 1984: A model for the shape of the Fourier amplitude spectrum of acceleration at high frequencies, *Bulletin of the Seismological Society of America*, 74(5), 1969-1993.

Chiaraluce, L., Festa, G., Bernard, P., Caracausi, A., Carluccio, I., Clinton, J., et al.; 2022: the near fault observatory community in Europe: A new resource for faulting and hazard studies, *Annals of Geophysics*, 65(3), DM316. https://doi.org/10.4401/ag-8778.

Currenti, G., Jousset, P., Napoli, R., Krawczyk, C., & Weber, M.; 2021: On the comparison of strain measurements from fibre optics with a dense seismometer array at Etna volcano (Italy), *Solid Earth*, *12*(4), 993–1003. https://doi.org/10.5194/se-12-993-2021

Hartog, H.A.; 2017: An introduction to distributed optical fibre sensors (A. H. Hartog, Ed.). CRC Press.

Iannaccone, G., Zollo, A., Elia, L., Convertito, V., Satriano, C., Martino, C., et al.; 2010: A prototype system for earthquake early-warning and alert management in southern Italy, *Bulletin of Earthquake Engineering*, 8(5), 1105–1129. https://doi.org/10.1007/s10518-009-9131-8.

Mousavi, S. M., Ellsworth, W. L., Zhu, W., Chuang, L. Y., Beroza, G. C.; 2020: Earthquake transformer—an attentive deep-learning model for simultaneous earthquake detection and phase picking, *Nature communications*, 11(1), 3952.

Sladen, A., Rivet, D., Ampuero, J. P., De Barros, L., Hello, Y., Calbris, G., Lamare, P.; 2019: Distributed sensing of earthquakes and ocean-solid Earth interactions on seafloor telecom cables, *Nature Communications*, 10(1). https://doi.org/10.1038/s41467-019-13793-z.

Trabattoni, A., Festa, G., Longo, R., Bernard, P., Plantier, G., Zollo, A., Strollo, A.; 2022: Microseismicity monitoring and site characterization with distributed acoustic sensing (DAS): The case of the Irpinia fault system (Southern Italy), *Journal of Geophysical Research: Solid Earth*, 127(9), e2022JB024529.

Trabattoni, A., Biagioli, F., Strumia, C., Van Den Ende, M., Scotto Di Uccio, F., Festa, G., Rivet, D., Sladen, A., Ampuero, J. P., Métaxian, J.-P., & Stutzmann, É.; 2023: From strain to displacement: using deformation to enhance distributed acoustic sensing applications, *Geophysical Journal International*, 235(3), 2372–2384. https://doi.org/10.1093/gji/ggad365

Vassallo, M., Festa, G., Bobbio, A.; 2012: Seismic ambient noise analysis in southern Italy, *Bulletin of the Seismological Society of America*, 102(2), 574-586.

Zhu, W., Beroza, G. C.; 2019: PhaseNet: A deep-neural-network-based seismic arrival-time picking method, *Geophysical Journal International*, 216(1), 261-273.

Corresponding author: Gaetano Festa (gaetano.festa@unina.it)

ML *vs* semi-automatic seismic catalogues: the L'Aquila 2009 earthquake sequence example

R. Fonzetti [1, 2], L. Valoroso [1], A. Govoni [1], P. De Gori [1], C. Chiarabba [1]

[1] *Istituto Nazionale di Geofisica e Vulcanologia (INGV), Rome (RM)*
[2] *Università degli Studi Roma Tre , Rome (RM)*

Nowadays the use of neural networks and artificial intelligence in seismology delivers high-resolution seismic catalogues including very small magnitude events that remained undetected by human analysts and standard monitoring room procedures. Here, we test the performance of such ML methods for their reliability in the high-seismic hazard area of the Central Apennines, Italy.
In this work, we apply the QuakeFlow (QF) workflow (Zhu et al., 2023), based on the PhaseNet (Zhu et al., 2019) and GaMMA (Zhu et al., 2022) modules for event detection and association respectively, to the L'Aquila 2009 seismic sequence involving 90 seismic stations and we benchmark our new catalogue against the high-resolution seismic catalogue of Valoroso et al., (2013) that used a semi-automatic procedure including detection and an automatic picking procedure for P and S waves (i.e., Manneken Pix algorithm, Aldersons et al., 2009).
We analysed the earthquakes that occurred during the entire 2009 year and obtained approximately 336,000 events vs the 182,000 from Valoroso et al., (2013) catalogue, obtaining about 85% more earthquakes. Thus, our new catalogue detected 154,452 more events (~ 85%) with respect to the Valoroso et al., (2013) catalogue.
We selected all events having at least 6 P- and 4 S- arrival times (i.e. about 222,000 earthquakes) and we computed 1D-locations using Hypoellipse (Lahr, 1999) with an ad-hoc velocity models for the Central Apennines (Fig. 1). The 1D-locations clearly highlight the geometric characteristics of the seismogenic faults activated during the sequence: the Paganica fault with its set of synthetic and antithetic minor faults (sections 13-19) and the Campotoso fault (sections 1-9). Finally, in the last sections (sections 19-23) a low-angle fault was activated during the sequence.
The comparison with the Valoroso et al., (2013) catalogue was obtained by using only those seismic stations which were in common between the two datasets (purple triangles in Fig. 2) and selecting the common earthquakes (i.e., events having P- and S- waves arrival times at a common station within 2 seconds, Fig. 2a-c). The ML- catalogue presents a larger number of phases with respect to the Valoroso et al., (2013) catalogue and lower GAP (°) values (Fig. 2d).
The application of this new methodology could speed up the time to analyse seismic sequences even in real time. Our findings are expected to help scientists to understand the earthquake generation mechanisms of the 2009 L'Aquila earthquake sequence in terms of nucleation processes, the underlying physical triggering processes leading to a richer aftershock catalogue, and revealing any hidden faults in the vicinity of well-known and mapped structures that remain unseen for the last two decades.

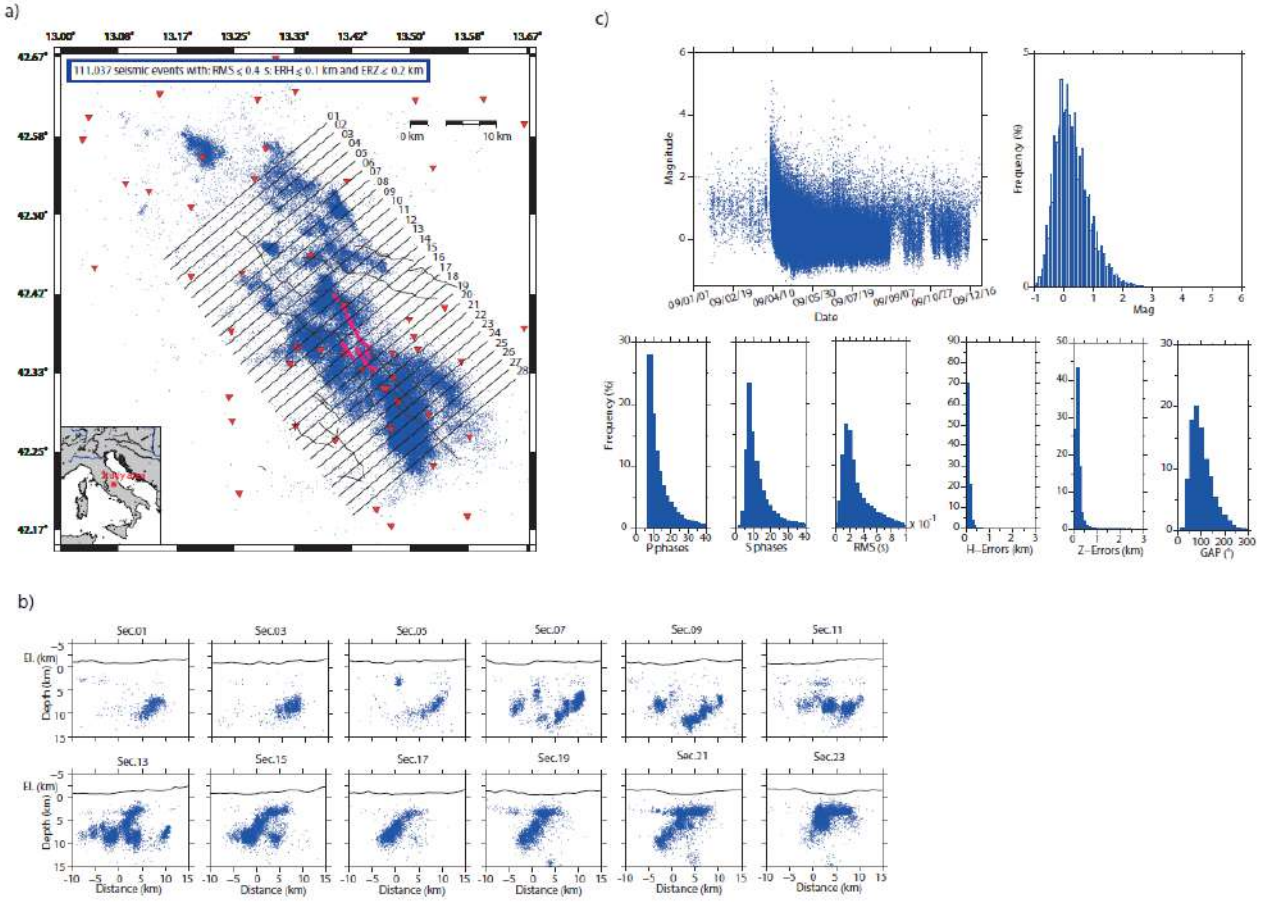

Fig.1 – a) The entire 2009 QF seismicity with at least 6 P- and 4 S arrival times (blue dots) relocated by using Hypoellipse with an optimised 1D-velocity model. The best locations (selecting criteria are specified in the upper left corner of the map) are shown. Red triangles are the seismic stations used by QF for the locations. Dark grey lines represent the main faults of the area. Pink lines are the evidence of surface rupture during the L'Aquila 2009 seismic sequence. Black straight lines are traces of vertical cross sections; b) some of the most interesting vertical sections (strike N°50E) showing the depth distribution of the seismic events occurred within ± 0.8 km distance from the sections; c) above, the magnitude vs time diagram and histogram of magnitude values; bottom) histograms showing the number of P- and S- waves, RMS (s), ERH (km), ERZ (km) and GAP (°).

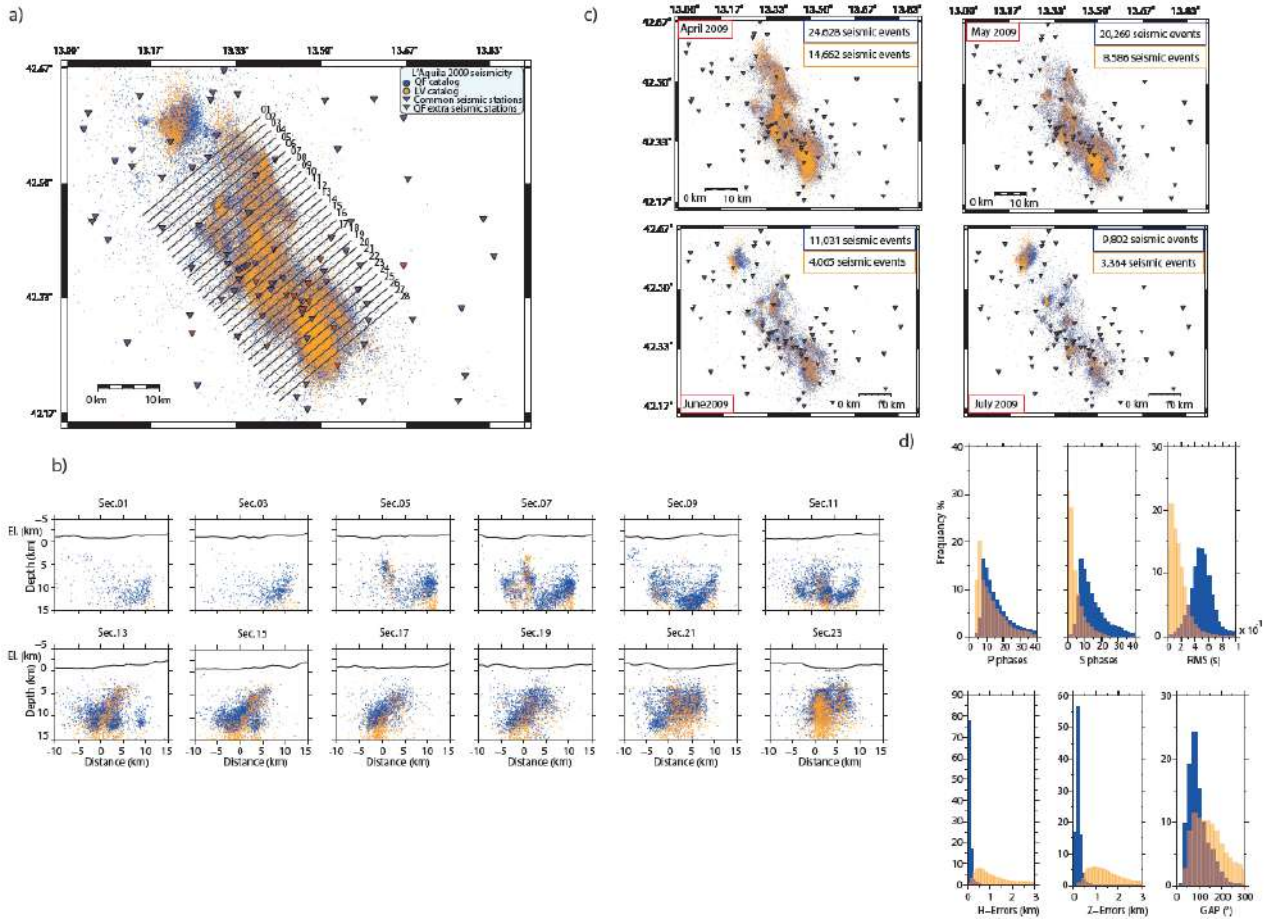

Fig.2 - a) Map view of the common seismic events from QF and Valoroso et al. (2013) catalogues. The best locations (the filters are specified in the boxes) are plotted. The purple triangles are the common seismic stations while the red ones are the extra seismic stations used by QF (not used for the LV processing). The black straight lines are traces of vertical cross sections; b) some of the most interesting vertical sections (strike: N°50E) which show the depth distribution of the seismic events occurring within ± 0.8 km distance from the sections; c) Snap-shot of the seismicity distribution during time (from April to July 2009); d) histograms showing the number of P- and S-waves, RMS (s), ERH (km), ERZ (km) and GAP (°).

References

Aldersons F., Di Stefano R., Chiaraluce L., Piccinini D. and Valoroso L.; (2009). Automatic detection and P- and S-wave picking algorithm: an application to the 2009 L'Aquila (Central Italy) earthquake sequence. http://adsabs.harvard.edu/abs/2009AGUFM.U23B0045A; https://zenodo.org/records/1471534.

Lahr, J. C. (1999). HYPOELLIPSE: A computer program for determining local earthquake hypocentral parameters, magnitude, and first motion pattern (p. 119). Reston, VA: US Geological Survey.

Valoroso, L., Chiaraluce, L., Piccinini, D., Di Stefano, R., Schaff, D., & Waldhauser, F. (2013). Radiography of a normal fault system by 64,000 high-precision earthquake locations: The 2009 L'Aquila (central Italy) case study. Journal of Geophysical Research: Solid Earth, 118(3), 1156-1176.

Valoroso, L., Chiaraluce, L., & Collettini, C. (2014). Earthquakes and fault zone structure. Geology, 42(4), 343-346.

Zhu, W., & Beroza G. B. (2019). PhaseNet: A Deep-Neural-Network-Based Seismic Arrival Time Picking Method. Geophysical Journal International, 216(1), 261-273.

Zhu, W., McBrearty, I. W., Mousavi, S. M., Ellsworth, W. L., & Beroza, G. C. (2022). Earthquake phase association using a Bayesian Gaussian mixture model. Journal of Geophysical Research: Solid Earth, 127(5), e2021JB023249.

Zhu, W., Hou, A. B., Yang, R., Datta, A., Mousavi, S. M., Ellsworth, W. L., & Beroza, G. C. (2023). QuakeFlow: a scalable machine-learning-based earthquake monitoring workflow with cloud computing. Geophysical Journal International, 232(1), 684-693.

Corresponding author: rossella.fonzetti@uniroma3.it

Do parallel active fault systems dream of Coulomb Stress Transfer?

A. Galderisi[1,2], P. Galli[3,2], E. Peronace[2]

[1]Dipartimento di Scienze della Terra, dell'Ambiente e delle Risorse, Università degli Studi di Napoli, Federico II, Italia

[2]CNR-IGAG, Roma, Italia

[3]Dipartimento Protezione Civile, Roma, Italia

Introduction. In this work, we have applied different analytical methodologies in order to explore the modes of frontal transfer of static Coulomb stress between various seismogenic fault systems. We started from the observation of a series of surface ruptures formed along the Norcia fault system (NFS) following the Mw 6.6 event of 30 October 2016. The 2016 sequence was not generated by the NFS, but from the Monte Vettore fault system (MVFS). Since the seismological data relating to this sequence (Chiaraluce et al, 2017; Improta et al, 2019) did not highlight any significant event associable to the NFS, we questioned the nature of these ruptures and the possible interaction between these two parallel fault systems. Firstly, a geological-structural survey was conducted along the entire NFS, mapping the coseismic ruptures and calculating the slip-vector. Then we calculated the change in Coulomb stress produced by the MVFS following the October 30 event. As a result, part of the static Coulomb stress was transferred from the MVFS to the NFS. We then compared paleoseismological data coming from the two fault system trying to understand whether these flange systems also interact over time. Finally, the same analysis methodology was applied to the seismogenic fault systems of the Gran Sasso (GSFS) and the Upper Aterno Fault System (UAFS).

Geological and seismotectonic framework. The MVFS and the NFS are two seismogenic normal fault systems that extend parallel for over 30 km in the N160° direction, at a distance of ~10 km from each other. Both are active in historical times, with evidence of surface ruptures at least throughout the Holocene (Galli et al, 2018 and 2019). Similarly, the GSFS and the UAFS are two seismogenic fault systems, located ~14 km distant. The GSFS shows a N120° direction, in the north and central sector, while NNW-SSE in the southern sector. Differently, the UAFS shows a unique master fault direction N160° (Galli et al, 2010; 2011 and 2022). The return times calculated from paleoseismological studies are ~1.8 kyr for the MVFS and NFS (Galli et al, 2018; 2019; Tab. 1), with a slip rate of 1.3 mm/yr and 1.2 mm/yr respectively. While the return times of the GSFS is 2.8 + 0.5 ky and of the UAFS 1-2 kyr (for large magnitude events), with a slip rate of 1.8 mm/yr for GSFS and 0.58 mm/yr for UAFS (Galli et al, 2010; 2011 and 2022, Tab. 1).

Tab. 1. Archaeo-paleoseismological records.

NFS	MVFS	GSFS	UAFS
1859	2016 CE.	1349 CE	2009 CE
1703 CE	443 CE	~2800 BP	1703 CE
1328	~4000 BP	~6100 BP	1461 CE
99 BCE	~5600 BP		801 CE
~3900 BP	~7400 BP		~3500 BP
~5300 BP			~6300 BP
~7600 BP			

Seismic sequence of 2009 and 2016. The disastrous earthquakes of 2009 and 2016 both involved central Italy, affecting the Abruzzo and Lazio-Umbria regions, respectively. The 2009 seismic sequence recorded a mainshock of Mw 6.3 (Chiarabba et al, 2009), with approximately 64k aftershocks (Valoroso et al, 2013). The arrangement of the aftershocks suggests that, beside the activation of the UAFS - which generated the main mainshock and the greatest number of aftershocks - the nearby GSFS fault system was also involved, without evidence of coseismic rupture along the fault planes of the GSFS (Galli et al, 2022, Fig. 1). Differently, the 2016 seismic sequence was produced first by the joint activation of the MVFS and the Laga Fault System on 24 August, Mw 6.2 (RCMT, 2016) and then only by the MVFS, first in the northern sector, 26 October, Mw 6.1 (RCMT, 2016) and later entirely on 30 October Mw 6.6 (RCMT, 2016). Following the 30 October event, ~2 km of coseismic ruptures were observed along the main fault planes of the NFS (Galderisi and Galli, 2019; 2020), although no aftershocks were observed along the NFS (Improta et al, 2019; Galderisi and Galli, 2020).

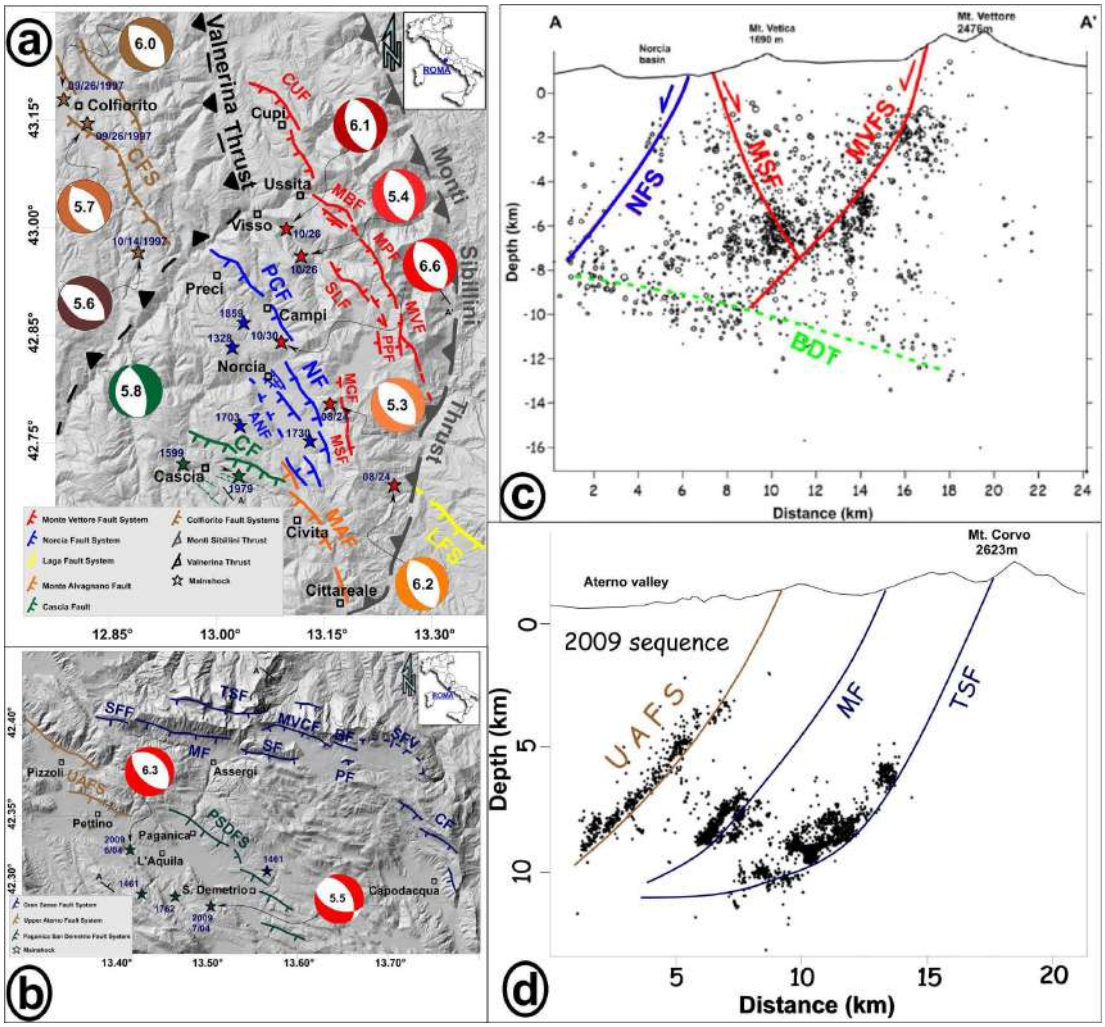

Fig. 1 – (a) Digital Terrain Model of the 2016 epicentral area with the main active fault segments. (b) Digital Terrain Model of the 2009 epicentral area with the main active fault segments. (c) Hypocentral distribution of the 2016 seismic sequence. (d) Hypocentral distribution of the 2009 seismic sequence.

Coseismic ruptures in the Norcia basin. The coseismic ruptures observed in the Norcia basin reflect the emergence of the master fault and the synthetic and antithetical splays already known and recognized as active in Galli et al. (2005; 2018; 2023). Following the earthquake of 30 October 2016, in total, over 2 km of coseismic ruptures with a maximum vertical offset of ~12 cm were measured. In December 2017, Galli et al. (2018) excavated a trench for paleoseismological studies along the coseismic rupture, where it was found that this rupture occurred in correspondence with the surface expression of the main splay observed on the walls of the trench.

Coulomb stress transfer. According to Coulomb stress change theory, following a seismic event part of the static stress can be transferred to nearby fault systems (King et al, 1994). Some authors have already analysed the variation in the static Coulomb stress produced by the 30 October event (Improta et al, 2019), with particular reference to the lateral interactions that occur between neighbouring seismogenic systems (Mildon et al, 2019). In our case, however, it is observed that part of the Coulomb stress is transferred frontally from the MVFS to the NFS. We then calculated the Coulomb stress changes generated on 30 October by the MVFS using the Coulomb 3.3 software (Toda et al, 2011). To define the Coulomb stress variation the software uses this equation:

$$\Delta CSC = \Delta\tau s + \mu\Delta\sigma n$$

where ΔCST is the change in Coulomb stress (Coulomb Stress Change – CSC), Δτs is the variation of shear stress, μ is the friction coefficient and Δσn is the variation of normal stress. The fault parameters entered into the software are:

• strike N160°; dip 70°; rake -90°; kinematic dip-slip; Mw 6.6; maximum slip -2 m for MVFS and -2.5 for NFS (INGV, 2016); friction coefficient μ=0.6 (typical of carbonate rocks). Two simulations were conducted, one activating the MVFS fault (S1), the other that of the NFS (S2) (Fig. 2).

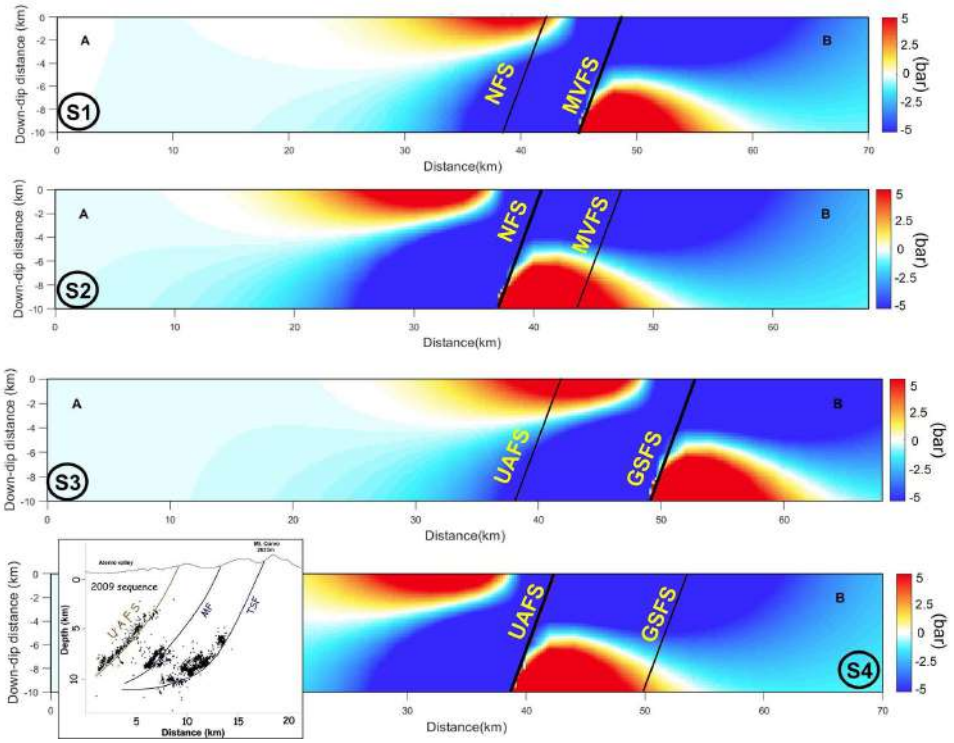

Fig. 2 – Simulation results for the calculation of the CST with the Coulomb 3.3 software. (S1) Cross-section with the activation of the MVFS. (S2) Cross-section with the activation of the NFS. (S3) Cross-section with the activation of the GSFS. (S4) Cross-section with the activation of the UAFS, with comparison of 2009 seismic sequence. Coulomb stress increase countering (red), Coulomb stress decrease countering (blue).

Similarly, two simulations were conducted for the GSFS (S3) and for the UAFS (S4), with parameters entered the software are:

• strike N160°; dip 70°; rake -90°; kinematic dip-slip; Mw 6.6; maximum slip -2.5 for both fault systems; friction coefficient μ=0.6 (Fig. 2).

Discussions and conclusions. The combination of all these analyses allowed us to hypothesize why the NFS was activated on the surface and how it interacts with the MVFS. The results obtained from the simulations for the calculation of the variation of the static Coulomb stress show that, in simulation S1, the formation of a stress growth lobe is observed in the first 2 km in the hanging-wall of the MVFS, corresponding to the superficial part of the NFS (Fig. 2). In simulation S2, however, a Coulomb stress increase lobe is observed at ~6.5 km depth in the footwall of the NFS,

corresponding to the deep part of the MVFS (Fig. 2). This suggests that, when the MVFS is activated, the static Coulomb stress is increased only in the most superficial portion of the crust crossed by the NFS, while when the NFS is activated, it is the static stress in the deep portion crossed by the MVFS that increases.

Considering that the 1) vector slips observed on the field along the coseismic breaks indicate pure dip-slip kinematics, while the slickenlines measured on the border fault planes indicate left oblique kinematics (Galderisi and Galli, 2020), and that 2) any significant seismicity has been detected at depth along the NFS (Improta et al., 2019), it is likely that the 30 October 2016 surface slip of the NFS cannot be attributed to deep deformation dynamics induced by Apennine tectonic stress release. Thus, excluding shaking-induced phenomena, as differential compaction or slope movements, both impossible in the splays of the plain, we hypothesize that the sudden increase in Coulomb stress induced by the activation of MVFS have triggered a slight passive slip along the pre-existing fault planes of the NFS, which accommodated also the abrupt, 12 cm uplift of the Norcia block (GSI, 2016; Bignami et al., 2019). Probably, due to the lack of sufficient lithostatic weight, friction was low and slip occurred seismically.

Considering the long paleoseismic history of the two fault systems (Galli et al., 2018; 2019; 2023), it is possible that the MVFS and the NFS have been interacting for thousands of years, mutually inducing variations in the Coulomb stress in the hanging wall of the other (Fig. 3). But while the activation of the MVFS seems to favour only the formation of superficial passive ruptures along the NFS, the activation of the NFS, which seems to precede that of the MVFS by 100-500 years, could act as a trigger for the complete rupture of the latter.

The same analysis methodology was applied for the GSFS and the UAFS. The results obtained from the simulations for the calculation of the variation of the static Coulomb stress show what was observed in the MVFS and NFS simulations (S3 and S4 in Fig. 2). This evidence suggests that the GSFS and the UAFS also interact by mutually inducing variations in the Coulomb stress in each other's hanging walls. The analysis of the aftershocks of the 2009 seismic sequence (Valoroso et al, 2013) unequivocally shows that the GSFS recorded seismicity, where the Coulomb stress growth lobe is created (Fig. 2). In fact, according to King et al, (2004) the increase of even just 1 bar would be sufficient to trigger slip on a fault system. In our case, the transfer of Coulomb stress from MVFS to NFS may reach 2–3 bars only in the upper lobe (Fig. 2). What is shown by the arrangement of the aftershocks of the 2009 seismic sequence, linked to the evidence of the 2016 coseismic ruptures observed along the NFS, shows that there is indeed an interaction between the parallel fault systems of the MVFS-NFS and the GSFS-UAFS, with possible Coulomb stress transfer.

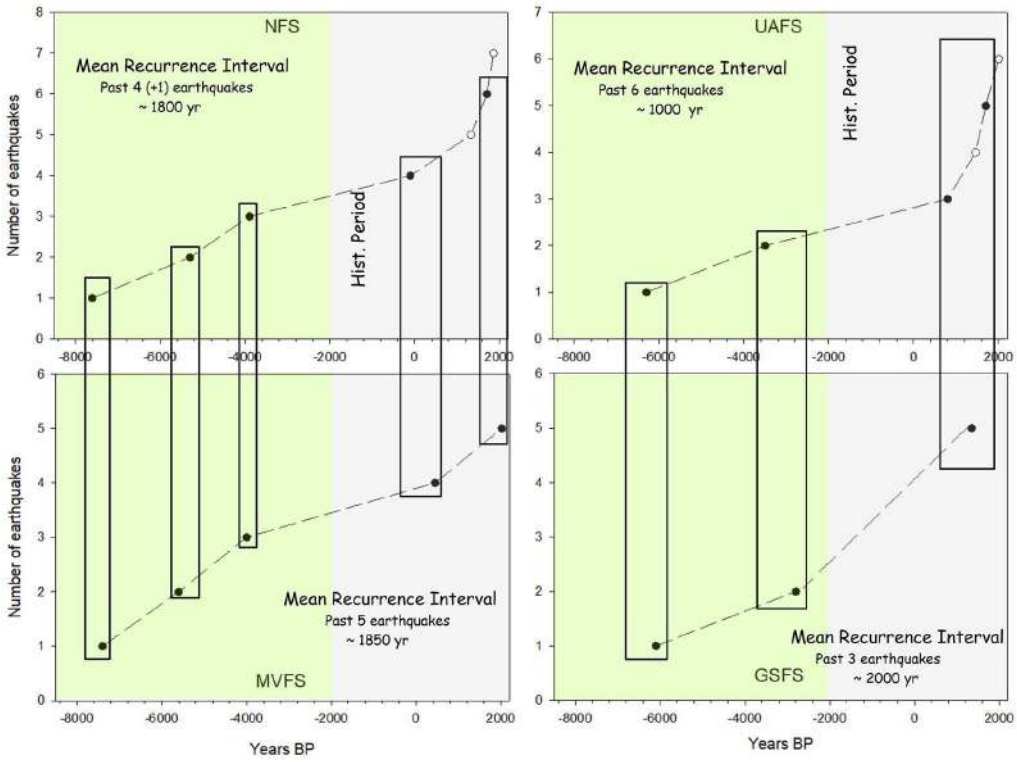

Fig. 3 – Comparison between the age of paleoearthquakes sourced by the NFS-MVFS and UAFS-GSFS. The white dots indicate seismic events known from historical bibliography but not recognized in the trenches.

The analysis of paleoseismological data shows that both the NFS-MVFS and the UAFS-GSFS recorded events at close times (Fig. 3). Differently, historical records show that the NFS and UAFS had greater activity, compared to the MVFS and GSFS (Fig. 3). In fact, the MVFS and the GSFS were classified as silent faults, as they did not show instrumental seismicity and even correlated historical seismic events. On the other hand, the seismic events of 1328 and 1859 for the NFS and 1461 for the UAFS were not observed in trenches. Even the 2009 seismic event didn't produce important surface coseismic ruptures, probably because not all the UAFS was activated. Considering only the earthquakes observed in the trenches, even in historical times a close activity is observed between the NFS-MVFS and UAFS-GSFS.

References

Bignami C., Valerio E., Carminati E., Doglion, C., Tizzani P., Riccardo Lanari R.; 2019. Volume unbalance on the 2016 Amatrice - Norcia (Central Italy) seismic sequence and insights on normal fault earthquake mechanism. Sci. Rep. 9, 4250.

Chiarabba C., et al; 2009. The 2009 L'Aquila (central Italy) Mw 6.3 earthquake: main shock and aftershocks. Geophys. Res. Lett. 36, 1–6.

Chiaraluce L., et al; 2017. The 2016 Central Italy seismic sequence: a first look at the mainshocks, aftershocks, and source models. Seismol. Res. Lett. 88, 757–771.

Galderisi A., Galli P.; 2020. Offset components and fault-block motion during the 2016 Central Italy earthquake (Mw 6.6, Monte Vettore Fault System). J. Struct. Geol. 134, 104014.

Galderisi A., P. Galli; 2020. Coulomb stress transfer between parallel faults. The case of Norcia and Mt Vettore normal faults (Italy, 2016 Mw 6.6 earthquake), Results Geophys. Sci. 1–4, 100003.

Galli P., Giaccio B., Messina P.; 2010. The 2009 central Italy earthquake seen through 0.5 Myr-long tectonic history of the L'Aquila faults system. Quat. Sci. Rev. 29, 3768–3789.

Galli P., Giaccio B., Messina P., Peronace E., Maria Zuppi G.; 2011. Palaeoseismology of the L'Aquila faults (central Italy, 2009,Mw 6.3 earthquake): implications for active fault linkage. Geophysical Journal International 187 (3), 1119–1134.

Galli P., Galderisi A., Ilardo I., Piscitelli S., Scionti V., Bellanova J., Calzoni F.; 2018. Holocene paleoseismology of the Norcia fault system (Central Italy). Tectonophysics 745, 154–169.

Galli P., Galderisi A., Peronace E., Giaccio B., Hajdas I., Messina P., Pileggi D., Polpetta F.; 2019. The awakening of the dormant Mt Vettore fault (2016 central Italy earthquake, Mw 6.6). Paleoseismic clues on its millennial silences. Tectonics 38, 687–705.

Galli P., A. Galderisi P. Messina, E. Peronace; 2022. The Gran Sasso fault system: Paleoseismological constraints on the catastrophic 1349 earthquake in central Italy, Tectonophysics, 822, 1–29.

GSI [Geospatial Information Authority of Japan] 2016. The 2016 Cen- tral Italy Earthquake: Crustal Deformation Detected by ALOS-2 Data.

King G.C.P., Stein R.S., Lin J.; 1994. Static stress changes and the triggering of earth- quakes. Bull. Seismol. Soc. Am. 84 (3), 935–953.

Improta L., et al, The Bollettino Sismico Italiano Work- ing Group; 2019. Multi-segment rupture of the 2016 Amatrice-Visso-Norcia seismic sequence (central Italy) constrained by the first high-quality catalog of Early After- shocks. Sci. Rep. 9, 6921.

INGV Working Group "Terremoto in centro Italia". Summary report on the October 30, 2016 earthquake in central Italy Mw 6.5; 2016.

Mildon Z.K., Roberts G.P., Faure Walker J.P., Toda S.; 2019. Coulomb pre-stress and fault bends are ignored yet vital factors for earthquake triggering and hazard. Nat. Commun. 10, 2744 .

RCMT., 2016: European-Mediterranean RCMT Catalog, web page: http://www.bo.ingv.it/RCMT/

Toda S., Enescu B.; 2011. Rate/state Coulomb stress transfer model for the CSEP Japan seismicity forecast. Earth Planets Space 63 (3), 171–185.

Valoroso L., Chiaraluce L., Piccinini D., Di Stefano R., Schaff D., Waldhauser F.; 2013. Radiography of a normal fault system by 64,000 high-precision earthquake locations: the 2009 L'Aquila (Central Italy) case study. J. Geophys. Res. Solid Earth 118, 1156–1176.

Corresponding author: a.galderisi92@gmail.com

Multidisciplinary analysis of 3D seismotectonic modelling: a case study of Serre and Cittanova faults in Southern Calabrian Arc (Italy).

S. Giuffrida[1*], F. Brighenti [1-4], F. Cannavò[3], F. Carnemolla[1-2], G. De Guidi[1-2], G. Barreca[1-2], S. Gambino[1], G. Barberi[3], L. Scarfì [3], C. Monaco[1-2-3]

1 Department of Biological, Geological and Environmental Sciences, University of Catania, Italy.
2 CRUST-Interuniversity Center for 3D Seismotectonics with territorial applications. U.R. Catania, Italy.
3 INGV-OE, National Institute of Geophysics and Volcanology-Etnean Observatory, Catania, Italy.
4 Department of Physics and Earth Sciences, University of Ferrara, Italy.

Introduction

The Calabrian Arc (CA hereinafter), in Southern Italy (Figure 1a,b,c), is an active structural domain where high-intensity historical and instrumental earthquakes with magnitude higher than 7 were recorded. In particular, some earthquakes in southern Calabria such as the seismic sequence of 1783, with the mainshock on February 5 (M 6.9–7.1; Jacques et al., 2001 (Figure 1a) have been regarded as the strongest seismic events of the Italian Peninsula. The seismogenic sources of major earthquakes occurred in the area are still debated, for instance, different interpretations were proposed regarding the location and the geometries of the causative faults responsible for the 1783 historical seismic sequence. In this work, a multidisciplinary approach has been followed to reconstruct, in the MOVE Software Suite environment (granted by Petroleum Experts Limited; www.petex.com), the 3D geometry of the Cittanova fault (CF) and Serre fault (SRF), the longest tectonic structures occurring in southern Calabria. These faults, belonging to the A2 category of the DISS (Database of Individual Seismogenic sources, https://diss.ingv.it/) (Fig.1 a), are defined by Jacques et al. (2001) and recently, starting from macroseismic data, by Andrenacci et al. (2023) as the seismogenic sources of the 5 and 7 February 1783 seismic events, whereas other authors (e.g., Cucci et al., 1996 and reference therein) consider the Gioia Tauro and Mesima faults, belonging to the A1 category, as the most likely sources for the same seismic events. The open debate between different geometric interpretations (E-dipping vs. W-dipping) reported in DISS and different schools of thought on the sources of the 1783 seismic sequence proves that the development of a 3D model for these faults may be crucial to better characterize the seismotectonics of the area and evaluate its seismic potential. Being characterized by clear surface evidence and seismic cluster at depth, we choose the CF and SRF for our analysis.

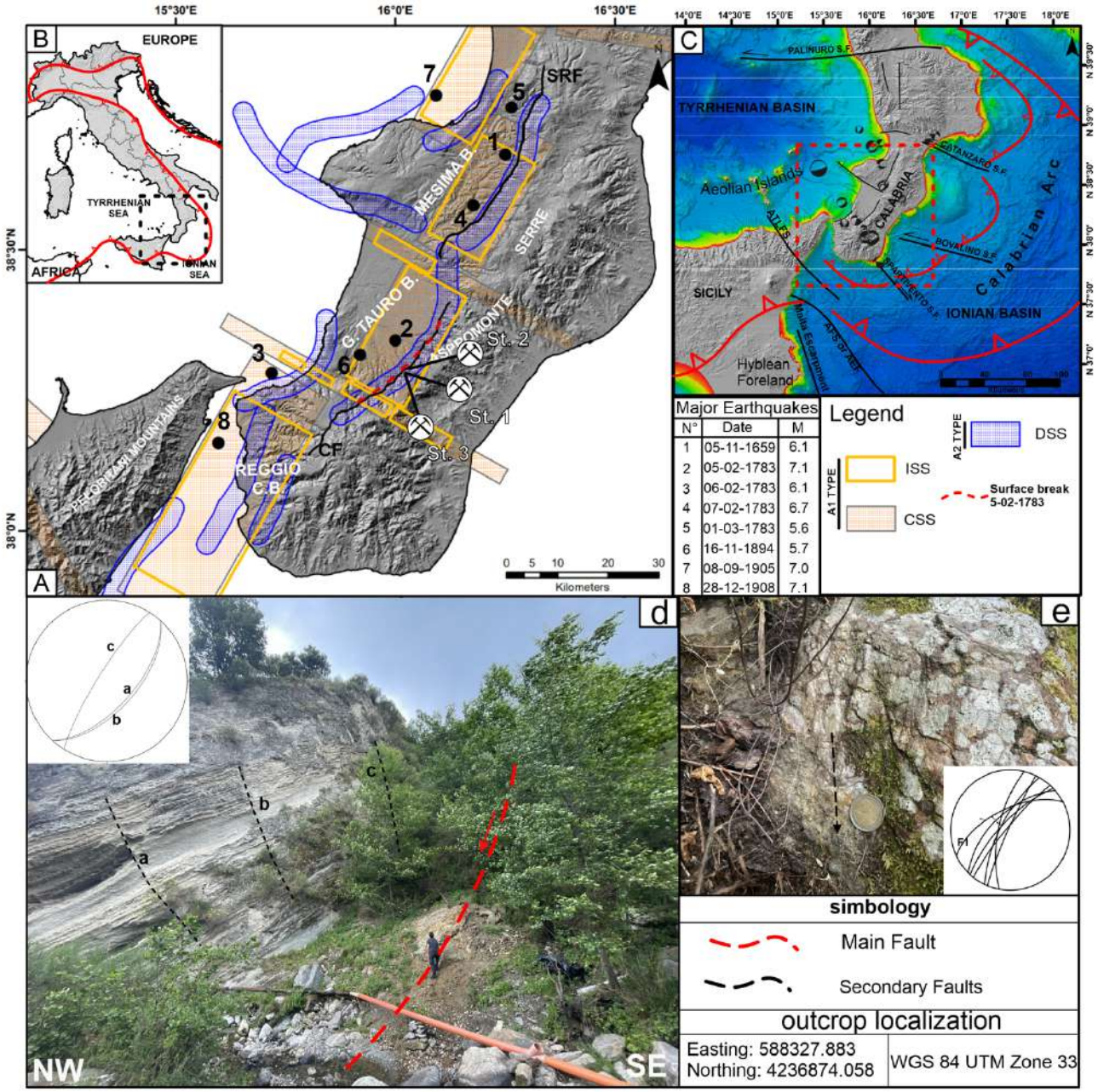

Figure 1: a) Map of seismogenic source types in southern Calabria and major historical earthquakes; The red dashed line represents the coseismic evidence of the 5 February seismic event. b) Front of the Appenninic–Maghrebian Orogen (red line) in the context of the Europe–Africa plate convergence. c) Simplified structural map of the Calabrian Arc domain; d) Upper Pleistocene deposits, tilted by the main fault activity. The main fault (red line) juxtaposes the Pleistocene sediments with the basement rocks. e) Slickenlines on the main fault plane (F1).

Previous seismic source models for the 1783 seismic sequence

The 1783 seismic sequence was characterized by the five events which the main occurred on February 5 that destroyed towns and villages located at the western foot of the northern Aspromonte (i.e., S. Cristina D'Aspromonte and S. Giorgio Morgeto). According to de Dolomieu (1784), after the 5 February mainshock, a 20-km-long scarplet that developed at the western foot of the Aspromonte Mountain between the village of S. Cristina and S. Giorgio Morgeto (red dashed

line in Figure 1a) was observed. Jacques et al. (2001) interpreted this as the coseismic reactivation of the west dipping CF during the 5 February mainshock. Concerning the seismic source models of 5 February, 7 February, and 1 March events, some authors proposed the CF and SRF west-dipping normal faults as responsible sources (Jacques et al., 2001) (Figure 1a, DSS; Debated Seismic Source). This hypothesis was supported by field geologic and morphotectonic data and observation by the distribution of the high-damage sites as exploited by the mesoseismal areas of the 1783 sequence (Baratta, 1901) and revisited macroseismic data (Andrenacci et al., 2023), the observed coseismic fracturing (de Dolomieu, 1784), and also by paleoseismological studies. Conversely, other authors inferred ruptures along the Gioia Tauro and the Mesima east-dipping blind low angle (~30°) normal faults for the same events (Loreto et al., 2013 and reference therein) (see also Figure 1a, ISS: Individual Seismic Source).

Structural data

The CF and SRF border the western sectors of the Aspromonte and Serre mountains, respectively. These NNE-SSW-oriented, west-dipping, and 40-km-long faults (Figures 1A, C) develop cumulative scarps of up to 450 m in height. In order to investigate the surface expression and the kinematic of the faults, a geological–structural survey was carried out. Unfortunately, due to the poorly conservative rock types cropping out in the investigated area, the kinematic indicators are difficult to observe (particularly in the SRF area). Structural data were collected in a few selected outcrops along the CF near Oppido Marmertina Village. Here we reported only the structural station 2 (Fig. 1d, e) (for further information please refer to Giuffrida et al., 2023). The outcrop is located southwest of Oppido Mamertina, along the Spilinga River where the fault meets the Aspromonte gneisses in the footwall and the Middle–Upper Pleistocene deposits in the hanging-wall. Pleistocene deposits are faulted and tilted toward the west (layer attitude 310/35). Minor faults are parallel to the master fault and show steep eastward dips (see also Jacques et al., 2001). The master fault (F1 in stereoplot in Fig. 1e and red line in Fig. 1d) is NE-SW-oriented and shows a set of slickenlines consistent with normal-oblique sinistral kinematics.

Seismological data: 3D fault modelling from earthquakes distribution

To investigate the recent kinematics of the faults affecting the studied area, we analysed the available focal solutions from ISC (http://www.isc.ac.uk/iscbulletin/search/fmechanisms/) and ISIDe (http://iside.rm.ingv.it/tdmt) databases (see Figure 1c). Moreover, earthquakes that have been instrumentally recorded since the early 1980s were used to infer the geometry of the studied faults at depth. We selected the seismic events occurred in the Calabrian Arc from the INGV databases (https://istituto.ingv.it/it/risorse-e-servizi/archivi-e-banche-dati.html) in order to enhance the picture derived from the seismic dataset (refer to Giuffrida et al., 2023 for further information). The final locations (approximately 8,500 seismic events with magnitudes ranging from 1 to 5.7) resulted with an average uncertainty of 0.20 ± 0. 15 km in both horizontal and vertical coordinates and an average root-mean-square travel-time residual of 0.02 s.

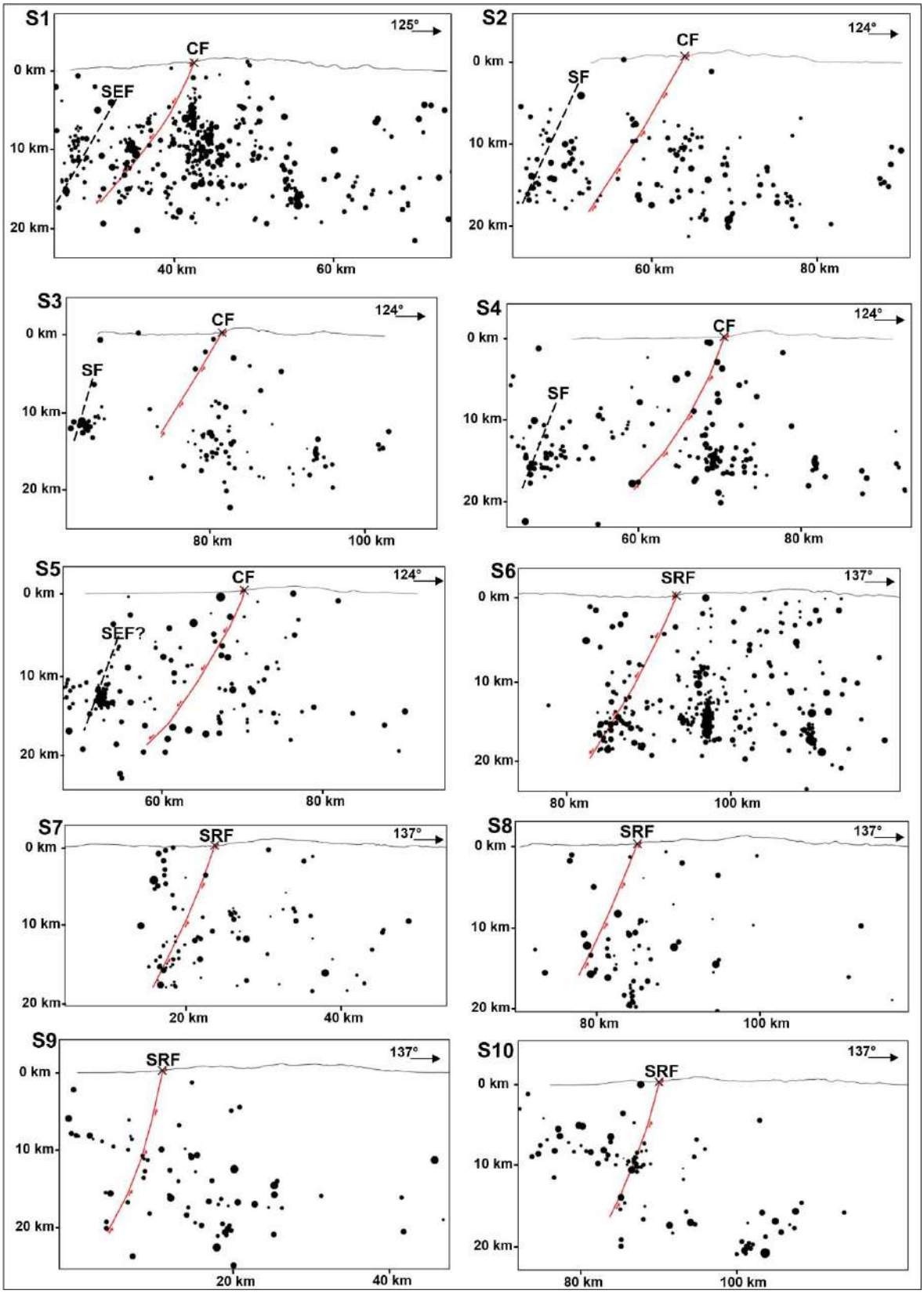

Figure 2: Seismological sections orthogonal to the Cittanova fault (S1–S5) and Serre fault (S6–S10). Crosses are the location of the studied faults at the surface. Black dashed lines are the inferred traces of other faults (SF, Scilla Fault; SEF, S. Eufemia Fault) slicing along the sections.

To constrain the depth geometry of Serre and Cittanova faults, a set of 10-km spaced seismological sections (five sections for each fault) with a buffer projection of 5 km was created (Fig. 2). the geometry at depth of the considered faults (red lines) was traced following earthquake clustering starting from the intersection of the fault on the surface (black crosses in Figure 2). Clusters are visible, especially in S1 and S6 corresponding to the southern tip areas of the CF and SRF, respectively. Despite the other sections that do not exhibit clear clusters useful to infer the attitude of the studied faults at depth, we traced their geometry considering the same trend of S1 and S6 and the earthquakes with the highest magnitude for each section. Subsequently, using a trial-and-error approach, we geometrically tested the modelled planes with the known empirical scaling in order to find a reliable solution for fault planes capable of generating events with a magnitude of 7.

Fault response modelling of the Cittanova and Serre faults

We combined the field structural data, literature data, and kinematics observed at surface with the seismic dataset in order to develop a reliable 3D model of the fault planes. According to the proposed fault model (Figures 3 a), the CF is an almost 44-km-long fault, roughly N40E-oriented with a plane dipping toward NW, whereas the SRF is a N30E-striking, 40-km long fault with a plane dipping toward NW. The average dip of the CF is 57°, while the SRF exhibits an average dip of approximately 60°. All geometric parameters are summarized in Table 1. The parameters derived from the 3D model were used to estimate the expected magnitude for each plane, assuming an activation of the faults for their entire length and using empirical relationships. We used the surface rupture length (SRL) and the rupture area (RA) vs. magnitude empirical scaling both for Wells and Coppersmith (1994) and Leonard (2010). The resulting magnitudes for the given faults are comparable (see Table 1). Moreover, the Fault Response Modelling (FRM) module was applied to kinematically test the model and verify the maximum vertical displacement and its spatial distribution associated with the activation of the fault planes for their entire length (which is consistent with a maximum expected magnitude of approximately 6.8 – 7). The first simulation (Figure 3c) shows the displacement field for the activation of both faults. The simulated vertical displacement ranges from 0.5 to 1.7 m (with a maximum value equal to 2.2 m). The correspondence of the mesoseismal areas of 5 and 7 February and for the 1 March shocks, macroseismic data and simulated coseismic displacement (Figure 3c) confirms the choice of the CF and SRF faults, respectively, as the most likely causative sources for the considered events. The second simulation (Figure 3d) shows the cumulative displacements ranging from −354 m to 112 m. In this case, the displacement values exhibit an abrupt change across the fault traces; the vertical cumulative displacement of CF and SRF reaches almost 450 m (see also the vertical displacement dz profiles shown in Figure 3f), which is consistent with the minimum vertical offset estimated for these faults (see also Jacques et al., 2001).

Geometric parameters and empirical relations								
		CF				SRF		
Av. Dip. Azimuth		313.96°				301.9°		
Av. Dip		57.73°				63.53°		
Dep. range and width (m)		min	Width	max		min	Width	max
		-19767	21070	1303		-21697	22305	608
Wells & Coppersmith (1996)	M vs SRL	6.98				7.14		
	M vs RA	6.99				7.02		
Leornad, (2010)	M vs SRL	6.9				6.93		
	M vs RA	6.98				7.01		
Tmax vs Lmax Manighetti et al., 2001		664m				697m		

Table 1

Slip Tendency

The slip tendency analysis (Figure 3 a, b) shows that both SRF and CF are under an almost unstable mechanical condition in the given remote stress state. Concerning the SRF, Ts ranges from 0.35 to 0.85, with the most frequent values ranging from 0.6 to 0.7, while CF exhibits Ts ranging from 0.45 to 0.80, with the most frequent values ranging from 0.62 to 0.68. Moreover, Ts value distribution for CF is more clustered than that for SRF which exhibits Ts spreading on its overall plane with another highly frequent minor distribution between 0.48 and 5.4, located especially near its northern and deepest portions. Note that the calculation was performed considering the saturated condition of the surrounding medium in order to take into account the worst condition for a potential reactivation of the fault planes.

Conclusion

The instrumental seismicity, merged with structural field investigation and literature data, provided useful constraints to infer the geometry on surface and at depth of SRF and CF. The geometric parameters obtained through the model of these faults are compatible with the empirical relationships (magnitude vs. rupture area and magnitude vs. fault length; Wells and Coppersmith, 1994; Leonard, 2010). Accordingly, we achieved the expected magnitude for CF and SRF and confirmed that these faults can be the probable sources of the mainshocks of the 1783 seismic sequence (5 February, 7 February, and 1 March, M = 6.9–7; Jacques et al., 2001). From the slip tendency analysis, we found that both fault planes are astride under the stable and unstable mechanical conditions in the given regional stress state. The response of the modelled fault planes

indicates that the simulated coseismic and cumulative vertical displacement fields agree with the historical observation of the slip along the fault planes and with actual height of the morphological scarps, respectively. Considering the lack of seismic profiles onshore, the proposed model can represent an important starting point for seismotectonic modelling.

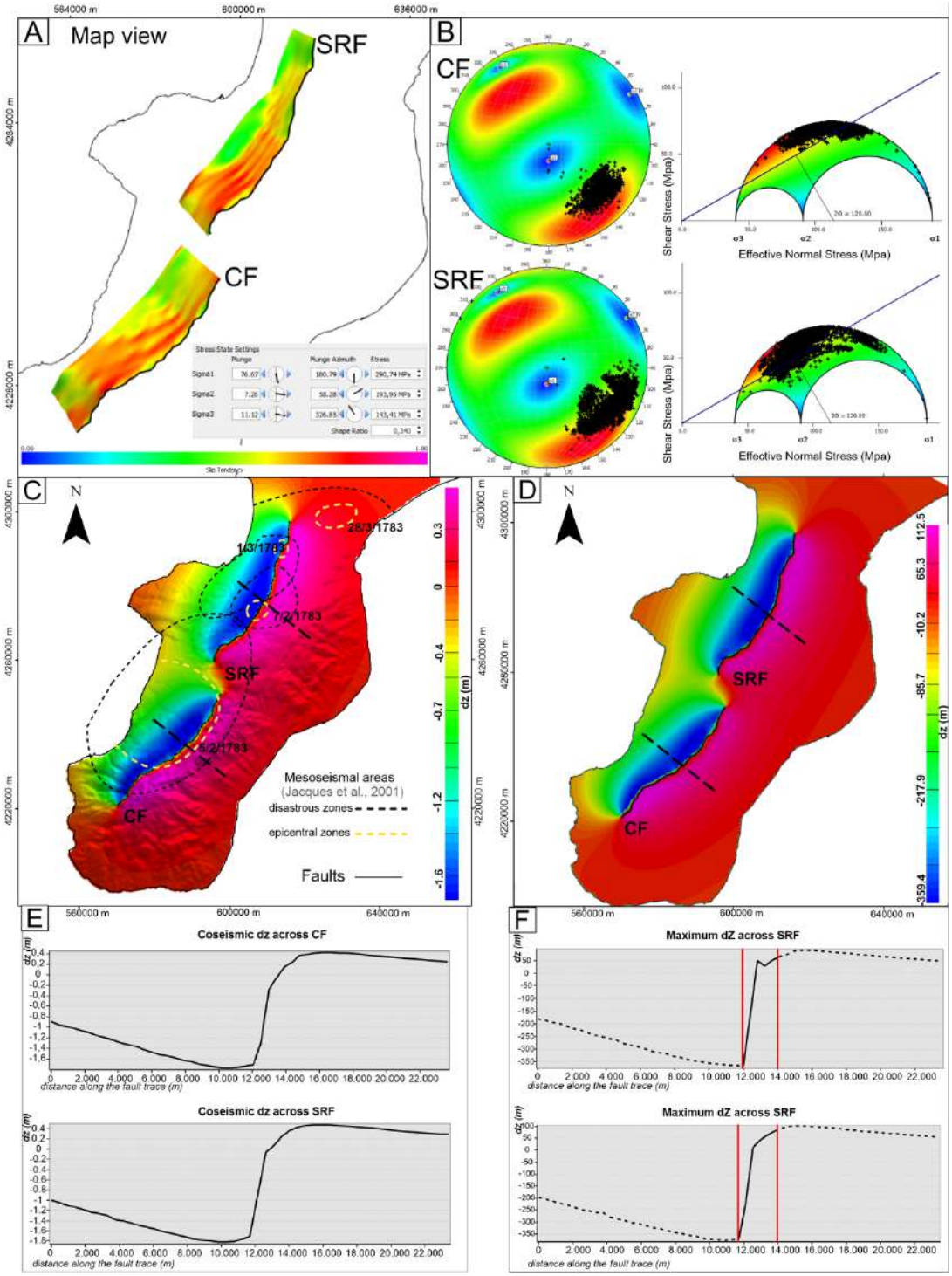

Figure 3: a) Map view of the 3D model of SRF and CF, fault planes are coloured in function of the Slip tendency (Ts). b) Confining stress state resolved at 10 km of depth. c) Vertical displacement (dz) computed for 3 m of uniform slip on the fault planes. Black and yellow dashed lines show the mesoseismal areas for the shocks of the 1783 seismic (see also Baratta, 1901; Jacques et al., 2001 for further information). d) Vertical displacement (dz) computed for Tmax values of 664 m and 697 m. e) Coseismic dz profile across CF and SRF. f) Cumulative dz profile across CF and SRF.

References

Andrenacci, C., Bello, S., Barbano, M. S., de Nardis, R., Pirrotta, C., Pietrolungo, F., et al. (2023). Reappraisal and analysis of macroseismic data for seismotectonic purposes: the strong earthquakes of southern Calabria, Italy. Geosciences 13, 212. doi:10.3390/ geosciences13070212.

Baratta, M. (1901). I terremoti d'Italia. Torino: Arnoldo Forni.

Cucci, L. (2022). NW-Dipping versus SE-dipping causative faults of the 1783 M7.1 southern Calabria (Italy) earthquake: the contribution from the analysis of the coseismic hydrological changes. Front. Earth Sci. 10, 987731. doi:10.3389/feart. 2022.987731.

de Dolomieu, D. (1784). Me´moire sur les Tremblemens de Terre de la Calabre Pendant l'Anne´e 1783. Rome: Fulgoni.

Jacques, E., Monaco, C., Tapponnier, P., Tortorici, L., and Winter, T. (2001). Faulting and earthquake triggering during the 1783 Calabria seismic sequence. Cambridge: Cambridge University Press.

Giuffrida S, Brighenti F, Cannavò F, Carnemolla F, De Guidi G, Barreca G, Gambino S, Barberi G, Scarfi L and Monaco C (2023), Multidisciplinary analysis of 3D seismotectonic modelling: a case study of Serre and Cittanova faults in the southern Calabrian Arc (Italy). Front. Earth Sci. 11:1240051. doi: 10.3389/feart.2023.1240051.

Loreto, M. F., Fracassi, U., Franzo, A., Negro, P., Zgur, F., and Facchin, L. (2013). Approaching the seismogenic source of the Calabria 8 September 1905 earthquake: new geophysical, geological and biochemical data from the S. Eufemia gulf (S Italy). Mar. Geol. 343, 62–75. doi:10.1016/ j.margeo.2013.06.016.

Corresponding author: salvatore.giuffrida@phd.unict.it

Integration of 3D P and S velocity model in SeisComP real time monitoring: an application to Northern Italy

F. Grigoli[1], C. Rossi[2], C. Cocorullo[2]

[1] *University of Pisa, Italy*
[2] *Seismix s.r.l., Italy*

The real-time microseismic monitoring represents a fundamental point in evaluating and managing the risks associated with industrial activities for geo-resources exploitation. SeisComP (Helmholtz Centre Potsdam GFZ German Research Centre for Geosciences and gempa GmbH 2008), a software package developed by the German Research for Geosciences (GFZ), stands out as one of the most extensively utilized tools for seismic monitoring: it facilitates automatic data acquisition and real-time or post-processing.

In this study, we illustrate a SeisComP optimization for real-time data processing applied to microseismic monitoring of an Underground Gas Storage field in Northern Italy. Our analysis encompasses two years of continuous seismic data obtained from a seismic network consisting of 15 stations, including both surface and borehole sensors. To better constrain the earthquakes' location, first, we applied a Joint Hypocenter and Velocity technique (Thurber, 1992; Kissling, et al. 1994) to compute a new P and S 1D velocity model for the gas storage field area.

Then, we derived a 3D P-wave velocity model at the reservoir scale by using migration velocity data from a 3D seismic reflection survey. To obtain the 3D S-wave velocity model, we used an average Vp/Vs value derived from the 1D velocity model and well-logs.

In the concluding phase, the different velocity models are compared by examining the earthquakes' locations obtained with each model. The results indicate a consistent enhancement in location accuracy (both in terms of RMS and waveform coherence) for events within the inner area when using the 3D model. For the other events, the earthquakes' locations computed with the optimized 1D velocity model are improved compared to those obtained by using the initial velocity model.

This seismic processing routine represents a pioneering application in Italy, demonstrating how a 3D velocity model can be fully integrated into real-time microseismic monitoring operations, in agreement with the recommendations of the Italian Guideline for Microseismicity Monitoring in Industrial Activities (Dialuce et al., 2014).

References

Dialuce, G., Chiarabba, C., Di Bucci, D., Doglioni, C., Gasparini, P., Lanari, R., . . . Zollo, A. (2014). Indirizzi e linee guida per il monitoraggio della sismicità, delle deformazioni del suolo e delle pressioni di poro nell'ambito delle attività antropiche.

Helmholtz Centre Potsdam GFZ German Research Centre for Geosciences and gempa GmbH. (2008). *The SeisComP seismological software package.* doi:10.5880/GFZ.2.4.2020.003

Kissling, E., Ellsworth, W., Eberhart-Phillips, D., & Kradolfer, U. (1994). Initial reference models in local earthquake tomography. *Journal of Geophysical Research, 99*(B10), 19635-19646. doi:10.1029/93JB03138

Thurber, C. (1992). Hypocenter-velocity structure coupling in local earthquake tomography. *Physics of the Earth and Planetary Interiors, 75*(1-3), 55-62. doi:10.1016/0031-9201(92)90117-E

Corresponding author: c.rossi@seismix.it

InSAR data analysis to investigate the 2009 post-seismic deformation in L'Aquila downtown

V. Guerriero[1], A. Sciortino[1], R. Marini[2], P. Mazzanti[2, 3], M. Tallini[1]

1 Dipartimento di Ingegneria Civile, Edile-Architettura e Ambientale, Università degli Studi dell'Aquila
2 NHAZCA S.r.l., start-up Università degli Studi di Roma "La Sapienza"
3 Dipartimento di Scienze della Terra & centro di ricerca CERI, Università degli Studi di Roma "La Sapienza"

Introduction

A statistical analysis of time series of A-DInSAR post-seismic data, acquired in the time range 2010-2021 from the Cosmo-SkyMed and Sentinel-1 missions, has been carried out. This has allowed analysing the relationships between ground deformations and geological, hydrogeological, and geomorphological features of the study area, located in L'Aquila (Italy) historical centre (LAHC). The correlation analysis between predisposing factors and SAR deformation has highlighted that subsidence is substantially controlled by the shalow lithology, showing how compositional variations within lithology can significantly influence ground deformations. Furthermore, hydrogeological features, such as water table depth and its seasonal fluctuations exhibit correlation with subsidence rates.
The analysis of these data is still ongoing and offers promising research perspectives in the field of geomechanical/geotechnical subsoil characterization, based on satellite ground deformation data, also useful in seismic hazard characterization and mitigation.

A-DInSAR Displacement Data by means of Multi-Satellite technology

The data set involved in the present study has been achieved by Advanced Differential Synthetic Aperture Radar Interferometry (A-DInSAR) technique, by integrating of ground displacement values from two active satellite SAR missions, namely Sentinel-1 (by ESA) and Cosmo-SkyMed (by ASI).
The resulting data sets consist of time series of 158 values of ground displacement, one for each monitored ground point, detected in the time range from April 14, 2010, to November 30, 2021. Figs. 1, 2 and 3 illustrate A-DInSAR data involved in this study, with their comparison with local geology.

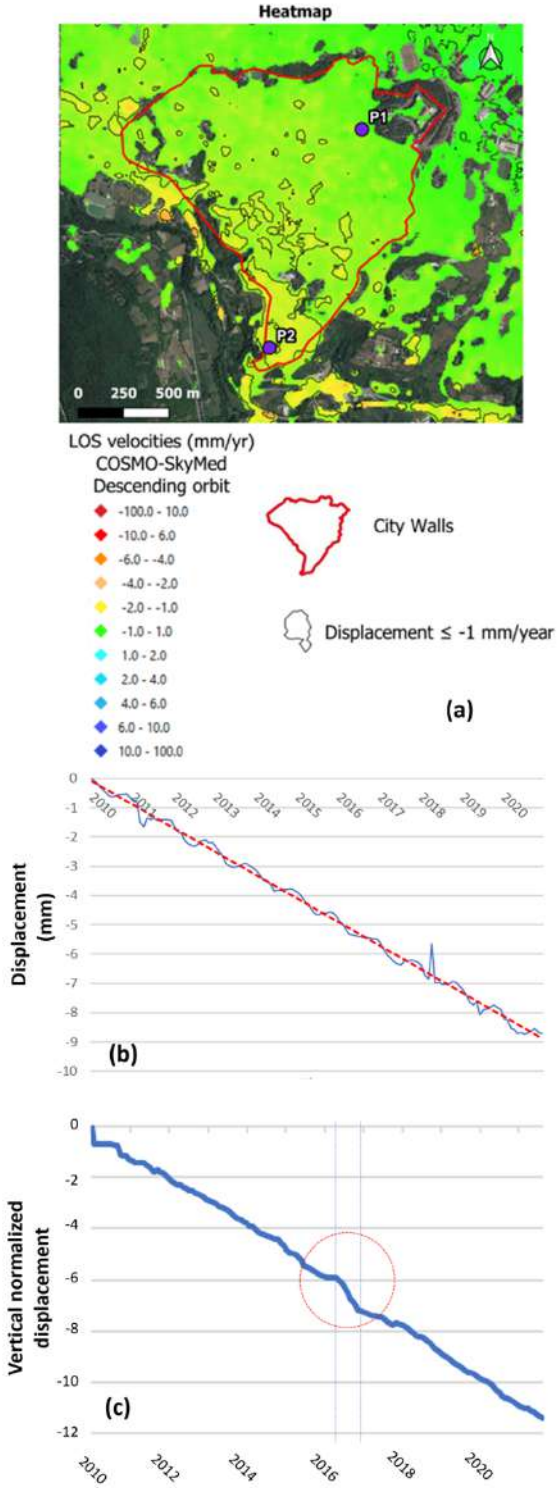

Figure 1 – a) A-DInSAR map resulting from the processing of April 14, 2010, to November 30, 2021, descending orbit images; b) time series of average displacements (i.e., spatially averaged over the studied area, within city walls) showing seasonal fluctuations around the trendline; c) time series of opportunely selected, normalized vertical displacement values in which seasonal oscillations have been removed. Each monthly value is calculated as the average of the values recorded in the previous and following six months. The red circle outlines an observed anomaly in the subsidence trend. The two vertical lines highlight the time range August-November 2016, in which the Amatrice-Norcia seismic sequence occurred.

The study area

L'Aquila downtown is placed in the L'Aquila-Scoppito intermontane basin (ASB) which is a half-graben bordered by SW-dipping normal mostly active faults located in its northern border, which are responsible for the historical and present seismicity. ASB is filled with approximately maximum 600 meters of Plio-Quaternary continental slope, colluvial and alluvial deposits which overlie unconformably the carbonate bedrock formed by Jurassic to Miocene marine carbonate units (Antonielli et al., 2020; Fig. 3).

Heterometric breccias with clayey-silty matrix (S. Demetrio-Colle Cantaro Unit) represent the first Plio-Quaternary detrital sedimentation in the ASB. These lithologies and the underlying bedrock are unconformably overlain by alluvial and marshy deposits composed by silt, clay, and sands (Madonna della Strada Unit – MDS, Early Pleistocene) (Tallini et al., 2019). The Fosso di Genzano Unit (FGS), incised into the earlier deposits, is composed by gravel and sand, pertaining to Middle Pleistocene alluvial fans.

The shallow part of the gently S-dipping hill, in which L'Aquila downtown is located, is mainly composed by 20-100 m-thick of L'Aquila Breccia Unit (LAB). LAB lays unconformably upon FGS and MDS and consists of heterometric poorly sorted carbonate clasts, sometimes with sandy-clayey calcareous matrix sedimented during the Middle Pleistocene with rock-avalanche process (Antonielli et al., 2020). In the southern part of L'Aquila hill, alluvial lens of sand and gravel (ALE) is interlayered within LAB (Fig. 3). The Red Soil Unit (RS) covers unconformably LAB (Tallini et al., 2020). RS includes reddish clayey colluvial sediment and epikarst deposits and exhibits highly variable thickness, reaching up to 30 meters. RS formed during a humid and warm interglacial phase of the Upper Pleistocene at the expense of LAB.

Data about geological features potentially controlling subsidence processes

To perform a geological and seismic characterization of the study area, a total of 142 Shear Wave Velocity (Vs) in-situ measurements, pertaining to the shallow lithologies within LAHC, were acquired from bibliographic sources (e.g., Amoroso et al., 2018). Furthermore, logs from an extensive dataset of 573 boreholes, many of which were drilled after the 2009 earthquake to facilitate the reconstruction of LAHC buildings, were integrated with geological data from the literature (e.g., Tallini et al., 2020).

The collected data formed a substantial database that facilitated numerous GIS-based processing, aimed to assess the surface geology and the RS thickness (Sciortino et al., 2023). Due to their high compressibility, RS have been recognized in various studies as lithology responsible for site-specific seismic amplifications (e.g., Tallini et al., 2020).

The produced geological map was rasterized, assigning a Vs (Shear Wave Velocity) value to each lithology based on literature data from Downhole (DH) and MASW in situ measurements (e.g., Amoroso et al., 2018).

Geomorphological and hydrogeological characterization of the LAHC area were carried out through the analysis of a digital terrain model (DEM) and of the piezometric level.

Results of the correlation analysis

To assess the relationship between the geological-geomorphological and hydrogeological study area features and ground deformation in LAHC, a correlation analysis has been carried out. We compared the vertical deformation, with slope maps, RS thickness, depth of regional aquifer and Vs of the outcropping lithologies. For each of these factors, the Pearson correlation coefficient with ground vertical average velocity has been calculated (Tab. 1).

Predisposing factor	Pearson coefficient
Depth of regional aquifer	-0.52
Ground slope	-0.22
Red Soil thickness	0.13
Vs of outcropping geology	0.46

Table 1 – Values of the Pearson coefficients calculated between the considered geological predisposing factors and subsidence velocities.

Furthermore, seasonal fluctuations of subsidence velocity, as evidenced in Fig 1b, have been analysed. To this end, the cross-correlation between quarterly average rainfall (mm/d) and detrended average subsidence rate (mm/y), has been analysed, in the time range 2010-2021. A statistically significant correlation value, equal to 0.56, has been individuated.

Discussion and perspectives for subsoil characterization by means of A-DInSAR displacement data

The correlation values in Tab. 1 are statistically significant, nevertheless, it is presumable that the subsidence process is mainly controlled by the kind and thickness of lithologies involved. The above illustrated correlation analysis provides a first result, which may be improved by a multivariate approach, as described below.

Fig.3 illustrates the velocity values associated with monitored points, falling in the strip (width: 50 m), indicated in semi-transparent red in Fig.3a, to achieve a more accurate comparison of ground displacement data with the subsurface structure. This band surrounds an accurate geological section accomplished by Antonielli et al. (2020; Fig. 3b). Subsidence velocities decrease going from LAB 3 (with abundant fine and more deformable fraction) to LAB 2 and LAB 1 (Fig. 2), whereas, local variations seem to be predominantly controlled by the RS thickness, as the trend of the point cloud in the diagram faithfully follows the thickness of the RS units (Figs. 3c and 3d).

The results illustrated in Fig. 3d lead to conclude that a significant contribution to the observed subsidence phenomenon is provided by the consolidation of Quaternary units. In In granular soils, seismic shaking produces well-known phenomena of variation in porosity, such as compaction or dilatancy. In the case of saturated fine-grained soils (even above the water table) a first phase of porosity variation occurs slowly, associated with fluid expulsion (Terzaghi consolidation), followed by a second phase of secondary consolidation, due to creep phenomena.

Therefore, the post-seismic velocity and displacement values of the monitored PS are given by the sum of effects of primary and/or secondary consolidation in saturated soils and the only secondary consolidation of non-saturated ones.

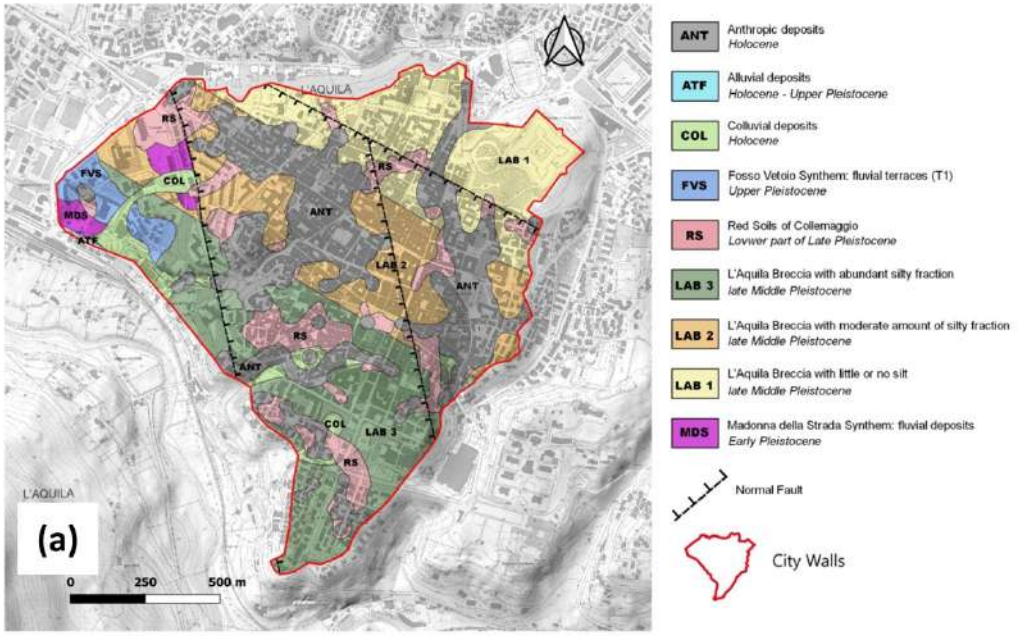

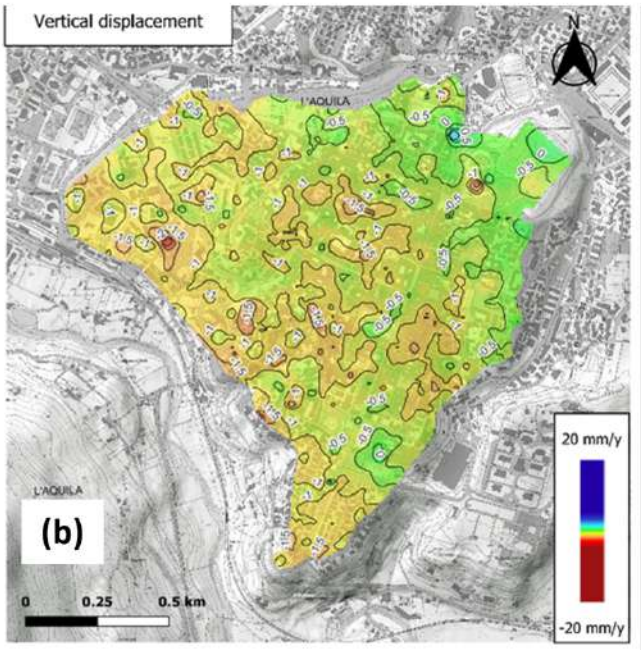

Figure 2 – a) Geological map with an internal division of LAB based on the abundance of the muddy-limestone matrix. From LAB 1 to LAB 3 the silt fraction increases; b) vertical velocity map achieved by means of interpolation of values calculated by combining Cosmo-SkyMed descending and Sentinel-1 ascending orbit data. Green colour, denoting velocity lesser tha 0.5 mm/y (in absolute value), is prevalent over LAB1, light green (velocity in the range 0.5-1 mm/y) over LAB2 and yellow (velocity >1 mm/y) over LAB3.

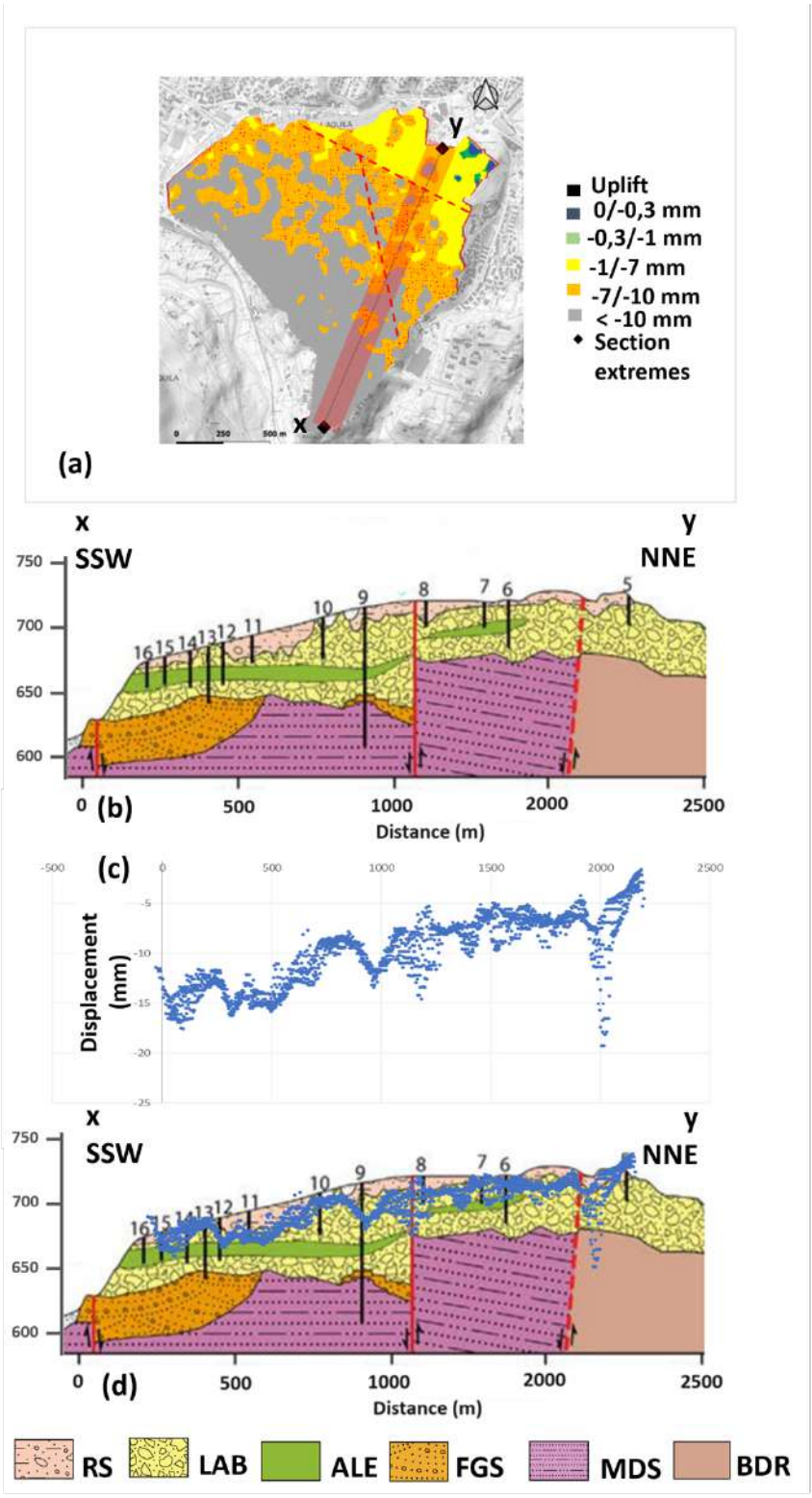

Figure 3 – a) Monitored points grouped in cumulative displacement classes (time range 2010-2021) in L'Aquila downtown; x-y: geological section reported in b and d; b) geological section; RS: Red Soil (Upper Pleistocene); LAB: L'Aquila Breccia (late Middle Pleistocene); ALE: Alluvial lens (sand and gravel, Middle Pleistocene); FGS: Fosso di Genzano Synthem (sand and gravel, Middle Pleistocene); MDS: Madonna della Strada Synthem (silt, clay and sand, Early Pleistocene); BDR: carbonate bedrock (Jurassic to Miocene); c) cumulative displacement values (mm) of the monitored points, falling in the red 50 m width semi-transparent band in panel a; d) the comparison of deformation and geology is shown through the superposition of the cumulative displacement of panel c and the geological section in panel b. Note the good matching between displacement with the Red Soil bottom boundary.

Let us consider a simple vertical strain model, made up of overlying layers (e.g., RS, LAB, etc.) in the consolidation phase. According to such a model, the subsidence velocity (or cumulated displacement in a given time interval) at a point is given by sum of contributions by the N layers under such point. Denoting by v such velocity value and by h_j the thickness of the j-th layer, then:

$$v = \sum_{j=1}^{N} C_j \bullet h_j, \quad (1)$$

where C_j are constants depending on the mechanical properties of the considered layers, which can be viewed as the contribution provided by each thickness unit (e.g., 1 m) of layer. If for M wells the thicknesses h_j are known, we have M equations like (1) in which v and h_j are known. Then, the constants C_j can be calculated by means of multivariate statistical analysis, e.g., by adopting a Least Squares or a Maximum Likelihood approach. Once C_j values have been evaluated, the thickness of shallow lithologies can be calculated for whatever point of the study area.

This may provide a promising powerful method of geotechnical characterization at urban scale and at a relatively low cost. This model may also be adapted to study variations in subsidence velocity over time, according to a multi-layer Terzaghi consolidation model. In this case, Eq. 1 would be nonlinear and, therefore, the analysis would follow a nonlinear multivariate approach.

Conclusion

- The A-DInSAR post-seismic data, recorded in the time range 2010-2021, revealed a subsidence phenomenon, still ongoing, due to the concurring effect of variation in pore pressures and secondary consolidation of shallow and deep rocks. The correlation analysis and the evidence illustrated in Fig. 3d allow us to conclude that subsidence velocities are mainly controlled by the properties and thicknesses of shallower rock layers, such as RS and LAB.
- The cross-correlation analysis highlighted a significant correlation between seasonal fluctuations in subsidence rate and rainfall variations.
- The seasonally adjusted A-DInSAR time series highlighted an anomaly in the subsidence trend, observable during the Amatrice-Norcia seismic sequence of 2016. The study of this anomaly deserves attention and will be the subject of future research.
- Ground deformations detected by means of A-DInSAR technology may provide a promising inversion criterion, enabling us to perform a geotechnical characterization of shallow rock layers, over large areas, at relatively low costs.

References

Amoroso, S.; Gaudiosi, I.; Tallini, M.; Di Giulio, G.; Milana, G. 2018: 2D site response analysis of a cultural heritage: the case study of the site of Santa Maria di Collemaggio Basilica (L'Aquila, Italy). Bull. Earthq. Eng., 16, 4443–4466, doi:10.1007/s10518-018-0356-2.

Antonielli B., Della Seta M., Esposito C., Scarascia Mugnozza G., Schilirò L., Spadi M., Tallini M. 2020: *Quaternary rock avalanches in the Apennines: New data and interpretation of the huge clastic deposit of the L'Aquila Basin (central Italy)*. Geomorphology, 361, 107194, doi: 10.1016/j.geomorph.2020.107194

Sciortino A., Guerriero V., Marini R., Spadi M., Mazzanti P., Tallini M. 2023: *Satellite A-DInSAR pattern recognition for seismic vulnerability mapping at city scale: insights from the L'Aquila (Italy) case study*. GIScience & Remote Sensing. https://doi.org/10.1080/15481603.2023.2293522

Tallini, M.; Lo Sardo, L.; Spadi, M. 2020: *Seismic site characterisation of Red Soil and soil-building resonance effects in L'Aquila downtown (Central Italy)*. Bull. Eng. Geol. Environ., 79, 4021–4034, doi:10.1007/s10064-020-01795-x.

Tallini, M.; Spadi, M.; Cosentino, D.; Nocentini, M.; Cavuoto, G.; Di Fiore, V. 2019: *High-resolution seismic reflection exploration for evaluating the seismic hazard in a Plio-Quaternary intermontane basin (L'Aquila downtown, central Italy)*. Quat. Int. 2019, 532, 34–47, doi:10.1016/j.quaint.2019.09.016.

Corresponding author: vincenzo.guerriero@univaq.it

Supervised and unsupervised machine learning approaches for identifying the preparatory process of moderate earthquakes at The Geysers, California

A.G. Iaccarino[1], M. Picozzi[1,2]

[1]Università degli Studi di Napoli "Federico II", Dipartimento di Fisica "Ettore Pancini", Napoli, Italy
[2]National Institute of Oceanography and Applied Geophysics, OGS, Sgonico, Italy

Earthquakes prediction is considered the holy grail of seismology. After almost a century of efforts without convincing results, the recent raise of machine learning (ML) methods in conjunction with the deployment of dense seismic networks has boosted new hope in this field. Even if large earthquakes still occur unanticipated, recent laboratory, field and theoretical studies support the existence of a preparatory phase preceding earthquakes, where small and stable ruptures progressively develop into an unstable and confined zone around the future hypocenter (Dresen et al., 2020; Kato & Ben-Zion, 2020; Mignan, 2012).

Here, we present two works focused on the induced seismicity at The Geysers geothermal field in California. Due to its complex geological structure, the industrial operations for energy production and the existence of a dense seismic network, the Geysers area represents a natural laboratory for seismicity studies (Bentz et al., 2019; Holtzman et al., 2018; Martínez-Garzón et al., 2020; Trugman et al., 2016).

We address the preparatory phase of Mw≥3.5 earthquakes identification problem by developing ML approaches to analyze time-series of physics-related features extracted from catalog information and estimated for events that occurred before the mainshocks. Specifically, we study the temporal evolution of the *b-value* from the Gutenberg-Richter (b), the magnitude of completeness (Mc), the fractal dimension (Dc), the inter-event time (dt), and the moment rate (Mr).

In a first work (Picozzi & Iaccarino, 2021), we use a supervised technique (Recurrent Neural Network, RNN) to reveal the preparation of 8 Mw≥3.9 earthquakes. In the second one (Iaccarino & Picozzi, 2023), we apply an unsupervised K-means clustering technique on 19 Mw≥3.5 events.

The results of the first work show that the preparatory phase for the three testing Mw≥3.9 earthquakes lasted from few hours to few days, in agreement with the short-time preparation process (~1 day) observed for a similar magnitude natural earthquake (De Barros et al., 2020).

In the second work, we show that out of 19 moderate magnitude events considered, a common preparatory phase for 11 events is clearly identified, plus other 5 events for which we can guess a preparatory phase but with different characteristics from the previous ones. The latter result confirms that even within the same tectonic context different possible activation behavior may exist. The duration of the preparatory process ranges between about 16 hours and 4 days. We observe that also for the retrieved preparatory process a decrease in b, and Dc, and an increase of Mr, as found by many authors (Gulia & Wiemer, 2019; Mignan, 2011; Picozzi et al., 2023). Finally, we find a clear spatial correlation (Fig. 1) between events with a preparation phase and the location of injection's wells, suggesting an important role of fluids in the preparatory process.

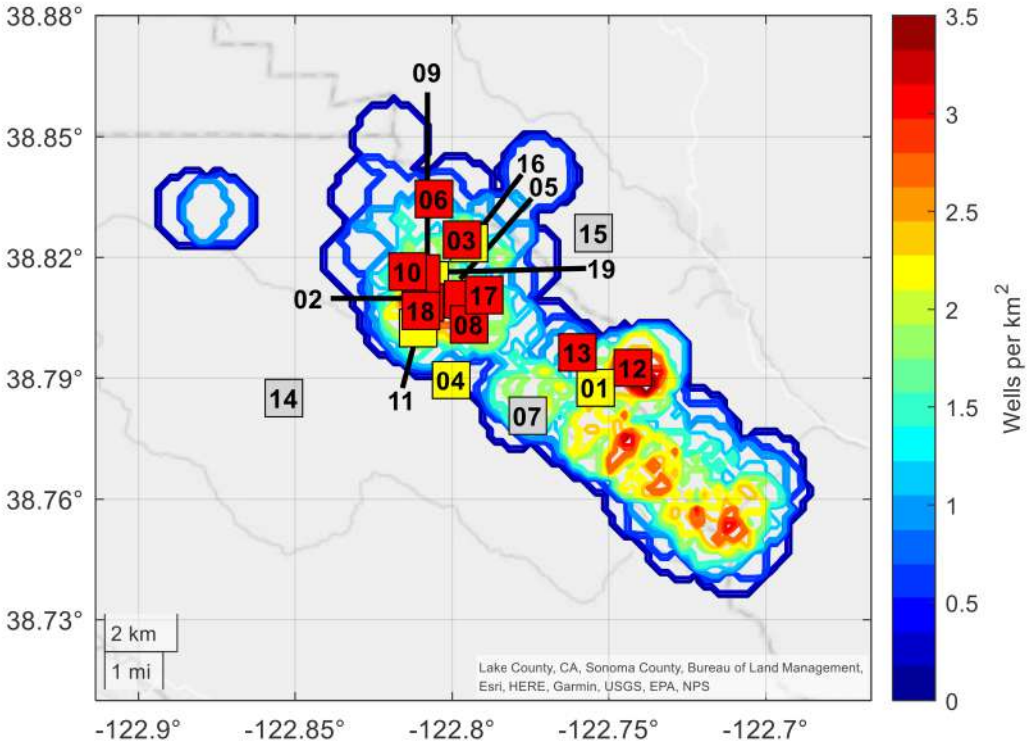

Fig. 1 – Maps of the M3.5 events compared to the areal well density (contour plot). The events with a preparatory phase are shown as red squares; yellow squares refer to the events with an unclear preparatory phase; the other M3.5 events as grey squares.

References

Bentz, S., Martínez-Garzón, P., Kwiatek, G., Dresen, G., & Bohnhoff, M. (2019). Analysis of Microseismicity Framing ML ' 2.5 Earthquakes at The Geysers Geothermal Field, California. Journal of Geophysical Research: Solid Earth, 124(8), 8823–8843. https://doi.org/10.1029/2019JB017716

De Barros, L., Cappa, F., Deschamps, A., & Dublanchet, P. (2020). Imbricated Aseismic Slip and Fluid Diffusion Drive a Seismic Swarm in the Corinth Gulf, Greece. Geophysical Research Letters, 47(9), e2020GL087142. https://doi.org/10.1029/2020GL087142

Dresen, G., Kwiatek, G., Goebel, T., & Ben-Zion, Y. (2020). Seismic and Aseismic Preparatory Processes Before Large Stick–Slip Failure. Pure and Applied Geophysics, 177(12), 5741–5760. https://doi.org/10.1007/s00024-020-02605-x

Gulia, L., & Wiemer, S. (2019). Real-time discrimination of earthquake foreshocks and aftershocks. Nature 2019 574:7777, 574(7777), 193–199. https://doi.org/10.1038/s41586-019-1606-4

Holtzman, B. K., Paté, A., Paisley, J., Waldhauser, F., & Repetto, D. (2018). Machine learning reveals cyclic changes in seismic source spectra in Geysers geothermal field. Science Advances, 4(5). https://doi.org/10.1126/SCIADV.AAO2929/SUPPL_FILE/AAO2929_SM.PDF

Iaccarino, A. G., & Picozzi, M. (2023). Detecting the Preparatory Phase of Induced Earthquakes at The Geysers (California) Using K-Means Clustering. Journal of Geophysical Research: Solid Earth, 128(10), e2023JB026429. https://doi.org/10.1029/2023JB026429

Kato, A., & Ben-Zion, Y. (2020). The generation of large earthquakes. Nature Reviews Earth & Environment 2020 2:1, 2(1), 26–39. https://doi.org/10.1038/s43017-020-00108-w

Martínez-Garzón, P., Kwiatek, G., Bentz, S., Bohnhoff, M., & Dresen, G. (2020). Induced earthquake potential in geothermal reservoirs: Insights from The Geysers, California. The Leading Edge, 39(12), 873–882. https://doi.org/10.1190/TLE39120873.1

Mignan, A. (2011). Retrospective on the Accelerating Seismic Release (ASR) hypothesis: Controversy and new horizons. Tectonophysics, 505(1–4), 1–16. https://doi.org/10.1016/J.TECTO.2011.03.010

Mignan, A. (2012). Seismicity precursors to large earthquakes unified in a stress accumulation framework. Geophysical Research Letters, 39(21), 21308. https://doi.org/10.1029/2012GL053946

Picozzi, M., & Iaccarino, A. G. (2021). Forecasting the Preparatory Phase of Induced Earthquakes by Recurrent Neural Network. Forecasting, 3(1), 17–36. https://doi.org/10.3390/forecast3010002

Picozzi, M., Iaccarino, A. G., & Spallarossa, D. (2023). The preparatory process of the 2023 Mw 7.8 Türkiye earthquake. Scientific Reports 2023 13:1, 13(1), 1–10. https://doi.org/10.1038/s41598-023-45073-8

Trugman, D. T., Shearer, P. M., Borsa, A. A., & Fialko, Y. (2016). A comparison of long-term changes in seismicity at The Geysers, Salton Sea, and Coso geothermal fields. Journal of Geophysical Research: Solid Earth, 121(1), 225–247. https://doi.org/10.1002/2015JB012510x: Title. Journal.

Corresponding author: antoniogiovanni.iaccarino@unina.it

Detection capability of earthquakes by a hydraulic pressure device in the Gran Sasso aquifer (central Italy)

D. Isaya[1], G. De Luca[2], M. Tallini[1]

1 Dipartimento di Ingegneria Civile, Edile-Architettura e Ambientale, Università degli Studi dell'Aquila
2 Istituto Nazionale di Geofisica e Vulcanologia

1. Introduction

The Gran Sasso aquifer (GSA) can be considered paradigmatic of the fissured-karst carbonate ones of the Mediterranean domain as concerns also the Earthquake Hydrology topic because (*i*) it is crossed by several active faults, (*ii*) it is placed in central Italy characterized by high Seismic hazard and (*iii*) it hosts the INFN underground laboratory (UL). UL is a strategic site for studying aquifer versus earthquakes because it represents a unique "window" within the deep saturated zone located in the GSA core which has above a very thick unsaturated zone (more than a thousand of meters). Therefore, UL rock mass volume is not involved by shallow hydrological processes and this opportunity generally it is very rare to find. For these considerations, UL was used to monitor groundwater parameters in the inter-, co- and post-seismic period above all of the recent 2009 L'Aquila earthquake and the 2016-2017 Central Italy seismic sequence (Adinolfi Falcone et al., 2012; De Luca et al., 2016; 2018; Petitta and Tallini, 2002).

As stated, we present further data concerning the estimation of the detection capacity of earthquakes by a hydraulic pressure device (in the following HPD) installed in the boreholes S13 and S14 (for their location see Fig. 1) by comparing earthquake detected by the INGV seismic station GIGS, placed in UL. The HPD measures at very high frequency (20 Hz) the hydraulic pressure and the boreholes S13 and S14 are located very near to UL. Moreover, the detection capability of earthquakes by the HPD installed in the boreholes S13 and S14 was compared to that due to earthquake-induced hydrological phenomena (liquefaction, stream discharge increase, mud

volcanoes) in worldwide sites (Galli, 2000; Manga and Wang, 2015).

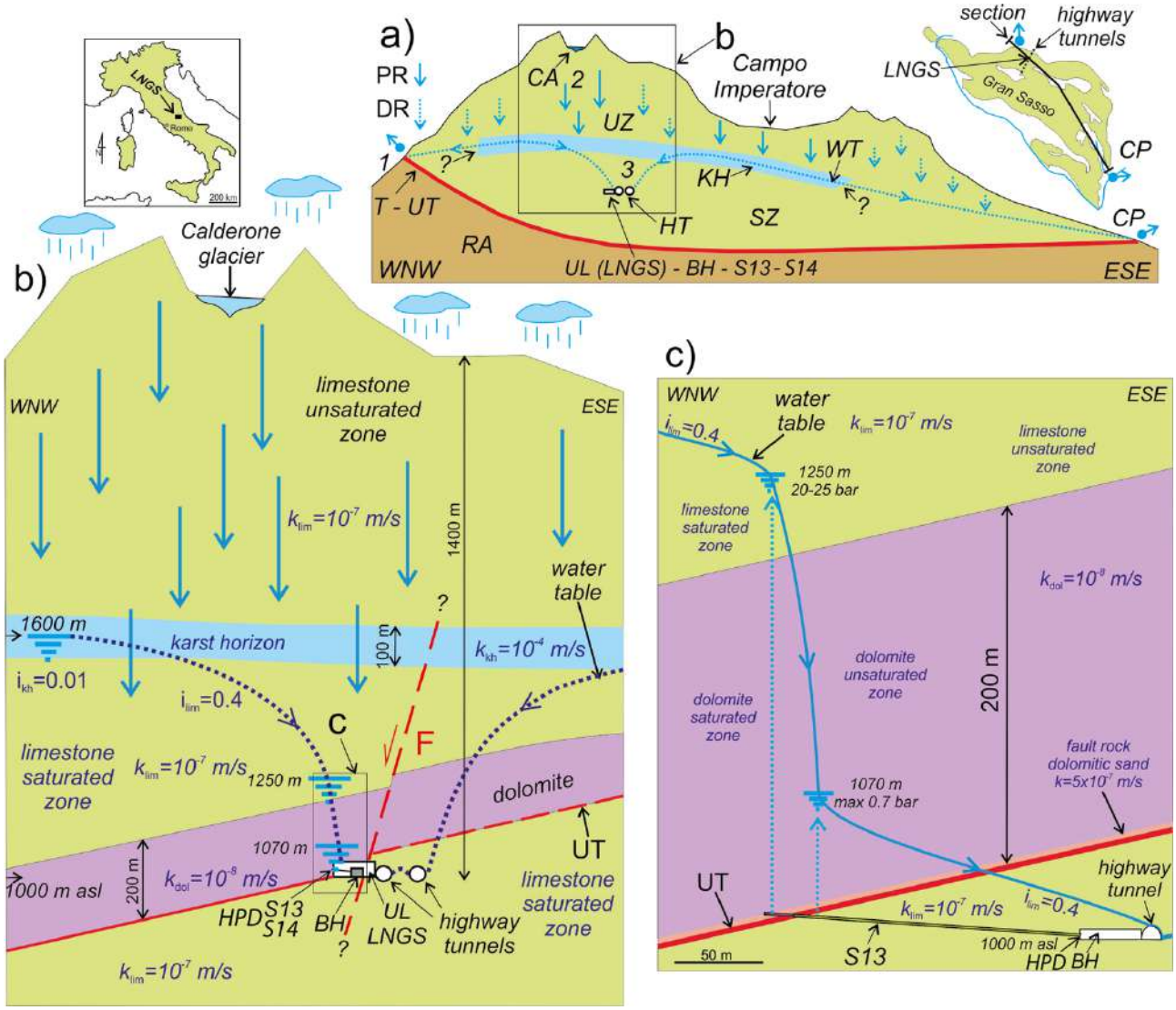

Figure 1 – (a) Sketch of GSA transversal to the highway tunnels and passing through UL and borehole S13 area. UZ: Unsaturated Zone; SZ: Saturated Zone; KH: Karst Horizon; RA: Regional Aquiclude; T: permeability boundary (regional Thrust); UT: local thrust named Upper Thrust; WT: Water Table; HT: Highway Tunnels; UL LNGS: Underground Laboratories; BH: Borehole Hall; CA: Calderone glacier (high elevation water reservoir – preferential recharge area); 1: overflow spring (CP: Capo Pescara spring); 2: preferential groundwater flowpath area; 3: preferential groundwater flowing toward the UL; PR: Preferential Recharge; DR: Diffuse Recharge; S13, S14: monitored horizontal boreholes, S14 is located very near to S13 (HPD). The hydrogeological relationships in the square are showed into details in (b). (b) Detailed hydrogeological relationships between Calderone glacier acting as a water reservoir for the carbonate aquifer down below; i: hydraulic gradient; k: hydraulic conductivity (m/s) (kh: karst horizon; lim: limestone; dol: dolomite). The hydrogeological relationships in the square are showed in detail in (c) (De Luca et al., 2018).

2. The water pressure device (HPD) and the INGV seismic station GIGS

The Borehole Hall (BH of Fig. 1), placed near UL at 965 m asl, hosts six horizontal boreholes (among which S13 and S14) and UL hosts the INGV seismic station GIGS located at around 250 m from BH. For the purposes of this work, boreholes S13 and S14, adjacent to each other, were monitored.

The borehole S13, has a horizontal length of 190 m, slopes gently upwards by ~5° and intercepts a fault near its end (UT of Fig. 1). The first 175 m of S13 are intubated, while the last 10 m drain

within the Upper Triassic dolomite (Fig. 1). The borehole S14, the same is 170 m long and drains within the same rocks as the borehole S13.

The boreholes S13 and S14 were equipped with a 3-channel, 24-bit analog-digital converter ADC (model SL06 by SARA Electronic Instrument company, http://www.sara.pg.it/), with a very high hydraulic pressure sampling frequency (20 Hz).

The hydraulic scheme of the experimental apparatus (showed in Fig. 5 in De Luca et al. 2018) is composed by (a) the horizontal boreholes; (b) an old analogic manometer; (c) a hydraulic valve always open during the data acquisition periods; (d) hydraulic pressure sensor; (e) hydraulic valve not completely close to enable the measurement of temperature and electrical conductivity in a container (h); (f) temperature sensor; (g) electrical conductivity sensor; (h) transparent plastic container housing the temperature and electrical conductivity sensors. Water is expelled when reaching about three quarters of the volume of the container.

The hydraulic pressure measured at the head of the 150-200 m long horizontal boreholes was about 0.5-0.7 MPa (piezometric height of 50-70 m), except for borehole S13, where a much higher pressure was recorded, about 2.0-2.5 MPa (piezometric head of 200–250 m).

Inside UL, the INGV seismic station GIGS, which was also adopted as part of the GINGER experiment used also to study the Rotational seismology (Belfi et al., 2017; Di Virgilio et al., 2017), is equipped with two broadband seismometers (Nanometrics Trillium 240 s and Guralp CMG 3T 360 s). This instrumentation is used both for continuous microseismic monitoring of GSA and for recording global seismicity (Italian seismicity and teleseismic events).

The main objective of the work was to identify and correlate the coincidences between earthquakes on a global, regional and local scale to the variations in hydraulic pressure within GSA detected by the HPD installed in the boreholes S13 and S14. To this end, we proceeded by comparing the hydroseismograms obtained from the hydraulic pressure values recorded in the HPD of the boreholes S13 and S14 and the seismograms recorded by the INGV seismic station GIGS.

The time interval for data acquisition, observation and analysis was between May 1st, 2015 and December 31st, 2022 and the monitoring is still going on.

3. Hydraulic pressure versus seismic data discussion

In the period May 2015 and December 2022, the HPD recognized 130 earthquakes compared to the 974 analysed. The event recognition by HPD means that (i) the hydraulic pressure signal recorded by the sensors is attributable to a hydroseismogram and, (ii) the time coincidence of the hydroseismogram with the seismogram of the same event recorded by the seismic station GIGS (Fig. 2).

Based on the elaboration of the above-mentioned hydraulic pressure versus seismic data it was possible to plot the diagrams of Fig. 3 which summarize the results.

The top plot of Fig. 3 shows two dotted lines: the grey line represents the sensitivity limit for the detection of seismic events reported by Manga and Wang (2015), as a result of a review of all similar studies until 2015; the blue line, obtained from the observation in the time interval of 15 months (May 2015-September 2016) by De Luca et al. (2016), is more sensitive, regardless of distances, with respect to that of Manga and Wang (2015). The slope of the blue line by De Luca et

al. (2016) is compatible with the results obtained with this study, despite the observation of a greater number of events due to a significantly longer observation period. However, approximately 20 events detected by the HPD with epicentral distances greater than 2000 km are located below the blue line (top plot, Fig. 3). On the other hand, 5 events with a Mw of 6.5 are superficial. Therefore, with the same magnitude and distance, deep events are not detected by the HPD.

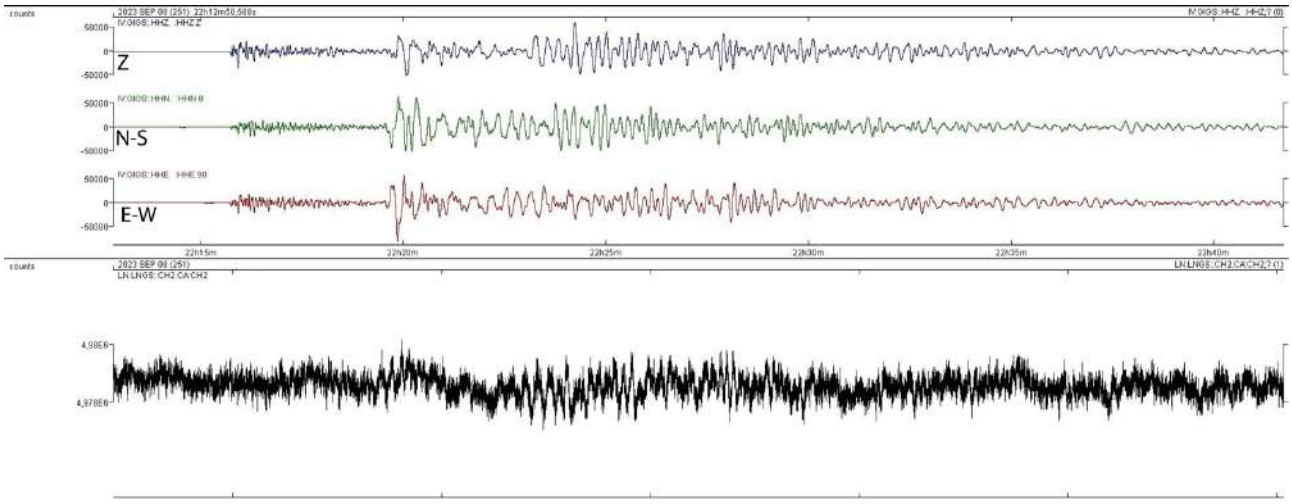

Figure 2 – Mw 6.8 earthquake occurred in Morocco on 9 September 2023 at 22:11:00 UTC. Top panel: The blue (Z), green (N-S) and brown (E-W) seismic traces refer to the vertical, N-S and E-W components, respectively, recorded by the INGV seismic station GIGS. Bottom panel: black trace is the hydraulic pressure signal recorded in the borehole S13 (i. e., hydroseismogram).

Events with an epicentral distance of less than 200 km, the hypocentral depth is low (about 5-20 km, shallow earthquakes). Beyond 200 km of epicentral distance, the first deep earthquakes that are identified with distances just over 200 km are those in the Tyrrhenian area, which however are not detected by the HPD system (bottom panel, Fig. 3). In accordance with the top plot in Fig. 3, HPD is more sensitive to surface events. Instead, the events detected with hypocentral depth greater than 80 km are significantly reduced.

Also note in the cluster at the top right (top plot of Fig. 3: A) as among the events at greater depth, i.e. greater than approximately 500 km, the HPD detected only two events (Mw 7.6 event located in the Sea of Japan at a depth of 675 km and epicentral distance of 10527 km, and the Mw 8.1 event located in the sea of Fiji Islands at a depth of 574 km and an epicentral distance of 17089 km).

In the most populous cluster (top plot of Fig. 3: B), consisting of events with a hypocentral depth between approximately 5 km and 20 km, HPD detectability is instead correlated to epicentral distance and magnitude.

Generally, events with a magnitude less than 3 and with an epicentral distance and hypocentral depth less than 20 km are not detected by the HPD.

Instead, most of the events detected by the HPD, regardless of the epicentral distance, have hypocentral depths generally less than 20 km as perhaps with the same magnitude the deep events generate smaller amplitudes of the surface waves which are normally particularly evident in the hydroseismograms.

Among the earthquakes with greater depth, i.e. greater than 80 km, only those of high magnitude greater than Mw 7.3 are detected by HPD (bottom plot, Fig. 3).

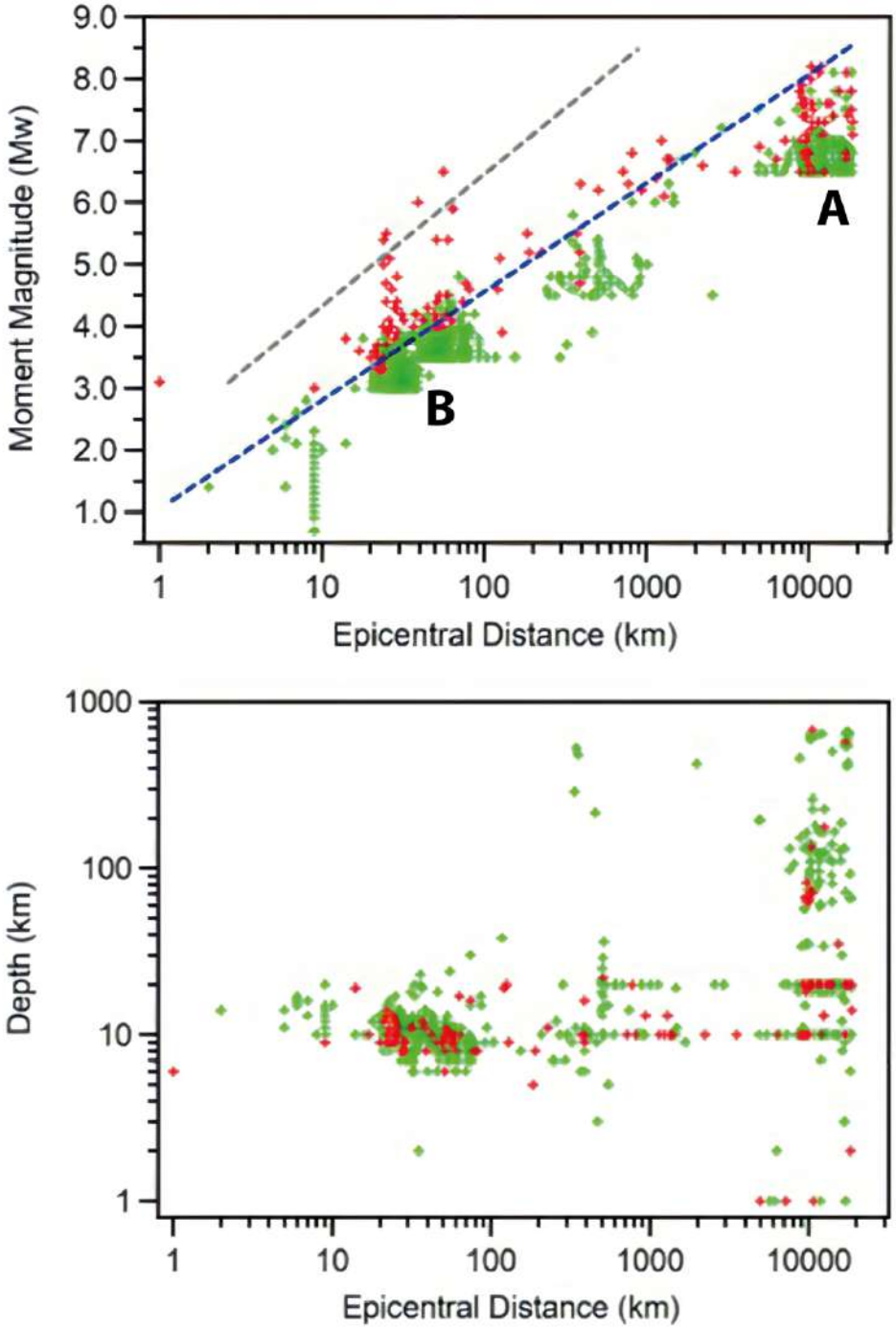

Figure 3 – Top: M_W versus epicentral distance (km) of earthquakes detected by HPD installed at boreholes S13 and S14 from May 2015 to December 2022. The blue line is the detection level obtained from De Luca et al. (2016), while the gray line refers to the detection level obtained from Manga and Wang (2015). A and B refer to the main cluster (see the text). Bottom plot: hypocentral depth (km) vs epicentral distance (km) of the same events population reported in the top plot. Red and green crosses represent earthquakes observed and not observed by the HPD, respectively.

4. Conclusions

We present further data concerning the estimation of the detection capacity of earthquakes by a hydraulic pressure device (HPD) (boreholes S13 and S14 in De Luca et al., 2018, Fig. 1) placed very near to UL, by comparing earthquakes detected by the INGV seismic station GIGS, located in UL.
The detection capability of the HPD was compared to the currently published bibliography (e.g., Galli, 2000; Manga and Wang, 2015).
In the period May 2015 and December 2022, the HPD recognized 130 earthquakes compared to the 974 analysed.
The results confirm the sensitivity of the HPD higher than the known values and recorded so far on a global scale (Manga and Wang, 2015).
Considering (i) the hydrogeological versus seismotectonic importance of GSA, (ii) the hydrological sensitivity to earthquakes of the HPD, which is placed in the GSA core, so that in a unique and strategic location, and (iii) the encouraging and significant results, the hydrological versus seismic monitoring of the HPD is continuing.

References

Adinolfi Falcone R., Carucci V., Falgiani A., Manetta M., Parisse B., Petitta M., Rusi S., Spizzico M., Tallini M.; 2012: *Changes on groundwater flow and hydrochemistry of the Gran Sasso carbonate aquifer due to the 2009 L'Aquila earthquake*. Ital. J. Geosci. (Boll. Soc. Geol. It.), 131, 459-474, doi: 10.3301/IJG.2011.34.

Belfi J., Beverini N., Bosi F., Carelli G., Cuccato D., De Luca, G., et al.; (2017): *Deep underground rotation measurements: Gingerino ring laser gyroscope in Gran Sasso*. Rev. Sci. Instrum. 88:034502, doi: 10.1063/1.4977051.

De Luca G., Di Carlo G., Tallini M.; 2016: *Hydraulic pressure variations of groundwater in the Gran Sasso underground laboratory during the Amatrice earthquake of August 24, 2016*. Annals of Geophysics 59, Fast Track 5, doi: 10.4401/AG-7200.

De Luca G., Di Carlo G., Tallini M.; 2018: *A record of changes in the Gran Sasso groundwater before, during and after the 2016 Amatrice earthquake, central Italy*. Scientific Reports, G:15982, doi: 10.1038/s41598-018-34444-1.

Di Virgilio, A.D.V. et al.; 2017: *GINGER: A feasibility study*. Eur. Phys. J. Plus, 132, 157, https:// doi.org/10.1140/epjp/i2017-11452-6.

Galli P.; (2000): *New empirical relationships between magnitude and distance for liquefaction*. Tectonophysics, 324, 169–187, doi: 10.1016/S0040-1951(00)00118-9.

Manga M., Wang C.-Y.; (2015): *Earthquake Hydrology*. In: Gerald Schubert (editor-in-chief), Treatise on Geophysics, 2nd edition, Vol 4. Oxford: Elsevier, 305–328, https://doi.org/10.1016/ B978-0-444-53802-4.00082-8.

Petitta, M., Tallini, M.; 2002: *Idrodinamica sotterranea del massiccio del Gran Sasso (Abruzzo): indagini idrologiche, idrogeologiche e idrochimiche (1994–2001)*. Boll. Soc. Geol. It., 121, 343–363.

Corresponding author: isayadomenico@live.it

Fault (re)activation, fluid-induced seismic activity and seismogenic potential in the Val d'Agri (southern Italy).

A. Lavecchia[1], V. Serlenga[2], M. Filippucci[1,3], T.A. Stabile[2], G. Prosser[4], A. Tallarico[1,3]

[1] University of Bari, Italy
[2] National Research Council of Italy, Institute of Methodologies for Environmental Analysis, Tito Scalo, Italy
[3] National Institute of Geophysics and Volcanology, Rome, Italy
[4] University of Basilicata, Potenza, Italy

The Val d'Agri is one of the regions around the globe where the relationship between fluids and earthquakes has been suggested. In this basin, wastewater reinjection led to the reactivation of the Costa Molina blind fault and the generation of a microearthquakes cluster. In addition, another cluster is observed within the basin and is related to seasonal variations of the Pertusillo Lake. The factors that led to the generation and reactivation of the fault systems responsible for both the Costa Molina and Pertusillo seismic clusters are still a matter of debate. Consequently, the characteristics of the seismic potential in the basin is largely uncertain. Therefore, we have built a 2D thermo-mechanical model to address the main mechanisms promoting the present-day tectonic setting of the Val d'Agri and assess the seismic hazard in the basin. Our findings suggest that deformation is mostly led by mechanisms of thin-skinned tectonics and the Burano Formation acts as a décollement layer between the sedimentary cover and the crystalline basement. Based on the quantification of the stress field in the region and estimations of the crust's Coulomb stress values, we suggest that the Val d'Agri sedimentary cover is characterized by a high seismic hazard, and therefore a careful approach is advisable when fluids injection and storage activities are programmed.

Corresponding author: alessio.lavecchia@uniba.it

From field geology to strain and stress inversion: multi-scale variations throughout peninsular Italy

G. Lavecchia[1,2], C. Andrenacci[1,2], S. Bello[1,2], F. Pietrolungo[1,2], D. Cirillo[1,2], A. Carducci[1,2], F. Ferrarini[1,2], F. Brozzetti[1,2], R. de Nardis[1,2]

[1] DiSPuTer, Università degli Studi "G. d'Annunzio" Chieti-Pescara, Chieti, Italy
[2] CRUST - Centro inteRUniversitario per l'analisi Sismotettonica Tridimensionale, Chieti, Italy

Exploring the complexities of stress field variations in regions beyond tectonic plate boundaries has become a central focus in innovative geodynamic and seismotectonic research. Traditional methodologies in this field encompass examining focal mechanisms and in situ stress data enriched by geological features and Quaternary fault-slip data. The formal inversion of stress, a critical step in establishing precise principal stress orientations and magnitudes, necessitates a wealth of input data, a resource more commonly abundant in seismological studies than geological investigations.

Italy has recently seen an increase in geological data availability by introducing two comprehensive databases containing Quaternary fault/striation pairs (FSP) records. These are represented by the QUIN 1.0 and 2.0 databases, collecting a total of ~8000 FSP in Lavecchia et al. (2022 and 2024) for Northern-Central and Southern Apennines, respectively. Together, the databases span the extensional intermountain seismogenic Province of the entire Peninsular Italy, encompassing approximately 2,500 kilometers along its strike length.

In the present study, we integrate the information from the two QUIN databases with additional data, forming a unified TOTOQUIN database. The latter serves as foundational input for conducting detailed strain analysis and formal stress inversion at three scales: 1) Structural site scale, 2) Fault system scale, and 3) Regional domains scale.

The multi-order principal stress attitudes and relative magnitudes obtained through TOTOQUIN inversion are analyzed and interpreted in light of the geometry and multi-scale segmentation pattern of the outcropping intra-Apennine fault system and the associated crustal structure. The analysis is further enriched by comparison with deformation trends derived from earthquake and geodetic data. Through this examination, the study validates the complete consistency between Italy's long-term and current stress fields, effectively bridging a crucial gap in the seismotectonic puzzle.

Beyond its evident applications in seismic hazard, seismotectonics, and geodynamics, the TOTOQUIN stress database holds the potential to optimize resource exploration strategy and

ensure the resilience of engineered structures in the intra-Apennines region. In general, the comprehensive insights derived from this study contribute to the scientific understanding of regional tectonics and have far-reaching implications for practical and strategic endeavors in the broader geological context.

References

Lavecchia, G., Bello, S., Andrenacci, C. et al. QUaternary fault strain INdicators database - QUIN 1.0 - first release from the Apennines of central Italy. Sci Data 9, 204 (2022). https://doi.org/10.1038/s41597-022-01311-8

Lavecchia, G., Bello, S., Andrenacci, C. et al. QUIN 2.0 - new release of the QUaternary fault strain INdicators database from the Southern Apennines of Italy. Sci Data (2024).

Corresponding author: glavecchia@unich.it

Analysis and preliminary results of the Mw 4.9, Marradi seismic sequence (September 18th, 2023), in the northern Apennines, carried out by the BSI working group.

A. Lisi, L. Arcoraci, P. Battelli, M. Berardi, B. Castello, D. Latorre, A. Marchetti, M. Michele, V. Misiti, A. Nardi, D. Piccinini, A. Rossi, Gruppo di lavoro del Bollettino Sismico Italiano*

*** A. Battelli, B. Cantucci, C. Castellano, D. Cheloni, M.G. Ciaccio, L. Colini, M. De Caro, A. Frepoli, L. Improta, A.M. Lombardi, A. Malagnini, L. Margheriti, M.T. Mariucci, G. Mele, C. Melorio, L. Miconi, G. Modica, C. Montuori, N.M. Pagliuca, M. Pastori, S. Pinzi, L. Pizzino, A. Sciarra, T. Sgroi, S. Spadoni, R. Tardini, C. Thermes, A. Bono, I. Carluccio, E. Della Bina, M. Fares, D. Franceschi, V. Lauciani, A. Mandiello, M. Maniscalco, S. Pintore, M. Quintiliani, M. Moretti, R. Di Stefano, L. Scognamiglio**

Istituto Nazionale di Geofisica e Vulcanologia, Roma, Italy

On September 18, 2023, an earthquake with a magnitude of M_L=4.8 (Mw=4.9) occurred a few kilometers SW of Marradi (FI) at a depth of about 8 kilometers. The computed TDMT solution of the mainshock suggests a normal fault oriented NW-SE (Scognamiglio et al., 2006).

The earthquake, preceded by a foreshock with a magnitude of M_L=3.3 (Mw=3.4), triggered a seismic sequence characterized, in the first two months, by approximately 700 aftershocks localized by the staff on duty in the Seismic Monitoring Room of the INGV in Rome, including 6 events with a magnitude of $M_L \geq 3.0$ occurred in the first two days.

The sequence occurred in a high seismic hazard region. The two closest historical earthquakes occurred in the Mugello area about 30 km SW of Marradi (and about 25 km north of Florence): one, whose magnitude (Mw) is estimated to be about 6.0, occurred on June 13, 1542 while the other with estimated magnitude (Mw) of about 6.4 occurred on June 29, 1919. The second one is among the strongest (most significant) Italian earthquakes of the 20th century, and also one of the strongest known to date with its epicentre in the northern Apennines. The affected area was that of Mugello, with extensive damage both in the province of Florence and on the Romagna side of the Apennines.

The analysts of the BSI (Italian Seismic Bulletin) reviewed the initial three days of the sequence, paying special attention to the hours directly following the mainshock. The BSI work mainly consists in revising the picking of P and S phases and assigning them appropriate weights, retrieving previously unused phases, and evaluating the maximum amplitudes necessary for calculating the value of M_L. The latter is a critical aspect of the initial phases of a seismic sequence; in fact, the occurrence of events is very close in time, making it challenging to estimate the

maximum amplitudes and, consequently, the magnitude automatically. Through this analysis, they have identified an earthquake with a magnitude of M_L=3.4, occurring approximately one minute after the mainshock and overlooked during the surveillance service. Furthermore, a comprehensive effort to recover smaller seismic events not initially analyzed in the Seismic Monitoring Room resulted in the localization of 498 earthquakes, nearly a 30% increase within the first three days. In Figure 1(a-d), hypocentral parameters and time readings of the 352 earthquakes detected in the Seismic Monitoring Room have been compared with those of the same events revised by the BSI. It is evident as both the horizontal and vertical errors, as well the seismic gap associated with the location decrease for the dataset analyzed from the BSI, while the number of P and S phases increases for the same dataset. Subsequently, the events revised from BSI were initially relocated by applying the NonLinLoc code (Lomax et al., 2000) using a 1D regional velocity model from Pastori et al. (2019). Following this, a double-difference technique (Waldhauser and Schaff, 2008) was applied to improve the geometries of the activated structures (see Figure 2).

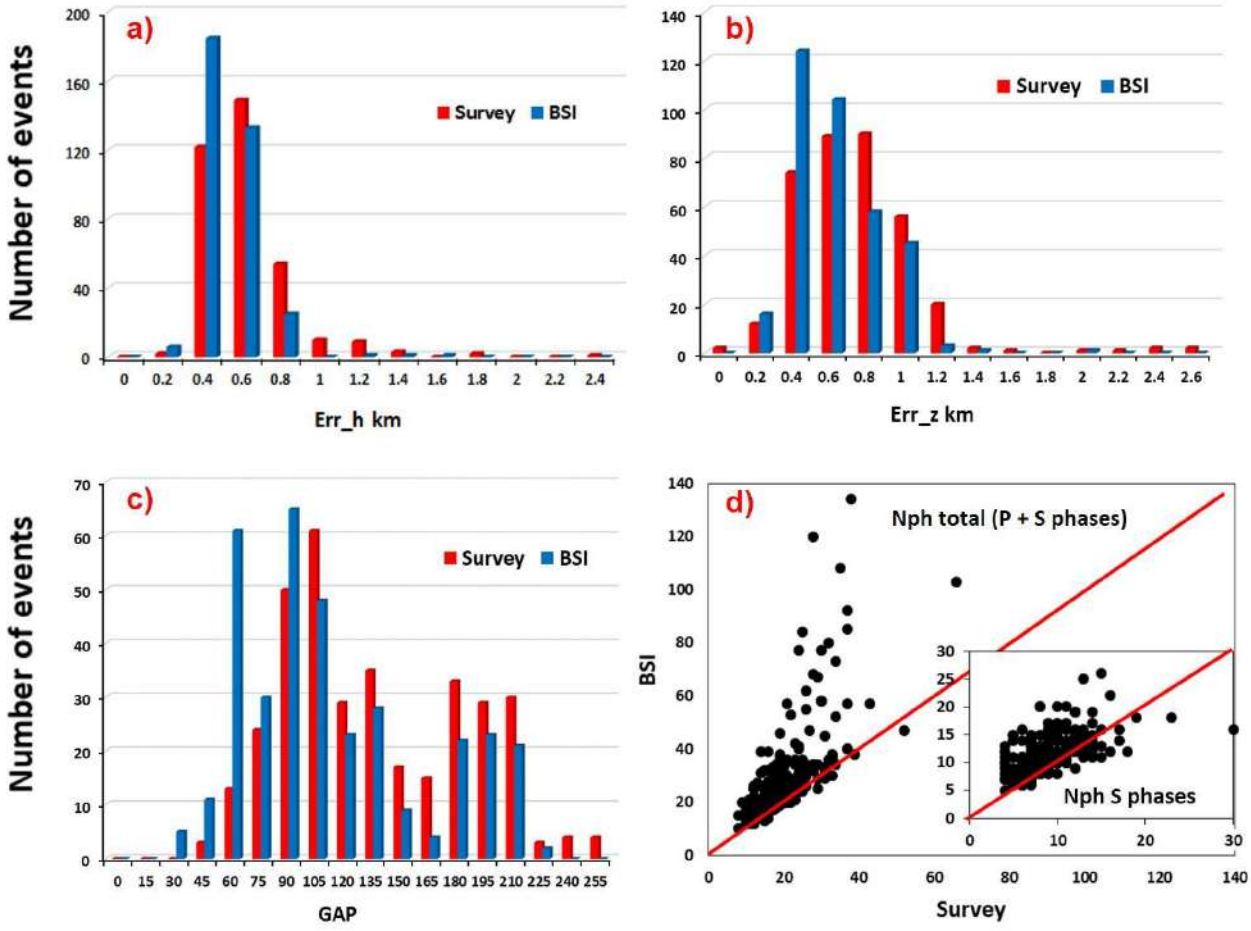

Fig.1 – Comparison between hypocentral parameters (a,b,c) and used time readings (d) for the same 352 earthquakes detected, during the first 3 days of the sequence, from seismic monitoring room and revised from BSI.

Concomitantly, an analysis using the *template-matching* technique was applied, for the period from September first to October 10th, to identify events overlooked by the Earthworm system in the Seismic Monitoring Room. The results are shown in Figure 3. It was found that the number of detections increased by approximately 60%. Furthermore, Figures 3c and 3d put in evidence as the

larger number of new detected earthquakes is characterized by lower magnitude. This result highlights the value of integrating this type of analysis to complement the efforts of the Italian Seismic Bulletin (BSI).

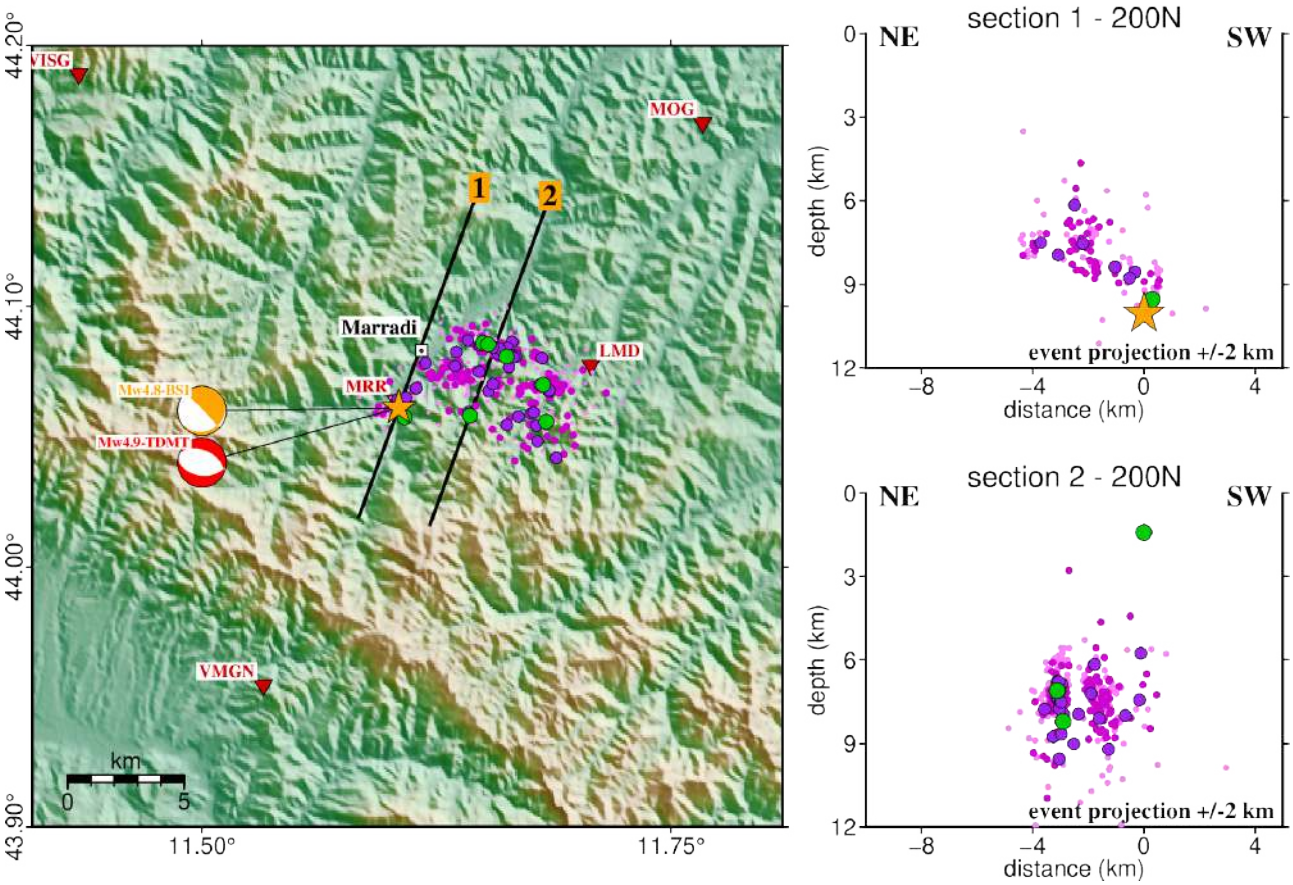

Fig.2 – Map view: Earthquakes recorded in the first 3 days of the sequence and revised by the BSI working group. Events are initially relocated using the NonLinLoc code (Lomax et al., 2000) and the local 1D velocity model from Pastori et al. (2019). Subsequently, a double-difference code (Waldhauser and Schaff, 2008) is applied to improve the geometries of the activated structures. The two vertical cross-sections are oriented perpendicular to the strike of the computed TDMT solution of the Mw=4.9 event (Scognamiglio et al., 2006).

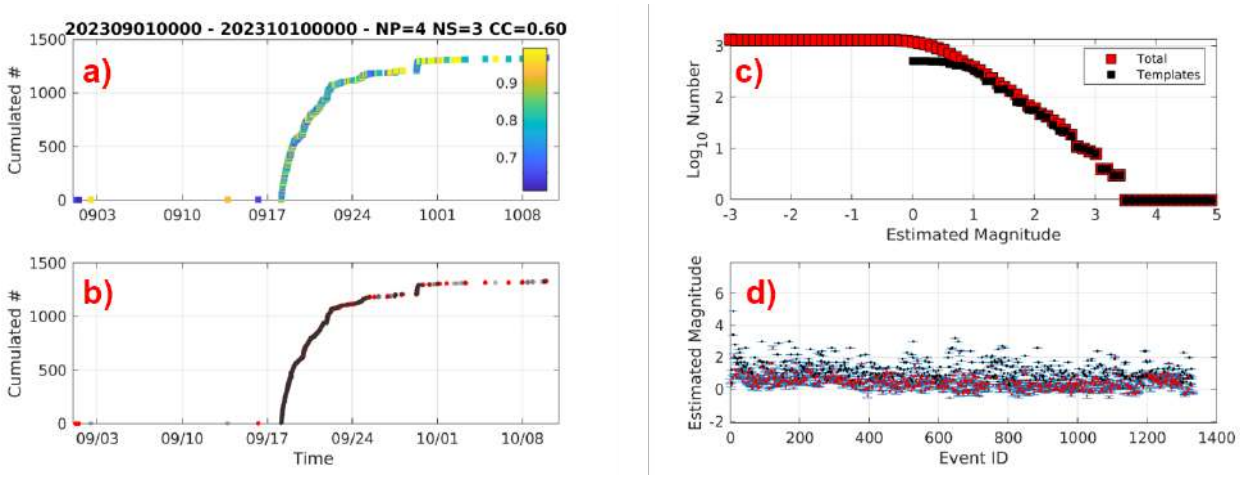

Fig.3 – Cumulative number of events over the time and relative magnitude distribution until October 10th. (a)The colours represent the average cross-correlation (CC) of each detected event. (b) New detected events are shown in red colour while the templates are in grey. (c) The Gutenberg - Richter relationship. (d) The magnitude of matched events (in red with their respective error bars) and that of the templates (in black).

References

Lomax, A., J. Virieux, P. Volant and C. Berge, 2000. Probabilistic earthquake location in 3D and layered models: Introduction of a Metropolis-Gibbs method and comparison with linear locations, in Advances in Seismic Event Location Thurber, C.H., and N. Rabinowitz (eds.), Kluwer, Amsterdam, 101-134.

Pastori M., Latorre, D., (2021). Report del Progetto DPC-B2-2019-2021, WP1-Task4.

Scognamiglio, L., Tinti, E., Quintiliani, M. (2006). Time Domain Moment Tensor (TDMT) [Data set]. Istituto Nazionale di Geofisica e Vulcanologia (INGV). https://doi.org/10.13127/TDMT

Waldhauser, F. and D.P. Schaff (2008), Large-scale relocation of two decades of Northern California seismicity using cross-correlation and double-difference methods. J. Geophys. Res., 113, B08311, doi:10.1029/2007JB005479.

Corresponding author: arianna.lisi@ingv.it

Studying the Viability of Kinematic Rupture Models and Source Time Functions with Dynamic Constraints

M.E. Locchi[1], F. Mosconi[1], M. Supino[2], E. Casarotti[2], E. Tinti[1,2]

[1] Sapienza Università di Roma, Rome, Italy;
[2] Istituto Nazionale di Geofisica e Vulcanologia, Rome, Italy;

Earthquakes are one of the greatest natural hazards and a better understanding of the physical processes causing earthquake ruptures is required for appropriate seismic hazard assessment. Progresses on the knowledge of the seismic source have been made in both modelling the increasingly dense geophysical data and through laboratory experiments. Kinematic modelling is a standard tool to provide important information on the complexity of the earthquake rupture process and for making inferences on earthquake mechanics.

Despite recent advances, kinematic models are characterized by uncertainties and trade-offs among parameters (inherent non-uniqueness of the problem). It has been documented that, for the same earthquake, source models obtained with different methodologies can exhibit significant discrepancies in terms of slip distribution, fault planes geometry and rupture time evolution.

Prescribing the slip velocity on causative faults (source time function) is one of the crucial components in the models because it contains key information about the dynamics and prescribes how fast each point on the fault reaches its final slip (Tinti et al, 2005). Such function is nonetheless one of the most poorly observationally constrained characteristics of faulting.

Recently, slip velocity time histories have been studied with laboratory earthquakes and a systematic change of mechanical properties and traction evolution has been observed to correspond with a change in the shape of slip velocity (Scuderi et al., 2020). However, this function is assumed a-priori following two different approaches: in the single window approach an analytic function is assumed; while in the multi window approach the complexity and heterogeneity of the process is simulated through the linear sum of cumulative slip at different time windows. The final effect is a heterogeneous function over time that accumulates the slip until it reaches the final slip. Multiple-window inversions impose the smoothness of the slip distribution, introduce a sort of causality but at the same time heterogeneity of the rupture front prescribed by the different time windows, solve for the evolution of rupture, allow the slip at each point to be determined by multiple time window functions with no predetermined shape, and observe the slip functions a posterior (Konca et al., 2013). Nevertheless, the limited resolution of the kinematic models prevents reliable constraints on the slip velocity time history.

To investigate the effect of the slip velocity function on the ground motion and on the inverted slip history on the fault we run a series of forward and inverse models. We generate spontaneous

dynamic models and use their ground motion as real events and we invert the data with kinematic models (Fig. 1).

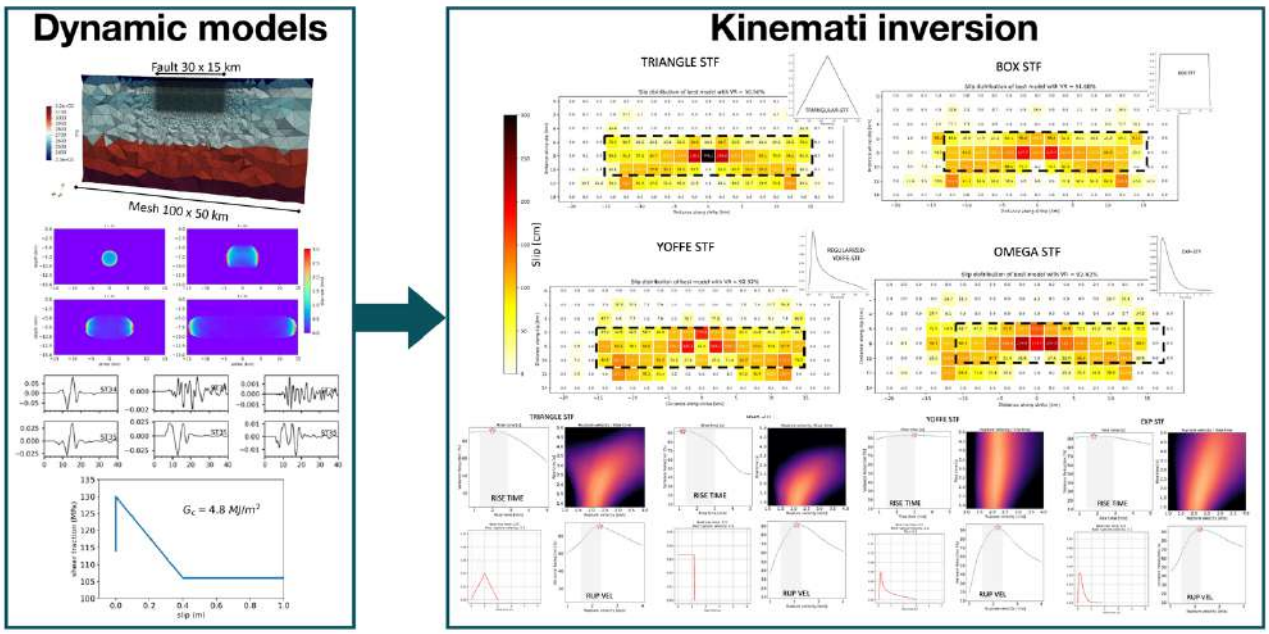

Fig. 1: Workflow for one model: results from spontaneous rupture of a bidirectivity model on the left; kinematic inversions results using ground-motion from dynamic model. For each source time function different rise time and rupture velocity were tested. The slip distribution from best models of each source time function.

The kinematic inversion has been conducted utilizing both single-time and multi-time windowing and to mitigate the uncertainties we adopt four different source time functions on the fault plane (triangular, box, regularized-yoffe and exponential). In this way we could examine how the slip velocity function influences the slip distribution on the fault plane and test if the inferred kinematic parameters are consistent with the dynamic models. We also examine the variability of the peak ground velocity (PGV) from forward modelling of synthetic seismograms up to 1 Hz, for a dense grid of phantom received, assuming the same slip distribution, rise time and rupture velocity, but changing the source time functions. Those results provide a glimpse of the variability that kinematic source time functions (dynamically consistent or not) might have when used as a constraint to model the earthquake dynamic.

Finally, we use the retrieved kinematic history on the pseudo-dynamic models to examine how different kinematic assumptions lead to a variability in the shear stress evolution. We focus on some dynamic parameters such as the breakdown work, the stress drop, and the Dc parameter. Those results provide a glimpse of the variability that kinematic source time functions (dynamically consistent or not) might have when used as a constraint to model the earthquake dynamic.

References

Ozgun Konca, A., Kaneko, Y., Lapusta, N., & Avouac, J. P. (2013). Kinematic inversion of physically plausible earthquake source models obtained from dynamic rupture simulations. *Bulletin of the Seismological Society of America*, *103*(5), 2621-2644.

Scuderi, M. M., Tinti, E., Cocco, M., & Collettini, C. (2020). The role of shear fabric in controlling breakdown processes during laboratory slow-slip events. *Journal of Geophysical Research: Solid Earth*, *125*(11), e2020JB020405.

Tinti, E., Fukuyama, E., Piatanesi, A., & Cocco, M. (2005). A kinematic source-time function compatible with earthquake dynamics. *Bulletin of the Seismological Society of America*, *95*(4), 1211-1223.

Corresponding author: mariaeugenia.locchi@uniroma1.it

Recalibration of the intensity prediction equation in Italy using the Macroseismic Dataset DBMI15 V2.0

B. Lolli[1], P. Gasperini[2,1], G. Vannucci[2]

[1]Istituto Nazionale di Geofisica e Vulcanologia, Sezione di Bologna
[2]Dipartimento di Fisica e Astronomia, Università di Bologna

We re-compute the coefficients of the intensity prediction equation (IPE) in Italy using the data of the DBMI15 V2.0 intensity database and the instrumental and combined (instrumental plus macroseismic) magnitudes reported by the CPTI15 V2.0 catalog. We follow the same procedure described in a previous article, consisting of a first step in which the attenuation of intensity *I* with respect to the distance *D* from macroseismic hypocenter is referred to the expected intensity at the epicenter I_E and a second step in which I_E is related to the instrumental magnitude M_i, the combined magnitude M_c, the epicentral intensity I_0 and the maximum intensity I_{max}, using error-in-variable (EIV) regression methods.

The main methodological difference with respect to the original article concerns the estimation of the uncertainty of I_E to be used for EIV regressions, which is empirically derived from the standard deviation of regression between I_E and M_i and also used for the regressions of I_E with M_c, I_0 and I_{max}.

In summary, the new IPE determined from DBMI15 V2.0 is

$$I = I_E - 0.0081\left(D - h\right) - 1.072\left[ln(D) - ln\left(h\right)\right]$$

where $D = \sqrt{R^2 + h^2}$, h=4.49 km and I_E can be calculated from the intensity data distribution of the earthquake. If the intensity data distribution is not available, I_E can be calculated from the following relationships

$$I_E = -2.578 + 1.867M_w$$

$$I_E = I_0$$

*Corresponding author: barbara.lolli@ingv.it

What is in the INGV ISIDe online database before 16 April 2005?

B. Lolli[1*], G. Vannucci[1] and P. Gasperini[2,1]

[1]Istituto Nazionale di Geofisica e Vulcanologia, Sezione di Bologna
[2]Dipartimento di Fisica e Astronomia, Università di Bologna

Abstract

The Italian Seismological Instrumental and Parametric Data-Base (ISIDe) is the recipient of earthquake data collected in real time by the Istituto Nazionale di Geofisica e Vulcanologia (INGV). When it went online, following a significant improvement of the seismic acquisition system of INGV, it was including only data since the second fortnight of April 2005. About ten years later, the data since the beginning of 1985 suddenly appeared without any other notice than the updating of the starting date of the dataset. However, the characteristics of the added data appeared clearly different from the following period both in terms of numbers of located earthquakes and of types of magnitudes provided. After having analyzed the numerical consistency and the calibration of magnitudes of ISIDe as a function of time from 1985 to 15 April 2005, we can say that such dataset is incomplete and poorly calibrated with respect to other catalogs of Italian seismicity (CSTI, CSI and HORUS) available for the same period. Hence, we suggest not to use it as it is for statistical analyses of Italian seismicity. However, it provides some magnitudes which are missed by other catalogs and thus might be used for improving such catalogs.

*Corresponding author: barbara.lolli@ingv.it

The implementation of the paleoseismological sites database into ITHACA Catalogue in the framework of the GeoScienceIR project

D. Maceroni[1], A.M. Blumetti[1], L. Bonadeo[2], M.P. Congi[1], V. Comerci[1], P. Di Manna[1], L. Guerrieri[1]

[1] ISPRA, Geological Survey of Italy, Roma, Italy
[2]Università degli Studi dell'Insubria, Dipartimento di Scienza ed Alta Tecnologia, Como, CO, Italy

The ITHACA (ITaly HAzard from CApable faults) Catalogue aims at collecting and summarising available information on capable faults affecting the national territory. ITHACA implementation started in the nineties, taking advantage from the knowledge deriving from siting studies of critical infrastructures (i.e., nuclear power plants, gas and oil pipelines, chemical plants, etc.). The first version was released for the 31st session of the International Geological Congress headed in Rio de Janeiro, Brazil, on August 6–17, 2000. Since then, the Catalogue has been continuously maintained and updated by the Geological Survey of Italy (ITHACA Working Group, 2019) and its present-day version is accessible through the following link: https://sgi.isprambiente.it/ithaca/viewer/index.html.

A capable fault is defined as an active fault able to produce permanent ruptures or deformation at or near the ground surface (surface faulting) during strong or moderate earthquakes (e.g. IAEA, 2015, 2022). The occurrence of surface faulting may cause serious damage to buildings and infrastructures and, therefore, it represents a geological hazard to be taken into due consideration at the local scale, particularly in the most densely populated and industrialised areas of the Italian territory. Consequently, the identification of capable faults and their characterization can provide useful information both for scientific research, aiming at seismotectonic studies, and for engineering purposes, intended for land use planning and management.

In this regard, in agreement with the "Guidelines for the management of territories affected by Active and Capable Faults" (Commissione Tecnica per la Microzonazione Sismica, 2015), the deepest degree of knowledge and insight achievable on capable faults require to perform paleoseismological investigations, site levels survey that allows to reconstruct the geological history of a given fault by analysing its past movements over the last few thousand years, providing useful information to define the seismogenetic and surface faulting potential of the fault.

For the same reason, since the very beginning of its implementation, the ITHACA Catalogue has included an information layer dedicated to paleoseismological sites (or paleosites). At that time, the compilation of the paleoseismological data in the Catalogue was in line with the available literature. Later, the collection of paleoseismological data has become insufficient and sparse in

comparison to the number of faults. As a result, it was decided not to include them in the public version of ITHACA.

However, in the last decade, also following the introduction of specific regulatory guidelines for fault displacement hazard assessment, paleoseismological studies have seen a significant increase, making available a large set of new data.

Given the relevance of this data for a better characterization of capable faults and, more broadly, to support the research aiming at minimising the risk associated with active and capable faults, it has become essential to make paleoseismological information again available within the ITHACA Catalogue. This choice will thus allow to improve the set of information associated with the archived faults, taking into account both the published studies on single faults and the already published inventories of paleoseismological data in Italy (e.g. Galli et al., 2008 and Cinti et al., 2021), and what is in the Catalogue, enriching the basket of information associated with the collected faults.

The paleoseismological sites database is implemented in the framework of the GeoSciencesIR project by collecting the information available from the published paleoseismological studies (Fig. 1a). The collected data are spatialized through GIS tools and organised in a relational database developed as a relational branch of the ITHACA Catalogue (Fig. 1a). The database consists of two main tables: the “Paleosites” attribute table and the “Paleoevent” related table. The first table refers to the identification of the paleoseismological site and provides geographic, geometric and descriptive attributes, including photographs and sketches of the trenches and evidence. The identification code (PaleoSiteCode) is linked to the FaultCode of the ITHACA fault, to which the paleoseismological study refers. Additional information is reported regarding the reference of the study and the location reliability of the site (Location Scale) (Fig. 1b). The second table provides a description of the paleoseismological evidence pointed out in the study, summarising the sequence of the faulting events and their characterization in terms of offset values and chronology, together with information on the type of sampled material and the dating methods applied for the age determination (Fig. 1c). To ensure a standardised compilation of field content, specific and detailed codelists have been arranged for each key domain. This enables driving and simplifying the compilation procedure and the dataset implementation, as well as ensuring that a certain field may only be populated with a list of preset attributes (Fig. 1d).

The paleosites database implementation in ITHACA enhances the set of information about capable faults collected in the Catalogue. The semantic and geographic link between the datasets in the Catalogue facilitates data access and cross-examination by offering an interactive view of fault traces and related paleoseismological evidence. This could be a useful tool for seismic hazard assessments, providing quick view of areas and faults where paleoseismological data is already accessible and, more importantly, facilitating access to the information for assessing the seismic and faulting potential of the mapped faults.

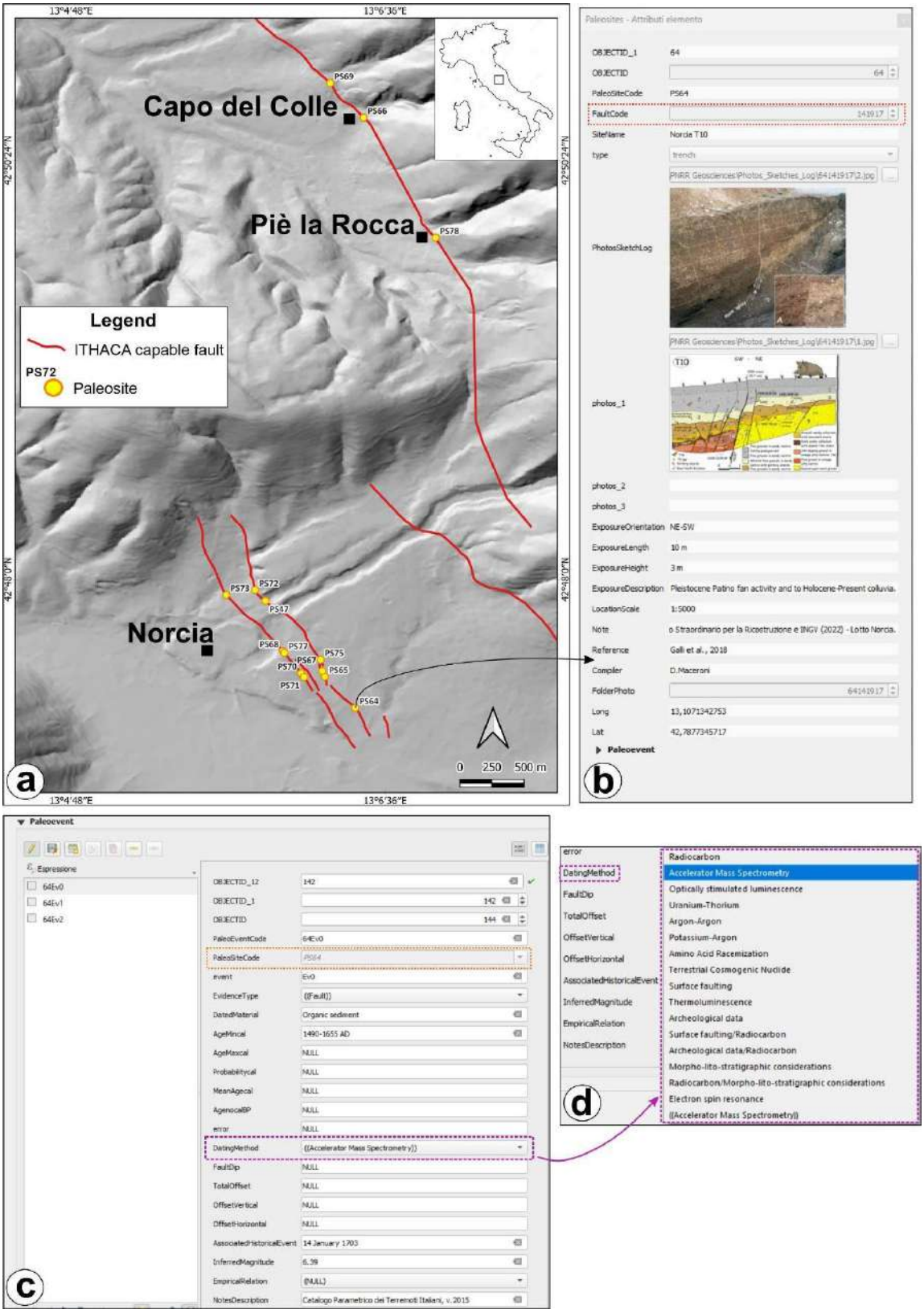

Fig. 4 – An example of a view of the ITHACA Catalogue that shows the geographic relations and architecture of the paleosites database, where each paleosites is connect to its respective ITHACA fault. a) View of the database for the Norcia-Campi basin, showing the traces of capable faults and the location of paleoseismological sites, labeled with specific identification codes (PaleoSiteCode); b) The "Paleosites" attribute table, which refers to the PS64 site. The link between the paleosite and the related capable fault is ensured by the "FaultCode" (dotted red box); c) The "Paleoevent" related table for the PS64 site. The connection is based on "PaleoSiteCode" (dotted orange box); d) A preset codelist for the "DatingMethod".

Finally, following the philosophy of open data fully adopted within the GeoSciencesIR project, the application of FAIR (Findable, Accessible, Interoperable and Reusable) principles to the entire ITHACA dataset has been promoted. Interoperability and data sharing will be ensured through the publication of OGC standard services (WMS, WFS and OFAPI). To simplify the resource reuse, the dataset will also be available in GeoPackage format with open licence attribution (CC BY 4.0).

Acknowledgments

The research activity described in this work is funded by European Union - NextGenerationEU programme- Mission 4 “Education and Research” - Component 2 “From Research to Business” – Investment 3.1 “Fund for the realisation of an integrated system of research and innovation infrastructures” - Project IR0000037 - GeoSciences IR. The Authors thank the Department of Earth, Environment and Resources Sciences of the University Federico II of Naples (Italy) for their help in collecting available paleoseismological data for the capable faults in central-southern Apennines.

References:

Cinti, F.R., Pantosti, D., Lombardi, A.M. & Civico, R. (2021). Modeling of earthquake chronology from paleoseismic data: Insights for regional earthquake recurrence and earthquake storms in the Central Apennines. Tectonophysics, 816, 10.1016/j.tecto.2021.229016

Dipartimento della Protezione Civile (2015). Microzonazione sismica. Linee guida per la gestione del territorio in aree interessate da faglie attive e capaci (FAC). http://www.protezionecivile.gov.it/media-comunicazione/pubblicazioni/dettaglio/-/asset_publisher/default/content/microzonazione-sismica-linee-guida-per-la-gestione-del-territorio-in-aree-interessate-da-faglie-attive-e-capaci-fac-

Galli, P., Galadini, F. & Pantosti, D. (2008). *Twenty years of paleoseismology in italy.* Earth-Science Reviewes 88 (2008) 89-117.

IAEA (2015). *The Contribution of Paleoseismology to Seismic Hazard Assessment in Site Evaluation for Nuclear Installations*. IAEA-TECDOC-1767. http://www.pub.iaea.org/MTCD/Publications/PDF/TE-1767_web.pdf

IAEA (2022). *Seismic Hazards in Site Evaluation for Nuclear Installations. Specific Safety Guide. IAEA Safety Standards*. Series SSG-9 (Rev.1) http://www.iaea.or/publications/14665/seismic-hazards-in-site-evaluation-for-nuclear-installations

ITHACA Working Group (2019). *ITHACA (ITaly HAzard from CApable faulting), A database of active capable faults of the Italian territory*. Version December 2019. ISPRA Geological Survey of Italy. Web Portal https://sgi.isprambiente.it/ithacaweb/Default

Corresponding author: deborah.maceroni@isprambiente.it

Seismic attenuation and stress on the San Andreas Fault at Parkfield: are we critical yet?

L. Malagnini*[1,2], R. M. Nadeau[2], and T. Parsons[3]

[1]Istituto Nazionale di Geofisica e Vulcanologia, Rome, Italy
[2]Berkeley Seismological Laboratory, University of California Berkeley, USA
[3]U.S. Geological Survey, Moffett Field, CA, 94035, USA

The Parkfield transitional segment of the San Andreas Fault (SAF) is characterized by the production of frequent quasi-periodical M6 events that break the very same asperity. The last Parkfield mainshock occurred on September 28th 2004, 38 years after the 1966 earthquake, and after the segment showed a ~22 years average recurrence time. The main reason for the much longer interevent period between the last two earthquakes is thought to be the reduction of the Coulomb stress from the M6.5 Coalinga earthquake of May 2nd1983, and the M6 Nuñez events of June 11th and July 22nd 1983.

Plausibly, the transitional segment of the SAF at Parkfield is now in the late part of its seismic cycle and current observations may all be relative to a state of stress close to criticality. This study aims at the recognition of the precritical state of the transitional segment of the SAF at Parkfield, in the hypothesis that the fluctuations of the attenuation parameter represent a proxy for the stress conditions in the crustal volume crossed by an active fault, even though the behaviour of the attenuation parameter in the last few years seems substantially different from the one that characterized the years prior to the 2004 mainshock.

A few questions arise from this study: (i) Does a detectable preparation phase for the Parkfield mainshocks exist, and is it the same for all events?; (ii) How dynamically/kinematically similar are the quasi-periodic occurrences of the Parkfield mainshocks? (iii) Are some dynamic/kinematic characteristics of the next mainshock predictable from the analysis of current data? (e.g., do we expect the epicenter of the impending failure to be co-located to that of 2004?) (iv) Should we expect the duration of the current interseismic period to be close to the 22-year “undisturbed” average value?

We respond to the questions above by analyzing the non-geometric attenuation of direct S-waves along the transitional segment of the SAF at Parkfield, in the close vicinity of the fault plane, between January 2001 and November 2023. Of particular interest is the preparatory behaviour of the attenuation parameter as the 2004 mainshock approached, on both sides of the SAF. We also show that the non-volcanic tremor activity modulates the seismic attenuation in the area, and possibly the seismicity along the Parkfield fault segment, including the occurrence of the mainshocks. The hypothesis is that the non-geometric attenuation is directly related to the bulk permeability of crustal rocks, which in turn is driven to crack density and interconnection.
Figure 1 shows a map of the investigated region, with the locations of the earthquakes in our dataset and more information of interest. An interesting observation is the 10-day smoothed rate of non-volcanic tremor (NVT) collected along the transitional segment of the SAF (Guilhem and

Nadeau, 2012). The long-term NVT rate (~8500 days, updated through November 15 2023) is plotted in red in Figure 2A, the cumulative NVT is plotted in black, and its detrended version is shown in Figure 2B. About 30-days prior to the 2004 Parkfield event a significant NVT fore tremor was observed (Nadeau and Guilhem, 2009; Guilhem and Nadeau, 2012). Prior to this fore tremor, a relatively quiescent period of ~120-days of NVT activity was also observed (Figure 2C).

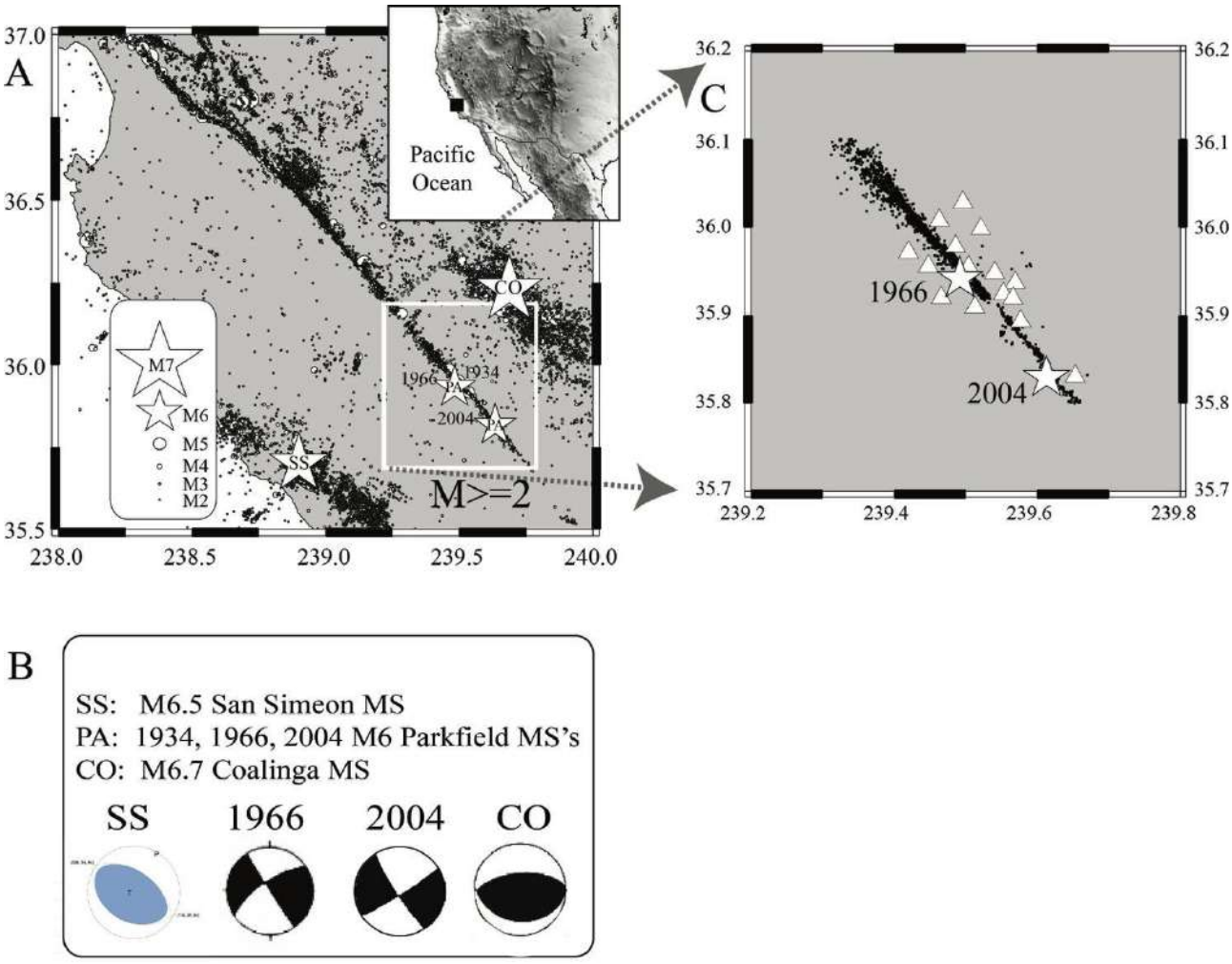

Figure 1. A: map of the region, showing the background seismicity and four mainshocks of specific interest in this study (white stars), whose focal mechanisms are indicated in B. C: i) epicentral locations of the SAF earthquakes used in this study; white triangles indicate the seismic stations of the HRSN.

A similar quiescent period also precedes the proposed foretremor of the next possible Parkfield M6 (Figure 2D). This 120-day quiescence is unusual for the majority of NVT episodes throughout the long-term NVT catalog (Figure 2A). The two pairs of dashed red vertical lines in Figures 2A,B correspond to the time windows of Figures 2C,D. Figure 2A suggests the presence of an anomaly in the tremor rate at Parkfield, which we call foretremor, between 15 and 30 days before the 2004 mainshock. A similar anomaly (another foretremor?) seems to characterize the tremor rate in

recent weeks (Figure 2B). Observations shown in Figure 2 are intriguing, although we can not produce solid proof of the recent anomaly being a foretremor.

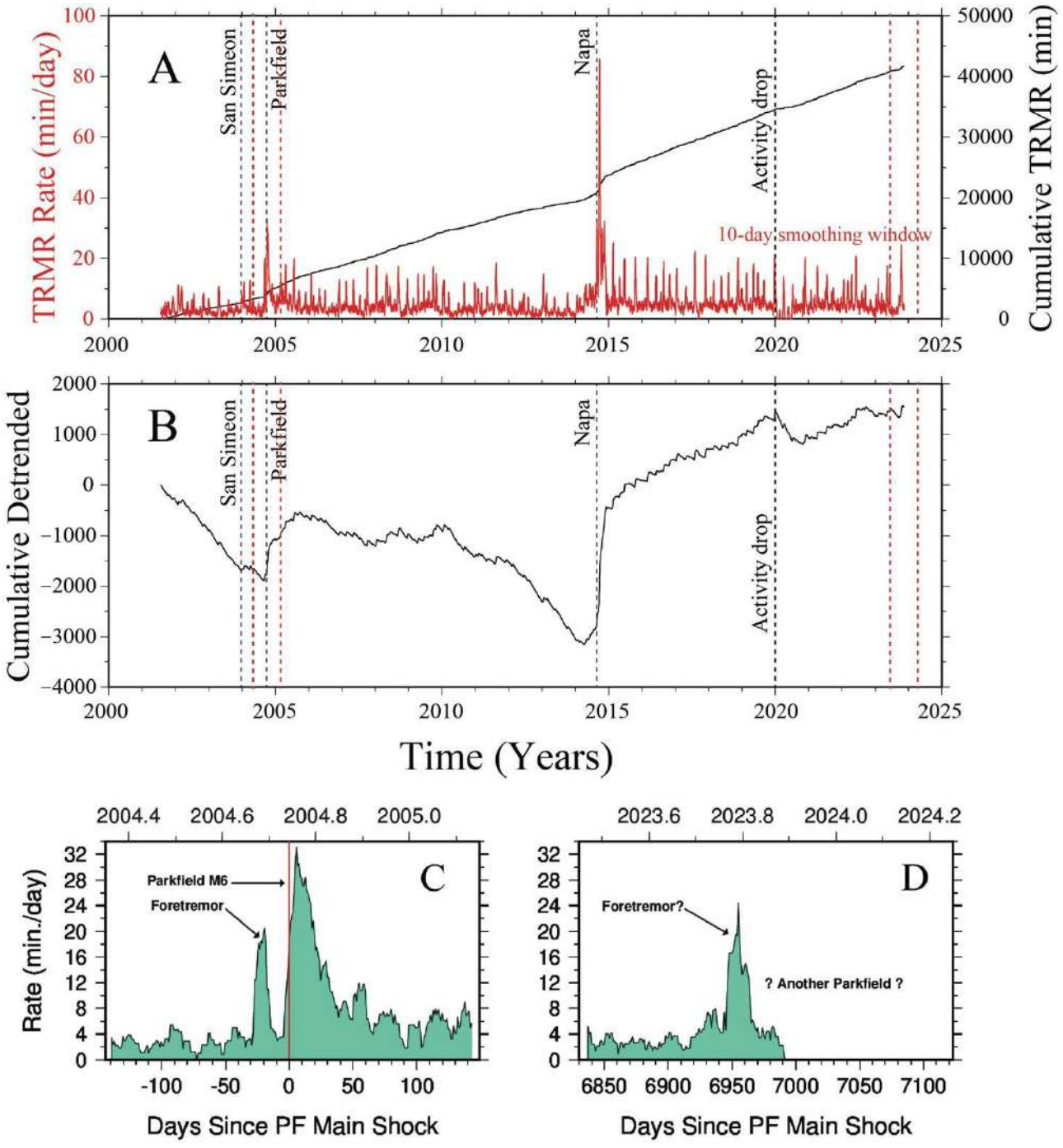

Figure 2. A) In red, the long term rate of non-volcanic tremor NVT (~8500 days) smoothed using a 10-day window (min/day); in black, the cumulative tremor activity (min). B) The detrended cumulative tremor activity. C) Rate of tremor 10-day smoothed (minutes/day) in the 293-day (9.7-month) 7-month time windows: May 7, 2004 - February 24, 2005. D) Rate of tremor 10-day smoothed (minutes/day) in the time window Jun 13, 2023 - April, 1, 2024. Bracketing dates of the two time windows of C and D are indicated in A and B by vertical dashed red lines.

The behaviour of the attenuation parameter during the latest portion of the earthquake cycle that ended with the mainshock of 28 September 2004 is shown in Figure 3, where are the logarithms of the ratios between spectral amplitudes taken at two specific hypocentral distances of 12 and 4 km

(the more such logarithms are negative, the stronger the attenuation). Spectral amplitudes are estimated through peak values of narrowband-filtered time histories: if *fc* is the central frequency, the bandpass filter is obtained by an eight-pole Butterworth low-pass filter with corner at $\sqrt{2}f_c$, followed by an eight-pole high-pass filter with a corner at $\frac{1}{\sqrt{2}}f_c$. After filtering, Random Vibration Theory (RVT) is applied to peak values to produce an estimate of spectral amplitude, given the time duration of the analyzed signal. Details can be found in Malagnini and Dreger (2016), and references therein.

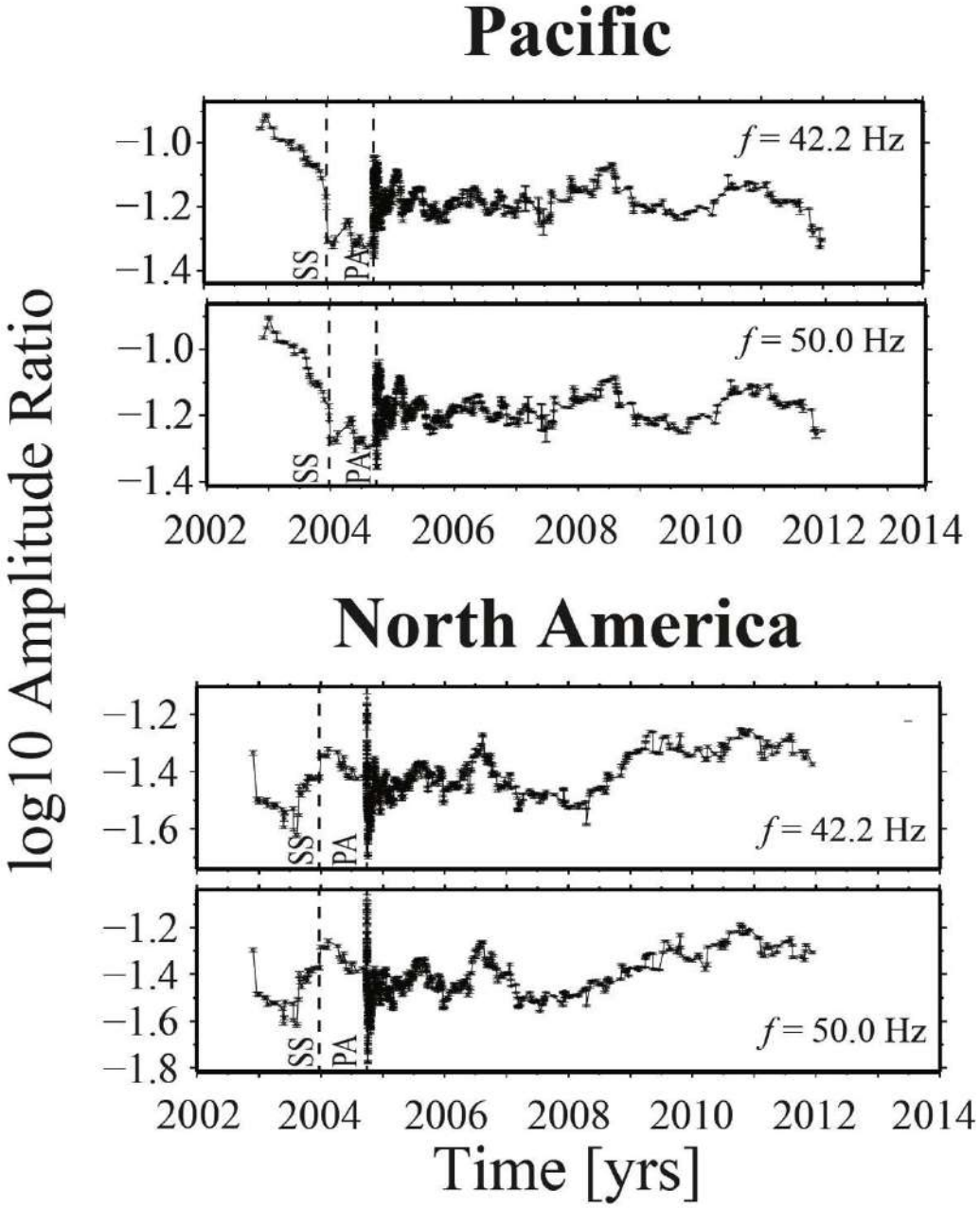

Figure 3. Logarithms of total attenuation experienced by direct S waves along the transitional segment of the SAF at Parkfield, between 4 and 12 km of hypocentral distance, at the indicated central frequencies of 42.2 and 50.0 Hz.

With Figure 4 we try to extract more specific information on two frequency bands at the two ends of the investigated spectrum: 2-5 Hz and 30-50 Hz. The quantities shown in Figure 4 are the stacked attenuation values that were calculated in the central frequencies contained in the

mentioned bands. Of great interest is the bifurcation of the stacked attenuation time histories that can be observed starting 6-8 weeks before the September 28, 2004 Parkfield mainshock. No bifurcation characterizes intermediate frequency bands.

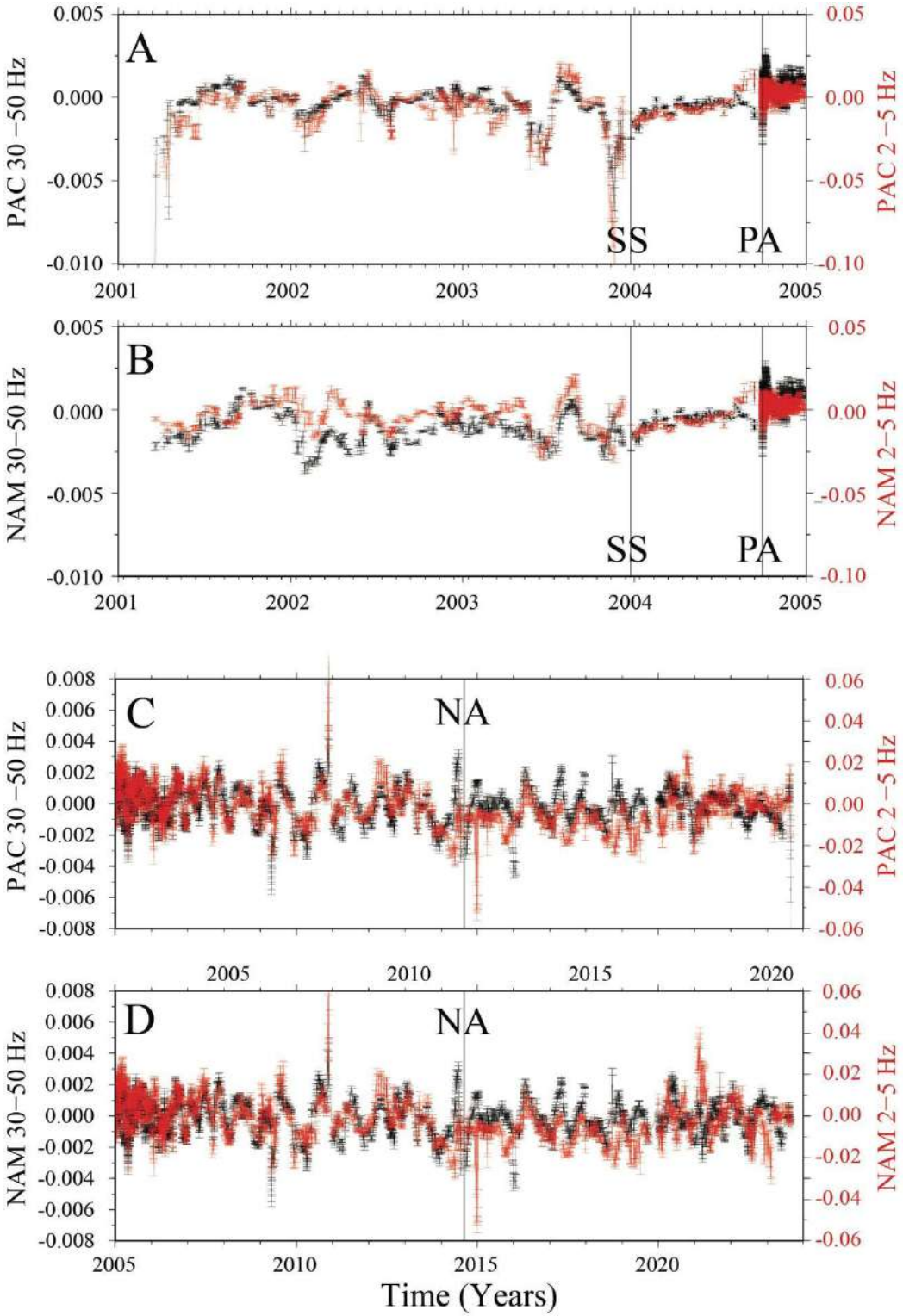

Figure 4. Stacked-averaged estimates of time histories of the variation of the attenuation parameter $\left(\delta\left(Q_S^{-1}(t,f)\right)\right)$ in two frequency bands: 2.0-5.0 Hz (black, left scale) and 30-50 Hz (red, right scale). In A and B the stacked-averaged values of the attenuation parameter are plotted in a three-year time window (01/01/2002 through 01/01/2005), whereas C and D show the stacked-averaged attenuation time histories between 01/01/2005 and the fall of 2023.

Following Sebastiani & Malagnini (2020), who provided a forecast for the next Parkfield mainshock via the analysis of the variability of the variance of the daily center of the seismic activity along the transitional segment of the SAF in the time window between 1973 and late 2019, we look at the variability of the variance of the attenuation anomalies as a function of time. Variances are computed over subsequent subsets of attenuation anomalies, and the latter are obtained as follows: after a number of samples is chosen (e.g. 40) , we look at the longest time window needed to gather 40 subsequent data points, then we apply that length to all the time windows that we analyze.

In each time window we randomly choose a subset of 40 data points to be used to compute the variance. We randomly choose 10% of data points to be eliminated from each subset and do multiple estimates of variance by looping through this bootstrap step of the analysis a number of times (10). We finally average all variance determinations. Time windows are moved, one data point at a time, toward more recent times. The analysis done without applying the bootstrapping/ averaging technique yields very similar results. In Figure 5 we plot the average variances, normalized by the length of the time window. We also point out that a single estimate of variance does not differ much from what we present here. Finally, Figure 6 shows the average attenuation parameter $\left(Q_S^{-1}(f) \right)$ calculated for the North American side (black) and for the Pacific side of the SAF (red), in the indicated time windows (2001-2004 and 2005-2019).

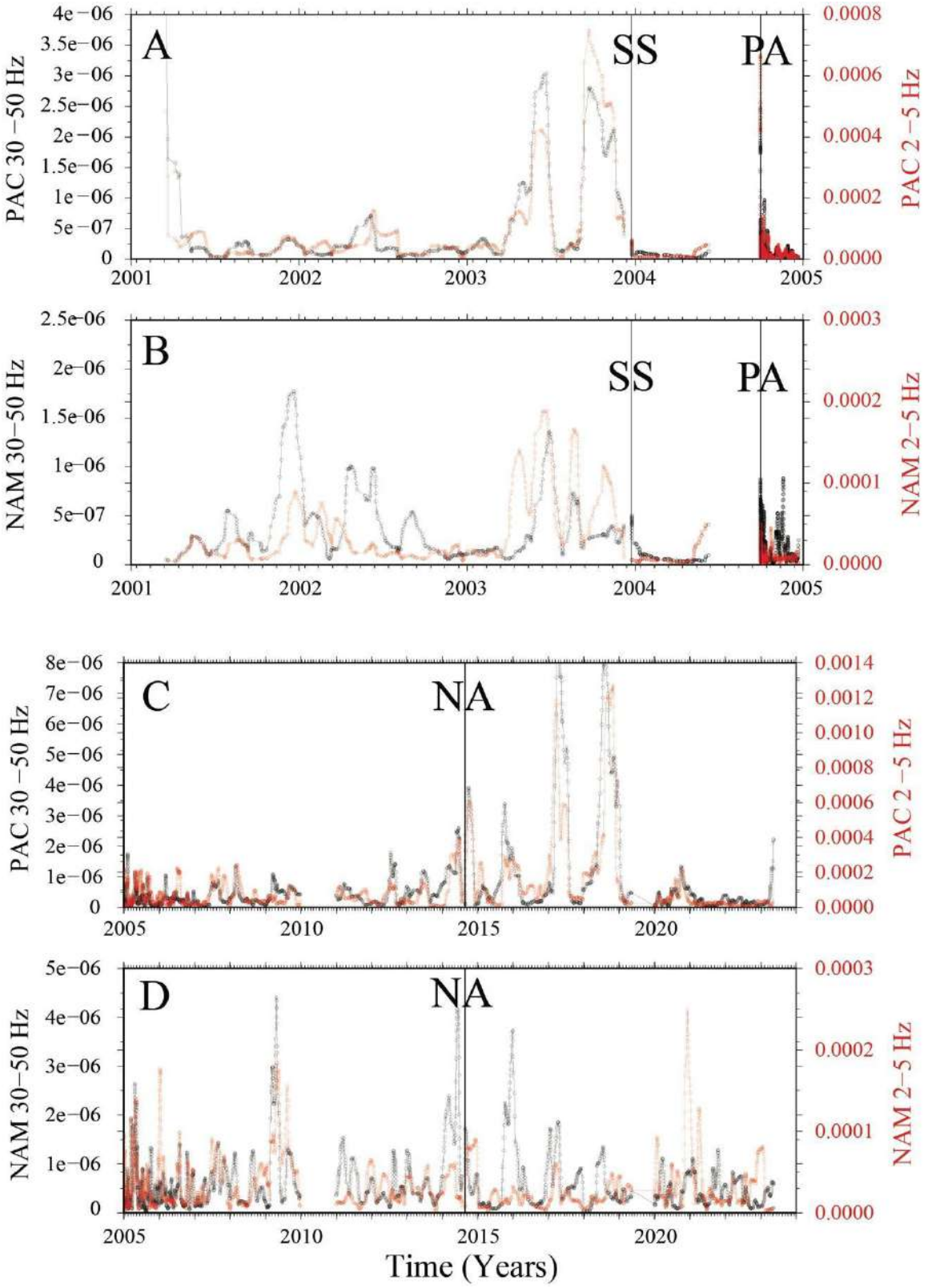

Figure 5. Variance of the stacked attenuation time histories of Figure 5 calculated on adjacent subsets of 40 data points. Note that, at the end of the previous seismic cycle, the San Simeon earthquake completely shuts off the variance of the attenuation time histories on both sides of the fault. Before being shut-off, variance shows an increasing trend on the Pacific side of the fault. During the current cycle, in the decade 2010-2020, a similar increasing trend is observed on the variance on the Pacific side of the SAF. SS, PA and NA indicate, respectively, the occurrences of the San Simeon, Parkfield, and Napa earthquakes. Comparing this Figure with Figure 2 we see a correspondence between the variance drop and a significant reduction of tremor activity in 2020, suggesting that the seismic attenuation (and possibly the main seismic activity) is modulated by the NVT rate.

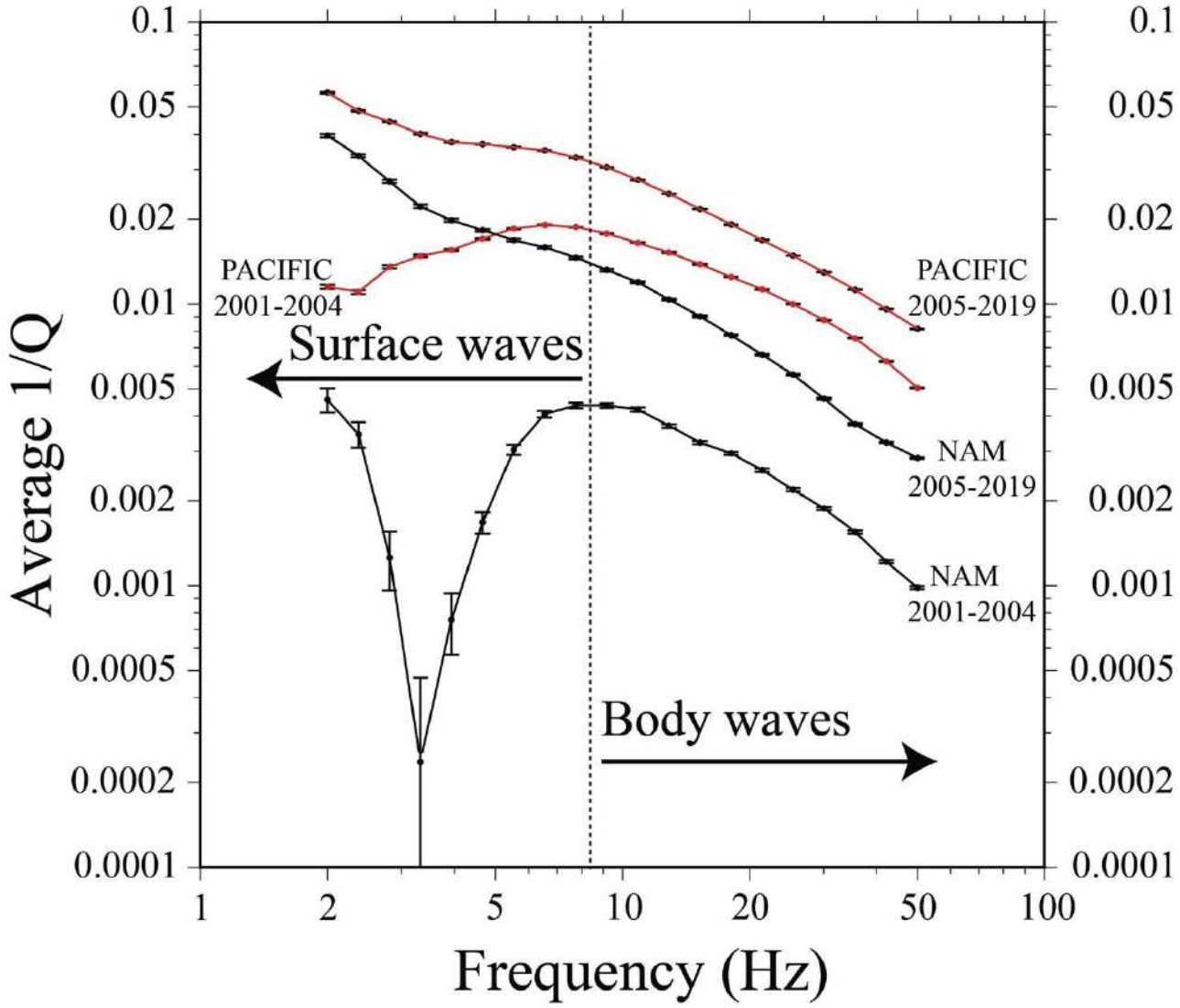

Figure 6. Average attenuation parameter $\left(Q_S^{-1}(f)\right)$ calculated for the North American side (black) and for the Pacific side of the SAF (red), in the indicated time windows (2001-2004 and 2005-2019). Below 8-10 Hz, all curves show a flattening that is stronger for the attenuation parameter calculated on both sides of the SAF in the 2001-2004 time window. Such behavior is consistent with the fact that the ground motion in the 2-8 Hz band is rich with surface waves, if not dominated by them.

Our study shows that, along the fault segment under scrutiny, the signature of the precritical state of the 2004 mainshock is represented by the variations in opposite directions of the low- and the high-frequency attenuation parameters as a function of time (low-frequency attenuation increases sharply, high-frequency attenuation decreases). The bifurcations are observed on both sides of the fault, and last 6-8 weeks. The precritical state of the Parkfield asperity emerges after a period of smooth variability of the attenuation parameter that lasts for about one year.

The bifurcation of the stacked seismic attenuation is the result of the different trends followed by the populations of cracks in the two ranges of frequency at both ends of the available spectrum: 2-5 Hz and 30-50 Hz. In order to interact with the seismic energy, cracks' lengths must form permeability structures with dimensions comparable to the wavelengths carried by the seismic radiation: 400-1500 m for the 2-5 Hz band, and 60-100 m for the 30-50 Hz band. The cracks in the

permeability structures with dimensions comparable to the short-wavelength radiation tend to close because crack coalescence causes strain localization into the macroscopic fracture, and compaction and stress relaxation in the surrounding volume. The long-wavelength radiation, on the contrary, gets more attenuated because the longer cracks that dominate the coalescence process increase the bulk permeability in the volume immediately around the fault plane by enhancing their aperture and interconnection. Finally, we observe that the 2-5 Hz band is dominated by surface waves that sample a shallower crustal structure than the direct S-waves of the 30-50 Hz band (see Figure 6).

About the intertwined behaviour of $\delta\left(Q_S^{-1}(t,f)\right)$ and the NVT activity, it is possible that the increased permeability along the very fault plane under subcritical conditions allows pore pressure to diminish at NVT depth (in our case, this would correspond to the observed decrease in NVT activity that starts in 2020), and to an upward pore fluid migration along the fault plane. In turn, the latter may weaken the fault and facilitate the occurrence of the mainshock. Within the limits of this hypothesis, monitoring the fluctuations of NVT activity along the SAF would be useful in recognizing the precritical state of the fault.

In the next few months (or years) the Parkfield segment of the SAF will provide most of the answers to our questions. In the meantime, it may be worthwhile applying our technique on different tectonic settings characterized by more complex fault geometries and ongoing NVT activity. Aside from more advanced theoretical developments and laboratory experiments on seismic attenuation under increasing differential stress, the most important ingredient for a successful use of non-geometric attenuation and NVT information would be the use of data from dense(r) seismic networks equipped with borehole sensors recording at high sampling rate.

References

Guilhen, A. and Nadeau, R.M. (2012), Episodic tremors and deep slow-slip events in Central California, EPSL, 357-358, 1-10.

Malagnini, L., Dreger, D. S., Bürgmann,R., Munafò, I., & Sebastiani, G. (2019). Modulation of seismic attenuation at Parkfield, before and after the 2004 M6 earthquake. Journal of Geophysical Research: Solid Earth,124, 5836–5853. https://doi.org/10.1029/2019JB017372.

Malagnini, L., & D.S. Dreger (2016). Generalized Free-Surface Effect and Random Vibration Theory: a new tool for computing moment magnitudes of small earthquakes using borehole data, Geophys J Int (2016) 206 (1): 103-113. https://doi.org/10.1093/gji/ggw113.

Nadeau, R.M., Guilhem, A. (2009). Nonvolcanic Tremor Evolution and the San Simeon and Parkfield, California, Earthquakes,Science 325, 191, DOI: 10.1126/science.1174155.

Sebastiani, G., & L. Malagnini (2020). Forecasting the Next Parkfield Mainshock on the San Andreas Fault (California), Journal of Ecology and Natural Resources, vol. 4, issue 3, https://doi.org/10.23880/jenr-16000218.

Corresponding author: luca.malagnini@ingv.it

Density values in the shallow crust: analysis and comparison of deep well data in the Adriatic region (Italy)

M.T. Mariucci[1], P. Montone[1], P. Balossino[2]

[1] Istituto Nazionale di Geofisica e Vulcanologia, Rome, Italy
[2] Former ENI S.p.A. Natural Resources, Italy

A detailed knowledge of rock densities helps in constraining the interpretation of crustal structures and their modelling. This work presents the results of a first systematic comparison between two datasets relative to density data of geological formations crossed by 13 deep wells. The wells are located in the Adriatic region and reach depths of over 5000 meters. The main lithologies involved include sedimentary rocks such as clays, sandstones, marls, evaporites, and carbonate rocks. The first dataset concerns density values obtained from the analysis of sonic logs recorded along the wells, by applying the relation proposed by Gardner et al. (1974). The second dataset refers to in situ density log measurements. We calculated the differences among the values in the two datasets. The comparison of the densities obtained from various lithologies and geological formations leads us to draw some initial considerations regarding the applicability and accuracy of Gardner's formula in the area we analyzed. In the Plio-Quaternary formations, characterized by clayey-sandy lithologies, the density values derived from sonic velocities are underestimated by at least 0.1 g/cm^3 with respect to the values measured by density logs. Whereas, densities of the carbonate sequences are overestimated by the same extent. Noteworthy, especially for gypsum units, the density estimates deviate from the real values, overestimating by a factor of approximately 0.3 g/cm^3. The results that we obtained emphasize the differences in density values when using the Gardner formula and suggest the need for taking into account the possible errors in the specific geological context or instead lithologies, such as those explored in this study. Since usually density values have to rely on evaluations and not real measurements, we should try to obtain the best possible estimates. We think that continuing in comparisons with as much data as possible of density log data and velocity-derived density data could produce also a numerical correction to adapt the Gardner rule to the Italian area.

References

Gardner G.H.F., Gardner L.W., Gregory A.R.; 1974: Formation velocity and density—the diagnostic basics for stratigraphic traps. Geophysics, 39, 770–780.

Corresponding author: mariateresa.mariucci@ingv.it

Earthquake swarms frozen in an exhumed hydrothermal system (Bolfin Fault Zone, Chile)

S. Masoch[1], G. Pennacchioni[1], M. Fondriest[1], R. Gomila[1], P. Poli[1], J. Cembrano[2,3], G. Di Toro[1,4]

1. Dipartimento di Geoscienze, Università degli Studi di Padova (Italy)
2. Departamento de Ingeniería Estructural y Geotécnica, Pontificia Universidad Católica de Chile (Chile)
3. Andean Geothermal Center of Excellence (Chile)
4. Sezione di Tettonofisica e Sismologia, Istituto Nazionale di Geofisica e Vulcanologia (Italy)

Earthquake swarms commonly occur in upper-crustal hydrothermal-magmatic systems and activate mesh-like fault networks within zones of fault geometric complexity. How these networks develop through space and time along seismic faults is poorly constrained in the geological record. Here, we describe a spatially dense array of small-displacement (< 1.5 m) epidote-rich fault-veins within granitoids, occurring at the intersections of subsidiary faults with the exhumed seismogenic Bolfin Fault Zone (Atacama Fault System, Northern Chile). Epidote faulting and sealing occurred at 3-7 km depth and 200-300 °C ambient temperature. At distance ≤ 1 cm to fault-veins, the magmatic quartz of the wall-rock shows (i) thin (<10- µm-thick) interlaced deformation lamellae, and (ii) cross cutting quartz-healed veinlets. The epidote-rich fault-veins (i) include clasts of deformed magmatic quartz, with deformation lamellae and quartz-healed veinlets, and (ii) record cyclic events of extensional-to-hybrid veining and either aseismic or seismic shearing. Deformation of the wall-rock quartz is interpreted to record the large stress perturbations associated with the rupture propagation of small earthquakes. In contrast, dilation and shearing forming the epidote-rich fault-veins are interpreted to record the later development of a mature and hydraulically-connected fault-fracture system. In this latter stage, the fault-fracture system cyclically ruptured due to fluid pressure fluctuations, possibly correlated with swarm-like earthquake sequences.

Corresponding author: Simone Masoch simone.masoch@phd.unipd.it

3D Hypocenters relocation in high-resolution central Mediterranean velocity model

I. Menichelli[1*], P. De Gori[1], C. Chiarabba[1]

[1] *Istituto Nazionale di Geofisica e Vulcanologia (Rome, Italy)*

In this study, a new 3D relocated hypocenters catalogue has been built for the Italian region using an updated 3D velocity model computed for the central Mediterranean area (Menichelli et al., 2023). Classical one-dimensional velocity models, due to their limitation in recovering lateral heterogeneous variations in the velocity structure, offer only a simplified depiction of the reality. For this reason, the necessity to use 3-D velocity models in the location of hypocenters, which consider the inhomogeneous structure of the different layers that constitute the earth's interior, has been emerging in recent years.

The 3D tomographic model used has been computed inverting P- and S- arrival times recorded between 2014-2021 by the RSN (Italian Seismic Network) and AlpArray (AlpArray 2015; Hetenyi et al., 2018) seismic network. In particular, the seismic data set includes Pg, Pn, Sg, and Sn, and the related arrival times were manually picked within a maximum epicentral distance of 1000 km.

We used the code Simulps 14 (Thurber 1983, 1999) to locate seismic events with the 3D velocity model. The method uses P and S–P arrival times to solve for hypocentral parameters while keeping fixed the Vp and Vs velocity structure.

We compute the hypocentral parameters for about 170.000 seismic events recorded by the INGV seismic network (RSD) that occurred in the period 2005–2023 starting from 1D absolute locations obtained using the best fit 1D Minimum Velocity Models and procedure presented in Menichelli et al., (2022). The decision to start with an already precise localization was made with the intention of improving the accuracy of localization as much as possible.

In order to determine stable solutions we selected only seismic events with at least 3 P-wave and 2 S-wave arrival times, the closest station within 50 km and *rms* ≤ 0.4 s. A further selection was also performed on the basis of the focal depth extracted from the previous 1D hypocentral locations: seismic events occurring at significant depths (≥ 80 km) were localized using a local model built ad hoc for the southern Tyrrhenian area using the arrival times of intraslab seismicity (Chiarabba et al., 2008). The decision was aimed at achieving accurate localization even at mantle depths.

The preliminary results obtained by the statistical analysis show low errors for the hypocentral coordinates (maximum peak at around 7 km for x and y-coordinates and at around 1-2 km for the z-coordinate) and small *rms* values (< 0.5 s).

The relocation process plays a key role in improving the accuracy of hypocenter determination, thus contributing significantly to the understanding of the intricate seismotectonic framework of the central Mediterranean region. By ensuring accurate relocation of seismic events, this method sheds light on the fundamental and deep crustal processes that define the structural dynamics of the Alpine and Apennine mountain ranges. In this way, the main seismic features, both large- and small-scale, within these regions are effectively highlighted.

In addition, through this work, the variation of the crustal seismogenic layer (CSL) along the Mediterranean area can be thoroughly evaluated. The delineation of the characteristics and variations of the crustal seismogenic layer in this area provides crucial insights into seismic potential and crustal behaviour, offering a comprehensive understanding of seismic hazards in this geologically complex area.

Furtherly, to test the performance of our location procedure, we performed detailed comparisons with the recent seismic catalogues obtained with both 1D (Menichelli et al., 2022) and 3D (CLASS, Latorre et al., 2023; CARS, Michele et al., 2023) velocity models. These kinds of studies turn out to be an important step forward in the assessment of the country's seismic hazard, aiming to improve the associated risk mitigation of the seismic activities.

References

Hetényi, G., Molinari, I., Clinton, J., Bokelmann, G., Bondár, I., Crawford, W. C., ... & AlpArray Working Group. (2018). The AlpArray seismic network: a large-scale European experiment to image the Alpine Orogen. *Surveys in geophysics*, *39*, 1009-1033.

Latorre, D., Di Stefano, R., Castello, B., Michele, M., & Chiaraluce, L. (2023). An updated view of the Italian seismicity from probabilistic location in 3D velocity models: The 1981–2018 Italian catalog of absolute earthquake locations (CLASS). *Tectonophysics*, *846*, 229664. Menichelli, I., De Gori, P., Lucente, F. P., Improta, L., Valoroso, L., Baccheschi, P., ... & Chiarabba, C. (2022). Minimum 1D VP and VP/VS models and hypocentral determinations in the central Mediterranean area. *Seismological Society of America*, *93*(5), 2670-2685.

Menichelli, I., De Gori, P., Lucente, F. P., Improta, L., & Chiarabba, C. (2023). Lithosphere Structure, Processes, and Physical State of the Alpine-Apennine System. Journal of Geophysical Research: Solid Earth, 128(4), e2023JB026411.

Michele, M., Di Stefano, R., Chiaraluce, L., Latorre, D., & Castello, B. (2023). *CARS-Catalog of Relative Seismic Locations of 1981-2018 Italian Seismicity* (No. EGU23-14033). Copernicus Meetings.

Thurber, C. H. (1983). Earthquake locations and three-dimensional crustal structure in the Coyote Lake area, central California. *Journal of Geophysical Research: Solid Earth*, *88*(B10), 8226-8236.

Thurber, C., & Eberhart-Phillips, D. (1999). Local earthquake tomography with flexible gridding. *Computers & Geosciences*, *25*(7), 809-818.

*Corresponding author: irene.menichelli@uniroma3.it

Exploring Italy's Present-Day Stress Field Complexity through Utilisation of Geophysical, Geological, and In Situ Drilling Data

P. Montone and M. T. Mariucci
Istituto Nazionale di Geofisica e Vulcanologia, Roma, Italy

Comprehensive understanding of the shallow crust's present-day stress field in Italy is crucial for enhanced crustal modelling and a more insight into tectonic processes and fault slip behaviour. Adhering to the guidelines of the World Stress Map, this study presents the latest findings on horizontal stress orientations and stress regime in Italy. The analysis is based on recent in situ drilling data and focal mechanisms of significant earthquakes (Figure 1). New borehole breakout analysis was conducted on 14 deep wells along the Adriatic coast and offshore, revealing horizontal stress orientations in nine wellbores. Stress orientations and tectonic regimes were deduced from the analysis of 21 earthquake focal mechanisms with magnitudes equal to or greater than 4, occurring between January 1, 2022, and October 31, 2023. The updated findings from 10 wells in the mid-southern Adriatic Sea, where no borehole ovalization was observed, highlight the absence of breakout zones along these wells.

These new data will be incorporated into the Italian Present-day Stress Indicators (IPSI) database, scheduled for release at the beginning of the year. The IPSI database, managed at INGV (Istituto Nazionale di Geofisica e Vulcanologia), serves as a georeferenced repository containing information on the present-day stress field of the crust.

The database includes horizontal stress orientations accurately analysed and standardised for global reliability and comparability, with 969 entries (all qualities) updated to October 2023. IPSI database consolidates information on contemporary stress within the Earth's crust's upper 40 km, derived from various stress indicators categorised into five main groups.

In the specific context of the Mw 5.5 2022-2023 Adriatic seismic sequence, newly acquired breakout data from deep boreholes exhibit coherent Shmin orientations ranging from N126 to N132, characterised by small standard deviations, indicating their high quality. These results, extending from the surface to approximately 4000 m, fill an information-deficient depth range, because the entire seismic sequence is positioned between 5 and 10 km depth. The seismic sequence, comprising six events with M≥4, yielded four available TDMT focal mechanisms, with three displaying pure thrust faulting and one a strike-slip mechanism. The consistently oriented minimum horizontal stress, evident in the N133 orientation for the Mw=5.5 event at 5 km depth, aligns with the northern Apennines' axis, confirming stress trends inferred from existing datasets in inland and southern sectors.

The intricate plate motions and the presence of multiple subduction zones have given rise to simultaneous and geographically proximate diverse stress regimes.

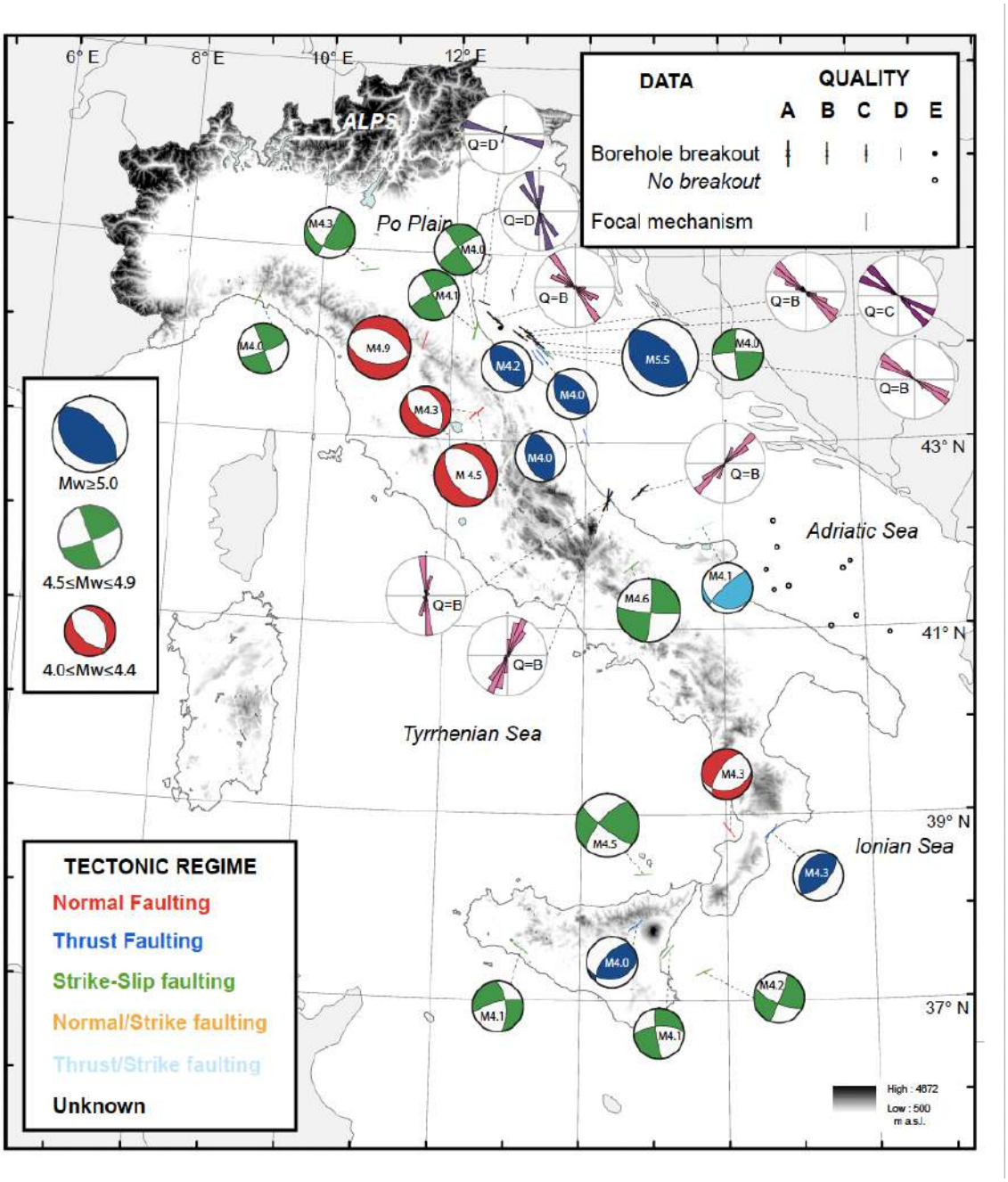

Fig. 1 – New data from 21 earthquake focal mechanisms and 9 breakout directions. Further 10 wells with no ovalization are highlighted with open circles.

Predominantly, extension is observable along the entire Apennine belt with a ~NE–SW orientation, transitioning to NW–SE in the Calabria region, following the curvature of the Calabrian arc. Thrust faulting is constrained to external areas, evident along the northern Apennine front (Adriatic foredeep) with a NE-oriented compression and offshore along the northern Sicilian coast, as well as in the Po Plain and Friuli regions. The stress orientation in the latter areas aligns closely with the ~N–S convergence of ongoing relative crustal motions between the Eurasia and Africa plates. Conversely, there is no apparent compression along the central and southern Apennines' external front based on present-day stress information. The active stress field so far not well defined in the offshore area of

the eastern Calabrian coast, seems to be today finally characterised by a compressive and strike-slip regime with the orientation of the maximum compression in a direction approximately NW-SE. In this area, the new data further highlights the clear separation between the western Tyrrhenian and eastern Ionian margins. Strike-slip faulting, the less prevalent tectonic regime in Italy, is spatially confined to areas along the southern Apennine foredeep and in eastern Sicily, both onshore and offshore in the Tyrrhenian and Ionian regions.

Situated within the broader context of Mediterranean tectonic plate boundary, the Adriatic area holds geological importance as a dynamic region, with the Adriatic microplate assuming a central role. Notably, recent revisions have been made to data from deep wells in the southern sector of the Adriatic Sea, characterised by a lack of seismic activity. The results of the analysis carried out along these wells have not shown borehole ovalization, thus indicating the absence of an anisotropic stress field.

References

ISIDe Working Group; 2007: Italian seismological instrumental and parametric database (ISIDe). Rome, Italy: Istituto Nazionale di Geofisica e Vulcanologia. doi:10.13127/ISIDE.

Mariucci M.T., Montone P.; 2022: IPSI 1.5, database of Italian present-day stress indicators. Rome, Italy: Istituto Nazionale di Geofisica e Vulcanologia. doi:10.13127/IPSI.1.5.

Montone P., Mariucci M.T.; 2023: Deep well new data in the area of the 2022 Mw 5.5 earthquake, Adriatic Sea, Italy: In situ stress state and P-velocities. Front. Earth Sci. 11:1164929. doi: 10.3389/feart.2023.1164929.

Montone P., Mariucci, M.T.; 2016: The new release of the Italian contemporary stress map. Geophys. J. Int. 205, 1525–1531. doi:10.1093/gji/ggw100.

Scognamiglio L., Tinti E., Quintiliani M.; 2006: Time domain moment tensor (TDMT). Rome, Italy: Istituto Nazionale di Geofisica e Vulcanologia. doi:10.13127/TDMT.

Corresponding author: paola.montone@ingv.it

Modeling dynamic ruptures on extended faults for microearthquakes induced by fluid injection

F. Mosconi[1], E. Tinti[1,2], E. Casarotti[2], A. A. Gabriel[3], R. Dorozhinskii[4], L. Dal Zilio[5], A. P. Rinaldi[5], and M. Cocco[2]

[1] Università la Sapienza, Rome, Italy
[2] Istituto Nazionale di Geofisica e Vulcanologia, Rome, Italy
[3] Scripps Institution of Oceanography, UC San Diego, La Jolla, CA 92093, USA
[4] Technical University of Munich, Germany
[5]Seismology and Geodynamics, Institute of Geophysics, Department of Earth Sciences, Swiss Federal Institute of Technology (ETH Zürich), Zürich, Switzerland

Understanding the dynamics of microearthquakes is a timely challenge to solve current paradoxes in earthquake mechanics, such as the stress drop and fracture energy scaling with seismic moment. Dynamic modeling of microearthquakes induced by fluid injection is also relevant for studying rupture propagation following a stimulated nucleation. We study the main features of unstable dynamic ruptures caused by fluid injection on a target pre-existing fault (50m x 50m) generating a M_w < 1 event. The selected fault is located in the Bedretto Underground Laboratory (Swiss Alps) at ≈1000m depth and these research activities are performed in the framework of the ERC Synergy project FEAR (Fault Activation and Earthquake Ruptures). We perform fully dynamic rupture simulations coupled with seismic wave propagation in 3D by adopting a linear slip-weakening friction law. We use the distributed multi-GPU implementation of SeisSol on the supercomputer Leonardo (CINECA).

Stress field and fault geometry are well constrained by in-situ characterization, allowing us to minimize the a priori imposed parameters. We investigate the dynamics of rupture propagation and arrest for a target M_w < 1 induced earthquake with spatially heterogeneous stress drops caused by pore pressure changes and different constitutive parameters (critical slip-weakening distance, D_c, dynamic friction μ_d). We explore different homogeneous conditions of frictional parameters, and we show that the spontaneous arrest of an unstable rupture is possible in the modeled stress regime (fig.1), by assuming a high ratio between strength excess and dynamic stress drop (the fault strength parameter S), characterizing the fault before the pore pressure change. The rupture arrest of modeled induced earthquakes depends on the heterogeneity of dynamic parameters due to the spatially variable effective normal stress, which controls the on fault G_c spatial increment. Moreover, for a fault with high S values (low rupturing potential), small variations of D_c *(≈0.45÷0.6 mm)* can significantly impact on the final earthquake size, particularly controlling the deceleration and arrest phase. Studying dynamic interactions (stress transfer) among slipping points on the rupturing fault provides insights on the dynamic load and shear

stress evolution at the crack tip. The inferred spatial dimension of the cohesive zone in our models is nearly ~0.3-0.4m, with a maximum slip of ~0.6 cm. Finally, from the generated synthetic waveforms, we examine the differences in the content of high-frequency radiation between self-arresting and run-away earthquakes, also providing an estimation of the source parameters obtained through the spectral inversion. This estimation is then compared with the forward models. Our results suggest that meso-scale processes near the crack-tip during the nucleation and acceleration of the rupture strongly affect dynamics of micro-earthquakes.

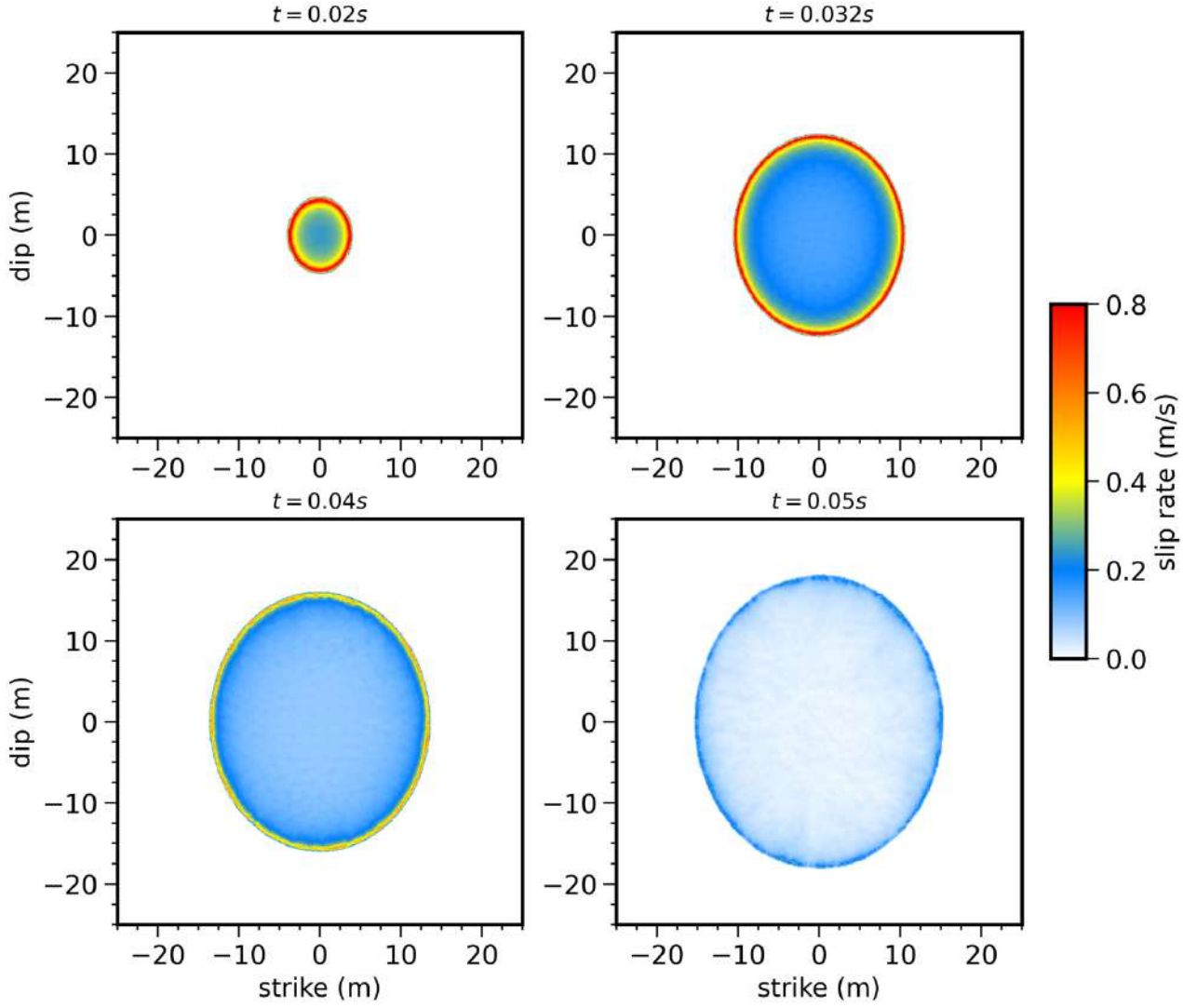

Fig. 1 Snapshot of the slip rate evolution during the rupture propagation of a microearthquakes (M_w = 0.71) in the context of fluid induced seismicity; for the model with D_c = 0.6mm.

Corresponding author: francesco.mosconi@uniroma1.it

Detect and characterize swarm-like seismicity

L. Passarelli [1], S. Cesca[2], L. Mizrahi[3], G. Petersen[2]

[1] INGV - Istituto Nazionale di Geofisica e Vulcanologia, sezione di Bologna, Bologna, Italy.
[2] GFZ – German Research Centre for Geosciences, Potsdam, Germany
[3] SED – Swiss Seismological Service, ETH Zürich, 8092 Zürich, Switzerland

Tectonic earthquake swarms do not follow the classical temporal and spatial pattern observed for mainshock-aftershock sequences. Unlike the typical occurrence of a largest mainshock that initiates the sequence and triggers aftershocks following an Omori-Utsu decay and productivity scaling with the mainshock magnitude, earthquake swarms show a distinctive increase of seismic activity without a clear mainshock. Typically, the largest earthquake(s) occur(s) later in a swarm sequence that often consists of multiple earthquake bursts that show spatial migration. This erratic clustering behavior of earthquake swarms comes from the interplay between the long-term accumulation of tectonic strain and short-term transient forces driving swarm-like seismicity. The detection and investigation of earthquake swarms challenges the community and ideally requires an unsupervised approach, and indeed numerous algorithms have emerged in the last decades for earthquake swarm identification.

In this study, we comprehensively review commonly used techniques for detecting earthquake clusters. We first applied those techniques to thousands synthetic earthquake catalogs produced with state-of-the-art ETAS model, featuring a time-dependent background rate to simulate realistic swarm-like sequences. Our approach enables us to identify boundaries in some parameters commonly used to distinguish earthquake clusters, says mainshock-aftershocks versus swarm sequences. The insights gained from synthetic data contribute to a more accurate classification of seismicity clusters in real earthquake catalogs. We therefore apply the same algorithm to real cases of seismicity where earthquake swarms have already been identified, i.e. the 2010-2014 Pollino seismic sequence; the Húsavík-Flatey transform fault seismicity and the regional catalog of Utah. However, applying these findings to real cases is contingent upon the clustering algorithm used, the statistical completeness of catalogs, and the spatial and temporal distribution of earthquakes. Unfortunately, full automation of swarm detection and characterization remains difficult to attain, necessitating manual verification and investigation of individual swarm-like sequences.

Corresponding author: luigi.passarelli@ingv.it

The Preparatory Process of the 2023 Mw 7.8 Türkiye Earthquake.

M. Picozzi[1,2], A.G. Iaccarino[2], D. Spallarossa[3]

[1] Istituto Nazionale di Oceanografia e di Geofisica Sperimentale - OGS, Italy.
[2]University of Naples Federico II, Italy.
[3]DISTAV, University of Genoa, Genoa, Italy.

To verify the existence of a preparatory process for the 6 February 2023, Mw 7.8 Kahramanmaraş earthquake, southern Türkiye, we analyze the temporal evolution of seismic catalog information for ~7500 earthquakes with magnitudes ML ≥ 1.5, which occurred along the main segments of the East Anatolian Fault (EAF) since 2014. We find the EAF fault segments showing different temporal patterns in the proportion of nonclustered seismicity, which we interpret as temporal variation of coupling. We also study the evolution of the b-value, fractal dimension and energy rate. These seismic features show for the Amanos and Pazarcık fault segments a long-term trend during the period 2020 – 2022 that might correspond to a quiescence phase. The latter is followed by a change in earthquake clustering and characteristics that starts about eight months before the Mw 7.8 Kahramanmaraş event. Our observations confirm the existence of a long-lasting preparatory phase for the 2023, Mw 7.8 Kahramanmaraş earthquake and can stimulate new investigations on the East Anatolian Fault mechanic. Intercepting when a fault starts deviating from its steady behaviour, might be the key for identifying the preparatory phase of large earthquakes and mitigate seismic risk.

Corresponding author: mpicozzi@ogs.it

ML-based workflow for earthquake detection and location: preliminary results from the northern Apennines with a model trained on local waveforms

G. Poggiali[1], S. Bagh[2], L. Chiaraluce[2], C. J. Marone[1], Z. E. Ross[3], E. Tinti[1], W. Zhu[4]

[1] La Sapienza Università di Roma, Rome, Italy

[2] Istituto Nazionale di Geofisica e Vulcanologia, Rome, Italy

[3] Seismological Laboratory, Division of Geological and Planetary Sciences, California Institute of Technology, Pasadena, CA, USA

[4] University of California, Department of Earth & Planetary Science, Berkeley, CA, USA

The analysis of microseismicity has a fundamental role in understanding earthquakes driving processes such as seismic sequences evolution and preparatory phase. Recent advances in machine learning (ML)-based detection and location techniques, coupled with dense seismic networks, have dramatically increased the quantity of low-magnitude earthquakes that can be recorded and properly located. This has led to the development of a new generation of earthquake catalogs illuminating fault systems in unprecedented detail.

We study data from the Alto Tiberina Near Fault Observatory (TABOO-NFO) located in the Apennines of central Italy where earthquake activity is intense. This is an ideal site to apply modern detection techniques and study in detail complex fault systems evolving in a shallow crust surrounded by deep fluid circulation. We build an earthquake catalog for the TABOO area using data from 2010 to present using a ML-based workflow tailored to this area.

We started from an updated version of the deep learning phase picker PhaseNet (Zhu and Beroza, 2019). This version of PhaseNet includes several improvements, such as polarity estimation and better detection of close-in-time events, which were often undetected in the original version. We trained PhaseNet on waveforms collected by the local TABOO seismic network that had been manually labelled by analysts (Cattaneo et al., 2017) with P, S phases and first arrivals polarity. We show that training the model with local data results in a significant improvement mainly in the picking accuracy of S-phases and also in polarity estimation.

The result of the detection step is a massive phase dataset composed of tens of millions of P and S phases making the association (e.g., binding) of events a challenge. For this task we used the Gaussian Mixture Model Association (GaMMA, Zhu et al., 2021) algorithm, which treats earthquake phase association as an unsupervised clustering problem in a probabilistic framework to estimate earthquake (preliminary) locations, origin times and magnitudes. We show the

statistics of associated events and phases as well as some examples that highlight the importance of fine-tuning the parameters, which becomes complex to do in the presence of very large datasets. This first part of the workflow (detection and association) resulted in 1.4M events.

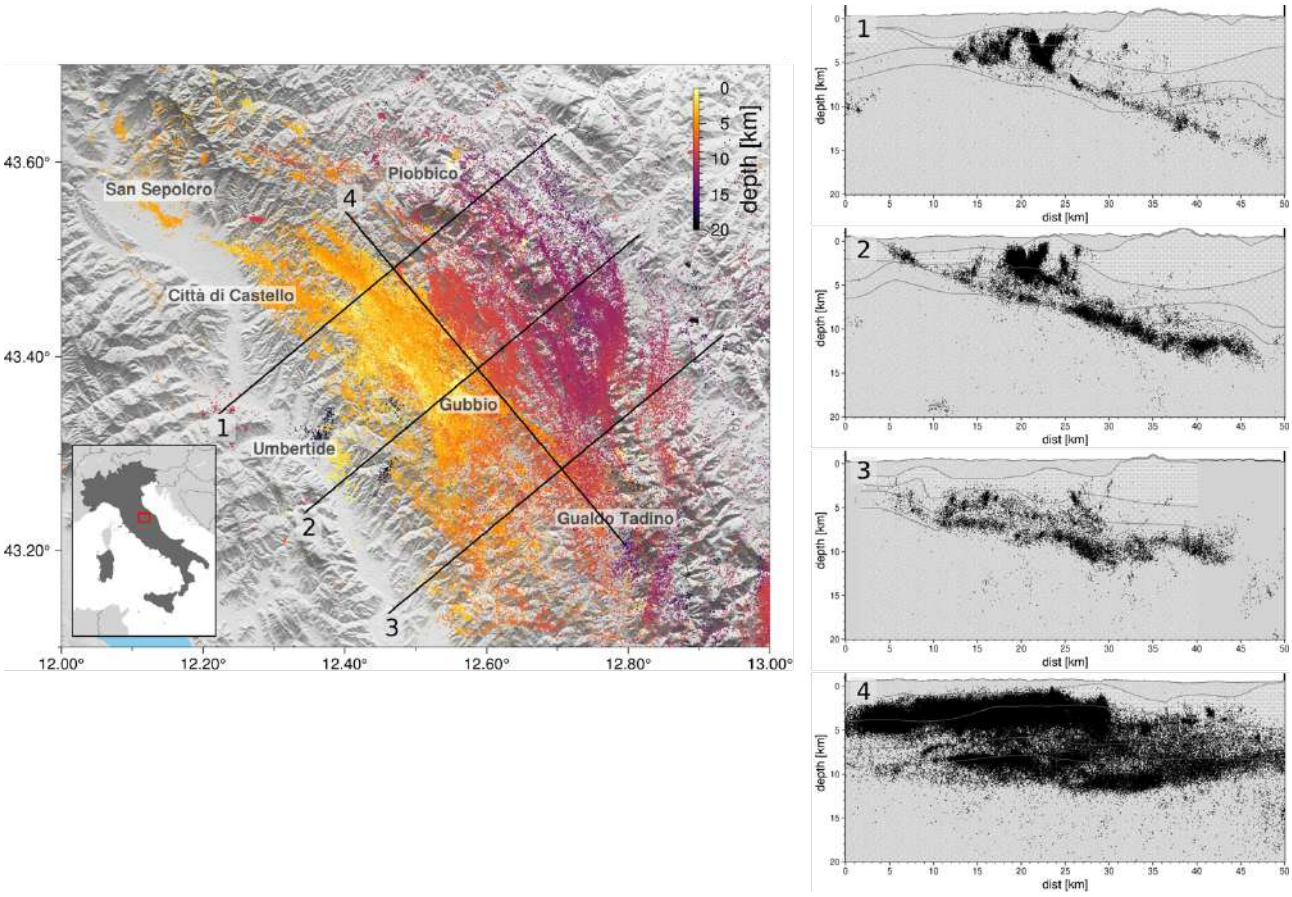

Fig. 1 – Map, cross sections (1-3, width=5km) and longitudinal section (4, width=20km). Cross sections 1 and 2 clearly depict the Altotibernia Fault at depth and the shallower seismicity pertaining to the Pietralunga (1) and Gubbio (2) sequences. The lithological model on the background is from Latorre et al., 2016.

To estimate the absolute hypocentral locations we use an updated version of HypoSVI (Smith et al., 2022), a probabilistic location method in which the forward model is based on a physics informed neural network trained to solve the Eikonal equation. The location procedure makes use of source-specific station terms (SSST) that can vary as a function of source position, allowing better correction for the unmodeled velocity structure with respect to the more classic static station corrections. During the location procedure, outlier picks are filtered out based on the statistics of the residuals. We provide absolute locations for more than 10 times the number of earthquakes recorded by the Italian seismic network, with a spatial distribution of seismicity that illuminates the expected crustal portions and agrees with independent information from a lithological model of the area (Fig. 1).

We are currently in the stage of waveform similarity analysis (cross correlation, CC). The CC refined traveltimes will be used to relocate the catalogue, providing a very detailed picture of the complex seismicity of the area. The similarity values will also be used to start investigating the presence of repeating earthquakes in order to better define the mixed distribution of locked and creeping

patches of The Alto Tiberina Fault and its interactions and coupling with the shallower system of faults. In the final stage we will approach focal mechanisms and moment magnitude estimation.

References

Cattaneo, M., Frapiccini, M., Ladina, C., Marzorati, S., & Monachesi, G. (2017). A mixed automatic-manual seismic catalog for Central-Eastern Italy: analysis of homogeneity. Annals of Geophysics.

Smith, Jonthan D, Zachary E Ross, Kamyar Azizzadenesheli, and Jack B Muir. 2022. "HypoSVI: Hypocentre Inversion with Stein Variational Inference and Physics Informed Neural Networks." Geophysical Journal International 228 (1): 698–710.

Zhu, Weiqiang, and Gregory C. Beroza. 2019. "PhaseNet: A Deep-Neural-Network-Based Seismic Arrival-Time Picking Method." Geophysical Journal International 216 (1): 261–73.

Zhu, Weiqiang, Ian W. McBrearty, S. Mostafa Mousavi, William L. Ellsworth, and Gregory C. Beroza. 2021. "Earthquake Phase Association Using a Bayesian Gaussian Mixture Model." Journal of Geophysical Research: Solid Earth, e2021JB023249.

Corresponding author: giulio.poggiali@uniroma1.it

NEW PALAEOSEISMOLOGICAL EVIDENCE OF COSEISMIC SURFACE RUPTURE ACROSS THE CARNIC PREALPINE FRONT (NE-ITALY): THE BUDOIA-AVIANO THRUST SYSTEM

M.E. Poli[1]; G. Patricelli[2]; E. Falcucci[3]; S. Gori[3]; G. Paiero[1]; E. Rizzo[2]; A. Marchesini[1]; R. Caputo[2]

(1) Università di Udine, Dipartimento di Scienze Agroalimentari, Ambientali e Animali
(2) Università degli Studi di Ferrara, Dipartimento di Fisica e Scienze della Terra
(3) Istituto Nazionale di Geofisica e Vulcanologia

In the framework of the PRIN_2020 “Fault segmentation and seismotectonics of active thrust systems: the Northern Apennines and Southern Alps laboratories for new Seismic Hazard Assessments in northern Italy (NASA4SHA)”, we conducted a palaeoseismological study into the area comprised between the Budoia and Aviano localities (western Carnic Prealps, NE Italy).

The investigated area, which is part of the external Plio-Quaternary front of the Eastern Southalpine Chain, is characterized by the presence of distinct WSW-ENE trending and S-verging reverse fault planes arranged in thrust systems and affecting the Quaternary succession (Poli et al., 2014).

In detail, the geological and morphotectonic survey highlighted many evidence of recent deformation affecting the Last Glacial Maximum alluvial fan of the Artugna Stream, including morphological anomalies of both the topography (scarps) and the hydrography of minor streams.

Following the multidisciplinary and multiscale approach, the preliminary geophysical survey, which included multiscale Electric Resistivity Tomograhy (DERT and ERT) and Ground Penetrating Radar (GPR), allowed us to identify the site for the excavation of two palaeoseismological trenches (Rizzo et al., this session)

The excavated walls intersected a set of medium-to-high angle reverse planes verging towards the North, which displace the alluvial fan stratigraphy and also affect the soil. At about 2 m depth from topography, we identified a paleosoil dividing two alluvial fan units and affected by deformation. The radiocarbon dating of the paleosoil sample revealed an age of about 16 ky BC.

The palaeoseismological analysis allowed us to estimate a cumulative slip, measured on all fault planes, of the order of at least 4.5 m. Moreover, we detected at least three seismic events, the most recent of which is possibly referable to the 1873 M 6.3 Alpago - Cansiglio earthquake (CPTI15, Rovida et al., 2022).

The reverse fault planes identified within the two excavated trenches define an about 20 m wide area of surficial deformation, developed at the hanging-wall of the main S-verging thrust plane and characterized by an ENE-WSW trending. If considering the lateral extension of this deformation area, it clearly affects industrial complexes, urban centres and sensitive structures of Budoia and Aviano localities. Therefore, the paleoseismological evidence collected so far provide implication which are relevant for the seismic hazard estimation of the area, and which must be necessarily considered in the framework of the regional planning.

REFERENCES

M.E. Poli, G. Monegato, A. Zanferrari, E. Falcucci, A. Marchesini, S. Grimaz, P. Malisan, E. Del Pin (2014). Seismotectonic characterization of the western Carnic pre-alpine area between Caneva and Meduno (Ne Italy, Friuli). DPC-INGV-S1 Project “Base-knowledge improvement for assessing the seismogenic potential of Italy” (D6/a2.1).

E. Rizzo, V. Giampaolo, F. Mucchi, P. Boldrin, G. De Martino, M.E. Poli, G. Patricelli, A. Marchesini, R. Caputo (2024). Multiscale geophysical investigation on the Budoia-Aviano thrust system (NE Italy): first results. GNGTS 2024.

A. Rovida, M. Locati, R. Camassi, B. Lolli, P. Gasperini, A. Antonucci (2022). Catalogo Parametrico dei Terremoti Italiani (CPTI15), versione 4.0. Istituto Nazionale di Geofisica e Vulcanologia (INGV). https://doi.org/10.13127/CPTI/CPTI15.4

Corresponding author: eliana.poli@uniud.it

Source parameters of the 2010-2014 Pollino (Italy) seismic sequence and their relationship with structural and geological setting of the area

M. Ponte[1], G. Calderoni[2], R. Di Giovambattista[2], M. La Rocca[1]

[1] Università della Calabria, Dipartimento di Fisica, Rende, Italy

[2] Istituto Nazionale di Geofisica e Vulcanologia, Rome, Italy

Between 2010 and 2014, a seismic swarm of thousands of events (Mwmax= 5.2) occurred in the Mt. Pollino area, between the Calabrian Arc and the Apennines, adjacent to the Ionian Subduction Zone. High resolution source location revealed that seismicity originated from two main clusters with opposite dipping orientations, with the main faults aligned along a NNW-SSE direction. Understanding the source parameters of these seismic events is crucial to get insight on the individual rupture process of the earthquake, the spatial evolution of the seismic sequence and the dynamic properties of the rupture, including the possible involvement of fluids.

We analyzed hundreds of earthquakes of the Pollino seismic sequence in order to investigate the following source parameters: the Brune stress drop ($\Delta\sigma$), the apparent stress (τa) and the Savage-Wood radiation efficiency ($\eta sw= \tau a/\Delta\sigma$). We identified 20 seismic events with $3.1 < Mw < 5.2$ with known TDMT solution and 80 smaller events with $2.4 < M_L < 3.0$ not present in the TDMT archive. For earthquakes not included in the TDMT archive we calculated the seismic moment through spectral scaling of the low frequency plateau in the displacement spectra using the corresponding target event selected on the basis of the distance, larger-magnitude, and greatest number of stations that recorded the event. The two stress parameters depict a similarly scattered trend, with the highest value corresponding to the main shocks. Seismic efficiency is substantially stable versus M0, with values mostly between 0.1 and 0.6, and a mean value of about 0.23, which corresponds to the expectation of the omega square model.

The area affected by the 2010-2014 sequence extends from the Mercure basin to the Campotenese and Morano Calabro basins and it is characterized by a complex system of normal and oblique normal faults (Fig. 1). The area towards the Tyrrhenian side (west) is made up of faults with a NS trend with E/NNE dip and dip-slip kinematics, alternating with segments of faults with WNW-ESE orientation with normal-slip kinematics whose anti-slip component is important. The intramontane area is characterized by NW-SE faults dipping towards the SW that are included in a "western system" and an "eastern" system.

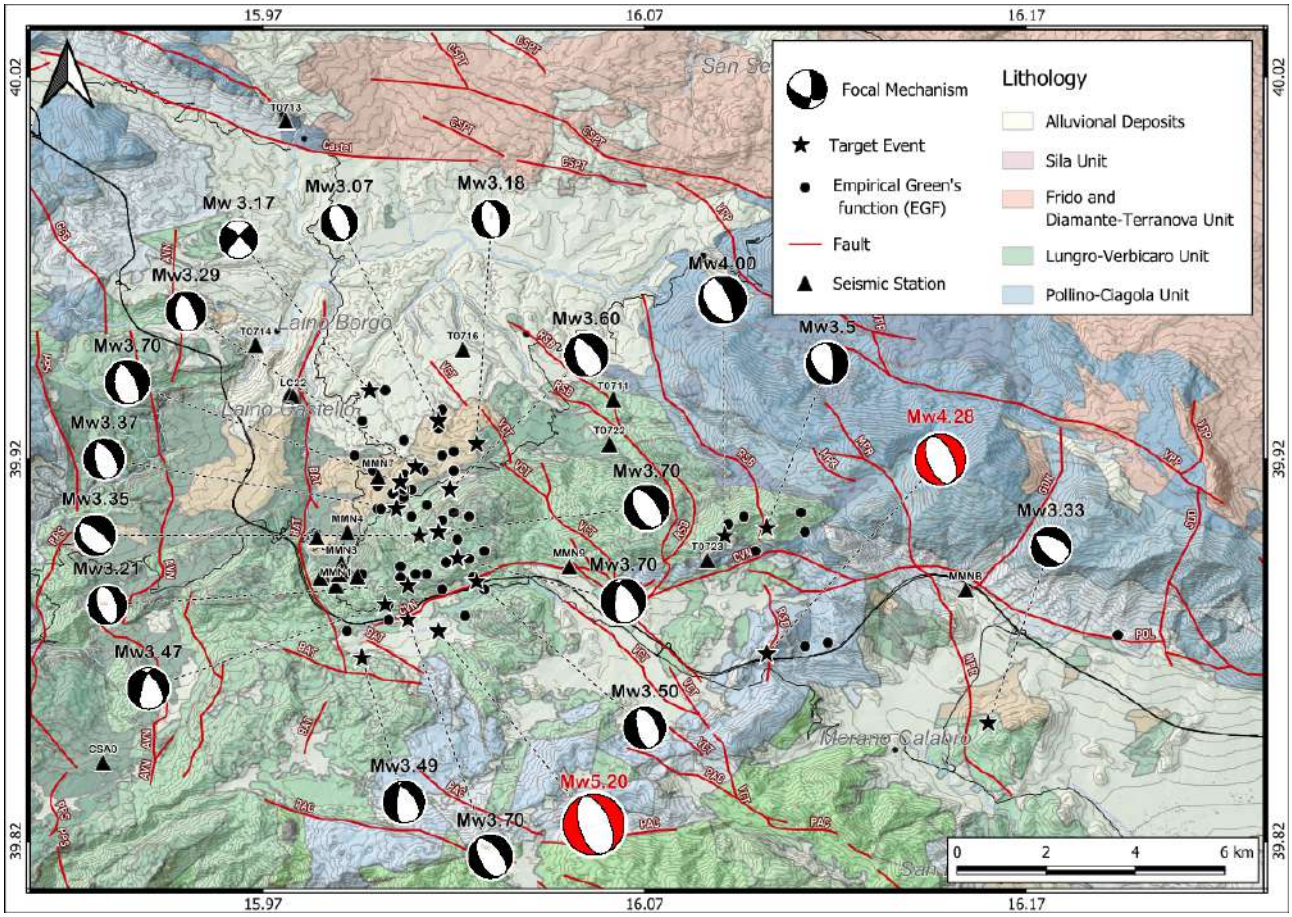

Fig. 1 - Map of the study area showing the main geologic units and structural elements, the seismic stations (black triangle), the seismic events with Mw 3.1 (black star), and 2.4 ML 3.0 (black circle). Beachballs represent the TDMT focal solution of Mw 3.1 and show predominantly normal kinematics with strike oriented in the N-NW/S-SE direction. The red beachballs correspond to the mainshocks (Mw5.20 and Mw4.28) of the seismic sequence nucleated on two different tectonic structures. Red lines represent known normal faults developed following the extensional tectonics during the Plio-Pleistocene. Two main fault systems are identified. The first includes main fault segments with a trend that varies southwards from N-S to WNW-ESE. The other two groups of faults have a NW-SE strike with SW dipping. The lithological basis is taken from the "Carta Geologica dell'area compresa tra Maratea, Castrovillari e Sangineto by A. Iannace; M. D'Errico; S. Vitale - (2004).

Other Quaternary faults are present in the area whose contribution plays an important role on the seismicity of the area. In this region two carbonate platforms, the Apennines Platform and the deeper Inner Apulian Platform, are believed to be overlapped at about 5 km depth. Recent papers describe results obtained from different analyses that indicate the presence of high pressure fluids in the seismogenic volume where the seismic sequence occurred (De Matteis et al., 2021; Pastori et al., 2021; Napolitano et al., 2021, 2023). The fluid moving along the faults causes the lubrification that facilitates the earthquake occurrence. A reduction of the dynamic strength due to high pressure fluid is expected to increase the seismic efficiency ηsw. From our analysis we find the highest ηsw values along the two main faults, reaching their maximum values at the tips of these faults. The concentration of elevated ηsw values at fault tips supports the observations that fluid-related processes play a significant role in the seismic activity within this particular area. The ηsw variability in the target area could be elucidated by considering fluid involvement in controlling

seismicity, a concept invoked by other researchers to explain observed Vp/Vs anomalies and anisotropy variations.

References

De Matteis R., Convertito V., Napolitano F., Amoroso O., Terakawa T., Capuano P.; 2021: Pore fluid pressure imaging of the Mt. Pollino region (southern Italy) from earthquake focal mechanisms. Geophysical Research Letters, 48, e2021GL094552. https://doi.org/10.1029/2021GL094552

Iannace A., D' Errico M., Vitale S.; 2004: Carta geologica dell'area compresa tra Maratea, Castrovillari e Sangineto. Stampa.

Napolitano F., De Siena L., Gervasi A., Guerra I., Scarpa R., La Rocca M.; 2020: Scattering and absorption imaging of a highly fractured fuid-filled seismogenetic volume in a region of slow deformation. Geosci. Front. 11 (3), 989-998. doi:10.1016/j.gsf.2019.09.014

Napolitano F., S. Gabrielli, L. De Siena, O. Amoroso, P. Capuano (2023). Imaging overpressurised fracture networks and geological barriers hindering fluid migrations across a slow deformation seismic gap. Scientific Reports 13:19680, https://doi.org/10.1038/s41598-023-47104-w

Pastori M., Margheriti L., et al.; 2021: The 2011-2014 Pollino Seismic Swarm: Complex Fault Systems Imaged by 1D Re ned Location and Shear Wave Splitting Analysis at the Apennines Calabrian Arc Boundary. Front. Earth Sci. 9:618293.doi: 10.3389/feart.2021.618293

Corresponding author: michela.ponte@unical.it

Geological field survey in the area affected by the 2023 devastating earthquake sequence (Turkey). Part I: the Hahramanmaraş-Pazarcık fault section

S. Pucci[1], M. Caciagli[1], R. Azzaro[1], P. Di Manna[2], A.M. Blumetti[2], V. Poggi[3], P.M. De Martini[1], R. Civico[1], R. Nappi[1], E. Ünsal[4], O. Tatar[5]

[1] Emergeo Working Group, Istituto Nazionale di Geofisica e Vulcanologia (INGV), Italy
[2] Istituto Superiore per la Protezione e la Ricerca Ambientale (ISPRA), Roma, Italy
[3] Istituto Nazionale di Oceanografia e di Geofisica Sperimentale (INOGS), Sgonico (TS), Italy
[4] Disaster and Emergency Management Authority (AFAD), Gaziantep, Turkey
[5] Disaster and Emergency Management Authority (AFAD), General Director of Earthquake and Risk Reduction, Ankara, Turkey

Introduction

Following the devastating M_w 7.8-7.6 earthquakes occurred on 6 February 2023 along the East Anatolian Fault (Fig. 1a), the Italian Civil Protection Department (DPC), in coordination with the Turkish Disaster and Emergency Management Authority (AFAD), set up a team of earthquake geologists belonging to its Competence Centres (INGV – Istituto Nazionale di Geofisica e Vulcanologia; ISPRA - Istituto Superiore per la Protezione e la Ricerca Ambientale; INOGS – Istituto Nazionale di Oceanografia e di Geofisica Sperimentale) to survey the coseismic surface faulting effects. In the period 6-13 May, the Italian team investigated six key-areas along the 140 km-long Nurdagi-Kahramanmaraş-Pazarcık fault section (Fig. 1) in the provinces of Gaziantep, Kahramanmaraş and Adıyaman.

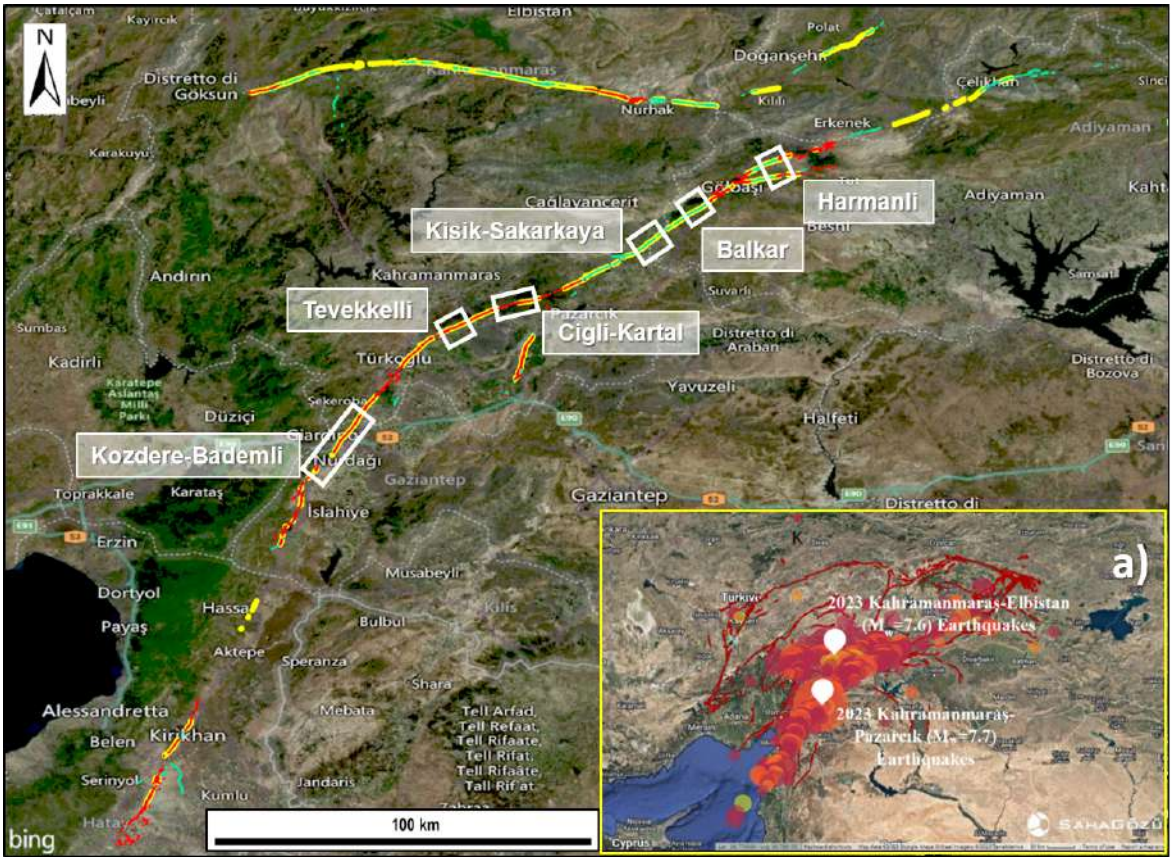

Fig. 1 – Locations of the investigated areas (white boxes) along the Kahramanmaraş-Pazarcık fault. Fault trace colors refer to different sources of data: yellow, AFAD; green, USGS; red, EMERGEO. Inset map (a) shows the regional framework affected by the 2023 seismic sequence (from Middle East Technical University, 2023).

This first mission, carried out within the clearinghouse system, has also allowed us to acquire useful information for planning further investigations, especially in the frame of the presently constituting European Earthquake Geology task force (EuQuaGe).

Methodological approach

The field survey was aimed at collecting data on the coseismic surface geological effects, particularly the primary effects (i.e. surface faulting), in order to contribute to the reconstruction of the near-fault slip distribution through the classical morphotectonic and structural geology approaches. Following the earthquakes, several international research teams began mapping the surface faulting traces by integrating different methodologies (field surveys, high-resolution (<1.0 m/pixel) optical image analysis (WorldView 1, 2, and 3; see Reitman et al., 2023) and remote sensing data processing). Three months after the events, a general overview of fault ruptures was already available, so we preferred to focus on some aspects of particular scientific interest, such as the relationship between coseismic deformation and long-term morphotectonic processes. In this way we concentrated our effort on specific situations that, at the same time, could ensure quickness in the field operations as well as significance of data collected.

First, in the phase of preparation for the mission, we analysed the pattern of fault rupture available on the Internet by different scientific institutions (USGS, METU) through the Google Earth® satellite

images, in some cases also comparing situations documented by both pre- and post-event images. This analysis allowed for the recognition of six key-areas (see labels in Fig. 1) where the interaction between long-term and coseismic deformation was immediately evident, each of them being characterised by different tectonic and morphological features. Then, in the field, we proceeded straight to the previously designated locations; however, it should be noted that in each region only a limited number of measurement points, even 1 km apart from each other, were considered. This operational approach differs significantly from that used in previous seismic emergencies in Italy (Pantosti et al., 2014), where measurement points were mapped extensively and practically in a continuous way along the fault. This strategy is motivated by the huge size of the coseismic phenomena to be mapped, as well as the limited time and personnel available.

In the field, for ground measurements, tapes and Leica DISTO™ laser distance meters have been used, as we have digital mobile devices equipped with Rocklogger® software to determine the position and orientation of the coseismic features. Moreover, in order to map the investigated areas homogeneously and obtain detailed 3D models, we used a DJI Mini 2 drone and tablet featuring a LIDAR scanner system (Polycam®). In addition, a huge amount of photographic documentation has been acquired by professional digital cameras.

Preliminary results

Overall, more than 600 structural and geomorphic data points, along with ca. 4,000 photos, were acquired in the field on orientation, position and dimension of the coseismic features, including the measurements of kinematics and offset components. A part of this dataset was shared in real-time with the MapLab at INGV in Rome, thanks to the tools of the GIS platform (ArcGIS Pro®). These georeferenced data pointed to reconstruct the deformational pattern at the local scale of the six key-areas. Morover, drone surveys provided images to reconstruct eight structure from motion (SfM) high-resolution (5 cm/pixel) digital surface models (DSM) (Fig. 2), and relative ortho-photomosaics. In addition, expeditious LIDAR-derived models representative of the expression of the surface faulting in four key-areas, were also obtained by a handheld device (Fig. 3). In this way it has been possible to derive analytical models of the coseismic mole-track along the fault trace that contain the georeferenced structural and geomorphic data.

In all the investigated key-areas, left-lateral displacements up to 5.0 m were measured and validated through the comparison of the same piercing points on pre-earthquake Google Earth® images through the same piercing points. Similarly, post-earthquake Google Earth® images allowed, at some places, to reproduce a detailed line drawing of the surface faulting in order to integrate the field mapping. This allowed us to highlight the relationships between coseismic surface faulting and tectonic long-term landforms (Fig. 3a).

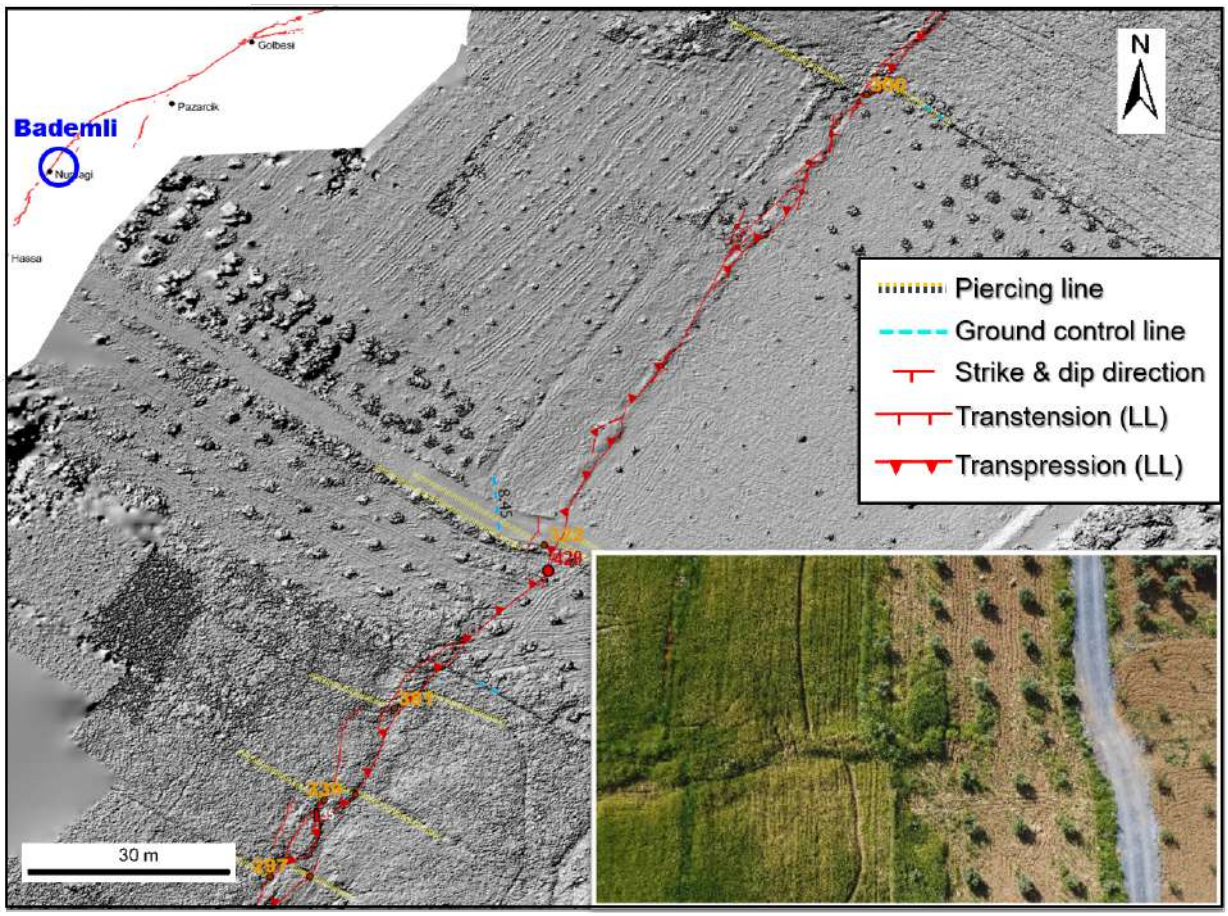

Fig. 2 – Example of a high-resolution digital surface model in the area of Bademli, districts of Nurdağı, and reconstruction of the structural pattern. Single mole-tracks and the horizontal offset component measured in the shifting of the tree rows are shown. The use of a drone represents a powerful tool to save time and resources, provided that control points in the field are calibrated.

The experience of our first mission in Turkey, carried out when national governmental and academic institutions were overwhelmed by the emergency of a devastating earthquake sequence, demonstrated that a relatively small team of experts may also provide external support to acquire detailed field observations and contribute to limiting the loss of data, typically short-lived features. Moreover, the integration of a ground-based traditional survey approach with drone surveys or LIDAR models, if well calibrated by control points in the field, proved to be a very powerful tool to optimise time and resources during a post-earthquake intervention.

Finally, the goal of this first cooperation, promoted by the Italian Civil Protection Department (DPC), was essential in defining a standardized methodology and shared tools for the next mission, held in October 2023 under the umbrella of the international EuQuaGe initiative.

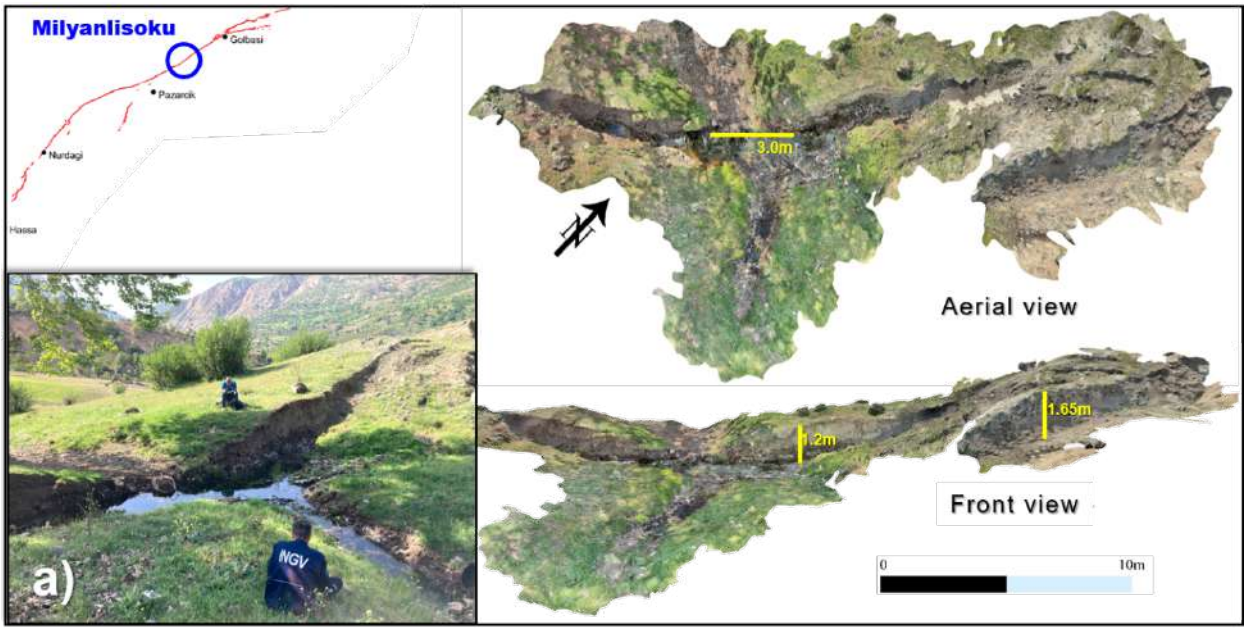

Fig. 3 – Example of speditive terrestrial acquisition by a tablet equipped with LIDAR sensor, in a site near Kartal. a) detail of the earthquake rupture interacting with geomorphological features in a mountain area: here the stream is dammed by the vertical apparent displacement produced by a left-lateral offset of 3 m.

References

Middle East Technical University; 2023: Preliminary reconnaissance report on February 6, 2023, Pazarcık M_w=7.7 and Elbistan M_w=7.6, Kahramanmaraş-Türkiye Earthquakes. Edited by K.Ö. Çetin, M. Ilgaç, G. Can and E. Çakır, Report N° METU/EERC 2023-01, Earthquake Engineering Research Center.

Pantosti D., Azzaro R., De Martini P.M., Moro M., Nappi R. and Pucci S.; 2014: QUI INGV - EMERGEO: un gruppo di lavoro INGV per lo studio degli effetti geologici cosismici. Progettazione Sismica, 2, 137-140.

Reitman N.G., Briggs R.W., Barnhart W.D., Thompson J.A., DuRoss C.B., Hatem A.E., Gold R.D., Akçiz S., Koehler R.D., Mejstrik J.D., Collett C.; 2023: Fault rupture mapping of the 6 February 2023 Kahramanmaraş, Türkiye, earthquake sequence from satellite data. U.S. Geological Survey data release, https://doi.org/10.5066/P985I7U2.

Corresponding author: raffaele.azzaro@ingv.it

The first manually revised catalog of micro-seismicity of Co. Donegal (Ireland): defining baseline seismicity in a region of slow lithospheric deformation.

F. Riva[1,2], N. Piana Agostinetti[2], S. Marzorati[3], C. Horan[4]

1. School of Advanced Studies, University of Camerino, Camerino, Italy
2. Department of Earth and Environmental science, University of Milano-Bicocca, Milan, Italy
3. Osservatorio Nazionale Terremoti, Istituto Nazionale di Geofisica e Vulcanologia (INGV), Ancona, Italy
4. Geophysics Section, Dublin Institute for Advanced Studies, Dublin, Ireland

INTRODUCTION

Ireland is a region of slow lithospheric deformation and at the present Co. Donegal, located in its northwestern part, is the only seismically active area in Ireland, with an average rate of an event every 3–4 years in the range of magnitude between 2-3. Regions of slow lithospheric deformations are characterized by a low seismicity rate and limited accumulation and release of tectonic energy, leaving open the question if such deformation is 'diffusely' accommodated along a wide fault system rather than clusterized along specific faults. Co. Donegal is also the site of post-orogenic radiogenic granites partly exposed along the NW Atlantic coast and potentially buried at shallow depth in the eastern part of the study region. For this reason, the area represents a target for deep (0–5 km depth) geothermal investigation (Goodman et al., 2004). Having a high quality of precisely located micro-seismicity is fundamental before the exploitation of geo-resources for investigating seismicity and rock physical properties in active tectonic and volcanic regions and for the definition of a 'baseline' seismicity, required for a safe future exploitation of georesource areas. For these two reasons, the final aim of our work is the precise location of both human-induced and natural micro seismic events of Co. Donegal, which could give new insights in the tectonic deformation mechanisms and help to find out granite volumes characterized by micro-fractures suitable for fluid circulation.

METHODS

The seismic data provided in this paper have been collected thanks to the SIM-CRUST project*: 'Seismic imaging and monitoring of the upper crust: exploring the potential of low-enthalpy geothermal resources of Ireland*' (https://sim-crust.dias.ie). The SIM-CRUST project provided a seismic network composed of 12 stations installed and maintained in Co. Donegal from August 2012 to June 2015 with the inter-station distance between 5 and 20 km. All stations were equipped

with broadband seismometers (Guralp CMG-40 T), with a flat response between 50 Hz and 60s. Continuous waveform data have been archived as 1-day MSEED files at DIAS (Dublin Institute for advanced Studies).

Our study focuses on the detection and location procedure through a Markov chain Monte Carlo approach of both natural and human-induced seismicity recorded from August 2012 to July 2015 by 12 broadband seismic stations. We compile a first manual-revised catalog of Donegal micro-seismicity, and we integrate it with the location of the seismic events occurred in a small seismic sequence during January 2012 in the study area.

In order to detect the seismic events, we analysed the continuous waveforms by applying a STA/ LTA network coincidence trigger algorithm (Team, 2017). Then, we performed a manual picking of P and S waves first arrival times of the events detected by the trigger algorithm (Goldstein and Snoke 2005) 2005). Finally, a total of 114 earthquakes were located using a hierarchical Bayes Markov chain Monte Carlo (McMC) algorithm, developed on purpose for this study. The Markov chain Monte Carlo method allows us to estimate the realistic uncertainties on the investigated parameters (Lomax et al., 2000). The strength of McMC method lies on the fact that the data uncertainties are also considered as part of the unknowns and are robustly estimated through the McMC sampling following a Hierarchical Bayes approach (Malinverno and Briggs 2004). Moreover, a detailed velocity model of the investigated area does not exist at the moment. This aspect can be easily solved by using our method because we just need to specify the minimum and maximum values of all the priors to define the prior probability distribution (i.e. the velocities of P and S waves).

For a more precise compilation of a seismic catalog, we also calculated the local magnitudes (ML) of the natural seismic events. We decided to use two different approaches for magnitude comparison due to scarceness of local seismicity and the consequent difficult calibration of existing magnitude values with respect to ours. We first used the classical formula for calculating the individual magnitude at each station provided by Richter (1935) that we call “MLRI352” in Table 2. For comparison, we then calculated the magnitude at each station using a calibrated local scale for Ireland, provided in the study of Grannell et al., 2018, where they used a station correction coefficient and a distance-dependant term accounting for geometrical spreading and anelastic attenuation, reported in Table 2 under the name “ML_Donegal”. We added a station correction term for the individual stations used by the Irish Seismic Network for both formulas. We then averaged the individual valued of ML resulted from each station discarding the single values that were more than two standard deviations from the mean ML value and we recalculated the final values of ML for each seismic event, as reported in Table 2.

RESULTS

We tested the performance of McMC algorithm statistically through frequency distribution histograms reported in Figure 1, where we chose a “reference event” from the list of located events. These histograms show the gaussian distribution of the eight parameters used to describe the mathematical model for the geophysical process of seismic wave propagation and thus the

location of each seismic event. Four parameters describe the event location in space and time (X, Y, Z, T0), two parameters represent the elasticity of the rock volume (Vp, Vs) and the last two are used to evaluate the data uncertainties ($\pi_{p,}$ π_s). The X and Y parameters show a Gaussian distribution with a standard deviation of about 1 km. The Z parameter (depth value) shows a Gaussian distribution with a mean value at around − 7 ± 3 km for this event. (Figure 1a–c). The velocity of P waves shows a Gaussian distribution with an average value between 5 and 6 km/s, whereas the velocity of S waves has the highest peak at 3.5 km/s with a standard deviation of about 1 km/s (Figure 1d, e). Both P ($\pi_{p,}$) and S wave uncertainties (π_s) have a Gaussian distribution with a narrow shape meaning that they have been well-constrained. The average value for π_s is 1.2, for π_s is 1.4, both with standard deviation lower than 1 (Figure 1g, h). Finally, the mean value for the Vp ⁄ Vs ratio of 1.69 with a standard deviation of less than 0.1.

The Figure 2 shows the located natural events within the Donegal Granite region. The natural seismicity is gathered between 55.12 and 55.22 N and between −7.59 and − 7.74 E (580–590 Km on the X coordinate and 6110–6120 Km on the Y coordinate) (Figure 2a). In the lower panel (panel b), the events are shown in cross-section along the track line A-B. The majority of the events is clearly aligned, showing a trend towards SE with a high dip angle. Figure 3 shows the distribution of located blast events within the Donegal area. Most of the blast events are concentrated in the proximity of active local quarries in the area. Table 1 resumes the geographical locations for the Donegal's quarries. Quarrie’s locations have been used to cross-validate the location of the recorded blast events. Comparing the position of the quarries and the clusters of localized blast events, the correlation between the two is clearly visible. This means that the majority of the anthropic events in Donegal are quarry blasts and they have been correctly localized by McMC procedure to their correspondent quarry.

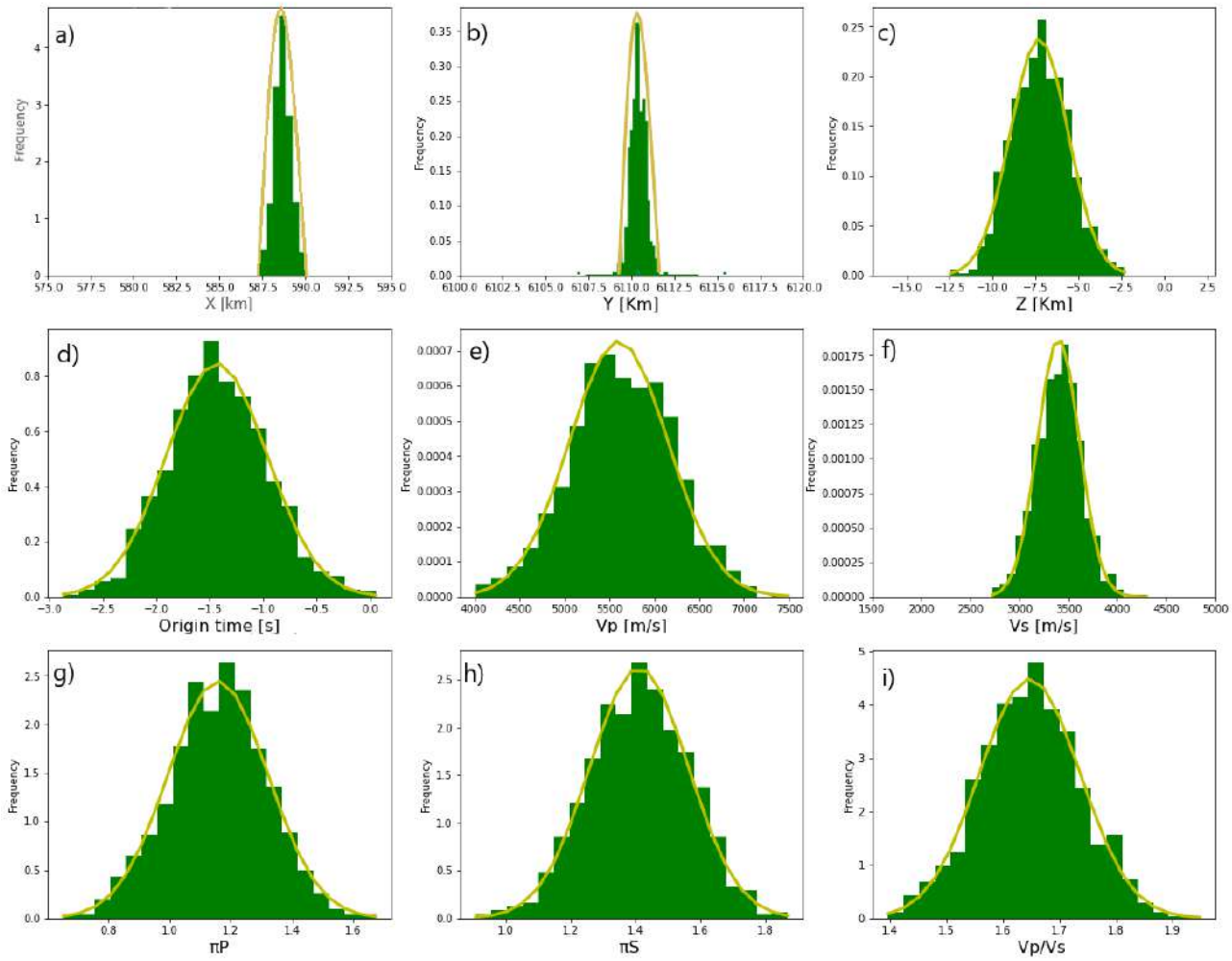

FIGURE 1. Gaussian distributions of (a) longitude [Km] (b) latitude [Km] (c) depth [Km] (d) origin time [s] (e) P-wave velocity [m/s] (f) S-wave velocity [m/s] (g) uncertainty related to the P-wave picking (h) uncertainty related to the S-wave picking (i) P- and S-wave velocity ratio for the “reference” event, chosen from the list of located natural events.

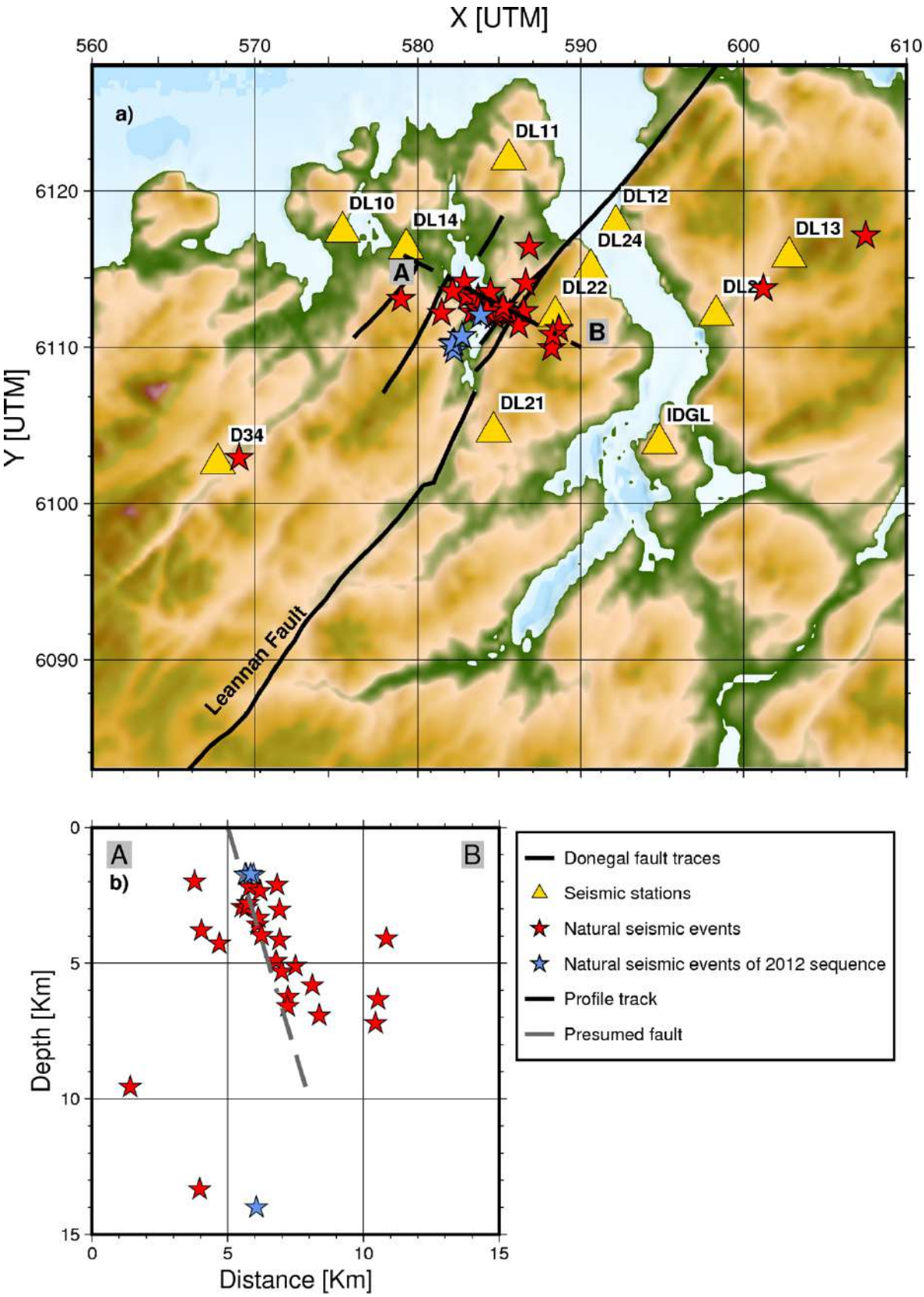

FIGURE 2. Natural seismic events plotted on the X-Y map and on the Z coordinate. Panel (a) shows the seismic stations and the track of the NW-SE profile. Panel (b) shows the natural events projected on depth and the presence of the presumed fault

.

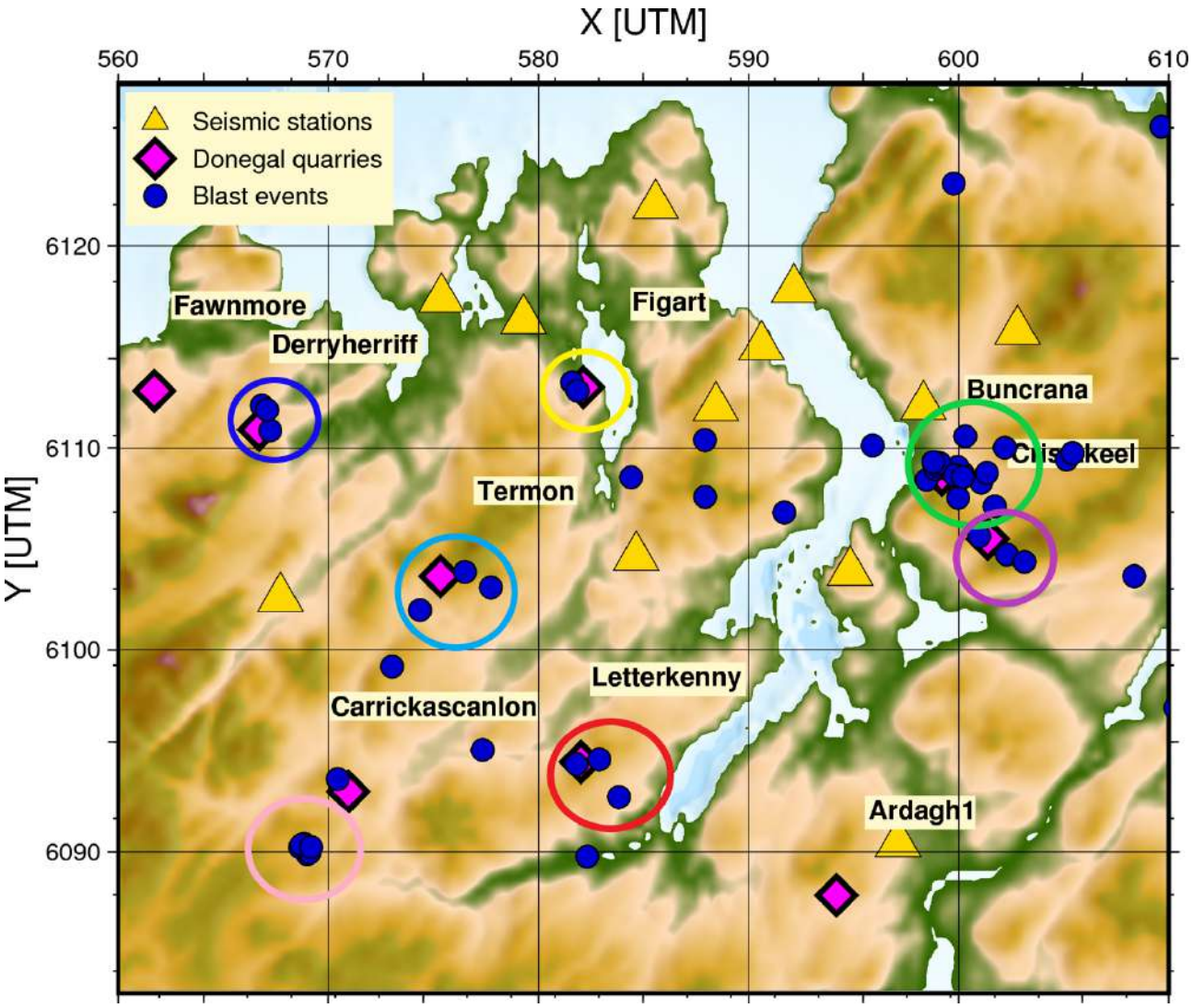

FIGURE 3. Blast events plotted on the X-Y plane. Clusters of events are related to local active quarries.

NAME	LAT	LON
Buncrana Co-Donegal	55,116	-7,440
Termon Co-Donegal	55,072	-7,820
Derryherriff Co-Donegal	55,136	-7,958
Carrickascanlon Co-Donegal	54,978	-7,890
Crislakeel Co-Donegal	55,088	-7,405
Letterkenny Co-Donegal	54,991	-7,714
Figart Co-Donegal	55,154	-7,712

TABLE 1. Donegal quarries' names and coordinates referred to the clusters of blast represented in Figure 3.

Idev num	idev	MLRI35	MLRI35 std	Num sta good	ML Donegal	ML Donegal std	Num sta good
1	20120928062959	1.6	0.3	4	1.2	0.1	4
2	20121024065903	1.5	0.3	6	1.3	0.2	6
3	20121031193817	1.5	0.3	6	1.0	0.6	6
4	20121122194654	1.9	0.4	7	2.3	0.1	6
5	20130210063823	1.5	0.2	6	1.2	0.2	6
6	20130402052503	2.3	0.3	7	1.3	0.3	7
7	20130405004553	2.8	0.3	7	3.7	0.2	7
8	20130405004643	1.4	0.3	7	0.9	0.2	7
9	20130503203415	1.5	0.3	7	1.7	0.3	7
10	20130521101615	1.4	0.3	6	1.5	0.2	6
11	20130523130545	1.4	0.3	6	1.7	0.3	6
12	20130528095326	1.4	0.3	7	1.0	0.4	7
13	20130602025737	1.6	0.4	7	1.2	0.2	7
14	20130608123331	1.4	0.3	7	1.2	0.7	7
15	20130609032716	1.4	0.3	7	0.4	0.1	7
16	20130622075627	1.4	0.3	7	1.2	0.1	6
17	20130625021853	1.4	0.3	7	0.2	0.3	7
18	20130625221351	1.4	0.3	7	0.5	0.5	7
19	20130720051915	1.5	0.2	8	0.5	0.6	8
20	20130925094650	1.8	0.3	7	1.2	0.3	7
21	20131231194717	1.5	0.2	8	1.1	0.4	8
22	20140314011925	1.5	0.3	8	0.7	0.4	8
23	20140401120612	1.5	0.2	8	1.7	0.2	8
24	20140429040202	1.5	0.2	8	1.4	0.3	8
25	20140519061145	1.5	0.2	8	1.1	0.2	7
26	20140611130418	1.5	0.3	8	1.4	0.3	8
27	20140619111118	1.6	0.4	8	1.5	0.3	8
28	20140706122114	1.5	0.2	8	0.6	0.4	8
29	20140706155212	1.5	0.2	8	0.8	0.3	8
30	20140728115302	1.5	0.3	8	1.2	0.3	7
31	20140805055249	1.5	0.2	8	1.8	0.3	8
32	20140818001902	1.5	0.3	8	1.0	0.2	7

33	20141209063409	1.4	0.3	6	1.8	0.2	6
34	20150521215759	1.5	0.3	5	0.9	0.1	5
35	20150701004049	1.4	0.4	3	0.4	0.1	3

TABLE 2. Magnitude values at each station calculated by using the first approach with equation for the magnitude 'MLRI35' and the second approach with equation for 'ML_Donegal', their standard deviations and the corresponding number of stations used to reach the final averaged ML value.

CONCLUSIONS

Our results indicate that the majority of the micro-seismicity is present with magnitudes lower than 2 (the highest magnitude is 2.8). The recorded seismicity is almost clustered along previously mapped NE-SW trending, steeply dipping faults and confined within the upper crust (focal depth less than 10 km). We also recorded anthropogenic seismicity mostly related to quarries' activity in the study area.

REFERENCES

Grannell, J., Arroucau, P., Lebedev, S., Moellhoff, M., & Bean, C. J. (2018). A Local Magnitude Scale for Ireland and its Offshore Regions, Poster Presentation, ESC General Assembly

Goldstein, P., and J. A. Snoke. 2005. "SAC Availability for the IRIS Community." *DMS Electronic Newsletter* 7 (1): 63. www.mathworks.com.

Goodman, R., Jones, G. L., Kelly, J., Slowey, E., & O'Neill, N. (2004). Geothermal energy exploitation in Ireland.

Lomax, A., Virieux, J., Volant, P., & Berge-Thierry, C. (2000). Probabilistic earthquake location in 3D and layered models (pp. 101–134). Springer Netherlands

Malinverno, A., & Briggs, V. A. (2004). Expanded uncertainty quantification in inverse problems: Hierarchical bayes and empirical bayes. Geophysics, 69, 1005–1016.

Richter, C. F. (1935). An instrumental earthquake magnitude scale*. Bulletin of the Seismological Society of America, 25, 1–32.

Team, T. O. D. (2017). Obspy 1.0.3.

Corresponding Author: federica.riva@unicam.it.

Multiscale geophysical investigation on the Budoia-Aviano thrust system (NE Italy): first results

E. Rizzo[1,2], V. Giampaolo[2], F. Mucchi[1], P. Boldrin[1], G. De Martino[2], M.E. Poli[3], G. Patricelli[1], A. Marchesini[3], R. Caputo[1]

[1] Dipartimento di Fisica e Scienze della Terra, University of Ferrara, Italy
[2]Consiglio Nazionale delle Ricerche, Istituto di Metodologie per l'Analisi Ambientale (CNR-IMAA), Tito Scalo (PZ), Italy
[3]Dipartimento di Scienze Agroalimentari, Ambientali e Animali, University of Udine, Italy

The work group is involved in the framework of the PRIN2020 research project (NASA4SHA), which aims to identify the complexity of faults in active thrust systems in Northern Apennines and Southern Alps in Italy. The paper describes the application of a multi-scale geophysical investigations applied on the Budoia-Aviano thrust system, that is part of the Polcenigo–Montereale fault system. The investigated area, which is part of the external Plio-Quaternary front of the Eastern Southalpine Chain, is characterized by the presence of distinct WSW-ENE trending and S-verging reverse fault planes arranged in thrust systems and affecting the Quaternary succession (Poli et al., 2014).

The proposed methodology included deep and shallow geoelectrical and GPR techniques to upscale the buried geological structures and to identify the site for the excavation of paleoseismological trenches. The adopted multiscale geophysical approach was applied in the studied area perpendicularly to the morphotectonic evidence of the Budoia-Aviano fault. The first step of the multiscale approach defined a Deep Electrical Resistivity Tomography (DERT). The DERT was long around 6000m, and it was able to obtain an investigation depth of about 1000m. The used DERT apparatus is a multichannel system designed and implemented by the CNR-IMAA (Rizzo et al.2004; Rizzo and Giampaolo, 2019). The acquired DERT data set was processed and elaborated through a procedure built ad hoc for this type of geoelectric surveys. While the first step highlighted the deep geological structure, several shallow high resolution geophysical surveys were planned close the morphotectonic evidence along the Budoia-Aviano thrust fault. Several shallow Electrical Resistivity Tomographies (ERT) with different electrode spacing were carried out. Three ERTs were carried out with an electrode spacing of about 5m obtaining an investigation depth of about 60m. Consequently, in order to increase the shallow resolution, a high resolution ERT with an electrode spacing of about 1m was acquired. The results of the shallow ERTs highlighted the buried geological structures in terms of subsurface faults and geological formations. Moreover, taking in account the previous results, several GPR profiles were carried out on the investigated area and the obtained results permitted to identify the site for the excavation of two

paleoseismological trenches (Poli et al., at this session 1.1). The GPR results well depicted the high-resolution image of the buried geological deformation, that were highlighted during the excavation phase (Poli et al., 2024). Finally, the multiscale geophysical approach allowed to improve the interpretation of previous geological and morphotectonic studies of the investigated area.

References

Poli M.E., Monegato G., Zanferrari A., Falcucci E., Marchesini A., Grimaz S., Malisan P., Del Pin E. (2014) Seismotectonic characterization of the western Carnic pre-alpine area between Caneva and Meduno (Ne Italy, Friuli). DPC-INGV-S1 Project “Base-knowledge improvement for assessing the seismogenic potential of Italy”.

Rizzo E., Colella, A., Lapenna, V. and Piscitelli, S. (2004). “High-resolution images of the fault controlled High Agri Valley basin (Southern Italy) with deep and shallow Electrical Resistivity Tomographies”. Physics and Chemistry of the Earth, 29, 321-327.

Rizzo E. & Valeria Giampaolo (2019) New deep electrical resistivity tomography in the High Agri Valley basin (Basilicata, Southern Italy), Geomatics, Natural Hazards and Risk, 10:1, 197-218, DOI: 10.1080/19475705.2018.1520150

Poli M.E.; Patricelli G.; Falcucci E.; Gori S.; Paiero G.; Rizzo E.; Marchesini A.; Caputo R. (2024). New palaeoseismological evidence of coseismic surface rupture across the Carnic Prealpine front (NE-Italy): the Budoia-Aviano thrust system. GNGTS 2024 (in this session).

Corresponding author: enzo.rizzo@unife.it

Preliminary results of the Non-Double-Couple seismic sources in the Southern Apennines

P. Roselli[1], L. Scognamiglio[2], F. Di Luccio[1], M. Palano[3], G. Ventura[1]

[1]Istituto Nazionale di Geofisica e Vulcanologia, Roma 1 (Roma, Italy)
[2]Istituto Nazionale di Geofisica e Vulcanologia, ONT (Roma, Italy)
[3]Istituto Nazionale di Geofisica e Vulcanologia, Osservatorio Etneo (Catania, Italy)

The seismic moment tensor analysis is an efficient way to better understand earthquake source processes as well as fault kinematics. Although earthquake sources are assumed to be shear ruptures with associated Double-Couple seismic moment tensors (DCMT), it is widely accepted that the faulting mechanism may include fracture opening and closing, rupture on a non-planar surface or multiple sub-ruptures that, in turn, produce significant Non-Double-Couple components of the moment tensor (Frohlich, 1994). Therefore, the seismic moment tensor can be decomposed into the isotropic (ISO), compensated linear vector dipole (CLVD) and double-couple (DC) components (Knopoff and Randall, 1970). The sum of the ISO and the deviatoric parts (DC and CLVD) constitute the full seismic moment tensor (FMT). DC represents the pure shear motion from two orthogonal vector pairs of equal magnitude but opposite sign; the ISO represents the isotropic volumetric change in the crack closures or implosions; the CLVD represents motion away or toward the earthquake sources with no net volume change and generally complex more physical interpretation (Frohlich, 1994; Julian et al., 1998; Martínez-Garzón et al., 2017). It is known that mixed shear-tensile earthquakes nucleate in geothermal and volcanic zones, where over-pressurized fluids concentrate (Ross et al., 1996; Saraò et al., 2010; Hrubcovà et al., 2021) and in areas of fluid extraction or injection, where hydraulic fracturing processes easily occur (Zoback, 2007; Ellsworth, 2013; Martínez-Garzón et al., 2017; Dost et al., 2020; Roselli et al., 2023). Here we investigate, the DCMTs and FMTs of the earthquakes from seismic sequences occurred in the Southern Apennine chain (Italy); these include the 2013-2014 Sannio-Matese (Di Luccio et al., 2018) and the 2010-2014 Pollino (Pastori et al. 2021; Napolitano et al., 2021) sequences. Our data-set consists of the waveforms ($M_L \geq 2.5$) recorded by both national permanent and local temporary networks operated by the Istituto Nazionale di Geofisica e Vulcanologia (http://www.orfeus-eu.org/data/eida/; Passarelli et al., 2012). To properly cover different magnitude ranges and to compare the results, we apply different approaches and specifically the Time Domain Moment Tensor (Dreger & Helemberger, 1993; Dreger 2003) and Isola (Sokos & Zahradník, 2018) for $M_L > 3.2$, hybridMT (Andersen, 2001; Kwiatek et al., 2016) for $M_L \leq 4$. Our primary goal is to understand the role played by fluids to define type and space-time variability of the source parameters and the behavior of the DC, ISO and CLVD components during the seismic sequences in the Southern Apennines.

References

Andersen L. M.; 2001: *A Relative Moment Tensor Inversion Technique Applied to Seismicity Induced by Mining*. Univ. of the Witwatersrand, Johannesburg, South Africa.

Di Luccio F., Chiodini G., Caliro S., Cardellini C., Convertito V., Pino N.A., Tolomei C., Ventura G.; 2018: *Seismic signature of active intrusions in mountain chains*. Sci. Adv. 4, e1701825.

Dost B., Stiphout A., Kühn D., Kortekaas M., Ruigrok E. and Heimann S.; 2020: *Probabilistic Moment Tensor Inversion for Hydrocarbon-Induced Seismicity in the Groningen Gas Field, the Netherlands*. Part 2: Application. Bull. Seism. Soc. Am., 110 (5): 2112–2123. Doi: https://doi.org/10.1785/0120200076.

Dreger D.S. and Helmberger D.V.; 1993: *Determination of source parameters at regional distances with 3-component sparse network data*. J. Geophys. Res., 98, 8107-8125.

Dreger D.S.; 2003: *Time Domain Seismic Moment Tensor INVersion*. International Handbook of Earthquake and Engineering Seismology, Volume 81(B), pp 1627.

Ellsworth W.L.; 2013: *Injection-induced earthquakes.* Science, 341(6142). doi: 10.1126/science.1225942.

Frohlich C.; 1994: *Earthquakes with Non-Double-Couple Mechanisms*. Science, 264 (5160), 804 -809. doi: 10.1126/science.264.5160.804.

Hrubcova P., Doubravová J., Vavrycuk V.; 2021: *Non-double-couple earthquakes in 2017 swarm in Reykjanes Peninsula, SW Iceland: Sensitive indicator of volcano-tectonic movements at slow spreading rift*. Earth and Planetary Science Letters. 563. 116875. 10.1016/j.epsl.2021.116875.

Istituto Nazionale di Geofisica e Vulcanologia (INGV); 2010-2014: *Rete Sismica Nazionale (RSN)*. doi: https://doi.org/10.13127/SD/X0FXnH7QfY.

Julian B.R., Miller A.D., Foulger G.R.; 1998: *Non-Double-Couple earthquakes 1: Theory*. Rev. Geophys., 36, 525-549.

Knoff, L. and Randall M.J.; 1970: *The compensated linear-vector dipole. A possible mechanism for deep earthquakes*. J. Gephys. Res., 75,1957-1963.

Kwiatek G., Martínez-Garzón P., Bohnhoff M.; 2016: *hybridMT: A Matlab/Shell environment package for seismic moment tensor inversion and refinement*. Seismol. Res. Lett., doi: 10.1785/0220150251.

Martínez-Garzón P., Kwiatek G., Bohnoff M., Dresen G.; 2017: *Volumetric components in the earthquake source related to fluid injection and stress state*. Geophys. Res. Lett., 44(2), 800-809, doi:10.1002/2016GL071963.

Napolitano F., Amoroso O., La Rocca M., Gervasi A., Gabrielli S., Capuano P.; 2021: Crustal Structure of the Seismogenic Volume of the 2010–2014 Pollino (Italy) Seismic Sequence From 3D P- and S-Wave Tomographic Images. Front. Earth Sci., Sec. Solid Earth Geophysics, 9. doi: 10.3389/feart.2021.735340.

Pastori M., Margheriti L., De Gori P., Govini A., Lucente F.P., Moretti M., Marchetti A., Di Giovambattista R., Anselmi M., De Luca P., Nardi A., Piana Agostinetti N., Latorre D., Piccinini D., Passarelli L., Chiarabba C.; 2021: *The 2011–2014 Pollino Seismic Swarm: Complex Fault Systems Imaged by 1D Refined Location and Shear Wave Splitting Analysis at the Apennines–Calabrian Arc Boundary*. Front. Earth Sci., Sec. Solid Earth Geophysics, 9. doi: 10.3389/feart.2021.618293.

Passarelli L., Roessler D., Aladino G., Maccaferri F., Moretti M., Lucente F.P., Braun T., De Gori P., Margheriti L., Woith H., Sebastian H., Eleonora R., Dahm T.; 2012: *Pollino Seismic Experiment (2012-2014)* [Data set]. Deutsches GeoForschungsZentrum GFZ. doi: 10.14470/9N904956.

Roselli P., Improta L., Kwiatek G., Martínez-Garzón P., Saccorotti G., Lombardi A.M.; 2023: *Source mechanisms and induced seismicity in the Val d'Agri Basin (Italy)*. Geophysical Journal International, 234 (3), pp 1617–1627

Ross A., Foulger G.R., Julian B.R.; 1996: *Non-double-couple earthquake mechanisms at The Geysers geothermal area California*. Geophys. Res. Lett., 23(8), 877-880. doi: 10.1029/96GL00590.

Saraò A., Cocina O., Privitera E., Panza G.F.; 2010: *The dynamics of the 2001 Etna eruption as seen by full moment tensor analysis*. Geophys. J. Int., 181(2), 951-965. doi: 10.1111/j.1365-246X.2010.04547.x.

Zahradník J. and Sokos E.; 2018: *ISOLA code for multiple-point source modeling –review. in Moment Tensor Solutions - A Useful Tool for Seismotectonics*. 1–28 (Springer Natural Hazards, 2018). doi:10.1007/978-3-319-77359-9.

Zoback M.D.; 2007: *Reservoir Geomechanics*. Cambridge University Press, 449 pp.

Corresponding author: pamela.roselli@ingv.it

Anatomy of clustering from parametric space-time analysis of seismicity.

G. Rossi[1], G. Bressan [2], C. Barnaba [1], A. Peresan [1]

[1] *National Institute of Oceanography and Applied Geophysics –OGS, Italy*
[2] formerly *National Institute of Oceanography and Applied Geophysics –OGS, Italy*

We propose a multiparametric approach to quantitatively describe the temporal and spatial evolution of seismicity in regions, where the spatial and temporal pattern of seismicity shows no obvious trends and cannot be resolved on well-defined fault planes (Bressan et al., 2021). We consider five different parameters. The spatio-temporal evolution of Shannon entropy quantifies the degree of organization or disorder in the energy distribution of an earthquake population (Telesca et al., 2004). The temporal changes in the classical estimates of the b-value from the Gutenberg-Richter (GR) law (Gutenberg and Richter, 1944) capture the balance between small and large-magnitude events. The temporal variation of the fractal dimension of hypocenters reflects the evolution of the spatial seismicity pattern. The “nearest neighbour" distance (Baiesi and Paczuski, 2004; Zaliapin and Ben-Zion, 2013) further enables characterizing the clustering properties of seismicity (Varini et al., 2021). Finally, the evolution of seismicity can be further investigated with multidimensional principal component analysis (PCA) (Rossi and Ebblin, 1990; Bressan et al. 2018a; 2021). Time adds to the spatial coordinates in the construction of the 4D-correlation matrix, which can be interpreted as a hyper-ellipsoid. The hyper-ellipsoid spatial axes projection onto a 3D space depicts the best-fit plane orientation and the extent of the volume interested by the aftershocks. The fourth axis projection onto space indicates the shock propagation direction and can be used to infer the relationships between the various planes that activate in time (Bressan et al., 2021).
We have focused on an area in northeastern Italy where the maximum interference between the NW-SE oriented Dinaric transpressive structures and the E-W oriented Alpine thrusts occurs, bound to the superposition of three main tectonic phases that affected the area through time (Ponton, 2010). The inversion of the focal mechanisms indicates a dominance of reverse mechanisms but the presence of strike-slip solutions is also relevant (Saraò et al., 2021). Comparison between the stress and strain tensors reveals planes of mechanical weakness that are oriented differently, often unfavourably with respect to the principal stress axes, suggesting heterogeneous crustal strength (Bressan et al., 2018b). This area is characterized by a relatively high seismic hazard and has experienced several destructive earthquakes in the past. The most severe ones occurred in 1700 (I0=VIII-IX MCS on the Mercalli-Cancani-Sieberg scale, Mw=5.7), 1788 (I0=IX, Mw=5.2), 1928 (I0=IX, Mw=6.0), 1959 (I0=VII-VIII, Mw=5.2) (Rovida et al., 2016; Bressan et al., 2019).

For our analysis, we considered a dataset of 1493 earthquakes that occurred between 2015 and March 2020 and whose magnitude M_D is between 0.4 and 4.0. The earthquakes were located

based on the 3D P-wave and S-wave velocity models. The mean values of the standard errors relative to the hypocentral coordinates are 0.07 km for the x- and y-coordinates and 0.23 km for the depth. Four events with a magnitude of more than 3.7 occurred in the time interval investigated: M_D=3.8 on January 19, 2018; M_D=3.9 on August 11, 2018; M_D=4.0 on June 14, 2019; and M_D=3.8 on September 22, 2019 (labelled E1, E2, E3, and E4 in Fig. 1).

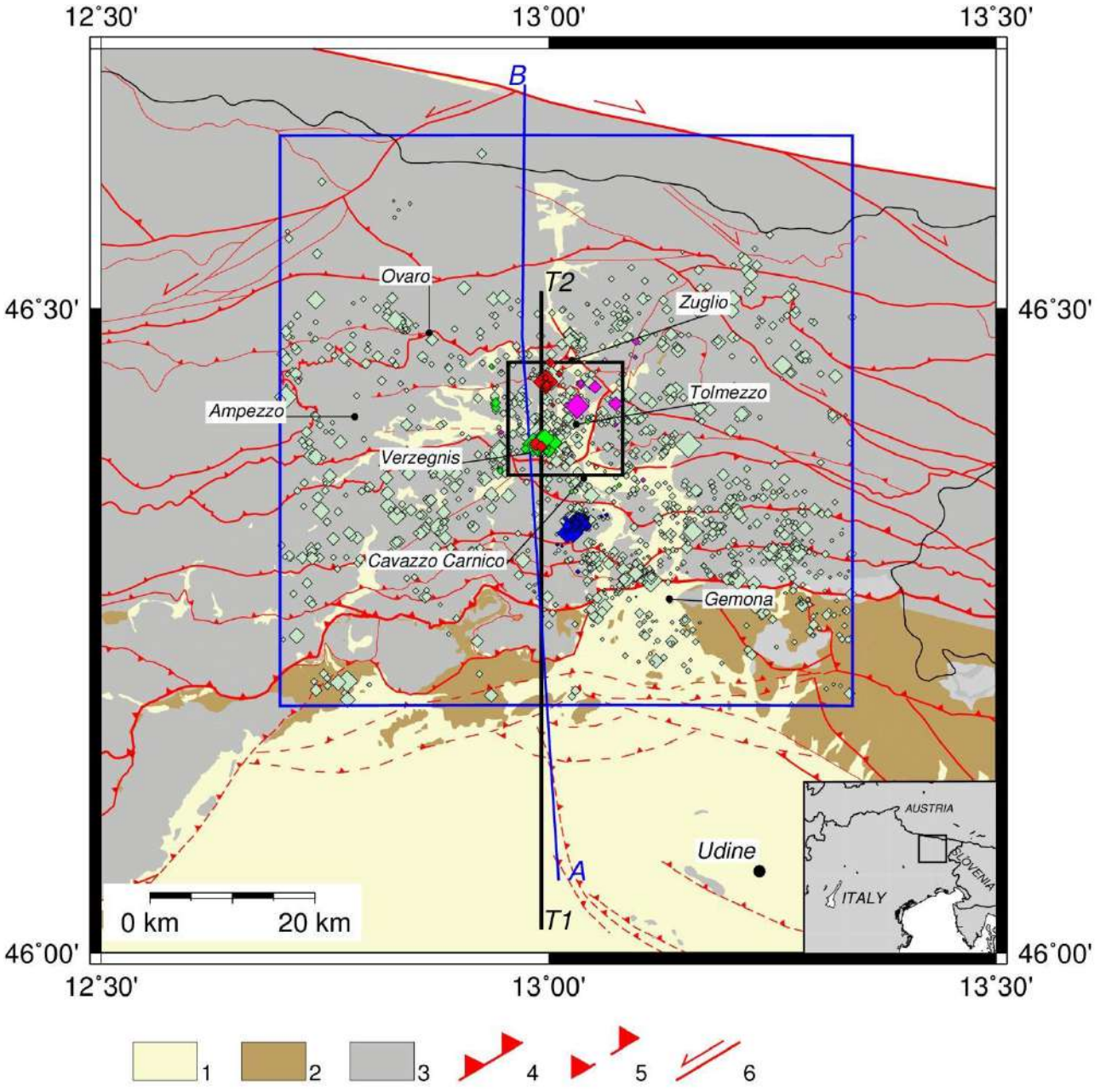

Fig. 1 –Simplified tectonic and geological sketch of the study area. The small black square indicates the central cell of the grid, where the most strongly radiated seismic energy is concentrated and the Shannon entropy was calculated. Light green diamonds: background seismicity from 2015 to March 2020. Magnitude values are given in coda duration magnitude MD. Fuchsia-coloured diamonds: earthquakes of the January 19 2018 MD 3.8 (E1) sequence. Blue diamonds: earthquakes of the sequence of August 11, 2018 MD 3.9 (E2). Green diamonds: earthquakes of the sequence of June 14, 2019 MD 4.0 (E3). Red diamonds: earthquakes of the sequence of September 22, 2019 MD 3.8 (E4). The blue line indicates the trace of the section along which the PCA analysis of Fig. 3 is performed.

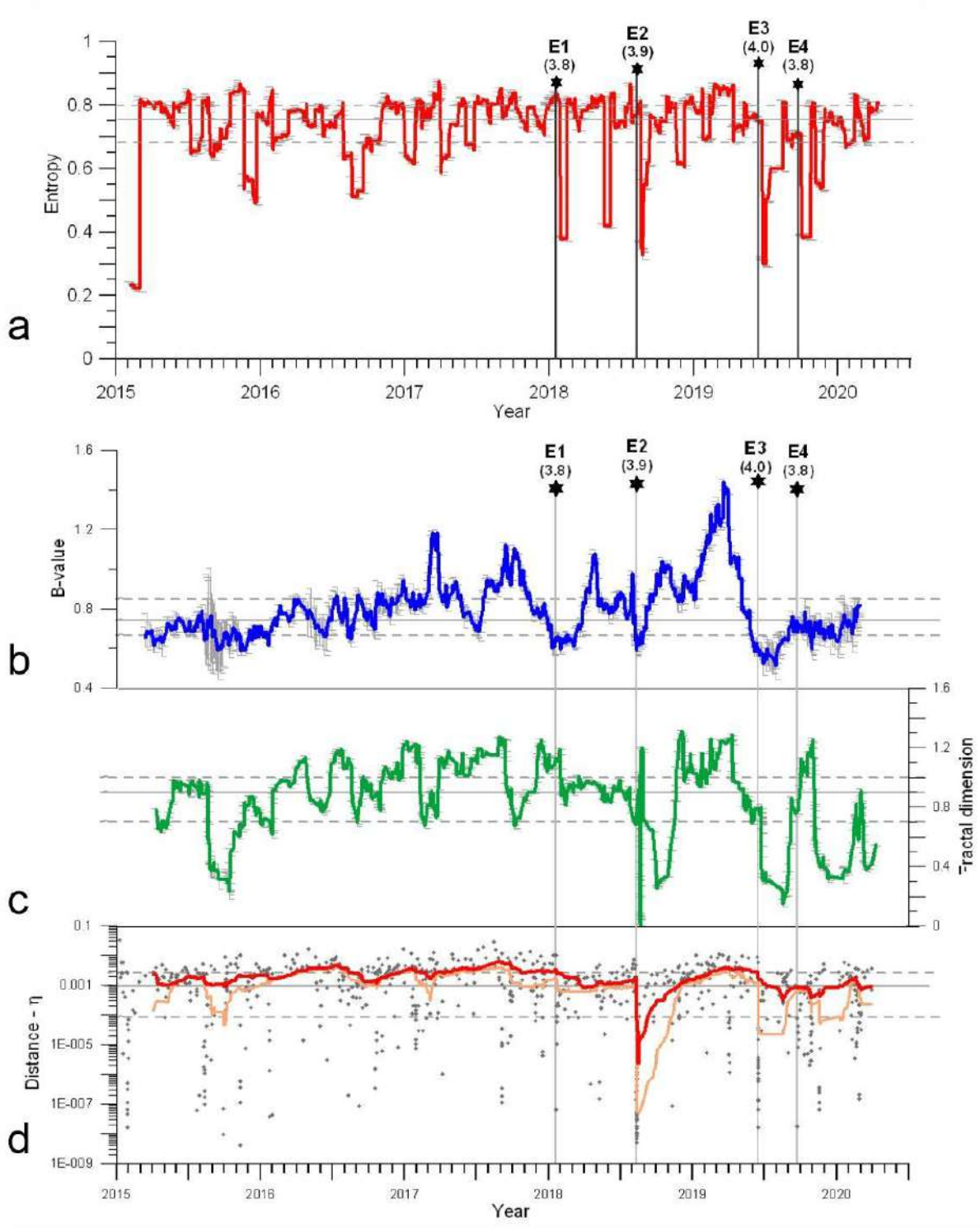

Fig. 2 – Temporal variations of a) Shannon entropy, b) b-value, c) fractal dimension, and d) Nearest-neighbour distances η_{ij}. The four main earthquakes, E1, E2, E3, and E4 are marked by stars with the corresponding magnitudes. For details about parameter computation, see Bressan et al. (2021).

Results

Two distinct periods of the temporal evolution of seismicity appear evident in the curves of Fig. 2: the period between preceding events E1 and E2 and the one following these events, since the beginning of 2017 characterized by marked fluctuations of all the parameters, and in particular b-values and fractal dimension (Fig. 2b, c). The temporal variation of the b-value can be related to crustal stress changes in a medium characterized by different mechanical properties. The fractal dimension time evolution indicates a prevailing clustering of the earthquakes with a tendency to propagate linearly. The temporal variations of the Shannon entropy (Fig. 2a) and η (Fig.2 d) quantify the evolving organization and correlation of seismicity within an area.

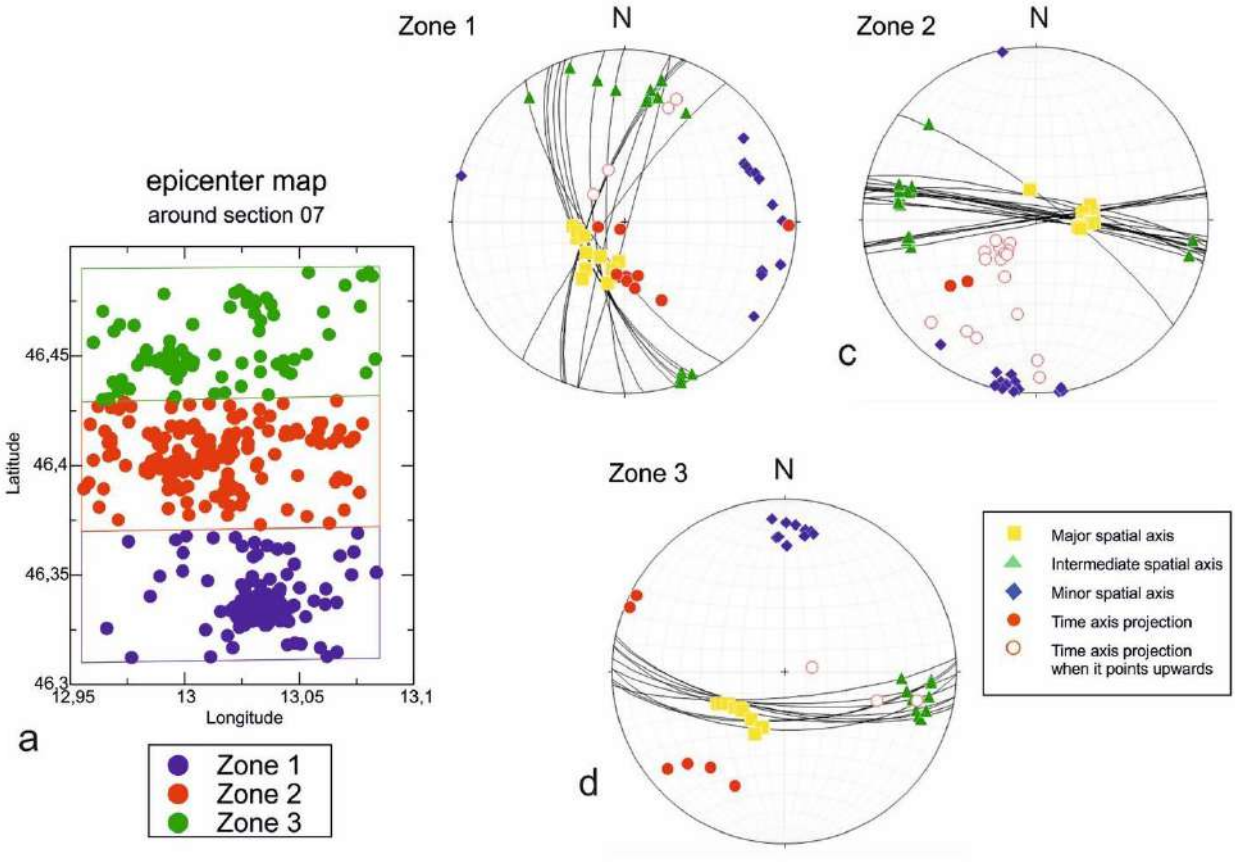

Fig. 3 - a) distribution of the epicentres of the events with M_C = 1 of the catalogue, in the region 10 km wide, centred on the section A-B of Fig. 1, in three spatial windows of about 10 km in longitude and 6.7 km in latitude. The circles are the epicentres of the earthquakes analyzed with PCA: blue circles: zone 1; red circles: zone 2; green circles: zone 3. b) PCA solutions obtained by sliding a 30 events window along the events in zone 1; c) PCA solutions obtained by sliding a 30 events window along the events in zone 2; d) PCA solutions obtained by sliding a 30 events window along the events in zone 3. Yellow square: Maximum spatial axis; green triangle: intermediate spatial axis; blue diamond: minimum space axis; red dot: time axis projection on the space volume: if hollow, the verse is upwards. Black lines: planes normal to the spatial minor axes (blue diamond). (from Bressan et al., 2021, modified).

The spatial distribution of seismicity is not uniform, but local clusters characterize it, as revealed by the fractal analysis and planes changing orientation with time, detected with the PCA method. The PCA solutions (Fig. 3) reveal mostly vertical and sub-vertical planes that fit the seismicity, changing orientation from south to north. The fracture propagates within the fracturing plane in the southern part (zone 1), with the activation of parallel planes in the central part (zone 2) and along weakness lines in the northern part (zone 3). Therefore, the stress concentrations and the localization of seismicity appear to be controlled by the geometric interaction between faults and by sharp variations of rock mechanical characters. Although performed in a narrow area and time span, the adopted procedures and the resulting observations can be applied to other areas of complex tectonics to investigate the time evolution of the seismicity and the damage.

Acknowledgements

The authors thank S. Urban and A. Magrin for help in graphics and critical reading of the manuscript. The local seismic network is managed by the Seismological Research Centre of the National Institute of Oceanography and Applied Geophysics – OGS with the financial contribution of the Regione Friuli Venezia Giulia (Bragato et al., 2021).

References

Baiesi, M., Paczuski, M.;2004: *Scale-free networks of earthquakes and aftershocks*, Phys. Rev. E., 69, 066106, doi:10.1103/PhysRevE.69.066106.

Bragato, P.L., Comelli, P., Saraò, A., Zuliani, D., Moratto, L., Poggi, V., Rossi, G., Scaini, C., Sugan, M., Barnaba, C., Bernardi, P., Bertoni, M., Bressan, G., Compagno, A., Del Negro, E., Di Bartolomeo, P., Fabris, P., Garbin, M., Grossi, M., Magrin, A., Magrin, E., Pesaresi, D., Petrovic, B., Plasencia Linares M.P., Romanelli, M., Snidarcig, A., Tunini, L., Urban, S., Venturini, E., Parolai, S.; 2021: *The OGS–Northeastern Italy Seismic and Deformation Network: Current Status and Outlook*, Seismological Research Letters 92 (3), 1704–1716, doi:10.1785/0220200372

Bressan, G., Barnaba, C., Gentili, S., Rossi, G.;2017: *Information entropy of earthquake populations in northeastern Italy and western Slovenia*, Physics of the Earth and Planetary Interiors, 271, 29–46, doi: 10.1016/j.pepi.2017.08.001.

Bressan G., Barnaba C., Peresan A., Rossi G.; 2021: *Anatomy of seismicity clustering from parametric space-time analysis*. Physics of the Earth and Planetary Interiors 320, 106787, doi:10.1016/j.pepi.2021.106787.

Bressan, G., Barnaba, C., Magrin, A., Rossi, G.; 2018a: *A study on off-fault aftershock pattern at N-Adria microplate*. J. Seismol., 22, 863-881, doi:10.1007/s10950-018-9737-x.

Bressan, G., Barnaba, C., Bragato, P., Ponton, M., and Restivo, A.; 2018b: *Revised seismotectonic model of NE Italy and W Slovenia based on focal mechanism inversion*, J. Seismol., 22, 1563–1578, doi:10.1007/s10950-018-9785-2.

Bressan, G., Barnaba, C., Bragato, P.L., Peresan, A., Rossi, G., Urban, S.; 2019: *Distretti sismici del Friuli Venezia Giulia*, Bollettino di Geofisica Teorica e Applicata, 60, s.3, s1-s74, doi: 10.4430/bgta0300.

Saraò, A., Sugan, M., Bressan, G., Renner, G., and Restivo, A.; 2021: *A focal mechanism catalogue of earthquakes that occurred in the southeastern Alps and surrounding areas from 1928–2019*, Earth Syst. Sci. Data, 13, 2245–2258, doi:10.5194/essd-13-2245-2021.

Ponton, M.; 2010: *Architettura delle Alpi Friulane*. Museo Friulano di Storia Naturale 52, Udine, 80 pp.

Rossi, G., Ebblin, C.;1990: *Space (3-D) and space-time (4-D) Analysis of aftershock sequences: the Friuli (Ne Italy) case*. Boll. Geof. Teor. Appl. 22, 37-49.

Rovida, A., Locati, M., Camassi, R., Lolli, B., Gasperini, P., (eds); 2016: *CPTI15, the 2015 version of the Parametric Catalogue of Italian Earthquakes*. Istituto Nazionale di Geofisica e Vulcanologia. doi:http//doi.org/10.6092/INGV.IT-CPTI15.

Telesca, L., Lapenna, V., Lovallo, M.;2004: *Information entropy analysis of seismicity of Umbria-Marche region (Central Italy)*. Nat. Haz. Earth Syst. Sci. 4, 691–695, doi: 10.5194/nhess-4-691-2004.

Varini, E., Peresan, A., Zhuang, J.; 2020: *Topological Comparison Between the Stochastic and the Nearest-Neighbor Earthquake Declustering Methods Through Network Analysis*. J. of Geophysical Research: Solid Earth, 125 (8), e2020JB019718, doi: 10.1029/2020JB019718

Zaliapin, I., Ben-Zion, Y.; 2013: *Earthquake clusters in southern California I: Identification and stability*, J. Geophys. Res. 118, 6, 2847–2864, doi:10.1002/jgrb.50179.

Corresponding author: grossi@ogs.it

Rheological behaviour along the Hellenic Wadati-Benioff zone

D. Russo[1,2] and R. Caputo[1,2]

[1] Department of Physics and Earth Sciences, University of Ferrara, Italy
[2] Centro Interuniversitario per La Sismotettonica Tridimensionale, CRUST-UR Ferrara, Italy

Following the method and the working flow proposed by Maggini et al. (2023) for reconstructing the 3D thermo-rheological modelling of the broader Aegean Region, the present note is focused on the rheological characteristics in correspondence of the Wadati-Benioff zone of the Hellenic subduction. The geometry of the interface has been reconstructed based on the results of Bocchini et al. (2018) and Halpaap et al. (2018). Figure 1a shows the isobaths, while Figure 1b the slope distribution.

The rheological model of Maggini et al. (2023) is based on a simplified approach, assuming frictional sliding and power-law creep as dominating deformational mechanisms for describing the brittle and the ductile behaviour, respectively. Calculations have been performed by means of several purposedly written MATLAB scripts (Maggini, 2020; Maggini and Caputo, 2020a, 2020b, 2021) allowing to calculate and reproduce the thermo-rheological features. In order to obtain a 3D cover for the whole investigated area, a number of 1D vertical logs were reconstructed in correspondence of the nodes of a horizontal regular grid (115 x 115 pixels) and were than interpolated to reconstruct a pseudo 3D model. Using common GIS tools, all the input parameters considered in the modelling (see Maggini et al., 2023 for details) were properly averaged at the selected pixel size of 10 x 10 km.

Based on the general results and for the purpose of the present note, we investigated a 500 m-thick volume on either side of the modelled slab interface (Figure 1a) conceptually corresponding to the core of the Wadati-Benioff zone separating the two plates. In particular, we implemented a dedicated MATLAB script to analyse the rheological behaviour of the lowermost portion of the upper plate and the uppermost one of the lower plate. Although, four different combinations between brittle versus ductile and upper versus lower plate could in principle occur, the results show that three conditions dominate the whole subduction zone, each uniformly and regularly covering wide sectors of the interface zone.

Figure 1c clearly shows that the most external and shallower zone (blue in Figure 1c), grossly at the base of the active accretionary wedge, is characterised by a brittle behaviour in both sides of the interface. In a progressively deeper sector, the model results indicate the contact between brittle rocks in the upper plate with ductile ones in the lower plate (purple zone in Figure 1c). Further deeper along the Wadati-Benioff zone, the modelled behaviour is ductile on either side (pink area in Figure 1c). Taking into account the resolution of the rheological model (10 x 10 km), only in a

very limited sector (in correspondence of Akarnania and Peloponnesus) the results indicate the contact between ductile rocks overlying brittle ones (yellow in Figure 1c).

Comparing the rheological results with the geometry characteristics of the interface, it is possible observe some peculiarity. For example, the transition from the brittle/brittle to the brittle/ductile behaviour occurs at the depth range between 20 and 25 km (Figure 1a), in a narrow sector where the slope progressively varies from less than 15°, characterizing the upper- and frontal-most portion of the slab, to more than 18°, therefore in correspondence of a dip-angle change along the interface. On the other hand, the deepest sector characterized by brittle rocks overlying the interface occur at 90-100 km in correspondence of a slope increase from less than 35° to more than 40°.

As a very preliminary conclusion of the rheological model, brittle and hence potentially seismogenic activity in correspondence of the Wadati-Benioff zone could occur only down to a depth of ca. 100 km as far as at greater depths the 1 km-thick modelled rock volume embedding the interpolates shear zone is entirely characterized by a ductile behaviour. Accordingly, though rarely recorded deeper seismicity should likely occur due to internal deformation of the subducting slab and not on the interface. This is in accordance with Halpaap et al. (2018); these authors, where the Wadati-Benioff zone was well-imaged, identified earthquake clusters standing out the intraslab seismicity between 40 km and 60 km depth. Also, in Bocchini et al. (2018) the interplate seismicity is imaged at depth shallower than 100 km, while in Meier et al. (2008) the relocated interplate seismicity, plotted on reconstructed profile across the Aegean, generally don't exceed 60 km depth, only few events are located between 80 km and 100 km.

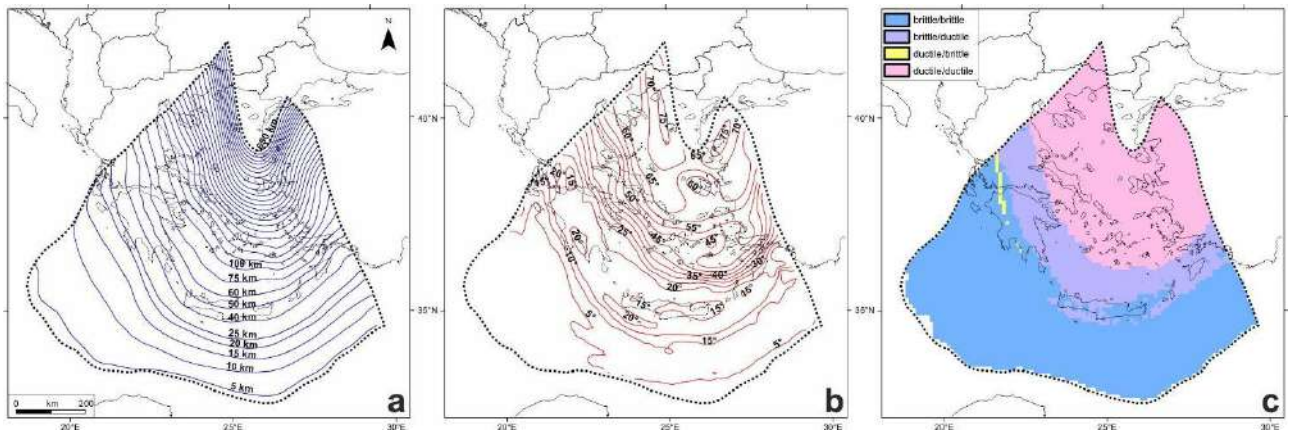

Figure 5: a) modelled Hellenic Subduction Zone (modified from Maggini et al., 2023 and references therein) with isobaths; b) slope distribution of the modelled Hellenic Slab; c) rheological behaviour in correspondence of the HSZ.

References

Bocchini G.M., Brustle A., Becker D., Meier T., van Keken P.E., Ruscic M., Papadopoulos G.A., Rische M. and Friederich W.; 2018: Tearing, segmentation, and backstepping of subduction in the Aegean: New insights from seismicity. *Tectonophysics*, 734-735, 96-118, doi: 10.1016/j.tecto.2018.04.002.

Halpaap F., Rondenay S. and Ottemoller L.; 2018: Seismicity, Deformation, and Metamorphism in the Western Hellenic Subduction Zone: New Constraints from Tomography. *J. Geophys. Res.: Solid Earth*, 123, 3000-3026, doi: 10.1002/2017JB015154.

Maggini M. and Caputo R.; 2020a: Sensitivity analysis for crustal rheological profiles: examples from the Aegean Region. *Ann. Geophys*., 63(3), SE334, doi: 10.4401/ag-8244.

Maggini M. and Caputo R.; 2020b: Rheological behaviour in collisional and subducting settings: inferences for the seismotectonics of the Hellenic Region. *Turk. J. Earth Sci.*, 29, 381–405, doi: 10.3906/yer-1909-4.

Maggini M. and Caputo R.; 2021: Seismological data *versus* rheological modelling: comparisons across the Aegean Region for improving the seismic hazard assessment. *J. Struct. Geol.*, 145, 104312, doi: 10.1016/j.jsg.2021.104312.

Maggini M., Russo D. and Caputo R.; 2023: A 3D rheological model for the Aegean Region: Mechanical layering and seismotectonic implications. *J. Struct. Geol.*, 175, 104956, 1-19, doi: 10.1016/j.jsg.2023.104956.

Meier T., Rische M., Endrun B., Vafidis A. and Harjes H.-P.; 2004: Seismicity of the Hellenic subduction zone in the area of western and central Crete observed by temporary local seismic networks. *Tectonophysics*, 383, 149 – 169, doi: 10.1016/j.tecto.2004.02.004.

Corresponding author: davide.russo@unife.it

Tracking the evolution of seismic sequences in the normal fault environment of Southern Apennines using deep catalogues

F. Scotto di Uccio[1], M. Michele[2], C. Strumia[1], G. Festa[1], M. Supino[2], L. Chiaraluce[2], N. D'Agostino[2], G. C. Beroza[3]

[1]Department of Physics 'Ettore Pancini', University of Napoli Federico II, Italy.
[2]Istituto Nazionale di Geofisica e Vulcanologia, Italy.
[3]Department of Geophysics, Stanford University, USA.

Seismic sequences, featuring events clustered in space and time and generating seismicity with a higher rate than the background, are a powerful tool for investigating the geometry and the mechanical state of faults that may host large magnitude earthquakes in the future. The knowledge about the involved structures and processes achievable from the analysis of the sequences strongly depends on the content and the magnitude of completeness of available catalogues. Enhanced catalogues obtained using advanced techniques, such as machine learning models or similarity-based detectors have contributed to decrease the magnitude of completeness of one point or more, increasing the number of events buried in the noise of more than one order of magnitude, with respect to manual earthquake identification. Furthermore, accurate location and source parameter estimation can provide direct access to mechanical properties of the structures hosting sequences. Earthquake location for deep catalogues can provide a high-resolution imaging of fault structures and their mutual interaction (e.g., Ross et al. 2019, Sugan et al. 2023) and define paths for fluid migration (Vuan et al. 2020), while evolutive models can be constructed accessing to the source parameters (Yoon et al., 2017).

In this study, we generated high resolution catalogues for seismic sequences in the complex normal fault system of Southern Apennines (Italy) by comparing and integrating advanced state of the art detectors (deep learning models and similarity-based detectors, Yoon et al. 2015, Chamberlain et al. 2018, Mousavi et al. 2020). We found that the integration of the machine learning and template matching detectors, the former providing templates for the cross-correlation, largely outperforms techniques based on autocorrelation and machine learning alone, featuring an enrichment of the existing automatic and manual catalogues of factors 21 and 7, respectively (Scotto di Uccio et al., 2023). Using deep catalogues of microseismic sequences, we performed accurate double-difference location, source parameter estimation and stress release modelling, that allows for addressing the spatiotemporal evolution and generation of the sequences. Relocated seismicity clearly identifies local patches on kilometric-scale structures, featuring an orientation coherent with the main faults of the area. When mapping the seismic sequences at depth, their location is generally not compatible with the faults that hosted the 1980, M 6.9 Irpinia event, looking at the fault traces on the Earth surface (Westaway & Jackson 1987), the event dip and the estimated geometry from inversion of seismic and levelling data (Bernard and Zollo, 1989). This indicates that seismic sequences ruptured small patches of secondary segments. When mapping the stress change on the fault plane, the inter-event distance compared to the size of the events suggests that the dominant triggering mechanism within the sequences is the (static) stress transfer, that allows the nucleation of individual events. The distribution of the events is not isotropic around the main events of the sequences, but small events tend to align dominantly along the dip direction, which also corresponds to the slip direction for normal faults. They can be interpreted as the boundary between locked and creeping domains (Rubin et al. 1999, Rubinstein and Beroza, 2007). The occurrence of an aseismic event appears to be more likely in the case of the 3-7 July 2020 Rocca San Felice sequence featuring the activation of two parallel clusters oriented along the dip direction but distant 5 km from each other. Although evident aseismic transients were not detected during the sequence, we evaluated the maximum average slip allowed on a deep dislocation whose displacement on the surface does not emerge within uncertainties from the noise level. We inferred that an aseismic event of Mw ~5.0 could have occurred during the sequence, transferring stress across the two asperities without producing a signal emerging at the GPS stations at the surface

References

Bernard, P., & Zollo, A. (1989). The Irpinia (Italy) 1980 earthquake: detailed analysis of a complex normal faulting. Journal of Geophysical Research: Solid Earth, 94(B2), 1631-1647.

Chamberlain, C. J., Hopp, C. J., Boese, C. M., Warren-Smith, E., Chambers, D., Chu, S. X., Kostantinos, M. & Townend, J. (2018). EQcorrscan: Repeating and near-repeating earthquake detection and analysis in Python. Seismological Research Letters, 89(1), 173-181.

Gualandi, A., Nichele, C., Serpelloni, E., Chiaraluce, L., Anderlini, L., Latorre, D., Belardinelli, M.E. & Avouac, J. P. (2017). Aseismic deformation associated with an earthquake swarm in the northern Apennines (Italy). Geophysical Research Letters, 44(15), 7706-7714.

Kaviris, G., Elias, P., Kapetanidis, V., Serpetsidaki, A., Karakonstantis, A., Plicka, V., ... & Bernard, P. (2021). The western Gulf of Corinth (Greece) 2020–2021 seismic crisis and cascading events: First results from the Corinth Rift Laboratory Network. The Seismic Record, 1(2), 85-95.

Mousavi, S. M., Ellsworth, W. L., Zhu, W., Chuang, L. Y., & Beroza, G. C. (2020). Earthquake transformer—an attentive deep-learning model for simultaneous earthquake detection and phase picking. Nature communications, 11(1), 3952.

Ross, Z. E., Trugman, D. T., Hauksson, E., & Shearer, P. M. (2019). Searching for hidden earthquakes in Southern California. Science, 364(6442), 767-771.

Rubin, A. M., Gillard, D., & Got, J. L. (1999). Streaks of microearthquakes along creeping faults. Nature, 400(6745), 635-641.

Rubinstein, J. L., & Beroza, G. C. (2007). Full waveform earthquake location: Application to seismic streaks on the Calaveras fault, California. Journal of Geophysical Research: Solid Earth, 112(B5).

Scotto di Uccio, F., Scala, A., Festa, G., Picozzi, M., & Beroza, G. C. (2023). Comparing and integrating artificial intelligence and similarity search detection techniques: application to seismic sequences in Southern Italy. Geophysical Journal International, 233(2), 861-874.

Sugan, M., Campanella, S., Chiaraluce, L., Michele, M., & Vuan, A. (2023). The unlocking process leading to the 2016 Central Italy seismic sequence. Geophysical Research Letters, 50(5), e2022GL101838.

Vuan, A., Brondi, P., Sugan, M., Chiaraluce, L., Di Stefano, R., & Michele, M. (2020). Intermittent slip along the Alto Tiberina low-angle normal fault in central Italy. Geophysical Research Letters, 47(17), e2020GL089039.

Westaway, R., & Jackson, J. (1987). The earthquake of 1980 November 23 in Campania—Basilicata (southern Italy). Geophysical Journal International, 90(2), 375-443.

Yoon, C. E., O'Reilly, O., Bergen, K. J., & Beroza, G. C. (2015). Earthquake detection through computationally efficient similarity search. Science advances, 1(11), e1501057.

Yoon, C. E., Huang, Y., Ellsworth, W. L., & Beroza, G. C. (2017). Seismicity during the initial stages of the Guy-Greenbrier, Arkansas, earthquake sequence. Journal of Geophysical Research: Solid Earth, 122(11), 9253-9274.

Corresponding author: francesco.scottodiuccio@unina.it

A preliminary computation of the seismic coupling for Italy

F. Sparacino[1], B. G. Galuzzi[2], M. Palano[1]

1 - Istituto Nazionale di Geofisica e Vulcanologia, Osservatorio Etneo - Sezione di Catania, Catania, Italy.
2 - Istituto di Bioimmagini e fisiologia molecolare, CNR, Milano, Italy.

In the last two decades, the worldwide growth of continuous and episodic GNSS stations as well as the seismic networks allowed the acquisition of extensive geodetic and seismological datasets. This aspect has recently allowed the possibility of comparing geodetic and seismic strain-rates at the scale of regional fault systems. Studies focusing on this topic have provided new insights on the partitioning between fault slip and bulk lithosphere permanent strain (Ferranti et al., 2014; Carafa et al., 2017, 2020). The basic idea is that, for a given region, the moment released by earthquakes mirrors the rate of tectonic deformation (Kostrov, 1974). Achieved results have allowed to identify regions where the crustal deformation budget is entirely released by seismicity (e.g. Mazzotti et al., 2011; Pancha et al., 2006; D'Agostino, 2014; Sparacino et al., 2020), as well as regions where the excess deformation can be released either as aseismic slip across faults or through large future earthquakes (Masson et al., 2005; Palano et al., 2018, 2020, Déprez, et al., 2013; Sparacino et al., 2022).

Here we provided a preliminary computation for Italy by adopting the seismogenic zonation of Meletti et al. (2004). To this aim, we compiled catalogs for both historical (since 1005) and instrumental crustal seismicity occurring in the investigated area (since 1985; http://iside.rm.ingv.it/). These catalogs have been used to estimate the seismic moment-rates along with the expected maximum magnitude, the seismogenic thickness, and the Gutenberg-Richter parameters. In addition, based on an updated GNSS velocity field we derived the geodetic moment-rates.

References

Carafa M.M., Valensise G. and Bird P.; 2017: Assessing the seismic coupling of shallow continental faults and its impact on seismic hazard estimates: a case-study from Italy. Geophys. J. Int., 209(1), 32-47, DOI 10.1093/gji/ggx002.

Carafa M.M., Galvani A., Di Naccio D., Kastelic V., Di Lorenzo C., Miccolis S., Sepe V., Pietrantonio G., Gizzi C., Massucci A., Valensise G. and Bird P.; 2020: Partitioning the ongoing extension of the central Apennines (Italy): Fault slip rates and bulk deformation rates from geodetic and stress data. J. Geophys. Res.: Solid Earth, 125(7), e2019JB018956, DOI 10.1029/2019JB018956.

D'Agostino N.; 2014: Complete seismic release of tectonic strain and earthquake recurrence in the Apennines (Italy). Geophys. Res. Lett., 41(4), 1155-1162, DOI 10.1002/2014GL059230.

Déprez A., Doubre C., Masson F. and Ulrich P.; 2013: Seismic and aseismic deformation along the East African Rift System from a reanalysis of the GPS velocity field of Africa. Geophys. J. Int., 193, 1353-1369, DOI 10.1093/gji/ggt085.

Ferranti L., Palano M., Cannavò F., Mazzella M.E., Oldow J.S., Gueguen E., Mattia M. and Monaco C.; 2014: Rates of geodetic deformation across active faults in southern Italy. Tectonophysics, 621, 101-122, DOI 10.1016/j.tecto.2014.02.007.

ISIDe Working Group 2007: Italian Seismological Instrumental and Parametric Database (ISIDe). Istituto Nazionale di Geofisica e Vulcanologia (INGV). Available online: DOI 10.13127/ISIDE (accessed on 18 December 2023).

Kostrov V.; 1974: Seismic moment and energy of earthquakes, and seismic Row of rock. Izv. Acad. Sci. USSR Phys. Solid Earth, 1, 23-44.

Masson F., Chéry J., Hatzfeld D., Martinod J., Vernant P., Tavakoli F. and Ghafory-Ashtiani M.; 2005: Seismic versus aseismic deformation in Iran inferred from earthquakes and geodetic data. Geophys. J. Int., 160, 217-226, DOI 10.1111/j.1365-246X.2004.02465.x.

Mazzotti S., Leonard L.J., Cassidy J.F., Rogers G.C. and Halchuk S.; 2011: Seismic hazard in western Canada from GPS strain rates versus earthquake catalog. J. Geophys. Res., 116, B12310, DOI 10.1029/2011JB008213.

Meletti C., Galadini F., Valensise G., Stucchi M., Basili R., Barba S., Vannucci G. and Boschi E.; 2004: Zonazione sismogenetica ZS9 [Data set]. Istituto Nazionale di Geofisica e Vulcanologia (INGV), DOI 10.13127/sh/zs9.

Pancha A., Anderson J. G. and Kreemer C.; 2006: Comparison of seismic and geodetic scalar moment rates across the Basin and Range Province. Bull. Seismol. Soc. Am., 96, 11-32, DOI 10.1785/0120040166.

Palano M., Imprescia P., Agnon A. and Gresta S.; 2018: An improved evaluation of the seismic/geodetic deformation-rate ratio for the Zagros Fold-and-Thrust collisional belt. Geophys. J. Int., 213, 194-209, DOI 10.1093/gji/ggx524.

Palano M., Ursino A., Spampinato S., Sparacino F., Polonia A. and Gasperini L.; 2020: Crustal deformation, active tectonics and seismic potential in the Sicily Channel (Central Mediterranean), along the Nubia-Eurasia plate boundary. Scientific Reports, 10, 21238, DOI 10.1038/s41598-020-78063-1.

Sparacino F., Palano M., Peláez J.A. and Fernández J.; 2020: Geodetic deformation versus seismic crustal moment-rates: insights from the Ibero-Maghrebian region. Remote Sensing, 12(6), 952, DOI 10.3390/rs12060952.

Sparacino F., Galuzzi B.G., Palano M., Segou M. and Chiarabba C.; 2022: Seismic coupling for the Aegean-Anatolian region. Earth-Science Reviews, 228, 103993, DOI 10.1016/j.earscirev.2022.103993.

Corresponding author: federica.sparacino@ingv.it

Analysis of the 1982-2016 seismicity of Aswan region (south Egypt)

T.A. Stabile[1], E.R. Fat-Helbary[2], V. Serlenga[1], S. Panebianco[1,3], P. Tizzani[4], R. Castaldo[4], L. Telesca[1], E.M. El-Amin[2], H. Ahmed[2]

[1] *Consiglio Nazionale delle Ricerche (CNR-IMAA), Italy*
[2] *National Research Institute of Astronomy and Geophysics, Egypt*
[3] *Dipartimento di Fisica e Scienze della Terra, Università di Ferrara, Italy*
[4] *Consiglio Nazionale delle Ricerche (CNR-IREA), Italy*

Lake Nasser is the Egypt's largest artificial water reservoir filled behind the Aswan High Dam. In this area a prolonged reservoir induced seismicity has been observed since the November 1981 Ms 5.3 earthquake. The dynamic interplay between loading and unloading operations at Lake Nasser, coupled with the increase of pore fluid pressure within the crustal rocks may lead the faults to go beyond the critical stress for failure (Gahalaut and Hassoup, 2012; Telesca et al., 2017). In response to the seismic concerns and the need for secure reservoir management, a permanent seismic network was established in 1982. This initiative has contributed significantly to the accumulation of an extensive seismological dataset.

From an initial catalogue encompassing 7833 natural and reservoir-induced seismic events recorded in the Aswan region from 1982 to 2016, our objective is to gain insights into the structure and triggering mechanisms of seismogenic faults within this complex tectonic system. To achieve this goal, we obtained a new 1-D velocity model of the area. Then, absolute and relative high-resolution earthquake locations for 2562 events have been determined. This process has enabled us to refine the fault structure in the Aswan region and better comprehend the spatio-temporal evolution of seismicity.

Our analysis revealed previously unmapped fault strands along the Kalabsha fault system and in the Wadi Kalabsha embayment area, enhancing the understanding of fault distribution beyond the original seismic catalogue. The spatio-temporal evolution indicated an eastward migration of seismicity with progressively shallower hypocentres, potentially linked to fluid migration processes and increased pore pressure in the Wadi Kalabsha embayment area. The combination of fluid pore-pressure diffusion and Coulomb stress variation from reservoir loading may also explain the variable faulting styles observed along an NW-SE striking alignment east of the Seyal Fault. We verified such hypothesis through a 3-D poroelastic simulation within a Finite Element (FE) framework. Specifically, we addressed both the time-dependent poroelastic equation and the linear elastic equation, employing a multiphysics approach through the use of the Comsol software package version 6.2.

Furthermore, the projection of earthquakes onto an E-W cross-section identified a seismic gap on the Kalabsha Fault, suggesting a locked fault patch approximately 11 km in length. According to Wells and Coppersmith (1994), such a segment could potentially trigger an earthquake with a magnitude up to Mw=5.9 in the event of a single rupture. Additionally, an earthquake clustering analysis revealed two clusters with prolonged swarm activity, driven by pore pressure diffusion, and four clusters characterized by seismic sequences and repeated earthquakes.

References

Gahalaut K. and Hassoup, A.; 2012: Role of fluids in the earthquake occurrence around Aswan reservoir, Egypt. J. Geophys. Res. 117, B02303.

Telesca L. et al.; 2017: Dynamical characterization of the 1982—2015 seismicity of Aswan region (Egypt). Tectonophysics 712-713, 132—144.

Wells D.L. and Coppersmith K.J.; 1994: New empirical relationships among magnitude, rupture length, rupture width, rupture area, and surface displacement. Bull. Seismol. Soc. Am. 84 (4), 974-1002.

Corresponding author: tonyalfredo.stabile@cnr.it

Synthesis of written, architecture, and geology information sources improving the understanding of seismic sequences in the Ferrara area

M. Stefani[1]

[1] *Università di Ferrara (Italy)*

This contribution is aimed at delving deeper into the impact of historic seismic events on the town of Ferrara and surrounding areas. The paper is based on the integration of the published palaeosismological research with the reconstruction of the architectural history of ancient buildings, and with the results of recent geological and microzonation investigations. The short article is not intended to provide a comprehensive seismological history, but to the interpretations of some significant seismic sequences, often characterized by the migration of the epicentre areas. Given the nature and size of the contribution, provide an exhaustive list of references and historic sources is impossible. The reader is therefore referred to the important contributions of Guidoboni 1984, Locati et al. 2016, Guidoboni et al. 2018 and 2019; Guidoboni and Valensise 2023, and to further references and quotations therein.

12th and 13th centuries earthquakes and the structural reconfiguration of the Cathedral.

The earliest known seismic effects are the local repercussion of the widespread earthquakes of 1117, and an event in 1128. A sequence of shocks occurred during the 1222 Christmas Day, between noon and sunset, within a seismic activity framework affecting large portions of the Po Plain, known as “the Brescia earthquake”. In Ferrara, the shocks induced at least the collapse of chimneys, while more severe damage cannot be ruled out. Another earthquake hit Ferrara on March the 20th 1234, associated with damage to buildings, in town and in the surrounding countryside, evaluated to the VII MCS, but the scantiness of the available documentation again prevents a precise estimation of the damage level. The earthquakes of the first half to the 13th century, together with the poor geotechnical properties of the foundation soils played a major, but previously undetected, role in the architecture evolution of the Cathedral. The building of the Romanesque five-nave church started in 1135 and continued through much of the century. The building was founded on Holocene, mainly cohesive sediments, deposited into interfluvial plain settings, the geotechnical properties of which were investigated through seismic cone penetration and dilatometer tests. The spatially varying load of the building induced differential foundation settlement, which, together with the seismic accelerations, damaged the thin wall structure of the

naves, triforium and clerestory. The analysis of the surviving Medieval structures and of the ancient written and drawn documentation supports a reconstruction of the building evolution. In the second quarter of the 13th century, probably between 1240 and 1250, the Cathedral underwent major structural changes, recording some of the earliest influences of the French Gothic in Italy. The damaged structures of the naves were repaired and reinforced through the building of flying buttresses (Fig. 1A) that conveyed downward the lateral forces pushing aside the nave walls, while the early overhanging façade was supported by two attached buttresses, on both sides of the porch, boasting the Last Judgment sculpture cycle, which is coaeval to the structural modification phase. The 13th century structural reinforcement was to play a major beneficial role during the numerous following seismic events.

Fig. 1 – **A** reconstructive cross section of the Ferrara Cathedral after the 13th century post-seismic restoration (drawing by A. Toma and V. Vona), **B** southern side of the Cathedral, with the main structural lesions induced by foundation settlement and seismic acceleration depicted in blue, **C** the south-eastern corner, with post-seismic collapse transept reconstruction in a backword position and "wall sewing up restoration" by reddish bricks, **D** the Renaissance transect rebuilt at the end of the 15th century and partially collapsed during the earthquake of 17 Novembre 1570.

Late medieval earthquakes.

Other earthquakes hit the town in 1285, 1339, and 1346. Near the half of the 14th century, likely during the 1346 earthquake, the belltower and roof of the San Nicolò Church and many noble family towers collapsed. At the time, churches were damaged, repaired or rebuilt, as S. Francesco and S. Domenico, but the following transformation makes the damage recognition presently impossible. In the early 15th century, an earthquake sequence affected the town over a 17-month interval, associated with repeated damages in the VII grade MCS range. The sequence started at 9

a.m. August 14th, 1409, with an earthquake epicentre near the town, followed by a stronger shock in the night between the 16th and 17th. Another earthquake is documented the 9th of May 1410, and the strongest of the sequence on the 9th of January 1411. Unspecified damage is reported to buildings; however, the following transformation prevents the present-day recognition of damage. Other earthquakes are known in 1445 and in 1483.

Fig. 2 – The hasty reconstruction of the ducal apartment over the Estense Castle southern barbican, using recycled bricks and limestone fragments, following the large collapse of November 17, 1570.

Early Modern Time earthquakes.

1495, on Sunday the 13th of December (Day of S. Lucia) an earthquake took place, certainly important, even if yet not mentioned in the seismic catalogues. At least a corner (*cantone*) of the cathedral collapsed, certainly in the eastern side, likely the Northeastern one. The upper part of the transept and the large new choir were then rebuilt in Renaissance forms by Biagio Rossetti (Fig. 1D). Post seismic restoration involved the twelfth steps leading from the naves to the raised presbytery area. The steps were previously incorrectly referred to the cathedral entrance. Severe damage and partial collapse also affected some portions of the Estense Castle and the towers of the Ducal Palace (Torre Rigobello) and of the Palazzo della Ragione (Torre Ribelli). The city then experienced the local effects of earthquakes generated in other areas (1505, 1511). In 1532, a seismic sequence, lasting at least 50 days, forced Alfonso I's court to take refuge into the Delizia del Barchetto, at the northeastern corner of the town walls; further seismic damage occurred in 1536. The 1561 earthquakes marked the onset of a long seismic phase that was to last until 1574. A seismic sequence (23.10-16.11.) was followed by a severely damaging earthquake (24.11) and by other shocks (13-14.12). Damage is reported to the Castello Estense, the North-East vaulted chapel

of the Cathedral (*Cappella del Santissimo Sacramento*), the synagogue (*Via dei Sabbioni* = Via Mazzini), and to the Belriguardo Palace, 14 km South-Est of the city. Less violent earthquakes followed in 1562, 1564. In 1569, seismic activity strongly affecting the western area of Pilastri and Bondeno, less so Ferrara.

The 1570-1574 Seismic Sequence and the repeated building damage and destruction.

After a sequence of gentle shocks (1-15.11.70), the city was struck by violent earthquakes on 16th, November and by even stronger shocks on the 17th. Several shocks were then perceived every and each day between the 17th of November and the 27th of February 1571, with possibly a single exception on 28th January. During several days of November, up to ten shock per day were perceived. Due to space limitations, an exhaustive list of damages is not here possible; therefore, attention is focused on some examples; further information is available in the aforementioned references. In the Cathedral, the façade increased its overhang and detached itself form the naves walls, as still partially visible, the south-eastern corner was also severely damaged (Fig. 1B, C). Portions of the transept collapses and its northern tympanum collapsed onto the opposite house, killing several people (17.11.70). In the churches of S. Francesco and S.M. in Vado, the upper portions of the façades and the nave vaults and domes collapsed (Fig. 3). The church of S. Giovanni Battista experienced an almost complete destruction, collapsing through several months of shocks, keeping some surviving walls only in the southern flank. In the Estense Castle, the ducal apartments built over the southern barbican *(rivellino*), internal cross vaults, the upper part of the four towers, and long portions of corbels collapsed (Fig. 2); the western wing was particularly damaged, losing vaults on all floors. Written sources do not clearly report major damage to the Diamanti Palace, which however at the time seems to have lost the porticoes previously built on all four sides of the courtyards. The palace certainly underwent a total reconstruction of the roof and major architecture modification and rebuilt, keeping the original configuration only in part of the lower order of the northern façade. In November 1570. coseismic liquefaction is documented in the granular sediments of the Medieval Po channel, founding the southernmost portion of the city. Liquefaction triggered lateral expansion toward the port basin and Po di Ferrara channel, induced the collapse of Castel Nuovo, and increased the damage to the 13th century fortification walls at the southern side of the city.

Fig. 3 – The upper portion of San Francesco, above the frame of the order, and the internal domes and circular windows rebuilt after the 1570 earthquakes. Italian quotation from Pirro Ligorio's writings, describing the collapse.

Distribution of the seismic sequence damage in time and space.

The reported damage induced by the 1570-1574 seismic sequence normally derived from the summation of the induvial shock effects, but specific damage events can be nevertheless detected. In Ferrara, damage and collapses occurred in the following dates: for the year 1570, 23.11 S. Domenico western façade, Castel Nuovo, portions of the city walls near Porta d'Amore; 3.12 almost complete collapse of S. Giovanni Battista; 13.12 city walls, 14-15.12 S. Andrea, S. Agostino, Palazzo Tassoni; 31.12 Lazzaretto in the Boschetto Island West of town, several churches and palaces; for the year 1571, 8.01. S. Andrea, 11.01 and 7.08 Cathedral, particularly in the transept; 12.01 Palazzo Montecuccoli, 25.08 portions of the new S.M. Angeli building under construction. Further damage took place during two 1574 earthquakes.

The clustering in space and time of the seismic damage and shock perception appears to suggest a migration of epicentres through different seismogenetic structures. Two earthquake cluster areas can be detected on the opposite sides of the city. When damage events in the two countryside clusters can be precisely dated, they are not synchronous with those affecting the city or the opposite cluster area. Areas of severe damage are separated by less affected zones.

(a) Western areas: 24.11.70 at about 8 p.m., deaths and damage in Bondeno and Ficarolo; 1.12.70, 5.03.71, 30.04, strong shocks in Bondeno, Palantone, Stellata and, North to the Po river, Ficarolo and Vico; 4.06, violent shocks inducing building damage in Parma, perceived as strong in Finale Emilia, S. Felice sul Panaro, and Stellata, as light in Ferrara. The destruction of the Castelmassa

church, and the damage to the Melara one, in the western portion of the modern Rovigo Province, respectively 34 and 42 km from the Ferrara epicentre, are noteworthy, considering that many building closer to town experienced only minor damage, as in Ravalle (VI MCS).

(b) South-Eastern Areas: 21-24.11.70 anomalous waves in the Po di Primaro channel; 5.12., 9.12, severe damage in the Belriguardo Palace, particularly in the entrance clock tower and in structures already damaged by the 1561 earthquake; 8.12 shock particularly strong in Montesanto; 14-15.12 the shocks damaging Ferrara were well perceived in S. Pietro in Casale, Bologna and Castelbolognese; 26.12. shocks in Belriguardo and Massa Lombarda, perceived as very light in Ferrara; 2.01.71 damage in Berliguardo and Runco, collapse of canal banks, and possible coseismic liquefaction; 3.01 strong shock perceived in Lugo, Imola, and Faenza; 23.12.71 new structural damage in Berliguardo. In the later area, during the seismic sequence, granular sediments deposited into the main Roman Time channel of the Po (*Eridanus*) were affected by important coseismic liquefaction, possibly associated with the outflowing of salty waters. Damage to churches in the cannot be normally dated with precision, but its areal distribution in the region south-east of Ferrara, is significant. Damage was severe (VII-VIII MCS) in sites surrounding the Belriguardo area, as in the churches of Cona, Masi Torello, Gaibanella, Runco, Gambulaga, S. Nicolò, Santa Maria Codifiume, but it was comparatively reduced in sites closer to the Ferrara epicentre, like Aguscello (3 Km from it), Focomorto, and Francolino.

Conclusions.

The architecture history of all major building in the Ferrara and surrounding area has been severely affected by the intense seismic activity. This is still evident, for instance, in the Cathedral and Estense Castle. A detailed study of the architecture history and of the damage and reparation phases still visible in many buildings can significantly integrate the knowledge generated by written sources, as it is the case of Palazzo dei Diamanti. Documented coseismic liquefaction is confined into the Roman and Medieval fluvial channel and proximal levee sediments. The seismic activity of the area has been often characterized by long seismic sequences, like the 1561-1574 one, recording the epicentre migration, associated to the activation of different seismogenetic fault systems, reflecting the structural intricacy of the buried foredeep external portions of the Apennines Chain.

References

Guidoboni E.; 1984: *Riti di calamità: terremoti a Ferrara nel 1570-74*, Quaderni Storici 55/ a. XIX, n. 1.

Guidoboni E., Valensise G.; 2023: *L'Italia dei Terremoti, l'Azzardo Sismico delle Città*. *Vol. 2, Centro-Nord*. Fondazione CNI, 668 pp.

Guidoboni E., Ferrari G., Mariotti D., Comastri A., Tarabusi G., Sgattoni G., Valensise G.; 2018: *CFTI5Med, Catalogo dei Forti Terremoti in Italia (461 a.C.-1997) e nell'area Mediterranea (760 a.C.-1500).* Istituto Nazionale di Geofisica e Vulcanologia (INGV).

Guidoboni E., Ferrari G., Tarabusi G., Sgattoni G., Comastri A., Mariotti D., Ciuccarelli C., Bianchi M.G., Valensise G.; 2019: *CFTI5Med, the new release of the catalogue of strong earthquakes in Italy and in the Mediterranean area.* Scientific Data 6, Article Number: 80 (2019).

Locati M., Camassi R., Rovida A., Ercolani E., Bernardini F., Castelli V., Caracciolo C.H., Tertulliani A., Rossi A., Azzaro R., D'amico S., Conte S., Rocchetti E.; 2016: *DBMI15, the 2015 version of the Italian Macroseismic Database*. Istituto Nazionale di Geofisica e Vulcanologia (INGV).

Corresponding author: marco.stefani@unife.it

A novel approach to earthquake source characterization using DAS strain rate data acquired along optical fibres

C. Strumia[1], A. Trabattoni[2], M. Supino[3], M. Baillet[2], D. Rivet[2], G. Festa[1]

[1]Università di Napoli Federico II, Physics Department, Complesso Monte S. Angelo, Napoli, Italy.
[2]Université Côte d'Azur, Observatoire de la Côte d'Azur, CNRS, IRD, Géoazur.
[3]Istituto Nazionale di Geofisica e Vulcanologia, Osservatorio Nazionale Terremoti, Roma, Italy.

In recent years Distributed Acoustic Sensing (DAS) is establishing as a powerful tool in seismology, allowing for continuous recordings of earthquakes, with unprecedented spatial sampling. DAS systems are interrogators connected to one end of an optical fibre cable, sending repeated laser pulses, and exploiting measurements of phase variations of the backscattered light with time to infer measurements of the strain rate along the direction of the fibre (Hartog, 2017). The cable, interrogated by the DAS system, behaves as an almost continuous array of single component seismic sensors.

The availability of existing cables deployed for telecommunication purposes and the simplicity of DAS installation opens up the possibility of investigating harsh environments, where deployments of standard instruments could be expensive or unpractical, such as glaciers, remote areas, sea bottoms, volcanic flanks, or geothermal sites (e.g., Walter et al., 2020; Hudson et al.; 2021, Sladen et al., 2019; Currenti et al., 2021; Tsuji et al., 2021). These cables can reach lengths up to hundreds of kilometers and can depict the long-range continuous, shallow propagation of seismic waves when interrogated through DAS. The high potential of these systems has been nowadays exploited in several seismological tasks, from earthquake location (Piana Agostinetti et al., 2022), subsurface characterization (Ajo-Franklin et al., 2019), focal mechanism inversion (Li et al., 2023a), tomography (Biondi et al., 2023), and source back projection (Li et al., 2023b).

Among the several seismological duties, characterizing source parameters allows for interpretation of the rupture process and its effects on the ground motion through the determination of its seismic moment and size. Unlike applications where only time information is needed, consolidated methods based on spectral inversion for the determination of source parameters cannot be directly applied to DAS data, that natively provide strain rate instead of acceleration and/or velocity time series. Using DAS amplitudes for earthquake source characterization leads to two possible alternatives: either converting recordings to kinematic quantities to apply existing physical models (Lior et al., 2021; 2023), or developing a novel forward modelling that directly digests DAS data. Despite conversion techniques have been proposed and validated (Trabattoni et al., 2023), moving to kinematic quantities pollutes the spectral content of the data, especially at low

frequencies. For this reason, we focus here on the development of a new mathematical formulation able to describe the source time function contribution contained in the far field strain domain, leading to forward modelling of time integrated strain spectra and evaluation of source parameters.

We validated the technique on two case-studies, for earthquakes in magnitude range $0.4 - 4.3$, by comparing the results with estimates from standard seismic instruments. When analysing earthquakes recorded on an off-shore, $150km$ long cable during a 1-month DAS survey in Chile, results exhibit scale invariant stress drop distribution between seismic moment and corner frequency estimates, with an average of $\Delta\sigma = (0.8 \pm 0.6)MPa$. Moreover, moment magnitude estimations agree with results from local seismic stations. The second case study involves DAS data acquired on a short cable ($1km$) deployed in the Irpinia region in the Southern Apennines during a 5-month temporary experiment. Here data show a dominance of site effects resulting in an apparent corner frequency around $5Hz$, while the low frequency content of signals gives estimates of moment magnitude in agreement with seismic stations. Nevertheless, the modelling of local site effect through a parametric EGF approach allows to determine corner frequencies for the largest magnitude events in the catalogue.

Overall, results highlight the potential of DAS systems in characterizing the seismic ruptures over different space scales, exploiting the redundancy of information available from the very-high spatial resolution of recordings.

References

Ajo-Franklin, J. B., Dou, S., Lindsey, N. J., Monga, I., Tracy, C., Robertson, M., Rodriguez Tribaldos, V., Ulrich, C., Freifeld, B., Daley, T., & Li, X; 2019: Distributed Acoustic Sensing Using Dark Fiber for Near-Surface Characterization and Broadband Seismic Event Detection. *Scientific Reports*, *9*(1). https://doi.org/10.1038/s41598-018-36675-8

Biondi, E., Zhu, W., Li, J., Williams, E.F., Zhan, Z.; 2023: An upper-crust lid over the Long Valley magma chamber. *Science Advances* https://doi.org/10.1126/sciadv.adi9878

Currenti, G., Jousset, P., Napoli, R., Krawczyk, C., & Weber, M.; 2021: On the comparison of strain measurements from fibre optics with a dense seismometer array at Etna volcano (Italy). *Solid Earth*, *12*(4), 993–1003. https://doi.org/10.5194/se-12-993-2021

Hartog, H.A.; 2017: An introduction to distributed optical fibre sensors (A. H. Hartog, Ed.). CRC Press.

Hudson, T. S., Baird, A. F., Kendall, J. M., Kufner, S. K., Brisbourne, A. M., Smith, A. M., et al.; 2021: Distributed Acoustic Sensing (DAS) for natural microseismicity studies: A case study from Antarctica. Journal of Geophysical Research: Solid Earth, 126, e2020JB021493. https://doi.org/10.1029/2020JB021493

Li, J., Zhu, W., Biondi, E., & Zhan, Z.; 2023a: Earthquake focal mechanisms with distributed acoustic sensing. *Nature Communications*, *14*(1), 4181. https://doi.org/10.1038/s41467-023-39639-3

Li, J., Kim, T., Lapusta, N. *et al.* The break of earthquake asperities imaged by distributed acoustic sensing. *Nature* 620, 800–806; 2023: https://doi.org/10.1038/s41586-023-06227-w

Lior, I., Rivet, D., Ampuero, J. P., Sladen, A., Barrientos, S., Sánchez-Olavarría, R., Villarroel Opazo, G. A., & Bustamante Prado, J. A.; 2023: Magnitude estimation and ground motion prediction to harness fiber optic distributed acoustic sensing for earthquake early warning. *Scientific Reports*, *13*(1). https://doi.org/10.1038/s41598-023-27444-3

Lior, I., Sladen, A., Mercerat, D., Ampuero, J. P., Rivet, D., & Sambolian, S.; 2021: Strain to ground motion conversion of distributed acoustic sensing data for earthquake magnitude and stress drop determination. *Solid Earth*, *12*(6), 1421–1442. https://doi.org/10.5194/se-12-1421-2021

Piana Agostinetti, N., Villa, A., & Saccorotti, G.; 2022: Distributed acoustic sensing as a tool for subsurface mapping and seismic event monitoring: A proof of concept. *Solid Earth*, *13*(2), 449–468. https://doi.org/10.5194/se-13-449-2022

Sladen, A., Rivet, D., Ampuero, J. P., De Barros, L., Hello, Y., Calbris, G., & Lamare, P.; 2019: Distributed sensing of earthquakes and ocean-solid Earth interactions on seafloor telecom cables. *Nature Communications*, *10*(1). https://doi.org/10.1038/s41467-019-13793-z

Trabattoni, A., Biagioli, F., Strumia, C., Van Den Ende, M., Scotto Di Uccio, F., Festa, G., Rivet, D., Sladen, A., Ampuero, J. P., Métaxian, J.-P., & Stutzmann, É.; 2023: From strain to displacement: using deformation to enhance distributed acoustic sensing applications, Geophysical Journal International, 235(3), 2372–2384. https://doi.org/10.1093/gji/ggad365

Tsuji, T., Ikeda, T., Matsuura, R., Mukumoto, K., Hutapea, F. L., Kimura, T., Yamaoka, K., & Shinohara, M.; 2021: Continuous monitoring system for safe managements of CO2 storage and geothermal reservoirs. *Scientific Reports*, *11*(1). https://doi.org/10.1038/s41598-021-97881-5

Walter, F., Gräff, D., Lindner, F, Paitz, P., Köpfli, M., Chmiel, M., Fichtner, A.; 2020: Distributed acoustic sensing of microseismic sources and wave propagation in glaciated terrain. *Nature Communications* 11, 2436 https://doi.org/10.1038/s41467-020-15824-6

Corresponding author: claudio.strumia@unina.it

Comparing Machine Learning to Manual Earthquake Location procedures: evaluating the performance of LOC-FLOW on a microseismic sequence occurred in Collalto area (NE Italy)

M. Sugan[1], L. Peruzza[1], M.A. Romano[1], M. Guidarelli[1], L. Moratto[1], D. Sandron[1], M.P. Plasencia Linares[1], M. Romanelli[1]

[1] National Institute of Oceanography and Applied Geophysics - OGS, Italy

Detecting earthquakes and picking seismic phases are fundamental elements in numerous seismological processes, being crucial in both seismic monitoring and in-depth seismological investigations. The utilization of machine learning (ML) techniques has experienced a notable improvement lately, offering a promising way to face the complexities associated with earthquake detection and localization.

The reliability of ML methods remains an open question in settings with dense and localized seismic networks. In such contexts, fast and accurate detection and localization of earthquakes are essential for decision-making, playing a pivotal role in seismic risk mitigation strategies, even for events of very low magnitude.

In the field of microseismic monitoring, ML applications are similar to those of earthquake monitoring, but have the task of processing weak seismic signals characterized by low signal-to-noise ratios at individual receivers or very short target time signals (Anikiev et al., 2023). Therefore, evaluating the performance of ML models trained on regional datasets in a microseismic sequence is challenging but crucial, especially for applications in the field of induced seismicity (e.g., Mousavi et al., 2016) or for activities of observatories near faults.

This study focuses on evaluating the performance of the PhaseNet algorithm (Zhu and Beroza, 2018), a prominent deep learning model for earthquake phase identification. The evaluation is conducted within the extensive LOC-FLOW workflow for earthquake location proposed by Zhang et al. (2022). The study is performed on the seismic events of the Refrontolo sequence that occurred in August 2021 on an antithetic fault segment of the Montello thrust system in the Pedemontana district of Southeastern Alps (Peruzza et al., 2022).

The seismic sequence displayed remarkable activity despite its low energy release (M_L 2.5 for the main event). The sequence consisted of 374 events occurring at approximately 9 km depth within a confined volume, and was monitored by the permanent Collalto Seismic Network (RSC). This

sequence is a significant case study for testing and refining automated techniques to detect and locate microearthquakes using machine learning.

The RSC is composed of 10 stations and has monitored microseismic activity potentially induced by underground gas storage activities since 2012. Rigorous manual processing conducted by the RSC, involving daily and monthly offline procedures, is undertaken to guarantee data accuracy and metadata reliability. Nevertheless, this approach can be time consuming and demanding, particularly in densely populated seismic sequences where very fast analysis is preferable.

Comparing seismic catalogs derived from associations approved by experienced analysts and revised manual picks with those generated using the PhaseNet integrated with LOC-FLOW provides a unique opportunity to evaluate the performance of ML methods in detecting and localizing local microearthquakes. Our particular focus includes:

1. PhaseNet phase picker performance: we examine the effectiveness of the PhaseNet phase picker in comparison to manual phase picks. This evaluation aims to assess the accuracy and reliability of PhaseNet's automated phase detection.

2. LOC-FLOW-generated earthquake catalogs: we analyse the earthquake catalogs produced by LOC-FLOW, evaluating both origin time and absolute locations. The examination involves comparing catalogs formed with PhaseNet picks against those created with the original RSC manual picks. This analysis offers insights into the coherence and efficacy of PhaseNet in creating the overall earthquake catalog.

3. Contribution of template matching: we assess the influence of template matching on the final catalog and compare it to the dataset obtained from the original RSC procedures. This evaluation aims to clarify the degree to which template matching enhances the accuracy and comprehensiveness of the earthquake catalog within the LOC-FLOW workflow.

4. Spatio-temporal characteristics of seismicity: furthermore, we assess the spatio-temporal characteristics of the acquired seismicity. This examination is useful to check the efficiency of the method in discerning tectonic structures activated during the sequence. Gaining insights into the spatial and temporal patterns of seismic activity offers valuable understanding of the underlying geologic processes.

We find that PhaseNet achieved a detection rate of 79% for manual P arrival times and 90% for S arrival times at the same stations. While P picks exhibited satisfactory accuracy, a noticeable delay was observed for S picks. This delay is presumed to be a common feature, even in other datasets, given the high quality of the manual picking used for comparison.

After integrating events identified by the template matching procedure, the final LOC-FLOW catalog is characterized by an increased number of events compared to the initial manual catalog. However, in our specific case study, PhaseNet did not contribute significantly to the augmentation of the earthquake count during the most active days of the sequence (e.g., 2-3 August), where template matching played a crucial role. Despite the observed lower accuracy in S picks,

PhaseNet's overall performance is commendable, especially when considering the time of processing, significantly reduced compared to manual picking. The seismicity pattern observed vividly depicted the geometry of the activated fault in both temporal and spatial dimensions (Sugan et al., 2023).

Funding

This study was carried out in the frame of the Italian PRIN Project 'Fault segmentation and seismotectonics of active thrust systems: the Northern Apennines and Southern Alps laboratories for new Seismic Hazard Assessments in northern Italy (NASA4SHA)' (PI R. Caputo, UR Responsible L. Peruzza). The research was also supported by OGS and CINECA under HPC-TRES program.

References

Anikiev D., Birnie C., bin Waheed U., Alkhalifah T., Gu C., Verschuur D.J., Eisner L.; 2023. Machine learning in microseismic monitoring. Earth-Science Reviews. 239:104371. https://doi.org/10.1016/j.earscirev.2023.104371.

Mousavi S.M., Horton S.P., Langston C.A., Samei B.; 2016. Seismic Features and Automatic Discrimination of Deep and Shallow Induced-Microearthquakes Using Neural Network and Logistic Regression. Geophys J Int. 207(1):29-46. https://doi.org/10.1093/gji/ggw258.

Peruzza L., Romano M.A., Guidarelli M., Moratto L., Garbin M., Priolo E.; 2022. An unusually productive microearthquake sequence brings new insights to the buried active thrust system of Montello (Southeastern Alps, Northern Italy). Front Earth Sci. 10:1044296. https://doi.org/10.3389/feart.2022.1044296.

Sugan M., Peruzza L., Romano M.A., Guidarelli M., Moratto L., Sandron D., Plasencia Linares M.P., Romanelli M.; 2023. Machine learning versus manual earthquake location workflow: testing LOC-FLOW on an unusually productive microseismic sequence in northeastern Italy. Geomatics, Natural Hazards and Risk, 14:1. https://doi.org/10.1080/19475705.2023.2284120.

Zhang M., Liu M., Feng T., Wang R., Zhu W.; 2022. LOC-FLOW: An End-to-End Machine-Learning-Based High-Precision Earthquake Location Workflow. Seismol Res Lett. 93(5):2426-2438. https://doi.org/10.1785/0220220019.

Zhu W., Beroza G.C.; 2018. PhaseNet: A deep-neural-network based seismic arrival-time picking method. Geophys J Int. 216(1): 261–273. https://doi.org/10.1093/gji/ggy423.

Corresponding author: msugan@ogs.it

SUPERSTUDIES: an approach for integrating macroseismic datasets of different nature

A. Tertulliani[1], A. Antonucci[2], F. Bernardini[3], V. Castelli[3], E. Ercolani[3], L. Graziani[1], A. Maramai[1] , M. Orlando[1], A. Rossi[1], T. Tuvè[4]

[1] Istituto Nazionale di Geofisica e Vulcanologia, Roma, Italy
[2] Istituto Nazionale di Geofisica e Vulcanologia, Milano, Italy
[3] Istituto Nazionale di Geofisica e Vulcanologia, Bologna, Italy
[4] Istituto Nazionale di Geofisica e Vulcanologia, Osservatorio Etneo, Catania, Italy

In recent decades, a huge amount of information on Italian seismic history has been produced, contributing to the compilation of the current seismic catalogues, CPTI15 (Rovida et al., 2020 and 2022) and CFTI5Med Guidoboni et al. 2018.). The last version of CPTI15 counts almost 5000 events from 1000 A.D. to 2020.

CPTI15 is fed by DBMI15 (Locati et al., 2022), a macroseismic database that derives its data from approximately 190 studies on single events, produced over time by the scientific community. DBMI15 contains over 120,000 Macroseismic Data Points (MDPs) related to more than 3200 earthquakes. The epicentral parameters and MDPs list of each event in the CPTI-DBMI catalogue are based on a single reference study (the “preferred” one), selected by a criterion based on the quality of the study itself and on the number and distribution of the intensity data it provides. However, in many cases, multiple studies are available in literature for the same event. For this reason, since 2017, the Italian Archive of Historical Earthquake Data (ASMI) has been published and it is continuously implemented (Rovida et al., 2017), collecting many references of interest for the thousands of earthquakes included in the catalogue. At present, ASMI stores about 450 studies dedicated to more than 6000 earthquakes. For many of these earthquakes, multiple studies, by different authors and of various kinds and complexity, are available, ensuring a multiplicity of views and types of information.

A screening of the available studies for different earthquakes showed that the "preferred" studies are not always those with the largest number of MDPs, or the most recent and up to date. In other words, there are cases in which the same earthquake has been investigated by different authors, who produced datasets that can differ in terms of MDPs, geographic coverage, and reference sources. This means that many available and published MDPs, are not included in the catalogue simply because they are not included in the “preferred” studies, and therefore, they cannot be used for any purpose. Earthquakes with multiple studies are particularly numerous in the period from 1985 to the present. A detailed analysis showed that these datasets could be, in many cases, complementary to each other.

In the light of this, we aimed at integrating the different existing datasets for a given event in a unique intensity compilation, thus optimising all the available intensity data. This possible data merging could give, for each studied earthquake, a significant increase both in MDPs number and

in the completeness of the listed localities' seismic histories. This operation could allow to systematize a considerable amount of data that so far has remained under-used or even unused.
We called "superstudy" this approach of integrating, in a single dataset, data derived from several different studies of the same event.
However, to carry out this task is not a straightforward procedure, and some critical issues exist, mainly due to the inhomogeneity of the different intensity dataset. This inhomogeneity is due to different methods of collecting information and assigning intensity, adopted by different research groups, in different "historical" periods, also sometimes using different intensity scales or different kinds of geolocalization (e.g. municipal area or hamlets).
The purpose of this work is to understand whether it is possible to integrate such different datasets into a coherent whole, quickly and efficiently (I.e. without performing a deep revision of each event), without lessening the quality of the resulting intensity assignments. To check this, we made an experiment that started with the selection of a number of earthquakes, occurred in the period from 1985 to 2006, for which several different studies are available.
The selected earthquakes are provided with studies of different kinds, from reports of macroseismic field surveys, to questionnaire data collections and to preliminary reviews.

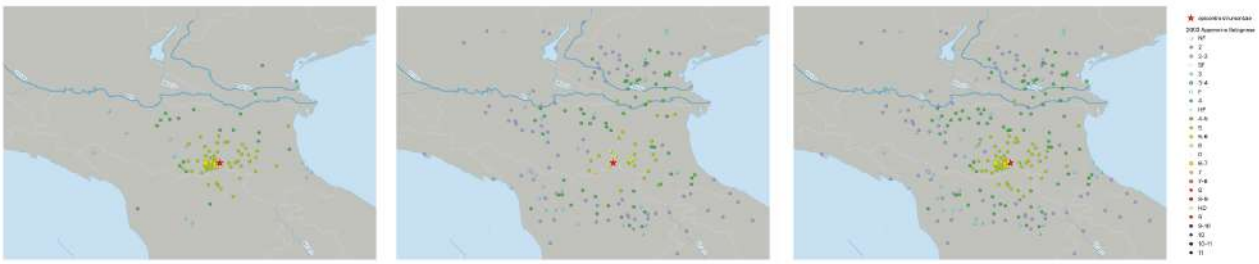

Fig.1 – Example of the superstudy of the September 9, 2003 earthquake. From the left to the right, CPTI15 preferred study (Bernardini et al., 2003) 134 Mdps, the other available source (BMING11, Gasparini et al., 2011) 613 MDPs and the final superstudy, MDPs 693 MDPs.

Integrating macroseismic studies of different nature does not simply mean combining intensity values as they are. On the contrary, it requires first to individuate some homogenization criteria that allow to optimize the quality and quantity of information. As mentioned above, dissimilarities in macroseismic data mostly result from the different practices of data collection followed at different times, according to the methodologies used, and from the kinds of intensity scale used and how they were used. The studies associated with the selected earthquakes provide data sets that differ both in the number of points and in the assessed intensity values. In some cases we find that a given locality is included in all studies, with coincident intensities or sometimes with different intensities. It can also happen that several MDPs are present in one only of the studies of the same earthquake.
To bring our appointed task to completion both efficiently and systematically, it is necessary to establish some criteria and accept some approximations about the nature of data, as for example, considering MCS and EMS intensities <5 to be equivalent. This project, at the moment, involves more than 40 earthquakes with a total of about 4,000 MDPs, which will increase to around 10,000

at the end of the work. The “superstudy” datasets will be compiled both in the MCS scale and in EMS-98. The unquestionable advantages of this operation are quite a number: feeding the catalogue with a great amount of MDPs not previously considered (example in Fig. 1); improving seismic histories with a large number of localities; increasing the knowledge of each event; enriching available datasets in both MCS and EMS-98 scales.

References

Bernardini F., Camassi R., Castelli V., Ercolani E., Frapiccini M., Vannucci G., Giovani L., Tertulliani A.; 2003: Rilievo macrosismico degli effetti prodotti dalla sequenza sismica iniziata il 14 settembre 2003 (Appennino Bolognese). Rapporto tecnico QUEST, Istituto Nazionale di Geofisica e Vulcanologia (INGV), Bologna, 10 pp. https://doi.org/10.13127/QUEST/20030914

Gasparini C., Conte S., Vannucci C. (ed); 2011: Bollettino macrosismico 2001-2005. Istituto Nazionale di Geofisica e Vulcanologia, Roma. CD-ROM

Guidoboni E., Ferrari G., Mariotti D., Comastri A., Tarabusi G., Sgattoni G., Valensise G.; 2018: CFTI5Med, Catalogo dei Forti Terremoti in Italia (461 a.C.-1997) e nell’area Mediterranea (760 a.C.-1500). Istituto Nazionale di Geofisica e Vulcanologia (INGV). doi: https://doi.org/10.6092/ingv.it-cfti5

Locati, M., R. Camassi, A. Rovida, E. Ercolani, F. Bernardini, V., Castelli, C. H. Caracciolo, A. Tertulliani, A. Rossi, R. Azzaro, et al.; 2019: Database macrosismico Italiano (DBMI15), versione 2.0, Istituto Nazionale di Geofisica e Vulcanologia (INGV), doi: 10.13127/DBMI/DBMI15.2 .

Rovida A., Locati M., Antonucci A., Camassi R. (a cura di); 2017: Archivio Storico Macrosismico Italiano (ASMI). Istituto Nazionale di Geofisica e Vulcanologia (INGV). https://doi.org/10.13127/asmi

Rovida, A., M. Locati, R. Camassi, B. Lolli, and P. Gasperini; 2020: The Italian earthquake catalogue CPTI15, Bull. Earthq. Eng. 18, 2953–2984, doi: 10.1007/s10518-020-00818-y

Rovida A., Locati M., Camassi R., Lolli B., Gasperini P., Antonucci A.; 2022: Catalogo Parametrico dei Terremoti Italiani (CPTI15), versione 4.0. Istituto Nazionale di Geofisica e Vulcanologia (INGV). https://doi.org/10.13127/CPTI/CPTI15.4

Corresponding author: andrea.tertulliani@ingv.it

Was the August 26, 1806 earthquake really the largest event in the Roman area ?

A. Tertulliani, C. Castellano

Istituto Nazionale di Geofisica e Vulcanologia, Roma, Italy

The August 26, 1806 earthquake, M_w 5.6 and I_0 8 MCS, with epicenter in the Alban Hills region, is known as the largest one that occurred in the Roman area (CPTI15, Rovida et al., 2020; 2022).

The shock occurred at 7:35 GMT, provoking damage in several localities, particularly severe in the villages of Genzano, Rocca di Papa and Velletri. Some sources have even mentioned the death and injury of some people in Genzano and Rocca di Papa. The earthquake was felt in Naples and caused light damage in Rome.

This is the summary of how the event is known so far in the catalogs (Guidoboni et al., 2018; Rovida et al., 2020).

However, some unique features of this event intrigued us, and motivated us to undertake in-depth research. A dedicated investigation showed that there was still room for improvement in the knowledge about this earthquake, in particular through the examination of archival documents, which had not been consulted by previous studies.

The aim of this work is to present the path of revision and enrichment of the knowledge about the earthquake of August 26, 1806, from which a rather different picture has emerged from what has been known and present in the catalogs so far.

References

Guidoboni E., Ferrari G., Mariotti D., Comastri A., Tarabusi G., Sgattoni G., Valensise G.; 2018: CFTI5Med, Catalogo dei Forti Terremoti in Italia (461 a.C.-1997) e nell'area Mediterranea (760 a.C.-1500). Istituto Nazionale di Geofisica e Vulcanologia (INGV). doi: https://doi.org/10.6092/ingv.it-cfti5

Rovida, A., M. Locati, R. Camassi, B. Lolli, and P. Gasperini; 2020: The Italian earthquake catalogue CPTI15, Bull. Earthq. Eng. 18, 2953–2984, doi: 10.1007/s10518-020-00818-y

Rovida A., Locati M., Camassi R., Lolli B., Gasperini P., Antonucci A.; 2022: Catalogo Parametrico dei Terremoti Italiani (CPTI15), versione 4.0. Istituto Nazionale di Geofisica e Vulcanologia (INGV). https://doi.org/10.13127/CPTI/CPTI15.4

Corresponding author: andrea.tertulliani@ingv.it

Recent activity of the Stradella fault (Emilia Arc, northern Italy) by a multi-scale approach

A. Tibaldi[1,2], R. de Nardis [3,2], P. Torrese [4,2], S. Bressan[1], M. Pedicini[1], D. Talone[2,3], F. L. Bonali[1,2], N. Corti[1], E. Russo[1,2], G. Lavecchia[3,2]

[1] Department of Earth and Environmental Sciences, University of Milan-Bicocca, Milan, Italy
[2] CRUST-Interuniversity Center for 3D Seismotectonics with Territorial Applications, Chieti, Italy
[3] Department of Psychological Sciences, Health and Territory, University of the Studies "G. d'Annunzio", Chieti, Italy
[4] Department of Earth and Environmental Sciences, University of Pavia, Italy

The deformation front of the northern Apennines - Italy - is mostly covered under the alluvial deposits of the Po Plain. Some of the folds and thrusts of this front show geological evidence of Late Quaternary activity, thus posing the need for an accurate seismic hazard assessment due to widespread housing settlements, industries, lifeline infrastructures, and large towns. We present new morphostructural, geophysical, and seismological data to discuss the recent activity of the Broni-Sarmato fault, an 18 km-long outcropping section of the north-verging Stradella thrust, located 50 km south of Milan, along the Pede-Apennine thrust front (PTF) in the rear of the Emilia Arc thrust system. The new geoelectrical surveys across the fault scarp show deformation of the shallow deposits. The outcropping deformations, with a fault scarp ranging up to 25.8 m, are investigated within the seismotectonic framework of the PTF and the Emilia Arc. The analysis of the associated seismicity and new focal mechanisms highlight two seismogenic contractional volumes dipping at low-angle southwest-ward, at upper (<12 km) and lower crustal depths (~20–30 km). The shallow seismicity partially illuminates the Stradella thrust and its alongstrike southeastward prosecution along the extent of the Stradella-Salsomaggiore Arc. Subordinately, it also illuminates some of the Emilia Arc thrust planes. The deeper seismogenic volume shows large patches of the basal thrust of the Emilia Arc fault system. We interpret the above multi-scale data as evidence of ongoing tectonic activity of the outer fronts of the Emilia Arc under a regional NNE-oriented compressional stress field, with some evidence of thrust involvement along the Pede-Apennine front. In our 3D fault-model reconstruction, all the analyzed thrust structures appear as expressions of a thick-skinned deformation that controls earthquake release at different structural levels. The results do not allow to establish if the Broni-Sarmato scarp really represents the emersion of the main fault or it can represent the frontal limb of a fault-propagation fold. In the latter case, the main thrust did not reach yet the surface, whereas the deformations of the shallow deposits, highlighted by geoelectrical surveys, may represent secondary structures.

Acknowledgments

Research activities have been carried out in the frame of the Italian PRIN Project (Research Projects of National Interest) “Fault segmentation and seismotectonics of active thrust systems: the Northern Apennines and Southern Alps laboratories for new Seismic Hazard Assessments in northern Italy (NASA4SHA)” (PI R. Caputo, UR Responsible A. Tibaldi), of the CRUST - Interuniversity Center for 3D Seismotectonics with Territorial Applications, and under the aegis of the International Lithosphere Program, Task Force II. We acknowledge PetEx that provided the Move 2019.1 suite software license and we thank Daniele Spallarossa and his colleagues for providing us the waveforms of the Regional Seismic Network of Northwestern Italy RSNI.

Corresponding author: alessandro.tibaldi@unimib.it

Integrated analysis of geophysical data: a case study from Central Italy

M.M. Tiberti[1], F.E. Maesano[1], M. Buttinelli[1], P. De Gori[1], F. Ferri[2], L. Minelli[1], M. Di Nezza[1], C. D'Ambrogi[2]

[1] Istituto Nazionale di Geofisica e Vulcanologia, Rome, Italy
[2]Istituto Superiore per la Protezione e la Ricerca Ambientale, Servizio Geologico d'Italia, Rome, Italy

We performed a 2D gravity modeling across the Central Apennines, spanning from the Tyrrhenian coast to the Adriatic Sea, in the area affected by the Amatrice-Visso-Norcia earthquakes.

The cross-section was built exploiting the results of the 3D model proposed by the RETRACE 3D project (*www.retrace3d.it*) and aimed at completing and verifying the crustal geometries resulting from the project itself.

The results were checked against the velocity model provided by local tomography (LET), adding further details, and, finally, against seismicity recorded during the 2016-2017 sequence.

The results indicate that the geometries proposed in the RETRACE 3D model fit well with the Bouguer anomalies, except for some local misfits.

We were also able to determine some new elements in the surroundings of the RETRACE study area, where the cross-section length exceeds the 3D model.

In addition, the gravity model allowed us to investigate the nature of the basement top and its relationship with seismotectonics.

Corresponding author: mara.tiberti@ingv.it

On-fault earthquake energy density partitioning from an exhumed seismic mid-crustal fault

G. Toffol[1], G. Pennacchioni[1], L. Menegon[2], D. Wallis[3], M. Faccenda[1], A. Camacho[4], M. Bestmann[5]

[1] Department of Geosciences, University of Padova, Padva, Italy
[2] Department of Geosciences, University of Oslo, Oslo, Norway
[3] Department of Earth Sciences, University of Cambridge, Cambridge, UK
[4] Department of Geological Sciences, University of Manitoba, Winnipeg, Canada
[5] Department of Geology, University of Vienna, Wien, Austria

The energy released during an earthquake is mostly dissipated in the fault zone and subordinately as radiated seismic waves. The on-fault energy budget is partitioned into frictional heat, generation of new grain surface by microfracturing, and crystal-lattice distortion associated with dislocation defects. The energy partitioning strongly influences earthquake mechanics; however, the relative contribution of the on-fault components is debated and difficult to assess.

Exhumed fault rocks bearing pseudotachylytes (quenched coseismic frictional melts, the geological record of earthquake failure) represent a fundamental source of information to understand earthquake mechanics. We used high-resolution scanning-electron-microscopy techniques to analyse shocked garnets in a fault wall-rock, to provide the first estimate of all three energy components for a seismic fault patch exhumed from midcrustal conditions. Fault single-jerk seismicity is recorded by the presence of pristine quenched frictional melt. The estimated value of energy per unit fault surface is ~ 13 MJ/m2 for heat, which is predominant with respect to both surface energy (up to 0.29 MJ/m2) and energy associated with crystal lattice distortion (0.02 MJ/m2).

Corresponding author: giovanni.toffol@unipd.it

Are productive gas fields anticorrelated with large seismogenic faults? Implications for hydrocarbon exploitation and seismic hazard

G. Valensise[1], F. Donda[2], A. Tamaro[2], S. Parolai[3]

[1] INGV, Rome, Italy
[2] OGS, Trieste, Italy
[3] University of Trieste, Italy

Thrust faulting earthquakes are an inherent occurrence in hydrocarbon-bearing active regions dominated by crustal shortening: they may be generated by regional-scale tectonic processes, but also triggered at all stages of hydrocarbon exploitation activities. Their occurrence, however, is highly heterogeneous, as earthquakes often appear scattered across relatively homogeneous tectonic trends. For instance, investigations of the seismicity of the Zagros region (southern Iran: Nissen et al., 2011), one of the largest oil and gas reserves worldwide, revealed (a) that thrust faulting earthquakes are less frequent than strike-slip events, despite the characteristic and actively deforming fold-and-thrust structure of the region; and, more importantly, that (b) the observed seismicity accounts for a small fraction of the region's shortening estimated from geodetic observations.

In a frictional regime, the fraction of fault slip that is released in earthquakes is generally referred to as seismic coupling, or *c*, a dimensionless parameter introduced in the 1970s based on observations of great earthquakes of the circum-Pacific belt (Kanamori et al., 1971). Investigations of the compressional domains encircling the Italian peninsula, most of which host important oil and gas reservoirs, have already suggested that the average *c* is about 50% (Carafa et al., 2017); half than that estimated for the extensional domains straddling the Apennines chain, which is close to 1.0. Is this the result of episodically aseismic behaviour of the large thrust faults occurring beneath Italy's hydrocarbon reservoirs? How else could it be exaplained?

These questions were initially addressed by Mucciarelli et al. (2015), moving from the evidence offered by the 20 and 29 May 2012, M_w 5.9-6.0, Emilia earthquakes. These workers focused on the 2D spatial relationships between some known seismogenic sources supplied by the DISS database (DISS Working Group, 2021), and the distribution of 455 gas fields falling in a ~ 10,000 km^2 portion of the central-southern Po Plain, using data supplied by the "Visibility of Petroleum Exploration Data in Italy" (ViDEPI) database run by the Italian Ministry of Economic Development (https://www.videpi.com/videpi/pozzi/pozzi.asp). Based on this exercise, they proposed the existence of an anticorrelation between productive reservoirs and the presence of relatively large seismogenic faults, i.e., faults capable of M_w 5.5 + earthquakes.

Later on, Valensise et al. (2022) investigated in 3D the spatial relationships among 18 known seismogenic faults and 1,651 wells drilled for gas exploitation in the main hydrocarbon province of northern-central Italy, based on the same DISS and ViDEPI databases. Together these data comprise a unique dataset worldwide. They adopted a robust statistical technique implemented in a GIS, and again found a significant anticorrelation between the location of productive wells and that of the considered seismogenic faults, which are often overlain or encircled by unproductive wells.

Their findings led to the following conclusions:

(a) over geological time, earthquake ruptures encompassing much of the upper crust may cause gas to be lost to the atmosphere from the potential reservoir formations;

(b) reservoirs underlain by smaller or aseismic faults are more likely to be intact. This implies that the May 2012 shocks may simply have been the most recent events released by faults having a long earthquake history; and

c) the limited seismic coupling observed by previous investigators does not just indicate diffuse aseismic behavior, but rather suggests that about 50% of the large thrust faults occurring beneath the Po Plain hydrocarbon province slip consistently in an aseismic fashion; the remainder are fully coupled, and hence capable of generating the largest possible earthquake allowed by their size. Recent works on the sources of the May 2012 Emilia earthquake suggested that stick–slip behaviour occurs only where previous tectonic histories caused high-stiffness rocks (e.g., Triassic and Jurassic limestones and dolostones) to be uplifted and brought in contact across the fault plane, up to the characteristic 3–10 km depth of local upper crustal thrust faults (Bonini et al., 2014).

These results, which are of inherently global relevance, have crucial implications for future hydrocarbon exploitation; for the public acceptance of energy-related facilities in tectonically active areas; and for or assessing the seismic–aseismic behaviour of large thrust faults, leading to a more accurate estimation of the local seismic hazard. They also suggest that in earthquake-prone areas, any facility for natural gas, hydrogen or CO_2 storage should (a) be located away from proven seismogenic faults, and (b) take full advantage of depleted gas reservoirs: in itself, the pre-exploitation performance of such reservoirs proves they can sustain the typical pressures of an intact gas-field, and should be free from the risk of being damaged by a large earthquake.

References

Bonini L., Toscani G., Seno S.; 2014: *Three-dimensional segmentation and different rupture behaviour during the 2012 Emilia seismic sequence (Northern Italy)*. Tectonophysics, 630, 33–42, DOI: 10.1016/j.tecto.2014.05.006.

Carafa M. M. C., Valensise G., Bird P.; 2017: *Assessing the seismic coupling of shallow continental faults and its impact on seismic hazard estimates: a case-study from Italy*. Geophys. J. Int., 209(1), 32–47, DOI: 10.1093/gji/ggx002.

DISS Working Group; 2021: Database of Individual Seismogenic Sources (DISS), Version 3.3.0: A compilation of potential sources for earthquakes larger than M 5.5 in Italy and surrounding areas. Istituto Nazionale di Geofisica e Vulcanologia (INGV), DOI: 10.13127/diss3.3.0.

Kanamori, H. Great earthquakes at island arcs and the lithosphere. Tectonophysics, 12, 187–198 (1971).

Mucciarelli M., Donda F., Valensise G.; 2015: *Earthquakes and depleted gas reservoirs: which comes first?* Natural Hazards and Earth System Sciences, 15(10), 2,201-2,208, DOI: 10.5194/nhess- 15-2201-2015.

Nissen E., Tatar M., Jackson J. A., Allen M. B.; 2011: *New views on earthquake faulting in the Zagros fold-and-thrust belt of Iran*. Geophys. J. Int., 186, 928–944, DOI: 10.1111/j.1365246X.2011.05119.x.

Valensise G., Donda F., Tamaro A., Parolai S.; 2022: *Gas fields and large shallow seismogenic reverse faults are anticorrelated*. Scientific Reports, 12(1), 1,827, DOI: 10.1038/s41598- 022-05732-8.

Corresponding author: gianluca.valensise@ingv.it

Investigating the Influence of Coulomb Stress Transfer in the Activity of the Central Apennine Fault System (CAFS) Over the Last Millennium

G. Valentini[1,2.], T. Volatili[1], P. Galli[3,4], E. Tondi[1,2]

1. School of Science and Technology - Geology Division, University of Camerino, Italy.
2. National Institute of Geophysics and Volcanology, Rome, Italy
3. Dipartimento Protezione Civile, Rome, Italy
4. Consiglio Nazionale delle Ricerche, Istituto di Geologia Ambientale e Geoingegneria, Rome, Italy

The active Central Apennine Fault System (CAFS) witnessed several destructive seismic events over the last millennia. Although numerous investigations have highlighted the role of Coulomb Stress Transfer (CST) in the onset of some of the most devastating earthquakes globally, there is limited scientific documentation pertaining to its specific impact within the CAFS. This research delves into and thoroughly examines the effects of CST on both historical and instrumental seismic events of significant magnitude associated with the CAFS.

15 seismic events within the CAFS region dating from 1279 to present with magnitudes higher than Mw 6.0 were selected. Specifically, 9 were selected for the CST investigation, based on their proximity to subsequently activated faults both spatially and temporally. Beyond analyzing the static stress transfer for each individual seismic event, the cumulative CST of recent instrumental earthquakes was also examined to provide a comprehensive overview of the current stress scenario. Leveraging an innovative approach, faults were modeled in three dimensions, adopting an ellipse as the most accurate representation of their 2D geometry. Considering the CST's sensitivity to strike variations, a variable strike three-dimensional elliptical model was therefore implemented, ensuring enhanced calculation accuracy.

Valentini et al. (2023) identify three prominent periods where most of the seismic moment was released. The initial phase spans from ~1300 CE to ~1400 CE, followed by a surge around 1700 CE, and the most recent phase extends from 1979 to 2016 with 300-350 years intervals. However, the scale of the released seismic moment varies across these distinct seismic periods. The first seismicity window cumulative seismic moment is approximately 1.35 times greater than the second phase and about 2.31 times that of the third phase. With the current data in consideration, it seems plausible to hypothesize the existence of a notable seismic gap in the ongoing historical period. Should this gap exist, it implies the need for a seismic event substantial enough to bridge this gap. Herein we will examine the factors that may influence this seismic gap and identify which

faults could potentially bridge it, in light of the Coulomb Stress Transfer analysis and the distribution of seismicity over the last millennium.

In recent times, there has been a renewed focus on investigating the tectonic and seismic features of the CAFS. This intensified commitment has fostered a deeper understanding of fault dynamics, stress interactions between them, and forecasts for future seismic activities. Given the intricate tectonic nature of the CAFS and its pronounced seismicity, the imperative for consistent research and monitoring in this domain becomes clear. A cornerstone in seismic risk assessment is grasping the Coulomb stress transfer mechanism among faults. This study delves into this particular facet within the CAFS, accounting for the most significant seismic events over the last 750 years. Both historic earthquakes and recent seismic occurrences are analyzed to determine potential future seismic scenarios. By evaluating both the magnitude and the proximity to other fault lines that ruptured shortly after the primary event, we have chosen to concentrate on 9 of these earthquakes in relation to the Coulomb stress transfer (CST). The comprehensive list of these earthquakes, along with their specific attributes, is presented in Table 1, highlighting the ones selected for the CST analysis. The seismic occurrence of 1349 AD was re-evaluated and updated based on the recent findings by Galli et al. (2022).

Within the framework of our research, we've operated under the assumption that subsequent to seismic activity on a specific fault, Coulomb stress can propagate to neighboring faults. If this stress is positive, it might encourage fault rupture, whereas if negative, it could deter it (King et al., 1994). Numerous factors, including the distance between the causative fault and its neighboring one, their shapes, positions, dynamics, and the slip of the source fault, influence the Coulomb stress changes. Utilizing the "Coulomb 3.4" software, we derived the CST using the equation (Lin and Stein, 2004; Toda et al., 2005):

$$\Delta CST = \Delta\tau s + \mu \Delta\sigma n$$

In this equation, ΔCST represents variations in Coulomb Stress Transfer, $\Delta\tau s$ corresponds to shifts in shear stress, while μ stands for the friction coefficient, and $\Delta\sigma n$ signifies alterations in normal stress. We adopted a friction coefficient of 0.6 (Galderisi and Galli, 2020) and opted for default spatial parameters with a Poisson's ratio of 0.25 and a Young's modulus of 800,000 bar.

Regarding the three-dimensional portrayal of faults within CST calculations, we leaned on the methodology proposed by Valentini et al., (2023). We integrated a three-dimensional model featuring strike variations and an elliptical shape into our CST algorithm, believing that an accurate representation of the CAFS is pivotal to reducing potential computational inaccuracies. In advancing with the CST simulations, we endeavored to mirror the real seismic rupture dynamics, factoring in variables such as the slip distribution or the partial or entire rupture.

To ensure sharp graphical detail and enhanced bar value precision, we established a 1 km grid for the fault modeling. Faults, perceived in an elastic half-space, were outlined as lines with variable strike and segmented into 1 km units. This intricate segmentation proved to be a balanced choice between output detail and modeling duration, deviating from the more typical practice of using 2 km segments for CST modeling. Subsequently, using the "Faults 3D" software (Mildon et al. 2016),

we were able to construct 3D fault models, drawing from actual traces and determining a slip distribution for each fault. We chose to compute the Coulomb stress for each fault segment, maintaining a consistent friction coefficient. Where available, we used actual slip data for recent earthquakes. For less documented seismic events, we assumed a centered slip distribution, reminiscent of a bull's eye pattern, depending on the relative seismic moment. In instances where the fault width wasn't specified in the reviewed literature, we used standard geometric relationships (Gupta and Scholz, 2000) to determine it, basing our calculations on a 1.5 aspect ratio (length/width). For faults with an extended length, their maximum depth was aligned with the thickness of the seismogenic layer, approximately 15 km (Gasparini et al., 1985; Chiarabba and De Gori, 2016). To optimize CST data comprehension, we crafted three distinct representations. Initially, a traditional CST map was produced at a depth of 5 km, in plan view, providing an approximation of CST distribution within the surrounding crust. This information was then translated to KML format for georeferenced visualization on Google Earth Pro. Lastly, we crafted cross-sections perpendicular to fault strikes and developed a 3D model of the fault planes, obtaining the CST values for each 1 km fault segment, thus ensuring heightened precision in the assessment of stress for each individual segment.

In many of the case studies, CST may have played an influential role within the CAFS (Fig. 1 and Fig.2), catalyzing the activation or inhibition of its faults. Several instances highlight fault reactivation following high stress transfer in short periods, some examples are described below:

- The 1279 Colfiorito earthquake positively stressed the northern tip of the Norcia fault, that ruptured in 1328.
- The 1703 Norcia earthquake positively stressed the Pizzoli fault, where few days later a huge earthquake nucleated, provoking a cascade effect engaging the Pettino and Paganica faults.
- The 24th august and 26th October 2016 earthquakes seems to have stressed the bends and the central portion of the Vettore fault, probably facilitating the 30th October complete rupture.
- The Colfiorito fault system stored conspicuous amount of positive stress from each of the earthquakes generated by the Norcia fault system probably influencing its reactivation in 1997.
- The 1703 Norcia earthquake generated a huge positive stress lobe towards the Fabriano area, where 38 years later a destructive earthquake struck.

Conversely, certain scenarios illuminate the calming effect of stress shadows. Some examples include:

- The Vettore fault generated only one earthquake during the last millennium, this could be linked to the parallel Norcia fault that ruptured 4 times in the same time span, transferring negative CST on the Vettore fault.

- The same hypothesis could be applicable on the Gran Sasso fault that ruptured in 1349, this is the only event in the last millennium. The Paganica fault generated 3 earthquakes that transferred negative Coulomb stress on the Gran Sasso fault.

The nuanced understanding of CST achieved through this research has both concrete and academic implications. By illuminating the interaction between faults in previous seismic episodes, it provides valuable insights into possible future earthquake sequences. Such awareness is essential: by anticipating seismic sequences, targeted risk mitigation tactics can be formulated, thereby protecting local communities from the catastrophic consequences of earthquakes.

Year	Month	Day	Epicentral Area	Lat	Lon	Io	Mw	ErrorMw	TMw	SOURCE
1279	4	30	Colfiorito	43.093	12.872	9	6.2	0.16	Mdm	CPTI15
1328	12	4	Valnerina	42.857	13.018	10	6.4	0.28	Mdm	CPTI15
1349	9	9	Gran Sasso	42.334	13.613	10	7.0	ND	Mdm	Galli et al., 2022
1461	11	27	L'Aquila	42.308	13.543	10	6.5	0.46	Mdm	CPTI15
1599	11	6	Cascia	42.724	13.021	9	6.0	0.24	Mdm	CPTI15
1639	10	7	Laga Mountains	42.639	13.261	9-10	6.2	0.15	Mdm	CPTI15
1703	1	14	Valnerina	42.708	13.071	11	6.9	0.1	Mdm	CPTI15
1703	2	2	L'Aquila	42.434	13.292	10	6.6	0.11	Mdm	CPTI15
1730	5	12	Valnerina	42.753	13.120	9	6.0	0.1	Mdm	CPTI15
1979	9	19	Valnerina	42.73	12.956	8-9	5.8	0.1	InsO	CPTI15
1997	9	26	Colfiorito	43.014	12.853	8-9	5.9	0.07	InsO	CPTI15/ISIDe
2009	4	6	L'Aquila	42.309	13.510	9-10	6.2	0.07	InsO	CPTI15/ISIDe
2016	8	24	Laga Mountains	42.698	13.233	10	6.0	0.07	InsO	CPTI15/ISIDe
2016	10	26	Valnerina	42.904	13.090		5.9	0.07	InsO	CPTI15/ISIDe
2016	10	30	Valnerina	42.83	13.109	11	6.5	0.07	InsO	CPTI15/ISIDe

Table 2 List of historical (Mw≥6) and instrumental (Mw≥5.8) seismic events from 1279 to 2016 caused by CAFS (from CPTI15; Rovida et al., 2022 and ISIDe seismic catalogues). The seismic events selected for simulations are highlighted in green.

Moreover, the complexity of the CAFS, observed in light of past seismic episodes like those in 1997, 2009, and 2016, underscores the intricate nature of stress patterns. These patterns emerge from interactions between seismic events, with stress lobes intertwining in ways that amplify, nullify, or diversify their impacts on nearby faults. It is noteworthy that while historically and currently seismic-active regions such as Fabriano and Sulmona have remained relatively quiescent, their potential for future activity and associated risks should not be overlooked. This research highlights the complex dynamics at play in a high-seismic-activity region like the CAFS. Through rigorous analyses and innovative modeling techniques, we offer insights that can guide future investigations and pragmatic strategies for seismic risk mitigation. This study stands as a testament to the profound ability of CST to influence the seismic narrative of a region and emphasizes the need for continued research in this field.

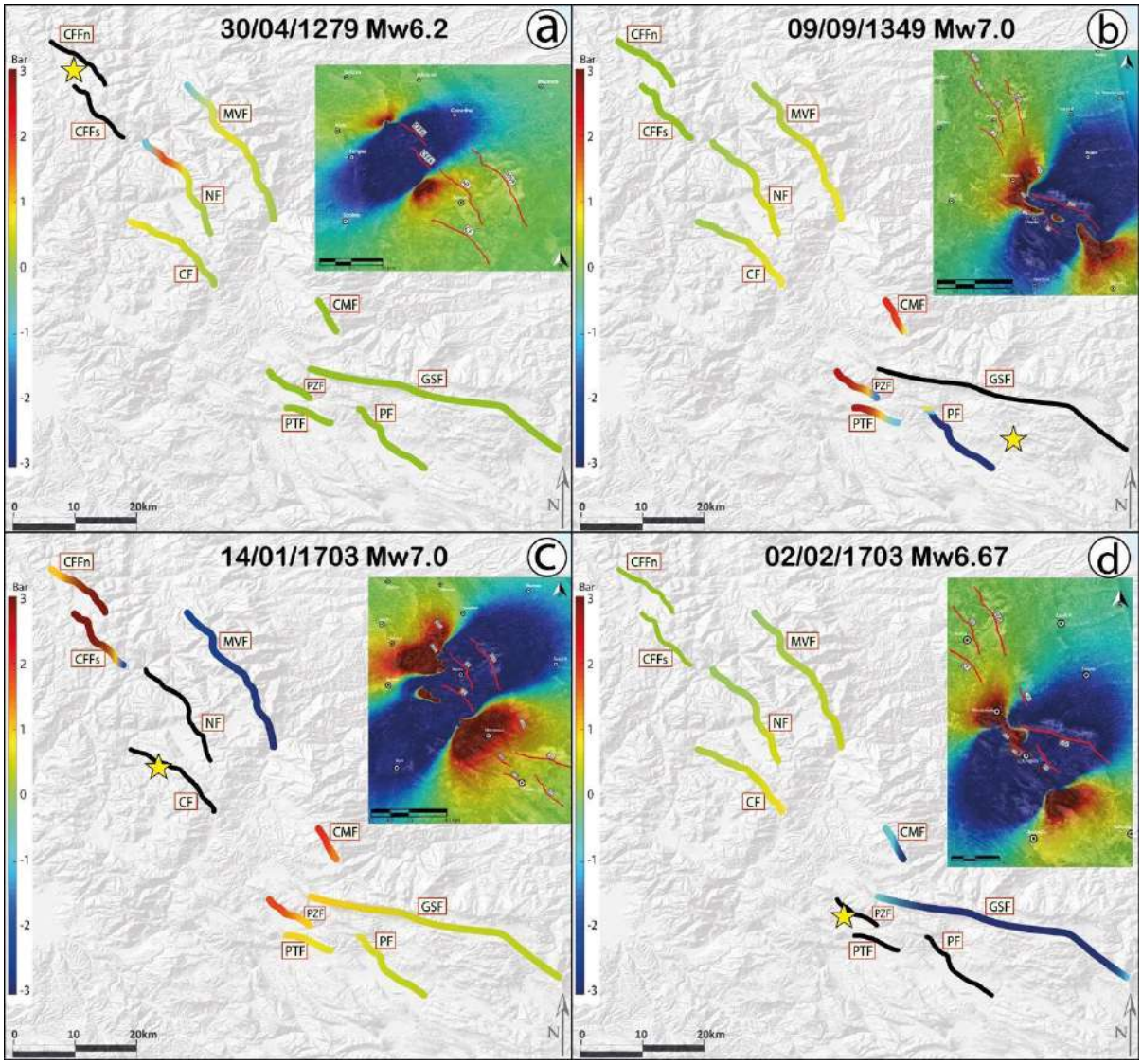

Figure 9 Summary visualization of the Calculated CST at a Depth of 5 km among the faults of the CAFS for each of the analyzed historical earthquakes. a) CST generated by the Colfiorito Fault System in April 1279. b) CST generated by the Gran Sasso Fault in September 1349. c) CST generated by the Norcia and Cascia Faults in January 1703. d) CST generated by the Paganica, Pizzoli, and Pettino Faults in February 1703. The fault traces drawn in black represent the causative faults. The insets of each figure illustrate the spatial distribution of the CST within the crust on a plane located at a depth of 5 km.

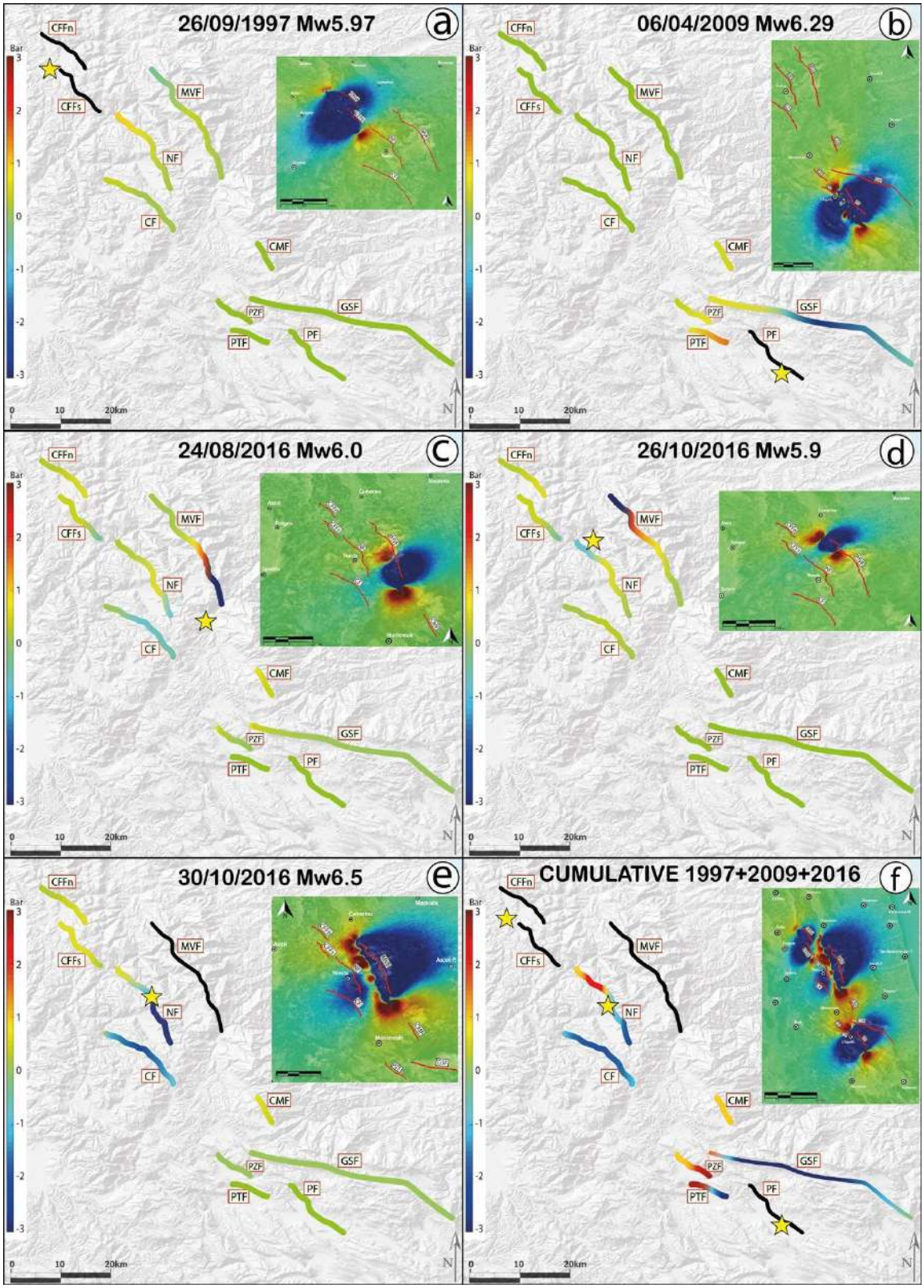

Figure 10 Summary visualization of the Calculated CST at a Depth of 5 km among the faults of the CAFS for each of the analyzed instrumental earthquakes. a) CST generated by the Colfiorito Fault System in September 1997. b) CST generated by the Paganica Fault in April 2009. c) CST generated by the southern portion of the Mt. Vettore fault in August 2016. d) CST generated by the northern portion of the Mt. Vettore fault in October 26th 2016. e) CST generated by the complete rupture of the Mt. Vettore fault in October 30th 2016. f) Cumulative CST from the last five instrumental earthquakes. The fault traces drawn in black represent the causative faults. The insets of each figure illustrate the spatial distribution of the CST within the crust on a plane located at a depth of 5 km.

Acknowledgments

We would like to acknowledge Dr. Zoë Mildon and Dr. Manuel-Lukas Diercks for their kind assistance in using the "3D-Faults" MATLAB code. This work was supported by the FAR Unicam project “Novel Approach for Seismic Hazard Analysis—NoHard'', responsible Emanuele Tondi.

References

Chiarabba C. and De Gori P.; 2016: *The seismogenic thickness in Italy: constraints on potential magnitude and seismic hazard*. Terra Nova, 28(6), 402-408.

Galderisi A. and Galli P.; 2020: *Coulomb stress transfer between parallel faults. The case of Norcia and Mt Vettore normal faults (Italy, 2016 Mw 6.6 earthquake)*. Results in Geophysical Sciences, 1, 100003.

Galli P., Galderisi A., Messina P. and Peronace E.; 2022: *The Gran Sasso fault system: Paleoseismological constraints on the catastrophic 1349 earthquake in Central Italy*. Tectonophysics, 822, 229156.

Gasparini C., Iannaccone G. and Scarpa R.; 1985: *Fault-plane solutions and seismicity of the Italian peninsula*. Tectonophysics 117, 59–78.

Gupta A. and Scholz C. H.; 2000: *A model of normal fault interaction based on observations and theory*. Journal of structural Geology, 22(7), 865-879.

ISIDe Working Group; 2007: *Italian Seismological Instrumental and Parametric Database (ISIDe)*. Istituto Nazionale di Geofisica e Vulcanologia (INGV). https://doi.org/10.13127/ISIDE

King G. C., Stein R. S. and Lin, J.; 1994: *Static stress changes and the triggering of earthquakes*. Bulletin of the Seismological Society of America, 84(3), 935-953.

Lin J. and Stein R. S.; 2004: *Stress triggering in thrust and subduction earthquakes and stress interaction between the southern San Andreas and nearby thrust and strike-slip faults*. Journal of Geophysical Research: Solid Earth, 109(B2).

Mildon Z. K., Toda S., Faure Walker J. P. and Roberts G. P.; 2016: *Evaluating models of Coulomb stress transfer: Is variable fault geometry important?*. Geophysical Research Letters, 43(24), 12-407.

Rovida A., Locati M., Camassi R., Lolli B., Gasperini P. and Antonucci A.; 2022: *Catalogo Parametrico dei Terremoti Italiani CPTI15, versione 4.0.*

Toda S., Stein R. S., Richards-Dinger K. and Bozkurt S. B.; 2005: *Forecasting the evolution of seismicity in southern California: Animations built on earthquake stress transfer*. Journal of Geophysical Research: Solid Earth, 110(B5).

Valentini G., Volatili T., Galli P. and Tondi E.; 2023: New methodological approach in the evaluation of faults interaction: insights from the central Apennine fault system. Bulletin of Geophysics and Oceanography.

Corresponding author: giorgio.valentini@unicam.it

Microseismicity and infrasonic monitoring at the Mefite d'Ansanto deep-CO_2-rich gas emission site (Southern Apennines, Italy)

L. Valoroso[1], S. Cianetti[2], P. De Gori[1], C. Giunchi[2], L. Improta[1], D. Piccinini[2], L. Zuccarello[1], F. Di Luccio[3]

[1] Istituto Nazionale di Geofisica e Vulcanologia (INGV), Osservatorio Nazionale Terremoti, Rome (Italy)
[2] Istituto Nazionale di Geofisica e Vulcanologia (INGV), Sezione di Pisa (Italy)
[3] Istituto Nazionale di Geofisica e Vulcanologia (INGV), Roma 1 (Italy)

The role of fluids in the earthquake nucleation process as well as in the evolution of aftershocks and swarms in space and time is well-documented, yet it is still an important issue for the seismological community to understand the physics governing the earthquakes. In particular, numerous studies evidence the primary role that mantle-derived fluids play in the generation of moderate to large upper crustal destructive earthquakes in extensional domains, where crustal-scale faults act as preferential hydraulic pathways.

In this study, we focus on the Mefite d'Ansanto degassing site (Southern Apennines, Italy) which is the largest low-temperature non-volcanic CO_2-rich gas emission site in the world, located at the northern tip of the Mw6.9 1980 Irpinia fault system. The study area experienced strong historical earthquakes (1702, 1732 and 1930 M6+ earthquakes) but it is characterised by a relatively low background seismicity rate with respect to the nearby Sannio and Irpinia regions.

To collect high-quality microseismicity data in this key sector of the southern Apennine extensional belt and investigate the relationship among seismicity, crustal fluids, and physical-hydraulic properties of the crust, we conducted a two years temporary experiment (June 2021 to May 2023) by installing a dense temporary network of 10 seismic stations equipped with short-period velocimeters (Lennartz 5sec). The temporary network covers an area of approximately 30x30 km^2 surrounding the Mefite d'Ansanto site and integrates with the numerous permanent stations of the INGV and ISNet permanent networks located at the boundary of the survey area. Within the Mefite area, we also deployed a temporary seismo-acoustic dense array to study two CO_2 degassing vents.

We show first results of the analysis of the seismicity recorded by the temporary network applying both standard (STA/LTA) detection algorithms or innovative enhanced techniques such as cross-correlation based template-matching algorithms (Chamberlain et al., 2018) and/or Deep-Learning-Phase-Recognition methods (Zhu and Beroza et al., 2018).

The activities are developed in the framework of the multidisciplinary project FURTHER (https://progetti.ingv.it/en/further).

References

Chamberlain C. J., Hopp C. J., Boese C. M., Warren-Smith E. , Chambers D., Chu S. X., Michailos K., Townend J. (2018). EQcorrscan: Repeating and Near-Repeating Earthquake Detection and Analysis in Python. Seismological Research Letters 2017; 89 (1): 173–181. https://doi.org/10.1785/0220170151

Zhu, W., & Beroza G. B. (2018). PhaseNet: A Deep-Neural-Network-Based Seismic Arrival Time Picking Method. Geophysical Journal International, 216(1), 261-273.

Corresponding author: luisa.valoroso@ingv.it

Vertical distributions of underground pore pressures from boreholes in the Southern Apennines and their seismotectonic implications

E. Vitagliano, N. D'Agostino, L. Improta, L. Pizzino

Istituto Nazionale di Geofisica e Vulcanologia (Rome, Italy)

Understanding subsurface pore pressures and crustal permeabilities is crucial for both resource exploitation and the mitigation of natural hazards. The pressure gradients inherent in the Earth's crust play an essential role in expelling geofluids and, more generally, in the underground fluid flows (groundwater, carbon dioxide, methane, etc.). Intensity and duration of the forces responsible for the pressure gradients are predominantly influenced by crustal permeability (Vannoli et al., 2021). In this context, unravelling the intricate dynamics of the pore pressure not only contributes to effective resource management but also enhances our ability to comprehend and address potential risks associated with seismic hazards.

The reconstruction of pore pressure regimes is normally inferred on the basis of indirect geophysical methods like the velocity ratios (e.g., Amoroso et al., 2017), which are suitable for large-scale studies and provide regional patterns often integrated with the geo-structural interpretation of the subsurface. However, these methods are limited, because they rely on certain assumptions about the subsurface, and their accuracy is contingent on the validity of these assumptions and can be influenced by the geological complexity of the study area. Conversely, direct pore pressure measurements from well data provide reliable information on in situ pressure conditions. These measures can be retrieved from formation and production tests and also derived from well logging by applying a properly calibration and validation procedure (e.g., Zhang, 2011).
Although future research will be addressed to combine both these approaches and thus providing a more comprehensive understanding of subsurface pressure conditions, in the present research we systematically investigate the vertical pressure trends using borehole data (mud weights, formation test and drill stem test pressures).

The proposed study is developed in the framework of the FLUIDS Project, funded by the Italian Ministry for Research with the aim at developing and applying an integrated multi-parametric and multi-disciplinary approach to image and track crustal fluids in different environments (e.g., tectonic, exploitation, volcanic). It deals with fluid movements, pore fluid-pressure diffusion and analysis of their correlation with the induced/triggered seismicity.

Moreover, our study focuses on the Irpinia and Sannio area, located in the northern part of the Southern Apennines. The Apennines has been generally explored in the last decades by many researchers to examine the relationship among tectonic processes, fluid movement and seismic

activity (e.g., Di Luccio et al., 2022). Regarding these topics, although many structural and geological aspects of the upper and lower crust of this chain are still unclear (e.g. Improta and Corciulo, 2006), it is overall accepted that the extensional tectonics has a primary role on CO_2 Earth degassing and that CO_2-rich fluids of mantle-origin is distributed in concomitance of the destructive Apennines seismic sequences (e.g., Chiodini et al., 2020 and references therein). The fluids, including CO_2, may contribute to the earthquake preparation, nucleation and evolution.

In the study area, the fold-and-thrust belt was under tectonic compression until the Pleistocene and is currently under extension (e.g., Improta et al., 2003). Moreover, the chain is nowadays the site of groundwater flow, natural gas circulation and seismicity (e.g., Fiorillo et al., 2010; Chiodini, 2014; D'Agostino et al., 2018). In particular, the fluids migrate across the crust, moving downward and upward through the orogenic wedge, whose upper part is composed by foredeep deposits and sediments formed in shallow, transitional, and deep-water environments. These sequences overlap with the carbonates of the Apulian Platform. Gas emissions collected at the Mefitiniella, Mefite, Malvizza and Telese sites testify that gas rises from great depths through the complex geological setting (e.g., Minissale, 2004). Moreover, in 1962 and 1980, two earthquakes of magnitude Mw>6 hit the region (Rovida et al., 2020; 2022), leading to the destruction of several municipalities in the provinces of Benevento and Avellino, and resulting in numerous fatalities, homeless people and extensive damages.

In the current work, 30 exploration wells available on open source (VIDEPI website) and drilled between 1961 and 1982 have been analysed. The pore pressures data were initially extracted from the well profiles, including mud weight and formation test pressures. Subsequently, the obtained pressures were normalized to a hydrostatic profile to better compare the pressure values at varying depths and different sites. Finally, observed hydrostatic and abnormal trends were compared to the fluids found at well sites to verify possible correlations.

Approximately half of the analysed wells identified carbon dioxide levels, either in sandy and calcareous formations across the hole or at the bottom hole reservoirs, such as the carbonates of the Apulian Platform. Since these boreholes allow us to extract pore pressure measurements up to a depth of 6 km, these wells offer a unique opportunity to investigate subsurface pore pressures and their interaction with the different fluid types (groundwater, hydrocarbons, carbon dioxide).

The study unveils that the CO_2 levels found in several wells (e.g., Circello 1 and Benevento 2) within the permeable layers of the Apulian Platform carbonates are in hydrostatic conditions, thus indicating that the storage of CO_2 is not necessarily correlated with the overpressures. Similarly, the CO_2 gas cap found in Monte Forcuso 1 and Monte Forcuso 2 wells is in hydrostatic conditions, thus suggesting that the CO_2 rising to the surface can occur without the generation of overpressures. In addition, moderate to high overpressured gradients are predominantly identified within allochthonous Miocene shaly-rich sequences, including the Irpinia/Sannio Units and the formations of the Rapolla Group, also associated with groundwater-fed levels, as evidenced by Panizza 1 and other wells.

References

Amoroso O., Russo G., De Landro G., Zollo A., Garambois S., Mazzoli S., Parente M., Virieux J.; 2017: From velocity and attenuation tomography to rock physical modeling: Inferences on fluid-driven earthquake processes at the Irpinia fault system in southern Italy. Geophys. Res. Lett., 44, 6752–6760.

Chiodini G., Cardellini C., Di Luccio F., Selva J., Frondini F., Caliro S., Rosiello A., Beddini G., Ventura G.; 2020: Correlation between tectonic CO2 Earth degassing and seismicity is revealed by a 10-year record in the Apennines, Italy. Sci. Adv., 6, eabc2938.

Chiodini G.; 2014: Gas emissions and related hazard in Italy. Mem. Descr. Carta Geol. d'It., XCVI, 189-194. In Italian

D'Agostino N., Silverii F., Amoroso O., Convertito V., Fiorillo F., Ventafridda G., Zollo A.; 2018: Crustal deformation and seismicity modulated by groundwater recharge of karst aquifers. Geophys. Res. Lett., 45, 12, 253–262.

Di Luccio F., Palano M., Chiodini G., Cucci L., Piromallo C., Sparacino F., Ventura G., Improta L. et alii; 2022: Geodynamics, geophysical and geochemical observations, and the role of CO2 degassing in the Apennines. Earth-Science Reviews, 234, 104236.

Fiorillo F., Guadagno F.M.; 2010: Karst spring discharges analysis in relation to drought periods, using SPI. Water Resource Manage, 24:1867-1884.

Improta L., Bonagura M., Capuano P., Iannaccone G.; 2003: An integrated geophysical investigation of the upper crust in the epicentral area of the 1980, Ms=6.9, Irpinia earthquake (Southern Italy). Tectonophysics, 361, 139-169.

Improta L., Corciulo M. (2006): Controlled source nonlinear tomography: A powerful tool to constrain tectonic models of the Southern Apennines orogenic wedge, Italy. *Geology*, 34 (11): 941–944.

Minissale A.; 2004: Origin, transport and discharge of CO2 in central Italy. Earth Sci. Rev. 66, 89–141.

Rovida A., Locati M., Camassi R., Lolli B., Gasperini P.; 2020: The Italian earthquake catalogue CPTI15. Bulletin of Earthquake Engineering, 18(7), 2953-2984.

Rovida A., Locati M., Camassi R., Lolli, B., Gasperini P., Antonucci A.; 2022: Catalogo Parametrico dei Terremoti Italiani (CPTI15), versione 4.0. Istituto Nazionale di Geofisica e Vulcanologia (INGV).

Vannoli P., Martinelli G., Valensise G.; 2021: The Seismotectonic Significance of Geofluids in Italy. Front. Earth Sci., 9:579390.

VIDEPI website, available at: https://www.videpi.com/videpi/videpi.asp. Accessed on 15 December 2023

Zhang J.; 2011: Pore pressure prediction from well logs: methods, modifications, and new approaches. Earth-Science Reviews, 108, 50-67.

Corresponding author: eleonora.vitagliano@ingv.it

The ‘Many’ Seismogenic Sources of the 1706, Mw=6.8, Maiella Earthquake: New Insights from Source Modelling

T. Volatili[1], V. Gironelli[1, 5], L. Luzi[2], P. Galli[3], M. M. C. Carafa[4], E. Tondi[1, 5]

1 Scuola di Scienze e Tecnologie – Sezione di Geologia, Università di Camerino, Italy
2 Istituto Nazionale di Geofisica e Vulcanologia, Milano, Italy
3 Presidenza del Consiglio dei Ministri, Dipartimento della Protezione Civile, Servizio Rischio Sismico - Roma, Italy
4 Istituto Nazionale di Geofisica e Vulcanologia, Sezione di Sismologia e Tettonofisica, L’Aquila, Italy
5 Istituto Nazionale di Geofisica e Vulcanologia, Sezione di Sismologia e Tettonofisica, Camerino, Italy

Introduction

Inner Abruzzi (central Italian Apennines), rank among the highest seismic hazard regions of Italy (Akinci et al., 2009; Petricca et al., 2015). All along the Apennines divide, a well-studied system of SW-dipping normal faults has been active both historically and in recent times, as evidenced by moderate-to-large earthquakes (Mw ≥ 5.5. Galadini and Galli, 2000). The most recent destructive seismic sequence occurred on April 6, 2009, (Mw = 6.3), known as the L’Aquila earthquake.

Following the events of 2009, there has been a growing interest in assessing the seismogenic potential of active faults in this region. Numerous studies have been conducted to identify active and potentially seismogenic structures. However, there are areas like the Maiella Massif, where both historical and instrumental seismicity are elusive, notwithstanding the occurrence of two strong events on November 3, 1706, and September 26, 1933, with Mw ~6.8 and 5.9, respectively (Rovida et al., 2022). According to Galli and Pallone (2019) and the Italian Macroseismic Database (DBMI15; Locati et al., 2022), these earthquakes caused severe damage over a wide area, with maximum epicentral intensities on the Mercalli-Cancani-Sieberg (MCS) scale reaching X-XI and IX, respectively. Despite being labelled as the Maiella earthquakes, the seismogenic structure responsible for these events remains controversial.

Various hypotheses have recently been proposed in the literature regarding the source of the 1706 earthquake. Before mentioning these hypotheses, it is worth noting that Pomposo and Pizzi (2009) have hypothesized that the area east of the Morrone-Porrara fault alignment is undergoing active compression, based on morphotectonic evidence of active anticline growth in the Orsogna area, suggesting a relationship with another strong event of the area (1881, Mw 5.4).

Galli and Pallone (2019), who re-evaluated the macroseismic intensity distribution on the basis of previously unknown historical sources, have suggested the activation of a blind backthrust that developed during Early-Middle Pleistocene in the footwall of the Maiella anticline as the potential

source for both the 1933 and 1706 earthquakes (labelled GALLI19 in Fig. 1). These authors also documented possible surface ruptures that occurred during the 1933 earthquake related with the Caramanico fault, a 26 km-long structure bounding westward the Maiella Massif. Although this surface evidence has been attributed to a likely passive slip of the Caramanico fault (Galli and Pallone 2019) we decided to test it anyway for the sake of completeness (labelled CARAMANICO in Fig. 1).

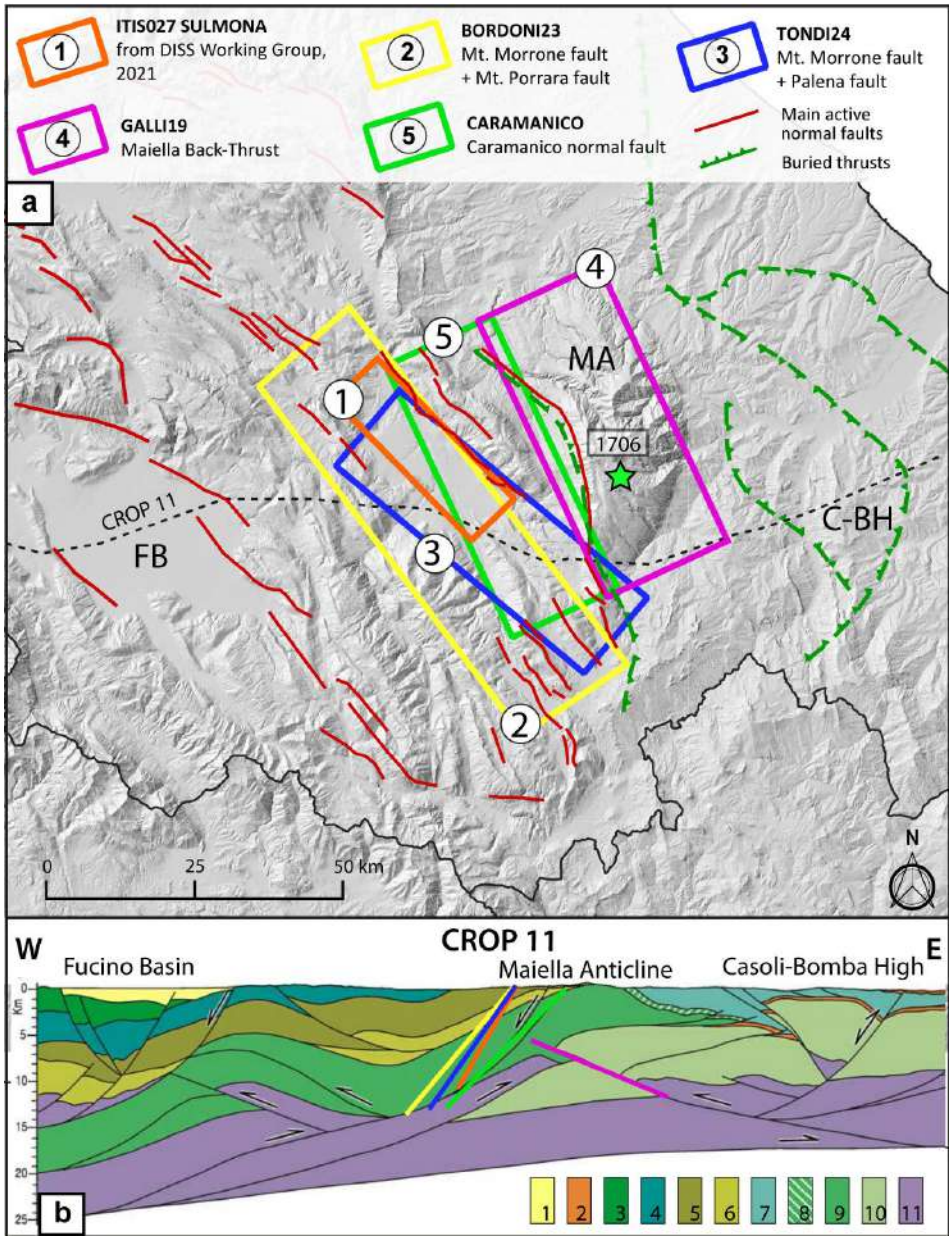

Figure 1. (a) Map showing the main tectonic structures of the study area (Galadini and Galli, 2000; Galli and Pallone, 2019) and the source models adopted for the simulations. (1) Seismogenic source "ITIS027" Sulmona from DISS (DISS Working Group, 2021); (2) Maiella back-thrust from Galli and Pallone (2019) for the 1933 earthquake; (3) Maiella back-thrust calibrated for the 1706 (Mw 6.8) earthquake, and (4) Non-Linear normal fault geometry proposal. (b) part of CROP-11 line interpreted by Patacca et al. (2008): 1, Pliocene-Quaternary continental deposits of intramontane basins; 2, Pliocene marine deposits conformably overlying the Apulia carbonates; 3, Western Marsica-Meta Unit; 4, Mount Genzana unit; 5, Mount Morrone-Porrara unit; 6, Upper Cretaceous-Pliocene Mount Queglia unit; 7, Molise units; 8, Lower Pliocene flysch of Maiella unit; 9, Mesozoic-Tertiary carbonates of Maiella unit; 10, Mesozoic-Tertiary carbonates of Apulia Platform; 11, Paleozoic-Triassic deposits.

Conversely, in the Database of Individual Seismogenic Sources (DISS – DISS Working Group, 2021; Basili et al., 2008) the 1706 earthquake, being the only meaningful seismic event in that area may relate with the largest and proximal individual seismogenic source labelled ITIS027 (see Fig. 1), associated with the Mt. Morrone fault. This consist of a dip-slip structure with surface expression consistent with a maximum magnitude of 6.7±0.1 (Galli et al., 2015), being composed by two major sub-parallel WSW-dipping splays, extending approximately 24 km across the western slope of Mt. Morrone. Lastly, Bordoni et al., (2023) presented a seismic scenario where the synchronous activation of both the Mt. Morrone fault and the Mt. Porrara fault, with a 43 km total fault length at surface and an 806 km2 maximum rupture area, would generate an earthquake consistent with the 1706 (labelled BORDONI23 in Fig. 1).

In this study we provide a comprehensive review of various hypotheses concerning the 1706 seismic source, along with another possible causative structure implying the dip-slip re-activation of the Mt. Morrone fault plus the Palena fault (labelled TONDI24 in Fig.1). As far as the Palena fault, Pizzi et al. (2010) hypothesized its Quaternary activity that, with an almost pure dip-slip kinematics, represents an inherited Pliocene syn-orogenic oblique structure. The results of this study, combined with the development of a shaking scenario, are expected to offer valuable insights to the earthquake geology community involved in studies on seismic risk assessment in this area.

Source Modelling

In our pursuit to identify the most likely source of 1706 Maiella earthquake, based on intensity data, we applied the procedure outlined by Gironelli et al. (2023) and schematised in the workflow in Figure 2. This methodology offers the advantage of testing various potential sources and conducting a quantitative interpretation of the earthquake-fault association.

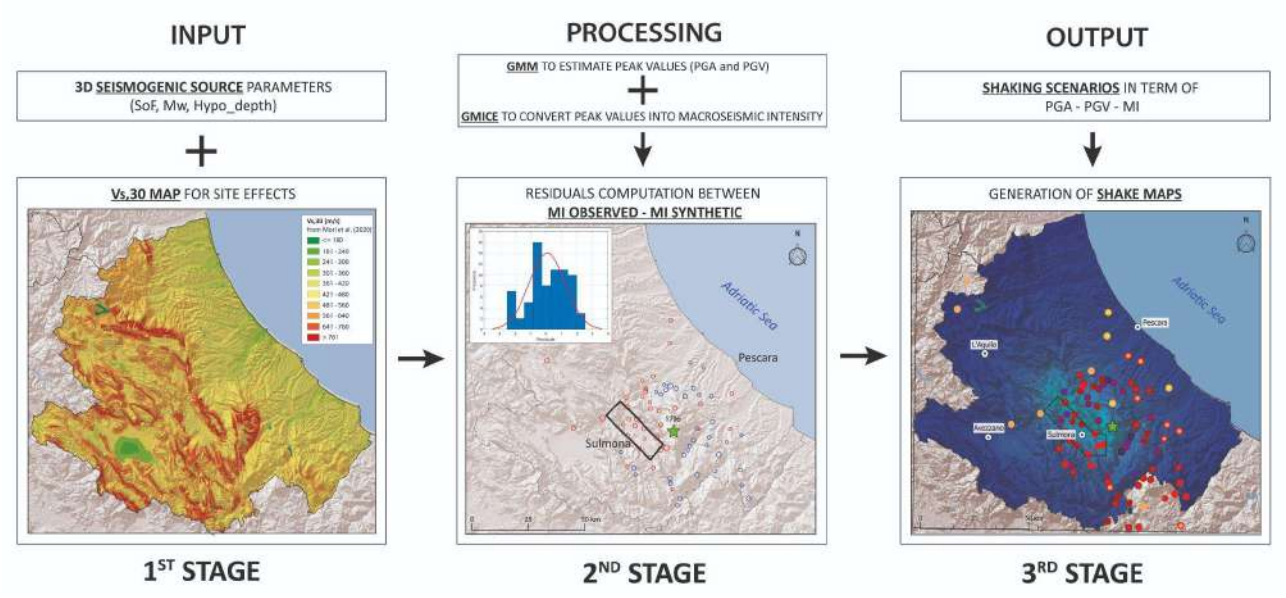

Figure 2. Summary workflow showing the main stages following Gironelli et al., 2023.

The analysis involves the creation of 3D seismogenic source models, considering the available geological and geophysical information. By varying individual source parameters such as dip angle and hypocentral depth, we estimate seismic scenarios in terms of macroseismic intensity. This is achieved by calculating synthetic peak ground motion values, including peak ground acceleration (PGA) and peak ground velocity (PGV), for each point within the 1706 macroseismic field (i.e., site). These peak values are subsequently converted into intensities using empirical relationships. This procedure incorporates site amplification effects into the synthetic ground motion calculations at each site within the macroseismic field. For this purpose, Vs,30 data representative of site effects are obtained from the more recent Vs,30 map proposed as a reference for Italy by Mori et al. (2020).

The determination of the best source model involves assessing the misfit (residuals) between the simulated macroseismic intensities and the observed ones. The accuracy of the simulated macroseismic field in reproducing the real field is evaluated by calculating the residual mean and the root-mean-square error (RMSE). The residual mean is deemed reliable if it is less than 0.1.

Our analysis shows a general fair matching between the synthetic and observed macroseismic field, especially using BORDONI23 and TONDI24 source models. However, the last surface rupture documented by paleoseismological survey in the northwestern sector of the Mt. Morrone fault dates back to the 2nd cent. CE (Galli et al., 2015), with no evidence at all of further activity (i.e., 1706 and 1933 events). Furthermore, the distribution of the macroseismic field, with the highest intensities surrounding the Maiella relief does not support the rupture of a normal fault dipping SW. On the other hand, the distribution of the macroseismic field may be biased by the settlement distribution itself, its characteristics, and relative site effects. In conclusion, it is evident that despite the possibility that this study might shed light on this open issue within the Apennine seismicity, there is still room for discussion and hopefully improvements to better constrain the seismic hazard of this region.

References

Akinci, A., Galadini, F., Pantosti, D., Petersen, M., Malagnini, L., & Perkins, D. (2009). Effect of time dependence on probabilistic seismic-hazard maps and deaggregation for the Central Apennines, Italy. Bulletin of the Seismological Society of America, 99(2A), 585-610.

Basili, R., Valensise, G., Vannoli, P., Burrato, P., Fracassi, U., Mariano, S., ... & Boschi, E. (2008). The Database of Individual Seismogenic Sources (DISS), version 3: summarizing 20 years of research on Italy's earthquake geology. Tectonophysics, 453(1-4), 20-43.

Bordoni, P., Gori, S., Akinci, A., Visini, F., Sgobba, S., Pacor, F., ... & Doglioni, C. (2023). A site-specific earthquake ground response analysis using a fault-based approach and nonlinear modeling: The Case Pente site (Sulmona, Italy). Engineering Geology, 314, 106970.

Galadini, F., & Galli, P. (2000). Active tectonics in the central Apennines (Italy)–input data for seismic hazard assessment. Natural Hazards, 22, 225-268.

Galli, P., Giaccio, B., Peronace, E., & Messina, P. (2015). Holocene paleoearthquakes and early–late pleistocene slip rate on the Sulmona fault (central Apeninnes, Italy). Bulletin of the Seismological Society of America, Vol. 105, No. 1, pp. 1–13, February 2015, doi: 10.1785/0120140029

Galli, P., & Pallone, F. (2019). Reviewing the intensity distribution of the 1933 earthquake (Maiella, Central Italy). Clues on the seismogenic fault. Alpine and Mediterranean Quaternary, 32(2), 93-100.

Gironelli, V., Volatili, T., Luzi, L., Brunelli, G., Zambrano, M., & Tondi, E. (2023). Ground motion simulations of historical earthquakes: the case study of the Fabriano (1741, Mw= 6.1) and Camerino (1799, Mw= 6.1) earthquakes in central Italy. Bulletin of Earthquake Engineering, 21(13), 5809-5830.

Gori, S., Giaccio, B., Galadini, F., Falcucci, E., Messina, P., Sposato, A., & Dramis, F. (2011). Active normal faulting along the Mt. Morrone south-western slopes (central Apennines, Italy). International journal of earth sciences, 100, 157-171.

Locati M., Camassi R., Rovida A., Ercolani E., Bernardini F., Castelli V., Caracciolo C.H., Tertulliani A., Rossi A., Azzaro R., D'Amico S., Antonucci A. (2022). Database Macrosismico Italiano (DBMI15), versione 4.0. Istituto Nazionale di Geofisica e Vulcanologia (INGV).

Mori, F., Mendicelli, A., Moscatelli, M., Romagnoli, G., Peronace, E., & Naso, G. (2020). A new Vs30 map for Italy based on the seismic microzonation dataset. Engineering Geology, 275, 105745.

Patacca, E., Scandone, P., Di Luzio, E., Cavinato, G. P., & Parotto, M. (2008). Structural architecture of the central Apennines: Interpretation of the CROP 11 seismic profile from the Adriatic coast to the orographic divide. Tectonics, 27(3).

Petricca, P., Barba, S., Carminati, E., Doglioni, C., & Riguzzi, F. (2015). Graviquakes in italy. Tectonophysics, 656, 202-214.

Pomposo, G., & Pizzi, A. (2009). Evidenze di tettonica recente ed attiva nel settore esterno sepolto dell'Appennino centrale abruzzese. In Rendiconti online della Società Geologica Italiana (Vol. 5, pp. 176-178). Società Geologica Italiana.

Rovida A., Locati M., Camassi R., Lolli B., Gasperini P., Antonucci A. (2022). Catalogo Parametrico dei Terremoti Italiani (CPTI15), versione 4.0. Istituto Nazionale di Geofisica e Vulcanologia (INGV). https://doi.org/10.13127/CPTI/CPTI15.4

*Corresponding author: tiziano.volatili@unicam.it

Interplay Between Fault Ruptures and Man-Made Structures Related With the 2023 Mw 7.8 and 7.5 Turkey Earthquakes

T. Volatili[1], A. Dall'Asta[2], S. Mazzoli[1], F. Micozzi[2], F. Stimilli[1], G. Valentini[1], M. Tümay[3], B. Aksay[3], A. Beycioğlu[3], E. Tondi[1, 4]

1 School of Science and Technology – Geology Division, University of Camerino, Italy
2 School of Architecture and Design, University of Camerino, Italy
3 Adana Alparslan Türkeş Science and Technology University, Turkey
4 National Institute of Geophysics and Volcanology, Seismology and Tectonophysics Division, Camerino, Italy

The February 6, 2023, earthquake twins, Mw 7.8 and 7.5, which struck Turkey and Syria on February stimulated scientific research on their geological and societal implications. Such destructive events, causing ca. 60'000 confirmed casualties, according to the Disaster and Emergency Management Authority (AFAD), was triggered by the partial re-activation of the Eastern Anatolian fault. Specifically, the southernmost segment of this left-lateral strike-slip structure produced fault ruptures at surface extending for ca. 500 km. Most of such fault expressions, clearly observable even from satellite images, were mapped soon after the mainshocks (Mai et al., 2023; Reitman et al., 2023).

The present study delved into the aftermath of this seismic upheaval: in 7 days of intense field survey (from 04/07/23 to 10/07/23), a total of 334 fault records were collected (Fig. 1) employing a multifaceted approach that combined traditional structural geology surveys with aero photogrammetric techniques. Covering the whole extent of the fault rupture at the surface, this research aimed to elucidate the manifold effects of surface faulting on both natural landscapes and human-built infrastructures and settlements.

Through meticulous structural geology surveys, the study catalogued the surface manifestations of the fault rupture, providing insights into the characteristics and behaviours of the ruptured fault segments. This in-depth analysis facilitated a comprehensive understanding of fault dynamics and their implications for seismic hazard assessments in the region. Moreover, the integration of aero photogrammetric surveys significantly expanded the scope and precision of the investigation. High-resolution aerial imagery enabled detailed mapping and three-dimensional reconstruction of fault rupture in key-zones. This comprehensive visualization proved instrumental in discerning fault displacement patterns and delineating the most susceptible areas to seismic activity.

Figure 1. a) spatial distribution of collected data from field (b) and drone (c) surveys. Surface ruptures highlighted in red.

One of the focal points of this study revolved around evaluating the impact of surface faulting on man-made structures and infrastructural facilities. Through meticulous field assessments and detailed analyses, the research documented the structural damage incurred by buildings, roads, bridges, and other vital infrastructures. By correlating the observed damage patterns with fault characteristics and ground motions, valuable insights were gleaned into the vulnerability of various structures (i.e., public, and private buildings) to seismic events of this magnitude. The findings of this study offer contributions to the fields of seismology, structural geology, and earthquake engineering. By elucidating the complex interactions between surface faulting and infrastructure vulnerability, the research provides a robust foundation for enhancing seismic risk assessments, informing urban planning strategies, and bolstering disaster preparedness and mitigation efforts in earthquake-prone regions.

In summary, this comprehensive investigation, blending traditional structural geology surveys with advanced aero photogrammetric techniques, presents a holistic understanding of the M7.8 and 7.5 Turkey earthquakes surface rupture effects. The implications of this study extend far beyond understanding the geological aspects, offering insights into the intricate interplay between seismic

events and the built environment, thus paving the way for more resilient and earthquake-resistant buildings and infrastructures in vulnerable regions worldwide.

References

Mai, P. Martin; Aspiotis, Theodoros; Aquib, Tariq Anwar; Cano, Eduardo Valero; Castro-Cruz, David; Espindola-Carmona, Armando; Li, Bo; Li, Xing; Liu, Jihong; Matrau, Rémi; Nobile, Adriano; Palgunadi, Kadek Hendrawan; Ribot, Matthieu; Parisi, Laura; Suhendi, Cahli; Tang, Yuxiang; Yalcin, Bora; Klinger, Yann; Jónsson, Sigurjón (2023). "The Destructive Earthquake Doublet of 6 February 2023 in South-Central Türkiye and Northwestern Syria: Initial Observations and Analyses". The Seismic Record. 3 (2): 105–115. doi:10.1785/0320230007

Reitman, Nadine G, Richard W. Briggs, William D. Barnhart, Jessica A. Thompson Jobe, Christopher B. DuRoss, Alexandra E. Hatem, Ryan D. Gold, John D. Mejstrik, and Sinan Akçiz (2023) Preliminary fault rupture mapping of the 2023 M7.8 and M7.5 Türkiye Earthquakes. DOI: https://doi.org/10.5066/P985I7U2

Corresponding author: tiziano.volatili@unicam.it

The role of long-range correlations and memory in earthquake occurrence

D. Zaccagnino[1*], L. Telesca[2], C. Doglioni[1,3]

[1] Sapienza University, Earth Sciences Department, Rome, Italy
[2] Institute of Methodologies for Environmental Analysis, National Research Council, Tito, Italy
[3] Istituto Nazionale di Geofisica e Vulcanologia (INGV), Rome, Italy.

Seismicity occurs because of strain accumulation in the brittle crust due to the action of tectonic forces. However, this background process is just one of numerous ones affecting earthquake occurrence. In the long run it controls the frequency of large events (Neely et al., 2023); conversely, at our time scales it is likely one of the less impactful. The spatial and temporal evolution of seismic sequences has been proposed to be driven by fluid migration and frictional instability and to be affected by stress perturbations as well as anthropic activities, rheology, structural properties of fault systems and by the tectonic regime (e.g., Rice & Cocco, 2007; Ellsworth, 2013; Ross & al., 2017). Consequently, several empirical relationships have been found connecting properties of seismicity with geophysical observables (pore pressure, differential stress, static friction etc.). We suggest that local variability of some routinely investigated parameters can be clarified considering few all-encompassing physical principles instead of advocating several hardly testable physical mechanisms. To provide an observational example, we analyse a high-definition regional seismic catalogue of seismicity in Central Italy (Tan et al., 2021). We identify a chain of relationships, starting with the properties of inherited structures and tectonic stress gradients directly affecting the fractal properties of fault systems, which, in turn, have an impact on the frequency-magnitude scaling of earthquakes. It produces implications for the duration of seismic sequences, complexity of the seismogenic source and the composition of moment tensors (Zaccagnino & Doglioni, 2022). Our approach has the advantage to be valid regardless of the specific rheology, lithology, tectonic setting, and state of stress. In this regard, we guess that such connections between seismicity and structural properties of fault systems are universal, being due to the action of feedback mechanisms and memory processes.

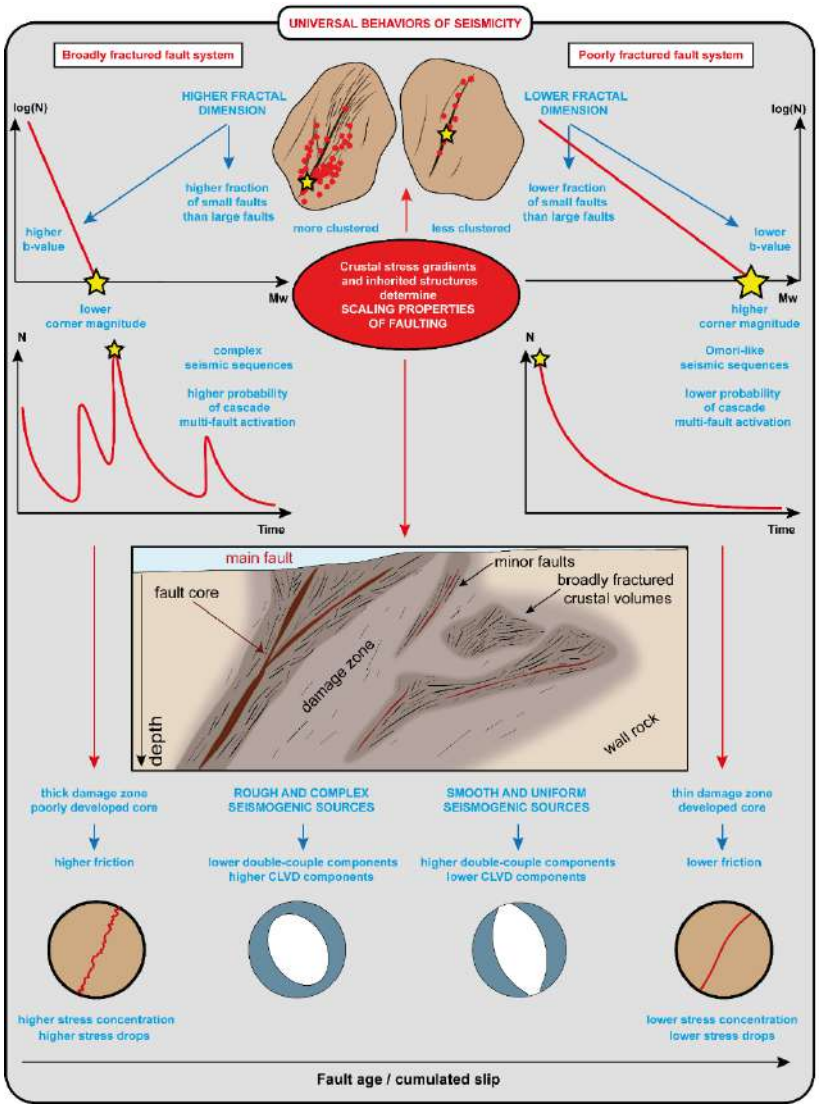

Fig. 1 - Universal properties of seismicity. Crustal stress gradients and inherited structures determine the scaling properties of seismicity, hence, the spatial organization of faults and fractures and its scaling properties. Higher fractal dimension of fractures and hypocenters produces strongly clustered seismicity in space with steeper Gutenberg-Richter law and lower corner magnitudes; hence, lower maximum magnitude and vice versa. Moreover, more developed fracturing with thicker damage zones and complex seismogenic sources promote stress accumulation because of higher internal friction within the boundary interface and, also, larger stress drops (magnitude fixed) during seismic events. At last, the interaction of fault planes with different spatial orientation is more likely in complex fault systems, which decreases the double-couple component of moment tensors of earthquakes.

References

Ellsworth W. L.; 2013: *Injection-induced earthquakes*. Science, 341(6142), 1225942.

Neely J. S., Salditch L., Spencer B. D. and Stein S.; 2023: *A More Realistic Earthquake Probability Model Using Long-Term Fault Memory*. Bull. Seismol. Soc. Am., 113(2), 843-855.

Rice J. R. and Cocco M.; 2007: *Seismic fault rheology and earthquake dynamics.* Tectonic faults: Agents of change on a dynamic earth, 99-137.

Ross Z. E., Hauksson E. and Ben-Zion, Y.; 2017: *Abundant off-fault seismicity and orthogonal structures in the San Jacinto fault zone*. Sci. Adv., 3(3), e1601946.

Tan Y. J., Waldhauser F., Ellsworth W. L., Zhang M., Zhu W., Michele M., ... and Segou M.; 2021: *Machine-learning-based high-resolution earthquake catalog reveals how complex fault structures were activated during the 2016–2017 Central Italy sequence*. The Seismic Record, 1(1), 11-19.

Zaccagnino D. and Doglioni C.; 2022: *The impact of faulting complexity and type on earthquake rupture dynamics*. Commun. Earth Environ., 3(1), 258.

Corresponding author: davide.zaccagnino@uniroma1.it

The 1783 Calabria earthquake sequence: a review of the coseismic effects on the natural environment

C. Zei[1,2], C. Ciuccarelli[1], M.G. Bianchi[1], G. Tarabusi[1], D. Mariotti[1]

[1] Istituto Nazionale di Geofisica e Vulcanologia, Italy
[2] Università degli Studi di Ferrara - Dipartimento di Fisica e Scienze della Terra, Italy

The primary goal of the initial versions of the CFTI (Boschi et al. 1995, 1997 and 2000) was to define the effects of strong earthquakes on the built environment. Consequently, the effects on the natural environment (EE) were not extensively studied but were considered as additional information.

In recent years, starting from the CFTI5med (Guidoboni et al, 2018 and 2019), special attention has been devoted to the retrieval and analysis of the EE.

Here we present a review of the effects on the natural environment of the 1783 Calabria earthquake sequence, starting from the data already included in the CFTI database.

The earthquake sequence began on 5 February 1783 and lasted for over three years, featuring five main shocks with a magnitude between 5.9 and 7.0 (5 February, 6 February, 7 February, 1 March, and 28 March 1783) and several hundred smaller shocks, which had cumulative devastating effects over an area of several thousand square kilometers. Within two months, from 5 February to 28 March, the earthquake activity migrated from the foothills of the Aspromonte to the area between the Golfo di Sant'Eufemia and the Golfo di Squillace.

Before this review, for the 1783 earthquake sequence the CFTI5med reported 222 EE, grouped into 14 different categories based on the observed natural phenomena. The most frequently observed typologies were landslides (67 observations), ground cracks (57 observations), and water effects (38). Only 2% of the 222 EE were assigned to a specific earthquake of the sequence. Other recent reviews (Cucci 2022) pointed attention to specific types of effects instead, in this work, we collected all the effects on the natural environment reported.

We focused on the review of 22 historical sources coeval with the earthquake, already archived in the CFTI5Med. These sources are the most reliable for the sequence, as many such as Vivenzio (1783) and Sarconi (1784), describe the effects on the natural environment after their survey of the epicentral area.

The CFTIvisual dataset (Bianchi et al., 2022) plays a central role in this work as it supplies over thirty historical original drawings that can be used to identify and locate the EE: indeed, they show

the coseismic effects in the territory as it appeared at the time, including cracks, landslides, effects on surface waters, liquefactions, appearance of ponds, etc. The detailed visual representation of the effects allowed for a better attribution to the correct effect category, compared to only consulting historical sources. Moreover, since in many cases it was possible to georeference the drawings accurately, we were able to improve the location of the effects.

As an in-depth part of this work, we also conducted a specific analysis of the Historical Earthquake-Induced Landslides (HEILs), in order to include new data in the CFTI Landslide (Zei et al., 2023). Our goal was to achieve a more accurate location and definition of the slope movement types of the HEILs, whenever the descriptions of the historical sources or drawings allowed it, through a geographical comparison with data of different origins. When possible, these effects were associated with the individual landslides reported in the IFFI database (https://www.progettoiffi.isprambiente.it/).

Our review led to a 120% increase in the pre-review number of effects, totalling 494 elements. Over 67% of the effects are now connected to a specific earthquake in the sequence, compared to the previous 2%.

The most numerous effects are those affecting the ground (69% of the total); within this class, the more common are landslides (59% of ground effects). Furthermore, the review returned effects related to seven EE categories for which there were no data (figure 1).

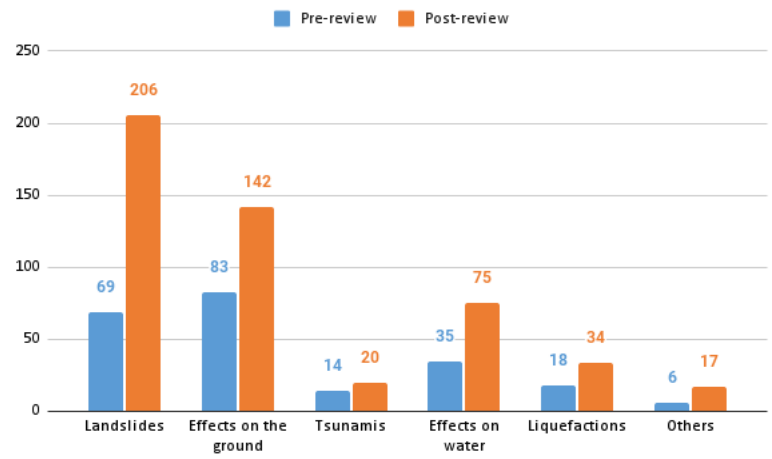

Fig.1 Pre- and post-review effects on the natural environment collected for the 1783 Calabria earthquake sequence.

Regarding HEILs, 36% of them have excellent/good location accuracy. All earthquake-induced landslides, along with their improvements in number, movement type and location, are now collected into the CFTILandslides database (Zei et al., 2023).

Acknowledgments

Part of the activities have been supported by a grant from Italy's Presidenza del Consiglio dei Ministri-Dipartimento della Protezione Civile. Nevertheless, the views and conclusions reported are the sole responsibility of the authors, and should not be interpreted as necessarily representing official policies, either expressed or implied, of the Dipartimento della Protezione Civile.

References

Bianchi M.G., Tarabusi G., Ciuccarelli C., Maresci M., Baranello S., Taccone R.C., Ferrari G.; 2022: *CFTIvisual, Atlante delle fonti visive dei terremoti italiani*. Istituto Nazionale di Geofisica e Vulcanologia (INGV). https://doi.org/10.13127/cfti/visual

Boschi E., Guidoboni E., Ferrari G., Mariotti D., Valensise G., Gasperini P. (eds); 200: *Catalogue of Strong Italian Earthquakes from 461 B.C. to 1997*. Annali di Geofisica, 43, 4, 609-868.

Boschi E., Ferrari G., Gasperini P., Guidoboni E., Smriglio G., Valensise G. (eds); 1995: *Catalogo dei forti terremoti in Italia dal 461 a.C. al 1980*. ING-SGA, Bologna, 970 pp.

Boschi E., Guidoboni E., Ferrari G., Valensise G. and Gasperini P. (eds.); 1997: *Catalogo dei forti terremoti in Italia dal 461 a.C. al 1990*, vol. 2. ING-SGA, Bologna, 644 pp.

Cucci L.; 2022: *NW-dipping versus SE-dipping causative faults of the 1783 M7.1 Southern Calabria (Italy) earthquake: The contribution from the analysis of the coseismic hydrological changes.* Front. Earth Sci. 10:987731. doi:10.3389/feart.2022.987731

Guidoboni E., Ferrari G., Mariotti D., Comastri A., Tarabusi G., Sgattoni G., Valensise G.; 2018: *CFTI5Med, Catalogo dei Forti Terremoti in Italia (461 a.C.-1997) e nell'area Mediterranea (760 a.C.-1500)*. Istituto Nazionale di Geofisica e Vulcanologia (INGV). https://doi.org/10.6092/ingv.it-cfti5

Guidoboni E., Ferrari G., Tarabusi G., Sgattoni G., Comastri A., Mariotti D., Ciuccarelli C., Bianchi M.G., Valensise G.; 2019: *CFTI5Med, the new release of the catalogue of strong earthquakes in Italy and in the Mediterranean area*, Scientific Data 6, Article number: 80. https://doi.org/10.1038/s41597-019-0091-9

Istituto Superiore per la Protezione e la Ricerca Ambientale (ISPRA); *IFFI, Inventario dei Fenomeni Franosi in Italia.* https://www.progettoiffi.isprambiente.it/

Sarconi M.; 1784: *Istoria de' fenomeni del tremoto avvenuto nelle Calabrie, e nel Valdemone nell'anno 1783 posta in luce dalla Reale Accademia delle Scienze e delle Belle Lettere di Napoli*, Napoli.

Tarabusi G., Ferrari G., Ciuccarelli C., Bianchi M.G., Sgattoni G., Comastri A., Mariotti D., Valensise G., Guidoboni E.; 2020: *CFTILab, Laboratorio Avanzato di Sismologia Storica. Istituto Nazionale di Geofisica e Vulcanologia (INGV)*. https://doi.org/10.13127/CFTI/CFTILAB

Vivenzio G.; 1783: *Istoria e teoria de' tremuoti in generale ed in particolare di quelli della Calabria, e di Messina del MDCCLXXXIII,* Napoli.

Zei C., Tarabusi G., Ciuccarelli C., Mariotti D., Baranello S., Sgattoni G., Burrato P., CFTI working Group; 2023: *A new database of historical earthquake-induced landslides in Italy*, 41st National Conference of the GNGTS, Bologna https://gngts.ogs.it/atti/GNGTS2023/HTML/212/

Corresponding author: caterina.zei@ingv.it

Session 1.2

Volcanoes and geothermal fields

GNGTS 2024

SEISMICITY, VOLCANOES, DATA AND MODELS

Session 1.2

Volcanoes and geothermal fields

Convenors of the session:
Mimmo Palano (INGV) – mimmo.palano@ingv.it
Francesca Forni (UniMI) – francesca.forni@unimi.it

- **Geophysical imaging**
- **Geochemical features**
- **Petrological data and analysis**
- **Field observations**
- **Remote sensing observation**
- **Geodetic data**
- **Hyperspectral imaging**
- **Volcanic unrest**
- **Effusive/explosive activity**
- **Models and inversion techniques**
- **Monitoring**
- **Hazard**

Volcanoes and geothermal fields are the best-known natural expression of the Earth's internal heat, which is mainly caused by the radioactive decay of isotopes in the mantle and the crust. The volcanic activity has played a fundamental role in the Earth's atmosphere and life development and represents the most important source of geothermal energy. Most of our current knowledge about volcanoes and geothermal fields comes from geological, petrological, geochemical and geophysical data and observations mainly collected in the last decades. All these data, along with extensive analysis and modelling, have provided useful information about the structure and geometry of magma storage in the crust and transfer of magmas and geothermal fluids in volcanic or geothermal areas.

Contributes including both observational and theoretical studies as well as summarizing the state-of-the-art and new research directions are also welcome. Moreover, contributes focusing on the ongoing crisis at the Phlegraean Fields are of relevant interest.

An AI-based emulator to enhance SPH lava flows simulations

E. Amato[1,2], V. Zago[1], C. Del Negro[1]

[1] *Istituto Nazionale di Geofisica e Vulcanologia, Osservatorio Etneo, Catania, Italy*

[2] *Department of Mathematics and Computer Science, University of Palermo, Palermo, Italy*

Lava flows are complex fluids, exhibiting non-Newtonian rheology with temperature-dependent viscosity and phase transition, capable of overcoming barriers and forming channels and tunnels (Cordonnier et al., 2016). While lava flows are generally not hazardous to nearby populations due to their slow velocities, their passage through towns can cause complete destruction. Therefore, reliable predictions of the areas likely to be inundated by lava flows are of obvious interest to hazard managers during a volcanic eruption (Del Negro et al., 2020). The main factors that govern lava-flow length include the discharge rate of lava at its vent, the lava composition, eruption temperature, cooling rate and the ground topography over which the lava flows. As a result, numerical simulations that consider the key factors influencing the extent of lava flow propagation are crucial for forecasting effusive scenarios (Del Negro et al., 2016). Due to the complex physics of volcanic phenomena and the unique characteristics of lava, mathematical models can assist in simulating the evolution of lava, providing accurate predictions of the spatio-temporal dynamics of the fluid. These kinds of simulations constitute a challenge for Computational Fluid Dynamics (CFD) (Anderson and Wendt, 1992).

Smoothed Particle Hydrodynamics (SPH) (Monaghan, 2005) is a potent CFD method particularly suited for simulating lava flows (Zago et al., 2017, 2018). It is a Lagrangian mesh-free numerical method based on a discrete approximation of the Navier-Stokes equations. It is a particle-based method, where the fluid is discretized using particles, and it has the capability to handle specific fluid details, such as viscous and thermal effects. In addition, it is parallelizable and executable on Graphics Processing Units (GPU), thereby accelerating simulations. However, SPH simulations still require extended run times and substantial computational resources, typically taking weeks to obtain a few minutes of simulation. This poses challenges for achieving real-time applications, especially in the context of volcanic hazard monitoring. While speed-ups of the simulations can be achieved by simplifying the model or increasing computational resources, a simplified version of the model may not capture the complex physical dynamics present in real world applications.

These limitations can be addressed by introducing the use of Artificial Intelligence (AI) (Goodfellow et al. 2016, Bonaccorso, 2017) to reduce the required computation. The combination of CFD and AI allows for the enhancement of fluid modeling performance and the extension of functionalities (Bortnik and Camporeale, 2021). AI algorithms can be trained on SPH simulated data to rapidly learn the behavior of the CFD reference model. Models of this nature are referred to as emulators

(Kasim et al., 2021). Specifically, an emulator is a model where AI algorithms complement the equation-based mathematical representation of physics. The emulator learns from CFD simulations how to reproduce the CFD reference model, enabling the solution of fluid dynamics problems in shorter times (Zago et al., 2023, Amato, 2023). While Eulerian methods have been extensively integrated with AI, providing high-fidelity and reliable results (*e.g.,* DENSE for weather prediction (Kasim et al., 2021)); the combination of AI and Lagrangian methods remains less consolidated.

Here, we introduce an AI-based emulator designed for a SPH model. This emulator, based on an Artificial Neural Network (ANN), is trained using SPH simulations of complex fluids, including viscous and thermal components, such as lava. It successfully replicates the underlying physical laws and accurately predicts their spatio-temporal behavior. To ensure the trustworthiness of the emulator results, it is crucial to validate its prediction ability and assess its generalization capability beyond the conditions encountered during the training phase. To achieve this, we conducted validation using benchmark tests representative of lava flows, characterized by high viscosity and temperature-dependent viscosities. We also tested the emulator's capacity to reproduce problems and settings with varying levels of complexity. The emulator results were then compared with the corresponding SPH simulations, demonstrating the model's good performance and highlighting its reliability and generalizability.

References:

Amato, E.; 2023: How a CFD Emulator Can Resolve the Boundary Conditions in a Viscous Flow. IEICE Proceedings Series, 76(B4L-42).

Anderson, J. D., & Wendt, J.; 1995: Computational fluid dynamics (Vol. 206, p. 332). New York: McGraw-hill.

Bonaccorso, G.; 2017: Machine learning algorithms. Packt Publishing Ltd.

Bortnik, J., & Camporeale, E.; 2021, December: Ten ways to apply machine learning in the Earth and space sciences. In AGU Fall Meeting Abstracts (Vol. 2021, pp. IN12A-06).

Cordonnier, B., Lev, E., & Garel, F.; 2016: Benchmarking lava-flow models. Geological Society, London, Special Publications, 426(1), 425-445.

Del Negro, C., Cappello, A., Bilotta, G., Ganci, G., Hérault, A., & Zago, V.; 2020: Living at the edge of an active volcano: Risk from lava flows on Mt. Etna. Bulletin, 132(7-8), 1615-1625.

Del Negro, C., Cappello, A., & Ganci, G.; 2016: Quantifying lava flow hazards in response to effusive eruption. Bulletin, 128(5-6), 752-763.

Goodfellow, I., Bengio, Y., & Courville, A.; 2016: Deep learning. MIT press.

Kasim, M. F., Watson-Parris, D., Deaconu, L., Oliver, S., Hatfield, P., Froula, D. H., ... & Vinko, S. M.; 2021: Building high accuracy emulators for scientific simulations with deep neural architecture search. Machine Learning: Science and Technology, 3(1), 015013.

Monaghan, J. J.; 2005: Smoothed particle hydrodynamics. Reports on progress in physics, 68(8), 1703.

Zago, V., Amato, E., Cariello, S., Corradino, C., Torrisi, F., & Del Negro, C.; 2023: On Artificial Intelligence-based emulators of physical models to forecast the evolution of lava flows (No. EGU23-16305). Copernicus Meetings.

Zago, V., Bilotta, G., Cappello, A., Dalrymple, R., Fortuna, L., Ganci, G., ... & Del Negro, C.; 2017: Simulating complex fluids with smoothed particle hydrodynamics. Annals of Geophysics.

Zago, V., Bilotta, G., Hérault, A., Dalrymple, R. A., Fortuna, L., Cappello, A., ... & Del Negro, C.; 2018: Semi-implicit 3D SPH on GPU for lava flows. Journal of computational physics, 375, 854-870.

Corresponding Author: eleonora.amato@ingv.it

Imaging the North-South deformation through the application of potential theory to InSAR measurements

A. Barone[1], P. Mastro[1], A. Pepe[1], M. Fedi[2], P. Tizzani[1], R. Castaldo[1]

[1] Istituto per il Rilevamento Elettromagnetico dell'Ambiente (IREA), Consiglio Nazionale delle Ricerche (CNR), Napoli, Italia.
[2] Dipartimento di Scienze della Terra, dell'Ambiente e delle Risorse (DiSTAR), Università degli Studi di Napoli Federico II, Napoli, Italia.

Synthetic Aperture Radar Interferometry (InSAR) is a well-established technique for monitoring and modeling the ground deformation field in volcanic areas and geothermal fields. Specifically, when SAR images are acquired along both the ascending and descending satellites orbits, the retrieval of the East-West (E-W) and vertical components of the related three-dimensional (3D) ground deformation field is conceivable; the North-South (N-S) one is usually not available and different techniques have been proposed to solve this task. However, the resolutions and accuracies of these retrieved measurements are not always satisfactory.

Here, we show a new approach for the retrieval of the N-S component and the reconstruction of the 3D ground deformation field in volcanic frameworks. The proposed methodology is based on the theory of the potential functions and the integral transforms of potential fields. We test our workflow on synthetic deformation datasets computed according to the commonly used analytic volcanic deformation sources (i.e., Mogi's, Okada's and Yang's models). The results show that the proposed technique allows the retrieval of the N-S deformation with negligible errors with respect to the expected one.

We then consider this approach to reconstruct the 3D ground deformation field that occurred at Sierra Negra volcano (Galapagos Islands, Ecuador) during the 2017 – 2018.5 unrest, which has led to the eruption. The comparison with GNSS data shows that we are able to image the pre-eruptive N-S deformation for this volcano with a mean error of about 5%, which is a surprising result for this kind of application.

The next step of this study is the modeling of the volcanic deformation sources through the use of the retrieved 3D ground deformation field and showing the impact in the framework of the ambiguity solving.

Corresponding author: barone.a@irea.cnr.it

STUDY OF ETNA LAVA FLOW DYNAMICS USING SAR AND OPTICAL SATELLITE DATA AND APPLICABILITY OF THE APPROACH IN OTHER VOLCANIC SETTINGS

L. Beccaro[1], E. Ferrentino[1], M. Albano[1], C. Tolomei[1], C. Spinetti[1], G. Pezzo[1], M. Palano[2], C. Chiarabba[1]

[1] Istituto Nazionale di Geofisica e Vulcanologia, Rome, Italy

[2] Istituto Nazionale di Geofisica e Vulcanologia, Catania, Italy

Introduction

The study of lava flows, among the most relevant products of volcanic activity, is definitely a topic for further study, being one of the main causes of displacement of volcanic edifices and therefore a relevant phenomenon to be considered for the proper study of the hazard associated with volcanic activity.

In this work, aiming at the characterization of the dynamics of the Mt. Etna volcano (Southern Italy) lava flows emplaced during the last decade (Figure 1 – left panel), we adopted a multidisciplinary approach comprising the processing of optical and radar satellite data through different remote sensing techniques. Long stacks of Synthetic Aperture Radar (SAR) data, acquired during Sentinel-1 (S1) satellite mission, were processed with the Small Baseline Subset (SBAS) SAR Interferometry (InSAR) technique to study the ground displacements evolution before (January 2016 – December 2018) and after (January 2019 – July 2021) the 24 December 2018 eruption. The validation of the InSAR results was performed by comparing the displacement time series (DTS) with GNSS measurements at some continuous stations located on the Mt. Etna edifice (Figure 1 – left panel). Then, Sentinel-2 (S2) optical data allowed us to identify the lava flows boundaries emplaced during December 2018 and May 2019 paroxysms. The subtraction of Digital Elevation Models (DEMs), generated through the application of the stereo radargrammetry technique to high-resolution COSMO-SkyMed (CSK) data, permitted to estimate the topographic changes caused by the lava emplaced during the aforementioned events. Results allowed the establishment of the influence that the physical mechanisms have on the observed motion, suggesting that thermal contraction of the lava body, viscous compaction of the substrate, and downslope sliding induce significant volcanic ground displacements, acting in different time periods and topographic conditions.

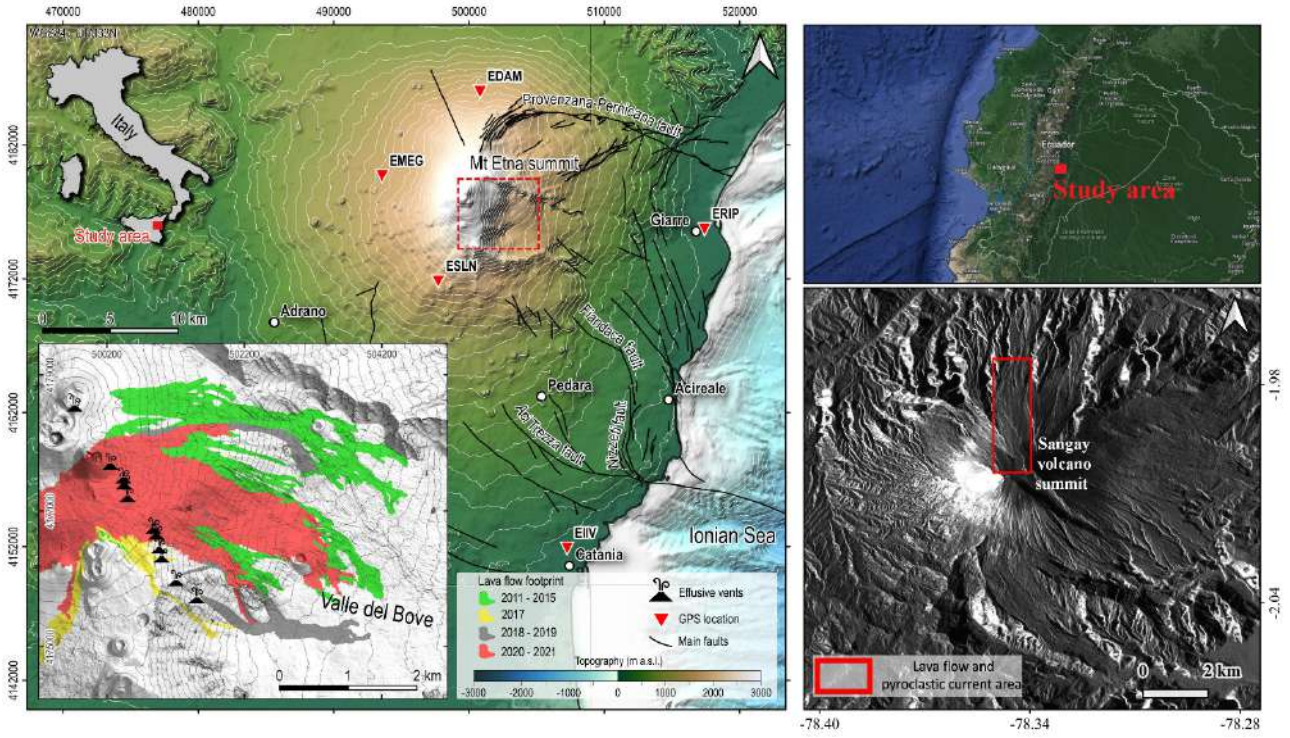

Figure 1 – The left panel shows the Etna volcano study area overview (from Beccaro et al., 2023). Black segments indicate the main tectonic structures, while the red triangles indicate the location of the selected GNSS stations used for InSAR results validation purposes. The dashed red rectangle delineates the study area zoomed in the inset panel where past (2011-2017) and recent (2018-2021) lava flow footprints are shown (data for the pre-2015 period are available from the Etna Observatory geoportal at http://geodb.ct.ingv.it/geoportale/; data for the 2017 and 2020-2021 period are available from Ganci et al. (2023) and De Beni et al. (2021)). The upper right panel shows the Sangay volcano study area location inside Ecuador country (from Google Maps), instead the lower right panel shows a Sentinel-1 amplitude image of the Sangay volcano with the area affected by the pyroclastic current and the lava flow emplaced at the end of 2021 (Hidalgo et al., 2022) and investigated in this work.

The applicability of the approach used for studying the dynamics of Etna lava flows was tested on an additional active andesitic stratovolcano, namely Sangay, located in Ecuador (Figure 1 – right panel). We applied the SBAS InSAR method to retrieve the ground displacements on the Sangay volcano from June 2021 to August 2023. Unfortunately, in this case, the lack of adequate (i.e., with low cloud cover) Sentinel-2 optical data and suitable (i.e., with sufficiently different angles of incidence) Cosmo-SkyMed data did not allow for delineating the boundaries of emplaced lava flow and generating DEMs to evaluate the lava body height. Therefore, aiming to correlate peculiar behaviors evidenced by the InSAR DTS with volcanic phenomena emitted during the investigated time period, i.e., lava flows and pyroclastic currents, we used a polarimetric change detection technique that exploits SAR data set collected before and after the event. Preliminary results made it possible to correlate the peculiar subsidence trend visible on the northern flank of the volcano with the pyroclastic current emitted on November 28, 2021.

Overview of the methods

Satellite Mission	Case Study	Methods	Time Interval	Products	Aim
Sentinel-1	Etna volcano	Small Baseline Subset InSAR approach	Before [Jan 2016 – Dec 2018] and after [Jan 2019 – Jul 2021] the 2018 eruption	Ground displacement maps & displacement time series	Displacements assessment on the entire volcano & displacements evolution study at the lava flows area
	Sangay volcano		Jun 2021 – Aug 2023		
		Polarimetric change detection approach	Before [Nov 2021] and after [Dec 2021] the eruption	Change detection map	Detection of lava flow and pyroclastic current phenomena
Cosmo-SkyMed	Etna volcano	Stereo radargrammetry technique	Before [Jun 2016] and after [Jul 2019] the 2018 eruption	Digital Elevation Models (DEM)	DEM difference analysis for estimating the topographic changes caused by the lava emplacement
Sentinel-2	Etna volcano	Visual inspection & reflectance analysis	December 2018 & May 2019	Lava flow boundaries vector files	Extension retrieval of the lava flows fields

Results

Figure 2 shows the main results obtained for the Etna case study. Displacement maps before the 24 December 2018 eruption (T1 period: January 2016 - December 2018) show general inflation reaching 7 cm/yr at summit areas. Eastward and westward movements are recorded along the eastern and western flanks, respectively. Instead, after the December event (T2 period: January 2019 - July 2021) we observe that the summit inflation decreases the spatial extent and localized patches of subsidence occur inside the Valle del Bove depression. Also, we note a seaward

acceleration of the eastern flank confined to the main tectonic features. The Etna summit blow-up exposes in detail the Valle del Bove area which accommodated the lava flows studied here in detail through the DTS analysis and the resultant ground displacement vector computation. This latter at the 2018 - 2019 lava flow area shows a contractional behavior typical of the cooling of young lava flows, suggesting that the thermal lava contraction is the main deformation cause. Instead, the comparable amplitude of subsidence and eastward motion for the overlapping portion of 2011 - 2015 and August 2020 - July 2021 lava flows, suggests that the combined effect of old lavas load and recent lavas thermal cooling should be taken into account. Finally, DTS in the T1 period highlight clear uplift and eastward trends related to volcanic inflation, except for older lava flow where the global uplift is masked by subsidence related to the existing lava flows load on the substrate. DTS executed for the T2 period exhibit subsidence and eastward trends that accelerate after the emplacement of new lava flows. These trends contrast only with the cyclic vertical oscillations recorded outside lava fields, reflecting Etna's breathing process.

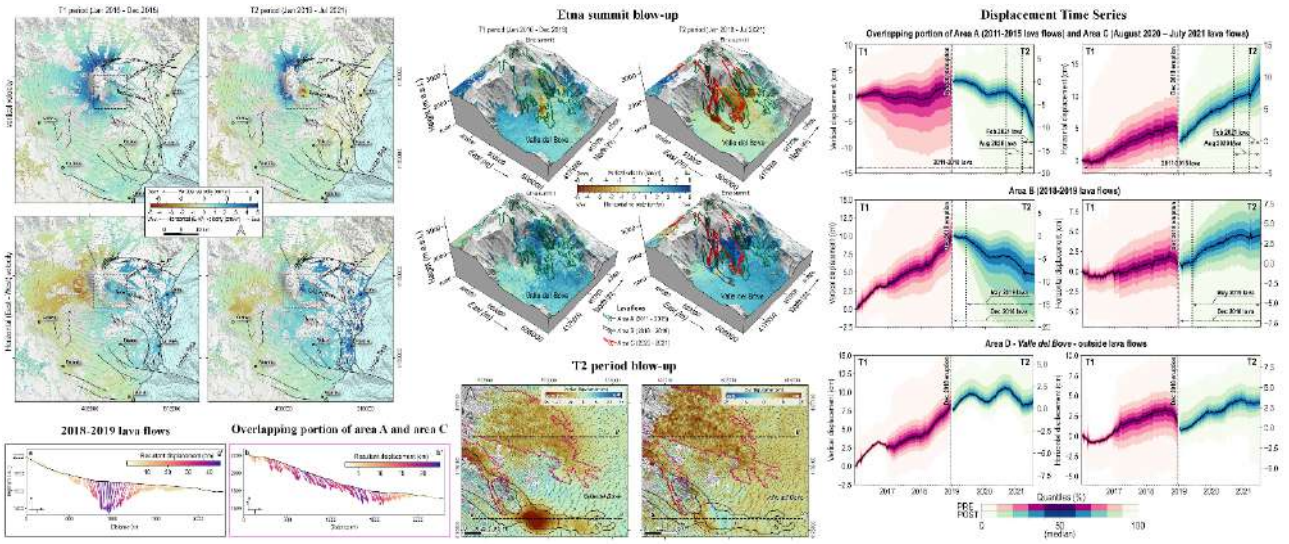

Figure 2 – Main outcomes for the Etna volcano area. From left to right: ground displacement maps, resultant ground displacement vectors for the indicated areas within the figure, and displacement time series.

Figure 3 shows the preliminary results of the Sangay volcano case study. Displacement maps show mainly westward and eastward directed movements of the western and eastern slopes, respectively. In addition, on the western flank of the volcano, clear inflation can be seen, which contrasts with the subsidence recorded on the northern and southeastern flanks. The time series performed along the N flank of the volcano, at the point indicated by the black triangle in the vertical displacement map visible in Figure 3, shows a clear subsidence since early December 2021. Using radar signal intensity variation analysis, it was possible to verify that the behavior can be associated with the cooling of the pyroclastic flow generated on November 28, 2021.

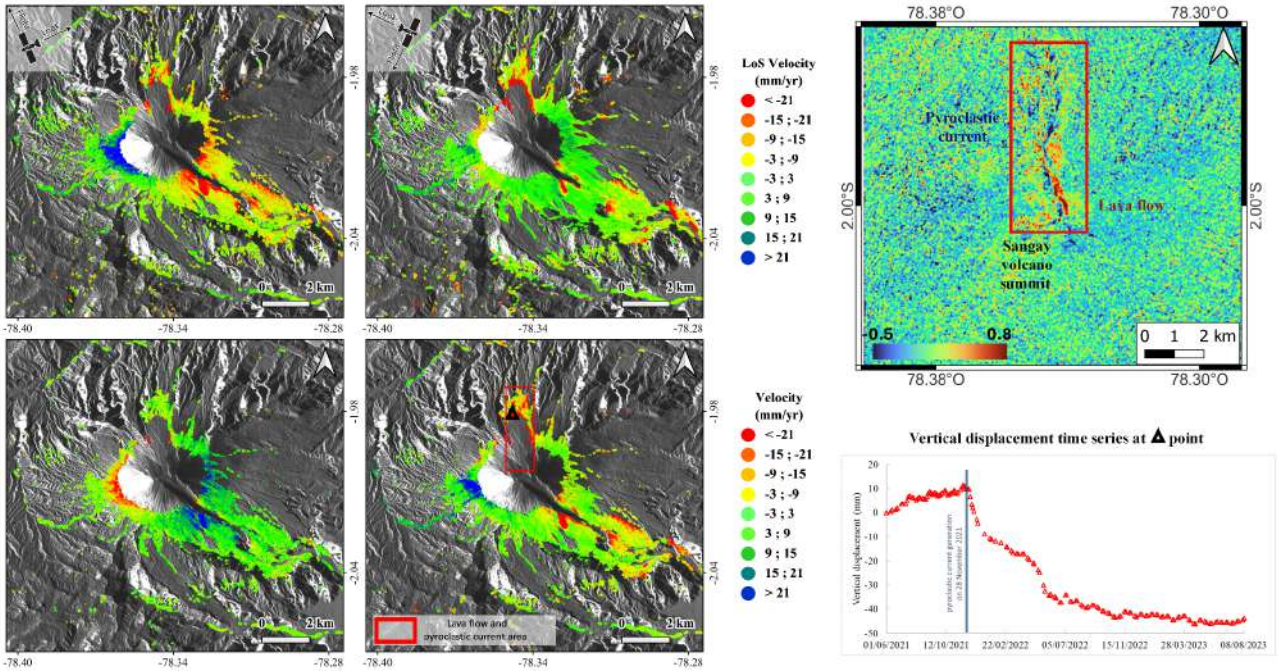

Figure 3 – Left panel: Ascending (upper left), descending (upper right), E-W (lower left) and vertical (lower right) ground displacement maps over Sangay volcano. In the upper right panel is visible the change detection map performed with S1 data acquired on 22 November and 4 December 2021, instead in the lower right panel the vertical displacement time series plotted at the black triangle can be appreciated.

Concluding remarks

Regarding Etna volcano, through InSAR methods we found out the presence of several subsidence areas that overlap with lava flow footprints identified by S2 and literature data. Horizontal displacements at lava flows are directed downslope on areas with high slope angles but directed upslope on areas characterized by low slope angles and larger lava thickness. Results also allowed us to establish the influence that the physical mechanisms have on the observed motion, suggesting that the main factors causing ground displacements are thermal contraction of the lava body and viscous compaction of the underlying substrate, the latter predominant for older lava flows. We tried to apply the same approach in the study of lava flows on Sangay volcano but, different climatic conditions and the inadequacy of some satellite datasets did not allow complete replicability. However, we were able to correlate the dynamics highlighted by the InSAR DTS analysis with the emplacement of a pyroclastic current in the N flank of Sangay at the end of November 2021 by using a polarimetric change detection approach that allows emphasizing changes due to the volcanic eruption.

As future developments, we plan to analyze in detail the displacement patterns measured by InSAR methods to relate them to other volcanic phenomena (e.g., inflation, lava flows, pyroclastic currents) by exploiting polarimetric change detection radar approach and also numerical modeling methods.

Acknowledgements

The present work is supported by the INGV research projects ATTEMPT – Integrated System for Multi-Hazard from Space over Mediterranean - and SAFARI - An artificial intelligence-based StrAtegy For volcAno hazaRd monItoring from space. Sentinel-1 and Sentinel-2 data are distributed by the European Space Agency. COSMO-SkyMed data were provided by the Italian Space Agency (Project ID: 607).

References

Beccaro, L., Albano, M., Tolomei, C., Spinetti, C., Pezzo, G., Palano, M., & Chiarabba, C. (2023). Insights into post-emplacement lava flow dynamics at Mt. Etna volcano from 2016 to 2021 by synthetic aperture radar and multispectral satellite data. Frontiers in Earth Science, 11, 1211450.

De Beni, E., Cantarero, M., Neri, M., and Messina, A. (2021). Lava flows of Mt Etna, Italy: the 2019 eruption within the context of the last two decades (1999–2019). Journal of Maps 17, 65–76. doi: 10.1080/17445647.2020.1854131.

Ganci, G., Bilotta, G., Zuccarello, F., Calvari, S., and Cappello, A. (2023). A Multi-Sensor Satellite Approach to Characterize the Volcanic Deposits Emitted during Etna's Lava Fountaining: The 2020–2022 Study Case. Remote Sensing 15, 916. doi: 10.3390/rs15040916.

Hidalgo, S., Vasconez, F. J., Battaglia, J., Bernard, B., Espín, P., Valade, S., ... & Ruiz, M. (2022). Sangay volcano (Ecuador): the opening of two new vents, a drumbeat seismic sequence and a new lava flow in late 2021. Volcanica, 5(2), 295-311.

Corresponding author: lisa.beccaro@ingv.it

ACU – Sviluppo di una rete prototipale per lo studio delle emissioni acustiche associate ai micro-processi dislocativi

C. Bidini [1], D. Sabatini [2], A. Govoni [3], G. Romeo [4], D. Famiani [4], G. Di Stefano [4], G. Spinelli [4], G. De Luca [3], M. Anselmi [3], A. Frepoli [3], A. Gattuso [5], T. Braun [1]

[1] Istituto Nazionale di Geofisica e Vulcanologia, Sezione di Roma1, Arezzo, Italy
[2] Università degli Studi "Roma Tre", Roma, Italy
[3] Istituto Nazionale di Geofisica e Vulcanologia, Sezione ONT, Roma, Italy
[4] Istituto Nazionale di Geofisica e Vulcanologia, Sezione di Roma1, Roma, Italy
[5] Istituto Nazionale di Geofisica e Vulcanologia, Sezione di Palermo, Milazzo, Italy

The main objective of the project ACU is to develop a prototypical network of infrasound sensors, for use on a national scale, dedicated to the monitoring of acoustic waves propagating in the atmosphere in the same frequency range as seismic waves. The range of applications to be covered by this new facility range from volcanic monitoring, detection of anthropogenic events and earthquake rumbles, as well as monitoring of other natural phenomena, like avalanches, landslides or rock falls.

Coupling of acoustic waves into the ground has been first noted on active volcanoes around the world, like e.g., Mt. S. Helens (Kieffer, 1981), Pavlov volcano (Mc Nutt, 1986; Garces et al., 2000); the identification of air-waves even in seismograms from moderate explosion-quakes and volcanic tremor was first reported by (Braun & Ripepe, 1993, Kedar et al., 1996; Ripepe et al., 1996; Hagerty et al., 2000).

The project is divided in the following steps:

- Development of an acoustic wave generator for calibration of the available sensors.
- Comparison and calibration of commercial infrasound sensors.
- Cost-benefit analysis
- Installation of an infrasonic array equipped with high-quality infrasound sensors for the detection and directional analysis of the recorded acoustic waves.
- Preparation of a portable infrasound network, to be deployed in the epicentral area in case of significant seismic events.
- Development and/or individuation of a low-cost sensor for a future widespread equipment of seismic and volcano-seismic networks by infrasound sensors.
- Test measurements in the ultrasonic range (> 20 kHz) inside the National Gran Sasso Laboratory (acoustic emission).

The INGV-laboratory has developed an electro-mechanical device based on a subwoofer, which can be used both as a sensor and as a source for calibration. In a passive “sensor”-mode the pressure acting on the membrane regulates the current inside the subwoofer’s voice-coil, while in an active “calibration”-mode a waveform generator steers the oscillation of the subwoofer’s membrane, whose amplitude is then controlled by a LVDT-interface. The pressure variations are then channelized through a hose directly to the sensor input pressure interface. As the desired frequency range is the same as for seismic stations, infrasound signals are recorded by commercial seismic digitizers, as e.g., Nanometrics CENTAUR, Cube or GAIA.

The presentation gives an update of the work in progress and will outline future perspectives.

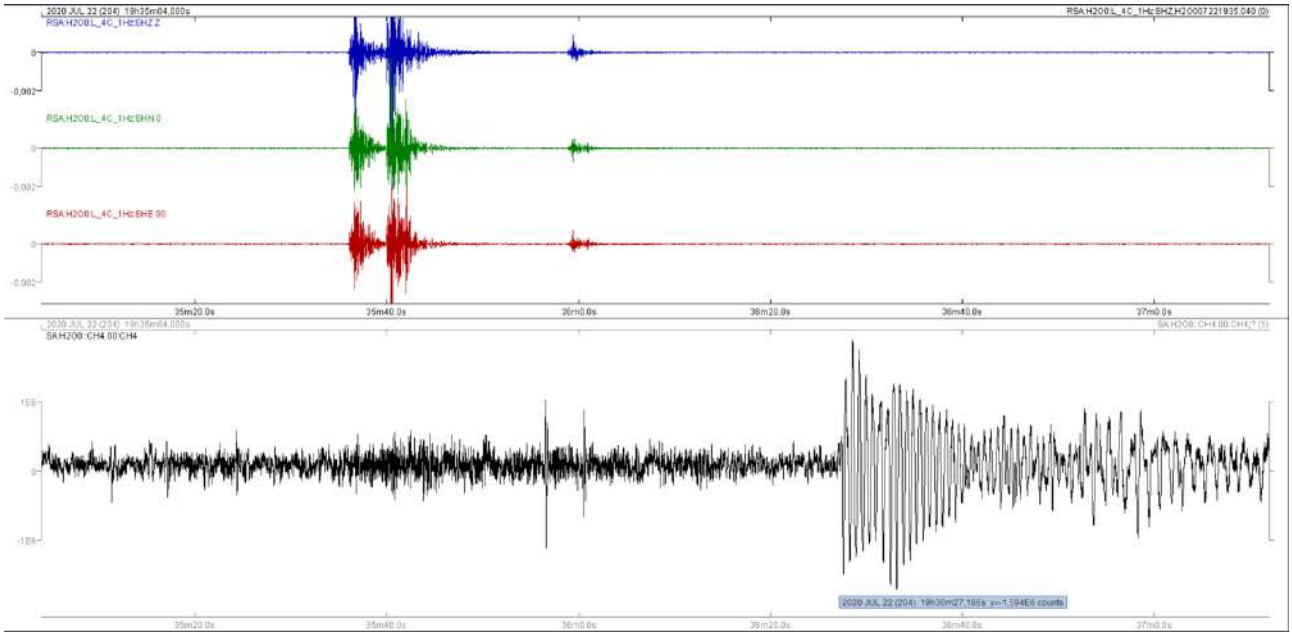

Fig. 1 – Example of an earthquake and rumble located on 22/07/2020 at 19:36 in the area of Montecassino (FR). Note the occurrence of three small seismic events (coloured traces) prior to the infrasound signal (black).

References

Braun T., Danesi S., and Morelli A.; 2020: Application of monitoring guidelines to induced seismicity in Italy. J. Seis.

Braun T. and Ripepe M.; 1993: Interaction of Seismic and Air Waves Recorded at Stromboli Volcano. Geophys. Res. Lett., 20(1), 65-68.

Garces M. A., McNutt S. R., Hansen R. A., Eichelberger J. C.; 2000: Application of wave-theoretical seismoacoustic models to the interpretation of explosion and eruption tremor signals radiated by Pavlof volcano, Alaska. J. Geophys. Res., 105(B2), 3039-3058.

Hagerty M. T., Schwartz S. Y., Garces M. A., Protti M.; 2007: Analysis of seismic and acoustic observations at Arenal Volcano, Costa Rica, 1995-1997. J. Volcanol. Geotherm. Res., 101, 27

Kedar S., Sturtevant B., Kanamori, H.; 1996: The origin of harmonic tremor at Old Faithful geyser. Nature 379, 708–711.

Kieffer, S. W. (1981). Blast dynamics at Mount St. Helens on 18 May 1980. Nature, 291, 568–570.

McNutt, S. R. (1986). Observations and Analysis of the B-Type Earthquakes, Explosions, and Volcanic Tremor at Pavlof Volcano, Alaska. Bull. of the Seismol. Soc. of Am., 76(1), 153-175.

Ripepe, M., Poggi, P., Braun, T., & Gordeev, E. (1996). Infrasonic waves and volcanic tremor at Stromboli. Geophys. Res. Lett., 23(2), 181-184.

Corresponding author: thomas.braun@ingv.it

HVSR analysis to investigate a possible correlation to a gas shallow reservoir in a mud volcanic field: the case of Nirano (MO)

A. Brindisi[1], D. Albarello[1,3], N. Carfagna[1], E. Paolucci[2]

[1] Dipartimento di Scienze Fisiche, della Terra e dell'Ambiente, Università degli Studi di Siena, Siena, Italy

[2] Dipartimento di Fisica ed Astronomia, Università degli Studi di Bologna, Bologna, Italy

[3] Consiglio Nazionale delle Ricerche, Istituto di Geologia Ambientale e Geoingegneria, Rome, Italy

Multiple studies highlight the evidence of a trough within the low-frequency range in HVSRs measurements performed over a gas field and attribute it to the presence of a hydrocarbon reservoir (Lambert et al., 2007; Saenger et al., 2007; Panzera et al., 2016; Antunes et al., 2022). To explain the natural emission of low-frequency signals Saenger et al. (2007) and Lambert et al. (2007) consider hydrocarbon-reservoir related microtremor, assuming that the reservoir itself acts as a (secondary) source of low-frequency seismic waves by a resonant amplification effect. Furthermore, Panzera et al. (2016) observe that the minimum is identified by an "inverse eye-shaped" feature in the Fourier spectra, related to an amplitude increase in the vertical component of motion due to a velocity inversion. This study focuses on the investigation of the spectral anomaly described above at Nirano mud volcano field, conducted through the analysis of the results obtained by seismic arrays and three directional velocimetric stations (HVSR) deployed in the site. After a cluster analysis carried out on HVSRs have been identified 3 groups of measurements, one of which include HVSRs located in the caldera-like basin area, marked by a minimum in the seismic spectrum at 0.53 Hz. The joint inversion procedure based on Genetic Algorithms of the HVSR curves and the Rayleigh waves dispersion curve shows that the minimum is well reproduced even without a velocity inversion. This proves that it is not uniquely correlated to the mechanisms proposed above and that, therefore, it may be linked to a stratigraphic effect that unites all the measurements concentrated in the group under examination or to the surface wave model used.

References

Antunes V., Planès T., Obermann A., Panzera F., D'Amico S., Mazzini A., Sciarra A., Ricci T., Lupi M.; 2022: Insight into the dynamics of the Nirano Mud Volcano through seismic characterization of drumbeat signals and V/H analysis. Journal of Volcanology and Geothermal Research, 431, 107619.

Lambert M., Schmalholz S. M., Saenger E. H. and Podladchikov Y. Y.; 2007: Low-frequency anomalies in spectral ratios of single-station microtremor measurements: Observations across an oil and gas field in Austria. In SEG Technical Program Expanded Abstracts 2007 (pp. 1352-1356). Society of Exploration Geophysicists.

Panzera F., Sicali S., Lombardo G., Imposa S., Gresta S. and D'Amico S.; 2016: A microtremor survey to define the subsoil structure in a mud volcanoes area: the case study of Salinelle (Mt. Etna, Italy). Environmental Earth Sciences, 75, 1-13.

Saenger E.H., Torres A., Rentsch S., Lambert M., Schmalholz S.M. and Mendez-Hernandez E.; 2007: A hydrocarbon microtremor survey over a gas field: Identification of seismic attributes. 77th SEG meeting, San Antonio, Texas, USA, Expanded Abstracts, 1277–1281.

Corresponding author: albachiara.brindi@student.unisi.it

Seismic monitoring of gas emissions at mud volcanoes: the case of Nirano (northern Italy)

N. Carfagna[1], A. Brindisi[1], E. Paolucci[2], D. Albarello[1,3]

[1] *Department of Physical Sciences, Earth and Environment, University of Siena, Siena, Italy*

[2] *Department of Physics and Astronomy, University of Bologna, bologna, Italy*

[3] *Consiglio Nazionale delle Ricerche, Istituto di Geologia Ambientale e Geoingegneria, Rome, Italy*

The Salse di Nirano site is a Natural Reserve in Italy distinguished by the presence of mud volcanic phenomena that have manifested in the formation of four main volcanic vents situated within its central part close to pools filled by low viscosity mud. The mud volcanoes of Nirano are relatively small, reaching a maximum of three meters height and exhibit minimal volcanic activity with weak, persistent surface degassing.

Seismic monitoring was conducted at the Nirano Mud Volcanoes during two distinct field campaigns in April 2021 and July 2023, with the aim of exploring the subsurface structure and the dynamics of the volcano. The seismic survey campaigns involved deploying small 'L-shape' seismic arrays composed of vertical geophones and three-directional sensors. Both active and passive seismic acquisition methods were also employed to characterize the first subsoil, focusing on shear wave velocity profiles.

During the recordings, a peculiar seismic pattern emerged, characterized by sequences of short impulsive events (0.1-0.2s) occurring at regular and irregular time intervals. These transient events, commonly referred to as 'drumbeats' by various authors (*Iverson et al., 2006*; *Lupi et al., 2016*), exhibit a spectral structure dominated by frequencies ranging between 10 and 30 Hz and by the presence of subsequent sharp peaks, for which a realistic explanation has been provided in this study.

A rapid automatic location procedure was deployed to identify seismic sources corresponding to these impulsive events, assuming a straight ray path from source to receiver. Approximately 5000 sources were identified over the 7-hour recording period (seven asynchronous arrays recording for one hour each) within a search area of few hundred meters. Most of the sources have been localized at shallow depths (<10m) with a minor contribution of deeper events (within few tens of meters from the surface).

The propagation velocities derived from the location procedure, coupled with the results of the conducted polarization analysis, suggest shear waves are responsible for most of the energy transmitted by these seismic signals.

Considering these findings, an interpretative source model for the recorded seismic pattern was attempted. This model proposes a stick-slip mechanism as the origin of the impulsive signals, due to the interaction between exsolved gas bubbles, mud plugs, and the vent walls.

Upon establishing a source model and proposing a dynamic relation between gas emission and seismic signals, an effort was made to provide an indirect estimate of the surface gas outflow. The outcomes of this analysis are in line with direct measurements of the average gas outflow (CO^2 and CH^4) conducted in the investigated area by other Authors (*Sciarra et al., 2019*).

References

Iverson, R. M., Dzurisin, D., Gardner, C. A., Gerlach, T. M., LaHusen, R. G., Lisowski, M., Vallance, J.; 2006: *Dynamics of seismogenic volcanic extrusion at Mount St Helens in 2004-05*. Nature, 444, 439-443.

Lupi, M., Ricci, B. S., Kenkel, J., Ricci, T., Fuchs, F., Miller, S. A., & Kemna, A.; 2016: *Subsurface fluid distribution and possible seismic precursory signal at the Salse di Nirano mud volcanic field, Italy*. Geophys.J.Int., 204, 907-917.

Sciarra, A., Cantucci, B., Ricci, T., Tamonaga, Y., & Mazzini, A.; 2019: *Geochemical characterization of the Nirano mud volcano, Italy*. Appl. Geochem., 102, 77-87.

Corresponding author: nicolo.carfagna@student.unisi.it

Unveiling hidden volcano dynamics with Artificial Intelligence (AI) and Earth Observation (EO)

S. Cariello[1,2], C. Corradino[1], F. Torrisi[1,2], G. S. Di Bella[1,2], C. Del Negro[1]

[1] Istituto Nazionale di Geofisica e Vulcanologia, Osservatorio Etneo, Catania, Italy

[2] Department of Electrical Electronics and Computer Engineering, University of Catania

Volcano hazard monitoring is essential for understanding the behavior of rapidly changing volcanoes and, consequently, for better forecasting volcanic hazards and related impacts. From this perspective, several satellite sensors are now available, providing thermal infrared data at various spatial resolutions and revisit times. Additionally, future satellite missions are being planned to maintain a near-constant "eye" on thermal volcanic activity across the planet. This huge volume of data necessitates the development of Artificial Intelligence (AI) tools to automatically extract relevant information on the volcano's state in a short time. Recently, we demonstrated the potential of a cascading pipeline for classifying high-temperature volcanic features and quantifying the spatial extension of thermal anomalies in high-resolution satellite data (Sentinel-2 MultiSpectral Instrument, S2-MSI). The ability to combine two separate machine learning models —a scene classifier and a pixel-based segmentation model (Corradino et al., 2022) —into a "top-down" cascading architecture makes this method highly effective, achieving an accuracy of 95%. These findings illustrate how the cascading technique can be used to fully characterize any accessible satellite image in almost real-time, offering valuable assistance in the mapping, monitoring, and characterization of volcanic thermal features. The model's high level of accuracy enables us to detect thermal signals that are often challenging to pick up with current detectors. Indeed, the thermal increase produced by intracrater activity during unrest phases provides valuable data for understanding volcanic phenomena, allowing the development of more accurate predictive models and a better understanding of the internal dynamics of volcanoes. While these thermal detections have already served as possible precursory signals for specific volcanoes, a comprehensive field investigation of such changes has not been conducted yet.

In this study, we aim to examine the thermal changes captured by satellite data on Etna and Stromboli, two of the most active and monitored volcanoes in the Mediterranean region. The objective is to identify and assess significant changes in thermal anomalies during periods of unrest, utilizing the outcomes generated by the cascading model.

Over the last two decades, the eruptive activity of Etna has been characterized by persistent degassing and a frequent intertwining of explosive and effusive eruptions from its four summit craters. Identifying the active craters and quantifying intra-crater budget emissions in terms of the areal coverage of thermal anomalies can unveil interesting scenarios associated with the volcano’s

dynamics. Using Google Earth Engine (GEE), we outlined each crater region and computed the contribution of each crater to the overall detected thermal anomalies; a circular area around each crater is considered, namely South-East (SE), North-East (NE), Bocca Nuova (BN) and Voragine (VOR). A period of intense eruptive activity began on December 14, 2020, with the first of 66 paroxysms producing several lava flows (Amato et. al., 2022), with the maximum area quantified being 1,800,000 m2 on 18 December. It is noteworthy that all the craters show consistent increases in the areal coverage of thermal anomalies before the first paroxysm (see Fig. 1), with NE and SE (see Fig. 2a-b) starting in June 2020. Lately, since June 2022, the most active crater has been BN. One of the most recent paroxysm events occurred on November 12, 2023, and was preceded by a net increase in thermal anomalies since October 16, 2023, when SE crater became active.

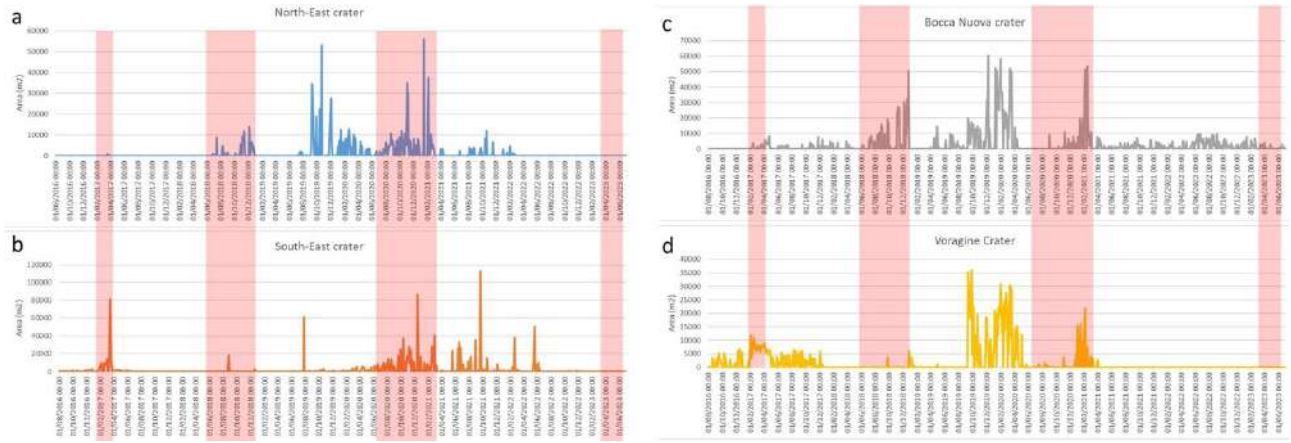

Fig. 1

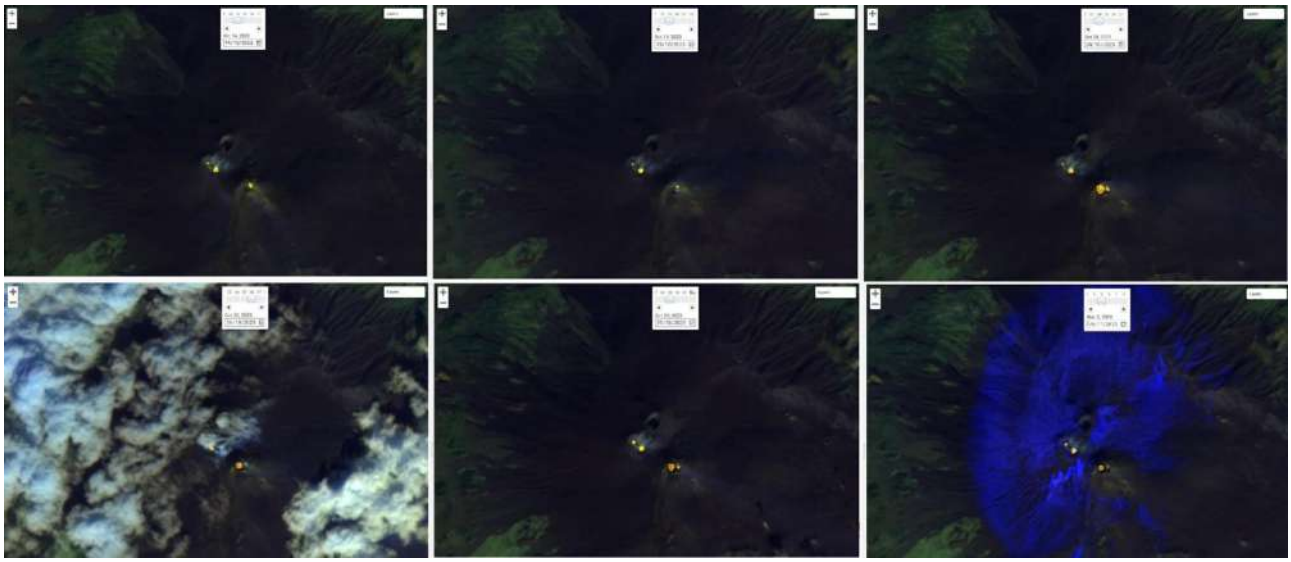

Fig. 2

Stromboli is characterized by persistent explosive activity that can sometimes escalate into more intense events, producing major explosions or paroxysmal events (Calvari et al., 2022, Giudicepietro et al., 2022). These events may lead to lava flows, as seen in October 2023 when a new eruptive activity commenced (Fig. 3). This activity was preceded by a steep increase in the

areal coverage of the thermal emissions starting from September 9, 2023, probably due to shallow magma dynamics. The first emplaced lava flow was identified by the cascading algorithm on October 4, 2023, estimating a hot area of about 55,000 m2.

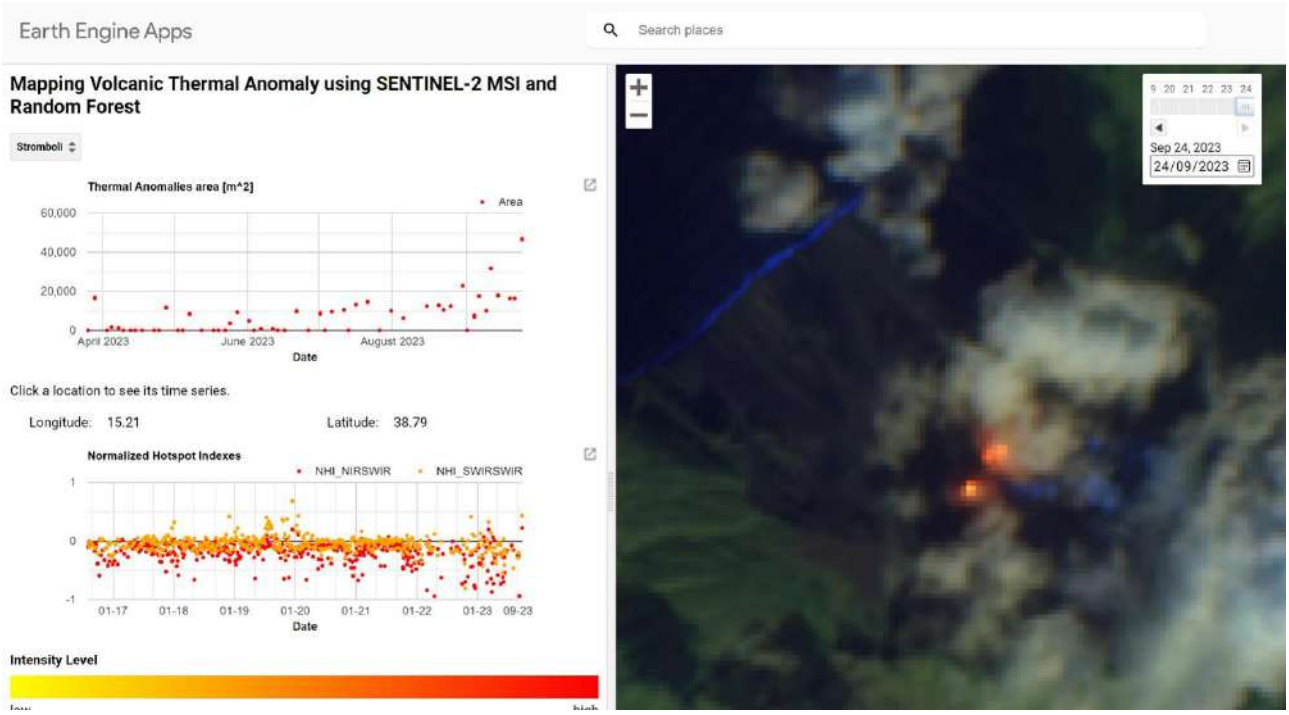

Fig. 3

In conclusion, identifying hidden growth trends within thermal data can be challenging, especially when it comes to identifying small, ever-increasing abnormalities that could be indicative of an imminent eruption. Therefore, the analysis of satellite thermal data, employing accurate AI detection techniques, is crucial for detecting significant thermal changes leading up to volcanic eruptive phenomena.

References:

Amato, E.; 2022: Machine Learning and Best Fit Approach to Map Lava Flows from Space. Il nuovo cimento C, 45, 1–12.

Calvari, S.; Di Traglia, F.; Ganci, G.; Bruno, V.; Ciancitto, F.; Di Lieto, B.; Gambino, S.; Garcia, A.; Giudicepietro, F.; Inguaggiato, S.; et al.; 2022: Multi-Parametric Study of an Eruptive Phase Comprising Unrest, Major Explosions, Crater Failure, Pyroclastic Density Currents and Lava Flows: Stromboli Volcano, 1 December 2020–30 June 2021. Frontiers in Earth Science.

Corradino, C., Amato, E., Torrisi, F., & Del Negro, C.; 2022: Data-Driven Random Forest Models for Detecting Volcanic Hot Spots in Sentinel-2 MSI Images. Remote Sensing, 14(17), 4370.

Giudicepietro, F.; Calvari, S.; D'Auria, L.; Traglia, F.D.; Layer, L.; Macedonio, G.; Caputo, T.; Cesare, W.D.; Ganci, G.; Martini, M.; et al.; 2022: Variations of Stromboli Activity Related to the 2019 Paroxysmal Phase Revealed by SOM Clustering of Seis-mo-Acoustic Data and Its Comparison with Video Recordings and GBInSAR Measurements; Copernicus Meetings.

Corresponding Author: simona.cariello@ingv.it

Dike-arrest vs dike-propagation: new insights from the Younger Stampar eruption (13th Century), SW Iceland

N. Corti[1], F. L. Bonali[1,2], E. Russo[1,2], K. Drymoni[1,3], F. Pasquarè Mariotto[4], A. Gudmundsson[5], A. Tibaldi[1,2]

[1] Department of Earth and Environmental Sciences, University of Milan-Bicocca, Milan, Italy;

[2] CRUST-Interuniversity Center for 3D Seismotectonics with Territorial Applications, Chieti Scalo, Italy;

[3] Earth and Environmental Sciences, Ludwig-Maximilians-Universität in Munich, Munich, Germany;

[4] Department of Human and Innovation Sciences, Insubria University, Como, Italy;

[5] Department of Earth Sciences, Queen's Building, Royal Holloway University of London, Egham, UK.

Unravelling the parameters that control dike arrest and dike propagation in the shallow crust, and subsequently the associated dike-induced deformation at the surface, is of paramount importance in volcanology. This is because dikes can select among many different paths towards the surface and either stall in the crust or, alternatively, feed volcanic eruptions.

In this work, we study two vertical dikes exposed in the sea-cliffs of the Reykjanes Peninsula (SW Iceland). Both dikes are associated with the Younger Stampar eruption (1210-1240 CE) and were emplaced in the same crustal segment, which includes lava flows and tuff layers. Although one of them fed a lava flow at the surface, the other dike, located at a distance of 30 m from the feeder, became arrested only 5 m below the surface of the active rift zone without inducing any brittle deformation. Hence, this outcrop represents an ideal case study to investigate the factors that favor dike arrest versus dike propagation, as well as the conditions that affect dike-induced brittle deformation.

We collected detailed structural data on the dikes and identified the stratigraphic sequence of the outcrop. We mapped the nearby crater rows of the Stampar eruptions and reconstructed a high-resolution 3D model through drone images and Structure from Motion (SfM) techniques. These data became inputs for 2D Finite Element Method (FEM) numerical models, using the COMSOL Multiphysics® software (v5.6), to explain mechanically the dike arrest and why there is no brittle deformation at the surface induced by the arrested dike. We tested the role of dike overpressure (P_o = 2-4 MPa), the stiffness (Young's modulus) of the layers, and the presence of an extensional or a compressional tectonic stress field.

Our structural data show that the strike of the Younger Stampar crater row is consistent with the strike of nearby historic and prehistoric eruptive fissures, as well as the orientation of the volcanic systems of the Reykjanes Peninsula. Our numerical models indicate that dike-induced compressive stress (caused by the earlier feeder dike), together with the contrasting stiffness of the layers, can explain the arrest of the later dike and the lack of brittle deformation at the surface. Specifically, the presence of a stiff lava flow on top of a soft tuff concentrated the feeder dike-induced compressive stress in the lava flow, favoring dike arrest at the tuff-lava contact. These results have implications for hazard studies in other volcanic areas, particularly as regards dike arrest at shallow depths, in Iceland and worldwide.

Corresponding author: noemi.corti@unimib.it

PROMUD Project – multidisciplinary monitoring of Mud Volcanoes

P. Cusano[1], P. Madonia[2], F. D'Ajello Caracciolo[3], C. Felli[4], F. Grassa[4], I. Nicolosi[3], A. Pesci[5], S. Petrosino[1], A. Sciarra[6], I. Aquino[1], V. Augusti[1], E. Bellucci Sessa[1], P. Bonfanti[4], G. Capasso[4], T. Caputo[1], A. Caracausi[4], C. Caracciolo[5], R. Carluccio[3], A. Cascella[7], A. Costanza[2], G. Etiope[3], E. Ferrari[8], G. Fertitta[2], A. La Spina[2], F. Loddo[5], M. Massa[8], L. Minelli[3], V. Misiti[3], L. Napoli[4], F. Pisciotta[4], C. Ricco[1], L. Spampinato[2], G. Tamburello[5], A. Venuti[3], D. Albarello[9], A. Ambrosone[10], G. Ciotoli[11], N. De Tommasi[10], C. Di Maggio[12], M. Falanga[10], S. Mancini[10], A. Mazzini[13], A. Piombo[14], A. Rizzo[15], G. Teza[14]

[1] Sezione di Napoli 'Osservatorio Vesuviano', INGV, Naples, Italy
[2] Sezione di Catania 'Osservatorio Etneo', INGV, Catania, Italy
[3] Sezione di Roma2, INGV, Rome, Italy
[4] Sezione di Palermo, INGV, Palermo, Italy
[5] Sezione di Bologna, INGV, Bologna, Italy
[6] Sezione di Roma1, INGV, Rome, Italy
[7] Sezione di Pisa, INGV, Pisa, Italy
[8] Sezione di Milano, INGV, Milan, Italy
[9] DSFTA, Università degli Studi di Siena, Siena, Italy
[10] Università degli Studi di Salerno, Fisciano (SA), Italy
[11] Istituto di Geologia Ambientale e Geoingegneria, CNR, Monteliberti, Italy
[12] DiSTeM, Università degli Studi di Palermo, Palermo, Italy
[13] Department of Geosciences, University of Oslo, Oslo, Norway
[14] Dipartimento di Fisica e Astronomia "Augusto Righi", Università degli Studi di Bologna, Bologna, Italy
[15] DISAT, Università degli Studi di Milano Bicocca, Milan, Italy

Mud or sedimentary volcanoes are geological structures built by the ejection of overpressured multiphase pore fluids, mainly composed of cold gases (principally methane), liquid hydrocarbons and high salinity waters, that episodically drag sediments and rock clast at surface. The fluids ascend along lithological or structural discontinuities, such as faults and fractures, or across permeable rocks. The cyclically alternation of eruptive activity and dormancy determines seepage features, i.e. mud cones, gryphons, pools and salsa lakes. Beyond their importance in the

monitoring of global warming being the second natural methane source (Mazzini et al., 2021; Etiope et al., 2019), mud volcanoes (MVs) can be a serious source for Geohazard. Sometimes MVs generate paroxysmal events, during which gas blasts and sudden expulsion, fallout and flooding of large amounts of mud can damage facilities and severely hurt persons in their proximity. During the paroxysm occurred at the Maccalube di Aragona (Sicily) in 2014 two children died. However, a monitoring protocols for MV surveillance have never been implemented.

MV monitoring to identify the triggering processes of paroxysms so far carried out is mainly based on the interplay with large earthquakes or hydrocarbon exploration drillings. Anyway a unanimous conclusion has not been reached yet. Other factors, such as the influence of regional tectonic stress, hydrological cycle or periodic inflation-deflation cycles at the crustal scale, as those driven by Earth tides, have been poorly investigated, as well as the MV buried structure. PROMUD project (https://progetti.ingv.it/it/promud) aims to fill these knowledge gaps through a multidisciplinary approach, whose ultimate goal is to intercept reliable precursors and to individuate activity state indicators of the evolution towards a paroxysm.

The Project

PROMUD ("definition of a multidisciplinary monitoring PROtocol for MUD volcanoes") is a 3-years (2023-2025) INGV project integrating geophysical (seismic, magnetic, geoelectric, environmental radioactivity), geodetic (GNSS and tilt), bio-geochemical (characterization of emitted fluids and vegetation analysis), topographic and geomorphological data, acquired by both permanent networks and spot field surveys.

The research is being carried out by 5 Working Packages (WPs), with their own specific objectives, that interplay and integrate with each other (Fig. 1).

WP1 - *Seismology, Tectonics, Tilt, hydrology and vegetation analysis*, deals with: the analysis of the background seismic noise wavefield and its role in the identification and monitoring of degassing sources and conduits; the response of the MV system to regional earthquakes; the possible link with the regional tectonic structures; the tiltmetric observations and their role in monitoring the MV activity; the hydrological regime and its influence on MV activity; evaluation of river network evolution as a consequence of MV activity; the vegetation pattern definition as a marker of MV evolution in space and time and radio nuclides emissions by soil.

WP2 - *Remote Sensing and Topography*, performs remote sensing for terrain and surface modelling aimed to identify morphological variations by compare multi-temporal models, searching for deformation patterns related to changes in styles, amplitude and rates of MV activity. The WP integrates data from surface variations by levelling and GNSS to estimate volume changes. The group intends to produce first images of a paroxysm, to identify inflation/deflation cycles as proxies of MV activity state. Moreover, the WP is carrying out a research of historical documents and testimonies, to assist the understanding of phenomena.

WP3 - *Geochemistry, Stratigraphy and Rock Magnetism*, foresees to characterize the fluid source by measuring the changes in flux/composition of emitted fluids as a proxy of MV activity state, to produce continuous visible video imagery of MV activity. Micropaleontological and stratigraphic study for depth determination of the mud source and investigations on active microbiological communities thriving within the erupted mud and around the seepage sites are in progress. Finally, the WP is performing a study of the magnetic properties of the mud collected in proximity of pools and cones and of the rocks outcropping nearby and recording the changes over time in the concentration, mineralogy and coercivity of the magnetic minerals.

WP4 – *Geophysics*, is carrying out several resistivity and magnetic anomaly surveys, for the definition of the subsoil configuration geometry by detecting eventual magnetic and electrical conductivity properties of the MV system.

WP5 - *Scientific Outreach*, manages the Website of the project, produces multimedia material (pictures and videos) and is in charge of the risk education activities in primary and secondary schools.

Study areas

We selected two main study sites, the Salse di Nirano (Northern Apennines, Fig. 2B) and the Maccalube di Aragona (Sicily, Fig. 2C). Both the areas are Nature Reserves: Comune di Fiorano Modenese and Ente Parchi dell'Emilia Centrale of Emilia Romagna Region and Legambiente, on behalf of the Sicilian Regional Government, respectively.

Final remarks

Many visitors closely approaching the active mud vents inside the two Natural Reserves and, therefore, to define a monitoring protocol for the mitigation of the risk related to possible paroxystic events, is imperative. For these reasons, the main stakeholders are the organizations that manage the two Reserves, which both are already providing their logistic support to this project and represent the end users of its outcomes.

In summary, PROMUD project has a two-fold challenge, that is to retrieve a model of the spatial and temporal evolution of MV systems from the multidisciplinary observations and the attempt of unravelling the transition from the background state to the paroxysm generation.

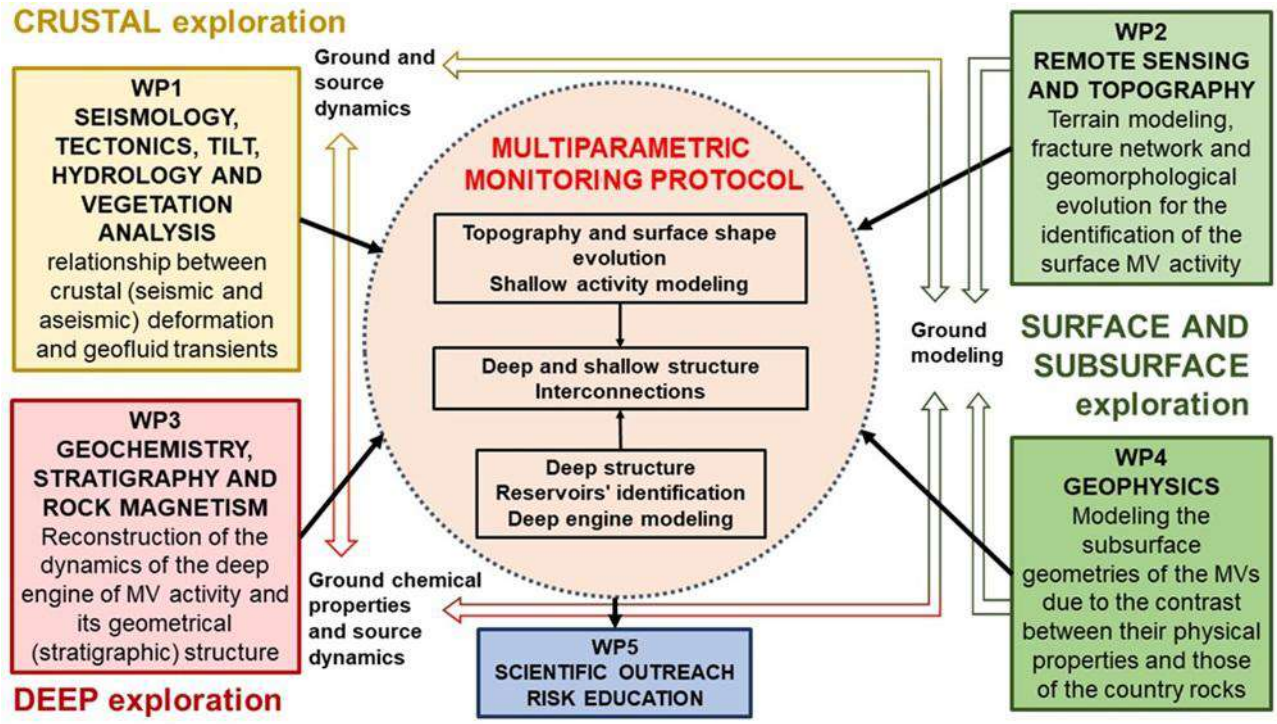

Fig. 1 – PROMUD conceptual scheme to illustrate how the project intends to achieve a significant improvement in the comprehensive knowledge of MVs deep engine and the interconnections with its activity at surface, and to define a correct and efficient multidisciplinary environmental monitoring directed to preserve human life and ecosystem by using this knowledge.

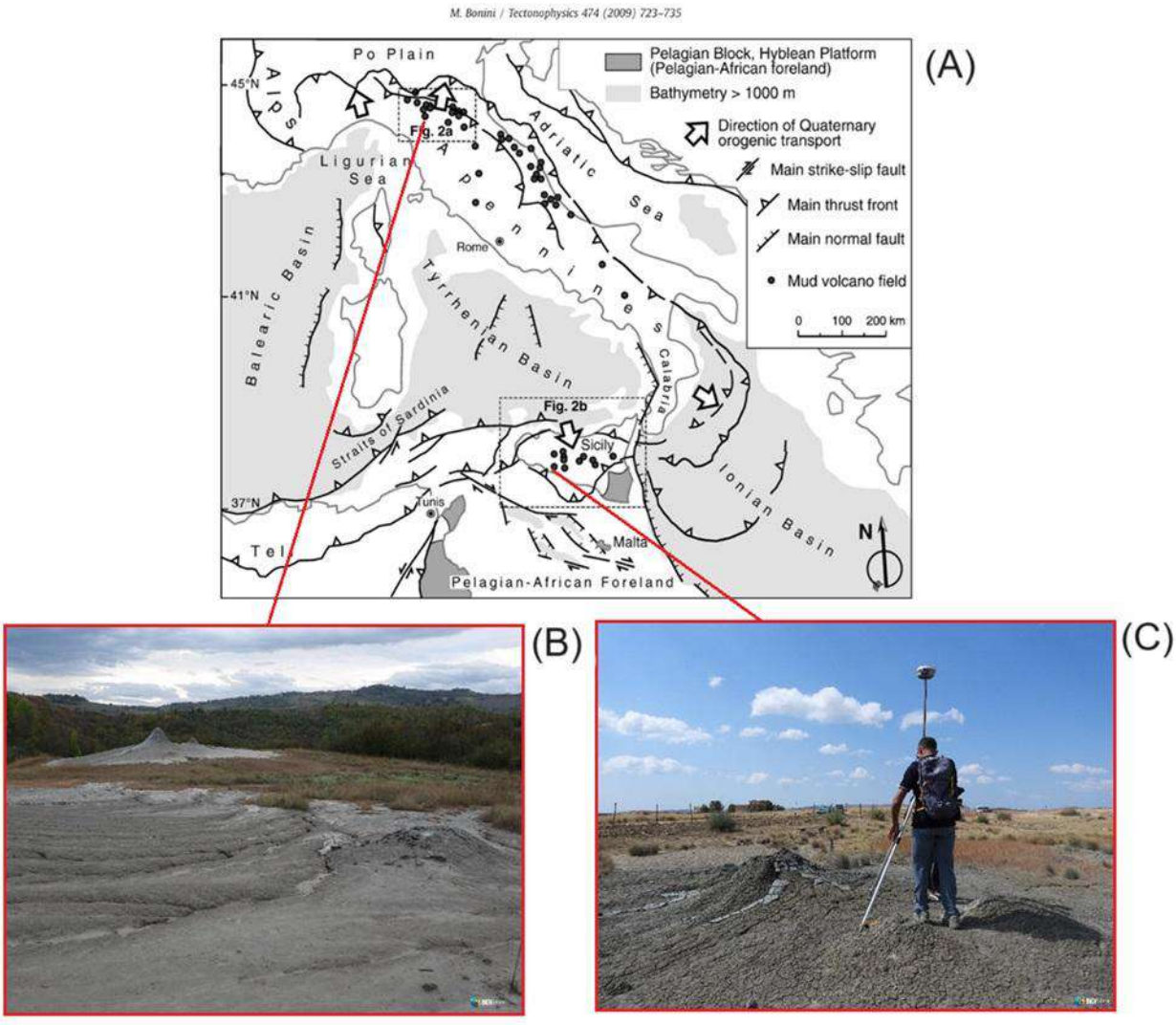

Fig. 2 – (A) Location of Mud volcanoes on the Italian territory (after Bonini, 2009). (B) Salse di Nirano (MO) and (C) Maccalube d'Aragona (AG) sites. Both the pictures were taken by the project staff (WP5 – Scientific outreach).

References

Mazzini A., Sciarra A., Etiope G., Sadavarte A., Houweling S., Pandey S. and Husein A.; 2021: Relevant methane emission to the atmosphere from a geological gas manifestation. Scientific Reports, doi:10.1038/s41598-021-83369-9.

Etiope et al. (2019). Earth Syst. Sci. Data, doi:10.5194/essd-11-1-2019.

Bonini M.; 2009: Mud volcano eruptions and earthquakes in the Northern Apennines and Sicily, Italy. Tectonophysics, doi: 10.1016/j.tecto.2009.05.018.

Corresponding author: paola.cusano@ingv.it

Statistical analysis of the seismicity of the last 30 years at Mt. Somma-Vesuvius

G. Dalla Via[1], P. Ricciolino[1], D. Lo Bascio[1], A. Tramelli[1]

[1] Istituto Nazionale di Geofisica e Vulcanologia, Sezione di Napoli, Osservatorio Vesuviano, Napoli, Italy

The last eruption of Mt. Somma-Vesuvius occurred in 1944, and since then has been quiescent showing only fumarole activity and moderate seismicity. The Md=3.6 event recorded on 09/10/1999 is the strongest record in the last 30 years.

Here we present an updated statistical analysis of the seismicity by analysing the three main seismic catalogues constantly filled in by INGV – Osservatorio Vesuviano:

- The catalogue of detected events at station OVO which starts in 1972 and counts 11783 earthquakes with duration magnitudes ranging from -1.5 to 3.6.
- The catalogue of detected events at station BKE which starts in 1998 and counts 20196 events.
- The catalogue of located events which starts in 1998 and counts 8558 events. Magnitudes of events in this and BKE catalogues range from -2.5 to 3.6.

The completeness magnitude computed for the OVO catalogue is Mc=1.9 and the b-value ranges between 1.0 and 2.5. The higher values correspond to the period 1980-1985, successively the b-value decreased to about 1.0 until the early 2000's. More recently, the b-value for the OVO catalogue slowly but steadily increased again to about 2.0 (~2014-2016), decreasing to 1.8 at present time. The annual occurrence rate is currently much lower than before 2000 (with a maximum of almost 700 events/year in 1999 when the Md=3.6 was recorded) and is generally lower than 100 events/year.

The analysis of the BKE catalogue gives an overall completeness magnitude of Mc=0.5 and a b-value in the range 0.8-1.2 in recent years. The annual seismicity rate, which reached values of 2000 events/year during 1999, decreased to less than 500 events/year in 2004. In successive years, seismicity grew up to about 750 and 1000 events/year in the period 2007-2010 and 2018-2022, respectively. However, the Gutenberg-Richter distribution shows a knee around Md=2.1. Our analysis, in agreement with previous results (D'Auria et al., 2013), suggests that at least two populations of earthquakes coexist in the BKE catalogue. This characteristic is mainly visible in the data before 2015, whereas it does not show up in more recent records. The two populations were analysed separately and gave values close to b=1 and b=1.7.

The main characteristic of the catalogue of located events is a significant variation in completeness magnitude with time, with completeness magnitude abruptly lowering during 2015 from about

Mc=1.5 to Mc=0.5-0.2. Our analysis shows how this dramatic change is produced by the improvement of the seismic network monitoring the volcano and by the increased sensitivity of the network. The annual rate of located events, in the order of hundreds per year in 1999/2000, dropped down to less than 100 events/year during the period 2001-2014. Since 2015, almost 1000 events/year have been recorded and located.

The GR analysis shows similar result with respect to the BKE catalogue, suggesting the presence of at least two populations of earthquakes also in the catalogue of located events. The first population is associated with earthquakes located within the cone of the volcano, above the sea level, whereas earthquakes belonging to the second class are located at greater depths well below the edifice.

References

D'Auria, L., et al.; 2013: The recent seismicity of Mt. Vesuvius: inference on seismogenic processes. ANNALS OF GEOPHYSICS, 56, 4, 2013, S0442; doi:10.4401/ag-6448.

Corresponding author: giorgio.dallavia@ingv.it

Trans-dimensional Mt. Etna P-wave anisotropic imaging

G. Del Piccolo[1], R. Lo Bue[1], B.P. VanderBeek[1], M. Faccenda[1], O. Cocina[2], M. Firetto Carlino[2], E. Giampiccolo[2], A. Morelli[3], J.S. Byrnes[4]

[1] *Dipartimento di Geoscienze, Università degli Studi di Padova*
[2] *Istituto Nazionale di Geofisica e Vulcanologia, osservatorio Etneo*
[3] *Istituto Nazionale di Geofisica e Vulcanologia, sezione Bologna*
[4] *School of Earth and Sustainability, Northern Arizona University*

Trans-dimensional inference identifies a class of methods for inverse problems where the number of free parameters is not fixed. In seismic imaging these methods are applied to let the data, and any prior information, decide the complexity of the models and how the inferred fields partition the inversion domains. Monte Carlo trans-dimensional inference is performed implementing the reversible-jump Markov chain Monte Carlo (rjMcMC) algorithm; the nature of Monte Carlo exploration allows the algorithm to be completely non-linear, to explore multiple possibilities among models with different dimensions and meshes and to extensively investigate the under-determined nature of the tomographic problems, showing quantitative evidence for the limitations in the data-sets used. Implementations of this method overcome the main limitations of traditional linearized solvers: the arbitrariness in the selection of the regularization parameters, the linearized iterative approach and in general the collapse of the information behind the solution into a unique inferred model.

We present applications of the rjMcMC algorithm to anisotropic seismic imaging of Mt. Etna with P-waves. Mt. Etna is one of the most active and monitored volcanoes in the world, typically investigated under the assumption of isotropic seismic speeds. However, since body waves manifest strong sensitivity to seismic anisotropy, we parametrize a multi-fields inversion to account for the directional dependence in the seismic velocities. Anisotropy increases the ill-condition of the tomographic problem and the consequences of the under-determination become more relevant. When multiple seismic fields are investigated, such as seismic speeds and anisotropy, the data-sets used may not be able to independently resolve them, resulting in non-independent estimates and corresponding trade-offs. Monte Carlo exploration allows for the evaluation of the robustness of seismic anomalies and anisotropic patterns, as well as the trade-offs between isotropic and anisotropic perturbations, key features for the interpretation of tomographic models in volcanic environments. The approach is completely non-linear, free of any explicit regularization and it keeps the computational time feasible, even for large data-sets.

Corresponding author: gianmarco.delpiccolo@phd.unipd.it

The state of art of the temperature monitoring network on La Fossa cone (Aeolian Islands, Italy)

I. S. Diliberto[1], M. G. Di Figlia[1]

[1] Istituto Nazionale di Geofisica e Vulcanologia, Sezione di Palermo

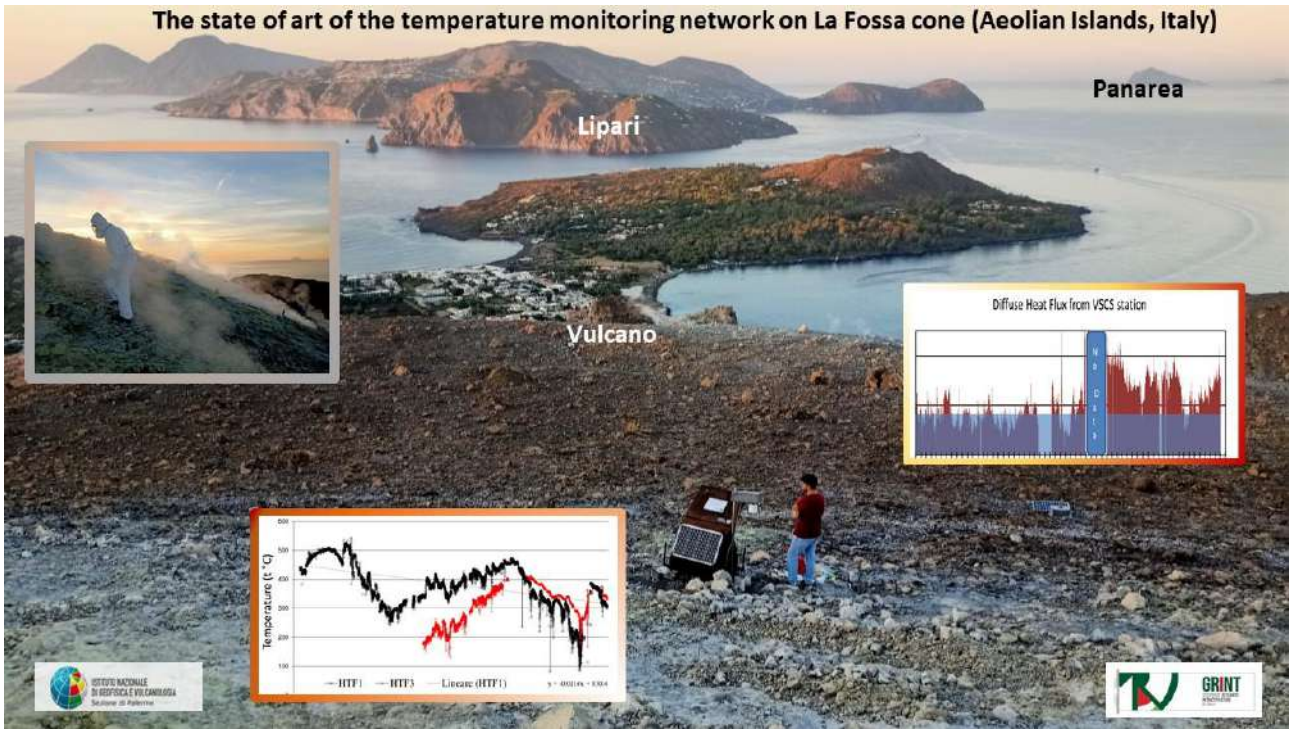

We present the long-term monitoring data, hourly recorded in the high temperature fumaroles (HTF) on the summit of La Fossa Cone, a close conduit volcano on the Island of Vulcano, and describe the actual implementation of the monitoring network. Its last eruption dates back to 1890. The thermal monitoring of the fumaroles output was included in the framework of geochemical monitoring activity in 1984 (Inguaggiato et al., 2018), the longest and uniform time series of data started in 1990 (fig 1) and is still uninterrupted. During 33 years the HTF temperature has been showing a general decreasing trend, some cyclic modulations (with the major periodical variation of about 20 years), with superimposed peaking variations (Diliberto, 2013). The peaking variations are correlated to unrest periods. The maximum temperatures recorded by the monitoring network ranged from 250 to 540 °C (Diliberto 2017). In 2023, this network has been implemented, and the number of monitored fumaroles increased to six high temperature vents (Fig. 2, HTF 1-6). Moreover, beside the HTF we started monitoring the temperature of the ground

in two diffuse degassing zones (Fig. 2, T gradient). The new HTF sites are located within two radial fractures elongated in the outer flank of the northern slope, with the outlet temperature reaching 320 °C, at the time of installation (December 2023). In the zones of diffuse degassing we have choosen two monitoring sites in a ground section of pyroclastic breccia (Fig. 2, T gradient), where we buried four sensors, at different depths. These diffuse degassing zones (DDZ) generally show at the surface a mild thermal anomaly because the ground is heated by the massive condensation of steam at shallow depth (a few meters below the line of sensors). At the time of installation of the monitoring profile (VSCS in …, G-Termis in November 2023, Fig. 2) the ground was permeable and dry, with temperature increasing at depth. In the DDZ, in the absence of water and steam, heat transfer is essentially diffusive and the convective component is negligible. In this dry condition, the temperature gradient is a proxy of the surface heat flux, being the only variable directly related to it. Moreover, the extrapolation of temperature gradient to the boiling temperature suggests a reference level for the minimum depth where the rising steam condenses within the ground. So, the continuous monitoring of the temperature gradient allows to track the local changes in heat flux and the vertical movements of the steam front in the summit area, at distance from the HTF zone. The G-Termis station is located about 190 m (linear distance) to the east of HTF zone, whereas the VSCS station is located about 210 m to the west of HTF zone (Fig. 2).

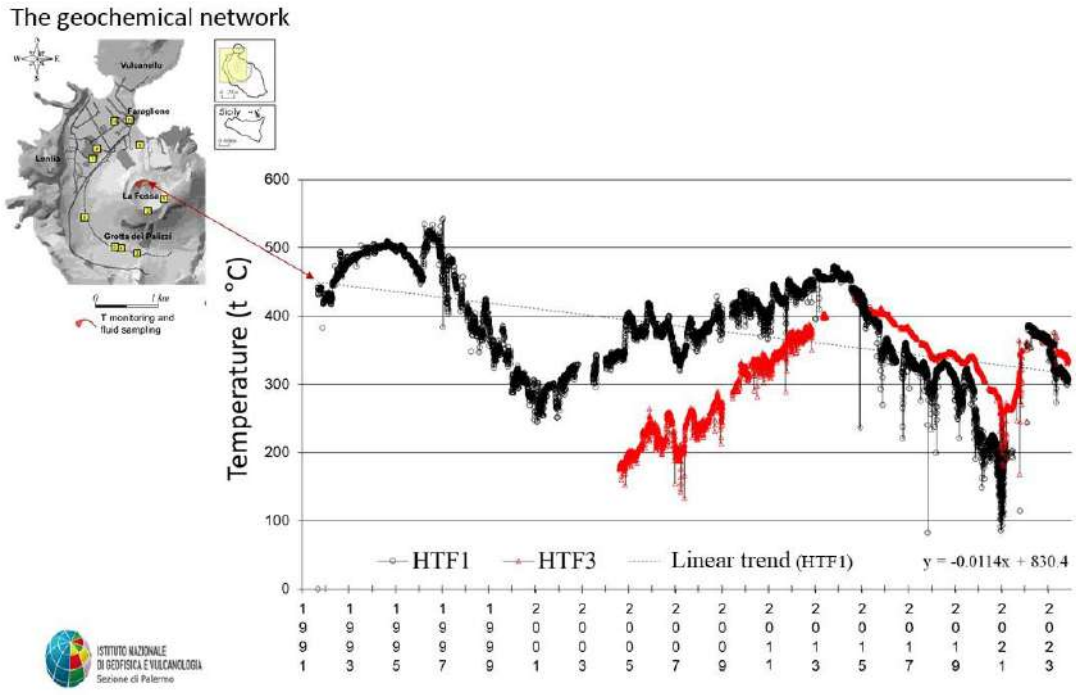

Fig. 1 – The longest time series of fumarole temperature recorded at La Fossa crater. The map showing the geochemical network is on the left corner.

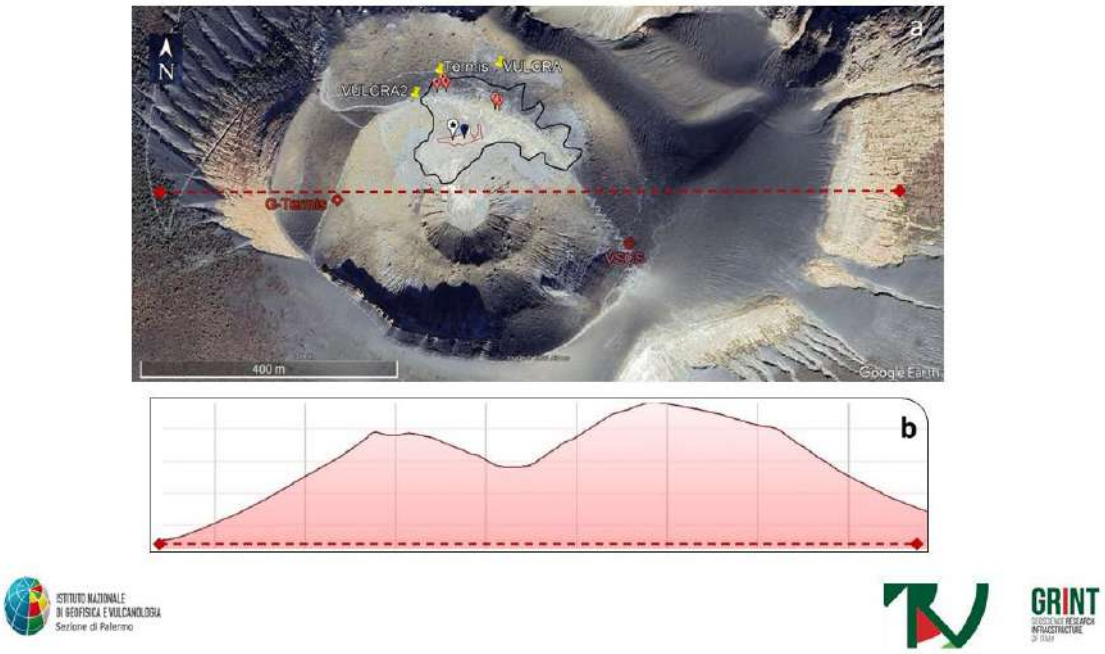

Fig. 2 – a) Google Image of summit area of la Fossa cone showing the temperature network for thermal monitoring of the active cone. The red line traces the profile reported in b. - b) E-W topographic profile of the summit area.

As an example of the information obtained by monitoring the temperature gradient in the diffuse degassing zone we show in Figure 3 the updated time series of heat flux, as it was registered at the VSCS station. The elaboration of the data set of temperatures revealed an increase of the thermal anomaly during the summer 2021, reaching the maximum intensity in September 2021 (Inguaggiato et al., 2022) due to the raising upward of a massive convective front below the VSCS station. The ground temperatures at VSCS station showed the highest peak with the maximum increasing rate registered from 17 September to October. To date even if the diffuse heat flux values from VSCS station, along with the other geochemical parameters are lowered from 2022, they have not yet returned to background values before the unrest of 2021. All the data recorded from the temperature monitoring network on La Fossa cone have been considered as ground control references for local application of thermal remote sensing (see for example Pailot et al., 2023; Silvestri et al. 2019). The updated time series are included in the periodical reports to the Italian Department of Civil Protection for volcanic surveillance.

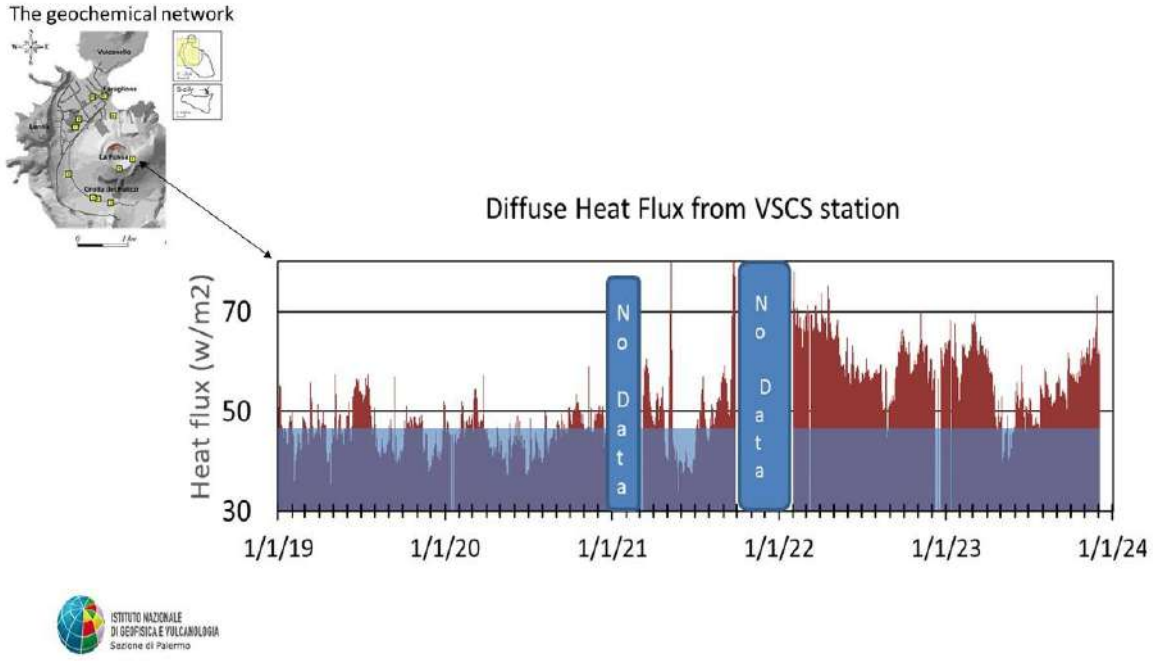

Fig. 3 – Heat flux variations evaluated from the time series of temperature gradients in a diffuse degassing zone. The blue shaded area shows the upper limit of background variations (47 w/m2); this value results from a statistic approach on the thermal records registered in the same site during a low degassing period. The map showing the geochemical network is on the left corner.

References

Diliberto I.S.; 2013: Time series analysis of high temperature fumaroles monitored on the island of Vulcano (Aeolian Archipelago, Italy). Journal of Volcanology and Geothermal Research 08/2013; 264., 150-163.

Diliberto I.S.; 2017: Long-term monitoring on a closed-conduit volcano: A 25 year long time-series of temperatures recorded at La Fossa cone (Vulcano Island), ranging from 250 to 520 °C. J. Volcanol. Geotherm. Res., http://dx.doi.org/10.1016/j.jvolgeores.2017.03.005 .

Diliberto, I.S.; 2021: Cyclic Behavior in the Fumaroles Output Detected by Direct Measurement of Temperature of the Ground. Eng. Proc. 2021, 5, 47. https://doi.org/10.3390/engproc2021005047.

Federico C.; Cocina O.; Gambino S.; Paonita A.; Stefano Branca S.; Coltelli; Italiano; Bruno; Caltabiano T; Camarda M.; Capasso G.; De Gregorio S., Diliberto I.S., Di Martino R., Falsaperla, Greco; Pecoraino; Salerno; Sciotto; Bellomo; Di Grazia; Ferrari; Gattuso; La Pica; Mattia; Pisciotta; Pruiti; Sortino; 2023: Inferences on the 2021 ongoing volcanic unrest at Vulcano Island (Italy) through a comprehensive multidisciplinary surveillance network (2023) Remote Sens. 15, 1405.https://doi.org/10.3390/rs15051405.

Inguaggiato, S.; Diliberto, I.S.; Federico, C.; Paonita, A.; Vita, F.; 2018: Review of the Evolution of Geochemical Monitoring, Networks and Methodologies Applied to the Volcanoes of the Aeolian Arc (Italy). Earth-Sci. Rev. 2018, 176, 241–276.

Inguaggiato, S., Vita, F., Diliberto, I.S., Mazot, A., Calderone, L., Mastrolia, A., Corrao, M.; 2022: The Extensive Parameters as a Tool to Monitoring the Volcanic Activity: The Case Study of Vulcano Island (Italy). Remote Sens. 2022, 14, 1283, doi:10.3390/rs14051283.

Pailot – Bonnétat, S.; Rafflin V.; Harris A.; Diliberto I.S.; Ganci G.; Cappello A.; Boudoire G.; Bilotta G.; Grassa F.; Gattuso A.; Ramsey M.; 2023: Anatomy of thermal unrest at a hydrothermal system: Case study of the 2021-2022 crisis at Vulcano. Earth Planet and Space 75:159. https://doi.org/10.1186/s40623-023-01913-5.

Silvestri M., et al.; 2019: Analysis of Thermal Anomalies in Volcanic Areas Using Multiscale and Multitemporal Monitoring: Vulcano Island Test Case Remote Sens. 2019, 11, 134; doi:10.3390/rs11020134.

Acknowledgements: The authors wish to thank the technical team of the Istituto Nazionale di Geofisica e Vulcanologia, Sezione di Palermo for their help in acquiring and processing data and for their support in field logistics. This research was funded by PON GRINT and the INGV-DPC (Istituto Nazionale di Geofisica e Vulcanologia-Italian Civil Protection Department) volcanic surveillance program of Vulcano Island.

Corresponding author: iole.diliberto@ingv.it

The magma chamber before the 79 CE Plinian eruption of Vesuvius

D.M. Doronzo[1], E. Trasatti[1], I. Arienzo[1], H. Balcone-Boissard[2], D. Barra[3], G. Aiello[3], V. Amato[4], M.A. Di Vito[1]

[1] *Istituto Nazionale di Geofisica e Vulcanologia, Italy;*

[2] *CNRS-Sorbonne Université, France;*

[3] *Università degli Studi di Napoli Federico II, Italy;*

[4] *Università degli Studi del Molise, Italy*

The 79 CE eruption of Vesuvius is the first documented Plinian eruption, also famous for the archaeological ruins of Pompeii and Herculaneum. Although much is known regarding the eruption dynamics and magma reservoir, little is known about the reservoir shape and growth, and related ground deformation. Numerical modelling by Finite Element Method was carried out, aimed at simulating the reservoir growth and ground deformation with respect to the reservoir shape (prolate, spherical, oblate) and magma overpressure. The modelling was tuned with volcanological, petrological and paleoenvironmental ground deformation constraints. Results indicate that the highest magma overpressure is achieved considering a prolate reservoir, making it as the most likely shape that led to eruption. Similar deformations but lower overpressures are obtained considering spherical and oblate reservoirs. These results demonstrate that ground deformation may not be indicative of eruption probability, style/size, and this has direct implications on surveillance at active explosive volcanoes.

References

Doronzo, D.M. et al. Magma reservoir growth and ground deformation preceding the 79 CE Plinian eruption of Vesuvius. Commun Earth Environ 4, 211 (2023). https://doi.org/10.1038/s43247-023-00880-9.

Corresponding author: domenico.doronzo@ingv.it

Mapping of volcanic deposits through the use of satellite techniques: the case of 2021 Mt. Etna eruptions

M. Dozzo[1], G. Ganci[1], S. Scollo[1], F. Lucchi[2]

[1] Istituto Nazionale Geofisica e Vulcanologia, Sezione di Catania - Osservatorio Etneo, Catania, Italy

[2] Dipartimento di Scienze Biologiche, Geologiche e Ambientali, Alma Mater Studiorum - Università di Bologna, Bologna, Italy

During explosive eruptions tephra fallout represents one of the main volcanic hazards and can be extremely dangerous for air traffic, infrastructures, and human health. Here we present a new technique aimed at identifying the urban areas covered by tephra after an explosive event based on the processing of PlanetScope satellite imagery. These recent multispectral data are acquired from a constellation of over 180 microsatellites and exhibits a relatively high spatial resolution (~ 3 m pixel size) covering once a day each point in the Earth surface.

Our technique is based on the introduction of a new index that we call 'Tephra Fallout Index (TFI)' computed from the mean reflectance values of the near infrared (NIR) band analyzing pre- and post-eruptive data in paved areas adjacent to the summit craters of Etna and more distal paved areas, to have an overall view of the distribution of the tephra deposit.

We use the Google Earth Engine computing platform and define a dynamic threshold for the TFI of different eruptive events to distinguish the areas affected by the tephra fallout.

We demonstrate our technique by applying it to the eruptive events that occurred in 2021 at Mt. Etna (Italy), which mainly involved the eastern and south-eastern flanks of the volcano, sometimes two or three times within a day, making field surveys difficult. Whenever possible, we compare our results with field data and find an optimal match.

The use of satellite imagery acquired from microsatellite constellations, such as PlanetScope, providing an optimal compromise between spatial and temporal resolution, may prove fundamental for identifying tephra deposits during eruptive episodes, such as those occurred in 2021 at Mount Etna volcano. In particular, our method provides a near real time result, making it ideal also for the mapping of other hazardous events worldwide.

Corresponding author: maddalena.dozzo@ingv.it

Monitoring of the radon emission from the surface soil in the Maccalube natural reserve

M. Falanga[1], S. Mancini[1], M. Guida[1], P. Madonia[2], P. Cusano[3]

[1] Università degli Studi di Salerno, Fisciano (SA), Italy

[2] Sezione di Catania, Osservatorio Etneo – INGV, Cefalù, Italy

[3] Sezione di Napoli, Osservatorio Vesuviano – INGV, Naples, Italy

The reserve of Maccalube di Aragona (Ag) in Sicily (Italy) is unfortunately known because of the death of two children in 2014 due to a sudden explosion of a mud volcano. Indeed, that reserve covers a large area made of mud volcanoes which emit different gases with high percentage of methane, followed by liquid hydrocarbons and high salinity waters [1-3]. Such overpressure fluids migrate towards the surface across discontinuities in subsoil often creating mud cones. The activity is generally of small intensity but, suddenly, as occurred in that tragic day of 2014, it could evolve in a paroxistic phase producing flooding which, in turn, causes damages and even injuries. For these reasons, mud volcanoes constitute a geohazard problem and, thus, are currently studied.

In the framework of the PROMUD Project (https://progetti.ingv.it/it/promud), in order to characterize the part of the reserve that is not under law restriction, in terms of environmental radioactivity, we performed measurements of radon in soil gas. Moreover, radon can be used as a naturally occurring tracer for environmental processes [4]. By means of grab-sampling or continuous monitoring of radon concentration, it is possible to assess several types of dynamic phenomena in the environmental matrices (air, water, etc). The preliminary survey was carried out at the end of November 2023 by using a radon and thoron detector (RAD7 Durridge) coupled with a soil probe for subsoil measurements and an accumulation chamber for surface emission [5]. The measurement points are in Fig. 1. Not negligible values of radon activity concentration at surface, of the order of thousands of Bq/m^3 in concomitance with the emitting active centers were detected, as well as values under the limit of detection (LD) elsewhere. Such high concentration at the only active centers could suggest that radon likely uses gases, i.e. methane, as carrier to way out from soil whereas no escape is possible due to the presence of a compact clay layer.

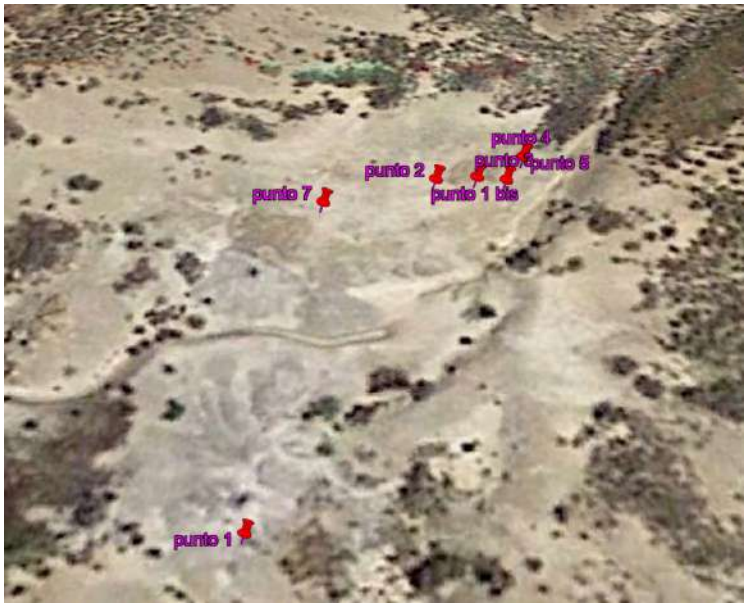

Fig. 1 – Measurement points at Maccalube reserve.

References

Etiope G.; Caracausi A.; Favara R.; Italiano F. & Baciu C.; 2002: Methane emission from the mud volcanoes of Sicily (Italy). Geophysical Research Letters, doi:10.1007/1-4020-3204-8_12.

Bonini M.; 2009: Mud volcano eruptions and earthquakes in the Northern Apennines and Sicily, Italy. Tectonophysics, doi: 10.1016/j.tecto.2009.05.018.

Cangemi M. & Madonia P.; 2013: 2014). GÖTTINGEN CONTRIBUTIONS TO GEOSCIENCES, doi: 10.3249/webdoc-3923.

Cuomo, Albina et al. “Using Radon-222 as a Naturally Occurring Tracer to investigate the streamflow-groundwater interactions in a typical Mediterranean fluvial-karst landscape: the interdisciplinary case study of the Bussento river (Campania region, Southern Italy).” The EGU General Assembly 12 (2010): 1-1.

Mancini, S., Guida, M., Cuomo, A., and Guida, D.: A geogenic approach for the Radon monitoring and the exposure assessment at a regional scale: The results of the Rad_Campania project, Adv. Geosci., 52, 87–96, https://doi.org/10.5194/adgeo-52-87-2020, 2020

Corresponding author: mfalanga@unisa.it

How multiple observations tracked the onset and evolution of the 2021-2023 unrest at Vulcano Island (Southern Italy), and unveiled the processes behind it

C. Federico[1], A. Paonita[1], S. Bellomo[1], R. M. R. Di Martino[1], A. Gattuso[1], L. La Pica[1], G. Lazzaro[1], M. Longo[1], G. Pecoraino[1], A. F. Pisciotta[1], F. Sortino[1].

[1] Istituto Nazionale di Geofisica e Vulcanologia, sezione di Palermo, Italy

In September 2021, the La Fossa volcano entered a new phase of unrest. The monitoring system recorded a sudden variation in seismicity, ground deformation, fumarole temperatures, and soil and plume degassing. These variations were ascribed to the fast vaporisation and expansion of the central hydrothermal system (Federico et al., 2023), strongly impacted by the input of heat and chemicals from the magmatic source. By the onset of the unrest, fumarole chemistry showed clear-cut variations, related to the dominant contribution of the magmatic gas over the hydrothermal one. The CO_2 content and the He isotopes of the magmatic gas revealed the appearance of a more primitive magma during the climax of the unrest. The increased contribution of magmatic gases was already evident since 2018, so the 2021 unrest could have been the outcome of a long-lasting preparatory phase. The anomalous outflow of magmatic gases gradually extended northwest of La Fossa cone and involved the thermal area of Baia di Levante, where several low-temperature (100°C) fumaroles emit a vapour coming from a local hydrothermal aquifer. The gas composition had been typical of hydrothermal systems, with equilibrium temperatures close to 200°C but, by the onset of the crisis, it was gradually modified by the magmatic gas. In May 2022, a sudden and likely explosive release of gas occurred in the Baia di Levante, which was testified by the whitening of the seawater in the bay, and by the appearance of typical pockmark structures on the seafloor. At that moment, the gas composition of the monitored fumarole on the beach closely approached that of crater fumaroles. This episode drove the attention of the scientific community to this area, for several months affected by a significant input of magmatic vapour, because of the risk related to the huge CO_2 emission and the eventual overpressurization of the local hydrothermal aquifer. The magmatic contribution is persistently high in the fumaroles of La Fossa crater by the time of this communication, whereas it is declining in the Baia di Levante. The gas output in the crater area, and at the base of the cone is declining as well.

References

Federico C., Cocina O., Gambino S., Paonita A., Branca S., Coltelli M., Italiano F., Bruno V., Caltabiano T., Camarda M., Capasso G., De Gregorio S., Diliberto I.S., Di Martino R.M.R., Falsaperla S., Greco F., Pecoraino G., Salerno G., Sciotto M., Bellomo S., Di Grazia G., Ferrari F., Gattuso A., La Pica L., Mattia M., Pisciotta A.F., Pruiti L., Sortino F.; 2023: Inferences on the 2021 Ongoing Volcanic Unrest at Vulcano Island (Italy) through a Comprehensive Multidisciplinary Surveillance Network. Remote Sensing, 15(5), 1405, doi.org/10.3390/rs15051405.

Corresponding author: cinzia.federico@ingv.it

Automated detection, characterization, and localization of Very Long-Period seismic events specifically designed for volcanic monitoring applications on Stromboli Island.

S. Gammaldi, D. Delle Donne, P. Cantiello, W. De Cesare, A. M. Esposito, R. Peluso, M. Orazi

Istituto Nazionale di Geofisica e Vulcanologia (INGV), Osservatorio Vesuviano, Sezione di Napoli.

Real-time applications in seismology have become essential for actively monitoring and surveilling volcanoes. They serve as valuable tools for promptly identifying volcanic unrest. In open-vent active volcanoes, the detection of Very Long Period (VLP) seismicity, typically associated with mild and persistent explosive activity, holds paramount significance in volcano monitoring. Variations in the occurrence rate and magnitude of VLP seismicity may indicate an impending phase of unrest. This study introduces a novel method for the automatic real-time detection and characterization of VLP seismicity at the Stromboli active volcano in Italy.

The detection algorithm relies on Three-Component Amplitude (TCA), derived from waveform polarization and spectral analysis of continuous recordings. It furnishes crucial information such as the time of detection, azimuth, incidence, amplitude, and frequency of the identified VLP. The automatically detected amplitude is then presented as peak-to-peak and root mean square amplitude, facilitating the automated amplitude localization of VLP.

The VLP detections and characterizations obtained through our automatic detection algorithm are compared with those derived from manual and automatic inspections of the seismic record, as well as with VLP time histories from existing published datasets. The comparison reveals that the VLP detection time series generated by the automatic algorithm effectively mirrors fluctuations in VLP activity, as manually identified by operators over an approximately 20-year period. This validation allows for the integration of the automatic algorithm into the real-time processing framework employed at Stromboli for volcano surveillance.

Corresponding author: sergio.gammaldi@ingv.it

Nonlinear convective motion of the asthenosphere and the lithosphere melting. A model for the birth of a volcano

C. Godano[1,2], S. Carlino[2], F. Oliveri[3], C. F. Mufanò[3]

[1] Department of Mathematics and Physics, Università della Campania "Luigi Vanvitelli", Caserta, Italy.
[2] INGV-Osservatorio Vesuviano, Napoli, Italy
[3] Department of Mathematical and Computer Sciences, Physical Sciences and Earth Sciences

The processes of heat transfer occurring between the Earth's asthenosphere and lithosphere are responsible for partial melting of rocks, leading to the magma generation and its migration and segregation in the crust and, possibly, to volcanoes generation at the surface. Convection is the dominant mechanism regulating the heat transfer from the asthenosphere to the lithosphere, although many aspects of the whole process are not yet clear. Therefore, the knowledge of the physical processes leading to the melting of the lithospheric rocks has important consequences in understanding the interior Earth dynamics, the surface volcanic dynamics, and its related hazards. Rock melting occurs when the temperature gradient meets the rock solidus. Here, we propose a nonlinear convective 1D analytical model (representing an approximation of more 3D complex models). The steady state solution of our equation is in good agreement with the estimated geotherms of the asthenosphere. A perturbative approach leads to a heat swelling at the boundary between asthenosphere and lithosphere able to determine its melting and the birth of a volcano. A generalization of the analytical model admits only numerical solution and put some constraint to the model.

Corresponding author: cataldo.godano@unicampania.it

An innovative system for the worldwide monitoring of volcanic thermal anomalies through Sentinel-2 and Landsat 8/9 data integration

F. Marchese[1,3], N. Genzano[2,3], N. Pergola[1,3],

[1] Institute of Methodologies for Environmental Analysis (IMAA)- National Research Council (CNR), 85050 Tito Scalo (Italy)

[2] School of Engineering (SI) - University of Basilicata (UNIBAS), 85100 Potenza (Italy)

[3] Space Technologies and Application Centre, Potenza, Italy

The NHI (Normalized Hotspot Indices) algorithm was developed to map high-temperature volcanic features through the analysis of near infrared (NIR) and shortwave infrared (SWIR) data, at mid-high spatial resolution (up to 20 m), from the Operational Land Imager (OLI) and the Multispectral Instrument (MSI), respectively aboard the Landsat-8/9 and Sentinel-2A/B satellites. The algorithm was then implemented within the Google Earth Engine (GEE) platform, which offers an extended dataset of geospatial data together with high computational resources. The developed GEE App enables the analysis of volcanic thermal anomalies at global scale, in terms of hotspot number, total SWIR radiance and hotspot area, without requiring any authentication from the users. The *NHI tool/system* then provides automated notifications about recent (over the past 48 hours) volcanic thermal activity globally, exploiting the increased temporal coverage of the combined Sentinel-2 and Landsat 8/9 observations. In this work, we present the NHI tool, and some recent results achieved by investigating eruptions occurred at different volcanoes (e.g., Mauna Loa, Kilauea, Ambrym, Etna). These results, providing accurate information about location, intensity, and spatial extent of hot targets (e.g., lava flows/lakes), which may be further enriched by quantitative characterization (e.g., in terms of volcanic radiative power), demonstrate the relevance of the developed GEE-App in the operational monitoring of active volcanoes, as a complement to the information provided by satellite systems offering higher temporal/lower spatial resolution products.

References

Genzano, N.; Pergola, N.; Marchese, F.; 2020. A Google Earth Engine tool to investigate, map and monitor volcanic thermal anomalies at global scale by means of mid-high spatial resolution satellite data. Remote Sensing, 12(19), 3232.

Marchese, F.; Genzano, N.; Neri, M.; Falconieri, A.; Mazzeo, G.; Pergola, N.; 2019. A multi-channel algorithm for mapping volcanic thermal anomalies by means of Sentinel-2 MSI and Landsat-8 OLI data. Remote Sensing, 11(23), 2876.

Marchese, F.; Genzano, N.; 2023. Global volcano monitoring through the Normalized Hotspot Indices (NHI) system. Journal of the Geological Society, 180(1).

Corresponding author: francesco.marchese@cnr.it

Thermo-poro-viscoelastic deformation sources

M. Nespoli[1], M. E. Belardinelli[1], M. Bonafede[1]

[1] Department of Physics and Astronomy, Alma Mater Studiorum, Università di Bologna, Bologna, Italy

1. Introduction. Thermo-poro-elastic (TPE) deformation sources allow to explain seismicity and deformation induced by pore-pressure (p) and temperature (T) changes in geothermal and volcanic environments. In the last years, TPE inclusions have been applied to model the displacement and the stress field in the caldera of Campi Flegrei (Italy), where pore-pressure and temperature changes are assumed to derive from the exsolution of fluids from a deep magmatic chamber. In the literature both analytical and numerical models of TPE inclusions with different geometries exist (Belardinelli et al., 2019, Mantiloni et al., 2020, Belardinelli et al., 2022, Nespoli et al., 2021 and 2022). While previous works were focused on TPE induced static deformation patterns, in the present work we show how to model the transient effects on displacement, strain and stress. Such transient effects can be modeled by extending the TPE models to the Thermo-Poro-ViscoElastic (TPVE) ones.

2. Method. The inclusion method allows us to model the static mechanical effects of pore-pressure and temperature changes occurring inside a closed volume (i.e. an inclusion) embedded in an elastic medium (Eshelby, 1957). To model transient mechanical effects one can include the effects of viscoelasticity. A viscoelastic behavior should be expected in high temperature and fluid saturated rocks, due to thermally activated and pressure-solution creep. The analytical thermo-poro-viscoelastic (TPVE) solutions for a disc-shaped inclusion embedded in a uniform viscoelastic medium can be obtained through the correspondence principle (Fung 1965, Nespoli et al., 2023a) assuming that the medium is a homogeneous Maxwell half space.

3. Discussion and Conclusions. The TPVE analytical solutions indicate that including the viscoelastic behavior inclusion can explain a decrease in seismicity rate accompanied by an increase of surface uplift, as was observed in the late stage of the 1982-84 unrest phase at Campi Flegrei. This behavior is in contrast with what is expected according to the elastic response, in which the seismicity increases during the uplift and decreases during the subsidence. Our approach allows us to extend the relevance of hot and pressurized inclusion models to the interpretation of transient mechanical effects, which can be observed in several areas of the World.

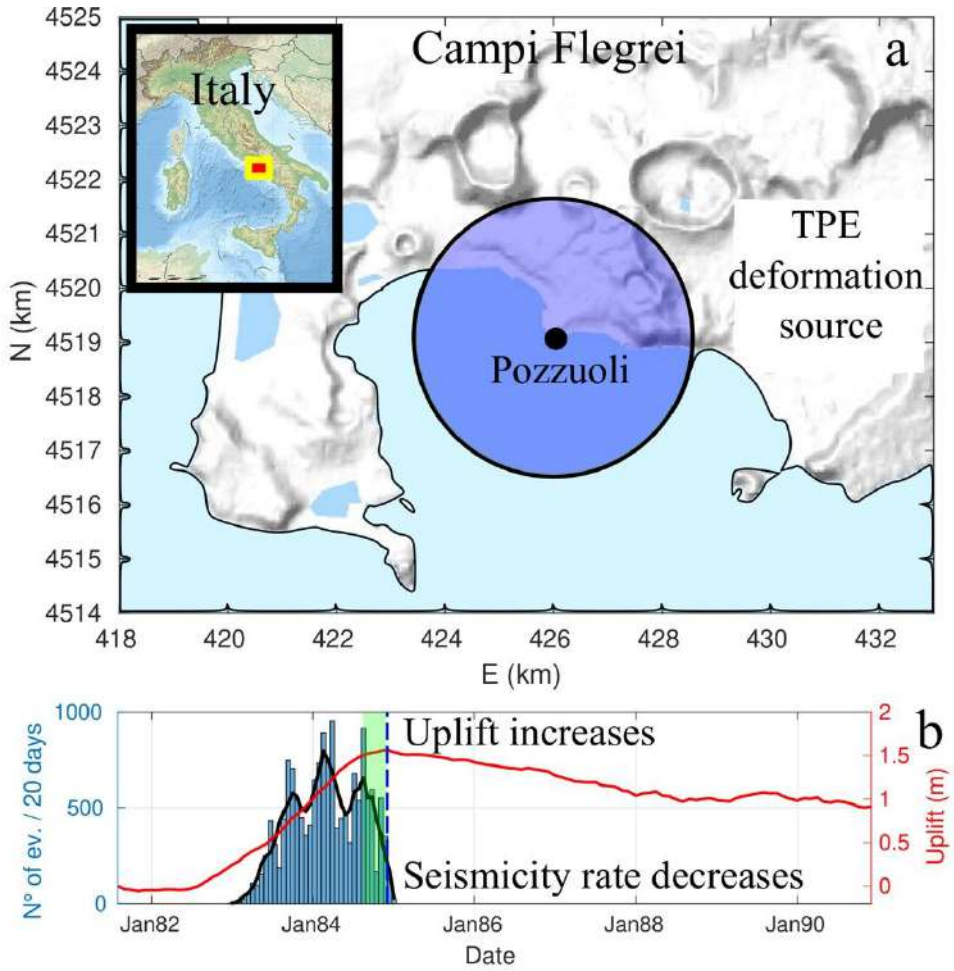

Figure 1. (a) Caldera of Campi Flegrei (Italy). The blue circle represents the projection of the TPE inclusion as inferred from the inversion of geodetic data measured during the period June 1980–1983 (Nespoli et al.2021). (b) Uplift (red curve) as a function of time, measured in the location of maximum measured uplift (Pozzuoli harbor) from 1980 to 1990. Histograms represent the number of events in time windows of 20 d. The black curve shows the number of events computed with a moving average.

References

Belardinelli, M., Bonafede, M. & Nespoli, M. (2019), 'Stress heterogeneities and failure mechanisms in-diced by temperature and pore-pressure increase in volcanic regions', Earth and Planetary Science Letters 525, 115765.

Belardinelli, M. E., Nespoli, M. & Bonafede, M. (2022), 'Stress changes caused by exsolution of magmatic fluids within an axi-symmetric inclusion', Geophysical Journal International . Ggac093. URL: https://doi.org/10.1093/gji/ggac093

Eshelby, J. D. (1957), 'The determination of the elastic field of an ellipsoidal inclusion, and related problems',Proc. R. Soc. Lond. A 241(1226), 376–396.

Mantiloni, L., Nespoli, M., Belardinelli, M. E. & Bonafede, M. (2020), 'Deformation and stress in hydrothermal regions: The case of a disk-shaped inclusion in a half-space', Journal of Volcanology and Geothermal Research 403, 107011.

Nespoli, M., Belardinelli, M. E. & Bonafede, M. (2021), 'Stress and deformation induced in layered media by cylindrical thermo-poro-elastic sources: An application to Campi Flegrei (italy)', Journal of Volcanology and Geothermal Research 415, 107269.

Nespoli, M., Belardinelli, M. E., Calò, M., Tramelli, A. & Bonafede, M. (2022), 'Deformation induced by distributions of single forces in a layered half-space: EFGRN/EFCMP', Computers and Geosciences 164, 105136. URL: https://www.sciencedirect.com/science/article/pii/S0098300422000930

Nespoli M, Belardinelli M.E. and Bonafede M. (2023a), Thermo-poro-viscoelastic response of a disc-shaped inclusion, Geophysical Journal International, Volume 235, Issue 1, October 2023, Pages 135–149, https://doi.org/10.1093/gji/ggad212

Corresponding author: massimo.nespoli2@unibo.it

Magnetic Anomaly Survey of the Martignano Lake maar center, Sabatini Volcanic District, Central Italy.

I. Nicolosi[1], F. D'Ajello Caracciolo[1], G. Sottili[2], N. Ricchetti[3], R. Carluccio[1]

[1] Istituto Nazionale di Geofisica e Vulcanologia

[2] Università di Roma, La Sapienza

[3] Via Vallelunga 7, Rignano Flaminio (RM) ,Italy

Introduction

A magnetic anomaly survey was conducted at the Martignano Lake volcanic center, which was formed during the final phases of the evolutionary history of the Sabatini Volcanic District (SVD) and persisted until 70 ka when the last documented SVD eruption took place at the Martignano maar (Marra et al., 2019).

The SVD became active 0.8 Ma and was characterized by explosive eruptions causing the deposition of pyroclastic flows and falls, surges and localized lava flows (Cioni et al., 1993). This volcanic activity developed during Pleistocene times due to the post-orogenic extensional tectonics that led to the Tyrrhenian Sea opening (Malinverno & Ryan, 1986). The SVD extends over an area of 1800 km^2 and is characterized by the lack of a central volcanic edifice as the activity was distributed over a large area. The SVD hydromagmatic centers mostly consist of tuff rings and subordinate tuff cones with maar-type craters located in the central area of the SVD, to the N and E of present-day Lake Bracciano (Sottili et al., 2012). The erupted tephra volumes from either monogenetic or polygenetic SVD maars ranged 0.004–0.07 km^3 during individual maar-forming eruptions.

The structure of Martignano lake was created by a sequence of hydromagmatic eruptions forming a composite maar type crater (Sottili et al. 2012).

The maar structure is a common volcanic morphology that occurs when magma interacts with groundwater, leading to multiple underground explosions and the formation of a crater that cuts into the pre-eruptive surface. Maar volcanoes subsurface structure is a cone-shaped geometry (diatreme) generated by mass deficiencies in the root zone, where the eruptive explosions occur; the diatreme and the maar crater are mainly due to explosions, collapse, and subsidence mechanism (Lorenz, 2003). Where no exposure of the diatreme exists, the application of geophysical modeling techniques can provide a method to model the geometry of a maar-

diatreme, its feeder dikes, and any intrusions (Skacelova, 2010, Blaikie et al., 2014, Mrlina, 2009). Potential field methods have proven valuable in providing information about volcanic structures and subvolcanic bodies, presenting a valid approach to probe through a volcanic pile (Nicolosi et al., 2014, 2016). Short wavelength magnetic anomalies have been observed inside maars craters, often associated with high gravimetric signature and interpreted as dikes that intruded the diatreme in the center of the main crater (Blaikie et al., 2014).

The Martignano lake survey

The magnetic survey of Martignano center represents a novelty, as this type of data has never been acquired for this volcanic center before. The survey was conducted using an inflatable boat designed for lake navigation and equipped with a GEM Systems GSM 19 magnetometer to measure the total magnetic intensity. Additionally, a GPS system for obtaining spatial coordinates of the magnetic measurements is integrated into the magnetometer platform.

The entire surface of the lake, which measures approximately 1890x1400m, was surveyed using profile lines oriented in the N-S direction and spaced 50 meters apart (Fig. 1). A series of Tie-lines E-W oriented were acquired to correctly level the main survey lines. While navigating the lake, echosounder measurements were conducted using a Garmin Striker V7 unit equipped with a transducer operating at 200 kHz. These measurements were gathered to construct a model of the lake's bathymetry and to examine morphological structures originating from volcanic activity. Throughout the measurements, numerous gas bubble emissions in the form of flares (continuous release of gas bubbles,) were observed. These emissions, characterized by high sonic impedance of the bubbles, scatter the echosounder signal, making them distinctly visible (Caudron et al. 2012). They were particularly concentrated in an area labeled FL in Fig. 3. Exploration of the lake bottom focusing on the region of higher density of observed flares was conducted using a submarine ROV (Remotely Operated Vehicle) equipped with a camera and a robotic arm.

Two aeromagnetic profiles, obtained during a previous survey covering the entire SVD, are situated to the west and east of the lake border in a north-south direction (referred to as L1 and L2, as shown in Fig. 2). The average altitude maintained during the aeromagnetic survey was 400 meters above ground level.

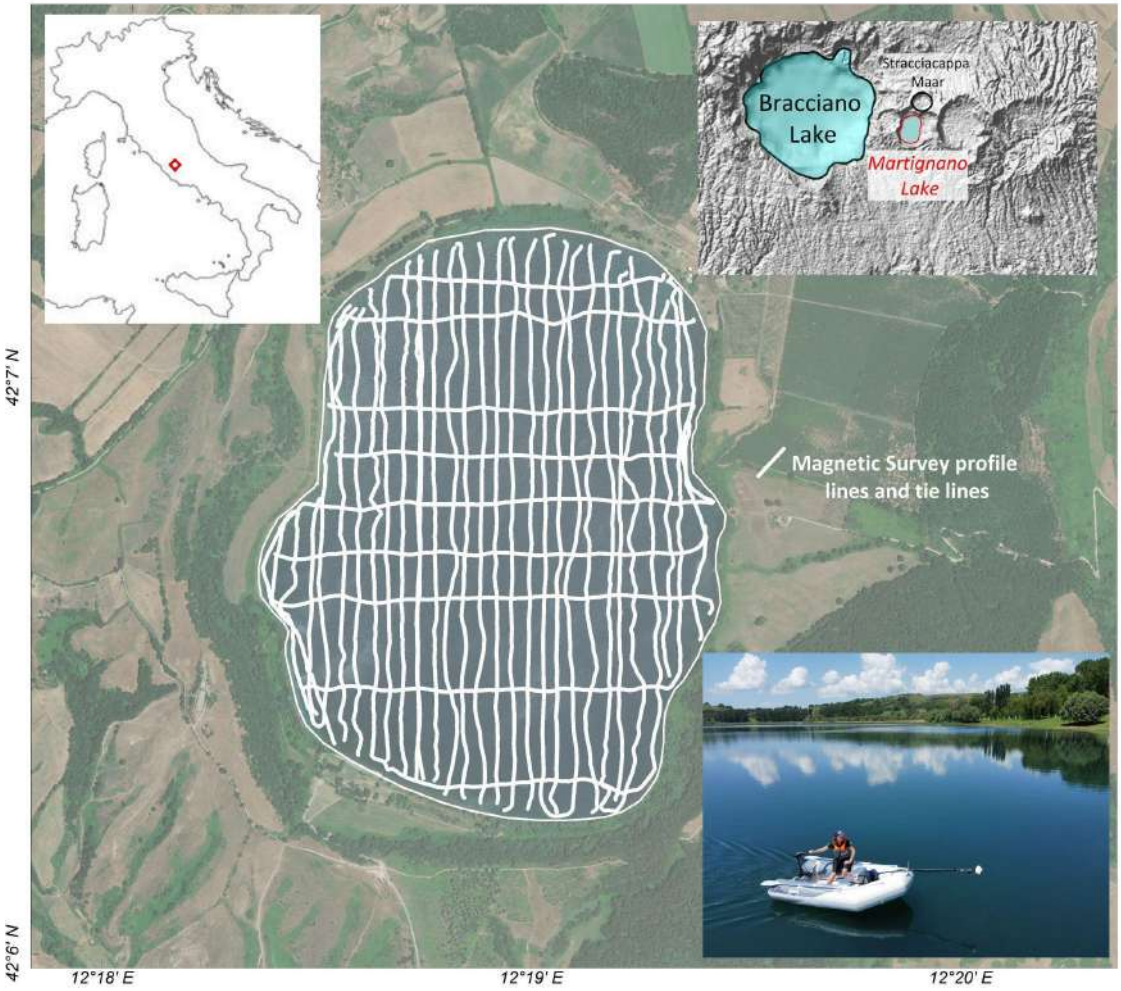

Fig. 1 - Location of the magnetic survey lines and tie lines acquired in Martignano Lake.

Results

The magnetic anomaly map resulting from the survey, shows that the Martignano magnetic anomalies are due to the presence of a negative magnetization contrast with the surrounding volcanic rocks; the primary dipolar structure of the magnetic intensities observed at the southern and northern borders of the lake (negative magnetic intensity lobe at point A and positive one at point B, Fig. 2) is attributed to the contrast in magnetization among the hydromagmatic products originating from the Martignano center, mostly consisting of stratified and cross-stratified tuffs with alternating fine-ash rich and coarse-ash to fine-lapilli rich horizons, the underlying structure of the maar, and the pre-maar composition, predominantly consisting of alternating pyroclastic deposits and lava flows from the SVD's activity. Nicolosi et al. (2019) estimated a bulk magnetization of 3 A/m for SVD products. This magnetization value surpasses the average values recorded from outcrops of the hydromagmatic products found at the Martignano lake by an order of magnitude, resulting in a significantly lower measurement. This contrast can also be considered representative for the diatreme and crater infill products.

The presence of decimetric lava lithics and bombs in the hydromagmatic deposits associated with the Martignano activity and the outcrop of a scoria cone deposit on the lake southern border (Sottili et al., 2012), suggests the presence of a highly magnetized lava plateau that was partly fragmented by the onset of the maar eruptive activity at Martignano. Anomaly D in Fig. 2 can represent the magnetic effect of the scoria cone deposits. The existence of a pre-eruptive 10-meter thick lava plateau is also documented for the nearby Stracciacappa maar crater (Moscatelli et al., 2021) (Fig. 1).

The negative magnetization contrast between Martignano and surrounding SVD products is testify by the two aeromagnetic profiles reported in figure 2, where a intense positive anomaly is observed along profile L1 and L2 at the northern border of the lake, mirroring the positive anomaly B of figure 2 and indicating the presence of higher magnetized material separating Martignano and Straccicappa maars (figure 1); this magnetic anomaly is not compatible with the presence of the low magnetized hydromagmatic products outcropping in the northern rim of the Martignano crater. Magnetic anomaly B in Figure 2 is therefore interpreted as the result of subsurface lava and pyroclastic products from the SVD which previously formed the topography of the pre-maar activity. The geometry of magnetic anomaly B suggests a thinning of the magnetized material and an inclined surface that deepens toward the center of the lake marking the contact surface between maar's diatrema and the pre-maar products;

The negative intensity sub-circular magnetic anomaly observed in the central region of the crater lake (G in Fig. 2) represents the effect of low magnetization material; this zone can be interpreted as the area where the magnetized pre-maar volcanic pile disappears due to the presence of the maar diatrema and infilling products.

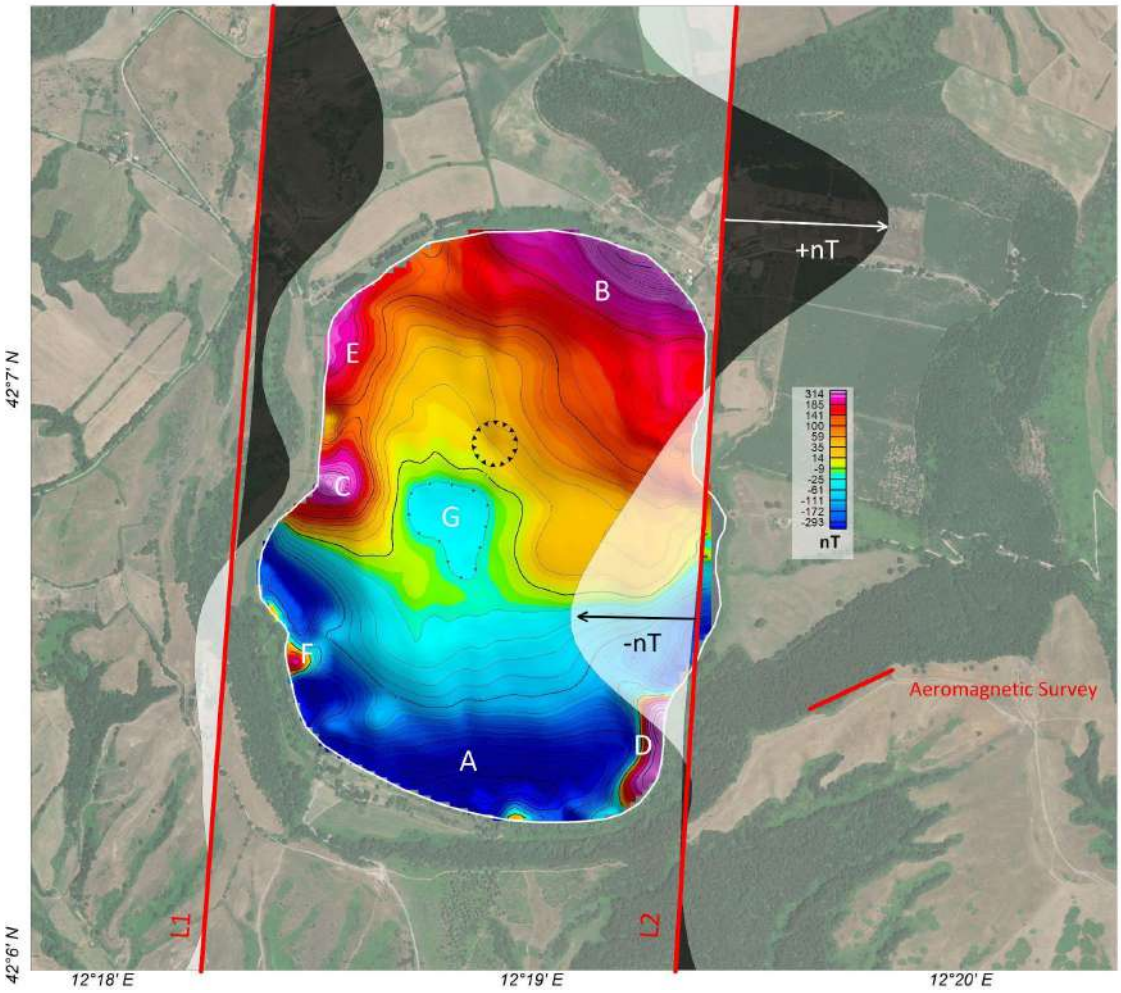

Figure 2 - Magnetic anomaly map of Martignano Lake displayed using a nonlinear intensity color scale and contour lines. Letters denote magnetic anomalies discussed in the main text. Red lines indicate survey lines from the 2008 aeromagnetic survey of the Sabatini Volcanic District (Nicolosi et al., 2019).

During the echosounder survey, numerous gas emission flares were observed across the entire lake bottom surface. A concentrated area with higher flare density was identified (FL, Fig. 3). This area coincides with a local magnetic anomaly minimum oriented in the N-S direction, with its southern boundary corresponding to the magnetic anomaly minimum G depicted in Fig. 2. Gas and fluid circulation might serve as an additional factor contributing to the reduction in magnetization properties of volcanic products. In this particular area, a submarine ROV was deployed to capture images of the emission sources originating from the lakebed. The acquired images depict an extensive field of gas sources emerging from small pockmarks and craters excavated in the mud due to gas efflux.

The lack of significant local magnetic dipolar anomalies within the crater perimeter suggests the absence of intrusions of dikes and lava effusions from the Martignano diatreme system.

The intense dipolar anomalies situated on the western border of the lake (E, F in Fig. 2) are associated with local lava outcrops whereas anomaly C is attributed to the presence of a bathymetric rock spur. This spur can be interpreted as a remnant of the fused crater rims resulting

from multiple explosions scattered within the lake perimeter, with non-coincident points of origin (Sottili et al., 2012).

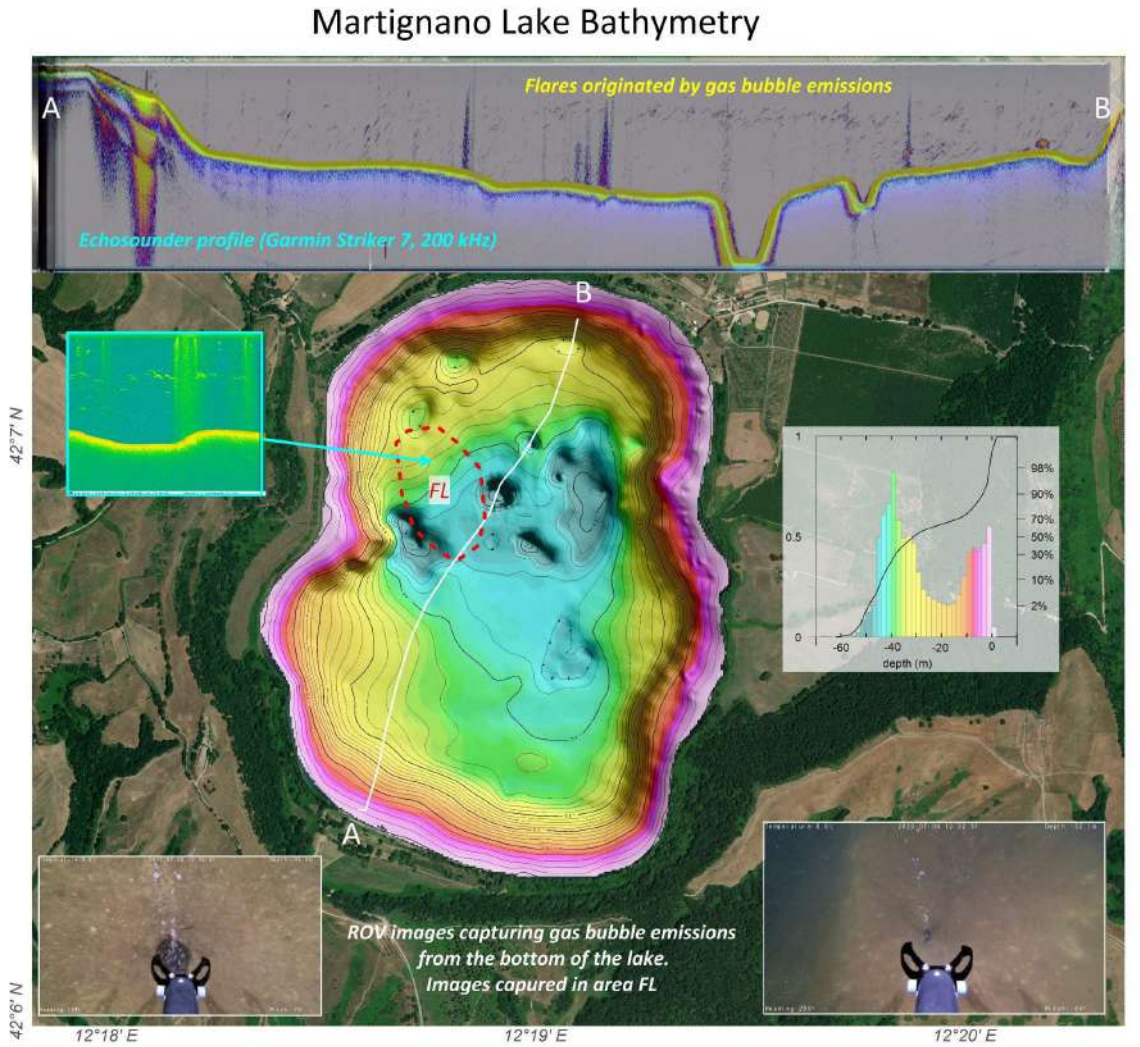

Figure 3: Bathymetry map of Martignano Lake displayed using a nonlinear color scale and contour lines. AB represents an echo-sounder profile line intersecting two craters.

References

Blaikie T.N. , L. Ailleres, P.G. Betts, R.A.F. Cas, (2014) A geophysical comparison of the diatremes of simple and complex maar volcanoes, Newer Volcanics Province, south-eastern Australia, Journal of Volcanology and Geothermal Research, Volume276, Pages 64-81, ISSN 0377-0273, https://doi.org/10.1016/j.jvolgeores.2014.03.001.

Caudron, C., A. Mazot, and A. Bernard (2012), Carbon dioxide dynamics in Kelud volcanic lake, J. Geophys. Res., 117, B05102, doi:10.1029/2011JB008806.

Cioni, R., Laurenzi, M.A., Sbrana, A., Villa, I.M., 1993. 40Ar/39Ar chronostratigraphy of the initial activity in the Sabatini volcanic complex (Italy), Boll. Soc. Geol. Ital.,112,251-263.

Lorenz Volker (2003), Maar-Diatreme Volcanoes, their Formation, and their Setting in Hard-rock or Soft-rock Environments, Geolines 15.

Malinverno, A., Ryan, W., 1986. Extension in the Tyrrhenian Sea and Shortening in the Apennines as Result of Arc Migration Driven by Sinking of the Lithosphere, Tectonics 5(2): 227-245, DOI:10.1029/TC005i002p00227.

Marra, F., Florindo, F., Jicha, B.R., Nomade, S., Palladino, D.M., Pereira, A., Sottili, G., Tolomei, C., 2019. Volcano-tectonic deformation in the Monti Sabatini Volcanic District at the gates of Rome (central Italy): evidence from new geochronologic constraints on the Tiber River MIS 5 terraces. Scientific Reports, 9:11496.

Moscatelli, M., Vignaroli, G., Pagliaroli, A. et al. Physical stratigraphy and geotechnical properties controlling the local seismic response in explosive volcanic settings: the Stracciacappa maar (central Italy). Bull Eng Geol Environ 80, 179–199 (2021). https://doi.org/10.1007/s10064-020-01925-5

Mrlina, J., Kampf, H., Kroner, C., Mingram, J., Stebich, M., Brauer, A., Geissler, W.H., Kallmeyer, J., Matthes, H., Seidl, M., 2009. Discovery of the first Quaternary maar in the Bohemian Massif, Central Europe, based on combined geophysical and geological surveys. Journal of Volcanology and Geothermal Research 182 (1–2), 97–112.

Nicolosi, I., D'Ajello Caracciolo, F., Branca, S., Ventura, G. and M. Chiappini, 2014, Volcanic conduit migration over a basement landslide at Mount Etna (Italy): Scientific Reports 01/2014; 4:5293. DOI: 10.1038/srep05293.

Nicolosi, I., D'Ajello Caracciolo, F., Branca, S., Ferlito, C., Chiappini, M. (2016). The earliest open conduit eruptive center of the Etnean region: evidence from aeromagnetic, geophysical and geological data, Bulletin of Volcanology, 78:50. DOI: 10.1007/s00445-016-1042-3.

Nicolosi, I., D'Ajello Caracciolo, F., Pignatelli, A., Chiappini, M., (2019), Imaging the Bracciano caldera system by aeromagnetic data inversion (Sabatini Volcanic District, Central Italy). Journal of Volcanology and Geothermal Research, 388, doi:10.1016/j.volgeores.2019.106680.

Skacelova, Z., Rapprich, V., Valenta, J., Hartvich, F., Sramek, J., Radon, M., Gazdova, R., Novakova, L., Kolinsky, P., Pecskay, Z., 2010. Geophysical research on structure of partly eroded maar volcanoes; Miocene Hnojnice and Oligocene Rychnov volcanoes (northern Czech Republic). Journal of Geosciences 55 (4), 333–345.

Sottili, G., Palladino, D.M., Marra, F., Jicha, B., Karner, D.B., Renne, P. (2010). Geochronology of the most recent activity in the Sabatini Volcanic District, Roman Province, central Italy. Journal of Volcanology and Geothermal Research 196 (2010) 20–30.

Sottili, G.,Palladino, M., Gaeta, M., Masotta, M., (2012), Origins and energetics of maar volcanoes: examples from the ultrapotassic Sabatini Volcanic District (Roman Province, Central Italy). Bull. Volcanol.., 74, 163-186. DOI 10.1007/s00445-011-0506-8

Corresponding author: iacopo.nicolosi@ingv.it

Twenty years of Campi Flegrei seismic monitoring by Istituto Nazionale di Geofisica e Vulcanologia- Osservatorio Vesuviano: history, performances and future developments

M. Orazi, D. Galluzzo, A. Benincasa, F. Bianco, A. Bobbio, G. Borriello, C. Buonocunto, M. Capello, A. Caputo, M. Castellano, V. Convertito, P. Cusano, G. Dalla Via, L. D'Auria, W. De Cesare, D. Delle Donne, A. Di Filippo, F. Giudicepietro, S. Guardato, R. Riccio, R. Esposito, G. Gaudiosi, M. La Rocca, F. Liguoro, D. Lo Bascio, M. Martini, R. Nappi, L. Nardone, R. Peluso, S. Petrosino, P. Ricciolino, G. Scarpato, M.G. Soldovieri, M.A. Di Vito

Istituto Nazionale di Geofisica e Vulcanologia, Sezione di Napoli, Osservatorio Vesuviano, Via Diocleziano 328, Napoli, Italy

The Campi Flegrei caldera is one of the highest-risk volcanic areas in the world due to the large number of people living there. In response to this high risk, the Campi Flegrei are one of the most monitored volcanoes in the world and the high level of anthropisation represents a constant challenge to improve the quality of monitoring data.

The INGV-Osservatorio Vesuviano (INGV-OV) is responsible for monitoring and studying the Campi Flegrei volcano and is the authoritative institution for the volcanic surveillance and monitoring.

The INGV-OV has been operating the instrumental seismic network in the Campi Flegrei since the 70s. Since then, this monitoring network has been constantly updated and upgraded in their instrumentation and topology.

At the present more than 30 stations are recording seismic data. All of them are equipped with velocimeters (SP, LP, BB and VBB sensors) and, among them, a subset is equipped with accelerometers. Moreover, by using multi channels digitizers, infrasound channels are also recorded (Figure 1).

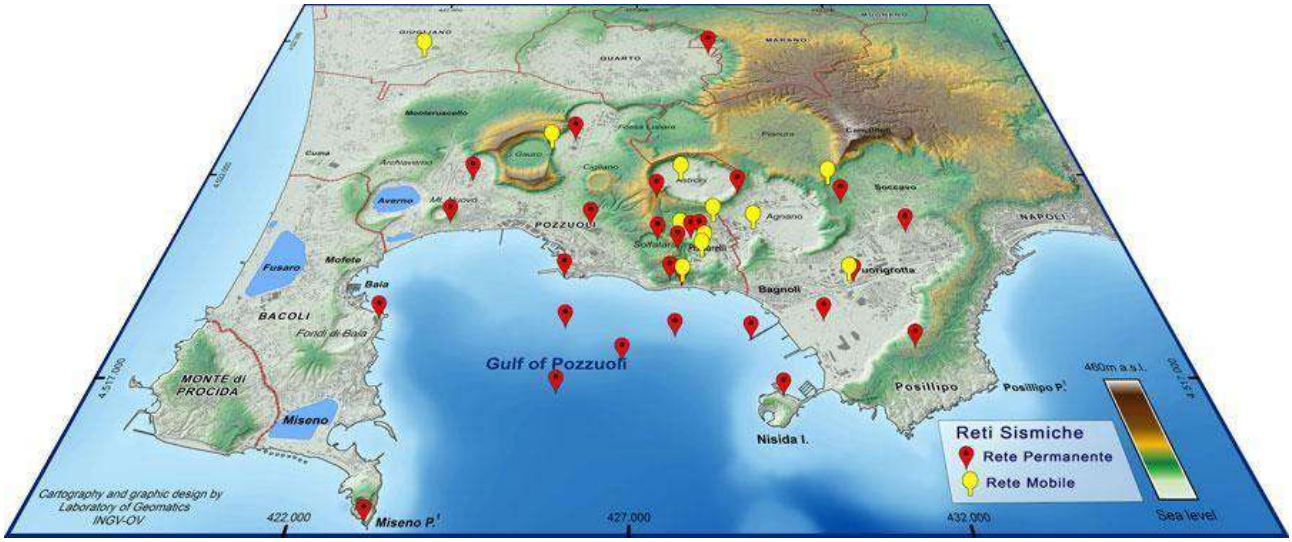

Figure 1 - The present Campi Flegrei seismic network. The map represents the permanent stations (red points) and mobile stations (yellow points). From http://www.ov.ingv.it

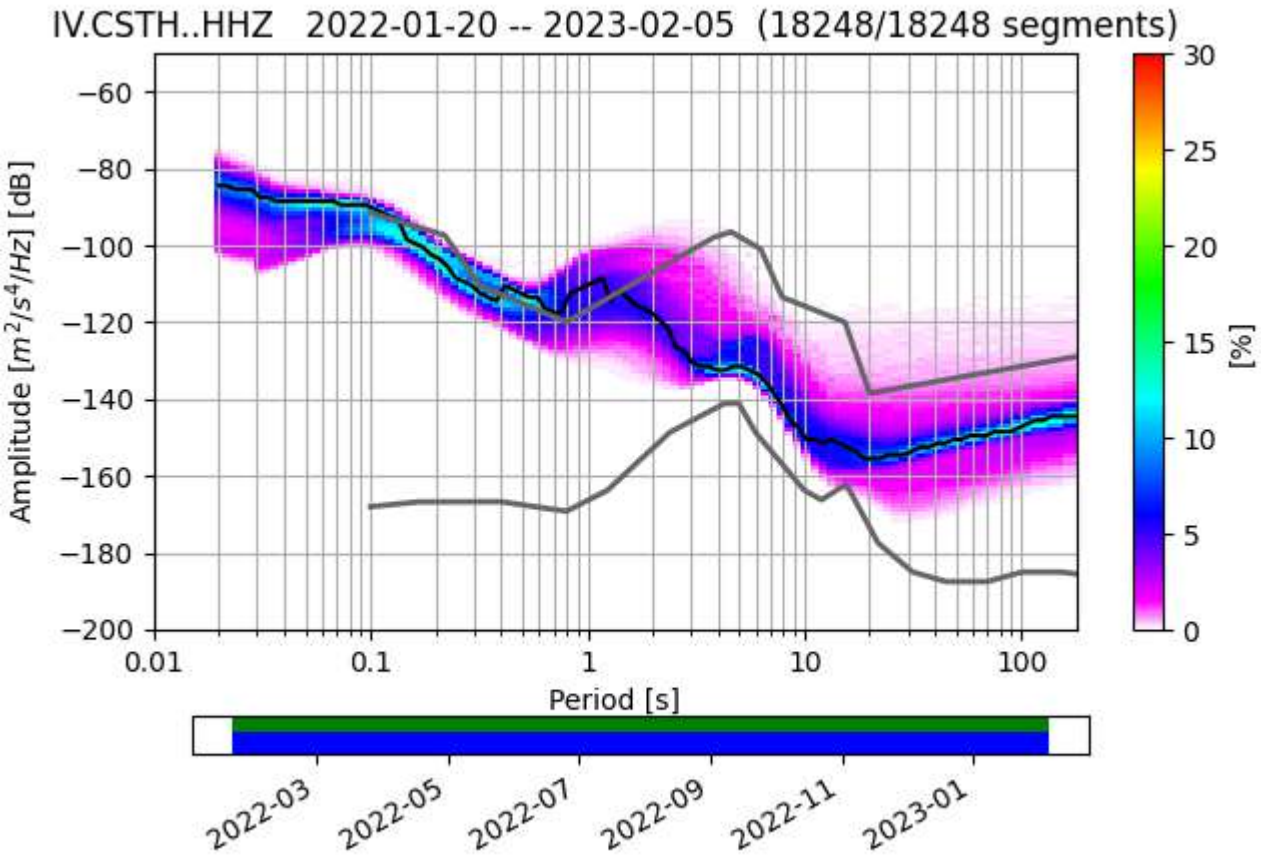

Figure 2 - Power Spectral Probability function of CSTH seismic station, which is the historical reference station for Campi Flegrei area. The plot represents about 14 months of data.

Over the past 20 years, European, Italian and Regione Campania supporting infrastructure projects have been the key factor in improving the equipment, while the implementation of digital communication network developed and managed in-house has led to an improvement in coverage of the area.

To better illustrate the current seismic monitoring network, we will also present the performance in terms of minimum detection magnitude over time and space, and other typical characteristics, such as the noise power spectral density of some key seismic stations (Figure 2).

Here we present this technological evolution aimed at improving the detection capability and at lowering the detection threshold.

Corresponding author: massimo.orazi@ingv.it

Preliminary characterization of the area of the Salse del Dragone mud volcano (Northern Italy) through surface-wave seismic prospecting

E. Paolucci[1], M. Zanetti[1], M. Antonellini[2], A. Armigliato[1], N. Carfagna[3], F. Zaniboni[1], A. Piombo[1].

[1] Department of Physics and Astronomy "A. Righi", University of Bologna, Bologna, Italy

[2] Department of Biological, Geological and Environmental Sciences, University of Bologna, Bologna, Italy

[3] Department of Physical Sciences, Earth and Environment, University of Siena, Siena, Italy

Mud volcanoes are geological structures due to the surface expulsion of fluids, such as mud, water and hydrocarbons which originate within a sedimentary sequence. In particular, the ascent of these materials is favoured by the presence of fluid-rich over-pressured deep sediments characterized by low density and viscosity respect to the surrounding deposits. The emission activities related to mud volcanoes have significant implications in terms of energy resource exploration, seismicity, atmospheric budget of greenhouse gases (Mazzini and Etiope, 2017) as well as geohazard assessment (e.g., Gattuso et al., 2021).

About 60 subaerial mud volcanoes exist in Italy, mainly located along the outer Apennine belt and Sicily (Martinelli and Judd, 2004). The structure known as "Salse del Dragone" is one of the 18 mud volcanoes located in the Emilia-Romagna region, specifically situated in the Northern Apennine belt about 20 km far from the city of Bologna. Actually, the area affected by clear emitted mud presence is about 1300 m^2 and the emission area (about 200 m^2) is characterized by a flattened positive structure with a plateau-like shape less than 0.5 m high (Martinelli and Judd, 2004). Although the emission activity currently appears to be quite bland, some historical references (Calindri, 1780; Bombicci, 1873) report intense and loud eruptions with huge mud emission: it is precisely this type of lively activity that gave the site its name ("Dragon Salsa"). Moreover, a large active mud debris flow originates from the emission area: actually, it is not clear if these deposits were generated directly from mud volcano flows, if are related to a surface flow of the outcropping formation ("Argille Varicolori"), or are a combination of both. In order to identify the main subsoil features of the area and try to understand the nature of the debris flow deposits, a preliminary seismic survey based on passive and active surface-waves acquisitions was carried out; in particular, several single-station and multiple-station measurements (e.g., Foti et al., 2018) were performed. The first ones were analyzed using the HVSR (Horizontal to Vertical Spectral Ratios) technique, while the latter were devoted to retrieve the Rayleigh wave phase velocity dispersion curves. The joint use of these two analyses made it possible to characterize the subsoil materials in

terms of shear-wave velocity values and to identify the main seismic impedance contrasts at depth. The preliminary outcomes show significant differences between the emission area and the zone affected by mud debris flow deposits.

References

Bombicci S.; 1873: Descrizione della mineralogia generale della Provincia di Bologna. Mem. Acc. SC. Istit. Di Bologna, vol 4, ser. 3, pp. 57-222.

Calindri S.; 1781: Dizionario corografico, georgico, orittologico, storico dell'Italia. Bologna 1781-1785, Ristampa Forni 1978.

Foti S., Parolai S., Albarello D. and Picozzi M.; 2011: Application of surface wave methods for seismic site characterization. Surv Geophys, 32(6), 777–825, https://doi.org/10.1007/s10712-011-9134-2.

Gattuso A., Italiano F., Capasso G., D'Alessandro A., Grassa F., Pisciotta A.F., Romano D.; 2021: The mud volcanoes at Santa Barbara and Aragona (Sicily, Italy): a contribution to risk assessment. Nat. Hazards Earth. Syst. Sci., 21, 3407-2419, https://doi.org/10.5194/nhess-21-3407-2021.

Martinelli G. and Judd A.; 2004: Mud volcanoes of Italy. Geological Journal 39, 49-61.

Mazzini A. and Etiope G.; 2017: Mud volcanism: An updated review. Earth Science Reviews., Vol.168, 81-112, https://doi.org/10.1016/j.earscirev.2017.03.001.

Corresponding author: enricopaolucci83@gmail.com

Geodetic imaging of magma ascent through a bent and twisted dike during the Tajogaite eruption of 2021 (La Palma, Canary Islands)

M. Przeor[1,2], R. Castaldo[3], L. D'Auria[1,2], A. Pepe[3], S. Pepe[3], T. Sagiya[4], G. Solaro[3], P.Tizzani[3], J. B. Martínez[1,2], N. Perez[1,2]

[1] *Instituto Volcanológico de Canarias (INVOLCAN), Granadilla de Abona, Tenerife, Canary Islands, Spain*

[2] *Instituto Tecnológico y de Energías Renovables (ITER), Granadilla de Abona, Tenerife, Canary Islands, Spain*

[3] *Istituto per il Rilevamento Elettromagnetico dell'Ambiente (CNR-IREA), Napoli (ITALY)*

[4] *Nagoya University, (JAPAN)*

On Sept. 19th, 2021, the Tajogaite eruption on the island of La Palma began with short precursors, lasting only eight days. The seismicity started on Sept. 11th with a westward and upward migration of hypocenters. Permanent GNSS stations started recording deformation on Sept. 12th on the island's western side, which reached more than 15 cm just before the eruption. After the eruption onset, the ground deformation increased, reaching a maximum on Sept. 22nd and showing a nearly steady deflation trend in the following months. To better understand the dynamics of the eruption, we exploited a joint dataset of GNSS and Sentinel-1 SBAS time series along both ascending and descending orbits. To obtain the geometry of the causative source of the ground deformation, we combined the result of a preliminary non-linear inversion and the precise location of the seismicity. The resulting geometry of the source is that of a twisted dike bending eastward.

We performed inverse modelling to obtain the spatiotemporal kinematics of the opening function of the dike. The forward modelling has been realised using a 3D finite-element approach considering the island's topography. Our findings reveal a close correspondence between the magmatic intrusion and pre-eruptive seismicity. The ascent of the magma occurred along two branches, and the rheology of a previously identified ductile layer strongly affected the magma propagation process. Finally, we found evidence of an early shallow deformation, which we interpret as the effect of ascending hydrothermal fluids. Our findings highlight the need for advanced modelling to understand pre-eruptive processes in basaltic volcanoes.

Corresponding author: solaro.g@irea.cnr.it

Determining the magmatic or hydrothermal nature of volcano unrest through Bayesian joint inversion of ground displacements and gravity changes.

E. Rivalta[1,2], M. Nikkhoo[1]

[1] Helmholtz Centre Potsdam GFZ German Research Centre for Geosciences, Germany

[2] Alma Mater Studiorum University of Bologna, Italy

Volcanic unrest may be caused by a replenishment of magmatic or hydrothermal reservoirs, or by fluid transport through the elastic brittle crust. In either case, the nature and amount of fluids involved in the unrest determine the hazard associated with any impending eruption. The key questions to be addressed are: what kind of fluid (magma or hydrothermal), and how much of it, is driving the unrest? We show how these questions may be answered, and uncertainties in the expected scenarios may be reduced, through joint inversions of surface displacements or other kinds of ground deformation data (baseline changes, uplift, tilt, strain) and gravity changes.

First, we present a new Bayesian approach to the joint deformation-gravity inversion, involving a rigorous treatment of the covariance between co-located uplift and gravity changes, and a simultaneous estimate of the optimal relative weights of different observation types. We show how this approach may help reduce the uncertainties on the inferred mass of the magmatic fluids and on the deformation source parameters, such as location and volume change of the source underlying the unrest.

Next, we show that the estimated mass and volume change, together with information on the density and compressibility of the fluids potentially involved in the process, can be used to constrain both the volume fraction of exsolved volatiles in the fluid intrusion, and the nature of the fluids. We show example applications to Long Valley Caldera and Mt. Etna.

References

Rivalta, E., Nikkhoo, M. (in preparation): Determining the exsolved volatile volume fraction of the fluids involved in volcanic unrest from joint analysis of ground deforma

Nikkhoo, M., Rivalta, E. (in preparation): Bayesian joint inversion of surface displacements and gravity changes.

Nikkhoo, M., Rivalta, E. (2023): Surface deformations and gravity changes caused by pressurized finite ellipsoidal cavities. - Geophysical Journal International, 232, 1, 643-655. https://doi.org/10.1093/gji/ggac351

Nikkhoo, M., Rivalta, E. (2022): Analytical solutions for gravity changes caused by triaxial volumetric sources. - Geophysical Research Letters, 49, e2021GL095442. https://doi.org/10.1029/2021GL095442

Corresponding authors: rivalta@gfz-potsdam.de, mehdi.nikkhoo@gfz-potsdam.de

Inverse modelling as a powerful tool for estimating gas flow emission rate from stationary hydrothermal vents

A. Semprebello[1], G. Lazzaro*[1], C. Caruso[1], S. Scirè Scappuzzo[1], S. Morici[1], A. Gattuso[1], M. Longo[1]

[1] National Institute of Geophysics and Volcanology – Palermo (INGV, Italy)

Submarine hydrothermal systems emit into the sea water huge amounts of both elements and energy, in terms of gas emissions, thermal water and solid deposition. The interest of the scientific community in these systems, classified as extreme environments in relation to their features (e.g. high temperature, low Ph) is increasing, especially in the last few years. However, direct measures can be challenging due to the extreme environmental conditions [Heinicke et al. 2009, Longo et al. 2021].

In this framework, passive passive hydroacoustics may represent a sustainable and safe method for both short- and long-term monitoring, since the typical source mechanisms present in the hydrothermal fields radiate sound pressure following different acoustic modes directly related to ascending fluids release (Dziak et al. 2002, Dziak et al. 2012, Li et al. 2021).

Particularly, the research activity presented here has been focused on the estimation of the gas flow emission rate from a stationary-high flux vent (Leifer and Tang 2007) located at ~16 meters depth, inside the hydrothermal field 2 miles East offshore Panarea island (see Fig. 1) in the NE sector of Aeolian arc (Aeolian Island, Italy).

Fig. 1 – Maps showing the position of Panarea Island in Southeastern Tyrrhenian Sea (red marker in left panel) and the position of the investigated vent (cyan marker in right panel).

To carry out the estimation of the gas volume emitted by the hydrothermal vent we implemented a spectral method (Leighton and White 2011, Roche et al. 2022), based on a specially developed inverse modelling algorithm. The adopted approach, founded on the assumption that the acoustic signature of a single bubble event evolves over time as a sinusoid that exponentially decays (Leighton et al. 2011, Walton et al. 2005), is based on the formulation of a forward model for the sound radiated by the bubbles plume, then the path is backward analysed to obtain an estimation of the flow emission rate.

High-resolution audio frames were recorded by using an autonomous smart hydrophone, able to collect and store digitised audio frames in the frequency band [1 - 12.800] Hz.

The hydrophone was deployed in mooring configuration in the proximity of the investigated vent, acquiring data for ~10 hours at the maximum sampling frequency. Hence the collected audio frames were treated with preliminary analyses, aimed to characterise the spectral features of the vent, thus identifying the acoustic signature of the source and the frequency range connected to signals attributable to the bubbling events. The analyses of the Power Spectral Density (PSD) and Pressure Power Spectrum show the presence of different persistent energetic frequency peaks over the environmental background noise which are compatible with the dynamic of the hydrothermal field (see Fig. 2).

Among these, the most energetic ones are likely due to the acoustic signal radiated by a huge, resonant bubble plume, consistently confirmed by the coupling of the estimated radius with direct observations.

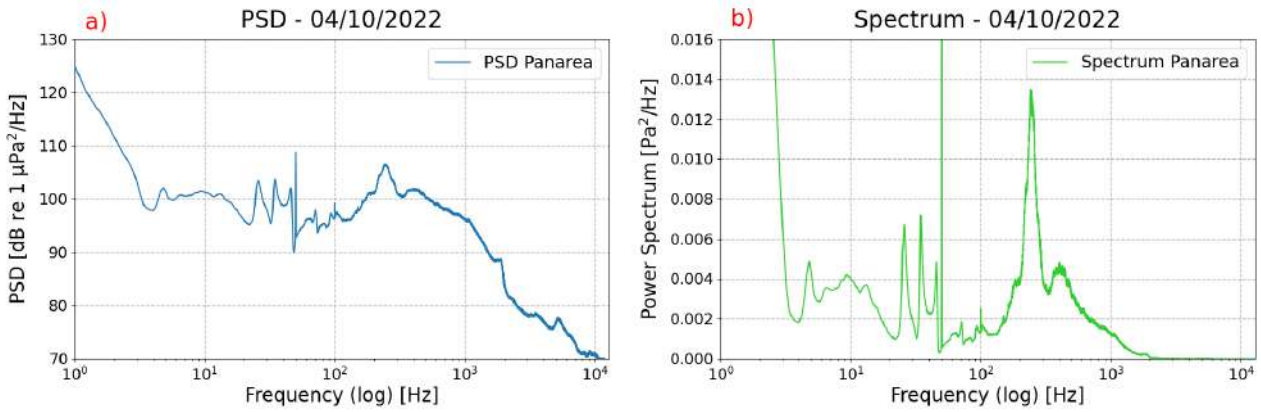

Fig. 2 – Power Spectral Density (PSD) (panel a) and Pressure Power Spectrum (panel b) of 04/10/2022.

The Spectrum analysis allows us to identify the main features of the vent, characterised by bubbles radii of 0.02 m that produce the main energetic peak centered at ~250 Hz, also visible in the Spectrogram along with smaller bubbles that produce less energetic peaks up to 2 kHz. Therefore, in the algorithm, we take into consideration a wide frequency range, spanning from 150 Hz to 2250 Hz, in order to estimate all the gas released by the vent.

The Spectrogram confirms that the energy spans in a wide bandwidth which is compatible with the size of the bubble observed.

In this framework, the inversion algorithm was applied to the dataset, considering the frequency range from 150 to 2250 Hz, as shown in Fig. 3.

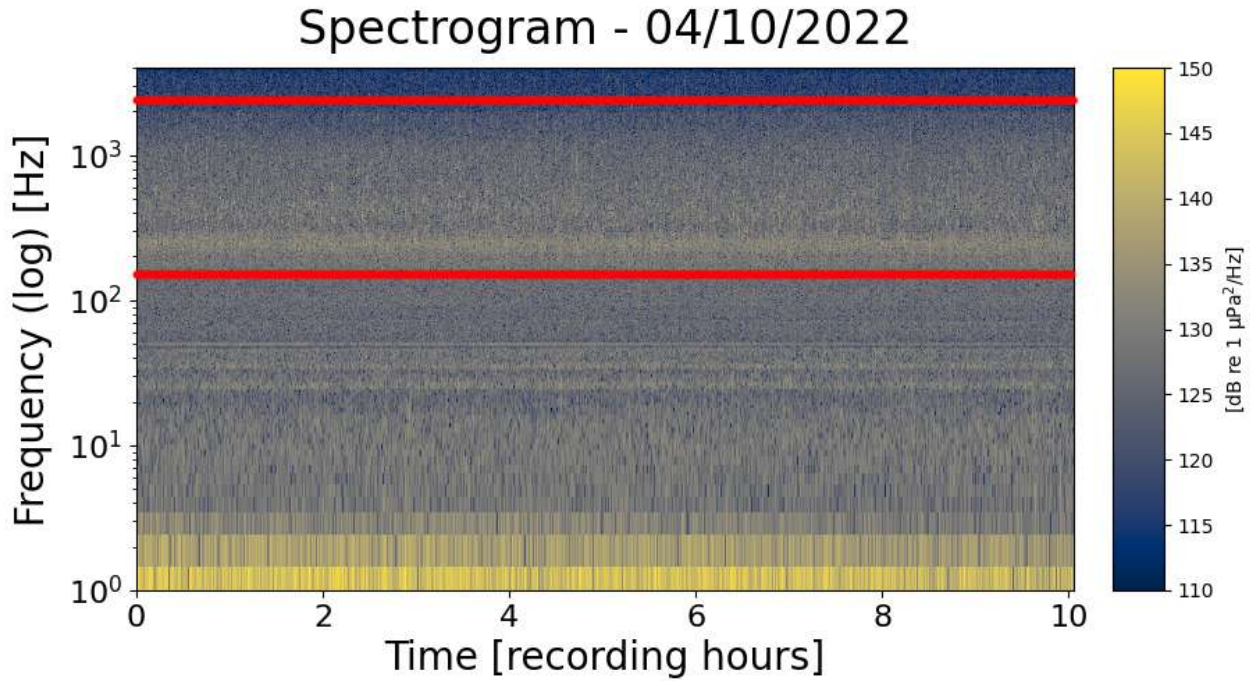

Fig. 3 – Charts showing the Spectrograms recorded on 04/10/2022 on which the inversion range is indicated (red lines).

The flow emission rate estimated through the inversion algorithm, which assumes a mean value of 8.32 liters per minute, is in good agreement with the direct observations. This confirms that

passive acoustic methods represent a valid and robust tool for both monitoring and research activity in submarine hydrothermal fields, providing to be also a long-lasting instrument able to detect the fluctuations connected to the variations of such natural systems.

References

Dziak, R.P.; 2002: Evidence of harmonic tremor from a submarine volcano detected across the Pacific Ocean basin. Journal of Geophysical Research, 107, https://doi.org/10.1029/2001jb000177

Dziak, R., Bohnenstiehl, D. and Smith, D.; 2012: Hydroacoustic monitoring of oceanic spreading centers: past, present, and future. Oceanography, 25, 116–127, https://doi.org/10.5670/oceanog.2012.10

Heinicke J., Italiano F., Maugeri R., Merkel B., Pohl T., Schipek M., and Braun T.; 2009: Evidence of tectonic control on active arc volcanism: the Panarea–Stromboli tectonic link inferred by submarine hydrothermal vents monitoring (Aeolian arc, Italy). Geophysical Research Letters, 36, https://doi.org/10.1029/2008gl036664

Leifer, I., and Tang, D.; 2007: The Acoustic Signature of Marine Seep Bubbles. J. Acous. Soc. doi:10.1121/1.2401227

Leighton T. G., and White P. R.; 2011: Quantification of undersea gas leaks from carbon capture and storage facilities, from pipelines and from methane seeps, by their acoustic emissions. Proceedings of the Royal Society A: Mathematical, Physical and Engineering Sciences, 468(2138):485–510.

Li, J., White, P. R., Roche, B., Bull, J. M., Leighton, T. G., Davis, J. W., et al.; 2021: Acoustic and Optical Determination of Bubble Size Distributions -Quantification of Seabed Gas Emissions. Int. J. Greenhouse Gas Control. 108, 103313. doi:10.1016/j.ijggc.2021.103313

Longo M., Lazzaro G., Caruso C. G., Corbo A., Sciré Scappuzzo S., Italiano F., Gattuso A., and Romano D.; 2021: Hydro-acoustic signals from the Panarea shallow hydrothermal field: new inferences of a direct link with stromboli. Geological Society, London, Special Publications, 519(1).

Roche B., White P. R., Bull J. M., Leighton T. G., Li J., Christie C., and Fone J.; 2022: Methods of acoustic gas flux inversion—investigation into the initial amplitude of bubble excitation. The Journal of the Acoustical Society of America, 152(2):799–806.

Walton A. J., Gunn M. G., and Reynolds, G. T.; 2005: The quality factor of oscillating bubbles as an indication of gas content with particular reference to methane. IEEE Journal of Oceanic Engineering, 30(4):924–926.

Corresponding author: gianluca.lazzaro@ingv.it

Dynamic and static strain sensitivity of velocity variations at Ischia Island, southern Italy

Stefania Tarantino[1], Piero Poli[2], Maurizio Vassallo[1], Nicola D'Agostino[1]

[1] *Istituto Nazionale di Geofisica e Vulcanologia*

[2] *Department of Goescience, University of Padova, Padova, Italy*

Ischia Island is the westernmost, active volcanic complex of the Campanian plain (Southern Italy, Civetta et al., 1991). A long-term depressurization (Sepe et al., 2007) in the local hydrothermal system is causing deflation and contraction (Galvani et al., 2021) of the surrounding volcanic edifice. In the 2017 a Mw 3.9 very shallow earthquake occurred in Casamicciola, in the northern part of the island, causing landslides and several collapse. Here we present dv/v measurements over 8 years (2016-2023) for variable coda waves time lapse using empirical Green's functions reconstructed by autocorrelation of seismic noise recorded at local velocimeters. We compared velocity variations time series with the temporal evolution of the strain, obtained at the network of GPS stations deployed on the island. We also investigated the coseismic variations of seismic waves velocity occurred during the 2017 earthquake. We found high values in both dynamic and static strain sensitivity of velocity variations with appreciable differences on the island, reflecting the anisotropic pattern of the depressurization. This also testify a significant non-linearity in the elastic properties of the local volcanic rocks, as expected for multi-fractured and heterogeneous materials where large amount of microcracks are commonly present.

References

Civetta, L., Gallo, G., & Orsi, G. (1991). Sr- and Nd-isotope and trace-element constraints on the chemical evolution of the magmatic system of Ischia (Italy) in the last 55 ka. *Journal of Volcanology and Geothermal Research*, *46*(3–4), 213–230. https://doi.org/10.1016/0377-0273(91)90084-D

Galvani, A., Pezzo, G., Sepe, V., & Ventura, G. (2021). Shrinking of Ischia Island (Italy) from Long-Term Geodetic Data: Implications for the Deflation Mechanisms of Resurgent Calderas and Their Relationships with Seismicity. *Remote Sensing*, *13*(22), 4648. https://doi.org/10.3390/rs13224648

Sepe, V., Atzori, S., & Ventura, G. (2007). Subsidence due to crack closure and depressurization of hydrothermal systems: a case study from Mt Epomeo (Ischia Island, Italy). *Terra Nova*, *19*(2), 127–132. https://doi.org/10.1111/j.1365-3121.2006.00727.x

Trasatti, E., Acocella, V., Di Vito, M. A., Del Gaudio, C., Weber, G., Aquino, I., Caliro, S., Chiodini, G., de Vita, S., Ricco, C., & Caricchi, L. (2019). Magma Degassing as a Source of Long-Term Seismicity at Volcanoes: The Ischia Island (Italy) Case. *Geophysical Research Letters*, *46*(24), 14421–14429. https://doi.org/10.1029/2019GL085371

Corresponding author: stefania.tarantino@ingv.it

The current unrest of Campi Flegrei caldera: seismicity and ground deformation

Anna Tramelli

and A. Benincasa, F. Bianco, A. Bobbio, C. Buonocunto, S. Caliro, A. Caputo, V. Convertito, P. Cusano, G. Dalla Via, P. De Martino, D. Delle Donne, R. Esposito, S. Gammaldi, G. Gaudiosi, D. Galluzzo, S. Guardato, D. Lo Bascio, R. Manzo, R. Nappi, L. Nardone, M. Orazi, R. Peluso, S. Petrosino, M.G. Soldovieri P. Ricciolino, G. Scarpato, M.A. Di Vito

Istituto Nazionale di Geofisica e Vulcanologia, Sezione di Napoli, Osservatorio Vesuviano, Via Diocleziano 328, Napoli, Italy

Campi Flegrei is one of the areas with the higher volcanic risk in the world due the active volcanic field and the presence of almost 500.000 people living in the area that could be invaded by pyroclastic flow in case of eruption. Its morphology is dominated by a large caldera collapsed during two caldera-forming eruptions. The caldera includes a continental sector and a submerged part, the Pozzuoli gulf. The caldera floor is punctuated by tens of craters' remains of monogenic volcanic activity origins. The Campi Flegrei area is characterised by intense uplift periods followed by subsidence phases (bradyseism). The area of the maximum uplift is located at Pozzuoli town and it decreases with a radially symmetrical shape. The uplift phases are associated with the unrests and are accompanied by seismicity that is usually shallow and with low-to-moderate magnitude. The Campi Flegrei caldera is currently in an unrest phase started at the end of 2005 when the subsidence phase, started at the end of 1984, was interrupted and the central part of the caldera started to uplift again. This trend persisted up till now with a varying rate. The increments in the velocity of the uplift are often associated with an increment in the earthquake occurrence rate.

In February 2022 the uplift at Pozzuoli exceeded the maximum level reached at the end of the last bradyseseimic crisis (1982-84). Between August and September 2023 an increment in the recorded seismicity in terms of rate and maximum magnitude was recorded. At the end of this period, 21-23 September, the uplift suffered an acceleration: almost 1 cm in 3 days. The rate of the earthquakes per month with MD>=2.0 passed from 5 between January and July 2023 to almost 20 in August and September. On September 27th a MD=4.2 was recorded by the seismic network of the INGV-Osservatorio Vesuviano. This is the highest magnitude earthquake recorded in the area since 1980.

The increment in the seismicity alerted the population and triggered a governative mitigation plan. At the same time the scientific community, already engaged in monitoring, focused even

more on understanding and studying the ongoing phenomenology. The researchers and technicians of the INGV-Osservatorio Vesuviano that is in charge of the monitoring of Campi Flegrei supplied all the data and possible interpretations to the authorities and to the decision maker.

A decrease in the rate of the seismicity and in the velocity of the uplift was recorded in October and November 2023. Other seismically anomalous periods like the one recorded in August-September were recorded during the current unrest of Campi Flegrei. But this last one was characterised by a rate of seismicity and magnitudes that made the authorities and population worried and recalled that both the volcanic and seismic risk are to be constantly faced in this area.

We will present the data collected by the monitoring system of the INGV-Osservatorio Vesuviano during this last period of the current unrest focusing mainly on the seismicity and ground deformation.

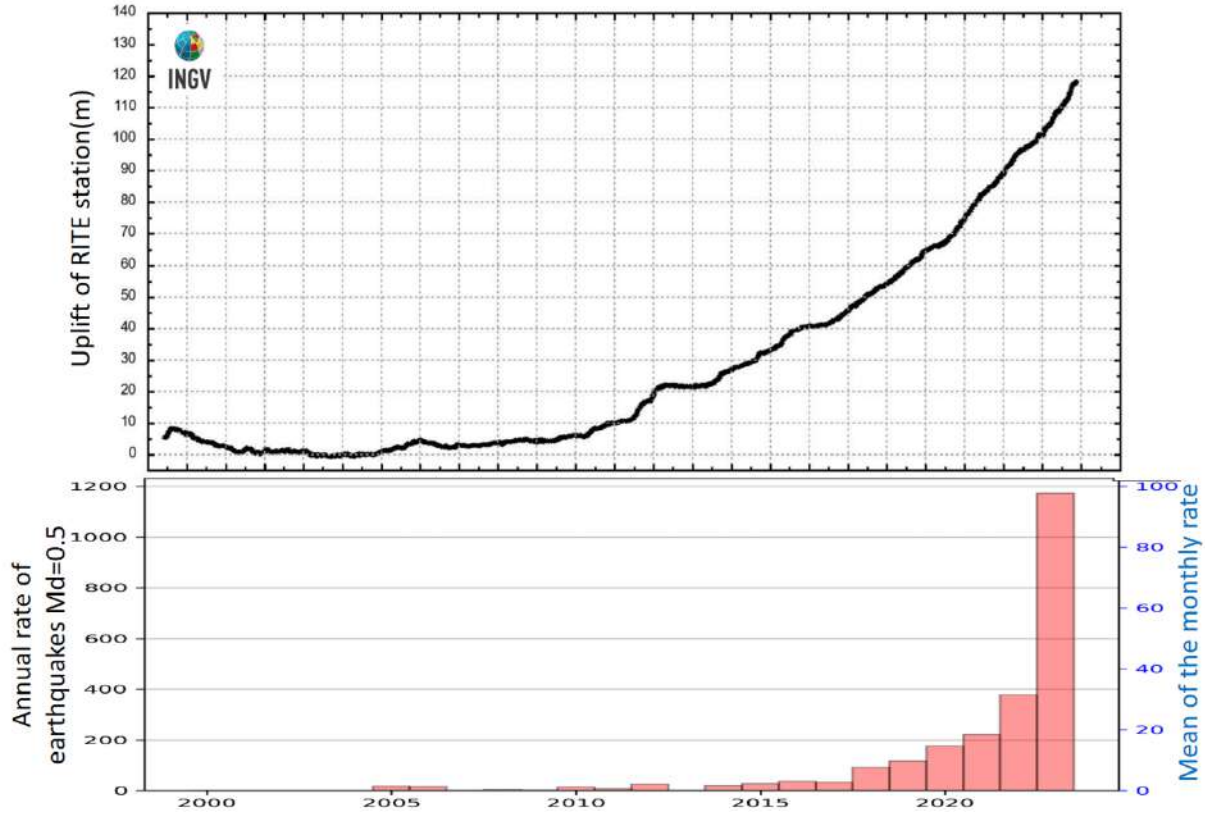

Figura 1 - Vertical displacement recorded at the station RITE (Rione Terra) and histogram of the number of earthquakes per year recorded at Campi Flegrei since 2000.

Corresponding author: anna.tramelli@ingv.it

b value tomography at Campi Flegrei: enlightening different rheological behaviour in volcanic areas

A. Tramelli[1], V. Convertito[2] and C. Godano[1.2]

[1] INGV-Osservatorio Vesuviano, Napoli, Italy
[2] Department of Mathematics and Physics, Università della Campania "Luigi Vanvitelli", Caserta, Italy.

The b-value represents the relative proportion of large and small events in the Gutemberg-Riechter relation:

$$\log(N)=a-bM$$

where N is the cumulative number of earthquakes with magnitude larger than M and a and b are constant that characterize the seismic catalogue and, consequently, the area where the catalogue is filled in. The b value is, generally, close to 1 in tectonic areas. Its value increases with the medium heterogeneity and temperature and it decreases with increasing stress.

We used the seismicity recorded in Campi Flegrei since 2005 to perform a tomography of the b value.

This tomography revealed values that ranges between 0.7 and 1.8.

A very good correlation with the structure of the hydro-thermal system at the basis of the bradiseismic phenomenon is evidenced. The lowest values characterize the caldera at depth of 2-4 km. The highest values characterize the shallower structures below Pisciarelli and Solfatara. More precisely we observe the smallest b values where we expect the higher stress concentration and for deepest seismicity. Conversely the highest b values are observed where the presence of a porous medium allows the passage of the volcanic gases. Values of b more close to typical tectonic ones are observed where the presence of faulting structure is documented.

Corresponding author: anna.tramelli@ingv.it

Multiscale Analysis of Physical Rock Properties at Stromboli Volcano: What controls the frictional properties?

S.C. Vinciguerra[1], T. Alcock[2], P.B. Benson[2]

[1] Department of Earth Sciences, University of Turin, Italy

[2] School of Earth and Environmental Sciences University of Portsmouth, England

The physical, mechanical and fracture properties at Stromboli volcano have been integrated at multiple scales to understand whether the interplay between a presumed NE/SW rift zone and the Sciara del Fuoco (SDF) depression has resulted in a zone of weakness able to promote fracturing prone to flank instability (Tibaldi et al., 2004; Alcock et al., 2024). Multiscale fracture quantification by imaging via FracPaQ toolbox both fractures and sample scale fractures has been integrated with rock physics and rock mechanics experiments on cm samples belonging to the Paleostromboli, Vancori, Neostromboli, Pizzo and Present Deposit volcanic cycles that have been taken from within and outside the rift zone. The structural changes to the edifice have been quantitively assessed by mapping at different scale fracture properties such density and orientation within and outside the rift zone allowing to identify the potential damaged zones that could reduce the edifice strength.

Results indicate that basalt textures, microfracture density, porosity, chemical zoning and preferential alignments, despite lithologically dependent, can be related to the NE/SW zone of weakness at the regional scale and to collapsed volumes that have been subject to continuous intrusive activity. Numerical inversion models have been performed to cross correlate fracture density in the basalts at multiple scales.

A link between microfracture density and seismic velocities has been also established via numerical modelling, allowing to interpret in terms of degree of fracturing the results of seismic tomographies at the field scale, providing a novel method to image crack damage evolution within the inner structure of the volcano edifice.

In order to image and constrain the fracturing mechanisms controlling the initiation of rupture in the instable sector of SDF in Stromboli a multiscale approach has been consequently designed by first identifying and analyzing via satellite fractures and then exploring via laboratory experiments how the initiation of rupture and the frictional properties evolve under different loading conditions, pore fluid content and effective pressure. An initial assessment on the potential frictional properties was performed by determining the slip tendency (Ts) from 2-D Imagery and sampling lithological units according to the remote sensing analysis and the location with respect

the instable sector of SDF (Fig.1). Triaxial direct-shear tests, via a purpose-built housing rig, equipped with two Piezo-Electric Transducers on 50 x 20 mm rectangular slabs at 5, 10 and 15 MPa both in dry and wet conditions were carried out to explore the coupled evolution of the frictional and seismic properties. Confining pressure and saturation have affected the friction coefficient. Rate and state friction parameters and friction coefficient are controlled by changing sliding velocity (Alcock et al., submitted). Microearthquakes recorded (Acoustic Emissions) and their key attributes, such amplitude, frequency and duration and their evolution confirm the relation to sliding velocity, confinement and porosity. Post mortem SEM analysis has revealed the impact that textural features on the evolution of fracture damage and their control on the frictional properties. These findings have been related to the field scale slip dilation analysis providing quantitative support for the identification of structurally weak zones across the SDF and constraint the mechanical behaviour of the fractured zones prone to instability.

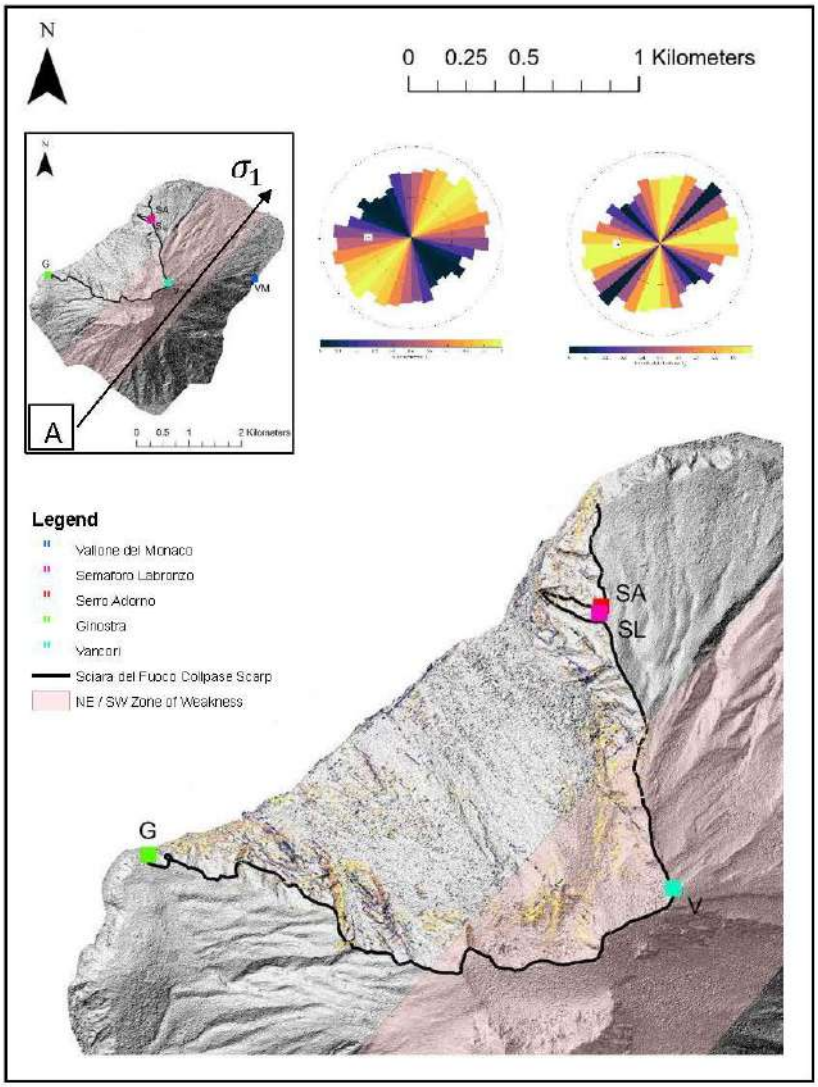

Fig. 1 - Slip tendency fracture map of the Sciara del Fuoco collapse scarp with sample site locations (A) of Vallone del Monaco (VM), Semaforo Labronzo (SL), Serro Adorno (SA), Ginostra (G) and Vancori (V) in relation to the NE/SW direction of σ1 aligned with the zone of weakness across the edifice. Rose diagrams of Td (B) and Ts (C).

References

Alcock T.; Vinciguerra S.; Benson. P.M.; Bullen D.; Multiscale fracture, physical and mechanical properties of Stromboli Volcano (Italy) edifice, Tectonophysics, in press

Alcock T.; Vinciguerra S.; Benson. P.M.; King T.; Frictional and seismic properties at Stromboli volcano: multiscale insights on the Sciara del Fuoco fracturing mechanics, Tectonophysics, in press

Tibaldi, A., 2004. Major changes in volcano behaviour after a sector collapse: Insights from Stromboli, Italy. Terra Nova 16, 2–8. https://doi.org/10.1046/j.1365-3121.2003.00517.x

Corresponding author: sergiocarmelo.vinciguerra@unito.it

AI-based emulators for data driven CFD model reconstruction

V. Zago[1], E. Amato[1,2], C. Del Negro[1]

[1] Istituto Nazionale di Geofisica e Vulcanologia, Osservatorio Etneo, Catania, Italy

[2] Department of Mathematics and Computer Science, University of Palermo, Palermo, Italy

Computational Fluid Dynamics (CFD) models have become fundamental tools for the study of fluids and the design of their applications. Their use becomes crucial when the fluid exhibits complex behaviors, which can be due to flow conditions or the physical properties of the fluid. Geophysical flows are good examples of these flows. Among these, a fluid with a high intrinsic complexity is Lava, which include non-Newtonian rheology, a behavior strongly dependent on temperature, and the coexistence of the three phases, solid, fluid and gas (Cordonnier et al., 2016). Numerous CFD approaches have been developed to simulate lava flows. The Smoothed Particle Hydrodynamics (SPH) has proven particularly suited for this application, thanks to its Lagrangian and mesh-free formulation (Zago et al., 2017, 2018). However, despite the good level of description that these models can provide, one of the main limitations in practical application to complex fluids comes from the epistemic uncertainty, which is due to the poor observability of these flows for which detailed studies and measurements are hard or impractical.

A solution to this lack of information can come from CFD models themselves, which can be used to get information about the real phenomena. For example, one can create the so-called digital twins of the studied system or perform reverse engineering. This potential becomes even higher if we consider the growing fusion between CFD methods and Artificial intelligence, which have highly increased the potentials of physical modeling (Kasim et al., 2021, Amato 2023, Amato et al, 2023A).

Here we present an illustrative application of a combined CFD-AI model adopted to retrieve information about the viscous model of Lava. The model that we use is an AI based emulator of the SPH method (Zago et al., 2023, Amato et al, 2023B), which is applied to a lava flow simulated with SPH, with a known acceleration field. The emulator can recreate pressure and viscous interaction forces, to reconstruct the SPH model originally adopted to generate the simulation, and to generate new simulations, emulating the behavior of the unknown SPH model. These results provide a concrete step toward the development of physically accurate models involving a minimal knowledge of the real phenomena.

References

Amato, E.; 2023: How a CFD Emulator Can Resolve the Boundary Conditions in a Viscous Flow. IEICE Proceedings Series, 76(B4L-42).

Amato, E., Zago, V., Del Negro, C.; 2023A: How AI can speed up SPH simulations. Proceedings of the 17th international SPHERIC workshop. Rhodes, Greece, 27-29 June, 2023.

Amato, E., Zago, V., Del Negro, C.; 2023B: A physically consistent AI-based SPH emulator for computational fluid dynamics. Accepted in Nonlinear Engineering Modeling and Application.

Cordonnier, B., Lev, E., & Garel, F.; 2016: Benchmarking lava-flow models. Geological Society, London, Special Publications, 426(1), 425-445.

Kasim, M. F., Watson-Parris, D., Deaconu, L., Oliver, S., Hatfield, P., Froula, D. H., ... & Vinko, S. M.; 2021: Building high accuracy emulators for scientific simulations with deep neural architecture search. Machine Learning: Science and Technology, 3(1), 015013.

Monaghan, J. J.; 2005: Smoothed particle hydrodynamics. Reports on progress in physics, 68(8), 1703.

Zago, V., Amato, E., Cariello, S., Corradino, C., Torrisi, F., & Del Negro, C.; 2023: On Artificial Intelligence-based emulators of physical models to forecast the evolution of lava flows (No. EGU23-16305). Copernicus Meetings.

Zago, V., Bilotta, G., Cappello, A., Dalrymple, R., Fortuna, L., Ganci, G., ... & Del Negro, C.; 2017: Simulating complex fluids with smoothed particle hydrodynamics. Annals of Geophysics.

Zago, V., Bilotta, G., Hérault, A., Dalrymple, R. A., Fortuna, L., Cappello, A., ... & Del Negro, C.; 2018: Semi-implicit 3D SPH on GPU for lava flows. Journal of computational physics, 375, 854-870.

Corresponding author: vito.zago@ingv.it

Session 1.3

Physical models for the Solid Earth and integration between modeling and data of different nature

GNGTS 2024

SEISMICITY, VOLCANOES, DATA AND MODELS

Session 1.3

Physical models for the Solid Earth and integration between modeling and data of different nature

Convenors of the session:
Anna Maria Marotta (UniMI) – anna.maria.marotta@unimi.it
Carla Braitenberg (UniTS) – berg@units.it
Barbara Orecchio (UniME) – barbara.orecchio@unime.it

Contributions recommended for this session:

- **Forward and inverse physical models of Solid Earth processes at different wavelengths and time scales**
  - **Surface tectonic deformation**
  - **Post glacial rebound**
  - **Mantle dynamics**
  - **Relative Sea level change**
  - **Earthquakes and the internal structure of the Earth**
- **Techniques and quantitative methods for analyzing large amounts of geophysical data of different nature and at very high resolution, both terrestrial and satellite (eg. GNSS, SAR, Gravitational, Seismological, Magnetometric, thermal)**
  - **Rheological characterization of the crust and mantle**
  - **Numerical models of geomagnetic anomalies**
  - **Shape and size of the Earth**
  - **Earth's gravitational field**
  - **Numerical modeling of Gravimetric Anomalies**
  - **Observation of the Earth from Space – GNSS, InSAR**
  - **Surface geodetic deformation**
- **Integrated analyses between physical modeling and data (natural, experimental and observational from satellite)**
- **Interactions between Solid Earth processes and the Hydrosphere and the Atmosphere**
- **Planetology studies regarding the internal physical processes occurring on planets, both internal and external to the solar system, are also welcome**

On opposite sides of Naples: an intriguing contemporaneous onset of deep deflation below Vesuvio and the ongoing Campi Flegrei uplift.

A. Amoruso[1], L. Crescentini[1]

[1] *Department of Physics, University of Salerno, Fisciano, Italy*

Campi Flegrei and Vesuvio volcanoes are located on opposite sides of Naples and it is of great interest to get clues of possible mutual interactions or coincidences in their recent deformation dynamics.

As for Campi Flegrei, after the large uplift occurred at the beginning of the 80s and the general subsidence from 1985 to 2001, since the early 2000s it is uplifting mostly at an accelerating rate and its dynamics is probably driven by deep magma inflation (Amoruso and Crescentini, 2022).

As for Vesuvio, we analysed the ground displacement time series in the whole Vesuvian area and its surroundings around the early 2000s, using 1993–2010 ERS/ENVISAT ascending- and descending-orbit line-of-sight displacements. Our computations show a sudden trend change around 2001: pre-2001 velocity maps indicate subsidence mainly occurring inside the caldera rim and in a few spots around 10 km from the summital crater, thus confirming previously published results by others; post-2002 velocity maps provide evidence of general subsidence in the whole Vesuvian area. This last arrangement of the ground displacement field is made even clearer by subtracting the post-2002 velocity from the pre-2001 one and is consistent with the deflation of a deep pressurised source and the decrease of Vesuvio's deep seismicity at the beginning of 2002. (Amoruso and Crescentini, 2023)

The reveal of the coincidence between the transition from deflation to inflation at Campi Flegrei and the onset of deflation below Vesuvio may suggest the possible transfer of magma and/or magmatic fluids and the influence of the dynamics of one plumbing system on the other.

Reference

Amoruso A. and Crescentini L.; 2022: Clues of Ongoing Deep Magma Inflation at Campi Flegrei Caldera (Italy) from Empirical Orthogonal Function Analysis of SAR Data. Remote Sens., 14, 5698, DOI 10.3390/rs14225698.

Amoruso A. and Crescentini L.; 2023: DInSAR Data Reveal an Intriguing Contemporaneous Onset of Deep Deflation below Vesuvio and the Ongoing Campi Flegrei Uplift. Remote Sens. 2023, 15, 3038. DOI 10.3390/rs15123038.

Corresponding author: aamoruso@unisa.it

Monitoring the Tonga volcano starting from the unrest of 2014/2015 to the 2021/2022 explosion with Sentinels

C. Braitenberg

Department of Mathematics, Informatics and Geosciences (MIGe), University of Trieste, Trieste, Italy,

This study explores the dynamic evolution of the Tonga volcano, Tonga, throughout its volcanic cycle, with a particular focus on the formation and subsequent disappearance of a new island between Hunga Tonga (HT) and Hunga Ha'Apai (HH) between 2014 and 2023. The island first increased its surface extension in 2015 and vanished in January 2022, by a significant eruption, characterized by a 50 km high ash plume and Tsunami. Leveraging remote sensing techniques, specifically multispectral imaging from the satellite missions Sentinel 2 and SAR imaging from Sentinel 1, the research employs a supervised Random Forest classification algorithm to track the changing subaerial surface area of the volcano. This approach enables the documentation of size variations in the islands, especially during weeks surrounding volcanic unrests. The classifier, trained on nearly cloud-free multispectral images, automatically defines surface area changes over the years. The temporal resolution of area change is constrained by images with less than 5% cloudiness, resulting in 113 Sentinel 2 images between 2016 and 2023, selected from 506 available images. The Sentinel 1 Synthetic Aperture Radar (SAR) images penetrate clouds, and are therefore complementary to the multispectral observations, with the drawback of observing the reflectivity only on up to two bands. Nonetheless the classifier is successful in distinguishing land from ocean, albeit with greater noise. The Sentinel 1 observations start in 2014, extending the time series to cover the volcano unrest of 2014/2015, totalling 213 images. The processing is fulfilled in the Earth Engine cloud computing data facility. Analysis reveals a slight decrease in area change after emplacement of a new island in 2015 and identifies the disappearance of the island bridge connecting HT and HH, along with two smaller islands south of HTHH in 2022. The 2022 unrest is preceded by an increase in island

area weeks before the volcano explosion. The global satellite coverage of the method suggests its potential applicability to automatically detect changes in oceanic areas, distinguishing between water and new volcanic island, thereby providing a means to anticipate upcoming volcanic unrests and document their evolution.

Corresponding author: berg@units.it

Update of the Northern Apennines and Southern Alps velocity field from historical GNSS measurement to the “0 point”.

F. Carnemolla[1], F. Brighenti[2], G. De Guidi[1], A. Di Pietro[2], P. Fabris[3], S. Giuffrida[1], A. Magrin[3], G. Rossi[3], D. Russo[2], L. Tunini[3], D. Zuliani[3].

[1] *Università degli Studi di Catania, Catania, Italy*
[2] *Università degli Studi di Ferrara, Ferrara, Italy*
[3] *Istituto Nazionale di Oceanografia e di Geofisica Sperimentale-OGS, Trieste, Italy*

In the framework of the PRIN 2020 - NASA4SHA Project (Fault segmentation and seismotectonics of active thrust systems: the Northern Apennines and Southern Alps laboratories for new Seismic Hazard Assessments in northern Italy), we have reoccupied 29 points belong to the IGM95 Network focusing on local transects orthogonal to the main compressive structures belong to the Northern Apennines and Southern Alps thrust belts (Fig. 1).

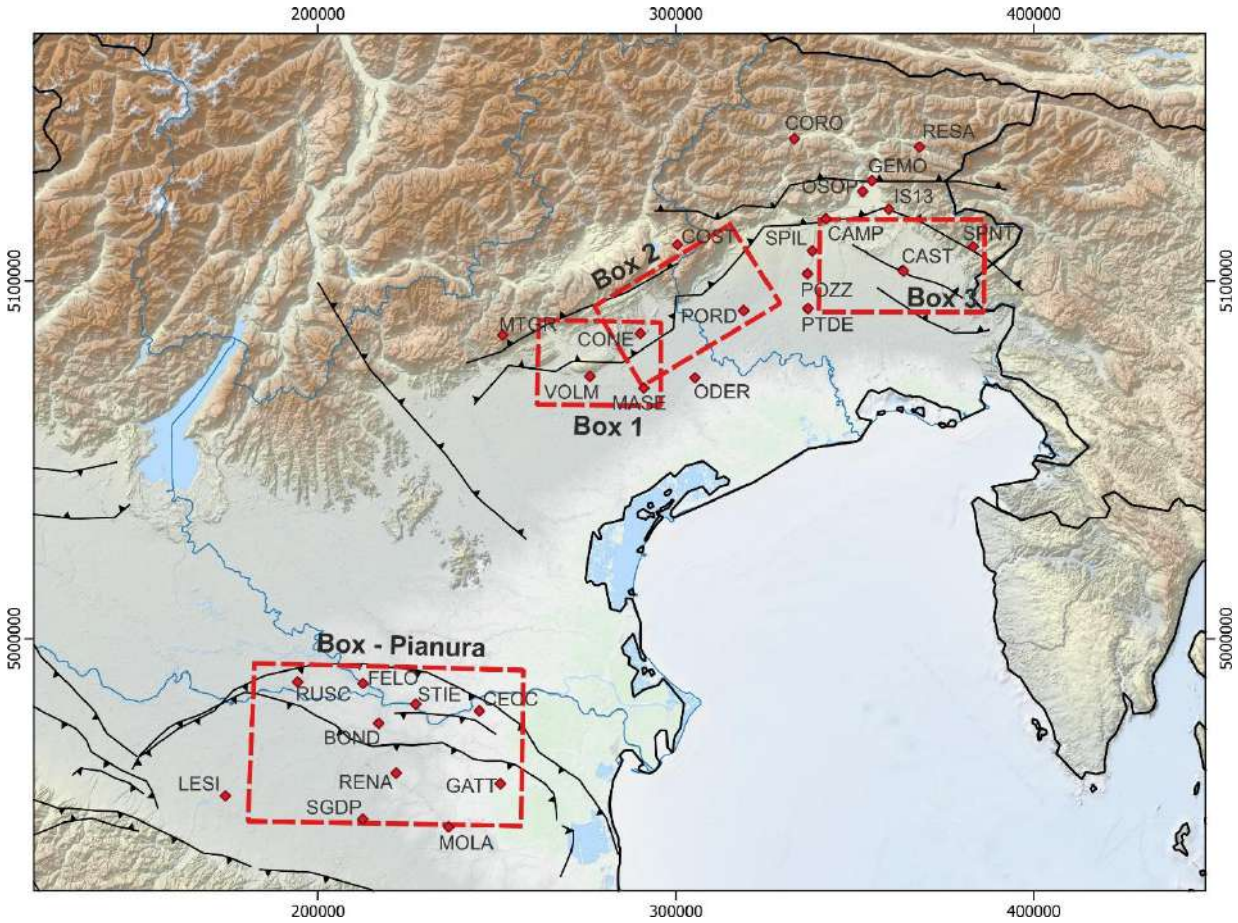

Fig. 1 – IGM95 points reoccupied during the 2023 campaigns

We selected these points, where possible, according to the following criteria:

1. Stability of the monuments;
2. Benchmarks build during the establishment of the IGM95 networks (1993-1995);
3. Number of occupations on the past;

Unfortunately, these criteria are not always respected in particular the second and third criteria, for example eight points (SPNT, PTDE, POZZ, MOLI, IS13, GEMO, CONS and CAMP) were built during the phase of densifications of the network (2000-2001) and four points have only one occupation (VOLM, PTDE, POZZ and MOLI). Moreover we have examined the duration of the measurement session for the old campaign, in particular, the first campaigns (1993) were characterised by an average of 4.5 hours measurement sessions, which decrease to 2 hours in the early 2000's (1996,2000,2006 and 2010).

In addition we have chosen same points close to same continues GPS stations, in order to compare our results to those obtain from the permanent stations.

Obviously, the IGM95 network was created for cartographic and topographic applications, for this reason most of the IGM95 beckmarks do not follow restrictive geodetic requirements for geophysical applications (duration, stability, use of tripod, Anzidei et al. 2008), but, in our opinion, these aspects are probably compensated by their long term velocity (30 years on 2023). However, these IGM95 points were selected in order to improve the strain rate, in term of resolutions, of selected structures on the Northern Apennines and Southern Alps thrust belt, and to establish a "0 points" for the future in order to improve our knowledge about these thrust belt.

The data were processed by Gamit-Globk software using double-difference phase observation with ambiguity resolutions, precise orbits and adopting the absolute phase center model for receiver and satellite antenna. The preliminary velocity field (Fig.2) is expressed in the IRTF14 reference frame with respect to the Eurasian plate (Altamini et al., 2017).

From a preliminary evaluation, the velocity field obtained by IGM95 sites is agree with the compressive dynamics and with that obtained by the permanent stations belong to the RING (Rete Integrata Nazionale GNSS) and FReDNet (Friuli Regional Deformation Network) networks, managed by INGV (Istituto Nazionale di Geofisica e Vulcanologia) and OGS (Istituto Nazionale di Oceanografia e di Geofisica Sperimentale) respectively in the framework of the PRIN2020 - NASA4SHA Project.

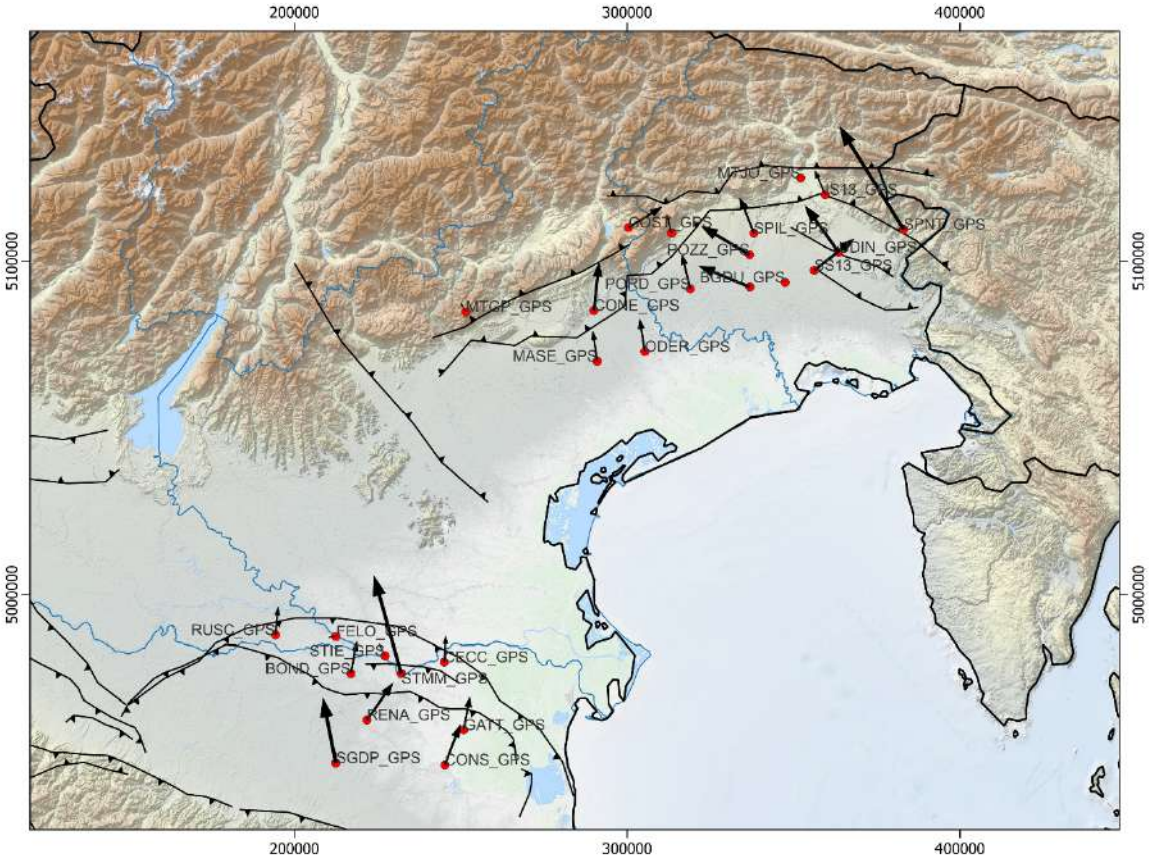

Fig. 2 – Velocity field obtained by IGM95 points.

References

Anzidei M., Baldi P., Serpelloni E.; 2008: The coseismic ground deformations of the 1997 Umbria-Marche earthquakes: a lesson for the development of new GPS networks, Annals of Geophysics, Vol. 51, N. 2/3, April/June 2008.

Altamimi Z., Métivier L., Rebischung P., Rouby H., Collilieux X.; 2017: ITRF2014 plate motion model, Geophys. J. Int., 209, 3, doi:10.1093/gji/ggx136..

Corresponding author: francesco.carnemolla@unict.it

Diffusivity analysis of clustered seismicity in Central-Southern Apennines

G.M. Cipressi[1], A. Vuan[4,5], M.A. Romano[4], G. Lavecchia[2,3], R. de Nardis[2,3]

1 Department of Engineering and Geology, University "G. d' Annunzio" of Chieti-Pescara, Italy

2 DiSPuTer - University of Chieti-Pescara 'G. d'Annunzio', Italy

3 CRUST- Interuniversity Center for 3D Seismotectonics with Territorial Applications, Italy

4 National Institute of Oceanography and Applied Geophysics (OGS), Italy

5 National Institute of Geophysics and Volcanology (INGV), Italy

Seismic swarms are defined as a set of clustered earthquakes with high spatio-temporal variability and with the absence of a main shock. They can originate in different tectonic contexts related to the migration of deep fluids that can alter the stress field (Roland et al., 2009). In particular, the diffusivity parameter, defined by Shapiro et al. (1997) and linked to the migration of the hypocenters over time, allows us to associate the swarms' temporal duration with the rocks' permeability characteristics. Swarms characterized by long durations (years) and low diffusivity values (10^{-3}-10^{-2} m^2/sec) are associated with low permeability fault systems. On the contrary, shorter durations (days) and high diffusivity values (0.5-1 m^2/sec or greater) indicate the presence of highly permeable systems in which seismicity is induced by the rise of fluids at high pressures (Amezawa et al., 2021). We focus on the clustered seismicity in the central-southern Apennines, which extends from the south of L'Aquila to Benevento, to analyze the spatio-temporal characteristics of the swarms and the relationship between their temporal duration and diffusivity.

Compared to the rest of the chain, this sector is characterized by (1) low seismicity rates, which do not allow us to follow the evolution of seismicity and the mechanisms underlying it, and (2) a high seismic risk, as demonstrated by the strongest and most destructive sequences recorded within the historical catalogs which magnitude M ~ 7.

We analyzed the seismicity reported in the catalog of absolute locations CLASS (Latorre et al., 2022), which describes Italian seismic activity over the past 37 years (1981-2018). Additionally, we augmented the catalog within a 7-year time window (2012-2018) using a template matching technique (Vuan et al., 2018). This choice was made based on the optimal distribution and operation of the seismic network. The initial catalog is improved, lowering the completeness magnitude by more than one degree (+ 20,000 events with -1.5<M<5.0). This approach allowed the analysis and comparison of clustered seismicity in two catalogs with different time extensions and resolutions.

Clustered seismicity is defined relative to the background using a nearest-neighbor technique (Zaliapin & Ben-Zion, 2020). Due to the great spatio-temporal variability of the seismic

phenomenon, no univocal methods in the literature can establish the spatial dimension and duration of the single cluster. The low seismicity rates of this area require a very detailed analysis on a small space-time scale and different methodological approaches. For the spatial definition, we used the Kernel Density calculation to determine an event's density probability in each radius. The time duration is defined using the approach described by Roland et al. 2009 based on the evaluation of the percentage of seismicity rate.

We identified 53 polyphasic seismic clusters in the complete catalog (37-year time window), and 30 in the improved catalog (7-year time window). The clusters were subsequently divided into swarms and sequences. The diffusivity was calculated for each cluster using the Shapiro et al. (1997) relationship.

Most of the seismicity is expressed as swarm-type and characterized by high diffusivity values (≥ 1m^2/sec) with short temporal durations (days-months). This result confirms that the clustered seismicity is linked to highly permeable fault zones and the natural injection of fluids under pressure. The swarms present in this sector of the Apennine chain can, therefore, be linked to the deep migration of CO2-rich fluids (Chiodini et al., 2004), which exploit pre-existing fault zones as a preferential path.

References

Amezawa Y., Taeta T., Kosuga M. (2021) Migration difusivity as a controlling factor in the duration of earthquake swarms;https://doi.org/10.1186/s40623-021-01480-7

Chiodini, G., C. Cardellini, A. Amato, E. Boschi, S. Caliro, F. Frondini, and G. Ventura (2004). Carbon dioxide Earth degassing and seismogenesis in central and southern Italy, Geophys. Res. Lett., 31, L07615. doi: 10.1029/2004GL019480

Latorre D., Di Stefano R., Castello B., Michele M., Chiaraluce L. (2022) Catalogo delle Localizzazioni ASSolute (CLASS): locations (Version 1). Istituto Nazionale di Geofisica e Vulcanologia (INGV). https://doi.org/10.13127/class.1.0

Roland E., Mc Guire J.J. (2009) Earthquake swarms on transform faults https://doi.org/10.1111/j.1365-246X.2009.04214.x

Shapiro A.S., Huenges E., Borm G. (1997) Estimating the crust permeability from fluid-injection-induced seismic emission at the KTB site https://doi.org/10.1111/j.1365-246X.1997.tb01215.x

Vuan A., Sugan M., Amati G., Kato A. (2018). Improving the Detection of Low-Magnitude Seismicity Preceding the Mw 6.3 L'Aquila Earthquake: Development of a Scalable Code Based on the Cross Correlation of Template Earthquakes.doi:10.1785/0120170106

Zaliapin, I., & Ben-Zion, Y. (2020). Earthquake declustering using the nearest-neighbor approach in space- time-magnitude domain. Journal of Geophysical Research: Solid Earth, 125, e2018JB017120. https://doi.org/ 10.1029/2018JB017120

Author: gemmacipressi@gmail.com

HOW ELASTIC IS ELASTIC DEFORMATION (IN GREENLAND)?

A. Consorzi, D. Melini, G. Spada

Glacial Isostatic Adjustment (GIA) is the time-dependent response of the Earth to spatio-temporal variations of surface loads. Since the seminal work of Wu and Peltier (1982), the GIA community has customarily adopted rheological models including a fluid core, a viscoelastic mantle and an elastic lithosphere. As a matter of fact, the focus of GIA modelling has always been the mantle viscoelastic rheology, that is the main driver of the deformation on the millennial timescale. This is motivated by the large size of the Late-Pleistocene ice sheets, which induce deformations that are mainly sensitive to the Earth's bulk properties. Presently, the highest rates of GIA deformation are measured in locations like Greenland, North America and Antarctica (Kremeer et al. 2018, Khan et al. 2016), where glaciers or ice sheets are still present. These ice masses are experiencing, in addition to the regular cycle of seasonal accumulation and ablation, a net loss caused by climate change (Osatoka et al. 2022). For this reason, GNSS stations located in the proximity of these glaciers are sensitive not only to the GIA-induced displacement but also to the elastic response of the lithosphere. Relatively small ice loads are expected to drive deformations that sense the fine structure of the Earth's outermost layers.

Even though it is undeniable that the lithosphere presents an elastic behaviour with respect to the underlying mantle, it is also true that *elasticity* is an ideal concept. In fact, rheology is a matter of time scales and, if we focus on those of GIA, the assumption of a purely elastic lithosphere is certainly unquestionable. Nevertheless, since we now dispose of high-quality geodetic records through the GNET (Bevis et al. 2009), it should be possible to identify lags between the load time evolution and the surface response. This becomes even more important when we perform local studies: especially nearby glaciers, the contribution of local processes such as underground water drainage, porosity or permafrost variations become more important and contribute to the inelasticity of the first lithospheric layers (Durkin et al. 2019, Mordret et al. 2016). Few other works in the literature have investigated this problem concerning possible phase lag due to periodic loading (Tang et al. 2020, Liu et al. 2017). Notably, Bevis et al. (2012) show a very good correlation between the global periodic loading (air mass + ice mass) and the global displacement, but it cannot be excluded that a more local-scale study might instead show delays in the Earth's response, especially in areas in which the lithosphere is weaker.

In this work we will compare the response to sinusoidal forcings of several Earth models with different lithospheric parameters, varying the thickness, rigidity, rheology and load size. We

will also consider two parallel families of models, one with a Maxwell mantle, and a second one with an Andrade (1910) mantle. Our goal is showing the role of every parameter in the determination of the response function or, in other words, the displacement. In particular, we will try to establish which combination of forcing period and load extent leads to the largest phase lag between the load history and the consequent response. As a preliminary experiment we performed a series of tests using the Earth Model from Barletta (2006). This model presents a thin elastic lithosphere of *18.5 km* and *5* viscoelastic layers of different viscosities (see Tab. 1). Firstly, with the ALMA code (Melini et al. 2022), we analysed the complex Love Numbers *h* and *l* associated with this model. Particularly, we were interested in the phase lag, namely

$$tan(\phi) = -Im[L_n(\omega)]/Re[L_n(\omega)] .$$

This quantity is of great interest since, through the relation $\Delta t = arcsin(Q^{-1})/\omega$, where Q is the quality factor and ω the tidal angular frequency (Tobie et al. 2019) , it allows us to evaluate the time delay between the load signal and the Earth's response. Results are shown in Fig. 1, where the plots display a quite complicated behaviour: the vertical Love number *h* presents, up to degree *n = 100*, a double-peak behaviour, while for higher degrees one peak only is observed. However, it is apparent that the more substantial phase lags occur for periods within 10^0 *kyr* < *T* < 10^2 *kyr*. By looking at the horizontal Love Number instead, we can clearly distinguish that, especially for degrees n > 10 and for shorter periods ($\sim 10^{-1}$ kyr), large phase lags are still visible.

Next, using the Taboo code (Spada et al. 2004) we computed the response of the model to a single disc load of semi amplitude α *= 1.5*° with a sinusoidal time history in which the ice height fluctuated between a maximum value of *10 m* and a minimum of *0 m*. We tested the sensibility of this model to different forcing periods, and we pushed our analysis up to the harmonic degree *128*. As we can see from Fig. 2, the findings of our previous analysis are confirmed: for periods of the order of 10^0 *kyr* the time lag between the load and the surface response is clearly visible, while for shorter forcing periods only horizontal displacements seem to preserve a distinguishable time lag.

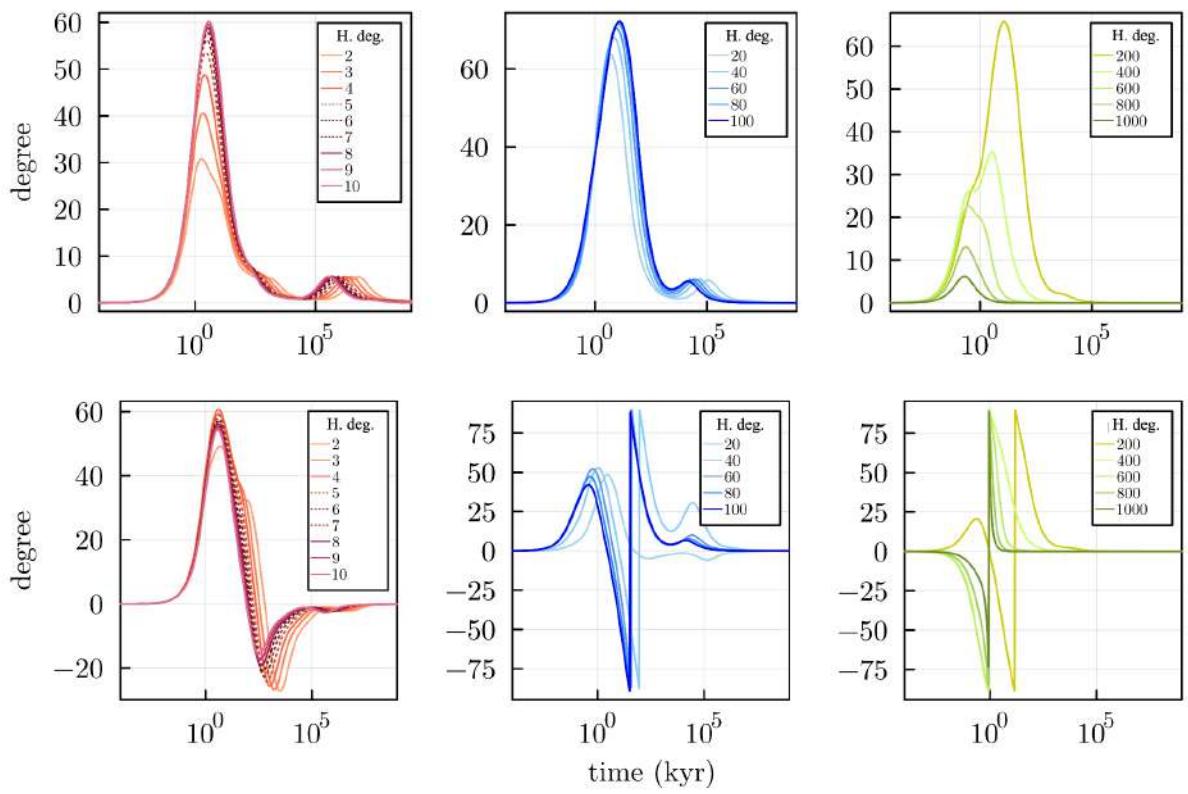

Fig. 1: Phase lag of Love numbers *h* (first row) and *l* (second row) for different harmonic degrees.

Depth (km)	Density (kg/m^3)	Rigidity (10^{10} Pa)	Viscosity (Pa · s)
6371	2650.0	2.97	$1.00 \cdot 10^{35}$
6352.5	2750.0	5.58	$2.15 \cdot 10^{19}$
6341.0	2900.0	6.81	$5.00 \cdot 10^{21}$
6331	3439.0	7.27	$4.64 \cdot 10^{20}$
5951	3882.3	10.9	$4.64 \cdot 10^{20}$
5701	4890.6	22.1	$1.00 \cdot 10^{21}$
3480	10932.0	0.00	0.00

Tab. 1: Earth model from Barletta 2006.

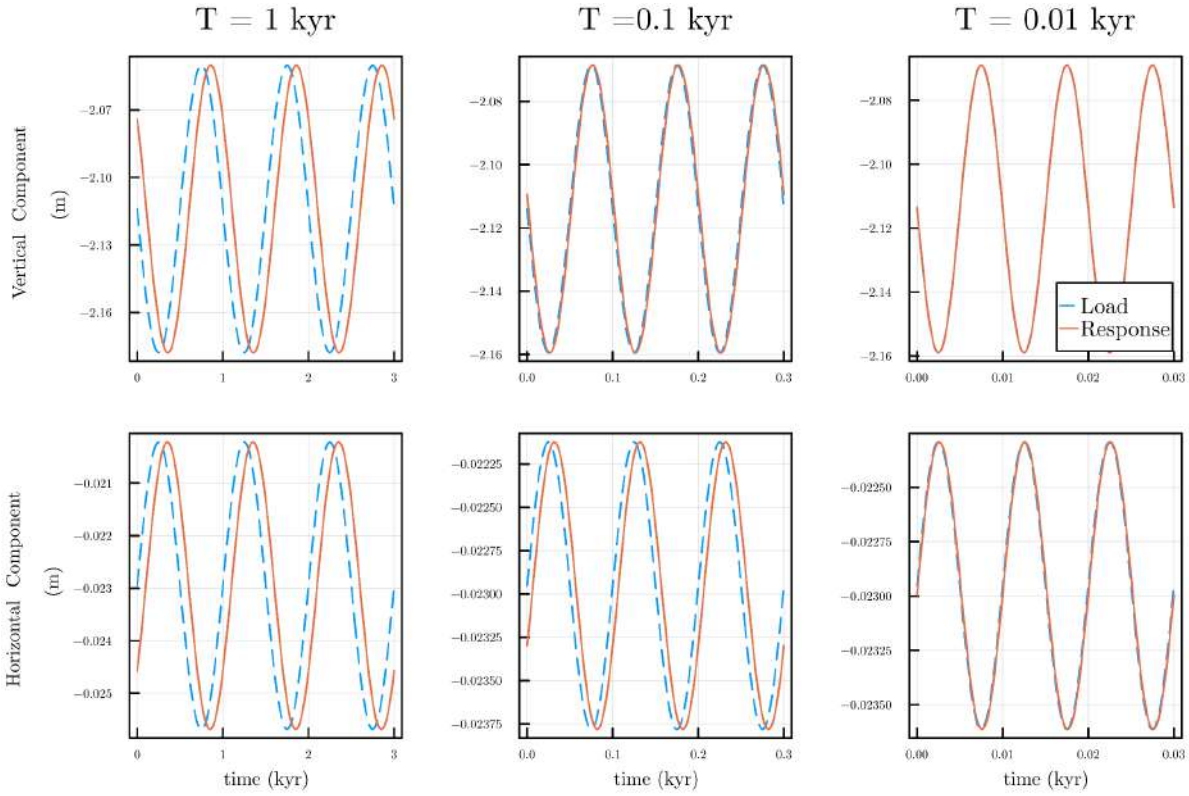

Fig. 2: Vertical (first row) and horizontal (second row) component of the displacement produced by a sinusoidal time history. The input load has been rescaled and inverted to ease the comparison between the two signals.

REFERENCES

Andrade, E. N. D. C. (1910). On the viscous flow in metals, and allied phenomena.

Proceedings of the Royal Society of London. Series A, Containing Papers of a Mathematical and Physical Character, 84(567):1–12.

Barletta, V. R., Ferrari, C., Diolaiuti, G., Carnielli, T., Sabadini, R., and Smiraglia, C. (2006). Glacier shrinkage and modeled uplift of the Alps. *Geophysical research letters*, *33*(14).

Bevis, M. G., Kendrick, E. C., Brown, A. K., Khan, S. A., Knudsen, P., Madsen, F., ...and Willis, M. J. (2009). Greenland GPS Network: Crustal oscillations and seasonal ice mass fluctuations. In *AGU Fall Meeting Abstracts* (Vol. 2009, pp. G43B-0728).

Bevis, M., Wahr, J., Khan, S. A., Madsen, F. B., Brown, A., Willis, M., ... and Francis, O. (2012). Bedrock displacements in Greenland manifest ice mass variations, climate cycles and climate change. *Proceedings of the National Academy of Sciences*, *109*(30), 11944-11948.

Durkin, W., Kachuck, S., and Pritchard, M. (2019). The importance of the inelastic and elastic structures of the crust in constraining glacial density, mass change, and isostatic adjustment from geodetic observations in Southeast Alaska. *Journal of Geophysical Research: Solid Earth, 124*, 1106–1119. https://doi.org/10.1029/2018JB016399

Khan, S. A., Sasgen, I., Bevis, M., van Dam, T., Bamber, J. L., Wahr, J., … and Munneke, P. K. (2016). Geodetic measurements reveal similarities between post–Last Glacial Maximum and present-day mass loss from the Greenland ice sheet. *Science advances*, *2*(9), e1600931.

Kreemer, C., Hammond, W. C., Blewitt, G. (2018). A robust estimation of the 3-D intraplate deformation of the North American plate from GPS. *Journal of Geophysical Research: Solid Earth*, 123, 4388–4412. https://doi.org/10.1029/2017JB015257

Liu, L., Khan, S. A., van Dam, T., Ma, J. H. Y., and Bevis, M. (2017). Annual variations in GPS-measured vertical displacements near Upernavik Isstrøm (Greenland) and contributions from surface mass loading. *Journal of Geophysical Research: Solid Earth*, *122*(1), 677-691.

Melini, D., Saliby, C., and Spada, G. (2022). On computing viscoelastic Love numbers for general planetary models: the ALMA3 code. *Geophysical Journal International,* 231(3), 1502-1517.

Mordret, A., Mikesell, T. D., Harig, C., Lipovsky, B. P., and Prieto, G. A. (2016). Monitoring southwest Greenland's ice sheet melt with ambient seismic noise. *Science advances*, *2*(5), e1501538.

Otosaka, I. N., Shepherd, A., Ivins, E. R., Schlegel, N. J., Amory, C., van den Broeke, M., ... and Wouters, B. (2022). Mass balance of the Greenland and Antarctic ice sheets from 1992 to 2020. *Earth System Science Data Discussions*, *2022*, 1-33.

Tang, H., Dong, J., Zhang, L., and Sun, W. (2020). Deformation of a spherical, viscoelastic, and incompressible Earth for a point load with periodic time change. *Geophysical Journal International*, *222*(3), 1909-1922.

Tobie, G., Grasset, O., Dumoulin, C., and Mocquet, A. (2019). Tidal response of rocky and ice-rich exoplanets. *Astronomy & Astrophysics*, 630, A70.

Spada, G., Antonioli, A., Boschi, L., Boschi, L., Brandi, V., Cianetti, S., … and Stocchi, P. (2004). Modeling Earth's post-glacial rebound.

Wu, P., Peltier, W. R. (1982). Viscous gravitational relaxation. *Geophysical Journal International*, *70*(2), 435-485.

Investigating the Tonga-Kermadec subduction zone from the study of the preparation phase of the June 15 2019 M7.2 Kermadec Islands (New Zealand) earthquake and the January 15 2022 Hunga Tonga-Hunga Ha'apai eruption

Serena D'Arcangelo, Mauro Regi, Angelo De Santis, Loredana Perrone, Gianfranco Cianchini, Maurizio Soldani, Alessandro Piscini, Cristiano Fidani, Dario Sabbagh, Stefania Lepidi, Domenico Di Mauro

The Tonga-Kermadec zone is one of the most active areas for the subduction continuous processes characterizing the area. In the recent few years, it was affected by two important geophysical events: first a strong earthquake of M7.2 on June 15 2019 with the epicentre in Kermadec Islands (New Zealand) and then an exceptional eruption of Hunga Tonga-Hunga Ha'apai volcano on January 15 2022. In order to better understand the geodynamics on the subduction area, we conducted a multi-parametric and multi-layer study on the phenomena occurred before both events basing on the lithosphere-atmosphere-ionosphere coupling (LAIC) models. We started with a seismic analysis of the earthquake sequence previous the June 15 2019 mainshock and of those anticipated the unique eruption, focusing on the circular area major affected to the preparation phase, i.e., the one defined by the Dobrovolsky strain radius. After that, we focused our attention on the atmospheric parameters generally influenced by seismic and volcanic events (skin temperature, outgoing longwave radiation, aerosol optical depth, and so on) applying the CAPRI algorithm to the ECMWF datasets to detect anomalies in their values. At the end, using the satellite data we studied the magnetic field and electron burst precipitations, looking for precursors of both events considered. All these observations together with their similarities and differences provide a better insight of the complex tectonic context. In conclusion, we reported evidence of the thermodynamic interaction between a stiff lithosphere and a more malleable asthenosphere inside the Kermadec-Tonga region. The presence of two distinct types of coupling among the geolayers was also proposed to explain the observed results.

SAR-TOOL: A new open-source software for the analysis of geospatial data in volcano-tectonic fields

S. D'Amico[1,3], F. Guglielmino[2]

[1] *Istituto Nazionale di Geofisica e Vulcanologia, Sezione Roma2, Rome, Italy*

[2] *Istituto Nazionale di Geofisica e Vulcanologia, Sezione di Catania - Osservatorio Etneo, Catania, Italy*

[3] *Department of Biological, Geological and Environmental Sciences, University of Catania, Catania, Italy*

Abstract

Since the last decade of the twentieth century, technological advancements and the availability of open-source satellite data have significantly increased geospatial analyses. Several software programs have been developed to process satellite INSAR data, including SNAP by ESA (European Space Agency), GAMMA (Wegmüller U. & Werner C.L., 1997), Sarscape, ROI_PAC/ISCE by NASA. In parallel, various algorithms have been proposed to compare, validate and integrate the satellite data with ground-based geodetic data. In particular, the SISTEM algorithm proposed by (Guglielmino et al., 2011) and based on elasticity theory, simultaneously integrates GNSS and INSAR data to provide 3D displacements maps of the study area. In order to (a) simplify the SISTEM pre-process work, (b) quickly analyse the outputs and (c) enhance the usability and ongoing development of SISTEM, we have developed SAR-TOOL, an open-source software in the Python language. Furthermore, we have developed an intuitive and lightweight GUI (Graphical User Interface), optimised to automatically adapt to different screen resolutions, ensuring an optimal user experience on any desktop, with ease of use designed especially for those without knowledge of computer programming. The GUI is structured with various frames to facilitate different operations on geospatial data, making the user interface organised and easy to navigate (Fig. 1).

From the SAR-TOOL GUI is possible:

- Visualise and convert the user's raster/vector data into various geospatial formats;
- Easily project data into various geographical reference systems;
- Crop and change the resolution of raster data;
- Homogenise input data through the development of a data intersection algorithm, which can then be supplied to the SISTEM algorithm;
- Generate synthetic data (DEM, synthetic Mogi source model (Mogi K., 1958) and synthetic GPS points) to associate with the modelled surface, in order to study the effects of inflation/deflation cycles as the parameters and position of the spherical source change (Fig. 2);

- Use the SISTEM algorithm effectively and interactively to obtain three-dimensional ground deformation maps, using one or more datasets of interferometric data as input.

SAR-TOOL utilises the open-source GDAL (Geospatial Data Abstraction Library) for the analysis of raster and vector data.

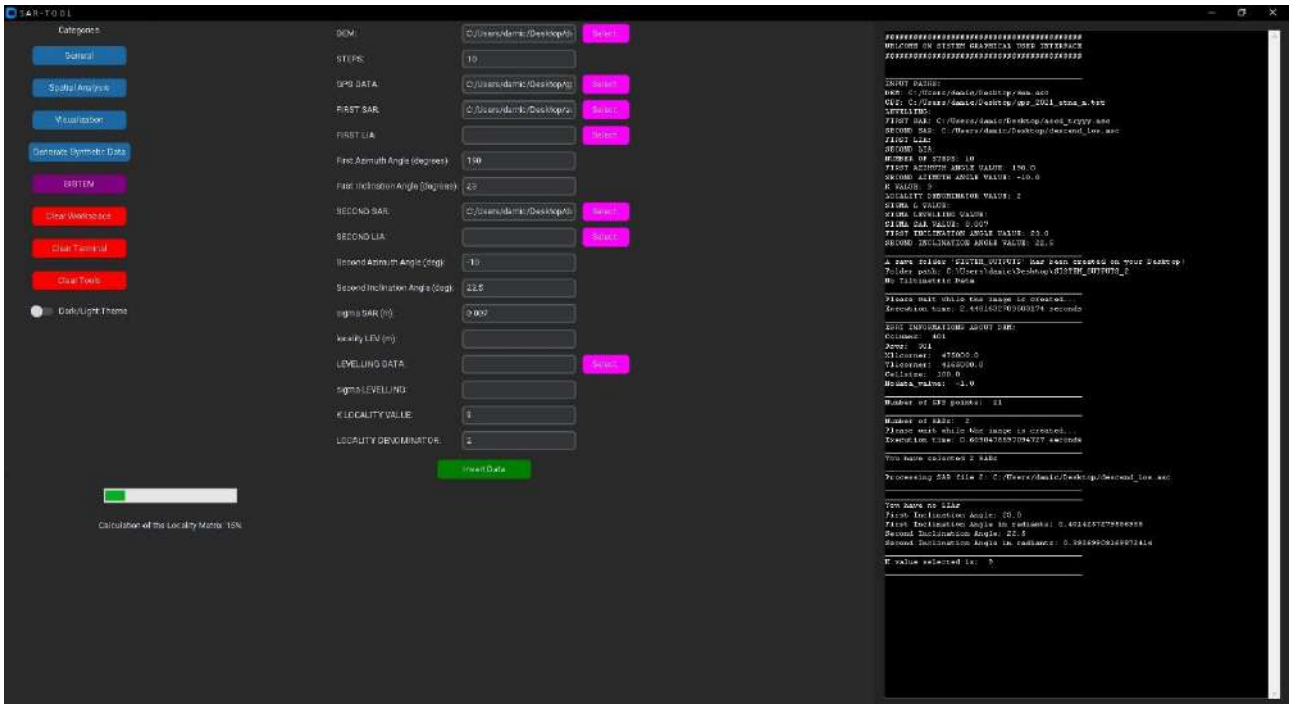

Fig. 1 - Main working screen of the open-source SAR-TOOL software. In particular, the figure shows a work session related to the interactive selection and addition of input data required by the SISTEM algorithm, featuring a terminal on the right showing both the parameters entered and those calculated by the algorithm.

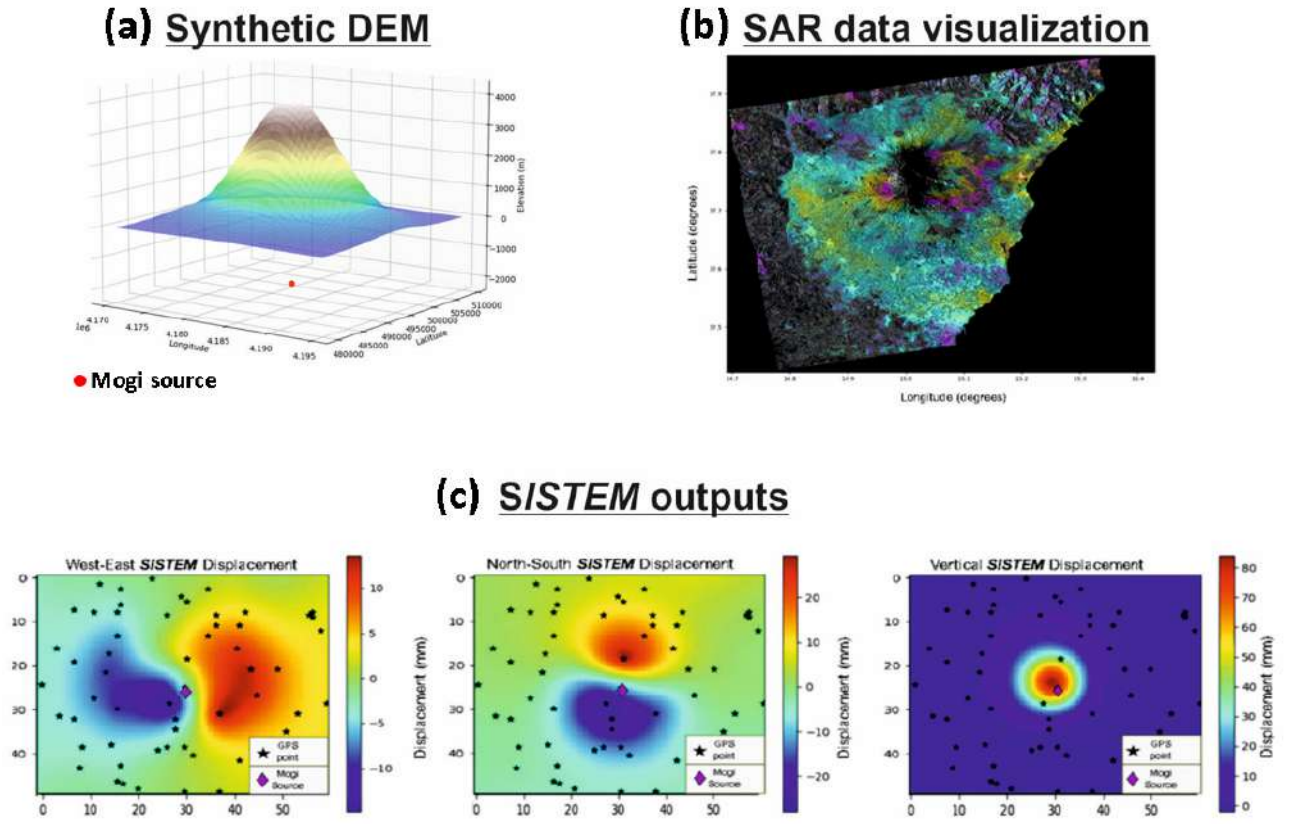

Fig. 2 - Examples of products obtained through SAR-TOOL. (a) Modelling of a synthetic DEM and a spherical Mogi source located at a depth of 2000 metres above sea level; (b) Visualisation of a phase interferogram relative to a ground deformation period at Etna volcano (Italy); (c) Output of the displacements generated by a spherical Mogi source and calculated by the SISTEM algorithm through interaction with 60 synthetic GPS points arranged in a random geometry within the grid.

References

Guglielmino F., Nunnari G., Puglisi G., Spata A.; 2011: Simultaneous and Integrated Strain Tensor Estimation from geodetic and satellite deformation Measurements (SISTEM) to obtain three-dimensional displacement maps. IEEE Trans. Geosci. Remote Sens. vol., 49, pp. 1815-1826.

Mogi K.; 1958: Relations between the eruptions of various volcanoes and the deformations of the ground surfaces around them. Bulletin of the Earthquake Research Institute, pp. 99-134.

Wegmüller U., Werner C.L.; 1997: GAMMA SAR processor and interferometry software. Proceedings 3rd ERS Scientific Symposium, Florence, Italy.

Corresponding author: salvatore.damico2@ingv.it

On constraining 3D mantle flow patterns in subduction, mid-ocean-ridge, and plume environments with teleseismic body wave data

M. Faccenda1 , B. P. VanderBeek1

[1] *Dipartimento di Geoscienze, Università di Padova, Padova, Italy*

Conventional seismic tomography studies consider the Earth's interior as mechanically isotropic, despite seismic anisotropy being widely observed. This current standard approach to seismic imaging is likely to lead to significant artefacts in tomographic images with first-order effects on interpretations and hinders the quantitative integration of seismology with geodynamic flow models. In this contribution we use geodynamic and seismological modeling to predict the elastic properties and synthetic teleseismic P- and S-wave travel-time datasets for three different tectonic settings: a plume rising in an intraplate setting, a divergent margin, and a subduction zone (Figs. 1, 2). Subsequently, we perform seismic anisotropy tomography testing a recently developed methodology that allows for the inversion of an arbitrarily oriented weakly anisotropic hexagonally symmetric medium using multiple body-wave datasets. The tomography experiments indicate that anisotropic inversions of separate and joint P- and S-wave travel-times are capable of recovering the first order isotropic velocity anomalies and anisotropic patterns. In particular, joint P- and S-wave anisotropic inversions show that by leveraging both phases it is possible to greatly mitigate issues related to imperfect data coverage common in seismology and reduce parameter trade-offs. In contrast, by neglecting seismic anisotropy, isotropic tomographic models provide no information on the mantle fabrics and in all cases are contaminated by strong velocity artifacts. In the inversions the magnitude of anisotropy (as well as that of seismic anomalies) is always underestimated owing to regularization procedures and smearing effects. It follows that the true seismic anisotropy of mantle rocks is likely higher than estimated from anisotropic tomographies, and more consistent with predictions from laboratory and numerical micro-mechanical experiments. Altogether, these results suggest that anisotropic body-wave tomography could provide unprecedented information about the Earth's deep geological structure, and that the latter could be better recovered by complementing teleseismic body-wave travel-times with other geophysical datasets (Faccenda and VanderBeek, 2023).

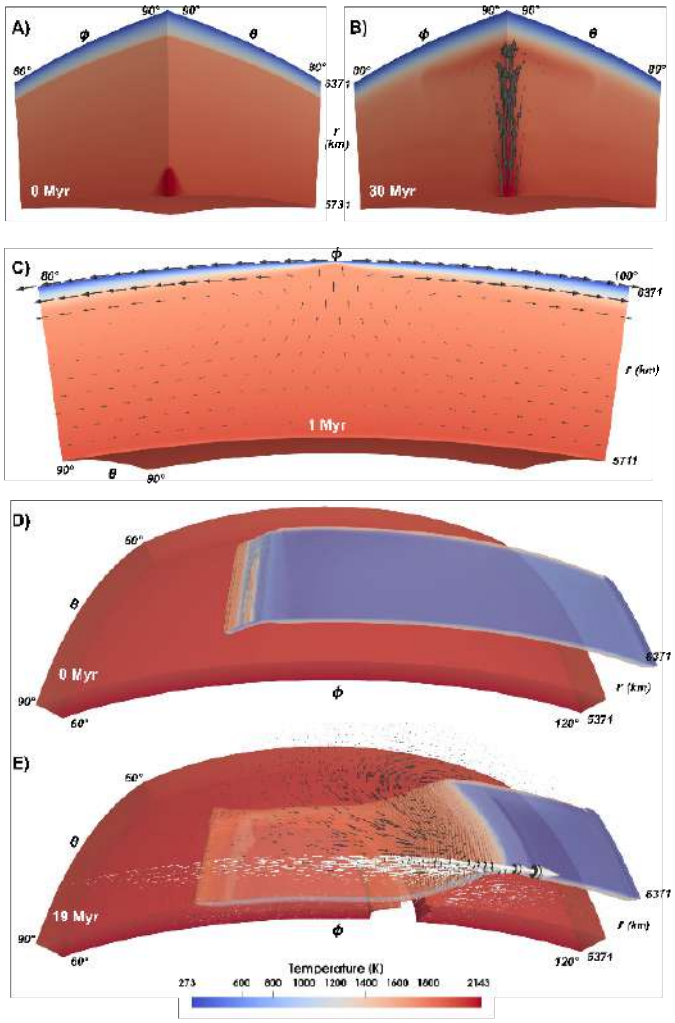

Fig. 1 – Temperature and velocity (arrows) fields for the three modeled tectonic settings as predicted by macro-scale geodynamic modeling. (A, B) Rising plume model initial setup and after 30 Myr. Only half of the computational domain (ϕ = 80° - 90°) is shown. The thermal anomaly is delimited by a 2D gaussian surface containing material at 2143 K, resulting in a 200-250 K temperature anomaly over the mantle transition zone. The 2D gaussian surface is centered at (ϕ, θ) = (90°, 90°), and has a radial extent of 1°, a horizontal standard deviation of 0.4° and a maximum amplitude of 100 km. (C) Oceanic spreading ridge model after 1 Myr. The arrows length at the surface is proportional to the imposed 2 cm/yr divergence rate. (D, E) Oceanic plate subduction model initial setup and after 19 Myr. The opaque surfaces enclose material with viscosity ≥ 10^{21} Pa s and are colored according to temperature. In (E) the white (dark grey) arrows indicate the poloidal (toroidal) component of the velocity field. The arrows length in (B) and (E) is downscaled by 10 and 4 times with respect to that in (C).

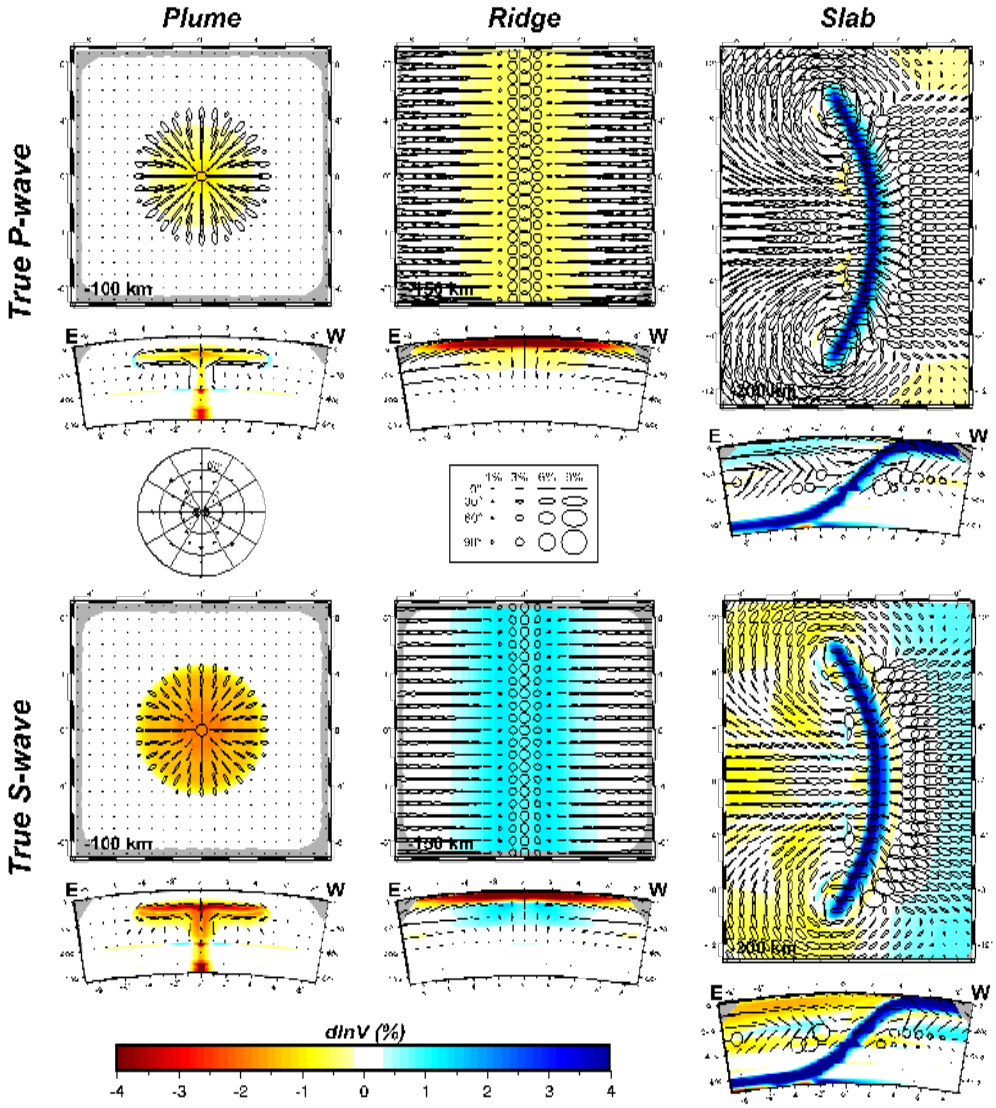

Fig. 2 - True P-wave (top two panels) and S-wave isotropic anomalies and fast symmetry axis orientations for the three modeled tectonic settings as predicted by micro-scale geodynamics modeling. Horizontal and E-W vertical cross sections (along the equatorial plane of the geodynamic model spherical domain) are shown. Velocity anomalies $\Delta lnV_{P,S}$ are computed (i) using the average of the three principal velocities, that for an hexagonally symmetric medium with a fast symmetry axis are V_{fast}, V_{slow}, V_{slow}, and (ii) with respect to reference radial velocity profiles taken at the corner of the computational domain with minimum the X-Z axes coordinates, which is representative of the far-field, unperturbed mantle. The P-wave low velocity and S-wave high velocity anomalies at 150 km in the ridge model, and the P-wave high velocity and S-wave low velocity anomalies in the subduction model mantle wedge, are caused by deviations from the hexagonally symmetry model. The length of the ellipses major axis is proportional to: $2f(\%) = \frac{\left(V_{fast} - V_{slow}\right)}{\left(V_{fast} + V_{slow}\right)} * 200\%$. The orientation of the fast symmetry axis is parallel to the major axis of the ellipses, while the length of minor axis is proportional to the dip relative to the cross section.

References

Faccenda, M., VanDerBeek, B.P., On constraining 3D seismic anisotropy in subduction, mid-ocean-ridge, and plume environments with teleseismic body wave data. J. Geodyn., 158, https://doi.org/10.1016/j.jog.2023.102003 (2023).

Corresponding author: manuele.faccenda@unipd.it

A dynamic identification of *continuous discontinuities* in geodynamic numerical models

V. Fedeli[1], A.M. Marotta[1]

[1] Dipartimento di Scienze della Terra "Ardito Desio" (Università degli Studi di Milano, Italy)

Discontinuities affect the Earth's dynamics, yet the Earth is often represented in geodynamical models as a continuous material. The challenge of representing discontinuities in numerical models has been addressed in several ways in literature. The split node method, originally introduced by Jungels (1973) and Jungels and Frazier (1973) for elastic rheology and then modified by Melosh and Raefsky (1981) to simplify its implementation, allows the introduction of discontinuity into a finite element model by imposing an a-priori slip at a designated node, where the displacement depends on the element which the node is referred to. Originally, this method requires that the discontinuity's geometry and slip are pre-established.

More recently, Marotta et al. (2020) modify this approach by introducing a coupling factor that indicates the percentage difference between the velocities of the element to which the slip node belongs, while the velocity consistently derives from the dynamic evolution of the system. However, this method still requires the pre-establishment of the discontinuity's geometry.

We here present a new technique that enables the dynamic identification of the discontinuity's during the thermomechanical evolution of the system, based on physical parameters and without predefining the slip or the geometry.

We have implemented a new algorithm that identifies one or more discontinuities in a finite-element scheme operating through two phases: nucleation and propagation. Nucleation involves selecting a yield physical property and identifying the potential slip nodes, i.e., nodes on which the chosen physical property exceeds a yield value. The nucleus is then identified as the potential slip node where the chosen property most exceeds the yield. Propagation can be performed by choosing between three approaches of propagation: single simple fault, multiple simple fault and single double fault; and three schemes for the identification of neighboring nodes: grid-bounded, pseudo-free and free. The resulting discontinuity is the line connecting the nucleus and the propagation nodes. Once the discontinuity has been identified, a coupling factor is introduced and the algorithm continues to operate following the Marotta et al., (2020)'s scheme.

The results of several benchmark tests, performed through both simple and complex finite-elements models, confirm the success of the algorithm in recognizing yield conditions and introducing a discontinuity into a finite-element model and demonstrate the correctness of the propagation's geometry.

References

Jungels P.H.; 1973: Models of tectonic processes associated with earthquakes. PhD thesis.

Jungels P.H., Frazier G.A. Frazier; 1973: Finite element analysis of the residual displacements for an earthquake rupture: source parameters for the San Fernando earthquake. Journal of Geophysical Research.

Marotta A.M., Restelli F., Bollino A., Regorda A., Sabadini R.; 2020: The static and time-dependent signature of ocean-continent and ocean-ocean subduction: The case studies of Sumatra and Mariana complexes. Geophysical Journal International.

Melosh H.J., Raefsky A.; 1981: A simple and efficient method for introducing faults into finite element computations. Bulletin of the Seismological Society of America.

Corresponding author: valeria.fedeli@unimi.it

PRIN 2020 NASA4SHA Project: A Combined Regional Velocity Field of Northern Italy

A. Galvani1, M. Albano1, C. Braitenberg2, F. Brighenti3, R. Caputo4, F. Carnemolla3, D. Cheloni1, G. De Guidi3, R. Devoti1, A. Magrin5, A. Pellegrinelli4, G. Pietrantonio1, G. Rossi5, S. Stramondo1, L. Tunini5, D. Zuliani5

[1] Istituto Nazionale di Geofisica e Vulcanologia, Rome, Italy
[2] Università degli Studi di Trieste, Trieste, Italy
[3] Università degli Studi di Catania, Catania, Italy
[4] Università degli Studi di Ferrara, Ferrara Italy
[5] Istituto Nazionale di Oceanografia e di Geofisica Sperimentale, Trieste, Italy

The activity presented in this note is part of the PRIN 2020 NASA4SHA Project (Fault segmentation and seismotectonics of active thrust systems: the Northern Apennines and Southrn Alps laboratorie for new Seismic Hazard Assessments in northern Italy). The project's objective is to define, through a multidisciplinary approach including geological, geophysical, seismological, paleoseismological, and geodetic methods at various scales (regional and local), the geometry and kinematics of the main compressive systems in the central – estern Southern Alps and Northern Apennines (Fig. 1).

Geodetic methods make it possible to reconstruct the ongoing deformation rate of the Earth's surface at regional and local scales (with high-density networks). This information, combined with the 3D model of tectonic structures present in the investigated region, can indicate areas/volumes where the tectonic activity and the deformation are either more or less intense, enabling a focus on fault zones where the stress is increasingly accumulated.

We analyzed data from continuous GNSS (Global Navigation Satellite Systems) stations covering the entire study area, belonging to the RING (Rete Integrata Nazionale GNSS) and FReDNet (Friuli Regional Deformation Network) networks, managed by INGV (Istituto Nazionale di Geofisica e Vulcanologia) and OGS (Istituto Nazionale di Oceanografia e di Geofisica Sperimentale - OGS) respectively, together with data from other permanent networks, managed by various institutions. In addition, we have resurveyed some vertices of the IGM95 geodetic network, focusing on local transects orthogonal to the main compressive structures, and we have analyzed the new discontinuous GNSS observations together with the previous ones performed in the past by IGM (Istituto Geografico Militare) on the same vertices.

Here, we present the regional velocity field (Fig. 2) of the GNSS permanent stations (discontinuous sites will be included in a second release), obtained as a result of the combination of two velocity

fields calculated by INGV and OGS, with different analysis softwares, Bernese and Gamit Globk

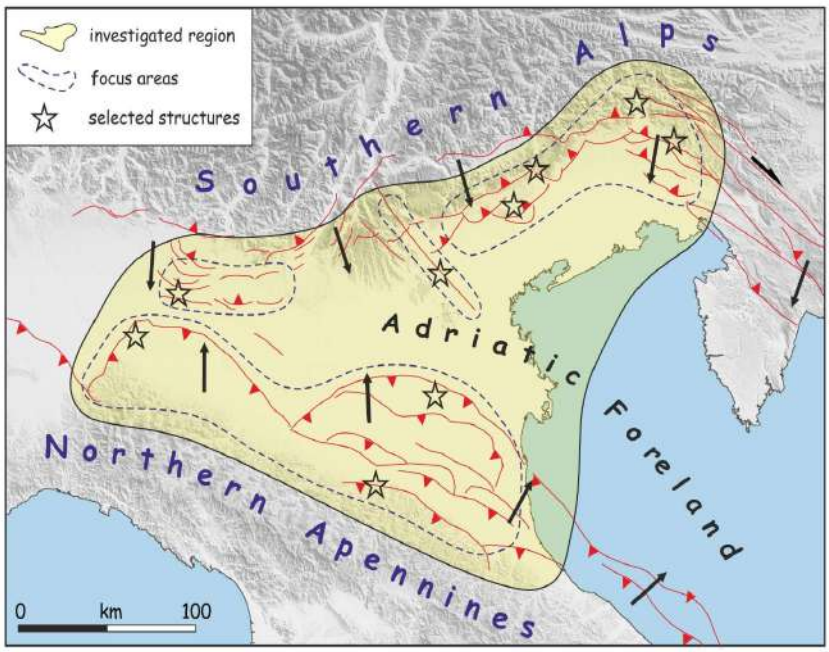

Fig. 1 – Map of the study area of the PRIN 2020 NASA4SHA Project.

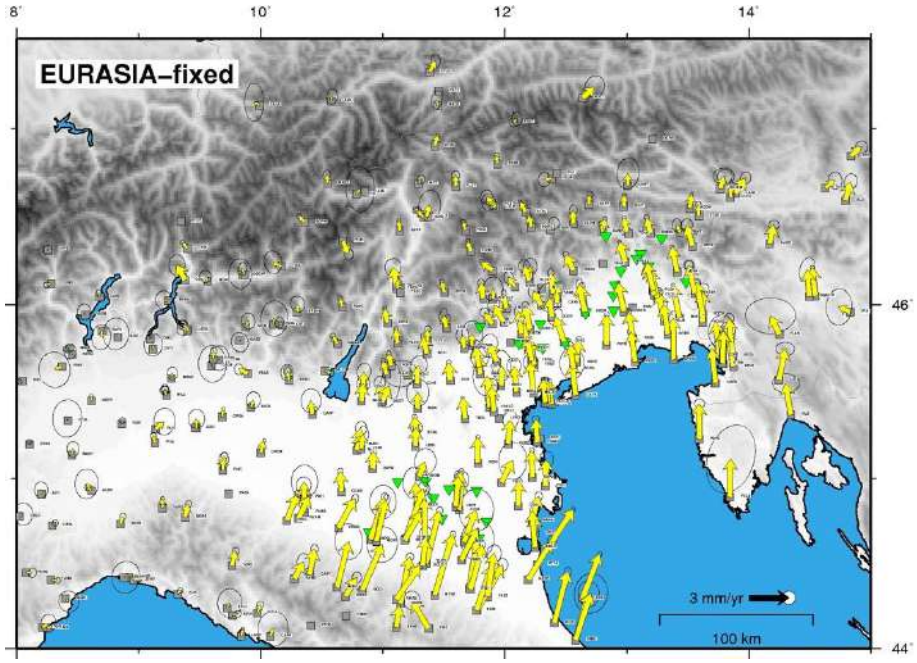

Fig. 2 – Map of the horizontal GNSS velocities in the Eurasian-fixed reference frame, from the combined solution. Error ellipses at 95%. The inverted green triangles are the locations of the resurveyed vertices of the IGM95 network.

respectively. The velocity field is expressed in the ITRF2014 reference frame, with respect to the Eurasian plate (Altamimi et al., 2017). The combination procedure described in Devoti et al., 2017, is based on a linear least-squares approach, where we consider each velocity field as a sample of the true velocity field and the combined velocity as the best estimate of the true velocity field. The combined solution allows a validation of the velocity field by assessing the velocity repeatability of velocities at the common sites and minimize the probability of including biased velocities.

The combined long-term horizontal velocity field is then used for obtaining the strain-rate field across the active deformation zones, by applying the classic approach based on GNSS velocity vectors converted in the strain-rate field (e.g., Beavan and Haines, 2001; Shen-Tu, 1998).

References

Altamimi Z., Métivier L., Rebischung P., Rouby H., Collilieux X.; 2017: ITRF2014 plate motion model, Geophys. J. Int., 209, 3, doi:10.1093/gji/ggx136.

Beavan J., Haines J.; 2001: Contemporary horizontal velocity and strain rate fields on the Pacific-Australian plate boundary zone through New Zealand. J. Geophys. Res., 106(B1), doi:10.1029/2000JB900302.

Devoti R., D'Agostino N., Serpelloni E., Pietrantonio G., Riguzzi F., Avallone A., Cavaliere A., Cheloni D., Cecere G., D'Ambrosio C., Falco L., Selvaggi G., Mètois M., Esposito A., Sepe V., Galvani A., Anzidei M.; 2017: A Combined Velocity Field of the Mediterranean Region. Annals of Geophysics, 60(2), doi:10.4401/ag-7059.

Shen-Tu B., Holt W.E., Haines J.; 1998: Contemporary kinematics of the western United States determined from earthquake moment tensors, very long baseline interferometry, and GPS observations. J. Geophys. Res., 103(B8), doi:10.1029/98JB01669.

Corresponding author: alessandro.galvani@ingv.it

Strength of the lithosphere derived by geological and geophysical data: the Graham Land (Antarctic Peninsula) case study

F. Linsalata[1], D. Melini[2], G. Spada[1]

[1] Dipartimento di Fisica e Astronomia (DIFA), Alma Mater Studiorum Università di Bologna, Italy
[2] Istituto Nazionale di Geofisica e Vulcanologia (INGV), Roma, Italy

One-dimensional lithospheric strength is usually represented by a diagram of shear-stress versus depth (Brace, 1980), known as the Brace-Goetze strength profile, or Yield Strength Envelope (YSE). The shape of this diagram, informally dubbed the 'Christmas tree', strongly depends on the composition of the constituent rocks. This constitutive property is usually extrapolated from centimeter-sized laboratory samples (e.g. Hirth and Kohlstedf, 2003; Zhang and Karato, 1995), from structural studies of naturally deformed rocks (e.g. Twiss, 1977; Tullis, 2002; Evans, 2005), or from a larger-scale perspective (e.g. Thatcher, 1983; Bird and Kong, 1994; Handy and Brun, 2004; Thatcher, 2009). However, the strength of the Earth's lithosphere has been debated since the beginning of the last century (Tesauro et al., 2009), when the concept of a strong lithosphere overlying a viscous asthenosphere was first introduced (Barrell, 1914). This concept played a major role in the development of plate tectonics (Le Pichon et al., 2013), and how the strength of the plates varies spatially and temporally is a fundamental question in geology and geodynamics (Jackson, 2002; Burov and Watts, 2006).

Yield Strength Envelopes have been calculated over the last few decades for a number of locations in Europe (e.g. Cloetingh and Burov, 1996; Cloetingh et al., 2005), America (Liu and Zoback, 1997) and Asia (Zang et al., 2007), but are not available on a regional scale for Antarctica. In this work, based on previously published data, we explore the strength of the lithosphere beneath the Graham Land region (Antarctic Peninsula, Fig. 1) using numerical modeling which simulates lithospheric deformation as a function of geological and geophysical parameters.

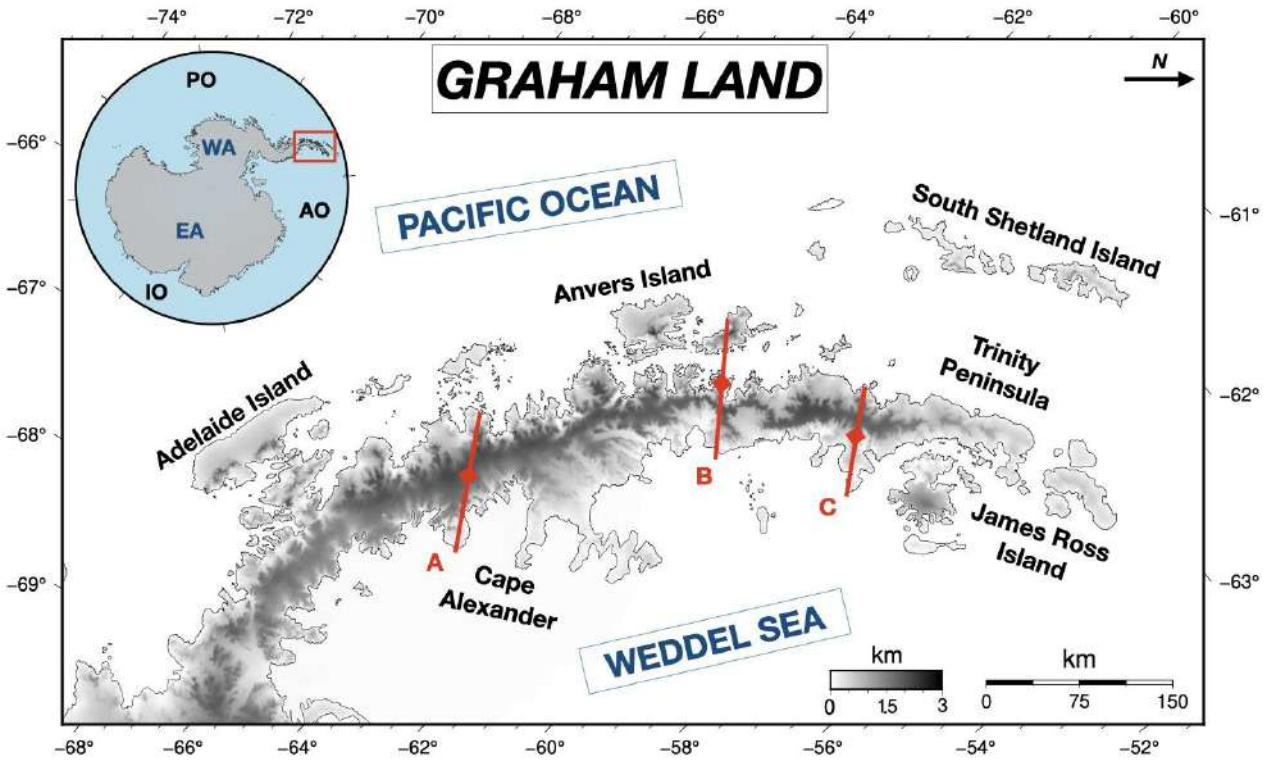

Figure 1. Detail of the study region, the Graham Land (Antarctic Peninsula) with major island. The red lines (A, B and C) indicate the location of three profiles considered in this study. The gray scale represents topography according to Global Earth Relief Grids (15 arc second). In the upper left frame, overview of the Antarctic continent with the study area highlighted by the red box. WE: West Antarctica, EA: East Antarctica, PO: Pacific Ocean, AO: Atlantic Ocean and IO: Indian Ocean.

First, we use the MIDAS algorithm (Blewitt, 2016) to process 21 GNSS time series spanning 1997–2022, provided by the Nevada Geodetic Laboratory, and we produce a robust tectonic velocity solution. Then, we calculate a new geodetic strain rate model using the VISR code (Shen et al., 1996; Shen et al., 2015), with an optimal mesh grid definition of 0.5x0.5 degrees, that best fits our study area. Second, we combine our new geodetic strain rate model with the Moho depth and rheological parameters (Tab. 1), such as Geothermal Heat Flow (GHF), heat production and thermal conductivity previously published in the literature to determine the YSE beneath Graham Land. We performed several numerical experiments in which the GHF and the rheological parameters were varied to compute predictions of the YSE. We explored the range of uncertainty in each parameter by a trial-and-error procedure with discrete sampling steps. Each combination of GHF and temperature coefficient for creep rheology constitutes an independent simulation. For each combination, the model predictions were computed with a MATLAB code; a flowchart illustrating our modeled workflow is shown in Fig. 2. The results of our study demonstrate that the “jelly sandwich” and the “crème brûlée” models are both valid for the Graham Land lithosphere, depending on specific thermal and rheological conditions considered.

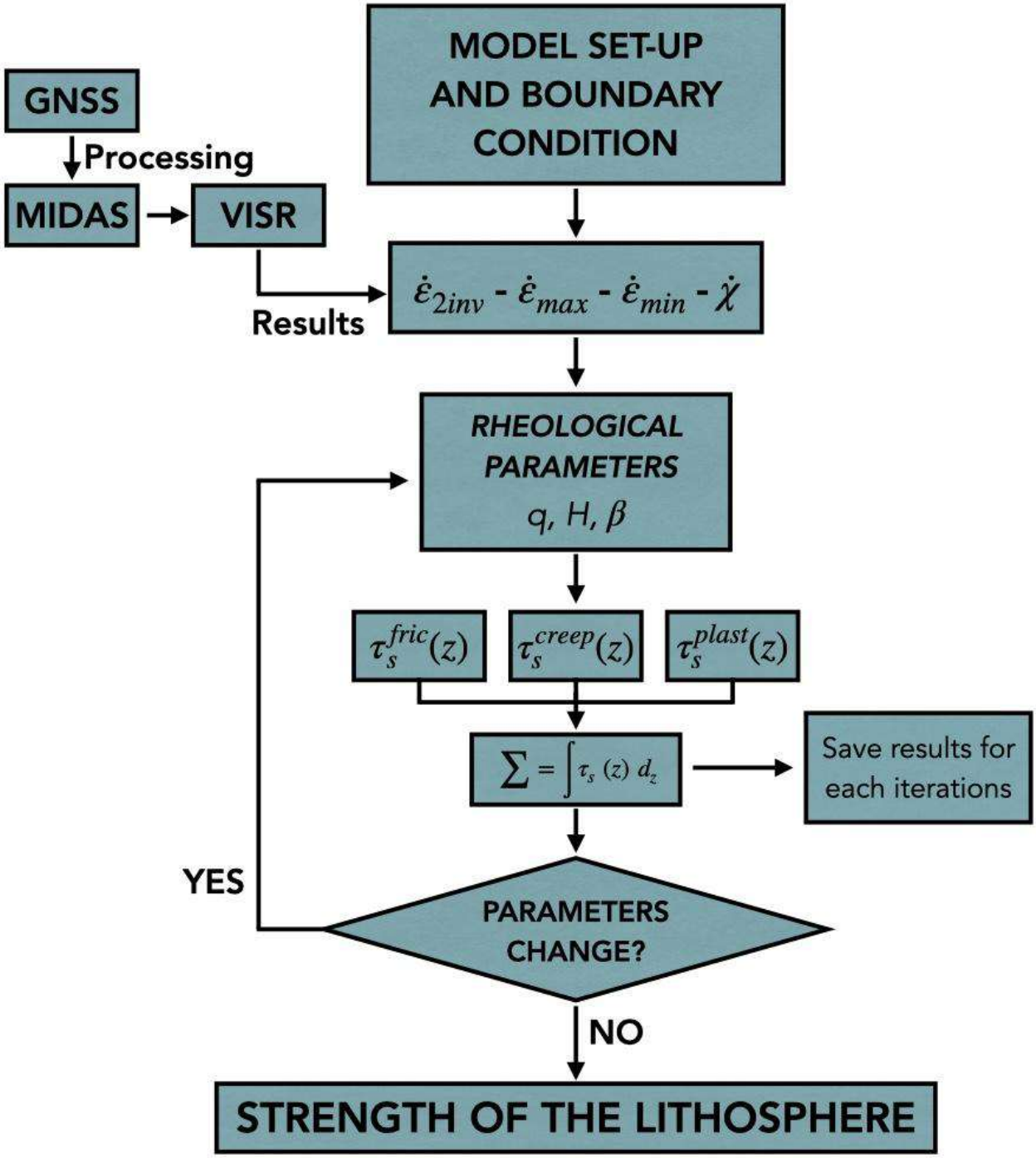

Figure 2. Modeling workflow adopted in our MATLAB Conde

Data availability statement

The MIDAS algorithm code is available from the Nevada Geodetic Laboratory (NGL) at the link http://geodesy.unr.edu/MIDAS_release/?C=M;O=A. Program to compute the strain rate is available from the Zheng-Kang Shen webpage at http://scec.ess.ucla.edu/~zshen/visr/. The numerical code implemented in MATLAB and the data underlying all figures shown in this work are available upon request from the corresponding author.

Acknowledgements

All figures have been drawn using the Generic Mapping Tools (GMT) of Wessel and Smith (1998). We acknowledge Nevada Geodetic Laboratory for making available the GPS data from the web http://geodesy.unr.edu/index.php and MIDAS software at the page http://geodesy.unr.edu/MIDAS_release/?C=M;O=A.

References

Barrell, J.; 1914. *The strength of the Earth's crust part I. Geologic tests of the limits of strength*. The Journal of Geology, 22(1), 28-48.

Bird, P., Kong, X.; 1994. *Computer simulations of California tectonics confirm very low strength of major faults*. Geological Society of America Bulletin, 106(2), 159-174.Blewitt, G., Kreemer, C., Hammond, W. C., & Gazeaux, J.; 2016. *MIDAS robust trend estimator for accurate GPS station velocities without step detection*. Journal of Geophysical Research: Solid Earth, 121(3), 2054-2068.Brace, W. F., Kohlstedt, D. L.; 1980. *Limits on lithospheric stress imposed by laboratory experiments*. Journal of Geophysical Research: Solid Earth, 85(B11), 6248-6252.

Burov, E. B., Watts, A. B; 2006. *The long-term strength of continental lithosphere: "jelly sandwich" or" crème brûlée"?*. Geological Society of America Today, 16(1), 4.

Cloetingh, S., Burov, E. B; 1996. *Thermomechanical structure of European continental lithosphere: constraints from rheological profiles and EET estimates*. Geophysical Journal International, 124(3), 695-723.

Cloetingh, S., Ziegler, P. A., Beekman, F., Andriessen, P. A. M., Hardebol, N., Dezes, P.; 2005. *Intraplate deformation and 3D rheological structure of the Rhine Rift System and adjacent areas of the northern Alpine foreland*. International Journal of Earth Sciences, 94, 758-778.

Evans, B.; 2005. *Creep constitutive laws for rocks with evolving structure*. Geol Soc Lond Spec Publ 245 (1): 329–346.

Handy, M. R., Brun, J. P.; 2004. *Seismicity, structure and strength of the continental lithosphere*. Earth and Planetary Science Letters, 223(3-4), 427-441.

Hirth, G., Kohlstedf, D.; 2003. *Rheology of the upper mantle and the mantle wedge: A view from the experimentalists*. Geophysical monograph-american geophysical union, 138, 83-106.

Jackson, J. A; 2002. *Strength of the continental lithosphere: time to abandon the jelly sandwich?*. Geological Society of America Today, 12, 4-10.

Le Pichon, X., Francheteau, J., Bonnin, J., X.; 2013. *Plate tectonics* (Vol. 6). Elsevier.

Liu, L., Zoback, M. D.; 1997. *Lithospheric strength and intraplate seismicity in the New Madrid seismic zone*. Tectonics, 16(4), 585-595.

Shen, Z. K., Jackson, D. D., Ge, B. X; 1996. *Crustal deformation across and beyond the Los Angeles basin from geodetic measurements*. Journal of Geophysical Research: Solid Earth, 101(B12), 27957-27980.

Shen, Z. K., Wang, M., Zeng, Y., Wang, F; 2015. *Optimal interpolation of spatially discretized geodetic data*. Bulletin of the Seismological Society of America, 105(4), 2117-2127.

Tesauro, M., Kaban, M. K., Cloetingh, S. A; 2009. *A new thermal and rheological model of the European lithosphere*. Tectonophysics, 476(3-4), 478-495.

Thatcher, W.; 1983. *Nonlinear strain buildup and the earthquake cycle on the San Andreas fault*. Journal of Geophysical Research: Solid Earth, 88(B7), 5893-5902.

Thatcher, W.; 2009. *How the continents deform: The evidence from tectonic geodesy*. Annual Review of Earth and Planetary Sciences, 37, 237-262.

Tullis, J.; 2002. *Deformation of granitic rocks: experimental studies and natural examples*. Reviews in Mineralogy and Geochemistry, 51(1), 51-95.

Twiss, R. J.; 1977. *Theory and applicability of a recrystallized grain size paleopiezometer*. Stress in the Earth, 227-244.

Wessel P., Smith W. H.; 1998: *New, improved version of Generic Mapping Tools released*, Eos, Transactions American Geophysical Union, 79(47), 579-579.

Zhang, S., Karato, S. I.; 1995. *Lattice preferred orientation of olivine in simple shear deformation and the flow geometry of the upper mantle of the Earth*. Nature, 375, 774-777.

Zang, S. X., Wei, R. Q., Ning, J. Y.; 2007. *Effect of brittle fracture on the rheological structure of the lithosphere and its application in the Ordos*. Tectonophysics, 429(3-4), 267-285.

Corresponding author: f.linsalata91@gmail.com, fernando.linsalata2@unibo.it

The coda attenuation method reveals a very high attenuating crust in the High Agri Valley (Southern Italy)

S. Lucente[a], V. Serlenga[b], S. de Lorenzo[a], E. del Pezzo[c,d], M. Filippucci[a,c], T. Ninivaggi[e], T.A. Stabile[b], A. Tallarico[a,c]

[a] *Università degli Studi di Bari Aldo Moro, Dipartimento di Scienze della Terra e Geoambientali, Bari, Italy*
[b] *CNR Institute of Methodologies for Environmental Analysis, IMAA, Tito Scalo, Italy*
[c] *Istituto Nazionale di Geofisica e Vulcanologia, Sezione di Napoli "Osservatorio Vesuviano", Napoli, Italy*
[d] *Instituto Andaluz de Geofisica, Universidad de Granada, Granada, Spain*
[e] *Istituto Nazionale di Geofisica e Vulcanologia, Sezione Irpinia, Grottaminarda, Italy*

High Agri Valley is an intermontane basin located in the axial portion of Southern Apennines, a fold and thrust chain originated starting from the late Oligocene (Patacca & Scandone, 2007). The investigated area is characterized by a very strong seismogenic potential as testified by the Mw=7.0 1857 earthquake. In the last decades, a low magnitude natural seismicity has been recorded by the stations belonging to both the trigger-mode monitoring network managed by ENI Oil Company and the Italian National Seismic Network managed by INGV. In addition to the natural seismicity, two anthropogenic seismicity clusters are documented (Stabile et al., 2014; Improta et al., 2017 among the others), located NE and SW of the artificial Pertusillo lake, respectively: a) fluid-induced microseismic swarms due to the injection, through the Costa Molina 2 well, of the wastewater produced by the exploitation of the Val d'Agri oilfield; b) protracted reservoir induced seismicity (RIS) caused by the combined effects of the water table oscillations of the Pertusillo lake, the regional tectonics and likely the poroelastic/elastic stress due to aquifers in the carbonate rocks (Picozzi et al., 2022). In order to gain insights on the attenuation properties of the crust of this region, we selected a dataset of about 1800 events acquired from 2001 to 2015 by the two above mentioned seismic networks, with local magnitude (ML) ranging from 0 to 3.3. The dataset is composed of triaxial recordings acquired by an average number of 14 stations.

We estimated the attenuation of S-coda waves Qc^{-1} from a linear regression analysis of the envelope of the amplitude decay curve (Sato, 1977). This parameter can give information about the physical state of the crust (possible presence of fluids, or thermal anomalies, or ductile rock volumes) and in tectonic context it is widely accepted that Q_c, estimated with the single scattering model at long lapse time, is representative of the intrinsic attenuation Q_i (Mayor et al. 2016). The method consists in the linear fitting of the decreasing trend on the envelopes of S coda waves in a selected time window. Moreover, we developed a method aimed at automatically finding the end-time (T_2) of the coda envelope, avoiding the manual and subjective criterion of selection of the end of coda. This method was tested on a significant sample of real data before of its application to the entire dataset. Only the components, for which the condition $T_1<T_L<T_2$ was fulfilled, were considered for the linear regression.
The Qc estimates were performed by using different time windows for the envelope fitting, starting from the time T_1 to the time T_L (the lapse time). In detail, we adopted, as T_1, 1.0*Ts, 1.5*Ts and 2.0*Ts (being Ts the S wave arrival time), and as T_L 10s, 15s, 20s, 25s and 30 s from the event origin

time. To evaluate the dependence of Q_c on frequency f, we filtered all the traces in bands centered around 1, 2, 3, 4, 5, 6, 8, 10, 12, 14 and 16 Hz of frequency (as suggested by Bianco et al., 2002, for Southern Apennines).

The obtained results show the increase of Q_c with f at all the considered T_L (Fig. 1). This dependence could be described by the general relation:

$$Q_c(f) = Q_0 f^{\alpha} \qquad (1)$$

where Q_0 is the Q_c at 1 Hz and α is the attenuation exponent. Our results show that in the High Agri Valley Q_0 ranges between 8 and 57, whereas α ranges between 0.66 and 1.14, indicating that the region is tectonically and seismically active, as found in other adjacent areas (Filippucci et al., 2021 and references therein). Compared with other tectonic regions worldwide, in the High Agri valley $Q_c(f)$ is very low at all the investigated frequencies (Fig. 2). This evidence could be interpreted as due to the fluid presence in the investigated crust, thus providing a further hint on the possible role of fluids in the seismicity of the area. A complete characterization of seismic attenuation of the studied area will require further investigations, that is the separation of scattering and intrinsic contributions in the total attenuation and a 3D imaging to highlight the possible relation between spatial attenuation anomalies and seismicity distribution in the investigated area.

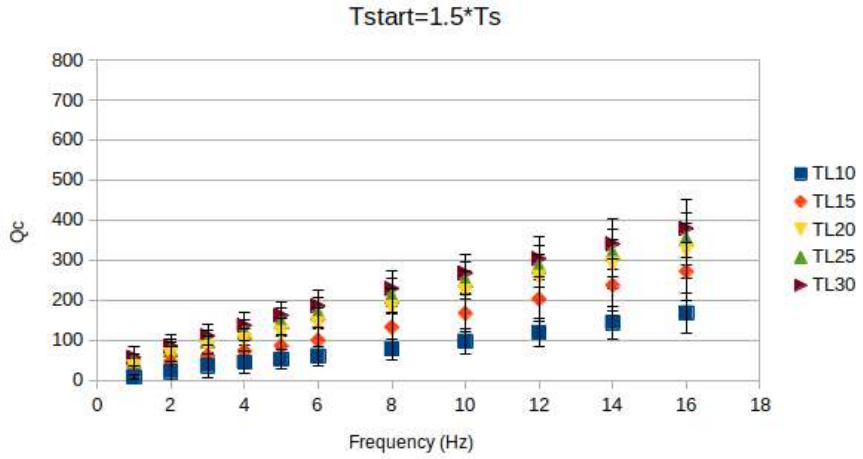

*Fig. 1 –Q_c distribution related to several time windows, starting from 1.5*Ts and ending at 10, 15, 20, 25 and 30 s.*

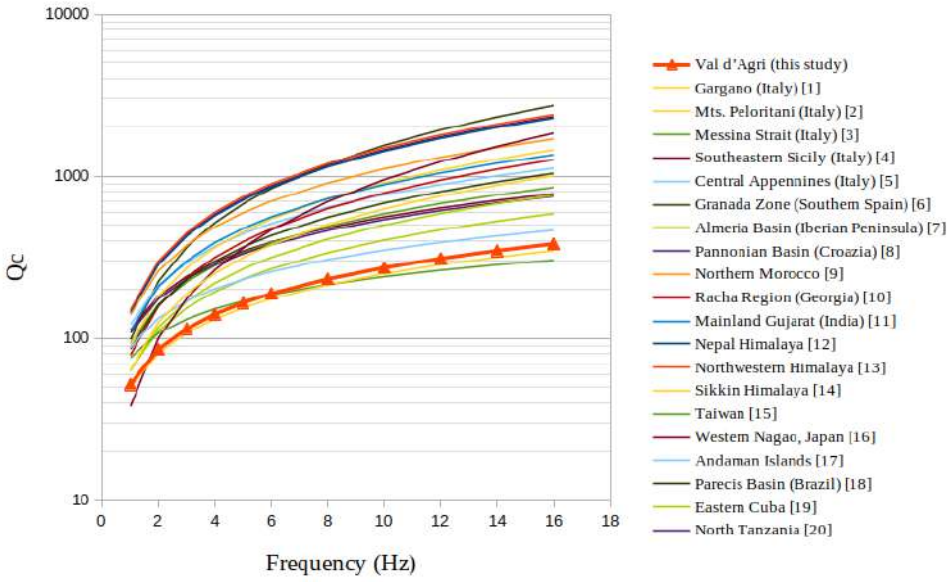

*Fig. 2 – Comparison between High Agri Valley Q_c (regression performed between 1.5*Ts and a lapse time of 30 s) and the same parameter obtained for other locations in the world.*

References

Bianco, F., Del Pezzo, E., Castellano, M., Ibanez, J., & Di Luccio, F. (2002). Separation of intrinsic and scattering seismic attenuation in the Southern Apennine zone, Italy. Geophysical Journal International, 150(1), 10-22.

Candela, S., Mazzoli, S., Megna, A., & Santini, S. (2015). Finite element modelling of stress field perturbations and interseismic crustal deformation in the Val d'Agri region, southern Apennines, Italy. Tectonophysics, 657, 245-259.

Filippucci, M., Lucente, S., Del Pezzo, E., de Lorenzo, S., Prosser, G., & Tallarico, A. (2021). 3D-Kernel Based Imaging of an Improved Estimation of (Qc) in the Northern Apulia (Southern Italy). Applied Sciences, 11(16), 7512.

Improta, L., Bagh, S., De Gori, P., Valoroso, L., Pastori, M., Piccinini, D., Chiarabba, C., Anselmi, M., Buttinelli, M. (2017). Reservoir structure and wastewater-induced seismicity at the Val d'Agri oilfield (Italy) shown by three-dimensional Vp and Vp/Vs local earthquake tomography. Journal of Geophysical Research: Solid Earth, 122.

Mayor, J., Calvet, M., Margerin, L. & Vanderhaeghe, O., 2016. Crustal structure of the Alps as seen by attenuation tomography, Earth planet. Sci. Lett., 439, 71–80

Patacca, E., & Scandone, P. (2007). Geology of the southern Apennines. Bollettino della Società Geologica Italiana, 7, 75-119.

Picozzi, M., Serlenga, V., Stabile, T.A. (2022). Spatio-temporal evolution of ground motion intensity caused by reservoir-induced seismicity at the Pertusillo artificial lake (southern Italy). Frontiers in Earth Science, 10, 1048196.

Sato H. (1977). Energy propagation including scattering effect: single isotropic scattering approximation. J. Phys. Earth, 25, pp. 27-41.

Stabile, T. A., Giocoli, A., Perrone, A., Piscitelli, S., & Lapenna, V. (2014). Fluid injection induced seismicity reveals a NE dipping fault in the southeastern sector of the High Agri Valley (southern Italy). Geophysical Research Letters, 41(16), 5847-5854.

Zolezzi, F., Morasca, P., Mayeda, K., Phillips, W. S., & Eva, C. (2008). Attenuation tomography of the southern Apennines (Italy). Journal of seismology, 12, 355-365.

Reference author: Salvatore Lucente, salvatore.lucente@uniba.it

MCMTpy waveform inversion package: testing a new method for moment tensor estimation

T. Mancuso[1], C. Totaro[1], B. Orecchio[1]

[1] *Department of Mathematical and Computer Sciences, Physical and Earth Sciences (University of Messina, Italy)*

Earthquake focal mechanism inversion is a seriously non-linear problem. It is well known that an accurate estimation of focal mechanisms is fundamental to obtain good constraints on regional stress field, to assess seismic hazard, and to better understand tectonic processes. The procedures commonly used to compute focal mechanism solutions are based on the polarity of P-wave first motion which may be biased by several factors (e.g., an inadequate coverage of seismic stations). Waveform inversion methods have so far demonstrated to be much more capable to furnish stable and reliable solutions (Presti et al., 2013), however needing a more accurate estimate of the associated errors which tend to be underestimated using linearized techniques (Scolaro et al., 2018). Bayesian inference is increasingly being applied to solve these non-linear problems because it has the advantage of quantifying uncertainties of parameters (Vasyura-Bathke et al., 2020).

In this work we present the application of a new Python package MCMTpy (Yin & Wang, 2022), which exploits the 'Cut-And-Paste' waveform inversion algorithm (CAP, Zhao & Helmberger, 1994; Zhu & Helmberger, 1996) and Bayesian inference, using Markov Chain to implement the source location and focal mechanism inversion in a unique workflow. The new approach can simultaneously invert for magnitude, focal mechanism, source location, source depth and origin time also providing a way to quantify uncertainties by statistical inference.

The main functions included in MCMTpy are source parameters inversion (i) under double-couple assumption with Markov-Chain Monte Carlo (MCMC) method, (ii) under double-couple assumption with a grid-search method and (iii) for the full moment tensor solution with MCMC method.

To test the robustness and limitations of the new package, we applied the MCMTpy to the 2016 M_w 6.0 Amatrice earthquake and to a smaller event (i.e., M_w 3.2) of the same sequence. We performed several tests by varying the starting solution, number of iterations, network geometry, and the type of computation (e.g., MCMC, grid-search method) and we compared our results with moment tensor solutions from other catalogues (e.g., Time Domain Moment Tensor). Test results were analysed in this study in order to evaluate reliability of moment tensor solutions and estimated uncertainties in different inversion settings.

References

Presti D., Billi A., Orecchio B., Totaro C., Faccenna C., Neri G.; 2013: Earthquake focal mechanisms, seismogenic stress, and seismotectonics of the Calabrian Arc, Italy. Tectonophysics, 602, 153–175, doi: 10.1016/j.tecto.2013.01.030.

Scolaro S., Totaro C., Presti D., D'Amico S., Neri G., Orecchio B.; 2018: Estimating Stability and Resolution of Waveform Inversion Focal Mechanisms. In Moment Tensor Solutions. Springer, 93–109, doi: 10.1007/978-3-319-77359-9_5.

Vasyura-Bathke H., Dettmer J., Steinberg A., Heimann S., Isken M. P., Zielke O., Mai P. M., Sudhaus H., Jónsson S.; 2020: The Bayesian earthquake analysis tool. Seismological Research Letters, 91 (2A): 1003–1018, doi: 10.1785/0220190075.

Yin F., Wang B.; 2022: MCMTpy: A Python Package for Source Parameters Inversion Based on Cut-and-Paste Algorithm and Markov Chain Monte Carlo. Seismological Research Letters, 93 (5): 2776–2792, doi: 10.1785/0220210336.

Zhao L. S., Helmberger D.; 1994: Source estimation from broad-band regional seismograms. Bulletin of the Seismological Society of America, 84 (1): 91–104.

Zhu L., Helmberger D.; 1996: Advancement in source estimation technique using broadband regional seismograms. Bulletin of the Seismological Society of America, 86 (5): 1634–1641.

Corresponding author: Thomas Mancuso - thomas.mancuso@studenti.unime.it

The gravitational signature of the dynamics of oceanization in the Gulf of Aden

A. M. Marotta[1], R. Barzaghi[2], A. Bollino[1], A. Regorda[1], R. Sabadini[1]

[1] *Department of Earth Sciences Ardito Desio, Universit`a degli Studi di Milano, Milano, Italy*
[2] *Department of Civil and Environmental Engineering, Politecnico di Milano, Milan, Italy*

We perform a new gravity analysis in the Gulf of Aden with the aim of finding new constraints on the geodynamic evolution of the area. Our analysis is developed within the frame of the recent GO_CONS_GCF_2_TIM_R6 global gravity model solution (Brockmann et al., 2021) that reflects the Earth's static gravity field as observed by GOCE (Gravity field and steady-state Ocean Circulation Explorer). We analyzed the solution at different harmonic degrees, to account for different depths and dimensions of the sources. Terrain correction has been performed by means of a spherical tesseroidal methodology (Marotta and Barzaghi, 2017) and the obtained corrected *Geodetic Residual Gravitation* has been compared to the *Model Residual Gravitation* predicted by means of a 2D visco-plastic finite element thermo-mechanic model that simulates the dynamics of the Gulf of Aden, from rifting to oceanization. In order to perform the comparison between observed and predicted gravitational features, data have been extracted along five profiles crossing the Gulf of Aden at different sectors, from the south-east to the north west. Via the *Model Residual Gravitation* we reproduce its geodetic counterpart, obtaining a characteristic hat-shaped pattern, with a central plateau portraying the highest values, flanked by two regions where the residual gravitation diminishes, finally reaching the lowest values at the far continental domains. The maximum variations of the residual gravitation values, from ridge to continental domain, range between 280 and 420 *mGal* and the steepest decrease occurs over distances of 200 km for the thick crust model and of 100–150 km for the thin crust model. Finally, the comparison between *Geodetic* and *Model Residual Gravitation* allows to further constrain the dynamics of the Gulf of Aden oceanization occurring by a slow passive rift of a hot 150 km thick lithosphere characterized by an initial 40 km thick crust.

References

Brockmann, J.M., Schubert, T., Schuh, W.D., 2021. An improved model of the Earth's static gravity field solely derived from reprocessed GOCE data. Surv. Geophys. 42, 277–316. https://doi.org/10.1007/s10712-020-09626-0.

Marotta, A.M., Barzaghi, R., 2017. A new methodology to compute the gravitational contribution of a spherical tesseroid based on the analytical solution of a sector of a spherical zonal band. J. Geod. 91, 1207–1224. https://doi.org/10.1007/s00190- 017-1018-x. Surname N.; 20xx: Title. Journal.

Corresponding author: anna.maria.marotta@unimi.it

Geofluids as a possible unconventional tool for Seismic Hazard Assessment.

G.Martinelli[1], L.Pierotti[2], G.Facca[2], F.Gherardi[2]

1 INGV, Dept.Palermo, Palermo, Italy

2 CNR-IGG, Pisa, Italy

In recent decades, phenomenological methods known as Recognition of Earthquake-Prone Areas (REPA) were set up for identifying potential sites of powerful earthquakes. The information on potential earthquake sources provided by the REPA method is an essential part of the seismic hazard assessment methodology. For the first time, we combined global-scale information on the geographic occurrence of geofluids with global-scale information on earthquake occurrence, heat flow distribution, and S-wave dispersion, to gain insight into the evolution of local stress-strain fields. We focused on areas characterized by the occurrence of thermal waters and/or by the release of deep-seated gases, as traced by the isotope composition of associated helium. We noticed that the geographical distribution of these geofluids might serve as an indirect indicator of crustal permeability anomalies generated by crustal deformation procedures. This study proposes adding geofluids to the list of fundamental geological parameters to be considered in hazard assessment research.

Corresponding author: giovanni.martinelli15@gmail.com

Joint inversion of gravity and magnetic data of the Cornubian Batholith (South-West UK)

G. Maurizio[1], C. Braitenberg[1]

1. Department of Mathematics, Informatics and Geosciences (MIGe), University of Trieste, Trieste, Italy,

The Inversion of the gravity and magnetic potential fields is a useful method to detect and identify a concealed crustal body. Depending on its physical properties and geometry, the positive or negative anomalies in the gravity and magnetic fields are detectable with appropriate instrumentation. The grav-mag method is a powerful tool in mineral exploration, used in first instance due to the natural 2D coverage of the data acquisition. The combination of magnetic and gravity datasets guarantees reliability to the inversion results and increases the probability that the detected bodies are realistic geological elements, resolving the ambiguity problem of the single field inversion result (Sampietro et al., 2022; Maurizio et al., 2023).

The Cornubian Batholith is a large early Permian granitic body in the south-west peninsula in Great Britain and is the post-collisional result of the Variscan orogeny. It is placed on the peninsula extending in west-southwest direction off-shore and is composed by six main plutons outcropping and cutting the upper Paleozoic coverage (Willis-Richards and Jackson, 1989). The five on-land plutons have been individually studied and it has been observed that each one has a distinctive mineralogy (Simons et al. 2016). The Cornubian Batholith has an important mining history, since from Prehistoric period. The ore fields were imposed in three distinct stages referred to as pre-, syn-, and post-batholith stages, in relation to the emplacement of the Cornubian Batholith (Willis-Richards and Jackson, 1989). Most of the mineralization took part simultaneously with the formation of the batholith, while remaining mineralization occurred with the thermal and tectonic evolution of the region (Willis-Richards and Jackson, 1989). Active mines are still present and are operative. The main activity in the area involves kaolin extraction, but several studies have shown its potential for Tin, Lithium and Tungsten production (Romer and Kroner, 2016; Simons et al., 2017), and for the exploitation of geothermal energy (Beamish and Busby, 2016; Reinecker et al., 2021).

To perform the inversion, we use the jif3d framework (Moorkamp et al., 2011) which is a jupyter collection of scripts for joint inversion of different datasets, in this case gravity and magnetic field measurements. Inversion was performed considering variation of information (Moorkamp, 2022): this means that the algorithm searches a one-to-one relation between the investigated properties. The inversion minimizes the misfit between observed and calculated fields and reduces the variation of information. At the end we obtain a model with density and susceptibility values that fit the observations and show correspondence between the two properties.

We propose the first results about our new model of the Cornubian Batholith, evidencing not only the edges of the body, but also the density and susceptibility distribution along the peninsula. The Cornubian ore field is a perfect area for studying granite-related hydrothermal mineralization, and a better appreciation of the physical properties distribution may allow it to be used as a perfect case study in the analysis of areas with similar geologic history, also considering its future importance regarding the mining industry and the green material transition.

References:

Beamish, D., Busby, J. (2016) The Cornubian geothermal province: heat production and flow in SW England: estimates from boreholes and airborne gamma-ray measurements. Geotherm Energy 4, 4. https://doi.org/10.1186/s40517-016-0046-8

Maurizio, G., Braitenberg, C., Sampietro, D., & Capponi, M. (2023). A new lithospheric density and magnetic susceptibility model of Iran, starting from high-resolution seismic tomography. Journal of Geophysical Research: Solid Earth, 128, e2023JB027383. https://doi.org/10.1029/2023JB027383

Moorkamp, M., Heincke, B., Jegen, M., Roberts, A. W., Hobbs, R. W. (2011). A framework for 3-D joint inversion of MT, gravity and seismic refraction data, Geophysical Journal International, Volume 184, Issue 1, Pages 477–493. https://doi.org/10.1111/j.1365-246X.2010.04856.x

Moorkamp, M. (2022). Deciphering the state of the lower crust and upper mantle with multi-physics inversion. Geophysical Research Letters, 49, e2021GL096336. https://doi.org/10.1029/2021GL096336

Reinecker, J., Gutmanis, J., Foxford, A., Cotton, L., Dalby, C., Law, R. (2021). Geothermal exploration and reservoir modelling of the United Downs deep geothermal project, Cornwall (UK), Geothermics, Volume 97, 102226, ISSN 0375-6505. https://doi.org/10.1016/j.geothermics.2021.102226.

Romer, R. L., Kroner, U. (2016). Phanerozoic tin and tungsten mineralization—Tectonic controls on the distribution of enriched protoliths and heat sources for crustal melting, Gondwana Research, Volume 31, Pages 60-95, ISSN 1342-937X. https://doi.org/10.1016/j.gr.2015.11.002.

Sampietro, D., Capponi, M., & Maurizio, G. (2022). 3D Bayesian inversion of potential fields: The Quebec Oka carbonatite complex case study. Geosciences, 12(10), 382. https://doi.org/10.3390/geosciences12100382

Simons, B., Shail, R. K., Andersen, J. C. Ø. (2016). The petrogenesis of the Early Permian Variscan granites of the Cornubian Batholith: Lower plate post-collisional peraluminous magmatism in the Rhenohercynian Zone of SW England, Lithos, Volume 260, Pages 76-94, ISSN 0024-4937. https://doi.org/10.1016/j.lithos.2016.05.010.

Simons, B., Andersen, J. C. Ø., Shail, R. K., Jenner, F. E. (2017). Fractionation of Li, Be, Ga, Nb, Ta, In, Sn, Sb, W and Bi in the peraluminous Early Permian Variscan granites of the Cornubian Batholith: Precursor processes to magmatic-hydrothermal mineralisation, Lithos, Volumes 278–281, Pages 491-512, ISSN 0024-4937. https://doi.org/10.1016/j.lithos.2017.02.007.

Willis-Richards, J., Jackson, N. J. (1989). Evolution of the Cornubian ore field, Southwest England; Part I, Batholith modeling and ore distribution. Economic Geology; 84 (5): 1078–1100. https://doi.org/10.2113/gsecongeo.84.5.1078

Upper Mantle structure below the Western Alps from P and S receiver functions

S. Monna [(1)], C. Montuori [(1)], F. Frugoni [(1)], C. Piromallo [(1)], L. Vinnik [(2)] and AlpArray Working Group

(1) Istituto Nazionale di Geofisica e Vulcanologia, Rome. Italy
(2) Institute of Physics of the Earth, Moscow. Russia

In spite of numerous active and passive seismological investigations on the Alpine orogen, many of the published observations focus on the Moho or the deeper part of the mantle, while reliable information on the LAB below the Alps is scarce.

We investigated the Moho and Lithosphere-Asthenosphere Boundary (LAB) for a broad region encompassing the Western Alps and including the Ivrea Geophysical Body (IGB), a fragment of mantle emplaced in the lower continental crust. After calculating a set of Receiver Function (RF) measurements from data recorded by the dense, broadband AlpArray Seismic Network, we produced seismic velocity profiles of the crust-uppermost mantle below each of the 50 analyzed stations down to about 250 km depth, through the joint inversion of P and S RFs. Lateral variations of the Moho and LAB topographies across the colliding plates, are constrained together with errors related to our measurements.

We considerably expand the published data of the Moho depth and add a unique set of new measurements of the LAB (Monna et al., 2022) and provide a contribution to the debate on the existence of continuous or interrupted continental subduction below the Western Alps. In fact, we find a comparable thickness (on average 90–100 km) of the Eurasia and Adria lithosphere, which are colliding below the IGB. Summarizing, Eurasia is not presently subducting below Adria with vertical continuity and there is a gap between the superficial (continental) European lithosphere and the deep (oceanic) lithosphere. These observations agree with the discontinuous structure of the Eurasia lithosphere imaged by some seismic tomography models (Fig. 1).

Corresponding authors: stephen.monna@ingv.it, caterina.montuori@ingv.it;

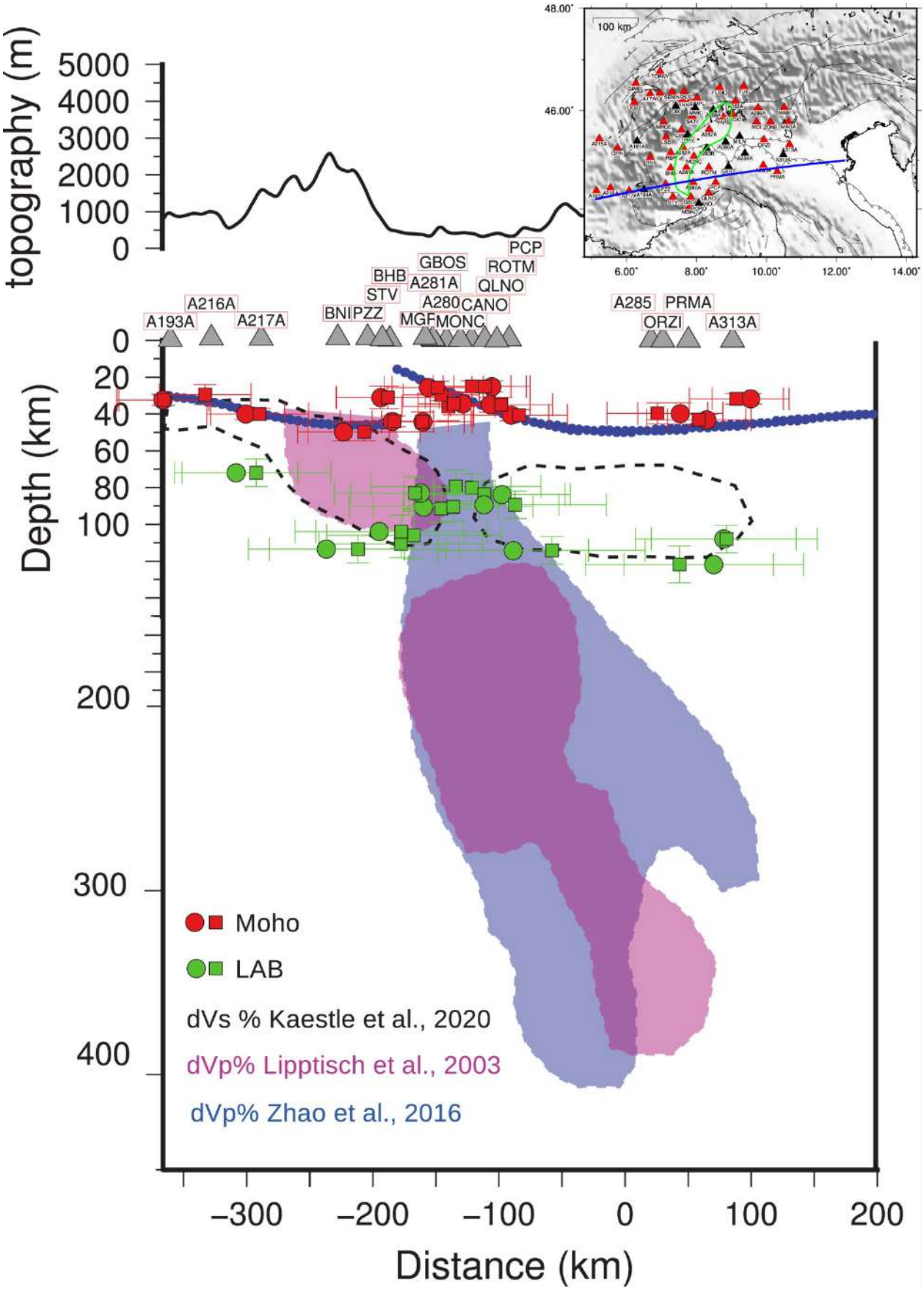

Figure 1- Moho (red symbols) and Lithosphere-Asthenosphere Boundary (LAB) (green symbols) depth for a profile shown in the inset. From Monna et al., 2022.

References

Monna, S., Montuori, C., Frugoni, F., Piromallo, C., Vinnik, L., & AlpArray Working Group (2022). Moho and LAB across the Western Alps (Europe) from P and S receiver function analysis. *Journal of Geophysical Research: Solid Earth*, 127, e2022JB025141. https://doi.org/10.1029/2022JB025141

Upper Mantle structure in the Tyrrhenian and Ionian basins (Central Mediterranean) from P and S receiver functions

C. Montuori [(1)], S. Monna [(1)], F. Frugoni [(1)], C. Piromallo [(1)], M. De Caro [(1)], A. Giuntini [(1)], G. Marinaro [(1)], V. Cormier [(2)] and L. Vinnik [(3)]

(1) Istituto Nazionale di Geofisica e Vulcanologia, Rome. Italy
(2) Dept. of Physics, University of Connecticut. USA
(3) Institute of Physics of the Earth, Moscow. Russia

We investigate the upper mantle discontinuities below the Tyrrhenian and Ionian basins by applying the P and S receiver function techniques to waveforms from broadband stations of the RSN network (Italy), located in Sicily, Ustica Island and Sardinia. These basins, with distinct characteristics in terms of age, origins, and crust-mantle structure, form part of the Central Mediterranean convective system. They are situated in different geological settings—the back-arc for the Tyrrhenian basin and the fore-arc for the Ionian basin—relative to the Calabrian slab. We model the 1D velocity structure below each station down to 250 km depth by joint inversion of P and S receiver functions through the Generalized Simulated Annealing method (Tsallis, 1988; Tsallis & Stariolo, 1996). Land-based observations are complemented with the analysis of data recorded by a broadband seismometer hosted on the NEMO-SN1 permanent observatory at 2100 m b.s.l (Western Ionian Regional Facility of EMSO ERIC, www.emso.eu). We show preliminary results for the Moho and Lithosphere-Asthenosphere-Boundary depth in the Ionian basin and integrate them with observations for the Tyrrhenian basin from our previous work (Monna et al., 2019).

We detect the mantle transition zone (MTZ) discontinuities (the '410' and '660') below the basins based on the receiver functions stacks and speculate on the origin of the observed MTZ thickness variations.

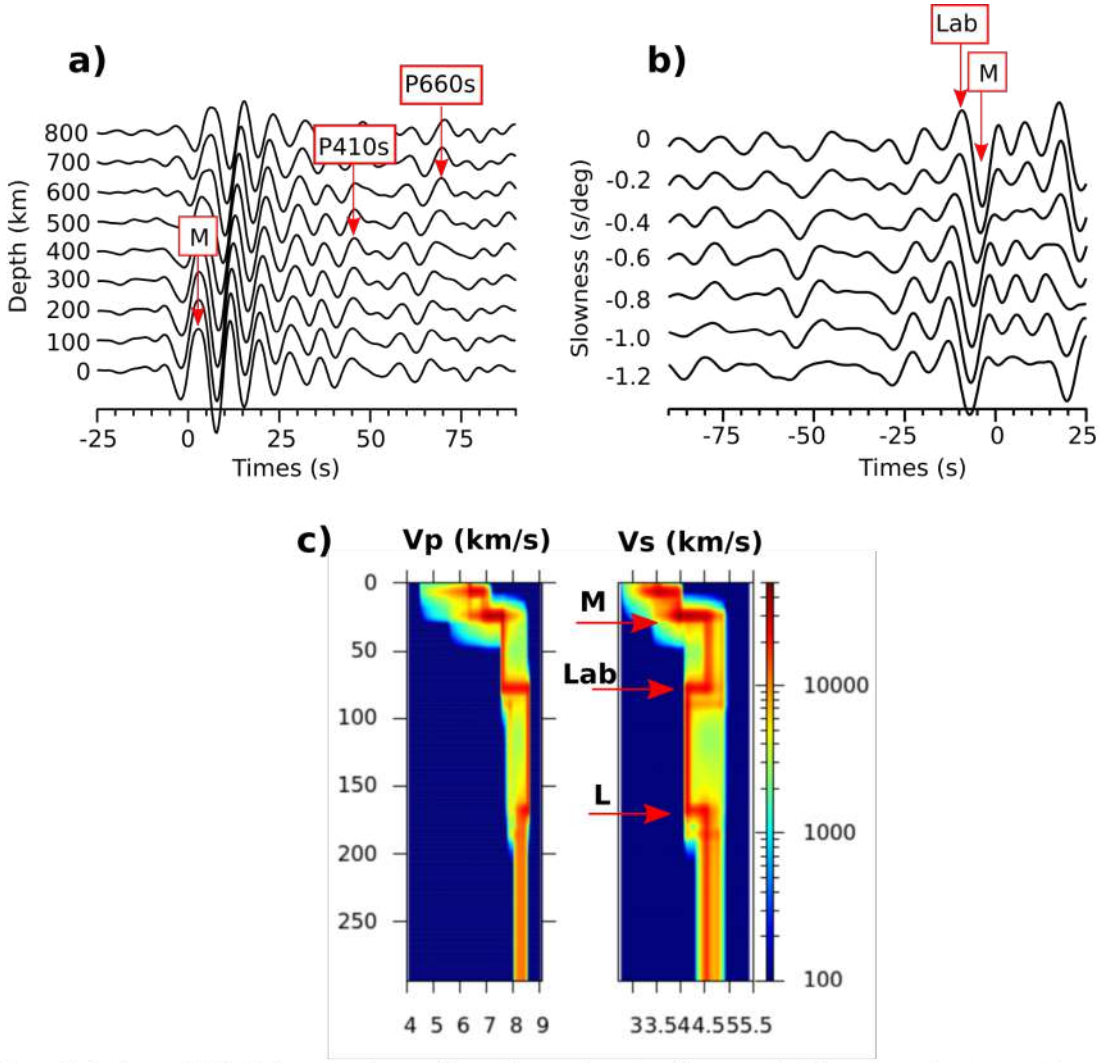

Fig. 1 – P (**a**) and S (**b**) receiver function stacks for a station located on the Hyblean Foreland (Sicily). **a**) Arrows indicate the positive phase converted at the Moho (M), at 410 km (P410s) and at 660 km depth (P660s). **b**) arrows indicate the negative phase converted at the Moho (M). Lab represents the positive candidate phase converted at the Lithosphere asthenosphere boundary. **c**) Vp and Vs velocity model obtained by joint inversion of P and S receiver functions. M: Moho; Lab: Lithosphere asthenosphere boundary; L: bottom of the asthenosphere.

References

Monna, S., Montuori, C., Piromallo, C., & Vinnik, L. (2019). Mantle structure in the central Mediterranean region from P and S receiver functions. Geochemistry, Geophysics, Geosystems, 20(10), 4545-4566. https://doi.org/10.1029/2019GC008496

Tsallis, C. (1988). Possible generalization of Boltzmann-Gibbs statistics. Journal of Statistical Physics, 52(1-2), 479-487. https://doi.org/10.1007/ bf01016429

Tsallis, C., & Stariolo, D. A. (1996). Generalized simulated Annealing. Physica A: Statistical Mechanics and its Applications, 233(1), 395-406. https://doi.org/10.1016/ s0378-4371(96)00271-3

Corresponding authors: caterina.montuori@ingv.it; stephen.monna@ingv.it

First evidence of water transport in the Earth's mantle from seismograms of Southern Tyrrhenian earthquakes

T. Ninivaggi[1], G. Selvaggi[2], S. Mazza[2], M. Filippucci2,[2,3], F. Tursi[4], W. Czuba[5]

[1] Istituto Nazionale di Geofisica e Vulcanologia, Sezione Irpinia, Grottaminarda, Italy
[2] Istituto Nazionale di Geofisica e Vulcanologia, ONT, Roma, Italy
[3] Dipartimento di Scienze della Terra e Geoambientali, Università degli Studi di Bari "Aldo Moro", Bari, Italy
[4] Dipartimento di Scienze della Terra, Università degli Studi di Torino, Torino, Italy
[5] Institute of Geophysics, Polish Academy of Sciences, Warsaw, Poland

Introduction

We have found a previously unreported later seismic phase in seismograms of European seismic stations from intermediate-depth and deep earthquakes of the Southern Tyrrhenian subduction system. We noticed the later phase on seismograms of a deep earthquake occurred in the Southern Tyrrhenian subduction region. The seismic phase, that we called the *x-phase*, appears few seconds after the direct *P*-wave, at stations located some hundreds of km away from the epicentre towards north (Fig. 1).
The interest in studying a later phase, detected after first arrivals, and observed in subduction zones, is motivated by the possibility to obtain indications on the slab properties (geometry, velocity anomalies, and petrology), because of their interaction with the subducting lithosphere. These later phases could be, for example, waves converted at the upper slab interface from the direct waves (e.g., Zhao et al., 1997) exploited to locate the upper boundary of the subducting plate. Later phases are also the depth phases, exploited to constrain hypocentral depths (e.g., Zhao, 2019). High frequency guided waves have been also interpreted as scattered seismic waves by heterogeneity in plate structure and enhanced by the presence of a metastable olivine wedge (Furumura et al., 2016).
As the *x-phase* is very likely linked to the subduction system, this research verifies the nature and the origin of the wave and gets new insights on the slab features.

Data and methods

To verify the robustness of the finding, we made a systematic analysis of the largest intermediate depth and deep earthquakes of the Southern Tyrrhenian subduction system, by selecting the 43 earthquakes occurred from 1990 to 2020 with magnitude ML ≥ 4.5 from the INGV Italian Seismological Instrumental and Parametric Database (http://cnt.rm.ingv.it/iside). The depth range is between 100 km and 644 km. The selected seismic stations are from 10° (central Africa) up to 71° North (Cape North in Norway) in latitude and between 10° (Portugal) West and 50° East (Mar Caspio) in longitude. We extracted and analysed about 25,000 digital waveforms from the

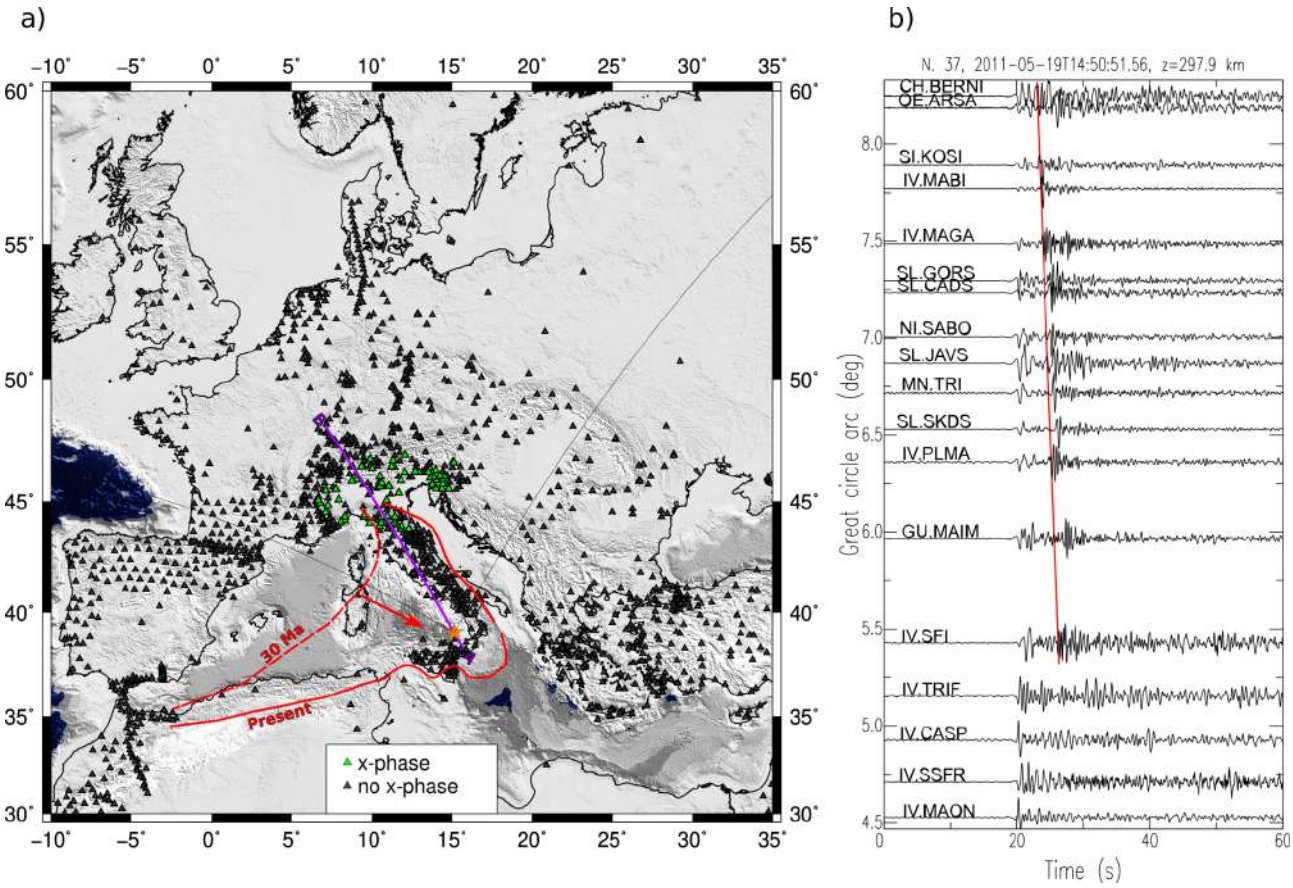

Fig. 1 – Observation of the later seismic phase. a) Stations which recorded the *x-phase* (green triangles). Seismograms of stations in black do not show the later arrival. Section trace AB of the Fig. 3, passing from the 2011 earthquake (n. 37). The red lines delineate the old (30 Ma) and the present subduction signature. The two thin black lines delineate the azimuths -60° and 30° starting from the epicentre. b) Time-distance vertical seismograms of the 2011 event aligned with P arrival time at 20 s. The red line marks the later phase arrivals.

European Integrated Data Archive, 2023 (EIDA, http://eida.ingv.it/) and from Incorporated Research Institutions for Seismology Data Management Centre, 2023 (IRIS DMC, https://service.iris.edu/).

We examined the seismological features of the wave to establish its nature by visual inspection of the waveforms and record sections. Later phases observed in a subduction context have characteristic features that allow to discern between the different type of waves interacting with the subducting lithosphere. We, therefore, compared the *x-phase* with seismic waves observed in subduction systems.

We finally reproduced its travel times and ray paths in a 2D velocity model with Seis83 software (Červený and Pšenčík, 1984) that makes use of ray-tracing technique (Červený et al., 1977). We used IASP91 velocity model (Kennett and Engdahl, 1991) to represent the velocity structure outside the slab. The slab boundaries were constrained by seismicity distribution of the Southern Tyrrhenian Sea, projected in the vertical section with trace AB in Figure 1a. According to tomographic studies (e.g., Amato et al., 1993; Scarfì et al., 2018), the subducting lithosphere is characterised by positive velocity anomalies. We increased the velocity inside the slab in different runs by a percentage between 1.5% and 5% to the IASP91 velocity values.

Results

The *x-phase* is prominent and easy to recognise. It often appears in the vertical and radial component as an impulsive arrival with a higher amplitude and frequency content than the first *P*-arrival. The *x-phase* shows a typical *P*-wave particle motion, and has an incidence angle always greater than the direct P. The travel time differences between the direct P wave and the *x-phase* decrease with increasing distances and with increasing depths of the earthquakes. The later phase has higher apparent velocities than P direct wave (about 11 km/s). These characteristics indicate that the *x-phase* is a compressional *P*-wave which leaves the source, travels downward, and interacts with an interface deeper than the hypocentre, in a less attenuating medium than the direct *P*-wave.

We observe this phase at stations from 6° to 9° from the epicentre, towards north (Fig. 2). Only seismograms of earthquakes located in a well-defined region of the slab, in the depth range of 215–320 km and below the eastern side of the Aeolian Arc, show the later *x-phase* (case 1 in Fig. 2). At greater distances, from 11° onwards, we found another arrival after the direct *P*-wave that is well reproduced by the 410 km discontinuity (P410P in the Fig. 2b, case 1 and 2). It is detected on earthquakes in the depth range of 200-400 km. Earthquakes deeper than 400 km, do not show neither of the two phases (case 3 in Fig. 2b).

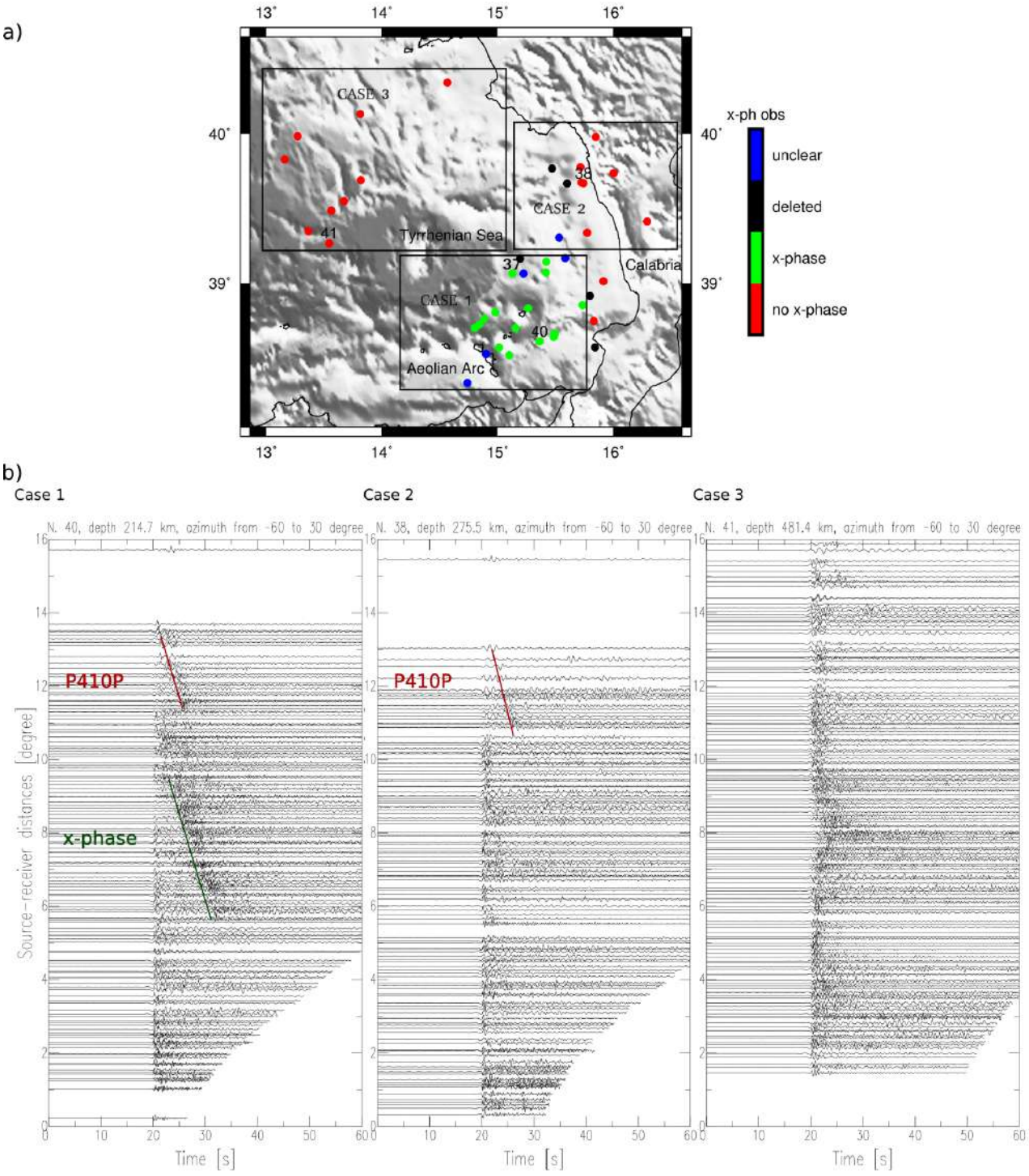

Fig. 2 – a) Map distribution of the earthquakes that show the later seismic phase (green dots), that do not show the *x-phase* (red dots) and those earthquakes where the presence of the *x-phase* is unclear (blue dots). Examples of record sections of the three cases we discuss in the text. The "N." in the title corresponds to number id in the map (N. 40, 38, 41). In the record section, each vertical waveform is normalised by its absolute maximum of amplitude, excluding *S*-waves from the plot and aligned by first arrival P, at 20 s. Waveforms are sorted by epicentral distances, shown on the vertical axis.

Arrival times indicate that the *x-phase* is not a depth phase, which shows an increasing difference of arrival time with the *P*-onset at increasing epicentral distances (Murphy and Barker, 2006). The *x-phase* is not even a *SP*-wave which is analysed by Zhao et al. (1997) for the Japan slab. It has an

apparent velocity almost equal or slightly smaller than the direct *P*-wave and the arrival time difference with the direct *P*-wave is constant. None of the main later phases associated to a subduction system and described in literature seems to be compatible with the seismological features found for the *x-phase*. The *x-phase* is a *P*-wave that propagates downward into the deepest portion of the subducted lithosphere below the Southern Tyrrhenian Sea.
The seismological constraints derived from the observations made in this work, allow us to design a simple 2D modelling by means of fitting the arrival times.
The arrivals of the direct *P*-wave are well fitted by a subducting lithosphere with an average increment of 1.5% of IASP91 velocity model, whereas the *x-phase* requires much faster velocities, at least 3% higher than IASP91 (Fig. 3a). Hence, we introduced a high velocity layer, HVL, in the region where we observe the hypocentre of the earthquakes with the later phase with an average increase of the velocity up to 3% with respect to IASP91. Following Pino and Helmberger (1997), the 410-km discontinuity is raised up to a depth of 370 km, as generally observed in subduction zones (Collier et al., 2001). The model can fit the arrival times of the x-phase for all the deep earthquakes below the Aeolian Island we have modelled (Fig. 3b-c). According to the final model, the *x-phase* is interpreted as a compressional wave that propagates downward in a "High Velocity Layer" (HVL) located in the subducted lithosphere and reflected from a shallower 410 km-discontinuity, located at 370 km of depth.

Discussion and conclusion

The 2D modelling states that a combination of velocity structure and geometric characteristics can reproduce rather well the *x-phase* observations and its travel times.
A 2D approach and a kinematic determination, however, is a first approximation to a more complex three-dimensional problem which need to be accompanied with a dynamic calculation in future research.
A HVL, as the one we have introduced in this work, has not been previously described from a seismological point of view. The tomographic images available for the Tyrrhenian subduction zone do not show such a HVL. However, the thickness of the HVL could be too narrow to be detected by the course grid used to model the mantle at those depths. The fact that we see the later *P*-arrival only in the Southern Tyrrhenian Subduction Zone, is probably due to the peculiar combination of the velocity structure, geometric conditions, and the station distribution in front of the slab.
Compressional velocities in the HVL between 250 and 370 km depth are from 8.9 to 9.15 km/s.
A simple explanation for the high velocity values of the HVL at those depths come from recent laboratory experiments on mineral transformations conducted at upper mantle conditions. The rocks that constitute the subducting lithosphere are locally hydrated with water incorporated into OH-bearing minerals (e.g., Hacker et al., 2003). One of the meta-stable minerals which compose the upper-mantle deep slabs is the dense magnesium hydrated silicate phase A. This mineral is considered the main responsible of the water transport into the deep Earth. Recent ultrasonic measurements of compressional waves on phase A in a cold subduction show an increase of *P*-velocities to the level introduced in the HVL model and at depths greater than 200 km (Cai et al., 2021). These depths are consistent with the range where we model the HVL in the Tyrrhenian subduction. Therefore, we interpret the HVL as related to the presence of the phase A, as inferred from laboratory experiments in cold subduction zones (van Keken et al., 2011; Cai et al., 2021), as the Tyrrhenian subduction seems to be. This is the first direct seismological observation of the phase A in the subduction process.

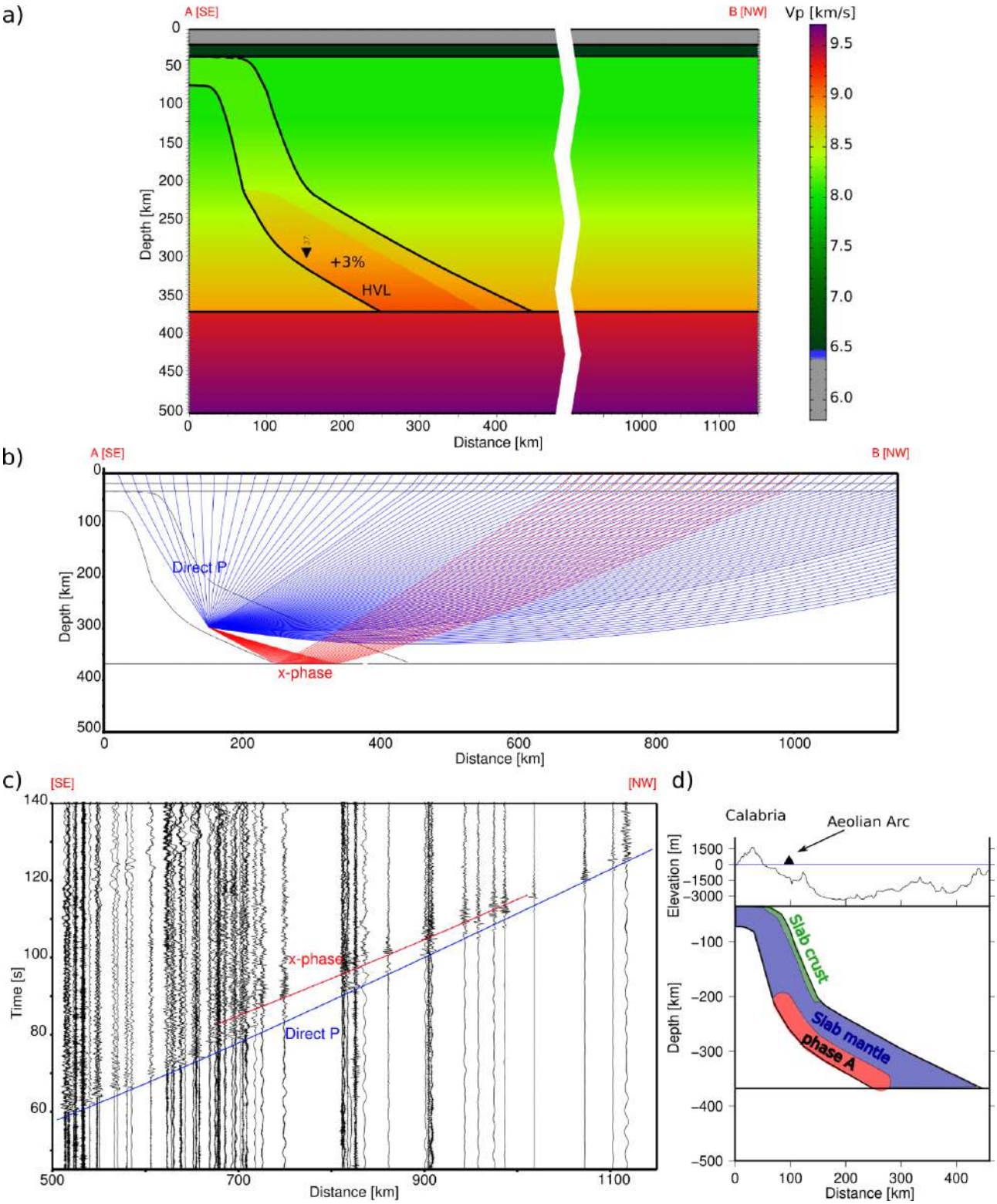

Fig. 3 (a) 2D velocity model, section trace AB in Fig. 1a (n.b. the section orientation is SE-NW to have increasing distances rightwards). The black triangle is the 2011 earthquake (N. 37) with *x-phase*; (b) Calculated ray paths for the earthquake N. 37; (c) calculated travel time curves on the observed record section of earthquake N. 37. The blue line shows the calculated direct P wave arrivals, and the red line is for the *x-phase*; (d) Sketch of the possible petrology and thickness of the HVL.

References

Amato, A., Alessandrini, B., Cimini, G., Frepoli, A., Selvaggi, G.; 1993: Active and remnant subducted slabs beneath Italy: evidence from seismic tomography and seismicity. Ann. Geophys. 36 (2) https://doi.org/10.4401/ag-4272.

Cai, N., Qi, X., Chen, T., Wang, S., Yu, T., Wang, Y., et al.; 2021: Enhanced visibility of subduction slabs by the formation of dense hydrous phase A. Geophys. Res. Lett. 48 (19), 1–10. https://doi.org/10.1029/2021GL095487.

Červený, V., Pšenčík, I.; 1984: SEIS83-Numerical modelling of seismic wave fields in 2-D laterally varying layered structures by the ray method. In: Engdahl, E.R. (Ed.), Documentation of Earthquake Algorithms, Report SE-35. World Data Center A for Solid Earth Geophysics, Boulder, pp. 36–40.

Červený, V., Molotkov, I.A., Pšenčík, I.; 1977: Ray method in seismology. Charles Univ. Press, Praha.

Collier, J.D., Helffrich, G.R., Wood, B.J.; 2001: Seismic discontinuities and subduction zones. Phys. Earth Planet. Inter. 127 (1–4), 35–49. https://doi.org/10.1016/S0031-9201(01)00220-5.

European Integrated Data Archive; 2023: http://eida.ingv.it/ (accessed 31 October 2021).

Furumura, T., Kennett, B.L.N., Padhy, S.; 2016: Enhanced waveguide effect for deep-focus earthquakes in the subducting Pacific slab produced by a metastable olivine wedge. J. Geophys. Res. Solid Earth 121, 6779–6796. https://doi.org/10.1002/2016JB013300.

Hacker, B.R., Abers, G.A., Peacock, S.M.; 2003: Subduction factory 1. Theoretical mineralogy, densities, seismic wave speeds, and H 2 O contents. J. Geophys. Res. Solid Earth 108 (B1), 1–26. https://doi.org/10.1029/2001jb001127.

ISIDe Working Group; 2007: Italian Seismological Instrumental and Parametric Database (ISIDe) [Dataset]. Istituto Nazionale di Geofisica e Vulcanologia (INGV). https://doi.Org/10.13127/ISIDE.

Incorporated Research Institutions for Seismology Data Management Centre; 2023: https://service.iris.edu/ (accessed 31 October 2021).

Kennett, B.L.N., Engdahl, E.R.; 1991: Traveltimes for global earthquake location and phase identification. Geophys. J. Int. 105, 429–465. https://doi.org/10.1111/j.1365-246X.1991.tb06724.x

Murphy, J.R., Barker, B.W.; 2006: Improved focal-depth determination through automated identification of the seismic depth phases pP and sP. Bull. Seismol. Soc. Am. 96 (4A), 1213–1229. https://doi.org/10.1785/0120050259.

Pino, N.A., Helmberger, D.V.; 1997: Upper mantle compressional velocity structure beneath the West Mediterranean Basin. J. Geophys. Res. 102 (B2), 2953–2967. https://doi.org/10.1029/96JB03461.

Scarfì, L., Barberi, G., Barreca, G., Cannavò, F., Koulakov, I., Patanè, D.; 2018: Slab narrowing in the Central Mediterranean: the Calabro-Ionian subduction zone as imaged by high resolution seismic tomography. Sci. Rep. 8 (1), 1–12. https://doi.org/10.1038/s41598.018-23543-8.

van Keken, P.E., Hacker, B.R., Syracuse, E.M., Abers, G.A.; 2011: Subduction factory: 4. Depth-dependent flux of H2O from subducting slabs worldwide. J. Geophys. Res. 116, B01401. https://doi.org/10.1029/2010JB007922.

Zhao, C.A.; 2019: Importance of later phases in seismic tomography. Phys. Earth Planet. Inter. 296, 106314 https://doi.org/10.1016/j.pepi.2019.106314.

Zhao, D., Matsuzawa, T., Hasegawa, A.; 1997: Morphology of the subducting slab boundary in the northeastern Japan arc. Phys. Earth Planet. Inter. 102 (1–2), 89–104. https://doi.org/10.1016/S0031-9201(96)03258-X.

Corresponding author: teresa.ninivaggi@ingv.it

Preliminary single-station template matching seismic catalogue for the area of Everest (Himalaya)

R Percacci[1], A Vuan[2], G Verza[3], M P Plasencia[2], D Sandron[2], F Pettenati[2]

1 Università degli studi di Trieste
2 Istituto di Oceanografia e di Geofisica Sperimentale, OGS, Trieste
3 EvK2cnr, Bergamo

From May 2014 to May 2023, we conducted a seismic monitoring project of the broadband station (IO.EVN), installed at the EvK2 Pyramid Laboratory/Observatory (Pettenati et al. 2014). The IO.EVN station, operated by OGS in the Everest region (Nepal) at an altitude of 5000 m above sea level. We applied the matched-filter method (Gibbons & Ringdal 2006; Vuan et al., 2018) to detect and locate seismic events within a 30 km radius from the station, using a catalogue of ~ 450 templates that we selected by a recursive STA/LTA trigger method based on a bandpass filter from 1 to 30 Hz and the coincidence of three channels. Single-station template matching is evaluated and improved by coupling the mutual information score and the cross-correlation values. We are currently analysing a rich catalogue of more than ~40000 events to distinguish between earthquakes, icequakes and rockfalls, and to identify any noise sources or artifacts related to the station operation or the surrounding environment.

References

Gibbons, S.J., Ringdal, F.; 2006: The detection of low magnitude seismic events using array-based waveform correlation. Geophys. J. Int. **165** (1), 149–166.

Pettenati F., C. Cravos, T. Dawa Sherpa, L. Adhikari Sherpa, M. P. Plasencia Linares, M. Romanelli, G. Verza; 2014: The installation of a new broadband seismometer to the EVK2-CNR Pyramid International Laboratory-Observatory (Everest, Nepal). 33° Convegno Nazionale Gruppo Nazionale di Geofisica della Terra Solida GNGTS. Bologna, 25-27 Novembre. 2014. Abstract.

Vuan A., Sugan M., Amati G., Kato A.; 2018: Improving the Detection of Low-Magnitude Seismicity Preceding the Mw 6.3 L'Aquila Earthquake: Development of a Scalable Code Based on the Cross Correlation of Template Earthquakes. *Bull Seismol Soc Am* 2018; **108** (1), 471–480. doi: https://doi.org/10.1785/0120170106

Space Weather: Central Italy Geoelectric-Field Mapping

G. Pignatiello[1], I. Coco[2], M. De Girolamo[2], F. Giannattasio[2], V. Materni[2], L. Miconi[2], G. Romano[1], V. Romano[2], V. Sapia[2], S. Tripaldi[1], R. Tozzi[2], A. Siniscalchi[1], P. De Michelis[2]

[1] Dipartimento di Scienze della Terra e Geoambientali, Università degli Studi di Bari, "Aldo Moro", Bari, Italy
[2] Istituto Nazionale di Geofisica e Vulcanologia, Roma, Italy

External dynamic processes related to extreme solar activity events can cause temporary disturbances of the Earth's magnetic field.

These geomagnetic disturbances induce geoelectric fields in the subsurface that generate low-frequency geomagnetically induced electric currents (GICs), which, flowing in metallic electrically conductive structures, can cause them to be damaged or malfunction.

Considering the sudden growth of the Sun's magnetic activity, which in the current solar cycle will peak in the year 2024, and the increasing dependence on electrical power and communication systems in our daily lives, many countries around the world are developing national strategies and risk assessment procedures for mitigating the risks associated with Space Weather events (A. Kelbert, 2020).

From the need to better understand the risk associated with the occurrence of GICs, the INGV research project called "MARGE", geoelectromagnetic risk mapping, was born. It aims to develop geoelectric field maps for real-time monitoring of ground effects related to Space Weather events as well as to define a 3D model of electrical resistivity at the regional scale of the middle crust and upper mantle of central Italy, so as to improve knowledge about the physical characteristics of the crust and mantle in the area under investigation.

This model will also be used for more accurate prediction of GICs.

This note will show the results of the analysis of simultaneous variable magnetic field recordings recorded in Central Italy observatories and electromagnetic field with broadband magnetotelluric stations at a distance of a few hundred km with a threefold purpose:

1. to estimate the transfer function for the magnetotelluric site for periods characterized by low Dst;
2. compare the electric field measured at periods with high Dst and compare it with that predicted by the magnetic field of the magnetic observatory in the same periods;
3. compare the transfer function at the site during periods of low Dst with that of high Dst.

References

Kelbert, A. (2020). The role of global/regional Earth conductivity models in natural geomagnetic hazard mitigation. Surveys in Geophysics,41, 115–166.https://doi.org/10.1007/s10712-019-09579-z

Corresponding author: Giulia Pignatiello (giulia.pignatiello@uniba.it)

Moment tensor inversion of the 1947 Squillace Basin earthquake (Southern Italy) using digitized analog seismograms

S. Scolaro[1*], J. Batlló[2], B. Orecchio[1], D. Presti[1], D. Stich[3], C. Totaro[1]

1.Department of Mathematics, Computer Sciences, Physics, and Earth Sciences, University of Messina, Italy
2.Institut Cartogràfic i Geològic de Catalunya, Barcelona, Spain;
3.Instituto Andaluz de Geofísica, Universidad de Granada, Spain

The importance of historical seismic data legacy has amplified within the scientific community due to its potential synergy with modern analysis techniques. Seismograms from the analog recording era cover more than a century of seismic activity, providing significant contributions especially in studying regions affected by major historical seismic events and minor activity in recent decades. We collected and digitized analog seismograms to investigate the 11 May 1947 earthquake that is, according to the CPTI15 catalog (Rovida et al., 2022), the largest seismic event (proxy Mw 5.7) instrumentally recorded in the Squillace Basin, at the Ionian offshore of central Calabria. This sector is a high seismic risk area framed in the complex geodynamic setting leaded by the NW-trending Nubia-Eurasia convergence and the southeastward Ionian slab rollback. Moreover, the presence of the lateral edge of the Ionian slab has been suggested and an intense debate is still open concerning the possible existence and the proper location of a Subduction-Transform Edge Propagator (STEP) fault zone.

Through a time-domain waveform inversion algorithm specifically developed for waveform inversion of analog seismograms (Stich et al., 2005) we computed the first moment tensor solution for the 1947 earthquake. Station bulletins and original seismograms recorded by medium-to-long-period seismographs have been collected, digitized and properly corrected for geometrical distortions. The moment tensor solution obtained for the 1947 earthquake indicates a strike-slip mechanism, focal depth of 28 km and Mw 5.1, that represents the first moment magnitude estimate directly computed from waveform analysis. The result has been accurately checked by performing several inversion tests and interpreted in the frame of the regional seismotectonic scenario (Orecchio et al., 2021 and references therein), where the obtained left-lateral kinematics on about WNW-ESE oriented fault are compatible with a STEP fault activity in the Squillace Basin area.

Our study demonstrates the invaluable and irreplaceable role of information derived from pre-digital seismograms in providing new constraints for local and regional seismotectonic modeling in high seismic risk regions like the Calabrian Arc. Furthermore, the presented analysis is also useful for sharing within the scientific community some methodological challenges linked to the management of historical seismograms.

References

Orecchio B., Scolaro S., Batlló J., Neri G., Presti D., Stich D., and Totaro C., (2021). New Results for the 1968 Belice, South Italy, Seismic Sequence: Solving the Long-Lasting Ambiguity on Causative Source, Seismol. Res. Lett., 92(4), 2364-2381. Doi:10.1785/0220200277

Rovida A., Locati M., Camassi R., Lolli B., Gasperini P., and Antonucci A. (2022). Italian Parametric Earthquake Catalogue (CPTI15), version 4.0. Istituto Nazionale di Geofisica e Vulcanologia (INGV). doi:10.13127/CPTI/CPTI15.4

Stich D., Batlló J., Macià R., Teves-Costa P., and Morales J. (2005). Moment tensor inversion with single-component historical seismograms: The 1909 Benavente (Portugal) and Lambesc (France) earthquakes, Geophys. J. Int., 162(3), 850–858. Doi: 10.1111/j.1365-246X.2005.02680.x

Corresponding author: silscolaro@unime.it

Thermo-poro-elastic modeling of the inflation phase during the 2021 Vulcano Island (Italy) unrest

S. C. Stissi[1], G. Currenti[1], F. Cannavò[1], R. Napoli[1]

[1] Istituto Nazionale di Geofisica e Vulcanologia (Catania, Italy)

Starting from September 2021, Vulcano Island has been affected by an unrest episode, characterised by the increase in gas emission, seismic activity, and edifice inflation (Aiuppa et al., 2022; Federico et al., 2023). The continuous and stable radial expansion of the volcano edifice continuing until mid-October 2021, that affected the GPS stations closer to the summit crater, suggested a deformation source located below La Fossa crater. The temporal evolution of the deformation pattern is indicative of a spatially stationary source. The deformation pattern and the lack of shallow VT seismicity ruled out a possible involvement of shallow magmatic intrusion. Therefore, it is likely that the observed displacements have been generated by the thermo-poro-elastic response of the rocks to the increase of hot fluid flow at shallow depth originating from the degassing of a deeper magma source.

With this in mind, we review and develop (semi-)analytical formulations to calculate the ground deformation induced by homogeneous distributions of pore-pressure and/or temperature changes within thermo-poro-elastic sources with simple geometries, embedded in an elastic, isotropic and homogeneous half-space. We investigate two models: spherical (Davies, 2003; Rinaldi et al., 2011) and cylindrical.

For homogeneous and isotropic distributions of rock elastic parameters and irrotational displacement fields, the deformations related to hydrothermal activity are given by the gradient of a potential that obeys a Poisson equation, establishing a mathematical analogy between displacement and gravitational problems in an infinite space (Wang, 2000). The semi-analytic formulation for the cylindrical source is derived as a function of this analogy starting from the solution to calculate the gravity changes due to homogeneous distributions of the density variations (Hemmings et al., 2016).

After checking the correctness of the developed thermo-poro-elastic displacement formulations through a comparison with the finite-element solutions (COMSOL, 2012), we verify whether the amplitude and extent of the deformation recorded on Vulcano Island from September to mid-October 2021 are consistent with a thermo-poro-elastic response of the rock, applying both models (sphere and cylinder) in the inversion of the GPS daily monitoring data. The inversion results have suggested a deformation source located below La Fossa crater at a depth of approximately 800 m from the ground surface undergoing a volume change of approximately 10^5 m^3(Stissi et al., 2023). The modeling results support the hypothesis that the observed deformation on the Island are induced by the circulation of fluids (Figure 1), fed by the degassing of a deeper magmatic system (Aiuppa et al., 2022; Federico et al., 2023) without necessarily invoking the migration of magma to shallow levels. We assume that a growing magmatic fluid input can explain both the source inflation and the simultaneous increase in gas emission from September to mid-October 2021. In particular, both, the fast deformation rate and the gas discharge, support the hypothesis that the inflation was engendered by the disequilibrium between the magmatic fluids entering the hydrothermal system and the hydrothermal-magmatic fluids released at the surface. Therefore, at the onset of the 2021 unrest, hot magmatic fluids raised from the deeper magmatic system, have reached the hydrothermal system at a shallower depth where they have generated a local overpressure, which produced the symmetric inflation pattern centred in the La Fossa crater. The stop in the increase in deformation starting from mid-October, and the continued gas emission at a level above the background, can be interpreted as a change in the response of the porous medium. Indeed, the interaction between rocks and fluid could have altered the permeability, the increase of which has favoured the fluid release and has hindered a further increase in pore-pressure.

Based on the observations and the obtained results, we can state that, despite the introduced simplifications, the derived thermo-poro-elastic solutions can provide a first-order approximation of ground displacements and source parameters. Therefore, they represent an excellent method for a first interpretation of geodetic data during unrest periods and for a better understanding of the evolution of the hydrothermal systems, contributing to the hazard assessment during volcanic crises.

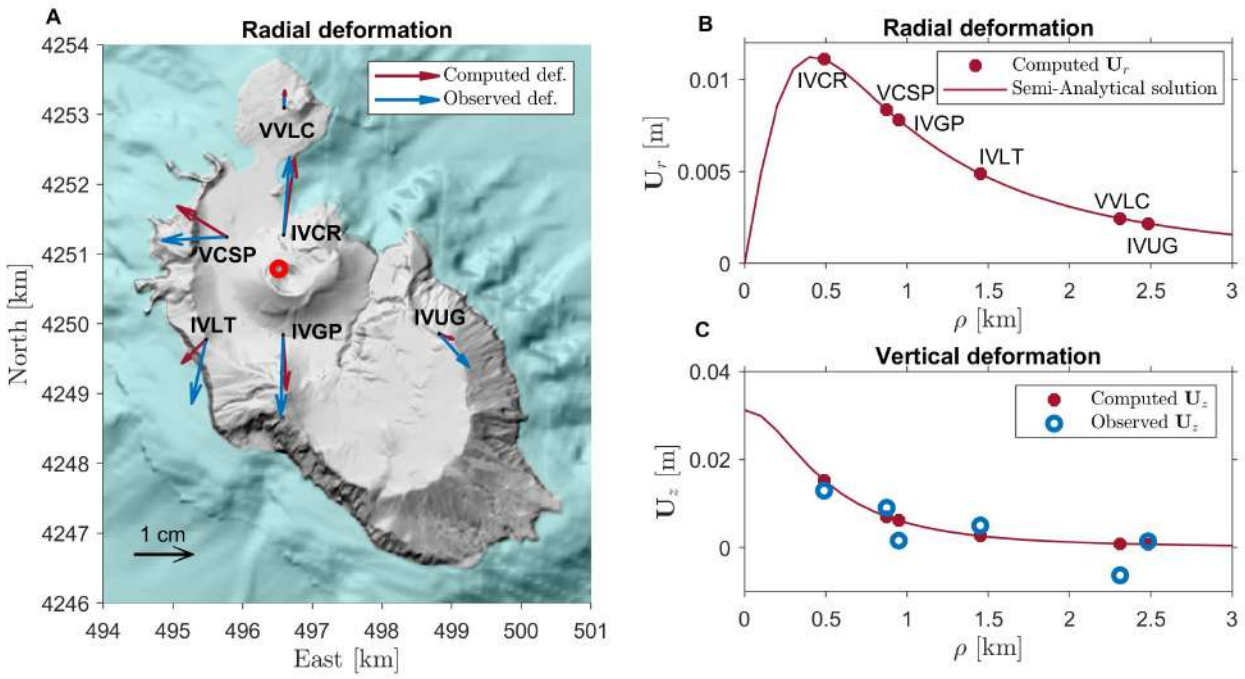

Figure 1: Comparison between observed and optimum computed deformation for the cylindrical source. **(A)** U_x and U_y components of the radial deformation in each monitoring station; the red circle indicates the position of the source. **(B)** Radial deformation U_r as a function of the radial distance ρ of the stations from the deformation source centre. **(C)** Vertical deformation U_z as a function of the radial distance ρ of the stations from the source centre.

References

Davies J. H.; 2003: Elastic field in a semi-infinite solid due to thermal expansion or a coherently misfitting inclusion. J. Appl. Mech. 70 (5), 655–660.

Federico C., Cocina O., Gambino S., Paonita A., Branca S., Coltelli M., Italiano F., Bruno V., Caltabiano T., Camarda M., Capasso G., De Gregorio S., Diliberto I. S., Di Martino R. M. R., Falsaperla S., Greco F., Pecoraino G., Salerno G., Sciotto M., Bellomo S., Di Grazia G., Ferrari F., Gattuso A., La Pica L., Mattia M., Pisciotta A. F., Pruiti L., Sortino F.; 2023: Inferences on the 2021 ongoing volcanic unrest at vulcano island (Italy) through a comprehensive multidisciplinary surveillance network. Remote Sens. 15, 1405.

Hemmings B., Gottsmann J., Whitaker F., Coco A.; 2016: Investigating hydrological contributions to volcano monitoring signals: A time-lapse gravity example. Geophys. J. Int. 207 (1), 259–273.

Rinaldi A. P., Todesco M., Vandemeulebrouck J., Revil A., Bonafede M.; 2011: Electrical conductivity, ground displacement, gravity changes, and gas flow at solfatara crater (Campi Flegrei caldera, Italy): results from numerical modeling. J. Volcanol. Geother. Res. 207 (3-4), 93–105.

Stissi S. C., Napoli R., Currenti G., Afanasyev A., Montegrossi G.; 2021: Influence of permeability on the hydrothermal system at Vulcano Island (Italy): inferences from numerical simulations. Earth, Planets Space 73, 179.

Stissi S. C., Currenti G., Cannavò F., Napoli, R.; 2023: Evidence of poro-elastic inflation at the onset of the 2021 Vulcano Island (Italy) unrest. Front Earth Sci 11:1179095.

Wang H. F.; 2000: Theory of linear poroelasticity with Applications to Geomechanics and hydrogeology. Princeton University Press.

Santina Chiara Stissi: santina.stissi@ingv.it

The Attenuation and Scattering Signature of Fluid Reservoirs and Tectonic Interactions in the Central-Southern Apennines (Italy)

D. Talone*[1,2], L. De Siena[2,3], G. Lavecchia[1,2], R. de Nardis[1,2]

[1]Department of Psychological Sciences, Health and Territory, University of the Studies "G. d'Annunzio", Chieti, Italy

[2]CRUST-Interuniversity Center for 3D Seismotectonics with Territorial Applications, Chieti, Italy

[3]Dipartimento di Fisica e Astronomia (DIFA), Alma Mater Studiorum-Università di Bologna, Bologna, Italy

For decades, seismic tomography techniques have imaged the Italian peninsula (Di Stefano and Ciaccio, 2014; Gualtieri et al., 2014; Scafidi et al., 2009; Zhao et al., 2016). Both large-scale and very local models have been produced, especially for the Northern and the Southern Apennines. Despite its seismotectonic interest, no seismic crustal image of the Central-Southern Apennines transition zone is currently available**,** primarily due to its low rates of seismic activity (Bagh et al., 2007; Frepoli et al., 2017; Romano et al., 2013; Trionfera et al., 2019).

Nowadays, the improvements in seismic detection infrastructures' sensibility and coverage allow the enrichment of seismic databases and the possibility of reliable geophysical imaging in these poor conditions. We applied the MuRAT package (De Siena et al., 2014; De Siena et al., 2014; Reiss et al., 2022) to perform 3D attenuation and scattering tomography, using seismic amplitudes from earthquake recordings to measure and model the total and scattering energy lost by P- and S-waves while propagating through space. The technique has been applied to volcanic contexts and tectonic frameworks showing high sensitivity to fluid-driven processes and strain accumulation (Amoroso et al., 2017; Di Martino et al., 2022; King et al., 2023, 2022; Sketsiou et al., 2021; Tisato and Quintal, 2014). Fracture networks and their potential fluid storage are thus ideal targets for these tomographic studies. By analyzing the peak delay of seismic envelopes and the coda-normalized energy loss, we interpreted the novel 3D models as images of the principal tectonic structures and fluid pathways.

The most relevant feature in the area is a high attenuation and scattering anomalies corresponding to almost the entire Apenninic Chain and related to its East- and West-dipping extensional Quaternary tectonic alignments. The fracture zones associated with the principal faults represent preferential ways for the circulation of CO^2-bearing fluids. A deep, wide, high-attenuation and high-scattering anomaly below the Matese extensional system appears the likely source of fluids feeding springs at its surface, while a smaller anomaly, at about 7 km depths, can be located in the proximity of the L'Aquila 2009 seismogenic area. The two attenuative areas are divided by a low attenuation and scattering volume acting as barriers for fluids and earthquake propagation. This detects a locked seismic zone with low seismic energy release corresponding to the Fucino and Morrone-Porrara fault systems and representing an area of stress accumulation and significant seismic hazard.

Amoroso, O., Russo, G., De Landro, G., Zollo, A., Garambois, S., Mazzoli, S., Parente, M., Virieux, J., 2017. From velocity and attenuation tomography to rock physical modeling: Inferences on fluid-driven earthquake processes at the Irpinia fault system in southern Italy: From Seismic Tomography to Rock Modeling. Geophys. Res. Lett. 44, 6752–6760. https://doi.org/10.1002/2016GL072346

Bagh, S., Chiaraluce, L., De Gori, P., Moretti, M., Govoni, A., Chiarabba, C., Di Bartolomeo, P., Romanelli, M., 2007. Background seismicity in the Central Apennines of Italy: The Abruzzo region case study. Tectonophysics 444, 80–92. https://doi.org/10.1016/j.tecto.2007.08.009

De Siena, L., Thomas, C., Aster, R., 2014. Multi-scale reasonable attenuation tomography analysis (MuRAT): An imaging algorithm designed for volcanic regions. Journal of Volcanology and Geothermal Research 277, 22–35. https://doi.org/10.1016/j.jvolgeores.2014.03.009

De Siena, L., Thomas, C., Waite, G.P., Moran, S.C., Klemme, S., 2014. Attenuation and scattering tomography of the deep plumbing system of Mount St. Helens. J. Geophys. Res. Solid Earth 119, 8223–8238. https://doi.org/10.1002/2014JB011372

Di Martino, M.D.P., De Siena, L., Tisato, N., 2022. Pore Space Topology Controls Ultrasonic Waveforms in Dry Volcanic Rocks. Geophysical Research Letters 49. https://doi.org/10.1029/2022GL100310

Di Stefano, R., Ciaccio, M.G., 2014. The lithosphere and asthenosphere system in Italy as inferred from the Vp and Vs 3D velocity model and Moho map. Journal of Geodynamics 82, 16–25. https://doi.org/10.1016/j.jog.2014.09.006

Frepoli, A., Cimini, G.B., De Gori, P., De Luca, G., Marchetti, A., Monna, S., Montuori, C., Pagliuca, N.M., 2017. Seismic sequences and swarms in the Latium-Abruzzo-Molise Apennines (central Italy): New observations and analysis from a dense monitoring of the recent activity. Tectonophysics 712–713, 312–329. https://doi.org/10.1016/j.tecto.2017.05.026

Gualtieri, L., Serretti, P., Morelli, A., 2014. Finite-difference P wave travel time seismic tomography of the crust and uppermost mantle in the Italian region: P WAVE TOMOGRAPHY OF THE ITALIAN REGION. Geochem. Geophys. Geosyst. 15, 69–88. https://doi.org/10.1002/2013GC004988

King, T., De Siena, L., Benson, P., Vinciguerra, S., 2022. Mapping faults in the laboratory with seismic scattering 1: the laboratory perspective. Geophysical Journal International 232, 1590–1599. https://doi.org/10.1093/gji/ggac409

King, T., De Siena, L., Zhang, Y., Nakata, N., Benson, P., Vinciguerra, S., 2023. Mapping faults in the laboratory with seismic scattering 2: the modelling perspective. Geophysical Journal International 234, 1024–1031. https://doi.org/10.1093/gji/ggad100

Reiss, M.C., De Siena, L., Muirhead, J.D., 2022. The Interconnected Magmatic Plumbing System of the Natron Rift. Geophysical Research Letters 49. https://doi.org/10.1029/2022GL098922

Romano, M.A., de Nardis, R., Garbin, M., Peruzza, L., Priolo, E., Lavecchia, G., Romanelli, M., 2013. Temporary seismic monitoring of the Sulmona area (Abruzzo, Italy): a quality study of microearthquake locations. Nat. Hazards Earth Syst. Sci. 13, 2727–2744. https://doi.org/10.5194/nhess-13-2727-2013

Scafidi, D., Solarino, S., Eva, C., 2009. P wave seismic velocity and Vp/Vs ratio beneath the Italian peninsula from local earthquake tomography. Tectonophysics 465, 1–23. https://doi.org/10.1016/j.tecto.2008.07.013

Sketsiou, P., De Siena, L., Gabrielli, S., Napolitano, F., 2021. 3-D attenuation image of fluid storage and tectonic interactions across the Pollino fault network. Geophysical Journal International 226, 536–547. https://doi.org/10.1093/gji/ggab109

Tisato, N., Quintal, B., 2014. Laboratory measurements of seismic attenuation in sandstone: Strain versus fluid saturation effects. GEOPHYSICS 79, WB9–WB14. https://doi.org/10.1190/geo2013-0419.1

Trionfera, B., Frepoli, A., De Luca, G., De Gori, P., Doglioni, C., 2019. The 2013–2018 Matese and Beneventano Seismic Sequences (Central–Southern Apennines): New Constraints on the Hypocentral Depth Determination. Geosciences 10, 17. https://doi.org/10.3390/geosciences10010017

Zhao, L., Paul, A., Malusà, M.G., Xu, X., Zheng, T., Solarino, S., Guillot, S., Schwartz, S., Dumont, T., Salimbeni, S., Aubert, C., Pondrelli, S., Wang, Q., Zhu, R., 2016. Continuity of the Alpine slab unraveled by high-resolution P wave tomography: Continuity of the Alpine Slab. J. Geophys. Res. Solid Earth 121, 8720–8737. https://doi.org/10.1002/2016JB013310

* **Reference author:** Talone Donato, donato.talone@unich.it

Twenty years of geodetic monitoring in NE-Italy

L. Tunini[1], A. Magrin[1], D. Zuliani[1], G. Rossi[1]

[1]National Institute of Oceanography and Applied Geophysics - OGS - Italy

North-Eastern Italy is part of the diffused tectonic boundary that accommodates the present-day convergence between the Adria microplate and the Eurasia plate. It is a region characterized by low deformation rates and moderate seismicity. It greatly benefits from continuous and high-precision geodetic monitoring, since it has been equipped with a permanent GNSS network providing real-time data and daily observations over two decades. This network, called Friuli Regional Deformation Network FReDNet (https://frednet.crs.ogs.it), has been established by the National Institute of Oceanography and Applied Geophysics - OGS with the aim of monitoring the distribution of crustal deformation and providing supplementary information for the regional earthquake hazard assessment (Zuliani et al., 2018). From the first stations installed in 2002, FReDNet has been continuously growing until counting, nowadays, 22 permanent GNSS stations covering homogeneously the eastern Alps, the alluvial plain, and the coastal areas of NE-Italy. Most of the time series are longer than 15 years.

Data from FReDNet are collected, quality-checked, transformed into RINEX-formatted files, and then released under a Creative Common license (CC BY-SA) along with their metadata, through a public ftp repository (FReDNet DC 2016), accessible at the link https://frednet.crs.ogs.it/DOI/.

We processed daily GNSS data from FReDNet and from other permanent networks, using the GAMIT/GLOBK software package version 10.71 (Herring et al., 2018). Data processing was performed on the HPC cluster GALILEO100 of CINECA, which uses the SLURM system for job scheduling and workload management (Tunini et al., 2023).

Here, we present the processing results focused on the NE-Italy, in terms of time-series and velocity field, and we illustrate the different aspects considered to test the reliability of the adopted processing procedure and of the obtained results, such as considering or avoiding tidal or non-tidal loadings or changing the reference stations, the influence of the type of GNSS monuments, or the location of the geodetic antenna (on a roof or in the free-field).

This research was supported by OGS and CINECA under the HPC-TRES program. In addition, we acknowledge the CINECA award under the ISCRA initiative, for the availability of high-performance computing resources and support (IscraC IsC83_GPSIT-2).

References

FReDNet DC; 2016: Friuli Regional Deformation Network Data Center. Istituto Nazionale di Oceanografia e Geofisica Sperimentale - OGS, Dataset, doi:10.6092/frednet.

Herring, T.A. and King, R., Floyd, M.A. and McClusky, S. C.; 2018: GAMIT Reference Manual: GPS Analysis at MIT, Release 10.7. Department of Earth. Tech. rep., Massachusetts Institute of Technology, Cambridge, Mass. URL: <http://geoweb.mit.edu/gg/Intro_GG.pdf>

Tunini, L., Magrin, A., Rossi, G., and Zuliani, D.; 2023: GNSS time series and velocities about a slow convergent margin processed on HPC clusters: products and robustness evaluation, Earth Syst. Sci. Data Discuss. [preprint], https://doi.org/10.5194/essd-2023-131, in review.

Zuliani, D., Fabris, P., Rossi, G.; 2019: FReDNet: Evolution of permanent GNSS receiver system. In: New Advanced GNSS and 3D Spatial Techniques Applications to Civil and Environmental Engineering, Geophysics, Architecture, Archeology and Cultural Heritage, Lecture Notes in Geoinformation and Cartography; Cefalo, R., Zielinski, J., Barbarella, M., Eds.; Springer: Cham, Switzerland, pp.123–137.

Lavinia Tunini, ltunini@ogs.it

Exploring Mantle Dynamics of the Cascadia Subduction System through Anisotropic Tomography with Transdimensional Inference Methods

Brandon P. VanderBeek[1], Gianmarco Del Piccolo[1], Manuele Faccenda[1]

[1]Dipartimento di Geoscienze, Università degli Studi di Padova, Padova, Italia

The Cascadia subduction system is an ideal location to investigate the nature of mantle flow and associated driving forces at a convergent margin owing to the dense network of on- and off-shore seismic instrumentation. While numerous shear wave splitting and tomography studies have been performed with these data, they have produced conflicting views of mantle dynamics collectively referred to as the Cascadia Paradox. On the overriding plate, splitting observations are consistent with large-scale 3D toroidal flow while off-shore splitting patterns are more easily explained by 2D plate-driven flow. Either geometry is difficult to reconcile with seismic tomographic models that image a fragmented Juan de Fuca slab descending beneath the Western USA. However, these observations offer only an incomplete image of Cascadia mantle structure. Shear wave splitting provides a depth integrated view of anisotropic fabrics making inferences regarding the 3D nature of mantle deformation difficult. Prior high-resolution body wave tomography typically neglects anisotropic effects which can in turn yield significant isotropic imaging artefacts that complicate model interpretation. To overcome these limitations, we invert P-wave delay times for a 3D hexagonally anisotropic model with arbitrarily oriented symmetry axes using the reversible jump Markov chain Monte Carlo algorithm. This stochastic imaging approach is particularly well-suited to the highly non-linear and under-determined nature of the anisotropic seismic tomography problem. The resulting ensemble of solutions allows us to rigorously assess model parameter uncertainties and trade-off between isotropic and anisotropic heterogeneity. We investigate whether the fragmented nature of the subducted Juan de Fuca slab is a well-resolved feature and to what extent its geometry trades off with anisotropic parameters. In light of our new 3D anisotropic model, we re-evaluate the Cascadia Paradox and attempt to reconcile disparate views of Western USA mantle dynamics.

Corresponding author: brandonpaul.vanderbeek@unipd.it

TOPIC 2

DISASTER RISK ANALYSIS AND REDUCTION

Session 2.1

Towards new approaches to estimate earthquake and tsunami hazard: a discussion

GNGTS 2024

DISASTER RISK ANALYSIS AND REDUCTION

Session 2.1

Towards new approaches to estimate earthquake and tsunami hazard: a discussion

Convenors of the session:

Daniela Di Bucci **– daniela.dibucci@protezionecivile.it**
Dario Albarello **– dario.albarello@unisi.it**
Bruno Pace **– bruno.pace@unich.it**

The workshop

Approaches for the evaluation of seismic hazard models in Italy

The session will host a workshop on "Approaches for the evaluation of seismic hazard models in Italy", which takes up and develops a previous event held Anacapri in September 2023 (https://www.reluis.it/it/divulgazione/eventi/266-workshop-approcci-per-la-valutazione-dei-modelli-di-pericolosita-sismica-in-italia.html).

The workshop aims at addressing issues related to the scientific and technical/applicative assessment of the various seismic hazard models that co-exist in various countries around the world (including Italy). They sometimes lead to the development of seismic hazard analyses whose results may differ in a way that is perceived as relevant.

The workshop will include contributions from eight invited speakers, followed by a general discussion.

Discussion on long term PSHA – a workshop

Daniela Di Bucci, Dario Albarello, Bruno Pace

Within the 2024 GNGTS Conference, Session "Towards new approaches to estimate earthquake and tsunami hazard: a discussion", a workshop has been organised, which aims at addressing issues related to the scientific and technical/applicative assessment of the various seismic hazard models that co-exist in various countries around the world, including Italy. They sometimes lead to the development of seismic hazard analyses whose results may differ in a way that is perceived as relevant.

The workshop takes up and develops a previous event held Anacapri in September 2023 (https://www.reluis.it/it/divulgazione/eventi/266-workshop-approcci-per-la-valutazione-dei-modelli-di-pericolosita-sismica-in-italia.html) and includes contributes from eight invited speakers, followed by a general discussion.

The focus is on long-term hazard in the Italian framework, at the national scale, in the Cornell-McGuire context, with a perspective on open problems that have not yet found a solution. This general theme has various possible areas of application in the background.

Italy represents a unicum with respect to the availability of input data, seismological, geological and historical data; are they all used, and at their best, in seismic hazard models? Is there scope for improving models by considering unused or underused input data?

The topic of uncertainties is developed in its different aspects: where do they lie with respect to the input data, where with respect to the modelling, how can they be correctly taken into account?

And, finally, what consequences the differences between the hazard models considered (different models, updating of existing models, etc.) have in the various fields of application is addressed.

In other words, what do we intend to do in this workshop?

- Discuss the topic of assessing seismic hazard models, in relation to both their scientific value and their practical use.
- Discuss the evolution of seismic hazard models over the last decades (including the role/development of uncertainties) and the consequences of this evolution on their use and on risk models.
- Identify proposals, possible solutions or aspects still to be explored

And what we do NOT intend to do in this workshop?

- Discuss specifically one or the other of the models produced, except for the purpose of exemplification within the more general topics
- Discuss the role of scientific commissions that play roles in seismic hazard studies
- Go into the decision-making processes of the actors using seismic hazard models

The applications of seismic hazard assessments in civil society and the impact of its variations

Mauro Dolce

Interuniversity Consortium ReLUIS

Whenever the results of seismic hazard analyses that enter into the decision-making processes of civil society (design, planning, etc.) have variations compared to previous ones, a great impact can be determined from different points of view. For example, due to the typical timing of the construction process of structures and infrastructures, new constructions or retrofitting interventions are designed for hazard values different from those of the models subsequently obtained and therefore, may be considered inadequate or excessively precautionary even before being built. This could imply a redesign and a further lengthening of construction times, or even retrofit immediately after their realisation. On the other hand, variations in hazard for models developed at different times can disorient people who are less experienced in probabilistic analysis of seismic hazard, causing a possible loss of confidence in the hazard assessments themselves.

In order to encourage discussion and exchange of ideas, the proposed speech identifies and describes, without claiming to be exhaustive, the areas of application of seismic hazard assessments and the implications of variations in the officially adopted hazard models. In particular, the following areas will be considered:

- Technical Standards for Construction (design of new buildings, safety assessment and risk classification of individual existing buildings, design of seismic retrofit
- Seismic classification of territories (eligibility of areas for incentives aimed at the reduction of the risk of individual buildings or areas on which to carry out structural and non-structural prevention actions - microzonation/territorial planning)
- Risk assessments at national and sub-national level (distribution of funds for seismic risk reduction, emergency planning)
- Risk communication (risk awareness of citizens and local administrators)
- Legal and judicial aspects (hindsight bias, according to which the varied hazard had to direct prevention interventions even before its official adoption)

The non-negligibility of the impact of hazard variations requires that particular attention be paid to the management of the use, in the various fields, of the scientific models that may be developed, taking into account the current state of knowledge, the considerable uncertainties in the knowledge of the fundamental parameters and the divergences of approach in the scientific community.

Uncertainty in source parameters and seismic hazard estimation

Stefano Parolai

Department of Mathematics, Informatics and Geosciences, University of Trieste, Via E. Weiss 2, 34128 Trieste, Italy

Seismic hazard assessment requires as a key ingredient a definition of earthquake magnitude both when using a probabilistic approach and through scenario calculations.

The estimation of the size of an earthquake event, represented by the magnitude, in fact makes it possible to calculate the level of ground shaking expected at a certain distance from the rupture (or epicenter, or hypocenter, depending on the metric used), and to calibrate the probability of occurrence of events of different magnitudes in a certain time period and in a certain space.

Over the years, thanks in part to the gradual introduction of new instruments, the development of seismic networks and the refinement of techniques for analyzing recorded data, different magnitude scales have gradually been proposed. For the same event, the magnitude estimates obtained may differ, being made on different frequency bands (period), of the recorded seismic signal, thus related to different processes of the seismic source.

Magnitude is also used to estimate, through empirical relationships, seismic energy. Moment magnitude (Mw), introduced to obviate the saturation problem that affected previous magnitudes (e.g., Ms, mb, Ml, Md), is determined using the long period (low frequency) amplitudes of the source Fourier spectra, controlled by the average dislocation on the rupture. However, these spectral periods are little affected by changes in the stress drop that determines the radiated energy in high-frequency seismic waves, which is extremely relevant to seismic action on a wide range of structures.

In this presentation, a brief review of some of the magnitude scales discussed above and their differences with a view to engineering applications will be proposed. The scales generally used for seismic hazard assessment and mainly now based on low-frequency spectral ordinates, scale reasonably well, at least within the Italian territory. In fact, the well-known saturation effects, for example for Magnitude Ms, occur only at values close to those of historically known maximum magnitudes. The reasonable scaling persists even when considering the level of uncertainty in magnitude estimation due to the limited observations and the observed shaking variations caused by propagation in the heterogeneous crust. However, this uncertainty must be taken into account for an appropriate treatment of this parameter. Finally, the effects that, due to the limitation of existing scales in capturing source processes, contribute to 'aleatoric uncertainty in ground shaking models will be illustrated.

The use of historical and geological data in seismic hazard assessment: available data, modeling opportunities, and uncertainties involved

Gianluca Valensise

INGV, Rome, Italy

Italy features what is probably the longest and most accurate earthquake record of the planet, plus one of the few compilations of seismogenic sources available worldwide. Not only these data are available to everyone, as they were collected by government agencies with the financial contribution of Italy's Department for Civil Protection; they are also stored in effective GIS-based databases, which makes it easy to explore them and extract the information needed by seismic hazard assessment (SHA) practitioners. Nevertheless, they are not error-free, and their uncertainties may reverberate on the quality of SHA at all scales.

Italian historical earthquake data are subject to uncertainties that concern the observed intensities and hence the focal parameters derived from them, or the ability to separate individual events within complex earthquake sequences – a common occurrence for over 50% of the country's earthquakes. Although there exist data documenting earthquakes that occurred in the Middle Ages, the record is well populated – i.e., complete – for only a few centuries back, depending on geographic regions and on their recording history; as the characteristic recurrence interval of most Italian quakes is in the order of a millennium, we are likely to have no record of the activity of many prospective seismogenic sources, which makes it hard to achieve the necessary completeness.

In their turn, Italian seismogenic sources are known to be hard to find and investigate; most of them are very deep or blind, some lie offshore. The country's geology is especially deceitful, as older faults are systematically more evident than their active and seismogenic counterparts, and there are very few cases of documented historical surface faulting. Also in this case, achieving completeness is definitely hard.

In addition to the mere identification of a large earthquake of the past, or of a large potential seismogenic fault, the potential inaccuracies of the historical and geological-tectonic records extend to the elaborations derived from them. Examples

include the assumption of a recurrence model, usually the same for all geographic areas and for all magnitude intervals; the subsequent derivation of a magnitude-frequency distribution, that sometimes contrasts with the evidence supplied by the earthquake record itself; the idea that all large active faults are fully coupled, and hence 100% seismogenic. These conditions should be sorted out beforehand by fostering the interaction of all scientists involved, so as to avoid turning the richness and uniqueness of the Italian historical and geological records into a limitation, rather than an advantage.

Historical and geological-tectonic data are inherently independent epistemically, and could hence support any seismicity model despite their respective incompleteness: but so far this circumstance has not been exploited to the fullest possible extent. I will briefly present examples of all these conditions, and illustrate how to get the best possible information from the multiplicity of data we already have, and where to go to find new supporting information.

Corresponding author: gianluca.valensise@ingv.it

Causes and ways for modelling complexity in fault-based seismic hazard studies

Bruno Pace

Dipartimento di Ingegneria e Geologia, Università di Chieti-Pescara, Chieti, Italy

Probabilistic fault-based and time-dependent seismic hazard studies are commonly used to forecast the time between consecutive earthquakes; however, the fault segmentation model and the slip rate variability over time are critical for obtaining accurate results. Complex coseismic ruptures observed in the last ~15 years (e.g., 2010 Mw 7.1 Canterbury NZ, 2012 Mw 8.6 Sumatra, 2016 Mw 7.8 Kaikōura NZ, 2016 Mw 6.5 central Italy, 2023 Mw 7.8 Turkey-Syria) have shown the need to consider different possible combinations of rupture scenarios. Moreover, geological and paleoseismological observations confirm the slip rate variability, but rarely seismic hazard models consider it. A possible explanation is the presence of networks of active faults, which interact in a complex manner. We present the results of some studies we have done on these topics. In terms of fault segmentation relaxation, we compare different methodologies to obtain fault-based seismic hazard estimates using several rupture scenarios combinations. In term of fault interaction, we show the importance considering the time-dependent viscoelastic relaxation of the lower crust and upper mantle as a possible additional source of stress changes at a regional scale to explain the concatenation of moderate-to-strong earthquakes. In addition to the development of realistic fault models (comprising detailed fault traces and geologic data to constrain surface and sub-surface fault geometry) and the collection of field observations (to constrain long-term slip rates), slip rate variability over time appears as another key parameter that needs to be considered in future fault-based seismic hazard models, given that both coseismic and postseismic processes are possible explanations of the observation. Finally, we suggest a way to better organize the fault data for a new generation of fault-based PSHA, with a transparent methodology to account for the best geological information available in a given region for seismic hazard and risk studies. The proposed approach empowers end-users and decision-makers to identify main fault and fault sections that participate the most to the seismic risk of a site.

Site-specific checks of probabilistic seismic hazard models with macroseismic historical records

Roberto Paolucci

Dipartimento di Ingegneria Civile e Ambientale, Politecnico di Milano, Milano, Italy

Abstract: Probabilistic Seismic Hazard Assessment (PSHA) provides estimates of annual probability of exceedance of ground motion amplitude at a site. Validation or falsification of PSHA results from ground motion records suffer of two main limitations: (i) since a sufficiently large amount of data should be collected at that specific site to make statistical analysis meaningful, checks cannot be carried out at the site scale, but by integrating records from a more or less large portion of the territory where the PSHA is carried out and (ii) the time interval is not sufficiently extended to cover those that are of relevance for the PSHA applications. In a nutshell, testing with ground motion records the PSHA result at a specific site (say, the town of Florence) is not presently feasible, unless very short return periods are considered that are of no relevance from the practical viewpoint. A different perspective comes if, instead or in addition to ground motion records, use is made of the macroseismic historical records. If reference is made to the Italian context, likely representing that of several European countries, completeness of the catalogue of locally observed macroseismic effects (including lack of effects)) during past earthquakes at many historical sites in terms of moderate-to-large values of macroseismic intensity may extend back to at least several centuries. While several researchers argue that correlations between ground motion and macroseismic intensity may be relatively poor, so to prevent the use of the latter one for PSHA testing, such lack of correlation occurs also because the ground motion amplitude recorded at a given site may not be in itself representative of that of a wider urban area, as, instead, is the case of the macroseismic intensity. With no ambition to introduce novel advanced approaches, in this contribution we will present criteria and application examples with reference to a consistency check, with macroseismic historical records, of the hazard estimates at several Italian towns from two seismic hazard models.

Some thoughts on the testing phase of seismic hazard models

W. Marzocchi

University of Naples Federico II

The intrinsic scientific nature of any probabilistic seismic hazard analysis (PSHA) – including national seismic hazard model (NSHM) – implies that its credibility has to be based (only) on a rigorous and extensive testing phase. However, this phase presents many challenges of different nature and limitations. Here we discuss in detail and with some real examples some of the most important ones.

The long-term time scale of NSHM (50 years) limits the possibility to *validate* a model, i.e., to check if NSHM describes satisfactorily independent data that were never used to build the model. However, past observations can be used to check the *consistency* of NSHM, i.e., if the model is able to explain the past observations. The difference between validation and consistency is not only semantic, because building and testing a model with the same past data can easily lead to overfitting, which may boost improperly the credibility of a model; conversely, overfitting is ruled out when testing model with independent data (validation). Being the consistency tests much more common, it must be kept in mind that the outcomes of this testing phase may not reflect the real goodness of a model, because of the unavoidable and often unquantifiable overfit.

Owing to the limited number of recorded ground shaking observations, the consistency of NSHM is also checked by analysing partial outcomes of the model, which may have more data available for testing (the number of data is linked to the power of the test). Specifically, a NSHM is a complex model with two major components: an earthquake rupture forecast model (ERFM) and a ground motion model (GMM). Hence, the consistency of NSHM can be also checked analysing its ERFM capability to describe satisfactorily the space-time distribution of the past large earthquakes. It goes without saying that this is a sine qua non condition, i.e., a reliable NSHM model has to be composed by a ERFM that describes satisfactorily the past earthquake occurrences, but the opposite is not true: an ERFM that describes well the past large earthquake occurrences does not necessarily lead to a good NSHM if the GMM is wrong. In essence, testing the consistency of ERFM can rise a red flag on the credibility of a NSHM model, but it cannot guarantee for its reliability.

Too often (and unfortunately), NSHM is still based on declustered earthquake catalogs, mimicking the ground shaking of the so-called mainshocks. However, a physics-based

method to distinguish mainshocks from all other earthquakes is not available (and maybe it does not exist at all), and the ground shaking of earthquakes that have been removed from the declustering technique (e.g., aftershocks) can be very damaging. Nonetheless, as regards the testing phase, to maintain coherency and to avoid the comparison of apples and pears, any consistency test should consider only data associated to the mainshocks selected, e.g., excluding strong ground shaking in some sites that were caused by aftershocks. If we want to consider all earthquakes or ground shaking data in the testing phase, the NSHM has to be corrected for declustering. Different techniques have been already proposed in scientific literature that are used in MPS19 (Meletti et al., 2019) and in the most recent NSHM of the United States (Field et al. 2023) and New Zealand (Gerstenberger et al., 2023).

One of the most remarkable features about NSHM in Italy is the rich database of macroseismic intensities, which are not measured ground shaking data, but they may be used to mimic them. However, such a kind of data may be affected by significant problems that have to be taken into account. Here, we just list some of the most important ones: (i) the large uncertainties in the transition from macroseismic intensity to numerical values of the shaking such as accelerations and speeds, and vice versa; (ii) the uncertainties on the macroseismic intensities of the past are affected by substantial uncertainties due, for example, to the cumulative effect of earthquakes of a seismic sequence and to the type of soil which is not considered in the hazard model (by definition, NSHM refers to a rigid ground); (iii) macroseismic intensity data sometimes depend on the research group estimating them.

Another point worth being mentioned is the fact that a rigorous testing phase must be based on solid statistical techniques. Sometimes, the outcomes of NSHM are analysed using ad hoc techniques whose statistical properties have not been properly investigated, or even based on untenable assumptions. It goes without saying that this attitude cannot lead to any reliable judgement on NSHM.

Last, but not least, almost all consistency tests that have been made so far are based on the mean (or median) hazard model, neglecting de facto the so-called epistemic uncertainty. In other words, two models having the same mean hazard, but a quite different dispersion of the branches of a logic tree (or alternative models) around the central value, are considered the same. It is easy to demonstrate that this attitude leads to asymmetrical conclusions, i.e., if a NSHM passes the test considering only the mean hazard it may be deemed as consistent with the data, but if it does not pass the test, it cannot be considered necessarily inconsistent with the data. In a more formal approach, the proper scientific interpretation of the seismic hazard estimates requires a probabilistic framework that admits epistemic uncertainties on aleatory variables. This is not straightforward because, to subjectivists, all probabilities are epistemic, whereas to frequentists, all probabilities are aleatory. The inadequacy of purely subjectivist and

purely frequentist interpretations of probability is made evident by examining the probabilistic meaning of the mean hazard in these contexts. Here we describe a unified approach (Marzocchi and Jordan, 2017) that may overcome this problem, allowing formal tests of NSHM.

References

Field, E. H., K. R. Milner, A. E. Hatem, P. M. Powers, F. F. Pollitz, A. L. Llenos, Y. Zeng, K. M. Johnson, B. E. Shaw, D. McPhillips, et al. (2023). The USGS 2023 Conterminous U.S. Time-Independent Earthquake Rupture Forecast, Bull. Seismol. Soc. Am., doi: 10.1785/0120230120

Gerstenberger, M. C., S. Bora, B. A. Bradley, C. DiCaprio, A. Kaiser, E. F. Manea, A. Nicol, C. Rollins, M. W. Stirling, K. KS. Thingbaijam, et al. (2023). The 2022 Aotearoa New Zealand National Seismic Hazard Model: Process, Overview, and Results, Bull. Seismol. Soc. Am., doi: 10.1785/0120230182

Marzocchi, W., T.H. Jordan (2017). A unified probabilistic framework for seismic hazard analysis. Bull. Seismol. Soc. Am., 107(6), 2738-2744.

Meletti, C., W. Marzocchi, V. D'Amico, G. Lanzano, L. Luzi, F. Martinelli, B. Pace, A. Rovida, M. Taroni, F. Visini (2021). The new Italian seismic hazard model (MPS19). Ann. Geophys., 64 (1), SE112

Corresponding author: warner.marzocchi@unina.it

How different PSHA is different enough?

I. Iervolino

[1] *Università degli Studi di Napoli Federico II.*

[2] *IUSS – Scuola Universitaria Superiore di Pavia.*

Probabilistic seismic hazard analysis (PSHA) is widely employed worldwide as the rational way to quantify the uncertainty associated to earthquake occurrence and effects. National-scale PSHA has its results typically expressed in the form of maps of ground motion measures intensities that all have the same exceedance return period. Classical PSHA relies on data that continuously increase due to instrumental seismic monitoring, and on models that continuously evolve with the knowledge on each of its many aspects. Therefore, it can happen that different, equally legitimate, hazard maps for the same region can show apparently irreconcilable differences, sparking public debate. This situation is currently ongoing in Italy, where the process of governmental enforcement of a new hazard map is delayed. The discussion is complicated by the fact that the events of interest to hazard assessment are intentionally rare at any of the sites the maps refer to, thus impeding empirical validation at any specific site. The presentation will show the result of two recent studies, which pursue a regional approach, regarding three different authoritative PSHA studies for Italy. The first one entailed formal tests on the output of PSHA against the observed ground shaking exceedance frequencies, obtained from about fifty years of continuous monitoring of seismic activities across the country (Iervolino et al., 2023a). The second compares the areas in which exceedance of PSHA-postulated ground motion intensity threshold is estimated according to ShakeMap for twelve years of instrumental earthquakes, with what expected from the considered PSHA models (Iervolino et al., 2023b). The bulk of analyses reveals that, apparently alternative hazard maps are, in fact, hardly distinguishable in the light of observations and ShakeMap estimations. This perspective, which may be relevant for the current debate, may be strengthened by the fact that recent studies (Baltzopoulos et al., 2023) also show that structural design, for example for reinforced concrete moment-resisting frames, is strictly dominated by seismic actions only in a fraction of the country, owing to the effect of building-code-prescribed minima and design for gravity loads.

References

Baltzopoulos, G., Grella, A., & Iervolino, I; 2023. Some issues in the practical application of risk-targeted ground motions. *Earthquake Engineering & Structural Dynamics*. DOI: 10.1002/eqe.4058

Iervolino, I., Chioccarelli, E., & Cito, P.; 2023a. Testing three seismic hazard models for Italy via multi-site observations. *PLoS one*, *18*(4), e0284909.x.

Iervolino, I., Cito, P., & Vitale A.; 2023b. Territorial exceedance of probabilistic seismic hazard from ShakeMap data. (In review.).

Corresponding author: iunio.iervolino@unina.it

Earthquake sequences and long-term seismic hazard maps: an oximoron?

P. Bazzurro

University School for Superior Studies (IUSS) in Pavia, Pavia, Italy

Seismic hazard maps for regional or national applications have no interest per se. Their importance resides in their critical support to earthquake risk assessment and, if needed, risk mitigation of specific structures or portfolios of structures. The oldest of the many possible applications of seismic hazard maps involves the definition of the ground motion loads to be used for designing new buildings in such a way that they possess the required level of safety or, equivalently, that have sufficiently low chance of becoming unfit for purpose in a given period of time. Another application, and arguably a more challenging one, involves their use at the basis for assessing the risk that existing buildings of different age and structural typology have to become unfit for occupancy or even to be destroyed by earthquakes in a given period of time. For these applications, and others not mentioned above, it is customary to require that these maps provide a long-term stationary view of the seismic hazard. This has been achieved by adopting a mainshock-only view of the earthquake phenomenon, a tenet that underpins essentially every single hazard map developed worldwide. Evidence has shown, however, that in most parts of the world, including Italy, earthquakes occur in sequences and that large damaging earthquakes not preceded or followed by other nearby events closely spaced in time are a rarity rather than the norm. The larger amount of damage that sequences cause when compared to the damage inflicted by the mainshock only has been apparent for a long time and the Central Italy sequence of 2016-17 is only one recent example. Therefore, given that hazard assessment should serve risk calculations and risk estimates are impacted by the occurrence of all damaging earthquakes, regardless of their label, it is clear that future seismic hazard maps should include the contribution of all earthquakes, not just the mainshocks. Several methods have been proposed to include earthquakes “other” than mainshocks in the hazard/risk calculations, some more elegant than others. We will present a method that allows the development of hazard maps that include the occurrence of realistic sequences that (i) are statistically consistent in time and space with those occurred in the region; (ii) include events with magnitude lower than that of the mainshock of the sequence and that may or may not occur along the same rupture of the mainshock. Such a method, if appropriately managed statistically, may yield maps that still reflect a long-term view estimate of the seismic hazard, but heightened if compared to the traditional hazard estimates that accounts only for mainshocks. The underestimation of the traditional seismic hazard due to the consideration of only mainshocks is, of course, more significant in regions where prolific sequences occur more often. From the risk side more refined engineering models that are able to capture damage accumulation in buildings due to multiple shocks are under development. There is no doubt that these maps are the way of the, hopefully, close future

The general session

Outlining the possible scenarios induced by the occurrence of earthquakes and tsunamis in the next future is an essential task of the seismological research. The close connection of these studies with the risk mitigation regulations has stimulated research in this direction but has also conditioned its development. Many studies have remained confined to restricted academic fields and this has progressively dried up part of the scientific debate, even at an international level. We want to stimulate a broader discussion on the topics, also because new and controversial strategies of analysis are appearing in the limelight. The session aims to reopen the debate on these issues of central importance for the research on hazards, also starting from a terminological redefinition of the problem, overcoming the apparent "sclerosis" of the discussion. The final aim is to outline a research path towards new approaches for seismic and tsunami hazards assessments over the next decade, also including a multi-hazard perspective.

In terms of earthquake hazard the following topics are encouraged:

- **Role and uncertainties of short-term seismic hazard models (days/months), both on statistical and deterministic basis, and how to give them a probabilistic form for their integration with medium-term (years) and long-term (tens of years) estimates.**
- **Seismic hazard estimates related to rare events and possible validation models of these estimates.**
- **Role of macroseismic studies and impact of their uncertainties in long-term seismic hazard definition.**
- **Methods of integrating geological and geophysical, surface and subsoil data, for parametric definition of the sources and their uncertainties, within a probabilistic formulation of hazard and event scenarios.**
- **Development of physics-based models of seismic sources and their interaction.**
- **Critical analysis of propagation models to support near-field and long-range ground motion estimates.**
- **Fault displacement hazard analysis, regarding in particular strategic infrastructures, and its possible integration into seismic hazard models.**
- **Systematic integration of local seismic hazard assessments into the regional scale ones.**

In terms of tsunami hazard the following topics are encouraged:

- **Tsunami hazard models for tsunamis generated by earthquakes, also in comparison with international experiences, and the possible integration with a probabilistic approach of other types of data.**

- **Development of event and impact scenarios and their constituent elements.**
- **Advances in knowledge and modelling for tsunami hazard for tsunamis not generated by earthquakes.**

An improved workflow to efficiently compute local seismic probabilistic tsunami analysis (SPTHA): a case study for the harbour of Ravenna, Italy

E. Baglione[1,2], B. Brizuela[2], M. Volpe[2], A. Armigliato[1], F. Zaniboni[1], R. Tonini[2], J. Selva[3]

[1] *Dipartimento di Fisica e Astronomia, Università di Bologna, Italy*
[2] *Istituto Nazionale di Geofisica e Vulcanologia, Italy*
[3] *Università di Napoli Federico II, Napoli, Italy*

Introduction

Tsunamis pose a significant threat to coastal communities worldwide, prompting the development of Probabilistic Tsunami Hazard Analysis (PTHA) to assess the hazard at varying Average Return Periods (ARPs), spanning from hundreds to thousands of years. By integrating data, physical and statistical models, and expert judgments, Probabilistic Tsunami Hazard Assessment (PTHA) provides a structured method for quantifying hazard and associated uncertainties (Grezio et al., 2017; Behrens et al., 2021; Davies et al., 2022). PTHA is increasingly recognized as the established best practice for effectively managing risk assessment and implementing risk mitigation measures (Løvholt et al., 2017; Tonini et al., 2020; Selva et al., 2021).

Offshore PTHA studies excel in characterising hazard across a broad spectrum of earthquake-tsunami sources over extensive spatial scales while quantifying uncertainties stemming from knowledge gaps. However, their primary drawback lies in the limited modelling of tsunami shoaling and inundation, providing restricted insights into local onshore hazard. Recognizing that regional models often lack the resolution to capture specific local characteristics, the development of a local hazard model becomes imperative.

A local model not only offers more accurate and detailed information but also facilitates more effective planning and mitigation strategies. Moreover, a local model proves invaluable for emergency responders and local authorities by enabling prompt and efficient evacuation and response efforts (Rafliana et al., 2022). Taking into account unique local features such as topography and coastal structures, a local model provides insights that may be overlooked in a regional model. This includes identifying vulnerable areas like small harbours or bays, which

might be particularly susceptible to tsunamis but are not easily discernible in broader regional models.

Hence, developing a local hazard model is an essential step in accurately forecasting the potential impact of tsunamis and developing effective mitigation and response strategies. But turning offshore into high-resolution onshore PTHAs, comprehensively capturing inundation hazard and uncertainty, while resolving spatial scales relevant to risk management on the order of 5-10 m, is a challenging task (Lorito et al., 2015; Lynett et al., 2017; Sepúlveda et al., 2019; Volpe et al., 2019; Gibbons et al., 2020; Tonini et al., 2021; Davies et al., 2022).

In this study we introduce an enhanced method for conducting a local Probabilistic Tsunami Hazard Assessment (SPTHA) based on a regional SPTHA without the need of HPC (High Performance Computing) resources (Fig. 1,a).

The method aims to reduce the computational effort required for a local tsunami assessment, updating and simplifying some previous approaches (Lorito et al., 2015, Volpe et al., 2019). The procedure is tested in the region of Catania, Sicily, south of Italy, and applied to the Ravenna harbour, situated in the Northern Adriatic Sea, Italy (Fig. 1,b).

The method

The developed method allows to refine the regional SPTHA by identifying the most significant tsunami sources that impact the local hazard. The resulting procedure simplifies some previous workflows (Lorito et al., 2015, Volpe et al., 2019) for quantifying local SPTHA and represents a useful tool that can be potentially applied wherever there is regional hazard information available, ultimately leading to improved accuracy in the assessment process.

The first and innovative step of our approach involves the application of an “importance” sampling technique that adopts regional hazard disaggregation as weighting information. A source refinement of the scenarios closest to the target is then applied to the new subset, enhancing the characterization of local sources, thereby improving hazard modelling by capturing natural variability (aleatory uncertainty) and reducing epistemic uncertainty. Offshore tsunami simulations are conducted on the retrieved scenarios and the water height profile over a series of points close to the target area; together with the coseismic field information, it represents the feature for a subsequent filtering operation to further reduce the number of high-resolution tsunami simulations required for the local hazard definition.

The workflow of the approach is reported in Fig. 1. and consists of four main steps: source preselection; source refinement; cluster analysis; local hazard quantification.

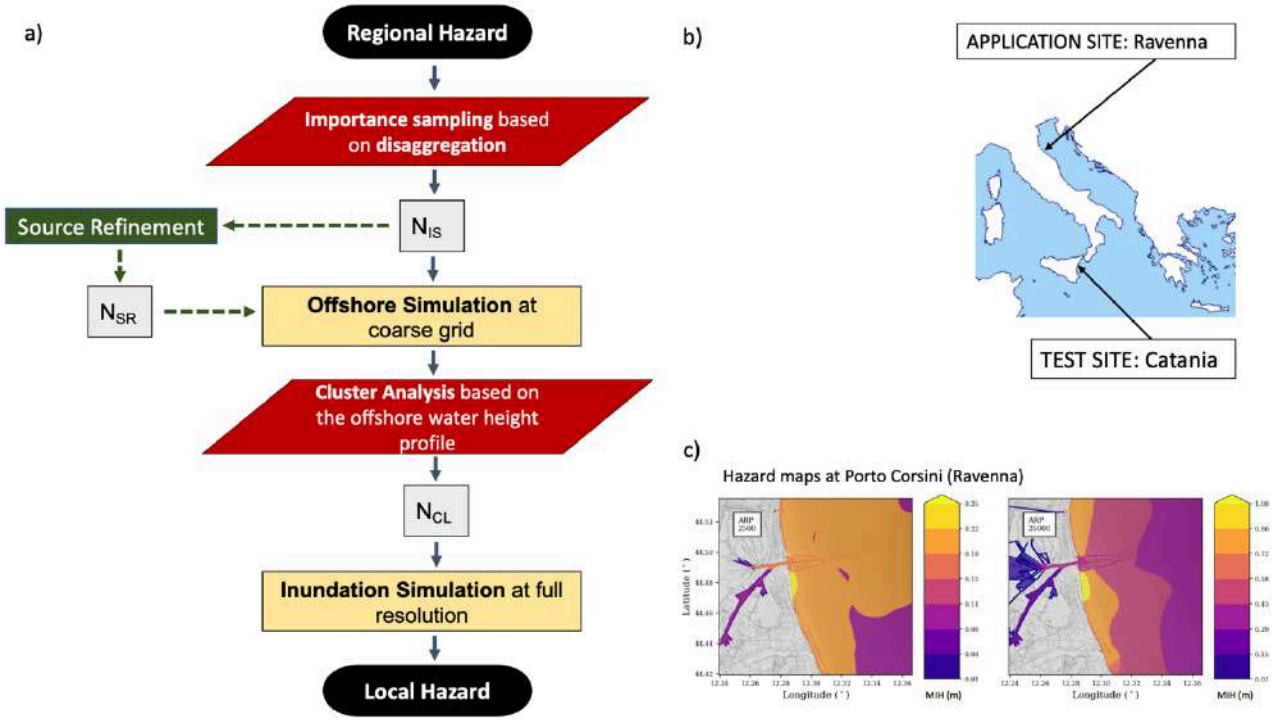

Fig. 1: a) *Schematic diagram of the adopted procedure for evaluating local SPTHA*. b) Spatial representation of Test and Application case sites. c) Hazard maps obtained at the Application site of Ravenna for two different Average Return Periods (ARPs).

Source Preselection

The presence of a Probabilistic Tsunami Hazard Assessment (PTHA) model holds significant importance as it enables the preselection of specific source areas of interest within the region. This capability results in essential time savings during calculations.

At local coastal sites, the offshore PTHA is not able to reproduce the tsunami, as only high-resolution onshore tsunami simulations can guarantee an acceptable level of detail for the description of the local hazard. However, regional PTHA makes a huge effort for homogeneously including all the potential sources of tsunami and for exploring existing aleatory and epistemic uncertainty (Basili et al., 2013, Selva et al., 2016; Davies et al., 2022). This effort allows quantitatively filtering out source areas that do not matter locally, without imposing any subjective qualitative choice.

Source disaggregation offers a quantitative assessment of the potential impact of a particular source area on the local tsunami hazard (Bazzurro and Cornell, 1999; Selva et al., 2016). Specifically, for a designated tsunami intensity threshold, hazard disaggregation provides a measure of the probability that a given source area can produce such an intensity of tsunami.

For a specified target, the regional hazard leads to a nearby point in the regional hazard, with the most representative point for the local target (e.g., the closest point) considered. Disaggregation enables the identification of earthquake scenarios that significantly contribute to the tsunami hazard for the preselected Point of Interest (POI).

The initial operation of our workflow consists of the employment of regional hazard disaggregation as weighting information for an “importance” sampling procedure. This enables sampling in areas of significance, where the likelihood of selecting scenarios that have the most impact on the hazard is higher. By choosing scenarios based on their "importance", this sampling strategy significantly enhances efficiency.

Source Refinement

The combination of importance sampling and hazard disaggregation provides us N_{IS} scenarios that comprehensively capture the total hazard at the most representative point for the target location. Given that the regional hazard is generated with a relatively coarse resolution for both the source and target points, it may be reasonable, at this juncture, to enhance the representation of both the source and target with a more localised perspective (Williamson et al., 2022). This refinement allows for an expanded source discretization, introducing greater variability for the local hazard. If specific local information is accessible, it becomes feasible at this stage to reassign probabilities based on such information, achieving a balanced consideration alongside the regional contribution. This involves perturbing each scenario by sampling alternative values of the source parameters that more accurately characterise it.

Following the refinement of the source, we obtain N_{SR} scenarios (greater than N_{IS}). To maintain the total contribution to the hazard, these new scenarios must undergo reweighting. In the absence of additional information, each new scenario can be assigned to the original scenarios, with equal weight assigned to all scenarios associated with the same original scenario. However, if new local information is accessible (e.g., insights into local fault positions), the weights can vary, with the constraint that they collectively sum to 1 for each original scenario, thus preserving their original balance.

Clustering

The results of offshore simulations serve as input for an additional filtering step before conducting coastal flood simulations on a fine grid. This step involves a cluster analysis of water column height profiles at specific points along a near-shore bathymetric depth, such as at 10 m. These points are strategically distributed in proximity to the site of interest, ensuring an adequate number for the final hazard calculation. It's important to note that without the application of the refinement step, these points might not be adequately resolved from the regional hazard results.

The water height profile, coupled with the vertical coseismic deformation at the corresponding profile location, serves as the proxy variable for the clustering filter (Volpe et al., 2019). For clustering, we employ a standard implementation of K-means clustering (Lloyd, 1982) provided by the Scipy sklearn package (Pedregosa et al., 2011). The selected metric is the Euclidean distance, computed as the square root of the sum of squares of differences in each of the two

proxy variables, and considers both the maximum wave height of the tsunami and the coseismic displacement at each target point. To cluster the N_{SR} original scenarios in proxy-space into N_{CL} clusters, we assign each scenario to the cluster with the closest centroid based on the selected metric.

To assess the convergence of results with an increasing number of clusters, we rely on the Within-Clusters Sum of Squared (WCSS) or inertia provided by the sklearn tool. This enables a quick visualisation of clustering behaviour and facilitates the identification of a suitable minimum number of clusters using the elbow rule. This approach helps determine the minimum clusters necessary for sufficient convergence of results. While larger numbers of clusters may enhance resolution, they come at the expense of increased computational effort.

Following the K-means clustering, a total of N_{CL} clusters are identified. These N_{CL} scenarios serve as a starting point for high-resolution simulations involving flooding at the target site.

For each cluster, we designate a representative scenario as the one whose water height profile deviates the least from the cluster's average. Assuming similar effects on near offshore points, scenarios within the same cluster can be reasonably regarded as inducing comparable inundation. The associated weight for each scenario representative is determined by summing the weights of all scenarios within that cluster. Without refinement, this sum corresponds to the number of scenarios in the cluster. It's worth noting that while K-means clustering is based on water height profiles, scenarios in the same cluster are expected to exhibit a relatively similar profile shape. However, this doesn't guarantee that all scenarios and clusters are equally representative of the final hazard: and that’s why the sum of all within-the-cluster scenarios rates is considered.

Local hazard quantification

High-resolution simulations can be performed for all representative scenarios identified by N_{CL}. The outcomes of these simulations will be utilised to generate hazard curves and maps, offering a representation of our local hazard model. The number of simulations N_{CL} is significantly reduced compared to the number of scenarios making up the initial ensemble: this allows resolution to be carried out even in the absence of a significant computing infrastructure.

The test case

To test the efficiency and validity of the method described, we considered the area of Catania, Sicily, South of Italy. In this test site, numerous numerical simulations have been produced with significant high-performance computing (HPC) resources for recent studies (Gibbons et al., 2020; Tonini et al., 2021). The 32,363 tsunami simulations were conducted through Tsunami-HySEA software over 4 levels of nested grids: one global 0-grid for the open ocean propagation covering the Mediterranean Sea and three local grids (with resolution 160 m, 40 m and 10 m respectively).

Since the available inundation simulations were obtained only for the NEAMTHM18 (Basili et al., 2021) discretization, to not produce further simulation, we skipped the source refinement. The available simulations were sufficient to produce the target point refinement. A set of 8 target points were defined along the 10 m bathymetric line, covering the entire target area (see Fig. 2,a). The results of simulations were retrieved at these new points. The convergence of hazard curves with the N_{IS} was checked also on these points (see Fig. 2,d-g).

Focusing on the results of simulations on these new points, we conducted the cluster analysis for different numbers of clusters N_{CL} (50, 100, 250): Fig. 2,b shows the WCSS applied to the N_{IS} ensemble. For each of these cluster sets we have reproduced the hazard curves (N_{CL}= 250 in Fig. 2,d-g) on the flow depth data on some points of the area of interest and the inundation maps (N_{CL}= 250 in Fig. 3), in order to compare the results obtained with those conducted starting from all the scenarios thanks to the HPC resources. As in Gibbons et al. (2020), no uncertainty is modelled in simulation results and a Heaviside step function is used that is 1 if the intensity computed by NLSW (Non-Linear Shallow Water) simulations for the scenario is greater than the reference MIH (Maximum Inundation Height) value, and 0 otherwise.

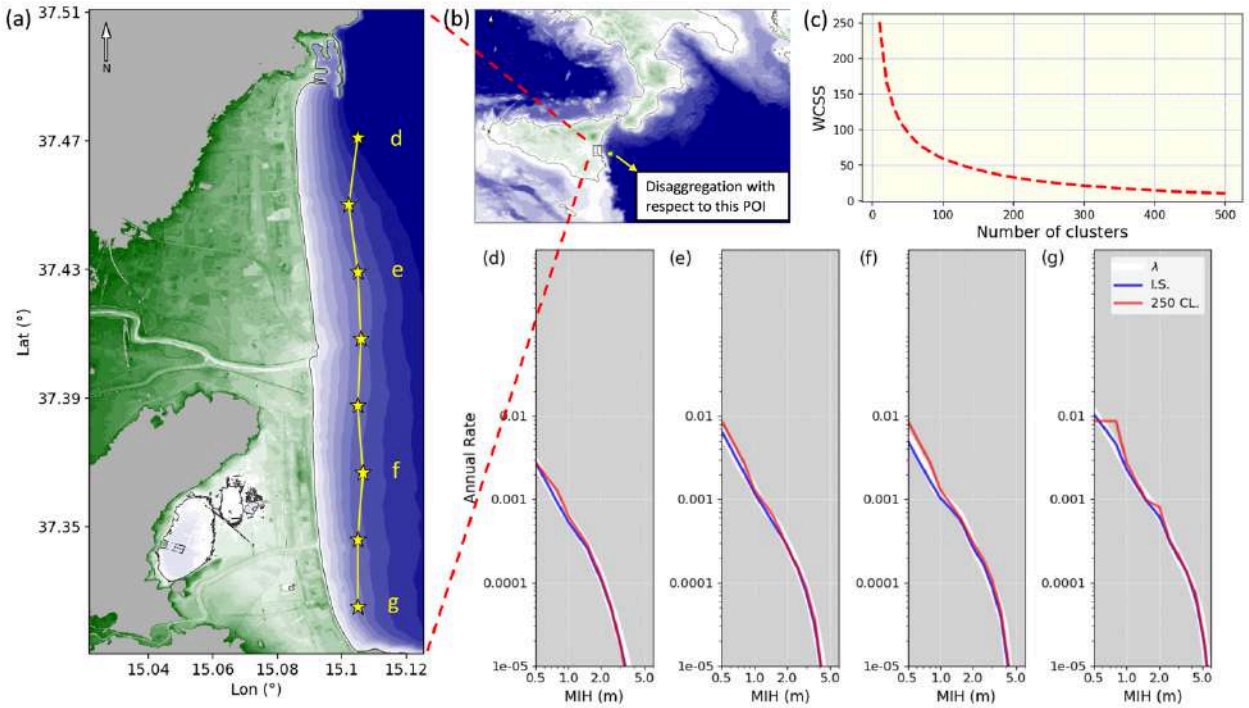

Fig. 2: a) Setup for the cluster analyses in the Catania site. Subplot (a) shows a zoom of the finest grid for the Catania harbour from: in the wider map (b) it is highlighted the location of the target site on the Sicilian Island, with respect to which the disaggregation was conducted. (c) subplot displays the WCSS (Within-Cluster Sum of Squares) behaviour for an increasing number of clusters. (d), (e), (f), (g) subplots are the annual rates evaluated for the total (white curve), importance sampling (blue curve) and cluster (red curve) rates respectively: the plots refer to the same letter locations highlighted in (a) subplot.

Hazard maps (for two different annual return periods) are displayed in Fig. 3: the differences between our results and the HPC ones are very small and nearly negligible for ARP 2500 yrs.

Considering the good results shown in the comparison with the outputs of the HPC implementation, we proceeded to apply the method implemented to the chosen case study.

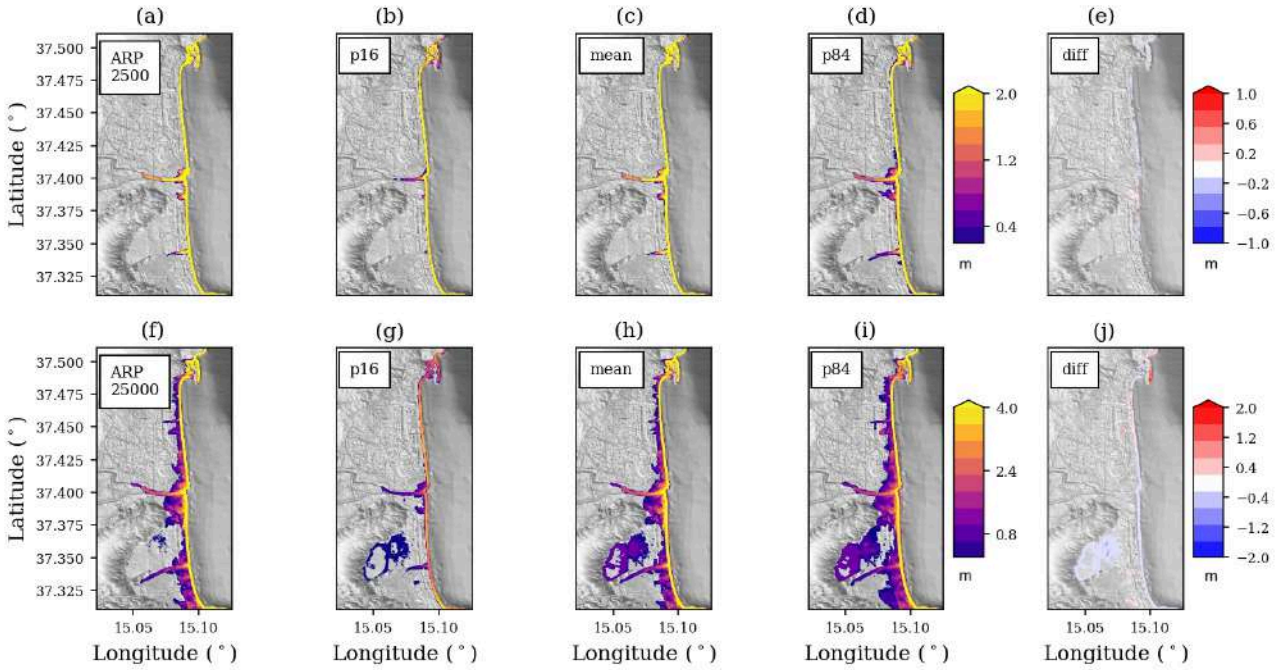

Fig. 3: a) Hazard maps for the flow-depth for different annual return periods. (a) and (d) plots represent our results for the 250 clusters. Plots in (b)-(g), (c)-(h), (d)-(i) represent the 16th percentile, the mean and the 84th percentile of the results obtained with the use of massive HPC. Last two columns (e) and (j) represent the difference between our results in the first columns and the mean values on the (c)-(h) columns.

The application

We applied the method to the North Adriatic region of Ravenna, particularly monitored for the subsidence that characterises the area and its important port. Porto Corsini, along the Adriatic coast, has consistently held a crucial role as a maritime hub (Perini et al., 2017; Armaroli et al., 2019). The port's strategic location has facilitated the efficient transportation of goods, people, and ideas throughout the region and beyond. With its proximity to major international trade routes, Porto Corsini has emerged as a crucial link connecting Italy to the broader global network of maritime commerce.

Studying the tsunami hazard in this area can play a useful perspective to help enabling the identification and implementation of effective mitigation measures to safeguard the port's infrastructure, maritime activities, and the surrounding coastal community from potential catastrophic events, ensuring the uninterrupted functioning of this vital maritime hub.

The bathymetric and topographic grid models for the simulations were built adopting the European Marine Observation and Data Network (EMODnet) project database (EMODnet DTM version released in 2018, http://portal.emodnet-bathymetry.eu/, last access: 23 April 2021), the European Digital Elevation Model (EU-DEM), version 1.1 (eu_dem_v11_E50N10). Superimposed on these grids, for greater detail in the target area, two nautical maps have been digitised. The

computational domain for tsunami propagation consisted of five levels of nested grids with increasing resolution approaching the Ravenna harbour (640, 320, 80, 20 and 5 m, respectively). The tsunami simulations were conducted with the Tsunami-HySEA software. Implemented in CUDA (Compute Unified Device Architecture) and parallelized for running in multi-GPU architectures (de la Asunción et al., 2013), the code solves the non-linear shallow water. It has passed proper benchmarking, in particular the National Tsunami Hazard and Mitigation Program, USA (Macías et al., 2017, 2020b, 2020a).

The method shown in Fig. 1,a diagram has been adopted. In addition to the Catania test case, we applied the source refinement step.

The regional model is again represented by the NEAMTHM18 tsunami hazard model (Selva et al. 2016, Basili et al., 2021). The first massive selection of scenarios involves the application of weighted importance sampling with disaggregation. This operation, carried out with a target near Ravenna, provides a total of about 1500 scenarios of the ensemble composing the regional hazard.

The close sources (within the first 125 km from the target location) are perturbed 10 times around their NEAMTHM18 values. The far sources are not perturbed. This operation widens the number of scenarios (about 4000) and considerably enriches the variability of the source: this can be a welcome operation in the passage from a regional description to a local one.

The obtained scenarios are the input for the first set of tsunami simulations conducted over 4 (6 for the more distant sources) hours of propagation on the first 3 grids of the bathymetrical domain. The water profiles over 7 points of the 80 m resolution grids, taken at an approximated depth of 10 m, are the inputs for the subsequent filtering conducted with a clustering algorithm.

The final set of simulations (on 250 cluster representative scenarios) is run over all the available grids, reaching the higher resolution of 5m in the proximity of the target area, the Ravenna harbour.

The results obtained with the fine grid simulations are used to produce the hazard maps for maximum inundation height (Fig. 1,c). Alongside the hazard results, the behaviour of the waves inside the Porto Corsini canal was studied, in order to retrieve useful information for sites and structures near the canal, taking advantage of the use of detailed bathymetry (5 m resolution).

Conclusion

In this study, we developed a local hazard model based on an existing regional model: this approach significantly reduces the computational workload without sacrificing precision or complexity. The key ingredient to reduce computational load and introduce an innovative strategy is represented by the coupling of the probabilistic insights gained from disaggregation with targeted sampling through importance sampling. This combination allows for an effective selection of scenarios that contribute most to the hazard, without the need for arbitrary and subjective cuts. The resulting ensemble is substantially reduced compared to the initial scenario

count: a refinement procedure is then applied to enhance information from the local source, thereby diminishing associated epistemic uncertainty. This step serves as the foundation for medium-scale simulations, maintaining a balance between comprehensiveness and detailed intricacies.

The offshore profiles of these simulations furnish the input for a subsequent filtering process using a K-means algorithm, which groups scenarios into clusters sharing similar wave shape and amplitude profiles. The representatives of these clusters are then selected for the final phase: conducting high-resolution flood simulations to define hazard curves and maps at the local level.

The method is tested and validated in the port area of Catania, thanks to the comparison with the already available results derived from massive simulations using high-performance computing. The results exhibit a good agreement between the proposed method and the exhaustive use of all scenarios in the ensemble. The new method is further applied to the port of Ravenna, where a high-resolution grid structure has been meticulously established.

References

Armaroli, C., Duo, E., and Viavattene, C. (2019). From Hazard to Consequences: Evaluation of Direct and Indirect Impacts of Flooding Along the Emilia-Romagna Coastline, Italy. *Frontiers in Earth Science* 7. Available at: https://www.frontiersin.org/articles/10.3389/feart.2019.00203 [Accessed June 28, 2023].

Basili, R., Tiberti, M. M., Kastelic, V., Romano, F., Piatanesi, A., Selva, J., et al. (2013). Integrating geologic fault data into tsunami hazard studies. *Natural Hazards and Earth System Sciences* 13, 1025–1050. doi: 10.5194/nhess-13-1025-2013.

Basili, R., Brizuela, B., Herrero, A., Iqbal, S., Lorito, S., Maesano, F. E., et al. (2021). The Making of the NEAM Tsunami Hazard Model 2018 (NEAMTHM18). *Front. Earth Sci.* 8. doi: 10.3389/feart.2020.616594.

Bazzurro, P., & Allin Cornell, C. (1999). Disaggregation of seismic hazard. *Bulletin of the Seismological Society of America*, *89*(2), 501-520.

Behrens, J., Løvholt, F., Jalayer, F., Lorito, S., Salgado-Gálvez, M. A., Sørensen, M., et al. (2021). Probabilistic Tsunami Hazard and Risk Analysis: A Review of Research Gaps. *Frontiers in Earth Science* 9. Available at: https://www.frontiersin.org/articles/10.3389/feart.2021.628772 [Accessed June 28, 2023].

Davies, G., Weber, R., Wilson, K., and Cummins, P. (2022). From offshore to onshore probabilistic tsunami hazard assessment via efficient Monte Carlo sampling. *Geophysical Journal International* 230, 1630–1651. doi: 10.1093/gji/ggac140.

De la Asunción, M., Castro, M. J., Fernández-Nieto, E. D., Mantas, J. M., Acosta, S. O., and González-Vida, J. M. (2013). Efficient GPU implementation of a two waves TVD-WAF method for the two-dimensional one layer shallow water system on structured meshes. *Computers & Fluids* 80, 441–452. doi: 10.1016/j.compfluid.2012.01.012.

Gibbons, S. J., Lorito, S., Macías, J., Løvholt, F., Selva, J., Volpe, M., et al. (2020). Probabilistic Tsunami Hazard Analysis: High Performance Computing for Massive Scale Inundation

Simulations. *Frontiers in Earth Science* 8. Available at: https://www.frontiersin.org/articles/10.3389/feart.2020.591549 [Accessed September 14, 2022].

Grezio, A., Babeyko, A., Baptista, M. A., Behrens, J., Costa, A., Davies, G., et al. (2017). Probabilistic Tsunami Hazard Analysis: Multiple Sources and Global Applications. *Reviews of Geophysics* 55, 1158–1198. doi: 10.1002/2017RG000579.

Lynett, P. J., Gately, K., Wilson, R., Montoya, L., Arcas, D., Aytore, B., et al. (2017). Inter-model analysis of tsunami-induced coastal currents. *Ocean Modelling* 114, 14–32. doi: 10.1016/j.ocemod.2017.04.003.

Lloyd, S. (1982). Least squares quantization in PCM. *IEEE Transactions on Information Theory* 28, 129–137. doi: 10.1109/TIT.1982.1056489.

Lorito, S., Selva, J., Basili, R., Romano, F., Tiberti, M. M., and Piatanesi, A. (2015). Probabilistic hazard for seismically induced tsunamis: accuracy and feasibility of inundation maps. *Geophysical Journal International* 200, 574–588. doi: 10.1093/gji/ggu408.

Løvholt, F., Bondevik, S., Laberg, J. S., Kim, J., and Boylan, N. (2017). Some giant submarine landslides do not produce large tsunamis. *Geophysical Research Letters* 44, 8463–8472. doi: 10.1002/2017GL074062.

Macías, J., Castro, M. J., and Escalante, C. (2020a). Performance assessment of the Tsunami-HySEA model for NTHMP tsunami currents benchmarking. Laboratory data. *Coastal Engineering* 158, 103667. doi: 10.1016/j.coastaleng.2020.103667.

Macías, J., Castro, M. J., Ortega, S., Escalante, C., and González-Vida, J. M. (2017). Performance Benchmarking of Tsunami-HySEA Model for NTHMP's Inundation Mapping Activities. *Pure Appl. Geophys.* 174, 3147–3183. doi: 10.1007/s00024-017-1583-1.

Macías, J., Castro, M. J., Ortega, S., and González-Vida, J. M. (2020b). Performance assessment of Tsunami-HySEA model for NTHMP tsunami currents benchmarking. Field cases. *Ocean Modelling* 152, 101645. doi: 10.1016/j.ocemod.2020.101645.

Pedregosa, F., Varoquaux, G., Gramfort, A., Michel, V., Thirion, B., Grisel, O., et al. (2011). Scikit-learn: Machine Learning in Python. *MACHINE LEARNING IN PYTHON*.

Perini, L., Calabrese, L., Luciani, P., Olivieri, M., Galassi, G., and Spada, G. (2017). Sea-level rise along the Emilia-Romagna coast (Northern Italy) in 2100: scenarios and impacts. *Natural Hazards and Earth System Sciences* 17, 2271–2287. doi: 10.5194/nhess-17-2271-2017.

Rafliana, I., Jalayer, F., Cerase, A., Cugliari, L., Baiguera, M., Salmanidou, D., et al. (2022). Tsunami risk communication and management: Contemporary gaps and challenges. *International Journal of Disaster Risk Reduction* 70, 102771. doi: 10.1016/j.ijdrr.2021.102771.

Selva, J., Tonini, R., Molinari, I., Tiberti, M. M., Romano, F., Grezio, A., et al. (2016). Quantification of source uncertainties in Seismic Probabilistic Tsunami Hazard Analysis (SPTHA). *Geophysical Journal International* 205, 1780–1803. doi: 10.1093/gji/ggw107.

Selva, J., Lorito, S., Volpe, M. *et al.* Probabilistic tsunami forecasting for early warning. *Nat. Commun*. 12, 5677 (2021). https://doi.org/10.1038/s41467-021-25815-w

Selva, J., Amato, A., Armigliato, A., Basili, R., Bernardi, F., Brizuela, B., ... & Zaniboni, F. (2021). Tsunami risk management for crustal earthquakes and non-seismic sources in Italy. *La Rivista del Nuovo Cimento*, *44*(2), 69-144.

Sepúlveda, I., Liu, P. L.-F., and Grigoriu, M. (2019). Probabilistic Tsunami Hazard Assessment in South China Sea With Consideration of Uncertain Earthquake Characteristics. *Journal of Geophysical Research: Solid Earth* 124, 658–688. doi: 10.1029/2018JB016620.

Tonini, R., Di Manna, P., Lorito, S., Selva, J., Volpe, M., Romano, F., et al. (2021). Testing Tsunami Inundation Maps for Evacuation Planning in Italy. *Frontiers in Earth Science* 9. Available at: https://www.frontiersin.org/articles/10.3389/feart.2021.628061 [Accessed June 28, 2023].

Volpe, M., Lorito, S., Selva, J., Tonini, R., Romano, F., and Brizuela, B. (2019). From regional to local SPTHA: efficient computation of probabilistic tsunami inundation maps addressing near-field sources. *Natural Hazards and Earth System Sciences* 19, 455–469. doi: 10.5194/nhess-19-455-2019.

Williamson, A. L., Rim, D., Adams, L. M., LeVeque, R. J., Melgar, D., and González, F. I. (2020). A Source Clustering Approach for Efficient Inundation Modeling and Regional Scale Probabilistic Tsunami Hazard Assessment. *Frontiers in Earth Science* 8. Available at: https://www.frontiersin.org/articles/10.3389/feart.2020.591663 [Accessed June 28, 2023].

Corresponding author: enrico.baglione@ingv.it

Comparison between alarm-based and probability-based earthquake forecasting methods

E. Biondini[1] and P. Gasperini[1,2]

[1] Dipartimento di Fisica e Astronomia, Università di Bologna, Italy
[2]Istituto Nazionale di Geofisica e Vulcanologia, Sezione di Bologna, Italy

In a recent work, we applied the Every Earthquake a Precursor According to Scale (EEPAS) probabilistic model to the pseudo-prospective forecasting of shallow earthquakes with magnitude $M \geq 5.0$ in the Italian region (Biondini et al., 2023). We compared the forecasting performance of EEPAS with that of the epidemic type aftershock sequences (ETAS) forecasting model, using the most recent consistency tests (Bayona et al., 2022) developed within the Collaboratory for the Study of Earthquake Predictability (CSEP). The application of such models for the forecasting of Italian target earthquakes seems to show peculiar characteristics for each of them. In particular, the ETAS model showed higher performance for short-term forecasting, in contrast, the EEPAS model showed higher forecasting performance for the medium/long-term. In this work, we compare the performance of EEPAS and ETAS models with that obtained by a deterministic model based on the occurrence of strong foreshocks (FORE model) using the alarm-based approach as described in Gasperini et al., (2021). We apply the two rate-based models (ETAS and EEPAS) estimating the best probability threshold above which we issue an alarm. The model parameters and probability thresholds for issuing the alarms are calibrated on a learning data set from 1990 to 2011 during which 27 target earthquakes have occurred within the analysis region. The pseudo-prospective forecasting performance is assessed on a validation data set from 2012 to 2021, which also comprises 27 target earthquakes. Tests to assess the forecasting capability demonstrate that, even if all models outperform a purely random method, which trivially forecast earthquakes proportionally to the space-time occupied by alarms, the EEPAS model exhibits lower forecasting performance than ETAS and FORE models. In addition, the relative performance comparison of the three models demonstrates that the forecasting capability of the FORE model appears slightly better than ETAS, but the difference is not statistically significant as it remains within the uncertainty level. However, truly prospective tests are necessary to validate such results, ideally using new testing procedures allowing the analysis of alarm-based models, not yet available within the CSEP.

References

Bayona, J. A., W. H. Savran, D. A. Rhoades, and M. J. Werner, 2022, Prospective evaluation of multiplicative hybrid earthquake forecasting models in California, Geophysical Journal International, 229, no. 3, 1736–1753, doi: 10.1093/gji/ggac018.

Biondini, E., D. A. Rhoades, and P. Gasperini, 2023, Application of the EEPAS earthquake forecasting model to Italy, Geophysical Journal International, ggad123, doi: 10.1093/gji/ggad123.

Gasperini, P., E. Biondini, B. Lolli, A. Petruccelli, and G. Vannucci, 2021, Retrospective short-term forecasting experiment in Italy based on the occurrence of strong (fore) shocks, Geophysical Journal International, 225, no. 2, 1192–1206, doi: 10.1093/gji/ggaa592.

Corresponding author: emanuele.biondini2@gmail.com

Imprints of the Earth's gravity on recent seismic events in Ceneselli, Italy

M. Campion[1], C. Fidani[2,3]

[1] *Gruppo Astrofili Polesani, Rovigo, Italy*
[2] *Istituto Nazionale di Geofisica e Vulcanologia, Roma, Italy*
[3] *Cenrtral Italy Electromagnetic Network, Fermo, Italy*

A laborious mechanical manufacture for the realization of a gravimeter was initiated at the beginning of 2000. The instrument manufacturer, Mario Giorgio Campion, put the gravimeter into operation at his home in via Arturo Toscanini 27 in Rovigo, Italy. The gravimeter is made up of a highly precise pendulum with damped oscillations: an integral accelerometer, which is able to detect oscillation times with precision and continuity (Campion, 2022). It was realized using materials and construction techniques to obtain the maximum rigour in the measurement of the variable (see Figure 1):

- it works under vacuum;
- with thermostatation;
- use rods in quartz and/or invar steel;
- synchronism with the focused laser;
- signals go throungh an optical fiber;
- times measured with a Rubidium clock;
- a computer controls and records data.

With these solutions, the variations of the period with respect to temperature were verified to be of the order of 1.65 μsec/°C. Through approximately 500 daily measurements, the instrument is able to measure local relative gravity continuously, over very narrow time intervals of approximately three minutes. Starting from 2000, the relative gravity recording went on for at least a decade; alternating intervals of stops of the gravimeter. The maintenance periods were useful in order to make necessary improvements to the system, therein reducing errors in the measurements both of random and systematic nature. This period was also useful to better understand the character of the captured data regarding the fundamental quantity of the gravity dependent on the mass of the Earth. Moreover, gravity is influenced by the nature of the subsoil, as well as by the geographical position of the location, and the altitude of the ground.

Fig. 1 – One of the damped pendulums self-built by Mario Campion in his laboratory. Note the vacuum pump connected to the base of the pendulum where the thermostat system is also located. The glass vacuum cylinder surrounds the pendulum made of invar steel. At the lower end of the rod there is a mass and the precision optical reading system of the instrument, this is connected via an optical fiber to the external rubidium clock.

As an element of credibility to validate the ability to record the gravity variations, the gravity trends, reconstructed starting from the measurements of this gravimeter, were compared to the tidal forces. The findings from a comparison carried out between the measurements of the damped pendulum and the tides is reported on the two plots of Fig. 1. Recordings concern the day 10 December 2019, 2 days before the New Moon, which were made simultaneously with two separate gravimeters, operating a few metres from each other with different oscillator periods. The traces in red on the graphs show the coincidence of the two maximums and the two minimums, both with the tide levels in Venice Lido, as well as with each other. Tide levels in Venice Lido were seen to have coincided exactly with the tide forces acting on the same location, most likely due to the complex resonance of the Adriatic Sea. Indeed, the plots do not show tide accelerations, but instead average oscillation times, this is because times are measured by damped oscillator through a focalized laser emitter detected by a Rubidium atomic clock. The period measure is also the motivation for measuring only a relative value of the gravity. In fact, the absolute value requiring the Kater's configuration would need repeated precise measurements of lengths (Lenzen and Multauf, 1964) which inevitably would lengthen measurement repetition times. Standard deviation of hourly averaged periods shown in Fig. 1 are a few units over ten millions. Its correspondent standard deviation on the gravity acceleration can be evaluated by

$$\Delta g/g=\Delta L/L+2\Delta T/T \quad (1)$$

where L (1 m) is the pendulum length and T (1.53 and 1.57 sec) the measured period. Being the pendulum under vacuum with thermostated (0.01 °C) quartz arm, $\Delta L/L < 10^{-8}$, Δg can be

evaluated by (1) in about 0.42 mGal for the gravimeter A on the top of Fig. 1, and in about 0.21 mGal for the

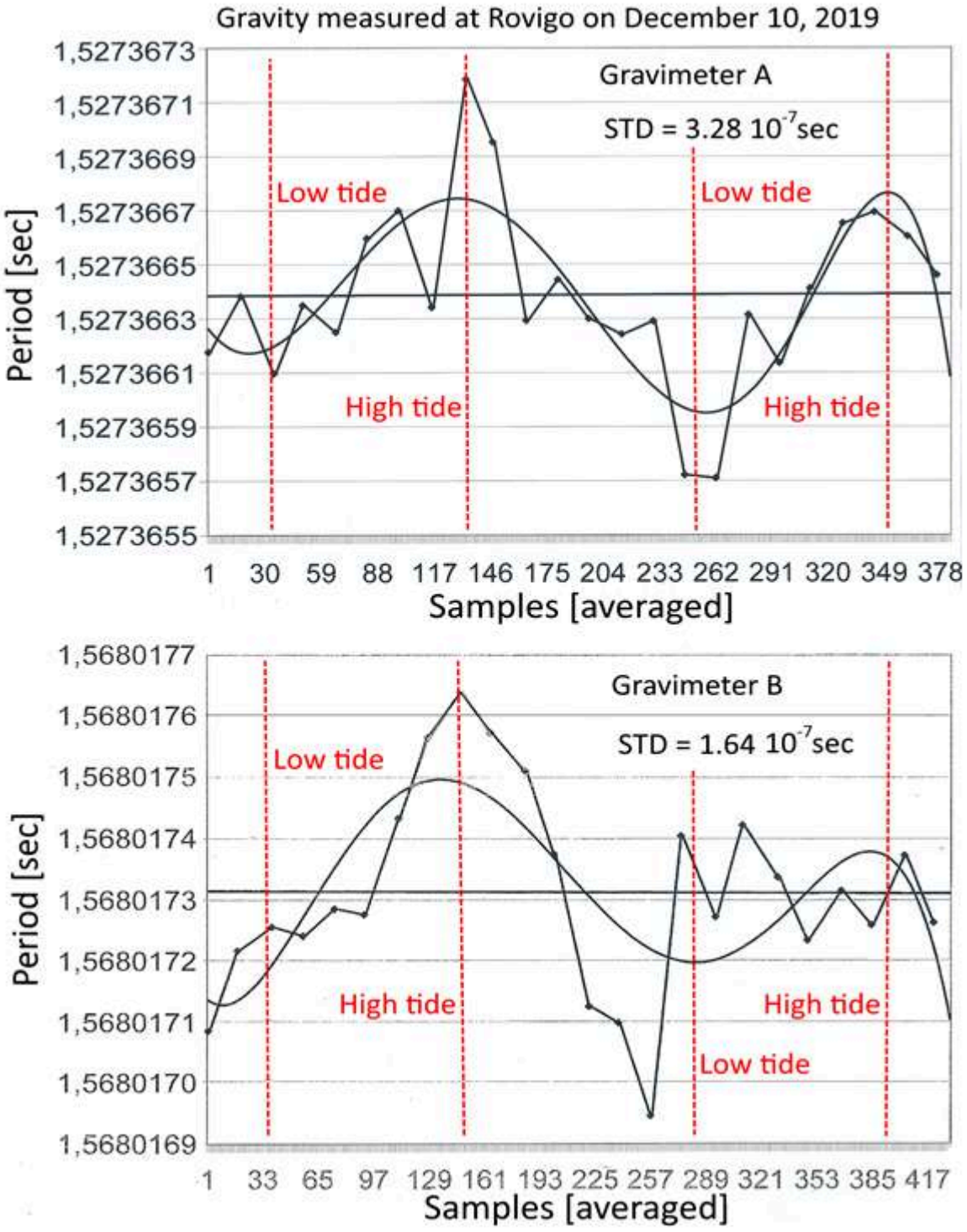

Fig. 2 – Two pendulum period recordings on December 10, 2019, where broken lines represent the union of the averaged points, continuos lines represent polynomial best fits, while red vertical dashed lines indicate tide phases at Venice Lido

gravimeter B on the bottom of Fig. 2. It should be highlighted that these are not the errors of the instruments as such standard deviations contain the tide contributions. The two graphs show on the abscissa the 378 and 417 measurements in the times of execution of the two gravimeters and on the ordinate the 24 values of the hourly averages joined by broken lines. Polynomial fits of the averaged periods are also reported to retrieve maximum and minimum periods corresponding to minimum and maximum gravity values, respectively. These graphs involve simultaneity and repetitiveness in the measurements of tidal forces validated by water levels in Venice on the same day and have surprised leading experts in the field of tidal study and tidal force recording.

Gravity data referred to a geographical point on Earth surface, which is usually a stable value, in turn is integrated with the addition of many very small perturbations. Generally of a transitory nature, small perturbations are observed to be induced by gravitational influences of the other celestial bodies of the solar system with greater mass (Campion, 2022), such as Jupiter and Saturn and/or from greater proximity such as Venus. These terrestrial gravity variations are difficult to determine with current gravimeters in a continuous way as they present variations in the sixth and seventh decimal of the period. Moreover, whenever detected in a sufficiently rigorous manner, gravity variations can provide valuable astronomical information. A further case concerns the ability of the damped pendulum gravimeter to highlight seismic events. It was used to record the gravity of the ground before, during, and after an earthquake highlighting some peculiar variations which were more intense during strong quakes (Campion, 2022).

Polesine had always been considered an area with low seismic risk, but the strong earthquake in Modena, Italy in 2012, which affected the upper part on the border with Emilia and Lombardy, suggested that this was not the case. The signal reported in Fig. 3 top coincided with the seismic shock of 17 July 2011 in Ceneselli, 33 km away from Rovigo, towards Lombardy, having a magnitude ML = 4.5 without causing any particular damage. The double recording of the event in Rovigo, with both the seismograph and the gravimeter, provided the possibility to observe the event in depth by integrating the information obtained with the two measurement systems. The two graphs were drawn vertically on the same Fig. 3 top, the seismogram upward and the gravity diagram downward, making the times of the two signals coincide, so as to carry out a comparison. The recording made by the seismograph produced the main wave detected by the gravimeter, while the second part of the same recording was attributable to the return to equilibrium of the ground. The first part of the gravimeter recording from 19:41:57 to 20:27:35, for a total of 45 minutes, shows three regular oscillations of the ground which were followed by a flat trend in gravity. The gravity flattening that preceded the seismic event could be interpreted as a sign of soil stretching and the critical phase before the shock. The shock itself, which seismic recording showed to last approximately 7 minutes, corresponds to a direct wave of the ground lasting 5 minutes and a reverse wave lasting 2 minutes, as measured by the gravimeter. Direct and reverse waves are due to the integration of seismic oscillations with the damped pendulum oscillations, these waves seem to indicate a first phase of gravity reduction followed by a rebound phase of gravity increases. A series of larger fluctuations followed the end of the event.

An earthquake of magnitude ML = 4.2 struck the area 1 km E in Ceneselli, on October 28, 2023, at 17:29:23 Italian time with geographical coordinates 45.015N, 11.388E at a depth of 8 km. The area affected by this earthquake was characterised by medium seismic danger and by strong earthquakes that had occurred in the past (INGV, 2015). The epicentre appears to fall in an area with few known earthquakes: the 2011 event discussed above, the sequence in the Po Valley in May-June 2012, and another event of magnitude ML = 4.2 occurred on October 25, 2023. The

measured period is reported in Fig. 3 bottom, it appeared to grow persistently for about half an hour before this minor event, which corresponded to a gravity decrease.

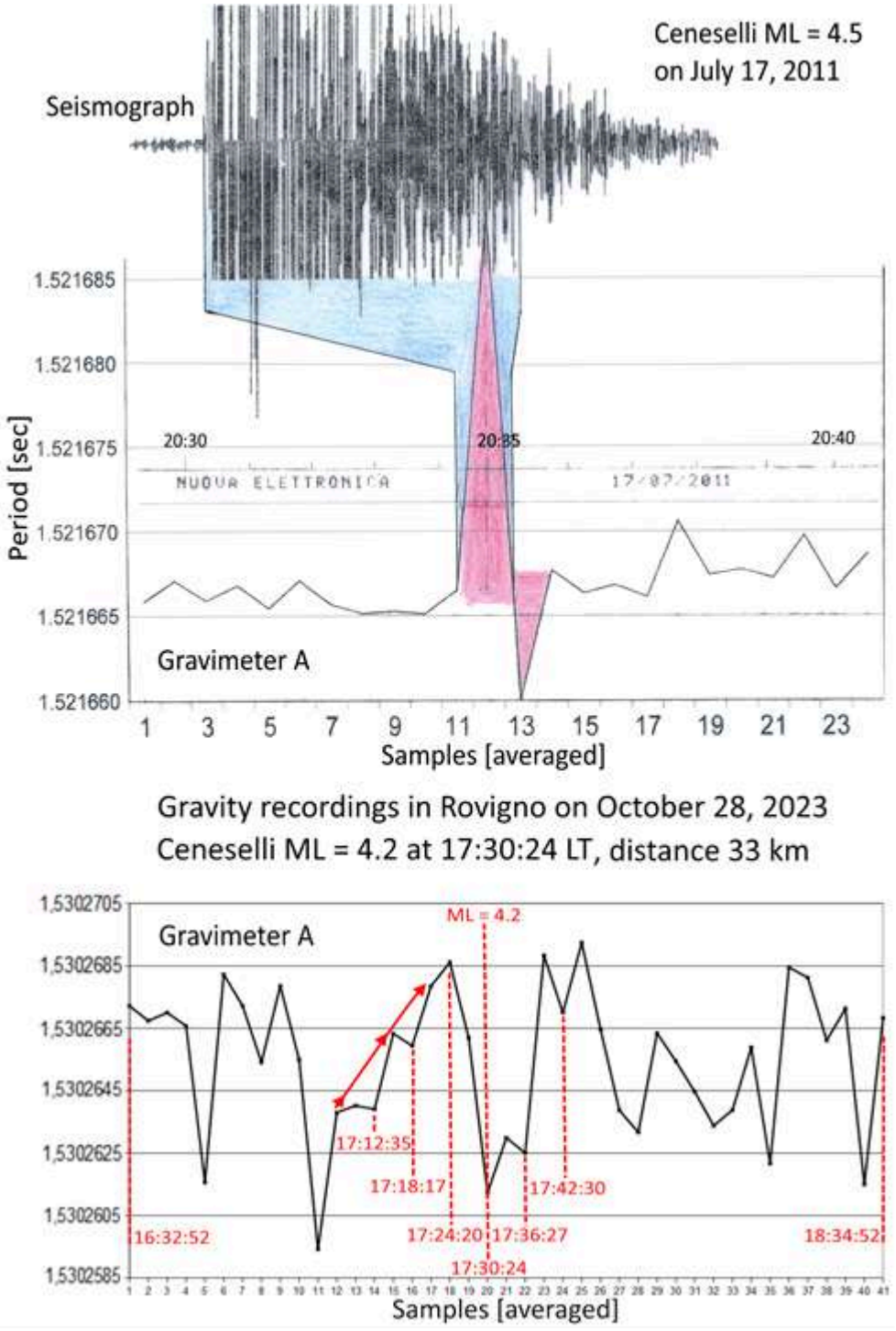

Fig. 3 – A gravity recording of the two hours between the seismic event occurred in Ceneselli on July 17, 2011. The seismogram recorded at the same position of the damped pendulum is reported on the top, where the blue area highlights the seismogram length while the red areas highlight direct and reverse gravimeter responses. Another gravity recording of the two hours between the seismic event occurred in Ceneselli on October 28, 2023, on the bottom. The gravity measurements are indicated by a broken line where the thick line indicates its average trend. Red areas evidence a trend of an increasing period that anticipated the shock, then the period suddenly decreased

References

Campion M.; 2022: Quanto ci può rivelare il tenue sussurro della gravità terrestre? Booksprint (13 Dec. 2022), p. 71.

INGV; 2015: CPTI15, Catalogo Parametrico dei Terremoti Italiani 2015, versione 4.0.

Lenzen V.F., Multauf R.P.; 1964: Development of gravity pendulums in the 19th century. United States National Museum Bulletin 240: Contributions from the Museum of History and Technology reprinted in Bulletin of the Smithsonian Institution. Paper 44. Washington: Smithsonian Institution Press., p. 307.

A data-driven parametrization of source-directivity effects: the study case of Central Italy

L. Colavitti [1,2], G. Lanzano [1], S. Sgobba [1], F. Pacor [1]

1 *National Institute of Geophysics and Volcanology, INGV*
Seismology applied to Engineering (Milan, Italy)
2 *University of Genoa, DISTAV*
Department of Earth, Environment and Life Sciences (Genoa, Italy)

INTRODUCTION

Assessing the spatial variability of seismic shaking in the epicenter zone is one of the major challenges to be addressed in seismic hazard estimates and ground motion scenarios generation. Among the various contributions causing the azimuthal variation of the shaking, source directivity plays a crucial role. As already proven by recent research, directivity effects, which are related to the characteristics of rupture propagation along the fault, can provoke ground motion amplifications in wider or narrower frequency ranges, even in small to moderate magnitude earthquakes (López-Comino et al., 2012; Pacor et al. 2016; Convertito et al. 2016). The scope of this work is to construct a fully data-driven directivity predictive model that can be used to estimate seismic ground motion amplification, using few independent parameters.

DATA AND METHOD

The dataset used in this research is the same used by Sgobba et al. (2021a) and Colavitti et al. (2022) and is formed by high-quality waveforms of Central Italy covering the period range from 2009 to 2018. In particular, we analyzed about 35,000 recordings from 460 stations (**Fig. 1a**) and 456 events (**Fig. 1b**), for which we computed the 5% acceleration elastic response spectra ordinates from 0.04 to 2 sec for shallow active crustal events (Spallarossa et al., 2023). The events spans from magnitude values between 3.2 and 6.5, and contain earthquakes of the sequence of L'Aquila in 2009 (Ameri et al., 2009; Calderoni et al., 2015) and Amatrice-Visso-Norcia in 2016-2017 (Chiaraluce et al., 2017; Michele et al., 2020).

The method to detect the effects of source directivity is the same implemented for the ordinates of the Fourier Amplitude Spectra (FAS) by Colavitti et al. (2022) and is based on the analysis of the residuals obtained from non-ergodic ground motion modelling. In particular, we identify the

systematic contributions of event, source, site and path effects thanks to a mixed effect calibration technique (Stafford, 2014). As already noted by Sgobba et al. (2023), the exceptional amount of information that has been produced in Central Italy, makes this area particularly suitable for a calibration of this kind of model.

The model calibrated in this study is a modified version of the one developed by Sgobba et al. (2021a) for the Central Italy and presents the following functional form:

$$log_{10}Y = a + F_M(M) + F_R(M,R) + \delta B_e + \delta S2S_s + \delta L2L_{source} + \delta P2P_p + \delta W_0 \quad [1]$$

where Y is the intensity measure, i.e. PGA or a spectral parameter (69 values logarithmically equispaced from 0.04 to 2 sec), a, $F_M(M)$, $F_R(M,R)$ are the fixed effects depending on magnitude M and distance metric R, while δB_e, $\delta S2S_{ref,s}$, $\delta P2P_p$ represents the zero-mean gaussian-distributed random effects.

Details on the fixed and random terms were provided in the paper of Sgobba et al. (2021); this study is based on the analysis of the azimuthal distribution of the leftover residual δW_0, which reflects the aleatory variability, net to the computation of the systematic effects. The azimuthal variation δW_0 is fitted starting from the general expression of the directivity factor C_d by Boatwright (2007):

$$C_d = \sqrt{\frac{k^2}{[1-(\frac{v_r}{c})cos(\theta-\theta_0)]^2} + \frac{(1-k)^2}{[1+(\frac{v_r}{c})cos(\theta-\theta_0)]^2}} \quad [2]$$

where $\frac{v_r}{c}$ is the Mach number from here on called α, θ_0 is the azimuth of the rupture direction and parameter k which spans from 0 to 1 indicates the relative portion of the rupture length along the rupture direction θ_0.

Taking into account that there is a trade-off between the fit parameters as α, k, θ and n, we have to assume fixed some of these values in order to vary others. After several tests, for this work we decided to fix k to 0.85 and α to 0.50 and then evaluating the directivity power by the parameter n. The constrained parameters are consistent with those reported in the literature (Ren et al., 2017; Convertito et al., 2017) and also ensure that we have a good fit in the majority of the events.

For the identification of directivity effects, we adopted the same criteria of Colavitti et al. (2022), which is based on these following points:

1. The coefficient of determination R^2 computed between the observed distribution of the aleatory residual δW_0 and the fit considering the C_d model is greater than 0.50 for at least 7 out of 69 periods investigated;

2. The standard deviation of the distribution of azimuths where n is maximized angle, θ_0, across all the vibration periods is smaller than 20°.

RESULTS

With the proposed methodology, we identified 175 out of 456 (38%) directive events that exhibits a clear azimuthal pattern and frequency dependence, representing the signature of source directivity. Comparison with the previous analysis in FAS shows that the directivity analysis carried out in SA extends to wider bands and that the directivity peak itself, defined by the value of n_{max}, is always higher than the corresponding peak in SA.

For directivity modelling, we focus on the spectral trend of the n parameter, which experimentally showed a curve that can be fitted with a Gaussian distribution, with the maximum value of n, n_{max} and the corresponding period called $T_{n_{max}}$. Since according to Colavitti et al. (2022) $T_{n_{max}}$ depends on the magnitude and the amplitude of n_{max} is proportional to the "strength" of the directivity, we need to normalize the parametrization curve for $T_{n_{max}}$ (period of the peak of the directivity) and n_{max} (the peak itself).

The normalized curves are shown in **Figure 1** and represent on average a Gaussian-like pattern with non-negligible variability. We decided to adopt a fit model based on a Gaussian distribution of order 1 which is defined by the following equation:

$$\frac{n}{n_{max}} = a_1 * exp^{\left(-\frac{\left(log_{10}\left(\frac{T}{T_{n_{max}}}\right)-b_1\right)}{c_1}\right)^2} \quad [3]$$

where $\frac{n}{n_{max}}$ represents the function to parametrize with respect to the x parameter (where $x = log_{10}\frac{T}{T_{n_{max}}}$), a_1 is the amplitude, b_1 the median value along x and c_1 is a coefficient that controls the width of the gaussian distribution bell. **Figure 1** shows the fit according to the first-order Gaussian constraining the model with $\frac{n}{n_{max}} = 1$ and $log_{10}\frac{T}{T_{n_{max}}} = 0$. In this way, c_1 is equal to 0.8229, which is the value for the median curve considering all the events.

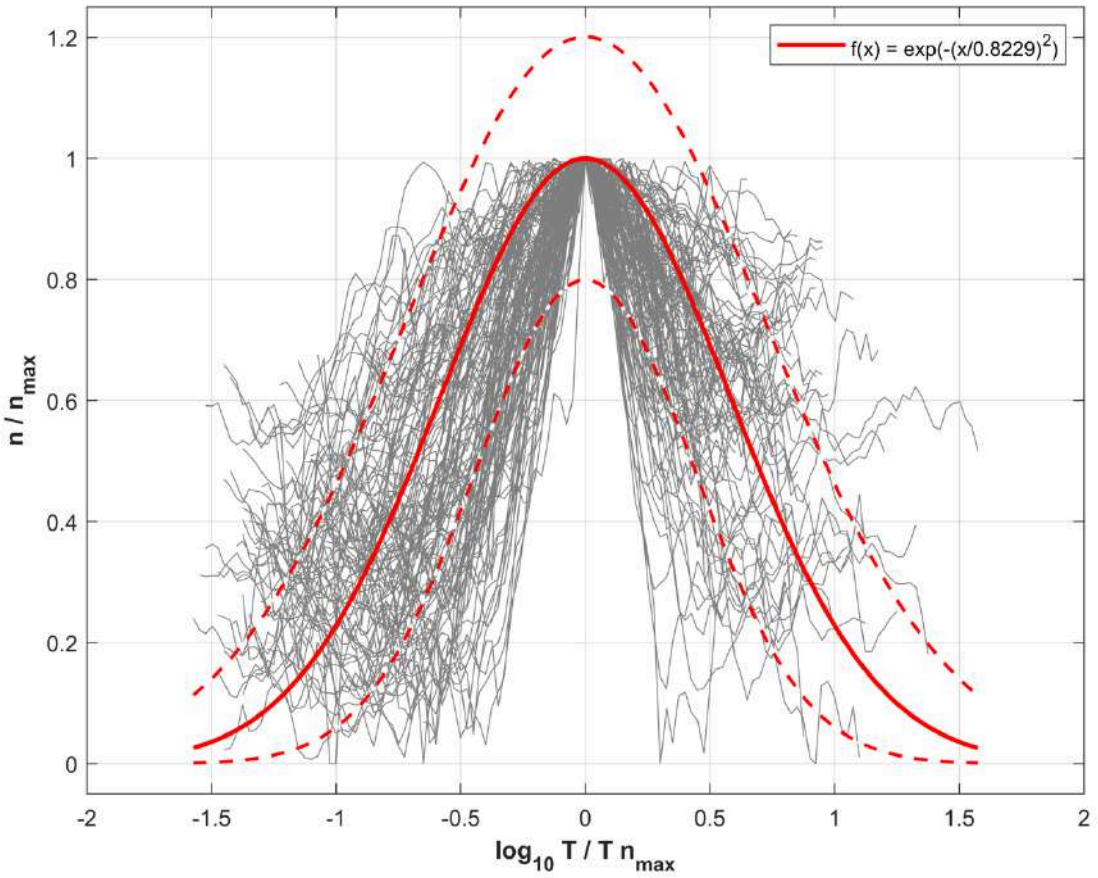

Figure 1. Relation between $\frac{n}{n_{max}}$ and $log_{10}\frac{T}{T_{n_{max}}}$ fitted with a Gaussian curve of order 1 and forcing the peak to the point 0,1. Grey lines are the events observed, red solid curve represents the best fit, while the standard deviation is shown by the red dashed curves. Some statistical parameters of the Gaussian: $c_1 = 0.8229$, fit $R^2 = 0.7822$, error $RMS = 0.0597$ and standard deviation $\sigma = 0.1980$.

CONCLUSIONS AND FUTURE PERSPECTIVES

Based on equation [3], we are able to provide a preliminary spectral parametrization of the amplitude of the source directivity, adopting a simple functional form with input values of $T_{n_{max}}$ and n_{max}. Based on several empirical models (see Sgobba et al., 2021b), $T_{n_{max}}$ is function of magnitude whereas the bandwidth can be modelled as directly proportional to the "strength" of the directivity.

At this stage, shaking scenarios in Central Italy can be generated including directivity contributions using non-ergodic ground motion models, once that the direction of rupture propagation and the level of source directivity is assumed *a priori*.

A future perspective of this work could be to extend the method into different tectonic contexts (e.g. 2019 Ridgecrest earthquake sequence, on a strike-slip fault domain) where we have a huge amount of recordings available and different styles of faults.

Acknowledgements

We are very grateful to Prof. Daniele Spallarossa (University of Genoa, Italy) for making available the dataset used in this work and to Prof. František Gallovič (University of Prague, Czech Republic) for the fruitful discussion about this work. This research is supported by the Italian Ministry of University and Research (MIUR) in the frame of the project SECURE: "Regional-Scale Earthquake Ground Motion PrediCtions ThroUgh Pyhsics-based and EmpiRical ApproachEs: A Case study Central Italy".

References

Ameri G., Massa M., Bindi D., D'Alema E., Gorini A., Luzi L., Marzorati S., Pacor F., Paolucci R., Puglia R., Smerzini C.; 2009.
The 6 April 2009 Mw 6.3 L'Aquila (central Italy) earthquake: Strong-motion observations. Seismol. Res. Lett., 80(6), 951-966. https://doi.org/10.1785/gssrl.80.6.951.

Boatwright J.; 2007. The persistence of directivity in small earthquakes. Bull. Seismol. Soc. Am., 97, 1850-1861. https://doi.org/10.1785/0120050228.

Calderoni G., Rovelli A., Ben-Zion Y. and Di Giovambattista R.; 2015. *Along-strike rupture directivity of earthquakes of the 2009 L'Aquila, Central Italy, seismic sequence.* Geophys. J. Int., 205, 399-415. https://doi.org/10.1093/gji/ggv275.

Chiaraluce L., Di Stefano R., Tinti E., Scognamiglio L., Michele M., Casarotti E., Cattaneo M., De Gori P., Chiarabba C., Monachesi G., Lombardi A., Valoroso L., Latorre D., Marzorati S.; 2017. *The 2016 central Italy seismic sequence: A first look at the mainshocks, aftershocks, and source models.* Seismol. Res. Lett., 88(3), 757-771. https://doi.org/10.1785/0220160221.

Colavitti L., Lanzano G., Sgobba S., Pacor F. and Gallovič F.; 2022. *Empirical evidence of frequency-dependent directivity effects from small-to-moderate normal fault earthquakes in Central Italy*. J. Geophys. Res: Solid Earth, 127, e2021JB023498. https://doi.org/10.1029/2021JB023498.

Convertito V., Pino N. A. and Di Luccio F.; 2010. *Investing source directivity of moderate earthquakes by multiple approach: The 2013 Matese (southern Italy) Mw=5 event.* Geophys. J. Int., 207, 1513–1528. https://doi.org/10.1093/gji/ggw360.

Convertito V., De Matteis R., Pino A.; 2017. *Evidence for static and dynamic triggering of seismicity following the 24 August 2016 Mw = 6.0, Amatrice (Central Italy) earthquake.* Pure and Appl. Geophys.,174, 3663-3672. https://doi.org/10.1007/s00024-017-1559-1.

López-Comino J. A., de Lis Mancilla F., Morales J. and Stich D.; 2012. Rupture directivity of the 2011, Mw 5.2 Lorca earthquake (Spain). Geophys. Res. Lett., 39, L03301. https://doi.org/10.1029/2011GL050498.

Michele M., Chiaraluce L., Di Stefano R. and Waldhauser F.; 2020. *Fine-Scale Structure of the 2016-2017 Central Italy Seismic Sequence from Data Recorded at the Italian National Network.* J. Geophys. Res.: Solid Earth, 125, e2019JB018440. https://doi.org/10.1029/2019JB018440.

Pacor F., Gallovič F., Puglia R., Luzi L. and D'Amico M.; 2016. *Diminishing high-frequency directivity due to a source effects: Empirical evidence from small earthquakes in the Abruzzo region, Italy*. Geophys. Res. Lett: Solid Earth, 43, 5000-5008. https://doi.org/10.1002/2016gl068546.

Ren Y., Wang H. and Wen R.; 2017. *Imprint of rupture directivity from ground motions of the 24 August 2016 Mw6.2 Central Italy earthquake.* Tectonics, 36, 3178-3191. https://doi.org/10.1002/2017tc004673.

Sgobba S., Lanzano G. and Pacor F.; 2021a. Empirical nonergodic shaking scenarios based on spatial correlation models: An application to central Italy. *Earthq. Eng. and Struct. Dynam*., 50(1), 60-80. https://doi.org/10.1002/eqe.3362.

Sgobba S., Felicetta C., Lanzano G., Ramadan F., D'Amico M., Pacor, F.; 2021b. *NESS2.0: An Updated Version of the Worldwide Dataset for Calibrating and Adjusting Ground-Motion Models in Near Source.* Bull. Seism. Soc. Am., 111(5), 2358-2378. https://doi.org/10.1785/0120210080.

Sgobba S., Lanzano G., Colavitti L., Morasca P., D'Amico M. C., Spallarossa D.; 2023. *Phyics-based parametrization of a FAS nonergodic ground motion model for Central Italy.* Bull. Earthq. Eng., 21, 4111-4137. https://doi.org/10.1007/s10518-023-01691-1.

Spallarossa D., Colavitti L., Lanzano G., Sgobba S., Pacor F., Felicetta C.; 2022. *CI-SA_Flatfile: Parametric table of the 5% Acceleration response Spectra ordinates and associated metadata for the shallow active crustal events in Central Italy (2009-2018)* [Data set]. Istituto Nazionale di Geofisica e Vulcanologia (INGV). https://doi.org/10.13127/CI_dataset/CI-SA_flatfile.

Stafford P. J.; 2014. *Crossed and nested mixed-effects approaches for enhanced model development and removal of the ergodic assumption in empirical ground-motion models.* Bull. Seism. Soc. Am., 104(2), 702-719. https://doi.org/10.1785/0120130145.

Corresponding author: leonardo.colavitti@edu.unige.it

Radon observations during the November 14 Montelparo, M = 4, and December 6 Allerona, M=3.6, earthquakes in 2023

G. De Antoni[1] C. Fidani[1,2,3,4] M. Siciliani[4] T. Milan[1]

[1] *Osservatorio Geofisico di Novara, Novara, Italy*
[2] *Istituto Nazionale di Geofisica e Vulcanologia, Roma, Italy*
[3] *Central Italy Electromagnetic Network, Fermo, Italy*
[4] *Osservatorio Sismico Andrea Bina, Perugia, Italy*

The Central Italy Electromagnetic Network (Fidani, 2011) was recently updated with a novel Radon detector (Fidani et al., 2022) developed by a project of the Novara Geophysical Observatory, at http://www.osservatorionovara.it/. A Radon detector prototype developed by the Novara Observatory team (De Antoni et al., 2011) was installed at the Fermo Station in January 2020. The installation followed the indications of the Novara Observatory team, which suggested to bury the pipe vertically with the bottom end open, and with the tube cap protruding a few cm from the ground. The scheme of the placement of the tube with a photo of the open cap is shown in Figure 1, note the bag that protects the sensor from condensation and the thermal insulating coating to reduce convective motions inside the pipe.

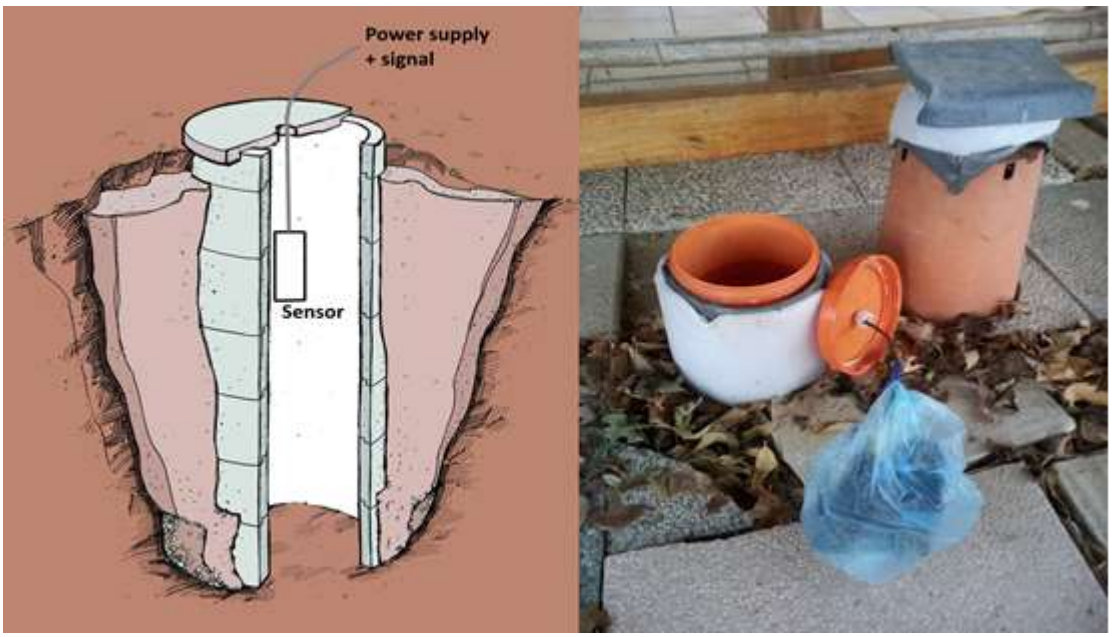

Fig. 1 – Scheme of the buried pipe with the sensor on the left, a photo of the top pipe open with the sensor placed outside on the right.

A year and half later, following the team indications, another three detectors were realized and installed; two in Gubbio and one at the Perugia Seismic Observatory Andrea Bina https://www.binapg.it/. The detectors are embedded in a network of observatories and have so far collected continuous recordings, separated by some interruptions due to the need for instrument maintenance, together with electric and magnetic detectors, gamma and air ions detectors, as well as meteorological stations https://cfidani.wixsite.com/cien. The objective of these instruments is to develop a physical model that links earthquake events to mutually interacting geophysical observables, in order to better understand the earthquake process manifested in the lowest surface atmosphere. Thus, for example, Radon escaping from the ground has been widely hypothesized to be driven by fluid migration towards the Earth's surface, and Radon plus fluids entering the atmosphere able to generate electromagnetic signals therein modifying meteorological conditions. Moreover, fluid migrations have been reported to be the primary trigger of Appennine earthquakes (Chiodini et al., 2004). Finally, the multi-parameter monitoring of the Central Italy Electromagnetic Network is mainly dedicated to the physical processes occurring on the ground-atmosphere interface.

Two moderately intense seismic events struck Central Italy between November-December 2023. An earthquake of magnitude ML = 4.0 occurred at about 3 km S Montelparo (Fermo), on November 14, 2023, 17:17:50 Italian time with geographical coordinates 42.996N and 13.537E at a depth of 21.6 km. The shock was generated by a compressional fault that is a typical mechanism of this area, due to the Apennine axis relaxation which towards the Adriatic Sea implicates a shortening belt. The area had been characterised by strong seismic events, as confirmed by the strong earthquakes of November 26, 1972, having an estimated magnitude Mw = 5.5, and of October 3, 1943, with an estimated magnitude Mw = 5.7 (INGV, 2015). The hourly decay counts of the 5 days preceding the November 14, 2023 shock are shown with a blue line in Fig. 2 bottom. Whereas, the red line in Fig. 2 bottom represents the 12-hour moving average of 12 previous counts reported in real time. Specifically, two decay increases are better visible by 12-hour moving averages, and these increases anticipated the seismic event indicated by a vertical red arrow in Fig. 2 bottom. The end of the smallest recorded average increase preceded the earthquake by two days, while the end of the largest recorded average increase preceded the earthquake by one day. The increases peak intensities were 30% for the smallest and of 120% for the largest. The meteorological instruments at the Fermo Station did not report any rain events or sudden pressure reductions during the peaks. However, a weak rain event registered prior to the quake was recorded between November 10th and 11th, 2023, with a cumulation of 7 mm.

These peaks were repeatedly detected before moderate seismic events at the Fermo Station. Furthermore, similar peaks were also detected before moderate seismic events in Central Italy by the stations located in Nepi (VT), Orvieto (TR), Campli (TE), and Gubbio (PG) http://www.osservatorionovara.it/. Other peaks and periodic variations having not been followed by moderate seismic events have been studied in relation to meteorological variables providing some interpretative agreement. Additional examples of increases, similar to those recorded a few days after the Montelparo event, occurred without any significant recorded seismic and meteorological events. On November 16, 2023, a sudden increase in the count decay was recorded to be 20 times the average, only to return to the initial value before the end of the same day, see Fig. 2 top. No rain or pressure variation events were recorded by the meteorological instruments before November 16. While a sudden and unexpected temperature

peak was recorded during the first hours of 17 November, 2023. The temperature peak reached 5 °C over a time interval during the early morning hours when the temperature is usually at its lowest. The time interval duration of around 4 hours from the 00:00 to 04:00 on November 17 is represented by a red line in Fig. 2 top, while the green line indicates the dew point. Data from the Montelparo meteorological instruments, and other stations positioned within 50 km, all reported significant increases in the temperatures during the same hours or over a longer time interval. Moreover, the temperatures recorded by meteorological stations more than 100 km from the Fermo Station did not detect any increases over the same hours. No increases in temperature were observed from Fig. 2 top after the December 13, 2023, peak.

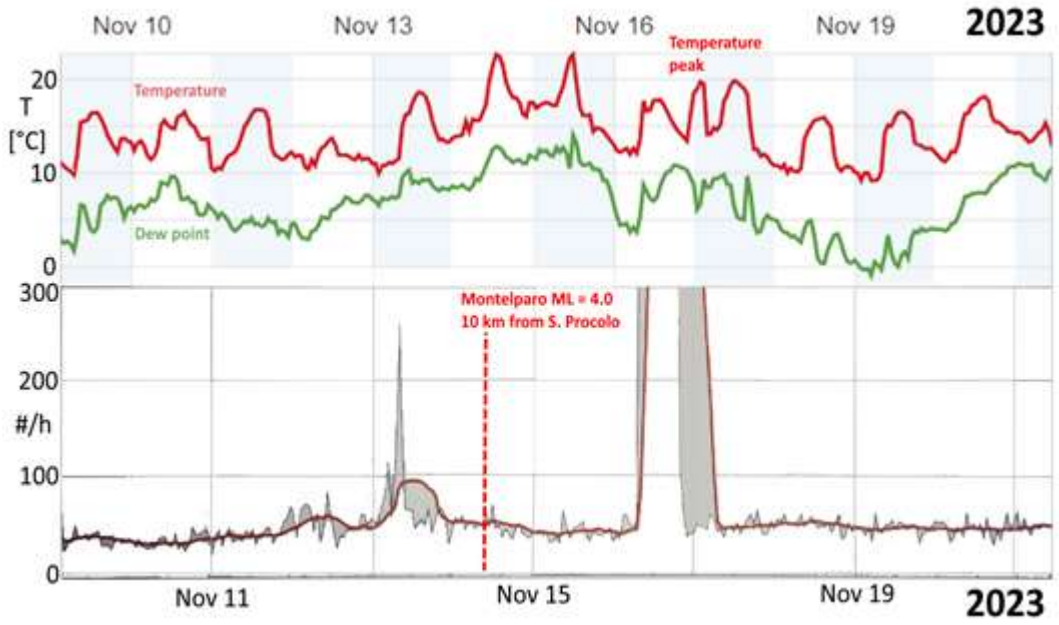

Fig. 2 – The Radon decay counts recorded at the San Procolo, Fermo Station, during the 5 days around the seismic event on the bottom, the temperature and the dew point trends along the same time interval on the top. The second recorded count decay peak is only partially shown here

An earthquake of a magnitude ML = 3.6 occurred 4 km SE Allerona (TR), on December 6, 2023, at 21:06:13 Italian time having geographical coordinates of 42.7960N and 12.0130E at a depth of 10.6 km (INGV, 2015). Its focal mechanism having been a strike sleep was unlike the Montelparo event. Strong earthquakes have occurred in the past in the same area although with a lower frequency than in the Marche Region. The active Radon detector nearest to the epicentre was the Perugia Seismic Observatory Andrea Bina https://www.binapg.it/, during the same period of the December 6 event, less than 50 km from the epicentre. The detector is located inside the San Pietro Abbey in Perugia and has been operative since the beginning of 2022. To date, this detector has counted an average low number of daily Radon decays, reaching a relative maximum on December 2, 2023. A relative minimum occurred about two day after the maximum on December 4, 2023, about two days before the shock, reported in Fig. 3. Pressure reported on the top of Fig. 3 evidenced a maximum of 1,019 mbar during the descending phase of the Radon count. Whereas, a 21 mm of cumulate rainfall was measured on December 5, 2023, and reported on the bottom of Fig. 3. No apparent influence of meteorological conditions on the Radon measurements were detected in Perugia over the same days. The data collected from both these recent events and all events in recent years proves to be valuable for testing the

monitoring network https://cfidani.wixsite.com/cien. This enables a statistical investigation into their correlation with seismic events.

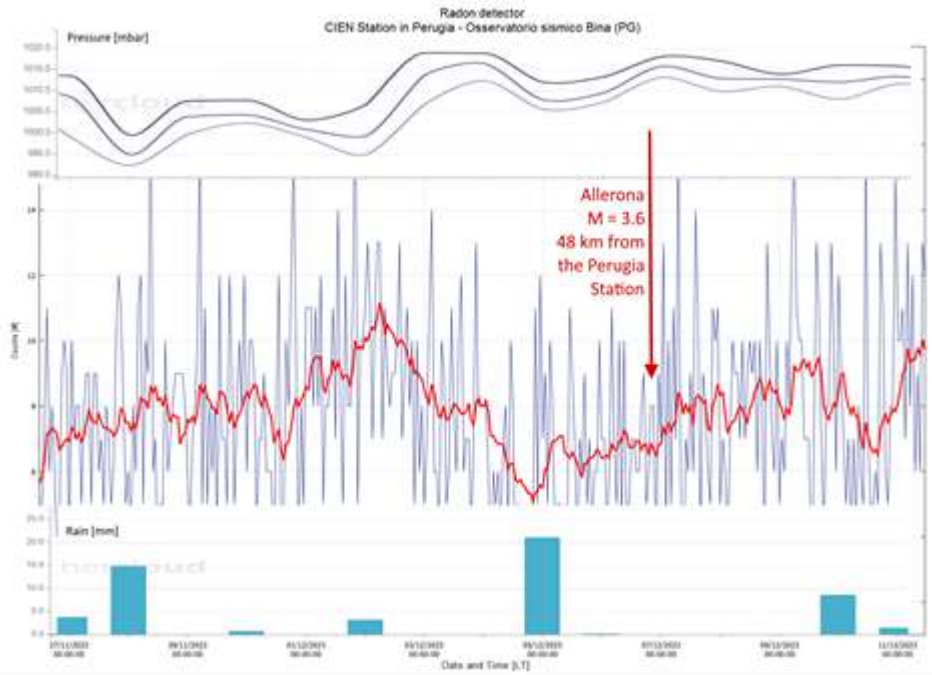

Fig. 3 – The Radon decay counts at the Andrea Bina Observatory, Perugia Station, measured during the days preceding and following the Allerona event, indicated by a vertical red arrow, and the superimposed meteorological trends of pressure on the top and rain on the bottom along the same time interval

References

Chiodini G., Cardellini C., Amato A., Boschi E., Caliro S., Frondini F., Ventura G.; 2004: Carbon dioxide Earth degassing and seismogenesis in central and southern Italy. Seismological Research Letters, 31, L07615.

De Antoni G., Milan T., Santini C., Baroffio E., Barile G.; Analisi della variazione del gas Randon lungo la Faglia della Cremosina e Sintesi sulla ricerca e sperimentazione di un nuovo sensore Radon. Osservatorio Geofisico di Novara, Progetto Gas Radon, pp. 40. http://www.osservatorionovara.it/1%20e%202%20Pubblicazione%20Radon.pdf

Fidani C.; 2011: The Central Italy electromagnetic network and the 2009 L'Aquila earthquake: observed electric activity. Geosciences, 1 (1), 3-25.

Fidani C., De Antoni G., Milan T., Siciliani M.; 2022: An update of the Central Italy Electromagnetic Network with Radon detectors, 40th GNGTS, Trieste, p. 47-51.

INGV; 2015: CPTI15, Catalogo Parametrico dei Terremoti Italiani 2015, versione 4.0.

Statistically interpreting multiple observations derived from one or more geophysical monitoring networks

C. Fidani[1,2]

[1] *Istituto Nazionale di Geofisica e Vulcanologia, Roma, Italy*
[2] *Cenrtral Italy Electromagnetic Network, Fermo, Italy*

Recent studies have unveiled significant statistical correlations between specific geophysical parameters and seismic activity. Statistical correlations for ULF geomagnetic fluctuations at ground stations have been calculated exclusively when considering moderate magnitude earthquakes (Schekotov et al., 2006). In alternative investigations, a lead time of 6–7 days for Pc1 was observed (Bortnik et al., 2008), VLF noise exhibited a lead time of 2 days (Oike and Yamada, 1994), lightning activities were noted to precede earthquakes by 17–19 days (Liu et al., 2015), and geoelectric fields demonstrated lead times ranging from days to weeks (An et al., 2020). A statistical correlation between earthquakes and VLF/LF signals, spanning approximately 10 years, was established using the Japanese VLF/LF network. The findings, as reported by Hayakawa et al. (2010), disclosed discernible perturbations in the signals occurring 3–6 days before the seismic wave paths. Low-orbit satellites provide the capability to observe extensive ground areas within a few hours, facilitating the monitoring of regions affected by seismic events. From this perspective, using the Intercosmos-24 satellite, Molchanov (1993) observed a 50% increase in the probability of charged particle burst observations occurring 6 to 24 hours before seismic events. Additionally, onboard the AUREOL-3 satellite, Parrot (1994) noted an augmentation in the average wave intensity correlated with seismic activity. The micro-satellite DEMETER enabled a statistical study of VLF electromagnetic wave intensity in the vicinity of earthquake epicenters (Nemec et al., 2008), evidencing a significant decrease in the measured wave intensity, 0–4 h before strong earthquakes. Analysing Total Electron Content (TEC) data from the global ionosphere map, researchers found that the highest occurrence rates of anomalies were associated with earthquakes of larger magnitudes and lower depths, 1–5 days before the seismic events (Zhu et al., 2018). This trend was corroborated by studies conducted in Japan (Kon et al., 2011) and China (Ke et al., 2016). Reports worldwide have documented concentrations of electron density and magnetic anomalies occurring more than two months to a few days before earthquake events (De Santis et al., 2019). Space-based observations have detected thermal infrared anomalies, and a comprehensive review by Tramutoli et al. (2015) has documented the major contributions and results achieved in over 30 years of correlating these anomalies with strong earthquakes. Finally, sudden variations in high-energy charged particles

have been linked to strong earthquakes, particularly during periods of low solar activity, as documented by Fidani (2015).

Currently, Earth is witnessing the development of numerous geophysical earth observation networks, each designed for specific purposes. These evolving networks aim to monitor various facets of our planet's geophysical activity. As highlighted above, recent findings suggest that many of these networks hold potential applications in earthquake studies. Satellite monitoring networks are implemented through various programs, including NOAA and MetOps, which focus on meteorological forecasting. Additionally, the Swarm constellation was operational for monitoring the geomagnetic field. Finally, Cses02 was scheduled to be launched after Cses01 was placed in orbit in 2018, creating a dedicated project for earthquake monitoring. A ground-based network is for example INTERMAGNET, see Fig. 1, a collaboration of digital magnetic observatories accessible at https://intermagnet.org/. INTERMAGNET adopts modern standard specifications for measuring and recording equipment, facilitating seamless data exchanges and the near real-time production of geomagnetic recordings. Furthermore, a long-term plan for the integration of existing national and trans-national research infrastructures for solid Earth science in Europe, EPOS at https://www.epos-eu.org/, sustains such a program through the utilisation of multidisciplinary solid Earth science data, data products, and services, along with physical access to facilities. It is in the process of developing a federated and sustainable research platform aimed at delivering coordinated access to harmonised and quality-controlled data spanning diverse Earth science disciplines. This platform will also offer tools for analysis and modelling. EPOS actively promotes global interoperability in Earth sciences and extends its services to a broad community of users. Such prospectives and discoveries have ignited a growing interest in investigating the feasibility of a comprehensive analysis that incorporates multiple parameters, both ground-based and space-based, to evaluate the occurrence of a seismic event.

Fig. 1 – Map distribution of geomagnetic observatories belonging to INTERMAGNET programme, red circles represent active international magnetic observatories while gray circles represent closed observatories

Defining the conditional probability of a noteworthy event, like an earthquake, involves analysing the variations in a geophysical observable that typically precedes it. In this context, time series representation involves binary events, with '1' indicating instances where the observable exceeds a certain magnitude threshold. For instance, these events could be seismic activities surpassing a specific magnitude or any observable exceeding its defined threshold. Subsequently, the likelihood of an earthquake is assessed by examining the correlation between these binary events. Or also, a probability increase for an earthquake can be defined by the probability gain

$$G_A = P(EQ|EA)/P(EQ), \quad (1)$$

where P(EQ) represents the frequency of the earthquake event of a magnitude greater than a fixed value, and EA represents the observable A event, being the conditional probability

$$P(EQ|EA) = P(EQ) + corr(EQ,EA)\ \{P(EQ)[1-P(EQ)][1-P(EA)]/P(EA)\}^{½}, \quad (2)$$

defined by the Pearson Coefficient R = corr(EQ,EA) and the frequency of the event A, P(EA). Such a relation (2) for the probability gain due to the observable A is valid only for binary event series. Let's explore the scenario where we observe two quantities, drawing from existing networks like the electromagnetic network in central Italy and the network comprised of NOAA satellites. The first network records magnetic field pulses, while the second detects electron precipitation. The magnetic pulses have the potential to alter the trajectory of electrons reaching the ionosphere, indicating compatibility and dependence between the two observables. These quantities can be observed concurrently (represented by the symbol ⋂) or individually, without distinction (represented by the symbol U). The correspondent probability gains (Fidani, 2021)

$$G_{EB\cap MP} = P(EB\cap MP|EQ)/P(EB\cap MP), \quad (3)$$

where EB is the electron burst event and MP is the magnetic pulse event, which reduces to $G_{EB}G_{MP}$ if the events were compatible but completely independent, and

$$G_{EB\cup MP} = \frac{G_{EB}P(EB) + G_{MP}P(MP) - G_{EB\cap MP}P(EB)P(MP)}{P(EB) + P(MP) - P(EB\cap MP)}, \quad (4)$$

which reduces to $[G_{EB}P(EB) + G_{MP}P(MP) - G_{EB}G_{MP}P(EB)P(MP)]/[P(EB) + P(MP) - P(EB)P(MP)]$ if the events were compatible but completely independent. In the case of compatible and dependent events it will be necessary to evaluate correlations of the type corr(EQ,EB⋂MP), i.e. concerning the concurrence of EB and MP events.

Ultimately, these probability gains define the increase in conditional probabilities of the occurrence of an earthquake of a certain minimum magnitude compared to the observation of the two observables together or only one of the two, regardless of which. In a model verification scenario, the region where the alarm is activated is specified for each observable, as illustrated in Fig. 2, for instance. If this region is not identical for both observables, then the probability gains of the observables need to be recalculated within the shared area. In the presence of

different networks, we could use the two gains, G∩ and GU, depending on whether we consider the observables distinct or indistinguishable in the intersection areas. The same parameter measured at different stations is combined as two different observations. Finally, G(∩) increases for highly intercorrelated parameters and G(U) increases for slightly intercorrelated parameters, consequently forecasting probabilities are given.

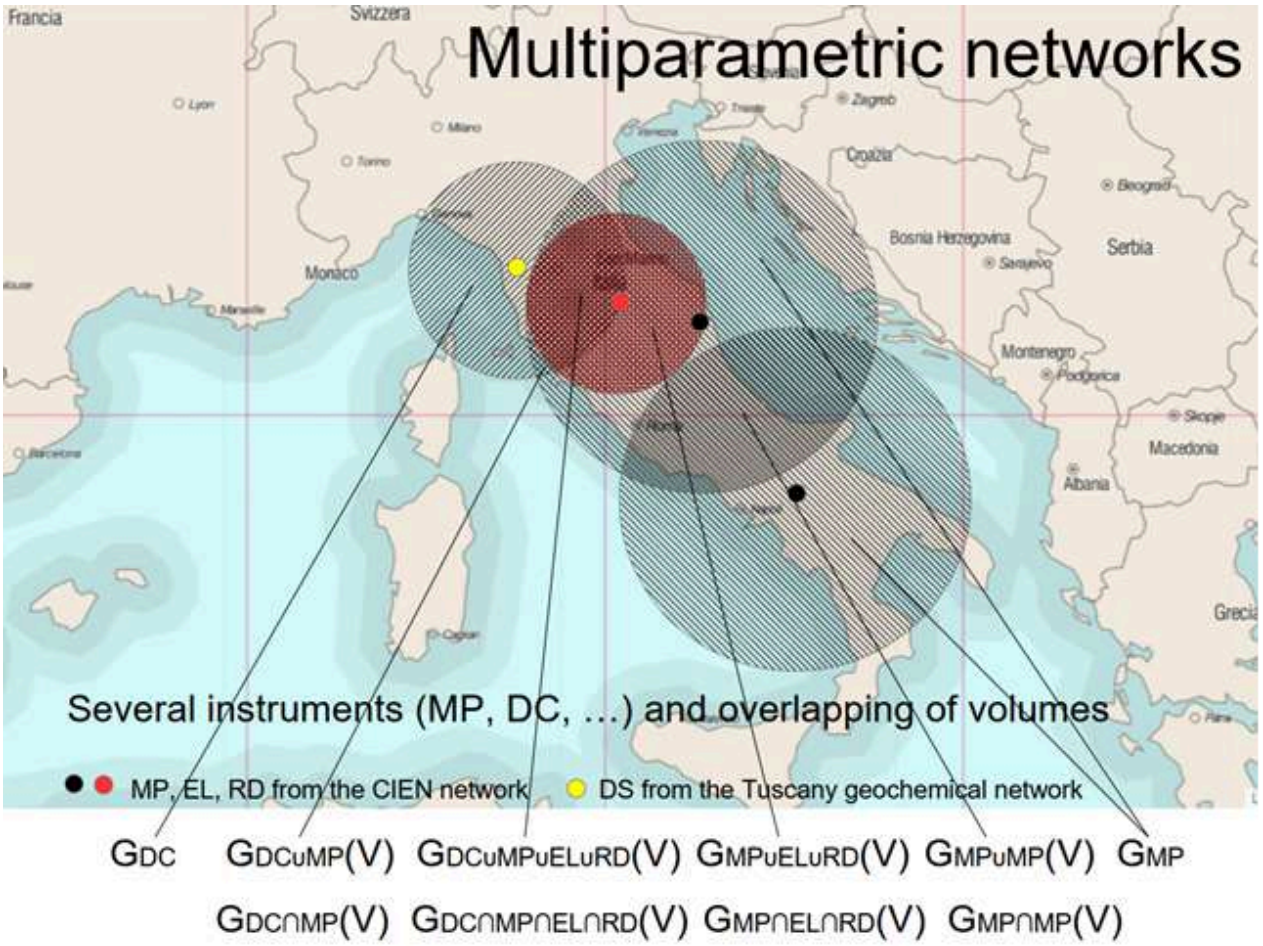

Fig. 2 – A potential scenario for testing a forecasting model in Italy involves leveraging the existing geophysical observational networks in the country

In summary, the verification process for this model is applicable to any observable, whether from ground-based or space-based sources. It necessitates the availability of geophysical observation datasets covering sufficiently long common time intervals. After establishing the elementary time interval, the initial step involves identifying anomalous events in the observable or, alternatively, events of interest, and assigning "1"s in the respective series. Subsequently, the series are correlated pairwise to identify any peaks. If correlation peaks are observed, the probability gains attributed to individual observables can be determined. From these gains, an attempt can be made to evaluate the probability gains resulting from data fusion. The process can be resumed in Fig. 3. The author thank the Limadou Scienza + (ASI) Project for the financial support.

Network	Observable	Studies of fluctuations	Binary series	Correlations	Conditional probabilities	Gains combined	Improved forecasting model
1) Seismic	... magnitude ...	Mo		1)-2) 1)-3)	P(1|2) P(1|3)	G2∩3 G2U3	P(1|2∩3)
2) A	1	threshold 1		2)-3)	Probability gains	using P(2|3)	P(1|2U3)
3) B	5 ...	threshold 2			G2 G3		

Fig. 3 – Steps of the process to improve forecasting

References

An Z., Zhan Y., Fan Y., Chen Q., Chen Q., Liu J.; 2019: Investigation of the Characteristics of Geoelectric Filed Earthquake Precursors: a Case Study of the Pingliang Observation Station, China. Ann. Geophys. 62 (5), 545.

Bortnik J., Cutler J. W., Dunson C., Bleier T. E.; 2008: The Possible Statistical Relation of Pc1 Pulsations to Earthquake Occurrence at Low Latitudes. Ann. Geophys. 26, 2825–2836.

De Santis A., Marchetti D., Pavón-Carrasco F. J., Cianchini G., Perrone L., Abbattista C., et al.; 2019: Precursory Worldwide Signatures of Earthquake Occurrences on Swarm Satellite Data. Sci. Rep. 9, 20287.

Fidani, C.; 2015: Particle Precipitation Prior to Large Earthquakes of Both the Sumatra and Philippine Regions: A Statistical Analysis. J. Asian Earth Sci. 114, 384–392.

Fidani C.; 2021: West Pacific Earthquake Forecasting Using NOAA Electron Bursts With Independent L-Shells and Ground-Based Magnetic Correlations. Front. Earth Sci. 9:673105.

Hayakawa M., Kasahara Y., Nakamura T., Muto F., Horie T., Maekawa S., et al.; 2010: A Statistical Study on the Correlation between Lower Ionospheric Perturbations as Seen by Subionospheric VLF/LF Propagation and Earthquakes. J. Geophys. Res. 115, A09305.

Ke F., Wang Y., Wang X., Qian H., Shi C.; 2016: Statistical Analysis of Seismo-Ionospheric Anomalies Related to Ms > 5.0 Earthquakes in China by GPS TEC. J. Seismol 20, 137–149.

Kon S., Nishihashi M., Hattori K.; 2011: Ionospheric Anomalies Possibly Associated with M≥6.0 Earthquakes in the Japan Area during 1998-2010: Case Studies and Statistical Study. J. Asian Earth Sci. 41, 410–420.

Liu J. Y., Chen Y. I., Huang C. H., Ho Y. Y., Chen C. H.; 2015: A Statistical Study of Lightning Activities and M ≥ 5.0 Earthquakes in Taiwan during 1993-2004.

Molchanov, O. A.; 1993: Wave and Plasma Phenomena inside the Ionosphere and Magnetosphere Associated with Earthquakes, in Review of Radio Science 1990–1992. Editor W Ross Stone (Oxford: Oxford University Press), 591–600.

Oike K., and Yamada T.; 1994: Relationship between Shallow Earthquakes and Electromagnetic Noises in the LF and VLF Ranges, in Electromagnetic Phenomena Related to Earthquake Prediction (Tokyo: Terra Scientific Publishing Company), 115–130.

Němec F., Santolík O., Parrot M., Berthelier J. J.; 2008: Spacecraft Observations of Electromagnetic Perturbations Connected with Seismic Activity. Geophys. Res. Lett. 35, L05109.

Parrot, M.; 1994: Statistical Study of ELF/VLF Emissions Recorded by a Low-Altitude Satellite during Seismic Events. J. Geophys. Res. 99 (A12), 339–347.

Schekotov A., Molchanov O. Hattori K., Fedorov E., Gladyshev V. A., Belyaev G. G., et al.; 2006: Seismo-ionospheric Depression of the ULF Geomagnetic Fluctuations at Kamchatka and Japan. Phys. Chem. Earth, Parts A/B/C 31, 313–318.

Tramutoli V., Corrado R., Filizzola C., Genzano N., Lisi M., Pergola N.; 2015: From Visual Comparison to Robust Satellite Techniques: 30 Years of thermal Infrared Satellite Data Analyses for the Study of Earthquake Preparation Phases. Boll. Geof. Teor. Appl. 56, 167–202.

Zhu F., Su F., Lin J.; 2018: Statistical Analysis of TEC Anomalies Prior to M6.0+ Earthquakes during 2003-2014. Pure Appl. Geophys. 175, 3441–3450.

A comparison between moment magnitude scales

P. Gasperini[1,2], B. Lolli[2]

[1] *Dipartimento di Fisica e Astronomia "Augusto Righi", Università di Bologna, Bologna, Italy*
[2] *Istituto Nazionale di Geofisica e Vulcanologia, Sezione di Bologna, Bologna, Italy*

Moment magnitude M_w was first defined by Kanamori (1977) and Hanks and Kanamori (1979) in the late 1970s, when the availability of new force balance seismometers made it possible to measure the seismic moment M_0 with virtually no limits in the frequency passband. For this reason, M_w does not become saturated even for the largest earthquakes ever recorded. M_w has been chosen in such a way that it coincides best with the previous definitions of magnitude (M_L, m_b, M_s etc.) on certain ranges of values but can deviate significantly from them within other ranges. A few years ago, a new moment magnitude scale M_{wg} was proposed by Das et al. (2019), with the aim of better reproducing the values of m_b and M_s over their entire range and to better predict the energy E_s radiated by earthquakes. In this work we show that there was no need to define such a new scale and that the latter is not even optimal to achieve the goal that the authors had set themselves.

References

Das, R., Sharma, M. L., Wason, H. R., Choudhury, D., and Gonzales. G. (2019). A Seismic Moment Magnitude Scale, Bull Seism. Soc. Am., 109/4, 1542–1555, doi: 10.1785/0120180338.

Kanamori, H. (1977). The energy release in great earthquakes, J. Geophys. Res. 82, 2981–2987.

Hanks, T. C., and H. Kanamori (1979). A moment magnitude scale, J. Geophys. Res. 84, 2348–2350.

Corresponding author: paolo.gasperini@unibo.it

Revealing anomalies in the Molise 2018 earthquake sequence

S. Gentili[1], P. Brondi[1], G. Rossi[1], M. Sugan[1], G. Petrillo[2,3], J. Zhuang[3], S. Campanella[1]

[1] National Institute of Oceanography and Applied Geophysics - OGS, Italy
[2]The Institute of Statistical Mathematics – ISM, Japan;
[3]Scuola Superiore Meridionale – SSM, Italy

Understanding the seismic clustering patterns in a region is crucial for statistical testing and forecasting. The NESTORE (NExt STrOng Related Earthquake – Gentili et al. 2023) algorithm has been shown to be a successful example of such applications of cluster analysis. It can be used for strong aftershock forecasting during an ongoing cluster. However, its forecasting performance can be compromised, if clusters are not properly detected.

With various approaches, including traditional window-based methods, complex network-based techniques, stochastic declustering methods rooted in the Epidemic Type Aftershock Sequence (ETAS) model, and Principal Component Analysis (PCA), this study investigates the seismic sequence in Molise (southern Italy) in 2018. Ambiguous results were obtained when applying the NESTORE method. We utilize an enhanced template matching catalog and four different methods to identify earthquakes belonging to the cluster. While two methods indicate the presence of two distinct clusters in the same area and time period (from April to November 2018), Principal Component Analysis and Nearest Neighbor suggest the presence of a single cluster.

Inconsistencies are attributed to the seismicity potentially being part of anomalous sequences. This research emphasizes the need for refined cluster identification methods and calls for further studies on how to characterize the specific seismic anomaly as in Molise in 2018.

Acknowledgements

Funded by a grant from the Italian Ministry of Foreign Affairs and International Cooperation

References

Gentili, S., P. Brondi, and R. Di Giovambattista; 2023: NESTOREv1.0: A MATLAB Package for Strong Forthcoming Earthquake Forecasting, Seismol. Res. Lett. 94, 2003–2013, doi: 10.1785/0220220327.

Corresponding author: sgentili@ogs.it

Time–Space Evolution of the Groningen Gas Field in Terms of b-Value: Insights and Implications for Seismic Hazard

L. Gulia

Università di Bologna, Bologna, Italia

The Groningen gas field, located in the northeast of The Netherlands, is the Europe's largest onshore gas field. It was discovered in 1959 and production started in 1963: Continuous production has led to reservoir compaction and subsidence, gradual loading of pre-existing faults and induced seismicity that started about 30 yr into the production. The seismic hazard and risk related to the induced seismicity is determined not only for the rate of activity, but it is also equally influenced by the relative size distribution of the seismicity—the b-value. I reanalyze the spatial and temporal evolution of the b-value in the field using an alternative approach to overcome magnitude in completeness heterogeneity, and link it to the evolution of fault loading and subsidence. Spatial variations of b-values are found to vary between 0.61 and 1.3, with the lowest observed values observed in the location of the 2012 M 3.6 Huizinge earthquake. In the last 10 years, the mapped b-values are more homogeneous throughout the field. The spatial and temporal evolution of the b-value in the field in this study is shown to be quite complex, and systematically linked it to the evolution of fault loading, absolute compaction, and the rate of compaction—an important finding that offers new insights into hazard reduction and mitigation strategies of extraction relation-induced seismicity. Compaction rates below 2 mm/yr are not correlated to seismicity above M 2.0 in the history of the field, suggesting that low-volume production may be safer than that previously assumed.

Corresponding author: laura.gulia@unibo.it

The new version of the Foreshock Traffic Light System

L. Gulia[1*], S. Wiemer[2], E. Biondini[1], G. Vannucci[3], B. Enescu[4]

[1] *University of Bologna, Department of Physics and Astronomy, Bologna, Italy*
[2] *Swiss Seismological Service, ETH Zurich, Zurich, Switzerland*
[3]*Istituto Nazionale di Geofisica e Vulcanologia, Bologna, Italy*
[4]*University of Kyoto, Kyoto, Japan*

After the occurrence of a moderate to large earthquake, the question shared between Civil Protection, scientists, the population, and all decision makers is only one: *Was it the mainshock or a bigger event has yet to come?*

According to standard earthquake statistics, the chance that after a moderate earthquake an even larger event will occur within five days and 10 km is typically 5% (Reasenberg and Jones, 1990). Recently, a more specific answer to this question has been given by the Foreshock Traffic Light System (FTLS, Gulia and Wiemer, 2019). The method allows the real-time discrimination between foreshocks and aftershocks in well-monitored regions.

However, some expert judgements are required in order to overcome local peculiarities (Brodsky, 2019) such as magnitude of completeness and the duration of the short-term aftershock incompleteness (STAI; Kagan, 2004).

We here introduce and test the new version of the code that, using the b-positive estimator (van der Elst, 2021), successfully overcomes the above-mentioned limits, allowing the implementation of the FTLS already in few hours after a M≥6 event without any specific expert judgements.

References

Brodsky, E. (2019). Predicting if the worst earthquake has passed. Nature, 574, 185-186.

Gulia, L., and S. Wiemer (2019). Real-time discrimination of earthquake foreshocks and aftershocks, Nature 574, 193–199.

Kagan, Y. Y. (2004). Short-term properties of earthquake catalogs and models of earthquake source. Bull. Seism. Soc. Am., 94(4), 1207–1228. https://doi.org/10.1785/012003098

van der Elst, N. J. (2021). B-positive: A robust estimator of aftershock magnitude distribution in transiently incomplete catalogs. J. Geophys. Res. Solid Earth, 126, e2020JB021027. https://doi.org/10.1029/2020JB021027

Corresponding author: laura.gulia@unibo.it

Fault System Finite-Element Geodynamical Modelling for Seismic Hazard Analysis of the Central Italian Apennines

A. Rood[1], M. Pagani[1], D. Di Bucci[2]

[1]*GEM Foundation, Pavia, Italy*
[2]*Dipartimento della Protezione Civile, Presidenza del Consiglio dei Ministri, Rome, Italy*

The structural complexity of the Italian Apennines, as a result of the sequential overprint of successive tectonic phases, presents a significant challenge in the study of the seismotectonics of the region for earthquake hazard analysis. Specifically, the effect of this structural complexity is that the interpretation of surface geological and geodetic observations may not completely characterise the 3-D distribution of fault geometries and their seismicity in the subsurface. Therefore, to understand the seismotectonics of the Apennines, for the goal of accurate seismic hazard analysis of this seismically active region, it is potentially valuable to characterise the seismogenic potential of faults both at surface and in the subsurface. The structural complexity of the Apennines and its consequences on the seismotectonic setting was recently emphasized by the pattern of seismicity across the Central Apennines during the 2016–2017 seismic sequence (Chiaraluce *et al.*, 2017). The reported fault segmentation, reactivation, and interaction within this fault system demonstrates the need for these phenomena to be taken into account when analysing the seismic hazard for this region (Buttinelli *et al.*, 2021a).

To achieve this goal, we employed the RETRACE-3D model (Buttinelli *et al.*, 2021b) of the fault system that characterises the crustal volume affected by the 2016-2017 seismic sequence (Di Bucci *et al.*, 2021; RETRACE-3D Working Group, 2021) for use in geodynamic modelling using the Geodynamic World Builder (Fraters *et al.*, 2019). We then integrated this model with the finite element code ASPECT (Bangerth *et al.*, 2022; Kronbichler *et al.*, 2012) to determine the instantaneous long-term strain rate of each fault in the fault system. This is a new application of ASPECT to the modelling of active faults systems for seismic hazard analysis. Perhaps not unexpected, we find that major faults take over most of the extension imposed as a boundary condition (Stemberk *et al.*, 2019) and that the interaction between the faults within the fault system is evident from the spatial variability of strain rate over an individual fault surface.

We utilised the OpenQuake engine (Pagani *et al.*, 2014) to then conduct a probabilistic seismic hazard analysis (PSHA) for the region that contains the RETRACE-3D model, using the ASPECT modelling results. The seismic moment rate of each fault was calculated from the total strain rate across the fault surface, which was then used to determine the rate of occurrence of a characteristic, full-fault rupture. Our RETRACE-3D hazard results show a good agreement with the hazard results using the ESHM20 fault model (Danciu *et al.*, 2021) at low probabilities of exceedance. Finally, disaggregation by source allowed the identification of the faults within the fault system that are the main contributors to the hazard for some representative sites. This innovative PSHA model for the Central Italian Apennines represents one of the first applications of geodynamic finite-element modelling of a highly complex fault system to characterise the 3-D distribution of seismic strain within the subsurface for a hazard analysis.

In this contribution, we present preliminary results, recognising that our work to date has revealed plenty of directions for subsequent work to be done. Such future work might include, for example, not only improving the rheology of the various components of the finite-element model but also abandoning the hypothesis of full segmentation. An approach to build a fault-based occurrence model by considering the full set of faults as part of an interconnected system of sections would be similar to the state-of-the-art hazard models in other regions of the world, such as California and New Zealand.

References:

Bangerth, W., Dannberg, J., Fraters, M., Gassmoeller, R., Glerum, A., Heister, T., Myhill, R., & Naliboff, J. (2022). ASPECT: Advanced Solver for Problems in Earth's ConvecTion, User Manual. https://doi.org/10.6084/m9.figshare.4865333.v9

Buttinelli, M., Petracchini, L., Maesano, F. E., D'Ambrogi, C., Scrocca, D., Marino, M., Capotorti, F., Bigi, S., Cavinato, G. P., Mariucci, M. T., Montone, P., & Di Bucci, D. (2021a). The impact of structural complexity, fault segmentation, and reactivation on seismotectonics: Constraints from the upper crust of the 2016–2017 Central Italy seismic sequence area. *Tectonophysics*, *810*, 228861. https://doi.org/10.1016/j.tecto.2021.228861

Buttinelli, M., Maesano, F. E., Petracchini, L., D'Ambrogi, C., Scrocca, D., Di Bucci, D., Basili, R., Cara, P., Castenetto, S., Giuliani, R., Salvi, I., Bigi, S., Cavinato, G. P., Di Filippo, M., Messina, P., Castaldo, R., De Novellis, V., Pepe, S., Solaro, G., . . . Ventura, R. (2021b). *RETRACE-3D Central Italy Geological Model.* Italian Institute for Environmental Protection and Research (ISPRA). https://doi.org/10.13127/RETRACE-3D/GEOMOD.2021

Chiaraluce, L., Di Stefano, R., Tinti, E., Scognamiglio, L., Michele, M., Casarotti, E., Cattaneo, M., De Gori, P., Chiarabba, C., Monachesi, G., Lombardi, A., Valoroso, L., Latorre, D., & Marzorati, S. (2017). The 2016 Central Italy Seismic Sequence: A First Look at the Mainshocks, Aftershocks, and Source Models. *Seismological Research Letters*, *88*(3), 757-771. https://doi.org/10.1785/0220160221

Danciu, L., Nandan, S., Reyes, C., Basili, R., Weatherill, G., Beauval, C., Rovida, A., Vilanova, S., Sesetyan, K., Bard, P.-Y., Cotton, F., Wiemer, S., & Giardini, D. (2021). *The 2020 update of the European Seismic Hazard Model: Model Overview*. https://doi.org/10.12686/a15

Di Bucci, D., Buttinelli, M., D'Ambrogi, C., Scrocca, D., & RETRACE-3D Working Group. (2021). RETRACE-3D project: a multidisciplinary collaboration to build a crustal model for the 2016-2018 central Italy seismic sequence. *Bollettino di Geofisica Teorica ed Applicata*, *62*, 1-18. https://doi.org/doi:10.4430/bgta0343

Fraters, M., Thieulot, C., van den Berg, A., & Spakman, W. (2019). The Geodynamic World Builder: a solution for complex initial conditions in numerical modeling. *Solid Earth*, *10*(5), 1785-1807. https://doi.org/10.5194/se-10-1785-2019

Kronbichler, M., Heister, T., & Bangerth, W. (2012). High accuracy mantle convection simulation through modern numerical methods. *Geophysical Journal International*, *191*(1), 12-29. https://doi.org/10.1111/j.1365-246X.2012.05609.x

Pagani, M., Monelli, D., Weatherill, G., Danciu, L., Crowley, H., Silva, V., Henshaw, P., Butler, L., Nastasi, M., Panzeri, L., Simionato, M., & Vigano, D. (2014). OpenQuake Engine: An Open Hazard (and Risk) Software for the Global Earthquake Model. *Seismological Research Letters*, *85*(3), 692-702. https://doi.org/10.1785/0220130087

RETRACE-3D Working Group. (2021). *RETRACE-3D: centRal italy EarThquakes integRAted Crustal modEl. Final report. eds. INGV, ISPRA, CNR-IGAG, DPC. Rome, p. 100.* https://doi.org/10.5281/zenodo.4604940

Stemberk, J., Moro, G. D., Stemberk, J., Blahůt, J., Coubal, M., Košťák, B., Zambrano, M., & Tondi, E. (2019). Strain monitoring of active faults in the central Apennines (Italy) during the period 2002–2017. *Tectonophysics*, *750*, 22-35. https://doi.org/https://doi.org/10.1016/j.tecto.2018.10.033

Corresponding Author: anna.rood@globalquakemodel.org

Performance of the Ground Motion Models to predict the significant durations in Italy

B. Shoaib[1], F. Ramadan[2], G. Lanzano[2], M. Sadek[3], H. EL Ghoche[3]

[1] *University of Camerino, Italy*
[2] *Istituto Nazionale di Geofisica e Vulcanologia, Italy*
[3] *Lebanese University – Faculty of Technology, Lebanon*

Within the framework of seismic probabilistic hazard analysis and other engineering-oriented applications, the common approach to predict the ground motion is to use ground motion prediction models (GMMs). Those models are empirically developed as a function of a few explanatory variables such as magnitude, source-to-site distance, site condition, and focal mechanism. Traditionally, GMMs are developed for peak ground acceleration (PGA), peak ground velocity (PGV), and the ordinates of the acceleration response spectra (SA); however, to fully describe the dynamic response, other intensity measurements should be considered, such as the Arias intensity and ground motion duration.

The main aim was to study the ground motion durations caused by moderate-to-high earthquakes in Italy and to contribute to the development of a new duration GMM within the Italian context, by analysing the performance of existing GMMs against recordings of recent earthquakes in Italy.

Among several definitions of waveform duration, we considered as a reference intensity measure the relative significant durations (DSR), that are related to Arias Intensity, according to two definitions (Bommer et al., 2009): i) the DSR(5-75) measures the time interval from the 5%up to 75% of the total AI; ii) the DSR(5-95) extends to 95% of the Arias intensity.

An Italian shallow crustal dataset (ITA18) (Lanzano et al., 2022) has been considered, already employed for the GMMs calibration of other strong motion parameters (Lanzano et al. 2019; Ramadan et al. 2021); the dataset presents records for 154 events taken from 1637 stations. The dataset is dominant with events of Mw<5, NF focal mechanism, and site type A and B (According to the EC8 site classification).

Based on the above mentioned definitions, DSR(5-75) and DSR(5-95) were computed for all records found in the dataset ITA18: Husid function (Arias intensity vs time) was estimated for each acceleration waveform to obtain the time frames corresponding at each specific percentage of the total arias intensity (5%, 75%, and 95%).

Figure 1 reports the correlogram of the intensity measures and explanatory variables: it shows the measures of the “strength” of the linear relationship between the DSRs and the variables: a strong positive correlation with RJB and a moderate positive correlation with Mw were observed, as expected. The correlations with the other variables are weaker, probably also due to the uncertainty associated with their estimation.

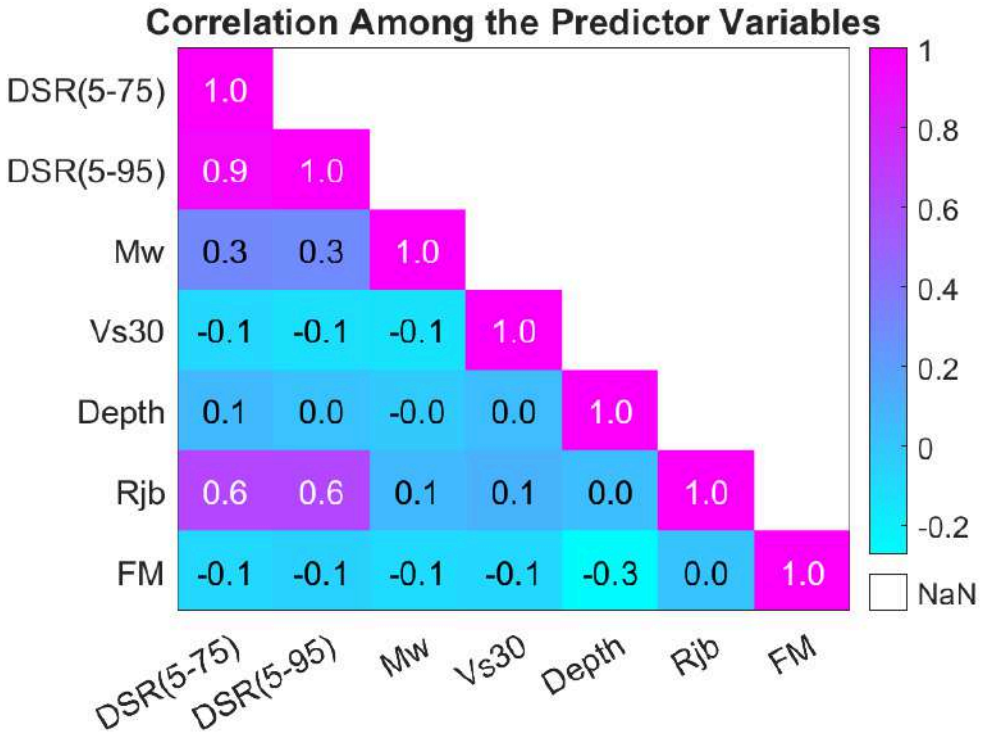

Figure 1: Durations' Correlations for Geometric Mean of the Horizontal Components with GMMs explanatory variables

Residuals were calculated, which represent the difference between the observed durations and the duration predicted by a specific model. It shows how well or poorly a model's predictions are close to the observed duration. After observing the duration, the predicted duration was calculated according to the models given by Bommer et al., (2009), Afshari and Stewart (2016), and Tafreshi and Bora (2023). Bommer et al., (2009) model and study were based on a strong motion dataset extracted from the database compiled for the NGA-West project (Chiou et al., 2008), whose main purpose is to calibrate GMM for active crustal earthquakes in the Western US. The dataset used consists of 2406 records from 114 earthquakes with moment magnitudes in the range from 4.8 to 7.9. Afshari and Stewart (2026) model was based on the NGA-West2 project (Ancheta et al., 2014), and it was reduced to 11,284 duration pairs of duration parameters for two as-recorded horizontal components with a Mw range between 3.0-7.9 events. Tafreshi and Bora (2023) model was calibrated on an Iranian strong motion database. The dataset used consists of 1749 records from 566 events with a Mw range from 3 to 7.5, recorded at 338 stations from 1976 to 2020. The total residual was calculated for each record by subtracting the logarithmic of the observed duration from the logarithmic of the predicted duration. Logarithmic was used since the durations are log-normally distributed. The distribution showed that all the models on average underestimated the observed durations, but the model by Afshari and Stewart (2016) has a better median performance and lower associated variability (Figure 2).

These results suggest that the functional form proposed by Afshari & Stewart (2016) is a good starting point for the calibration of a new predictive model for duration in Italy.

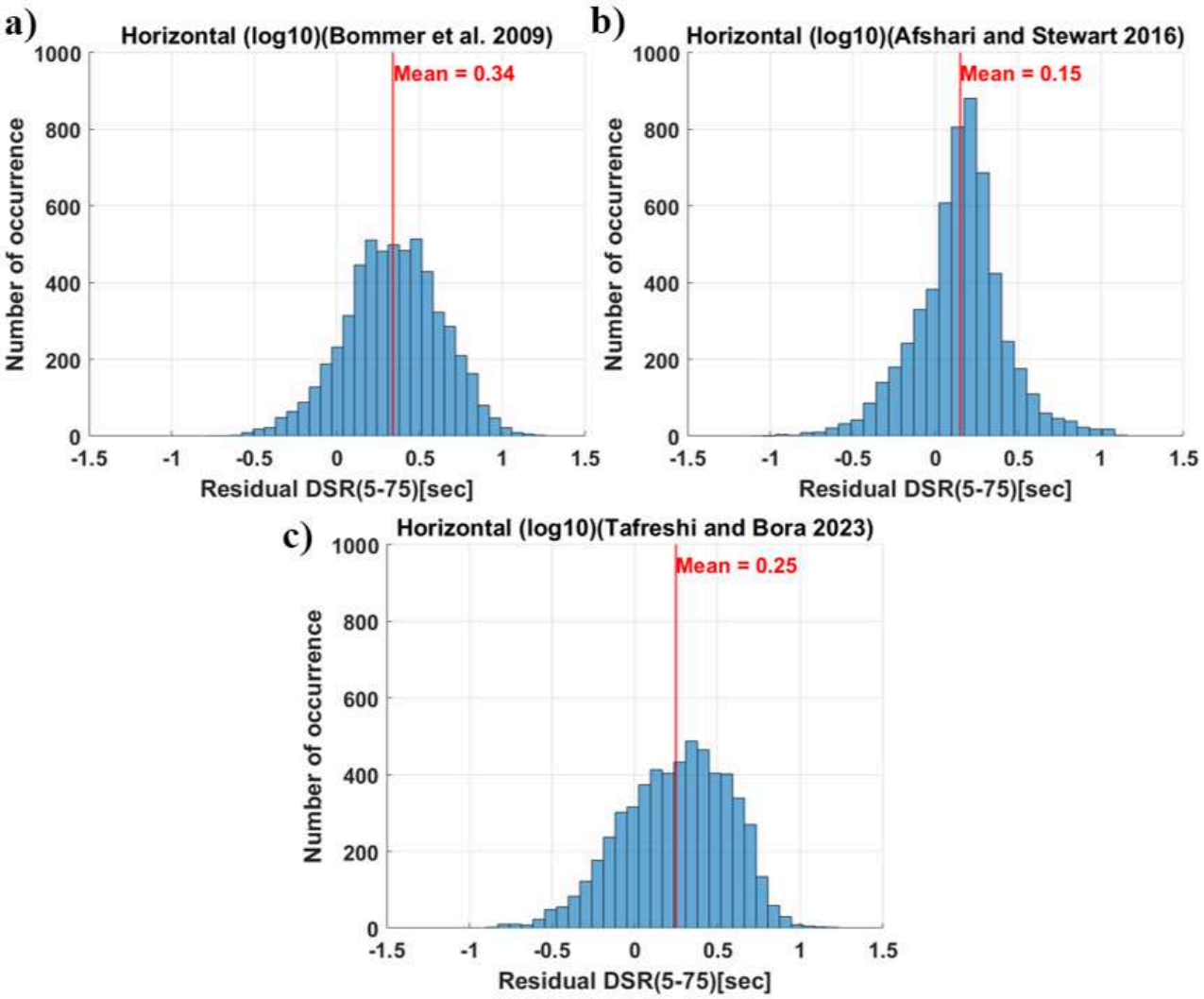

Figure 2: Residual for the horizontal DSR(5-75) for the Three Models: a) Bommer et al. 2009, b) Afshari and Stewart 2016, and c) Tafreshi and Bora 2023

The residuals were subsequently decomposed by applying the random effects approach (Al Atik et al. 2010) into offset (a0), between event (δBe), site-to-site (δS2Ss), and event-and-site corrected (δW0es) terms to check that the scaling with magnitude, distance, and V_{S30} (which are the main explanatory variables) of the considered models are compatible with those observed for ITA18. The results showed that all the models did not capture the magnitude scaling of ITA18 data: Bommer et al. (2009) and Tafreshi and Bora (2023) have similar trends, underestimating the low magnitude durations and overestimating the high magnitude ones. Afshari & Stewart (2016) GMM has a better median performance, but the duration observed for high magnitude earthquakes are underestimated (Figure 3-a,d & g). The other residuals did not exhibit significant bias, except for the event and site corrected residuals of Tafreshi and Bora (2023), which showed a different scaling with distance, probably because the model mimics the regional attenuation characteristics of Iran, for which the model was calibrated.

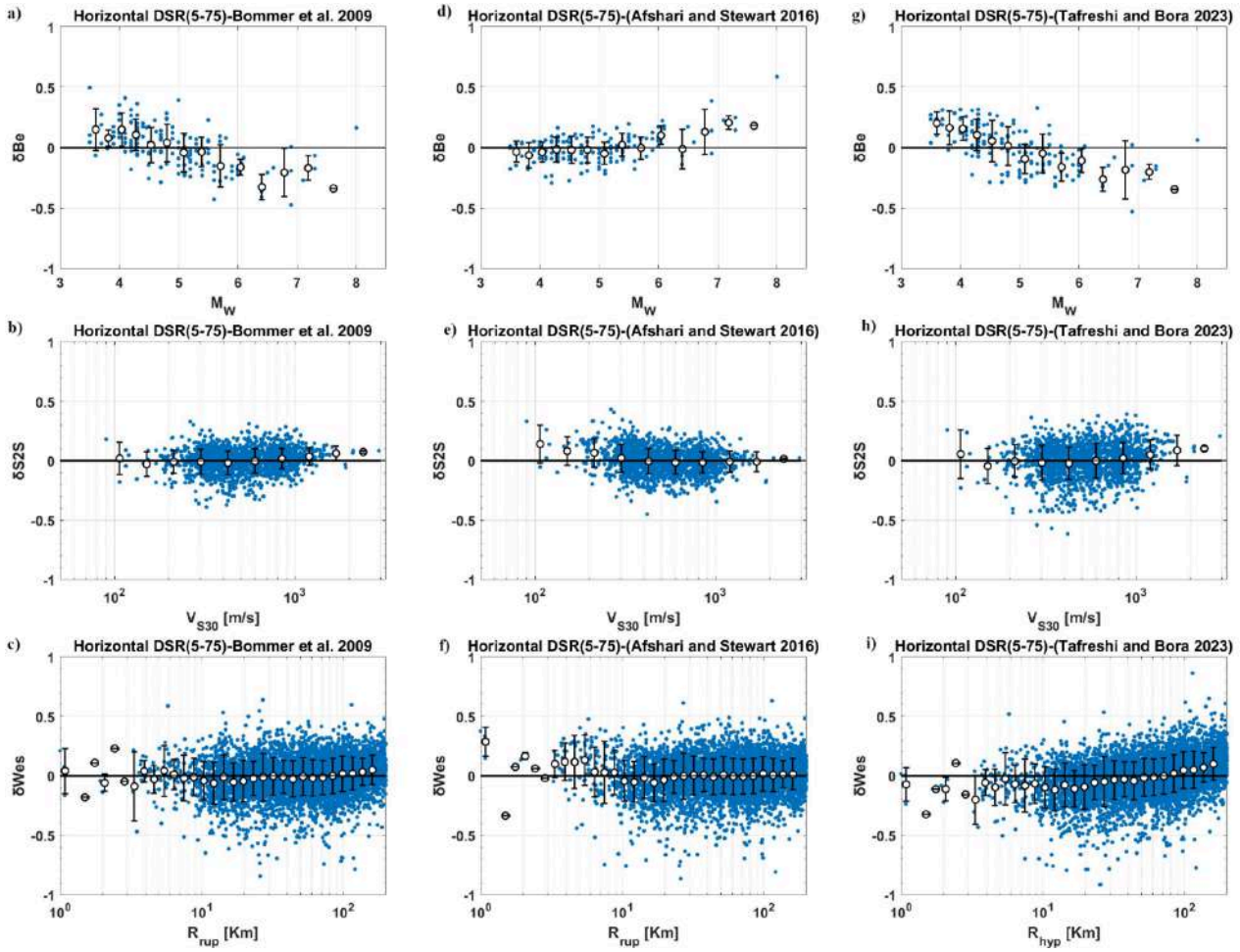

Figure 3: Distribution of a) between events residuals for Bommer, et al., (2009) model, b) site-to-site residuals for Bommer, et al., (2009) model, c) event-and-site residuals for Bommer, et al., (2009) model, d) between events residuals for Afshari & Stewart, (2016) model, e) site-to-site residuals for Afshari & Stewart, (2016) model, f) event-and site residuals for Afshari & Stewart, (2016) model, g) between events residuals for Tafreshi and Bora (2023) model, h) site-to-site residuals for Tafreshi and Bora (2023) model, i) event-and-site residuals for Tafreshi and Bora (2023) model.

References

Afshari K., and Stewart J. P.; (2016): Physically Parameterized Prediction Equations for Significant Duration in Active Crustal Regions. Earthquake Spectra, 29.

Al Atik L., Abragamson N., Bommer JJ., Scherbaum F., Cotton F., Kuehn N., The variability of ground-motion prediction models and its components. Seismol Res Lett. 2010;81(5):794-801.

Ancheta T. D., Darragh R. B., Stewart J. P., Seyhan E., Silva W. J., Chiou B. S.-J., Wooddell K. E., et al.; (2014): NGA-West2 Database. Earthquake Spectra, 30, 989–1005.

Bommer J. J., Stafford P. J., and Alarcón, J. E.; (2009): Empirical Equations for the Prediction of the Significant, Bracketed, and Uniform Duration of Earthquake Ground Motion. Bulletin of the Seismological Society of America, 99(6), 3233.

Chiou B., Darragh R., Gregor N., and Silva W.; (2008): NGA Project Strong-Motion Database. Earthquake Spectra, 24(1), 23–44.

Lanzano G., Luzi L., Pacor F., et al.; (2019): A revised ground-motion prediction model for shallow crustal earthquake in Italy. Bull Seismol Soc Am.; 109(2):525-540.

Lanzano G., Ramadan F., Luzi L., Sgobba S., Felicetta C., Pacor F., D'Amico M.C., Puglia R., Russo E.; (2022): Parametric table of the ITA18 GMM for PGA, PGV and Spectral Acceleration ordinates. Istituto Nazionale di Geofisica e Vulcanologia (INGV). <https://doi.org/10.13127/ita18/sa_flatfile>

Ramadan F., Smerzini C., Lanzano G., Pakor F.;(2021): An empirical model for the vertical-to-horizontal spectral ratios for Italy. Earthquake Engineering and structural dynamics; 50(15): 3937-4219.

Tafreshi M. D., and Bora S. S.; (2023): Empirical ground motion models (GMMs) and associated correlations for cumulative absolute velocity, Arias intensity, and significant durations calibrated on Iranian strong motion database. Bulletin of Earthquake Engineering, 21, 4139–4166.

Corresponding author: batoul.a.shoaib@gmail.com

The database of the Catalogue of Strong Earthquakes in Italy and in the Mediterranean Area (CFTI): exploring historical seismology through modern web tools

G. Tarabusi[1], C. Ciuccarelli[1], M.G. Bianchi[1], C. Zei[1,2], D. Mariotti[1], G. Sgattoni[1], R.C. Taccone[1], G. De Francesco[1], G. Ferrari[1], G. Valensise[1], CFTI working group

[1] *Istituto Nazionale di Geofisica e Vulcanologia, Italy*
[2] *Dept. of Physics and Earth Sciences, Ferrara University, Italy*

CFTI, the Catalogue of Strong Earthquakes in Italy and in the Mediterranean Area, is an analytical inventory that stores in a large database the results of four decades of research in Historical Seismology on Italy and on the Mediterranean area.

CFTI is both parametric and analytical, as for most of the analysed earthquakes it features descriptive summaries of both the effects of each specific event at each individual location, and of its overall social and economic impact. But it is also a fully transparent database, as for each investigated earthquake sequence it provides a complete bibliography of all available testimonies of scholars and casual observers: many of such testimonies are supplied on-line, either in the form of the original source or as a transcription.

Since the beginning of the research in 1983, the Working Group developed a specific computerised cataloguing scheme of all historical materials identified along selected research paths. The work was extremely extensive from its very beginning; numerous previously unknown or poorly known earthquakes were added to the previously available wealth of knowledge. The method used for unearthing and organising the new information and the resulting elaborations has been gradually refined and consolidated in the subsequent versions of the CFTI.

The current version of the catalogue, termed CFTI5Med (Guidoboni et al., 2018; Guidoboni et al., 2019), includes 1,167 earthquakes for the Italian area and 473 earthquakes for the extended Mediterranean region (the latter section deals exclusively with ancient and medieval events). It hence draws from an extremely valuable and unique documentary and historical heritage: one of the most important in the world, in terms of quantity, quality and geographic distribution of the available information, and also in terms of the relevant chronological interval, spanning over two millennia (from the 8th century B.C. to the 15th century for Mediterranean area; from the 5th century B.C. to the 20th century for Italy).

Since the release of CFTI5Med, which features an entirely renovated and advanced web interface, we added various datasets and developed new IT tools, all accessible via the CFTILab web portal (Tarabusi et al., 2020), which are the result of synergistic collaboration among the various skills that exist in the CFTI Working Group. Our aim was to enable multiple specialist and non-specialist users – including scholars, civil protection officers, teachers, students, professionals, and simply curious citizens – to explore and analyse efficiently the extensive wealth of data stored in the Catalogue. We briefly present here four of its main components (tools and datasets).

CFTIcompare is a web-based tool that allows for a visual comparison of the effects of two different earthquakes, or of the intensity data supplied by two different studies of the same earthquake.

The comparison is performed on a geographical basis, and may concern either data from the CFTI alone (which are shown along with summaries of the effects for each individual location) – for example to compare the effects of two earthquakes that occurred in adjacent areas – or from other databases (e.g. ASMI, DBMI, Hai sentito il terremoto?).

The user may also use his/her own dataset, provided that it is organised following one of the three allowed input formats.

CFTIvisual (Bianchi et al., 2022) is the Atlas of visual sources on Italian historical earthquakes (Fig. 1).

About four decades of investigation of Italian historical earthquakes led to the retrieval of many visual sources, including engravings, paintings, photographs, film documents, etc. They may be useful to scholars from different disciplines for supplementing information on the estimation of damage, on the response of institutions, on scientific observations, etc.

Currently the Atlas allows for advanced consultation of all visual sources that concern Italian earthquakes and can be freely published. Dedicated links allow connecting the sources to contextual descriptive information from CFTI.

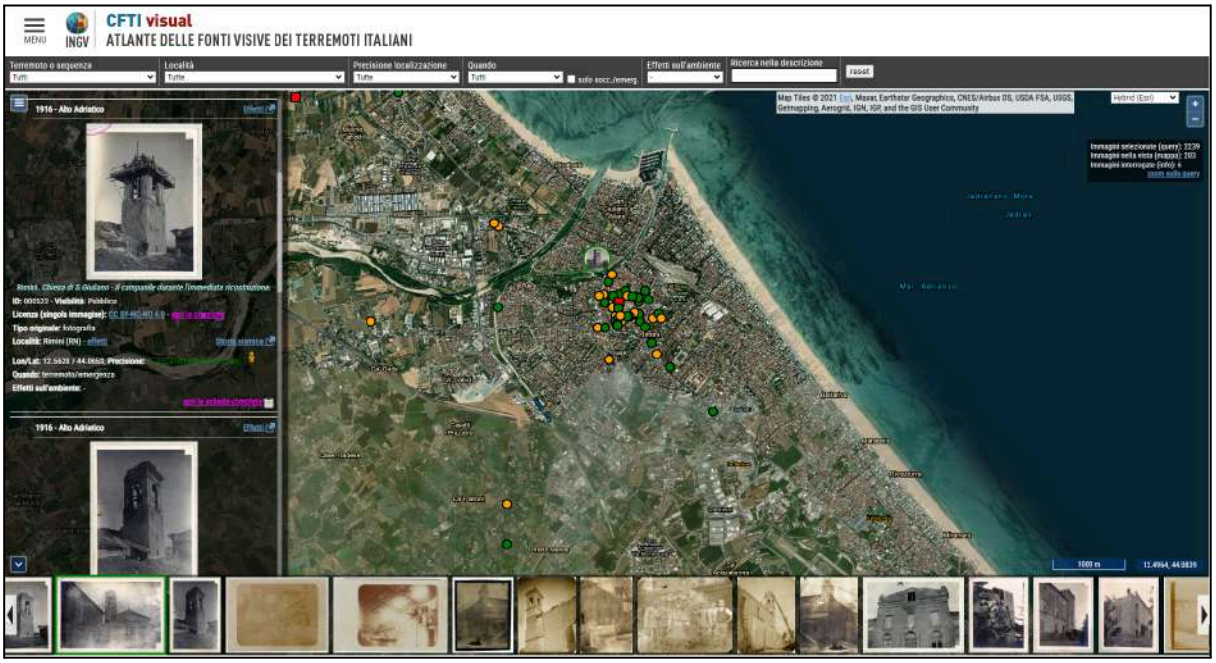

Fig. 1 - CFTIvisual web interface.

CFTIsequences displays the earthquake sequences through interactive graphs and maps (Fig. 2). This result has been made possible through extensive data review of historical sources aimed at integrating and validating data related to the chronology, the location, and the effects of individual shocks.

It allows users to consult the available data for individual shocks and for individual locations while keeping all descriptive textual comments visible.

Since the publication of its first release (1995), the CFTI paid much attention to the existence of any foreshocks and aftershocks and of their time and space evolution. This was accomplished by dedicating a specific descriptive commentary to these shocks.

This product is fully functional: it currently contains two sequences for demonstration purposes only, but will soon provide data from more than 100 sequences stored in the CFTI.

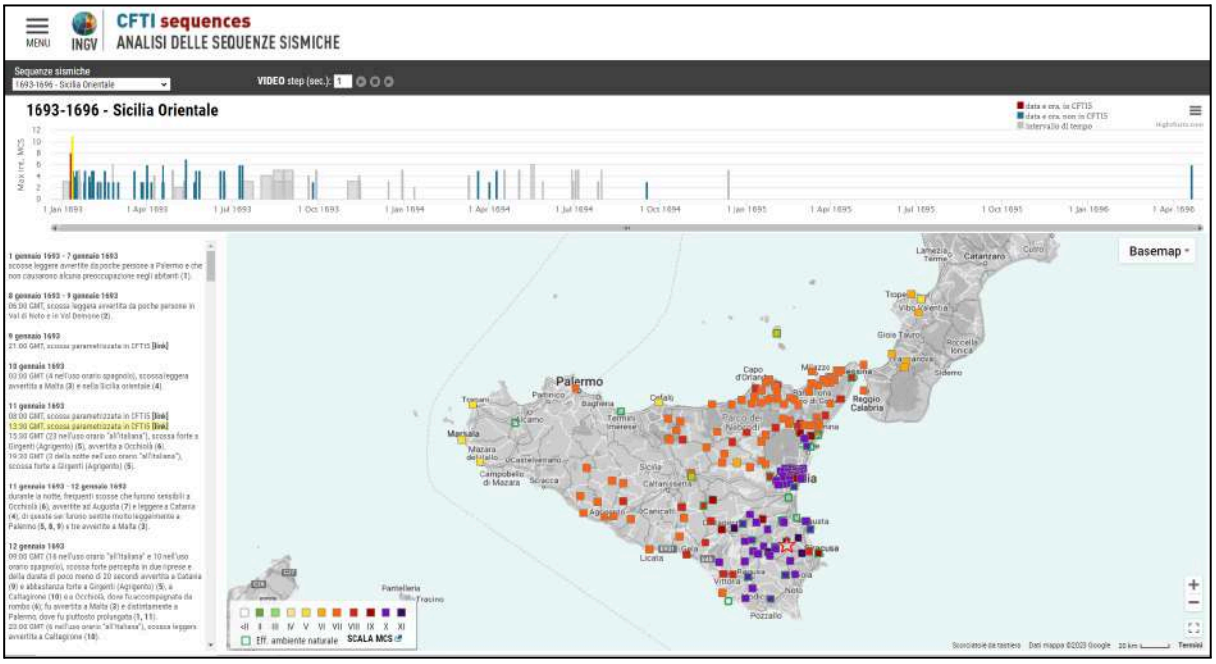

Fig. 2 - CFTIsequences web interface.

CFTIlandslides (Zei et al., 2023) is the Italian database of historical earthquake-induced landslides (Fig. 2).

The investigation of earthquake-induced environmental phenomena is becoming increasingly critical for civil protection agencies. In particular, earthquake-triggered landslides may cause significant losses and may delay rescue operations across large areas.

The combination of a relatively frequent seismic release with a very high landslide susceptibility makes the Italian territory especially prone to the occurrence of earthquake-induced landslides.

This is a new dataset that was developed starting from the effects on the natural environment stored in CFTI5Med. It features over 1,200 landslides, subdivided into classes based on location accuracy and type of movement. It is addressed to a large audience of potential users, including researchers and scholars, administrators and technicians belonging to local institutions, civil protection authorities.

A single, comprehensive web portal is currently under development to provide access to all these products.

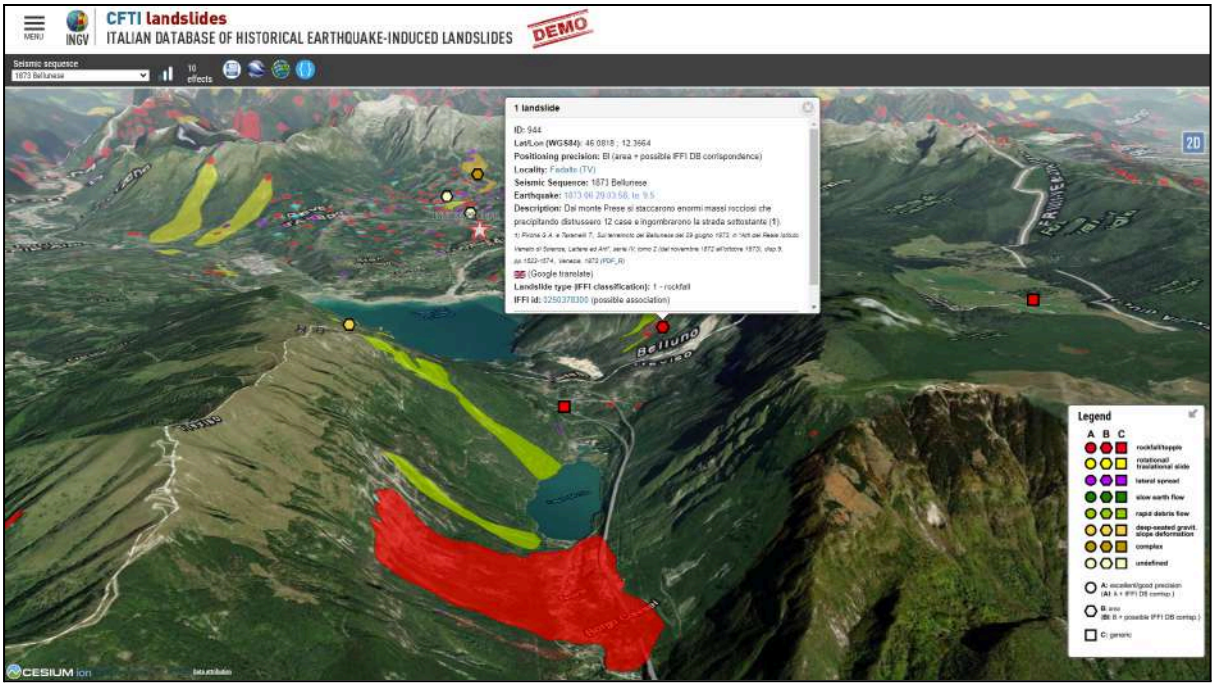

Fig. 3 - CFTIlandslides web interface (3D Map View).

Acknowledgments

Part of the activities have been supported by a grant from Italy's Presidenza del Consiglio dei Ministri-Dipartimento della Protezione Civile. Nevertheless, the views and conclusions reported are the sole responsibility of the authors, and should not be interpreted as necessarily representing official policies, either expressed or implied, of the Dipartimento della Protezione Civile.

References

Bianchi M.G., Tarabusi G., Ciuccarelli C., Maresci M., Baranello S., Taccone R.C., Ferrari G., 2022. CFTIvisual, Atlante delle fonti visive dei terremoti italiani. Istituto Nazionale di Geofisica e Vulcanologia (INGV). https://doi.org/10.13127/cfti/visual

Guidoboni E., Ferrari G., Mariotti D., Comastri A., Tarabusi G., Sgattoni G., Valensise G., 2018. CFTI5Med, Catalogo dei Forti Terremoti in Italia (461 a.C.-1997) e nell'area Mediterranea (760 a.C.-1500). Istituto Nazionale di Geofisica e Vulcanologia (INGV). doi: https://doi.org/10.6092/ingv.it-cfti5

Guidoboni E., Ferrari G., Tarabusi G., Sgattoni G., Comastri A., Mariotti D., Ciuccarelli C., Bianchi M.G., Valensise G., 2019, CFTI5Med, the new release of the catalogue of strong earthquakes in Italy and in the Mediterranean area, Scientific Data 6, 80. doi: https://doi.org/10.1038/s41597-019-0091-9

Tarabusi G., Ferrari G., Ciuccarelli C., Bianchi M.G., Sgattoni G., Comastri A., Mariotti D., Valensise G., Guidoboni E. , 2020, CFTILab, Laboratorio Avanzato di Sismologia Storica. Istituto Nazionale di Geofisica e Vulcanologia (INGV). https://doi.org/10.13127/CFTI/CFTILAB

Zei C., Tarabusi G., Ciuccarelli C., Mariotti D., Baranello S., Sgattoni G., Burrato P., CFTI working Group; 2023: *A new database of historical earthquake-induced landslides in Italy*, 41st National Conference of the GNGTS, Bologna https://gngts.ogs.it/atti/GNGTS2023/HTML/212/

Corresponding author: gabriele.tarabusi@ingv.it

The estimation of b-value of the frequency-magnitude distribution and of its one-sigma intervals from binned magnitude data

S. Tinti[1], P. Gasperini[1,2]

[1] *Dipartimento di Fisica e Astronomia "Augusto Righi", Università di Bologna, Bologna, Italy*
[2] *Istituto Nazionale di Geofisica e Vulcanologia, Sezione di Bologna, Bologna, Italy*

The estimation of the slope (b-value) of the frequency magnitude distribution of earthquakes is based on a formula derived by Aki (1965) decades ago, assuming a continuous exponential distribution. However, as the magnitude is usually provided with a limited resolution, its distribution is not continuous but discrete. In the literature this problem was initially solved by an empirical correction (due to Utsu, 1966) to the minimum magnitude, and later by providing an exact formula such as that by Tinti and Mulargia 1987, based on the geometric distribution theory. A recent paper by van der Elst (2021) showed that the b-value can be estimated also by considering the magnitude differences (which are proven to follow an exponential discrete Laplace distribution) and that in this case the estimator is more resilient to the incompleteness of the magnitude dataset.

In this work we provide the complete theoretical formulation including i) the derivation of the means and standard deviations of the discrete exponential and Laplace distributions; ii) the estimators of the decay parameter of the discrete exponential and trimmed Laplace distributions; and iii) the corresponding formulas for the parameter b. We further deduce iv) the standard one-sigma intervals for the estimated b. Moreover, we are able v) to quantify the error associated with the Utsu (1966) minimum-magnitude correction.

We tested extensively such formulas on simulated synthetic datasets including complete catalogues as well as catalogues affected by a strong incompleteness degree such as aftershock sequences where the incompleteness is made to vary from one event to the next.

References

Aki, M. (1965). Maximum likelihood estimate of b in the formula log N = a – bM and its confidence limits, Bull. Earthquake Res. Inst., Tokyo Univ. 43, 237-239. https://doi.org/10.15083/0000033631.

Tinti, S. & Mulargia, F. (1987). Confidence intervals of b values for grouped magnitudes. Bull. Seism. Soc. Am., 77, 2125-2134. Doi: 10.1785/BSSA0770062125.

Utsu, T. (1966). A statistical significance test of the difference in b-value between two earthquake groups, J. Phys. Earth 14, 34–37. https://doi.org/10.4294/jpe1952.14.37.

van der Elst, N. J. (2021). B-positive: A robust estimator of aftershock magnitude distribution in transiently incomplete catalogs. J.of Geophys. Res.: Solid Earth, 126, e2020JB021027. https://doi. org/10.1029/2020JB021027.

Corresponding author: paolo.gasperini@unibo.it

The Multi Synthetic Catalog Analysis (MSCA) as a tool to evaluate seismic hazard, risk and resilience

T. Tufaro[1]

[1] *School of Civil Engineering, University of Basilicata, I-85100 Potenza, Basilicata, Italy*

The classical approach to seismic hazard evaluation is the PSHA method (Cornell, 1968). It is still an excellent approach if we are interested in computing seismic hazard only. However if we wish to include other quantities such as risk or resilience it is better to follow a different method.

The proposal presented here is based on the concept of building a very large number of synthetic catalogs (up to several hundred thousands) that will result in tens of millions of events. It naturally allows for inclusion of:

Risk and resilience scenarios probability;

Time evolution.

The acceleration is computed at each site and the damage is evaluated: each event generates a complete probabilistic scenario. Let us suppose focusing on bridges; a damage scenario where fragility curves can be considered also probabilistic, will lead to the possibility of computing the total repairing cost and necessary timing. This in turn will allow for evaluating the disturbance to local communities, the interruption of local traffic and the overall time necessary to recover it. All of the aboves can be evaluated with a probabilistic setting. The statistics are then conducted on all scenarios. The underlying idea is that, set the quantity we are looking for, let us say the numbers of days commuters loose because of road interruption, and set the number of synthetic catalogs, let us say 100.000, we will select the 100.000 largest values (out of even tenths of millions of events) where the 10% probability threshold will be the one at the 90.000 largest value. Every scenario has a centroid, so the process can be repeated for every possible centroid location. It is obviously a very computationally heavy approach but it can give the appropriate view where major issues are expected. Moreover it is possible to introduce a full time dependent seismic evaluation of the hazard. Fig.1 shows the hazard due the classical seismic zoning (attenuation: Bindi et al., 2011). Since the attenuation law is different from those used in the MPS04, it looks obviously slightly different but it conveys the idea of the equivalence of the two approaches.

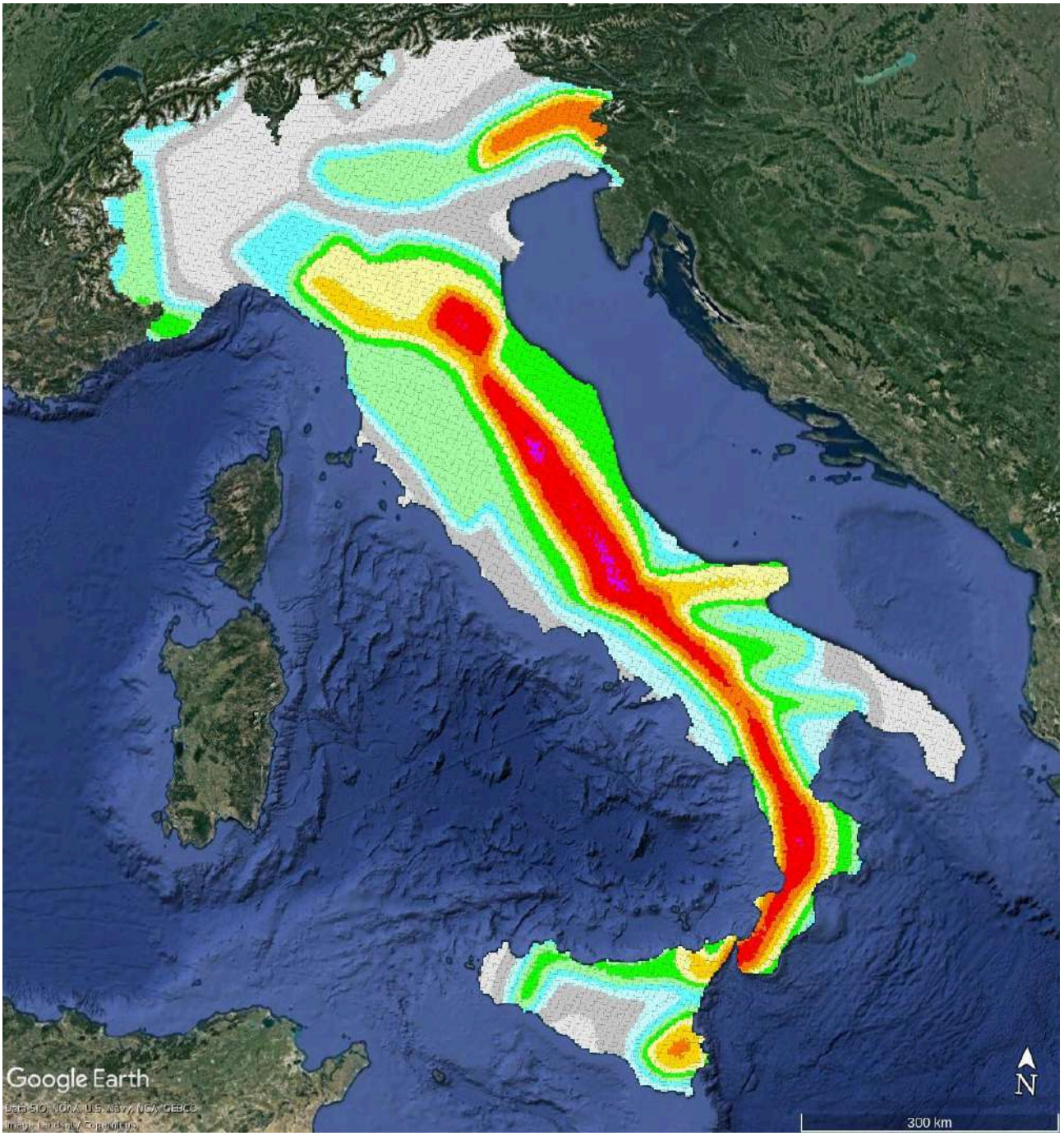

Fig.1 Hazard map due to classical seismic zoning (attenuation: Bindi et al., 2011).

To give a flavour of what the proposed method can achieve, Fig.2 shows the results of a prototypical non poissonian approach where the 10% exceeding probability is not in 50 years but in the next 50 years.

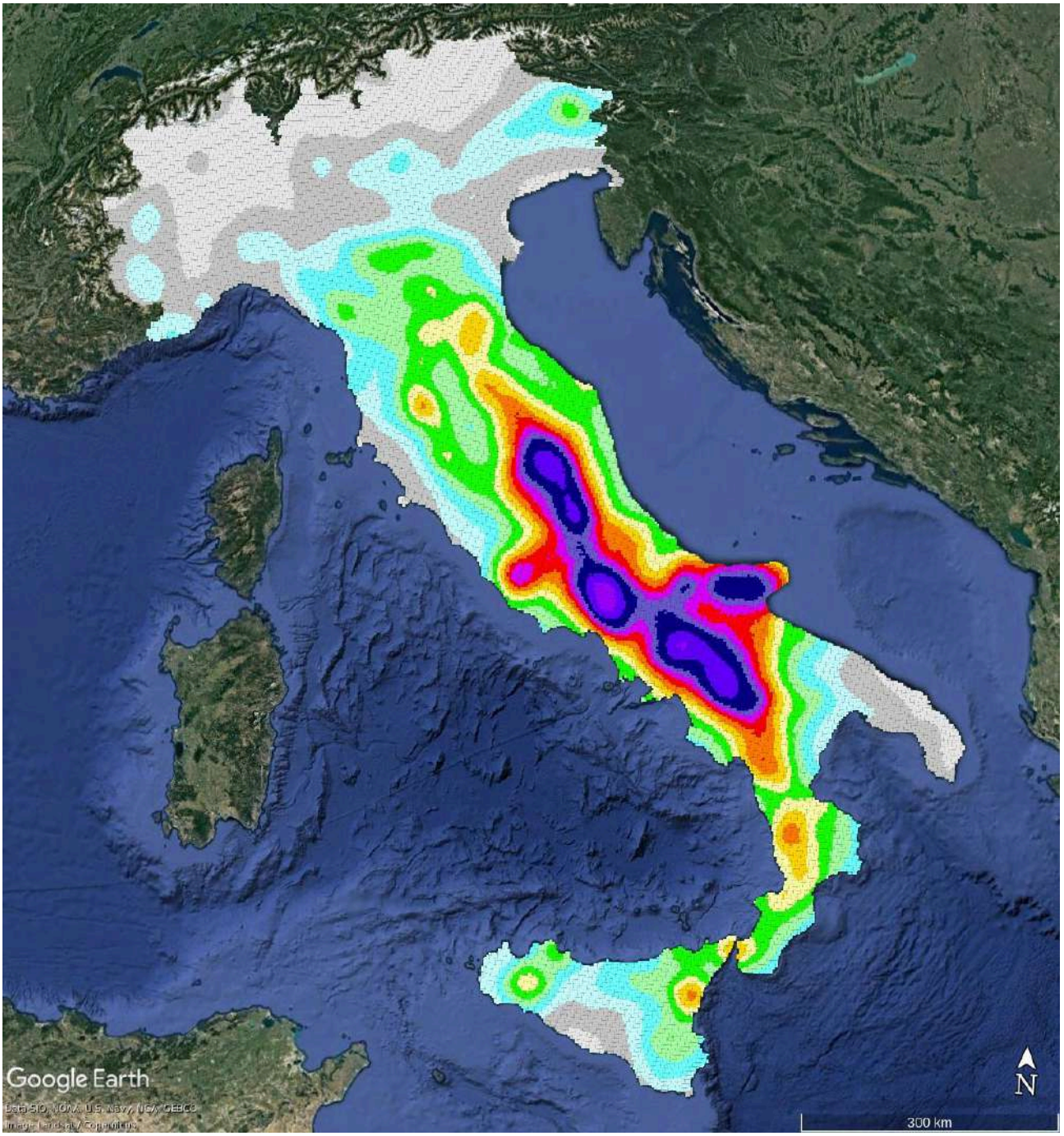

Fig.2 Thematic map of the results obtained through a prototype non-Poissonian approach in which the probability of exceeding 10% is not in 50 years but in the next 50 years.

This model was kindly given by the group (based in University of Basilicata, OGS, INGV-OV, and University of Trieste) that is developing it, and it is based on an extension of Harabaglia (2020) approach. It is based on earthquake data (HORUS) of Lolli et al., (2020) with magnitude M>3.95 in the time interval 1960-2022, and it takes into account the historical locations of the CPTI15 catalog (Rovida et al., 2022) in the time interval 1000-1959. It must be no means be intended as an actual proposal of earthquake hazard in the next 50 years, since the model must still be tuned, but only as an example of what the MSCA can do.

References

Bindi D., Pacor F., Luzi L., Puglia R., Massa M., Ameri G., Paolucci R.; 2011: Ground motion prediction equations derived from the Italian strong motion database. Bull Earthquake Eng, 9(6), 1899–1920. doi:10.1007/s10518 -011-9313.

Cornell; C.A. 1968: Engineering seismic risk analysis. Bull. Seismol. Soc. Am 58, 1583-1606.

Harabaglia P.; 2020: Non-Poissonian Earthquake Occurrence Probability through Empirical Survival Functions Appl. Sci. 2020, 10(3), 838; https://doi.org/10.3390/app10030838 Submission received: 13 December 2019 / Revised: 15 January 2020 / Accepted: 18 January 2020 / Published: 24 January 2020

Lolli B., Randazzo D., Vannucci G., Gasperini P.; 2020: The Homogenized Instrumental Seismic Catalog (HORUS) of Italy from 1960 to Present, Seismol. Res. Lett, doi: 10.1785/0220200148.

Rovida A., Locati M., Camassi R., Lolli B., Gasperini P., Antonucci A.; 2022: Catalogo Parametrico dei Terremoti Italiani (CPTI15), versione 4.0. Istituto Nazionale di Geofisica e Vulcanologia (INGV). https://doi.org/10.13127/CPTI/CPTI15.4.

Corresponding author: ttufaro250@gmail.com

Un confronto teorico tra scale macrosismiche utilizzate in Italia

G. Vannucci[1], B. Lolli[1], P. Gasperini[2,1]

[1]Istituto Nazionale di Geofisica e Vulcanologia, Sezione di Bologna, Bologna, Italy
[2]Dipartimento di Fisica e Astronomia "Augusto Righi", Università di Bologna, Bologna, Italy

In un recente lavoro (Vannucci et al., 2021) abbiamo evidenziato alcune discrepanze empiriche tra le stime dell'intensità macrosismica in Italia nell'ultimo decennio rispetto ai precedenti periodi. Una possibile ragione potrebbe essere la progressiva adozione da parte dei ricercatori italiani della Scala Macrosismica Europea (EMS, Grünthal et al., 1998) al posto della scala Mercalli Cancani Sieberg (MCS; Sieberg, 1912, 1932) utilizzata invece in maniera prevalente fino al 2009. In teoria, in un insediamento moderno in cui gli edifici in cemento armato (RC) stanno sempre più sostituendo quelli in muratura, l'intensità EMS dovrebbe sovrastimare quella MCS perché la prima tiene conto della minore vulnerabilità degli edifici in RC, mentre la seconda non menziona affatto gli edifici in RC poiché questi erano quasi assenti all'epoca in cui fu compilata. Tuttavia, tale deduzione teorica è contraddetta dall'evidenza empirica che, in media, le intensità MCS realmente stimate in Italia nell'ultimo decennio sovrastimano leggermente la EMS e non viceversa come dovrebbe essere. Una possibile spiegazione è che la scala EMS non sia stata ben calibrata per riprodurre la MCS come era nelle intenzioni dei suoi autori. Un'altra possibile ragione delle discrepanze tra l'ultimo decennio e i precedenti potrebbe essere che la scala MCS applicata oggi non è la stessa definita da Sieberg all'inizio del XX secolo. Per comprendere meglio le possibili cause di queste discrepanze, presentiamo qui un confronto formale tra le definizioni dei diversi gradi di tali scale macrosismiche.

References

Grünthal, G. (Editor) (1998). European Macroseismic Scale 1998, Vol. 13, Conseil de l'Europe, Cahiers du Centre Européen de Géodynamique et de Séismologie, Luxembourg, Luxembourg, 99 pp.

Sieberg, A. (1912). Über die makroseismische Bestimmung der Erdbebenstärke. Ein Beitrag zur seismologische Praxis, G. Gerlands Beitr. Geophys. 11, nos. 2/4, 227–239 (in tedesco).

Sieberg, A. (1932). Erdebeben, in Handbuch der Geophysik, B. Gutenberg (Editor), Vol. 4, 552–554 (in tedesco).

Vannucci G, Lolli B, Gasperini P (2021) Inhomogeneity of macroseismic intensities in Italy and consequences for macroseismic magnitude estimation. Seism Res Lett 92:2234–2244. Doi: 10. 1785/0220200273.

Corresponding author: gianfranco.vannucci@ingv.it

Do not call them foreshocks

D. Zaccagnino[1*], L. Telesca[2], C. Doglioni[1,3]

[1] *Sapienza University, Earth Sciences Department, Rome, Italy*
[2] *Institute of Methodologies for Environmental Analysis, National Research Council, Tito, Italy*
[3] *Istituto Nazionale di Geofisica e Vulcanologia (INGV), Rome, Italy*

One of the most intriguing issues in earthquake science concerns the discrimination between foreshocks and swarms. We investigate relocated seismic catalogues in California and Italy and provide a theoretical explanation of our results.

Foreshocks and swarms share the same scaling behaviours and are likely generated by the same physical mechanism; however, statistical analyses highlight that foreshocks spread over larger areas, are featured by larger and more energetic clusters with also higher variance of magnitudes and relative Tsallis and Shannon entropies. On the other hand, foreshocks have duration, seismic rates, and moment rates, as well as magnitude trends and clustering properties indistinguishable from swarms. Our results prove that mainshocks can occur with or without foreshocks with extremely variable magnitudes. In fact, in crustal volumes, the value of stress at a certain time depends on the history of recently happened variations of the stress itself, depending on memory kernels, and fine-scale structural details of fault interfaces and tectonic forces. This means that even two identical seismic clusters can flow into a large mainshock, moderate events or a swarm depending on the action of tiny details in the evolution of stress gradients. On the other hand, two completely different seismic patterns can give rise to seismic events with similar features. This result strongly challenges the possibility of accurate earthquake prediction, both in terms of time to failure and magnitude, at least just considering past seismic activity. A mathematical model is realized to explain our observations.

Clusters covering large areas are displays of long-range correlations within larger crustal volumes. As tectonic strain increases the level of stress, faults become more and more unstable, until a spontaneous rupture develops on the weakest interface. Static and dynamic stress variations trigger further events afterwards within the crustal volume showing significant correlations with the hypocenter, i.e., sensitivity to stress perturbations. The larger the region close to instability, the more seismic events can be triggered and with statistically higher magnitudes. This is the reason why mainshocks tend to happen after clusters spread over larger areas, with higher number of events and magnitudes not because such seismic activity ultimately triggers them. However, foreshocks are not “fore-shocks''; they are not informative about the magnitude or time-to-failure of the eventually impending earthquake. Earthquakes ultimately grow to become giant events because of fine details of differential stress patterns and

fault strength, regardless of previous seismic activity, if the extension of the prone-to-failure volumes is large enough.

References

Shannon C.E. (1948). A mathematical theory of communication. Bell Syst. Tech. J., **27**(3), 379-423.

Tsallis C. (1988). Possible generalization of Boltzmann-Gibbs statistics. J. Stat. Phys., **52**, 479-487.

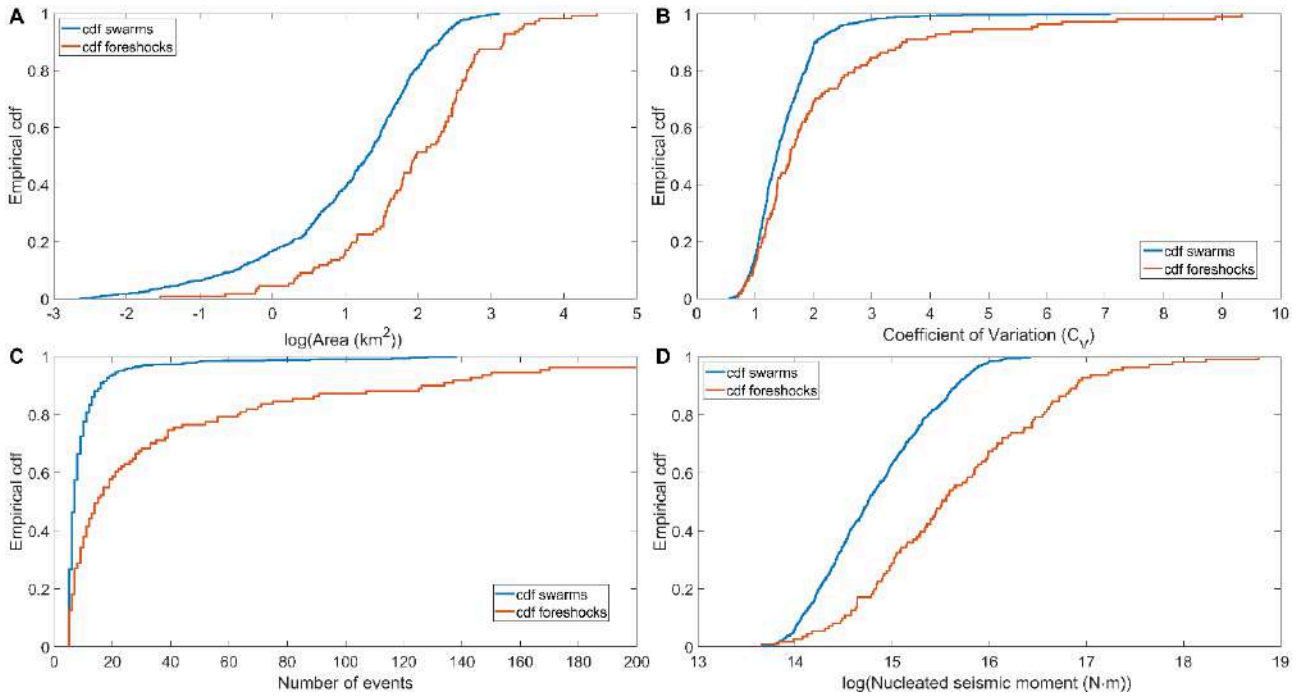

Fig. 1: Cumulative distribution of the number of seismic events in each cluster until the mainshock as a function of their various features: area (A), global coefficient of variation (B), number of events (C), nucleated seismic moment (D) in Southern California from 1981 to 2022 (only events with Mw > 2.5 are included in the analysis).

Possible applications of self-similarity in earthquake clustering to seismic hazard

D. Zaccagnino[1*], L. Telesca[2], C. Doglioni[1,3]

1 Sapienza University, Earth Sciences Department, Rome, Italy

2 *Institute of Methodologies for Environmental Analysis, National Research Council, Tito, Italy*
3 Istituto Nazionale di Geofisica e Vulcanologia (INGV), Rome, Italy

We perform an analysis to understand what information may be hidden in partial, limited earthquake catalogues only containing mid-size and a few large seismic events (or even no one) about the largest possible ones using clustering properties of recorded events. We consider the local and global coefficients of variation, the scaling exponent of the Gutenberg–Richter law, the fractal dimension of epicentral series D_f, the seismic rate and the number of events. We find that the largest earthquakes occur in locally Poissonian systems (local coefficient of variation of interevents L_V 1) with globally clustered dynamics (global coefficient of variation C_V1). While local clustering in time is strongly dependent on the size of the catalogue, so that longer databases tend to be less regular and more Poissonian than shorter ones, the global coefficient seems to be a reliable parameter even in cases of rather limited available information, e.g., few thousand events (Zaccagnino et al., 2023a). We analyse regional seismicity in different tectonic settings getting analogous results, e.g., Southern California, Cascadia (Zaccagnino et al., 2022), Italian Apennines, New Zealand (Zaccagnino et al., 2023a), and Turkey (Zaccagnino et al., 2023b). The fractal dimension of spatial series is positively correlated with the seismic rate, C_V and the maximum listed magnitude. Conversely, the b-value does not show any correlation with the principal observables except for the number of earthquakes. We explain this phenomenon considering the different sizes of mainshocks in various tectonic settings. We propose that the predictive power of clustering properties stems from the self-similar nature of slow dynamics producing the emergence of slips in complex systems such as the brittle crust. Prospectively, this approach can be of great interest, once tuned, to extrapolate the features of extreme, still unobserved events given a limited database.

References

Zaccagnino D., Telesca L. and Doglioni C.; 2022: Variable seismic responsiveness to stress perturbations along the shallow section of subduction zones: The role of different slip modes and implications for the stability of fault segments. Front. Earth Sci., 10, 989697.

Zaccagnino D., Telesca L. and Doglioni, C.; 2023: Global versus local clustering of seismicity: Implications with earthquake prediction. Chaos Solit. Fractals, 170, 113419.

Zaccagnino D., Telesca L., Tan O. and Doglioni, C.; 2023: Clustering Analysis of Seismicity in the Anatolian Region with Implications for Seismic Hazard. Entropy, 25(6), 835.

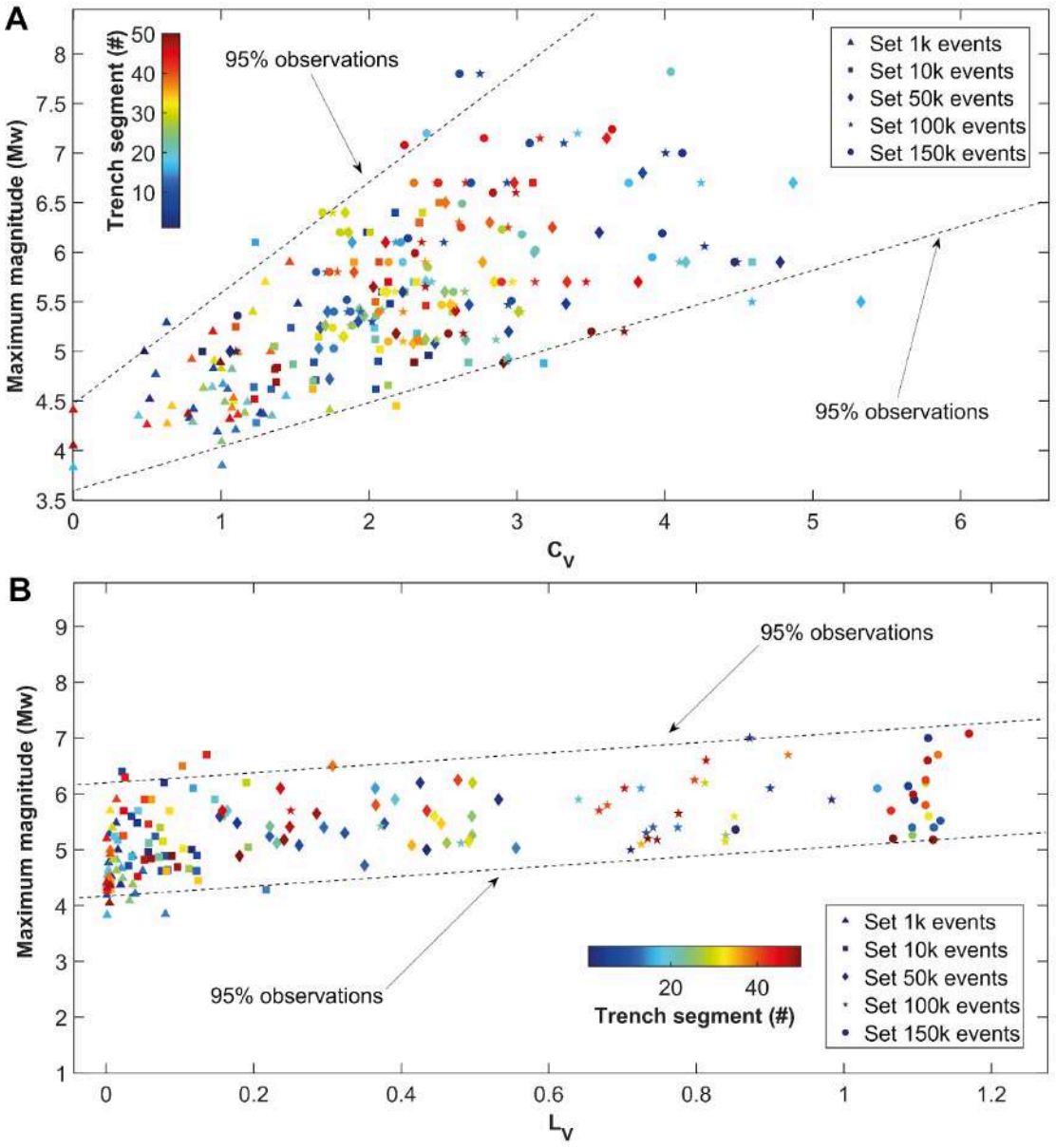

Fig. 1 (A) Maximum observed magnitude in catalogue vs global coefficient of variation for fifty segments of seismogenic sources in New Zealand (represented by the colour) calculated using different portions of the seismic catalogue (Mw>Mc, depth < 50 km, 1985-2022), i.e., < 1%, ~ 7%, ~ 1/3, ~ 2/3 and full catalogue, one of each kind, in chronological order. This situation simulates how clustering properties of seismicity change with time as the amount of recording increases. Extremely short catalogues (corresponding to few months of recordings) are almost Poissonian with low maximum magnitude, while mid-length and long catalogues showcase clustered seismicity. The behaviour of seismic activity in the latter cases seems to be long-term time invariant, i.e., the degree of global clustering increases almost linearly. Therefore, regions with higher CV fixed the size of the catalogue may be prone to larger earthquakes. (B) Maximum observed magnitude in catalogue vs local coefficient of variation. While extremely short catalogues are locally periodic, mid-length and long catalogues showcase locally-Poissonian seismicity. Only slight positive correlation is observed between maximum magnitude and the local coefficient of variation.

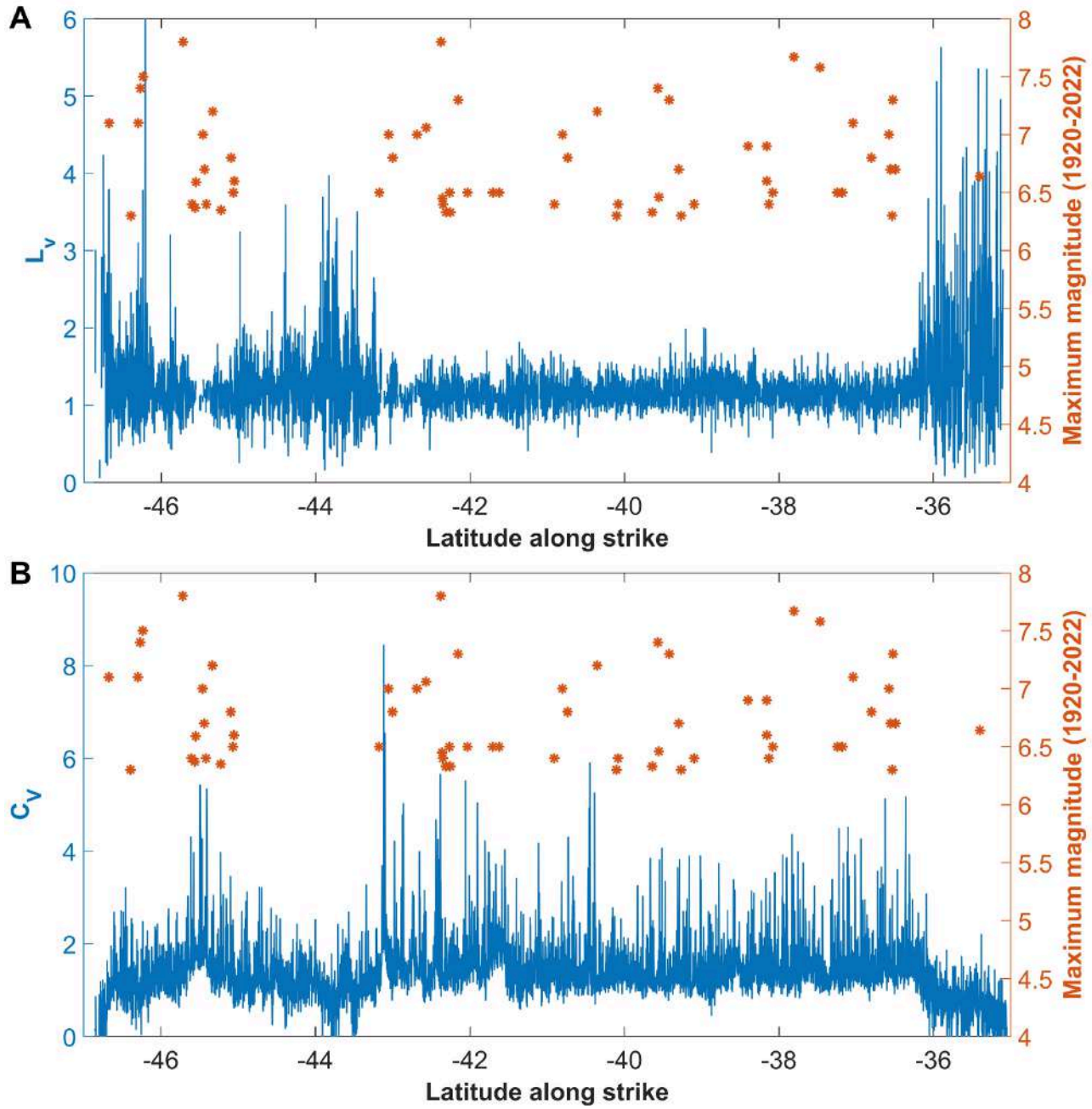

Fig. 2: Coefficients of variation for seismicity along the most important seismogenic structures in New Zealand between 1985 and 2022. (A) Local coefficient of variation and maximum observed magnitudes from 1920 and 2022 above Mw 6.0. Large seismic events tend to occur where seismic activity is locally Poissonian. (B) Global coefficient of variation and maximum historical magnitudes from 1920 and 2022. Large seismic events tend to occur where seismicity is globally clustered.

Session 2.2

Science and technology to support earthquake prevention and preparedness

GNGTS 2024

DISASTER RISK ANALYSIS AND REDUCTION

Session 2.2

Science and technology to support earthquake prevention and preparedness

Convenors of the session:
Mauro Dolce (UniNA) – mauro.dolce@unina.it
Francesca Pacor (INGV) – francesca.pacor@ingv.it
Maria Polese (UniNA) – mapolese@unina.it

Contributions recommended for this session:

- Monitoring networks for the knowledge of seismic hazard and for rapid response
- Shaking scenarios at different territorial scales for seismic risk evaluations: methodological approaches, uncertainty management and input data
- Assessment of seismic risk and its engineering components (vulnerability and exposure) at different territorial scales and with different methodologies, and development of the necessary tools and databases
- Methodologies and examples of multi-risk analysis associated to seismic risk (e.g. earthquakes and tsunamis)
- Civil protection planning and urban planning tools for seismic risk mitigation
- Techniques and examples of seismic strengthening or retrofit interventions of rapid execution and having low impact on the service continuity of the building, also integrated with energy efficiency interventions and considering circular economy principles
- Tools for the safety assessment of individual buildings, including on-site and remote monitoring and related analysis methodologies
- Contributions for the improvement of seismic standards for different structural types (buildings, bridges, warehouses, large structures, etc.) and for different structural materials (masonry, reinforced concrete, steel, wood, etc.) for the design of new buildings or interventions on existing buildings, including the evaluation of seismic design actions

Seismic risk mitigation is a rapidly evolving field, as scientific, engineering and technological developments are providing new elements for the prevention, preparedness, response and recovery of the system and population to the effects of

earthquakes. Moreover, the need to combine the seismic risk reduction with the reduction of other risks, coupled with the requirement to consider present and future climate change issues, foster the adoption of a more articulated and complete approach, where the risk scenarios encompass also compound and induced events (e.g. tsunamis), and where the prevention actions on constructions take into account the needs for energy efficiency. This session has the scope to collect those contributions that could represent an advancement in seismic reduction strategies, also in a broader perspective to other risks.

A systematic analysis at stations of the Italian seismic network to test the role of local topographic effect.

M. Ariano[1], P.L. Fantozzi[1], D. Albarello[1]

[1]Department of Physics Sciences, Earth and Environment, University of Siena, Siena, Italy

The Italian seismic code (NTC18) provides indications about the expected effects of some morphological configurations on the expected ground motion during earthquakes. In particular, two main 2D morphologies are identified as reference: cliffs and crests. Based on numerical simulations, the value of St is assumed to depend on the steepness of the cliffs and aspect ratio of the crest. A critical aspect of these estimates is that the considered configurations are defined in terms of steepness angles and aspect ratios, without any scale indication. Moreover, the considered morphologies are very schematic, and this prevents their simple application in the natural context: in most cases an expert judgement is necessary, and this makes the final estimates potentially controversial and difficult to validate on the basis of empirical observations. To face this problem, in the frame of the PRIN project "SERENA", a procedure has been developed for the automatic identification of areas prone to morphological amplification effects by following NTC18 prescriptions, based on the Digital Terrain Model. The proposed approach allows the full exploitation of topographical data at the maximum resolution available. After a first application to restricted areas, the proposed procedure has been applied at National scale at the seismometric and accelerometric sites managed by INGV. The aim is twofold: first comparing outcomes of the new approach with the ones proposed by other Authors at the same sites, second to provide a sound basis of a coherent and reproducible estimate of St values to be compared with possible empirical evidence. In the presentation, the results obtained about the first aim will be presented and discussed.

Seismic vulnerability of masonry buildings in Montenegro: a heuristic model

F. Aloschi[1], M. Polese[1], J. Pejovic[2], N. Serdar[2]

[1] Department of Structures for Engineering and Architecture (DiSt), University of Naples Federico II, Naples, Italy
[2] Faculty of Civil Engineering, University of Montenegro UCG, Podgorica, Montenegro

Background, motivation, and scope

The first step to perform a vulnerability assessment is to classify buildings, recognizing the typological characteristics that define the seismic behavior of a *class*. The typological characteristics are discernible when conducting analyses at the territorial scale (Polese *et al.* 2019). After selecting the damage scale, vulnerability functions are assessed as a measure of the likelihood for building classes to experience damage due to earthquakes of given intensity. Main approaches for estimating the vulnerability of buildings may be distinguished as: i) empirical, where models are based on statistical processing of damage data collected from past earthquake events, ii) analytical, where fragility is computed according to an analytical-based estimation of the buildings' response, iii) hybrid, where features of i) and ii) are combined, and iv) heuristic, expert based methods with subsequent empirical calibration by observational data. Heuristic approaches were largely adopted in the last two decades as they ensure physically consistent results and fairly accurate fittings with actual damage (Lagomarsino *et al.* 2021). In this paper, we propose a heuristic approach, hereafter referred to as EXPLORA, to evaluate the vulnerability model (VM) for masonry residential buildings in Montenegro. In particular, building classification is based on the SERA model (Crowley *et al.* 2020) suitably enriched to account for building features that influence the vulnerability. The SERA model is based on the Global Earthquake Model (GEM) (Silva *et al.* 2020) and was developed to work jointly with GEM's analytical fragility curves. However, these curves were developed for global applications and were not calibrated with observed damage data. Thus, they cannot adequately capture the behaviour of buildings in specific geographic areas.

In this work, masonry buildings in Montenegro are initially subdivided in 3 building classes, namely: 1) unconfined stone masonry buildings (URM-St), 2) unconfined brick masonry buildings (URM-Br), and 3) confined masonry (CFM). In the context of Montenegro, specific VMs have not been developed as yet. To address this gap, we firstly compare Montenegrin building typologies with the SERA typologies, based on the GEM taxonomy (Scawthorn *et al.* 2013), and with those of Serbia (Blagojević *et al.* 2023), Slovenia (Babič *et al.* 2021; Polese *et al.* 2023), and Italy (Rosti *et al.* 2021; Polese *et al.* 2023). This allows a re-classification of the Montenegrin typologies according to

different VMs and a preliminary vulnerability evaluation. However, the capability of existing VMs to represent effective susceptibility to damage must be tested with real damage data. To this end, data pertaining to the April 15, 1979, Montenegro Earthquake, referred to as the Seismic Event (SE), are considered. Ultimately, damage data extracted and revised from historical reports are used to calibrate a heuristic VM that suitably combines existing VMs for similar typologies.

Damage data analysis

In Montenegro, the data on historical earthquakes and relevant damages are not collected in systematic way and there is a lack of structural database which can provide information on events and direct effects of earthquakes. However, the SE left an indelible mark on the collective memory of Montenegrins, and a few initiatives were taken to assess the extensive damage caused by this catastrophic event. We rely on two of them: the historical Report IZIIS (Petrovski *et al.* 1984) and the work by Pavićević (Pavićević Božidar S 2004). In both reports, the classification of damage differs from the European Macroseismic Scale 1998 (EMS98) (Grünthal & European Seismological Commission 1998) notation. Therefore, following an approach similar to Rota et al. (Rota *et al.* 2008), we have developed the conversion scheme reported in Tab. 1.

Usability	**Report IZIIS 84-085** (Petrovski *et al.* 1984)	**EMS 98** (Grünthal 1998)
Usable	**11** - no damage	DS0
	12 - no damage of LBS	DS1
	13 - damages of LBS	DS1
Temporary unusable	**21** - damaged LBS	DS2
	22 - heavy damages of LBS	DS2
Unusable	**31** - severely damaged	DS3
	32 - partially collapsed	DS4
	33 - collapsed	DS5

Tab. 1 – Conversion scheme for damage levels into EMS98 damage states (DSs). Note: LBS stands for load-bearing system.

The earthquake's hypocenter was located offshore, and the coastal municipalities suffered the most severe impact of the devastation. A shake map for this event is available from United States Geological Survey (USGS) (U.S. Department of the Interior 2023). In the present study, Peak Ground Acceleration (PGA) is selected as the Intensity Measure (IM). For the coastal cities a Modified Mercalli intensity (MMI) between VIII and IX was reported in (Blagojević *et al.* 2023); by adopting the I-PGA conversion law proposed in Trifunac et al. (Trifunac MD *et al.* 1991), a reasonable agreement of the corresponding PGA with the values from the USGS shake map can be observed. These shake map values are reported in Tab. 2.

	Ulcinj	Bar	Budva	Tivat	Kotor	Herceg Novi	Cetinje
Modified Mercalli Intensity (MMI)	VII	VIII	IX	VIII	IX	VI	VII
Peak Ground Acceleration (PGA) [g]	0.4	0.5	0.65	0.45	0.37	0.3	0.32

Tab. 2 – Seismic event (SE) intensities identified in 7 municipalities.

(Petrovski *et al.* 1984) classifies buildings based on their construction materials, namely: i) unconfined stone masonry buildings (URM-St), ii) unconfined brick masonry buildings (URM-Br), and iii) confined masonry (CFM). For each one of these building classes, the respective DS associated with all surveyed buildings is recorded. These results are reported in Fig. 1 (a) - (c). Conversely, in (Pavićević Božidar S 2004) the DSs are indicated for the 7 municipalities reported in Tab. 2. Being characterized by MMI ≥ VI, it is assumed that all the municipalities were completely inspected, consistently with what was observed in (Dolce & Goretti 2015) after the L'Aquila earthquake. This assumption ensures the availability of unbiased data for damage characterization. The damage data encompassed all types of construction materials, including masonry, reinforced concrete (RC), and steel. Acknowledging that masonry buildings constituted approximately 90% of the entire building dataset across all municipalities, we hypothesized that all damage pertained to masonry structures. The resulting damage data extracted from (Pavićević Božidar S 2004) is summarized in the histograms in Fig. 1 (d) - (l). One can note that the report (Pavićević Božidar S 2004) does not indicate specific building classes, such as URM-St, URM-Br, or CFM.

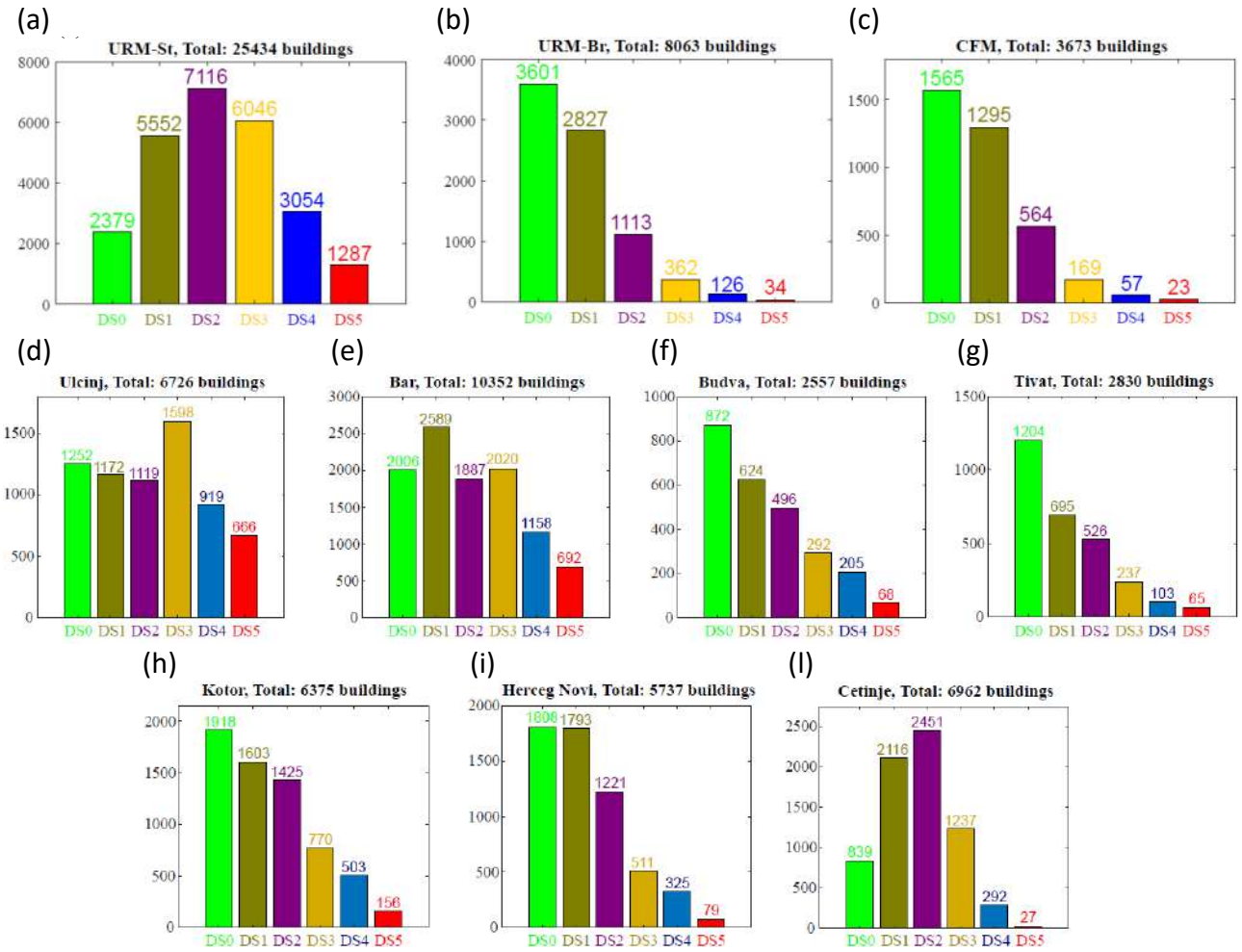

Fig. 1 – Damage data extracted from (Petrovski *et al.* 1984): a) unconfined stone masonry buildings (URM-St), b) unconfined brick masonry buildings (URM-Br), and (c) confined masonry (CFM). From (d) to (l): damage data extracted from (Pavićević Božidar S 2004) for 7 municipalities.

Given that both reports (Petrovski *et al.* 1984) and (Pavićević Božidar S 2004) are derived from surveys related to the same SE, we conducted data manipulation to extract pertinent information for establishing anchor points in fragility functions. Specifically, we initially computed, based on Fig. 1 (a) - (c), the percentage of URM-St, URM-Br, and CFM buildings within each DS. This information has been compiled and is presented in Tab. 3.

Damage State	URM-St	URM-Br	CFM
DS0	32%	48%	21%
DS1	57%	29%	13%
DS2	81%	13%	6%
DS3	92%	6%	3%
DS4	94%	4%	2%
DS5	96%	3%	2%

Tab. 3 – Distribution of building classes across damage states: derived from Fig. 1 (a) - (c).

Then, by applying the percentages of Tab. 3 to the data in Fig. 1 (d)-(l), we determine the number of buildings corresponding to each class falling in each DS. For the sake of conciseness, we do not

report this info in this paper; however, the outcomes of this manipulation will be clearly displayed in the forthcoming subsection.

The proposed heuristic model (EXPLORA)

In Montenegro, data on building structures is obtained from the 2011 census, which provides info on dwellings and their construction dates. There is no specific information detailing the typological characteristics of buildings, which is crucial for creating comprehensive building classes. Hence, the SERA exposure model (Crowley *et al.* 2020) for Montenegro is used as a reference. It defines common building classes in Montenegro based on the year of construction and location (urban or rural). With the aim of comparing the typologies with those considered in (Blagojević *et al.* 2023)-(Rosti *et al.* 2021; Polese *et al.* 2023), additional features are considered. Firstly, the SERA model (Crowley *et al.* 2020) is enriched according to the GEM building taxonomy (Scawthorn *et al.* 2013), and buildings are subdivided according to height classes Low (**L**: 1-2 stories) or Medium (**MH**: ≥ 3 stories). The percentage distribution in height classes is derived from the SERA model for Montenegro (Crowley *et al.* 2020). Next, the presence of flexible or rigid slab floors is considered, assigning equal probability. The resulting building classes are outlined on the left side of Tab. 4.

Montenegro building classes	**Lateral load resisting system (LLRS)**	**Design Code and Age of Construction**	**Floor type**	**Height**		**SERA typologies** (Scawthorn *et al.* 2013; Crowley *et al.* 2020)	**VM Serbia** (Blagojević *et al.* 2023)	**VM Italy** (Rosti *et al.* 2021)	**VM Slovenia** (Babič *et al.* 2021)
URM-St	Stone walls in both directions without tie-rods	**CDN** pre-code **1919-1964**	50% Flexible (wooden slab) 50% Rigid (RC slab)	90% Low (**L**) 1 - 2 stories 10% Medium (**MH**) ≥ 3 stories	→	**MUR-STDRE_LWAL-H1** (λ_{S1}=0.45) **MUR-STDRE_LWAL-H2** (λ_{S2}=0.45) **MUR-STDRE_LWAL-H3** (λ_{S3}=0.10)	**M1**, **M2** (λ_{Sr1}=0.5) **M3** (λ_{Sr2}=0.5)	**B-L** (λ_{It1}=0.45) **B-MH** (λ_{It2}=0.05) **C1-L** (λ_{It3}=0.45) **C1-MH** (λ_{It4}=0.05)	**1** (λ_{SI1}=0.9) **2** (λ_{SI2}=0.1)
URM-Br	Brick walls in both directions without tie-rods	**CDL** low code **1964-1980**	50% Flexible (wooden slab) 50% Rigid (RC slab)	90% Low (**L**) 1 – 2 stories 10% Medium (**MH**) ≥ 3 stories	→	**MUR-CL99_LWAL-H1** (λ_{S1}=0.45) **MUR- CL99_LWAL-H2** (λ_{S2}=0.45) **MUR- CL99_LWAL-H3** (λ_{S3}=0.10)	**M1**, **M2** (λ_{Sr1}=0.5) **M3** (λ_{Sr2}=0.5)	**B-L** (λ_{It1}=0.45) **B-MH** (λ_{It2}=0.05) **C1-L** (λ_{It3}=0.45) **C1-MH** (λ_{It4}=0.05)	**3** (λ_{SI1}=0.9) **4** (λ_{SI2}=0.1)
CFM	Brick or stone walls with vertical and horizontal RC elements without tie-rods	**CDM** moderate code **1981-2011**	50% Flexible (wooden slab) 50% Rigid (RC slab)	71% Low (**L**) 1 - 2 stories 29% Medium (**MH**) ≥ 3 stories	→	**MCF/LWAL+DUL/H:1** (λ_{S1}=0.42) **MCF/LWAL+DUL/H:2** (λ_{S2}=0.29) **MCF/LWAL+DUL/H:3** (λ_{S3}=0.29)	**M3** (λ_{Sr}=1)	**C1-L** (λ_{It1}=0.71) **C1-MH** (λ_{It2}=0.29)	**5** (λ_{SI1}=0.71) **6** (λ_{SI2}=0.29)

Tab. 4 – Association of renowned vulnerability models (VMs) to the Montenegro building classes.

Adding to the details of the SERA model and Tab. 4, it's worth mentioning that we assumed all buildings under CDN were constructed with stone masonry, while those under CDL were built with

brick masonry. In Tab. 4, the building classes identified for Montenegro are associated with the VMs of Serbia (Blagojević *et al.* 2023), Slovenia (Babič *et al.* 2021) and Italy (Rosti *et al.* 2021). Slovenia and Italy VMs were chosen because they are well-recognized in the seismic community and have undergone validation over the years. On the other hand, the Serbia VM is relatively recent, but is the result of a comprehensive effort involving also structural engineers from the Balkans with extensive experience in the local built environment. Thus, to exploit the common features of these three VMs, we created a heuristic VM called EXPLORA. Specifically, the fragility curves of EXPLORA are represented as cumulative distribution functions (CDFs) of lognormal distributions. These distributions show the probability of exceeding a certain DS at various IMs. The EXPLORA VM is designed in a way that its fragility curves are a linear combination of the VMs from (Blagojević *et al.* 2023), (Babič *et al.* 2021) and (Rosti *et al.* 2021), in terms of mean and standard deviation, as follows:

$$\Theta = w_S \vartheta_S + w_{Sr} \vartheta_{Sr} + w_{It} \vartheta_{It} + w_{Sl} \vartheta_{Sl} , \quad (1)$$

$$B = w_S \beta_S + w_{Sr} \beta_{Sr} + w_{It} \beta_{It} + w_{Sl} \beta_{Sl} , \quad (2)$$

where Θ and B are the heuristic mean and standard deviation of the EXPLORA VM, while ϑ and β are the mean and standard deviation of the employed VMs: SERA (S), Serbia (Sr), Italy (It) and Slovenia (Sl). The weights w are calculated such that:

$$w_S + w_{Sr} + w_{It} + w_{Sl} = 1. \quad (3)$$

In Eqs. (1) and (2), the means ϑ and standard deviations β are derived by weighting the various VMs' fragility curves with predetermined weights λ. These weights are indicated in Tab. 4 and are applied similarly to Eqs. (1) and (2) for each building class and VM. This step is taken to consider the potential influence of flexible and rigid diaphragms, as well as the variability in building heights (**L** or **MH**), which are unfortunately missing in the damage data. Next, to leverage the damage information, the weights w in Eqs. (1) and (2) are fine-tuned by minimizing the error between the final weighted solution and a linear regression from the damage data pertaining DS2. Currently, this error minimization is done by means of a trial-and-error process, but a more advanced procedure is planned for future stages of this research. The weights w computed for the EXPLORA VM, which characterizes the seismic vulnerability of Montenegro, are detailed in Tab. 5.

Building class	w_S	w_{Sr}	w_{It}	w_{Sl}
URM-St	0.30	0.15	0.10	0.45
URM-Br	0.20	0.05	0.70	0.05
CFM	0.35	0.03	0.55	0.07

Tab. 5 – Weights w of each building class for the EXPLORA VM defined in Eqs. (1) and (2).

The ultimate fragility curves for each building class of Tab. 4, derived from the EXPLORA approach outlined in Eqs. (1) and (2), are depicted in Fig. 2 and offer a visual comparison with the aforementioned damage data.

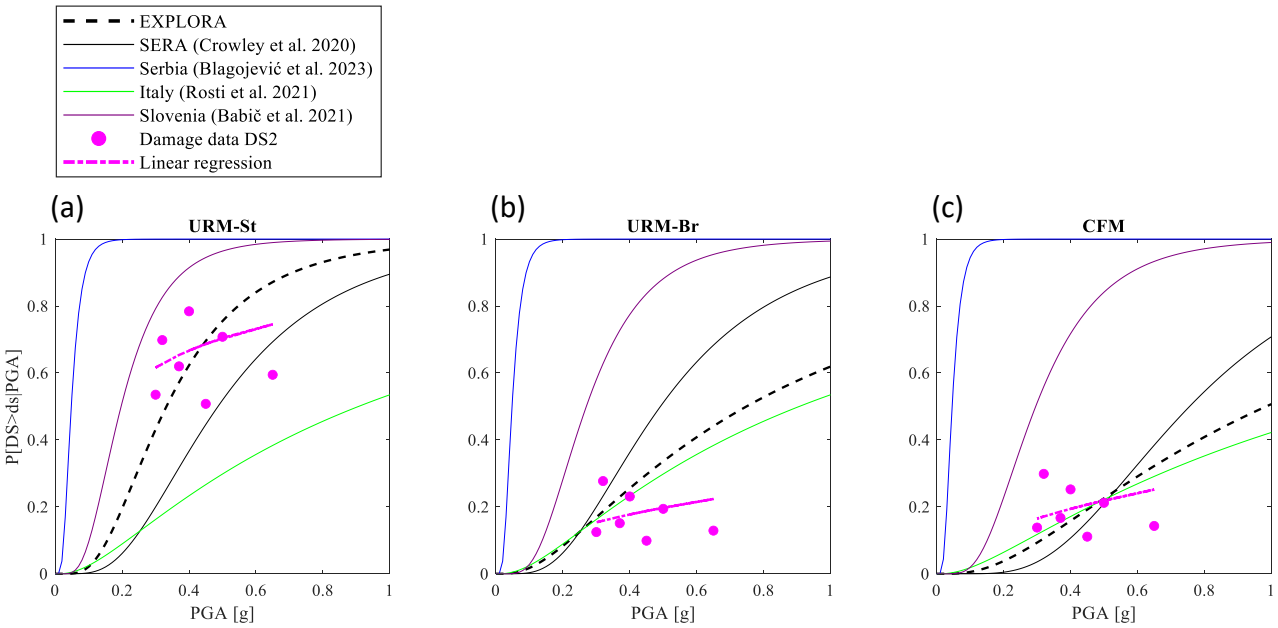

Fig. 2 – Visual comparison between the weighted DS2 EXPLORA VM and the SERA (Crowley et al. 2020), Serbia (Blagojević et al. 2023), Slovenia (Babič et al. 2021) and Italy (Rosti et al. 2021) VMs.

The weights calibrated in correspondence of the DS2 are then applied to all the DSs of each building class. The complete EXPLORA VM is depicted in Fig. 3 in comparison with the relevant damage data.

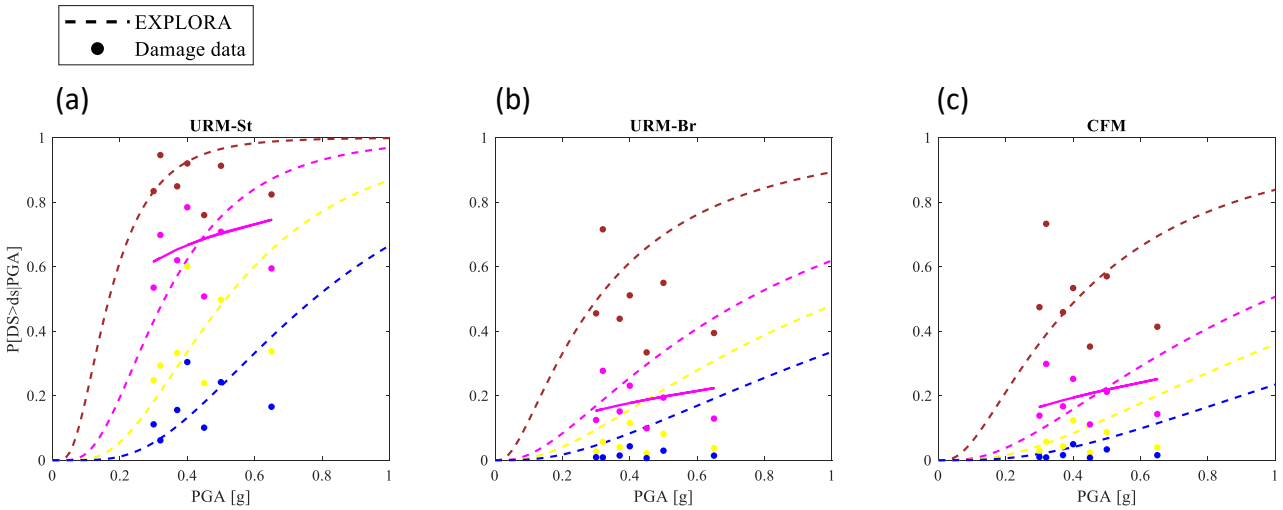

Fig. 3 – Visual comparison between the EXPLORA VM and the damage data for all the damage states (DSs): DS1 (brown), DS2 (magenta), DS3 (yellow), and DS4 (blue).

As shown in Fig. 3, the proposed EXPLORA VM reasonably captures the empirical behavior of the building classes identified for Montenegro, particularly for the URM-St and CFM. However, a slightly worse comparison is observed for the URM-Br building class. This discrepancy arises because the various VMs chosen for comparison do not accurately represent the damage data for this specific building class in DS2, as can be observed in Fig. 2 (b).

Acknowledgements

This study was performed within EXPLORA project, co-financed by Ministero degli Affari Esteri e della Cooperazione Internazionale in Italy and by the Ministarstvo nauke i tehnološkog razvoja in Montenegro.

Furthermore, we thank the authors of (Blagojević *et al.*, 2023) for sharing the fragility curve parameters from their vulnerability model for Serbia.

References

Babič, A., Dolšek, M. & Žižmond, J. 2021. Simulating Historical Earthquakes in Existing Cities for Fostering Design of Resilient and Sustainable Communities: The Ljubljana Case. *Sustainability 13(14),* 7624. DOI 10.3390/su13147624

Blagojević, N., Brzev, S., Petrović, M., Borozan, J., Bulajić, B., Marinković, M., Hadzima-Nyarko, M., Koković, V. & Stojadinović, B. 2023. Residential building stock in Serbia: classification and vulnerability for seismic risk studies. *Bulletin of Earthquake Engineering 21(9),* 4315–4383. DOI 10.1007/s10518-023-01676-0

Crowley, H., Despotaki, V., Rodrigues, D., Silva, V., Toma-Danila, D., Riga, E., Karatzetzou, A., Fotopoulou, S., Zugic, Z., Sousa, L., Ozcebe, S. & Gamba, P. 2020. Exposure model for European seismic risk assessment. *Earthquake Spectra 36(1_suppl),* 252–273. DOI 10.1177/8755293020919429

Dolce, M. & Goretti, A. 2015. Building damage assessment after the 2009 Abruzzi earthquake. *Bulletin of Earthquake Engineering 13(8),* 2241–2264. DOI 10.1007/s10518-015-9723-4

Grünthal, Gottfried. & European Seismological Commission. Working Group 'Macroseismic Scales.' 1998. *European Macroseismic Scale 1998 : EMS-98*. 99 pp. European Seismological Commission, Subcommission on Engineering Seismology, Working Group Macroseismic scales.

Lagomarsino, S., Cattari, S. & Ottonelli, D. 2021. The heuristic vulnerability model: fragility curves for masonry buildings. *Bulletin of Earthquake Engineering 19(8),* 3129–3163. DOI 10.1007/s10518-021-01063-7

Pavićević Božidar S. 2004. *An Integrated Approach to Seismic Risk Reduction through the Experience after Montenegro Earthquake 1979, Tehnika-Naše Građevinarstvo 58.2 (2004): 1-9.*

Petrovski, J., NOCEVSKI, N., RISTIC, D., MILUTINOVIC, Z., STANKOVIC, V. & PAVICEVIC BOZIDAR S. 1984. Report IZIIS 84-085 (1984) in Montenegrin.

Polese, M., Gaetani d'Aragona, M. & Prota, A. 2019. Simplified approach for building inventory and seismic damage assessment at the territorial scale: An application for a town in southern Italy. *Soil Dynamics and Earthquake Engineering 121,* 405–420. DOI 10.1016/j.soildyn.2019.03.028

Polese, M., Tocchi, G., Dolsek, M., Babič, A., Faravelli, M., Quaroni, D., Borzi, B. & Prota, A. 2023. Seismic risk assessment in transboundary areas: the case study on the border between Italy and Slovenia. In: *Procedia Structural Integrity*. 123–130. DOI 10.1016/j.prostr.2023.01.017

Rosti, A., Rota, M. & Penna, A. 2021. Empirical fragility curves for Italian URM buildings. *Bulletin of Earthquake Engineering 19(8),* 3057–3076. DOI 10.1007/s10518-020-00845-9

Rota, M., Penna, A. & Strobbia, C.L. 2008. Processing Italian damage data to derive typological fragility curves. *Soil Dynamics and Earthquake Engineering 28(10–11),* 933–947. DOI 10.1016/j.soildyn.2007.10.010

Scawthorn, C., Charleson, A., Allen, L., Greene, M., Jaiswal, K. & Silva, V. 2013. *GEM Global Earthquake Model GEM Building Taxonomy Version 2.0 Exposure Modelling*.

Silva, V., Amo-Oduro, D., Calderon, A., Costa, C., Dabbeek, J., Despotaki, V., Martins, L., Pagani, M., Rao, A., Simionato, M., Viganò, D., Yepes-Estrada, C., Acevedo, A., Crowley, H., Horspool, N., Jaiswal, K., Journeay, M. & Pittore, M. 2020. Development of a global seismic risk model. *Earthquake Spectra 36(1_suppl),* 372–394. DOI 10.1177/8755293019899953

Trifunac MD, Lee VW, Zivcic M & Manic MI. 1991. On the correlation of Mercalli-Cancani-Sieberg intensity scale in Yugoslavia with the peaks of recorded strong earthquake ground motion. *European Earthquake Engineering (1)(5),* 27–33.

U.S. Department of the Interior. 2023. https://www.usgs.gov/programs/earthquake-hazards.

Corresponding author: fabrizio.aloschi@unina.it

Correlation between site effects proxies: the case of Argostoli basin (Greece)

D. Attolico[1,2], G. Cultrera[1], V. De Rubeis[1], N. Theodoulidis[1]

[1] Istituto Nazionale di Geofisica e Vulcanologia (INGV, Italy)
[2] Asset - Agenzia regionale Strategica per lo Sviluppo Ecosostenibile del Territorio (Regione Puglia, Italy)

The purpose of this work is to explore the potential of multivariate statistical analysis method to define possible correlations between site response properties. The considered data are seismological instrumental observations and geological-geophysical parameters that could be used as proxy for the characterization of local site effect wherever seismological observations are not available.
The study area is the Argostoli basin (Greece), chosen for both the amount of earthquake and seismic noise recordings, and the geological and geophysical available information (Figure 1).
We follow the approach of Attolico et al. (2022) where multivariate statistical analysis was used to evaluate the most important site effect indicators and to deduce how the geological context influences their behaviours.
The statistical Factor Analysis technique has been applied to the different available or computed parameters including Horizontal-to-Vertical spectral ratios on earthquakes (HVSR) and noise (HVNSR), averaged over 4 frequency intervals (see Cultrera et al., 2014, for further details), the predominant frequency of HVSR and corresponding amplitude, maximum duration lengthening value (calculated from the frequency dependent mean group delay of the Fourier spectrum phases, as proposed by Sawada, 1998) and the corresponding frequency; thicknesses of the 3 lithological contrasts identified inside the basin; Vs average within the 3 aforementioned thicknesses (from Cushing et al., 2020); PGA normalized to magnitude and hypocentral distance; depth of seismic events.
The findings of this study suggest that the statistical variation of ground motion is influenced by the location of the seismic stations around and inside the basin, and by the type of lithology present underneath the site. Additionally, duration lengthening parameter is strictly correlated with the basin morphology and it is a useful tool to describe the seismic motion prolongation estimation for the site effects studies.

Towards an earthquake-induced landslide triggering map for Italy

S. Azhideh, S. Barani, G. Ferretti, D. Scafidi, G. Pepe

[1] *Università degli Studi di Genova, Genova, Italy*

Landslides are one of the most frequent geohazards that have caused devasting damage throughout history. Landslides often occur as a consequence of other natural hazards among which earthquakes can be considered as one of the main triggering factors. When an earthquake occurs, the effects of the induced ground shaking are often sufficient to cause failure of slopes that were marginally to moderately stable before the earthquake.

In the present study, we present a first attempt to define a screening map for all of Italy that classifies sites in terms of their potentiality of triggering earthquake-induced landslides based on seismic hazard. To this end, we analyze seismic hazard disaggregation results on a national scale (Barani et al., 2009) and compare magnitude-distance (*M*-*R*) scenarios with the upper-bound *M*-*R* curves defined by Keefer (1984) for different types of landslides: disrupted slides and falls, coherent slides, and lateral spreads and flows. For a given magnitude value, these curves define the critical distance below which earthquake-induced failures may occur and, as a consequence, the possibility of triggering a landslide can not be discounted.

First, for all computation nodes considered in the hazard assessment of Italy (MPS Working Group, 2004; Stucchi et al., 2011), joint distributions (i.e., probability mass functions, PMFs) of *M* and *R* are analyzed to identify all modal scenarios (i.e., local maxima). To this end, we treat each PMF as an image and apply morphological image processing techniques to find local maxima. Specifically, we apply the maximum (dilation) filter operation (e.g., Gonzales and Woods, 2018). Each *M*-*R* scenario in the PMF matrix is treated as a pixel. Each pixel is updated based on comparing it against the surrounding pixels in a running window process (a 3-by-3 square window around the target pixel is used). Specifically, the maximum filter replaces the value of the PMF associated with the central pixel with the greatest one in the running window. Finally, local maxima in the distribution are obtained by checking for element-wise equality within the original and filtered matrices, creating an array of Boolean values (Boolean matrix) within which True values indicate the modes. Figure 1 shows an example *M*-*R* distribution with indication of the modal scenarios resulting from maximum filtering and Boolean mask.

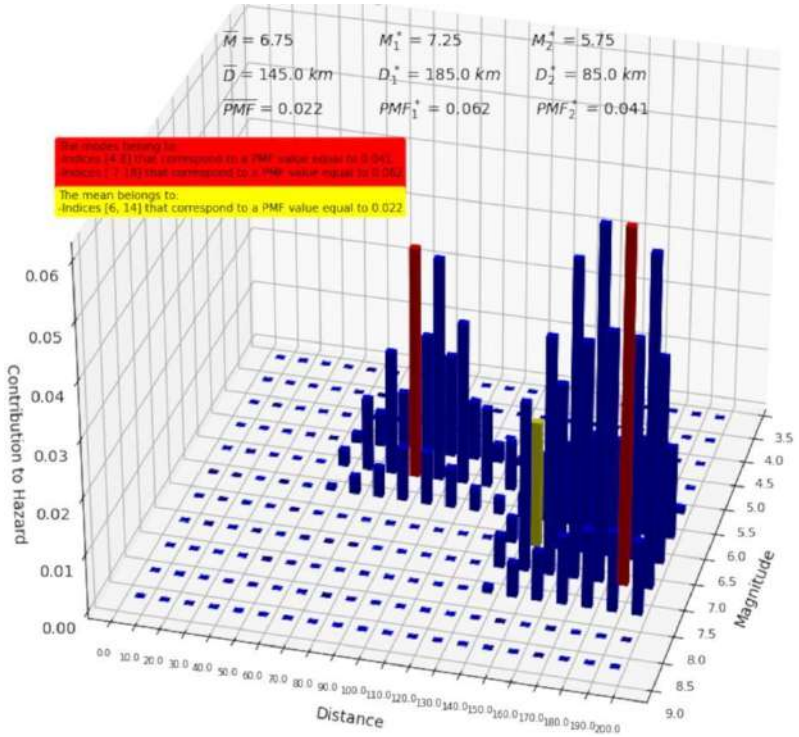

Fig. 1 Example distribution of *M* and *R* with indication of the mean and modal scenarios.

For each distribution, mean and modal scenarios of *M*-*R* are then compared to the upper-bound curves defined by Keefer (1984) and the preferred magnitude is selected as follows:

- if all *M*-*R* pairs stand above the reference upper-bound curve, then the triggering of earthquake-induced landslides can be neglected.
- if at least one *M*-*R* pair is below the reference upper-bound curve, then the triggering of earthquake-induced landslides can not be discounted.
- if more than one *M*-*R* pair lies below the reference upper-bound curve, then the triggering of earthquake-induced landslides can not be excluded and the *M*-*R* scenario that contributes the most to hazard (i.e., the *M*-*R* pair with the largest PMF value) is selected as the preferred magnitude.

Figure 2 shows an application of the criteria above to the case displayed in Figure 1.

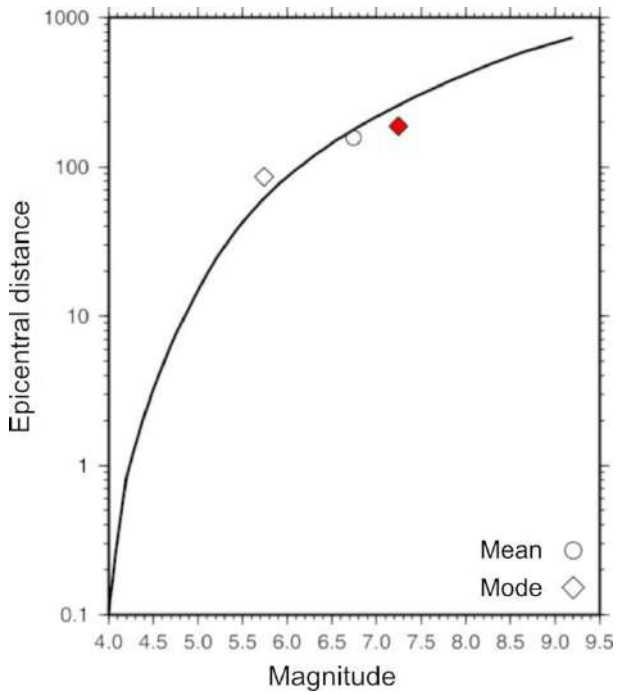

Fig. 2 Comparison of the mean and modal *M*-*R* scenarios shown in Figure 1 with the upper-bound curve for disrupted slides and falls proposed by Keefer (1984). The preferred *M*-*R* pair is displayed in red.

Figure 3 shows the geographic distribution of the preferred values of *M* and *R* resulting from the application of the methodology described above to the *M*-*R* distributions obtained from the disaggregation of the PGA hazard for a 475-yr return period together with the relevant triggering map.

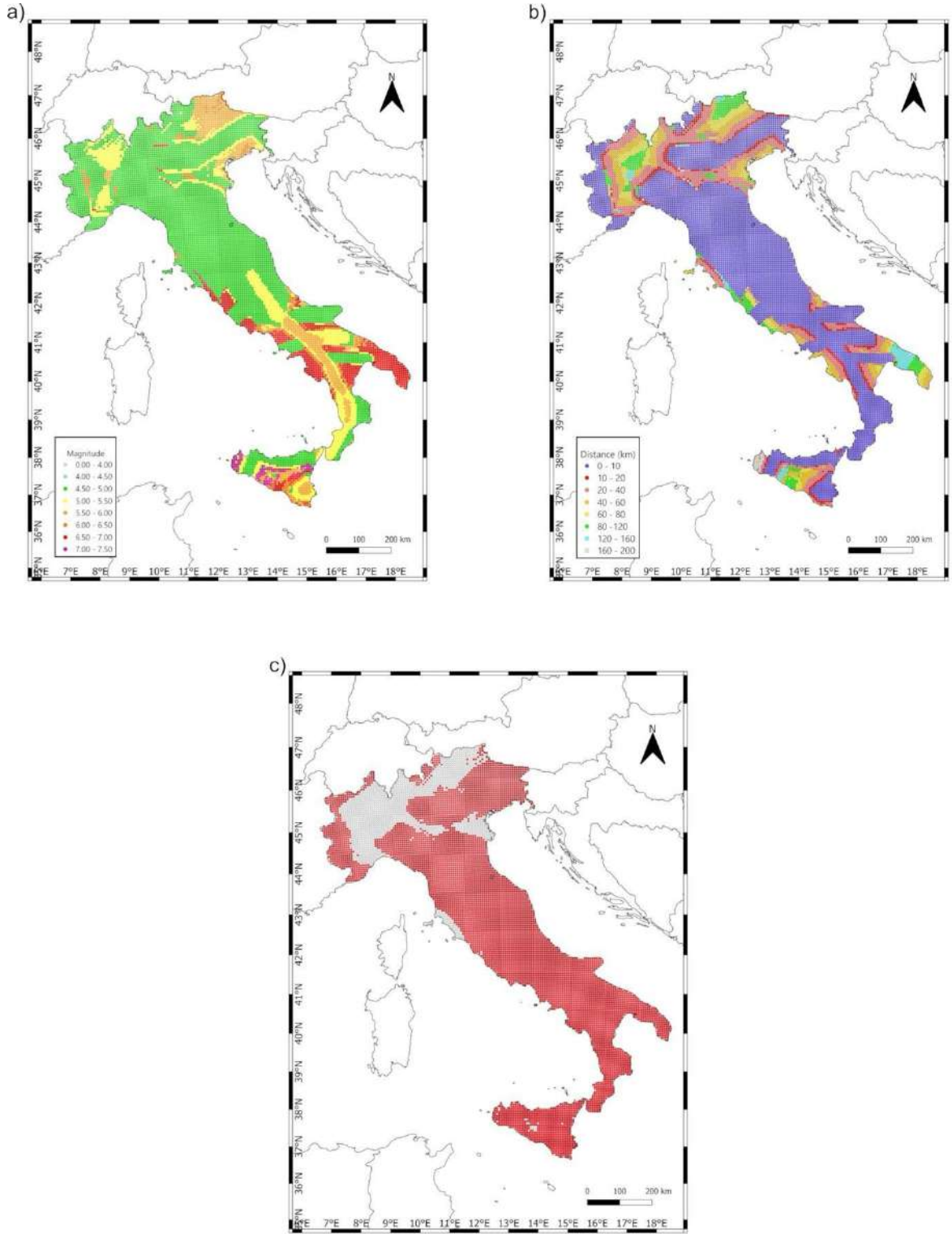

Fig. 3 Map of preferred magnitude (a) and distance (b) associated with the PGA hazard for a 475-yr return period and corresponding earthquake-induced landslide triggering map (c). In the latter, red points are nodes for which the triggering of earthquake-induced landslides can not be excluded.

Analyzing the triggering map in Figure 3c clearly shows an over-conservative scenario as the triggering of earthquake-induced slope failures can not be excluded in most of the Italian territory. It is worth noting, however, that the effect of other parameters related to the triggering of landslides deserve future consideration, particularly slope angle and stratigraphic

conditions. Moreover, can the selected *M-R* pairs produce acceleration levels above a certain critical value, thus inducing permanent slope displacement? It follows that some condition on critical acceleration (i.e., minimum acceleration to produce slope instability) should be incorporated in our methodology. Moreover, following Barani et al. (2023), future development of the work should include disaggregation results for different spectral periods as a function of soil classification. It is known, indeed, that soils resonate at different periods depending on local stratigraphic conditions (e.g., Kramer, 1996) and that disaggregation results are sensitive to the response period considered (i.e., the larger the spectral period, the greater the contribution from distant, higher magnitude events).

References

Barani S., Ferretti G., and Scafidi D.; 2023: *Evaluation of liquefaction triggering potential in Italy: a seismic hazard-based approach*. Nat. Hazards Earth Syst. Sci., 23, 1685-1698.

Barani S., Spallarossa D. and Bazzurro P.; 2009: *Disaggregation of probabilistic ground-motion hazard in Italy*. Bull. Seismol. Soc. Am., 99, 2638-2661.

Gonzales R. C. & Woods R. E.; 2018: *Digital image processing*. Pearson, New York, 1019 pp.

Keefer D. K.; 1984: *Landslides caused by earthquakes*. Bull. Geol. Soc. Am., 95, 406-421.

Kramer, S. L.; 1996: *Geotechnical Earthquake Engineering*. Prentice-Hall, Upper Saddle River, New Jersey, 653 pp.

MPS Working Group; 2004: *Redazione della mappa di pericolosità sismica prevista dall'Ordinanza PCM 3274 del 20 marzo 200*3, Final Report. INGV, Milano-Roma 2004, 65 pp + 5 appendixes.

Stucchi M., Meletti C., Montaldo V., Crowley H., Calvi G. M. and Boschi E.; 2011: *Seismic hazard assessment (2003-2009) for the Italian building code*. Bull. Seismol. Soc. Am., 101, 1885-1911.

Corresponding author: Azhideh_sina@yahoo.com

One-dimensional numerical approach VERSUS experimental quantifications of site effect parameters: the Ferrara test area

C. Barnaba (1), L. Minarelli (2), G. Di Giulio (2), G. Laurenzano (1), A. Affatato (1), P. Taverna (1), M. Vassallo (2), R. Caputo (3), G. Cultrera (2)

[1] National Institute of Oceanography and Applied Geophysics –OGS, Italy
[2] National Institute of Geophysics and Volcanology –INGV, Italy
[3] University of Ferrara - Italy

Within the work package WP06 - Empirical Testing and Calibration of the ongoing project PRIN-SERENA (Mapping Seismic Site Effects at REGional and NAtional Scale), we test the predicted estimates of ground motion parameters with the experimental values in an area with high-density geophysical investigations. The study area belongs to the lower alluvial Po plain, near Ferrara, and corresponds to an external buried portion of the Apennines foredeep basin, involved into active thrust-fold compressive structures (Martelli et al. 2017), of late Neogene-Quaternary age (Ghielmi et al., 2013). The active faults induce an important earthquake activity, documented by many historic events (Guidoboni et al., 2018, 2019), including the most recent ones in May 2012. The subsurface thick unlithified terrigenous Quaternary successions record an evolution from deep marine to alluvial plain environments. The successions are characterized by low seismic velocities (Minarelli et al. 2016; Petronio et al. 2023), and reduced seismic impedance contrasts (Mascandola et al., 2021).

Shortly after the event of May 20, 2012, the Istituto Nazionale di Geofisica e Vulcanologia (INGV) and the Istituto Nazionale di Oceanografia e di Geofisica Sperimentale (OGS) set up a dense temporary network of 18 stations (see Moretti et al., 2012; Priolo et al.,2012; Bordoni et al., 2012; Milana et al., 2014), equipped with short period and strong motion sensors. In addition, geophysical data were collected from microzonations studies and research projects performed by the city of Ferrara as well as by INGV and OGS. Around 200 single-station ambient noise measurements, 300 Vs profiles derived by seismic cone (SCPT) and 6 deep seismic boreholes (DH) were carried out.

The large amount of geophysical data (Vp, Vs, DH, noise measurements) and the availability of earthquake records, combined with the flat topography, make the Ferrara area the perfect site to test the resolving power of the one-dimensional numerical approaches (e.g. Falcone et al., 2021) to determine the amplification factors.

We collected and organized all available information in a dedicated geographic information system (GIS, Fig. 1) and reprocessed the earthquake records of all temporary seismological stations in the area.

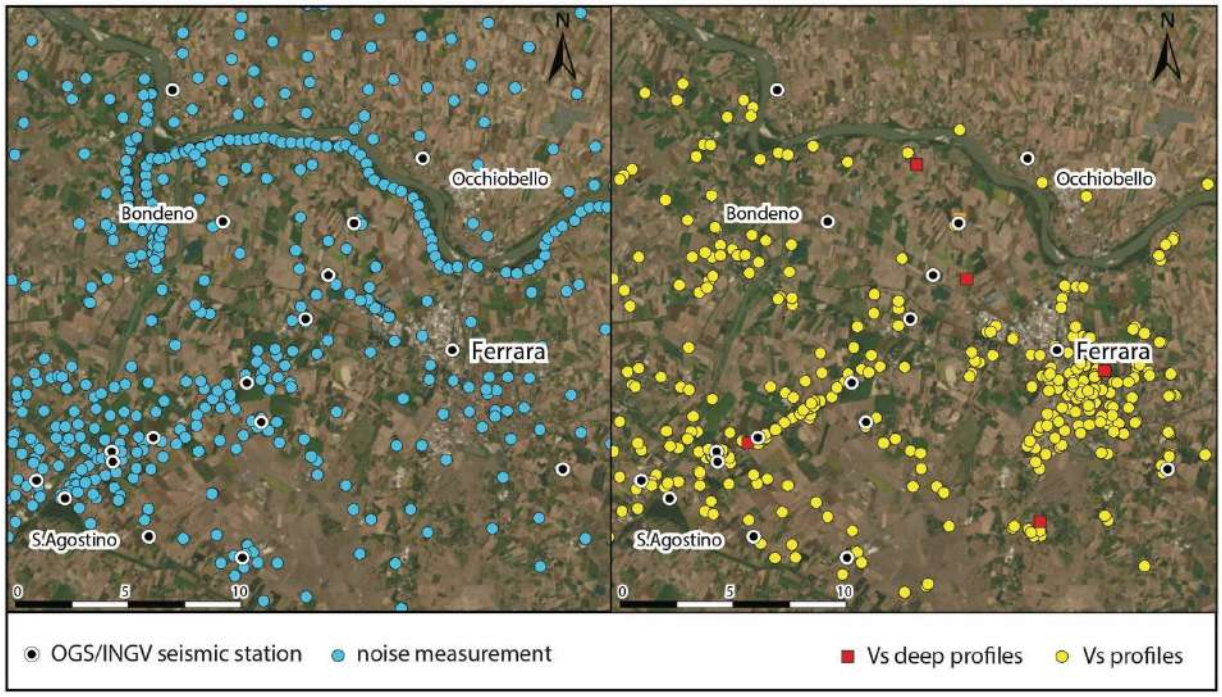

Fig. 1: The study area in the Po plain, near the city of Ferrara: on the left, noise measurements and seismic station position; on the right, Vs profiles available.

Since the Ferrara area is located in the alluvial deposits, far from rocks on the surface, the standard approach of spectral ratio to the reference site is not applicable for the assessment of FAs. To circumvent this, we computed the amplification function using the generalized inversion technique (GIT), using as reference site a virtual site (as proposed by Laurenzano et al., 2017) that mimics the conditions of the reference site considered by the building code (class A soil, with Vs=800 m/s). Due to the large amount of Vs profiles and data available at the Casaglia well, we constrained the virtual site at the surface and calculated the seismic ground motion parameters (PGA, PGV, FA, etc.). We plan to extend the pointwise results at the seismic network sites by a cluster analysis applied to the denser network of noise measurements and the Vs profiles, and compare the results with the numerical predictions of the one-dimensional approach.

References

Bordoni P., Azzara R. M., Cara F., Cogliano R., Cultrera G., Di Giulio G., Fodarella A., Milana G., Pucillo S., Riccio G., Rovelli A., Augliera P., Luzi L., Lovati S., Massa M., Pacor F., Puglia R., Ameri G.; 2012: Preliminary results from EMERSITO, the rapid response network for site effect studies. Annals of Geophysics, 55, 4, 599-607; DOI: 10.4401/ag-6153

Falcone G., Acunzo G., Mendicelli A., Mori F., Naso G., Peronace E., Porchia A., Romagnoli G., Tarquini E., Moscatelli M., 2021. Seismic amplification maps of Italy based on site-specific

microzonation dataset and one-dimensional numerical approach. Engineering Geology, 289, 106170. https://doi.org/10.1016/j.enggeo.2021.106170

Guidoboni E., Ferrari G., Mariotti D., Comastri A., Tarabusi G., Sgattoni G., Valensise G.; 2018: CFTI5Med, Catalogo dei Forti Terremoti in Italia (461 a.C.-1997) e nell'area Mediterranea (760 a.C.-1500). Istituto Nazionale di Geofisica e Vulcanologia (INGV).

Guidoboni E., Ferrari G., Tarabusi G., Sgattoni G., Comastri A., Mariotti D., Ciuccarelli C., Bianchi M.G., Valensise G.; 2019: CFTI5Med, the new release of the catalogue of strong earthquakes in Italy and in the Mediterranean area. Scientific Data 6, Article Number: 80 (2019).

Laurenzano, G., Priolo, E., Mucciarelli, M., Martelli, L., Romanelli, M., 2017. Site response estimation at Mirandola by virtual reference station. Bull. Earthquake Eng., 15:2393-2409, https://doi.org/10.1007/s10518-016-0037-y

Mascandola, C., Barani, S., Massa, M., & Albarello, D. (2021). New insights into long-period (> 1 s) seismic amplification effects in deep sedimentary basins: A case of the Po Plain basin of northern Italy. Bulletin of the Seismological Society of America, 111(4), pp.2071-2086.

Milana, G., Bordoni, P., Cara, F., Di Giulio, G., Hailemikael, S. and Rovelli, A., 2014. 1D velocity structure of the Po River plain (Northern Italy) assessed by combining strong motion and ambient noise data. Bull Earthquake Eng 12, 2195–2209 (2014). https://doi.org/10.1007/s10518-013-9483-y.

Minarelli, L., Amoroso, S., Tarabusi, G., Stefani, M., & Pulelli, G. (2016). Down-hole geophysical characterization of middle-upper Quaternary sequences in the Apennine Foredeep, Mirabello, Italy. Annals of Geophysics, 59(5), p. S0543, https://doi.org/10.4401/ag-7114.

Moretti, M., et al. (2012). Rapid response to the earthquake emergency of May 2012 in the Po Plain, northern Italy, Annals of Geophysics, 55 (4); doi:10.4401/ag-6152

Petronio, L., Baradello, L., Poggi, V., Minarelli, L., Böhm, G., Affatato, A., Barbagallo, A., Cristofano, G., Sorgo, D., Martelli, L., & Lai, C.G. (2023). Combining SH-and P-wave seismic reflection survey to support seismic response analysis. A case study from Cavezzo (Italy) after the 2012 Emilia earthquake. Engineering Geology, 313, p.106916. https://doi.org/10.1016/j.enggeo.2022.106916

Priolo, E., Romanelli, M., Barnaba, C., Mucciarelli, M., Laurenzano, G., Dall'Olio, L., Abu Zeid, N., Caputo, R., Santarato, G., Vignola, L., Lizza, C., Di Bartolomeo, P., 2012. The Ferrara thrust earthquakes of May-June 2012: Preliminary site response analysis at the sites of the OGS temporary network. Annals of geophysics, 55. 10.4401/ag-6172.

Corresponding author: cbarnaba@ogs.it

A dense accelerometric network supporting rapid damage estimation in Veneto

P.L. Bragato[1], J. Boaga[2], G. Capotosti[1], P. Comelli[1], S. Parolai[1,3], G. Rossi[1], H. Siracusa[1], P. Ziani[1], D. Zuliani[1]

[1] National Institute of Oceanography and Applied Geophysics – OGS, Italy
[2] University of Padova, Italy
[3] University of Trieste, Italy

On 20 April 2020 Regione del Veneto and the Italian National Institute of Oceanography and Applied Geophysics – OGS signed an agreement for the deployment of a dense accelerometric network covering over 50% of the municipalities in Veneto. The project continued similar initiatives undertaken by OGS in recent years (Bragato et al., 2021): its main objective was to give reliable shaking scenarios after severe earthquakes, allowing rapid damage estimations for civil protection purposes (Poggi et al., 2021). The network was built in less than nine months between February and October 2022 and currently comprises 312 three-component MEMS accelerometers each one installed in the basement of a building (Fig. 1). Twenty-two edifices were also equipped with an accelerometer at the top for studying their dynamical response. In order to reduce the administrative work and the number of formal agreements, the edifices were chosen among the headquarters of organizations of volunteers coordinated by the Civil Protection of Regione del Veneto, telephone exchange buildings of TIM s.p.a., and post offices of Poste Italiane s.p.a. (129, 120 and 42 structures, respectively). Another 21 buildings were made available by municipalities (mainly town halls). Seismic noise characterization has been performed for 100 sites and will be continued for the other ones. The network is based on the accelerometer ADEL ASX2000, developed and tested in close collaboration between OGS and the manufacturer, highlighting the interconnection between research and the private sector. It is a cost-effective instrument that guarantees mechanical robustness, quality of the recordings and sufficient sensitivity to give usable signals in the near field roughly from ML=2.5. The seismic recordings are transmitted in real-time by means of LTE internal modems using the “seedlink” protocol. The data are acquired on a virtual machine in the cloud hosted by TIM s.p.a. All the adopted solutions aim to allow the technical and economical sustainability of the network in the long term, so that similar monitoring systems can be proposed for other regions in Italy. The network proved its validity for two earthquakes that occurred in southern Veneto on 25 and 28 October 2023 (magnitude ML 4.4 and 4.3, respectively).

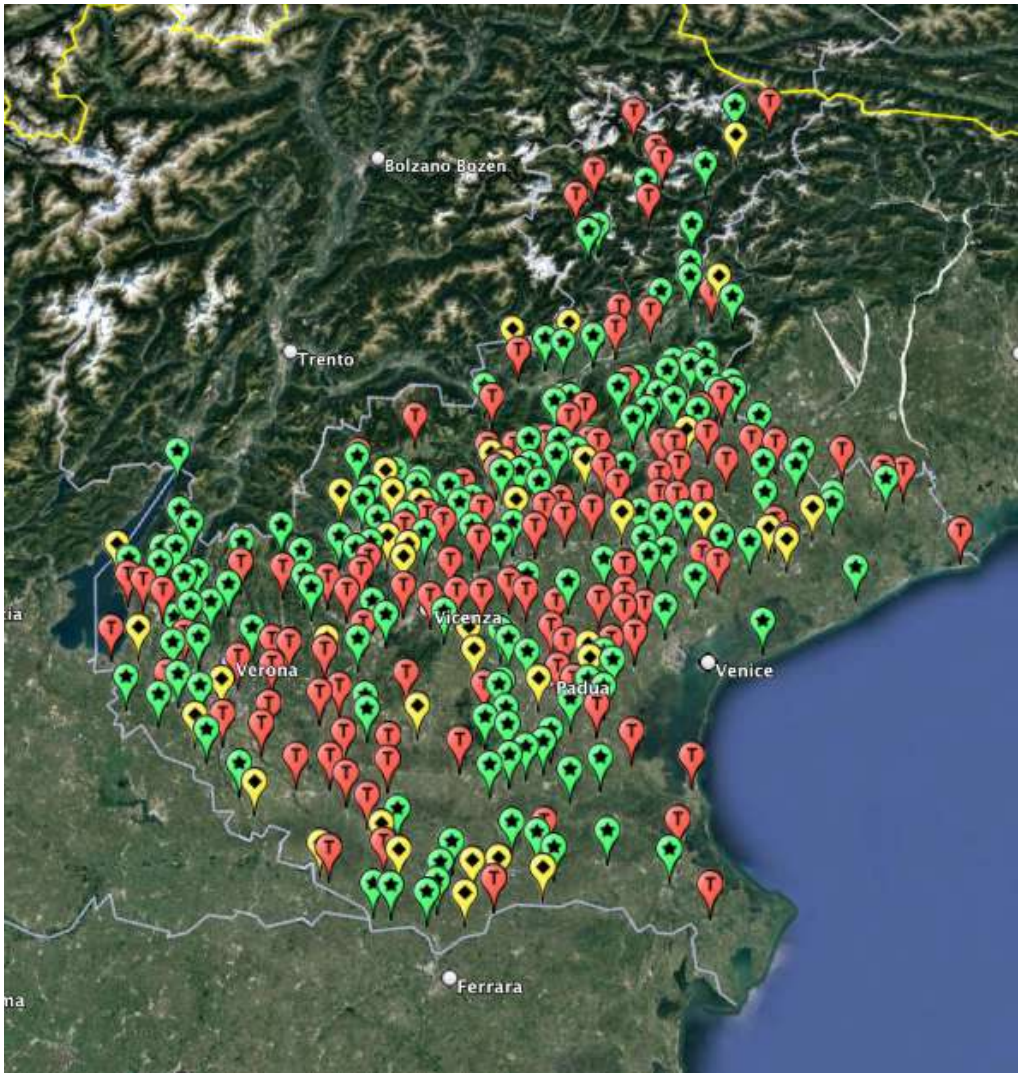

Fig. 1 – Stations composing the dense accelerometric network in Veneto: green, organizations of volunteers and other public edifices; red, telephone exchange buildings of TIM s.p.a.; yellow, post offices of Poste Italiane s.p.a.

Acknowledgements

This project was financed by the programme POR-FESR Regione Veneto 2014–2020, Action 5.3.1.

References

Bragato P.L., Comelli P., Saraò A., Zuliani D., Moratto L., et al.; 2021: The OGS–northeastern Italy seismic and deformation network: current status and outlook. Seismol. Res. Lett. 92, 1704–1716.

Poggi V., Scaini C., Moratto L., Peressi G., Comelli P., Bragato P.L., Parolai S.; 2021: Rapid damage scenario assessment for earthquake emergency management. Seismol. Res. Lett. 92, 2513–2530.

Corresponding author: pbragato@ogs.it

A GEOLOGICAL GEOPHYSICAL APPROACH FOR THE LARGE-SCALE EVALUATION OF SEISMIC AMPLIFICATION IN THE PLAIN AREA: EXAMPLE OF THE BRESCIA BASIN (PIANURA PADANA)

G. Caielli[1], R. de Franco[1], I. Gaudiosi[2], A. Mendicelli[2], M. Moscatelli[2], G. Norini[1], D. Rusconi[1], M. Simionato[2].

[1] ISTITUTO DI GEOLOGIA AMBIENTALE E GEOINGEGNERIA – CNR - Milano - Italy
[2] ISTITUTO DI GEOLOGIA AMBIENTALE E GEOINGEGNERIA – CNR - Montelibretti - Italy

This presentation aims to answer the scientific question: how to model the expected effects of site seismic amplification at different scales in a plain environment where the informative contribution of the geological-morphological survey is almost nil but widespread spatial information deriving from well geo-stratigraphy and few direct geophysical measurements in the well and indirect from surface are available.

We present the result of the analyses of the data available from surface geophysical studies with the aim of creating a database of the physical parameters characterizing the lithotypes outcropping to the depth of the “seismic” bedrock that is hypothesized coinciding with the top of the early Pleistocene, named “red discontinuity)”, in the area of the Brescia basin (CARG-ISPRA).

Quaternary deposits will be analyzed in order to associate geological units with engineering-geological units (UGT) and attribute the Vs and Vp values. For the reconstruction of the surface part, it has been decided to use seismic microzonation studies (MS). The data and information retrieved and analyzed have been collected in a data-base, each survey contains the identification code, the geographical coordinates, layer thickness and velocity values.

The fundamental objective of the work is the association of UGT to each layer identified and inserted in the tables of geophysical measurements. Then using well for the hydrogeological data, we try to assign to each layer the UGT. The results of 246 geophysical surveys and 623 hydrogeological data, mainly water wells, were analyzed. These were the starting point for the statistical analyses carried out with ArcGis and ArcGis Pro. The statistical analyses carried out relate above all to the velocities Vs and available Vp subset. Using the information derived from the analysis, it has been possible the attribution of the velocity range Vs to each UGT recognized within the Brescia basin.

This allow us to obtain a big set of seismostratigraphies for which we can calculate the site amplification and then study statistically the seismic response for the Brescia basin.

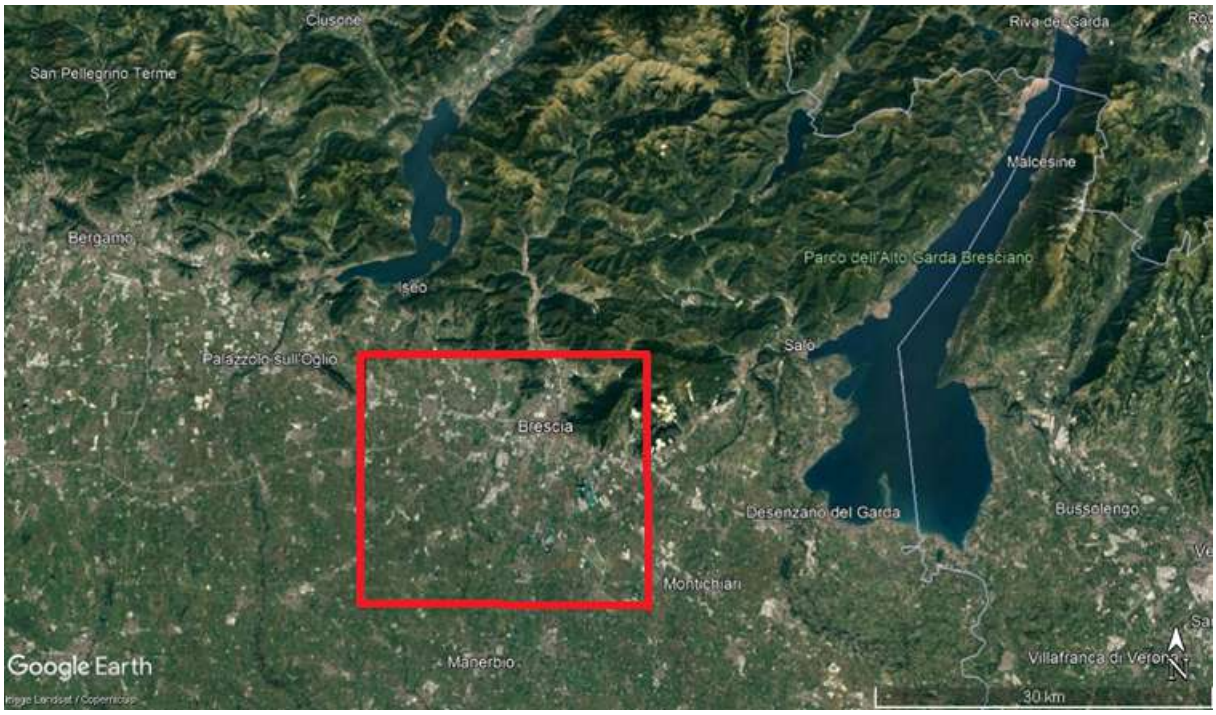

Fig. 1 – Map of the studied area.

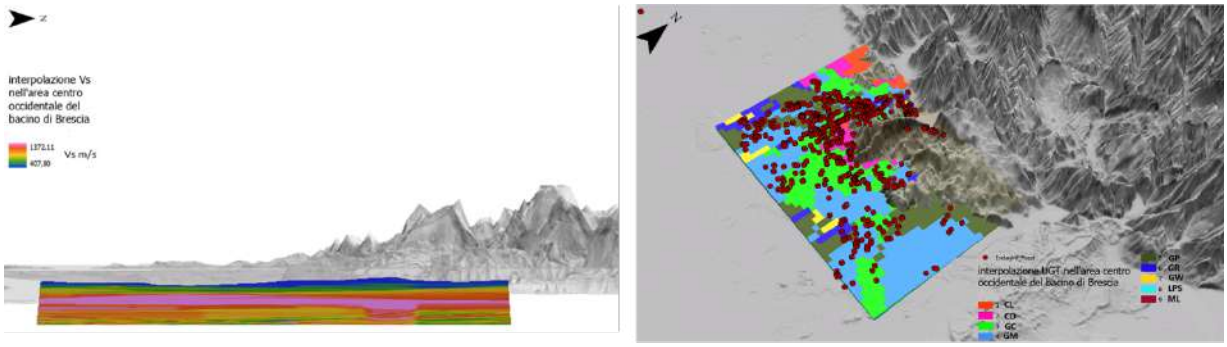

Fig. 2 – Left panel: Vp section of the 3D geological-geophysical model. Right panel: Interpolation of outcropping UGT in the western part of the Brescia basin.

References

Gino Romagnoli, Emanuele Tarquini, Attilio Porchia, Stefano Catalano, Dario Albarello, Massimiliano Moscatelli, 2022 - Constraints for the Vs profiles from engineering-geological qualitative characterization of shallow subsoil in seismic microzonation studies, Soil Dynamics and Earthquake Engineering, 161, 107347, https://doi.org/10.1016/j.soildyn.2022.107347.

Geoportale Regione Lombardia https://www.cartografia.servizirl.it/viewer32/index.jsp?config=config_caspita.json.

Acknowledgments

This work was carried out as part of the projects:
DTA.AD004.330 - CARG-BS - Realizzazione della Carta Geologica e Geotematica d'Italia Foglio 121 Brescia.
DTA.AD003.757 - PRIN-SERENA MUR-2020MMCPER - Mapping seismic site effects at regional and national scale.

Corresponding author: davide.rusconi@igag.cnr.it

Mapping seismostratigraphical amplification effects at regional scale from geological data

N. Carfagna[1], P. Pieruccini[2], P. Fantozzi[1], D. Albarello[2,3]

[1] Department of Physical Science, Earth and Environment, University of Siena, Siena, Italy
[2] Department of Earth Science, University of Turin, Turin, Italy
[3] Consiglio Nazionale delle Ricerche, Istituto di Geologia Ambientale e Geoingegneria, Rome, Italy

It is widely recognized that the amplification of ground motion during earthquakes is attributed to the interference of seismic waves trapped between the free surface and impedance contrasts in the shallow subsoil. Seismic Microzonation (SM) studies are devoted to evaluating these site effects, but their application in wider contexts is a hard and expensive task. To estimate seismic site effects at regional scale, the most viable approach is to utilize detailed geological and geomorphological data (1:10.000-1:50.000), which are available for a large part of Italy.

In the frame of the national research project “SERENA”, in this study a procedure is proposed and tested to constrain the entity of 1D seismostratigraphical ground motion amplification based on geological information at the most detailed scale available. In particular, amplification factors are estimated for Seismically Homogeneous Microzones (SHM) defined on the basis of geological information. Each SHM is represented as a stack flat homogeneous layer, each characterized in terms of engineering-geological units by following the seismic microzonation standards (*Commissione Tecnica, 2018; SM Working Group, 2015*). Seismic properties of each layer (shear waves velocity, density, damping and G/G0 curves) and respective range of variability are determined on the basis of the most recent literature (*Romagnoli et al., 2022*; *Gaudiosi et al., 2023*).

This information feeds a linear equivalent numerical approach and the Inverse Random Vibration Theory (*Kottke and Rathje, 2008*) to compute the expected seismic response at each SHM. To account for the relevant uncertainty, 100 random profiles were generated for each SHM, which were compatible with available data. Outcomes of the relevant numerical simulations were considered to assess uncertainty affecting amplification estimates at each SHM.

Through this procedure, approximately 4000 Seismically Homogeneous Microzones were identified, distributed across over 80,000 formation outcrops mapped on Geological map of Tuscany Region, selected by dedicated ArcgisPro ™/Arcpy ™ scripts elaborated for this aim. The 50th percentile of the amplification factor (AF) distribution for each SHM was taken into consideration. This process aimed to create a new map of amplification factors for the entire territory of Tuscany, achieving an optimal spatial resolution of 1:10,000.

To assess the reliability of the results obtained from numerical simulations, and evaluate the possible presence of biases, outcomes of the numerical procedure here considered were

compared with those from second and third levels of Seismic Microzonation studies available in Tuscany. Approximately 1500 benchmark samples were identified, revealing distinct trends among various SHM, particularly between those with outcropping sedimentary covers and those with exposed geological bedrock.
In general, amplification estimates provided by the approach here proposed provide a slight overestimate of the ones provided by the detailed seismic microzonation studies (less than 10% on average). However, this overestimate is largely within the range of uncertainty affecting regional estimates and mostly concerns SHMs where bedrock outcrops.
It is worth to note that by no way the proposed approach should be considered as a substitute for detailed local studies. Anyway it could be considered to provide ex-ante evaluations to be used as a preliminary reference for large scale risk analysis and for a preliminary assessment of expected ground motion effects where more detailed studies are not available so far.

References

Commissione Tecnica MS; 2018: Standard di rappresentazione e archiviazione informatica degli studi di MS vers.4.1.

Gaudiosi I., Romagnoli G., Albarello D., Fortunato C., Imprescia P., Stigliano F. Moscatelli M.; 2023: G/G 0 (γ) and D(γ) curves joined with engineering geological units in Italy. In press on Sci.Data,

Romagnoli G., Tarquini E., Porchia A., Catalano S., Albarello D., Moscatelli M.; 2022: The possible use of engineering-geological qualitative characterization of shallow subsoil for a preliminary estimate of the Vs profile in seismic microzonation studies. Soil Dyn. Earthq. Eng., 161, 107347,

SM Working Group; 2015: Guidelines for Seismic Microzonation, Conference of Regions and Autonomous Provinces of Italy – Civil Protection Department, Rome.

Corresponding author: nicolo.carfagna@student.unisi.it

Seismic isolation for Glass Curtain Walls

N. Cella, C. Bedon

University of Trieste, Department of Engineering and Architecture, Trieste, Italy

Introduction

Glass curtain walls (GCWs) are a typical component of modern buildings, providing them a sleek and modern aesthetic. However, glass façades are also a criticality for buildings, and require special design strategies under extreme design loads like earthquakes. The main reason is the brittle behaviour of glass, which makes these composite systems a potential hazard for life.

Several surveys conducted after natural earthquakes, as well as extensive laboratory experimental campaigns, highlighted the high vulnerability and susceptibility of GCWs to major damage following inter-story drifts, even in those buildings that have suffered for minimal damage in structural members (Bedon et al., 2017). This damage is generally due to an incompatibility between the deformation of the primary structure and the façade components. As such, there is a major need to develop technological solutions to optimise the capability of GCWs to satisfy these displacement demands caused by seismic actions. Possible approaches – like the device fabricated by Heonseok et al. (2021) – should be able to offer energy dissipation and flexibility to accommodate the seismic shock and demand.

In this paper, the in-plane lateral performance of a full-scale case-study glass façade (Aiello et al., 2018) is numerically investigated to explore its criticalities and to assess the potential and feasibility of a possible isolation system inspired by the well-known rubber seismic isolators for structures. The discussion of numerical comparative results poses attention on the different behaviour of the reference “fixed” façade and the “isolated” façade configurations, highlighting the potential benefits in terms of seismic demand reduction.

Case study

As a reference for the numerical modelling, the GCW presented in Aiello et al. (2018) was taken in account.

The tested façade is a typical stick system with five mullions and twenty transoms in extruded aluminium (alloy EN-AW 6060, supply type T5). The GCW is 7.80 m high and 5.38 m wide with a constant inter-story height of 3.4 m. The transom to mullion connection is made through a U-shaped steel joint fixed to the mullion with two stainless steel screws.

Glass panels (1300x1900h mm) consist of insulated glass units (IGUs) where two laminated elements (4+4 mm thick annealed glass panels with two PVB interlayers) are spaced by a 16 mm cavity. Each panel is supported by two setting blocks made of aluminium alloy with a layer of plastic material (rubber pad) on top, located at about L/10 from the end of the transom, where L is the length of the transom. Glass panels are then fixed in position by means of pressure plates, which are screwed to the aluminium frame. The clearance between glass panels and frame is about 6 mm.

Finite Element model

A geometrically simplified and computationally efficient numerical model - inspired by the strategic modelling steps discussed by Caterino et al. (2017) - was implemented in SAP2000 (Fig. 1(a)).

The model consists of 1D beam elements to accurately represent the mechanical properties of the aluminium frame mullions and transoms. The latter are assumed to be hinged at both ends. 2D shell elements are employed to describe the insulated glazing units (IGUs), with their total thickness corresponding to the sum of the glass layers (thus excluding cavity and PVB layers). A linear constitutive law is adopted for both glass and aluminium, with input material properties summarized in Tab. 1. Two different link types available in SAP2000 are employed to reproduce the mechanical interactions between the different components of the façade:

- "Gap" links are used to represent potential contact between IGUs and frame members following clearance closure. To account for the role of setting blocks, the gap value for the respective links is set to zero.
- "Wen" links are used to characterize the mechanical behaviour of the gaskets.

The typical simulation consisted of nonlinear Direct-Integration time-history analysis in displacement control. For the validation of the numerical model, the experimental displacement time-history was applied to the intermediate constrained joints, while the displacement obtained from a natural earthquake record (Newhall - Los Angeles County Fire Station) was used to evaluate the effectiveness of the isolation system (Fig. 1(b)). The chosen mesh size results in approximately 450 frame elements, 1200 shell elements, and 1600 joints.

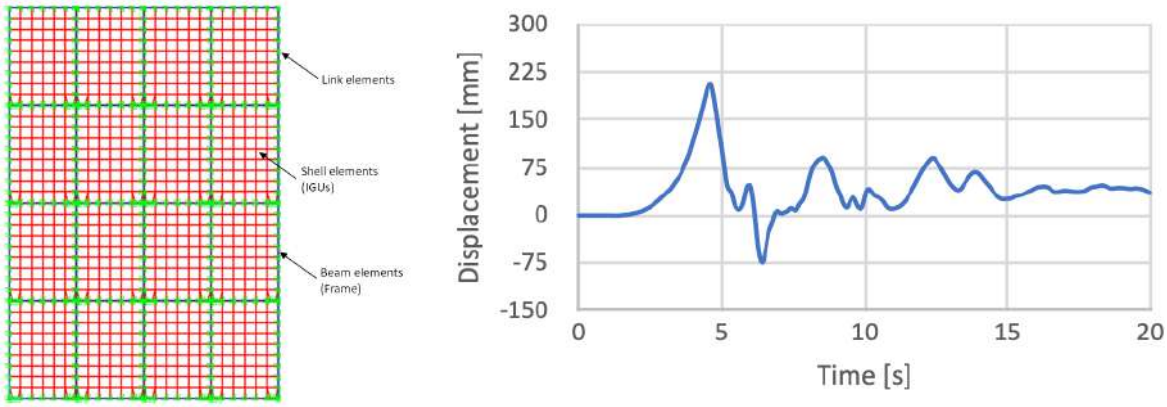

(a) (b)

Fig. 1– (a) Numerical model in SAP2000 and (b) Displacement Time-History from a natural earthquake.

Material	Density [kg/m³]	Modulus of elasticity [MPa]	Poisson' coefficient [-]
Aluminium (6060 T5)	2700	70,000	0.3
Annealed glass	2500	70,000	0.23

Tab. 1 – Input material properties.

To assess the effect and potential of the seismic isolation system, the "fixed" model was modified by introducing a set of linear links with specific stiffness components. In addition, the position of the lower constraints was changed by assuming that the façade is supported at the base.

The linear links in use for the isolation system are characterized by two different stiffness values in the three translational directions. For the present investigation, the isolator is assumed to be rigid along the direction of the link (i.e., the Fixed option of SAP2000 is used). The stiffness in the other two directions is calculated following the design approach for rubber seismic isolators. Specifically, given the period of the isolated system, T_{isol}, the stiffness of the isolation system is given by:

(1)

$$k_{isol} = \left(\frac{2 \bullet \pi}{T_{isol}}\right)^2 \bullet M$$

Where $M = 1880kg$ is the total mass of the GCW. The stiffness of the isolator is thus calculated as follows:

(2)

$$k_{isol,i} = \frac{k_{isol}}{n}$$

where $n = 15$ is the number of isolators.

The input features of isolating system were chosen to result in a vibration period of the isolated system of 2.0 seconds. For comparison, the "fixed" configuration has an in-plane vibration period of 0.0053 seconds. An equivalent viscous damping coefficient of 10% was also considered for the isolated system. It is worth noting that, assuming a dynamic shear modulus of 0.4 MPa for the rubber layers and a cylindrical shape for the isolator, the stiffness corresponds to a ratio $\frac{r^2}{h} = 0.98$ (e.g., a 30 mm high rubber cylinder with a radius of 5.4 mm).

The above link parameters have been calibrated as shown in Tab. 2.

Parameter	Gap	Wen	Linear
Stiffness [N/mm]	75	500	1.24
Damping [N·s/m]	-	-	78.75
open [mm]	6	-	-
ratio [-]	-	0	-
yield [kN]	-	50	-
exp [-]	-	1	-

Tab. 2 – Link parameters.

It is important to note that the parameters for Wen and Gap links were chosen with the aim of achieving the best agreement between the numerical results and the experimental data.

Discussion of numerical results

Fig. 2(a) shows the numerical response of the façade subjected to in-plane lateral displacement as a function of the corresponding reaction force, compared to the reference literature experiment (Aiello et al., 2018). The numerical results have good agreement with the test, confirming the goodness of the modelling strategy proposed by Caterino et al. (2017) and further elaborated in Aiello et al. (2018) for predicting the global seismic behaviour of a stick curtain wall.

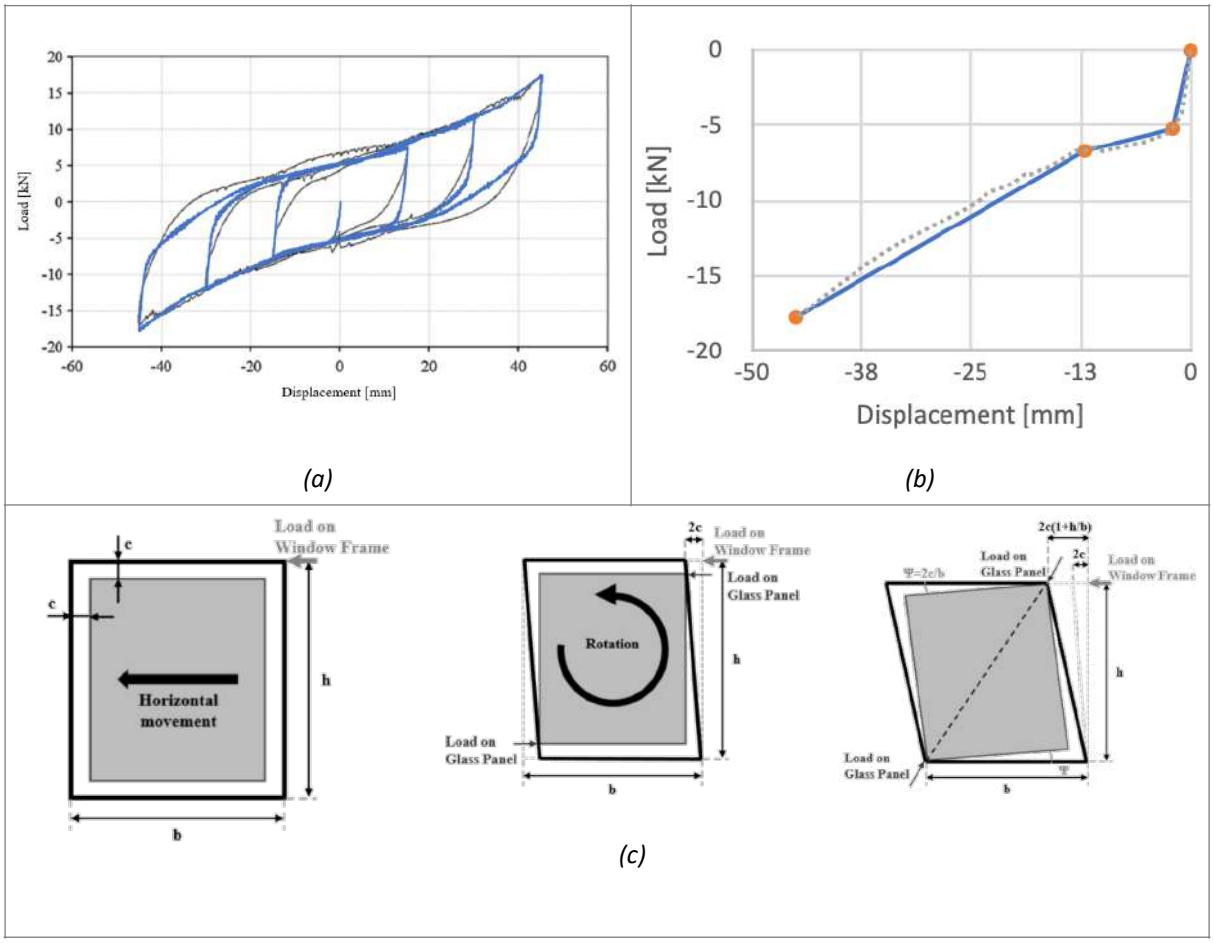

Fig. 2 – (a) Load-displacement response compared to the reference experiment (Aiello et al., 2018) for the "fixed" model; (b) Schematization of the load-displacement response; (c) Movement of a glass panel under in-plane seismic action (Sucuoğlu & Vallabhan, 1997).

The load-displacement response of the façade can be schematize as shown in Fig. 2(b), where it is possible to subdivide it into three branches:

1. The first branch, AB, is governed by friction between glass panels and gaskets.
2. The second one, BC, is governed by the lateral stiffness of the bare aluminium frame.
3. In the point C the glass panels make contact with the aluminium frame; in the last branch, CD, glass panels start to contribute to the global stiffness of the façade.

The movement of a glass panel within the frame can be summarized as in Fig. 2(c) (Sucuoğlu & Vallabhan, 1997):

1. Rigid horizontal movement of the panel until the contact with the frame.
2. The contact happens in two opposite glass corners and the panel start to rotate.
3. When the two opposite glass panel corners make contact with those of the surrounding frame, the panel acts like a diagonal strut.

The final configuration may result in either a compressive crushing failure or the practically intact glass panel falling out due to the loss of support on the contour.

Fig. 3(a) and (b) show the deformed shape of the “fixed” and “isolated” models at the maximum imposed displacement. The effect of the adopted isolation system is evident and corresponds to a major reduction in the frame deformation, as well as a decrease in its absolute in-plane lateral displacement. The latter is also highlighted by Fig. 3(c), where the displacement of the same control point is reported for the two configurations. The reduction corresponding to the maximum imposed displacement is - 67%. Such a major decrease in the in-plane bending frame deformation naturally leads to a reduction of stress peaks in both metal and glass components, as Fig. 3(d) shows. In this case, the stress reduction corresponding to the maximum imposed displacement is quantified in - 99%.

As shown in Fig. 2(c), breaking of the glass or its fall-out depends to the contact with the frame. Fig. 3(e) shows the relative distance between two joints, one from a glass panel and one from the frame, connected with a link. Fig. 3(e) shows a constant relative distance for the “isolated” model, equal to the initial clearance of 6 mm. This confirms the possibility of avoiding glass failure adopting the seismic isolation system presented. Additionally, Fig. 3(e) highlights an intrinsic limitation of the modelling strategy adopted for the “fixed” model in the local performance assessment as the relative distance becomes negative.

Conclusions

Due to brittle behaviour of glass, façades are vulnerable building components, especially under extreme actions, such as earthquakes. In this paper, preliminary considerations and numerical results about the effects of a seismic isolation system inspired by rubber seismic isolators are presented. The attention was given primarily to reduction in displacement and stress peaks through a comparison between the numerical results of an experimental tested glass façade and the same GCW equipped with the isolation system. In this regard, a - 67% reduction in maximum frame displacement and a - 99% reduction in peak frame stress was recorded. In addition, the absence of relative displacement between glass and frame was noted for the “isolated” façade. In this sense, the analysis of present results confirms the positive effects of such a system in reducing damage of GCWs subjected to in-plane lateral displacement.

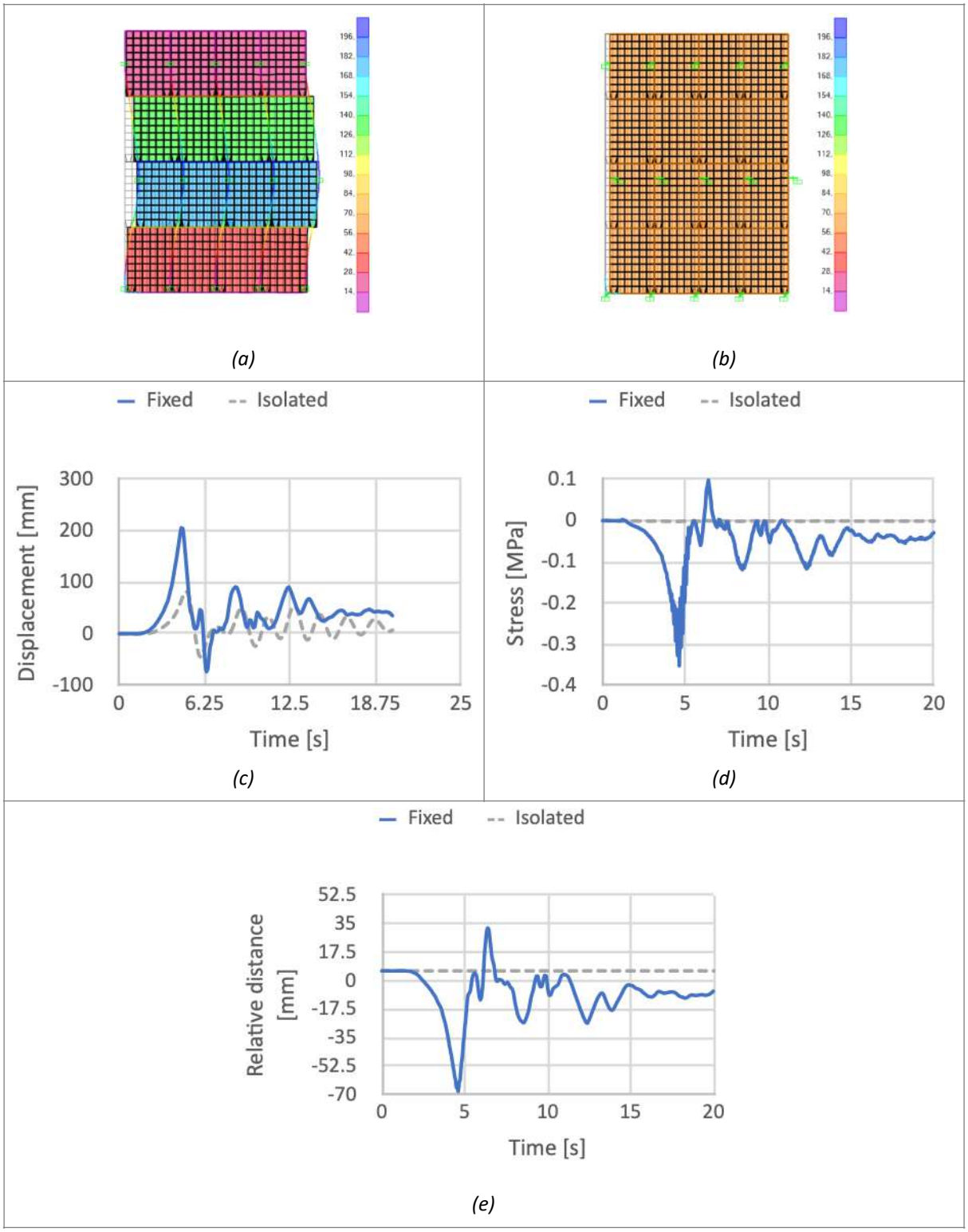

Fig. 3 – Deformed shape for (a) "fixed" and (b) "isolated" model and comparison for (c) frame absolute displacement, (d) frame stress and (e) glass-frame relative distance.

References

Aiello C., Caterino N., Maddaloni G., Bonati A., Franco A., Occhiuzzi A.; 2018: Experimental and numerical investigation of cyclic response of a glass curtain wall for seismic performance assessment. Construction and Building Materials.

Bedon C., Zhang X., Santos F., Honfi D., Kozłowski M., Arrigoni M., Lange D.; 2017: Performance of structural glass façades under extreme loads - Design methods, existing research, current issues and trends. Construction and Building Materials.

Caterino N., Del Zoppo M., Maddaloni G., Bonati A., Cavanna G., Occhiuzzi A.; 2017: Seismic assessment and finite element modelling of glazed curtain walls. Structural Engineering and Mechanics.

Heonseok L., Myunghwan O., Junwon S., Woosuk K.; 2021: Seismic and Energy Performance Evaluation of Large-Scale Curtain Walls Subjected to Displacement Control Fasteners. Applied Sciences.

SAP2000 Static and Dynamic Finite Element Analysis of Structures; 2014: Berkeley, USA. Computers and Structures Inc.

Sucuoğlu, H., Vallabhan, C.; 1997: Behaviour of window glass panels during earthquakes. Engineering Structures.

Corresponding author: chiara.bedon@dia.units.it

The state of art of the Italian National Seismic Network

L. Chiaraluce, A. Mandiello, M. Massa, D. Piccinini and RSNM-BOARD[1]

[1] *Istituto Nazionale di Geofisica e Vulcanologia (INGV, Italy)*

The National Seismic Network (RSN) is a research infrastructure that must allow the scientific community to practise and develop cutting-edge seismological research topics. To do this, the RSN must have a configuration able to guarantee the continuous production in real time of high-quality data, in standard formats, correctly described and easily and freely accessible to all users. It is our opinion that if the RSN allows the development of front-line scientific research, it will easily be able to allow a detailed monitoring service of seismic activity throughout the whole national territory.

In this context, network configuration and technology play a fundamental role. For this reason, we have established a series of analyses aimed at evaluating the quality of the data produced by both the velocity and accelerometer stations of the IV and MN Networks managed by the INGV. Thus, through a complex analysis of the signal's characteristic and continuity and instruments association from which the data are produced, we have therefore generated a sort of quality ranking of the stations managed by INGV.

The result of this study will serve not only to carry out interventions aimed at improving the qualitatively less performing stations and to decide on a maintenance policy based on the importance of the specific station, but also to allow us to propose a new project for the true modernization of the National Network. Modernization that will pass not only through a simple densification, but also through an implementation of instrumentation, acquisition technology and installation methods.

Corresponding author: lauro.chiaraluce@ingv.it

Regional scale geological/geotechnical parametrization for seismic amplification abacuses – a global approach in the Piedmont Region.

C. Comina [1], G.M. Adinolfi[1], A. Bertea[2], C. Bertok[1], V. Giraud[2], P. Pieruccini[1]

[1] Università degli studi di Torino, Department of Earth Sciences; Torino, Italy.
[2] Seismic Sector, Piedmont Region; Pinerolo, Italy.

Introduction

Amplification abacuses are widely diffused simplified tools for the quantification of local stratigraphic amplifications of the seismic ground motion over large areas, i.e. Regions. To be effective, the abacuses should be representative of a geological/geotechnical model including all possible seismo-stratigraphical settings of the study area (Pieruccini et al., 2022). Thus, abacuses must be the result of a compromise between generalization and specialization (Peruzzi et al., 2016) and several approaches have been adopted in the past for their formulation (e.g. Pagani et al., 2006). Most of these approaches include as fundamental steps: 1) geological/geotechnical modelling, 2) parameterization, 3) numerical simulations, 4) statistical analysis and the final compilation of representative abacuses. The first two phases are undoubtedly the most important and troublesome. An extensive characterization of the study area is required, preferably based on geological, geotechnical and geophysical databases from Regional Authority's repositories. The statistical significance of the collected data should be resumed in a proper parameterization of the geological/geotechnical model of the area of study, in terms of potential seismo-stratigraphical settings. We present in this study the preliminary work done for the assessment of the Piedmont Region (Northern Italy) amplification abacuses focussing on the shear wave velocity (Vs) distribution of the Geological Domains (GD) within the Region that will be adopted as a driving tool for the following numerical simulations and statistical analysis.

Methodology

The first step was the assessment of the Engineering Geological Model for the Piedmont Region by the identification and mapping of the different Geological Domains (GD), each one characterised by an homogeneous Geological and Geomorphological setting, including a number of litho-stratigraphical logs. The original regional database was 1:250.000 scale Geological Map that allowed the identification of 13 different GDs (Figure 1).

Each GD is characterized by different bedrock typologies and potentially different litho-stratigraphic settings, including Cover Terrains. The GDs are related to: a) the Alpine mountain chain with different bedrocks (GD 1 to 4) including the main Alpine valleys (GD 5); b) the foreland hilly landscape both with different bedrock and cover terrains typologies and thicknesses (GD 6 and 7); c) the Po river plain, fed by alpine rivers, with thick mostly coarse-grained Quaternary deposits overlying at depth different bedrocks (GD 8); d) minor alluvial plains fed by rivers coming from the Apennines and the foreland hills with thick mostly fine-grained Quaternary deposits overlying at depth different bedrocks (GD 9 and 10); e) the morain amphitheatres and the associated fluvio-glacial and lacustrine deposits (GD 11 and 12); f) the complex successions belonging to the Ligurian Units (GD 13).

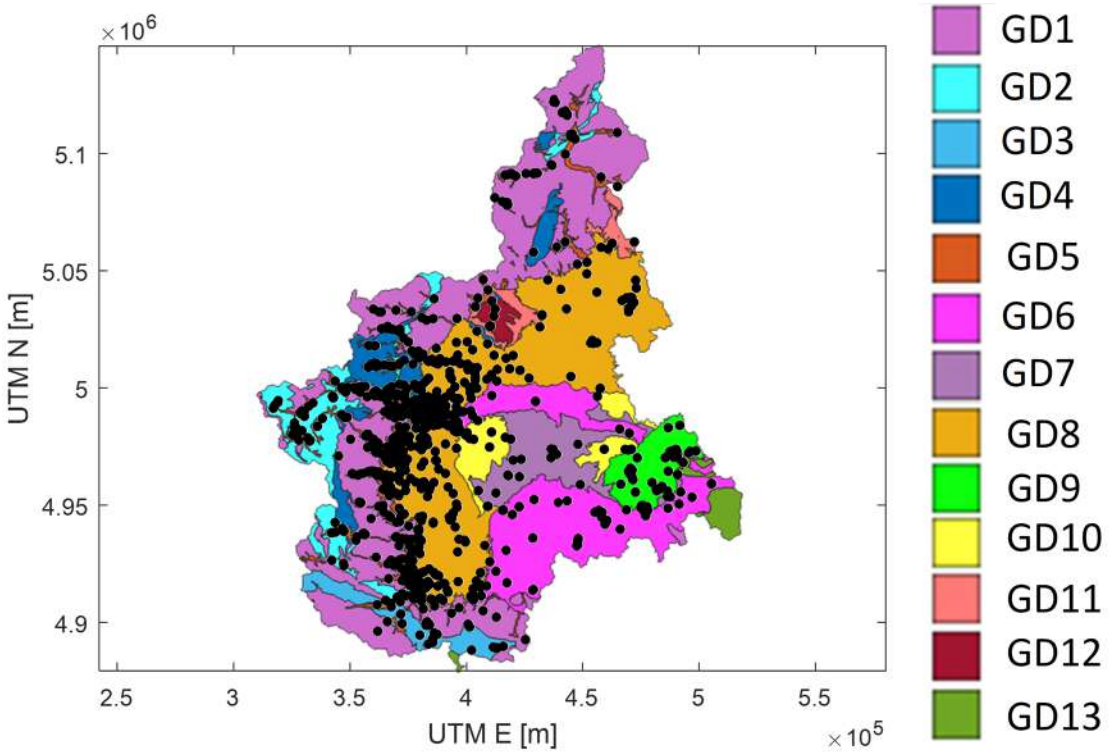

Figure 1 – Map of the Geological Domains within the Piedmont Region, black dots represent the available geophysical information in terms of shear wave velocity profiles from Regional repository database, on purpose implemented information and specific field tests executed.

Once the GDs were identified the available geotechnical and geophysical databases from Regional authority's repositories were used for the geological/geotechnical characterization and for parameterization within each GD. One of the main parameters to be considered in the study of stratigraphic amplifications is the seismic bedrock depth and the shear wave velocity (Vs) of the different units overlaying the seismic bedrock. With this respect the analysis of the Regional geophysical database allowed the assessment of about 1200 Vs profiles. In order to fill the gap in the geographic data distribution we added more Vs profiles thanks to the collaboration with Techgea S.r.l., a leading geophysical society at Regional scale (about 300 Vs profiles) and by performing specific field tests or implementing specific information from literature data (about 50 Vs profiles).

All the available data underwent specific Quality Control (QC) in order to consider only reliable and state of the art information. Data deriving from MASW tests (the most widely diffused technique for Vs profile determination) underwent a specific QC control consisting in checking: 1) the consistency of the dispersion curve, that should present a clearly visible and continuous fundamental mode in the frequency band of interest; 2) in case of presence of multiple modes of vibration, they should be well separable, well distinguishable and reliably interpretable independently; 3) the picking of the dispersion curve that should be reliable and fitting with the spectral maxima of the seismogram transform used for the analysis; 4) the inversion of the data should lead to a synthetic dispersion curve very close to the experimental data *i.e.* good correspondence between the experimental data and the results of the inversion; 5) the depth of the Vs profile should be compatible with the minimum frequencies observed in the analysis of the dispersion curve, *i.e.* investigation depth less than at least the maximum wavelength (preferably half the maximum wavelength); 6) the Vs profile should match the minimum parametrization criterion, *i.e.* number of analyzed layers compatible with the experimental information.
The results of the QC are about 1000 Vs profiles distributed over all the GDs (Figure 1), concentrated near the main urban settlements and most populated areas that are the main targets for such types of studies. The final step is the evaluation of specific Vs profile distribution within each GDs and their comparison among different GDs.

Results and Discussion

As an example, the results of the performed analysis over the GD 8 (Po plain fed by alpine rivers) are reported in Figure 2. In this GD 362 Vs profiles were available (Figure 2a) of which 66 reached the seismic bedrock (Figure 2b). The average Vs of the bedrock is 975 m/s and its depth is between 5 and 46 m. The Vs,z (harmonic average velocity) distribution of the non-bedrock layers was also computed for each profile (Figure 2c) together with the resulting Vs,h according to NTC (Figure 2d). The Vs,z is indeed usually considered as a closer representation of the physics of the problem than the Vs layered profile (Comina et al., 2022). This allowed also to obtain a representative median Vs,z profile for the GD (together with its standard deviation).
Median Vs,z profiles were then analysed in the different GDs (Figure 3). The distribution of the median Vs,z profiles show groups of GDs with very similar behaviours, reflecting the similarities in the properties of the non-bedrock deposits. Following a global approach to the data analysis the median Vs,z profiles, eventually merged between similar GDs, will be the basis for the following randomization and simulation steps. For this purpose specific randomization approaches, based on the same Vs,z (Passeri et al., 2020) or on usually adopted randomization criteria (e.g. Toro, 2022) will be evaluated. This proposed global approach allows to overcome the limitations inherited by the uncertainties of the specific litho-stratigraphic settings within each GD, due to the regionality scale of observations and the quality of the existing databases.

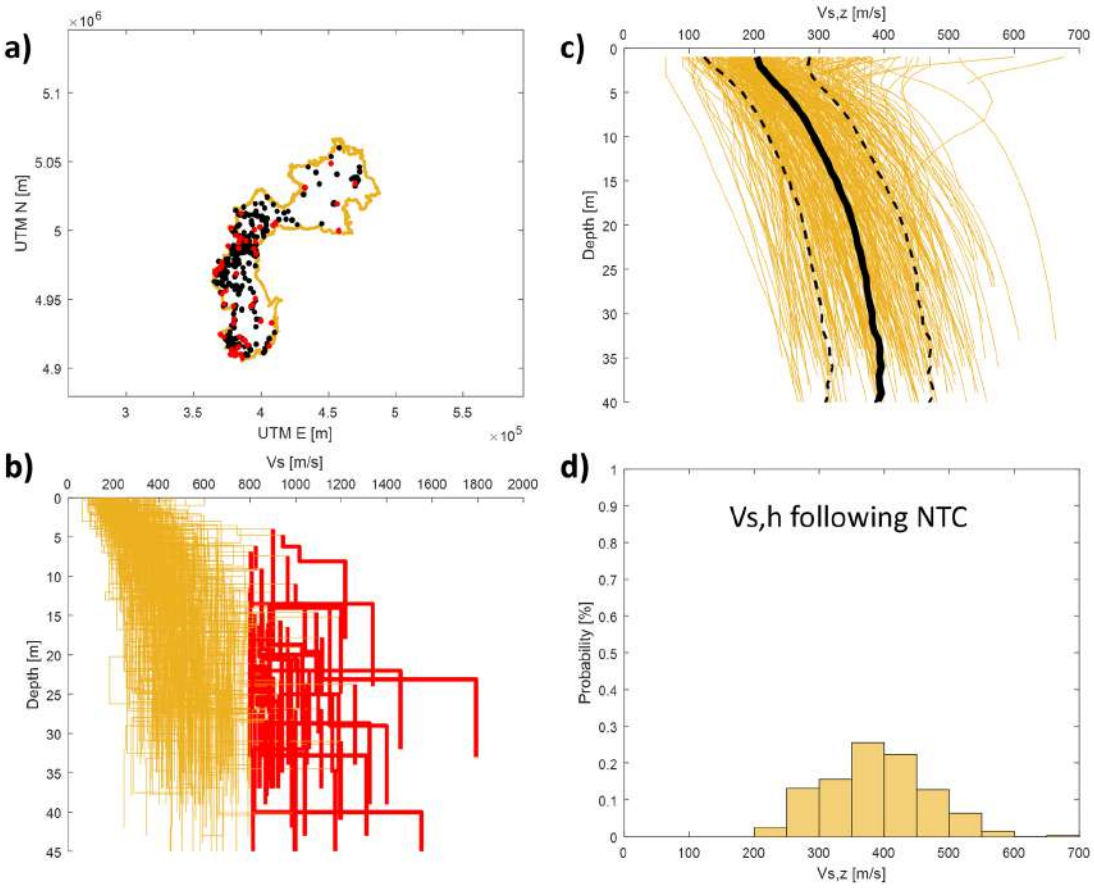

Figure 2 – Example results of the performed analysis over GD 8 – Po plain: a) Vs profile availability within the GD (black dots) and evidence of the Vs profiles reaching the seismic bedrock (red dots); b) All available Vs profiles (orange lines) with evidence of the bedrock velocities (red lines); c) Vs,z profiles for the non-bedrock units and their mean (continuous black line) and standard deviation (dashed black lines); d) Vs,h distribution following NTC.

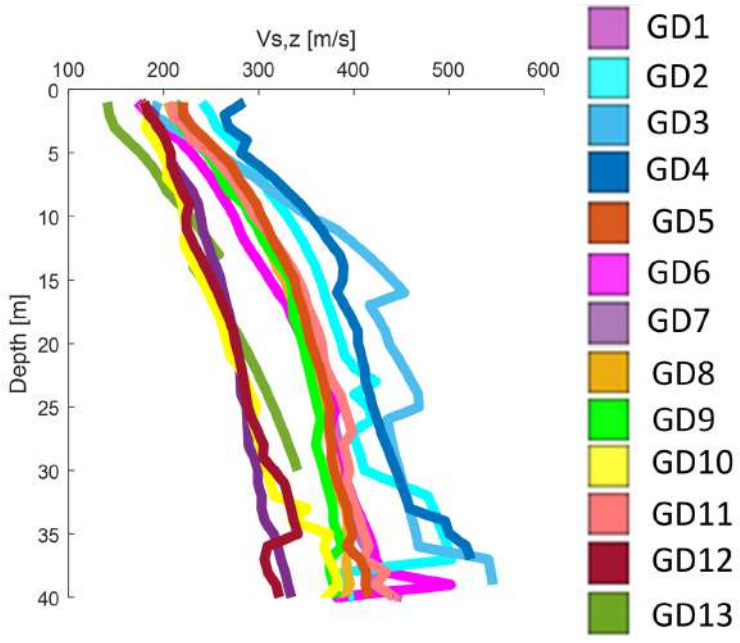

Figure 3 – Average Vs,z profiles for the non-bedrock units for each GD.

Conclusions and future work

The preliminary work done for the construction of the Piedmont Region amplification abacuses is presented and discussed in this study with particular attention in the definition of the shear wave velocity distribution of the different identified Geological Domains (GD). For this purpose, an extensive database of about 1000 Vs profiles was assessed for the randomization approaches to abacuses construction. Moreover, the median properties of the distribution of the Vs profiles within the GDs might provide useful data for similar materials in analogous geological contexts. Further work will include the analysis of available borehole logs in the Region and the definition of decaying curves to be adopted in the execution of specific numerical simulations.

Acknowledgements

Authors are indebted with the Seismic Sector of Piedmont Region for their support and data availability, with Techgea S.r.l. for the sharing of additional shear wave velocity profiles, fundamental to complement the data.

References

Acunzo G., G. Falcone, A. di Lernia, F. Mori, A. Mendicelli, G. Naso, D. Albarello, M. Moscatelli, 2023, NC92Soil: A computer code for deterministic and stochastic 1D equivalent linear seismic site response analyses, Computers and Geotechnics 165 (2024) 105857.

Comina C., Foti S., Passeri F., Socco L.V., 2022, Time-weighted average shear wave velocity profiles from surface wave tests through a wavelength-depth transformation, Soil Dynamics and Earthquake Engineering, 2022, 158, 107262.

Pagani M., Marcellini A., Crespellani T., Martelli L., Tento A., Daminelli R., (2006) Seismic microzonation regulations of the Emilia-Romagna Region (Italy). Third international symposium on the effects of surface geology on seismic motion, Grenoble, France, 30 August–1 September 2006.

Passeri F., Foti S., Rodriguez-Marek A., 2020, A new geostatistical model for shear wave velocity profiles, Soil Dynamics and Earthquake Engineering, 2020, 136, 106247.

Peruzzi G., D. Albarello, M. Baglione, V. D'Intinosante, P. Fabbroni, D. Pileggi, 2016, Assessing 1D litho-stratigraphical amplification factor for microzoning studies in Italy, Bull. Earthquake Eng. 14:373–389.

Pieruccini P., Paolucci E., Fantozzi P.L, Naldini D., Albarello D., 2022. Effectiveness of Geological-Geomorphological modelling for Seismic Microzonation studies. Nat Hazards 112, 451–474.

Toro G.R., 2002, Uncertainty in Shear-Wave Velocity Profiles, J Seismol (2022) 26:713–730.

Corresponding Author: cesare.comina@unito.it

Using data from CRISP database to infer site response behaviour

G. Cultrera[1] , A. Mercuri[1]

(1) Istituto Nazionale di Geofisica e Vulcanologia, Roma - Italy

The CRISP archive is a web portal that collects site information of the Italian National Seismic Network RSN (website crisp.ingv.it; Mercuri et al., 2023). It is organized to contain all the information useful for the site characterization, such as: thematic maps on geological characteristics; information on station and housing (location, instrumentation, data quality, housing type); geological data under and around the station (stratigraphy, geological review, morphological, lithological and geological classification, cross section); seismic analysis on recordings (spectral ratio on noise and earthquake, signal polarization); geophysical investigations (Vs profile, non linear curve); topography and soil class. CRISP is populated with heterogeneous data coming from pre-existing INGV archives or having different origins, such as: maps and geological description from ISPRA (https://www.isprambiente.gov.it/), results of seismological analyses and geophysical surveys specifically performed or inferred from literature, site and topography classification using different available information. It represents a continuously expanding database being updated with new stations added to the national network and with new data gradually becoming available from new sources.

With 340 stations present at the beginning of 2023, in the framework of the national research PRIN project SERENA - Mapping Seismic Site Effects at REGional and NATIONAL Scale, (WP6 - Empirical Testing and Calibration) CRISP represents a good starting point for systematising the information related to the site characterization with the aim to identify a site amplification model based on site condition indicators.

A preliminary selection of representative proxies drove us to extract and compare the indicators related to the morphological and lithological classification, site classification and seismological analysis. Specifically, we selected the slope of morphology, lithological type, soil consolidation degree, amplitude and frequency peaks of Horizontal-to-Vertical spectral ratio (HVSR) on noise and earthquakes, frequency and direction of polarization, topography class and site class from EC08 and NTC18.

In order to identify the significant indicators and recognize their dependencies, we first analysed the distribution of each indicator (see histograms of Lithological classification groupments and site class in Fig.1).

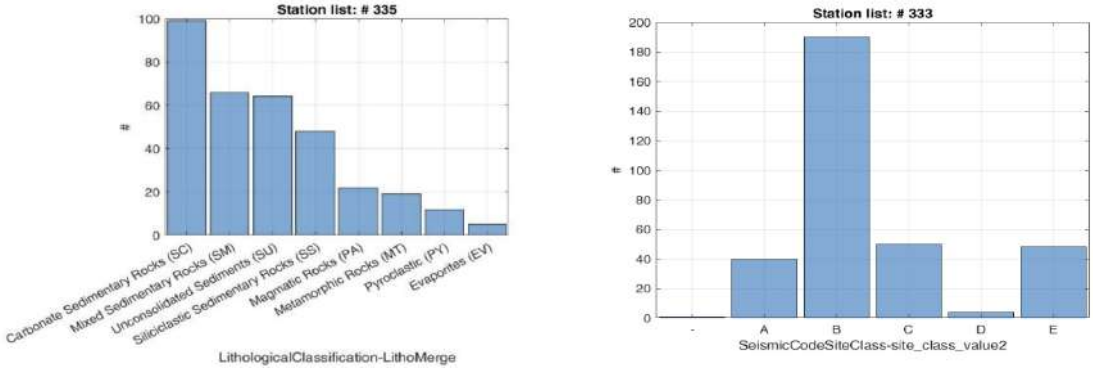

Fig. 1 – Data distribution for lithological classification grouped by rock categories with similar genesis(left) and Site classification from NTC18 (right).

We then looked for possible correlation between different parameters. Fig. 2 shows the comparison between the resonance frequency (f0) values from HVSR on noise and earthquakes at all stations: in general, for frequencies larger than about 2 Hz, the peak amplifications from noise are found at larger frequencies than from earthquakes.
Moreover these proxies are compared with magnitude residual from Di Bona et al. (2016), to look for an additional relationship helping to determine a site amplification model. For example the Fig.3 shows the distribution of f0 from HVnoise: the magnitude residuals tend to positive values as f0 increases.
Furthermore, the availability of numerous HVSR curves can be grouped by means of the cluster analysis for the recognition of similar characteristics.

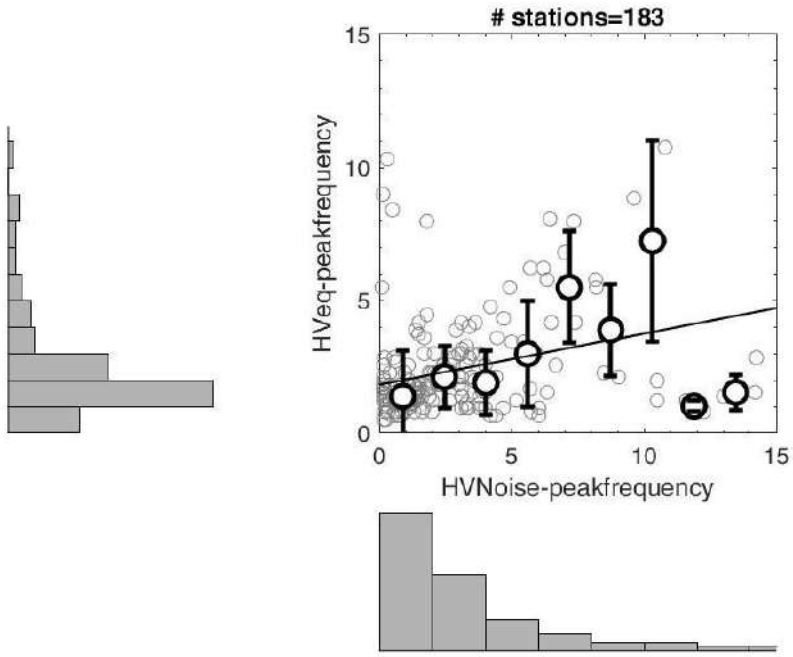

Fig. 2 – Example of correlation between f0 from HVSR on noise and earthquakes, having amplitude A0 >= 2.

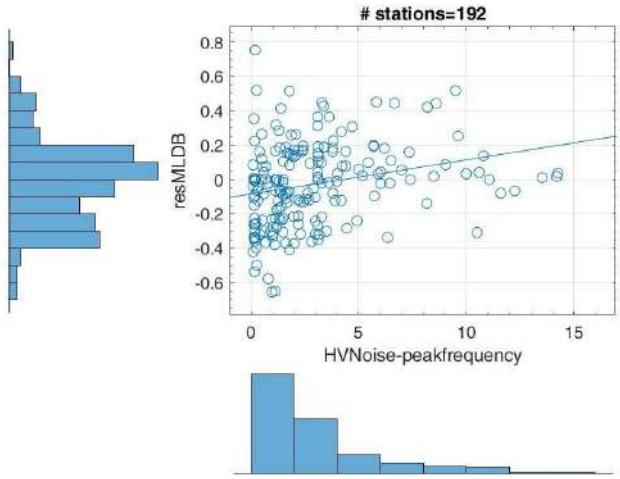

Fig. 3 – Distribution of f0 from HVnoise, with respect to the magnitude residuals.

References

Cultrera G., Bordoni P., Mercuri A., Quintiliani M., Minarelli L., Famiani D., Casale P., Pischiutta M., Ladina C., Cara F., Di Giulio G., Pucillo S., Monti G., and CRISP Working Group (2022). Database for site characterization of permanent seismic stations (CRISP). Istituto Nazionale di Geofisica e Vulcanologia (INGV). https://doi.org/10.13127/crisp

Mercuri A., G. Cultrera, L. Minarelli, M. Quintiliani, P. Bordoni, D. Famiani, P. Casale, M. Pischiutta, C. Ladina, F. Cara, G. Di Giulio, S. Pucillo, G. Tarabusi, and INGV CRISP Working Group. CRISP: an archive for the site characterization of permanent Italian seismic stations. Accepted by Bulletin of Earthquake Engineering (2022). https://doi.org/10.1007/s10518-023-01618-w

Russo E, Felicetta C, D Amico M, Sgobba S, Lanzano G, Mascandola C, Pacor F, Luzi L (2022). Italian Accelerometric Archive v3.2 - Istituto Nazionale di Geofisica e Vulcanologia, Dipartimento della Protezione Civile Nazionale. doi: 10.13127/itaca.3.2

Corresponding author: alessia.mercuri@ingv.it

Automated Stratigraphic Reconstruction and Spatialization for Seismic Site Effect Analysis

A. D'Agostino[1], A. Porchia[2], G. Cavuoto[3], F. Pavano[3], M. Moscatelli[2], G. Tortorici[2], S. Catalano[1,2]

[1] Department of Biological, Geological and Environmental Sciences (DBGES) – Section of Earth Science, University of Catania.
[2] IGAG-CNR - Institute of Environmental Geology and Geoengineering of the Italian National Research Council, Area Della Ricerca di Roma 1.
[3] ISPC-CNR - Institute of Heritage Science of the Italian National Research Council, Napoli.

In the frame of the PRIN project "Mapping seismic site effects at regional and national scale – SERENA", we have developed a set of Python scripts within a GIS environment, aimed at reconstructing and spatializing stratigraphies. These codes represent an integral part of a workflow designed to divide the territory into stratigraphically homogeneous areas, providing representative stratigraphic columns for modeling and determining seismic amplification factors.

The code set consists of two scripts for stratigraphic reconstructions and a third script for their spatialization. The first unsupervised script operates on a raster base and generates stratigraphies based on a predetermined total thickness. The second supervised script works on vector cartographic bases and produces stratigraphies through individual steps. This procedure allows a progressive verification of the stratigraphic column under construction. These first two scripts analyze the lateral contacts between the outcropping units, placing them in stratigraphic order based on a geometric position index (Cesarano et al., 2022) and calculating the cumulated thickness.

The third unsupervised script performs the spatialization by assigning the same ID to each unique reconstructed stratigraphic column. The final output is a 2D map made of polygons populated by the same column ID.

In order to generate and spatialize the stratigraphies, the employed raster or vector cartographic base must contain polygonal elements representing the Engineering-Geological Units – EGU (Technical Commission for Seismic Microzonation, 2020). Each polygon must include a unique geometric position index and a thickness value.

The scripts were validated on the 428 km^2 wide Territorial Context (TC) of Cariati (Calabria, Italy) (Regione Calabria DGR 498/2019), since the EGUs had already been geometrically indexed (Fig. 1) and the stratigraphic columns manually reconstructed by Cesarano et al. (2022). In this study, the stratigraphic columns were represented in a matrix form. The

developed scripts successfully reproduced the same stratigraphic columns manually obtained by Cesarano et al. (2022), confirming their efficiency (Fig. 2). The entire process required about ten minutes.

Currently, a fourth script for automated thickness calculation is under development with the main goal of defining realistic thickness values that take into account the effects of the erosional processes. This script, using the same cartographic base employed in the previous scripts along with a digital elevation model, analyzes the boundaries between different EGUs and reconstructs their subsoil geometry to assess the thickness of each outcropping unit.

These tools, combined with geophysical and geotechnical data, such as the variability of shear wave velocity in relation to EGUs (Romagnoli et al., 2022) and shear modulus reduction and damping ratio curves (Gaudiosi et al., 2022), represent a significant advancement in the analysis of seismic hazards on a large scale. Their ability to provide detailed and realistic stratigraphies for local seismic response analysis greatly contributes to improving the calculation of seismic amplification factors (AF). This refines the current procedure based on the identification at a national scale of homogeneous morphological-geological and lithological areas (Falcone et al. 2021).

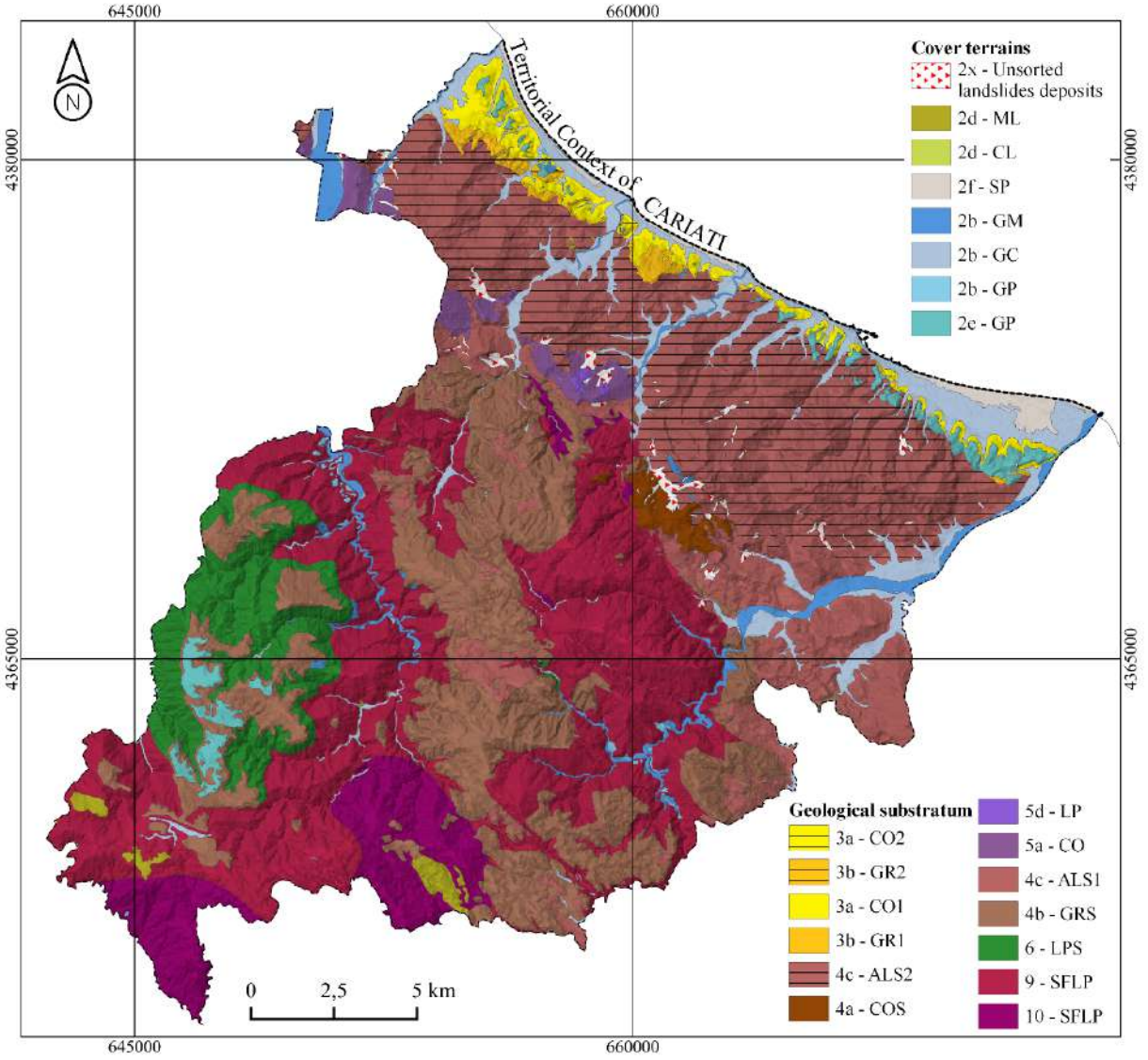

Fig. 1 – Engineering-geological map of the Territorial Context of Cariati (from Cesarano et. al, 2022).

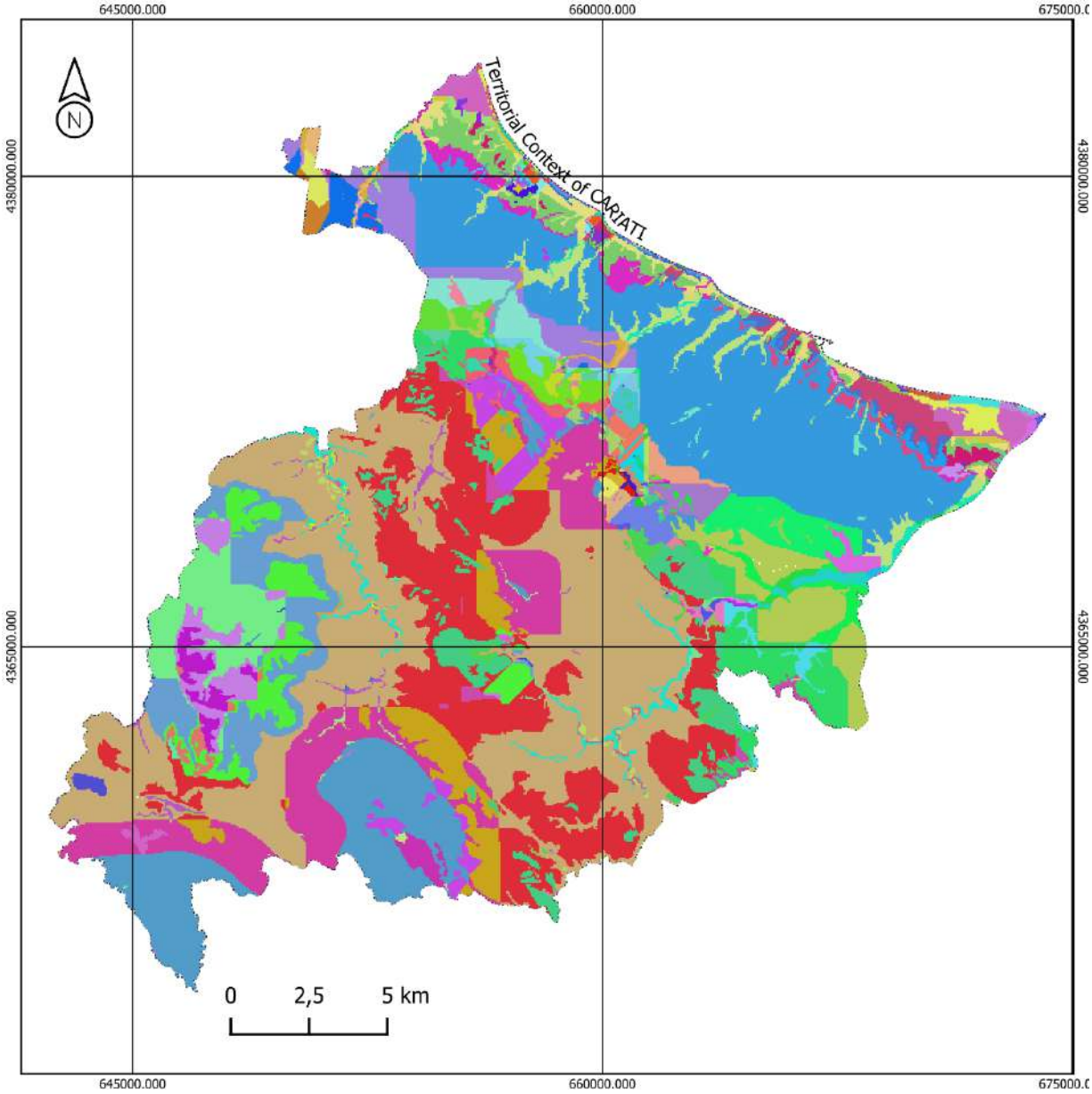

Fig. 2 – Result of the spatialization process in the Territorial Context of Cariati. Each color represents a unique stratigraphic column.

References

Cesarano M., Porchia A., Romagnoli G., Peronace E., Mendicelli A., Nocentini M., Naso G., Castenetto S., Catalano S. & Moscatelli M.; 2022: Multiscale geothematic maps for using the database from the Italian Seismic Microzonation Project: an example of application in the Calabria Region (Southern Italy). Ital. J. Geosci, 141(1), 35-52. https://doi.org/10.3301/IJG.2022.03.

Falcone G., Acunzo G., Mendicelli A., Mori F., Naso G, Peronace E., Porchia A., Romagnoli G., Tarquini E., Moscatelli M.; 2021: Seismic amplification maps of Italy based on site-specific microzonation dataset and one-dimensional numerical approach, Engineering Geology, 289, 2021, 106170, ISSN 0013-7952. https://doi.org/10.1016/j.enggeo.2021.106170.

Gaudiosi, I., Romagnoli, G., Albarello, D., Fortunato, C., Imprescia, P., Stigliano, F., Moscatelli, M.; 2023: Shear modulus reduction and damping ratios curves joined with engineering geological units in Italy. Sci Data 10, 625. https://doi.org/10.1038/s41597-023-02412-8

Regione Calabria; DGR n. 498 del 25 ottobre 2019: Prevenzione del rischio sismico. Adozione documento Contesti Territoriali e Comuni di Riferimento della Regione Calabria redatto dal Dipartimento Nazionale Protezione Civile. Revoca DGR n. 408 del 24.10.2016.

Romagnoli G., Tarquini E., Porchia A., Catalano S., Albarello D., Moscatelli M.; 2022: Constraints for the Vs profiles from engineering-geological qualitative characterization of shallow subsoil in seismic microzonation studies, Soil Dynamics and Earthquake Engineering, 161, 2022, 107347, ISSN 0267-7261. https://doi.org/10.1016/j.soildyn.2022.107347.

Corresponding author: alberto.dagostino@phd.unict.it

Site-dependency of fragility functions

M. Fasan[1], C. Bedon[1], F. Romanelli[2]

[1] University of Trieste, Department of Engineering and Architecture
[2] University of Trieste, Department of Mathematics and Geosciences

Introduction

This work focuses on investigating the potential impact of site conditions on fragility curves, considering factors like source effects, wave propagation, and local site characteristics. Utilizing physics-based numerical simulations, the study examines a hypothetical site using a single seismic source with varied crustal and stratigraphic models.

Through nonlinear dynamic analyses the response of a reinforced concrete frame structure is assessed, leading to the evaluation of fragility curves using the cloud analysis method. The study emphasizes the frequently overlooked impact of crustal models through comparisons among curves for various configurations. The primary objective is to comprehend physical parameter influences on the seismic response of buildings in a hypothetical setting.

Methodology

The methodology of this study delves into ground shaking simulation and seismic source modeling to explore the factors affecting seismic responses. Ground shaking, influenced by rupture processes, rupture propagation, and slip distribution on the fault plane, exhibits high variability in expected acceleration. Synthetic accelerograms are computed through the tensor product of earthquake source representation and Green's function of the medium, considering local site effects and crustal layer characteristics (Chieffo et al., 2021; Hassan et al., 2020). The simulations encompass a hypothetical seismic scenario, evaluating various configurations by employing two realistic deep crustal models (propagation effects) and two local stratigraphic models (site effects, within the same category according to EC8). The earthquake source is modeled as a distributed slip field on the fault surface, employing a Monte Carlo approach to account for spatiotemporal variability in rupture evolution. Seismogram calculations use two techniques, Modal Summation (MS) and Discrete Wave Number (DWN), ensuring accurate simulation of ground motion under different conditions. The limitation to a maximum frequency of 10 Hz is a compromise for simulation accuracy, available information, and computation time.

The fragility curves in this study are derived through the "cloud" methodology, employing unscaled signals and assuming a linear correlation between the logarithms of signal intensity

measures (IM) and engineering demand parameters (EDP)(Jalayer & Cornell, 2009). This linear relationship, expressed as:

is determined by parameters a and b through linear regression. Assuming a lognormal distribution, the fragility function can be expressed as:

Here, is the standard normal cumulative distribution and the logarithmic standard deviation of linear regression.

The methodology can accommodate aleatory and epistemic uncertainties, considering variations in structural response, mechanical properties, capacity thresholds, and model parameters.

Aleatory uncertainties, linked to record-to-record variability, mechanical properties, and capacity thresholds, contribute to fragility functions. Record-to-record variability is naturally considered by the initial data cloud .

Furthermore, epistemic uncertainty in model parameters is addressed through a bootstrap procedure involving resampling with replacement, resulting in n different realizations of , leading to n fragility curves and regressions. The report adopts n=1000 bootstrap samples, providing a comprehensive approach to assessing fragility curves that considers multiple uncertainties and enhances the understanding of probabilistic seismic vulnerability.

Modeling choices

Ground accelerations are influenced by source, path, and site effects. Key source modelling parameters include magnitude (M_w), source rupture process (nucleation point, rupture front evolution, slip distribution, depth), path effects, site stratigraphy, receiver-source distance (R), and source-receiver angle.

The seismic source, modeled after the "Medea" fault, undergoes one hundred different rupture process realizations (Fig.1). Parameters from the DISS database and source functions proposed by Magrin et al. (2016) are employed. Crustal models (CR1 and CR2) and local stratigraphies (L1 and L2) are used to capture the source-to-site path effects. The physical properties of the crustal models are extracted from literature (Brandmayr et al., 2010). These cellular structures represent realistic configurations present in the Italian territory and were obtained through a nonlinear optimized inversion of the dispersion curves of surface waves. Both local stratigraphies belong to category B according to Eurocode 8 classification, but L1 can be considered moderately faster (V30= 695 m/s), and L2 slower (V30= 366 m/s). As a result, in common practice, all the presented outcomes would represent equivalent scenarios in the selection of real signals to be used in nonlinear dynamic analyses. The receiver was placed approximately 26 km from the fault center.

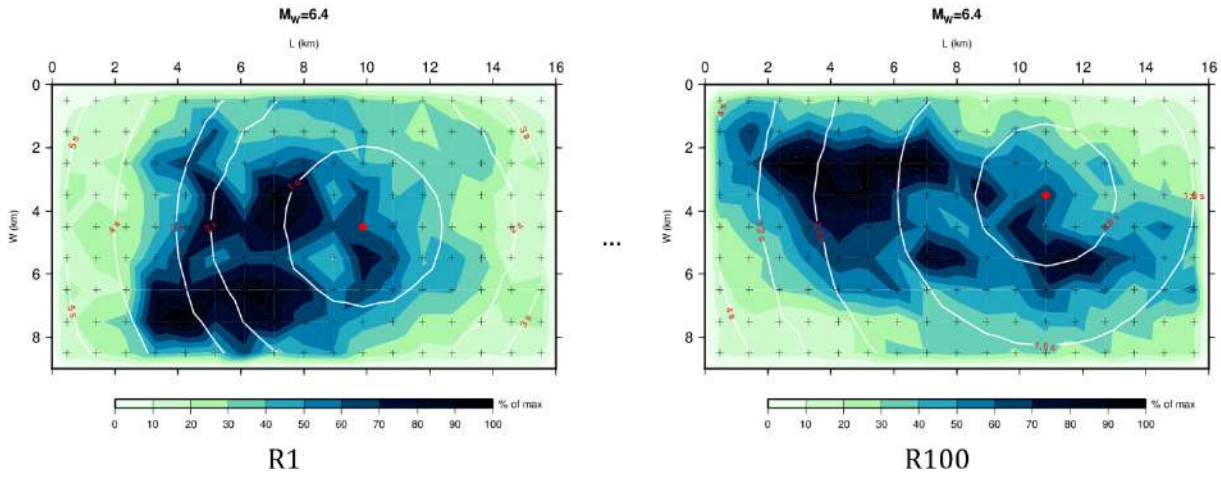

Fig. 1 – Example of different realizations of the rupture process

The reference structure is a five-story reinforced concrete frame designed according to Italian regulations. The structure has a 15m wide square plan with three bays, each 5m long. Each floor is 3m high, totaling 15m. Gravitational permanent loads include self-weight of structural elements, and an accidental load of 2 kN/m2 is applied to each floor. The roof has a snow load of 0.8 kN/m2. Seismic action is considered based on the Italian Building Code for a moderately hazardous site.

A spectral analysis determines maximum stress values, and beams and columns are designed with low ductility (Class B) and a behavior factor of 3.9. Design criteria ensure weak beam/ strong column capacity. Nonlinear time history analyses (NLTHA) are performed using Seismostruct software, considering both material and geometric nonlinearities. Inelastic force-based beam elements are used for material nonlinearities. Concrete strength class C28/35 and steel reinforcement class B450C are adopted.

Rayleigh damping is applied, and the Hilber-Hughes-Taylor integration scheme is used. The summary outlines the structural design, seismic considerations, material properties, and analysis methods employed in evaluating the behavior of the reinforced concrete frame under various conditions.

Scalar intensity measures such as peak ground acceleration (PGA), spectral acceleration at the first mode Sa(T1), and average spectral acceleration () are employed for fragility curve construction. Since the reference structure is 3D, the IM should account for the main vibrational properties in both directions. Therefore, here the spectral acceleration is evaluated for an average period calculated as the mean of the fundamental period values in each direction (FEMA, 2018):

$$S_a(T_{1m}) = S_a(\frac{T_{1x} + T_{1y}}{2})$$

Average spectral acceleration is defined as the geometric mean of spectral accelerations over a range of periods (Eads et al., 2015):

$$S_{a,avg}(T_i) = \left[\prod_{i=1}^{n} S_a(T_i)\right]^{1/n}$$

The period range is selected to including the effects of higher modes and period elongations due to damage accumulation. Five periods are selected, including modes with a mass participation greater than 10%:

$$T_i = \left[T_{2m}, min\left[(T_{2m} + T_{1m})/2,\ 1.5T_{2m}\right], T_{1m}, 1.5T_{1m}, 2T_{1m}\right]$$

Where is the mean of the second mode periods in the two orthogonal directions.

Results

The findings encompass accelerograms, intensity parameter distributions, regressions, and fragility curves derived from four distinct configurations. Various crustal and local models, yielding four configurations: CR1-L1, CR2-L1, CR1-L2, and CR2-L2. While the seismic source remains constant, 100 variations in rupture processes are considered to capture variability.

Accelerograms resulting from the combined models exhibit significant variations in shape and amplitude. Distributions of ground motion parameters, including Arias Intensity, Significant Duration, PGA, PGV, and Response Spectra in Acceleration, underscore the impact of the chosen configurations.

The Arias Intensity distributions highlight the influence of crustal model CR2 on signal energy, while the coupling of local model L2 with CR1 increases Arias. Signal duration, crucial for structures with cyclic strength degradation, shows greater dispersion in configurations coupling CR2 and L2. Notably, PGA, a historically pivotal intensity measure, displays no clear increase when transitioning from fast to slow B soil, emphasizing the intricate interplay between crustal and local models.

The fragility curves, representing the structure's vulnerability, reveal intriguing insights. For the sake of brevity only results for PGA are reported, hence for regressions of parameter MIDR (Maximum Interstorey Drift Ratio) as a function of $PGA_{GMRotD50}$ (median value of the geometric mean of the two horizontal components rotated through all nonredundant period-dependent angles (Boore et al., 2006)) in the bi-logarithmic plane. Regressions associated with crustal model CR1 appear less steep due to higher standard deviation, indicating greater uncertainty. Conversely, the reliability of estimates is higher for crustal model CR2, influenced by a more consistent distribution of intensity measures (Fig. 2).

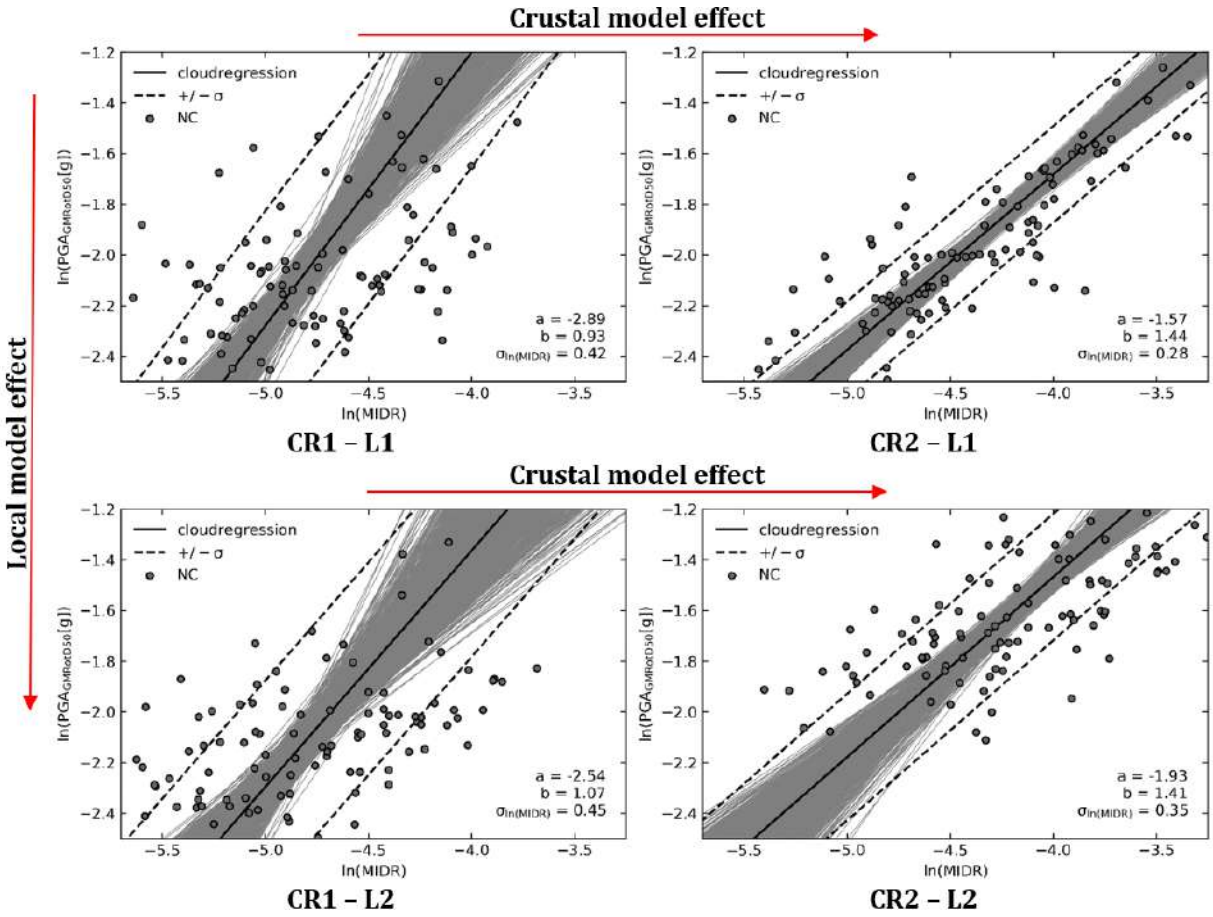

Fig. 2 – Cloud data (indicated with NC) and regressions obtained for the four studied configurations (PGA)

This study challenges the assumption that identical seismic scenarios, at least in terms of commonly used seismological parameters (magnitude, focal mechanism, site conditions, source-to-site distance) produce uniform structural responses. The observed variations in fragility curves, here reported only for the life safety (LS) performance level, underscore the need for an understanding of crustal and local model interactions in seismic risk assessment, emphasizing the importance of considering various configurations for a comprehensive analysis (Fig. 3).

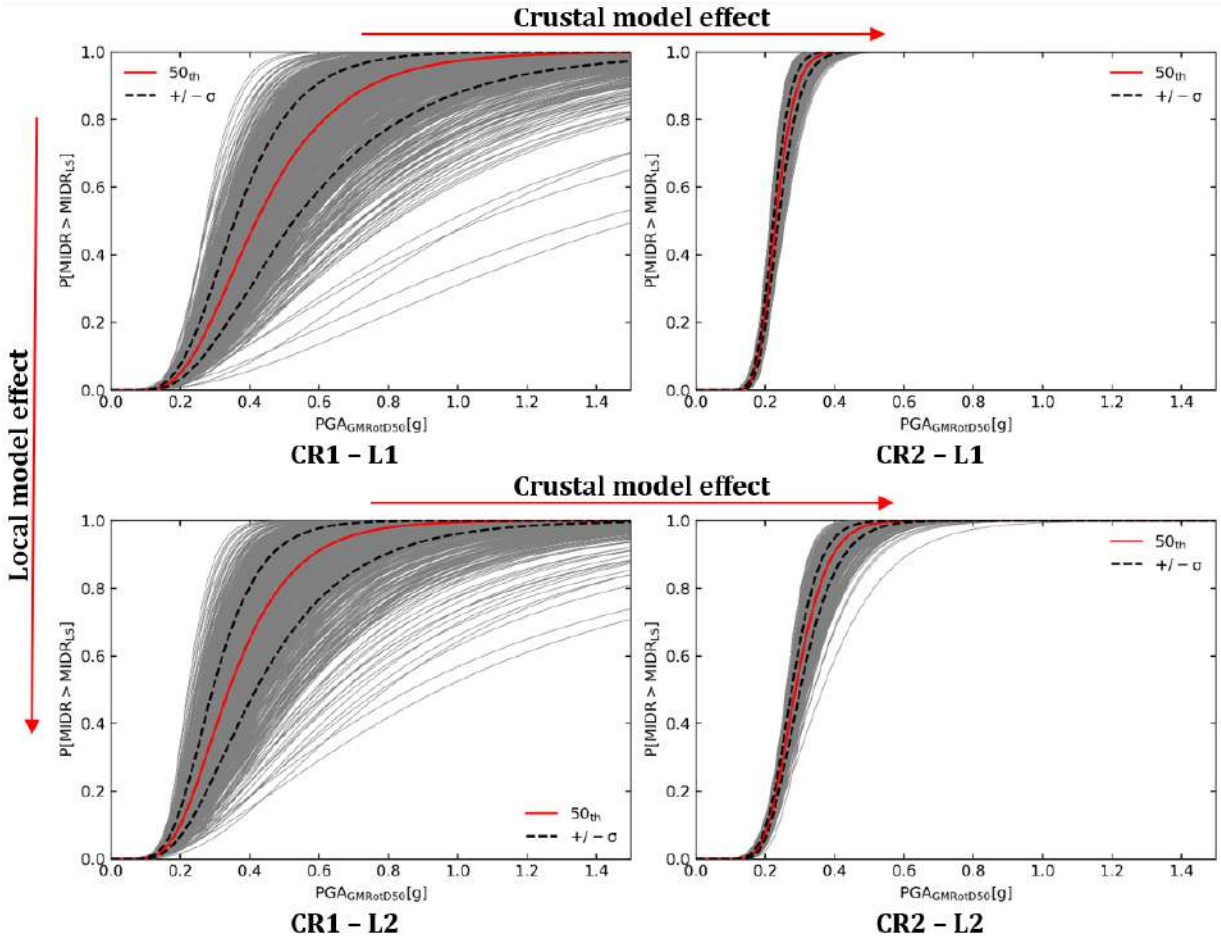

Fig. 3 - Fragility curves obtained for the four studied configurations (PGA)

Conclusions

In this work, four possible configurations of crustal and local structural models were analyzed to identify their influence on the IM-EDP relationship and, consequently, on fragility curves. In terms of demand, reflecting the distribution of possible signal intensity measures, configurations where crustal model CR2 is present showed higher values. The influence on the intensity measure values of crustal models seems to be, in the analyzed cases, more significant than that of local models.

Examining the IM-EDP relationship and consequently the fragility curves, it is observed that the regressions performed on IM-EDP pairs do not overlap. This implies that the intensity measures analyzed are not sufficient even in the studied case, where a single scenario is represented. In particular, the dependence of these measures on local and crustal structural models has been highlighted.

Acknowledgements

DPC-RELUIS is gratefully acknowledged for funding the present research activity under the MARS-2 research project.

References

Boore, D. M., Watson-Lamprey, J., & Abrahamson, N. A. (2006). Orientation-independent measures of ground motion. *Bulletin of the Seismological Society of America*, *96*(4 A), 1502–1511. https://doi.org/10.1785/0120050209

Brandmayr, E., Raykova, R. B., Zuri, M., Romanelli, F., Doglioni, C., & Panza, G. F. (2010). The lithosphere in Italy: structure and seismicity. *Journal of the Virtual Explorer*, *36*. https://doi.org/10.3809/jvirtex.2010.00224

Chieffo, N., Fasan, M., Romanelli, F., Formisano, A., & Mochi, G. (2021). Physics-Based Ground Motion Simulations for the Prediction of the Seismic Vulnerability of Masonry Building Compounds in Mirandola (Italy). *Buildings*, *11*(12), 667. https://doi.org/10.3390/buildings11120667

Eads, L., Miranda, E., & Lignos, D. G. (2015). Average spectral acceleration as an intensity measure for collapse risk assessment. *Earthquake Engineering & Structural Dynamics*, *44*(12), 2057–2073. https://doi.org/10.1002/eqe.2575

FEMA. (2018). *Seismic Performance Assessment of Buildings, FEMA P-58-1*.

Hassan, H. M., Fasan, M., Sayed, M. A., Romanelli, F., ElGabry, M. N., Vaccari, F., & Hamed, A. (2020). Site-specific ground motion modeling for a historical Cairo site as a step towards computation of seismic input at cultural heritage sites. *Engineering Geology*, *268*(February), 105524. https://doi.org/10.1016/j.enggeo.2020.105524

Jalayer, F., & Cornell, C. A. (2009). Alternative non-linear demand estimation methods for probability-based seismic assessments. *Earthquake Engineering & Structural Dynamics*, *38*(8), 951–972. https://doi.org/10.1002/eqe.876

Magrin, A., Gusev, A. A., Romanelli, F., Vaccari, F., & Panza, G. F. (2016). Broadband NDSHA computations and earthquake ground motion observations for the Italian territory. *International Journal of Earthquake and Impact Engineering*, *1*(1/2), 28. https://doi.org/10.1504/IJEIE.2016.10000979

Corresponding author: mfasan@units.it

Development of a hybrid method for ground shaking map reconstruction in near-real time

S. F. Fornasari , V. Pazzi , G. Costa

Dipartimento di Matematica, Informatica e Geoscienze (MIGE - Università degli Studi di Trieste, Italia)

Introduction

Real-time seismic monitoring is of primary importance for rapid and targeted emergency operations after potentially destructive earthquakes. A key aspect in determining the impact of an earthquake is the reconstruction of the ground-shaking field, usually expressed as the ground motion parameter. Traditional algorithms (e.g. ShakeMap®) compute the ground-shaking fields from the punctual data at the stations relying on ground-motion prediction equations (GMPEs) computed on estimates of the earthquake location and magnitude when the instrumental data are missing. The results of such algorithms are then subordinate to the evaluation of location and magnitude, which can take several minutes.

Since machine learning techniques have already been proven capable of estimating the ground motion parameters (Fornasari et al., 2023), a hybrid method has been developed to integrate neural networks in the ShakeMap® workflow to speed up the current ground-shaking map evaluation process.

The core idea is to adopt the ShakeMap® multivariate normal distribution (MVN) method for the intensity measure (IM) interpolation and use a neural network, in place of the ground motion prediction equations (GMPEs), to estimate the IM conditional expected value and uncertainty at the target sites based only on data available in real-time and thus do not wait for the magnitude and location estimates.

Furthermore, by reusing the ShakeMap® framework, the complexity of the model is reduced with improvements in the interpretability of the results.

Method

The proposed hybrid method consists of two steps: first, the expected IM values (and their uncertainties) are computed at the stations and target locations; then the recorded and expected IMs are passed to the MVN to compute the ground-shaking map (and its uncertainty).

The approach adopted to replace the GMPE is called Convolutional Conditional Neural Process (ConvCNP, Gordon et al., 2019): starting from sparse randomly sampled observations, a functional representation of them is computed, discretized to a regular grid and fed to a backbone neural network whose outputs are converted from the function space to the

original space of the intensity measures such that the output, for each target point, is a conditional distribution.

The input and output of the ConvCNP are expressed in log-units and thus assumed to be corrected for site effects: the effects of local geology are removed from the IMs recorded at the stations and reintroduced into the estimated IMs at the target points using the corresponding amplification factor by Falcone et al. (2021). The choice of using the amplification factors (instead of, for example, a Vs30-based approach) to address the site effects is double-fold: on one hand, it simplifies the ConvCNP process by operating on uniform inputs and outputs (which is especially useful since the encoder and decoder can seamlessly handle input and output points affected by different local effects); on the other hand, it improves the interpretability of the results by separating the contribution of local geology to the final results.

The implemented MVN is based on the formulation by Worden et al. (2018) and the correlation function by Loth and Baker (2013) is adopted: the choice of a correlation function independent of the epicentral distance and the event magnitude is required to obtain a workflow no longer dependant on the evaluation of the source parameters.

A flowchart of the hybrid method is shown in Fig. 1:

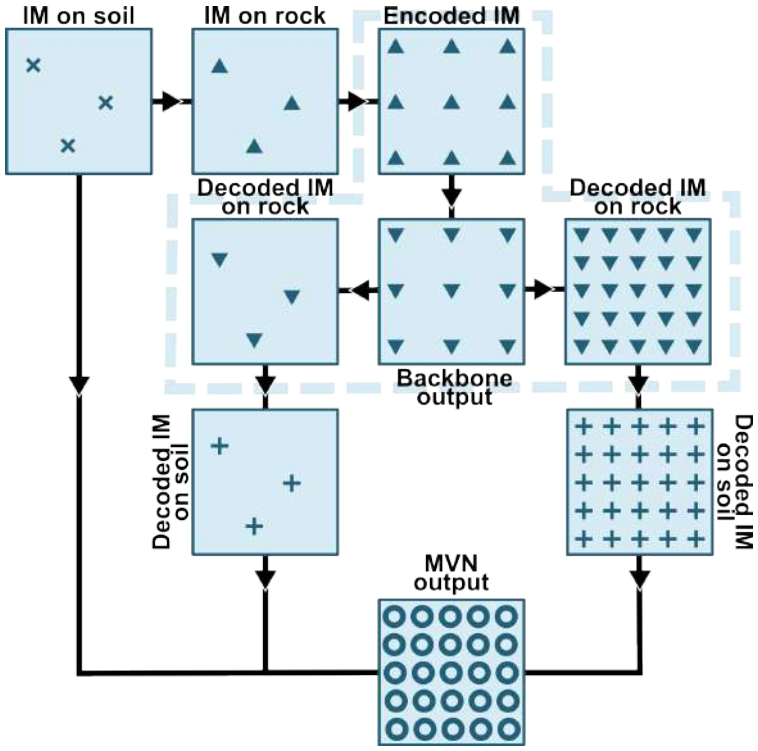

Fig. 1 – ShakeRec-hybrid flowchart: real-time data are corrected for the site effects with an amplification factor and passed to the ConvCNP (defined by the dashed line). IM values are estimated both at the station locations and the target points (here represented by a regular grid) and the soil effect is reintroduced by the corresponding amplification factors. These outputs and the real-time original inputs are then passed to the MVN to compute the ground-shaking maps.

The functional encoding and decoding are performed using rational quadratic kernels k_{rq} based on the great distances d_{ij} between the input and output points:

$$k_{rq}(d_{ij}) = (1 + \frac{{d_{ij}}^2}{2\alpha\lambda^2})^{-\alpha}$$

with $\lambda > 0$ and $\alpha > 0$ being two learnable parameters called length scale and the scale-mixture, respectively.

The backbone neural network has a custom architecture, shown in Fig. 2, consisting of a common sequential network that leads into two different branches for the evaluation of the mean IM values and the associated standard deviations, respectively.

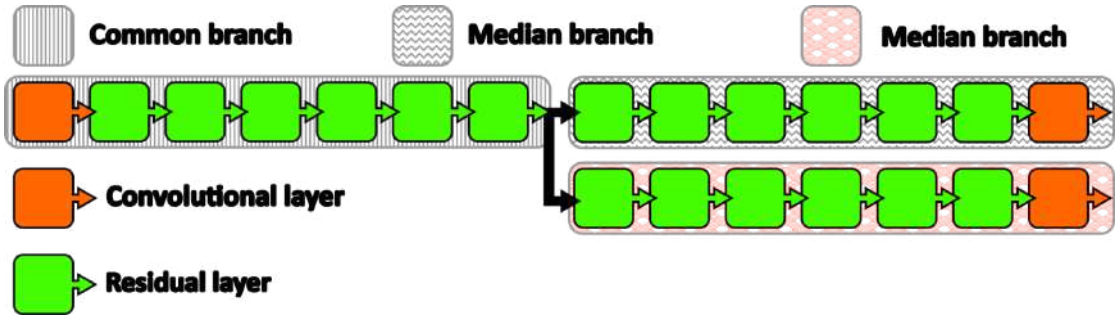

Fig. 2 – Schematic diagram of the ConvCNP backbone neural network architecture.

Model training

The model has been trained with a combination of synthetic and recorded data.

Numerical simulations provide a cost-effective way to acquire more data to train neural networks that allows building datasets whose dimension can meet the actual requirements for training and in which the distribution of the events can be balanced, generating more scenarios for rare events with high magnitudes (generally under-represented in recorded data). Furthermore, different scenarios can be generated including different noise levels in the input data leading to models more robust to input noise.

A synthetic dataset has been created by simulating multiple events over the Italian territory: the source characteristics have been taken within the ranges provided by the Database of Individual and Composite Seismogenic Sources, considering for each source multiple scenarios for different magnitudes.

The ShakeMap® INGV catalogue has been considered as the source for recorded data: specifically, the database considered contains 4925 events whose magnitude ranges between M3.0 and M6.5.

The model is trained to learn a conditional log-normal distribution over the expected GMPE output in two stages: first, a new model has been pre-trained on the synthetic dataset; then, the pre-trained model has been fine-tuned using the real data.

For each event (both synthetic or recorded), a variable number of context points (i.e., the IM values at the stations) and a fixed number of target points have been considered: the context points are corrected for the site effects using the amplification factors by Falcone et al. (2020) evaluated at the station locations.

The target points have been randomly selected with a radial uniform distribution around the epicentre.
To avoid any bias introduced by the training data, the "computational" grid is randomly shifted with respect to the epicentre position for each event.
The loss function L used to train the model is a linear combination of negative log-likelihood (NLL) and Frechet inception distance (FID): $L = w_{NLL}NLL + w_{FID}FID$.
Effectively, the adopted loss can be seen as a Wasserstein distance with a negative log-likelihood penalty term introduced to regularise the results and provide a better connection between the mean and standard deviation.

Results and Conclusions

The proposed hybrid method implements a multi-step approach in which the neural network performs a very specific task: while it still maintains some aspects of a black box-like algorithm, the results of this implementation are much more interpretable, specifically with the possibility to address the role of the different components in the final result.
The use of data augmentation is beneficial even in cases where a good amount of recorded data is available to train the models, because the greater control over synthetic data could allow the development of more balanced datasets that can, in turn, promote the model to learn more useful low-level features while the fine-tuning phase using real data seems promising in training models able to generate more realistic results.
The proposed method proved to be robust to network geometry changes (both in terms of the number of stations and their spatial distribution) and to noise.
The 30 October 2016 M_w6.5 Norcia earthquake has been chosen to benchmark the method against ShakeMap®.
Even though it doesn't represent an exhaustive analysis, the Norcia event, which required mobilisation of emergency response, is indicative of the behaviour of the method for the archetype of the seismic event it has been developed for, being a strong event recorded by a high number of stations with good coverage.
In Fig. 3, the PGA median and standard deviation obtained with the proposed method and ShakeMap® are compared. In the epicentral area, thanks also to the high density of stations, both methods provide similar results in terms of median values (panels a) and c) in Fig. 3). Considering the standard deviations, the hybrid method generates values that are overall more similar, although consistently greater, than ShakeMap® (panels b) and d) in Fig. 3). Given the PGA probability distributions at each target point from the hybrid method f_H and ShakeMap® f_{SM}, the map of the overlapping coefficient $OVL = \int_R min(f_1(x), f_2(x))dx$ has been computed (panel e) in Fig. 3) showing great compatibility between the two methods and thus the quality of the hybrid method.
Despite being non-predictive (i.e. it reconstructs the ground-shaking field to be consistent with the values recorded until that moment rather than foresee future ones), the hybrid

method allows to update the ground-shaking maps every few seconds and to obtain the final ground-shaking map for inland events within a minute of their origin time.

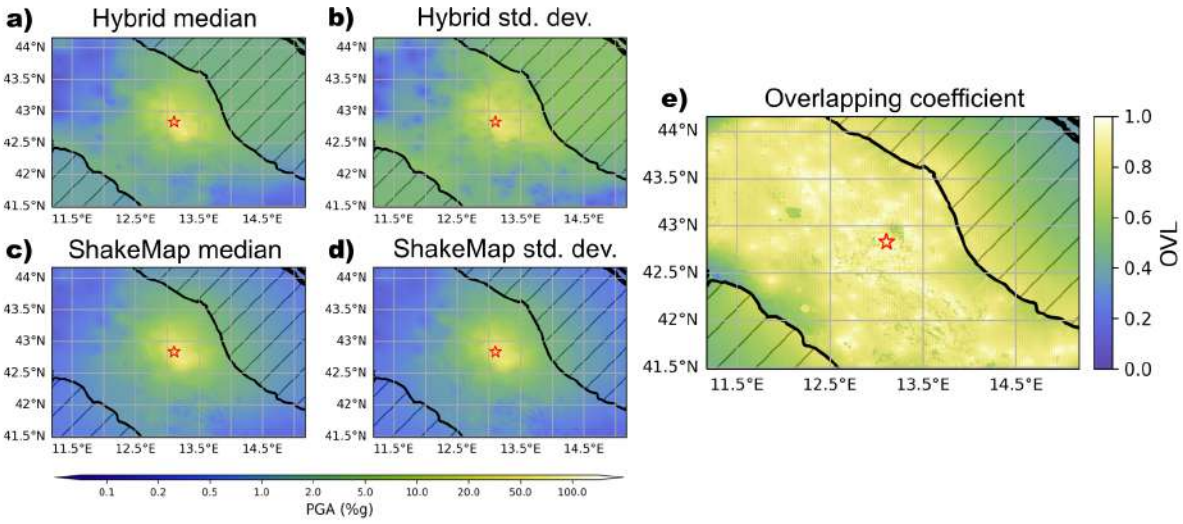

Fig. 3 – Reconstruction of the PGA median and standard deviation using the hybrid method (panels a) and b), respectively) and using ShakeMap® (panels c) and d), respectively) for the $M_w 6.5$ Norcia earthquake. Panel e) shows the overlapping coefficient between the PGA reconstructions obtained with the two methods.

Acknowledgement

This research received financial support from the Italian Civil Protection Department - Presidency of the Council of Ministers (PCM-DPC), to whom I am grateful, under the agreement “Accordo ai sensi dell’art. 15 della legge 7 agosto 1990, n. 241 e dell’art. 4 del decreto legislativo 2 gennaio 2018, n. 1 tra la Presidenza del Consiglio dei Ministri dipartimento della Protezione Civile e l’Università degli Studi di Trieste per il monitoraggio accelerometrico in Friuli Venezia Giulia e Veneto e la consulenza sull’elaborazione dei dati della rete accelerometrica nazionale" (2023-2024) between DPC and University of Trieste.

References

Falcone G., Acunzo G., Mendicelli A., Mori F., Naso G., Peronace E., Porchia A., Romagnoli G., Tarquini E., & Moscatelli M.; 2021: Seismic amplification maps of Italy based on site-specific microzonation dataset and one-dimensional numerical approach. Engineering Geology, 289:106170

Falcone, G., Boldini, D., Martelli, L., & Amorosi, A.; 2020: Quantifying local seismic amplification from regional charts and site specific numerical analyses: a case study. *Bulletin of Earthquake Engineering*, *18*, 77-107.

Fornasari, S. F., Pazzi, V., & Costa, G.; 2022: A Machine-Learning Approach for the Reconstruction of Ground-Shaking Fields in Real Time. Bulletin of the Seismological Society of America, 112(5), 2642-2652.

Gordon, J., Bruinsma, W. P., Foong, A. Y., Requeima, J., Dubois, Y., & Turner, R. E.; 2019: Convolutional conditional neural processes. arXiv preprint arXiv:1910.13556.

Loth C., and Baker J. W.; 2013: A spatial cross-correlation model of spectral accelerations at multiple periods. Earthquake Engineering & Structural Dynamics 42.3.

Worden, C. B., Thompson, E. M., Baker, J. W., Bradley, B. A., Luco, N., & Wald, D. J.; 2018: Spatial and spectral interpolation of ground-motion intensity measure observations. Bulletin of the Seismological Society of America, 108(2), 866-875.

Corresponding author: simonefrancesco.fornasari@phd.units.it

On the reconnaissance of slopes susceptible to co-seismic failures in Daunia (Apulia, Southern Italy)

F. Fredella[1], V. Del Gaudio[1], N. Venisti[1], J. Wasowski[2]

[1]Dipartimento di Scienze della Terra e Geoambientali, Università degli Studi di Bari "Aldo Moro", Bari

[2]Consiglio Nazionale delle Ricerche, Istituto di Ricerca per la Protezione Idrogeologica, Bari

Introduction

Co-seismic landslides are capable of causing significant damage even to structures and infrastructures that resist the direct effects of earthquake ground shaking. It is therefore important to identify the slopes potentially exposed to seismic destabilization for hazard mitigation and prevention. A regional- to local-scale investigation of sites susceptible to co-seismic failure requires allocation of considerable resources, which should be prioritized by focusing attention on slopes with greater probability of being mobilized by seismic shaking.

Here we explore the potential of reconnaissance-type identification of slopes susceptible to co-seismic failures in the Daunia Mountains, at the NW border of the Apulia region. This is done by comparing the resistance demand placed by local seismicity on slope sites and the actual slope resistance. To this end, we take into account i) the basic seismic hazard inferred at regional scale from earthquake records, ii) the local effects of site amplification phenomena and iii) expeditious estimates of slope resistance to seismic shaking.

Our study benefits from the large amount of data acquired in the ongoing seismic microzonation (SM) studies of the Apulia region. We focus on the Daunia Mts., which are known for the widespread presence of marginally stable slopes consisting of clay-rich flysch materials and rainfall-triggered landsliding (e.g., Wasowski et al. 2010). Although Daunia is exposed to earthquakes generated in the surrounding areas, little is known about the susceptibility of its slopes to seismic failure.

Basic slope resistance demand

A first stage for the identification of slopes subject to seismically induced landslides consists in defining the resistance demand placed on slope by the regional seismicity. For this purpose, the starting point is the assessment of the basic seismic hazard, represented as a probabilistic

estimate of seismic shaking expected at a site. This depends on the location of the surrounding seismogenic zones, whose seismicity rate can be inferred from historical and instrumental records. Then, ground motion prediction equations (GMPE) are used to estimate the probability of a site to experience seismic shaking of different levels on a flat surface with outcropping stiff lithology. These site conditions, however, differ from those of slopes susceptible to seismically induced landslides, where the slope response to seismic waves can considerably aggravate the destabilizing effects of shakings.

A method for a probabilistic evaluation of the resistance demand was proposed by Del Gaudio et al. (2003) through the quantity $(A_c)_x$, which represents the critical acceleration A_c that a slope must have to keep the probability of landslide triggering, for expected earthquakes, within a pre-defined probability level (e.g., 10% in 50 years). The condition of landslide triggering is identified by the exceedance of a critical threshold x of the permanent displacement induced by seismic shaking, measured, according to the Newmark (1965) model, as Newmark displacement D_N. The calculation of $(A_c)_x$ is based on an empirical relation calibrated by Romeo (2000), in which D_N is expressed as a function of the Arias Intensity (Arias, 1970) (which measures the ground shaking) and of the slope critical acceleration a_c (which measures the slope resistance to failure).

In their first application of the proposed method Del Gaudio et al. (2003), produced a map of slope resistance demand in terms of $(A_c)_x$ values for the area of Daunia Mts. (Fig. 1 a). They exploited the following data and tools available at that time: the ZS4 seismogenic zonation (Scandone, 1997), a GMPE for Arias Intensity published by Sabetta and Pugliese (1996) and the SEISRISK III software (Bender and Perkins, 1987) to calculate the seismic shaking probabilities. The map shows the results in terms of critical acceleration that slopes must have to keep within 10% in 50 years the probability that D_N exceed 10 cm. Site amplification effects were not considered.

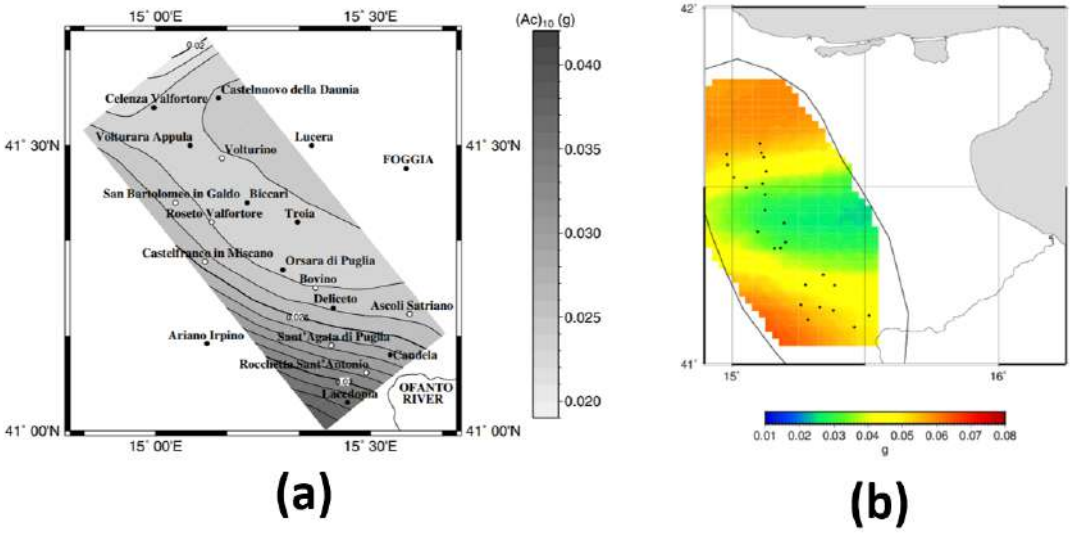

Fig. 1: Basic resistance demand maps calculated for the Daunia area, expressed through the quantity $(A_c)_{10}$: (a) results obtained by Del Gaudio et al. (2003); (b) new version of the same map obtained using updated versions of the seismogenic zonation and of the earthquake catalogue.

Figure 1b shows an updated version of the map of slope resistance demand. It relies on more recent information and tools, namely the ZS9 seismogenic zonation (Meletti et al., 2004), the latest attenuation relation for Arias Intensity published by Sabetta et al., (2021) and the software R-CRISIS for the seismic hazard assessment (Ordaz et al., 2017).

A comparison of the two maps reveals significant differences, in particular an increase of the maximum value of $(A_c)_{10}$ from 0.04 to 0.06 g. The spatial distribution of $(A_c)_{10}$ values is strongly influenced by the geometry of the seismogenic zones, which cause a minimum in the central part of Daunia and higher values both in the northern and southern parts. Higher $(A_c)_{10}$ values coincide with the areas including many old, large deep-seated landslides of unknown origin (Ardizzone et al., 2023). These landslides are generally larger than the recent slope failures triggered by rainfall, and Wasowski et al. (2022) presented circumstantial evidence for their co-seismic origin.

Data on site resonance properties

Our previous study on slope resistance demand in Daunia have not incorporated the effect of site amplification. At present, a software package like R-CRISIS allow taking into account the site effects providing in input a matrix of the spatial distribution of amplification factors. A detailed evaluation of such effects requires the acquisition of many data, which is not feasible for regional scale studies. Thus, for a preliminary estimate of the influence of site effects on slope resistance demand, we explore the utility of information on site resonance properties obtained from ambient noise analysis carried out during the 1st level of Seismic Microzonation of the Daunia urban and peri-urban areas.

A large set of noise recordings (about 1000) have been acquired on different lithologies and slope stability conditions. We initially examined the results obtained from their processing with the HVNR method (Nakamura, 1989), which identifies local site conditions from peak values in the ratios between the spectral amplitudes of the horizontal and vertical components of the recordings. For each Daunia municipality, the resonance amplitudes and frequencies and the lithology at the measurement sites were identified, distinguishing whether these sites are on landslide or stable areas.

The following flysch formations are most common at the measurement sites:

FAE - **Flysch di Faeto** (Upper Burdigalian-Lower Tortonian). Limestone-marly-clayey alternation with a bentonite base. It is divided into a predominantly pelitic facies (FAEp) and a predominantly calcarenitic facies (FAEc).

FYR – **Flysch Rosso** (Cretaceous-Aquitanian). Grey-green to reddish mudstones alternating with blackish layers of jaspers, with intercalations of breccias, calcarenites and calcilutites.

Fig. 2 shows the distribution of resonance frequencies and H/V peak amplitudes resulting from noise measurements. The most recurring frequencies are between 0.9 and 4 Hz, while the most recurrent peak amplitudes are between 2 and 4. The attention is focused on sites

where H/V peak values are greater than 3, which should indicate a significant level of site amplification. Peak values of this amount are found to be slightly more frequent for the sites on landslides (44%) than on stable areas of (38%). This can be expected because a pre-existing landslide creates velocity contrasts with the substratum.

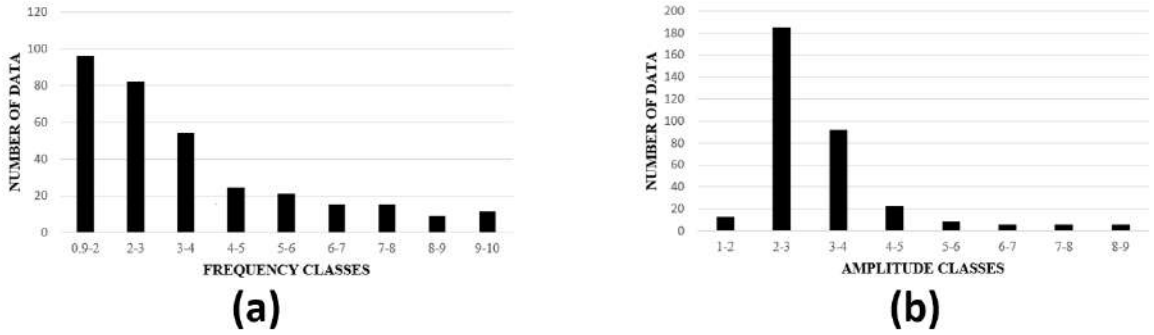

Fig. 2: Distribution of resonance frequency (a) and H/V peak amplitude (b) based on ambient noise in Daunia.

However, resonance conditions are not ubiquitous and 7.9% of landslide and 6.9% of stable ground areas showed no site effects. Furthermore, resonances appeared rather weak and this could be the effect of the “slow” flysch substratum, which causes weak velocity contrasts with the surficial material.

Between the two most common flysch formations, FAE appear characterized by a slightly greater diversity of resonance frequencies with higher mean amplitudes, in comparison to FYR whose resonance frequencies are concentrated around lower values and amplitudes. The sites on landslides in FAE, however, show a larger recurrence of lower frequency and higher amplitude, likely as an effect of the reduced velocity of slope materials. The sites on FYR, besides an increase of mean amplitude, show a frequency re-distribution towards intermediate frequency from the lowest (< 2 Hz) and the highest (> 8 Hz) frequencies. Furthermore, resonance is absent in 9.4% of FAE and 22.5% of FYR sites.

Given the differences in dynamic response, the estimates of amplification factors from the results of noise analysis may require the use of differentiated relations for the two units. However, additional efforts are needed considering that, with regard to H/V peak amplitude measurements, the HVNR technique suffers from a strong dependence on environmental conditions. For this reason the recordings are being reanalysed with the HVIP technique (Del Gaudio, 2017), which extracts from the noise the Rayleigh waves and measures their ellipticity, thus providing more stable H/V values better correlated to the local amplification factor. Fig. 3 shows a comparison between the results obtained by the two types of noise analyses.

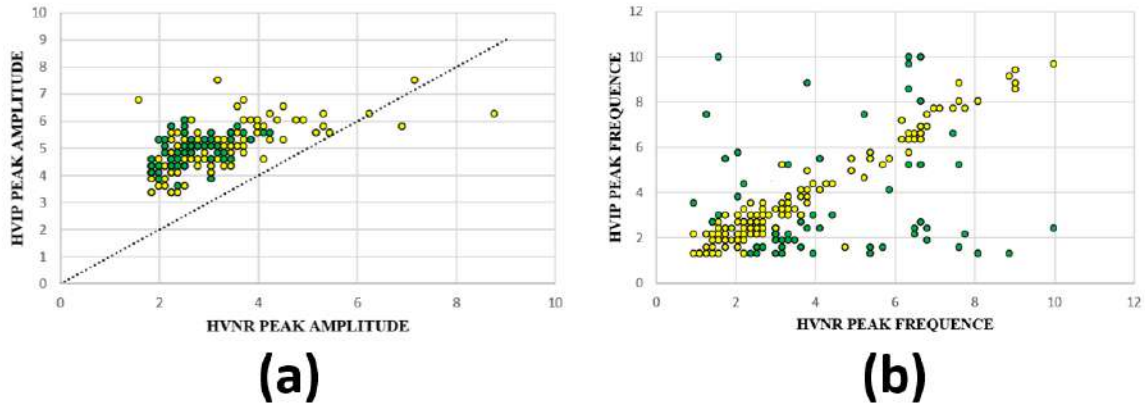

Fig. 3: Comparison of the results of HVIP and HVNR analysis of Daunia noise recordings: (a) peak frequencies and (b) peak amplitudes. Green dots mark the cases for which the main resonance frequency identified by the two techniques differs by more than 1 Hz.

The amplitudes of the HVIP peaks (which represent Rayleigh wave ellipticity) are usually greater than those of the HVNR peaks. The main peak frequency identified by the two techniques differs by more than 1 Hz in about 40% of sites. This seems related to the complex resonance pattern of flysch units, with multiple peaks of similar amplitude.

Future work

The results of ambient noise analysis will be compared with the outcomes of numerical modeling of the local seismic response in order to seek possible correlations useful to estimate the amplification factors from ambient noise data. Such modelling will rely on the detailed auxiliary data collected for Seismic Microzonation of the Daunia Mts urban and peri-urban areas, including borehole stratigraphies and results of geophysical surveys. A major contribution is expected from the study sites which, thanks to a large availability of data, will allow a 3D modelling of the local seismic response, to be compared with the results of simplified (1D and 2D) modelling; this will help evaluating uncertainties introduced by the simplification. The objective is to expand as much as possible the data set for the calibration and validation of empirical relation providing estimates of amplification factors in terms of Arias Intensity. Where the presence of site amplification effects will be recognised through the noise measurements, the resistance demand values $(A_c)_x$ will be accordingly modified, introducing the estimated amplification factors in the calculation of exceedance probability of Arias Intensity.

Finally, the $(A_c)_x$ values corrected for site amplification effects will be compared with the slopes' critical acceleration values a_c based on local topography and geotechnical properties of slope material. This should allow us to identify slopes most susceptible to co-seismic failure.

Acknowledgements

Study carried out within the RETURN Extended Partnership with funds from the European Union Next-Generation EU (National Recovery and Resilience Plan – NRRP, Mission 4, Component 2, Investment 1.3 – D.D. 1243 2/8/2022, PE0000005). Data acquired within the seismic microzonation studies of Apulia supported by the National Department of Civil Protection and the Civil Protection Office of the Apulian Regional Administration.

References

Ardizzone F., Bucci F., Cardinali M., Fiorucci F., Pisano L., Santangelo M. and Zumpano V.; 2023: Geomorphological landslide inventory map of the Daunia Apennines, southern Italy. Earth System Science Data, 15, 2, pp. 753-767.

Arias A.; 1970: A measure of earthquake intensity, in Seismic Design for Nuclear Power Plants, R. J. Hansen (ed), MIT Press, Cambridge, Massachusetts, pp. 438-483.

Bender B. and Perkins B.; 1987: SEISRISK III: A Computer Program for Seismic Hazard Estimation. U.S. Geological Survey Bulletin 1772.

Del Gaudio V.; 2017: Instantaneous polarization analysis of ambient noise recordings in site response investigations. J. Geophys. Int., 210, pp. 443-464.

Del Gaudio V., Pierri P. and Wasowski J.; 2003: An Approach to Time-Probabilistic Evaluation of Seismically Induced Landslide Hazard. Bulletin of the Seismological Society of America, 93, 2, pp. 557-569.

Meletti C., Galadini F., Valensise G., Stucchi M., Basili R., Barba S., Vannucci G. and Boschi E.; 2004: Zonazione sismogenetica ZS9 [Data set]. Istituto Nazionale di Geofisica e Vulcanologia (INGV).

Nakamura Y.; 1989: A method for dynamic characteristics estimation of subsurface using microtremor on the ground surface. Q. Report Railway Tech. Res. Inst., 30, pp. 25-33.

Newmark N. M.; 1965: Effects of earthquakes on dams and embankments, Geotechnique, 15, pp- 139-160.

Ordaz M., Martinelli F., Aguilar A., Arboleda J., Meletti C. and D'Amico V.; 2017: R-CRISIS. Program and platform for computing seismic hazard.

Romeo R.; 2000: Seismically induced landslide displacements: a predictive model. Eng. Geol., 58, 3-4, pp. 337-351, doi:10.1016/S0013-7952(00)00042-9.

Sabetta F. and Pugliese A.; 1996: Estimation of response spectra and simulation of nonstationary earthquake ground motions. Bull. Seism. Soc. Am., 86, 2, pp. 337-352.

Sabetta F., Pugliese A., Fiorentino G., Lanzano G. and Luzi L.; 2021: Simulation of non-stationary stochastic ground motions based on recent Italian earthquakes. Bull. Earth. Eng., 19, pp. 3287-3315, doi.org/10.1007/s10518-021-01077-1.

Scandone P.; 1997: Linea di ricerca 2 "Sismotettonica". In: Corsanego A., Faccioli E., Gavarini C., Scandone P., Slejko D. and Stucchi M. (eds), L'attività del GNDT nel triennio 1993 -1995, CNR-GNDT, Roma, pp. 67-96.

Wasowski J., Lamanna C. and Casarano D.; 2010: Influence of land-use change and precipitation patterns on landslide activity in the Daunia Apennines, Italy. Quarterly J. Eng. Geology and Hydrogeology, 43, 4, pp. 387–401.

Wasowski J., Del Gaudio V., Pisano L., Fazio N. L., De Lucia D., Ugenti A., Zumpano V., Filice F., Casarano D., Santaloia F., Gallicchio S. and Lollino P.; 2022: Unravelling the origin of large ancient landslides in low elevation Daunia Mountains, Italy. AGU Fall Meeting Abstracts, NH22A-07.

Corresponding author: flaviana.fredella@uniba.it

Temporal and Spatial Variability of Anelastic Attenuation and Its Effects on Ground Motion Characteristics in Central Italy

Simona Gabrielli (1), Aybige Akinci (1), Carolina Gutierrez (2), Javier Ojeda Vargas (2), Sebastian Arriola (3) and Sergio Ruiz (2)

1 Istituto Nazionale di Geofisica e Vulcanologia (INGV), Via di Vigna Murata 605, 00142, Rome, Italy

2 Departamento de Geofísica, Universidad de Chile, Blanco Encalada, 2002, Santiago, Chile

3 Centro Sismológico Nacional Universidad de Chile, Santiago, Chile

In recent decades, Central Italy has experienced seismic sequences resulting in casualties and significant building damage, as the one of 2016-2017, started with the Amatrice mainshock (Mw6.2) in August 2016, followed by the Visso (Mw5.9) and Norcia (Mw6.5) events in October 2016 (hereafter, AVN). Considering the frequent seismic activity and elevated seismic risk in the region, employing ground-motion simulations is essential for assessing seismic risk and earthquake engineering applications. Previous studies focused on ground motion characteristics of the Mw6.2 Amatrice and Mw6.5 Norcia earthquakes using stochastic and numerical approaches (Pischiutta et al., 2020; Ojeda et al., 2021; Pitarka et al., 2021).

The definition of attenuation characteristics and their relationship with ground motion models have already been used for predicting ground motions from hypothesized events, which are fundamental to defining the accuracy of seismic assessments. Recent studies applied non-ergodic approaches to reduce the uncertainties in ground motion models, taking into account a range of physical parameters linked to both the seismic source and wave propagation, along with heterogeneities specific to the path.

Here, we explore the seismic wave attenuation variability on strong-ground motion simulation in the Central Apennines, using stochastic simulations (Ojeda et al., 2021). First, we calculate the quality factor Q values for the area, obtaining the total attenuation Q as a function of frequency for the 2016-2017 seismic sequence. In order to map this variation, we applied a 2D kernel-based imaging of coda-Q space variation, which confirmed the differences in attenuation between the pre-sequence and the AVN, with an increment in attenuation during the 2016 time period in the fault plane zones.

Then, we integrate the obtained frequency-dependent Q value as input parameters for strong-ground motion simulations, considering earthquake-induced ground motions. This stochastic methodology simulates the strong-ground motion at high frequencies, mimicking

the source rupture fault mechanisms, slip distribution, stress drop and radiation pattern, and obtaining horizontal and vertical accelerograms. The estimations are correlated and validated against observed peak ground accelerations and spectral acceleration for the Amatrice and Norcia fault plane, and then compared with the ground motion prediction equations used for the region (Lanzano et al., 2019).

Stochastic modelling as a method for providing seismic hazard estimates of site effects over wide areas

I. Gaudiosi[1], G. Acunzo[2], D. Albarello[3], M. Moscatelli[1]

[1] Istituto di Geologia Ambientale e Geoingegneria (CNR, Italy)
[2] Theta Group (Italy)
[3] Dipartimento di Scienze Fisiche, della Terra e dell'Ambiente (Università degli Studi di Siena, Italy)

Numerical simulations of seismic site response require the characterization of the nonlinear behaviour of shallow subsoil and their mechanical characterization. When extensive evaluations are of concern, as in the case of seismic microzonation studies, funding problems prevent a systematic use of laboratory tests or S-waves velocity profiles to provide detailed evaluations.

For this purpose, we investigate the use of statistical laws for both the main mechanical and dynamic parameters. A statistical analysis of the data were carried out in previous studies (Romagnoli et al., 2021; Gaudiosi et al., 2023) with the aim of shedding light on the significant difference between the laboratory and in situ classification of samples and soils and the macroscopic/engineering geological one, provided during seismic microzonation studies.

Since the engineering geological classification plays a prominent role in extensive site response evaluations, the outcomes of the present work may be of help at least when preliminary seismic response estimates are of concern. The preliminary tests carried out in the framework of the PRIN SERENA Projects provide reference information that can serve as key data for large-scale hazard assessments in the Italian territory.

The variability of the synthetic hazard parameters may be modelled throughout the NC92 code (Acunzo et al., 2024) by considering the probability distributions obtained for each seismo-stratigraphy. These probability distributions may be combined in the frame of a Bayesian approach to determine a probabilistic estimate of the hazard parameters at output nodes, as well as its variability range.

References

Acunzo G., Falcone G., di Lernia A., Mori F., Mendicelli A., Naso G., Albarello D., Moscatelli M.; 2024. *NC92Soil: A computer code for deterministic and stochastic 1D equivalent linear seismic site response analyses*. Computers and Geotechnics, **165**, 105857.

Gaudiosi I., Romagnoli G., Albarello D., Fortunato C., Imprescia P., Stigliano F., Moscatelli M.; 2023. Shear modulus reduction and damping ratios curves joined with engineering geological units in Italy. Scientific Data **10**, 625. https://doi.org/10.1038/s41597-023-02412-8

Romagnoli G., Tarquini E., Porchia A., Catalano S., Albarello D., Moscatelli M.; 2022. *Constraints for the Vs profiles from engineering-geological qualitative characterization of shallow subsoil in seismic microzonation studies*. Soil Dynamics and Earthquake Engineering, **161**, 107347. https://doi.org/10.1016/j.soildyn.2022.107347

Acknowledgments

This research was supported by the PRIN SERENA project (scientific coordinator: D. Albarello; Prot. 2020MMCPER; Decreto 374 Direttoriale n. 223 del 18/02/2022 del Ministero dell'Università e della Ricerca, Segretariato Generale Direzione Generale della 375 ricerca).

Corresponding author: iolanda.gaudiosi@cnr.it

Testing synthetic site amplification maps through comparison with empirical estimates in Central Italy

S. Hailemikael[1], G. Cultrera[1], C. Barnaba[2], G. Laurenzano[2], G. Martini[1,3], A. Peloso[3], F. Cara[1], G. Di Giulio[1], D. Famiani[1]

[1] Istituto Nazionale di Geofisica e Vulcanologia (INGV), Rome, Italy.
[2] Istituto Nazionale di Oceanografia e di Geofisica Sperimentale (OGS), Trieste, Italy.
[3] Agenzia Nazionale per le Nuove Tecnologie, l'Energia e lo Sviluppo Economico Sostenibile (ENEA), Frascati, Italy.

In the framework of the national research project SERENA - Mapping Seismic Site Effects at REGional and NATIONAL Scale, the work package 6 (WP6) aims to test the ground motion amplification maps developed within the project by means of empirical estimates. The target maps will be mainly generated by a hybrid geological-geomorphological classification of the national territory and stochastic 1D equivalent linear numerical simulations (synthetic approach) based on seismic microzonation data collected over the last decade (Moscatelli *et al.*, 2020).

To this end, we collected and enriched the database of experimental site-specific amplification estimates originally gathered by Priolo *et al*. (2020) for Central Italy and compared these estimates with those obtained in a study preceding this project by implementing a synthetic approach similar to what will be developed in SERENA (Falcone *et al.*, 2021). In particular, the empirical estimates for about 240 seismic monitoring sites in Central Italy were obtained by evaluating more than 45000 seismic records processed with a standardised approach to derive site amplification factors (FA). The FA values are calculated within three period intervals, defined by the current seismic microzonation guidelines (SM Worging group 2015) and representative of short, medium and long period ground-motion amplification (namely 0.1s-0.5s, 0.4s-0.8s, 0.7s-1.1s).

We calculated and compared the statistical distributions of experimental and synthetic FA (FA_exp and FA_syn, respectively) for the 240 sites in Central Italy, also by means of specifically developed GIS tools. We found that the FA_syn distributions are within the range 1-2 for all considered periods, while all FA_exp distributions have median values equal to or greater than 2 and large upper tails, with amplification values up to 7.5. The distribution of FA_exp also shows values below 1 for a few sites, indicating de-amplification compared to the considered reference motion.

The distributions of the residuals between FA_exp and Fa_syn (in natural logarithmic units) were then evaluated for each considered site and the influence of the period interval and the

available site parameters on the residual value were investigated. The distributions of the residuals (Fig. 1) show a positive mean term, which clearly indicates an underestimation of empirical amplification by the synthetic approach. The mean underestimation term increases with the considered period interval, while the associated uncertainty (σ of such distributions) is almost constant with respect to the period. The distributions also show negative tails, which are related to those sites having experimental de-amplification of ground motion.

Despite the lack of detailed geological information for the studied sites, the uniform geo-lithological classification of the national map at 1:100.000 scale (http://www.pcn.minambiente.it/mattm) revealed that most of the sites (65%) for which the synthetic approach underestimates the observed amplification are located on alluvial deposits and chaotic sedimentary complexes, while the sites for which an overestimation was calculated by FA_syn are located on bedrock formations and mostly correspond to sites with the FA_exp < 1.

These preliminary results suggest that the amplification maps produced prior to the SERENA project using the synthetic approach may significantly underestimate the experimental ground-motion amplifications. Therefore, the approach should be improved so that the FA_syn values can cover a wider range (max FA_syn >> 2). Furthermore, the analysis of the residuals suggests that larger discrepancies between the experimental and synthetic estimates occur for long-period amplifications, which may be caused by: i) bedrock definition in 1D simulations for those sites located on large intermountain basins characterised by large bedrock depths (> 100 m) and ii) 2D/3D site effects.

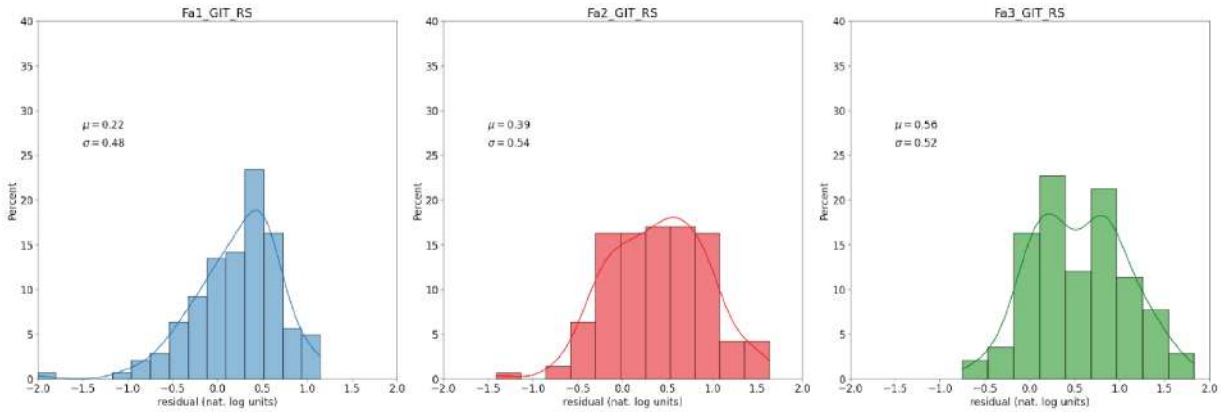

Fig. 1 - Distribution of residuals between median FA_exp and Fa_syn values (in natural logarithmic units) as a function of period: short (FA1 blue), intermediate (red) and long periods (green).

References

Falcone G., Acunzo G., Mendicelli A., Mori F., Naso G., Peronace E., Porchia A., Romagnoli G., Tarquini E. and Moscatelli M.; 2021: *Seismic amplification maps of Italy based on site-specific microzonation dataset and one-dimensional numerical approach*. Engineering Geology, Vol. 289, 106170, https://doi.org/10.1016/j.enggeo.2021.106170.

Moscatelli M., Albarello D., Scarascia Mugnozza G. and Dolce M.; 2020: *The Italian approach to seismic microzonation*. Bull Earthq Eng 18, 5425–5440. https://doi.org/10.1007/s10518-020-00856-6

SM Working Group; 2015: *Guidelines for seismic microzonation, conference of regions and autonomous Provinces of Italy—Civil Protection Department, Rome*. http://www.protezionecivile.gov.it/httpdocs/cms/attach_extra/GuidelinesForSeismicMicrozonation.pdf.

Priolo E., Pacor F., Spallarossa D., Milana G., Laurenzano G., Romano M.A., Felicetta C., Hailemikael S., Cara F., Di Giulio G., Ferretti G., Barnaba C., Lanzano G., Luzi L., D'Amico M., Puglia R., Scafidi D., Barani S., De Ferrari R. and Cultrera G.; 2020: Seismological analyses of the seismic microzonation of 138 municipalities damaged by the 2016–1017 seismic sequence in Central Italy. Bull Earthq Eng 18:5553–5593. https://doi.org/10.1007/s10518-019-00652-x

Corresponding author: salomon.hailemikael@ingv.it

Site Response Analysis in the Agri valley (Basilicata) using the Generalized Inversion Technique

G. Laurenzano[1], N. Tragni[2], P. Klin[1], TA Stabile[2], MR Gallipoli[2] & *PRIN SERENA WP06 WG*

[1] Istituto Nazionale di Oceanografia e di Geofisica Sperimentale – OGS (Triste, Italy)
[2] National Research Council of Italy - CNR-IMAA (Tito Scalo, Italy)

The inclusion of site amplification effects caused by local geo-lithological features could bring a considerable improvement in the assessment of seismic hazard (e. g. Mascandola et al., 2023). A wide range of approaches is used today to analyze the site response, but the modalities for their optimal application are still under debate. As part of the work package "Empirical testing and calibration" of the ongoing PRIN project "Mapping seismic site effects at regional and national scale - SERENA", this study presents the application of the Generalized Inversion Technique - GIT (Castro et al., 1990) to evaluate the frequency-dependent local seismic amplification at 24 sites in the Agri Valley (southern Basilicata). The Agri Valley is a NW-SE trending intermontane basin, which mainly developed during Quaternary draining of a large sector of the Southern Apennines. The High Agri Valley is a tectonically active area characterized by high seismic hazard related to fault systems capable of generating up to M = 7 earthquakes (i.e., the 1857 Mw = 7 Basilicata earthquake). The analyzed sites are distributed over an area of about 800 km^2 and correspond to the locations of seismic stations that belong to three permanent seismic networks. The sites are characterized by a variety of lithologies, ranging from alluvial, lacustrine, swamp and marine deposits to eluvial and colluvial deposits, siliciclastic sedimentary rocks and carbonate rocks. Site amplification functions are estimated by means of an implementation (Klin et al., 2021) of the one-step nonparametric GIT based on the conventional decomposition of the S-wave phase in terms of source, propagation, and site response. The used database of earthquake recordings consists of more than 2000 waveforms recorded between 2016 and 2018 and includes local and regional events in a distance range of up to 400 km, ensuring good azimuthal coverage for each station. The evaluated site amplification functions are compared to both earthquake and micro-tremor horizontal-to-vertical spectral ratios. Finally, the amplification functions are used to evaluate the FA amplification factors in three period bands of engineering interest (0.1 – 0.5 s, 0.4-0.8 s, and 0.7-1.1 s). The results evidence high FA amplification factors (up to values of the order of 5) in the low and medium period bands for stations located on sedimentary deposits. A more detailed investigation on possible correlations between the measured amplification and the site geomorphological characteristics is under progress.

References

Castro R.R., Anderson J.G. and Singh S.K.; 1990: Site response, attenuation and source spectra of S waves along the Guerrero, Mexico, subduction zone. Bull. Seismol. Soc. Am., 80 no. 6A, 1481–1503.

Klin P., Laurenzano G., Barnaba C., Priolo E. and Parolai S.; 2021: Site Amplification at Permanent Stations in Northeastern Italy. Bull. Seismol. Soc. Am., 111 no. 4, 1885–1904, DOI 10.1785/0120200361.

Mascandola C., Barani S. and Albarello D.; 2023: Impact of Site-Response Characterization on Probabilistic Seismic Hazard in the Po Plain (Italy). Bull. Seismol. Soc. Am., 113 no. 3, 1269–1285, DOI 10.1785/0120220177.

Corresponding author: nicolatragni@cnr.it

MUDA: a new geophysical and geochimical MUltiparametric DAtabase for real-time multidisciplinary monitoring networks

Massa M.[(1)], Rizzo L.A.[(2)], Ferrari E.[(1)], Lovati S.[(1)], Scafidi D.[(3)] and MUDA working group

[(1)] Istituto Nazionale di Geofisica e Vulcanologia, sezione Milano
[(2)] Università di Milano Bicocca, DISAT
[(3)] Università di Genova, DISTAV

MUDA (geophysical and geochemical MUltiparametric DAtabase) is a new infrastructure of the National Institute of Geophysics and Volcanology (INGV, www.ingv.it) serving geophysical and geochemical multiparametric data, designed as part of the INGV Pianeta Dinamico (PD) 2020-2022 project and now implemented as a part of the ongoing INGV Pianeta Dinamico 2023-2025 PD-GEMME (Integrated Geological, gEophysical and geocheMical approaches for 3D Modeling of complex seismic site Effects) project.

MUDA is a dynamic and relational database based on MySQL (https://www.mysql.com) with a web interface realised in php (https://www.php.net) using a responsive design technique. The multi-parametric data are stored and organised using a table-structure able of correlating different types of data that allow possible future integration with new type of data acquired through both real-time and off-line transmission vectors.

MUDA collects information from different types of sensors, such as seismometers, accelerometers, hydrogeochemical sensors, sensors for measuring the flux of carbon dioxide on the ground (CO_2), sensors for detecting the concentration of Radon gas and weather stations with the aim of making possible correlations between seismic phenomena and variations in environmental parameters such as the level of groundwater as well as its temperature and electrical conductivity (e.g, Barberio et al. 2017; Chiodini et al., 2020; Mastrorillo et al. 2020).

MUDA archives and publishes data of multiparametric stations belonging both to permanent (e.g. National Seismic Network, RSN-INGV, https://www.fdsn.org/networks/detail/IV/) or temporary (e.g. PDnet, Massa et al., 2021, https://www.fdsn.org/networks/detail/ZO_2021/) INGV seismic networks, as well as data from a multi-parametric Salse di Nirano Reserve (MO) site in cooperation with the PD PROMUD 2023-2025 (Definition of a multidisciplinary monitoring PROtocol for MUD volcanoes) project and two additional multi-parametric sites installed in the inter-mountain basin of Norcia, as a part of the GEMME 2023-2025 project. Data from Radon stations belong to the INGV-IRON national network (Italian Radon Monitoring Network, https://www.ingv.it/en/monitoring-and-infrastructure/monitoring-networks/ingv-and-its-networks/iron).

MUDA daily publishes multi-parametric data updated to the previous day and offers the chance to view and download dynamic time series for all available data and for different periods, up to a maximum of 30 days. For longer periods, users can request data to muda@ingv.it.

MUDA is now published at http://muda.mi.ingv.it (doi.org/10.13127/muda)

Bibliografia

Barberio M.D., Barbieri M., Billi A., Doglioni C., Petitta M. (2017), Hydrogeochemical changes before and during the 2016 Amatrice-Norcia seismic sequence (central Italy). Scientific Reports, 7:11735, doi:10.1038/s41598-017-11990-8.

Chiodini G., Cardellini C., Di Luccio F., Selva J., Frondini F., Caliro S., Rosiello A., Beddini G., Ventura G. (2020), Correlation between tectonic CO2 Earth degassing and seismicity is revealed by a 10-year record in the Apennines, Italy. Sci. Adv. 2020; 6 : eabc2938

Massa M., Rizzo A.L., Lorenzetti A., Lovati S., D'Alema E., Puglia R., Carannante S., Piersanti A., Galli G., Cannelli V., Luzi L. (2021), La rete del lago di Garda: una nuova infrastruttura dell'INGV per il monitoraggio multiparametrico, blog INGV dipartimento terremoti, https://ingvterremoti.com/2021/12/10/la-rete-del-lago-di-garda-una-nuova-infrastruttura-dellingv-per-il-monitoraggio-multiparametrico/

Mastrorillo L, Saroli M, Viaroli S, Banzato F, Valigi D, Petitta M. (2020), Sustained post-seismic effects on groundwater flow in fractured carbonate aquifers in Central Italy. Hydrological Processes, 34:1167–1181. https://doi.org/10.1002/hyp.13662

Correponding author: marco.massa@ingv.it

In-plane strengthening of timber floors to improve the seismic response of masonry structures: a 18thcentury case-study

A. Mazelli[1,2], C. Bedon[2], A. Morassi[1]

[1] University of Udine, Polytechnic Department of Engineering and Architecture, Udine, Italy
[2] University of Trieste, Department of Engineering and Architecture, Trieste, Italy

Introduction

Existing masonry buildings are often complex structures, and their seismic performance evaluation represents a challenge. The high variability of mechanical characteristics of unreinforced masonry and the presence of flexible floors that are poorly anchored to the walls make identifying their dynamic behaviour tough.

A solution to improve the seismic behaviour of existing / historic masonry structures is the floor reinforcement, by stiffening and connecting them efficiently to vertical structures, and facilitating an effective distribution of the seismic action with a box-like behaviour. Various solutions have been proposed over the years, using steel, wood or fibre-reinforced materials, and their effectiveness on the building seismic behaviour has been addressed by push-over (Ortega et al. 2018, Jiménez -Pacheco et al. 2020) or nonlinear dynamic analyses (Scotta et al. 2018, Gubana and Melotto 2019).

The main goal of current work is to evaluate the effectiveness of several floor stiffening solutions, by means of push-over analysis, to improve the seismic performance of a case-study historic building.

Description of the case-study building

The case-study building is a noble Villa in north-eastern Italy (Pordenone) built in the early 18th century (Fig. 1a,b). The building has a compact rectangular plan shape (16x15 m) and four levels. The upper floors were added after a renovation (end of 18th century), and for this reason the internal walls layout of new and lower floors has no correspondence (Fig. 1c,d). Moreover, the floor at the tympanum level has smaller dimensions.

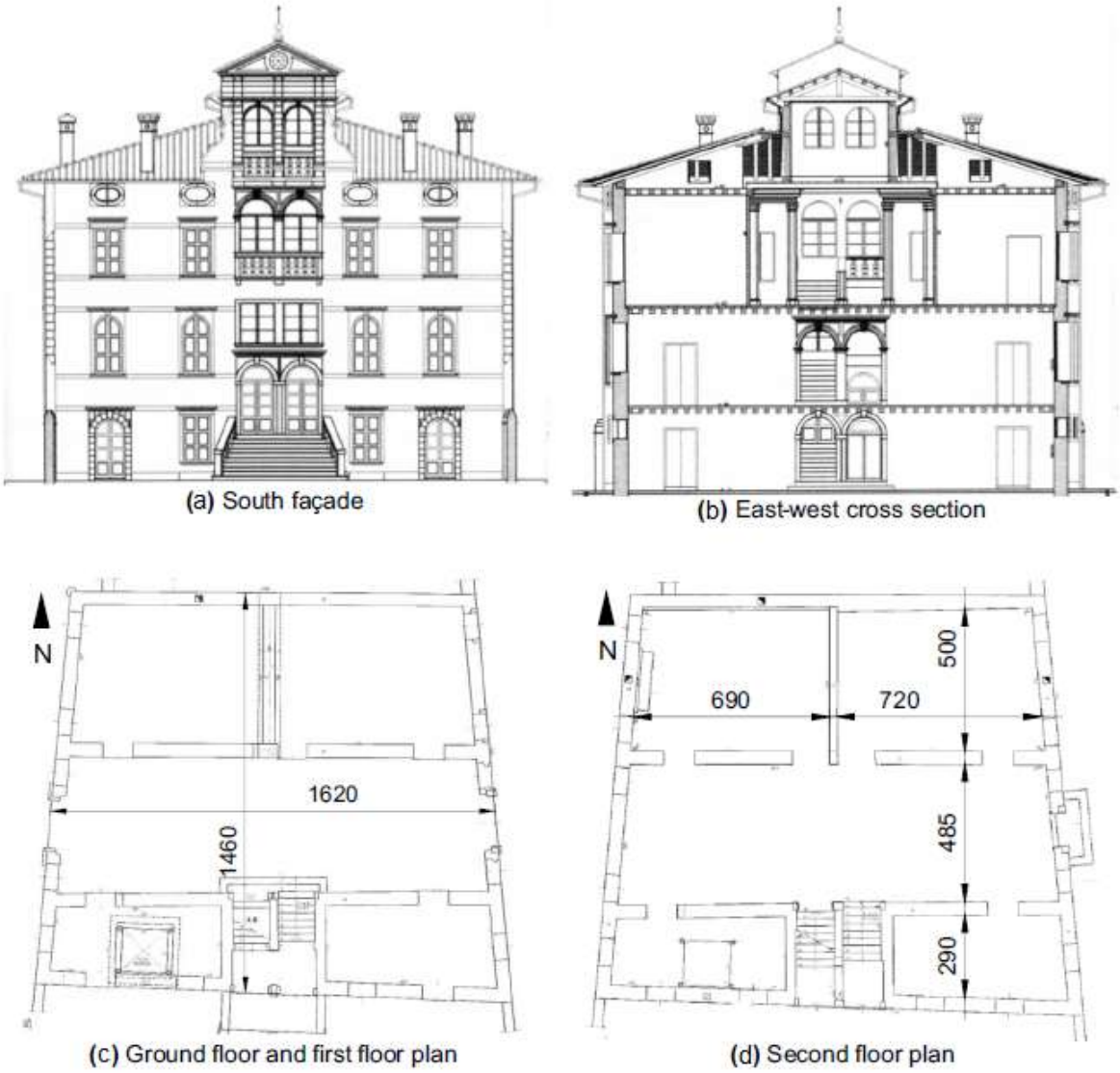

Fig. 1 – Drawings of the case-study historic Villa (measurements in centimetres).

The walls are made of rubble stone masonry (mean compressive strength f_c=2.17 MPa, elastic modulus E=1500 MPa, shear modulus G=500 MPa) varying in thickness from 50 cm (ground floor) to 42 cm (upper storeys). The existing floors consist of timber joists and nailed planks, with beams oriented North-South.

Structural numerical model

The case-study villa was modelled in Sap2000 using a simplified but efficient approach, which was validated towards the earlier DEM modelling strategy presented in (Gubana and Melotto 2021a). To this aim, the façade shape was slightly simplified in geometry, in accordance with (Gubana and Melotto 2021a). Moreover, the roof and the 4th storey were described in terms of equivalent masses only (applied to the 3rd floor). The tympanum floor consists in a timber reticular system with negligible contribution to the overall stiffness of the building (Gubana and Melotto 2021a).

The walls were modelled with an equivalent frame strategy (Fig. 2). Each pier and spandrel were associated with two flexural hinges at the ends, and a shear hinge at mid-span. Ultimate bending moment, shear and corresponding drifts were assumed in accordance with the Italian Building Code and the CNR-DT 212/2013.

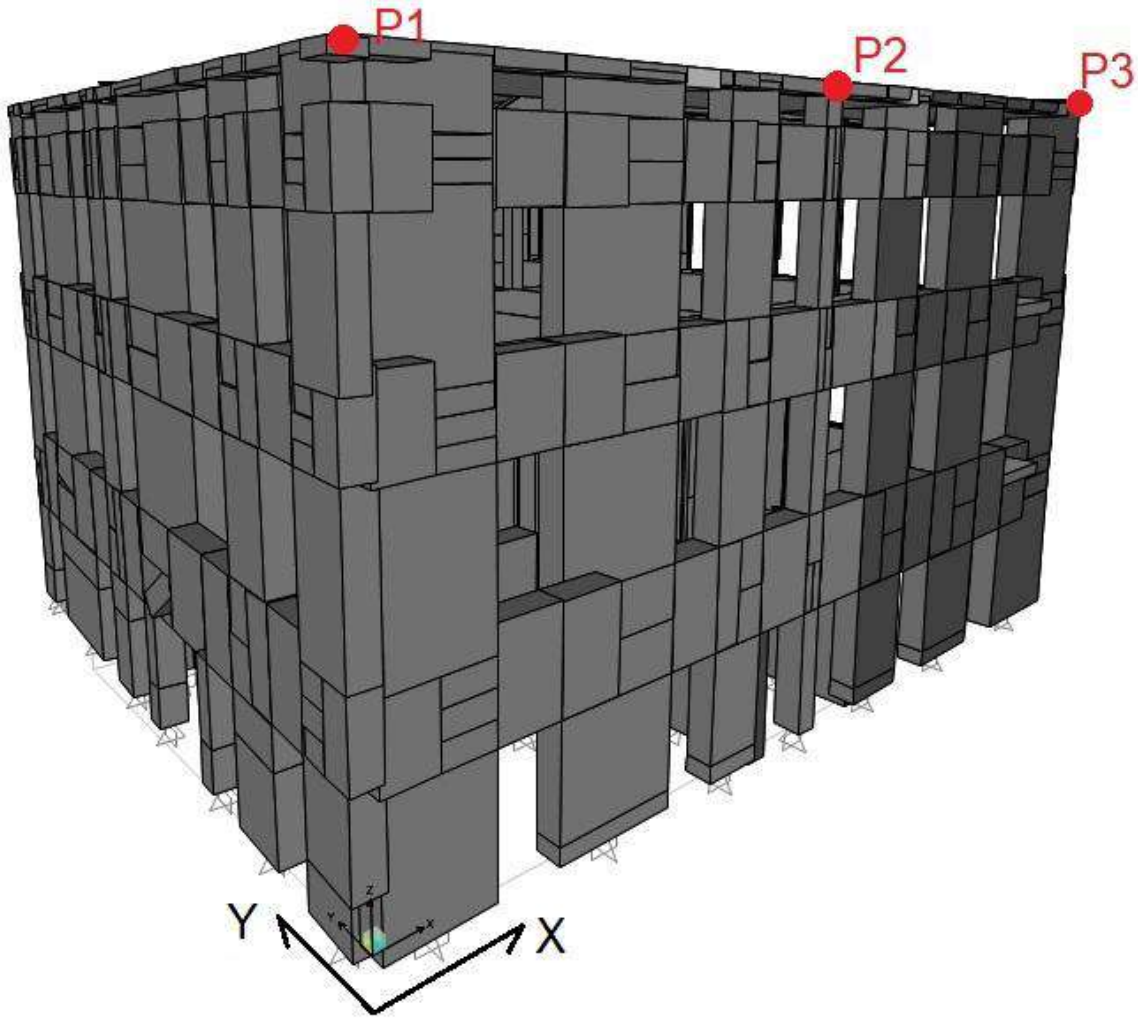

Fig. 2 – Structural FEM model of the Villa and control points on the top floor (Sap2000).

Six different models of the Villa were developed, by varying the in-plane reinforcement strategy for timber floors (Table 1). The mechanical parameters for the reinforcement characterisation were taken from a previous extensive experimental campaign (Gubana and Melotto 2021b). The equivalent stiffness of the floor was evaluated by means of equation 1:

$$G = \frac{F/B}{\gamma} = \frac{F/B}{\frac{\sqrt{B^2 + H^2}}{BH}\frac{d_1 - d_2}{2}} \quad (1)$$

Where F is the applied load, B and H are the floor dimensions parallel and orthogonal to the orientation of the beams respectively, and d_1 and d_2 are the length variation of the diagonals. Values of the equivalent stiffness are shown in Table 1. A first shear stiffness $G_{0\text{-}30}$ was calculated between 0% and 30% of the maximum shear load carried by the sample, while a second value ($G_{10\text{-}40}$) between 10% and 40% of the maximum load, in accordance to UNI-EN12512 (2006). Two non-reinforced floors (TF-UR-G and TF-UR-NG) were selected for the analyses: the first with gaps between the planks and the second without gaps. Their difference is emphasized by the $G_{0\text{-}30}$ stiffness, which is eighteen times higher for the NG case, where the friction between the parts of the floor plays an important role. The influence of the initial stiffness is partially lost when evaluating $G_{10\text{-}40}$. Three types of reinforced floors were considered. TF-OSB-N and TF-OSB-S were stiffened with 25 mm thick OSB panels and ringed-nails (N case) or screws (S case). On the other hand, TF-CLT-S floor was reinforced with 60 mm thick CLT panels, which were fastened with screws. Each floor was modelled as an equivalent shell element with an elastic behaviour. Furthermore, the case of rigid diaphragm was also taken into account (TF-RIGID).

Table 1 – Timber floor typologies considered for the non-linear analysis of the case study Villa, as derived from the experimental investigations in (Gubana and Melotto 2021b)

ID	Features	Reinforcement type	Connectors	$G_{0\text{-}30}$ [kN/mm]	$G_{10\text{-}40}$ [kN/mm]
TF-UR-G	With gaps	-	-	0.09	0.06
TF-UR-NG	No gaps	-	-	1.66	0.65
TF-OSB-N		OSB panel	Ringed-Nails	19.52	5.92
TF-OSB-S		OSB panel	Self-tapping screws	10.49	3.81
TF-CLT-S		CLT panel	Self-tapping screws	5.69	2.83
TF-RIGID		-	-	-	-

Results

The parametric numerical results were analysed in term of displacements. A comparison between base shear and top displacement obtained for each configuration of Table 1 was also carried out.

Pushover analyses were performed in the North-South direction (Y direction according to Fig. 2), which corresponds to the orientation of timber joists. In accordance with the Italian Building Code, a mass proportional (Group 1) and an acceleration proportional (Group 2) configuration were considered for loading.

Fig. 3 shows the displacements on the top storey of the South façade of the Villa for all floor configurations, normalized to the displacement of control point P2 in the TF-UR-NG arrangement ($d_{P2,TF\text{-}UR\text{-}NG}$). A red dot highlights the control point P2 defined in Fig. 2. The graphs in Fig. 3 confirm the significant contribution of the interventions in reducing the out-of-plane bending of the south wall, and so the possibility to avoid the activation of local out-of-plane mechanisms. The effect can also be seen graphically, considering the less convex shape of the deformed curves in the reinforced cases.

In the TF-UR-G case, the structure exhibits a different behaviour, where in Fig. 3a,d a considerable slip is visible at x = 0 m, due to the collapse of the corresponding shear wall.

For each type of floor, the ratio between the out-of-plane deflection of the south façade and the total displacement was evaluated, referring to control point P2. For the TF-UR-NG case, the ratio varies between 20% (Group 2 negative) and 46% (Group 1 negative). These percentages drop significantly for strengthen floors.

When the floor is reinforced with OSB panels and ringed-nails, the incidence of the out-of-plane bending varies between 11% and 22% for Group 2 and Group 1 in the positive direction respectively. The results are further improved if OSB panels and screws are considered: in this case, the incidence is limited between a minimum of 7% (Group 2 negative) and a maximum of 15% (Group 1 positive).

In the TF-CLT-S case, the ratio varies between 7% (Group 2 negative) and 30% (group 1 positive). It is worth noticing that this solution allows achieving higher global displacements in the negative direction.

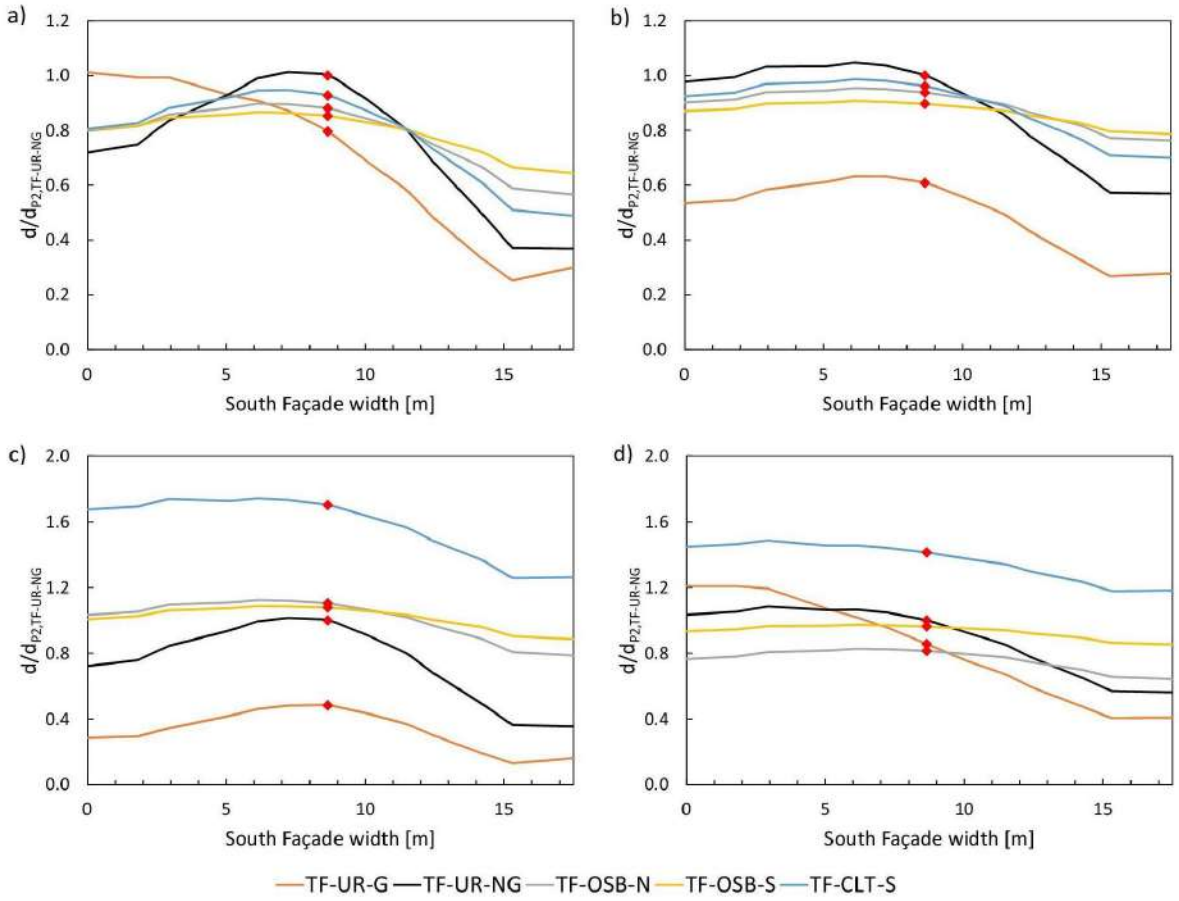

Fig. 3 – Normalised displacements of the main South façade for Group 1 and Group 2 loading configurations in positive (a and b) and negative (c and d) directions.

Furthermore, Table 2 shows the influence of the reinforcement on the maximum base shear F_{max} and the maximum displacement d_{max} of the control point in the center of mass of the top floor. The results were considered in terms of percentage variation compared to the TF-UR-NG case.

The high displacements of the TF-UR-G case are due to the premature collapse of a shear wall, as already seen in Fig. 3. The effect is visible in the decrease in the total force at the base compared to the TF-UR-NG case.

The reinforced cases exhibit a slight increase in the maximum base shear, due to the improved distribution of the seismic forces on the resistant structures. Furthermore, in most cases, the ultimate displacement decreases. It is worth noticing that this is not a decrease in the ductility of the structure, which is low because its global response is governed by brittle shear failures. The smaller displacement is due to the greater stiffness of the reinforced floors.

As already seen in Fig. 3, the CLT case in the negative direction has an excellent performance. It limits the out-of-plane displacements of the south façade and, at the same time, the

maximum shear obtained is increased. Among all cases, the TF-CLT-S is the one more similar to the ideal behavior of a rigid diaphragm, as already noted in (Gubana and Melotto 2021a).

Table 2 – Influence of the reinforcement of the floors on the base shear F_{max} and on the maximum displacement d_{max} with respect to the TF-UR-NG case.

	GROUP 1				GROUP 2			
	Positive		Negative		Positive		Negative	
	ΔF_{max} [%]	Δd_{max} [%]	ΔF_{max} [%]	Δd_{max} [%]	ΔF_{max} [%]	Δd_{max} [%]	ΔF_{max} [%]	Δd_{max} [%]
TF-UR-G	-8.6	131.2	-28.7	47.6	-16.7	24.7	-5.6	74.7
TF-UR-NG	-	-	-	-	-	-	-	-
TF-OSB-N	7.0	-33.2	12.0	-16.7	5.7	-24.4	1.8	-35.5
TF-OSB-S	7.9	-37.4	14.4	-21.7	7.1	-29.4	8.8	-25.1
TF-CLT-S	5.5	-25.8	24.6	34.8	4.4	-19.4	10.4	17.5
TF-RIGID	91.0	83.0	48.2	-34.6	37.4	52.7	22.6	-21.9

Conclusions

Pushover numerical analyses to evaluate the influence of the in-plane strengthening of timber floors were carried out on a historical masonry Villa.

Three cases of reinforcement with OSB and CLT panels, with nails and screws, were considered, and their performances were compared with two unreinforced cases. The equivalent stiffness of the floors was assumed from experimental tests.

The investigation confirms the capacity of the reinforced floors to limit the out-of-plane bending of the Villa's façade. The incidence of out-of-plane on the total displacement varies from 20-46% in the unreinforced case to 7-15% in the case reinforced with OSB panels and screws. This reduction indicates that it is possible to avoid the activation of local out-of-plane mechanisms with a timber reinforced floor. Furthermore, the proposed stiffening interventions allows to obtain a slight increase in the maximum base shear, between 2% and 25% with respect to the unreinforced case.

References

CNR-DT 212/2013 Instructions for the Reliability Assessment of Seismic Safety of Existing Buildings, National Research Council, Rome 2013 (in italian)

CS.LL.PP. 2018 Ministery Decree 17/01/2018 - Italian National Building Code NTC 2018 (in Italian).

Gubana A., Melotto M.; 2019: Discrete-element analysis of floor influence on seismic response of masonry structures. Proceedings of the Institution of Civil Engineers - Structures and Buildings 174:459-472. doi.org/10.1680/jstbu.19.00099

Gubana A., Melotto M.; 2021a: Evaluation of timber floor in-plane retrofitting interventions on the seismic response of masonry structures by DEM analysis: a case study. Bull Earthquake Eng 19, 6003–6026. https://doi.org/10.1007/s10518-021-01190-1

Gubana A., Melotto M.; 2021b: Cyclic numerical analyses on wood-based in-plane retrofit solutions for existing timber floors. Structures 33:1764-1774. doi.org/10.1016/j.istruc.2021.05.037

Jiménez-Pacheco J., González-Drigo R., Pujades Beneit L.G., Barbat A.H., Calderón-Brito J.; 2020: Traditional High-rise Unreinforced Masonry Buildings: Modeling and Influence of Floor System Stiffening on Their Overall Seismic Response. International Journal of Architectural Heritage. doi:10.1080/15583058.2019.1709582

Ortega J., Vasconcelos G., Rodrigues H., Correia M.; 2018: Assessment of the influence of horizontal diaphragms on the seismic performance of vernacular buildings. Bulletin of Earthquake Engineering. doi:10.1007/s10518-018-0318-8

Scotta R., Trutalli D., Marchi L., Pozza L.; 2018: Seismic performance of URM buildings with in-plane non-stiffened and stiffened timber floors. Engineering Structures 167:683–694.

UNI-EN 12512:2006 Timber structures. Test methods. Cyclic testing of joints made with mechanical fasteners.

Acknowledgment

This work was carried out as part of the DPC-ReLUIS 2022-2024 project financed by the Department of Civil Protection.

Corresponding author: alessandro.mazelli@phd.units.it

Mapping recent flood covers using machine learning techniques.

A. Mendicelli[1], F. Mori[1], C. Varone[1], M. Simionato[1], M. Moscatelli[1]

1 CNR-IGAG, Istituto di Geologia Ambientale e Geoingegneria, Area della Ricerca di Roma 1, Via Salaria km 29.300, 00015 Monterotondo Stazione, Rome, Italy)

Abstract

At present, the most detailed geological map covering the entire Italian national territory is the 1:100,000 scale geological map of Italy created by ISPRA. To estimate the stratigraphic amplification of seismic motion at the surface over a large area, it is crucial to better define the geological and lithotechnical characteristics of covering soils and geological bedrocks. This work is aimed at improving the definition of recent alluvial covers (Holocene and Upper Pleistocene deposits) compared to the 1:100,000 geological map of Italy. For this purpose, a methodology based on machine learning models has been developed. It considers both categorical and numerical variables to predict the presence/absence of recent flood coverage with good accuracy.

To train the machine learning model, both geomorphometric parameters and geological databases at different scales were used. Initially, the methodology was tested in the Calabria Region and in the Marche Region, for which promising results were obtained with good performances in the external test. The next step, still in the development phase, consists in the application of the methodology in a wider area which includes not only the Calabria and Marche regions but also Tuscany, Emilia-Romagna and Umbria. The model thus obtained will be tested across the entire national territory.

Acknowledgements

This research was supported with funds from the PNRR, from the project: “National Center for HPC, Big Data and Quantum Computing – HPC – SPOKE 5” – CN00000013.

Corresponding author: amerigo.mendicelli @cnr.it

Local seismic effects forecast supporting risk mitigation in the Ferrara area.

L. Minarelli[1], M. Stefani[2], S. Amoroso[3-1], G. Tarabusi[1]

[1]Istituto Nazionale di Geofisica e Vulcanologia, Italy
[2]University of Ferrara, Italy
[3] University of Chieti-Pescara, Italy

Introduction

The history of Ferrara has been marked by many significant earthquakes, documented since 1117 (Guidoboni 1984; Locati et al. 2016; Guidoboni et al. 2018 and Guidoboni et al. 2019). The worst documented damage occurred during the 1570 earthquakes. The seismic activity was generated by reverse and, sometimes, strike-slip faults of the Apennines chain front, buried under thick Plio-Pleistocene foredeep deposits. The damage to the anthropic structures was modulated by local seismic effects, reflecting the complex stratigraphical, geophysical, and geotechnical features of the area. The subsurface architecture induced seismic wave amplification and, at sites, coseismic liquefaction of water-saturated granular sediments, as occurred in the urban area of Ferrara during the 1570 earthquakes (Guidoboni and Valensise 2023), and in adjacent areas in the year 2012 (Minarelli et al. 2022). For developing the research, over 4,000 pre-existing geophysical, stratigraphical, and geotechnical investigations were collected into a homogeneous database, and analyzed together with the new investigations we carried out, such as seismic noise measurements, seismic piezocone, and seismic dilatometer tests. Numerical modeling for the seismic response analysis was also performed.

Geology and Stratigraphy

The distribution and properties of the outcropping fluvial sediments were reconstructed through remote sensing, field investigation, and geotechnical testing. The Po channel sands (Fig. 1a), mainly Medieval in age, form elongated bodies in northern areas, whereas, in southern zones, the Reno channel silty sand and silts accumulated during the XVII century. In south-eastern areas, Roman Times Po and Reno channel bodies are sub-outcropping. The fluvial channel deposits are flanked by finely granular natural levee belts. Most of the study area consists of mainly cohesive, argillaceous sediments, accumulated into interfluvial settings (Fig. 1a). The conceptual correlation of the abundant cone penetrations tests and stratigraphic cores generated a subsurface geological model, developed throughout the wide Ferrara Municipality area, integrated, in the urban and peri-urban zone, by a lithostratigraphy 3D model, produced by automated interpolation techniques. To generate the model, synthetic lithological columns were derived from the comparison of the tip resistance and lateral friction values, interpreted according to the Roberston classes (Robertson 1990, 2009). The synthetic lithological logs and the actual stratigraphic cores were then laterally correlated, using trilinear and tricubic interpolation algorithms, to generate continuous 3D subsoil models of the first 40 m of subsurface (Fig. 1b, c).

In northern areas, the lower part of the study stratigraphic interval consists of Wuermian synglacial sands, sedimented by the river Po, which southward give way to finer grained units, mainly accumulated by Apennines rivers (Fig. 1c). Throughout the area, the synglacial units are topped by a terraced discordance surface, followed by syn-transgressive continental silty deposits, and by Holocene highstand fine grained sediments, associated with Po River channel sands and, in southern areas, with finer grained sediments of Apennines provenance. Based on the two geological models, 21 stratigraphic microzones (MOPS), homogeneous from a seismic response point of view, have been defined in the first 30 m of subsurface. The petrophysical properties of the microzones control the near surface seismic wave amplification and liquefaction hazard.

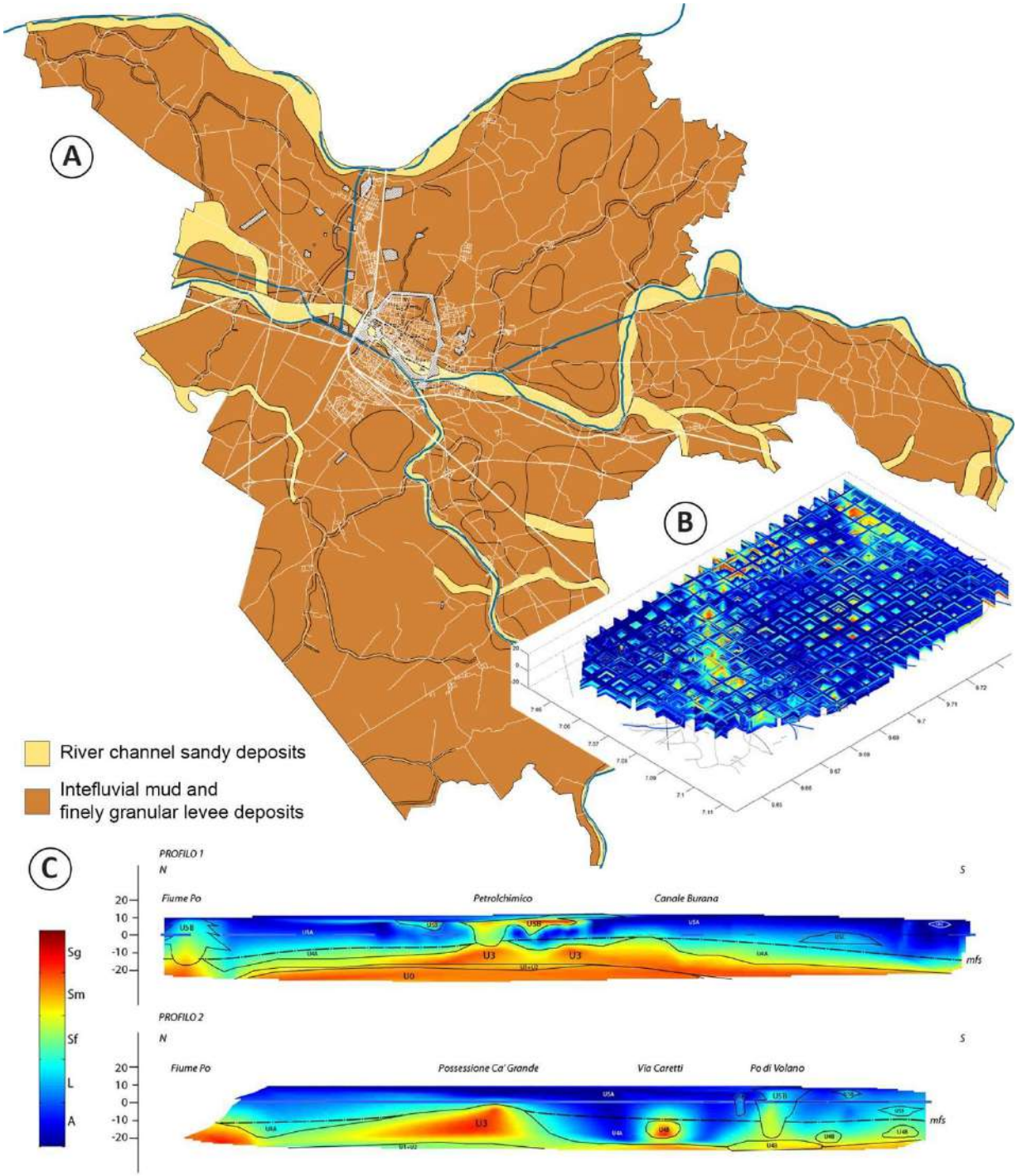

Fig. 1 – (A) Engineering-geological map of the Ferrara municipality area, the yellow ribbons depict Po and Reno channel sand bodies; (B) enclosure diagram extracted from the the 3D model of the first 40 m of the urban area subsurface, derived from the automated tricubic interpolation of more than 1000 subsurface logs; (C) N-S sections extracted from the same model, sand lithologies are depicted in red, cohesive muds in blue, late Pleistocene synglacial sands are covered by Holocene lower alluvial plain deposits.

Seismic amplification and local response

The spectral selective amplification of seismic waves shows rapid spatial variations, even within the comparatively small urban area of Ferrara, due to the complex geological architecture. The seismic bedrock, defined by rocks with S-waves speed exceeding 800 m/s, is everywhere covered by thick unlithified late Quaternary units. The bedrock rises in the

anticline area (Casaglia) to its minimum depth, at about 100 m, and largely sinks towards the subsiding southern syncline zone, where normally exceeds 300 m in depth. The deepening of the seismic substratum shifts the amplification peaks toward lower frequencies. To evaluate the forecasted acceleration at the surface, seismic microzonation studies require to input the seismic intensity, estimated on the bedrock top, with a 10% occurrence probability, over a 50-year time interval, which is provided by the Italian seismic hazard map (Meletti et al. 2006; Stucchi et al, 2011).

To evaluate the seismic motion amplification induced by the unlithified stratigraphic units overlaying the bedrocks, the amplification factor abacuses proposed by the Emilia-Romagna Region for alluvial plain areas were initially used. Two separate abacuses were applied. The "Pianura 2" abacus was used for the areas where the bedrock top is less than 150 m deep, while for the greater portion of the municipal area, with bedrock exceeding 300 m in depth, the "Pianura 3" one was applied. The amplification factors predicted by the abacuses were compared with those derived from our detailed local seismic response analyses (Fig. 2). The good match of the results supports the use of the abacuses approximation. The response analyses was performed in the anticline area and in different portions of the historic center, developed on fluvial sands or on interfluvial muds (Fig. 1, 2). We then forecasted the areal distribution of damage, according to the "synthetic damage constrained parameter" (HSM, Naso 2019), related to the forecasted site shaking, expressed in cm/s^2. The HSM values in turn support the damage estimation. Medium to severe damage is expected for the largest portion of the Municipality of Ferrara, including the whole urban area.

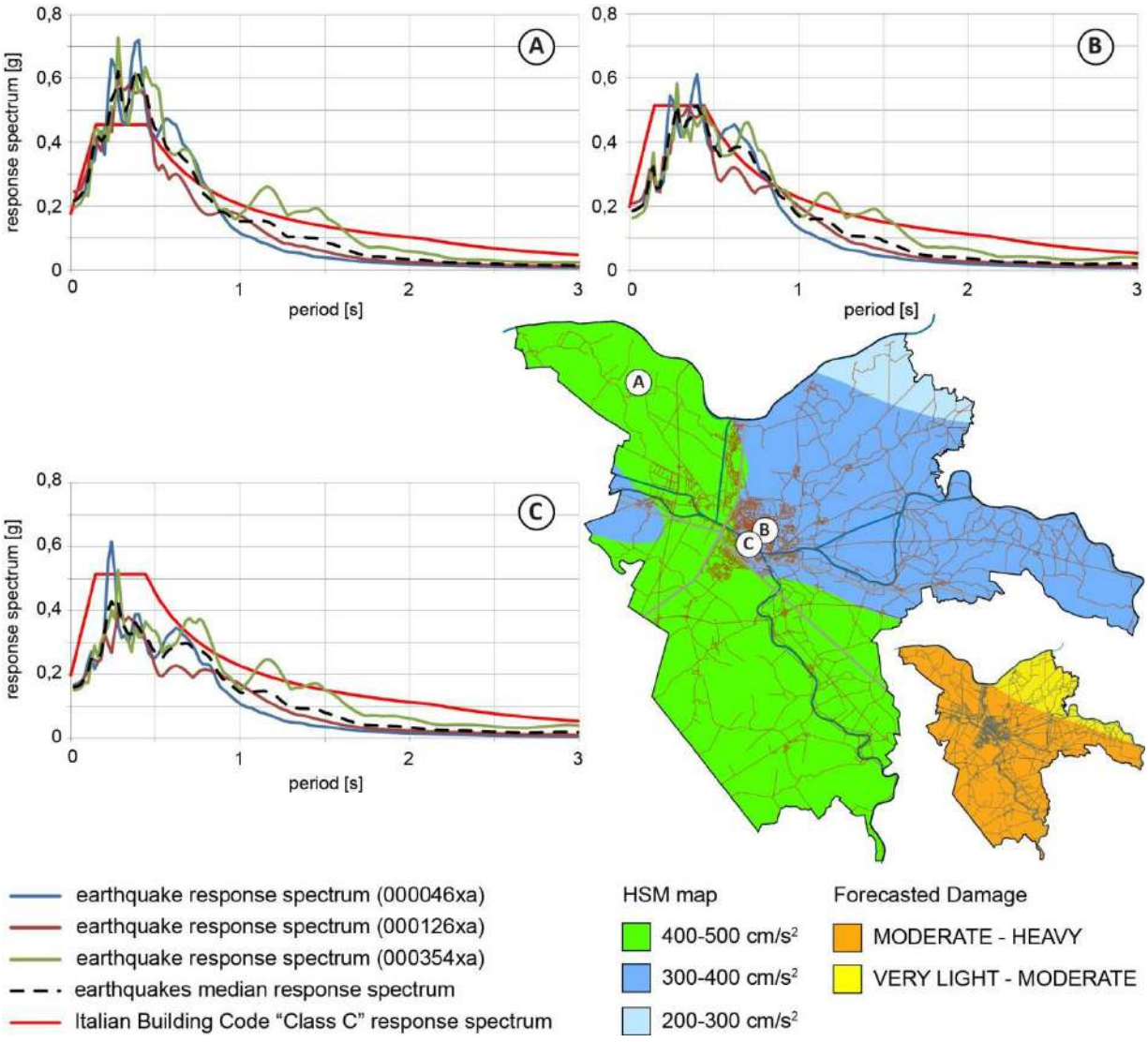

Fig. 2 – Distribution of the damage parameter expressed as acceleration in cm/s² and of the expected damage estimation: Medium-Severe damage is forecast for the urban area. Green areas indicate higher acceleration values than in the blue ones, orange zones more severe damage than the yellow ones. The three graphs illustrate the different spectrally selective amplification responses to the seismic acceleration, in the structural high area (A), and in the urban center, respectively on the Po channel sand body (B) and on interfluvial mud areas (C).

Coseismic liquefaction hazard

To evaluate the local liquefaction hazard, more than 400 punctual analyses were performed, processing cone penetration data through the Boulanger and Idriss (2014) "simplified method". Liquefaction hazard maps were then generated through the geology-based surface interpolation of the punctual estimations. The Liquefaction Potential Indexes LPI (Iwazaki et al., 1982) were subdivided into classes (Sonmez, 2003), to distinguish areas of low ($0 < LPI \leq 2$), moderate ($2 < LPI \leq 5$), and high ($5 < LPI \leq 15$) hazard. A high liquefaction susceptibility is mainly confined to the channel sand bodies deposited by the Po. The sites where the 1570 liquefaction is documented show medium to high hazard index values, validating the estimation procedure, as in the southern portion of the Medieval town and at Torre Fossa (Fig. 3). The forecasted effects of the liquefaction will be largely increased by the presence of

slopes and artificial embankments, which can trigger gravitational lateral spreading. The remaining portions of the study area are generally spared from the liquefaction hazard but are subject to seismic settlements and significant seismic amplification factors.

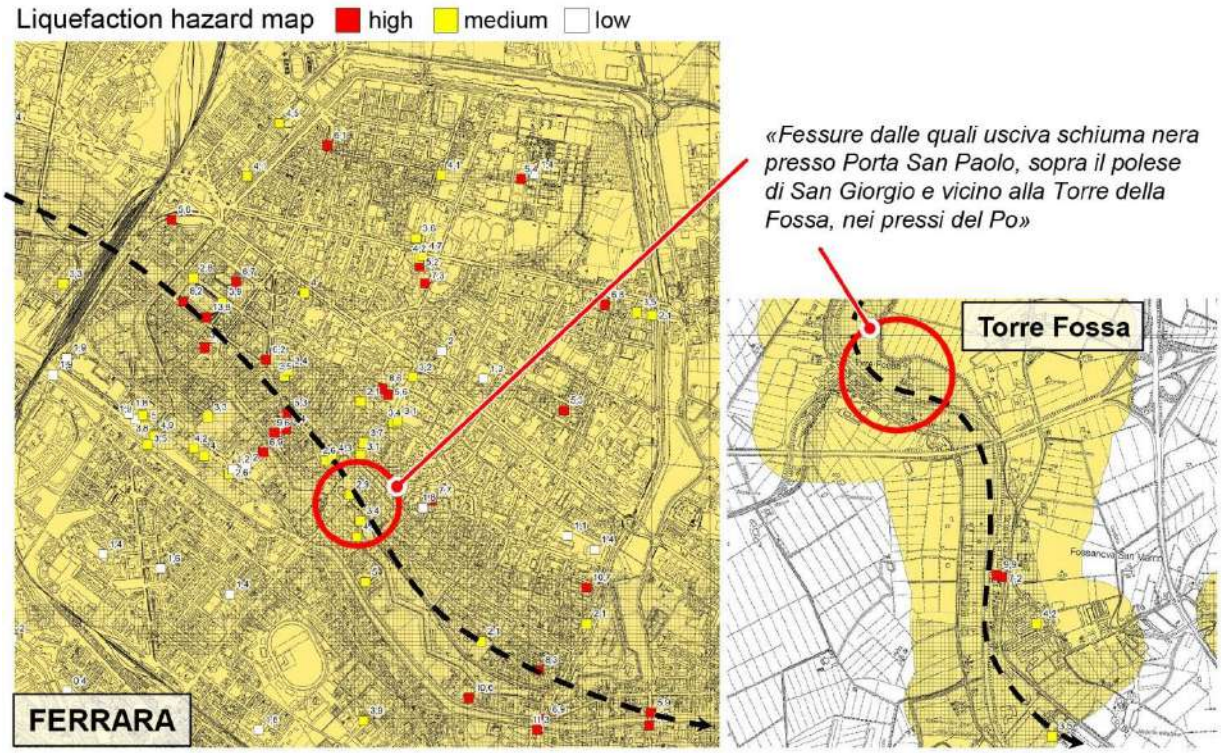

Fig. 3 – Liquefaction hazard map, red squares indicate points of high liquefaction hazard, the Po channel sands always show high or intermediate values. The circles indicate areas where liquefaction was reported in November 1570, near Castel Nuovo – Porta San Paolo and Torre Fossa. The quotation is from a manuscript describing the November 1570 earthquake (Guidoboni 1984).

Conclusions

Interdisciplinary research, integrating geological, geotechnical, geophysical, and computational geostatistics techniques, supported an accurate microzonation of the seismic hazard of the study area. Large spectral selective amplification was demonstrated, showing strong spatial variation gradients. Medium-severe damage is forecasted throughout much of the municipality area. Moderate to high liquefaction hazard characterizes the late Holocene Po channel sand bodies, on which the southern portion of the Medieval town developed. The outskirt areas built on both Po and Reno granular sediments are also subject to significant liquefaction hazard. The impact of the coseismic liquefaction will be multiplied by the lateral spreading of embankments and ridges. The remaining portions of the municipality are developed on cohesive interfluvial sediments and are therefore spared from liquefaction hazard, but still subject to significant seismic wave amplification. The research was aimed at supporting the development of appropriate urban planning and politics. The spatial distribution of the areas subject to liquefaction must be considered in the design of anti-seismic buildings and architecture restoration procedures. The increased knowledge of the risk affecting the town should prompt a massive effort to mitigate the expected damage, by improving the seismic response of both ancient and modern buildings, especially for the many of them built before the Italian seismic code implementation. Improved public

awareness should spur action to mitigate the serious risks to which both buildings and people's lives are now subject.

References

Boulanger R. W., Idriss I. M.; 2014: CPT and SPT based liquefaction triggering procedures. Report No. UCD/CGM-14/01, Center for Geotechnical Modeling, Department of Civil and Environmental Engineering, University of California, Davis, CA, 134 pp.

Guidoboni E.; 1984: Riti di calamità: terremoti a Ferrara nel 1570-74, Quaderni storici 55/ a. XIX, n. 1.

Guidoboni E., Valensise G.; 2023: *L'Italia dei Terremoti, l'Azzardo Sismico delle Città*. Vol. 2, Centro-Nord. Fondazione CNI, 668 pp.

Guidoboni E., Ferrari G., Mariotti D., Comastri A., Tarabusi G., Sgattoni G., Valensise G.; 2018: *CFTI5Med, Catalogo dei Forti Terremoti in Italia (461 a.C.-1997) e nell'area Mediterranea (760 a.C.-1500).* Istituto Nazionale di Geofisica e Vulcanologia (INGV). Guidoboni E., Ferrari G., Tarabusi G., Sgattoni G., Comastri A., Mariotti D., Ciuccarelli C., Bianchi M.G., Valensise G.; 2019: *CFTI5Med, the new release of the catalogue of strong earthquakes in Italy and in the Mediterranean area.* Scientific Data 6, Article Number: 80 (2019).

Iwasaki T., Arakawa T., Tokida K.; 1982: Simplified procedures for assessing soil liquefaction during earthquakes. Proceedings of the Conference on Soil Dynam, p. 49-58.

Locati M., Camassi R., Rovida A., Ercolani E., Bernardini F., Castelli V., Caracciolo C.H., Tertulliani A., Rossi A., Azzaro R., D'amico S., Conte S., Rochetti E.; 2016: *DBMI15, the 2015 version of the Italian Macroseismic Database*. Istituto Nazionale di Geofisica e Vulcanologia.

Meletti C., Montaldo V., Stucchi M., Martinelli F.; 2006: *Database della pericolosità sismica MPS04*. Istituto Nazionale di Geofisica e Vulcanologia (INGV).

Minarelli L, Amoroso S., Civico R., De Martini P.M., Lugli S., Martelli L., Molisso F., Rollins K.M., Salocchi A., Stefani M., Cultrera G., Milana G., Fontanta D.; 2022: *Liquefied sites of the 2012 Emilia earthquake: a comprehensive database of the geological and geotechnical features (Quaternary alluvial Po plain, Italy)*. BULLETIN OF EARTHQUAKE ENGINEERING, v. 20, p. 3659-3697.

Naso G., Martelli L., Baglione M., Bramerini F., Castenetto S., D'Intinosante V., Ercolessi G.; 2019: *Maps for land management: from geology to seismic hazard*. Boll. Geof. Teor. App. Vol. 60, n.2, June 2019, p. 277-294.

Robertson P.K.; 1990: *Soil classification using the cone penetration test*. Canadian Geotechnical Journal, 27(1), p. 151-158.

Robertson P.K.; 2009: *Interpretation of cone penetration tests — a unified approach*. Can. 34 650 Geotech. J. 46, p. 1337–1355.

Stucchi M., Meletti C., Montaldo V., Crowley H., Calvi G.M., Boschi E.; 2011: *Seismic Hazard Assessment (2003-2009) for the Italian Building Code.* Bull. Seismol. Soc. Am. 101(4), p. 1885-1911.

Sonmez H.; 2003: Modification to the liquefaction potential index and liquefaction susceptibility mapping for a liquefaction-prone area (Inegol-Turkey). Environ. Geology 44(7), p. 862-871.

Corresponding author: luca.minarelli@ingv.it

Seismic-induced Landslide Scenarios with Physically-based Models at Regional Scale

N. Monte, I. Marchesini, P. Reichenbach , M. Alviol , F. Bucci, M. Santangelo

CNR IRPI, via della Madonna Alta 126, I 06128 Perugia, Italy

The software r.slope.stability (M. Mergili et al, 2014a; M. Mergili et al, 2014b) is a tool for evaluating regional-scale slope stability (up to hundreds of square kilometers) perfectly integrated within a GIS environment (GRASS GIS – GRASS GIS Developers team, 2024). This software considers multiple potential sliding surfaces, three-dimensional in nature (more precisely, 2.5D), approximated by portions of ellipsoids or truncated ellipsoids. It also relies on the characterization of key geotechnical features of materials and layers used to describe variations in mechanical properties with depth. It employs a limit equilibrium approach and the Mohr-Coulomb criterion to assess the stability factor or, considering uncertainty in input parameters, to define a landslide susceptibility.

The software is freely accessible (https://www.slopestability.org) and constantly evolving. Recently, thanks to collaborations between CNR IRPI and Mundialis GmbH & Co. and the significant contribution of the University of GRAZ, it has been enriched with new functionalities aimed at evaluating the propensity of the territory to experience landslides under the influence of seismic forces (Mergili, M., 2014-2021). The seismic input is integrated via pseudo-static analysis, where seismic forces are directly included in the calculation of destabilizing and resisting forces, utilizing peak ground acceleration and a seismic coefficient. A Newmark approach is also applicable when the hipocenter of the earthquake is known or supposed.

This contribution outlines the software's characteristics and presents preliminary results of its expedited application over an area covering almost the entire region of Molise.

Reference

Mergili, M., 2014-2021. r.slope.stability - The slope stability model. https://www.slopestability.org

GRASS Development Team 2024. Geographic Resources Analysis Support System (GRASS GIS) Software, Version 8.3 https://grass.osgeo.org

Corresponding author: nunzia.monte@irpi.cnr.it

Towards a multi-risk deterministic scenario in the Mt. Etna area

V. Pessina[1], F. Meroni[1], E. Varini[2], M. Longoni[1], R. Rotondi[2], S. D'Amico[3], A. Cappello[3] e Panacea Group*

[1] Istituto Nazionale di Geofisica e Vulcanologia – INGV, Milan, Italy
[2] CNR Istituto di Matematica Applicata e Tecnologie Informatiche "Enrico Magenes", Milan, Italy
[3] Istituto Nazionale di Geofisica e Vulcanologia – INGV, Catania, Italy

* *A full list of authors appears at the end of the abstract*

1. Multi-risk analysis in the Panacea project

Etna (Sicily, Italy) is an active volcano characterized by effusive and explosive eruptions, often accompanied by intense seismic activity. Its densely urbanized territory on the eastern flanks can suffer severe impacts due to lava flows, earthquakes, and tephra, while pyroclastic flows only affect the summit area of the volcano.
As part of the Panacea project (Probabilistic AssessmeNt of volCano-related multi-hazard and multi-risk at Mount EtnA), seismic and volcanic hazard scenarios were generated; consequently risk scenarios for built-up places, lifelines and communication systems were assessed at very different scales, from local to sub-regional. In general, in case of a multi-risk project, it is necessary to identify the elements exposed to the volcano's effects, assess their vulnerability to each different hazard and proceed to complex risk analyses (Meroni et al., 2022, Pessina et al., 2022).
Mt. Etna's hazard studies provided interesting insights (Del Negro et al., 2019) but it is the first time that a multi-risk analysis has been carried out in the area. For this reason, in this study the analyses have been limited to the estimation of direct losses (in terms of structural damage, victims, and loss of functionality) and more complex risk analyses, such as multi-risk and cascade assessments, have not yet been taken into consideration.

2. The hazard scenarios

During the three years of the project, deterministic damage scenarios were created for the calibration and development of damage estimation methods. In this short note, we present

the risk results for 6 municipalities in the Etna area (Milo, Giarre, Riposto, Santa Venerina, Zafferana Etnea, Acireale) for a hypothetical reference scenario.

Two days after the Etna eruption of 24 December 2018 (Alparone et al., 2020), a strong earthquake (M_W 5.0) hit the lower south-eastern flank of the volcano, causing extensive damage in the area between the municipalities of Acireale and Zafferana, with over 1,100 homeless (Pessina et. Al, 2021). It represents the largest event occurred in the area in the last 70 years.

The flank eruption at the volcano started with an intense degassing from the summit craters, an opening of eruptive fissure with a lava flow that ended on December 27.

The (hypothetical) Tephra and Lava scenarios were generated assuming that the 2018 eruption was not interrupted, and significant values of input parameters were assumed in the simulation process to create realistic scenarios of lava invasion and ash ground loads, which are sufficiently important to cause damage to buildings and infrastructure. Fig. 1 shows the seismic scenario of December 26th 2018, and hypothetical scenarios for lava and tephra loads. More comprehensive studies are being published (Sandri et al.)

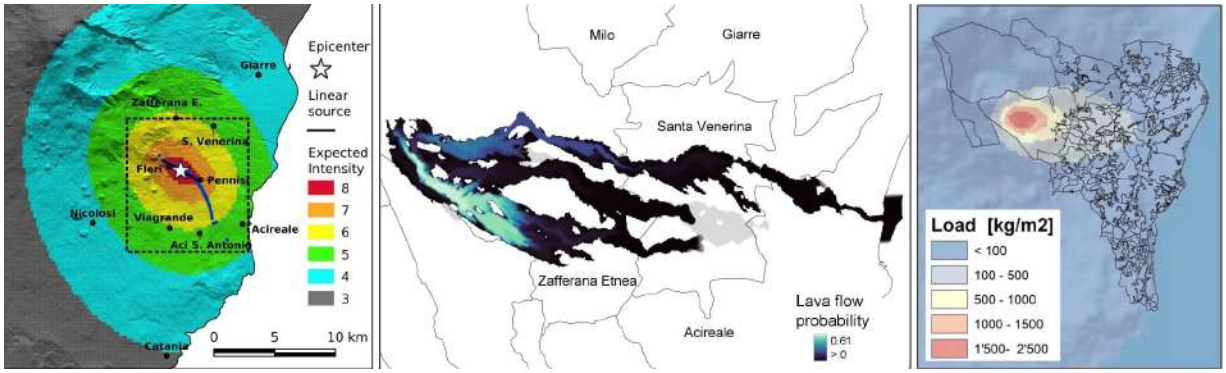

Fig.1 – From left to right: seismic scenario, represented in terms of EMS-98 Intensity, for the December 26, 2018 earthquake, and hypothetical scenarios for lava flow and tephra loads.

3. The risk scenarios

Damage assessment was calculated for residential buildings. Using data collected by the Italian Institute of Statistics (ISTAT, 2011), that are updated and spatially detailed, residential buildings were classified as masonry, reinforced concrete (RC) and other construction type, according to the method illustrated in Dolce et al. (2021). For the assessment of the seismic vulnerability and damage we used the model of Lagomarsino et al. (2021) for masonry buildings and that of Rosti et al. (2021) for RC ones.

Since the new models use both pga values, it was necessary to develop an ad hoc conversion relationship between EMS98 intensity and pga, for this type of event of volcanic origin in the Etna area. The new conversion relationship is the following:

$$\log_{10}(pga) = 0.346\ I_{EMS\text{-}98} - 0.190$$

With reference to the definition of the 5 damage levels of the EMS-98 scale (Grünthal, 1998), Fig. 2a shows the number of heavy damaged buildings (damage level (D4 + D5) in each census tract).

Through remote sensing analysis, the project's colleagues estimated the percentage of pitched and flat terrace roofs of the buildings. These distributions, together with the analysis of AeDes data for the identification of building types and their vulnerability, made it possible to identify the distribution of roofs in four vulnerability classes (Spence et al., 2005). The distribution of buildings with total collapse of the roof due to tephra load – if no cleanup action is taken- is shown in Fig 2c, but it is necessary to highlight the very low probability to have such a level of loads.

In case of lava flow hazard, the level of risk is independent of the vulnerability of the buildings. For each ISTAT census section, the number of buildings damaged by lava is calculated proportionally to the percentage of the section's area occupied by the flow (Fig. 2b).

Once assessed the damage level of the buildings, the totally collapsed buildings, the unusable one, the number of the possible victims or of homeless are calculated in each census section.

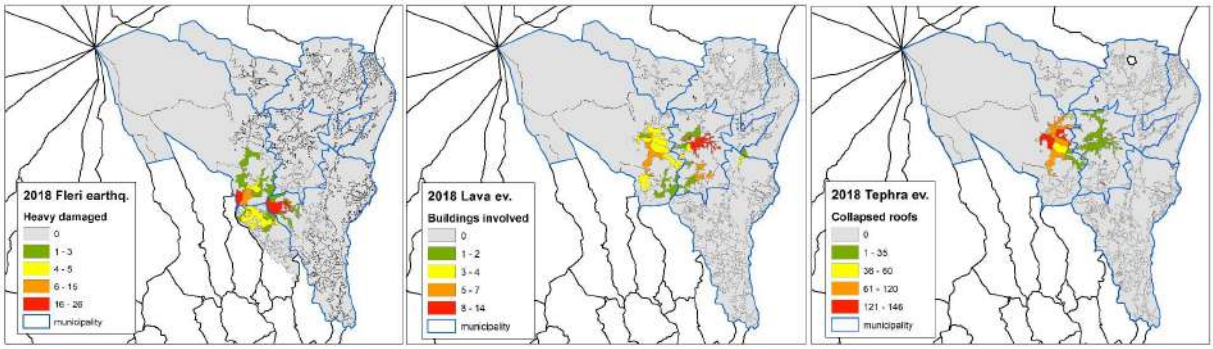

Fig.2 – Damage map of residential buildings due to the earthquake, lava and tephra flows scenarios.

Damage scenarios due to ash loads, lava flows and earthquakes have been estimated to road and power systems, too. Tab. 1 illustrates damage to the power system (pylons, medium voltage (MV) and high voltage (HV) substations and transformers) reach by lava flow with different probability of invasion, as well as the length of invaded road and number of affected buildings.

Tab. 1 – Damage due to the 2018 lava flow scenario

POWER SYSTEM	Road system	Residential

Probability	Pylons	Power MV	Power HV	Transformer	[km]	buildings
0.000358	15	52	1	10	23.82	737
0.005	2	10	-	1	6.27	181
0.01	4	23	-	2	12.61	596
0.025	3	20	-	4	15.69	639
0.05	2	3	-	3	5.37	148
0.1	4	14	-	1	8.31	205
0.3	0	4	-	-	0.74	1
0.5	1	1	-	-	0.79	2
Tot	31	127	1	21	73.6	2509

4. Conclusions

High-impact deterministic scenarios were generated to test the models to be applied for the seismic and volcanic risk of buildings (residential and strategic) and lifelines (electricity grid, roads, etc.) in the Etna area.This exercise, among other things, led to the implementation of a PGA-intensity conversion relationship for Etna earthquakes, as well as the characterization of roof vulnerability in the study area.

Apart from earthquake, expected damage from tephra and lava flow are unlikely to reach high level of damage(D4 and D5). Anyway the interruption of services and other inconveniences are foreseeable at lower damage levels (D2 and D3).

Due to the characteristics of Mount Etna eruptions, lava flow (which are slow) or ash accumulation does not generate victims. Instead, it is possible to find an interdependence on risk scenarios: even a thickness of a few centimetres of ash can make roads dangerous or even just unusable, making rescue operations difficult in the event of an earthquake or in the event of a fire triggered by the eruption.

Thanks to a probabilistic estimate of the expected damage, still in progress, it will be possible to quantify the influence of seismic hazard, lava flow and tephra accumulation in appropriate exposure times.

Acknowledgements

This work was carried out within the PANACEA project that benefited from funding provided by the MIUR (Minitero Istruzione Università e della Ricerca) - Decreto MIUR 1118 del 04/12/2019, within the Pianeta Dinamico project.

References

Alparone, S., Barberi, G., Giampiccolo, E.,Maiolino, V., Mostaccio, A., Musumeci, C., et al.; 2020: Seismological constraints on the 2018 Mt. Etna (Italy) flank eruption and implications for the flank dynamics of the volcano. Terranova 32, 334–344. doi: 10.1111/ter.12463

Del Negro C., Cappello A., Bilotta G., Gangi G., Hérault A., Zago V.; 2019: *Living at the edge of an active volcano: Risk from lava flows on Mt. Etna.* GSA Bulletin; Month/Month 2019; 0; p. 1–11; https://doi.org/10.1130/B35290.1

Dolce, M., Prota, A., Borzi, B., da Porto, F., Lagomarsino, S., Magenes, G., Moroni, C., Penna, A., Polese, M., Speranza, E., Verderame, G. M., Zuccaro, G.; 2021: *Seismic risk assessment of residential buildings in Italy*. Bull Earthquake Eng 19, 2999–3032, https://doi.org/10.1007/s10518-020-01009-5

Grünthal, G.; 1998: *European macroseismic scale 1998 (EMS-98)*. In: Cahiers du Centre Européen de Géodynamique et de Séismologie, Vol. 15. Luxembourg: Conseil de l'Europe

ISTAT (2011) 15° Censimento generale della popolazione e abitazioni.Retrieved February, 2022, from http://dati-censimentopopolazione.istat.it/Index.aspx?lang=it

Lagomarsino S., Cattari S., Ottonelli D.; 2021: *The heuristic vulnerability model: fragility curves for masonry buildings*. Bull Earthquake Eng 19, 3129–3163. https://doi.org/10.1007/s10518-021-01063-7

Meroni F., Pessina V., Azzaro R., D'Amico S., Scollo S.; 2022: *From seismic damage assessment to a risk volcanic scenarios in the area of Mount Etna (Sicily)*. 2nd Int. Conf. on Urban Risk, 30 june-2 July, Lisbon

Pessina V., Meroni F., Azzaro R., D'Amico S.; 2021: *Applying simulated seismic damage scenarios in the volcanic region of Mount Etna (Sicily): a case-study from the MW 4.9, 2018 earthquake*. Front. Earth Sci. 9:629184. doi: 10.3389/feart.2021.629184 https://www.frontiersin.or g/articles/10.3389/feart.2021.629184/full

Pessina, V., Garcia, A., Meroni, M., Sandri, L., Selva, J., Azzaro, R., Bevilacqua, A., Bilotta, G., Branca, S., Coltelli, M., D'Amico, S., de' Michieli Vitturi, M., Esposti Ongaro, T., Ganci, G., Mereu, L., Scollo S., and Cappello, A.; 2022: *From multi-hazard to multi-risk at Mount*

Etna: approaches and strategies of the PANACEA project, 3rd Int. Workshop on Natural Hazards, 26-27 May, Terceira Island, Azores, 6 pp

Rosti A., Del Gaudio C., Rota M., Ricci P., Di Ludovico M., Penna A., Verderame G.M.; 2021: *Empirical fragility curves for Italian residential RC buildings*. Bull Earthquake Eng 19, 3165–3183, https://doi.org/10.1007/s10518-020-00971-4

Sandri L. , Garcia A., Proietti C., Branca S., Ganci G., Cappello A.; :*Where will the next flank eruption at Etna occur? An updated spatial probabilistic assessment*. Preprint (on Discussion) https://doi.org/10.5194/egusphere-2023-2624

Spence R., Kelman I., Petrazzuoli S., Zuccaro G.; 2005: *Residential Buildings and Occupant Vulnerability to Tephra Fall.* Nat. Hazards Earth Syst. Sci. Eu.Geosciences Union, 1–18.

PANACEA GROUP

Azzaro R., Bilotta G., de' Michieli Vitturi M., Esposti Ongaro T., Ganci G., Garcia A., Mereu L., Sandri L., Scollo S., Tuvé T., Zuccarello F.

Corresponding author: vera.pessina@ingv.it

SISMIKO: the operational task force for seismic networks rapid deployments and integration in the INGV monitoring system.

D. Piccinini[1], E. D'Alema[1], S. Marzorati[1], M. Moretti[1], L. Margheriti[1] and SISMIKO Group

[1] *Istituto Nazionale di Geofisica e Vulcanologia (Italia)*

SISMIKO is the operational group within the Istituto Nazionale di Geofisica e Vulcanologia responsible for deploying a temporary seismic network as a rapid response to significant seismic events [Moretti et al., 2023; https://sismiko.ingv.it/]. The purpose of the temporary seismic network is to complement the RSNi (Rete Sismica Nazionale integrata) by reducing the inter-station distances of permanent stations, where necessary. SISMIKO has a distributed structure across various INGV headquarters nationwide and in recent years has equipped itself with a consistent set of around 50 seismo-accelerometric stations and an autonomous acquisition system. This system makes the acquired data available, without restrictions, to the entire scientific community through the Italy node of the European Integrated Data Archive (EIDA [Danecek et al., 2021]) portal, ensuring a high level of data quality.

To ensure a rapid response following an earthquake and rapid integration of data collected by emergency stations, a codified procedure has been established. Through this procedure, the metadata of each station is pre-configured and the data flow coming from these stations is collected within an acquisition system [D'Alema et al., 2022]. This setting allows the rapid use, if necessary, of the data obtained by SISMIKO - after a quality control - by the seismologists on duty at the INGV Operations Room [Margheriti et al., 2021].

Today, over 100 INGV personnel join SISMIKO group: technicians, technologists and researchers from each of the headquarters distributed across the national territory. A new configuration in Activity Groups allows to coordinate the distributed personnel and to cover all the aspects in the preparation of the emergency such as the technical management of the instrumentation, the field operations, to maintain contacts with the INGV Crisis Unit and the other Operational Groups and to develop automatic procedures to analyse real time seismic data (Fig 1).

Besides the operational aspects, in recent years SISMIKO has promoted the recovery of continuous data recorded by temporary seismic stations installed during past seismic sequences such as in L'Aquila 2009, Po Plain 2012 and Central Italy 2016. By reconstructing the complete station's metadata, it is now possible to distribute the data to the scientific community through the EIDA portal.

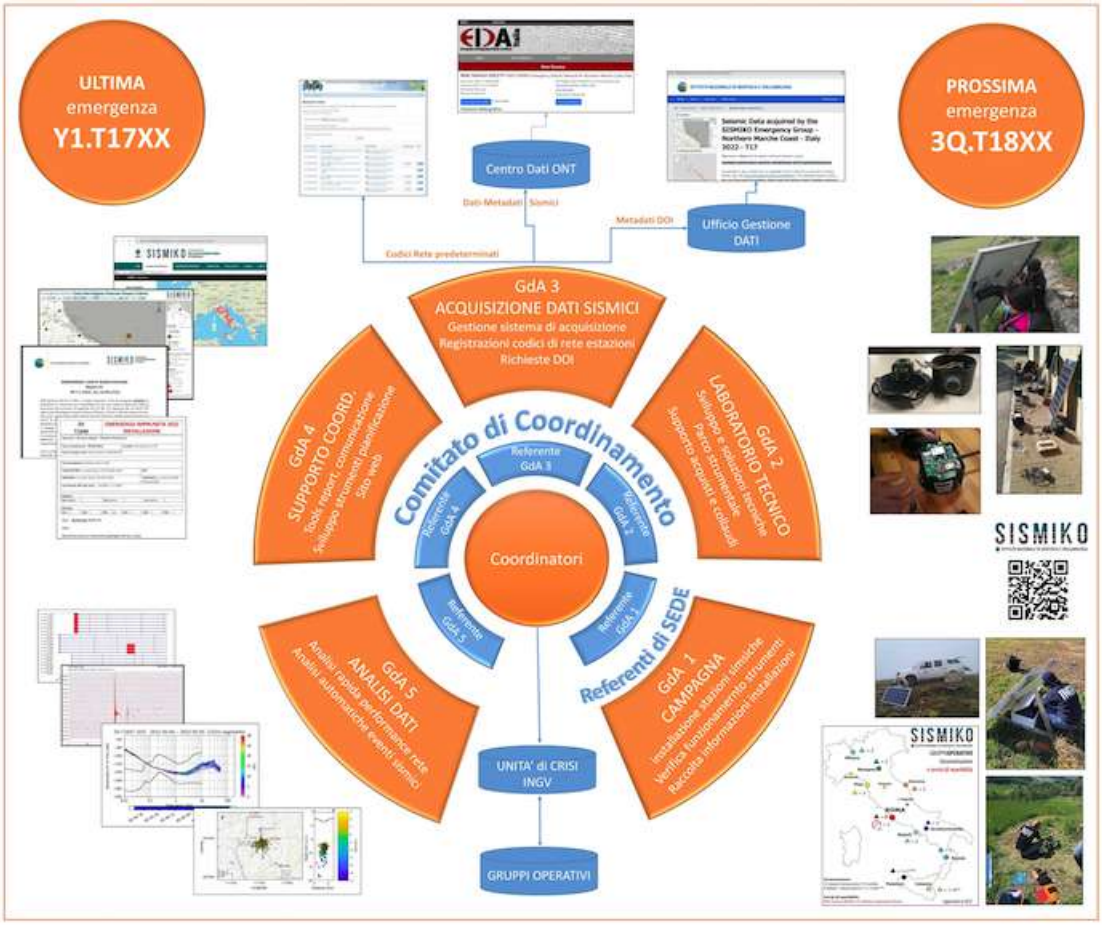

Fig. 1. Schematic representation of the current structure and activities of the SISMIKO Operational Group.

References

D'Alema E., Giunchi C., Marzorati S., Piccinini D., Moretti M.; 2022: SISMIKO: il nuovo sistema di acquisizione dati sismici in tempo reale. Rapp. Tec. INGV, 445: 1-126, https://doi.org/10.13127/rpt/445.

Margheriti, L., et al.; 2021: Seismic Surveillance and Earthquake Monitoring in Italy. Seismological Research Letters. 2021; 92 (3): 1659–1671. doi: https://doi.org/10.1785/0220200380.

Moretti M., Margheriti L., D'Alema E. and Piccinini D.; 2023: SISMIKO: INGV operational task force for rapid deployment of seismic network during earthquake emergencies. Front. Earth Sci. 11:1146579. doi: 10.3389/feart.2023.1146579.

Danecek, D., Pintore, S., Mazza, S., Mandiello, A., Fares, M., Carluccio, I., et al.; 2021: The Italian Node of the European Integrated Data Archive. Seismological Research Letters 92 (3): 1726–1737. doi: https://doi.org/10.1785/0220200409.

Corresponding author: davide.piccinini@ingv.it

Software applications for multi-level safety management of healthcare facilities network

Sandoli[1,2], D. Gargaro[3], D. Gentile[4], M. A. Notarangelo[3], G. Fabbrocino[1,2]

[1] University of Molise, Dept. of Biosciences and Territory, Campobasso, Italy
[2] Institute for Construction Technologies ITC-CNR, National Research Council, L'Aquila, Italy
[3] S2X S.r.l., Campobasso, Italy
[4] University of Molise, Dept. of Medicine and Health Sciences, Campobasso, Italy

Introduction

Earthquakes occurred worldwide demonstrated that hospital infrastructures have often experienced significant damage to structural and non-structural components, producing difficulties during the post-event emergency management phases and economic losses [1]. Collapses or severe damage of hospitals in a given area have had tremendous consequences on both injured peoples, which need immediate medical attention, and patients in the hospitals, thus reducing the resilience of the communities. This phenomenon is particularly felt in the so called Inner or Peripheric Areas, where the health infrastructure network is composed with few hospitals often not well interconnected among them, making difficult the emergency management.

In this framework, it appears evident the needs of identifying safety management strategies of the health infrastructure network, based on multi-level approach, i.e. involving management strategies from large scale (Regional or sub-Regional) up to single-scale building approach. On the other hand, it is also true that the management of healthcare facilities engages a transversal concept of safety which must be regarded at different levels: it involves the safety of structural and non-structural elements under severe and moderate seismic events and that of workers in workplaces in the sense of the Italian Legislative Decree n.81 released in 2008 [2]. The LD81/08 supplies general measures aimed at protecting the safety and the health of workers in workplaces, valid for all private and public activity sectors and for all types of risk [3]. These measures - of primary importance for developing a complete framework for seismic risk assessment of health services in the post-event and for strategizing risk mitigation plans - should be conveniently implemented in probabilistic safety assessment methods. This paper presents an operational framework supported by software applications aimed at approaching from an engineering perspective the management of the occupational health and safety in critical infrastructures [4]. Attention herein is focussed on the multi-level safety management of health services network. The first part is devoted to data collection regarding safety assessment of workers conditions in the workplace, while the second part is devoted at performing Probabilistic Structural Safety Assessment (PSSA) of health facilities with an integrated approach at different scales.

Definition of a comprehensive framework for occupational safety and health management

Safety management of existing health facility structures represents a complex task, because involving the “container” (i.e., structural and non-structural components) and the “content” i.e., safety of workers in workplaces as defined by the LD 81/08. In this regard, a general multi-scale framework to support the safety management of the health facility structures is proposed in Fig. 1, discussed in the following. With the term “multi-level” is here intended scalable datasets and procedures oriented to safety assessment at different levels of deepening. The scales can be substantially organized in three different macro-levels: large- (Level 1), medium- (Level 2) and single-scale buildings (Level 3). The large-scale evaluations involve the safety assessment of a network of heath facility structures located in a given area whose extension coincides with Regional of sub-Regional boundaries; medium scale concerns a group of building constituting the hospital campus, while a single-scale refers to single building belonging to the health facility.

For safety management purposes involving the Levels 1 and 2, data can be conveniently collected in remote through web-based crowd-sourcing technologies, eventually complemented with data coming from on-site surveys. In the case of the Level 3, on-site inspections - eventually integrated with data coming from structural health monitoring - are necessary to collect structural-typological information and details regarding the building characteristics. In addition, on-site inspections to collect data regarding the condition of workers on workplaces are necessary.

Once the data are collected, different procedures of data treatment can be adopted depending on the scale level required to conduct safety assessment. Less detailed data in the case of procedures involving probabilistic-based structural safety evaluations at large and medium scale are required, while more detailed information in the case of single-scale building are necessary (both from structural and safety on workplace point of view). Data, collected and filtered as a function of the considered scale-level, represent the input for implementing multi-level safety assessment methodologies, the latter chosen among those available in literature. As a result, a baseline for defining risk mitigation strategies against natural events of health facilities network is obtained. Note that, data collection, data treatment and safety assessment are procedures which can be by automated through digital tools, facilitating the multi-level management phases of the infrastructure network from the Authorities both in case of emergency or in to plan mitigation strategies.

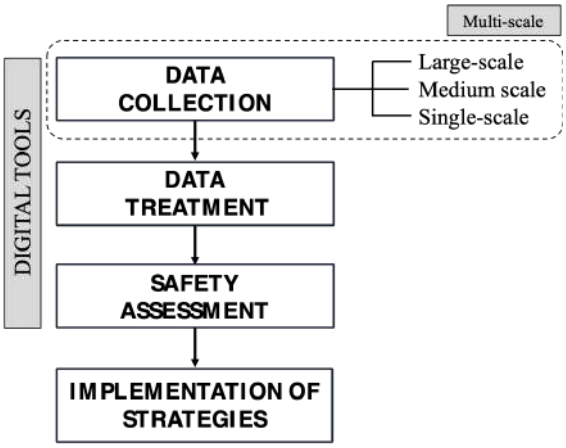

Fig. 1 – Multi-level framework for safety management of health facilities structures

Digital tools for safety assessment and management

In this paper two software devoted to support the implementation of safety management strategies of health facility structures are presented. The software are named as follows:

HF-INSPECT, allows on-site data collection regarding (i) risks related to safety of workers in workplaces as defined by the LD81/08 (electric, biologic attacks, fire, etc.) and (ii) structural typological characteristics of buildings (material-type, age of construction, structural details).

HF-ALL RISKS, enables a comprehensive PSSA of the health facilities (i.e., referred to a network of structures or to single buildings). Data to be included in the software can be collected through web-mapping procedures, eventually combined with on-site surveys.

HF- INSPECT includes a digital form to support on site census activity. Data collection regards: (i) information on personnel working inside the structure, (ii) metric data (i.e. plan and sections) of the structure and their use destination, (iii) layout of the installations, (iv) list of electromedical devices, (v) identification of the risks affecting the specific working place according to LD81/08 (Fig. 2). This survey activity is integrated with interviews to medical personnel operating in the structure. Moreover, HF-INSPECT includes a specific layout called as “structural form” which allows to collect data related to safety and operational conditions of the structure. In particular, the form allows to upload data relative to age of construction, structural characteristics, type of soil, presence of structural interventions and seismological data. Information relative to structural characteristics are of paramount importance to implement PSSA analysis and they are directly interconnected with the HF-ALL RISKS software.

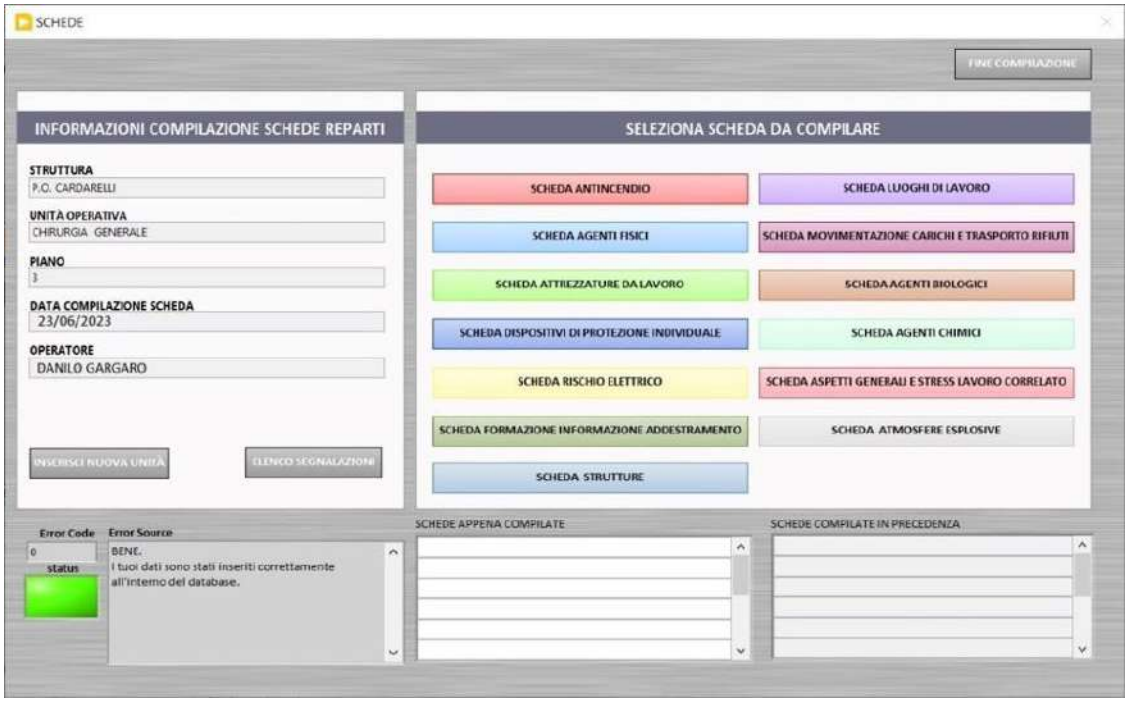

Fig. 2 – HF-INSPECT software

HF-ALL RISKS generates multi-scale PSSA of health facility structures using the Typological Fragility Matrices (TFM) [5]. Typically, such type of analysis is conducted by developing typological fragility curves, which provide the exceedance probability of a Limit State threshold associated with conventional earthquakes conditioned to an IM parameter described through peak-ground, spectral or macroseismic parameters. Instead, TFM computes the exceedance probability using a vectorial form of the IM, for instance composed by magnitude M and distance R, leading to a three-dimensional representation of the fragility (Fig. 3). The change of variable from a single peak-ground/spectral or macroseismic

parameter to (M-R) is obtained by disaggregating the ground motion through Ground Motion Prediction Equations (GMPE). To develop the software, the GMPE provided by Bindi et al. 2011 [6] was used, which consider the magnitude of the event, the epicentral distance, type of soil and type of fault.

The software allows to estimate the PSSA based on the three fundamental steps: a) structural-typological classification of the building classes, b) computation of fragility, c) definition of a safety threshold defining a demand-to-capacity ratio.

As far as the building classes is concerned, each analysed hospital structure is associated to a structural-typological building class. Basically, within the software, the five classes of masonry buildings and the four classes of reinforced concrete ones defined in [7] have been considered, but they can be also changed with other building classes available in the literature. The association to the building class is based on the information available in HF-INSPECT integrated with web-mapping cataloguing procedures. For each building class, the software estimates the TFM computing the Cumulative Density Function (CDF), as follows [5]:

$$CDF = P\left[PGA^{-}\right] = \int_{0}^{PGA^{-}} f(im)dim = \int_{0}^{PGA(M,R)} f(im)dim$$

where PGA is the peak-ground acceleration threshold, M the magnitude of the event, R the epicentral distance, LS the Limit State considered for the structure (in this case the Ultimate Limit State). By cutting the TFM with a M-CDF or R-CDF plane the corresponding fragility curves are also provided by the software. Moreover, the report of the conducted analysis can be downloaded in *.pdf* format. Finally, by selecting a set of earthquake scenarios in terms of (M, R), for instance those provided by the Probabilistic Seismic Hazard Analysis (PSHA) or with reference to an earthquake occurred at a given epicentral distance between with respect a hospital infrastructure and characterized with a given magnitude, the probabilistic structural safety level of the investigated structure can be identified.

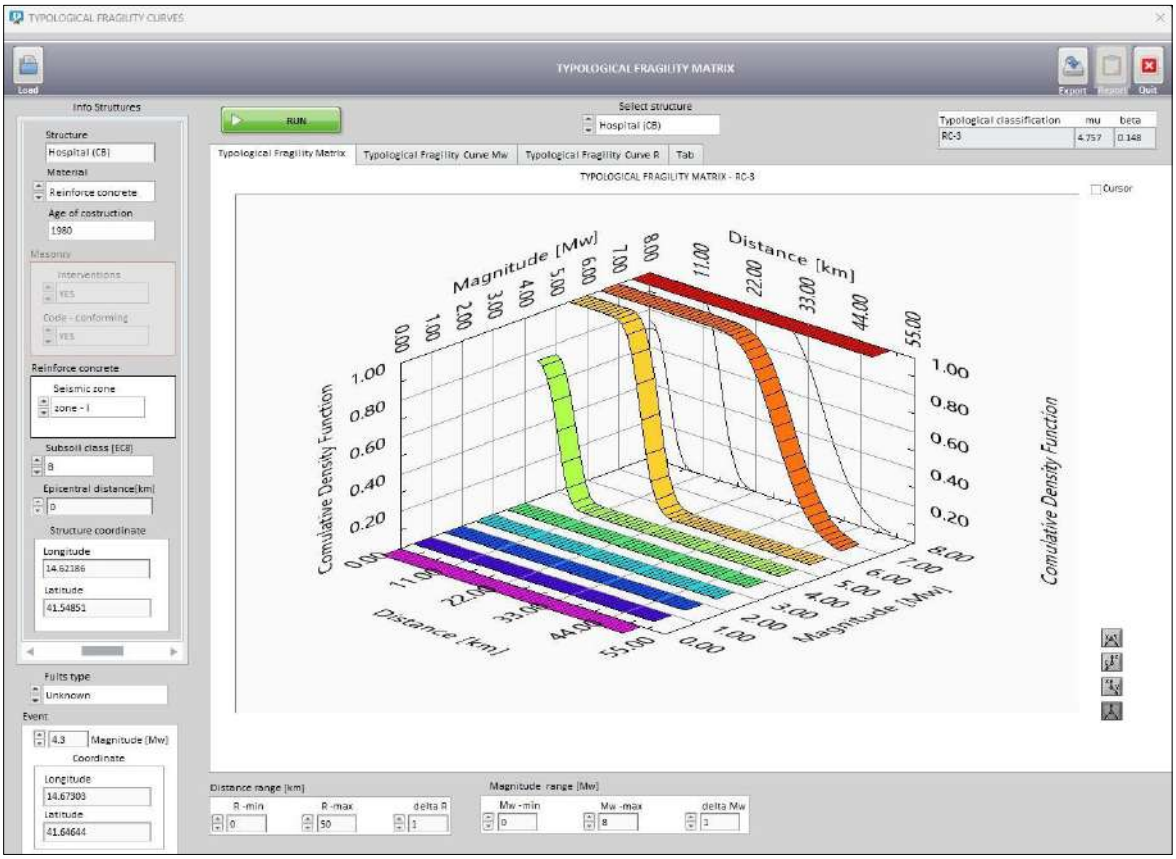

Fig. 3 – HF-ALL RISKS software (the figure illustrates the TFM for the hospital of Campobasso)

Acknowledgements. This study received financial support by research project PON CADS 2020–2023 (Creating a safe home environment) promoted by the Italian Ministry of University and Research.

References

[1] Miranda E, Taghavi S. 2003. Estimation of seismic demands on acceleration-sensitive nonstructural components in critical facilities, Proc. of the seminar on seismic design, performance, and retrofit of non- structural component in critical facilities, ATC 29-2, Newport Beach.

[2] Legislative Decree LD 81/08 – Ministry of work. DL 9 Aprile 2008 n. 81. Testo unico sulla salute e sicurezza sul lavoro. Gazzetta ufficiale n. 101 del 30 aprile 2008- suppl. ordinario n. 108.

[3] Notarangelo MA, Rainieri C, Fabbrocino G. 2016. Strumenti informatici integrati per le indagini conoscitive finalizzate alla valutazione dei rischi sul logo di lavoro in strutture sanitarie e presidi ospedalieri. Proc. of Conf. Proc of the Conf Valutazione e Gestione del Rischio negli Insediamenti Civili ed Industriali VGR 2016. Rome, Italy, 13-15 September 2016.

[4] Ghasemi F, Doosti-irani A, Aghaei H. 2023. Applications, Shortcomings, and new advances of job safety analysis (JSA): findings from a systematic review. Safety and Health at Work 14, 153-162.

[5] Sandoli A, Lignola GP, Prota A, Fabbrocino G. 2023. Seismic fragility assessment of inner peripheries of Italy through crowd-sourcing technologies. Buildings, 13(2), 562.

[6] Bindi D, Pacor F, Luzi L, Puglia R, Massa M, Ameri G, Paolucci R. 2011. Ground motion prediction equations derived from the Italian strong motion database. Bull of Earth Eng 9, 1899-1920.

[7] Sandoli A, Lignola, GP, Calderoni B.; Prota, A. 2021. Fragility curves for Italian URM buildings based on a hybrid method. Bull Earth Eng 19, 4979–5013.

Corresponding author: antonio.sandoli@unimol.it

Capturing spatial variability of empirical site amplification functions δS2S: a case-study in Central Italy

S. Sgobba[1], C. Felicetta[1], G. Lanzano[1], F. Pacor[1] , T. Bortolotti[2], A. Menafoglio[2]

1. *Istituto Nazionale di Geofisica e Vulcanologia, INGV (Milan, Italy)*
2. *MOX, Department of Mathematics, Politecnico di Milano (Milan, Italy)*

Among the techniques for predicting seismic shaking for damage scenarios or regional hazard and risk assessment, the empirical methods based on the use of a ground motion model (GMM) are probably the most rapid and widespread. However, to produce the estimates at ground-level, we need a key-proxy to describe the effect of the local site response, which is usually represented by the shear wave velocity in the first 30 m depth (Vs30) from in situ geophysical measurements or inferred from other proxies (geology, topography, etc.). Although Vs30 has the advantage of being a synthetic predictor, on the other hand it has been shown that it is not truly representative of site response (Castellaro et al., 2008; Luzi et al., 2011; Bergamo et al., 2021), thus, alternative site proxies called site-to-site terms (δS2S) are being explored; they represent systematic deviations of observed amplification at a site from the median values predicted by a partial or fully non-ergodic GMM calibrated on a set of reference rock sites (Lanzano et al., 2022; Kotha et al., 2020). To date δS2S can be considered the most reliable representation of empirical site response if estimated from a sufficient number of site-specific ground-motion observations (Bard et al., 2020; Loviknes et al., 2021).

To increase the use of δS2S for site characterization studies, there is a need to map this parameter at locations in space that lack direct observations. Geostatistical methods, such as the simple Kriging technique, are commonly used for this purpose, but limitations arise in less densely sampled areas or in complex regions (e.g. characterized by the presence of different geological and tectonic structures, alluvial basins, mountain chains, etc. within a few kilometers) due to a too coarse interpolation.

To address this issue, we explore the statistical correlations of δS2S in terms of PGA and elastic spectral acceleration (SA) up to 2s, with other mappable site proxies, in order to calibrate a parametric model capable of constraining the spatial predictions to other proxies or geological/lithological information that are available in the area. In our case the proxies are: Vs30 measurements, high-frequency attenuation decay parameter κ0 (Anderson and Hough, 1984), topographic slope from the Tinitaly DEM at 40m (Mascandola et al., 2021) and local descriptions of the litho-stratigraphic units of the region from large-scale maps (i.e. the

chart of ISPRA 1:100.000 and the classification provided by Forte et al., 2019). On the basis of the resulting correlations, we construct a geostatistical methodology to model the spatial dependencies observed in the site terms, testing both the spatial stationary and non-stationary hypotheses; for the latter, we apply the Universal Kriging technique that captures the local variability and allows us to produce high-resolution maps of δS2S that are constrained to other parameters; i.e. the Vs30 data and the other site-related proxies.

The need for dense information in the region and low-uncertain estimates of ground motion parameters, motivates the choice of central Italy as a case-study area. In this region, in fact, we dispose of a very high number of seismic events recorded in the last 20 years (more than 30.000 records of events with magnitude ranging from 3.2 and 6.5) and the calibration of specific regional GMMs in a completely non-ergodic framework (Sgobba et al., 2021; Sgobba et al., 2023).

Key-findings

- The statistical correlation analysis shows that the δS2S estimates at different spectral periods are mostly correlated with Vs30 measurements, especially at longer periods (from about 0.3s), while are less dependent on the other investigated proxies (κ0, slope, lithology, etc.);
- The best model of δS2S (**Figure 1**) is obtained with a non-stationary parametrization based on geographical coordinates (x, y) and a combined Vs30-map *ad-hoc* developed for the study . The parametric functional form (the same for all spectral parameters) is the following: $\delta S2S \sim \beta0 + \beta1x + \beta2\ y + \beta3\ (x*y) + \beta4\ (Vs30\text{-}map)$ + model error.

  Note that the Vs30-map was constructed by combining the dataset of observations and estimates inferred from the topographic slope (Vs30-WA), according to Wald and Allen's global empirical relationship (Wald and Allen, 2007), and the Italian map (Vs30-Mori) provided by Mori et al. (Mori et al., 2020); indeed, we observed that neither Vs30-WA nor Vs30-Mori alone were able to capture the full range of variability of Vs30 observations;

- Non-stationary spatial models including lithology were also tested but they are not able to significantly improve the predictions of δS2S, suggesting that the current lithological classification or resolution may not be useful for constructing spatial models of the investigated parameters;
- The final optimal model is able to capture the main trend of the empirical site response in central Italy, but it shows some limitations in reproducing the full range of local amplifications and the observed variability between different frequencies, suggesting that additional key-proxies are needed, such as the fundamental frequency of soil deposit f0, the sediment thickness, as well as alternative maps of geo-lithological complexes.

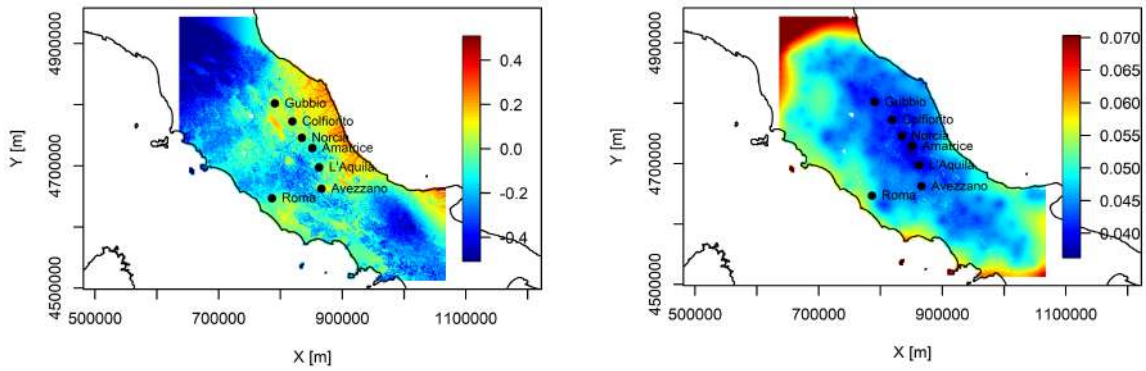

a) **b)**

Figure 1. Maps (coordinate system UTM zone N32) of the best δS2S model: median predictions (log10 units) (a) and associated variance (b) for PGA.

Acknowledgements

This work was partially supported by the Italian Ministry of University and Research (MIUR) in the framework of the project PRIN-SERENA, coordinated by Prof. Dario Albarello of the University of Siena and by the Centrum of Seismic Hazard (CPS, INGV) within the WP4 - Shaking Scenarios. The authors wish to thank the Working Group of Work Package 06 “Empirical Testing and Calibration” and their coordinator Giovanna Cultrera of INGV-Roma.

References

Anderson, J., Hough, S. (1984). *A model for the shape of the Fourier amplitude spectrum at high frequencies.* Bulletin of the Seismological Society of America. 74. 1969-1993.

Bard P. Y. Bora S. S. Hollender F. Laurendeau A., and Traversa P. (2020). *Are the standard Vs30-kappa host-to-target adjustments the only way to get consistent hard-rock ground motion prediction?* Pure Appl. Geophys. 177, 2049–2068.

Bergamo, P., C. Hammer, and D. Fäh (2021). *Correspondence between Site Amplification and Topographical, Geological Parameters: Collation of Data from Swiss and Japanese Stations, and Neural Networks-Based Prediction of Local Response*, Bull. Seismol. Soc. Am. 112, 1008–1030, doi: 10.1785/0120210225

Castellaro S. Mulargia F., and Rossi P. L. (2008). *Vs30: Proxy for seismic amplification?* Seismol. Res. Lett. 79, 540–543, doi: https://doi.org/10.1785/gssrl.79.4.540

Forte, G., Chioccarelli, E., De Falco, M., Cito, P., Santo, A., & Iervolino, I. (2019). *Seismic soil classification of Italy based on surface geology and shear-wave velocity measurements*. Soil Dynamics and Earthquake Engineering, 122, 79-93.

Kotha, S.R., Cotton, F., Bindi, D. (2018). *A New Approach to Site Classification: Mixed-effects Ground Motion Prediction Equation with Spectral Clustering of Site Amplification Functions*. Soil Dynamics and Earthquake Engineering. 10.1016/j.soildyn.2018.01.051.

Lanzano G, Felicetta C, Pacor F, Spallarossa D, Traversa P. (2022). *Generic-to-reference rocks scaling factors for seismic ground motion in Italy*. Bull Seismol Soc Am. https://doi.org/10.1785/0120210063.

Loviknes, K., Kotha, S. R., Cotton, F., Schorlemmer, D. (2021): *Testing Nonlinear Amplification Factors of Ground-Motion Models*. - Bulletin of the Seismological Society of America, 111, 4, 2121-2137.

Luzi, L., Puglia, R., Pacor, F., Gallipoli, M.R., Bindi, D., Mucciarelli, M. (2011). *Proposal for a soil classification based on parameters alternative or complementary to Vs,30*. Bulletin of Earthquake Engineering 9, no. 6, 1877-1898

Mascandola, C., Luzi, L., Felicetta, C., Pacor, F. (2021). *A GIS procedure for the topographic classification of Italy, according to the seismic code provisions*. Soil Dynamics and Earthquake Engineering. 148. 106848. 10.1016/j.soildyn.2021.106848.

Mori, F., Mendicelli, A., Moscatelli, M., Romagnoli, G., Peronace, E., & Naso, G. (2020). *A new Vs30 map for Italy based on the seismic microzonation dataset*. Engineering Geology, 275, 105745.

Sgobba S., Lanzano G. and Pacor F. (2021). *Empirical nonergodic shaking scenarios based on spatial correlation models: An application to central Italy*. *Earthq. Eng. and Struct. Dynam*., 50(1), 60-80. https://doi.org/10.1002/eqe.3362.

Sgobba S., Lanzano G., Colavitti L., Morasca P., D'Amico M. C., Spallarossa D. (2023). *Phyics-based parametrization of a FAS nonergodic ground motion model for Central Italy.* Bull. Earthq. Eng., 21, 4111-4137. https://doi.org/10.1007/s10518-023-01691-1.

Wald DJ, Allen TI (2007). *Topographic slope as a proxy for seismic site conditions and amplification*. Bulletin of the Seismological Society of America, 97(5), 1379-1395.

Corresponding author: sara.sgobba@ingv.it

GIS spatial modelling for seismic exposure assessment: a case study over Central Asia.

A. Tamaro, C. Scaini

National Institute of Oceanography and Applied Geophysics - OGS, Trieste, Italy

Introduction

Exposure assessment is of paramount importance in order to produce reliable risk estimates. However, there are many challenges associated with exposure assessment, in particular due to the lack of data on the spatial distribution of assets. Exposure analyses, in fact, identify the main exposed assets and their spatial location. In addition, it allows the assessment of the reconstruction costs for each asset.

Here, we present a methodology to assess exposed population and residential buildings based on a combination of regional-scale and national-scale data, and apply it to Central Asia. The adopted approach combines the most recent datasets and technologies, which allowed the development of high-resolution datasets (e.g., the Facebook high-resolution population grid, https://data.humdata.org/organization/facebook) and local-scale official data (e.g., population census). All collected data were harmonized in order to produce a regionally-consistent exposure database for Central Asia. The exposure database was developed during the project "*Regionally consistent risk assessment for earthquakes and floods and selective landslide scenario analysis for strengthening financial resilience and accelerating risk reduction in Central Asia*" funded by the European Community and implemented by the World Bank. The project saw the development of multiple exposure layers for the different exposed asset types identified in Central Asia:

- · population
- · residential buildings
- · non-residential buildings (schools, healthcare facilities, industrial and commercial buildings)
- · transportation system (roads, railways and bridges)
- · croplands
- A more detailed explanation of the methodology and the results obtained can be found in Scaini et al. (2023, a,b) In this short note we will only present the methods and results of the exposure model for the population and residential buildings, discussing the applicability of this method to other contexts.

Methodology

The methods adopted in this project allowed us to combine the available exposure data at different spatial resolutions (global, regional, national and sub-national) and produced under several past projects based on cutting-edge technologies. In particular, remote sensing data are very important in order to derive exposure datasets that allow covering large areas, but also allow to assess the location and specific characteristics of selected sites. These data were combined with local-scale information provided by local partners in each of the 5 Central Asia countries that enabled us to grasp the differences among the national contexts. The collected information was then homogenized in order to provide regionally-consistent aggregated results for the entire Central Asia region.

Exposure datasets are, by definition, spatial datasets, that is, digital maps where the exposure information is associated to spatial coordinates. In fact, the location of exposed assets (e.g., where different building types are located within a country) is required in order to perform the risk assessment. In absence of information on the asset location (e.g., address, coordinates), a common method to infer the buildings' or facilities' location is to distribute them spatially based on proxies such as population or land use maps. This operation, also called 'spatial disaggregation', and other spatial operations of the kind (e.g., merging of databases, intersection of different maps) were performed using the QGIS open-source program (https://www.qgis.org/en/site/).

Population

In this project, we developed a population dataset at 100m resolution that includes specific demographic attributes (age, gender) for the whole Central Asia. This dataset was based on data from several data sources, used as a starting point for the development of the exposure layers. In particular, the consortium used the Facebook high-resolution dataset (https://data.humdata.org/organization/facebook), which provides population, gender and age information at approximately 20 m in Central Asia. The Facebook population data, retrieved for 2020, was distinguished into three age classes: younger than 5 years old, older than 60 years old or the intermediate age class. The population layers were assembled as follows:

First, the total population in the Facebook dataset was compared with the WorldPop dataset (https://www.worldpop.org/), that provides total population (but no information on age and gender fractions) for 2020. The comparison was performed after aggregating the Facebook data at the resolution of the WorldPop layer (100 m) and showed a good agreement. This operation was performed directly on the spatial layers using the QGIS open-source program.

Second, population, age and gender data in the Facebook dataset was compared with national census data collected by local partners. Local partners retrieved the available population data from national sources, including population data by age and gender in each country and sub- national administrative units (Oblasts). The collected data were extracted from the latest available population census or equivalent data source (2021 for Uzbekistan, 2020 for Kazakhstan and Kyrgyz Republic, 2019 for Turkmenistan, and 2018 for Tajikistan).

Finally, for each Oblast, the Facebook base layer was corrected according to the recent national-scale data. This is done under the assumption that recent national census data is more reliable than global datasets. The difference was greater than 20% in 7 Oblasts of the 4 considered countries. In all regions, the 100-m population grid was corrected proportionally to the estimated difference with the national census data. The correction was performed also for a number of cities in Kyrgyz Republic, Kazakhstan and Turkmenistan, for which data were available. Gender and age percentages were also corrected based on the national data collected after 2019, when available from country-based data (table 1 only for Kazakhstan). The exception of the elder fraction (greater than 60 years old) was maintained from the Facebook population dataset because the data at national scale was only available for different age thresholds (e.g., 70 for Kyrgyz Republic and Uzbekistan, 63 for Kazakhstan).

Figure 1 shows a detail of the population exposure dataset provided by the high-resolution Facebook dataset and the grid developed at 100m resolution in this project (bottom) showing that it matches successfully the building's distribution in the aerial image (top).

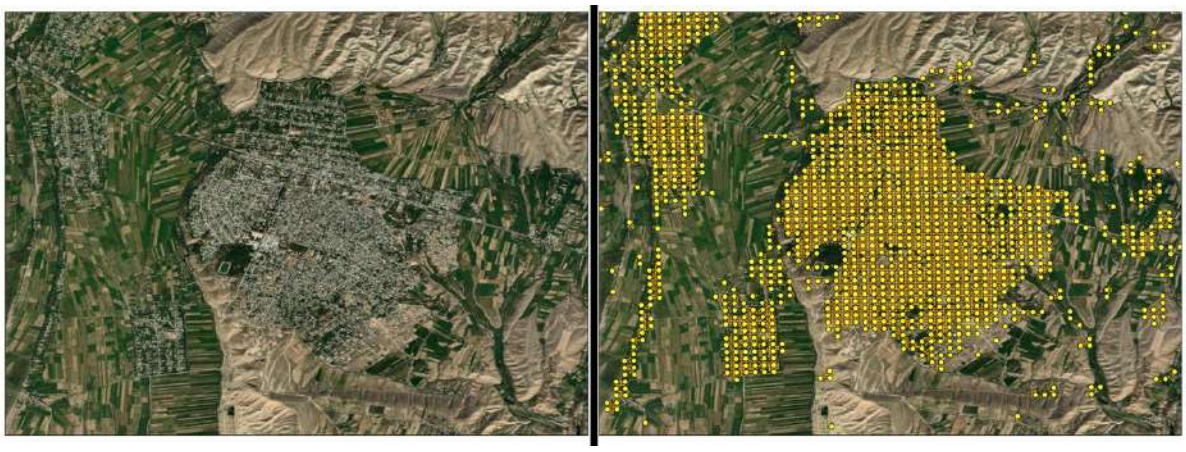

Fig. 1. Distribution of the buildings based on an aerial image in a village in Jalal-Abad Oblast, Kyrgyz Republic (top), (bottom) population grid at 20m (Facebook) and 100m resolution (orange and yellow dots respectively).

Country	Oblast	Total	Men	Women	>60 years old	<5 years old
Kazakhstan	Akmola	1.732.686	831.689	900.996	190.595	138.614

Aktobe	915.196	439.294	475.902	100.671	73.215
Almaty	2.440.375	1.171.380	1.268.995	268.441	195.230
Almaty (city)	1.437.016	689.767	747.248	158.071	112.961
Atyrau	653.678	318.765	339.912	71.904	52.294
East Kazakhstan	1.431.196	686.974	744.222	157.431	114.495
Jambyl	1.166.798	560.063	606.735	128.347	93.343
Karagandy	1.439.313	690.870	748.443	158.324	115.145
Kostanay	907.530	435.614	471.915	99.828	72.602
Kyzylorda	832.005	399.362	432.642	91.520	66.560
Mangystau	711.729	341.630	370.099	78.290	56.938
North Kazakhstan	786.807	377.667	409.140	86.548	62.944
Pavlodar	784.726	376.668	408.057	86.319	62.778
Shymkent (city)	1.038.152	500.439	537.713	78928	n.a.
Turkestan	3.084.568	1.480.593	1.603.975	339.302	246.765
West Kazakhstan	682.746	327.718	355.028	75.102	54.619
Total	19.006.369	9.123.054	9.883.309	2.090.693	1.520.503

Table 1. Population in each Oblast of Kazakhstan according to the Facebook layer and the national census. Total population and gender and age fractions in Kazakhstan country and for the whole region.

Residential buildings

The method adopted here for developing exposure maps of residential buildings consists of refining the exposure model of Pittore et al. (2020) by increasing its spatial resolution and by better characterizing the residential building typologies. The building typologies used in the exposure model of Pittore et al. (2020) were defined during the Earthquake Model Central Asia project (EMCA, http://www.emca-gem.org/) and will be referred to here as 'EMCA' typologies. Each typology and sub-typology is associated to a description and a taxonomy, which can also specify if the structure is designed to be Earthquake Resistant (ERD). The taxonomies are expressed based on the GEM building taxonomy (https://taxonomy.openquake.org/).

The spatial layer produced by Pittore et al. (2020) has a variable resolution ranging from a few hundred meters in urban areas to several km in rural areas. This layer was developed specifically for earthquake damage and risk assessment purposes, for which the spatial resolution was appropriate. However, in order to perform a risk assessment for fluvial and pluvial hazard, spatial resolution needs to be increased considerably. During this project, we increased the layer spatial resolution in order to produce a residential buildings exposure layer on a constant-resolution grid. Local partners collected and provided information on the number of buildings or households by Oblast or city and, when available, the number of buildings for each structural typology. For two countries, Kazakhstan and Uzbekistan, local partners provided the information about the number of households by Oblast and load-bearing material (which were associated to EMCA structural typologies). This information was used to update the spatial distribution of building typologies in each country of Central Asia based on national-scale data. The method for deriving the final residential buildings exposure layer has 4 main phases:

The original polygons from Pittore et al. (2020) were classified into urban and rural areas based on the urbanized areas mask provided by the GRUMP dataset (Center for International Earth Science Information Network - CIESIN, 2021, Figure 2a)

For each country and Oblast, the number of buildings in each typology (provided by local partners) was distributed into the urban and rural polygons identified in the previous step (Figure 2b). This method was applied to the countries where local data were available. Buildings were distributed based on the population in the buildings in each polygon (provided by Pittore et al., 2020). The fraction of different typologies in urban and rural areas of each Central Asia country was extracted from Wieland et al. (2015).

For each building type, the total number of buildings was distributed among the sub-typologies (EMCA) based on the relative fraction of each sub-typology in the Pittore et al. (2020) dataset. This operation was carried out for each polygon.

Finally, residential buildings in each polygon were distributed spatially based on the population layer developed for Central Asia at 100m resolution. This allowed increasing the resolution and obtaining an equally spaced grid of 100-m resolution (Figure 2c).

Figure 2 shows examples of the exposure development main steps for Eastern Uzbekistan. Figure 2a shows the urban and rural mask provided by the GRUMP dataset. Figure 2b shows an example of how data provided by locals for each country's Oblast (e.g., Navoi province, Tajikistan) are distributed on the existing variable-resolution grid. Figure 2c shows how the data are distributed on the population grid in order to reach higher resolution. The result of this procedure is an equally-spaced grid of 100m resolution with the number and type of buildings in each sub-typology (EMCA). Finally, the information was aggregated on a regular 500 m grid to better manage the spatial data. Information on exposed residential buildings is

therefore provided in aggregated format (i.e., a number of buildings are located on a point belonging to a constantly-spaced grid).

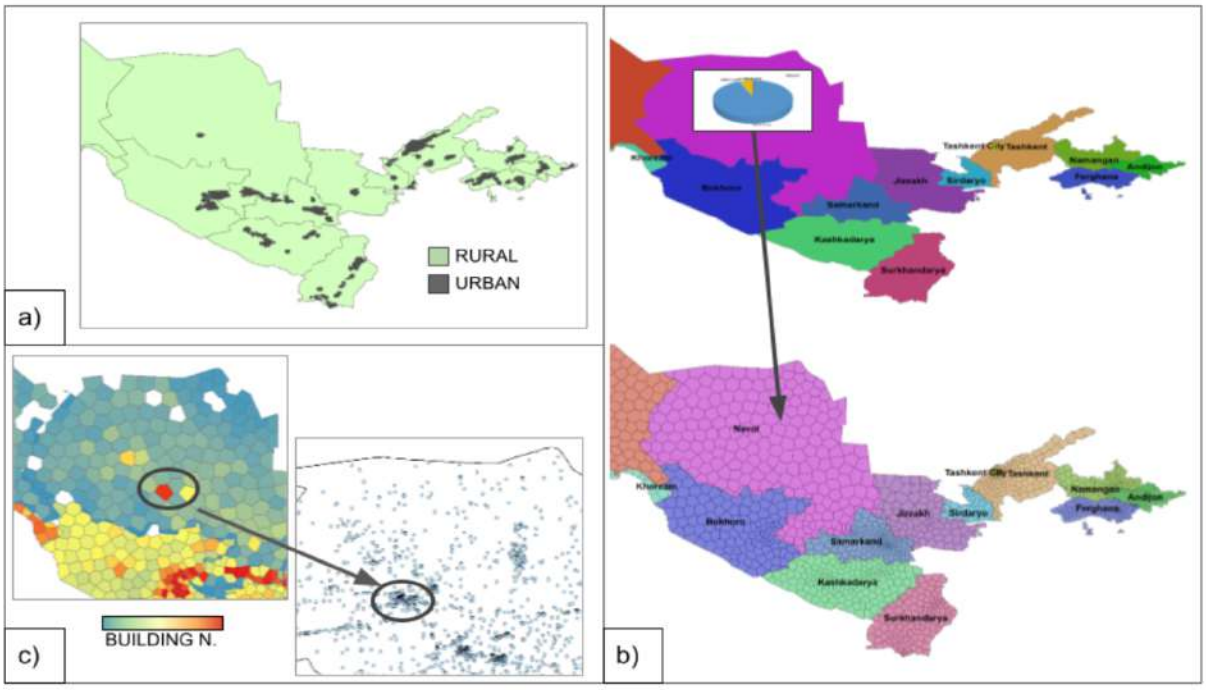

Fig. 2. a) Urban and rural mask provided by the GRUMP dataset, b) example of distribution of national and sub-national scale buildings data on the variable-resolution grid (Pittore et al., 2020), c) distribution of buildings data on the high-resolution Facebook population grid.

The building typologies were enriched with age information based on the characteristics extracted from past projects and from local partners' data. As for the storey number, similarly for the age of construction, a value was associated to each building typology based on the information provided with the EMCA macro typologies (see Wieland et al., 2015 for details) and on the data collected from past projects and/or provided by local partners.

Figure 3 (above) shows examples of images of residential buildings provided by local partners in the Kyrgyz Republic and Tajikistan (left and right columns) for typical precast panel buildings (a, b) and adobe buildings (d, e). These images contributed to the characterization of the building types and were used for the elaboration of the capacity building activities and especially for the training material. Figure 3 below shows the spatial distribution of one sub-typology of the EMCA1 typology, unreinforced masonry (URM). The map shows the spatial distribution of buildings in the entire Central Asia region (left) and for a selected study area (right) with a resolution of 500 metres. Similar maps can also be created for other building typologies.

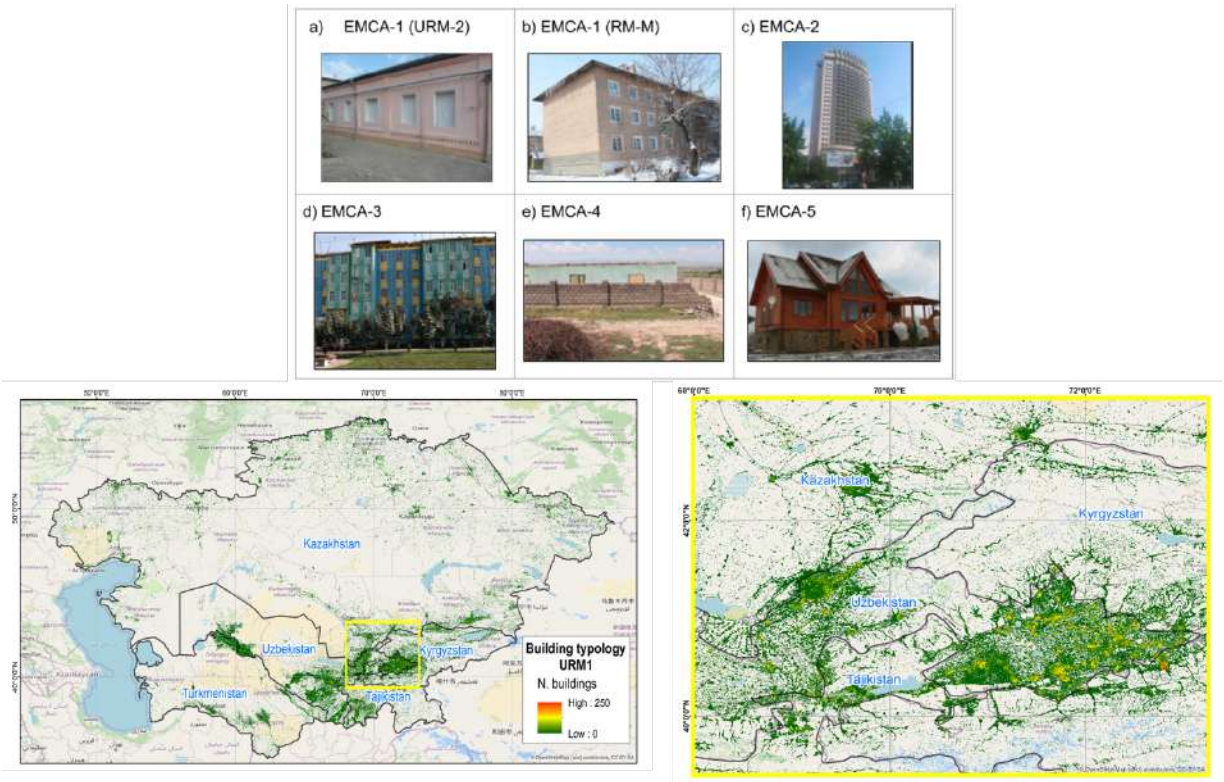

Fig. 3. Above examples of residential building images provided by local partners for selected EMCA typologies; in particular, two types of EMCA1 are shown (URM-2 and RM-M). typical precast panel buildings (a, b) and adobe buildings (d, e), which correspond to the EMCA3 and EMCA4 typologies, respectively. Below, examples of the number of buildings in each 500 m cell belonging to one sub-typology of EMCA1 (unreinforced masonry, URM1) in the entire Central Asian region (left) and in a selected area (right).

Reconstruction costs of residential buildings:

Past research projects provided an estimate of reconstruction costs for residential building typologies (Pittore et al., 2020) and other assets (Project 'Measuring Seismic Risk in Kyrgyz Republic', World Bank project P149630). Here, we updated the information with reconstruction costs retrieved by local partners for each country. Costs provided by local partners were compared with each country's GDP 2020 per capita, and across the different countries. In order to reduce discrepancies between country-specific costs, and to provide a regionally-consistent dataset of reconstruction costs. The final exposure layers contain, for each asset type, the average reconstruction cost for each country, converted from local currency to USD (Table 2). The residential buildings content cost can be estimated based on the procedure described in the HAZUS inventory technical manual (2021). The content cost is expressed as a percentage of the building structural cost, and is 50% for all residential building types.

Type EMCA	Material	Kazakhstan	Kyrgyz Republic	Tajikistan	Uzbekistan	Turkmenistan
EMCA 1	Unreinforced masonry (URM)	190	175	175	175	105
EMCA 2	Reinforced concrete frame (RC)	570	400	425	400	180
EMCA 3	Reinforced concrete precast (RCPC)	425	425	425	400	180
EMCA	Adobe	125	125	125	190	125
EMCA	Wood	330	330	177.5	300	648
EMCA	Steel	175	175	175	175	175

Table 2. Reconstruction unit costs (in 2021 USD/m²) defined in this project for each EMCA residential building typology in each Central Asia country.

Conclusion

This short note describes the exposure model (population and residential buildings) developed for Central Asia within the project "*Regionally consistent risk assessment for earthquakes and floods and selective landslide scenario analysis for strengthening financial resilience and accelerating risk reduction in Central Asia*".

The regional exposure database relies on the previous exposure assessments carried out in Central Asia. However, it introduces substantial improvements by including up-to-date local-scale data for each Central Asia country and by homogenizing these data into a single, regionally-consistent database. In particular, the exposure assessment allows to increase the spatial resolution of the previously existing exposure layers, comprise a large number of assets into a single and consistent regional dataset, and include exposure attributes that were not characterized prior to this project (e.g., country-based reconstruction costs).

Results of the exposure assessment show that the exposed assets in central Asia are distributed heterogeneously, with large differences between urban and rural areas. In particular, a large fraction of residential reconstruction costs is located in the main cities and urbanized areas. One of the challenges when developing such a comprehensive database is the difficulty of gathering data and combining different data sources together. The work presented here relies on the available global and regional-scale datasets, mostly provided by third-parties, which are paramount in order to collect exposure layers in a timely manner. To the extent possible, such data underwent specific validation procedures, made possible by

the use of national and sub-national data and remote sensing images. The global and regional-scale datasets were substantially improved also thanks to the large amount of country-based data provided by local partners. Such data were collected for each country in Central Asia as a result of an extensive effort, carried out in cooperation with the consortium partners in the region (See Peresan et al., 2023 for details). We are therefore thankful to all the working team for their contributions to the development of the exposure layers.

References

Peresan A., Scaini C., Tyagunov S., Ceresa P.; 2023: Capacity Building Experience for Disaster Risk Reduction in Central Asia. Natural hazard and Eart System Sciences. https://doi.org/10.5194/nhess-2023-156. Preprint. Discussion started: 6 September 2023.

Pittore M., Haas M. and Silva V.; 2020: Variable resolution probabilistic modeling of residential exposure and vulnerability for risk applications. Earthquake Spectra, 36(1_suppl), pp. 321–344. doi: 10.1177/8755293020951582.

Wieland M., Pittore M., Parolai S., Begaliev U., Yasunov P., Niyazov J., Tyagunov S., Moldobekov B., Saidiy S., Ilyasov I., Abakanov T.; 2015: Towards a cross-border exposure model for the Earthquake Model Central Asia. Ann. Geophys58.

Scaini C., Tamaro A., Adilkhan B., Sarzhanov S., Ismailov V., Umaraliev R., Safarov M., Belikov V., Karayev J., Faga E.; 2023a: A new regionally consistent exposure database for Central Asia: population and residential buildings. Natural hazard and Eart System Sciences.https://doi.org/10.5194/nhess-2023-94. Preprint. Discussion started: 19 June 2023.

Scaini C., Tamaro A., Adilkhan B., Sarzhanov S., Ismailov V., Umaraliev R., Safarov M., Belikov V., Karayev J., Faga E.; 2023b: A regional scale approach to assess non-residential buildings, transportation and croplands exposure in Central Asia. Natural hazard and Eart System Sciences. https://doi.org/10.5194/nhess-2023-95. Preprint. Discussion started: 21 June 2023.

Corresponding author: atamaro@ogs.it

A new service for the exchange of national and transboundary station information: *STATION* (*Seismic sTATion and amplificatION service*)

G. Tarchini[1], D. Spallarossa[1], D. Scafidi[1], S. Parolai[2], M. Picozzi[3], D. Bindi[4]

[1] *DISTAV, University of Genoa, Genoa, Italy*
[2] *Department of Mathematics, Informatics and Geosciences, University of Trieste, Trieste, Italy*
[3] *National Institute of Oceanography and Applied Geophysics – OGS, Udine, Italy*
[4] *Helmholtz Centre Potsdam, GFZ German Research Centre for Geosciences, Potsdam, Germany*

STATION (*Seismic sTATion and sIte amplificatiON* – https://distav.unige.it/rsni/station.php) is the prototype of a web interface and service for the exchange and dissemination of 'seismological' data related to seismic stations installed since 2005 on Italian territory and in cross-border areas that have recorded seismic events with local magnitude values greater than 1.8. By 'seismological data' we mean products from the processing of seismic signals that are useful for a 'seismic' characterisation of the station: for example, horizontal-to-vertical spectral ratios from noise and S phases as well as residuals of magnitude.
Processing is quasi-automatic based on *INGV* reference data. It consists of:

- the selection of data records within a radius of 120 km from the event;
- the automatic picking of P and S phases;
- the calculation of horizontal-to-vertical spectral ratios, average and NS and EW components separately, both for the S-wave phase and noise windows; and
- the calculation of station magnitude, and subsequently of the residual of magnitude.

Currently, the STATION database includes more than 2,200 seismic stations throughout the entire national territory and neighbouring states (Fig. 1) and was created by processing data of more than 15,000 seismic events and two million of waveforms. In this way, about four million values for magnitude residuals and horizontal-to-vertical curves were obtained.
For each station a dedicated webpage is available (Fig. 2), developed according to *FAIR* principles, through which it is possible to access general station information and seismological data. Each station webpage contains:

- an interactive map showing the station location;
- a table containing site name, station code, network, location, channel, link to station metadata, link to station data in the *Earthquake Strong Motion* (*ESM*) database, and the link to download a PDF summary document of the station;
- another table containing the number of S phases and noise time-windows analysed, magnitude and hypocentral distance ranges, start time and end time; and
- plots of noise spectra (mean) and horizontal-to-vertical spectral ratios – average and NS and EW components separately – for both the S-wave phase and noise windows.

There are many possible applications for this service. For example:

- STATION is the only seismological service that allows to view the map of all the stations installed on Italian territory and in the neighbouring regions (whether they are still operating or have been decommissioned, but whose data are in any case 'open');
- the database contains information on 559 seismic stations of the INGV national monitoring network (network code IV) and information on 753 stations of the monitoring network of the Italian Civil Protection Department (network code IT);
- the stations of many temporary networks are also included (*e.g.*, *'AlpArray'* (network code Z3) and '*Centro di microzonazione sismica Network, 2016 Central Italy seismic sequence*' (network code 3A));
- in the event of a seismic 'crisis', the available services could be effectively used both to define the characteristics of a temporary monitoring network and to support microzonation activities.
-

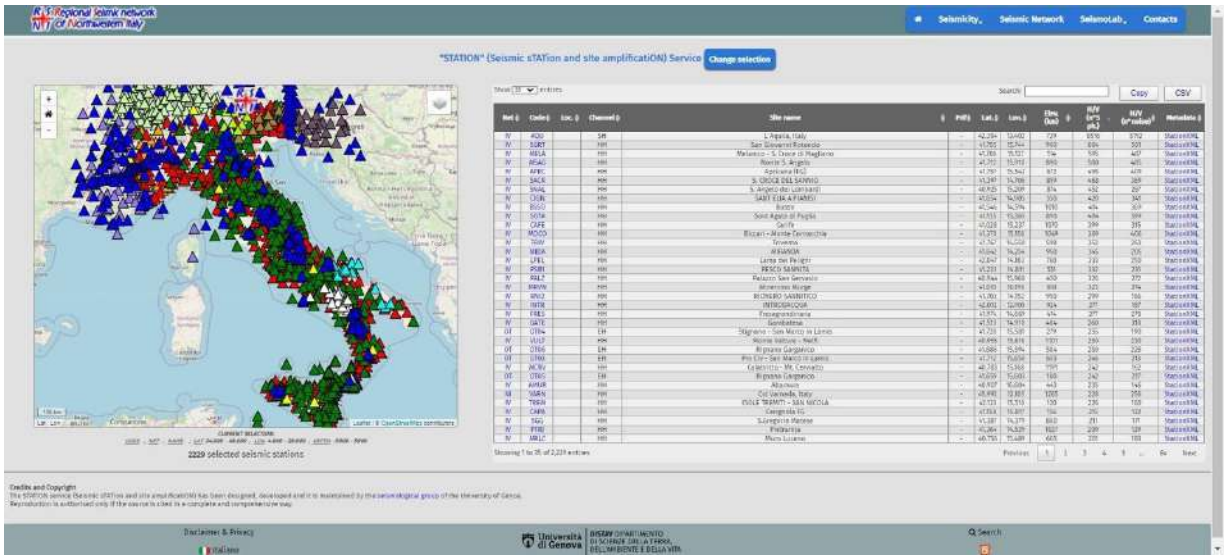

Fig. 1 – STATION main webpage.

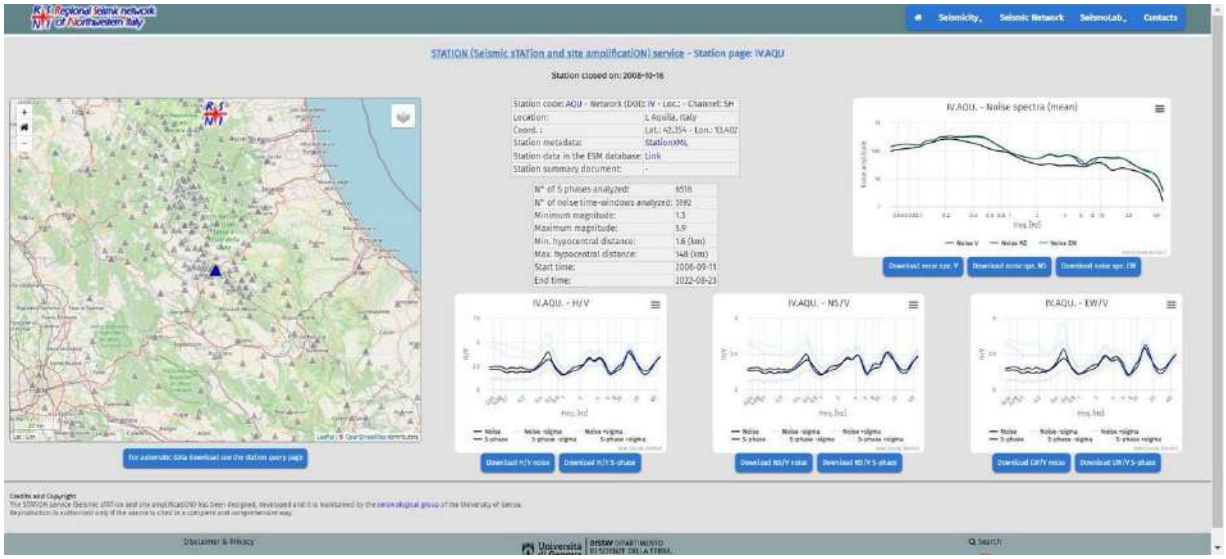

Fig. 2 – Example of specific webpage for the station IV.AQU.

Corresponding author: Gabriele Tarchini – gabriele.tarchini@edu.unige.it

SDQ: a new tool for the evaluation of seismic-accelerometric data quality

F. Varchetta[1], M. Massa[1], R. Puglia[1], P. Danececk[2], S. Rao[2], A. Mandiello[2], D. Piccinini[3]

[1] INGV, sezione di Milano, Italia

[2] INGV, ONT, Osservatorio Nazionale Terremoti, Roma, Italia

[3] INGV, sezione di PISA, Italia

Abstract

In recent years, many works have focused their attention on the issue of data processing and verification procedures, in particular of strong-motion data because of their fundamental role in the case of strong earthquakes At the national level in Italy, there are currently two web portals available for checking seismic data quality: EIDA Italia (https://eida.ingv.it/it/getdata) and ISMDq (http://ismd.mi.ingv.it/quality.php). The EIDA Italia (Danecek et al., 2021) employs the data quality tools directly from the ORFEUS website (http://www.orfeus-eu.org/data/eida/quality/), while ISMDq (Massa et al., 2022) is a recent system for dynamic quality check both of continuous data stream and earthquake data.

In this work, we introduce the SDQ (Seismic Data Quality) project, a new open-source Python tool freely available and downloadable. It is designed for the automatic monitoring of sismo-accelerometric stations by analyzing both events - selected based on magnitude and distance - and continuous data streams.

Regarding earthquake data, the quality of individual waveforms is assessed by comparing the ground motion parameters derived from co-located accelerometers and velocimeters. SDQ operates by utilizing a simple external input file containing the INGV event identifier, station, and network codes. SDQ is organized into three main phases: acquisition, pre-processing, and processing. In the acquisition phase, event information, station metadata, and waveforms are downloaded from FDSN (https://www.fdsn.org/) web services (https://www.fdsn.org/webservices/). Initially, the waveforms are analyzed to identify event and pre-event noise windows. Then, the data are converted into physical units, accounting for pre-filter parameters and exclusion conditions. Finally, each single waveform is assigned to a quality class ranging from A (excellent) to D (data to be rejected) based on time- and frequency-dependent algorithms. Thresholds for classification were empirically obtained by combining visual signal inspection and statistical analysis. Tests were performed considering about 15,000 waveforms in the time interval from January 2012 to June 2023, encompassing all 6-channel stations of the IV (National Seismic Networks (https://www.fdsn.org/networks/detail/IV/)) and MN (MedNet network, https://www.fdsn.org/networks/detail/MN/), both managed by the Italian National Institute for Geophysics and Volcanology (INGV, https://www.ingv.it/).

Concerning continuous ambient noise data streams, 24-hour mini-seed recording signals are analyzed at each selected station to set empirical thresholds considering data metrics and data availability. The goal is to build a station-quality archive.
Users can select and build the time history for each network, station, stream data type, and single ground motion component related to selected input data included in a local mini-seed data archive representing the starting point of the procedure.
Data metrics are evaluated considering RMS (Root Mean Square, Bormann, 2012) and PSD (Power Spectral Density, Bormann, 2012) in several frequency intervals (i.e., 0.01-0.1; 0.1-1; 1-5; 5-10; 10-20; 20:50 Hz).
For availability, the graphs show the results in terms of daily %gap, maximum daily availability, sum of the time gaps, and maximum duration of the maximum daily gap. Daily results are represented by static images related to the 24 hours of the data selected at each target station. Daily results include the PDF (Probability Density Function, McNamara and Buland, 2004), the frequency-dependent PSD, the comparison between RMS and PSD variations, time histories, and spectrograms. SDQ provides final summary tables for both earthquake and continuous data, collecting all relevant parameters for each processed waveform and data stream, along with explanatory text files (log and warning files), allowing the user to better evaluate the results.
Although SDQ is currently under development, the release presented and discussed in this work is uploaded to the INGV GitLab platform and is available at: https://gitlab.rm.ingv.it/EIDA/quality/sdq.

References

Bormann P.; 2012: New manual of seismological observatory practice (NMSOP-2). IASPEI, GFZ Ger. Research Centre for Geosciences.

Danecek P., Pintore S., Mazza S., Mandiello A., Fares M., Carluccio I., ... & Michelini A.; 2021. The Italian node of the European integrated data archive. *Seismological Research Letters*, *92*(3), 1726-1737.

Massa M., Scafidi D., Mascandola C., & Lorenzetti A.; 2022: Introducing ISMDq - A web portal for real-time quality monitoring of italian strong-motion data. *Seismological Research Letters*, *93*(1), 241-256.

McNamara D. E., and R. P. Buland; 2004: Ambient noise levels in the continental United States, Bull. Seismol. Soc. Am. 94, no. 4, 1517–1527.

Varchetta F., Massa M., Puglia R., Danecek P., Rao S., Mandiello A., Piccinini D.; 2023: SDQ: a python-based open-source to improving data quality check of the INGV Italian Seismic Network, *Rapporti Tecnici INGV* (in revisione).

Corresponding author: fabio.varchetta@ingv.it

Machine Learning-based modelling for Near Real-Time prediction of liquefaction

C. Varone[1], F. Mori[1], A. Mendicelli[1], G. Ciotoli[1], G. Acunzo[2], G. Naso[3], M. Moscatelli[1]

[1] *CNR Italian National Research Council, Institute of Environmental Geology and Geoengineering (IGAG), Montelibretti, Italy*
[2] *Theta Group Srls, Rome, Italy*
[3] *Presidenza del Consiglio dei Ministri, Dipartimento della Protezione Civile (DPC), Rome, Italy*

The occurrence of an earthquake may involve extensive consequences, highlighting the critical requirement from prompt and reliable information to minimize the effects of the disaster. The rapid execution of emergency response strategies also depends on the accurate prediction of seismically induced effects. This study aims to develop an approach based on machine learning to predict seismically induced liquefaction phenomena in near real-time. This method combines factors such as ground shaking scenarios (Magnitude and Peak Ground Acceleration PGA), shear-waves velocity to a depth of 30 meters (Vs30), and groundwater table depth to predict the likelihood of liquefaction phenomena. The implementation is planned within the SEARCH (Seismic Emergency Assessment and Response Computing Hub) software, which is an innovative solution able to generate impedance maps for landslides, liquefaction, and building collapses. These maps provide valuable assistance for emergency management.

Corresponding author: chiara.varone@cnr.it

Session 2.3

Risk Communication

GNGTS 2024

DISASTER RISK ANALYSIS AND REDUCTION

Session 2.3

Risk Communication

Convenors of the session:
***Serena Tagliacozzo (IRPPS, CNR)* – serena.tagliacozzo@irpps.cnr.it**
***Valentina Rizzoli (CORIS, Sapienza University of Rome)* – valentina.rizzoli@uniroma1.it**

Interventions can address – but are not limited to – the following areas and topics:

- **Information and communication technologies for risk and crisis communication (e.g., social media, citizen sensors)**
- **Relationship between risk perception and communication**
- **Risk communication and behavioural change**
- **Multi-hazard risk communication**
- **Risk communication for disaster prevention, preparedness, response, and recovery**
- **Targeted risk communication (i.e., involving diverse groups such as vulnerable populations, young people, and gender-sensitive communication)**
- **Risk education**
- **Ethics in risk communication.**

Risk and crisis communication is an essential component for disaster risk prevention and management and, to be effective, it requires multidisciplinary and multi-actors efforts. Risk communication should therefore be implemented in all the phases of the disaster cycle (e.g. prevention, preparedness, response and recovery). This session welcomes contributions from researchers and practitioners working on different research streams and hazards from a multi-hazard risk perspective. Relevant topics include -but are not limited to – opportunities offered by information and communication technologies for tailoring the message to the specific needs of diverse groups and sub-populations; social media and social construction of risk; the role of risk education in communication; drivers of risk perception and behavioural change.

Towards the IT-ALERT implementation. Early warning and cell-broadcast systems in the context of risk and crisis communication

L. Cugliari[1,2], A. Amato[1], A. Cerase[2], F. Comunello[2], M. Crescimbene[1]

[1] Istituto Nazionale di Geofisica e Vulcanologia, 00153, Roma, Italia

[2] Università di Roma La Sapienza, dipartimento di Comunicazione e Ricerca Sociale, 00198, Roma, Italia

Introduction

Communication is one of the most effective - and at the same time complex - processes to mitigate risks to the population. Indeed, it allows protecting the safety of citizens in peacetime: following an ongoing process (Coombs, 2007; Palttala & Vos, 2012) that, through the timely activation of relational practices and (in)formative processes involves institutions, citizenship, and the media (Zimmerman, 1987; Johnson, 1999; Comunello, 2014; Cerase, 2017; Comunello and Mulargia, 2017; Renn, 2020; Rafliana et al., 2022) or-as in the specific case study-a few minutes or seconds before a damaging event hits the population (WMO, 2022).

Technological progress has actually transformed the communication of anthropogenic and natural hazards. This has engaged institutions, and still requires them energy and effort, to identify the "communicative optimum" time after time, trying to identify the best strategies to disseminate information including through Social Network Sites (SNS) (Stieglitz & Dang-Xuan, 2013; Alexander, 2014). In this framework, driven by the widespread use of mobile devices, the United Nations Foundation (2010) argues that: "if communities, to survive in times of crisis, depend on information, then communication technologies constitute their lifelines."

The online environments activate seamless communicative dynamics (Baym, 2015) that engage citizens in an active role in terms of demands towards risk management institutions (Kasperson & Kasperson, 2012). The direct, two-way exchange, in which SNS and platforms are seen as discussion environments, has required further adaptation of communication modalities both on the part of the institutions responsible for risk communication and from the point of view of scientists, researchers, local managers, and stakeholders dealing - at various levels - with risks, in order to respond clearly, punctually, quickly, and, possibly, by personalizing the response, for citizens who in an "always on" (Baron, 2008) perspective become "prosumers" of information and knowledge.

As for risk communication, citizens, driven by growing information needs in peacetime as well as in crises, rely on the information and answers they find on the web (verified or not). In our case,

these needs are mainly to be found in the spheres of cognitive needs, to obtain information about risks independently, and of integrative personality needs to search for post-emergency information should they be involved in a disaster event (Wachinger et al., 2013). In this case, one of the strengths that enabled the self-information of online environments to reach the general public sooner also concerns regulatory management.

While the early warning broadcast systems provide for centralized management with a strong normative and accountability component - as well as relevant technological systems managed by experts in the field - (Valbonesi et al, 2019,2021) the internet is not jurisdictional with regard to the sharing of communicative content except from the point of view of data protection, and mild regulations exercised by private individuals operating SNSs, it is multi-modal and the communication that takes place in it is self-generated in terms of content, self-directed in terms of emission mechanisms, and self-selected in terms of reception.

The Early Warning System for Natural Hazards

Early warning systems (EWS) are part of the risk communication framework. According to the 2006 report of the United Nations General Office for Disaster Risk Reduction (UNDRR), communication is one of the four components of an EWS together with risk knowledge, monitoring, warning and message dissemination.

In 2017, the UNDRR defines an early warning system as *"An integrated system of hazard monitoring, forecasting and prediction, disaster risk assessment, communication and preparedness activities systems and processes that enables individuals, communities, governments, businesses and others to take timely action to reduce disaster risks in advance of hazardous events".* The provided definition actually follows point-by-point the alert process, which needs specific instruments and expert human resources to be issued.

For this study proposal, rather than the systems and protocols for sending/receiving the message, I will focus on the socio-demographic, gender, cultural and livelihood aspects of the recipients, in order to better target users' actions according to the alert and facilitate the operations of emergency managers.

For this I started from a preliminary survey conducted in New Zealand by J. Becker et al. where, as of 2020 - the year of the study - an early warning system for earthquakes had not yet been implemented. Becker's team, in that context, conducted a survey of the public's acceptability, attitudes and perceptions regarding the development and reception of earthquake early warnings, before the government decided to invest money in the technology. The interviewees in that case expressed a positive opinion about the system, suggesting some substantial information regarding, for example, the warning threshold, the actions they would take within a few seconds before they felt the earthquake and those they would take within a few minutes before the tremor started. An applicable and replicable methodology, useful to produce relevant and directly usable information for risk mitigation institutions.

Cell-broadcast warning systems and IT-ALERT as case studies

To date, broadcast technology represents the most stable and reliable communication channel even in emergency situations. The broadcast communication flow actually involves: the signal source through which the process begins, the modulation or transformation of the signal into a transferable format, the transmission through a medium that carries the signal, the reception by devices in the network and capable of receiving the specific signal, the demodulation or decoding that allows the signal to acquire its original format again, and the reproduction or display of the initial message. Widely used and recognised throughout the world, broadcast technology recognises and supports the C.A.P. (Common Alerting Protocol), which is an international standard initially used in the military field and now adapted to the communication of emergency alerts and alarms. Among the strengths of the C.A.P. protocol is firstly the interoperability that allows the same message to be decoded by different devices and platforms, and secondly the simplicity and, if desired, schematic nature of the message. European Directive 2018/1972 of 11 December 2018 establishes the European Electronic Communications Code (EECC). Article 110 of the EECC makes it mandatory that as of 21 June 2022, when public warning systems are in place, "in the event of imminent or ongoing major emergencies and disasters, providers of mobile interpersonal communication services, based on the mobile phone number, shall transmit public alerts to the end users concerned". The legislation is not mandatory regarding the setting up of public warning systems, although it regulates the character of the warning.

In Italy, to date, no official channels are in place to issue rapid emergency information. There are also several apps made by third-party developers that, with different application interfaces and in different contexts, have been adopted by various municipalities. The Italian Presidency of the Council of Ministers, with the directive of 7 February 2023, decides the experimentation, on the Italian territory, of the IT-Alert public alert system with reference to the Civil Protection activities in order to conform the alerting procedures to the above-mentioned European regulations (G.U. Serie Generale n.91 of 18-04-2023).

The IT-Alert system, which is now operational, will directly inform the population at risk by sending an information message to geographically located mobile phones. Users, in order to receive the message, will need to have their mobile phone and - for now - the public alert messaging service, in the mobile phone's settings, active.

Below are some preliminary percentage frequencies extracted from the questionnaire administration test on 13.12.23 at the Information Engineering Faculty of the Università Politecnica delle Marche. 114 questionnaires were collected for the test. For this specific research, an ad-hoc section was added to the questionnaire developed by Backer et al. in New Zealand to survey some of the respondents' opinions about IT-ALERT.

- 86% of the respondents know IT-ALERT, 14% are not.
- 71% received the system test message, 29% did not.

- More than 50% of the respondents affirmed that one test was not enough to be clear about how IT-ALERT works.
- About 80% of the respondents wouldn't feel anxiety if they received an alert message sent by the IT-ALERT system.
- Most respondents knew IT-ALERT through social media or through the Civil Protection's testing of the system.

References:

Alexander, D. E. (2014). Social media in disaster risk reduction and crisis management. Science and engineering ethics, 20, 717-733.

Baron, N. S. (2008). Always on: Language in an online and mobile world. Oxford University Press. http://dx.doi.org/10.1093/acprof:oso/9780195313055.001.0001

Baym, N. K. (2015). Personal connections in the digital age. John Wiley & Sons. ISBN: 978-0-745-67033-1

Becker, J. S., Potter, S. H., Vinnell, L. J., Nakayachi, K., McBride, S. K., & Johnston, D. M. (2020). Earthquake early warning in Aotearoa New Zealand: A survey of public perspectives to guide warning system development. Humanities and Social Sciences Communications, 7(1), 1-12. https://doi.org/10.1057/s41599-020-00613-9

Cerase, A. (2017). Rischio e comunicazione Teorie, modelli, problemi. Rischio e comunicazione Teorie, modelli, problemi, 1-290.

Comunello, F. (ed.) (2014). Social media e comunicazione d'emergenza, Guerini e Associati, Milano.

Comunello, F., Mulargia, S. (2017). Tra risposte protocollate e «social sensing». L'uso dei social media per la comunicazione d'emergenza nelle istituzioni locali italiane in "SOCIOLOGIA E RICERCA SOCIALE " 112/2017, pp 111-137, DOI: 10.3280/SR2017-112006

Coombs, W. (2007). Protecting Organization Reputations During a Crisis: The Development and Application of Situational Crisis Communication Theory. Corp Reputation Rev 10, 163–176. https://doi.org/10.1057/palgrave.crr.1550049

G.U. Serie Generale, Anno 164° n.91 del 18-04-2023 http://www.gazzettaufficiale.it/eli/gu/2023/04/18/91/sg/pdf

Johnson, B. B. (1999). Ethical issues in risk communication: Continuing the discussion. Risk analysis, 19, 335-348. https://doi.org/10.1023/A:1007084108903

Kasperson, R. E., & Kasperson, J. (2012). Social contours of risk: Volume I: Publics, risk communication and the social. Routledge. ISBN 978184407073

Palttala, P., & Vos, M. (2012). Quality indicators for crisis communication to support emergency management by public authorities. Journal of Contingencies and Crisis Management, 20(1), 39-51. https://doi.org/10.1111/j.1468-5973.2011.00654.x

Rafliana, I., Jalayer, F., Cerase, A., Cugliari, L., Baiguera, M., Salmanidou, D., ... & Hancilar, U. (2022). Tsunami risk communication and management: Contemporary gaps and challenges. International Journal of Disaster Risk Reduction, 70, 102771. https://doi.org/10.1016/j.ijdrr.2021.102771

Renn, O. (2020). Risk communication: Insights and requirements for designing successful communication programs on health and environmental hazards. In Handbook of risk and crisis communication (pp. 80-98). Routledge.

Stieglitz, S., & Dang-Xuan, L. (2013). Social media and political communication: a social media analytics framework. Social network analysis and mining, 3, 1277-1291.

UNDRR (United Nations for Disaster Risk Reduction). (2006). Developing early warning systems: from concept to action. A checklist. Third international conference on early warning, United Nations (UN), Bonn, Germany. https://www.undrr.org/quick/10879 accessed 21 August 2023

UNDRR (United Nations International Strategy for Disaster Reduction). (2015). Sendai framework for disaster risk reduction 2015–2030. A/CONF.224/CRP.1. Geneva, Switzerland. https://www.undrr.org/quick/11409

United Nations Foundation (2010). New technologies in emergencies and conflicts report: The role of information and social networks (New York: United Nations Foundation, 2010).

Valbonesi, C., Amato, A., & Cerase, A. (2019). The INGV Tsunami Alert Centre: analysis of the responsibility profiles, procedures and risk communication issues. Bollettino di Geofisica Teorica ed Applicata. https://doi.org/10.4430/bgta0252

Valbonesi, C. (2021). Between necessity and legal responsibility: the development of EEWS in Italy and its international framework. Frontiers in Earth Science, 9, 685153. https://doi.org/10.3389/feart.2021.685153

Wachinger, G., Renn, O., Begg, C., & Kuhlicke, C. (2013). The risk perception paradox—implications for governance and communication of natural hazards. Risk analysis, 33(6), 1049-1065.

WMO (World Meteorological Organization) (2022). Early Warning and Anticipatory Action. In Bulletin Vol. 71 (1). http://public.wmo.int/en/resources/bulletin accessed 14 Dec 2023

Zimmerman, R. (1987). A process framework for risk communication. Science, Technology, & Human Values, 12(3/4), 131-137. http://www.jstor.org/stable/689393

Corresponding Author: lorenzo.cugliari@uniroma1.it

Tsunami Ready: some steps for a people-centred tsunami risk approach

L. Cugliari[1,2], A. Amato[1], C. Valbonesi[1,3], I. Moreschini[1], F. Romano[1], L. Graziani, S. Filosa[1], M. Crescimbene[1], F. La Longa[1]

[1] Istituto Nazionale di Geofisica e Vulcanologia, 00153, Roma, Italia

[2] Università di Roma La Sapienza, dipartimento di Comunicazione e Ricerca Sociale, 00198, Roma, Italia

[3] Università degli Studi di Roma UNITELMA Sapienza, 00185, Roma

Abstract

The Tsunami Ready (TR) programme, developed in the United States of America by the US National Weather Service (NWS) and the National Ocean and Atmospheric Administration (NOAA), is aimed at ensuring greater tsunami risk awareness and more effective tsunami risk management by coastal communities, which are called to take an active role in the definition and implementation of life-saving measures. The UNESCO International Oceanographic Commission, assuming the programme as one of its main objectives, has developed international and standard guidelines for the accreditation of individual municipalities wishing to be declared “Tsunami Ready”. The guidelines, based on decades of experience in protecting coastal communities from tsunami risk, have been tested in various tsunami-prone regions around the world (UNESCO, 2022). The Tsunami Ready programme has been identified as a priority in the framework of the Ocean Decade for Sustainable Development, established by the United Nations for the period 2021-2030 (Franke et al., 2023).

A detailed, universally applicable - and traceable - grid consisting of three thematic sections and 12 indicators underpins this approach.

	TSUNAMI READY INDICATORS
I	**ASSESSMENT (ASSESS)**
1	**ASSESS-1**. Tsunami hazard zones are mapped and designated.
2	**ASSESS-2**. The number of people at risk in the tsunami hazard zone is estimated.
3	**ASSESS-3**. Economic, infrastructural, political, and social resources are identified.
II	**PREPAREDNESS (PREP)**
4	**PREP-1**. Easily understood tsunami evacuation maps are approved.
5	**PREP-2**. Tsunami information including signage is publicly displayed.
6	**PREP-3**. Outreach and public awareness and education resources are available and distributed.
7	**PREP-4**. Outreach or educational activities are held at least 3 times a year.
8	**PREP-5**: A community tsunami exercise is conducted at least every two years.
III	**RESPONSE (RESP)**
9	**RESP-1**. A community tsunami emergency response plan is approved.
10	**RESP-2**. The capacity to manage emergency response operations during a tsunami is in place.
11	**RESP-3**. Redundant and reliable means to timely receive 24-hour official tsunami alerts are in place.
12	**RESP-4**. Redundant and reliable means to timely disseminate 24-hour official tsunami alerts to the public are in place.

Table 1: Tsunami Ready programme indicators

Among the strengths of the programme is the voluntary, performance-based community recognition to promote prevention and preparedness through the active collaboration of national and local civil protection agencies, land management authorities, scientists and citizens. Therefore, Tsunami Ready can be considered in a mixed-methods framework. Besides a methodology based on standard indicators, there is an underlying qualitative approach that promotes interaction and participation between the various parties involved at various levels. These principles are embedded both between the SDGs of the UN 2030 agenda and Sendai Framework for Disaster Risk Reduction to “Make cities and human settlements inclusive, safe, resilient and sustainable” and to highlight the need to invest in, develop, maintain and enhance multi-hazard, multi-sectoral early warning and forecasting systems (UNISDR, 2018). Such systems should be user-oriented, adopting a participatory, people-centred approach, and include effective risk communication mechanisms in disaster and emergency situations. In table below we condensed the strengths and criticalities emerged from the application (described below).

Strenghts	Problems/Criticalities
A clear strategy with a finite number of objectives (12)	Careful definition of the inundation areas (need for detailed DTM and local scale modeling)
The international (IOC-UNESCO) framework limits the sphere of possible liability of local authorities and collaborators /scientists	Bureaucracy (Mayor’s election, complex purchase procedures, …)
Inducement to risk education for young citizens (schools)	Funding (specific resources not available, must be allocated)

Strenghts	Problems/Criticalities
Inducement to formation and information for the population, including the attitude towards a self protective approach	Competition with other more frequent hazards (floods, storms, fires, earthquakes) and local problems (traffic, streets conditions, seaside facilities management, …)
Motivation for a multi-risk approach	Difficulty in spreading TR to tens/hundreds coastal localities without a continuous support by scientific and CP experts (reaching the Ocean Decade target of 100% within 2030)

Table 2: strengths and weaknesses for the Tsunami Ready programme

In Italy, the Tsunami Ready initiative was launched in 2020-2021 with the establishment of the National Committee (composed by the National Department of Civil Protection, ISPRA and INGV) and the identification of three pilot coastal municipalities (Valbonesi, 2022).

The first three coastal municipalities to join the Tsunami Ready programme are: Minturno, in southern Latium, Palmi in Calabria and Pachino/Marzamemi in Sicily. In 2023, the Municipality of Otranto (LE) in Apulia also joined the programme. We are currently waiting for the municipal resolution of the municipality of Lipari (ME), which will join the programme with Stromboli Island.

The Italian coastal municipalities that joined the program are located in different areas of the peninsula, these areas also differ among themselves in I) tsunami hazard II) urban and environmental context III) socio-demographic composition.

Municipalities involved in achieving recognition have enthusiastically embraced the initiative and are moving forward, even if at different speeds, point by point through the grid indicators. Below we provide a summary map with some photographic and detailed elements for the initiatives that, to date, have actively involved the population (at various levels) in the pilot sites (Amato et al., 2023).

Italian National Tsunami Ready Board: Dec 15, 2023

A- Minturno, Latium, Pop. 19,700 Medium-Low Hazard Local TR Board: 03/2021

B- Palmi, Calabria, Pop. 17,000, Medium-High Hazard, Local TR Board: 12/2020

C- Marzamemi-Pachino, Sicily, Pop. 376 / 21,000, Ionian - High Hazard, Local TR Board: 04/2021

D- Otranto, Apulia, Pop. 5,769, Adriatic - High Hazard, In progress (2023)

E- Stromboli volcano, Tyrrhenian sea, Pop. 450 / n,000 (summer), High Hazard , In progress (2023)

References:

Amato, A., Valbonesi, C., Cugliari, L., Graziani, L., & Romano, F. (2023). Tsunami Ready in Italy: towards the UNESCO recognition (No. EGU23-15864). Copernicus Meetings.

Franke, A., Peters, K., Hinkel, J., Hornidge, A. K., Schlüter, A., Zielinski, O., ... & Hillebrand, H. (2023). Making the UN Ocean Decade work? The potential for, and challenges of, transdisciplinary research and real-world laboratories for building towards ocean solutions. People and Nature, 5(1), 21-33. https://doi.org/10.1002/pan3.10412

UNESCO (2022). Standard guidelines for the Tsunami Ready Recognition Programme. IOC/2022/MG/74. https://unesdoc.unesco.org/ark:/48223/pf0000381353

UNISDR United Nations Office for Disaster Risk Reduction (2018). Global Capacity Development Strategy to Support Implementation of the Sendai Framework for Disaster Risk Reduction, 23 February 2018, https://www.preventionweb.net/files/56922_sfdrrcdstrategyzerodraft20180223.pdf

Valbonesi, C. (2022, May). Tsunami Ready Programme in NEAM region: strategies, responsibilities and further advancements to protect communities from tsunamis. In EGU General Assembly Conference Abstracts (pp. EGU22-11876).

Corresponding Author: lorenzo.cugliari@ingv.it

“A Scuola di Terremoto”: a targeted risk education project in Calabria (South Italy) to promote behavioural change

E. Ercolani[1], R. Camassi[1], V. Pessina[2], F. Brasini[3], P. Del Gaudio[4], A. Giambattista[1], M. Lopez[1]

1 Istituto Nazionale di Geofisica e Vulcanologia – INGV, Bologna, Italy
2 Istituto Nazionale di Geofisica e Vulcanologia – INGV, Milano, Italy
3 CUG | Con Un Gioco, Cooperativa sociale, Roma, Italy
4 Istituto Nazionale di Geofisica e Vulcanologia – INGV, Rende (CZ), Italy

1. The project “A Scuola di Terremoto”

“A Scuola di Terremoto” (“At Earthquake School", in the following ASdT) is a seismic risk education project addressed to secondary schools and aimed at offering both educational training for teachers and activities with students in the classroom. The goal is to motivate, deepen, and consolidate knowledge throughout an occasion of “discovery”, where reflection and engagement can lead to a better understanding of the concept of earthquakes.

Based on more than 20 years of experience within Edurisk (www.edurisk.it), we designed the ASdT project to raise awareness among teachers and their students about seismic risk and the possible consequences of an earthquake, and to create a network of shared experiences throughout schools in the region.

The project started in February 2022 and continued and refined in the following year. The data presented here refer to the status of the project at the end of the 2022-2023 school year. The activity is currently underway for the 2023-2024 school year, with well-established methods and activities (Fig.1). The project was promoted by the Calabria Region, which is well aware of seismic hazard and the high level of risk in its territory (Camassi, 2008).

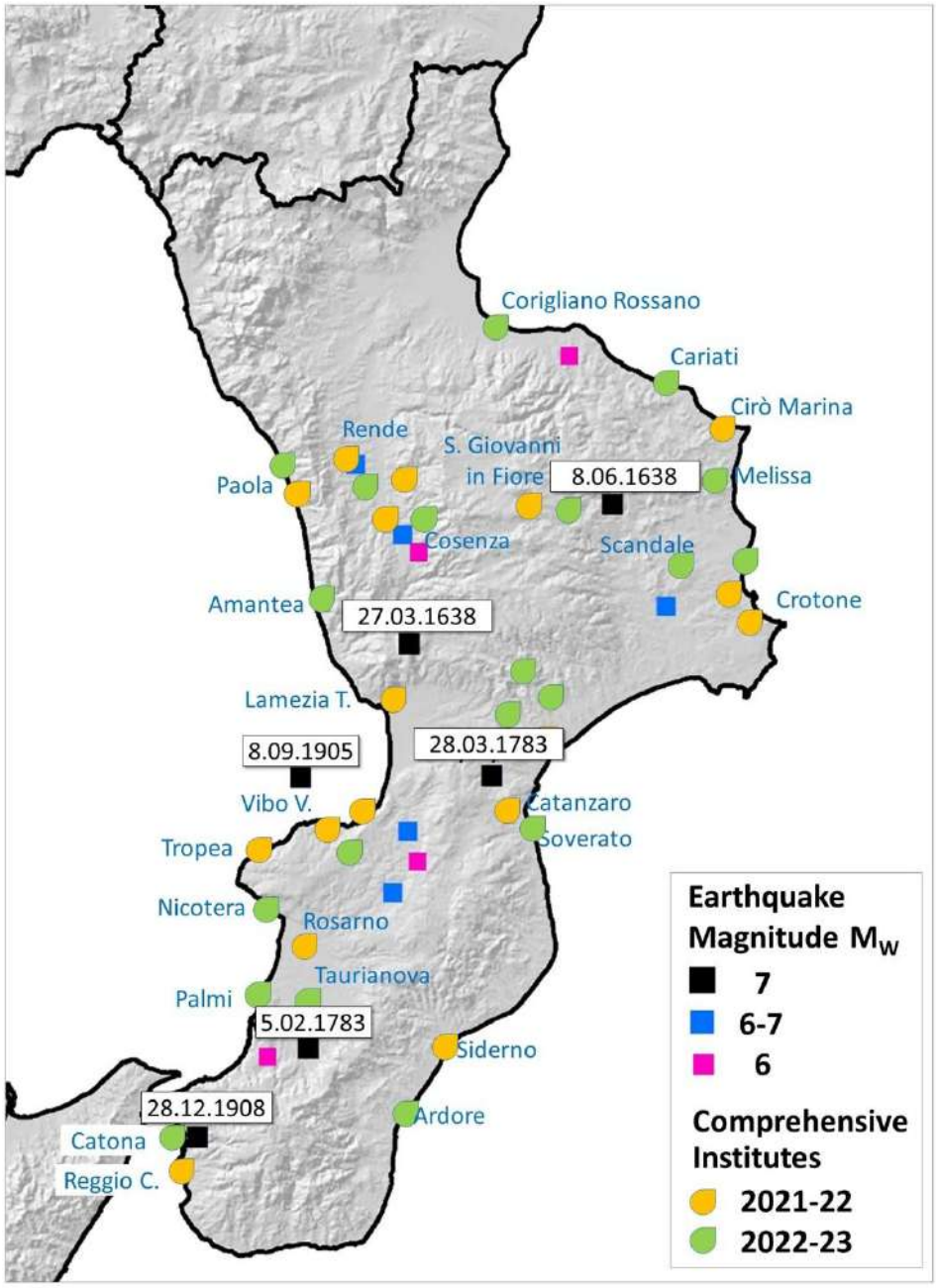

Fig.1 - Map of the Comprehensive Institutes participating in the ASdT project and distribution of the major historical earthquakes in Calabria (data from CPTI15, Rovida et al., 2021)

2. The numbers of the project

2.1. Experimental phase (AS. 2021-2022)

The project initiated in February 2022 and, thanks to the close collaboration with the Regional School Office of Calabria, it involved 41 teachers, 17 classes, and 17 Comprehensive Institutes (Tab. 1).

According to the Italian school system, nursery, primary and lower secondary schools, close to each other in the area and connected for administrative purposes, are brought together in a single Comprehensive Institute (Istituto Comprensivo), that is a multi-sit school. Outside the cities and the most populated centres, the Comprehensive Institutes can gather schools of even 5-6 municipalities, and also have a dozen or more schools buildings ("plesso").
The project is structured in two main parts: in the first we proceed with the training of teachers through three dedicated meetings of a couple of hours each.
The first meeting was held in Calabria where the ASdT team was present in three different locations in the area to give all teachers a chance to participate (Fig. 2, left); the other two training meetings were held remotely, in afternoon-evening hours, to meet the needs and availability of teachers.
The other part of the project took place directly in classrooms: the ASdT team organized playful, interactive and multidisciplinary workshops with the support of teachers. Again, the first workshop in the classrooms was carried out in person (Fig. 2, right), while the other two were carried out remotely, agreeing on the relevant schedule with the teachers.

Fig.2 - Teachers training (left) at Siderno (Reggio Calabria) and workshops in the classrooms (right) on March 2022

2.2. Refinement phase (AS. 2022-2023)

With the start of the 2022-2023 school year, we worked to refine the educational programming and extend the network of involved schools. We held a series of meetings open to all teachers to present the overall project. Almost all Comprehensive Institutes activated in 2021-2022 decided to continue the project, and 21 new institutes joined the existing network with the involvement of 58 teachers and 45 classes. Among the new institutes were some upper secondary schools for which ad hoc activities had to be planned (Tab. 1).

2.3. Current activities (AS. 2023-2024)

The project is currently underway in 20 Comprehensive Institutes (Tab. 1). Some of the schools that have already participated (8) have proposed to continue the activity in new classrooms and

have shown interest in training new teachers (49). 12 schools, however, are joining for the first time.

Tab. 1 – Number of involved Comprehensive Institutes

Scolastic year	Comprehensive Institutes	Trained teachers	Classes with an avarage of 20 students/classe
2021-2022	17	41	17
2022-2023	21	58	45
2023-2024	20	49	--

Training courses for teachers and activities with students

The three training meetings for teachers covered the following topics:

Some activities were proposed to check motivations for participating in the project, and others to discuss and compare their own views of the earthquake. Techniques such as discussion and role-playing games were used that can be replicated later by teachers in classroom activities. The initial meeting aimed to bring out the questions they personally considered most important and the most sensitive topics, which were then discussed in subsequent meetings.

The second meeting aimed to understand how to build knowledge about the earthquake by delving into the topic of earthquake risk. Through the flipped classroom model (Bergmann and Sams, 2012; Maglioni and Biscaro, 2014), some important topics were explored in depth through the use of scientific models, historical documents, scientific documentation and discussions with "experts." Teachers then brainstormed and shared the information gathered.

Finally, with work developed in small groups, the topic of educational planning was addressed, building and sharing working hypotheses to be implemented in classrooms.

The activities proposed to students in the classrooms are the following:

The workshop on risk was proposed in the form of a comparison game. Two stories of common life situations (a walk in the woods and a trip to the mountains) are presented in which risky conditions are included. The students' behaviour choices become an opportunity to confront each other on the different propensity and acceptance of the level of risk, and respect for rules to safeguard themselves and the community

The second workshop was devoted to exploring the imagery of the earthquake (how it occurs, what is its impact, how people react) through the invention of stories, illustrated and described by

the students. Through this work, they had the opportunity to show what they know or imagine about earthquakes and to represent what the occurrence of an earthquake means, questioning its possible consequences in both the short and long term.

A key element of the project is to increase students' and adults' awareness of the hazard characteristics of the area where they live, and thus its seismicity and seismic history. For this reason, in the third workshops, students were invited to collect testimonies and memories of family members or acquaintances related to seismic experiences.

4 Conclusions

After the initial calibration phase that saw an important presence of the ASdT team in the Calabrian territories for a couple of years, the project is now being organized to be self-sustainable and easily reproducible for all Calabrian schools.

The constant demand for participation from schools (this year the number of schools has increased) and the enthusiasm shown by teachers who have already participated and are renewing their presence, suggest the goodness and quality of the educational proposal. This finding is not surprising because the educational proposal is consistent with the philosophy of Edurisk, which for more than 20 years has been offering training to teachers to be able - together - to educate students (Pessina and Camassi, eds., 2012; Camassi et al. 2016). This approach has also proven effective in recent experiences in other Italian territories in the northern Apennine area (Camassi et al., 2021; Ercolani et al., 2022).

Frontal lectures, imparting notions, were banished, but mutual acquaintance activities were proposed to assess the teachers' level of knowledge and degree of curiosity and interest. Students were offered active-learning laboratory activities with the involvement of families and relatives.

Wide-ranging topics were covered, from the concept of generic risk to seismic issues, dropped into the local reality, albeit with due local difference.

In fact, one of the ultimate goals of this project is to provide an opportunity to verify personal experiences within one's family or social context: people are invited to search for traces of past earthquakes (recent or otherwise), through memories or signs on the territory for full awareness leading to risk reduction choices.

Greater knowledge of risks and preventive measures can make the difference between an effective response to an earthquake and a disaster situation. Awareness campaigns through schools help identify specific community needs and customize awareness strategies, stimulating collective efforts to minimize risks.

Acknowledgements

The study presented in this article was developed under the agreement between INGV and the Department of Civil Protection of the Calabria Region, with the collaboration of the Regional School Office.

The planned activities were successfully carried out thanks to the willingness and passion of the heads and teachers of the Institutes that joined the project.

References

Bergmann J., Sams A.; 2012: Flip Your Classroom: Reach Every Student in Every Class Every Day. International Society for Technology in Education, Washington DC, 112 pp.

Camassi R.; 2008: Educazione e Rischio a cento anni dal terremoto del 1908. 1908 - 2008 Scienza e Società a cento anni dal Grande Terremoto. Riassunti estesi del convegno, Reggio Calabria, 10-12 December, Miscellanea INGV, 3, pp. 25-26.

Camassi R., Ercolani E., Brasini F., Modonesi D., Pessina V., Castelli V., Meletti C.; 2021: One hundred years after: The results of an educational project, 37° European Seismological Commission General Assembly, ESC2021, Virtual, 19-24th September, Abstract ESC2021-S06-292

Camassi R., Pessina V., Bernardini F., Castelli V., Crescimbene M., Ercolani E., La Longa F., Nostro C., Pignone M.; 2016: EDURISK, 15 years of risk education, state of the art. 35th European Seismological Commission General Assembly, ESC2016, September, Trieste, Abstract ESC2016-667.

Ercolani E., Camassi R., Brasini F., Modonesi D., Castelli V., Pessina V.; 2022: Comunicare ed educare al rischio, le strade possibili. Quaderni di geofisica, 182, pp. 40, ISSN: 1590-2595

Maglioni M., Biscaro F.; 2014: La classe capovolta. Innovare la didattica con il flipped classroom. Erickson, 87 pp.

Pessina V., Camassi R. (eds); 2012: EDURISK 2002-2011: 10 anni di progetti di educazione al rischio. Roma, 30 novembre 2011. Miscellanea INGV, 13, 77 pp.

Rovida A., Locati M., Camassi R., Lolli B., Gasperini P., Antonucci A.; 2021: Catalogo Parametrico dei Terremoti Italiani (CPTI15), versione 3.0. Istituto Nazionale di Geofisica e Vulcanologia (INGV). https://doi.org/10.13127/CPTI/CPTI15.3

Corresponding author: emanulea.ercolani@ingv.it

Insights into risk communication from the analysis of earthquake light phenomena reports in Turkey and Morocco

C. Fidani[1,2]

[1] *Istituto Nazionale di Geofisica e Vulcanologia, Roma, Italy*

[2] *Central Italy Electromagnetic Network, Fermo, Italy*

Recently, a 6.8-magnitude earthquake struck Morocco on September 8, 2023, at 11.11 p.m. local time. Video footage has emerged capturing unusual light phenomena during this seismic event. The first recording, Fig. 1a, available at https://www.albawaba.net/editors-choice/mysterious-blue-light-flashes-moroccan-earthquake-1533613, features blue flashes in Agadir originating from the ground. This video, dated 11.08 p.m. on September 8, 2023, was captured by a surveillance camera. Another video, Fig. 2, documenting the 7.8-magnitude earthquake in Turkey on February 7, 2023, displays flashes with less defined origins where public illumination is on during the first flash, Fig. 2a, while public illumination is off during the following flash, Fig. 2b. Both recordings were taken in residential areas, the first by a surveillance camera and the second via a mobile phone. A separate video, Fig. 1b, accessible at https://video.corriere.it/video-virali/strane-luci-apparse-cieli-marocco-prima-devastante-terremoto/fa2e4bc6-5179-11ee-929c-7dcc808a97b8, depicts six bright points moving across the desert sky. Unfortunately, details such as the times and locations of these observations are not provided by newspapers.

Fig. 1 – Two photograms of the two videos capturing unusual light phenomena of the Morocco earthquake, flashes in a and luminous points in b

Video footage capturing similar phenomena has become increasingly common in the aftermath of numerous recent earthquakes, facilitated by the widespread use of mobile phones and surveillance systems. Consequently, the term "seismic lights" is now regularly employed, surfacing multiple times each year, within a progressively expanding community of journalists and bloggers. The implications of this growing awareness present an intriguing aspect. The phenomena associated with strong earthquakes, often serving as precursors, consistently contribute to ongoing discussions. Yet, an essential gap warrants examination before delving into the implications, namely, the absence of a critical perspective in the reporting of these recordings.

Fig. 2 – Two photograms of the same video in two different moments capturing flashes of the Turkey earthquake, during the first flash in a and during a following flash in b

Indeed, a significant portion of recent filming has concentrated in inhabited areas where the population resides, coinciding with the presence of an electricity distribution network. As seismic waves traverse through, the anchoring points of the electrical grid oscillate, causing electrical cables to stretch and break at vulnerable points, Fig. 3. During the 2009 L'Aquila earthquake (Fidani, 2010), numerous accounts described electrical cables detaching from the corners of houses at the moment of the tremor, emitting sparks ranging from red to blue. Furthermore, there were discharges observed between high-voltage cables in the vicinity of the city during the earthquake, resulting in prolonged illuminations resembling lightning from a thunderstorm. Many instances of seismic lights may have originated from short circuits in the electrical grid and are not mysterious phenomena without clear explanations. Regarding bright spots in the sky, historical testimonies abound, and several videos have consistently reported them, displaying stable light characteristics with oscillating colours transitioning from red to yellow to white. In some recent cases, explanations have been offered, ranging from the mention of Chinese lanterns to attributions of the phenomenon to drone movements, and even digital artifacts intentionally created to suggest extraterrestrial visits. Regardless of the interpretation, it is crucial that when a digital document captures an unusual phenomenon, it should include essential details such as the date, time, and location of the observation.

Fig. 3 – Photo taken February 16, 2010, a man walks down an earthquake damaged street with fallen electrical lines in downtown Port-au-Prince; source: The Associated Press

On the flip side, individuals captivated by the mystery these phenomena evoke are undoubtedly inclined to seek explanations. It remains a possibility that some are driven solely by the desire to write articles that garner the highest number of reads. However, does this account for the actual absence of a critical perspective? Generally, incorporating a degree of criticism tends to enhance the appeal of an article. Could it be that our accustomed mode of communicating science, synonymous with presenting only established results, stifles critical observation? In this context, the reality of numerous imperfect endeavours, striving for limited and incremental outcomes, gets lost in communication. It seems that the role of those reporting news is reduced to merely cataloging observations as scientific findings. In this process, there is no space for questions, no allowance for error, and no opportunity for a genuine effort at understanding. Instead, there exists only the cataloging of consolidated results as the "product" of science. Yet, every result, sooner or later, will face scrutiny and potential refutation within its scientific domain. Consequently, science cannot be exclusively identified with its outcomes, and relying solely on results in communication appears to foster a lack of critical thinking.

Cloudless and thunderless lightning, along with subdued discharges of electric lights and a widespread reddening of the sky, are frequently observed hours before the occurrence of the main earthquake event. Centuries of collecting testimonies have revealed some common traits, such as their prevalence in rift zones (Thériault et al., 2014). Despite being regularly observed,

photographed, and filmed, these phenomena lack unequivocal and certain interpretations. Instead, they represent phenomena that necessitate further study to unveil their connection with earthquakes. The essence of science lies not in providing definitive interpretations but in the approach and method employed for study, encompassing hypotheses, tests, and attempts that may occasionally prove incorrect. Can seismic lights be interpreted as a signal of the impending strongest event during a seismic swarm? The answer is not without uncertainty. Even with instrumental observations, which have been feasible for some time (Fidani, 2010), and can be activated in the event of a swarm in the area of interest, uncertainties persist. While personal awareness of seismic lights can serve as a means of self-protection or safeguarding one's family (Witze, 2014), the collective utilization of this awareness necessitates the preparedness of the population to discuss such a possibility.

Finally, earthquake lights serve as a compelling topic for initiating discussions surrounding these tragic events. They engage both those who haven't directly experienced the tremor and those who have experimented with memories of deafening thuds, screams, helplessness, and pain. For the former, these lights are spectacular phenomena highlighting the immense energies unleashed, involving the atmosphere, yet underscoring the recurring nature of such tragedies. Hopefully, for those who lived through the earthquake, discussions unfold from the days before and after, gradually converging on the moment of tragedy. This approach allows individuals to revisit the traumatic experience, starting from a calmer perspective. The collection of testimonies following the earthquake in L'Aquila revealed the facilitation that this topic provides in sharing personal experiences. It's not merely a therapeutic exercise aimed at dispelling lingering fears but a valuable contribution to "save" those destined to undergo a similar experience, transforming trauma into something constructive. Conversations about lights, unique observations, and the behaviour of domestic animals hold great potential in the more serene re-enactment of the event in childrens. Recognizing that dear pets and companions have also experienced it creates a shared understanding that helps individuals discuss their emotions, potentially making the event seem less daunting.

What favors this form of communication from the typically probabilistic communication? Individuals who undergo the harrowing ordeal of an earthquake often wonder if they will face such an experience again. However, the probabilistic approach states that we don't know and that it is not possible to know. Moreover, a purely probabilistic approach concentrates exclusively on the epistemological aspects of acquiring information about future earthquakes by relying on past series of events. It overlooks the essential consideration of the earthquake's nature, its ontology. Consequently, communication based on a probabilistic approach falls short.

References

Fidani C.; 2010: The earthquake lights (EQL) of the 6 April 2009 Aquila earthquake, in Central Italy, Nat. Hazards Earth Syst. Sci., 10, 967–978.

Thériault R., St-Laurent F., Freund F. T., Derr J. S.; 2022: Prevalence of Earthquake Lights Associated with Rift Environments, Seismological Research Letters, 85 (1): 159–178.

Witze A.; 2014: Earthquake lights linked to rift zones. Nature, doi.org/10.1038/nature.2014.14455.

Corresponding author: c.fidani@virgilio.it

E se… (What if…) a game to learn about risk perception

M. V. Gargiulo[1], G. Woo[1], R. Russo[1], F. Napolitano[1], O. Amoroso[1], B. Massa[2], P. Capuano[1]

[1] Department of Physics – University of Salerno, Italy,
[2]Department of Science and Technology – University of Sannio

The role of science and its public perception is pivotal for societal resilience, a fact underscored by the profound impact of COVID-19. How society responds to scientific findings and the trust citizens place in them is closely tied to the effectiveness of scientific communication (Reuter and Spielhofer, 2017). Consequently, it is imperative to formulate innovative strategies and protocols for communicating science and risk (Appleby-Arnold et al, 2021).

Italy, geologically one of the most complex and scientifically intriguing countries globally, faces significant seismic and volcanic hazards. Focusing on the Campania region, particularly the Phlegraean Fields, a supervolcano near Naples, the area exhibits unique geological features, including 24 craters and volcanic edifices, many submerged. The region experiences hydrothermal activity and bradyseismic phenomena, with recent reports indicating inflation around Pozzuoli and increased seismic activity.

In light of these geological challenges, public awareness and education about general and seismic risks, especially among younger generations, assume paramount importance. Recognizing the influential role of the younger demographic in societal scientific awareness, it is crucial to employ effective language and engagement strategies (Musacchio et al., 2023).

In this context, the use of Serious Games, a balance of serious and playful elements, emerges as an innovative science communication tool (Veldkamp et al., 2021). These games actively involve participants, enhancing their learning experience.

In parallel, integral to risk analysis is the use of downward counterfactual analysis, a cognitive psychology concept. While people often contemplate how situations could have been better, considering how they might have been worse is less common. In the realm of risk assessment, the downward counterfactual is a valuable tool. It prompts a deliberate examination of how events might have taken a more adverse turn, contributing to enhanced disaster preparedness and avoiding unexpected surprises.

The preparedness for risk, intertwined with the identification of danger factors and anticipation of their impacts, can be nurtured through exercises that cultivate counterfactual thinking and associated intelligences. This approach finds application in addressing extreme natural risks such as volcanic eruptions and periods of volcanic unrest.

Bagnoli, venue of the Science Fair “Futuro Remoto”, situated in the Phlegraean Fields caldera, presents a scenario where public perception of volcanic risk is low. To elevate awareness, a democratic and egalitarian role-playing game has been designed for the 2023 edition of “Futuro Remoto”, offering an interactive and instructive experience for participants.

The initiative aims to place participants at the core of the learning process, fostering not only the acquisition of scientific knowledge but also the development of problem-solving and leadership skills.

Participants engage in a roundtable of Counterfactuals in the Negative, imagining historical volcanic eruptions as having worse outcomes. This interactive exercise enhances individual risk intelligence.

Finally, an evaluation protocol has been developed to assess the impact of the experience on risk perception. This presentation focuses on presenting the outcomes of this evaluation after the 2023 edition of “Futuro Remoto”, where almost 200 participants joined the game.

Fig. 1 – Poster of the Activity at Futuro Remoto 2023

References

Appleby-Arnold, S.; Brockdorff, N., and Callus, C. (2021). Developing a “culture of disaster preparedness”: The citizens’ view, Int. J. Disaster Risk Reduct.,Vol. 56,102133,ISSN 2212-4209. doi:10.1016/j.ijdrr.2021.102133

Musacchio G, Saraò A, Falsaperla S and Scolobig A (2023), A scoping review of seismic risk communication in Europe. Front. Earth Sci. 11:1155576. doi: 10.3389/feart.2023.1155576

Reuter, C., and Spielhofer, T. (2017). Towards social resilience: A quantitative and qualitative survey on citizens' perception of social media in emergencies in Europe, Technol. Forecast. Soc. Change, Vol. 121, Pages 168-180, ISSN 0040-1625. doi: 10.1016/j.techfore.2016.07.038

Veldkamp, A., Knippels, M.C.P.J., and van Joolingen W.R. (2021). Beyond the Early Adopters: Escape Rooms in Science Education. Front. Educ. 6:622860. doi:10.3389/feduc.2021.622860

Corresponding author: mgargiulo@unisa.it

Preparing for disasters through games: a worth taking bet?

M. Giuffrè[1], M. S. Benigni[1], I. Gaudiosi[1], M. Mancini[1], M. Moscatelli[1]

[1] Istituto di Geologia Ambientale e Geoingegneria (Consiglio Nazionale delle Ricerche, Italia)

The risk education represents a significant factor in improving the awareness and knowledge required to reduce the impact of earthquakes on the territories (UN, 2015). For this reason, the Institute of Environmental Geology and Geoengineering of the National Research Council has established an educational laboratory aimed at helping students understanding the concept of seismic risk and disseminating knowledge about mitigation measures to reduce the impact of disasters (Gaudiosi et al. 2022). The chosen target was also calibrated in light of the young people's renewed interest in new technologies and different editorial forms (comics and graphic novels).
The laboratory hopes to transmit methods for sismic microzonation and earthquakeresistent city planning (Benigni et al. 2022), through tabletop games and three-dimensional representations of the territory (Gaudiosi et al. 2023). The direct and shared participation in laboratory activities, combined with game experience (Filomena et al. 2023), promotes understanding of the physical phenomenon of the earthquake, its consequences and effects, and the discussion of one's own prejudices.
The measurement of acquired awareness is carried out using appropriate questionnaires.
Finally, the goal of this contribution is to establish a cross-institutional network in which the authors participate in order to disseminate and confront proposals for integrated risk communication methods throughout the scientific community.

References

Benigni M. S., Fontana C., Giuffrè M., Tomassoni V.; 2022. L'analisi della Condizione Limite per l'Emergenza a dieci anni dalla sua istituzione: limiti attuali e potenzialità future, Urbanistica informazioni. ISSN: 2239-4222

Filomena M. G., Pace B., De Acetis M., Aquino A., Crescimbene M., Pace M., & Alparone F. R.; 2023. Play to Learn: A Game to Improve Seismic-Risk Perception. Sustainability, 15 (5), 1-11.

Gaudiosi I. et al.; 2022. From the Institute of Environmental Geology and Geoengineering of the National Research Council (CNR IGAG) to schools: introducing cultural heritage into classrooms to foster awareness about natural risk prevention. Rendiconti Online della Società Geologica Italiana. DOI: 10.3301/ROL.2022.14;

Gaudiosi I., Mancini M., Caielli G., de Franco R., Moscatelli M., Stigliano F.; 2023. Microzonazione sismica: quali scenari per il futuro? Geologicamente, 10. ISSN: 2705-0149 https://doi.org/10.3301/GM.2023.01

UN – United Nations; 2015. Sendai Framework for Disaster Risk Reduction 2015-2030. https://www.preventionweb.net/files/43291_sendaiframeworkfordrren.pdf

Corresponding author: margherita.giuffre@cnr.it

From risk to safety for a resilient governance

S. Grimaz [1], P. Malisan [1]

[1] SPRINT-Lab, Polytechnic Department of Engineering and Architecture, University of Udine (Italy)

Background and motivations. Events and phenomena with a strong impact on the territory are increasingly common and are exacerbated by climate change (UNDRR, 2015). They include natural hazards (e.g., floods, tornadoes, earthquakes, hydrogeological instability phenomena), as well as human activities (e.g., air pollution, water pollution, deforestation, soil degradation) or combinations of both. These events occur with greater frequency and intensity, affecting all countries around the world.

The interactions between natural and human systems further complicate risks. Infrastructure development in hazardous zones, such as coastal areas prone to hurricanes or earthquake-prone regions, elevates exposure to natural disasters, increasing the potential for widespread damage and disruption. Simultaneously, degraded ecosystems, such as deforested lands or polluted water sources, diminish their natural buffering capacity, leaving communities more vulnerable to the adverse impacts of environmental changes.

The complex interplay between natural and human systems underscores the importance of holistic approaches to risk management, necessitating strategies that consider both environmental and societal factors to build resilient and sustainable communities. At the same time, social and economic networks have become deeply interconnected locally and globally. Disruptions to any part of complex, cross-border systems can trigger widespread cascading impacts difficult to predict and manage. Interdependencies between infrastructure, supply and value chains mean disturbances are more system-wide with the potential for massive harm.

These multifaceted issues demand holistic, intersectoral approaches respectful of territorial specificities. While climate adaptation and disaster risk reduction are priorities, siloed actions are insufficient. Cooperation across governments, private stakeholders, scientists and communities is necessary to understand dynamic risk contexts and cocreate adaptive solutions. In this process, an effective communication plays a strategic role.

Recognizing the scale and urgency of these sustainable development challenges, the UN's 2030 Agenda (United Nations General Assembly, 2015) aims to build resilience through policy and financing coherence, ecosystem protection, social inclusion, innovation and preparedness. Yet integration of risk knowledge and management into strategies, planning and decision-making remains fragmented.

The COVID-19 crisis further underscored gaps, particularly regarding coordination of emergency responses, continuity of critical services and support for vulnerable populations. It revealed deficiencies in integration and social protection requiring attention in recovery agendas. The EU's "Next Generation EU" recovery plan (European Union, 2023) and related framework emphasize building back in a manner that is greener, fairer, and more resilient against future adversities.

To achieve disaster risk reduction, as indicated by the Sendai Framework (UNDRR, 2015), it will be imperative to reduce hazards and vulnerabilities through coordinated territorial action. International cooperation on evidence-based risk assessment, management of cross-border risks, knowledge exchange and capacity building should be scaled up. Strong multilevel governance and

cooperation between countries are needed to align risk reduction with sustainable development trajectories and ensure balanced, resilient pathways ahead.

Dealing with the complex interconnected challenges of risk, climate change and development requires approaches that embrace uncertainty and evolve over time. Systems thinking acknowledges the high degree of unpredictability from emergent, nonlinear dynamics between interacting social, ecological, technological and infrastructure components. Events often occur in unforeseen ways and new risks can materialize that previous risk assessments did not anticipate. Continuous learning and adaptations are necessary to incorporate evolving understandings of complexity into flexible management strategies. Surprises are inevitable, so building in redundancy, modular solutions and feedback loops helps sustainable development pathways absorb disruption. Cross-disciplinary integration of perspectives from social, natural and engineering sciences also aids accounting for unknown unknowns (Grimaz et al., 2024). Scenario methodologies and adaptive governance enable recalibration of policies and projects to surprise outcomes within an overall risk-informed strategic direction. Such innovation and preparedness help promote resilient pathways despite a substantial immeasurable component of risks in complex, evolving systems.

In addition, the UNDRR Global Assessment Report 2022 (UNDRR, 2022) recognizes that achieving transformative change to build disaster and climate resilience requires transforming governance systems. Traditional top-down, rigid governance approaches are inadequate to address complex, interconnected risk in a volatile world. The report advocates for more flexible, inclusive and collaborative modes of governance termed "transforming governance". The report emphasizes the need for transforming governance, taking into account aspects of systemic risk, uncertainty and the needs to take actions in order to build resilience and achieve the UN sustainable Development Goals.

Discussing on the key aspects highlighted by the UN Agenda 2023, the Sendai Framework and the Global Assessment Report 2022, the researchers of the Safety and Protection Intersectoral Laboratory (SPRINT-Lab) of the Polytechnic Department of Engineering and Architecture at the University of Udine, also UNESCO Chair on Intersectoral Safety for Disaster Risk Reduction and Resilience, started an interdisciplinary process of discussions to work across silos and face the issues related to the resilience to disasters for a sustainable development. In detail, this paper aims to rise attention on the need to improve communication for transforming governance, considering the disaster prevention, preparedness, response, and recovery, in order to pass from an approach focused mainly on the risk assessment to a risk-informed approach finalized to reach safety.

Governance as “play the game”. In the Global Assessment Report 2022, the transition to systemic risk governance is presented through the metaphor of “playing the game” (North, 2008; Shepsle, 2012). In this report, the metaphor of "playing the game" is employed to denote the systems, arrangements, structures, strategies, and processes involved in agreeing upon and formulating rules, laws, and policies, as well as making and implementing collective decisions. These elements are not rigid and can vary. Effective governance models have the ability to adapt, facilitating prompt responses to crises and monitoring gradual changes, allowing for the implementation of longer-term measures (IRGC, 2018; UNDRR, 2022).

Overall, transforming governance through collaborative, multi-level "game playing" is key to adaptively governing complex, multicausal and evolving disaster and climate risks.

Traditionally, governance has followed a top-down, segmented approach to addressing societal challenges like risk. Problems are understood through the narrow lens of separate government

ministries and agencies. Decisions are made by political officials with limited stakeholder input. Actions are implemented according to rigid plans with few feedback loops to course correct.
However, the COVID-19 pandemic and climate change have proved the limitations of such linear, siloed governance in our modern, complex world. Risks emerge from dynamic interactions across many interconnected human and natural systems, defying segmentation. Uncertainty and emergent, non-linear behaviours demand continual learning and adaptation not allowed for in rigid structures. Vulnerable communities fall through cracks without grassroots collaboration.
Crucially, "playing the game" fosters adaptive processes wherein actions are continuously calibrated alongside monitoring and feedback. Plans evolve in tandem with changes in conditions on the context or new insights. Responses fill emergent needs through grassroots action complementing strategy. Governance demonstrates agility unseen in rigid, compartmental approaches.
Governance is a multifaceted process that involves understanding complex problems, making informed decisions, and implementing actions to achieve specific goals (Fig. 1). In today's intricate and uncertain world, marked by systemic risks, this process becomes even more crucial. Effective governance demands a dynamic and adaptive approach, recognizing the interconnections and uncertainties inherent in our complex global landscape.

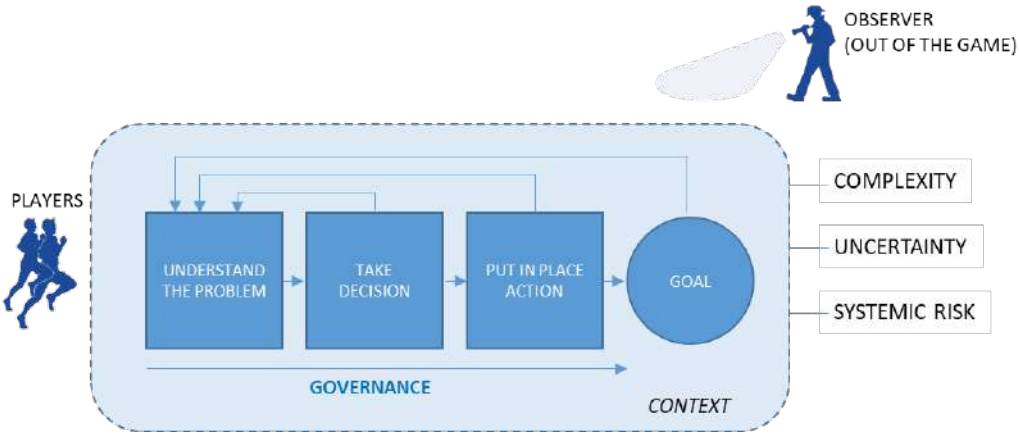

Fig. 1 - Non-linear governance process in a changing context: different perspectives of the different subject.

An essential passage in governance is gaining a deep understanding of the problem at hand. In our modern world, issues are rarely isolated; instead, they are embedded in a web of interconnected factors. This complexity requires a nuanced understanding of the root causes, potential impacts, and the broader context in which the problem exists.
The governance process requires making decisions that are both strategic and contextually relevant. Decisions must be informed by a comprehensive understanding of the complexity, considering the diverse and often interdependent factors that contribute to the issue. The decision-making process should be agile, allowing for adjustments based on emerging information and changing circumstances.
Putting in place actions is the means for passing from decision to goal attainment. Actions must be carefully crafted to address the specific facets of the problem. This requires a proactive stance, adapting to unforeseen challenges and leveraging opportunities as they arise.
In the dynamic landscape of contemporary governance, each passage — understanding, decision-making, and implementation — demands a continuous feedback loop. Regular assessments and evaluations ensure that strategies remain effective and adaptable. Feedback mechanisms provide

insights into the evolving nature of the problem, enabling governance structures to evolve in tandem.

In this framework, governance unfolds through two distinct perspectives:

- the actively engaged players, i.e. those called to endeavour for reaching the goal. Players, whether individuals, organizations, or governments, navigate the complexities firsthand, making decisions and implementing actions.
- the observers who analyse, critique, and learn from the process, checking the outcomes and verifying the respect of the rules of the game. Observers contribute by providing critical assessments, learning from outcomes, and offering insights that can inform future governance endeavours.

Just as games require collaboration between diverse players operating within flexible yet coherent rules, risk governance too requires opening up decision-making arenas. By "playing the game", problems can be understood more holistically by incorporating local risk knowledges alongside technical expertise. Participatory platforms allow stakeholders to jointly frame issues, trade-offs and solution space, building ownership over top-down plans. In short, "governing as playing the game" offers a promising metaphor for the flexible, inclusive, adaptive forms of multi-stakeholder participation with multiple perspectives, and joint problem-solving demanded by today's complex risk governance challenges.

The governance process has to be applied in the four phases of the Disaster Risk Management Cycle (UNDRR) (Fig. 2), adapting goals and strategies to the current context.

The view in Fig. 1 permits to emphasise also the importance of communication both among all the passages of the governance process and among involved subjects.

In particular, it is important to pass knowledge from those called to understand the problem, those called to take decisions and those called to implement actions. The endeavours and activities in each passage strongly rely on the comprehension of the main requirements and specificities of the other passages, and this aspect can be achieved only through a proper communication (bridge).

For example, understanding the problem requires knowing which is the goal of the governance, which are the requirements of decision-makers and which could be possible and feasible actions to reach the goal. Without this entire knowledge, every understanding would remain an end in itself, potentially compromising attempts to make decisions and implement actions in the context. A proper communication approach, that is aware of the requirements of all the other passages and of the context in which it is developed is an essential aspect to transform governance.

Resilience. The Disaster Risk Management Cycle (DRMC) conceptualization (Fig. 2) forms the basis for the disaster preparedness policies established by the United Nations in recent decades (Ahmad Basri et al., 2022). In the DRMC resilience can be interpreted as the ability to reach a condition of “normality” (or “new normality”) as quickly as possible; this means the ability to close the loop of the post-event phases (response and recovery) in a fast and effective way. This capacity is closely related to what has been done and invested before the event, i.e., in the prevision-prevention and preparation phases, and to what has been capitalized from positive and negative experiences in previous events.

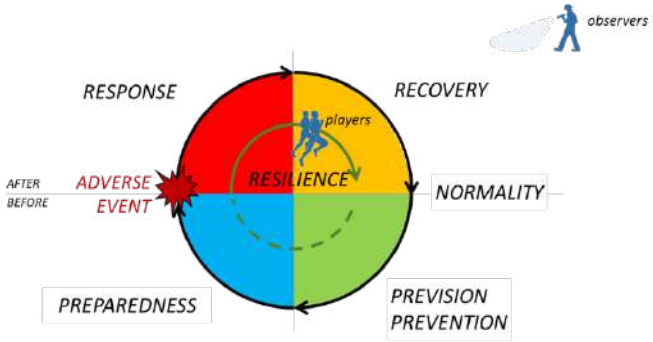

Fig. 2 - The Disaster Risk Management Cycle and the resilience: different points of view of the subjects

It's worth noting that an effective and good recovery should result in a new normality at a level better than the pre-event, introducing elements of improvement and regeneration compared to the pre-event state. To improve resilience, the system uses not only its ability to respond and recover, but also its ability to anticipate, regenerate and learn. These capabilities are particularly important given that adverse events may recur over time and the system has the ability to prepare in advance for future events. The ability to learn from the gained knowledge gives the system a potential evolutionary capacity. An ecological-evolutionary approach involves assuming the role of the active agent, i.e., as the player, whether as an individual, a group, or a community. In this perspective, the system's resilience is contingent upon the capabilities of these players, including their knowledge, strategies, and tools used to comprehend the issue, make decisions, and implement actions. The correctness, relevance, timeliness, contextualization, and effectiveness of these actions (or inactions) collectively determine the system's resilience.
Moreover, there are external observers, who have a comprehensive overview of the entire situation. They analyse the outcomes resulting from the actions of the players, considering the entire process, or even during the development of each step, as well as the appropriateness, effectiveness, and efficacy of the entire process. However, these observations are conducted with an ex-post point of view or ex-ante (but out of the game). External observers possess knowledge of how the system evolved under the specific circumstances and on which have been the results of the actions. In this case, the task of the observer is to interpret the situation to gather knowledge and experience that can be applied to future events.
In dealing with complex systems where continuous environmental changes occur, the focus shifts to navigation, requiring monitoring, anticipation, adaptation, and learning. Safety management in today's complex world must consider numerous risks, dimensions, and disciplines, accounting for the open and unpredictable nature of the system.
In response to these challenges, the player’s perspective becomes pivotal in determining the right actions at the right time, especially in the face of unpredictable events. The intersectoral approach strives to link technical aspects with socio-economic and human behaviour, fostering interdisciplinary and inter-institutional synergies to enhance contextualization, finalization, and resilience in safety management.

From risk to safety. Effective disaster risk reduction (DRR) is a critical component of ensuring the safety and resilience of communities and nations. The journey from risk to safety involves a comprehensive shift in governance strategies, acknowledging the dynamic nature of hazards and emphasizing proactive measures and the need of a constant contextualization. Disaster risks are complex and ever-evolving, influenced by factors such as climate change, urbanization, and socio-economic conditions. Approaching DRR solely through risk management is akin to playing catch-up

with an unpredictable adversary. As hazards become more intricate, the need for a paradigm shift becomes evident.

Transitioning from risk to safety involves a shift from reactive measures to proactive, preventive actions. Instead of primarily focusing on responding to disasters, safety-oriented governance aims to prevent or minimize their impacts through strategic planning, investment in resilient infrastructure, and community empowerment.

Safety-focused governance demands an integrated and inclusive approach. Governments, communities, and stakeholders must collaborate to develop and implement policies that consider the multi-dimensional aspects of disaster risk. This entails breaking down silos and fostering coordination among various sectors such as health, education, infrastructure, and environment.

Shifting the focus from managing risks to enhancing safety requires passing to action, through substantial investments and endeavours in resilient infrastructure, early warning systems, and capacity-building programs. Allocating resources strategically based on vulnerability assessments is crucial for long-term safety, however any endeavour relies on a combination of strategic planning, skilled execution, adaptability, effective governance, stakeholder engagement, monitoring and evaluation, risk management, ethical considerations, and a commitment to continuous improvement.

The transition from risk to safety is a fundamental shift in mindset and strategy, requiring a holistic and forward-looking approach to disaster risk reduction. Governments must lead this transformation by adopting integrated and inclusive governance, investing in resilience, empowering communities, and crafting adaptive policies. Embracing safety as a core principle ensures that nations are not merely reactive to threats but are actively working towards creating a safer, more resilient future for all.

Conclusion. Governance in our complex and uncertain world is a dynamic process that requires a holistic understanding, strategic decision-making, and a contextualized and adaptive implementation. Systemic risks add layers of complexity, emphasizing the need for continuous feedback loops to navigate challenges effectively. The dual perspectives of players and observers contribute to a comprehensive and evolving approach to governance, fostering resilience and sustainable solutions in an ever-changing global landscape. The governance framework emphasises the importance of knowledge transfer between passages, especially the one between science and decision-makers. New challenges are open for defining and implementing effective communication for resilient governance.

Acknowledgements. We would like to express our sincere gratitude to the members of the UNESCO Chair at the University of Udine for their interdisciplinary observations and contributions to the reflections presented here. These insights have also served as a source of thoughtful discussions during the activities of the ResiliEnhance platform within the Central European Initiative projects.

References

Ahmad Basri, S. A., Syed Zakaria, S. A., A.Majid, T., & Yusop, Z. (2022). Exploring awareness and application of disaster risk management cycle (DRMC) from stakeholder's perspective.

International Journal of Disaster Resilience in the Built Environment, 13(4). https://doi.org/10.1108/IJDRBE-09-2020-0105

European Union. (2023). Next Generation EU. https://next-generation-eu.europa.eu/index_en

Grimaz, S., De Toni, A. F., Malisan, P., Torres, J., Aristei, A., & Maiolo, A. (2024). 8. Safety and resilience for navigating towards sustainable development in the age of complexity. In F. Bucci, A. Colonna, E. Fioretto, & N. Lombardini (Eds.), KNOWLEDGE DISSEMINATION FOR THE SUSTAINABLE DEVELOPMENT (pp. 114–127). Springer Nature.

IRGC. (2018). Guidelines for the Governance of Systemic Risks. In Guidelines for the Governance of Systemic Risks. Lausanne: International Risk Governance Center (IRGC).

North, D. C. (2008). Institutions and the Performance of Economies over Time. In Handbook of New Institutional Economics. https://doi.org/10.1007/978-3-540-69305-5_2

Shepsle, K. A. (2012). The rules of the game: What rules? Which game? In Institutions, Property Rights, and Economic Growth: The Legacy of Douglass North. https://doi.org/10.1017/CBO9781107300361.006

UNDRR. (2015). *Sendai Framework for Disaster Risk Reduction*. http://www.unisdr.org/we/coordinate/sendai-framework

UNDRR. (2022). *Global Assessment Report on Disaster Risk Reduction 2022 (GAR2022)*. https://www.undrr.org/gar2022-our-world-risk

United Nations General Assembly. (2015). Transforming our world: The 2030 agenda for sustainable development. *Https://Sustainabledevelopment.Un.Org/Content/Documents/7891Transforming%20Our%20World. Pdf*, *1*, 35. https://doi.org/10.1007/s13398-014-0173-7.2

Corresponding author: stefano.grimaz@uniud.it

Tsunami risk perception of the touristic population of Stromboli Island: towards effective risk communication strategies

I. Moreschini[1], L. Cugliari[1,2], L. Cerbara[3], F. La Longa[1], M. Crescimbene[1],A. Amato[1]

[1] National Institute of Geophysics and Volcanology, Rome, Italy

[2] Department of Communication and Social Research, La Sapienza University, Rome, Italy

[3] Institute for Research on Population and Social Policies, National Research Council, Rome, Italy

Abstract

Stromboli volcanic island has experienced six mass-flow induced tsunamis since 1916, accounting for more than a third of the tsunamis recorded in the Aeolian Islands in international catalogs (Maramai et al., 2019). Among these, the 2002 tsunami triggered by a collapse on the Sciara del Fuoco highlighted the need for effective risk mitigation measures, prompting universities' and research centers' efforts for volcanic and tidal monitoring of the island. Beyond probabilistic modeling of tsunamis and warning systems, effective disaster response relies significantly on studies of tsunami risk perception to improve communication and preparedness of communities most exposed to tsunami risk. Among these, transient populations such as tourists hold particular significance in risk perception studies, as their needs intersect with those of the local population, necessitating considerations in planning risk mitigation measures. As tourism attracted by the volcano is the primary revenue source for the island's community, steps are to be taken to ensure the industry's sustainability over time and prevent collapses due to exogenous shocks (Orchiston, 2011).

Methodology

As part of the B2 Stromboli Project (DPC-INGV Agreement 2022-2023), a specific research task was funded to investigate the fundamental knowledge of tourists and the resident population to develop solid risk communication strategies. A multilingual survey (n = 699) was conducted between July and September 2023 to assess tourists' risk perception and preparedness. A web-based survey instrument was chosen to allow respondents flexibility in completing the survey, and both sampling and selection errors must be considered when interpreting the data. (Moreschini et al. submitted)

Indicators of tsunami risk perception were developed to gather respondent perception of concepts derived from studies on probabilistic assessment of tsunami hazard (Basili et al., 2018) and quantitative assessment of risk (Cadorna et al., 2012) helping the identification of areas for risk communication intervention, in terms of both target and content.

Results

Results indicate that tourists correctly recognize Stromboli as subject to a relatively higher probability of being hit by a tsunami than most of the Mediterranean Sea but underestimate the overall hazard to which they are exposed.

Tourists' representations often mischaracterize tsunamis, overlooking safety threats posed by smaller events and revealing deficiencies in current communication approaches.

The data gathered allowed the development of a conceptual typology based on tourists' exposition to information on risk-related behaviors and shows how more than half of the tourists lack any information on the behaviors to follow in case of emergency. The typology was used to identify variables that influence the probability of being adequately informed by means of logistic regressions.

Given the practices within the tourism industry on the island, effective communication strategies for tourists should prioritize providing comprehensive information within the initial 24 hours of their arrival. Moreover, given the high percentage of tourists visiting the island for a few hours and within specific time slots, we encourage the authorities to provide this information before they land.

Communication strategies to achieve adequate awareness levels rely on residents' and industry operators' acceptance of new roles and on the integration of their actions with opportunities provided by communication technologies, to expand the reach and ensure the sustainability of a continuous act of communication.

References

Basili, R., Brizuela, B., Herrero, A., Iqbal, et al. (2018) NEAM Tsunami Hazard Model 2018 (NEAMTHM18): online data of the Probabilistic Tsunami Hazard Model for the NEAM Region from the TSUMAPS-NEAM project. Istituto Nazionale di Geofisica e Vulcanologia (INGV); https://doi.org/10.13127/tsunami/neamthm18

Cardona, O.D., M.K. van Aalst, J. Birkmann, M. Fordham, G. McGregor, R. Perez, R.S. Pulwarty, E.L.F. Schipper, B.T. Sinh, H. Decamps, M. Keim, I. Davis, K.L. Ebi, A. Lavell, R. Mechler, M. Pelling, J. Pohl, A. Oliver-Smith, F. Thomalla (2012). Determinants of risk: Exposure and vulnerability. Managing the Risks of Extreme Events and Disasters to Advance Climate Change Adaptation [Field, C.B., V. Barros, T.F. Stocker, D. Qin, D.J. Dokken, K.L. Ebi, M.D. Mastrandrea, K.J. Mach, G.-K. Plattner, S.K. Allen, M. Tignor, and P.M. Midgley (eds.)]. A Special Report of Working Groups I and II of the Intergovernmental Panel on Climate Change (IPCC). Cambridge University Press, Cambridge, UK, and New York, NY, USA, pp. 65-10

Maramai A., Graziani L., and Brizuela B. (2019). Euro-Mediterranean Tsunami Catalogue (EMTC), version 2.0. Istituto Nazionale di Geofisica e Vulcanologia (INGV). https://doi.org/10.13127/tsunami/emtc.2.0

Moreschini I., Cugliari L., Cerbara L., La Longa F., Crescibmene M., Amato A. (submitted) Stromboli Risk perception of the Touristic Population of Stromboli Island: towards effective risk communication strategies.

Orchiston C. (2011) Seismic risk scenario planning and sustainable tourism management: Christchurch and the Alpine Fault zone, South Island, New Zealand, Journal of Sustainable Tourism, 20:1, 59-79, DOI: 10.1080/09669582.2011.617827

Aknowledgments: The present research is developed as part of the agreement between the Department of Civil Protection and the National Institute of Volcanology and Geophysics which provides for the strengthening of service activities in accordance with the provisions of the art. 6 of the Framework Agreement between DPC and INGV (period 2022 – 2025). The study has benefited from the financial contribution of the Italian Presidenza del Consiglio dei Ministri, Dipartimento della Protezione Civile. The publication does not necessarily reflect the position and policies of the Italian Presidenza del Consiglio dei Ministri, Dipartimento della Protezione Civile.”.

Corresponding author: iacopo.moreschini@ingv.it

Risk education and communication: the experience of serious games and *Situated Learning Episodes (ELS)* in Pandemic

G. L. Piangiamore [1] and A. Maramai [2]

[1] Istituto Nazionale di Geofisica e Vulcanologia, Sezione Roma2, Sede di Lerici, 19032 Lerici, Italy

[2] Istituto Nazionale di Geofisica e Vulcanologia, Sezione Roma1, Sede di Roma, 00143 Rome, Italy

Natural risk education is an essential component for disaster risk prevention: school education is crucial in the enhancement of knowledge and in risk awareness, to trigger changes towards rights choices for the Society as a whole.

The researchers of the Istituto Nazionale di Geofisica e Vulcanologia (INGV) activities devoted to schools bring students closer to the world of Research, focussing on earthquakes, tsunamis, floods issues in a non-formal context. The main aim is to train future proactive and resilient citizens, encouraging the personal development of the contents discussed with the experts, by using *trasformational learning* activities through digital games and *Episodes of Situated Learning (ESL)* (Rivoltella, 2013a).

During the COVID19 Pandemic, we have experienced, by remote learning, different *active learning* methods to enhance *behavioral change* in order to ease the automation of best practices of Civil Protection.

Dealing inductively with concepts of hazard and risk, a set of digital scientific games, participative escape rooms and *ESL*s have been designed, involving more than 10,000 students from Primary, Middle and High schools in the last four years. The answers of both teachers and students to the satisfaction questionnaires submitted at the end of each scientific special event, showed that these experimentations have turned out to be tools of school-based civic education.

During online scientific special venues, such as the European Researchers' Nights 2020-2023, the World Water Day 2021, the World Earth Day 2021, the Rome Science Festival 2021, the 10th anniversary of the 2011 Ligurian floods and the World Environment Day 2022, World Environment Day 2022, EPALE EDU HACK 2022 competition, and Fosforo Science Festival of Senigallia (MC) 2023, different activities were implemented. In particular, our didactic multihazard serious games concerning earthquakes, tsunami, flood and climate change, were used to explain natural phenomena and to communicate science. Salvina's *adventures* have been created: a young girl faces several hazardous situations, from earthquake to flood, to environmental issues. She is the protagonist of four educational quizzes: *"Salvina and the earthquake: what will she do?", "Salvina and the flood: what will she do?", "Salvina and the environment: what will she do?" and "Salvina and the 4Rs: what* will she do?" and of the online Escape Room "Let's free Salvina!" to elude natural risks. A second Escape, *"4S: Salvina and Samanta Save the Species"*, dealing with environmental issues to promote sustainable behavior, was designed in a participatory approach

with a second class of Middle school supported by teachers and INGV researchers. Each game was played as a challenge that had to be overcome to advance in the game as the result of *cooperative learning* by the whole class in the competition. These gaming competitions are all designed on *inquiry-based learning* and have been enthusiastically played simultaneously by students from all over Italy (Piangiamore & Maramai, 2022).

In the reduction of natural hazards, knowledge of the past plays a key role. This is why, experimenting with a new didactic model experienced and based on the *ESL* at school, we decided to focus the activity on the study of past earthquakes and tsunamis for facing the future with greater awareness.

ESL suggests an innovative way of studying with the use of new technologies, as a new way for teaching and learning based on a flipped-up approach. This activity facilitates the development of all key competences and citizenship skills, stimulating discussion among peers and with adults and fostering critical thinking development (Rivoltella, 2013b; Piangiamore et al., 2016).

In particular, two *ESL* project addressed to High schools have been realized: *"Earthquakes: history teaches us the future: researchers for a day with experimentation in didactics for ESL"* and *"Tsunamis: history teaches us the future researchers for a day with experimentation in didactics for ESL"*. In both activities students design a final digital communication product developing life skills, focusing on historical seismic studies of both past earthquakes and tsunamis. The experiences triggered students' interest, favoring learning at a distance in a context that challenges knowledge, skills, attitudes and competences. On the other hand, teachers can evaluate all the three phases of *ESL* activity to reach a formative assessment (Rivoltella, 2014).

The above-mentioned experiences underlined that risk education and best practices of natural risk reduction can be instilled automatically to promote safe behaviors to be implemented during natural events, building a *lifelong-lifewide* resilience (Piangiamore et al., 2021).

References

Piangiamore, G.L.; Maramai, A. Gaming and Resilience: Teaching by Playing Together—Online Educational Competition at School during the Pandemic. Appl. Sci. 2022, 12, 11931. https://doi.org/10.3390/app122311931

Rivoltella, P.C. Fare didattica con gli EAS - (Episodi di Apprendimento situato); La Scuola Ed.; Brescia, IT, 2013a.

Rivoltella, P.C. L'agire didattico. Manuale per l'insegnante; La Scuola Ed.; Brescia, IT, 2013b.

Rivoltella, P.C. Episodes of Situated Learning. A New Way to Teaching and Learning. Research on Education and Media, 2014, VI, N. 2, 79-87.

Piangiamore, G.L.; Musacchio, G.; Devecchi, M. Episodes of Situated Learning: natural hazards active learning in a smart school. In Interactive Learning: Strategies, Technologies and Effectiveness; Lewis M. Hunt Eds.; Nova Science Publisher: New York, USA, 2016; ISBN 978-1-63484-198-6.

Piangiamore, G.L.; Falsaperla, S.; Eva, E.; Musacchio, G. Seismic risk communication: Let's students show their own way. Ann. Geophys. 2021, 64, 1–16.

Corresponding authors: giovanna.piangiamore@ingv.it

alessandra.maramai@ingv.it

Real-time seismicity on your smartphone

M. Pignone[1], E. Casarotti[2], V. Lauciani[1], C. Nostro[1], C. Meletti[3], A. Amato[1]

[1] Istituto Nazionale di Geofisica e Vulcanologia, Osservatorio Nazionale Terremoti, Roma, Italy
[2] Istituto Nazionale di Geofisica e Vulcanologia, Sezione Roma1, Roma, Italy
[3] Istituto Nazionale di Geofisica e Vulcanologia, Sezione di Pisa, Pisa, Italy

The INGVterremoti mobile application for smartphones and tablets is a tool designed to provide real-time earthquake information and updates on seismic activity in Italy and around the world. Developed by the Terremoti Department of the Istituto Nazionale di Geofisica e Vulcanologia (INGV), this App offers a user-friendly interface combined with powerful features to stay informed about seismic events and earthquake research and monitoring activities.

Since March 10, 2011 (one day before the 2011 Tohoku earthquake), the INGVterremoti App for iOS has been distributed in the App Store. It was the first seismological App released by a scientific institution. The goal was to provide fast communication about seismic information tailored to users with mobile devices, an audience that was beginning to be dominant. This first version of the App showed data on the most recent earthquakes on Italian territory and the strongest events in the rest of the world. In addition through the "Search" section it allowed the visualisation of Italian seismicity from 2005 onward.

Already from the first version, special attention was also paid to scientific information about earthquakes by directly linking to the contents, pages and articles, of the blog-magazine INGVterremoti.com. This included educational and popular content to improve users' understanding of seismic activity, explanations of the science behind earthquakes, how to prepare for and behave in case of an earthquake event. This educational component made the app useful not only during emergencies but also as a learning resource.

When the App was first released, the smartphone and tablet app market was in its infancy, at least in Italy. Therefore, because of the novelty and effectiveness of a product released by a well-known scientific institution, during the earthquake crises from March 2011 to July 2013 the INGVterremoti App was repeatedly ranked in the top 10 positions among the most downloaded Apps in the Apple Store (Italy).

Over the years this App has been constantly updated (with 3 major releases) both due to the evolution of the technological platforms in which it operates and due to changes in the INGV seismicity information service of which they are an integral part. In 2011, the main innovation was the ability to consult the entire INGV Italian seismic catalogue since 2005 by downloading it directly to the device during installation to allow the App to work without a data connection (e.g., in remote areas or during an earthquake emergency). The improvement of mobile data coverage in Italy and the creation of APIs to programmatically access the INGV earthquake database allowed in

2016 the release of a completely new version of the INGVterremoti App, finally distributed not only for iOS but also for Android. Among the main new features is the ability to consult seismicity since 1985.

In 2022, the iOS version (and in the following months also the Android version) was completely rewritten and deeply renewed in graphics and released in the Stores. The user interface was changed to a cleaner and more intuitive design, making it accessible to users of all levels of technological expertise. The interface prioritises ease of navigation, ensuring that users can quickly access the information they need during critical moments.

Changes have also been made on the map interface that displays earthquake data in a simpler way in terms of symbology and interaction. Users can explore recent earthquake events, view their location on the map, and access detailed information about each earthquake on the information pages of the portal http://terremoti.ingv.it.

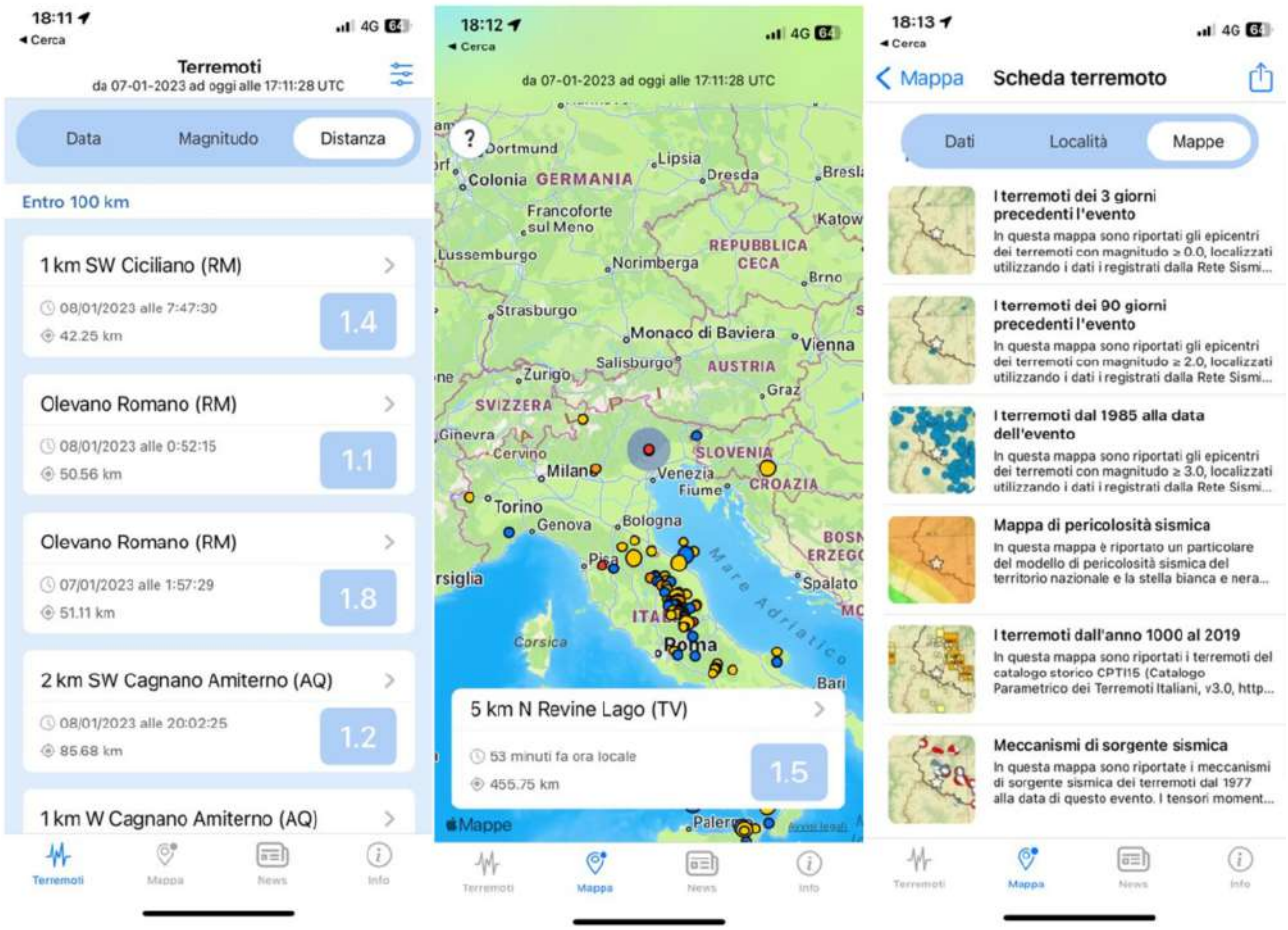

Fig. 1 – The user interface of the latest version of the INGVterremoti App. The figure shows the list of the latest earthquake events, the corresponding map, and a sample of the information available for each earthquake.

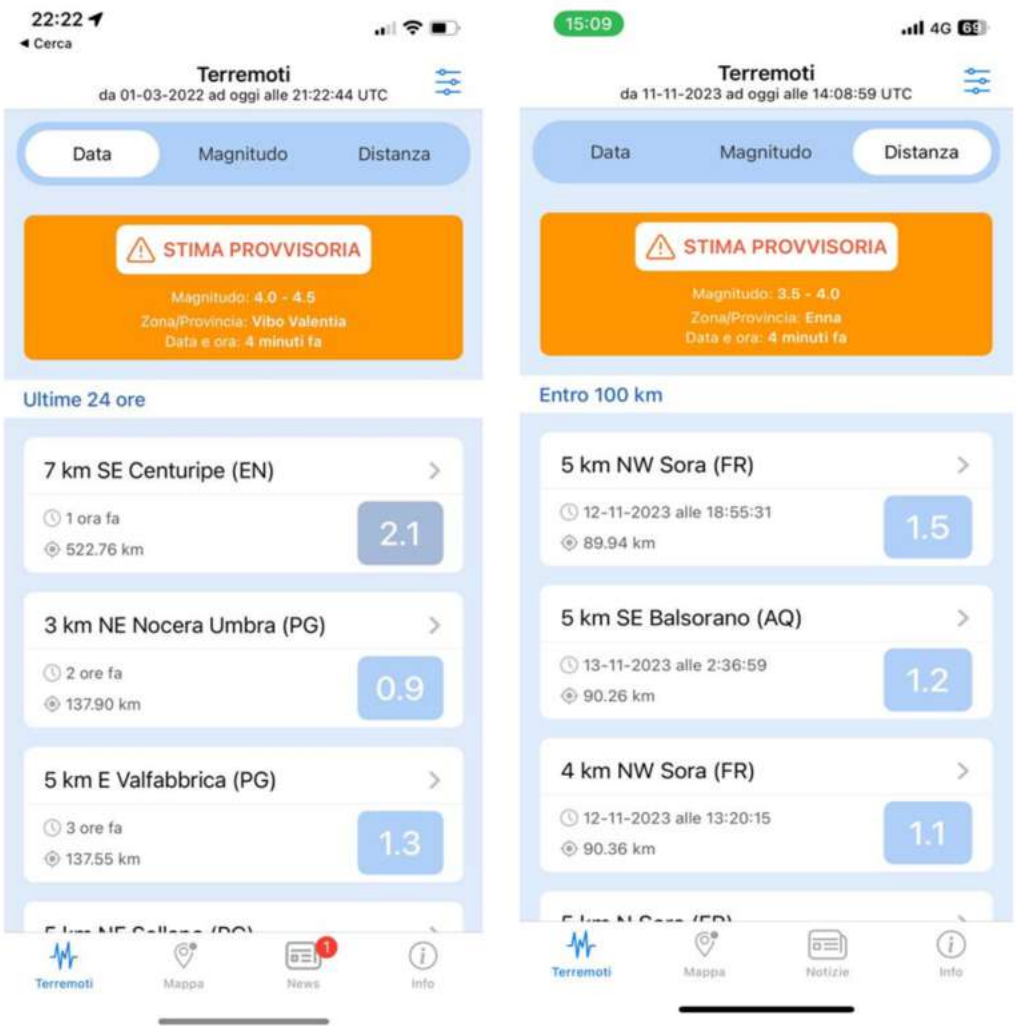

Fig. 2 – Two examples of the "provisional estimate" message displayed in the list of latest earthquakes in the App interface.

Fig. 3 – A card posted on INGVterremoti social media to launch the latest version of the App. It also features QR codes to download the two versions for IOS and Android.

The most important change in recent years is the publication of automatic localizations (provisional estimate) for events of magnitude greater than 3 occurring over the national territory, including coastal and border areas. Only events that have good localization parameters are published to avoid false events and Italian volcanic areas are excluded, for the moment.

The message of the provisional estimate reports the same information already published since 2018 on the Twitter channel @INGVterremoti and on the portal http://terremoti.ingv.it: the time of the event, a magnitude interval, the epicentral zone.

In recent months, work is being done to include in the next version of the App a push notification service that is highly requested by users. The service is currently in an advanced testing phase and will provide early warnings about major earthquakes, ensuring that users receive instant notifications about seismic activity in their region. The notification system will be customizable and will allow users to set parameters based on magnitude and proximity to their location, ensuring personalised and relevant updates.

References

Comunello, F., Polidoro, P., Lauciani, V., Mulargia, S., and Casarotti, E. (2015). “No misunderstandings during earthquakes: Elaborating and testing a standardized tweet structure for automatic earthquake detection information,” in ISCRAM 2015 Conference Proceedings 12th International Conference on Information Systems for Crisis Response and Management, (Kristiansand, Norway University of Agder (UiA)). Editors M. Büscher, T. Comes, and A. Hughes 7, 2411–3387.

Pignone, M., Nostro, C., Amato, A., Casarotti, E., and Piromallo, C. (2012). The INGVterremoti blog: A new communication tool to improve earthquake information during the Po Plain Seismic sequence. Ann. Geophys. 55, 42. doi:10.4401/ag-6179

Pignone M, Amato A, Nostro C, Casarotti E, Meletti C, Quintiliani M and Lauciani V (2022), Public earthquake communication in Italy through a multisource social media platform: The INGVterremoti experience (2010–2022). Front. Earth Sci. 10:1003867. doi: 10.3389/feart.2022.1003867

Corresponding author: maurizio.pignone@ingv.it

Trust in authorities and experts as shaping factor of risk perception

R. Russo[1], M. V. Gargiulo[1], R. Iorio[2], G. Cavalca[2], P. Capuano[1]

[1] *Università degli Studi di Salerno, Department of Physics "E.R. Caianiello", Fisciano (SA), Italy*
[2] Università degli Studi di Salerno*, Department of Political and Social Studies, Fisciano (SA), Italy*

In September 2019, the United Nations Secretary-General, António Guterres, remarked that our global community is experiencing a significant challenge known as 'Trust Deficit Disorder'. He noted a decline in people's trust in political institutions, a growing polarization, and the increasing prevalence of populism.

The decline in trust among European and non-European citizens is spanning various institutional levels and is a concerning aspect of the turbulent times experienced in Europe and beyond.

In such a context, trust plays a pivotal role in all facets of disaster resilience, encompassing the relationships between citizens and institutions, citizens and experts, policymakers and experts, and among different governance levels. Risk perception arise from an intricate interplay involving individuals, communities, institutions, and experts.

The H2020 CORE (sCience and human factOr for Resilient sociEty) project conducted a survey whose main scope is to understand the role of trust in scientific experts (virologists, geoscientists, biologists, and experts in general in the disaster resilience field) in determining citizens' risk perception. The tool is also targeted to disseminate proposed strategies to policymakers and practitioners useful to increase social acceptance of emergency procedures and risk mitigation actions. The CORE questionnaire was developed using the SurveyMonkey tool and was designed to explore the connection between trust in authorities and experts and risk perception, specifically concerning various risks such as earthquakes, tsunamis, pandemics, flash floods, industrial accidents, wildfires, and terrorist attacks. It was available in multiple languages, including Italian, English, French, German, Hebrew, and Tagalog.

The survey questions were catalogued in three different blocks, i.e. *trust in Authorities and experts*, *risk perception*, and *disasters' preparedness*. A fourth block of questions, useful to stratify the sample, concerns *socio economic and demographic characteristics*.

Based on the existing literature in the investigated topics, we expect that data analysis will reveal the significance of trust in institutions, including government authorities, the national health system, enforcement authorities, rescue authorities, and NGOs, as well as scientific experts. Thus, it should highlight the central role of trust in shaping risk perception. The ultimate goal of the research is to promote the development of a two-way trust: from citizens to institutions, from experts to citizens, and vice versa. This aims to establish a collaborative framework for effective action in reducing and preparing for disaster risks, and fostering the behavioral change.

References

Algan, Y., Cohen, D., Davoine, E., Foucault, M., & Stantcheva, S. (2021) - Trust in scientists in times of pandemic: Panel evidence from 12 countries. Proceedings of the National Academy of Sciences, 118(40), e2108576118, https://doi.org/10.1073/pnas.2108576118.

Bronfman, N. C., Cisternas, P. C., López-Vázquez, E., & Cifuentes, L. A. (2016) - Trust and risk perception of natural hazards: implications for risk preparedness in Chile. Natural hazards, 81, 307-327, https://doi.org/10.1007/s11069-015-2080-410.1007/s11069-015-2080-4

Wachinger, G., Renn, O., Begg, C., & Kuhlicke, C. (2013) - The risk perception paradox—implications for governance and communication of natural hazards. Risk analysis, 33(6), 1049-1065, https://doi.org/10.1111/j.1539-6924.2012.01942.

Acknowledgements

The present abstract has been produced for the H2020 CORE (sCience and human factOr for Resilient sociEty) project that has received funding from the European Union's Horizon 2020 research and innovation programme under grant agreement No 101021746.

Corresponding author: rarusso@unisa.it

Seismic risk communication in Europe over the last two decades

G. Musacchio[1], A. Saraò[2], S. Falsaperla[3], A. Scolobig[4]

[1]Sezione di Milano, Istituto Nazionale di Geofisica e Vulcanologia (INGV), Italy
[2]Istituto Nazionale di Oceanografia e di Geofisica Sperimentale (OGS), Italy
[3]Sezione di Catania, Osservatorio Etneo, Istituto Nazionale di Geofisica e Vulcanologia (INGV), Italy
[4]Institute for Environmental Sciences, University of Geneva, Switzerland; Equity and Justice Group, International Institute for Applied Systems Analysis, Austria

Introduction

Risk communication is a key component of risk management. It can raise risk awareness, increase preparedness and promote the adoption of protective measures before, during and after disaster events. To enable risk reduction and resilience, risk communication should be a two-way, dynamic and interactive process, rather than a one-way transfer of information from experts to citizens.

Since the Seveso Directive I (1982), international guidelines such as the Yokohama Strategy (IDNDR, 1994), the Hyogo Strategy (UNISDR, 2005) and the Sendai Framework (UNISDR, 2015-2030) have recognized the potential of risk communication to promote community empowerment. From the Yokohama Strategy to the Sendai Framework, communication approaches have evolved from the prevailing one-way model to more comprehensive transdisciplinary strategies that envision working directly with communities at risk to motivate them to take precautionary action. The Sendai Framework promotes communication approaches that are tailored to the needs and capacities of different groups and communities. It emphasizes the importance of a whole-of-society approach to risk communication that involves all stakeholders, including governments, civil society, the private sector, academia, the media and communities. Effective communication requires different strategies for each disaster phase: mitigation, preparedness, response and recovery. An analysis of risk communication strategies can be found in the mid-term review of the implementation of the Sendai Framework (United Nations Official Documents, 2023). Nevertheless, an in-depth analysis of earthquake risk communication practices is still a research gap. This study aims to fill this gap by focusing on seismic risk communication and its development in Europe.

Methodology and analysis

We applied the scoping review method (see Musacchio et al., 2023 and reference therein) and structured our analysis around the following questions: “What are the main characteristics of earthquake risk communication practises and research in Europe?” and “Have they changed over time?”. To answer these questions, we analysed selected publications from three scholar databases, i.e., Scopus, Web of Science and Google Scholar, to obtain the most comprehensive overview of scientific publications.

Before beginning our analysis, we examined how the literature on seismic risk communication has evolved over time, starting in 1970. The Google Scholar database shows that the number of

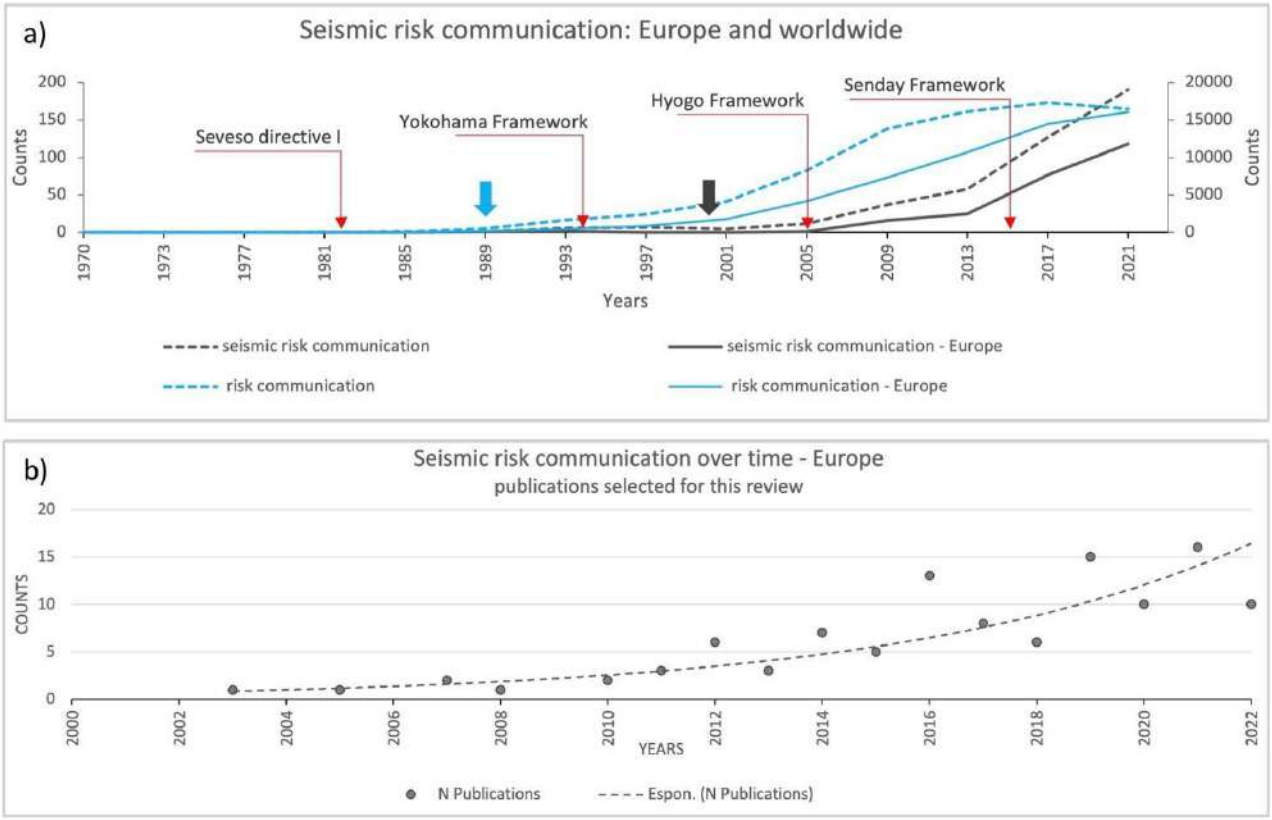

Fig. 1 – a) Publications on seismic risk communication over time. Raw data from Google Scholar database searches according to the strings listed in the text are plotted for all risks (right y-axis) and seismic risk communication (left y-axis) in Europe and worldwide; b) publications shortlisted for this review study.

publications increased significantly after the year 2000 (Fig. 1a), whereas it was negligible before. Therefore, we filtered out publications with the following terms in the period 2000-2022 (Fig. 1b): seismic risk communication; earthquake risk communication; seismic risk education; earthquake risk communication; educational seismology; seismic risk education campaign(s); seismic risk awareness campaigns. Other criteria included peer-reviewed full-text publications in English and case studies from European countries. Some additional documents were found via citations in the selected publications.

We shortlisted 482 documents that underwent further screening after reading the title, abstract or main text to remove duplicates, grey literature (conference proceedings, abstracts, reports, dissertations, web documents, magazine/newspaper articles), documents not strictly focused on earthquake risk communication or not dealing with case studies in Europe. Finally, 109 publications were considered for the scoping review (see Musacchio et al., 2023 for more details).

The 109 selected publications were examined on the basis of six key aspects of risk communication (Fig. 2), namely when the communication takes place, who communicates what to whom, why and how. We divided the publications among all co-authors in order to be able to read and categorise them in detail.

Results

The interest of the scientific literature in the communication of seismic risks seems to begin shortly after the Hyogo framework (Fig. 1a). The first paper in our selected collection was published in 2003 (Fig. 1b); the analysed publications were mainly published in geoscience journals (45%), risk or disaster journals (18%) and books (17%). The main topics covered are disasters, preparedness, risk perception and social issues, and the most frequently mentioned country is Italy. Following the structure of the key questions described in the previous section (Fig. 2), we summarise the main findings below (more details are reported in Musacchio et al., 2023).

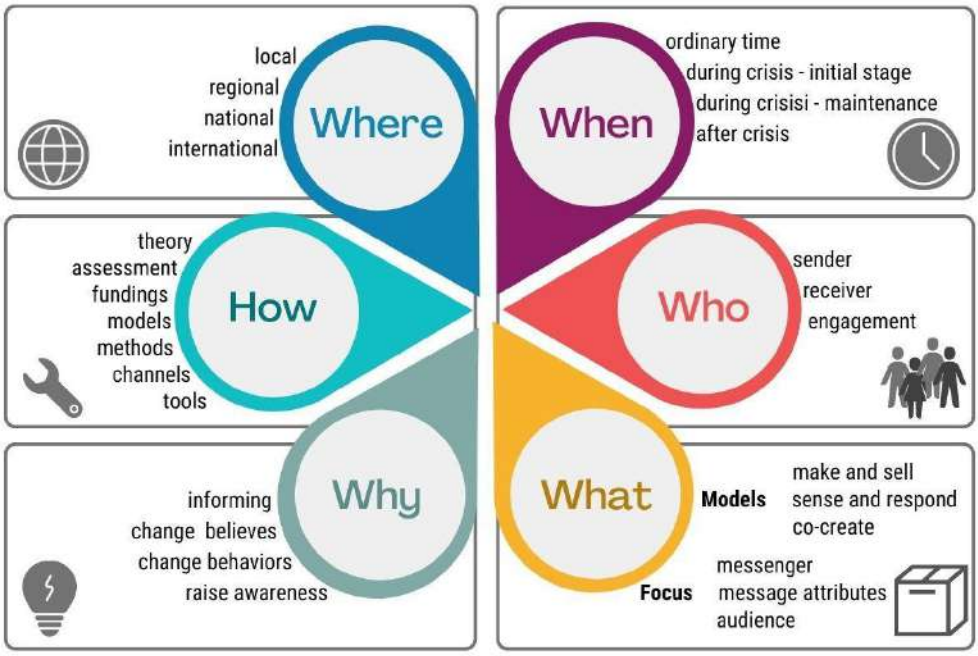

Fig. 2 – Issues under investigation for the screening of the selected publications.

When - The overwhelming majority of the selected documents (75%) dealt with earthquake risk communication in ordinary time (Fig. 3a) i.e., in the pre-event phase of the disaster risk management life cycle.

Who - Research centres and universities are among the main senders/organisers of communication activities (72%). Pupils and students (40%) and citizens (27%) are the main recipients. Recipient engagement is described in about half of the publications (46%). The vast majority use a joint development or implementation model between experts and the public, while only a few publications describe a joint evaluation model.

What - Since 2013, the two-way (43%) communication model (see Stewart et al., 2023 for description of the communication models) has been the most widely used (Fig. 3b). However, the one-way model is still mentioned in a fairly large number of publications (29%). Interestingly, the three-way model ("instruct and co-create") was adopted by less than 20% of authors, although its prevalence increased over time.

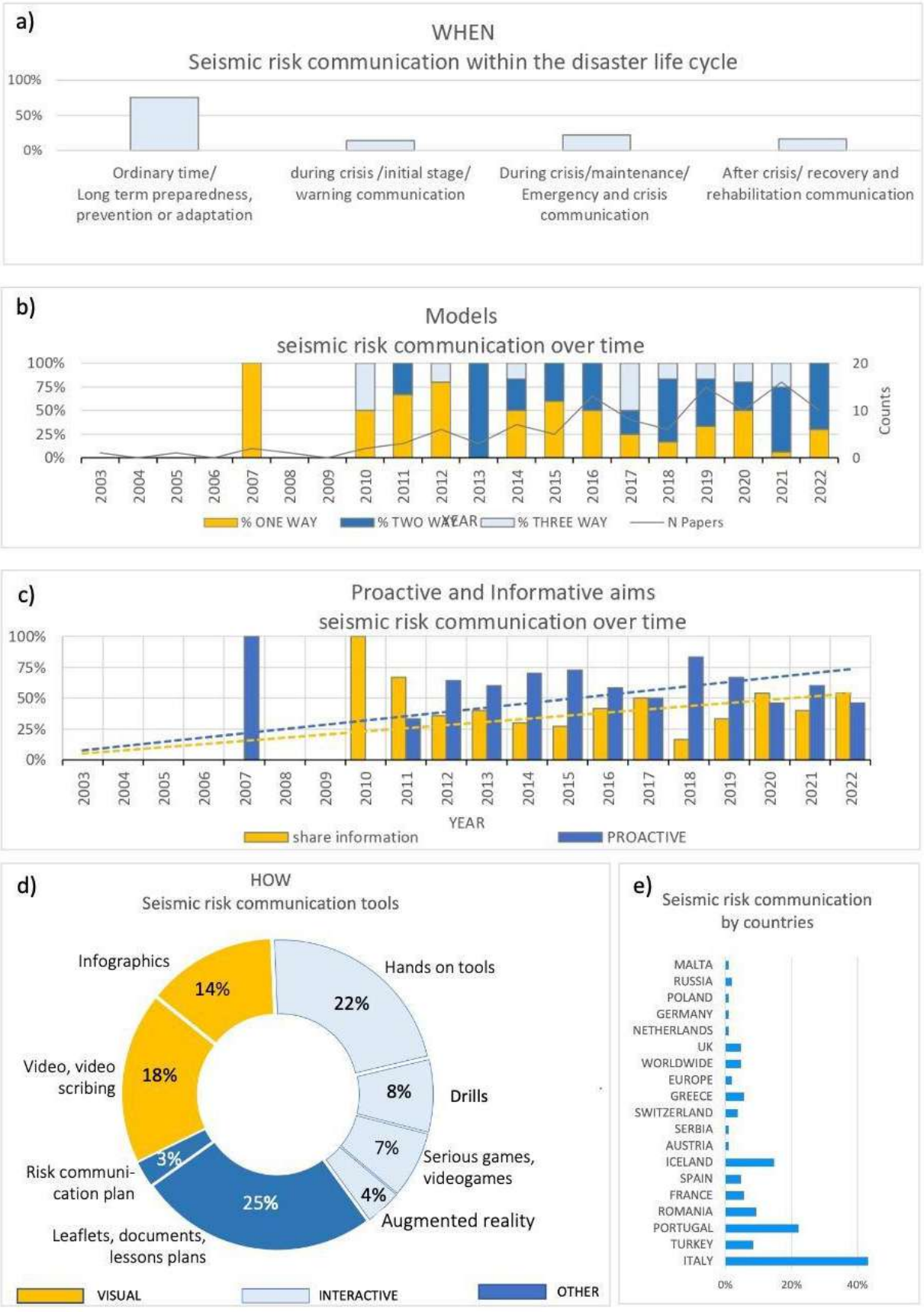

Fig. 3 – a) The selected publications on seismic risk communication within the disaster life cycle; b) the communication models used over time; c) the communication objectives mentioned in the publications; d) the tools used for communication; e) Countries of the case studies reported in the selected publications.

Why - The stated goals of seismic risk communication (multiple responses) are to share information (62%), raise awareness (47%), change behaviours (27%), change beliefs (16%), and increase preparedness (4%). Over time, communication has become more proactive than informative (Fig. 3c).

How - Interactive and visual language tools were mentioned most frequently, regardless of the temporal distribution (Fig. 3d). Serious games and augmented reality have only appeared in our data sample since the beginning of 2016. Personal communication (face-to-face, 39 %) far outperformed the internet (7 %) and even the mass media (4 %). However, the evolution of communication techniques is clearly evident in the use of social media, which enables rapid interpersonal communication and collaboration even during disasters (e.g., Saraò et al., 2023).

The methods used for communication practices were mostly surveys (18%) and classroom activities (16%), while focus groups, outreach events and interviews were the least used. However, multiple methods were reported in 24% of publications.
Risk communication research and practice is mainly funded by public international (29%) and national (26%) institutions. Only about half of the publications report on the evaluation of the efficiency/performance of seismic risk communication. The majority of publications (80%) do not explicitly formulate their theoretical basis. When theories are mentioned, deficit and behavioural models are the most frequently cited.

Where - Seismic risk communication started at the local level with the documentation of practices implemented in different countries and then took on an increasingly international character over the years. Seismic risk communication in Europe is unevenly distributed across countries, with Italy having the highest number of documents in the analysed dataset, followed by Portugal, Iceland, Romania, Turkey, France and Greece (Fig. 3e). This could be related to our criteria for the selection of documents and does not necessarily indicate a lack of interest in seismic risk communication. However, with regard to Italy, we mention two earthquakes that had a strong impact on seismic risk communication in Italy. These are the 2002 earthquake in San Giuliano di Puglia (Mw=5.7), which led to the collapse of a school and the death of 26 children and their teacher, and the 2009 earthquake in L'Aquila (Mw=6.3) and the well-known legal dispute associated with it.

Conclusions

Although earthquakes are a threat in many countries and considerable resources have been invested in safety regulations, communities at risk often lack awareness and preparedness. In this study, we reviewed the literature on earthquake risk communication in Europe published since 2000. We analysed the approaches, messages, tools and channels used for communication and how they have changed over time. The main objectives of seismic risk communication over the last two decades were to share information, raise awareness, change behaviours/beliefs and increase preparedness. Communication has mainly taken place in the pre-crisis phase of a disaster's life cycle, when risk awareness and the ability to cope with hazards can be effectively built. Pupils, students and citizens were the main recipients of the communication activities.

Over the years, two-way, transdisciplinary and bottom-up communication models have prevailed over the one-way model. In addition, communication has increasingly aimed at encouraging proactive behaviour rather than simply informing the public. Face-to-face conversations, hands-on

activities and serious games are the main tools used to engage with the public. The findings also show the growing importance of social media to reach different audiences, provide timely and actionable information in times of crisis and engage citizens. Furthermore, communication about seismic risks is practised in different ways in different countries.

As with any review study, we recognise that the results and their interpretations apply only in the context of the selected scientific literature, which does not include grey literature and documents in languages other than English. Nevertheless, we believe that the main features we have identified provide an interesting overview of the topic and can serve as a reference for future studies. The future agenda for seismic risk communication should focus on building trust with the public, tailoring communication to their needs and moving towards a three-way model of seismic risk communication that engages stakeholders from different sectors - academia, business, government and civil society — for the common goal of earthquake safety and seismic resilience.

References

Musacchio G.; Saraò A.; Falsaperla S.; Scolobig A.; 2023: A scoping review of seismic risk communication in Europe. Front. Earth Sci. 11:1155576. https://doi.org/10.3389/feart.2023.1155576

Saraò A.; Tamaro A.; Sandron D; Slejko D.; Rebez A.; 2023: On the crowdsourcing of macroseismic data to characterize geological settings. Int. J. Dis. Risk Red. 96: 103934, https://doi.org/10.1016/j.ijdrr.2023.103934

Stewart I.S.; Sevilla E.; Barragán K.; Yahya Menteşe E.; 2023: Disaster risk communication requires dissemination, dialogue and participation. Nat. Rev. Earth. Environ 4. https://doi.org/10.1038/s43017-023-00506-w

United Nations Official documents (2023). Main findings and recommendations of the midterm review of the implementation of the Sendai framework for disaster risk reduction 2015–2030. https://www.undrr.org/publication/report-main-findings-and-recommendations-midterm-review-implementation-sendai-framework

Corresponding author: asarao@ogs.it

Schools-tailored activities to communicate seismic risk

M. G. Sestito[1], S. Zidarich[1], E. Ferrari[1], M. Longoni[1], F. Varchetta[1], F. Meroni[1], S. Lovati[1], D. Piccarreda[1], L. Zarrilli[2], S. Puccillo[2], M. Massa[1], S. Mirenna[1], A. Goretti[3], G. Musacchio[1]

[1] Sezione di Milano, Istituto Nazionale di Geofisica e Vulcanologia (INGV), Milan, Italy

[2] Sezione Irpinia, Istituto Nazionale di Geofisica e Vulcanologia (INGV), Milan, Italy

[3] Dipartimento della Protezione Civile (DPC), Rome, Italy

INTRODUCTION

Risk communication is a crucial element in the management of risks: it has a great potential to raise awareness, increase preparedness, and promote legislative interventions.

Uncertainty, lack of scientific knowledge, misunderstanding, misinformation, cognitive bias, and distrust in authorities are among the major threats of effective risk communication. Nonetheless recent studies have highlighted that seismic risk communication practices have been increasing during the last decades although still more work needs to be done (Musacchio et al., 2023).

There are different models of risk communication: the majority refer to the public understanding paradigm, in which information are given in a “one-way” direction to the public, and to the public engagement paradigm, in which stakeholders are meant to participate in the building process of knowledge. In preparing a risk communication campaign, the school target has revealed as one of the most important to address, given its high potential to influence a risk-resilient society (Musacchio & Solarino, 2019).

In this paper, activities to communicate seismic risk communication specifically designed to engage middle school students are presented. Science communication with teen audiences has a unique challenge: there is a fundamental need to design activities that can help them feel involved.

The work presents the framework within which the activity is done. It describes the communication goals, learning methodology and present some of the activities that have been included in a format suitable for open-door outreach events. The activities discussed in this work were tested within two open-doors events that were held at the Milano division of the National Institute for Geophysics and Volcanology in the year 2023.

BACKGROUND FRAMEWORK

In Italy according to OPCM 3274 of 2003, 4 seismic zones were established. Highest hazard areas are spread along the Apennine, in the south and eastern part of the country. The Lombardy region is among the areas where seismic hazard is relatively low. Most of its land belongs to Seismic Zones 3 and 4 (Fig. 1).

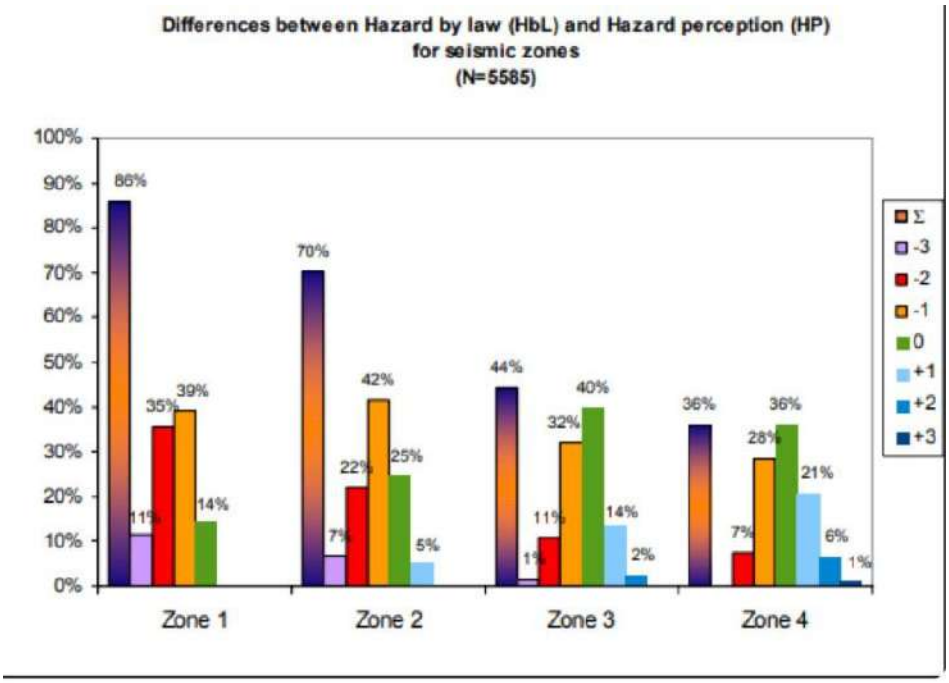

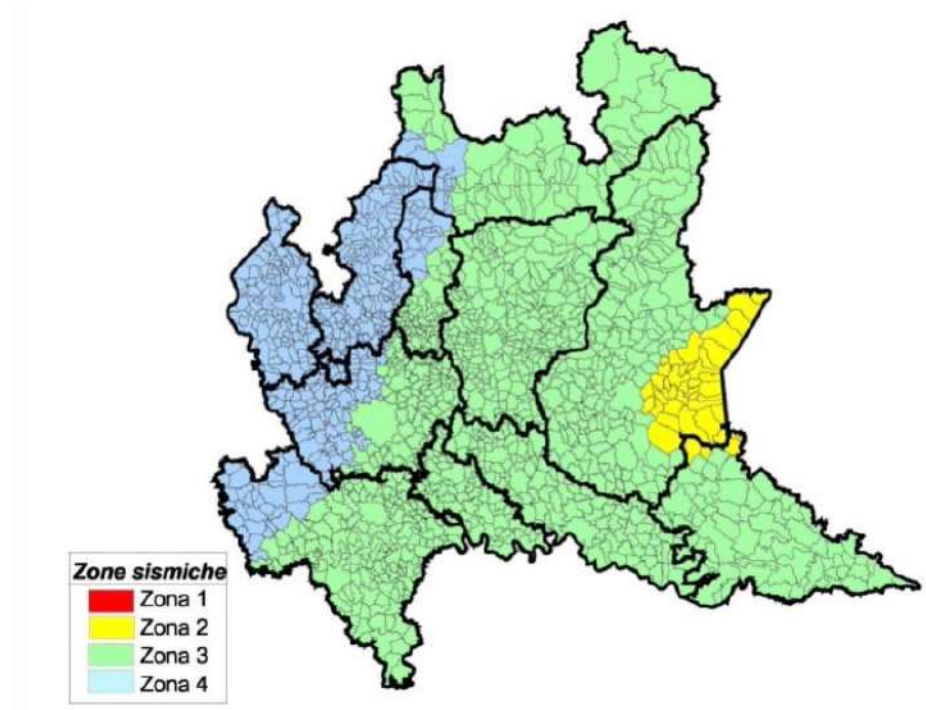

Fig. 1: Real and perceived seismic hazard. The diagram presents the frequency distribution of differences in hazard perception for Italian seismic zonation (Crescimbene et al., 2015); the map displays the seismic classification of the Lombardy region where no more than 40% of the population perceives seismic hazard properly.

The Milan Metropolitan area is located in the seismic zone 3 at the lower limit of the peak ground acceleration range of 0.05g-0.075g. This range is expected to cause damage to non-structural elements of buildings, which is typically underestimated in many European countries (Ferreira et al., 2021). Most of the buildings and infrastructures are likely to be vulnerable to such damage as specific measures are not provided by the building code.

The Milan metropolitan area's relatively low-risk level is not in line with its real risk, which affects densely populated areas with strategic infrastructure. This brings the earthquakes' issue prone to be mostly underestimated. Recent studies highlight a low-risk perception (Crescimbene et al., 2015; Crescimbene et al., 2016) that might cause communities to be unprepared to cope with the hazard.

Two earthquakes of low magnitude have shaken the area surrounding Milan in the last two years, which people did not expect but were clearly felt. On December the 17th 2020 a Mw3.8 earthquake occurred southwest of Milan next to the town of Pero; one year later, on December the 18th 2021 a Mw3.9 earthquake occurred northeast of Milan next to the city of Dalmine. They both drew attention on the seismic risk of the area. But since risk perception is still low the community is likely to be heavily unprepared.

The school context also shows the underestimation of seismic risk. The perception of seismic hazard in schools' staff and students is mostly incorrect (Bandecchi et al., 2019). Moreover there is a lack in staffs' competence to educate students to risk prevention and textbooks do not provide specific information on the topic (Musacchio et al., 2020). For these reasons, it is critical for the seismic risk subject to be more included in the school programs, and to engage students in risk communication campaigns, so they can contribute to promote awareness and preparedness on seismic risk in the society.

METHODS

The Milano Division of the Istituto Nazionale di Geofisica e Vulcanologia annually hosts schools and undertakes with them activities highly interactive mostly framed in the serious gaming approach. In this work we select educational laboratories and activities to describe three aspects of seismic risk: (1) the role of seismic site effects on the ground shaking, (2) buildings response to ground shaking and (3) key-issues on community preparedness.

The role of seismic site effects on the ground shaking: the Site-effects laboratory

Seismic site effects are a cause of damage that is often unknown by the general public. Geological, geomorphological, and geotechnical conditions modify the amplitude and frequency of seismic motion as it propagates in the final layers of soil before reaching the surface. Lithostratigraphic (Cara et al., 2019) or topographic (Massa et al., 2014) amplifications or induced phenomena, such as landslides, avalanches, or the liquefaction of sandy soils are examples of seismic site effects. A recent example that has reached the public debate in the media occurred during the 2012 Emilia earthquake sequence (Emergeo working group, 2012).

During outreach events for the secondary school, we show models displaying some aspects of seismic site effects (Fig. 2a). Two seismometers installed into sand and gravel filled buckets are used to show lithostratigrafic seismic amplification. A jump by students simulates earthquake shaking and waveforms from the seismometer installed on soft soil (sand) are visually compared with those recorded on hard soil (gravel).

Soil liquefaction is shown with a model of buildings at a small scale placed on top of water-saturated sand. A small engine shakes the sand until the typical shear strength is drastically reduced by the increasing pore pressures. The phenomenon can be observed by the appearance of water that overturns scaled models of buildings.

Buildings response to ground shaking: the Shake-It! Laboratory

The general public often asks questions such as “why do buildings collapse?”. To explore in depth the concept of vulnerability to seismic ground shaking, a laboratory about buildings’ resonance has been implemented. The dynamic characteristics of buildings play an important role in predicting their seismic behaviour and therefore their vulnerability. This parameter is highly important during an earthquake, since, if an earthquake carries significant energy near the natural period of the structure, or if the foundation’s soft soil has its predominant period near the structure’s period, the physical phenomena of resonance could happen (Mucciarelli et al., 2002).

In the “Shake it!” laboratory key aspects of this concept have been addressed highlighting that the largest oscillations occur when earthquake frequency matches the building’s natural frequency. A metal structure building-model placed on a unidirectional small-scale educational shaking table was used to visualize the downscale phenomenon of earthquake building resistance. A wi-fi accelerometer placed on top of the building, and a second one on the platform, that Is at the base of the building-model, were used to measure the ground-shaking displayed on a monitor. A real earthquake and a synthetic sinusoidal signal, in a 2Hz to 10Hz frequency range, were used as input for the shaking table. While the real signal was used to highlight the difference between the shaking at the ground and that on top of the building, the synthetic sinusoidal allowed to visualize the phenomenon of the resonance (Fig. 2b).

After watching the shake table experiment the class was asked to make its own experiment. The building-model had to be done using spaghetti and marshmallows and the shake table was made by a cardboard platform on top of a small electrical engine. The challenge was to build the frame structure as tall and stable as possible. To have a more stable structure it was suggested to add braces. The building-models were placed on the shake-box to verify its seismic performance (Fig. 2c).

Key-issues on community prevention and preparedness: Videogaming activity

Risk communication must enhance both prevention and preparedness to a seismic event. These concepts could be summarized by two key questions:

-why should I care about seismic risk?

-what can I do to protect myself?

We used 3 interactive videogames to address the above questions. These videogames have been designed in the framework of the ENP-CP project on the Seismic Risk Sensibilization, and successfully used in interactive hybrid events for the schools (Goretti and Musacchio, 2022). We chose the games not only as a tool to better capture the teenagers' attention but also to aid them get across some otherwise heavy-handed subjects.

The first question was addressed with the videogame "Catch the Plate" that is based on Plate Tectonics. The activity helps acknowledge that earthquakes are a natural phenomenon. Emphasis is placed on the knowledge of the territory where one lives, the geological features characterizing it and therefore the seismic hazard.

The second question was answered by highlighting the need to be prepared as a mean to prevent damage and be able to cope with emergency situations. Two games address this question and provide suggestions concerning those actions that can make the difference in case of an earthquake. The game "Make your room ready" ask the players to decrease seismic vulnerability in the places where youth spend most of their time during the day (i.e., bedroom, classroom). It stands upon three keywords matching crucial simple actions that can reduce seismic vulnerability to non-structural elements inside a building, and namely move-protect-secure (Ferreira et al., 2020).

The game "Emergency bag" highlights that as we live in a seismic country, it is fundamental to know how to cope with the issue of evacuation in case of an earthquake. The April 6th, 2009, L'Aquila event is just an example of an earthquake catching people off-guard in the middle of the night. Thus, it is crucial to have an emergency bag to be ready to go out of a building with only the most useful stuff. The game wants to make young people think about proper objects to stay a few hours away from home.

The take-home message is to be ready for a seismic event means to know where I live and how to act in the most efficient and safe way.

Fig. 2: Snapshots of the activities implemented in 2023 at the Milano Division of the Institute of geophysics and Volcanology during the events of ScienzAperta for schools and the Week of Planet Earth. From top to bottom: "Site-effects" laboratory: analogue models for the lithostratigraphic amplification and liquefaction (a); Shake it!" laboratory: a ground shaking simulation using an educational small-scale shaking table (b) and an example of a marshmallow building frame structure placed on the shake box (c); "Videogaming" activity: prevention and preparedness issues addressed with videogames (d).

CONCLUSION AND DISCUSSION

In this paper, a format for seismic risk communication specifically designed to engage middle school students is proposed, with the aim to increase scientific knowledge, and promote the awareness in the community about the seismic risk.

In the Lombardy region seismic hazard is relatively low since most of its land belongs to Seismic Zones 3 and 4. The relatively low hazard level of the Milan Metropolitan area is apparently at odds with the actual risk. Moreover, in the last two years the area surrounding Milan was shook by two low magnitude earthquakes that people clearly felt, and that were yet unexpected.

The Milano Division of the Istituto Nazionale di Geofisica e Vulcanologia is engaged in science communication activities that are intended for a school audience. Although schools are referred to as a strategic public in risk communication to build a risk-resilient society, topics addressing seismic risk are underestimated in educational programs. It's critical to invest more in the design of effective seismic risk communication campaigns for the school target.

The format described in this paper includes three activities: in the Site effects laboratory we show models displaying some aspects of these phenomena; in the Shake-it! laboratory seismic vulnerability is discussed through an experiment on scaled-down shaking table model and by letting the students reproduce it with marshmallows, spaghetti and a cardboard shaking-table; finally, we propose video games designed to learn where do earthquakes usually occur, how to secure the house from ground shaking and how to get ready for a seismic emergency. The three activities share features responding to modern communicative and didactic methodologies, inspired on active learning, that has proven to be one of the most effective in enhancing students' capability in achieving an in-depth knowledge in STEM disciplines (Freeman et al., 2013; Michael, 2006). Interactivity, team play, problem-solving, hands-on activities, multiple communicative channels, from graphic to linguistic, are the techniques used to contrast the students' disengagement and by doing this to adapt the seismic risk communication campaign to the specific target. All these techniques stood on the fruitful interaction between students and scientists.

Each activity had a focus on a single aspect of the seismic risk, to raise from time-to-time awareness on the different factors involved in seismic risk: the site effects, the buildings vulnerability, and the preparedness were addressed one by one allowing students to strengthen their understanding of specific scientific concepts. The digital game-based learning proposed in the preparedness laboratory has shown as one of the most effective ways to communicate with the so called "millennial" students, a digital native generation with specific concentration attitudes (Roelh et al., 2013).

The activities were tested within the two open-doors events that the Milano Division of the Istituto Nazionale di Geofisica e Vulcanologia offered to schools in the year 2023 hosting about 200 students and teachers.

An excellent participation among students and teachers was recorded, with students actively collaborating with each other during hands on activities and showing a great curiosity towards the seismological models. Videogames confirm their effectiveness in capturing the teenagers' attention, aiding them to get across some otherwise heavy-handed subjects. A recap-game was used to understand to what extent the proposed concepts were grasped: students had to fill a text with words representing the topics addressed during the activities. The results indicate the efficacy of this methodology to communicate risk to schools and reiterate the need to increase the communication practices for this specific form of risk.

Acknowledgements

The videogames presented in this work have been implemented within the ENP-CP European Neighbourhood Policy - Civil Protection (ENP-CP) EU-funded project. The activities are a follow-up of the "Know your city, Reduce seISmic risK through non-structural elements" (KnowRISK) DG-ECHO program funded project. They are also based on the exhibition "Terremoti: Attenti agli Elementi!-Dettagli che salvano la vita" that was presented at the 2019 edition of the Genova Science festival.

References

Asteris P. G., Tsaris A. K., Cavaleri L., Repapis C. C., Papalou A., Di Trapani F., & Karypidis D. F. (2016). Prediction of the fundamental period of infilled RC frame structures using artificial neural networks. Computational Intelligence and Neuroscience, 2016, 20-20.

Bandecchi A. E., Pazzi V., Morelli S., Valori L., & Casagli N. (2019). Geo-hydrological and seismic risk awareness at school: Emergency preparedness and risk perception evaluation. International journal of disaster risk reduction, 40, 101280.

Cara F., Cultrera G., Riccio G., Amoroso S., Bordoni P., Bucci A., ... & Mancini M. (2019). Temporary dense seismic network during the 2016 Central Italy seismic emergency for microzonation studies. Scientific data, 6(1), 182.

Crescimbene M., La Longa F., Camassi R., & Pino N. A. (2015). The seismic risk perception questionnaire. Geological Society, London, Special Publications, 419(1), 69-77.

Crescimbene M., La Longa F., Pessina V., Pino N. A., & Peruzza L. (2016). Seismic Risk Perception compared with seismic Risk Factors. European Geosciences Union General Assembly.

Emergeo Working Group. (2013). Liquefaction phenomena associated with the Emilia earthquake sequence of May–June 2012 (Northern Italy). Natural Hazards and Earth System Sciences, 13(4), 935-947.

Ferreira M.A., Oliveira C.S., Lopes M., Mota de Sá F., Musacchio G., Rupakhety R., Reitano D., Pais I. (2021) Using non-structural mitigation measures to maintain business continuity: a multi-stakeholder engagement strategy. Annals of Geophysics, 64, 3, https://doi.org/10.4401/ag-8559

Freeman S., Eddy, S. L., McDonough M., Smith M. K., Okoroafor N., Jordt, H., & Wenderoth M. P. (2014). Active learning increases student performance in science, engineering, and mathematics. Proceedings of the national academy of sciences, 111(23), 8410-8415.

Goretti A., and Musacchio G. (2022). Report on the Interactive Hybrid Event@Schools on Seismic Risk Sensibilisation, Activity 4.3 Participation to MS awareness and educational campaigns, WP4 Strengthening awareness raising initiatives and educational campaigns in the area of seismic risk, Preparedness action for European Neighbourhood Policy countries – Civil Protection Project (ENP-CP). Agreement No. ECHO/SUB/2019/B1/816935

Massa M., Barani S., & Lovati S. (2014). Overview of topographic effects based on experimental observations: meaning, causes and possible interpretations. Geophysical Journal International, 197(3), 1537-1550.

Mayhew M. A., & Hall M. K. (2012). Science Communication in a Café Scientifique for High School Teens. Science Communication, 34(4), 546-554. https://doi.org/10.1177/1075547012444790

Michael J. (2006). Where's the evidence that active learning works?. Advances in physiology education.

Mucciarelli M., Masi A., Gallipoli M. R., Harabaglia P., Vona M., Ponzo F., & Dolce M. (2004). Analysis of RC building dynamic response and soil-building resonance based on data recorded during a damaging earthquake (Molise, Italy, 2002). Bulletin of the Seismological Society of America, 94(5), 1943-1953.

Musacchio G., Eva E., Crescimbene M., Pino N. A., & Cugliari L. (2021). A protocol to communicate seismic risk in schools: design, test, and assessment in Italy. Annals of Geophysics.

Musacchio G., Falsaperla S., Solarino S., Piangiamore G. L., Crescimbene M., Pino N. A., ... & Accardo M. (2019). KnowRISK on seismic risk communication: The set-up of a participatory strategy-Italy case study. In Proceedings of the International Conference on Earthquake Engineering and Structural Dynamics (pp. 413-427). Springer International Publishing.

Musacchio G., Saraò A., Falsaperla S., & Scolobig A. (2023). A scoping review of seismic risk communication in Europe. Frontiers in Earth Science, 11, 1155576.

Roehl A., Reddy S. L., & Shannon G. J. (2013). The flipped classroom: An opportunity to engage millennial students through active learning. Journal of Family and Consumer Sciences, 105(2), 44.

Reference author: mariagiovanna.sestito@ingv.it

Seismic risk perception in italian hospitals: The role of non-structural elements

S. Zidarich[1], M.G. Sestito[1], M. Crescimbene[2], G. Musacchio[1], D. Reitano[3], D. Perrone[4], D. D'Angela[5], G. Magliulo[5]

[1] Sezione di Milano, Istituto Nazionale di Geofisica e Vulcanologia (INGV), Milan, Italy

[2] Sezione di Roma, Istituto Nazionale di Geofisica e Vulcanologia (INGV), Roma, Italy

[3] Osservatorio Etneo, Istituto Nazionale di Geofisica e Vulcanologia (INGV), Catania, Italy

[4] Università degli Studi del Salento, Lecce, Italy

[5] Università degli Studi di Napoli Federico II, Napoli, Italy

INTRODUCTION

The ENRICH (ENhancing the Resilience of Italian HealthCare and Hospital Facilities) project deals with seismic resilience of hospitals and healthcare facilities. It is a three-years project funded by the Ministry of University and Research as part of the major national interest programme, PRIN, 2022-2025, led by the University of Neaples Federico II and involving the Universities of Sannio and Salento, the Istituto per le Tecnologie della Costruzione of the National Research Council and the Istituto Nazionale di Geofisica e Vulcanologia.

Seismic performance of non-structural elements and their functional adaptability are the two pillars of ENRICH. However, since regulatory provisions are likely to become more effective if stakeholders are aware of the associated risks and benefits (Solarino et al. 2020; Musacchio et al. 2021), the project couple engineering technological advancement to risk perception studies.

Hospitals are at the forefront of responding to disasters, including those associated with earthquakes, providing essential medical care, public health services and coordination efforts to mitigate the impact of disasters on individuals and communities by providing immediate assistance to those affected. Furthermore, in addition to receiving and treating patients, they must be able to ensure prevention for any epidemics.

The disproportionate impact of earthquakes on critical structures such as hospitals can often be attributed to the inadequate seismic response of non-structural elements. While the structural integrity of buildings is crucial, the non-structural components and systems within such buildings play a significant role in ensuring the continued functioning of essential structures during and after an earthquake. Damaging these elements would mean hindering the overall functionality of healthcare facilities.

Risk perception is a key element in the definition and adoption of preventive countermeasures. To develop effective risk information and communication strategies, it is necessary to know risk perception and the factors that influence it (Slovic, 1987; Peters & Slovic, 1996; Renn, 2008).

METHODS AND RESULTS

The objective of this research was to investigate (1) how the healthcare facilities' staff perceives the seismic risk in their workplace and territory, (2) how they perceive the risk associated with the non-structural elements in the hospital buildings, and (3) what are in their opinion the main factors influencing risk. At this purpose, a mixed methodology that combines quantitative and qualitative techniques was adopted, consisting on a focus group and a survey, and it was proposed to the healthcare staffs in the pilot sited selected in the framework of the ENRICH project. The pilot sites were the Lecce healthcare unit, and the Caserta healthcare unit, both in the South of Italy. These two pilot sites are located in two different seismic hazard areas: Lecce is located in the low-to-moderate seismic hazard area 4, while the Caserta area is area 2, where strong earthquakes are possible.

The focus group was implemented in order to achieve an in-depth knowledge about the subject of seismic risk perception: it was offered a list of assessed questions, starting from the general topic of the personal experience with earthquakes and progressively went into detail about the seismic risk perception in the healthcare framework and the prevention issue, but encouraging the spontaneous contribution of participants. The analysis of data has followed the grounded theory framework, by applying a coding process to the text extrapolated from the discussion and creating general interpretative categories basing on that code (Sargent et al., 2016). The quantitative questionnaire was expressly designed to measure the seismic risk perception in healthcare staff: it includes 10 sections with questions evaluating the resilience of the hospital structure, of non-structural elements, of the territory, and of the staff itself, to score on a semantic differential for each item.

Results from preliminary analysis on the data collected indicate that there is an underestimation of the risk, both as regards the geographic areas, respectively Lecce city and Caserta city, and as regards the role of non-structural elements in determining the damage inflicted by an earthquake. However, the participants seem generally aware that the risk is underestimated, and the importance of prevention seems to be properly perceived. Moreover, both groups looked very curious, especially about geological and scientific issues, and eager to fill the knowledge gap by means of informative events and initiatives addressing specifically the seismic risk topic.

The aim of the ENRICH project by conducting this research is to actively involve the healthcare facilities' staff in the risk communication process, and to use the gathered data and suggestions in the developing of future risk communication strategies and campaigns, more effective and more targeted to the communities to address. One of the tasks scheduled by the project is the informative materials production, including that of a citizen-science app, and the design of

informative events in order to raise awareness towards the seismic risk and the non-structural elements resilience, in the healthcare framework and among the general public.

REFERENCES

Musacchio G., Eva E., Crescimbene M., Pino N.A., Cugliari L. (2021). A protocol to communicate seismic risk in schools: design, test and assessment in Italy. *Annals of Geophysics*, 64, 3, https://doi.org/10.4401/ag-8533.

Peters E., Slovic P. (1996). The role of affect and worldviews as orienting dispositions in the perception and acceptance of nuclear power. *Journal of Applied Social Psychology* 26(16):1427–1453.

Renn O. (2008). Risk governance: coping with uncertainty in a complex world. Earthscan, London, p. 110.

Sargent S., Samanta J., & Yelden K. (2016). A grounded theory analysis of a focus group study. *SAGE Research Methods Cases Health*.

Slovic P. (1987). Perception of risk. *Science* 236:280–285.

Solarino S., Amaral Ferreira M., Musacchio G., Rupakhety R., O'Neill H., et al. (2020). What scientific information on non-structural elements seismic risk people need to know? Part 2: tools for risk communication. *Annals of Geophysics* 2020; 63(Vol 63): 2.

Corresponding author: silvia.zidarich@ingv.it

TOPIC 3

APPLIED GEOPHYSICS FOR ENERGY, ENVIRONMENT AND NEW TECHNOLOGIES

Session 3.1

Energy transition and resources

GNGTS 2024

APPLIED GEOPHYSICS FOR ENERGY, ENVIRONMENT AND NEW TECHNOLOGIES

Session 3.1

Energy transition and resources

Convenors of the session:
***Michela Giustiniani* – mgiustiniani@ogs.it**
***Paolo Mazzucchelli* – paolo.mazzucchelli@aresys.it**
***Vincenzo Lipari* – vlipari@ogs.it**

Contributions recommended for this session:

- **Innovative geophysical technologies;**
- **Integration of geophysical methods;**
- **Petrophysical characterization of the subsurface;**
- **Geophysical data processing;**
- **Geophysical borehole logging;**
- **Geophysics to characterize georesources (i.e., Oil & gas, mining, geothermal, water);**
- **Geophysics for reaching the net zero carbon (i.e., CCS, hydrogen storage);**
- **Artificial intelligence techniques applied to Geophysics;**
- **Natural Hazard;**
- **Case studies.**

Geophysical prospecting is widely used to both identify and store natural resources underground.
Different investigation techniques characterize the subsurface with different resolutions and at
different depths, such as reflection and refraction seismic, gravimetric, magnetic, electrical methods.
These technologies and tools also contribute to the mix of strategies to address anthropogenic CO2 emissions and to achieve net-zero carbon emissions goals.
The session welcomes contributions that illustrate methodological innovations, processing methods, case studies and applications in the fields of exploration of georesources, as well as in the field of resource and greenhouse gas storage.

Sustainable geothermal energy for two Southern Italy regions: geophysical resource evaluation and public awareness

O. Amoroso[1], V. Giampaolo[2], M. Balasco[2], M. Blasone[1], D. Bubbico[3], P. Capuano[1], G. De Martino[2], M.V. Gargiulo[1], F. Napolitano[1], A. Perrone[2], S. Panebianco[2], R. Russo[1], V. Serlenga[2], T.A. Stabile[2]

[1] Università degli Studi di Salerno, Dipartimento di Fisica "E.R. Caianiello"

[2] Consiglio Nazionale delle Ricerche, Istituto di metodologie per l'analisi ambientale (IMAA)

[3] Università degli Studi di Salerno, Dipartimento di Studi Politici e Sociali/DISPS

The deployment and sustainable use of Italy's geothermal resources could represent a key asset to increase renewable energy production and reduce greenhouse gas emissions in the coming years. The primary benefits of geothermal energy generation and geothermal heating and cooling are that the sources are local, adaptable, and resistant to the price volatility that impacts fossil fuels. Furthermore, they are renewable energy sources that allow for energy mix diversification, resulting in less energy dependency and higher supply security. As a result, geothermal energy is a realistic choice and an urgent cure for reducing Italy's reliance on the import of fossil energy resources and improving energy efficiency in building air conditioning and the execution of numerous industrial operations. Finally, recent studies have shown that high- to low-enthalpy fluids could represent an unconventional source of lithium, a critical material for the energy transition (Dini et al., 2022).

In this setting, there is an obvious need for programs to improve subsurface geothermal resource extraction while maintaining environmental sustainability. These designs need knowledge of the subsurface, which, owing to its complexity, renders traditional diagnostics ineffective. Assessing the potential exploitation requires knowing the type of geothermal system, the likely temperature and characteristics of the reservoir rocks and fluids. The volumetric or stored heat method (White and Williams, 1975) and its revised versions are the most widely used tools for quantifying geothermal resource capacity. However, these methods suffer from several major uncertainties depending on reservoir temperature, porosity, saturation, and resource size (volume) (Ciriaco et al., 2020).

To reduce these uncertainties, it is possible to estimate these parameters by adopting geophysical methods. Electrical and electromagnetic ones, such as Magnetotelluric (MT) and deep electrical resistivity tomography (DERT), have been proven to be powerful tools for investigating and characterising geothermal reservoirs on a wide range of depths and at different scales, since measured electrical resistivity depend on temperature, porosity, percentage of fluid saturation, and permeating fluid type (Manzella et al., 1999; Tamburiello et al., 2008; Rizzo et al., 2022). Local

earthquake tomography (LET) has been used for imaging the crustal elastic properties in seismically active geothermal settings in terms of 3D P-and S- wave velocity models (Toledo et al., 2020; Amoroso et al., 2022), while ambient noise tomography (ANT) is widely adopted in shallower geothermal settings (Toledo et al., 2020). The VP and VS parameters result in being mainly sensitive to lithology changes, whereas their ratio (VP/VS) provides precious hints on the fluid composition and its pore pressure Mavko et al. (2009). Finally, the anelastic parameters, described by the quality factor Q, strictly depend on some rheological properties like the temperature and the percentage of fluid saturation in rocks, key factors in the investigation of occurring subsurface geothermal processes (Chiarabba, 2021).

Social and environmental considerations are important in the long-term utilization of geothermal energy resources. Recently, the procedures of assessing and mitigating the environmental impact of energy exploitation have included the engagement of the local community to avoid any potential environmental dispute. The increased attention of public opinion to issues of environmental sustainability and ecology in general has favored the emergence of both greater sensitivity and a risk-predictive culture over time, enhancing the conflict between fears about human health risks and scientific knowledge beliefs. In this regard, geothermal energy, for example, is frequently not presented as a renewable energy source (Benighaus and Bleicher, 2019). This implies that planning procedures must be distinguished by the pursuit of common solutions via an appropriate assessment technique.

In this study we propose a novel geophysical multi-messenger technique, which provides unique and useful insights into the features and activities of examined geothermal reservoirs. These findings stem from the complementary information carried by subsoil electrical resistivity and elastic/anelastic characteristics related to fluid presence. The proposed method will be tested in two test regions in Southern Italy that are appropriate for low to medium-enthalpy geothermal extraction. The initiative is specifically focused on field investigations in: 2) Contursi Terme (Campania) and Tramutola (Basilicata). Contursi Terme is one of the most appreciated thermal sites in the whole Campania region. Here, 77 springs with temperatures ranging from 21°C to 30°C are present, furthermore, 72 shallower and deeper wells for the pumping of hot waters with temperatures ranging from 38°C to 43°C are used for balneotherapy (Celico P. et al 1979). The Tramutola test site is located on the western side of the Agri Valley which is home to Europe's biggest onshore hydrocarbon reserve. During the drilling of the "Tramutola2" well (404.4 m) in 1936, a significant volume of sulphureous hypothermal water (28 °C with a flow rate of 10 l/s) with accompanying gases (mostly CH4 and CO2) was discovered (Cazzini, 2018).

At the same time, we propose appropriate communication strategies in order to contribute to the acceptance of geothermal energy sources based on its raising awareness and direct involvement of stakeholders on the studied territories.

Acknowledgements

This work is supported by project TOGETHER - Sustainable geothermal energy for two Southern Italy regions: geophysical resource evaluation and public awareness financed by European Union – Next Generation EU (PRIN-PNRR 2022, CUP D53D23022850001).Acknowledgements

References

Amoroso O. et al. (2022) 3D seismic imaging of the Nesjavellir geothermal field, SW-Iceland. Front. Earth Sci. 10:994280. doi: 10.3389/feart.2022.994280 https://doi.org/10.3389/feart.2022.994280

C. Benighaus, A. Bleicher, (2019). Neither risky technology nor renewable electricity: Contested frames in the development of geothermal energy in Germany, Energy Research & Social Science, Volume 47, Pages 46-55, ISSN 2214-6296, https://doi.org/10.1016/j.erss.2018.08.022.

Cazzini, F. F. (2018). The history of the upstream oil and gas industry in Italy. Geological Society, London, Special Publications, 465(1), 243-274.

Celico P. et al 1979 – Le sorgenti termominerali della valle del Sele (Salerno): indagini strutturali, idrogeologiche e geochimiche. Rendiconti della Società Italiana di Mineralogia e Petrologia, 35 (1), pp. 389-409

Chiarabba, C. (2021). Local Earthquake Tomography (2021): pp. 610-621. https://doi.org/10.1016/B978-0-08-102908-4.00077-1

Ciriaco, A. E., Zarrouk, S. J., and Zakeri, G. (2020). Geothermal resource and reserve assessment methodology: Overview, analysis and future directions. Renewable and Sustainable Energy Reviews, 119, 109515.

Dini, A. et al. (2022) Lithium Occurrence in Italy—An Overview. Minerals, 12, 945. https://doi.org/10.3390/min12080945.

Manzella, A., Mackie, R., and Fiordelisi, A. (1999). A MT survey in the Amiata volcanic area: a combined methodology for defining shallow and deep structures. Physics and Chemistry of the Earth, Part A: Solid Earth and Geodesy, 24(9), 837-840.

Mavko, G., Mukerji, T., and Dvorkin, J. (2009). The rock physics handbook. Second Edition. New York: Cambridge University Press.

Rizzo, E., et al. (2022). 3D deep geoelectrical exploration in the Larderello geothermal sites (Italy). Physics of the Earth and Planetary Interiors, 329, 106906.

Tamburriello, G., et al. (2008). Deep electrical resistivity tomography and geothermal analysis of Bradano foredeep deposits in Venosa area (Southern Italy): preliminary results. Annals of geophysics.

Toledo, T., et al. (2020). Local earthquake tomography at Los Humeros geothermal field (Mexico). Journal of Geophysical Research: Solid Earth, 125(12), e2020JB020390.

White, D. E., & Williams, D. L. (1975). Assessment of geothermal resources of the United States, 1975 (No. 726-730). US Department of the Interior, Geological Survey.

Corresponding author: oamoroso@unisa.it

The European project SUCCEED for coupling Geothermal Energy and CCUS: innovative monitoring technologies by active-source seismic data acquisition

C. Bellezza, E. Barison, F. Poletto, A. Schleifer, F. Meneghini, G. Böhm, B. Farina

OGS - National Institute of Oceanography and Applied Geophysics, Italy

Geothermal energy is a natural and renewable energy source, but geothermal power production generates greenhouse gas (GHG) emissions, in particular CO_2. Some studies estimated that the GHG emission from geothermal power plant can be higher than 1000 g/kWh (Fridriksson et al., 2017).

In the view of reducing CO_2 emissions from geothermal power plants, for climate change mitigation (carbon capture utilization and storage - CCUS) purposes, the Synergetic Utilisation of CO_2 Storage Coupled with Geothermal Energy Deployment (SUCCEED) ACT project (2019-2023) aims to prove the feasibility of re-injecting the emitted CO_2 into the same geothermal system to improve its performance and in the meanwhile to permanently storage the CO_2 by mineralization.

The project investigated two different existing geothermal power plants, one is the Kizildere geothermal field, located in the East of Büyük Menderes graben in Western Anatolia, Turkey, the other is the Hellisheiði geothermal field, in Iceland. Here we present the work done for the geophysical monitoring and the results achieved at the Hellisheiði geothermal field.

In the framework of the project, our research focused on the development of innovative reservoir-monitoring technologies at the Hellisheiði geothermal field, an active geothermal power plant located in the southern part of the Hengill volcanic system in the southwestern Iceland, close to the city of Reykjavik. The Hengill volcanic system is constituted by a central volcano and a fissure swarm with a graben structure that extends to the northeast and southwest and it is located at the junction of Reykjanes Volcanic Belt (RVB), the Western Volcanic Zone (WVZ) and the South Iceland Seismic Zone (SISZ) (Jóhannesson and Sæmundsson, 1998).

The Hellisheiði geothermal field has a temperature higher than 300°C at a depth of 1000 m below sea level and the steam combined heat and power plant is one of the biggest in the world with an installed production capacity of 303 MWe and 210 MWh of energy. The CO_2 is added to the re-injected geothermal fluid as dissolved gas. The monitoring experiment consisted in a baseline survey and a time lapse survey after a long-lasting, continuative (a few months) injection of CO_2. The monitoring is performed by active-source seismic data acquisition using a novel electric seismic vibrator source (E-Vibe) and permanently installed Helically Wound Cable (HWC) fibre-optic distributed acoustic sensors (DAS) in shallow trenches. We present the resulting time-stacked section from the baseline HWC DAS acquisition (July 2021) to investigate the complex basaltic system prior the CO_2 injection. At the same time, two co-linear acquisitions have been done with two- and three-components geophones to validate the results from the baseline HWC DAS system. The results showed a good consistency in the reflected events and helped to define the reservoir where we expect the injected CO_2 to be stored (Bellezza et al., 2023, under revision). We also show

the preliminary results from the time-lapse acquisition acquired by the only HWC DAS system (June 2022) to highlight the variation in the reflected events after the injection of the CO_2.

Acknowledgements

The SUCCEED project is funded through the ACT – Accelerating CCS Technologies (Project No 294766) programme. Financial contributions by the Department for Business, Energy & Industrial Strategy UK (BEIS), the Ministry of Economic Affairs and Climate Policy, the Netherlands, the Scientific and Technological Research Council of Turkey (TUBITAK), Orkuveita Reykjavíkur/Reykjavik Energy Iceland (OR) and National Institute of Oceanography and Applied Geophysics - OGS Italy are gratefully acknowledged. We also acknowledge all the SUCCEED partners.

References

Bellezza C.; Barison E.; Farina B.; Poletto F.; Meneghini F.; Böhm G.; Draganov D.; Janssen M.T.G.; van Otten G.; Stork A.; Chalari A.; Schleifer A., Durucan S.; 2023-under revision. Helically Wound Cable (HWC) Distributed Acoustic Sensors (DAS) and co-located geophones data: a multi-sensor seismic processing approach in the monitoring of CO2 storage at the Hellisheiði geothermal power plant in Iceland. Sustainability, S.I. Geological Insights for a Carbon-Free, Sustainable Environment.

Fridriksson T.; Merino A. M.; Orucu A. Y.; Audinet P.; 2017: Greenhouse Gas Emissions from Geothermal Power Production. Proceedings, 42nd Workshop on Geothermal Reservoir Engineering Stanford University, Stanford, California, February 13-15, 2017.

Jóhannesson, H.; Sæmundsson, K.; 1998: Geological Map of Iceland, 1:500.000. Bedrock Geology; Reykjavík.

Corresponding author: Erika Barison ebarison@ogs.it

Salt domes modelling through magnetic data: an unconventional tool for challenging scenarios

L. Bianco[1], M. Abbas[1], L. Speranza[2], B. Garcea[2], M. Fedi[1]

[1] Department of Earth, Environmental and Resources, University of Naples "Federico II", Naples, Italy.
[2] Energean, Milan, Italy.

We demonstrate that the analysis of magnetic data in salt basins could often represent a fundamental tool. The analysis was carried out on the data of a deep-water area in the Eastern Mediterranean, offshore Egypt. The reduced to pole (RTP) magnetic anomalies were filtered for the regional-residual separation with the discrete wavelet transform (DWT). The resulting magnetic anomalies were interpreted as generated by the contrast between the salt bodies and the surrounding sedimentary layers. We extracted many lineaments representative of the salt bodies from the multiscale boundary analysis of the produced anomalies. Moreover, we inverted the data using a 3D non-linear non-iterative inversion technique jointly with Euler deconvolution. This procedure has led to an interesting salt map, which is by the fact exclusively based on magnetic data. This result agrees well with the seismic interpretation of the top of the salt. This is a not obvious result, which demonstrates an advantageous and low-cost use of magnetic surveys for the exploration of salt basins, especially when seismic data are inaccessible or suffer of possible pitfalls in such scenarios.

Corresponding author: luigi.bianco2@unina.it

Monitoring and No-Money-toring of Oil & Gas exploitation in Italy

T. Braun[1], S. Danesi[2]

[1] *Istituto Nazionale di Geofisica e Vulcanologia, Sezione di Roma1, Arezzo, Italy*
[2] *Istituto Nazionale di Geofisica e Vulcanologia, Sezione di Bologna, Bologna, Italy*

The Val d'Agri basin (VA) is a Quaternary extensional basin bounded by two parallel and oppositely dipping normal fault systems. A M~7 earthquake that struck the VA in 1857 testifies the high seismic hazard of the region. The VA basin hosts the largest on-shore oil field in on-shore Europe, producing hydrocarbon since the 1990s from a high-productive reservoir consisting of fractured, low-porosity Cretaceous limestones from production wells drilled at 2 to 3 km depth below sea level (Buttinelli et al., 2016).

The ENI petroleum company is the main concessionaire in VA, operating 25 productive wells located between the eastern side of the basin and the eastern ridge, and reaching production rates around 90000 oil barrels/day. Since 2002, the operator installed a local seismic network to monitor the seismicity of the area and to study the potential influence of industrial activities on it. On 2014, the Italian Government decided to assign the monitoring duties to an independent external consultant (Struttura Preposta al Monitoraggio, SPM, in Italian) and published experimental guidelines (ILG) (Dialuce et al., 2014) describing the recommendations to be followed for the geophysical monitoring of hydrocarbon production, waste-water injection and gas storage.

Only in the case of the injection of incompressible fluids, the ILG propose the application of a Traffic Light System that defines a response scheme when seismic parameters exceed specific thresholds. Parameters like Peak Ground Velocity (PGV), Peak Ground Acceleration (PGA) and magnitude (ML) must be monitored when hypocentres are located within a defined spatial domain around the injection well. (Braun et al., 2020).

In 2017, the Italian Ministry for Economic Development commissioned INGV to act as monitoring agency (SPM) for the VA concession for exploiting hydrocarbons. In the standard operation mode, the SPM is responsible for monitoring seismic parameters in near-real time, and analysing them in conjunction with ground deformation (GPS and INSAR) and pore pressure fluctuations on a biannual basis. The ILG define the monitoring domains (Figure 1): an Extended (DE) and an Internal Domain (DI) based on the border of the Oil-Water contact of the reservoir, as well as a Reference Domain (DR), a cylindrical volume with a radius of 5 km along waste-water reinjection well Costa Molina 2 (CM2). Important to note that the Traffic Light Protocol only applies to the DR (Braun and Danesi, 2022).

Wastewater associated with oil production has been re-injected into the CM2 well, an unproductive marginal section of the carbonate reservoir, from 2890m to 3096m depth (well bottom) since June 2006. The variable injection rates have reached maximum values of 2800–3000 m^3/d (normal 2000 m^3/d), while the well-head pressure has never exceeded 13–14 MPa. CM2 can be classified as a long-term, high-rate disposal well (e.g., Stabile et al. 2014, Improta et al., 2015).

The two-year experimental period of the ILG came to an end in the middle of the COVID-19 pandemic in April 2021, and for the sake of simplicity it was extended for a further 12 months. Due to an unfavourable superposition of individual administrative difficulties by the involved public administrations, the originally common target of a straight and uninterrupted transition from the experimentation to the application of the ILG, could not be realized. This led to a contractual and financial discontinuity for a period of more than 20 months, which will now probably end with the signing of a long-term agreement between the different parties.

Mother nature does not mind if monitoring agreements are active! … and sometimes earthquakes may also occur during times, when monitoring is not adequately covered by fundings. The question rises whether monitoring should continue anyway, or should rather follow the economic availability? with other words: “In case that financing funds may temporarily thrust out should the SPM still continue monitoring?”. This is the inauspicious circumstance, when “No-Money-toring” starts.

Without deepening this issue, INGV decided, however, to continue the monitoring activity; a decision that turned out to be useful, due to a non-neglectable seismic activity, occurring during 2023 (Figure 2). Our contribution will report about scientific and non-scientific aspects experienced during Monitoring and No-Money-toring phase of the VA project.

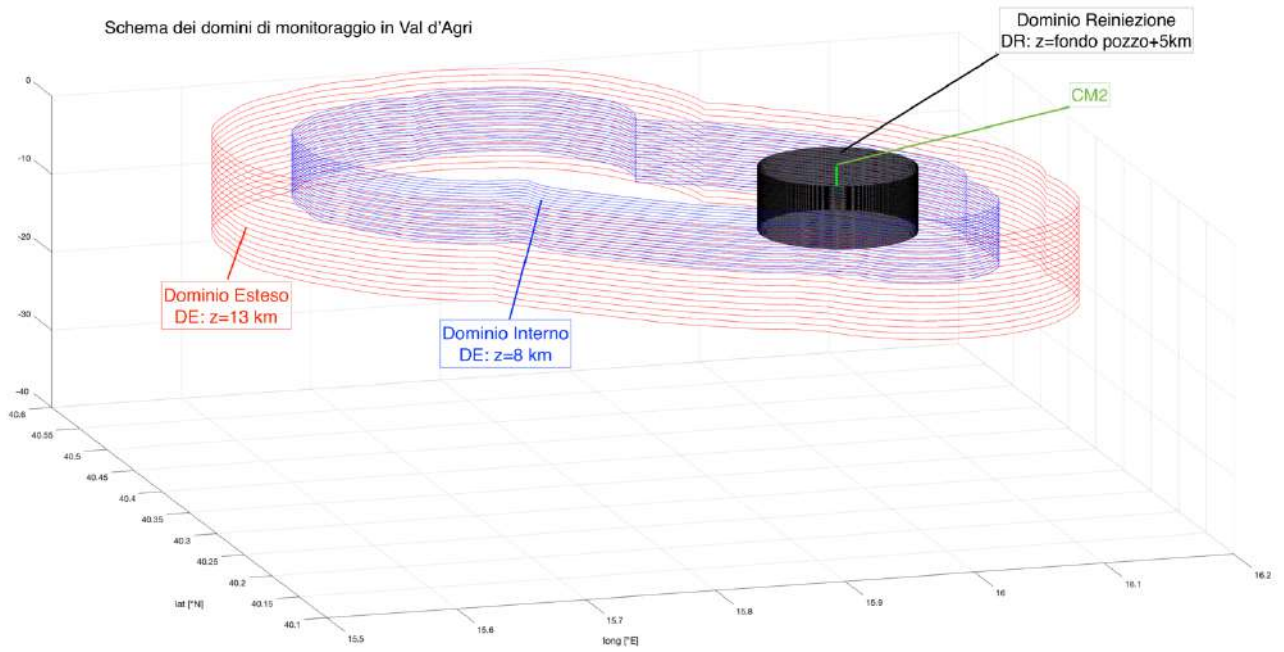

Fig. 1 – Monitoring domains DE, DI and DR defined for the monitoring of the hydrocarbon exploitation in VA (after Danesi et al., 2021)

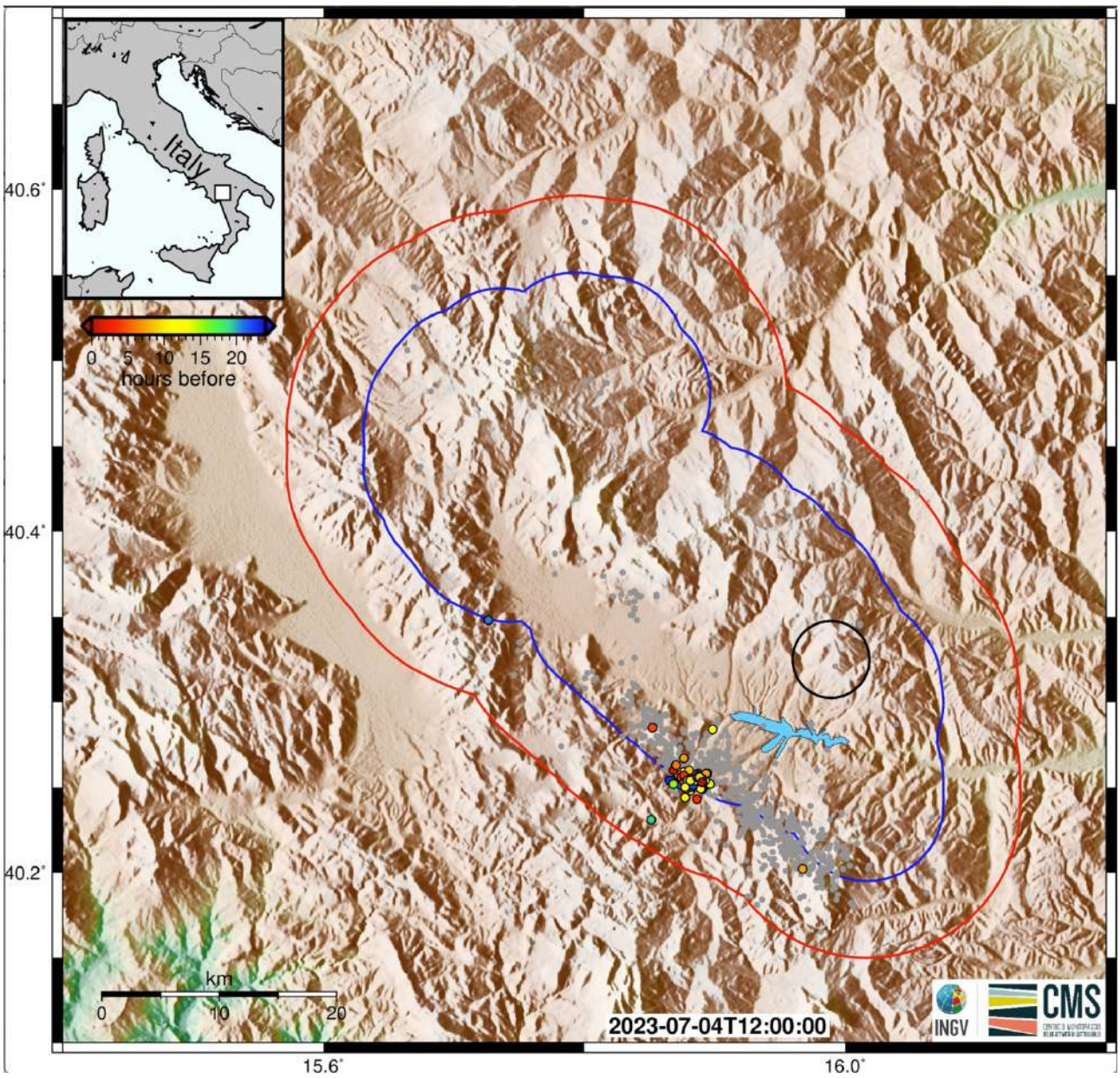

Fig. 2 – Example screenshot of the seismic activity in VA recorded in 2023 by INGV.

References

Braun T., Danesi S., and Morelli A.; 2020: Application of monitoring guidelines to induced seismicity in Italy. J. Seis.

Braun T. and Danesi S.; 2022: Il monitoraggio sismico delle attività di produzione idrocarburi in Val d'Agri. Risk Elaboration.

Buttinelli M., Improta L., Bagh S. and Chiarabba C.; 2016: Inversion of inherited thrusts by wastewater injection induced seismicity at the Val d'Agri oilfield (Italy). Sci. Rep. 6, 37165.

Danesi S. et al.; 2021: Relazione semestrale 2021/I, Progetto di Monitoraggio concessione Val d'Agri.

Dialuce G., Chiarabba C., Di Bucci D., Doglioni C., Gasparini P., Lanari R., Priolo E. and Zollo A. (2014). Indirizzi e linee guida per il monitoraggio della sismicità, delle deformazioni del suolo e delle pressioni di poro nell'ambito delle attività antropiche. GdL MiSE, Roma.

Improta L., Valoroso L., Piccinini D. & Chiarabba C. (2015). A detailed analysis of wastewater-induced seismicity in the Val d'Agri oilfield (Italy). Geophys. Res. Lett. 42, 2682–2690.

Stabile T. A., Giocoli A., Lapenna V., Perrone A., Piscitelli S. & Telesca L.; 2014: Evidence of low-magnitude continued reservoir-induced seismicity associated with the Pertusillo artificial lake (southern Italy). Bull. Seismol. Soc. Am. 104, 1820–1828.

Corresponding author: thomas.braun@ingv.it

Comparison and calibration of Traffic Light Protocols applied in different countries, in the framework of the ENSURE-project

T. Braun[1], S. Danesi [2]

[1] *Istituto Nazionale di Geofisica e Vulcanologia, Sezione di Roma1, Arezzo, Italy*
[2] *Istituto Nazionale di Geofisica e Vulcanologia, Sezione di Bologna, Italy*

Innovative strategies for risk reduction are feasible in the context of induced seismicity, as it is possible to manage risk through hazard control, in contrast with standard seismic risk mitigation that considers only vulnerability and exposure (Bommer et al., 2006). Traffic Light Protocols have been proposed to determine the risk level condition associated with induced seismicity, with the goal of reducing or stopping industrial operations in case it reaches an unacceptable level. The protocol also includes restarting operations once the situation is deemed safe on the basis of quantitative criteria (Figure 1). Country specific regulations defined by national laws and different types of operation have led to specific TLPs customized for the different anthropogenic activities, as e.g., proposed by (Bommer et al., 2006; Zoback, 2012; Grigoli et al, 2017; Bohnhoff et al., 2018; Baisch et al., 2019; Braun et al., 2023). In the first instance, TLPs are used to classify monitoring results ad report them to the authorities according to a "communication scheme". Sometimes, TLPs serve as "reaction scheme", to take action in respect of the operations and reduce or interrupt, and eventually restart anthropogenic activities.

With regard to Italy, the Ministry of Economic Development proposed "Guidelines for the monitoring of seismicity, soil deformation, and pore pressure in relation to anthropic activities" (Dialuce et al., 2014; Braun et al., 2020), to be applied for the monitoring in Italy of artificial water basins, mining drilling (caves, mines, hydrocarbons), tunnel excavations, methane gas and CO_2 storage. The ILG describe standards for monitoring relevant geophysical observables; outline roles and responsibilities of the different actors involved in monitoring activities; define procedures to be followed in case of significant changes of the monitored parameters, propose a decision-making model based on the exceeding of predetermined thresholds, a so-called traffic light protocol (TLP). The TLP becomes exclusively applied in case of reinjection of incompressible fluids (production waste waters, but not methane or CO_2).

For concessions of national competence, the ILG define the constitution of a "Committee", composed by the Ministry representatives on a national level (DGS-UNMIG), the regional government, the industrial operator and the monitoring agency (in Italian: Struttura Preposta al Monitoraggio SPM). The role of the Committee is to manage the monitoring of a concession, on the basis of the monitoring recommendations. The primary SPM's task is to calculate hypocentral coordinates of seismic events and discriminate whether they are within previously defined monitoring volumes (spatial threshold). For events that meet the specified criteria, the SPM

computes the seismic parameters Magnitude, PGV (Peak Ground Velocity), and PGA (Peak Ground Acceleration), determines if any of these parameters exceed the thresholds established in the TLP (parametric threshold), and reports the outcome to the committee (==> communication process). On the basis of the SPM's analyses, three of the committee members (UNMIG, Region, Concessionaire) are then responsible for deciding on the type of intervention to be applied, classified as “Ordinary” (green), ”Attention” (yellow), “Reduction” (orange) or “Suspension” (red) of the industrial activities (==> reaction scheme). The definition of the intervention measure is a political decision, based on the SPM's technical assessment.

The project “Effective moNitoring of long-term site Stability for transparent carbon captUre and storage hazaRd assEssment” (ENSURE) aims to (i) identify common traits between seismicity occurring in different settings with respect to calibrate TLPs, (ii) correlate seismological with reservoir engineering parameters, (iii) compare results to existing TLPs from other industrial monitoring systems. As a deliverable it is planned to propose an evaluation of monitoring parameters (as e.g., M, PGV, PGA, Hypo) and their uncertainties for a conversion into effective TLPs- threshold values, especially for the case of Carbon Capture and Storage (CCS). As CCS will be introduced soon also in Italy, and based on the experiences of INGV as SPM during the experimental monitoring phase of pilot concessions, a revision of the ILG is absolutely essential. We will present the preliminary analyses achieved in the framework of ENSURE, which give important indications for calibrating also the national TLPs, effective for 10 years.

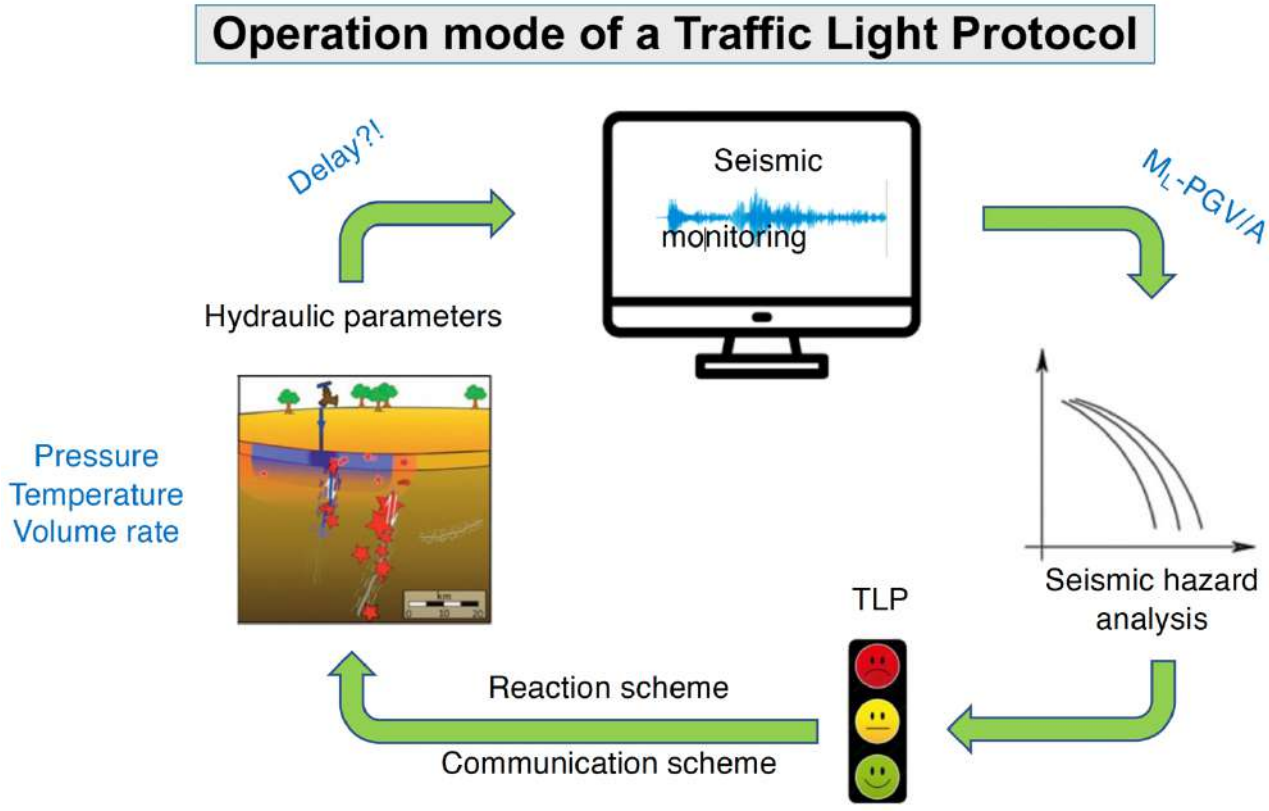

Fig. 1 – Operation principle of a Traffic Light Protocol

References

Baisch et al.; 2019: Traffic Light Systems: To What Extent Can Induced Seismicity Be Controlled? Seis. Res. Lett. 90(3), 1145-1154

Bohnhoff et al.; 2018: Suggested best practice for seismic monitoring and characterization of non-conventional reservoirs. First Break, pp. 59–64.

Bommer J.J., Oates S., Cepeda J.M., Lindholm C., Bird J., Torres R., Marroquin G., and Rivas J.; 2006: Control of hazard due to seismicity induced by a hot fractured rock geothermal project. Engineering Geology, 83(4), 287–306.

Braun T., Danesi S., and Morelli A.; 2020: Application of monitoring guidelines to induced seismicity in Italy. J. Seis.

Braun T., Schmidt B., Wassermann J., 2023: Esempi nel mondo di sismicità indotta dalla produzione geotermica: considerazioni e proposte di monitoraggio. Quaderni di Geofisica.

Dialuce G., Chiarabba C., Di Bucci D., Doglioni C., Gasparini P., Lanari R., Priolo E. and Zollo A; 2014: Indirizzi e linee guida per il monitoraggio della sismicità, delle deformazioni del suolo e delle pressioni di poro nell'ambito delle attività antropiche. GdL MiSE, Roma.

Grigoli et al.; 2017: Current challenges in monitoring, discrimination and management of induced seismicity related to underground industrial activities: a European perspective. Rev. Geophys., 55, pp. 310–340.

Zoback M.D.; 2012: Managing the seismic risk posed by waste water disposal. EARTH Magazine 57(38).

Corresponding author: thomas.braun@ingv.it

The MARE (MARine Energy) project Assessment of energy production potential from marine waves and currents: a case study from Aegadian archipelago

A. D'Alessandro[1], A. Sulli[2], M. Agate[2], P. Capizzi[2], C. Caruso[1], L. Cocchi[2], R. D'Anna[2], A. Di Benedetto[2], A. Figlioli[1], M. Gasparo Morticelli[2], A. Mandiello[1], R. Martorana[2], A. Pisciotta[1], S. Speciale[1], S. Sciré Scappuzzo[1], S. Scudero[1], G. Vitale[1]

[1] Istituto Nazionale di Geofisisica e Vulcanologia, Italy
[2] Università degli Studi di Palermo, Italy

Introduction

World energy consumption will grow considerably in the next decades, as well as that of the European Union. At the same time, the Member States' awareness that traditional energy production seriously contributes to environmental pollution, making the need for a non-polluting generation of energy. As part of the technological evolution of renewable energy, the marine energy is emerging. In fact, this source arouses growing interest from governments and industries, despite being relatively new, and with non-competitive costs such as wind power.

An important characteristic of the sea is that it has the highest energy density of all renewable sources. The most important advantages are the high availability and high predictability of the resource, while the technology is characterized by a low visual impact and no CO2 emissions. Marine waves and currents can thus contribute to a renewable energy mix to help curb the current dependence on fossil fuels. Italy has a geographical position that allows exploitation of different sources of renewable energy; among these sources, the sea should have a prominent role due to the large amount of Italian coastline.

After more than thirty years confined to academic research, the progress of marine energy has reached an almost mature stage, presenting itself as a potential industry for the future. The sea contains an enormous amount of energy, which theoretically can be exploited by man for his own energy needs. It is present in several forms, including tides, surface waves, currents, the thermal gradient and the salinity gradient. We refer to kinetic energy with regard to tidal currents or sea currents, which are moved by gravitational forces, while the waves of the sea, pushed by the wind, derive indirectly from solar energy . All these different forms can be used for the generation of electricity, through the use of the most modern technologies.

The estimated global potential resource for each of these sources is as follows:

- Wave energy 80000 TWh/year,
- Tidal energy > 300 TWh/year,
- Current 800 TWh/year,
- Salinity gradient 2000 TWh/year,
- Thermal gradient 10000 Twh/year.

The idea of converting surface wave energy into useful forms of energy is not a recent one. The first patent, known for using the energy of sea, dates back to 1799, and was filed in Paris by Girard and his son. Recently, following the problems of climate change, a new interest in renewable energy has grown around the world and the scientific community examined the potential for generating electricity from the sea.

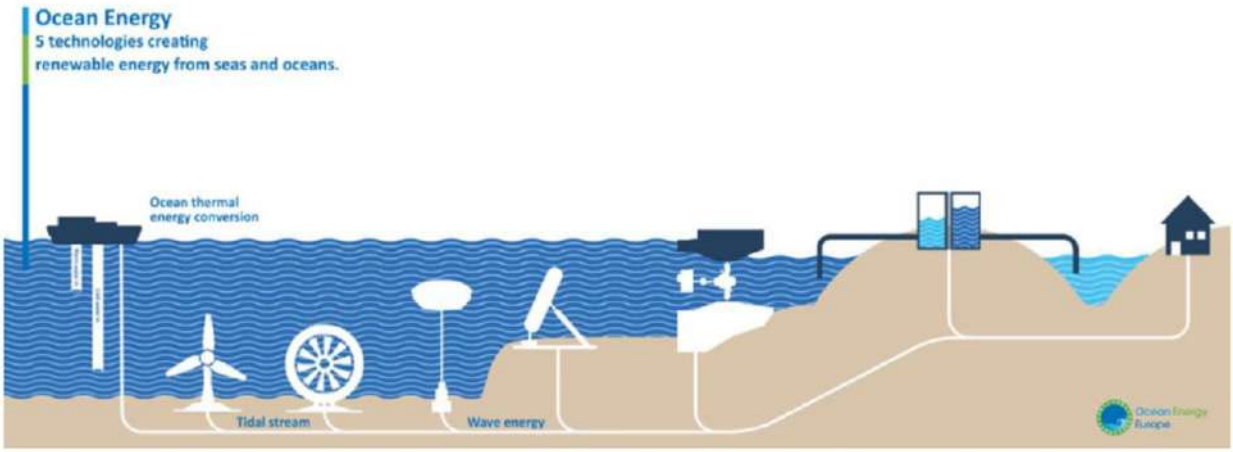

Fig. 1 – Different types of technologies for the exploitation of marine energy (Energy, 2017).

A large number of technologies (Fig. 1) have been developed for the exploitation of sea energy. More than a thousand patents have been registered around the world, but none of these technologies has yet established itself as the dominant one. The most used parameters to distinguish the different technologies are: the position with respect to the coast, the principle of operation and the power take-off system. A detailed description of the technologies currently available is outside the topics of interest; therefore, reference should be made to the available scientific literature.

Many are the projects dedicated to marine energy that have been funded and implemented in Europe like: Pico, Lysekil Project, European Marine Energy Centre, DanWEC Hanstholm, Wave Hub, Yongsoo, Bimep, Oosterschelde Tidal Project, Belmullet, Santoña wave farm, FlanSea Project, Pilot Zone, Perth Wave Energy Project, Limpet, Mutriku, Aguçadoura, Bernera, Aegir, Lewis Wave Energy Farm, Reedsport OPT Wave Park, Coos Bay OPT Wave Park. Some of these led to the creation of wave farms in Italy like: Iswec (La Spezia, Alghero and Pantelleria), SouthEnergy (Tuscan Archipelago, Punta Righini - Castiglioncello) and Rewec (several italian ports).

Recently, atlases of wave energy of the Italian coasts have been developed, using wave parameters measured by buoys positioned off the coast (ENEA, 2011). Wave buoys provide accurate and direct measurements of wave parameters. However, the time series obtained from the buoys describe swell climates only locally, and often have large data gaps caused by temporary buoy failures, or by maintenance operations routine. Wave height and period do not generally show high spatial gradients in the open ocean, but substantial spatial variations are observed in enclosed seas, where ground obstacles strongly influence wave generation and propagation. We can therefore conclude that at the moment, an accurate and detailed estimate of wave energy of the Italian seas is not yet available.

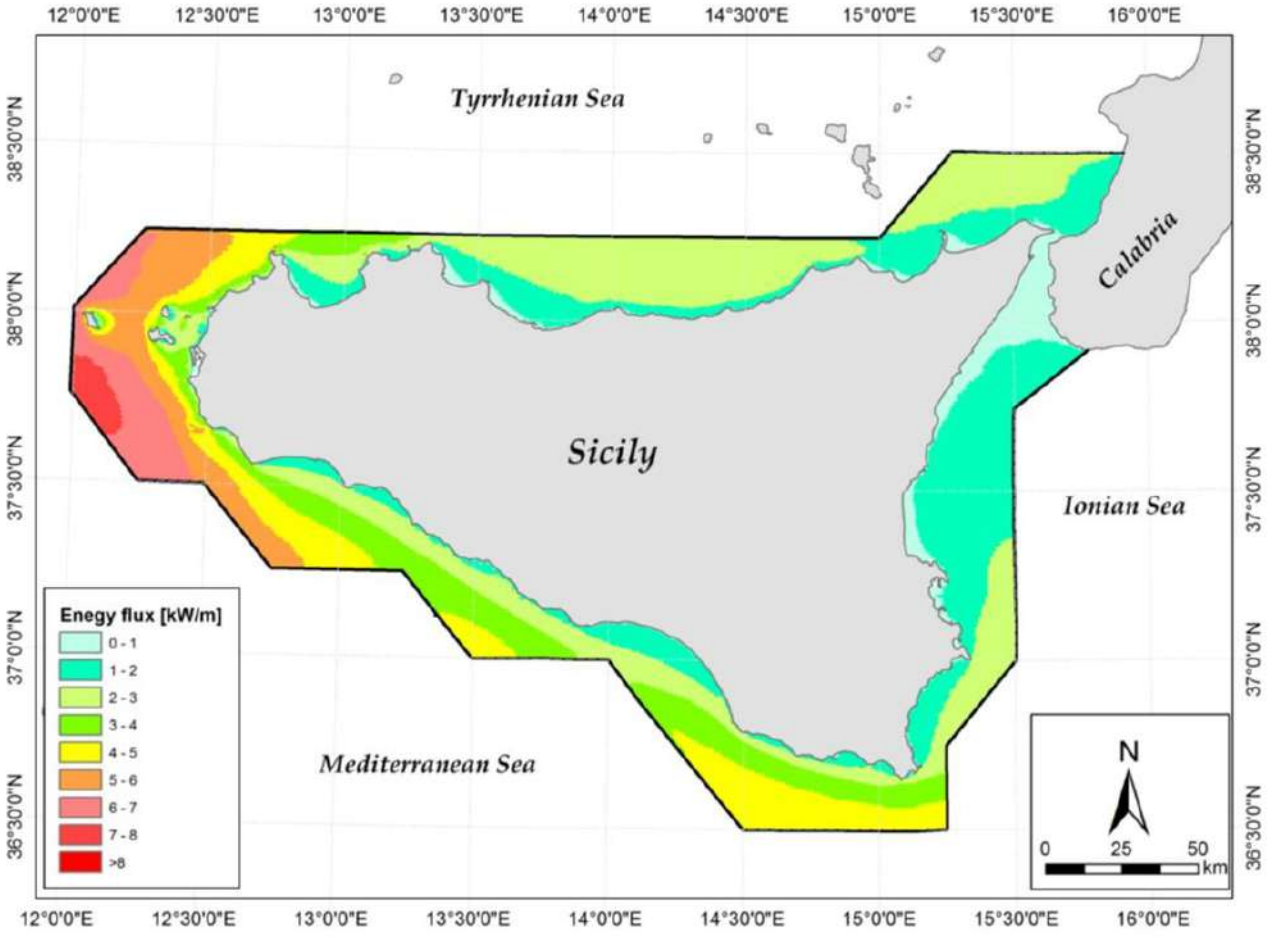

Fig. 2 – Distribution of the average wave energy flux per unit crest length within the computational domain (from Iuppa et al., 2015).

The MARE (MARine Energy project), funded in the framework of PRIN PNRR, arises from the premise that for the energy production from marine sources, becoming an important piece in the mosaic of renewable energies, the available resource must be well assessed, in order to demonstrate the real productive possibilities and attract investors. The activity presents the potential tools identified for the definition of a methodology capable of determining the potential of energy producibility from sea waves and marine current along the territorial waters of the Aegadian Archipelago.

As regards energy supply, most of the Minor Islands are not interconnected to the National Transmission Grid (NTG) being managed by small vertically integrated electricity companies and 8 are managed by ENEL Produzione. The production plants are currently made up of diesel units, whose overall power is always oversized to ensure the quality and continuity of the service. The supply of fuel takes place with tankers, with inevitable associated environmental risks, (pollution, greenhouse emissions, etc).

To assess the potential for the marine energy it is opportune to employ the most suitable methodologies for the analysis of such a particularly complex system. The MARE project aims to contribute to the necessary knowledge so that the energy production from marine waves and currents may become a real resource for small islands. The Aegadian archipelago is proposed as a case study.

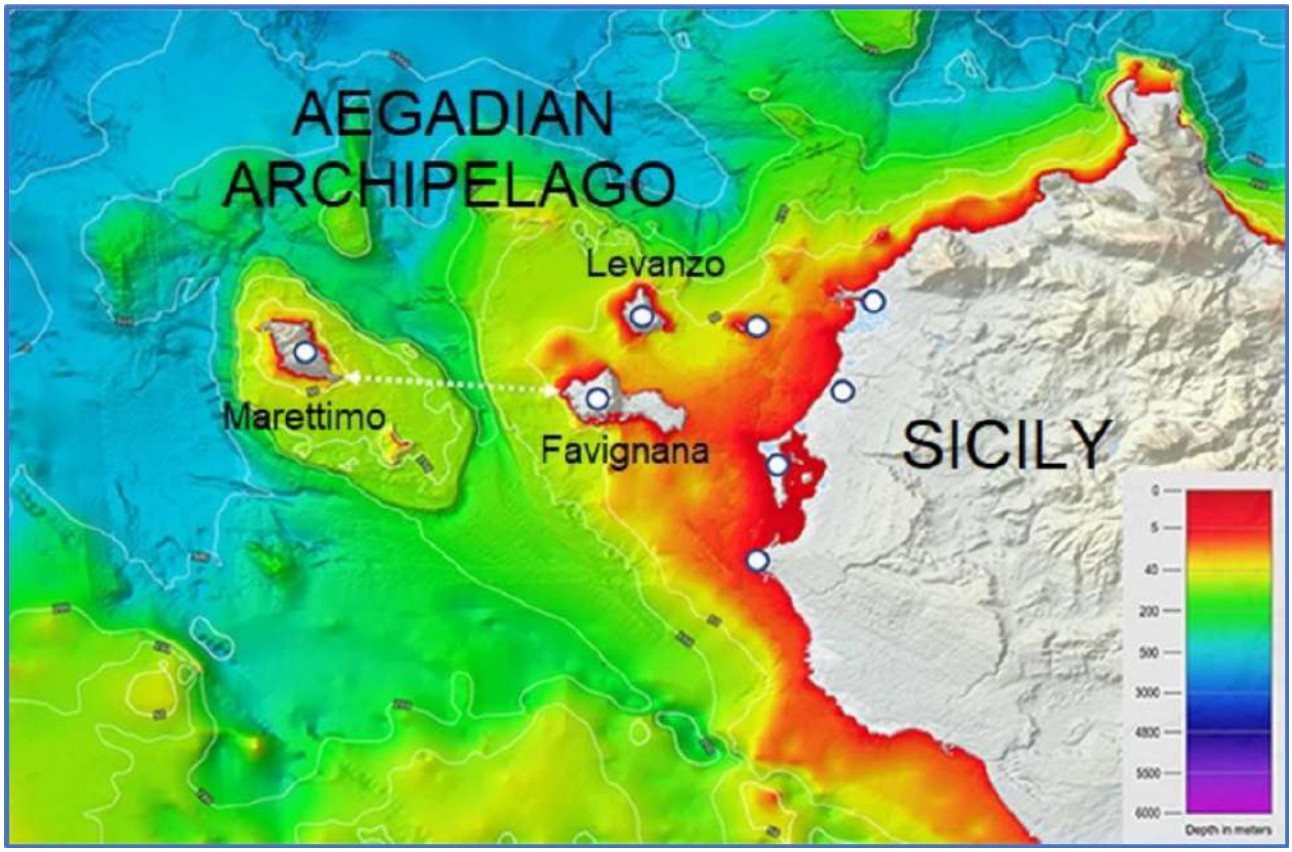

Fig. 3 – Bathymetric map of the study area.

The Aegadian Archipelago is composed of the islands of Favignana, Levanzo and Marettimo and it is located off the -western coast of Sicily. The population of the whole archipelago is not distributed equally, Favignana is the larger island (37 km2) with 3,407 inhabitants, Marettimo (12 km^2) has 648 inhabitants, while Levanzo (6 km^2) is the smallest of the three with 208 inhabitants. Favignana, Levanzo and Marettimo are not interconnected with the mainland and neither among themselves, each Island has a local Distribution System Operators that provides electric energy using diesel plants. In the last years, the Municipality of Favignana has strongly pushed several clean energy-oriented projects. At present, the whole archipelago hosts only about 300 kW of

photovoltaic power, since the regional regulatory framework forbids the establishment of any wind power plants.

Wave energy atlases are based on measurements from buoys, satellite observations and from models. In recent years, several authors have presented global wave energy atlases. These works do not include observations from the Mediterranean Sea; rather they are based on models, with a spatial resolution too coarse, to be able to distinguish, on a smaller scale, the spatial variations of the availability of wave energy. These details are important to identify suitable sites for the production of electricity in relatively small basins like the Mediterranean, and especially for minor islands.

Generally speaking, islands are the ideal laboratory of sustainability and they are today, all over the world, in a dimension of great interest where ambition and concreteness are combined. The challenge is to make the smaller Italian islands a vanguard in the world in the dissemination of innovative and economically sustainable solutions on energy and water, in the circular economy and sustainable mobility. A perspective that, as the international experiences, can help to revive the economy and attract tourism to the islands because it preserves these unique ecosystems, making them attractive precisely for their landscape and environmental qualities (Legambiente, 2018).

Previous studies have shown that wave farms could be implemented at some sites. For example, Vicinanza et al. (2011) reported the offshore wave energy potentials of the Italian seas. The results highlighted that the west coasts of Sicily are the most energetic among the Italian coasts. Indeed, the highest energy values were obtained for the buoys of Mazara del Vallo, which corresponded to 4.75kWm-1. Fig. 2 shows the average wave energy of the Sicilia coasts (Iuppa et al., 2015a). The average wave energy has a not negligible spatial variability even over distances of the order of 20km. This variability cannot be adequately described by local buoy measurements, or by models with a lower spatial resolution. The average power is a useful parameter to identify promising areas for the production of wave energy, its value however is presented as a contribution of the individual states of the sea, distributed over a range of wave heights, periods and directions. On the west coast of Sicily, the average power flow is between 5 and 6 kW/m, which increases gradually, up to average value of 6 kW/m, in the Aegadian Archipelago (Iuppa et al., 2015a,b). The Aegadian islands are among the most productive in the Mediterranean Sea and surely the most promising of the Italy.

The MARE project focused on two main lines:

- The collection, organization and analysis of available environmental data, with particular reference to those strictly related to the studied problem;
- The identification, on the basis of geological, geophysical and geochemical investigation of the potential for energy production of the highlighted case of study.

And includes the following types of surveys in the Aegadian Archipelago and surroundings:

- bathymetric surveys

- seismic microtremor investigations
- current meter surveys
- investigations of temperature and salinity parameters

For the following purposes:

- Assessment of Energy Production Potential from marine waves motion;
- Assessment of Energy Production Potential from marine currents.

The first main aim of the MARE project is to assess the marine wave motion in terms of amplitude, frequency and seasonal stability by exploiting an indirect method widely tested in the literature. Sea waves are among the important sources of seismic noise recorded by seismic stations.

The second main aim of the MARE project is to assess the current velocity characteristics at different depths and estimate their theoretical potential. The objective is to calculate the potential energy generated from streams at different depth layers and detect the optimal one.

The final objective of the project is the production of maps of marine energy potential indicators with different spatial resolution, from a few km to a few hundred meters for the case of study proposed that will be characterized by a significant energy potential. For the latter it will also be possible to evaluate the real amount of energy that can be extracted according to the different exploitation technologies that can be used.

References

Ardhuin, F., et al. (2011). Ocean wave sources of seismic noise, J. Geophys. Res., 116, C09004.

Ardhuin, F., et al. (2012). From seismic noise to ocean wave parameters: methods, J. Geophys. Res., 117, C05002.

Berger, J., et al. (2004). Ambient Earth noise: a survey of the global seismographic network. J. Geophys. Res., Solid Earth109 (B11), B11307.

Bernard, P., 1990. Historical sketch of microseisms from past to future, Phys. Earth Planet. Inter., 63, 145–150.

Bromirski, P., et al. (1999). Ocean wave height determined from inland seismometer data: implications for investigating wave climate changes in the NEpacific, J. Geophys. Res., 104(C9), 20753–20766.

Bromirski, P. et al., (2002). The near-coastal microseism spectrum: spatial and temporal wave climate relationships, J. Geophys. Res., 107, B82166.

Ebeling, C. W. (2012). Inferring Ocean Storm Characteristics from Ambient Seismic Noise: A Historical Perspective. Advances in Geophysics, 53, 1.

Energy, E.O. (2017). Europe needs ocean energy. Retrieved April 23, 2019.

Falcao, A. (2010). Wave energy utilization: A review of the technologies, Renewable and Sustainable Energy Reviews 14, 899–918.

Ferretti, G., et al. (2016), Applicability of an empirical law to predict significant sea-wave heights from microseisms along the Western Ligurian Coast (Italy), Continental Shelf Research 122, 1, 36-42.

Gimberta, F., et al. (2015). Predicting short-period, wind-wave-generated seismic noise in coastal regions, Earth Planet. Sci. Lett. 426, 280–292.

Guandalini, R., et al. (2010). Indagini per la valutazione del potenziale di producibilità energetica dal moto ondoso e dalle correnti marine, lungo la fascia di acque territoriali italiane, Rapporto ERSE, pp 41.

Grevemeyer, I., et al. (2000). Microseismological evidence for a changing wave climate in the northeast atlantic ocean. Nature, 408, 349–352.

Iuppa, C., et al. (2015a). Investigation of suitable sites for wave energy converters around Sicily (Italy), Ocean Sci., 11, 543–557.

Iuppa, C., et al., (2015b). Potential wave energy production by different wave energy converters around Sicily, J. Renewable Sustainable Energy 7, 061701.

Legambiente (2018). Isole Sostenibili, Osservatorio sulle isole minori, 2nd ediction.

McNamara, D.E., Buland, R.P. (2004). Ambient noise levels in the continental United States. Bull. Seismol. Soc. Am.94 (4), 1517–1527.

Rhie, J., Romanowicz, B. (2006). A study of the relation between ocean storms and the earth's hum, Geochem. Geophys. Geosyst., 7(10).

Schulte-Pelkum, V., et al. (2004). Strong directivity of ocean-generated seismic noise, Geochem. Geophys. Geosyst., 5, Q03004.

Stutzmann, E., et al. (2000). Geoscope station noise level, Bull. seism. Soc. Am., 90(3), 690–701.

Stutzmann, E., et al., (2012). Modelling long-term seismic noise in various environments. Geophys. J. Int. 191, 707–722.

Vicinanza, D., et al. (2011) Estimation of the wave energy in the Italian offshore, J. Coastal Res., 64, 613–617.

Corresponding author: antonino.dalessandro@ingv.it

Airborne and Ground IP: an integrated approach for exploration

F. Dauti[1], A. Viezzoli[2], G. Fiandaca[1]

[1] The EEM Team for Hydro & eXploration, Dep. of Earth Sciences A. Desio, Università degli Studi di Milano, Via Botticelli 23, Milano (Italy)
[2] Emergo s.r.l., Via XX Settembre 12, Cascina (Pisa), Italy

Introduction

The Iberian Pyrite Belt (IPB) is one of the oldest and still active mining districts in the world. In the last decade, a renewed mining activity and scientific research have led into a wealth of new data and new geological hints for explorers and for the academic community, making the IPB one of the most important and dynamic mining districts in Europe (Inverno et al, 2015). In this region, the great number of different signatures related to the ore body and to its vectors call for an integrated use of complementary geophysical methods. The sulfides targets show contrast in both density and electrical properties, and historically gravity has played a crucial role for exploring in the IPB. These methods have been later accompanied by EM methodologies, both airborne and ground, given their high sensitivity to conductive targets (Menghini et al, 2022).

With this contribution we will focus on an application of a novel modelling approach that aims to properly extract the Induced Polarization (AIP) effects from the Airborne Electromagnetic (AEM) data. The AEM survey has been acquired in the IPB for mineral exploration to localize the VMS deposit. After the AIP modelling, we will show a comparison between the airborne chargeability and some overlapping ground IP models from the same area. This comparison aims to better understand the potential in the use of AIP for exploration and to attempt an improvement in the definition of the sensitivity field of the airborne technique, as well as its relationships with ground IP. Then, a joint inversion between the two methods will be presented.

Inductive Induced Polarization - theory and modelling

It is known and accepted that the Electromagnetic methods are sensitive to Induced Polarization effects (AIP) when acquired over a polarizable medium (Kratzer and Macnae, 2012; Viezzoli et al., 2013). From a physical point of view, the polarization processes generate currents in the ground (polarization currents) with an opposite direction respect to the pure EM currents (eddy currents) that proceed downward with a diffusive regime. These effects generate a distortion of the recorded electromagnetic signal which often culminate in its change of sign at late times when the halfspace is particularly polarizable. In general, the distortions generated from IP have two signatures in the EM data: a faster decay (respect to the purely resistive forward response) and/or negative voltages. Under these conditions, the standard EM modelling, which does not account for

polarization currents, ceases to be valid (Smith and Klein, 1996): the negative data cannot be fitted and the fast-decaying signals are modelled as strong resistors, generating artifacts.
To avoid the mis-modelling of EM-IP affected data, it is necessary to use a dispersive-resistivity model (such as the Cole & Cole one) to compute the forward response and considering the capacitive nature of the ground. This approach gives the opportunity to map, as well as the resistivity, the chargeability of the ground that is often related to significant economic (or signatures of) mineralization. At the same time, it complicates the inversion process adding three more parameters and expanding the model space generating equivalent domains. It follows that an appropriate parameters management during the inversion process is crucial to properly retrieve the ground description and to maximize the AIP sensitivity to geological and mineral targets.

Geophysical and geological description

The Airborne EM data have been acquired in spring 2022 with the NRG XCite Time Domain system, with a 25Hz base frequency, and the acquisition lines are illustrated in black lines in *figure 1*. In the same area, 18 Iris VIP 1000 (transmitter) lines (0.125Hz of base frequency, 50% duty cycle) of ground Time Domain DCIP have been acquired (red lines in figure 1).

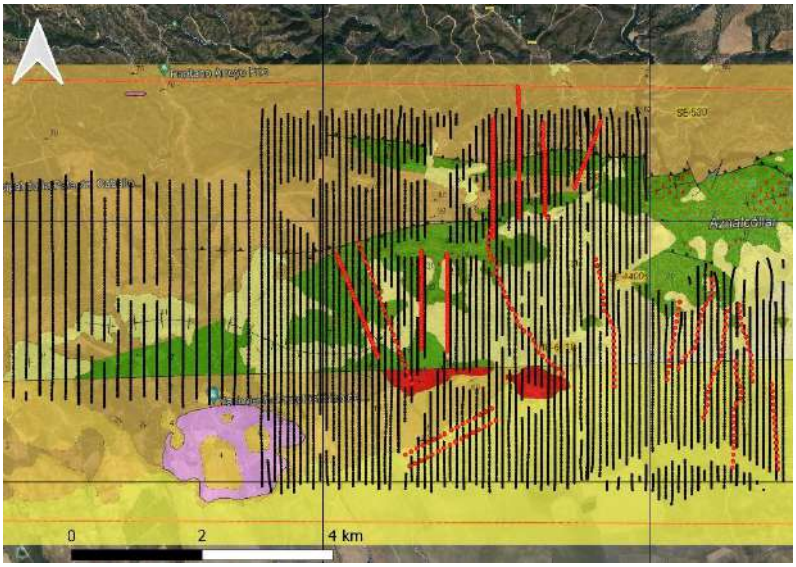

Figure 1. Survey location. In black the Airborne EM lines are displayed, in red the DCIP.

In the base map of *figure 1* the local geology is shown. Two main domains are visible: a volcanic intrusive one in the north, where Rhyolite and Dacite are presented in red and green, and a more recent sedimentary domain that covers the outcrop is in yellow in the southern area. The main tectonic features are represented in black and outcrops in the northernmost part of the investigated area.

Data modelling and inversion

Among the differences between Airborne and Ground IP, the most obvious are in the in footprint, depth of investigation and spectral content, with AEM data's frequency bandwidth usually a couple

of orders of magnitudes higher than that of ground IP data. Beside these problems, another major issue, not always recognized, is the difference in the modelling approach. Ground IP data is usually modelled dropping the spectral information, e.g., turning a full secondary voltage decay into a single value of integral chargeability (e.g. Oldenburg and Li, 1994). Moreover, the effect of current waveform is often not modelled, resulting in inversion models in which the retrieved polarization magnitude strongly depends on the acquisition settings of the current waveform, making a quantitative comparison between AIP and Ground IP impossible (Olsson et al., 2019).
On the contrary, in this study we model the IP spectral content in both AIP and Ground IP data with the same modelling approach, in terms of data-preparation, model space management and inversion approach.
In particular, the galvanic data have been modelled in 2D in terms of full-voltage decay (instead of the integral chargeability), taking into account the transmitter waveform and the receiver transfer function (Fiandaca et al., 2012; Fiandaca et al., 2013; Bollino and Fiandaca, 2024). The inductive data have been modelled in 1D, and to reduce the model space and to enhance the spectral resolution, the frequency dependence and time constant parameters have been set to vary only horizontally (while resistivity and maximum phase change also with depth).
For both the methos, the Maximum Phase Angle (MPA) re-parametrization of the Cole & Cole model has been used (Fiandaca et al., 2018). In the MPA Cole-Cole model, the maximum phase φ_{max} of the complex conductivity and the phase relaxation time τ_φ are used instead of m_0 and τ_ρ (of the classic Cole & Cole model). The phase of the complex conductivity can be defined in terms of both *equations 1 and 2* as:

$$\varphi(\omega) = tg^{-1}\left(\frac{\sigma''(\omega)}{\sigma'(\omega)}\right) = -\,tg^{-1}\left(\frac{\rho''(\omega)}{\rho'(\omega)}\right) \qquad \text{(eq. 1)}$$

The phase reaches his maximum φ_{max} at an angular frequency $\omega \equiv 1/\tau_\varphi$ as:

$$\varphi_{max} = tg^{-1}\left(\frac{\sigma''(1/\tau_\varphi)}{\sigma'(1/\tau_\varphi)}\right) = tg^{-1}\left(\frac{\rho''(1/\tau_\varphi))}{\rho'(1/\tau_\varphi)}\right) \qquad \text{(eq. 2)}$$

Finally, the model space of the MPA Cole-Cole model can be written as:

$m_{MPA\ Cole\text{–}Cole} = \{\rho_0, \varphi_{max}, \tau_\varphi, C\}$

The MPA parametrisation replace the strongly-correlated parameters m_0 and C of the classic Cole-Cole model with the weakly-correlated parameters φ_{max} and C (Fiandaca et al., 2018), to improve the resolution retrieved from inversion IP data of the classical Cole-Cole model.
The inversions have been performed with the inversion with EEMverter (Fiandaca et al., 2024), following a modelling scheme that uses voxel model mesh to map the solved parameters via an interpolation of the forward mesh solutions. The decoupling of the model mesh and the forward mesh allows to work with more flexible and manageable spaces (forward and model) to perform joint inversions and time laps inversions. In our inversion procedure, in order to increase the parametrical resolution and the phase sensitivity in depth, we parametrized the spectral parameters (τ_φ, C) on an independent mesh respect to resistivity and phase, with different lateral constraints and vertically fixed (as proposed by Viezzoli and Fiandaca in 2021).

Results

In *figure 2a* and *2b* the results are shown, with a comparison between a portion of the airborne and the ground DCIP modelled chargeability (phase) with our modelling approach.

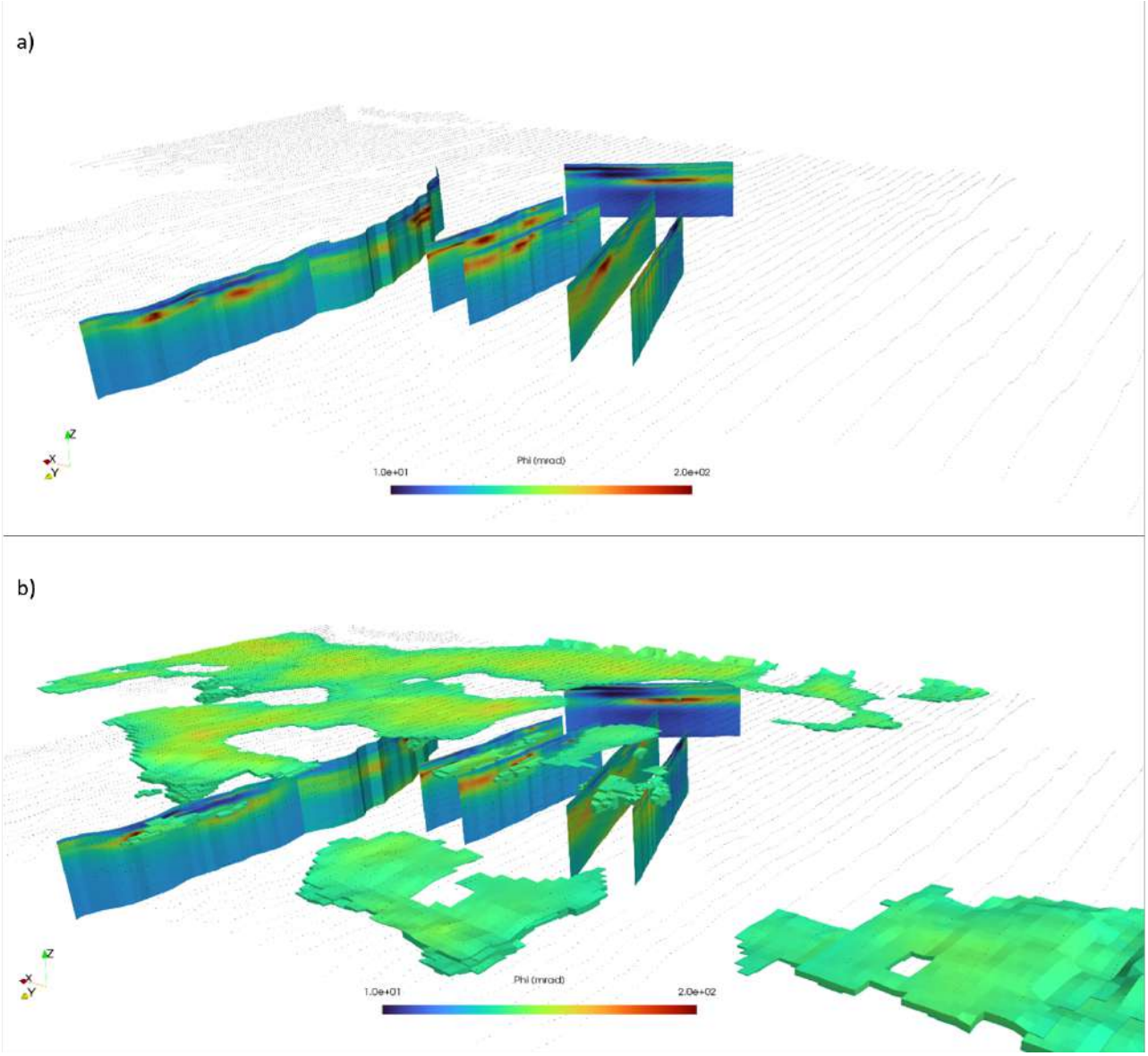

Figure 2. a) Example of ground DCIP phase results and, in dashed line, the AEM survey flown above; b) Partial Ground DCIP vs Airborne IP phase results

As visible from the figures, a great correlation between the airborne and ground is obtained when modelling with the presented approach. The airborne chargeability model shows a consistent structure with the ground model in depth and a geology-controlled behaviour in the shallower near surface. A known mineralization has also been mapped with the AIP. The differences in the near surface are a consequence of the big electric dipoles dimension used for the ground DCIP

(100m). For this dataset, all the airborne IP chargeability anomalies have been confirmed from the ground IP.

After this, we performed a joint inversion between all the ground DCIP lines (17) and the entire AEM survey. For the joint inversion we used the AEM model (for all the parameters) as starting model for the joint inversion. In *figure 3* the results are shown.

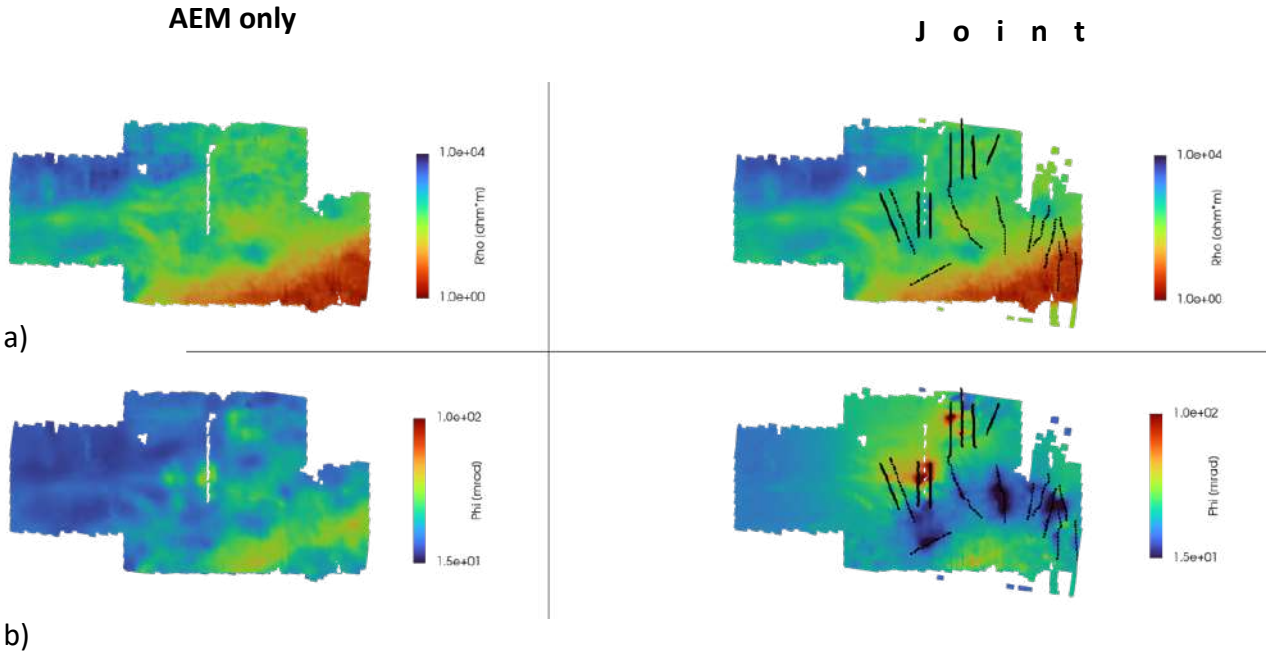

Figure 3. Comparison between AEM only model (on the left) and Joint Inversion model (on the right) for a slice at 60 m of depth. Figure 3a shows a comparison between the resistivities while figure 3b a comparison between chargeabilities.

In *figure 3a* a comparison between the AEM only and joint inversion resistivity is presented. As visible, the main structural are mantained in the inversions. Differently, in *figure 3b*, it appears that introducing the ground DCIP lines in the inversion add structure in the chargeability model for the entire survey area. In terms of misfit, the general misfit of the AEM only inversion is 1.6 while the misfit for the joint inversion is 1.7, confirming how the AEM data accept the jointly obtained chargeability model obtained together with the ground IP.

Conclusions

This study shows encouraging results in the using of the Airborne Induced Polarization for chargeability mapping for airborne-scale areas. In particular it results that:

- Reducing the equivalences in the AEM-IP modelling is a key to unlock the understanding of the AIP sensitivity to geological and mineral targets.
- For this case study, the airborne chargeability shown sensitivity to deep chargeable bodies.
- All of the airborne chargeability anomalies have been confirmed from the ground DCIP models, demonstrating an overlapping field of sensitivity between the methods.
- Known mineralizations have been mapped with the AIP.
- The joint inversion between the DCIP and the AIP is possible and shows how the AEM data not only is compatible with the joint model, but also contribute in the chargeability mapping.

References

Bollino, A., Fiandaca G. (2024). Full-decay spectral modelling of time-domain induced polarization decoupling model and forward meshes. GNGTS 2024, 13-16 February 2024, Ferrara, Italy.

Fiandaca, G., Gazoty, A., Auken, E., & Christiansen, A. V. (2012). Time-domain-induced polarization: Full-decay forward modeling and 1D laterally constrained inversion of Cole-Cole parameters. Geophysics, 77, E213-E225.

Fiandaca, G., Ramm, J., Binley, J., Gazoty, A., Christiansen., A.V., Auken, E., Resolving spectral information from time domain induced polarization data through 2-D inversion, Geophysical Journal International, Volume 192, Issue 2, February 2013, Pages 631–646.

Fiandaca, G., Madsen, L.M. and Maurya, P.K. (2018), Re-parameterisations of the Cole–Cole model for improved spectral inversion of induced polarization data. Near Surface Geophysics, 16: 385-399.

Fiandaca, G., Zhang, B., Chen, J., Signora, A., Dauti, F., Galli, S., Sullivan, N.A.L., Bollino, A., Viezzoli, A. (2024). EEMverter, a new 1D/2D/3D inversion tool for Electric and Electromagnetic data with focus on Induced Polarization. GNGTS 2024, 13-16 February 2024, Ferrara, Italy.

Inverno, C. & Díez-Montes, A. & Rosa, Carlos & Garcia-Crespo, Jesus & Matos, João & García-Lobón, J. & Carvalho, João & Bellido, F. & Castello-Branco, J. & Ayala, Conxi & Batista, M. & Rubio, Felix Manuel & Granado, Isabel & Tornos, F. & Oliveira, Jose & Rey, C. & Araujo, Vitor & Sanchez-Garcia, Teresa & Pereira, Zelia & Sousa, P., (2015). Introduction and Geological Setting of the Iberian Pyrite Belt. 10.1007/978-3-319-17428-0_9.

Kratzer, T. and Macnae, J., 2012, Induced polarization in airborne EM, Geophys-ics, 77(5), E317–E327.

Oldenburg, D.W. & Li, Y., 1994. Inversion of induced polarization data, Geophysics, 59, 1327–1341.

Leistel, J.M., Marcoux, E., Thieblemont., D., Quesada, C., Sanchez, A., Almodovar G.R., Pascual, E., Saez, R., (1998). The volcanic-hosted massive sulphide deposits of the Iberian Pyrite Belt. Review and preface to the special issue: Mineralium Deposita, v. 33, p. 2-30

Menghini, A., Fernandez, I., Viezzoli, A., Pushing Exploration in the Pyrite Belt Around Aem, Conference Paper, NSG2022 3rd Conference on Airborne, Drone and Robotic Geophysics, Sep 2022, Volume 2022, p.1 – 5, Belgrade, Serbia.

Olsson, P. I., Fiandaca, G., Maurya, P. K., Dahlin, T., & Auken, E. (2019). Effect of current pulse duration in recovering quantitative induced polarization models from time-domain full-response and integral chargeability data. Geophysical Journal International, 218(3), 1739-1747.

Pelton W.H., Ward S.H., Hallof P.G., Sill W.R., Nelson P.H. Mineral discrimina-tion and removal of inductive coupling with multifrequency IP, Geophysics, 1978, vol. 43 (pg. 588-609).

Smith, R.S., and J. Klein, 1996, A special circumstance of airborne induced polar-ization measurements, Geophysics, 61, 66–73.

Viezzoli, Andrea & Fiandaca, Gianluca & Auken, Esben & Christiansen, Anders & Sergio, Simonetta. (2013). Constrained inversion of IP parameters from Airborne EM data. ASEG Extended Abstracts. 2013. 1. 10.1071/ASEG2013ab274.

Corresponding Author: francesco.dauti@unimi.it

UAS photogrammetry analysis for coastal hazard assessment: the case study of Maronti landslide (Ischia, 2022)

N.A. Famiglietti[1], A. Memmolo[1], P. Miele[1], E. Marotta[2], P. Belviso[2], G. Avvisati[2], C. Grasso[1], R. Moschillo[1], A. Vicari[1]

[1] Istituto Nazionale di Geofisica e Vulcanologia- Sezione Irpinia, Italy
[2] Istituto Nazionale di Geofisica e Vulcanologia- Osservatorio Vesuviano, Italy

Continental and marine processes drive coastal areas' landscape changes. The morphoevolution results from both rapid catastrophic events and slower continuous processes such as landslides, storms, and coastal land use, influenced by sea actions. The cliff erosion rates are linked to geological features, including rock mass strength and fracture system properties. The assessment of erosion processes and quantification of coastal retreat are crucial for effective coastal planning and engineering mitigation (Callaghan et al., 2009). Various methods, including geological processes monitoring, are used to assess coastal hazards (Quesada-Román and Peralta-Reyes, 2023).

The present study focuses on Maronti Bay's coastal evolution on Ischia Island, which has historically been affected by slope stability issues due to volcanic activity, earthquakes, and coastal erosion (Del Prete and Mele, 1999). In this perspective, researchers of the INGV (Istituto Nazionale di Geofisica e Vulcanologia) carry out periodical surveys of the Ischia territory. Drone surveys were used to evaluate the difference between pre- and post-landslide Digital Surface Models (DSMs) to focus on the November 26th, 2022 landslide event (Figure 1b). That event affected the volcanic cliff and can be classified as debris avalanche (Hungr et al., 2014) causing severe problems to the nearby structures and a remarkable scarp retreat of about 20 m. Consequently, debris and large blocks with the creation of a deposition area invaded the beach.

The pre (acquired on December 15th, 2021) and the post (acquired on January 31, 2023) datasets have been orthorectified and georeferred with PPK (Post Processing Kinematic) workflow (Famiglietti et al., 2021) using as GNSS base the station SANT (Santantuono) managed by INGV and located onto the Ischia island. Thanks to very high spatial resolution of products (1.7 cm) this analysis estimates mobilized volumes (Figure 1c) allowing the comparison with results presented by other authors (Massaro et al., 2023). The adopted approach offers a geometric understanding of coastal cliff evolution after the landslide impact. These insights are crucial for managing landslide risks on Ischia and for other similar environments, guiding the development of mitigation strategies to protect the environment and ensure residents' and visitors' safety.

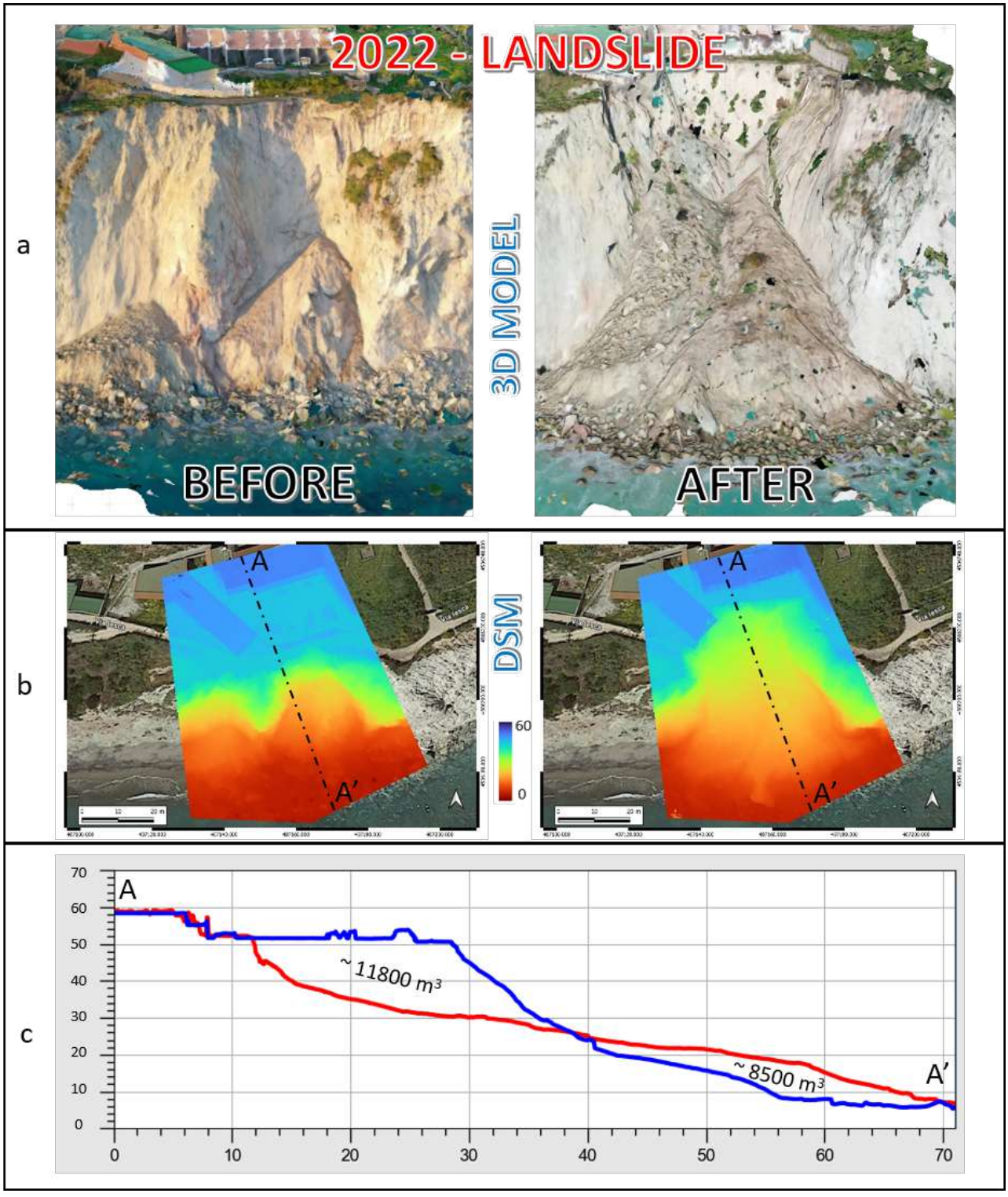

Fig. 1 – Pre and post 3D models, DSMs and section of the investigated area.

References

Callaghan, D.P., Roshanka, R., Andrew, S., 2009. Quantifying the storm erosion hazard for coastal planning. Coastal Engineering 56, 90–93. https://doi.org/10.1016/j.coastaleng.2008.10.003

Del Prete, Mele, 1999. L'Influenza dei fenomeni di instabilità di versante nel quadro morfoevolutivo della costa dell'isola d'Ischia. Bollettino Della Società Geologica Italiana 339–360.

Famiglietti, N.A., Cecere, G., Grasso, C., Memmolo, A., Vicari, A., 2021. A Test on the Potential of a Low Cost Unmanned Aerial Vehicle RTK/PPK Solution for Precision Positioning. Sensors 21, 3882. https://doi.org/10.3390/s21113882

Hungr, O., Leroueil, S., Picarelli, L., 2014. The Varnes classification of landslide types, an update. Landslides 11, 167–194. https://doi.org/10.1007/s10346-013-0436-y

Massaro, L., Forte, G., De Falco, M., Santo, A., 2023. Geomorphological Evolution of Volcanic Cliffs in Coastal Areas: The Case of Maronti Bay (Ischia Island). Geosciences 13, 313. https://doi.org/10.3390/geosciences13100313

Quesada-Román, A., Peralta-Reyes, M., 2023. Geomorphological Mapping Global Trends and Applications. Geographies 3, 610–621. https://doi.org/10.3390/geographies3030032

Acknowledgments

Special thanks to INGV - Osservatorio Vesuviano for providing the GNSS data used.

Corresponding author: nicola.famiglietti@ingv.it

InGEO: Innovation in geothermal resources and reserves potential assessment

A. Manzella[1], G. Gola[2], M. Tesauro[3], A. Galgaro[4]

[1] Istituto di Geoscienze e Georisorse, Consiglio Nazionale delle Ricerche, Pisa, Italy
[2] Istituto di Geoscienze e Georisorse, Consiglio Nazionale delle Ricerche, Torino, Italy
[3] Università degli Studi di Trieste, Dipartimento di Matematica e Geoscienze, Trieste, Italy
[4] Università degli Studi di Padova, Dipartimento di Geoscienze, Padova, Italy

In agreement with the European Green Deal, setting the ambitious target of reducing CO2 and climate-altering gas emissions by 55% by 2030 (from 1990 levels) and climate neutrality by 2050, the geothermal energy sector is expected to grow steadily. For many decades geothermal energy has been used on a large scale by tapping into hot water-bearing layers at 0 – 4 km depth. The geographical limitation of large-scale geothermal plants is going to be overcome by recent advancements, which demonstrate that it is possible to produce energy also by deep closed-loop heat exchanger systems in the subsurface (Gola et al., 2022). While research in this field develops, it is strategic to estimate - on a regional scale, down to a depth of 10 km - how much energy can be concentrated and extracted from upper-crustal layers.

The InGEO project (Innovation in GEOthermal resources and reserves potential assessment for the decarbonization of power/thermal sectors) aims to define a method to quantify the energy realistically producible from deep geothermal energy sources at the regional level to be used for specific technologies, e.g. to generate electricity or for district heating. Starting from a review of the existing techniques for the evaluation of the technical and economical-technical potential based on the volume method (Trumpy et al., 2016), further innovations will be included. Key challenges, considering a regional scale example as a test site, consist of: (i) developing a robust assessment of the deep geothermal resources, considering the local geological conditions, the thermal regime and the heat exchange capacity; (ii) defining operative solutions for heat extraction, including the exploitation of natural hydrothermal systems, the deep closed-loop heat exchangers as well as the thermal energy storage technologies, to optimise the thermal performance; and (iii) validating the regional scale approach with site-specific information.

The study area includes the sector of the buried fold and thrust belt of the Northern Apennine belonging to the Romagna and Ferrara Folds (Figure 1). This area has been the target of previous studies focused on both hydrocarbon and geothermal exploration activities. More than 500 boreholes with available lithostratigraphic and bottom hole temperature information have been selected. Locally, thermal data highlight positive heat flow anomalies attributable to the deep fluid circulation within the deep-seated carbonate sequences of Mesozoic age (Pasquale et al., 2013).

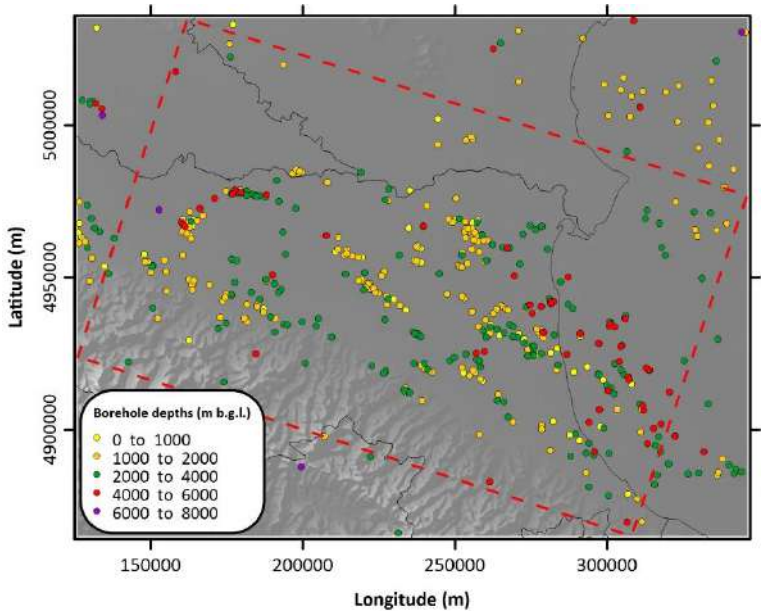

Figure 1. Area of study (dotted rectangle) and location of the selected deep boreholes as function of the total depth (meters below ground level).

The project will demonstrate an innovative exploration workflow to integrate geophysical data (e.g. Spada et al., 2013; Magnoni et al., 2022) to reconstruct the crustal and subcrustal structures (Figure 2). Moreover, taking advantage of the different sensitivity that geophysical data have on physical rock's parameters (temperature and composition), the optimized geological and thermal models will be the input of the resource assessment. The calculation of the deep geothermal energy potential for hydrothermal systems, deep closed-loop heat exchangers and thermal storage technologies will be performed by developing an open-source and web-based GIS tool, namely GEOTHERMOS.

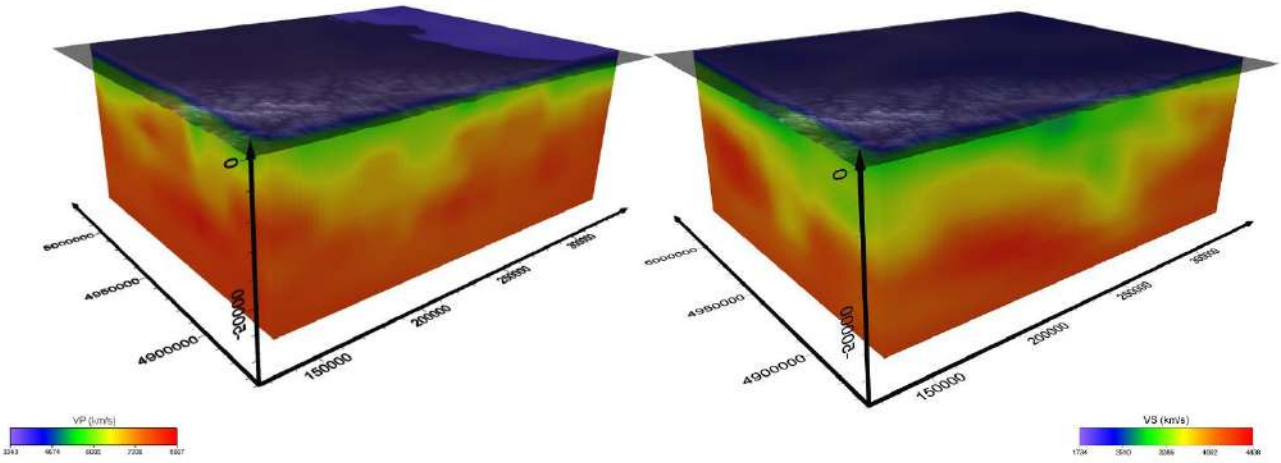

Figure 2. Distribution of the seismic velocities (Vp on the left, Vs on the right) beneath the area of study (from Magnoni et al., 2022).

The project is expected to have a significant impact on the geothermal community. The outcomes of InGEO are designed for use by investors, regulators, governments and consumers. InGEO sets the cornerstone for comprehensive deep geothermal potential estimation at the regional level.

Stakeholders will have the opportunity to compute the potential for any area where deep geological and thermal models will be available. The research units involved into the project will continue to improve the GEOTHERMOS tool by inserting their data also for other regions in Italy and will invite the scientific and industrial community to contribute to the feasibility.

Acknowledgements

The InGEO project has received founding from the European Union – NextGenerationEU

References

Gola, G., Di Sipio, E., Facci, M., Galgaro, A., & Manzella, A. (2022). Geothermal deep closed-loop heat exchangers: A novel technical potential evaluation to answer the power and heat demands. Renewable Energy, 198, 1193–1209. https://doi.org/10.1016/j.renene.2022.08.071

Spada, M., Bianchi, I., Kissling, E., Piana Agostinetti, N., Wiemer, S., 2013. Combiningcontrolled-source seismology and receiver function information to derive 3-DMoho topography for Italy. Geophys. J. Int. http://dx.doi.org/10.1093/gji/ggt148

Pasquale, V., Chiozzi, P., Verdoya, M. (2013). Evidence for thermal convection in the deep carbonate aquifer of the eastern sector of the Po Plain, Italy. Tectonophysics, 594, 1-12. https://doi.org/10.1016/j.tecto.2013.03.011

Trumpy, E., Botteghi, S., Caiozzi, F., Donato, A., Gola, G., Montanari, D., Pluymaekers, M.P.D., Santilano, A., van Wees, J.D., Manzella, A. (2016). Geothermal potential assessment for a low carbon strategy: A new systematic approach applied in southern Italy. Energy, 103, 167-181. https://doi.org/10.1016/j.energy.2016.02.144

Corresponding author: gianluca.gola@igg.cnr.it

Time-lapse Gravity Monitoring at surface and Excess Mass Estimation of CO_2 Stored in Deep Saline Aquifers

M. Milano[1], M. Fedi[1]

[1] Department of Earth, Environmental and Resources Sciences, University of Naples Federico II, Napoli, Italy.

This study regards the assessment of surface gravity surveying for CO_2 plume monitoring in a deep saline aquifer (Milano and Fedi, 2023). We simulated surface gravity monitoring of CO_2 storage for the injection and post-injection phases and using different injection rates. We show that time lapse gravity data can be used to successfully estimate the CO_2 stored mass by means of DEXP multiscale analysis, even when the anomaly is incompletely defined, due to a not proper areal coverage of the survey. The DEXP method has proven to be very stable with respect to noise and to be an efficient technique for simultaneously determining the CO_2 plume depth, its geometrical features and stored mass.

We used the available benchmark model of the Johansen reservoir to conduct the simulation. We calculated the gravity response at surface from the estimated models of reservoir density and saturation at different time intervals and for different injection rates. We used a new approach for monitoring the mass stored into the reservoir based on the DEXP method. DEXP allows an effective reduction of interference effects from nearby sources and it can be applied to high-order vertical or horizontal gradients of the field, maintaining high stability with respect to high-wavenumber noise. Moreover, this technique does not require any a-priori information about the geometry and physical parameter (density) of the source.

The results show that the baseline scenario of 15 kg/s of CO_2 injected for 25 years resulted in a weak gravity response. Conversely, for a rate of 60 kg/s we observe a maximum amplitude of about -16 μGal at the end of the injection period, while preserving low bottom hole pressure within the reservoir. We also show that we can track the migration of the CO_2 plume and contemporary the migration of the brine with respect to the well position. We also show that, by using the DEXP method, we can easily estimate the mass changes associated with the stored CO_2 for each injection rate, which we found to be very close to the true values. DEXP analysis has also proven to be very stable vs. noise. Compared to the results inferred from other methods, we showed that the DEXP analysis can simultaneously provide results about the depth to the source, the source geometry and, most importantly, an accurate estimate of the stored mass.

This study clearly shows that the appropriate choice of the injection rate strongly impacts on the ability to recover useful gravity signal at the surface, beyond the measurement error threshold. We provide an in-depth analysis of the effect of noise on the mass change estimates. Our approach

could be a valid tool for conducting real time monitoring of the CO_2 as it could accurately determine the effective mass stored in the reservoir. This is particularly important as it does not require information about the source and could make surface gravity surveying as an independent monitoring strategy.

References

Milano, M. & Fedi, M. Surface Gravity Response of CO_2 Storage in the Johansen Deep Reservoir. IEEE Trans. Geosci. Remote Sens. 61, 1–14 (2023)

Corresponding author: maurizio.milano@unina.it

SpiderTherm: Optimizing Geothermal Extraction for Sustainable Energy Transition

A. Molossi[1], G. Gola[2], A. Manzella[2], M. Pipan[1]

[1] *Università di Trieste, Dipartimento di Matematica e Geoscienze, Via E. Weiss 1, Trieste, Italy.*

[2]*Institute of Geosciences and Earth Resources, National Research Council, via Giuseppe Moruzzi, 1, 56124, Pisa, Italy*

The geothermal resource presents at least three advantageous aspects: i) it is a ubiquitous and continuous source of energy; ii) it can contribute to the thermal and electrical energy needs in residential and industrial sectors; iii) it can aid the energy transition process towards renewable energy sources. Geothermal fluids are valuable energy sources with various applications depending on their temperature range: between 40°-60°C, they are mainly used for greenhouse heating and aquaculture; between 60°-70°C, common applications include building conditioning and domestic water heating; above 70°-80°C, water can be integrated into industrial processes or used for absorption chillers in refrigeration cycles; and starting from 100°C, the primary fluid can be used in binary geothermal systems for electricity production.

Conventional geothermal applications utilizing natural hydrothermal systems face challenges in exploration due to uncertainty in subsurface lithology and fluid distribution, corrosion and mineral precipitation during production, and environmental impacts such as subsidence and induced seismicity. Economic feasibility is another limitation, primarily due to high drilling costs, but retrofitting abandoned wells, originally drilled for the oil industry, offers a cost-effective alternative.

An unconventional approach to harness geothermal energy is the deep borehole heat exchanger (DBHE), involving coaxial pipes in single wells. However, its low efficiency restricts its applicability in geothermal power production compared to conventional systems. Recently, deep closed-loop geothermal systems (DCHE) have been proposed to enhance efficiency by connecting multiple wells horizontally, demonstrating potential for geothermal power production under favourable conditions.

The energy performance of DCHE depends on various parameters, such as environmental, design, and operational variables. With respect to the different parameters, Gola et al. (2022) demonstrated by a sensitivity study that the following factors play a primary role: the undisturbed geothermal gradient, the dimensions (vertical depth and horizontal length) of the closed-loop, , the flow rate, , and injection temperature.

This study aims to analyze the long-term performance of an innovative DCHE configuration, varying the number of reused exploration wells (N), vertical (H) and horizontal (L) lengths, flow rate per well (q), injection temperature (Tin), heat exchange (DT), and geothermal gradient (Ggeo). The goal is to identify conditions that achieve the recommended minimum long-term production temperature of 100°C for binary geothermal power plants.

We did this with a numerical simulation approach using COMSOL 6.1. However, numerical simulations can suffer high computational time , which can become a limitation.Machine learning, specifically Long-Short Term Memory (LSTM) neural networks, is explored for predicting long-term production temperatures based on the mentioned variables, offering a faster alternative to numerical simulations.

To do that, we used the COMSOL results of each DCHE as a training set for the LSTM system. So far, the tested LSTM system is a very shallow network with three hidden layers with 24, 14, and 7 neurons, respectively. Given the low number of training instances, we were interested in testing different learning strategies to observe which was faster in convergence and determine the best in temperature forecasting after ten years of production. These strategies are the curriculum and the non-curriculum learning (standard).

We applied the proposed concepts in a specific case study in Cesano, integrating available geological and geothermal information. The simulation assessed the production temperature after 10 years for a 3-branch DCHE configuration in the Cesano area, known for its abundance of abandoned or depleted wells and a high geothermal gradient.

The results from the numerical simulation indicate that the production temperature in such a DCHE configuration would be 139.57 °C. Our analysis using a Long-Short Term Memory (LSTM) neural network trained with curriculum and non-curriculum learning strategy predicted a value of 136.8 °C and 95.7 °C with an absolute error of 2.77 °C and 41.1°C, respectively. This suggests that the LSTM can provide accurate predictions for long-term production temperatures, offering an efficient alternative to more time-consuming numerical simulations.

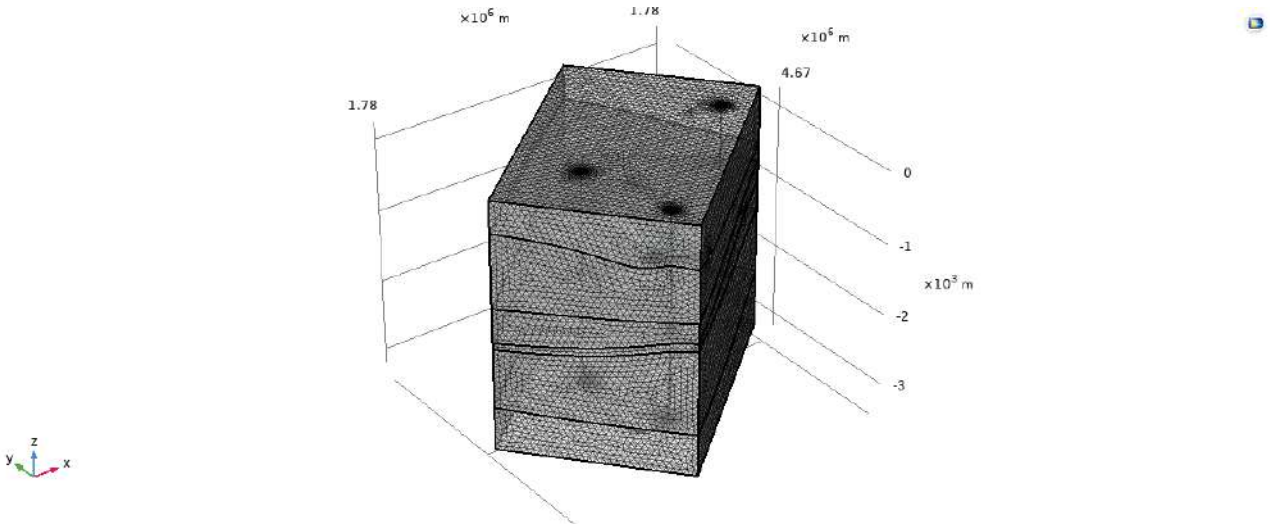

Figure 1 3D view of the Deep Closed-Loop Heat Exchanger (DCHE) model in the Cesano area made up of three reused geothermal wells (2 injections and 1 production boreholes). The surfaces delineating the lithothermal units as well as the numerical mesh are displayed.

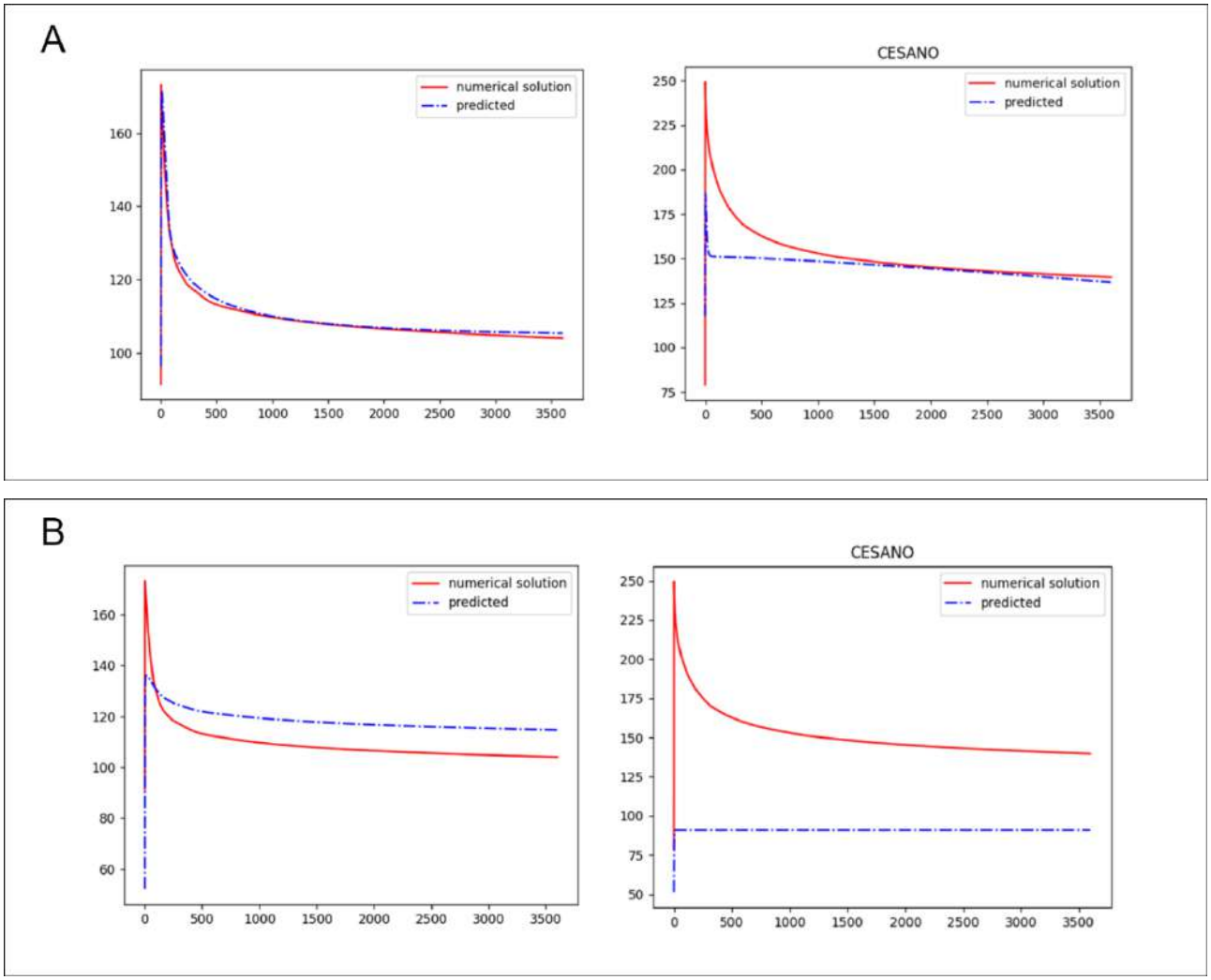

Figure 2. LSTM production temperatures forecasting versus simulated ones obtained by curriculum-learning (a) and non-curriculum (b) strategies. On the left the results refer to the synthetic scenarios and on the right to the Cesano area case study.

References

Alimonti, C., Berardi, D., Bocchetti, D., & Soldo, E. (2016). Coupling of energy conversion systems and wellbore heat exchanger in a depleted oil well. *Geothermal Energy*, *4*(1), 11. https://doi.org/10.1186/s40517-016-0053-9

Alimonti, C., & Soldo, E. (2016). Study of geothermal power generation from a very deep oil well with a wellbore heat exchanger. *Renewable Energy*, *86*, 292–301. https://doi.org/10.1016/j.renene.2015.08.031

Chen, S., Zhang, Q., Andrews-Speed, P., & Mclellan, B. (2020). Quantitative assessment of the environmental risks of geothermal energy: A review. *Journal of Environmental Management*, *276*, 111287. https://doi.org/10.1016/j.jenvman.2020.111287

DiPippo, R. (2007). Ideal thermal efficiency for geothermal binary plants. *Geothermics*, *36*(3), 276–285. https://doi.org/10.1016/j.geothermics.2007.03.002

Doran, H. R., Renaud, T., Falcone, G., Pan, L., & Verdin, P. G. (2021). Modelling an unconventional closed-loop deep borehole heat exchanger (DBHE): Sensitivity analysis on the Newberry volcanic setting. *Geothermal Energy*, *9*(1), 4. https://doi.org/10.1186/s40517-021-00185-0

Eavor-Lite™—Eavor—Demonstrating a New Energy Solution. (s.d.). *Eavor*. Recuperato 28 novembre 2023, da https://www.eavor.com/eavor-lite/

Falcone, G., Liu, X., Okech, R. R., Seyidov, F., & Teodoriu, C. (2018). Assessment of deep geothermal energy exploitation methods: The need for novel single-well solutions. *Energy*, *160*, 54–63. https://doi.org/10.1016/j.energy.2018.06.144

Gangwani, P., Soni, J., Upadhyay, H., Joshi, S., & Student, M. (2020). *A Deep Learning Approach for Modeling of Geothermal Energy Prediction*. *18*(1).

Geothopica. (s.d.). Recuperato 28 novembre 2023, da https://geothopica.igg.cnr.it/index.php?lang=en

Gola, G., Di Sipio, E., Facci, M., Galgaro, A., & Manzella, A. (2022). Geothermal deep closed-loop heat exchangers: A novel technical potential evaluation to answer the power and heat demands. *Renewable Energy*, *198*, 1193–1209. https://doi.org/10.1016/j.renene.2022.08.071

Gupta, S., Chakraborty, G., Kanungo, U. S., & Bharsakale, A. (2006). Dattatraya K. *Reservoir delineation of lower Kalol pays and field growth in Wadu And Paliyad Areas, Cambay Basin, India. In*, 2006. Scopus.

Home | Sustainable Development. (s.d.). Recuperato 28 novembre 2023, da https://sdgs.un.org/#goal_section%20last

Hu, X., Banks, J., Guo, Y., & Liu, W. V. (2021). Retrofitting abandoned petroleum wells as doublet deep borehole heat exchangers for geothermal energy production—A numerical investigation. *Renewable Energy*, *176*, 115–134. https://doi.org/10.1016/j.renene.2021.05.061

Kujawa, T., Nowak, W., & Stachel, A. A. (2006). Utilization of existing deep geological wells for acquisitions of geothermal energy. *Energy*, *31*(5), 650–664. https://doi.org/10.1016/j.energy.2005.05.002

Liao, Y., Sun, X., Sun, B., Wang, Z., Wang, J., & Wang, X. (2021). Geothermal exploitation and electricity generation from multibranch U-shaped well–enhanced geothermal system. *Renewable Energy*, *163*, 2178–2189. https://doi.org/10.1016/j.renene.2020.10.090

Lund, J. W. (2003). The use of downhole heat exchangers. *Geothermics*, *32*(4), 535–543. https://doi.org/10.1016/j.geothermics.2003.06.002

Moore, J. N., & Simmons, S. F. (2013). More Power from Below. *Science*, *340*(6135), 933–934. https://doi.org/10.1126/science.1235640

Nadkarni, K., Lefsrud, L. M., Schiffner, D., & Banks, J. (2022). Converting oil wells to geothermal resources: Roadmaps and roadblocks for energy transformation. *Energy Policy*, *161*, 112705. https://doi.org/10.1016/j.enpol.2021.112705

Palomo, E., Colmenar-Santos, A., & Rosales-Asensio, E. (2022). Measures to Remove Geothermal Energy Barriers in the European Union. In E. Palomo, A. Colmenar-Santos, & E. Rosales-Asensio (A c. Di), *Potential of Low-Medium Enthalpy Geothermal Energy: Hybridization and Application in Industry* (pp. 9–45). Springer International Publishing. https://doi.org/10.1007/978-3-030-95626-4_2

Saltelli, A., Ratto, M., Andres, T., Campolongo, F., Cariboni, J., Gatelli, D., Saisana, M., & Tarantola, S. (2008). *Global Sensitivity Analysis: The Primer*. John Wiley & Sons.

Shi, Y., Song, X., & Song, G. (2021). Productivity prediction of a multilateral-well geothermal system based on a long short-term memory and multi-layer perceptron combinational neural network. *Applied Energy*, *282*, 116046. https://doi.org/10.1016/j.apenergy.2020.116046

Trumpy, E., & Manzella, A. (2017). Geothopica and the interactive analysis and visualization of the updated Italian National Geothermal Database. *International Journal of Applied Earth Observation and Geoinformation*, *54*, 28–37. https://doi.org/10.1016/j.jag.2016.09.004

ViDEPI. (s.d.). Recuperato 28 novembre 2023, da https://www.videpi.com/videpi/pozzi/pozzi.asp

Wang, N., Chang, H., Kong, X., Saar, M. O., & Zhang, D. (2022). *Deep learning based closed-loop optimization of geothermal reservoir production* (arXiv:2204.08987). arXiv. https://doi.org/10.48550/arXiv.2204.08987

Witter, J. B., Trainor-Guitton, W. J., & Siler, D. L. (2019). Uncertainty and risk evaluation during the exploration stage of geothermal development: A review. *Geothermics*, *78*, 233–242. https://doi.org/10.1016/j.geothermics.2018.12.011

Yuan, W., Chen, Z., Grasby, S. E., & Little, E. (2021). Closed-loop geothermal energy recovery from deep high enthalpy systems. *Renewable Energy*, *177*, 976–991. https://doi.org/10.1016/j.renene.2021.06.028

Corresponding author: attilio.molossi@phd.units.it

Machine learning classification of seismic tremor associated with the Mefite d'Ansanto CO_2 gas emission.

S. Panebianco[1,2], C. Satriano[3], G. Vivone[2], M. Picozzi[4], A. Strollo[5], T.A. Stabile[2]

[1] *Dipartimento di Fisica e Scienze della Terra, Università di Ferrara, Italy*
[2] *Consiglio Nazionale delle Ricerche (CNR-IMAA), Italy*
[3] *Université Paris Cité, Institut de physique du globe de Paris, France.*
[4] *Istituto Nazionale di Oceanografia e di Geofisica Sperimentale - OGS, Italy.*
[5] *GFZ German Research Centre for Geoscience, Potsdam, Germany.*

The focus of this study is framed around the development of automatic methods to track the spatio-temporal evolution of deep-origin, non-volcanic gas emissions. It is widely recognized that crustal fluids play a crucial role in the earthquake nucleation process, and the characterization of their emissions on the surface can be essential for better understanding crustal source mechanisms.

We investigated seismic tremors recorded at the gas-emission of Mefite d'Ansanto, situated within one of the highest seismic hazard areas of Southern Apennines, at the northern end of the fault system that generated the Mw 6.9 1980 Irpinia Earthquake. Mefite d'Ansanto is currently considered to be the largest natural emission of deep-source, non-volcanic, CO_2-dominated gases on Earth, with an estimated total gas flux of about 2000 tons per day.

We studied seismic tremor recorded between 30-10-2019 and 02-11-2019 recorded by a dense temporary seismic network (4 broadband and 7 short-period sensors) deployed around the emission area. Tremor signals were identified by developing an automated detection algorithm, based on non-parametric statistics of the recorded signal amplitudes. At the same time, we extracted signals characteristics parameters like the RMS amplitude and the statistical moments of amplitude distributions, both in time and frequency domains. These were used as features for training and optimizing station-based KNN (k-Nearest-Neighbors) binary classifiers, which were then used to classify and discriminate the target tremor from anthropogenic and background noise. The trained classifiers showed good performances, with a median overall accuracy of 92.8%. The comparison of the classified tremor across all stations revealed common features: a variable duration (16 s to 30-40 mins), a broad-frequency band (4-20 Hz) with varying amplitudes peaks at different stations, and two kinds of signals: (a) long-duration, high-amplitude tremors, (b) pulsating tremors. The higher amplitude of classified tremors recorded at stations located close to bubbling and pressurized vents suggests the presence of multiple local sources.

Corresponding author: serenapanebianco@cnr.it

Mapping the thermophysical properties of Apennines rocks (Central Italy): implications for the temperature state of crust.

Sabatini A.[1], C. Pauselli[1], S. Fuchs[2], M. Ercoli[1], P. Mancinelli[1]

[1] Università degli Studi di Perugia, Dip. Fisica e Geologia, Italy.
[2] GFZ German Research Centre for Geosciences, Germany.

This work presents the results obtained from the laboratory analysis of the thermophysical properties of carbonate rocks and turbidites present in the northern Apennines. The aim was to determine and relate the thermophysical properties of outcropping carbonate rocks belonging to the main geological formations that characterize western Umbria (central Italy). The determinations were carried out to observe the heat transfer capacity of these rocks, with varying temperatures and both in dry and saturated conditions; the porosities, that results less than 5%; the densities and the mineralogical composition of 70 samples.

The thermal conductivity values measured in dry conditions with three different devices based on the transient technique, differ by percentages of less than 10%.

Mineralogical analysis indicates that the formations under examination are mainly composed of calcite, with an abundance of quartz for some samples.

The thermal conductivity values at ambient temperature of 20 – 25°C measured in dry conditions vary from 1.8 to 3.0 W/mK for samples with predominant calcite, and greater than 3.6 W/mK for samples with larger quantities of quartz. The decrease in conductivity up to 200°C is about 30% for most samples.

Theoretical equations based on the mineralogical composition and porosity were analysed to find the right fit with the measured values, with the possibility of extending the results to other parts of the world.

The results obtained from the study represent the basis for a more complete evaluation of the temperature trend with depth, useful for the evaluation of geothermal systems and for defining the rheological behaviour of the crust.

Corresponding author: alessandro.sabatini1@studenti.unipg.it

ISTRICI - STRUCTURAL INVERSION OF COMMON IMAGE GATHERS

U. Tinivella[1], M. Giustiniani[1]

1 National Institute of Oceanography and Applied Geophysics – OGS, Trieste, Italy

In this paper, we present a free package consisting of codes developed by us and Seismix Unix (SU; Cohen and Stockwell, 2008), an open-source software package for seismic data analysis, to determine the seismic velocity field in different geologic settings. This package, called ISTRICI, was developed to facilitate the use of Seismic Unix, a free software designed to process seismic data. Seismic Unix is a powerful tool for performing pre-stack depth migration and using the residual parameters to update the seismic velocity model based on the pre-stack depth migration results. What is missing are codes and scripts that allow practical, interactive, and easy application of the Seismic Unix algorithms. Therefore, ISTRICI was developed to fill this gap.

ISTRICI consists of three workflows (INTER, CIG and TRAD; Tinivella and Giustiniani, 2023) for interactively performing residual velocity analysis and pre-stack depth migration, switching from one workflow to the next depending on the characteristics and type of seismic data. The PreStack depth migration (PSDM) adopted in SU is based on the method of Liu and Bleistein (1995); the PSDM output consists of two migration sections characterised by the same phase, but different amplitudes. The algorithm performs the PSDM using the input and perturbed velocity models. The ratio of the amplitudes of these two PSDM sections is used to evaluate the residual velocity (i.e.,Vargas-Cordero et al., 2010). The result of the migration can be organized into CIGs: if the migrated reflections in the CIGs are flat, it means that a correct migration velocity was used to migrate the data (Yilmaz 2001). By contrast, the slope of the reflections in the CIGs indicates an error in the migration velocity, which can be corrected by analyzing the residual energy and then updating the velocity (code available in SU; Liu and Bleistein, 1995). The residual energy (called the r-parameter) is a measure of the flatness deviations of the reflections along the offset in each CIG (i.e., Tinivella et al., 2009). A zero value for the r-parameter means that the velocity is corrected at the corresponding reflection. If the r-parameter has a negative/positive value, it means that the velocity must be increased/decreased. Then, using the theory of Liu and Bleistein (1995), the r-parameter is converted to a residual velocity used to update the input velocity. It is important to remember that, when the medium has strong lateral velocity variations, the algorithm works adequately even with small velocity corrections. All steps, such as PSDM, CIG analysis, r-parameter evaluation, velocity update, are performed iteratively until all reflections in the CIGs are reasonably flat, i.e. when the variation of the depth of the reflector versus offset is sufficiently small in each CIG (Vargas-Cordero et al., 2010).

The novelty of the ISTRICI package is to propose three different ways to organize the CIGs to improve the seismic velocity analysis depending on different elements, such as targets and characteristics of the data, optimizing the result quality and reducing the time needed to analyze the r-parameters in the residual semblances. ISTRICI has been developed on the basis of the most common cases: (i) the continuity of some reflections along the seismic line, such as the seafloor, suggests that the picking procedure can be performed semi-automatically in the residual semblance; (ii) the availability of the interpretation of the seismic section suggests that the velocity analysis can be performed along the interpreted reflectors; (iii) in complex geological settings and/ or in the presence of non-continuous reflectors, the velocity analysis can be performed as a function of depth rather than in a layer-stripping approach. The user can choose and move from one workflow to another in order to better resolve the targets and/or scientific questions on the basis of the characteristics of the data. Moreover, for the same purposes, the user can update and modify the codes related to the velocity analysis. The STEP 1 of all workflows consists of performing PSDM obtaining two outputs: the standard migration and the additional migration with extra amplitude (see details in Liu and Bleistein, 1995). Before this step, an initial velocity model has to be created, which is input into the workflow along with the seismic data for the first step. In the INTER workflow, the r-parameter analysis is performed along a selected reflector. The procedure of INTER consists of four steps (Fig. 1). First, after PSDM, the migrated section is interpreted by picking the selected reflector; then, the picks are interpolated to obtain one pick for each migrated trace (STEP 2). Then, in a selected range of CIGs, residual propagation analysis is calculated over the depth of the selected reflector with a defined window based on the wavelength of the reflection.Then, the operator simply selects the r-parameter along the reflector; the selections are interpolated to obtain an r-parameter value for each CIG (STEP 3). STEP 4 consists of evaluating the velocity and updating the reflector depth for each CIG based on the r-parameter value and migration results. The procedure is repeated from STEP 1 to STEP 4 until the difference between two successive iterations is less than a certain threshold. The final velocity model is composed of the selected layers. In each layer, the velocity changes in horizontal direction, but is constant in depth.

In the CIG workflow, the analysis of the r-parameters is performed along a selected reflector, but unlike the INTER workflow, the picking is performed by analysing the total semblance at each selected CIG (see also Vargas-Cordero et al., 2010). This workflow also requires four STEPS, as described in Fig. 2. In STEP 2, the migrated section is interpreted and the picking of a reflection is performed. As in the INTER workflow, the picks are interpolated along the seismic section. STEP 3 consists of picking the r-parameter at depth in proximity of the picked reflector at selected CIGs. To help the user, the code specifies the depth of the selected reflector at the semblance to pick the r-parameter where the energy is higher. In this way, the interpretation of the seismic line (i. e., the depth of the target interface) is changed according to the maximum coherence of the semblance. STEP 4 is the same as the one in the INTER workflow as well as the final result. Also in this case, STEPs 1-4 are repeated until the difference between successive iterations is less than a certain threshold.

The TRAD workflow is different from the other two workflows because STEP 2, dedicated to the interpretation of the migration section, is not required. In fact, only two STEPs are required in this workflow in addition to STEP 1 (Fig. 3). STEP 2 consists in selecting the maximum energies in the semblance at selected CIGs. Of course, the number of models in selected layers when an interpretation of the seismic line is provided. In this way, it is possible to switch from one workflow to another at each stage of the inversion. Once the procedure is completed, ISTRICI can include a velocity gradient below the last inverted layer or a defined surface before performing the final

PSDM to improve the seismic imaging.

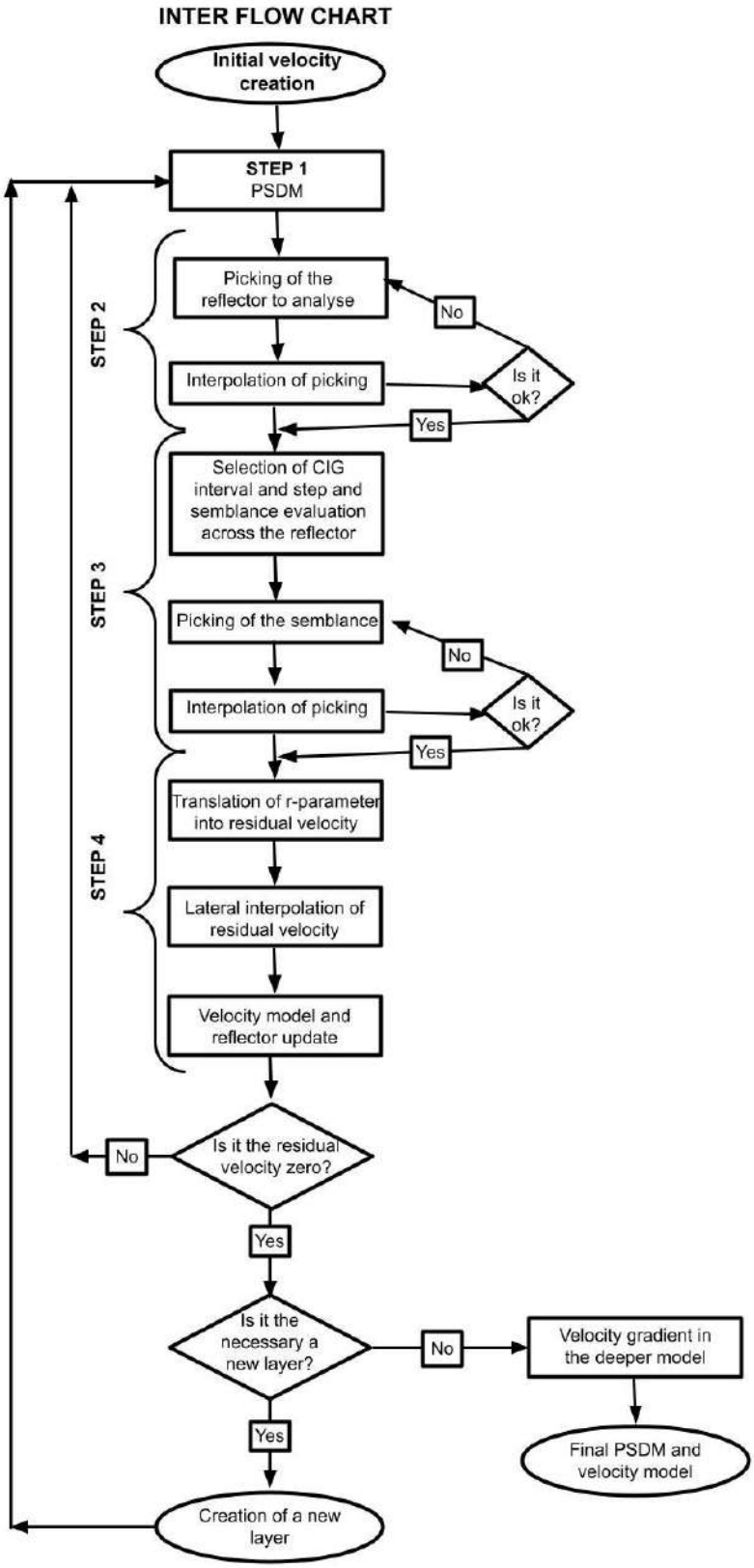

Fig. 1 - Flowchart of INTER

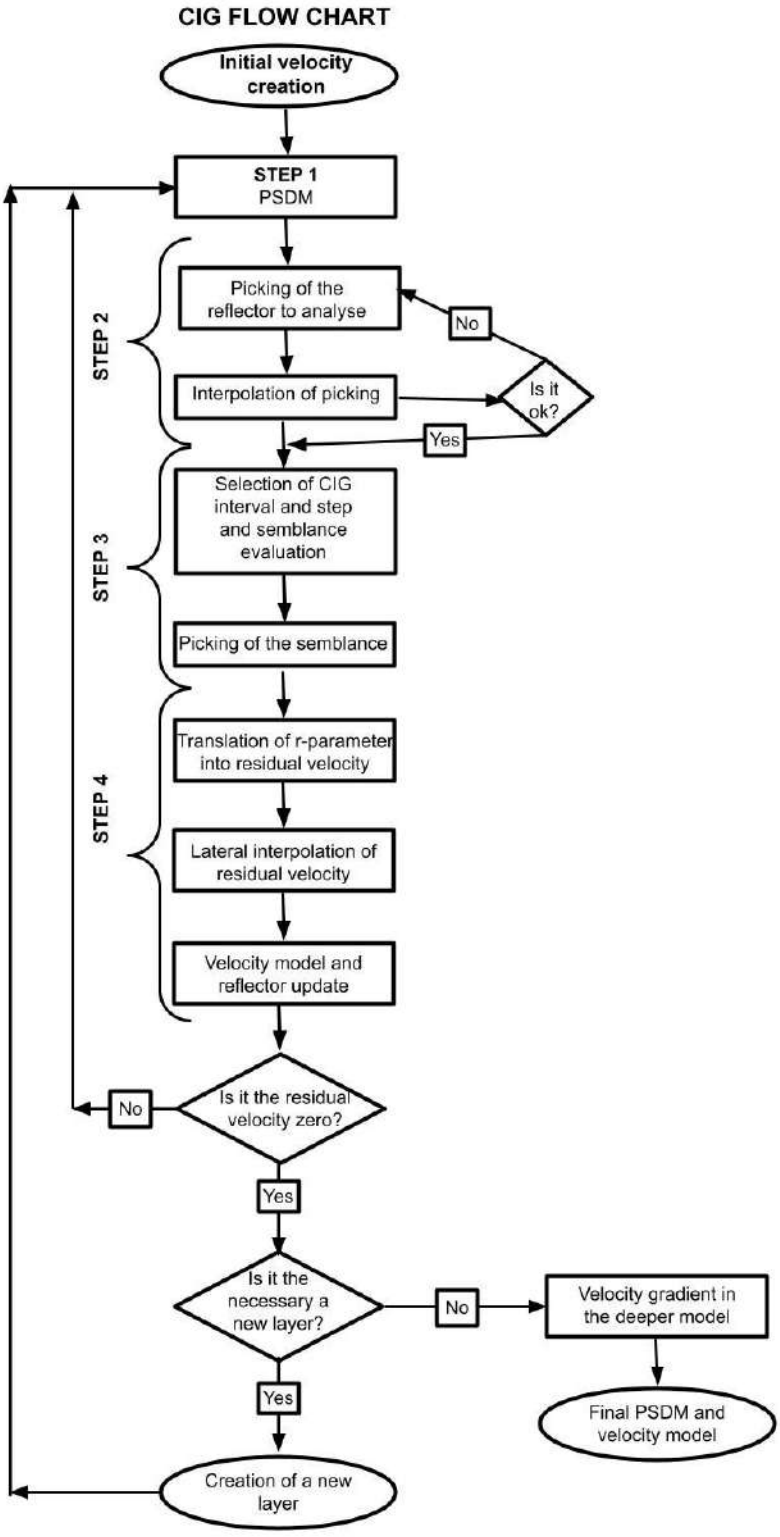

Fig. 2 - Flowchart of CIG

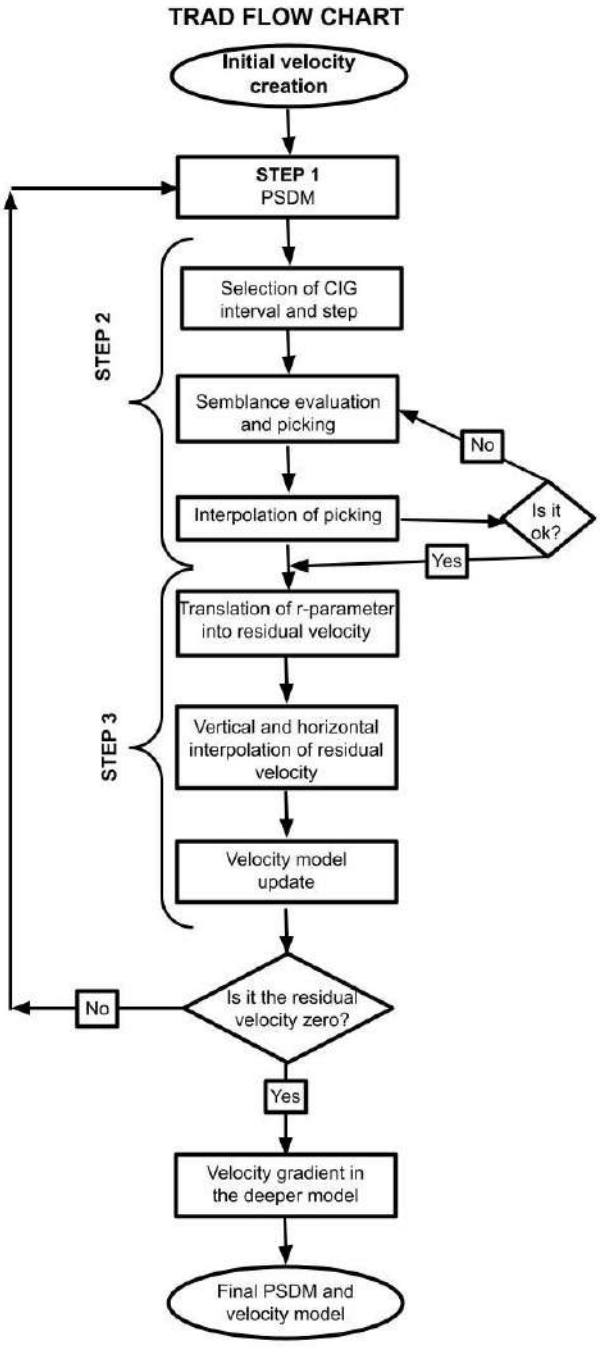

Fig. 3 - Flowchart of TRAD

ISTRICI package has been tested on different dataset with excellent results (i.e., Tinivella et al., 2009; Vargas et al., 2010; Vargas et al., 2016). Our codes were developed and improved after many tests that allowed identifying critical steps. As mentioned before, it is worth highlighting that the codes and scripts can easily be modified by the user if necessary. ISTRICI can be downloaded from the following public repository: https://github.com/utinivella/ISTRICI; a README file is provided for each workflow (INTER, CIG, and TRAD); an example is also available. ISTRICI uses codes from

Seismic Unix, free software that can be downloaded here: https://wiki.seismic-unix.org/doku.php. Information about the use of ISTRICI at the Authors is appreciated. Finally, ISTRICI can be used in the present form for multichannel seismic data, ocean bottom seismometer data, ocean bottom cable data as well as land data.

Acknowledgements

This study was supported by the Italian Ministry of Education, Uni- versities and Research in part under the extraordinary contribution for Italian participation in activities related to the international infrastructure PRACE-The Partnership for Advanced Computing in Europe (www.prace-ri.eu; Decreto MIUR No. 631 of August 8, 2016) and in part by the PRIN Project entitled: “Methane recovery and carbon dioxide disposal in natural gas hydrate reservoirs”.

References

Cohen J.K., Stockwell Jr., J.W.; 2008: CWP/SU: Seismic Unix Release No. 41: an Open Source Software Package for Seismic Research and Processing. Center for Wave Phenomena, Colorado School of Mines.

Liu Z., Bleistein N.; 1995: Migration velocity analysis: theory and an iterative algorithm. Geophysics, 60, 142e153.

Tinivella U., Loreto M.F., Accaino F.; 2009: Regional versus Detailed Velocity Analysis to Quantify Hydrate and Free Gas in Marine Sediments: the South Shetland Margin Case Study. Geological Society Special Publication, 319, 103–119.

Tinivella U., Giustiniani M.; 2023: ISTRICI – Tools for facilitating seismic depth imaging and velocity analysis with seismic unix. Computers & Geosciences, 180, 105458.

Vargas-Cordero I., Tinivella U., Accaino F., Loreto M.F., Fanucci F.; 2010: Thermal state and concentration of gas hydrate and free gas of Coyhaique, Chilean Margin (44◦30′ S). Mar. Petrol. Geol., 27 (5), 1148–1156.

Vargas-Cordero I.C., Tinivella U., Villar-Mu˜noz L., Giustiniani,M.; 2016: Gas hydrate and free gas estimation from seismic analysis offshore Chilo´e island (Chile). Andean Geol. 43 (3), 263–274.

Yilmaz O.; 2001: Seismic Data Analysis: Processing, Inversion and Interpretation of Seismic Data, second ed. Society of Exploration Geophysicists, Tulsa, Oklahoma, p. 2027.

Corresponding author: utinivella@ogs.it

Methane recovery and carbon dioxide disposal in natural gas hydrate reservoirs

U. Tinivella[1], S. Cannone[2], B. Castellani[3], M. Ciulla[4], P. Di Profio[4], A. Nicolini[3], M. Filipponi[3,6], R. Fazioli[5], A. M. Gambelli[3], R. Giovannetti[6], M. Giustiniani[1], A. Lanzini[2], L. Mascali[2], G. Minelli[3], A. Rossi[6], M. Santarelli[2], D. Schiera[2], F. Trippetta[7], M. Zannotti[6], F. Rossi[3]

[1] Istituto Nazionale di Oceanografia e di Geofisica Sperimentale—OGS, Sgonico, Italy;
[2] Energy Department, Politecnico di Torino, Torino, Italy;
[3] University of Perugia, Perugia, Italy;
[4] University of Chieti, Chieti, Italy;
[5] University of Ferrara, Ferrara, Italy;
[6]Chemistry Division, School of Science and Technology, University of Camerino, Italy;
[7]University of Rome "La Sapienza", Italy.

The present paper presents the results obtained in a three-year national research project on natural gas hydrate exploitation and carbon dioxide disposal. The consortium of partners is led by University of Perugia (UNIPG), which includes the Applied Physics group and the Structural Geology group. The other partners are the University of Camerino (UNICAM), the Politecnico di Torino (POLITO), the Istituto di Oceanografia e Geofisica Sperimentale (OGS) and the University of Ferrara (UNIFE).

The proposed project aims to develop an innovative technological solution for the extraction of methane from marine natural gas hydrates and the simultaneous sequestration of carbon dioxide in a single process (Fig. 1; Gambelli et al., 2021). The obtained fuel is neutral in terms of climate changing emissions and therefore equivalent to renewable energy sources. The multidisciplinary expertise of the consortium is focussed on the pursuit of five specific objectives:

1. Analysis of marine hydrate reservoirs, potentiality and infrastructures for their exploitation

2. Reproduction of hydrate sediments in the laboratory and determination of kinetic and thermodynamic parameters

3. CO2 replacement in methane hydrates

4. Development of a scalable technology for CO2 injection/CH4 extraction in natural hydrate reservoirs

5. Theoretical model applicable of marine hydrate reservoir and energy/environmental assessment of the proposed process.

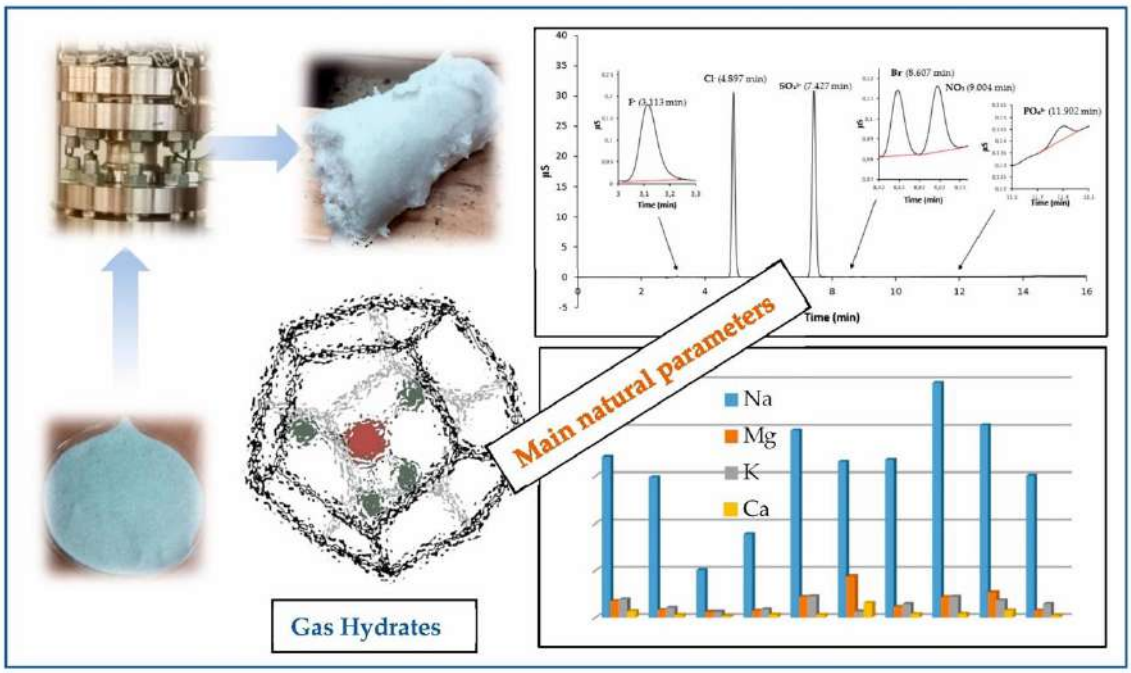

Fig. 1 – Simplified scheme of the adopted approach

The first three objectives aimed at gaining a body of knowledge on the chemical, physical and geotechnical properties of marine natural gas hydrates and on the CH4-CO2 replacement mechanism. For the activities in these three objectives, laboratory facilities of UNIPG and UNICAM are used. In addition, laboratory facilities of "D'Annunzio" University of Chieti-Pescara (UNICH) are employed since UNICH has available a patented reactor to study the kinetics of the hydrate formation process. Objective 4 concerns the design and construction of a scalable device for methane extraction and CO2 replacement. It is integrated with a methane purification and CO2 recirculation section and tested in a seafloor simulator, where water-rich natural gas hydrates sediment reproduction and in-situ measurements will be performed. Finally the last objective focuses on the development of a theoretical geophysical model of the marine natural gas hydrates reservoir and final evaluations on energy, environmental and economic impact of the proposed process and technological solution. The starting point for the development of a theoretical model is the method proposed by Tinivella (1999), which is based on the Biot-Geerstma-Smit equations. The input data are the results of laboratory analysis, which provide various parameters such as bulk density, P-wave velocity, S-wave velocity and porosity. To estimate the stiffness and compressibility of the sediments and the hydrate, these two parameters were varied until obtaining the P-wave and S-wave velocity obtained in the laboratory.

References

Gambelli M.A.; Tinivella U.; Giovannetti R.; Castellani B.; Giustiniani M.; Rossi A.; Zannotti M.; Rossi F.; 2021: Observation of the Main Natural Parameters Influencing the Formation of Gas Hydrates. Energies 14, 1803.

Tinivella U.; 1999: A method for estimating gas hydrate and free gas concentration in marine sediments. Bollettino di Geofisica Teorica ed Applicata 40(1), 19-30.

Corresponding author: utinivella@ogs.it

Seismic attribute analyses for geothermal applications: a case study from the geothermal potential assessment in the Valle Latina area (Central Italy).

G. Vico[1,2], R. Maffucci[2], S. Bigi[1]

[1] Dipartimento di Scienze della Terra, Università di Roma La Sapienza, Italy
[2]Istituto Nazionale di Geofisica e Vulcanologia, Roma, Italy

Introduction

We reprocessed the seismic public profiles acquired in the Valle Latina in the last century for a Ph.D. project focused on identifying potential geothermal reservoirs. Our main target was to depict faults, fracture zones, and strong AI contrast, reprocessing the VIDEPI seismic reflection profiles with the application of an advanced Matlab code (i.e., WIGGLETOSEGY by Sopher, 2018). Using this code allowed us to digitize the seismic traces of the vintage seismic profiles to obtain major quality data for seismic attribute analysis to detect faults and fracture zones that may have a great influence in the behavior of a geothermal reservoir.

The main goal of this integrated PhD project is to provide an accurate characterization of specific geothermal systems located in central Italy. The focus is defining their potential for geothermal energy planning and elaborating a potential reservoir assessment. The ultimate aim is to develop a map of the geothermal potential structures and identify one or more case studies in the southern Latium, particularly in the Valle Latina area of interest. In the southernmost part of Latium, in correspondence with the Mesozoic carbonate reservoir, hot waters were found within 1-1.4 km depth in the areas of (i) Latina (60 °C at 1.4 km); (ii) Fogliano (80 °C at 1 km); (iii) in the Valle Latina (50-70 °C at 1-2 km); and (iv) near the Terme di Suio (50-100 °C at 0.5-1 km) (Buonasorte et al., 2011).

Data and Methods

In order to describe the structural features of Valle Latina, we analyzed a huge hydrocarbon exploration dataset consisting of geophysical and stratigraphic well-logs, along with seismic reflection profiles. The geophysical data comprised public data from the ViDEPI project database and literature and private data provided by Pentex Italia Ltd. The seismic profiles were recorded from various acquisition surveys conducted in the 1980s and 1990s by AGIP, Sovereign, and Pentex for hydrocarbon exploration. The seismic dataset includes both the stack and the migrated versions.

WIGGLE2SEGY is a code developed by Sopher in 2017 using Matlab. It is available to the scientific community to convert scanned images of stacked reflection seismic data to the standard SEG-Y format. The code is designed to work directly on the image characteristics and can recognize and eliminate the signal associated with timelines and baselines. This code is particularly useful in removing noise associated with paper data due to the storage and retention of the data itself. Moreover, WIGGLE2SEGY applies a frequency filter to eliminate artifacts with frequencies outside the bandwidth of the data, as described in Buttinelli et al. (2022). Before the application of seismic attribute analysis, an AGC (automatic gain control) was applied to seismic data to bring up weak signals. The further step is the application of seismic attributes to highlight and identify some discontinuities in the seismic data that are helpful for fault and fracture characterization (Fig. 1).

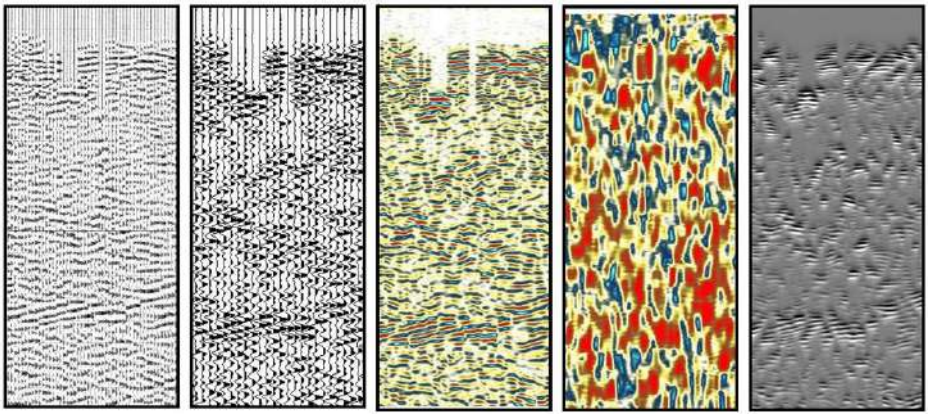

Fig. 1 - An example of vectorization results from the VIDEPI dataset, using the process described in this study. a) Scanned image of line FR-309-80. b) SEG-Y file extracted from the scanned image in a), plotted with similar parameters to the original, c) same SEG-Y data as in b) plotted with a variable density display. d) application of seismic attribute “semblance”; e) application of seismic attribute “pseudo-relief”.

Results

Analysis of attributes integrated into the reflection seismic interpretation, mainly for 2D and 3D seismic data, allowed better detection of faults and fractures of the carbonate reservoir in the project's area of interest. Some vintage 2D seismic lines were tested using several post-stack attributes, including semblance/coherence and pseudo-relief, using OpendTect software.

This method has created a dataset of vectorized seismic profiles that can be shared with the scientific community. This helped with the structural interpretation of the study area, improving the public structural isochrone maps available in the public database. In this case, we have used scientific analyses like seismic attributes despite having only 2D seismic data. Seismic attributes can detect faults and fractures, stratigraphic discontinuities, and identify hydrocarbon volumes. Our study displays the outcome of vectorization and enhancement of seismic data by applying attributes like automatic gain control and convolve and other seismic attributes such as coherence, curvature, and pseudo-relief, which are suitable for characterizing geothermal reservoir structures (Fig. 2).

Thanks to the new digitalized and vectorized dataset and the application of seismic attributes analysis, it has been possible to a better definition and interpretation of the interface between

Upper Miocene siliciclastic deposits and Mio-Cretaceous carbonate platform in the area of study, characterized by strong acoustic impedance contrast. The identified reservoir structures will be simulated according to their geothermal potential. Seismic attributes (i.e., semblance and pseudo-relief) were applied to identify discontinuities caused by faults in the fractured carbonates.

Conclusions

This approach of seismic attribute analysis is extremely useful for geothermal exploration of similar fields and reservoirs with a strong AI contrast and the construction of more predictive static and dynamic reservoir models based on discontinuity detected by attribute analysis and seismic interpretation. Seismic attributes are very useful in characterizing faults and fractures also in 2D seismic data volumes. The pseudo-relief attribute application made the interpretation of the main unconformities and structural features possible.

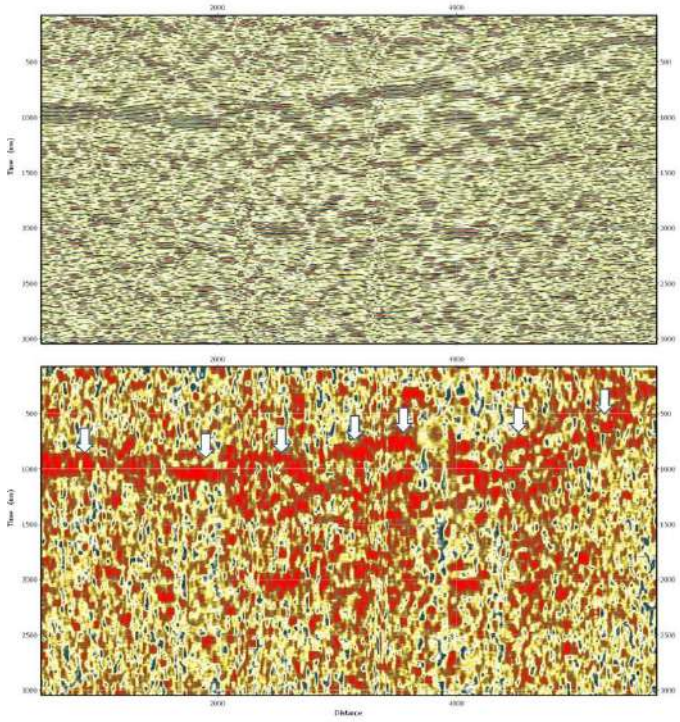

Fig. 2 - (a) FS-03-90 available publicly stack seismic profile in vectorized SEG-Y format via WIGGLE2SEGY Matlab-based tool. (b) The second panel shows the semblance attribute calculated in OpendTect software to detect AI contrast, faults and fractured reservoirs.

References

Buonasorte G., Cataldi R., Franci T. et al., 2011: Previsioni di crescita della geotermia in Italia fino al 2030–Per un Nuovo Manifesto della Geotermia Italiana, Pacini, UGI Special Publication.

Buttinelli, M., Maesano, F. E., Sopher, D., Feriozzi, F., Maraio, S., Mazzarini, F., Improta L., Vallone R., Villani F. & Basili, R., 2022: Revitalizing vintage seismic reflection profiles by converting into SEG-Y format: Case studies from publicly available data on the Italian territory. Annals of Geophysics. https://doi.org/10.4401/ag-8883

Sopher, D., 2017: Converting scanned images of seismic reflection data into SEG-Y format, Earth Sci. Inform., 11, 2, 241-255; https://doi.org/10.1007/s12145-017-0329-z

VIDEPI project, 2015. https://www.videpi.com/videpi/videpi.asp

Corresponding author: giuseppe.vico@uniroma1.it; giuseppe.vico@ingv.it

Electromagnetic Induction Data Inversion: Realistic Prior Models and Spatial Regularization with Respect to Known Structures

N. Zaru[1], M. Rossi[2], G. Vacca[1], G. Vignoli[1,3]

[1] DICAAR - University of Cagliari, Italy
[2] Engineering Geology Division – Lund University, Sweden
[3] Near Surface Land and Marine Geology Department - GEUS, Denmark

Introduction

Geophysical techniques, including electrical resistivity tomography (ERT) and electromagnetic induction (EMI), play a crucial role in non-invasive subsurface characterization. While ERT involves galvanic contact with the ground of arrays of electrodes, EMI enables contactless measurements and is frequently employed for (quasi-)3D resistivity mapping, particularly in large-scale surveys, often carried out with helicopter-mounted systems (Karshakov, 2017; Yin, 2007). Calibration differences between the two methods pose challenges, as ERT relies on internal resistances, while EMI demands meticulous adjustments for absolute measurements (Finco, 2023; Minsley, 2012). Both ERT and EMI inversions are ill-posed problems. The selection of a unique and stable solution relies on prior knowledge, incorporated either as regularization term (deterministic approaches) or as prior distribution (probabilistic strategies) (Tarantola, 1982; Zhdanov, 2002). The present study focuses on enhancing 1D EMI inversion by making use of: 1) realistic prior samples, ensuring compatibility with subsurface expectations, and 2) spatial constraints with geologically meaningful features (e.g., from 2D ERT sections or their geological interpretations). We verified the performance of the proposed approach in a field test by comparing our results against ground-penetrating radar (GPR) measurements.

Methodology

Within this research, a strategic shift was undertaken to significantly enhance computational efficiency. The proposed approach consists of formulating the prior information in terms of an ensemble P consisting of 1D resistivity models m and the corresponding forward response $d = F(m)$ computed for the model m. The core principle underpinning this approach involves an exploration of the solution space for the inverse problem using a substantial number of pre-computed (d, m) couples, typically in the range of 10^5 - 10^6 samples. Consequently, the challenge no longer revolves around the continual generation of a solution, which is computationally intensive, but instead centers on the search for a suitable one from the pre-existing array of possibilities. When correctly implemented, particularly by harnessing the computational power of Graphics Processing Units (GPU), this method demonstrates a speed advantage of at least two orders of magnitude over traditional deterministic algorithms (McLachlanet al. 2021).

The discrimination criterion is given by the chi-squared value, defined as

$$\chi^2 = N^{-1}\left\|\delta^{-1}\left(F(m) - d\right)\right\|_2^2, \quad (1)$$

where N is the number of frequencies for each observation, δ represents the uncertainty associated with each of the measured data d and $F(m)$ is the forward response of the model m. Clearly, retrieving the inverse model m by simply minimizing Eq. 1 would be challenging because of non-uniqueness and instability of the solution with respect to the data. In the deterministic inversion framework, the originally ill-posed problem is turned into a conditionally well-posed one by minimizing a stabilizing term (formalizing the available prior information; e.g. the presence of smooth transitions between lithologies) with the constraint that $\chi^2 = 1$. A common choice for the stabilizing term is $s(m) = \left\|m - m_{apr}\right\|_2^2$; in this specific case, the solution m is selected as it produces a response compatible with the observed data ($\chi^2 = 1$) while being as close as possible to the reference model m_{apr}. Within this research, the reference models are the 1D models constituting the 2D resistivity section crossing the survey area (Fig. 1b), obtained through the inversion of ERT data. However, in the proposed scheme, this spatial constraint enforced by the stabilizing term acts uniquely in the lateral direction, whereas, along the vertical direction, the prior information is incorporated by selecting the possible solutions among the realization of the ensemble P. In this way, the information provided by the reference model is laterally propagated across the entire survey and the possibly very complex (and realistic) prior information is infused into the solution by selecting it among the element of the ensample P (supposedly generated in accordance with our expectations about the subsurface).

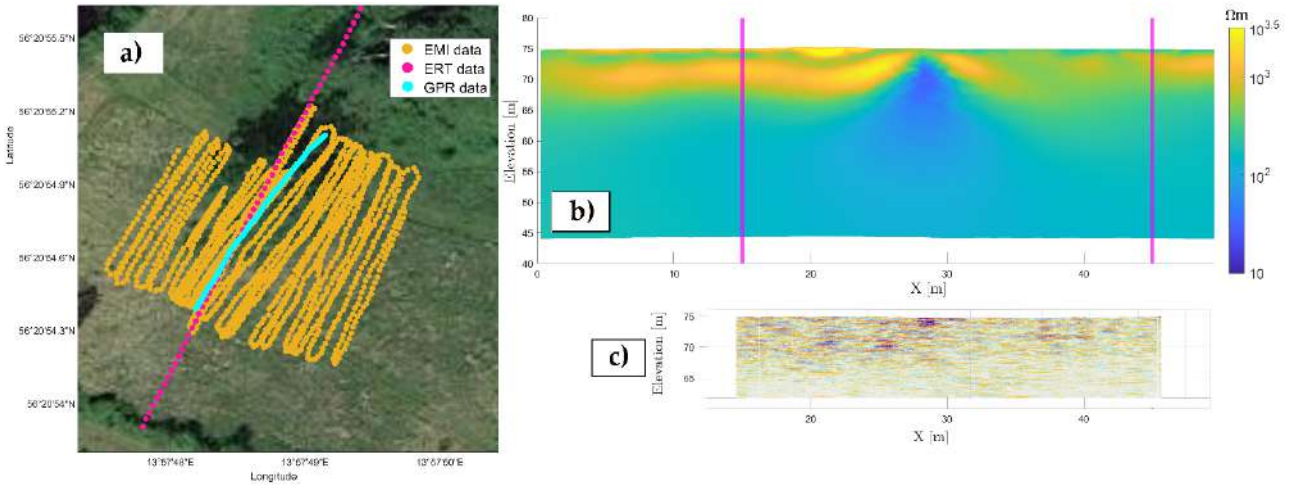

Fig. 1 – Field data. **a**) the location of the collected EMI, ERT and GPR data; **b**) the result of the ERT inversion (the vertical lines delineate the portion crossing the EMI survey area); **c**) the GPR section.

To validate the proposed approach, we conducted various geophysical measurements on a test site located in the south of Sweden. Specifically, we acquired 1550 frequency soundings using the Profiler EMP-400 from GSSI at three frequencies: 5, 10, and 15 KHz. Additionally, an ERT line was collected across the EMI area using the Terrameter LS2 instrument from GuidelineGeo (Fig. 1). Lastly, we performed a grid of Ground Penetrating Radar (GPR) measurements that overlapped with the EMI area. It's important to note that the GPR data was utilized uniquely for validating the

results of the EMI-ERT constrained inversion and was not incorporated into the inversion process itself.

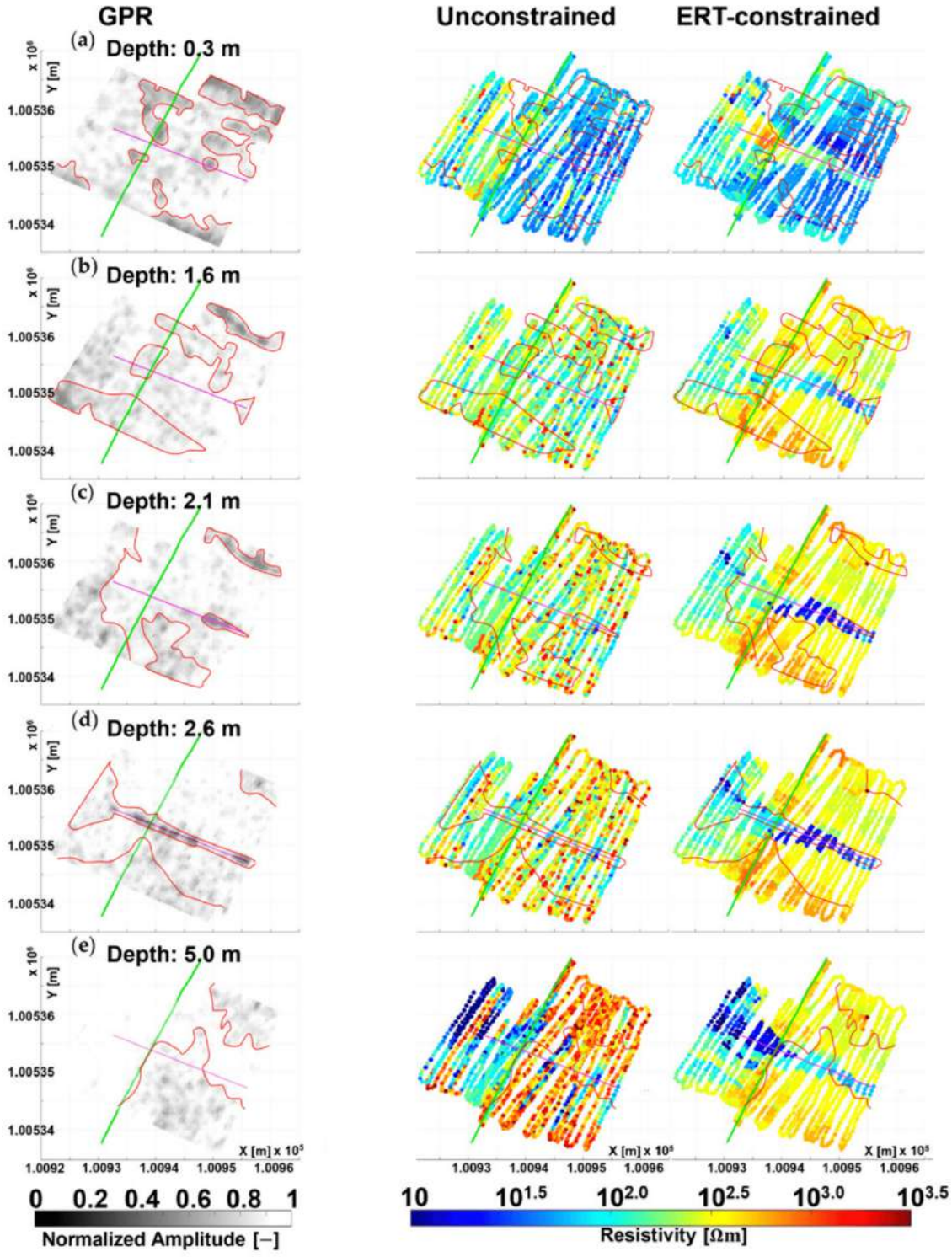

Figure 2 - Horizontal sections of the GPR and of the resistivity volumes obtained with and without constrain. Each row corresponds to a different depth: (**a**) 0.3 m; (**b**) 1.6 m; (**c**) 2.1 m; (**d**) 2.6 m and (**e**) 5.0 m. The location of the ERT section (and its geoelectrical interpretation) is shown as a green solid line. The assumed position of a pipe is plotted in purple. The red contours are shown as references to the GPR anomalies; their purpose is merely to make the comparisons easier, and they are not necessarily connected to any specific geological features.

Results

The field test produced the two EMI inversions shown in Figure 2, showcasing: 1) the unconstrained outcome (Figure 2a-f, middle column), in which the solutions are obtained by simply minimizing Eq. 1 within the ensemble P, and 2) the constrained inversions (Figure 2a-f, rightmost column) that incorporates information from both the ensemble P and the 2D ERT section. The unconstrained result tends to be more resistive than the constrained inversions, illustrating the impact of ancillary information from the ERT section on spatial consistency and on the reduction of erratic variations between adjacent 1D models. Figure 2 offers a comparative analysis at different depths, in which horizontal slices of GPR reflections' envelope can be checked against the corresponding slices of EMI volumes obtained with and without the ERT constraint. This comparison highlights the effectiveness of schemes incorporating ancillary information, as seen in the detection of a conductive anomaly related to a pipeline, particularly visible in Figure 2c-d at the depth of 2.1 m to 2.6 m. Differently from existing spatially constrained schemes, the present approach does not rely (vertically) on smooth/sharp regularizations (Klose et al. 2022; Klose et al.2023); still vertical consistency is enforced by selecting the model in the ensemble P that, by construction, is generated in accordance with our expectations (Zaru et al. 2023). In summary, the proposed inversion scheme, utilizing an arbitrarily complex prior distribution and ancillary information, generates a unique EMI inversion result. The ability to formalize information through prior distribution samples and reference models proves crucial for achieving spatially consistent and reliable reconstructions. In addition, the method effectively integrates ancillary data, presenting a robust solution that aligns with geological descriptions, GPR reflections, and borehole logs.

Conclusion

In conclusion, this research presents some of the results discussed in Zaru et al. 2023 which introduces an inversion scheme for EMI data, employing a realistic prior distribution for vertical conditioning and incorporating ancillary information from an ERT cross-sections for lateral consistency in the final (pseudo-)3D resistivity volume. Our results highlight the severe non-uniqueness of EMI data inversion, emphasizing the importance of formalizing information through prior distribution samples and reference models. The proposed constrained scheme, integrating ancillary observations ab initio, demonstrate their effectiveness in addressing the ill-posedness of the original problem. Comparisons with the GPR cross-sections validate the proposed approach's capability to detect lithological interfaces and resistivity contrasts with decent resolution, considering the amount of information provided by the EMI survey is contained in just 3 frequencies. The computational efficiency of the strategy, coupled with its ability to provide a single reliable model, opens avenues for future exploration, including the potential implementation of a probabilistic solution to assess feature probabilities across different realizations of the posterior distribution. Overall, the proposed inversion strategy enhances the reconstruction of 3D resistivity volumes from EMI measurements, offering improved agreement with independent geophysical observations.

References

Finco, C.; Rejiba, F.; Schamper, C.; Fraga, L.H.C.; Wang, A. Calibration of near-surface multi-frequency electromagnetic induction data. Geophys. Prospect. 2023, 71, 765–779.

Karshakov, E.V.; Podmogov, Y.G.; Kertsman, V.M.; Moilanen, J. Combined Frequency Domain and Time Domain Airborne Data for Environmental and Engineering Challenges. J. Environ. Eng. Geophys. 2017, 22, 1–11.

Klose, T.; Guillemoteau, J.; Vignoli, G.; Tronicke, J. (2022) Laterally constrained inversion (LCI) of multi-configuration EMI data with tunable sharpness. J. Appl. Geophys., 196, 104519.

Klose, T.; Guillemoteau, J.; Vignoli, G.; Walter, J.; Herrmann, A.; Tronicke, J. Structurally constrained inversion by means of a Minimum Gradient Support regularizer: Examples of FD-EMI data inversion constrained by GPR reflection data. Geophys. J. Int. 2023, 233, 1938–1949.

M Minsley, B.J.; Smith, B.D.; Hammack, R.; Sams, J.I.; Veloski, G. Calibration and filtering strategies for frequency domain electromagnetic data. J. Appl. Geophys. 2012, 80, 56–66.

Tarantola, A.; Valette, B. Generalized nonlinear inverse problems solved using the least squares criterion. Rev. Geophys. 1982, 20, 219–232..

Yin, C.; Hodges, G. 3D animated visualization of EM diffusion for a frequency-domain helicopter EM system. Geophysics 2007, 72, F1–F7.

Zaru, N., Rossi, M., Vacca, G. and Vignoli, G., 2023. Spreading of Localized Information across an Entire 3D Electrical Resistivity Volume via Constrained EMI Inversion Based on a Realistic Prior Distribution. *Remote Sensing*, *15*(16), p.3993.

Zhdanov, M. S. (2002). Geophysical inverse theory and regularization problems. *Elsevier, 36*.

Corresponding author: n.zaru@studenti.unica.it

Probabilistic Petrophysical Inversion of Ground-Based FDEM Data for Alpine Peatland Characterization: A Case Study in the Italian Dolomites

N. Zaru[1], S. Silvestri[2], M. Assiri[3], P. Bai[4], T.M. Hansen[5], G. Vignoli[1,6]

[1] DICAAR - University of Cagliari, Italy
[2] University of Bologna, Italy
[3] University of Padua, Italy
[4] SINOPEC, China
[5] Aarhus University, Denmark
[6] Near Surface Land and Marine Geology Department, GEUS, Denmark

Introduction

Peatlands, vital carbon reservoirs, often pose challenges in efficiently and reliably characterization of their geometry and volumes, particularly in alpine settings (Silvestri et al., 2019). Here, we investigate a probabilistic petrophysical method applied to ground-based frequency-domain electromagnetic induction (FDEM) data to quantify peat thickness and extension in an alpine bog situated in the Italian Dolomites, where peat overlays an electrically conductive clay substrate. While traditional FDEM inversion retrieves electrical resistivity, a direct estimation of the probability of peat or clay occurrence is preferable as that is the ultimate goal of the geophysical investigation (Grana et al., 2022). Additionally, the proposed probabilistic strategy addresses the limitations of oversimplified constraints and has practical applications for real-time fieldwork optimization. Generally, the ill-posedness of FDEM data inversion necessitates prior information. Traditional deterministic approaches utilize regularization terms, such as the L2-norm of the model gradient, which may oversimplify complex geological structures (Klose et al., 2022; Klose et al., 2023). The proposed probabilistic approach is capable to accommodate more complex (and realistic) prior information. Additionally, it naturally provides uncertainty estimates, crucial for the assessment of the reliability of inferred geological features. In this study, we apply probabilistic petrophysical inversion to an FDEM dataset collected on an alpine peatland, comparing results against traditional deterministic Occam's inversions and borehole logs.

Methodology

The research is focused on characterizing Alpine peatland structures in the Italian Dolomites through ground-based Frequency Domain Electromagnetics (FDEM). The study area is situated near Danta di Cadore in the North of Italy, encompassing a peatland of particular interest. A systematic survey was conducted across this targeted peatland area using the GEM-2 instrument

from Geophex (Haoping & Won, 2003). FDEM measurements were collected at the following frequencies: 1025, 1525, 2875, 5825, 7775, 12775, 15325, 25525, 36225, 63025, and 80225 Hz. A total of 153,621 soundings were acquired. To model uncertainties inherent in the petrophysical properties of the peatland structure, a probabilistic inversion procedure was employed. The procedure utilized an independent extended Metropolis algorithm - a variant of the conventional extended Metropolis algorithm proposed by Mosegaard and Tarantola (1995). In our specific implementation, an infinitely long step-length was selected; this implies that each new model proposal from the prior distribution represented a completely independent realization. Based on our expectation about the target, we created a prior ensemble of 10^5 1D models consisting of 200 layers (each 0.1 m thick),. The synthetic set of 1D models is realized by establishing a prior distribution based on the assumption of two distinct lithologies: peat and clay. Each geological model is considered made of three lithological units, allowing for varied configurations without imposing specific vertical arrangements, with interface depths and lithology assignments randomly generated. Resistivity values for each layer are drawn from distributions representing expected resistivity ranges for peat and clay, followed by a smoothing process to introduce vertical spatial coherence. The resistivity ranges associated with each category are consistent with relevant literature examples for peat and clay soils. For each sounding location, the response $F(m)$ of each prior realization was compared
against the observed data d using the conditional probability (and assuming normally distributed noise in the measurements):

$$p(m) = k_d exp\left(-\frac{1}{2} \left(d - F(m)\right)^T C_d^{-1} \left(d - F(m)\right) \right), \quad (1)$$

where k_d is a normalization factor, C_d takes into account the data covariance, and often selected such that $diag\left(\sigma_d\right)^{-2} = C_d^{-1}$, with each component of the vector σ_d being the standard deviation of the corresponding data element. Notably, this inversion scheme was implemented using the SIPPI toolbox (Hansen et al., 2013a; Hansen et al., 2013b).

Results

Figure 1 shows the horizontal slices at the depths of 3.0 m and 7.0 m, depicting the realization of the posterior distribution with maximum likelihood and the probabilities of encountering peat and clay. Peat is predominant in the northern-central area, extending from the surface to depths exceeding 7.0 m, with a shallower deposit in the southern part. The spatial coherence of the results is noteworthy, considering that each sounding was inverted separately without spatial constraints.

Verification against boreholes reveals the geophysical reconstruction aligns well with the morphology of the peat unit (Fig. 2). Some mismatches can be potentially attributed to 3D effects (Bai et al. 2021) or actual distance from the inverted and the borehole locations (for instance, borehole B31* is approximately 4 m away from the inverted section). Moreover, boreholes were originally drilled aiming at reaching the top of the clay layer but that was not always possible. In this respect, only those actually hitting the top of the clay unit are denoted with an asterisk, such as B31*. The maximum likelihood model exhibits spatial coherence without explicit regularization, emphasizing the impact of prior information on stability. Comparisons in terms of data fitting show the maximum likelihood model closely matches the observations, exhibiting a chi-squared value

generally lower than 1 (Fig. 2 – top panel). For sake of completeness, the probabilistic inversion was

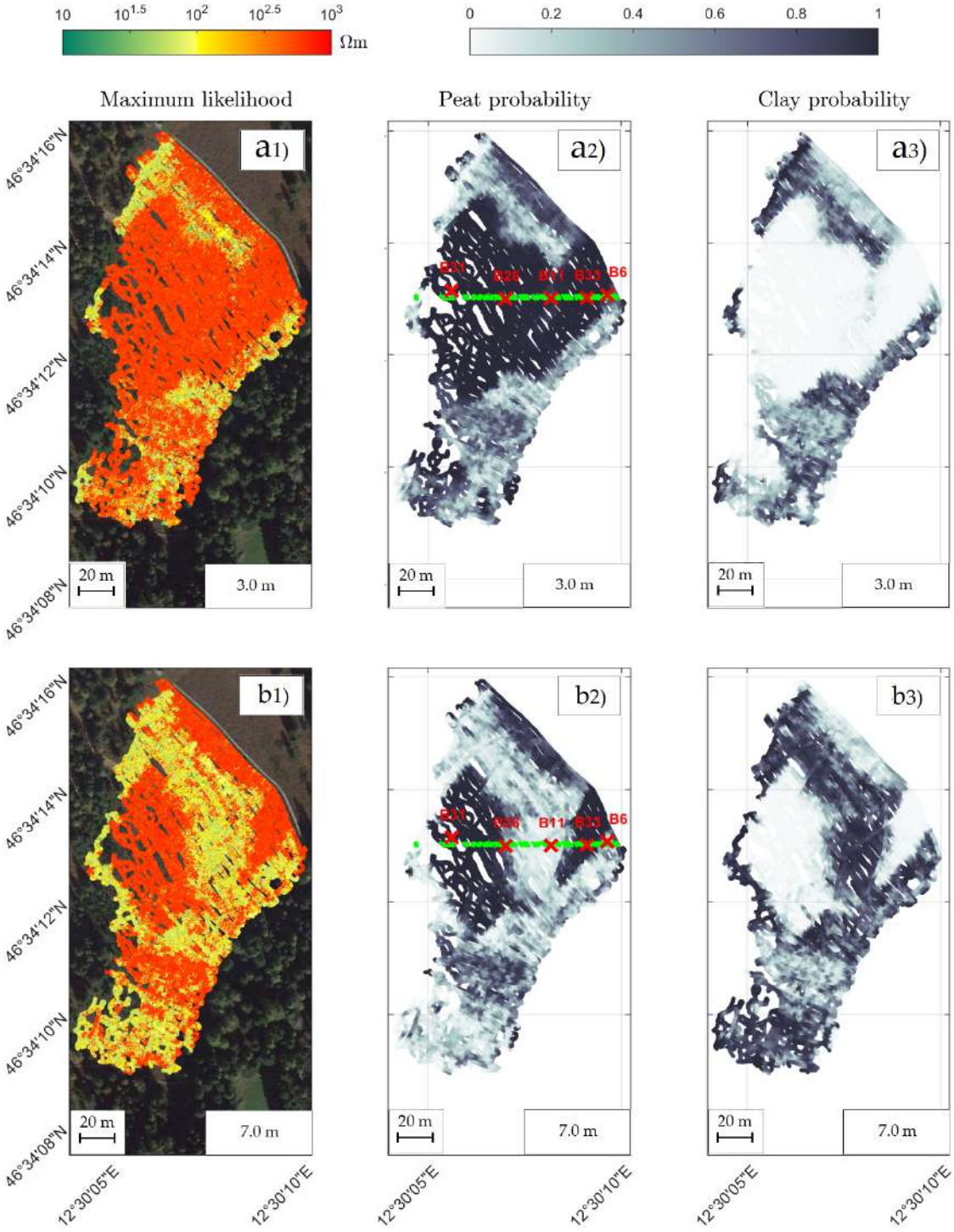

Fig. 1 – Horizontal slices presenting the inversion outcomes derived from the Frequency-Domain Electromagnetic Induction (FDEM) data collected across the Danta peatland in Italy. Each row shows the resistivity model with maximum likelihood and the probability of encountering peat or clay. Rows (a-b) depict these models and probabilities at depths of 3.0 m and 7.0 m respectively. In the third column, above the peat probability, the figure displays the profile's location shown in Figure 2 (highlighted in bright green), along with the positions of associated boreholes marked by red X.

compared against the traditional Occam's inversion (Fig. 2 – middle panel) obtained by using EMagPy (McLachlan et al., 2021). In the case of deterministic inversion, special care was devoted to the selection of the Tikhonov's parameter to reach the chi-squared values in the range of the optimal value 1 (Fig. 2 – top panel). Despite the similar data fitting, the deterministic inversion seems to favor vertically elongated structures (opposite to our expectation about the presence of a peat-clay interface and the information from the boreholes). In contrast, the probabilistic approach, whose spatial consistency is attributed to complex prior information, seems to offer a more accurate portrayal of the peat unit's morphology.

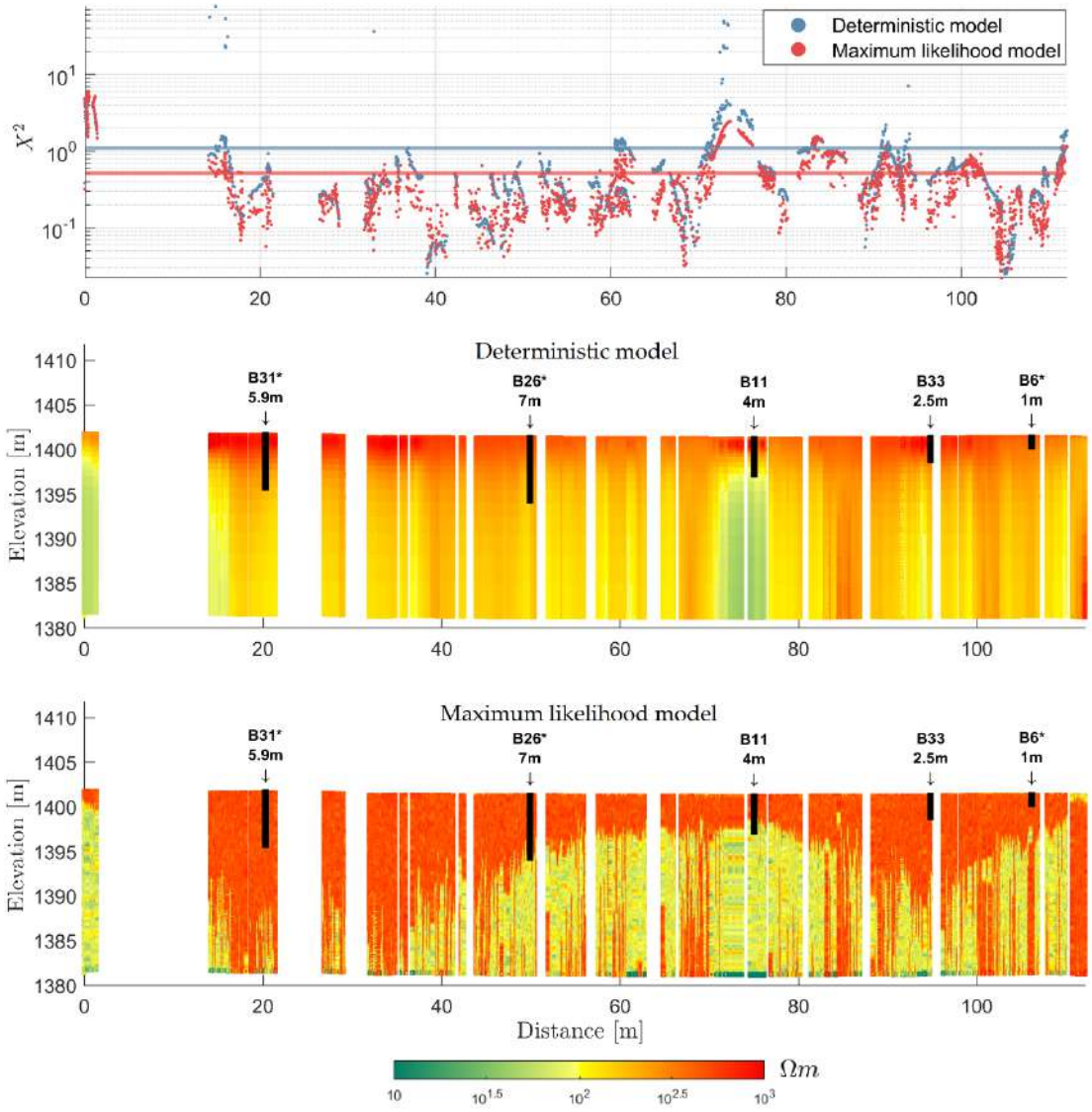

Fig. 2 – Vertical profile presenting the chi-squared value of the deterministic (blue) and maximum likelihood (red) models in the top panel. The deterministic model obtained with the standard Occam's inversion is shown in the middle panel; the maximum likelihood model obtained with the probabilistic inversion in the bottom panel. The horizontal blue and red lines in the fist panel represent the average chi-squared values associated with the two models.

Figure 3 depicts the probability of having peat and clay in the examined section. Clearly, the portion between the boreholes B26* and B11 is well correlated with the peat-clay interface. The big difference between the peat probability and the Occam's result highlights one more time the influence of different prior information in the two approaches (probabilistic and deterministic): the

detailed information represented by samples in the prior distribution facilitates the reconstruction of a geologically consistent structure of the peat unit, whereas the deterministic method is forced to provide (vertically) smooth solution. It is worth noting that B26* is the most reliable borehole as, unlike the others, its core has been extracted and analyzed (Poto et al., 2013), proving the presence of 6 meters of peat followed by roughly 1 meter of gyttja (more decomposed peat).

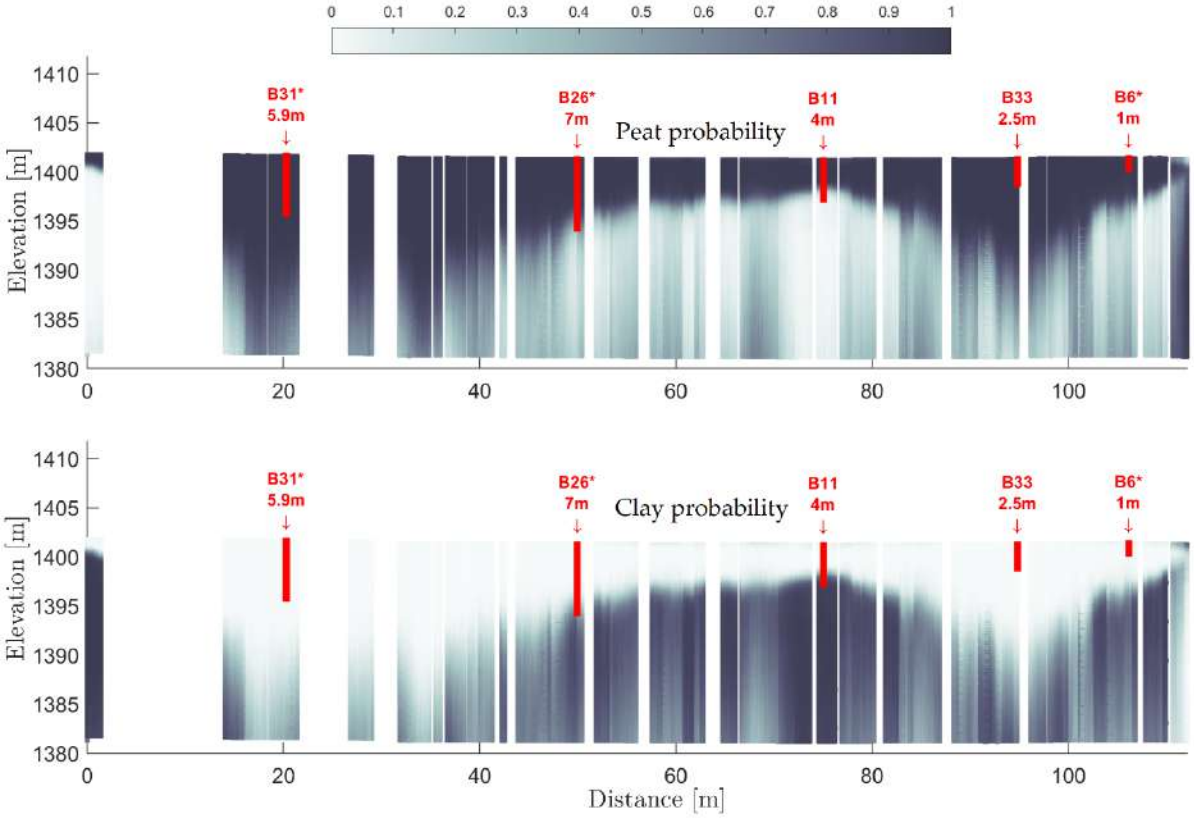

Fig. 3 – Vertical profile presenting the inversion outcomes derived from the Frequency-Domain Electromagnetic Induction (FDEM) data collected across the Danta peatland in Italy.

In terms of inversion performance, the probabilistic approach, relying on forward calculations of prior samples, proves computationally efficient and parallelizable. The calculation of conditional probability for the entire dataset takes around one hour, while generating prior samples and associated measurements adds another hour. In contrast, a deterministic inversion of the entire dataset was computationally infeasible as it required more than a day for the inversion of the 2D section considered here.

Conclusion

This research demonstrates the efficacy of a probabilistic petrophysical inversion approach in characterizing the complex subsurface structures of alpine peatlands. By applying ground-based frequency-domain electromagnetic induction (FDEM) technology to an Italian Dolomite peatland, where peat overlays a conductive clay substrate, the study surpasses the limitations of traditional deterministic Occam's inversions. The probabilistic approach, rooted in Bayes' theorem, allows for the incorporation of realistic prior information, offering a more geologically meaningful representation of the subsurface. The spatial coherence observed in the results highlights the

stability and accuracy of the proposed approach, even if each sounding is independently inverted without explicit spatial constraints (Zaru et al. 2023). Verification against boreholes and comparisons with deterministic results highlights the reliability and efficiency of the proposed strategy. Moreover, the probabilistic approach inherently provides an estimation of the uncertainty of the results that is quite problematic in deterministic framework.

Reference

Bai, P., Vignoli, G. & Hansen, T.M. 2021. “1D stochastic inversion of airborne time-domain electromagnetic data with realistic prior and accounting for the forward modeling error.” *Remote Sensing* 13 (19): 3881.

Grana, D., Russell, B. & Mukerji, T. 2022. “Petrophysical inversion based on f-s-r amplitude-variation-with-offset linearization and canonical correlation analysis.” *Geophysics* 87 (6): M247-M258.

Hansen, T. M., Cordua, K. S., Looms, M.C., & Mosegaard, K. 2013b. “SIPPI: A Matlab toolbox for sampling the solution to inverse problems with complex prior information: Part 2 -Application to crosshole GPR tomography.” *Computers & Geosciences* 52: 481-492.

Hansen, T. M., Cordua, K.S., Looms, M.C., & Mosegaard, K. 2013a. “SIPPI: A Matlab toolbox for sampling the solution to inverse problems with complex prior information: Part 1-Methodology.” *Computers & Geosciences* 52: 470-480.

Haoping, H., & Won, I.J. 2003. “Real-time resistivity sounding using a hand-held broadband electromagnetic sensor.” *Geophysics* 68 (4): 1224-1231.

Klose, T., Guillemoteau, J., Vignoli, G., & Tronicke, J. 2022. “Laterally constrained inversion (LCI) of multi-configuration EMI data with tunable sharpness.” *Journal of Applied Geophysics* 196.

Klose, T., Guillemoteau, J., Vignoli, G., Walter, J., Herrmann, A., & Tronicke, J. 2023. “Structurally constrained inversion by means of a Minimum Gradient Support regularizer: examples of FD-EMI data inversion constrained by GPR reflection data.” *Geophysical Journal International* 233 (3): 1938-1949.

McLachlan, P., Blanchy, G. & Binley, A. 2021. "EMagPy: Open-source standalone software for processing, forward modeling and inversion of electromagnetic induction data." Computers & Geosciences, 146, 104561.

Mosegaard, K., & Tarantola, A. 1995. “Monte Carlo sampling of solutions to inverse problems.” *Journal of Geophysical Research: Solid Earth* 100 (B7): 12431-12447.

Silvestri, S., Christensen, C. W., Lysdahl, A. O. K., Anschütz, H., Pfaffhuber, A. A., & Viezzoli, A. 2019. “Peatland volume mapping over resistive substrates with airborne electromagnetic technology.” *Geophysical Research Letters* 46: 6459-6468. doi:10.1029/2019GL083025.

Zaru, N., Rossi, M., Vacca, G. and Vignoli, G., 2023. Spreading of Localized Information across an Entire 3D Electrical Resistivity Volume via Constrained EMI Inversion Based on a Realistic Prior Distribution. *Remote Sensing*, *15*(16), p.3993.

Corresponding author: n.zaru@studenti.unica.it

Session 3.2

Near surface geophysics

GNGTS 2024

APPLIED GEOPHYSICS FOR ENERGY, ENVIRONMENT AND NEW TECHNOLOGIES

Session 3.2

Near surface geophysics

Convenors of the session:

***Emanuele Forte* – eforte@units.it**
***Chiara Colombero* – chiara.colombero@polito.it**
***Michele Cercato* – michele.cercato@uniroma1.it**

Contributions recommended for this session:

- **Innovative geophysical techniques;**
- **Quantitative data integration;**
- **Geophysical data processing;**
- **Geophysical modeling;**
- **Time-lapse geophysical approaches;**
- **Geophysics for hydrogeological properties and hydrological dynamics (Hydrogeophysics);**
- **Geophysics for biological interactions (Biogeophysics);**
- **Geophysics for cultural heritage (Archaeogeophysics);**
- **Geophysics for environmental risks (Environmental Geophysics);**
- **Geophysics for applied geology and engineering (Engineering Geophysics).**

There is a growing need to quantitatively characterize the near surface and related anthropic structures, providing a reliable estimate of their geometric, mechanical and hydraulic characteristics through the use of high-resolution, environmentally and economically sustainable techniques.
This session is open to contributions that illustrate methodological innovations, processing methods, case studies and applications of different geophysical methods, typically at high resolution, in all the above mentioned fields.

Applicability of cheap and lightweight magnetic sensors to geophysical exploration

F. Accomando[1] and G. Florio[1]

[1] Dipartimento di Scienze della Terra, dell'Ambiente e delle Risorse – Università di Napoli "Federico II", Italia.

In recent years, there was a notable technological advancement in geophysical sensors. In the case of magnetometry, several sensors were used having the common feature to be miniaturized and lightweight, thus idoneous to be carried by UAV in drone-borne magnetometric surveys. Moreover, such sensors have the common feature to be very cheap, so that it is in principle very easy to have the resources to combine two or three of them to form gradiometers. Nonetheless, another common feature is that their sensitivity ranges from 0.1 to about 200 nT, thus not comparable to that of alkali vapor, standard flux-gate or even proton magnetometers. However, their low-cost, small volume and weight remain as very interesting features of these sensors. In this communication, we want to explore the range of applications of small tri-axial magnetometers commonly used for attitude determination in several devices. We compare the results of ground-based surveys performed with conventional geophysical instruments with those obtained using these sensors.

Corresponding author: filippo.accomando@unina.it

Exploring rockfall precursors through unsupervised deep-learning clustering analysis

G.M. Adinolfi [1] , C. Comina [1], S.C. Vinciguerra [1]

[1] *Department of Earth Sciences, University of Turin, Turin, Italy*

Studying rock mass stability is greatly enhanced by the powerful tool of seismic monitoring. This technique allows for continuous recording, making it easier to analyse spatiotemporal activity related to gravitational instabilities. Seismic monitoring is essential for detecting and assessing damage and cracking processes as precursors to macroscopic failures.

In this research, we present initial findings from seismic monitoring conducted at a test site where a rockfall occurred shortly after deploying a small-aperture array of three seismic stations, covering approximately 100 meters. These stations were equipped with a tri-axial velocimetric sensor and data-loggers sampling at 250 Hz. The specific focus of the seismic array was to survey potential instabilities originating from structural weaknesses, including deformation bands, joints, and lithological contacts. The installation of the site-specific seismic array preceded a rockfall event by about a month. The rockfall occurred at the lithological contact between folded gneisses and a unit of dolomitic limestones, predominantly composed of dolomites and dolomitic saccharoid marbles. The seismic signature of the rockfall persisted for approximately 10 seconds, and spectral analysis revealed the occurrence of multiple sub-episodes of slip triggered by the initial rupture.

No apparent correlations between precursory activity and the rockfall occurrence were identified through traditional seismological approaches. In response to this challenge, we applied a recently developed unsupervised deep-learning method for clustering signals in continuous multichannel seismic time series. This method combines a deep scattering network for automatic feature extraction with a Gaussian mixture model for clustering. Our successful application of this approach led to the identification of seismic signals associated with the rockfall, encompassing various slip episodes, along with their initiation and propagation. Additionally, we detected precursory activity occurring approximately 2 hours before the rockfall, consistently identified through the clustering analysis (Fig. 1).

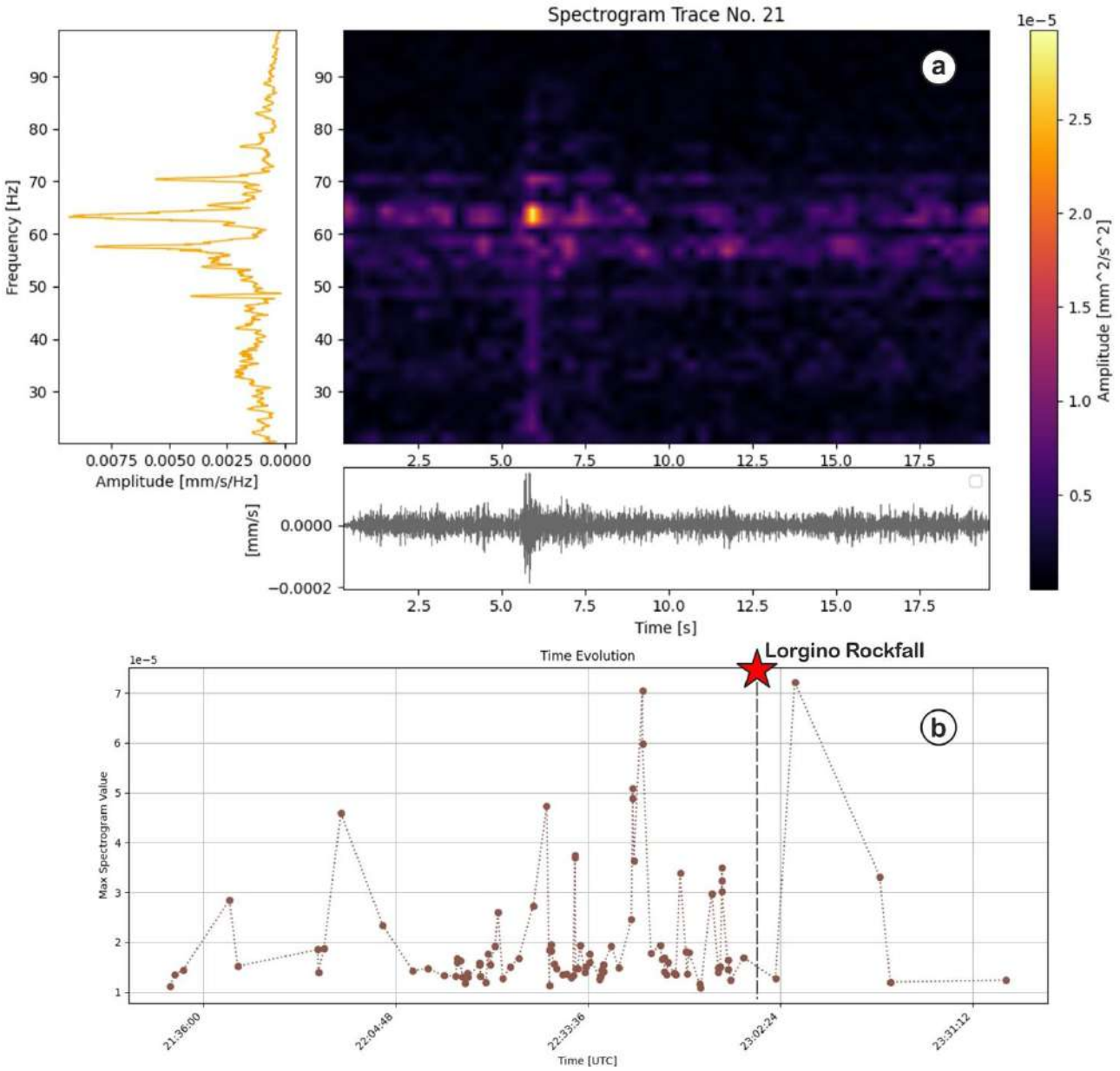

Figure 1 a) Example of time-frequency analysis for a precursory event. b) Amplitude vs time of precursory seismic signals

Preliminary results indicate a slow initiation process, potentially linked to a precursory nucleation phase driven by an intermittent preparatory process before the large stick–slip acceleration accompanying the rock mass failure. Despite their low amplitude and absence of direct visibility in raw seismic records, these signals were effectively discerned through the deep learning analysis.

References

Seydoux, L., Balestriero, R., Poli, P., Hoop, M. D., Campillo, M., & Baraniuk, R.; 2020: *Clustering earthquake signals and background noises in continuous seismic data with unsupervised deep learning.* Nature communications, 11(1), 3972.

Corresponding author: guidomaria.adinolfi@unito.it

Combined 3D surface wave and refraction analysis around the Scrovegni Chapel in Padua, Italy

I. Barone[1], M. Pavoni[1], J. T. F. Ting[1], J. Boaga[1,3], G. Cassiani[1,3], D. Dupuy[4], R. Deiana[2,3]

[1] Università degli Studi di Padova, Dipartimento di Geoscienze, Padova
[2] Università degli Studi di Padova, Dipartimento dei Beni Culturali, Padova
[3] Università degli Studi di Padova, Centro Interdipartimentale di Ricerca Studio e Conservazione dei Beni Archeologici, Architettonici e Storico-Artistici (CIBA), Padova
[4] Geo2x SA, Yverdon-les-Bains, Svizzera

The Scrovegni Chapel in Padua (Italy) is part of the Padua UNESCO World Heritage site since 2021. The chapel hosts a worldwide famous fresco cycle of Giotto dating back to the 14th century, and it is located in a complex archaeological area hosting remains of several periods. In particular, the façade of the chapel stands on the remains of the elliptical middle wall of a Roman amphitheatre. Many aspects are still unclear, especially regarding the interconnection between the two monuments and the presence of buried radial walls of the amphitheatre in that area (Deiana et al., 2018).

Following the previous studies from Barone et al. 2022 and Barone et al. 2023, a new active seismic data acquisition has been carried out using 28 source locations and 188 seismic nodes, placed all around the chapel on a regular grid of 3 m spacing in both spatial directions (Fig. 1). The new survey area partially overlaps the previously investigated areas. The source used is a weight drop with a 50 kg mass falling from a height of approximately 2 m. Each shot was repeated twice to increase the signal-to-noise ratio. A combination of single-component (1C) and three-component (3C) nodes was used. Although only the vertical component was considered for the analyses described hereinafter, the 3C recordings were used to study the seismic waves ellipticity.

The same shot records have been analysed with two different methods: surface wave tomography and first arrival traveltime tomography. As for the surface wave analysis, the same procedure used in Barone et al. 2022 was used, including: preliminary analysis for modes identification, pseudo 2D f-k filtering to remove higher-modes and backscattering, phase unwrapping, traveltime extraction and Eikonal tomography (Lin et al. 2009). The outcome of this procedure consists in a series of phase velocity maps, each referring to a different frequency of analysis between 10 Hz and 50 Hz. Autospectrum gradient maps were also computed, which reflect sudden amplitude changes due to abrupt lateral velocity variations.

The 3D first arrival traveltime tomography (Heincke et al. 2006) included the picking of the first breaks for all 3D gathers and inversion through the software GEOGIGA (Technology Corp.). Some preliminary analysis was needed in order to find the optimum parameters for inversion, including the generation of synthetic 2D and pseudo 3D models. Picking of first break times for the real 3D dataset was done manually and revealed the most time-consuming processing step, due to the high level of urban noise polluting the data.

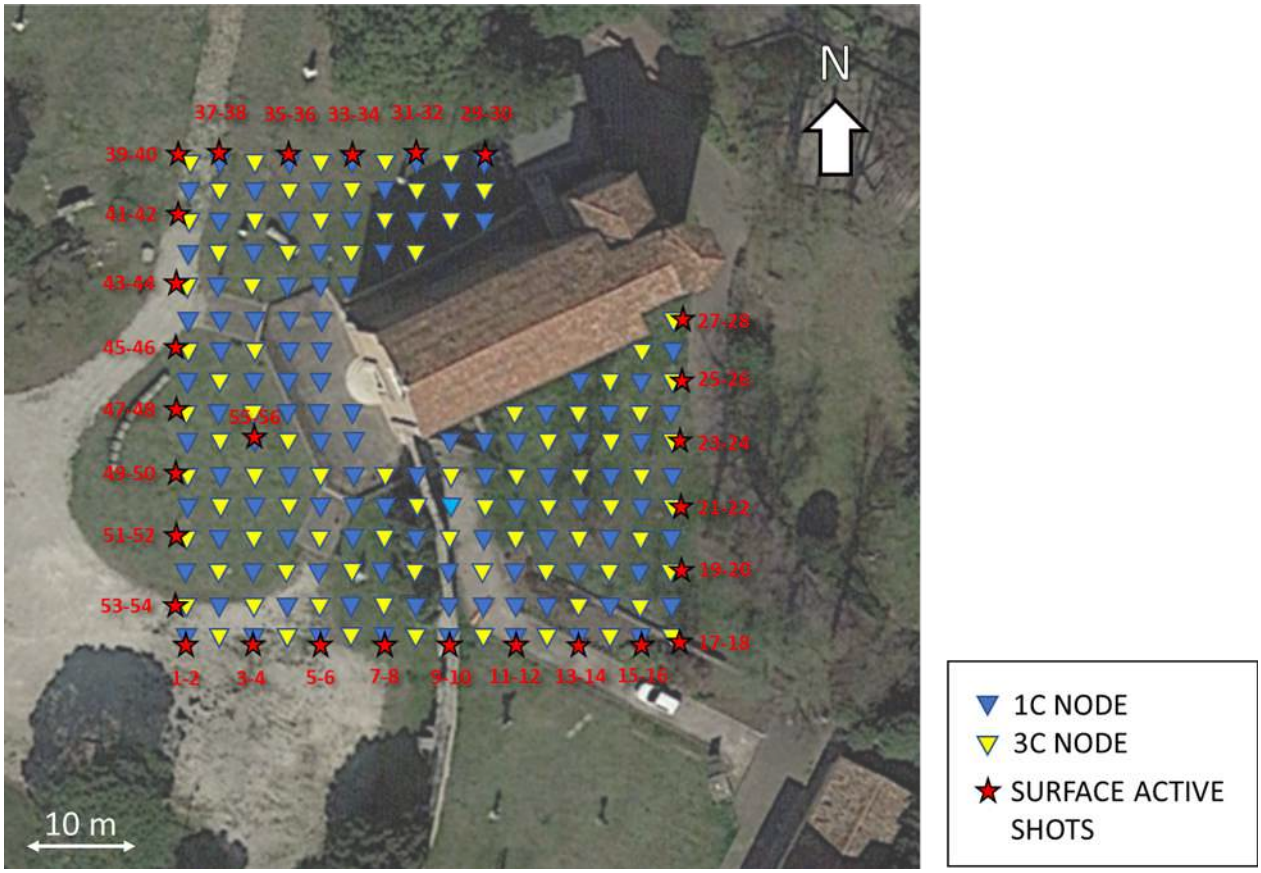

Fig. 1 – Acquisition scheme for the dense 3D seismic survey. 1C and 3D seismic nodes are represented as blue and yellow triangles, respectively, while active source locations are represented as red stars.

The phase velocity maps, the autospectrum gradient maps and the 3D Vp model from first arrival traveltime tomography reveal the same velocity anomalies, corresponding to known archaeological features such as the walls of the Roman amphitheatre and probable reinforced concrete structures built during the Second World War in order to protect the chapel. A low-velocity area in the south-western side of the study area, already mapped in Barone et al. 2022 and Barone et al. 2023, is clearly visible. Finally, a high-velocity area in the eastern side is also imaged, whose origin is uncertain and that will need further investigations.

In conclusion, this study demonstrates that a combined surface wave and refraction analysis using dense 3D seismic data can be helpful for archaeological prospection. Despite the noisy urban context, the limited number of sensors (with respect to our previous studies) and the non-optimum geophone spacing, especially for surface wave analysis, a spatial resolution of a few

meters was obtained. Further work will include depth inversion of phase velocity maps, in order to obtain a pseudo-3D Vs model.

Acknowledgments

This study, made possible by the willingness and support of the Culture Office of the Municipality of Padua, was funded under the agreement between the Veneto Regional Secretariat of the Italian Ministry of Culture (MiC) and the CIBA Interdepartmental Research Center of the University of Padua under the umbrella of WCRI SYCURI.

References

Barone, I., Cassiani, G., Ourabah, A., Boaga, J., Pavoni, M. and Deiana, R.; 2022: Surface wave tomography using dense 3D data around the Scrovegni Chapel in Padua, Italy. Scientific Reports, v. 12, 11806. doi: 10.1038/s41598-022-16061-1

Barone, I., Cassiani, G., Ourabah, A., Boaga, J., Pavoni, M. and Deiana, R.; 2023: Integrating controlled-source and ambient noise seismic measures for archaeological prospection: the Scrovegni Chapel case. Geophysical Journal International, v. 232, pp. 1944–1956. doi: 10.1093/gji/ggac432

Deiana, R.; 2018: L'importanza dell'approccio multidisciplinare: considerazioni a valle del progetto dell'Università di Padova sulla Cappella degli Scrovegni. In La Cappella degli Scrovegni nell'anfiteatro romano di Padova: nuove ricerche e questioni irrisolte, Padova University Press.

Heincke, B., Maurer, H., Green, A. G., Willenberg, H., Spillmann, T. and Burlini, L.; 2006: Characterizing an unstable mountain slope using shallow 2D and 3D seismic tomography, GEOPHYSICS, v. 71, n.6, B241-B256.

Lin, F.C., Ritzwoller, M.H. and Snieder, R.; 2009: Eikonal tomography: surface wave tomography by phase front tracking across a regional broad-band seismic array. Geophysical Journal International, v. 177, pp. 1091-1110. doi: 10.1111/j.1365-246X.2009.04105.

Corresponding author: ilaria.barone@unipd.it

P-and S-velocity 3D model for the characterisation of the subsurface beneath the village of Arquata del Tronto

G. Böhm[1], A. Affatato[1], L. Baradello[1], G. Brancatelli[1], E. Forlin[1], F. Meneghini[1]

[1] National Institute of Oceanography and Applied Geophysics – OGS (Italy)

1. Introduction

The 2016-2017 seismic sequence in the Central Apennines has, once again, demonstrated the importance of different seismic effects in complex geological contexts at short distances (e.g., valleys filled with soft sediments, hilltops, complex buried geometries). The severe damage reported by ancient settlements located on the top of a rocky hill, as in the case of Arquata del Tronto, has underlined the need to define an accurate three-dimensional numerical model (topography, seismo-stratigraphic, geomechanical, geotechnical characteristics, etc.) in order to best model the local seismic response through appropriate numerical simulations.
This work describes the results of a high-resolution reflection seismic acquisition (P-wave and S-wave) carried out at the Arquata del Tronto (AP) site for the geophysical characterization of the subsurface, as part of the public intervention "Progetto di suolo (terrazzamenti)" in the historic centre of Arquata del Tronto (AP). The final product of this study was a 3D velocity model obtained by the travel time tomography of the picked first break from the acquired seismic survey.

2. Seismic acquisition

The seismic survey made at this site consists of 3 separate lines (Fig. 1).
The acquisition of Line 1 (source spacing 4 m, group spacing 2 m), was carried out in 3 phases, using the electrodynamic vibrator (ELVIS VII) with 20-220 Hz, 10 seconds sweep as the source:
- with the P source and P geophones (10 Hz);
- with the S source oriented at an angle of 5° N (corresponding to the average strike direction of the outcropping formations) and the S geophones (14 Hz single component geophones oriented at the same angle of 5° N), called SA;
- with the S source oriented at an angle of 95° N (perpendicular to the strike direction) and the S geophones (single component geophones oriented at the same angle of 95° N), called SB.
Line 2 (source spacing 4 m, group spacing 2 m), was acquired with the shotgun as the source and the P geophones.
Line 3 (source spacing 8 m, group spacing 4 m), was acquired in 2 stages using the P-source ELVIS VII (20-220 Hz, 10 s sweep) and S-source MiniVib IVI T-2500 (20-200 Hz, 10 s sweep):
- with the P source and P geophones;
- with the S source aligned perpendicular to the local direction of the line and the S geophones (single component geophones, all oriented at an angle of 5° N);

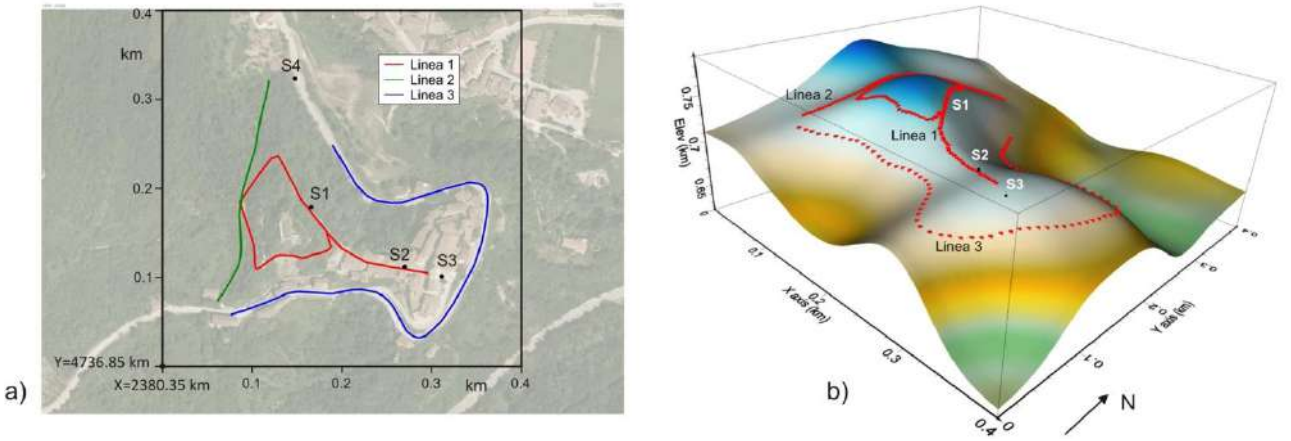

Fig. 1 – a) Location of the 3 seismic lines and the area used for the tomographic model (black rectangle) with the aerial image of the Arquata del Tronto area in transparency. The black dots represent the locations of the wells drilled in the area (S1, S2, S3 and S4). The coordinates of the lower right vertex are given in the Monte Mario/Italy Zone 2 reference system B) 3D view of the line positions with respect to the topography of the area.

3. 3D velocity model

All 3 seismic lines were taken into account in the reconstruction of the 3D velocity model (Figg. 2, 3). All coordinates (referred to Monte Mario/Italy zone 2, in the Gauss-Boaga projection) were referenced to an X=0 Y=0 origin, which corresponds to the point X=2380.35 km and Y=4736.85 km (Fig. 1).

The Cat3D software developed by OGS was used for the inversion of the arrival times. The tomographic method used for these data is based on a ray tracing algorithm (Böhm et al., 1999) for the direct model and the iterative method SIRT (Simultaneous Iterative Reconstruction Technique) (Stewart, 1991) for the travel time inversion. In addition, a model optimization technique based on the staggered grid method (Vesnaver and Böhm, 2000) was applied, which increases the resolution of the final inversion model by summing multiple tomographic solutions obtained from a well-conditioned (low null space) base grid shifted in the X and Y directions, while preserving the reliability of the tomographic solution proper to the base grid.

In general, the acquired seismic data showed the presence of coherent noise (air waves, ground roll, diffractions), which in some cases was relevant, especially in the acquisitions with S waves source. This is partly due to the presence of loose sediments or filling material below the surface (especially in the area of the old village) and the presence of walls, ditches and scarps close to the survey lines, which sometimes led to interference in the data caused by reflected and/or refracted lateral arrivals from these elements.

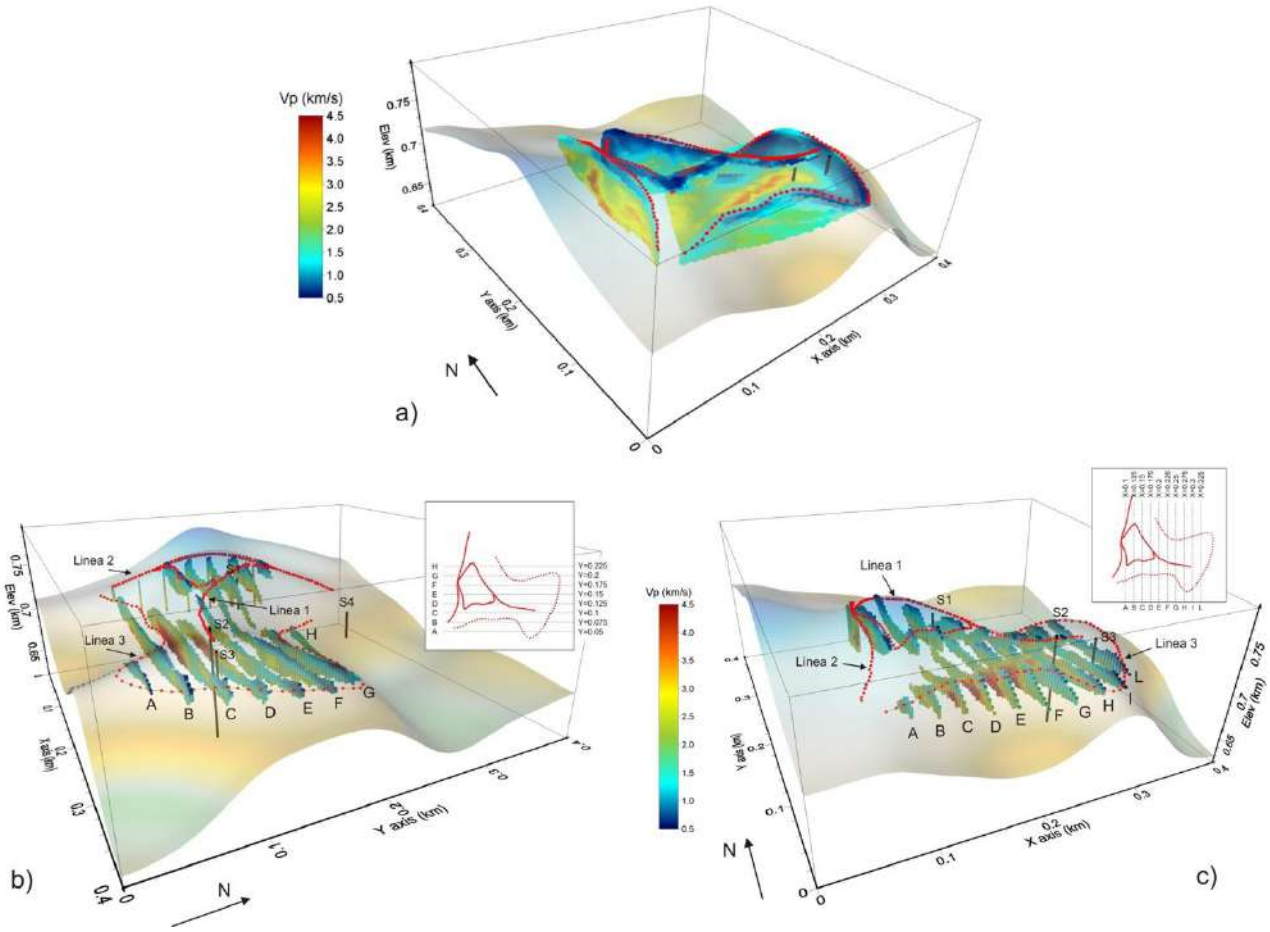

Fig. 2 – Complete 3D Vp model from the travel time tomography of the three lines. a) 3D view. b) Vertical sections extracted along the east-west direction and spaced 25 m apart (see map top right). c) Vertical sections extracted along the north-south direction and spaced 25 m apart (see map top right).

For each line, we inverted the travel times of the first arrivals , which were treated as related to diving waves in the ray tracing used for the inversion.

The resolution of the final tomographic models for Lines 1 and 2 is 2.5 m both in horizontal and vertical directions, starting from a base grid of 10x10 m (horizontally), while for Line 3, the resolution of the final velocity model is 5 m (horizontally) per 2.5 m (vertically), starting from a base grid of 15x15 m (horizontally).

For each inversion, the reliability of the tomographic solution was checked by analysing the time residuals (difference between the observed travel times and those calculated on the final model). In all instances of inversions based on the P times, root mean square (rms) values for the time residuals were approximately 3.5% in relation to the observed times. This corresponds to about 2.3 ms for Line 1, 3.1% with 1.3 ms for Line 2, and 1.6% along with 1.5 ms for Line 3 (which exhibited the lowest residuals).

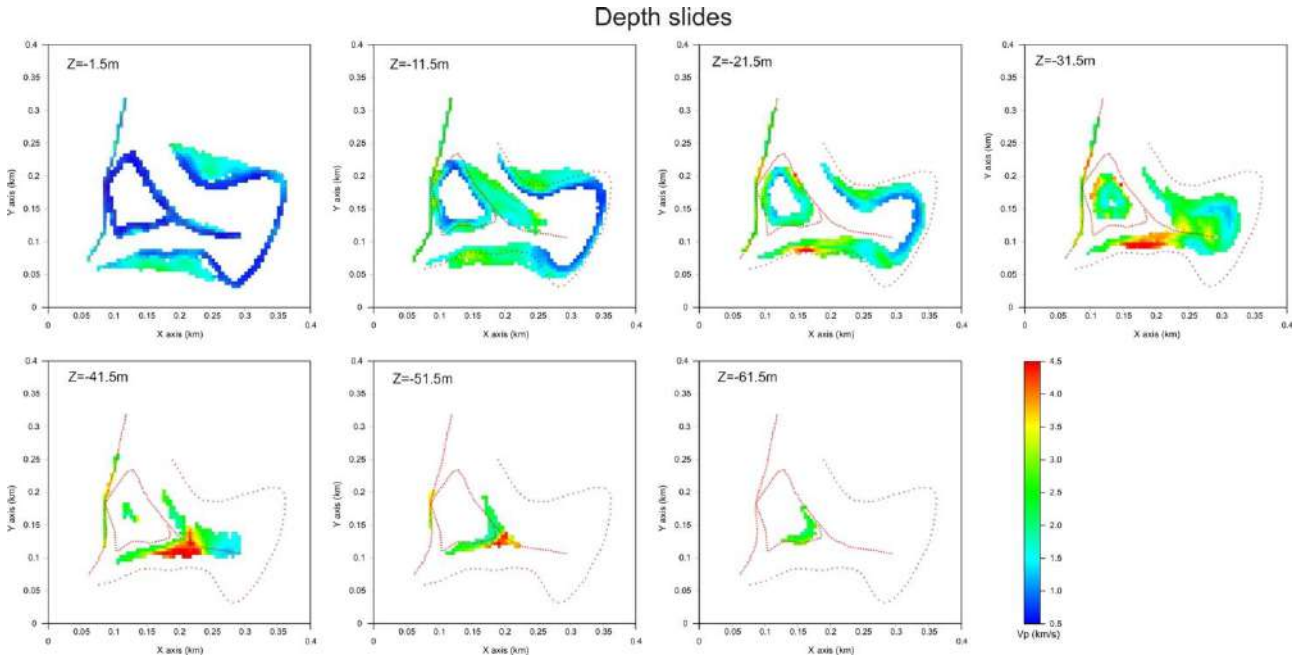

Fig. 3 – Horizontal slices corresponding to different depths of the final 3D tomographic P velocity model. The Z coordinate denotes the depth in relation to the corresponding topographic elevation.

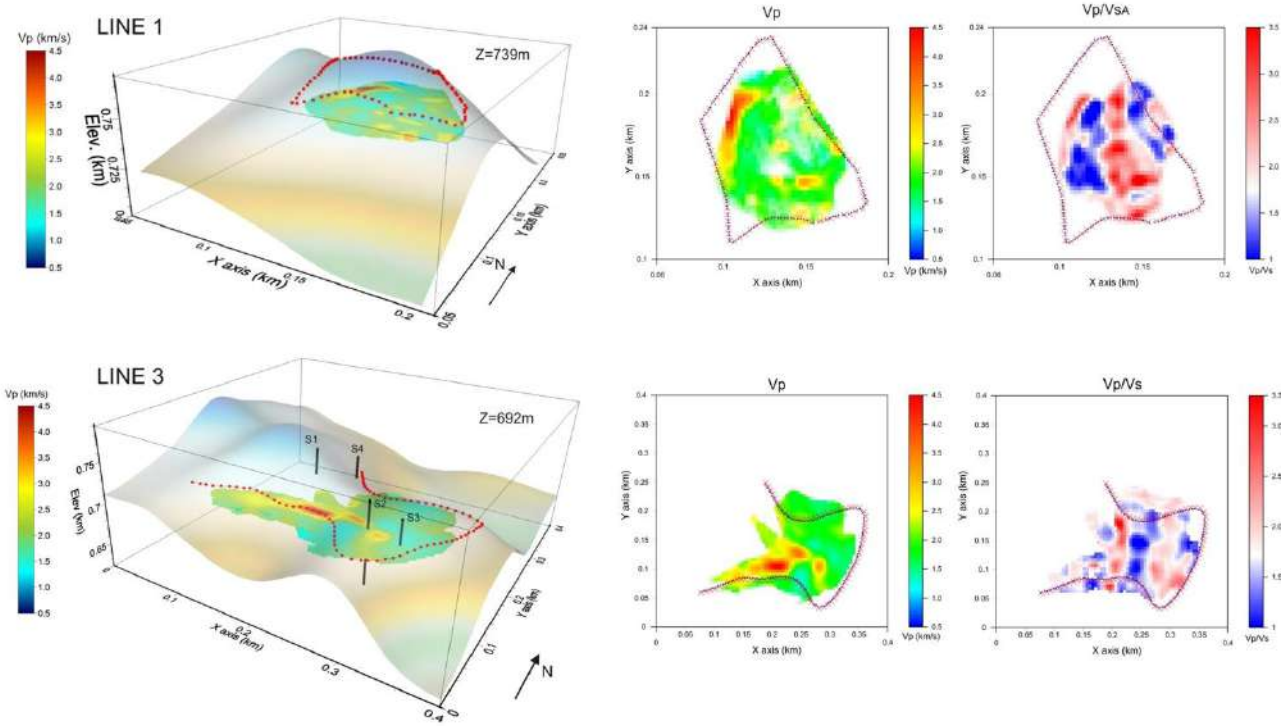

Fig. 4 – Horizontal sections of velocity volume corresponding to Z = 0.739 m (Line 1) and Z = 692 m (Line 3) for P velocity and Vp/Vs ratio.

4. Results and conclusions

In the surveyed area, there exist regions with elevated P velocities ranging between 3.5 and 4.5 km/s, extending to relatively shallow depths, even beneath Line 2. Conversely, in other zones,

heightened P velocities are observed primarily in the southernmost part of the hill, approximately 30 meters below the topographic surface. Notably, the structure directly beneath the centre of the old village exhibits comparatively lower P velocities. The region enclosed by the perimeter of Line 1 displays a heterogeneous distribution of P and S velocities, with the exception of the high-velocity zone on the western side, aligning with the elevated velocities detected beneath Line 2. Regarding S velocities, the reliability of the inversion is compromised by increased noise compared to P data, exacerbated by lateral events interfering with the first break signals used for inversion. Despite these challenges, an analysis of the Vp/Vs ratio maps (Fig. 4) reveals a discernible pattern showcasing alternating low and high values, following bands oriented in a north-south direction. This pattern broadly corresponds to the strike values of subsurface formations identified in the area.

Acknowledgments

The authors thank the entire OGS acquisition group for the professional level demonstrated in the tough acquisition task, the Marche Region Special Reconstruction Office (USR) for the permission to publish these data and results, Prof. Carlo G. Lai (Eucentre Foundation, Pavia), Prof. Alessandro Pagliaroli and Prof. Alberto Pizzi of the University of Chieti for their advice and valuable suggestions.

References

Böhm G., Rossi G., Vesnaver A.; 1999: Minimum-time ray tracing for 3-D irregular grids. Journal of seismic exploration, 8, 117-131.

Stewart R.; 1991: Exploration Seismic Tomography: Fundamentals. Course note series, vol. 3, S. N. Domenico, Editor. SEG - Society of Exploration Geophysicists.

DOI: https://doi.org/10.1190/1.9781560802372.

Vesnaver A., Böhm G.; 2000: Staggered or adapted grids for seismic tomography? The Leading Edge 19(9), 944-950. DOI: https://doi.org/10.1190/1.1438762.

Corresponding author: gbohm@ogs.it

Monitoring of the saline wedge in the Po di Goro river.

P. Boldrin[1], E. Ferrari[1], F. Droghetti[1], A. Bondesan[2], E. Rizzo[1]

[1] *University of Ferrara (Dipartimento di Fisica e Scienze della Terra, Ferrara, Italy)*
[2] *Consorzio di Bonifica di Ferrara (Italy)*

Keywords: salt wedge intrusion, EM, climate change, tides

Seawater intrusion in coastal aquifers is a worldwide problem caused, among other factors, by aquifer overexploitation related to human activities, such as irrigation and drinking water supply, and the reduction in natural groundwater recharge due to climate change [1]. In order to prevent or limit the degradation of both surface water and groundwater quality due to saltwater contamination, research studies have been conducted to gain a comprehensive understanding of the issue, identify fundamental parameters, and assess possible corrective measures.

The territory of the Po Delta is characterized by minimal slopes and it is largely situated below sea level. The elevation profile of the territory significantly influences land management. The morphological characteristics of the Po Delta make the largest Italian wetland particularly unstable and very fragile when subjected to human pressure. Only the application of careful policies concerning coastal defence, flood mitigation, anthropogenic subsidence reduction and salt wedge intrusion control will allow reduction of the present or predicted negative effects [2].

In order to detect the salinity of the water river, a probe system that measure the water conductivity (EC) is necessary. Typical monitoring system for EC data involves moving boat acquisitions, which depict a low resolution of the salt wedge detection. Moreover, long rivers are not suitable for point acquisition approach as they require long acquisition times. To overcome these limitations, geophysical methods could appear as a good alternative for fast mapping and detailed resolution. Taking in account these aspects, a monitoring research activity was applied along the Po di Goro River by geophysical method. In detail, a FDEM system was used to carry out the in-phase and out-phase components, in order to obtain the ECa distribution along the river. The geophysical monitoring began in summer 2022 [3], during the last salt wedge crisis along the Po River, and continued this summer. The first results of the Summer 2022 data set highlighted the saline wedge intrusion, on the contrary the Summer 2023 data set showed that saline intrusion was absent in the same investigated area. Anyway, the acquired data during last summer permitted to observe the influence of the tide on the advance and retreat of the salt wedge along the river (Fig.1). The results highlight the significant potential of the proposed geophysical

approach to monitor the salt wedge phenomenon during the warmer periods with increased drought but also on a daily basis due to the influence of tides.

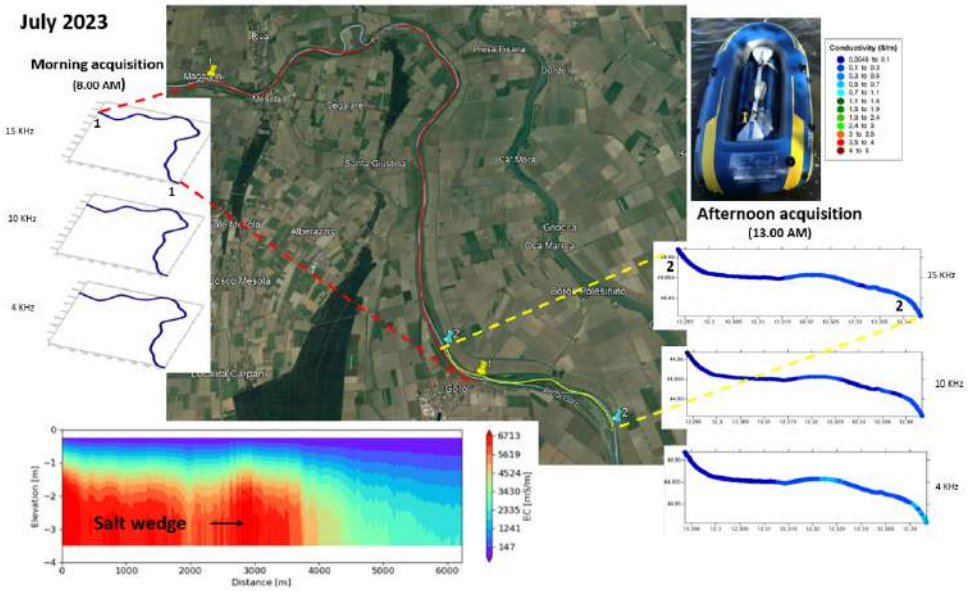

Fig.1: The map shows the pathway of the acquisitions. The acquisitions carried out in two different times of the day along part of Po di Goro (15 Km). During the morning (8.00 AM) when there was low tide and during the afternoon (13.00 PM) when there was a peak of maximum tide. The two paths have an overlap of about 1.5 Km. The different EMs were performed using different frequency of Profiler. It was located on a inflatable boat pulled by a kayak.

References

[1] Crestani E., Camporese M., Belluco E., Bouchedda A., Gloaguen E., Salandin P.; 2022: Large-Scale Physical Modeling of Salt-Water Intrusion. Water. https://doi.org/10.3390/w14081183

[2] Umberto S. Corbau C.; 2009: A review of the Delta Po evolution (Italy) related to climatic changes and human impacts. Geomorphology. http://dx.doi.org/10.1016/j.geomorph.2008.11.004

[3] Boldrin P., Bondesan A., Droghetti F, Ferrari E., Fornasari G., Neri F., Rizzo E.; 2023: DC and FDEM monitoring of the salt wedge on the Po di Goro river (Italy). Atti del 41° Convegno Nazionale del GNGTS.

Corresponding author: bldpla4@unife.it , enzo.rizzo@unife.it

Deep Electric Resistivity Tomography (DERT) on the Cazzaso Landslide

A. Bratus[1], F. Agliardi[2], O. Araujo[3], G.B. Crosta[2], G. Dattola[2], R.G. Francese[3], P. Frattini[2], M. Giorgi[1], F. Kranitz[4], S. Picotti[1]

[1] OGS – Istituto Nazionale di Oceanografia e di geofisica Sperimentale, Trieste, Italia.
[2]DISAT – Dipartimento di Scienze dell'Ambiente e della terra, Università degli Studi Milano – Bicocca, Milano, Italia.
[3]SCVSA - Dipartimento di Scienze Chimiche, della Vita e della Sostenibilità Ambientale, Università di Parma, Parma, Italia.
[4]Servizio Geologico, Regione Autonoma Friuli Venezia Giulia, Trieste, Italia.

Introduction

The Cazzaso landslide affects the eastern slope of Mt. Diverdalce, in the central part of the Fusea - Cazzaso - Sezza plateau, on the orographic right of the But River valley (Tolmezzo, Udine).
The complexity geological and geomorphological setting in which the landslide developed motivated the Geological Survey of the Autonomous Region of Friuli Venezia Giulia to collaborate with the OGS (National Institute of Oceanography and Experimental Geophysics), to better constrain the hydrogeological instability phenomena associated to the Cazzaso landslide by using cutting edge geophysical techniques. The resulting geophysical model of the subsoil was then exploited to study the landslide instability by the Department of Environment and Earth Sciences (DISAT) of the Bicocca University of Milan.

Geological, geomorphological and landslide settings

The Cazzaso landslide complex, reported since 1807 and reactivated as of October 1851, displaced the entire Cazzaso village up to 24 m causing the destruction of some buildings (Zuliani et al., 2021). Currently, three landslide perimeters are defined in the Italian landslide inventory (IFFI) (Trigila and Iadanza, 2007): two translational slides and one complex landslide.
Rock outcropping in the area belong to the sedimentary sequence of the Late Triassic Raibl group (Carnic). The Raibl group, between the formation of the Schlern and the Main Dolomite, consists of a very heterogeneous lithological succession, including black limestone and red sandstone, lastroid limestone, quaternary surface deposits of both morainic and slope origin, characterized by high heterogeneity.
The sequence is cut into multiple blocks by a complex network of major faults associated to the Sauris line, the most important structural feature in central-western Carnic Alps, whose main branch leads the Permo-Werfen to cover the Carnic (Carulli, 2006).
The Local geomorphology is substantially defined by the structural and lithological characteristics, which were shaped by glacial, river and gravitational activity, determining today's morphological appearance.

The Cazzaso landslide complex shows three markedly distinct sectors, with different morphological characteristics, notwithstanding the main morphogenetic agents (tectonic activity, glacial action, gravitational phenomena) are the same.
The western sector, higher in altitude, includes the large area dissected by the landslide movement. The morphology of this area is characterized by the presence of an upper slope with constant inclination and regular profile, morphologically interrupted by a well-delineated 30-m high detachment scarp, which delimits the landslide body that extends below this scarp.
The central part of the slope is occupied a morainic shelf on which the Cazzaso village stands, characterized by a slight slope towards E and locally interrupted by escarpments, which has its eastern limit at the increase in slope gradient.
The eastern part of the slope has a regular course, of medium acclivity, with outcropping rocky substratum that progressively connects with the deposits of the valley floor.

The geoelectric survey

The purpose of the geoelectric prospecting campaign was to contribute to the construction of a conceptual model of the landslide. The use of high-power transmitters (Rizzo and Gianpaolo, 2019) is a further expansion of the Electrical Resistivity Tomography (ERT) delivering a larger depth of exploration so that the method is often indicated as Deep ERT (DERT) (Bocchia et al., 2021). The survey was made using new generation instrumentation and was divided into two phases (Fig 1).

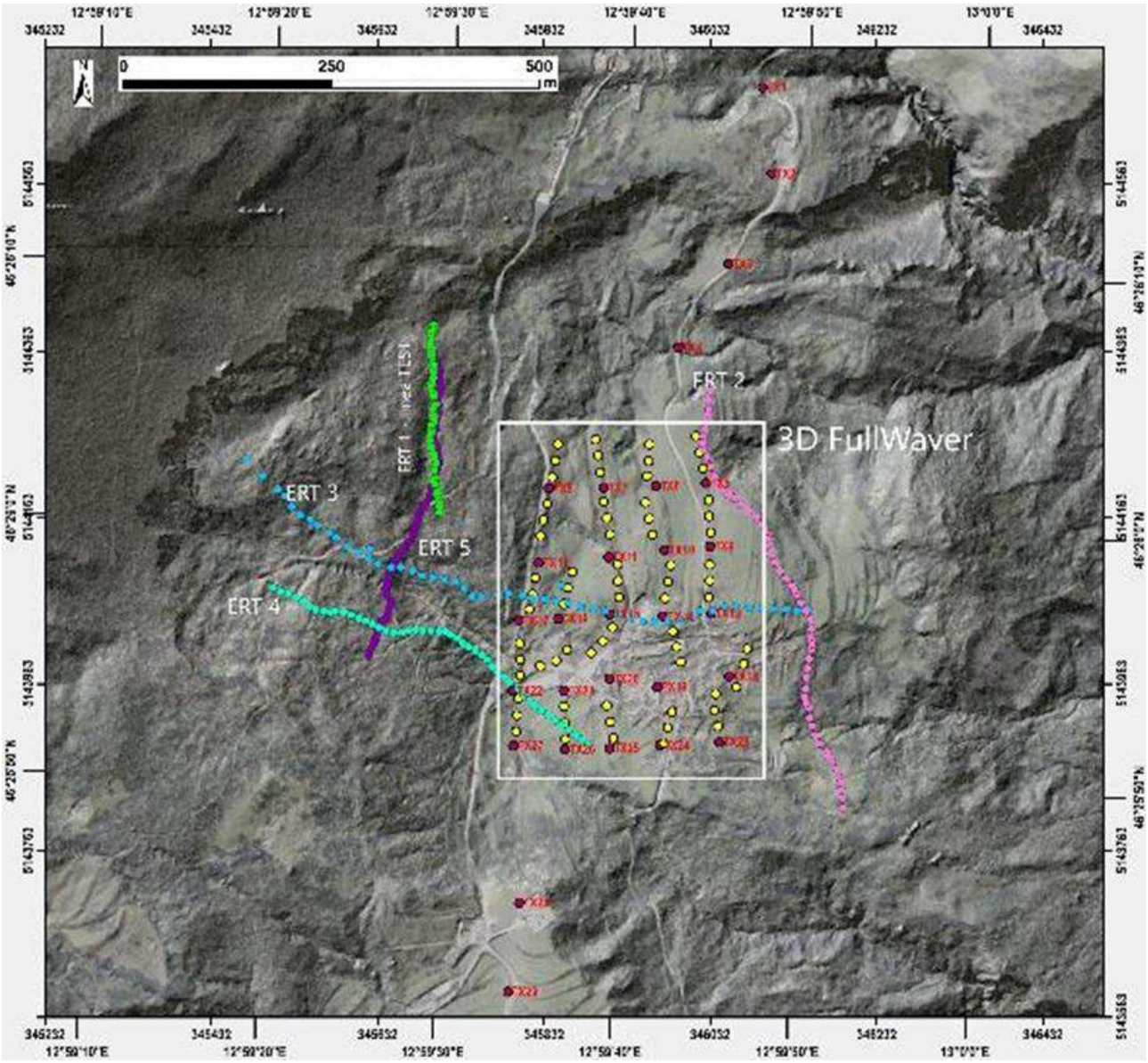

Fig 1 Layout of the MS and FW profiles in the area of the Cazzaso landslide.

In the first phase, a Multi-Source (MS) Wireless Data Acquisition was used. MS introduced a new approach for collecting DERT data (LaBrecque et al., 2013). The MS resistivity-meter has the peculiarity to control transmitting (Tx) and receiving (Rx) dipoles with short, isolated wires. It is a modular system based on stand-alone units remotely controlled via radio signals. Modularity eases the use of the system, but the real innovative and most important feature is its capability of injecting current simultaneously with different dipoles.

The campaign operations were preceded by a survey design phase which allowed to optimize the acquisition geometries. Moreover, a preliminary ERT test allowed to analyze the geophysical response of the subsurface. Then, 4 DERT lines were acquired: 2 lines transverse to the landslide (approximately in the N-S direction), and 2 longitudinal lines (approximately in the E-W direction). This arrangement enabled the investigation of both the western sector and the central sector of the slope.

16 MS units were used for a total of 48 electrodes placed on the ground. All the surveys were carried out adopting a in-line quadrupole acquisition geometry, with both single- and simultaneous multi-source (2 Tx and 4 Tx) transmitters (Bocchia et al., 2021). Further supplementary acquisitions

were carried out with the Tx/Rx dipoles translated at variable distances, internally to the line, according to a "pseudo-gradient" geometry.
In the second phase three-dimensional DERT survey was performed on the central part of the slope using the FullWaver system (Leite et al., 2017; Gance et al., 2021).
The FullWaver devices (Iris Instruments) have been designed for the measurement of resistivity, Induced Polarization and Self Potential on large 3D surfaces with complex topography. Depending on the size of the area to investigate, many V-FullWaver devices can be located on the surface of investigation, performing a continuous measurement. In the meantime, the operator moves a transmitter and the I-FullWaver on the same surface, to perform different current injections according to the survey geometry.
In our case 27 V-FullWaver were used, with a current transmission system TIPIX 3000 capable of injecting current up to 13 A.
The energization patterns were the following. A first set of 29 transmissions consists of a fixed pole A (labelled as TX 1) and a second transmitter B moving from TX2 to TX29, where the dipole aperture reaches the maximum value of about 1100 m. This acquisition sequence was followed by a backward energization scheme with the pole A fixed in TX29 and the pole B moving from TX28 to TX1. The combination of these dipole transmission patterns allowed to acquire different type of electrode arrays: dipole-dipole type, when the transmission dipole is very far from the receiving dipole; pole-dipole type, when the mobile transmitter B is close to the receiving dipole; gradient type, when both transmitters A and B are external and away from the receiving dipole.

Data Processing and inversion

ERT data processing and inversion were carried out by using the ERTLab Studio software (Fischanger et al., 2013), modified to manage both MS and FW measurements.
The application of the two methodologies produced a robust dataset where the 2D MS data and the 3D FW data are in good agreement. The maximum investigation depth, of about 110 - 120 m, has been reached by the FullWaver system under the village of Cazzaso.
The inversion algorithm is based smoothness-constrained least squares approach under the Occam assumptions and consists in minimizing the differences between calculated and measured difference of potentials (Fischanger et al., 2013).

Data Interpretation

In agreement with the geological setting, the measured physical parameters of the subsoil have been interpreted by assuming the landslide body composed by four main formations: inconsistent material; prevalence of sandstone, calcarenites; prevalence of shale and silt; dark stratified limestone and dolomite.
The interpretation of the DERT sections describes some important peculiarities, the most evident is the presence of a deep and large resistive body ascribable to the dolomite formation that increases towards the south and constitutes a barrier to the more conductive materials of the western and more steep part of the slope (fig 2).

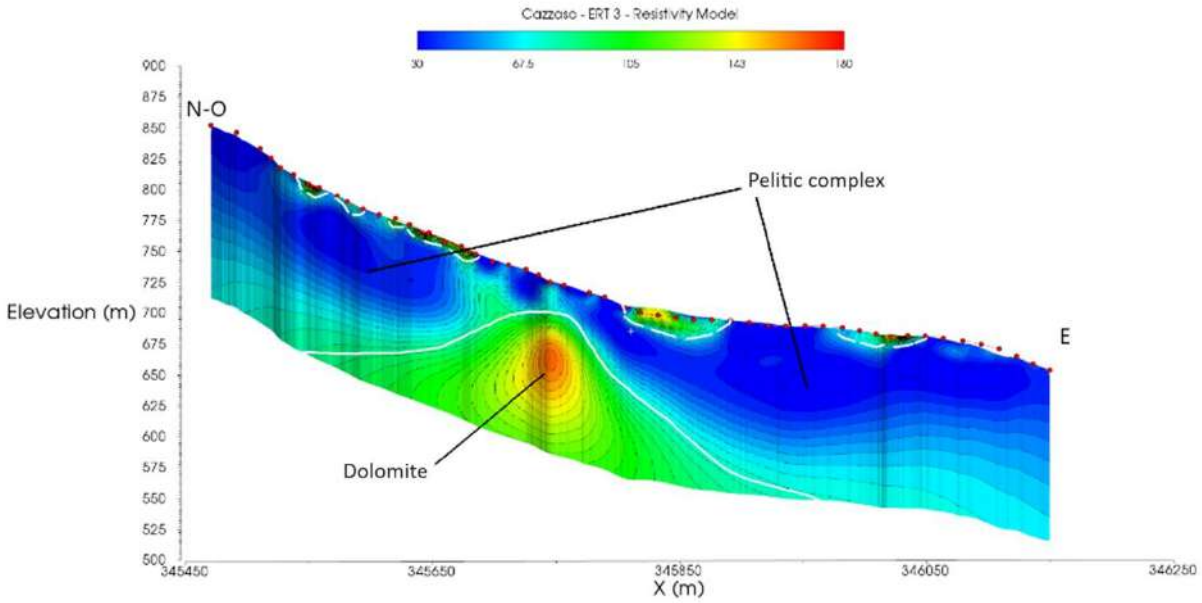

Fig 2 Resistivity model of the ERT3 line, in the transverse direction respect to the landslide.

The availability of three-dimensional resistivity model and of the of the chargeability distribution of the subsoil, up to a depth of about 100 m below the surface, has highlighted the main lithological, hydrogeological and geo-geological characteristics, identifying in detail the geometries of the conductive pelitic complex and of the surface separating this formation by the dolomite. (Fig 3)

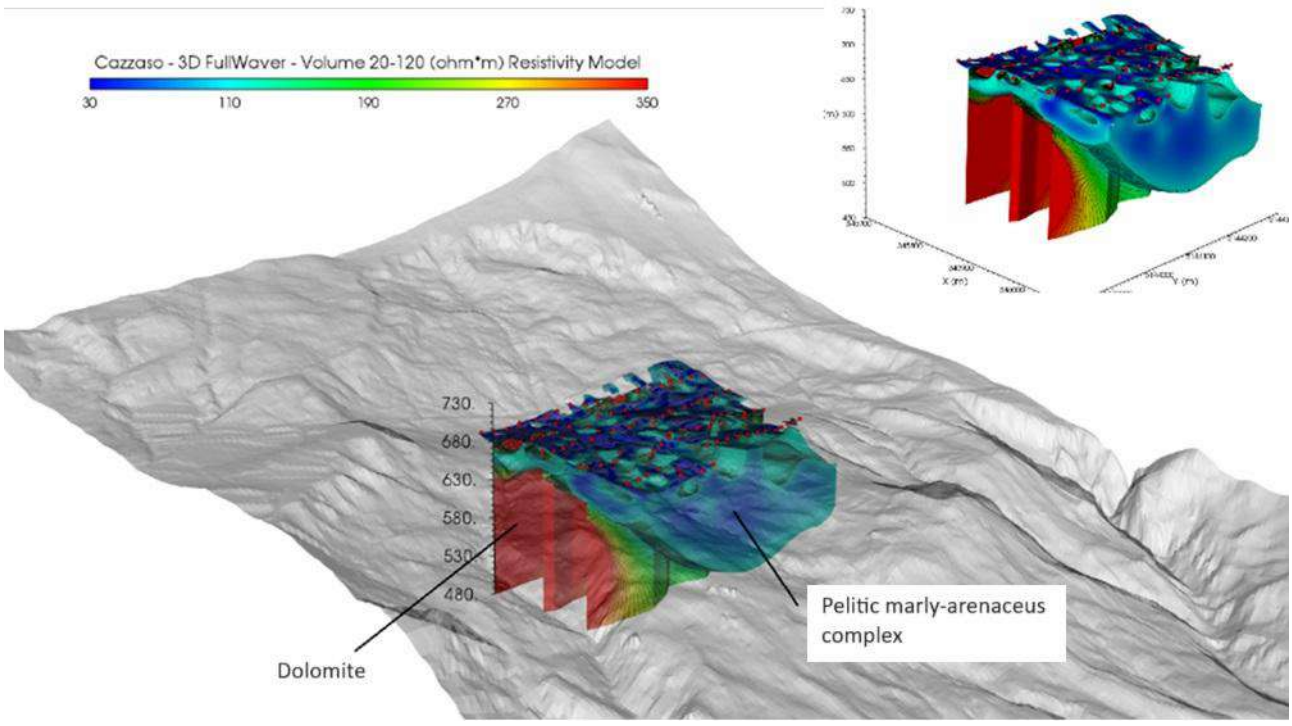

Fig 3 Resistivity volume (20 - 120 Ωm) extracted from the FullWaver cube showing the whole conductive pelitic complex and the contact between this and the dolomite.

Conclusions

The use and integrated application of innovative geophysical prospecting methodologies allowed to acquire high quality resistivity datasets, thus granting an adequate resolution even in the deepest parts of the investigated subsoil. This allowed to obtain imaging of the subsoil up to depths greater than 100 m from the surface, i.e. the depth of lithological and structural features directly constraining the development of the main Cazzaso landslide.

The geophysical models of the subsoil derived from the DERT profiles were capitalized by the study of the landslide by the University of Milano – Bicocca that drew important conclusions about the instability phenomena in the area of Cazzaso. The two slope areas, western with a higher slope, and central that refers to the terrace on which the Cazzaso village stands, are affected by phenomena of different types. The upper part of the landslide is more superficial and characterized by rapid phenomena with evolution in some cases such as to give significant displacements. The second part of is a slower and more continuous deep-seated landslide, probably with a superficial component superimposed on a very deep one that is still not well evaluated.

References

Bocchia, F., Francese, R. G., Giorgi, M., Fischanger, F., Picotti, S.; 2021: The impact of multiple transmitters on signal strength in Deep Electrical Resistivity Tomography data: an experiment in the Vajont valley (north-eastern Italy). Bulletin of Geophysics and Oceanography, Vol. 62, n. 4, pp. 687-706.

Carulli, G.B.; 2006: Note Illustrative della Carta Geologica del Friuli Venezia Giulia, Scala 1:150000; Regione Autonoma Friuli Venezia Giulia, Direzione Centrale Ambiente e Lavori Pubblici, Servizio Geologico Regionale; SELCA: Milano, Italy, pp. 1–44.

Fischanger, F., Morelli, G., Ranieri, G., Santarato, G. & Occhi, M.; 2013: 4d cross-borehole electrical resistivity tomography to control resin injection for ground stabilization: a case history in Venice (Italy), Near Surf. Geophys., 11(1), 41–50.

Gance, J., Leite, O., Lajaunie, M., Susanto, K., Truffert, C., Maillard, O., Bertrand, C., Ferhat, G., and Malet, J.-P.; 2021: Dense 3D electrical resistivity tomography to understand complex deep landslide structures, EGU General Assembly 2021, online, 19–30 Apr 2021, EGU21-14522, https://doi.org/10.5194/egusphere-egu21-14522.

LaBrecque D.J., Morelli G., Fischanger F., Lamoureux P. and Brigham R.; 2013: Field trials of the multi-source approach for resistivity and induced polarization data acquisition. In: Abstracts, AGU Fall Meeting, American Geophysical Union, San Francisco, CA, USA, NS34A-03

Leite, O., Truffert, C., Gance, J., Texier, B., Bernard, J.; 2017: A New Distributed and Cable Less System For Large 3D Electrical Resistivity Ert And Induced Polarization Tomography, 9th Congress of the Balkan Geophysical Society, Nov 2017, Volume 2017, p.1 – 5.

Rizzo E. and Giampaolo V.; 2019: New deep electrical resistivity tomography in the High Agri Valley basin (Basilicata, southern Italy). Geomatics, Nat. Hazards and Risk, 10, 197-218, doi: 10.1080/19475705.2018.1520150

Triglia, A., Iadanza, C.; 2007: “Il Progetto IFFI - Metodologia, risultati e rapporti regionali” Rapporto sulle frane in Italia, (APAT, Roma).

Zuliani, D.; Tunini, L.; DiTraglia, F.; Chersich, M.; Curone, D.; 2022: Cost-Effective, Single-Frequency GPS Network as a Tool for Landslide Monitoring. Sensors, 22, 3526. https://doi.org/10.3390/s22093526.

Corresponding author: abratus@ogs.it

What does the seismic record of a World War II bomb-explosion look like? observations from a controlled detonation in 26 november 2023 near Ferrara, Italy

Authors: *F. Brighenti[1], A. Garcia[2], R. Caputo [1]*

[1]Dipartimento di Fisica e Scienze della Terra, Università degli Studi di Ferrara, Italy
[2]Istituto Nazionale di Geofisica e Vulcanologia, Sezione di Bologna, Bologna, Italy

During restoration operations at the former Convent of San Benedetto in Corso Porta Po, in Ferrara (Italy), an unexploded aeroplane bomb from War World II (WWII) was found on the first floor of the church (see e.g., press release from the Prefecture (Prefettura - Ufficio territoriale del Governo di Ferrara 2023). In the morning of 26 November 2023 the bomb was removed from this location and later, at 14:19 (UTC), a controlled detonation of the war device was performed in a cave about 7 km NW of the city. The cave where the explosion occurred is located in an area in which a local seismic monitoring network, the SNet4Fer 3.0, operates for monitoring microseismicity around the Casaglia geothermal field (Fig. 1). SNet4Fer 3.0 is an evolution of the previous SNet4Fer 2.0 network, which is still in operation, and represents an improvement of the monitoring capabilities of the anthropogenic activities that can potentially induce seismicity in the geothermal field (Abu Zeid et al., 2017). Both networks are operated by the University of Ferrara.

The NetFer 3.0 network consists of 7 seismic stations, each equipped with a surface accelerometer and a three-component, 2 Hz borehole seismometer (with the exception of station FEM0, which has a broadband borehole seismometer), all located 148 m below ground level. In addition, the NetFer 2.0 network consists of five stations equipped with single-component (with the exception of the PONT station, which has a three-component instrument) borehole seismometers located at depths ranging from 12 to 57 m below ground level.

Figure 2 shows some examples of the seismic records of the bomb explosion; in the records it is possible to distinguish relatively, weak P and S phase arrivals as well as the seismic trace of the airwave from the airblast. Despite the energy of the explosions being relatively low, if compared to earthquakes, the records in the nearby stations can provide interesting data for different analyses as e.g., for studying the anatomy of the records, for performing forensic analyses related with the equivalent charge of the war device, and also for checking the installation of the borehole instrumentation. In this work, we present some preliminary analyses of the seismic records of this explosion.

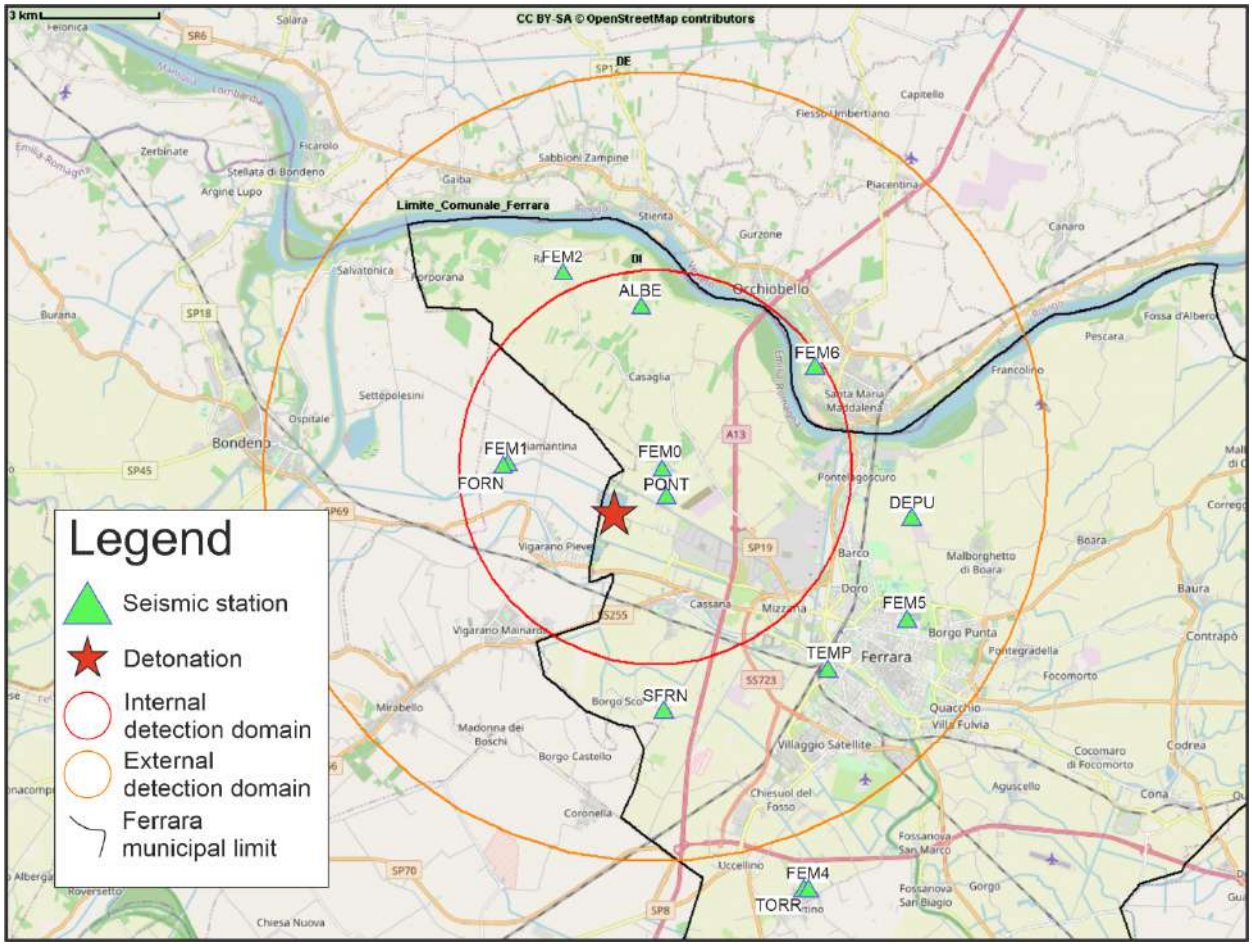

Figure 1: SNet4Fer 2.0/3.0 seismic networks (green triangles). The red star represents the point where the WWII bomb was detonated; the circles represent the internal (red) and external (orange) monitoring domains of the Casaglia geothermal field.

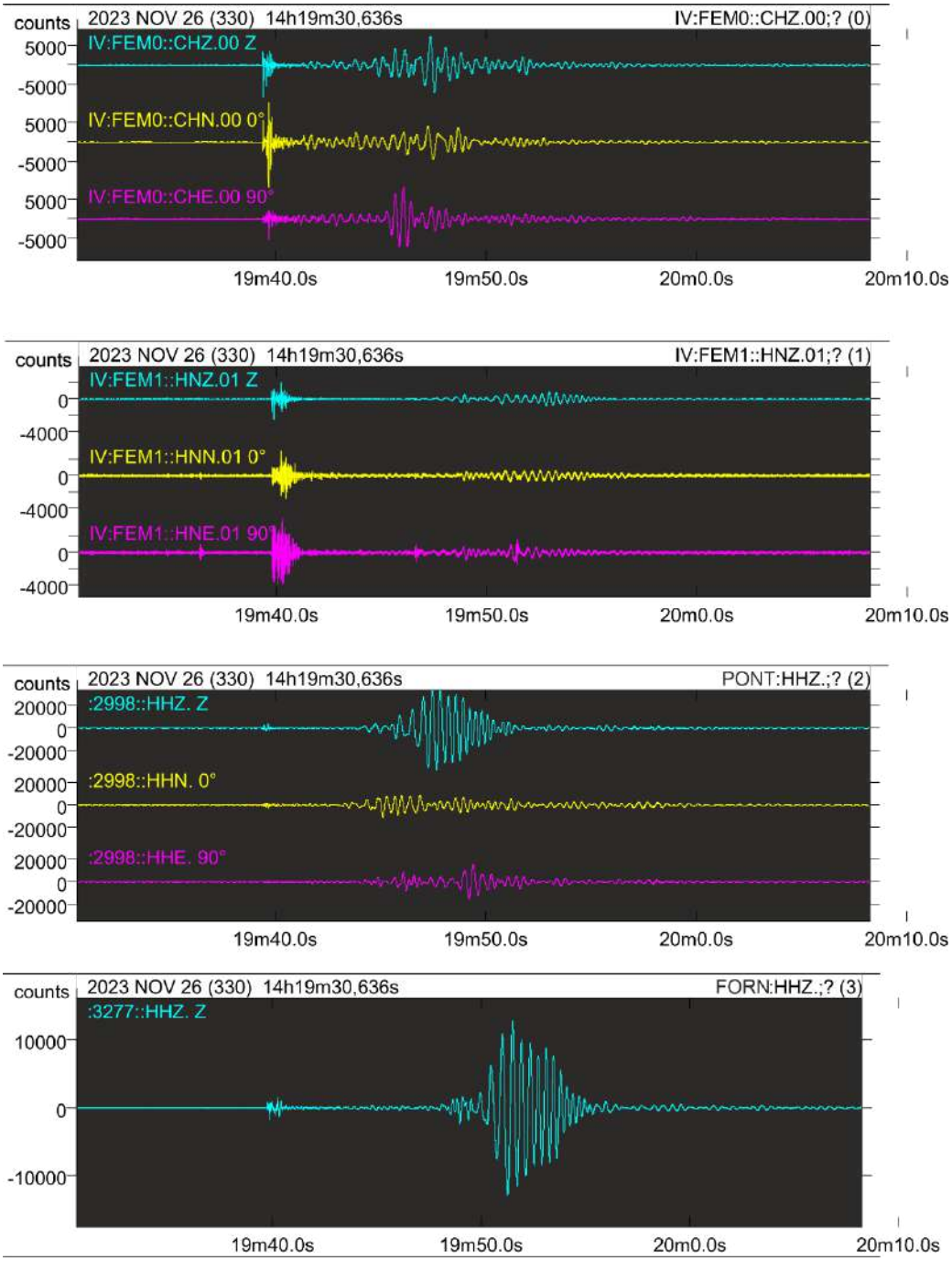

Figure 2. Examples of the bomb explosion seismograms recorded in stations from the SNet4Fer network. The first two panels show the 3-component records in the SNet4Fer 3.0 stations FEM0 and FEM1 (the seismograms are from the borehole sensors). The third and fourth panels show the records of two NetFer2.0 stations: PONT (3 components) and FORN stations (1 component).

References

Abu Zeid, N., Dall'olio, L., Bignardi, S., and Santarato, G., (2017). “Past, present and future improvements of the efficiency of the local seismic network of the geothermal reservoir of Casaglia, Ferrara (North Italy)”. 19th EGU General Assembly, 23-28 April, 2017, Vienna, Proceedings, 19172.

Prefettura - Ufficio territoriale del Governo di Ferrara (2023). Comunicato stampa del 26 novembre 2023. Link: https://www.prefettura.it/ferrara/contenuti/Neutralizzato_l_ordigno_bellico_inesploso_rinvenuto_nell_ex_convento_di_san_benedetto-18065660.htm (last accessed: 15 december 2023).

Corresponding author fabio.brighenti@unife.it

GPR investigations in the Santa Maria di Vezzolano rectory (AT)

M.F. Alberghina[1,2], V. Barberis[3], P. Capizzi[4], G. Comello[3], G. Milazzo[3], S. Schiavone[2]

[1] Department of Biology, Ecology and Earth Sciences (DiBEST), University of Calabria, Ponte P. Bucci, Cubo 12b, II Piano 87036, Arcavacata di Rende (CS), Italy

[2] S.T.Art-Test di S. Schiavone & C sas, via Stovigliai, 88 93015 Niscemi (CL), Italy,

[3] Regional Directorate of Piedmont Museums, Ministry of Culture, Via Accademia delle Scienze, 5, 10123 Torino (TO), Italy, valentina.barberis@cultura.gov.it

[4] Department of Earth and Marine Sciences (DiSTeM), University of Palermo,Via Archirafi 26 90123 Palermo (PA), Italy

The rectory of Santa Maria di Vezzolano in Albugnano (Asti, Italy) was founded in 1095 AD. Between the 12th and 13th centuries the structure experienced its period of maximum magnificence, followed by a phase of progressive decline which lasted until 1800. In 1937 the complex was handed under the management of the Italian State and is now part of the cultural heritage sites of the Regional Directorate of Piedmont Museums, peripheral institute of the Ministry of Culture.

Among the non-invasive investigations, geophysical methodologies were conducted to deepen the knowledge of any architectural elements under the pavement not yet detected. In particular, ground penetrating radar (GPR) investigations (fig. 1) with a 200/600 MHz multi-channel antenna were carried out on the internal flooring of the church and in the area in front of the façade to identify cavities, discontinuities or underground architectural structures. Ground Penetrating Radar (Conyers and Leckebusch, 2010; Goodman and Piro, 2013) is today a consolidated method widely used for diagnostics and research in archaeological prospecting and in other fields of cultural heritage (Deiana et al., 2018; Cozzolino et al., 2020; Capizzi et al., 2021).

All GPR profiles were carried out with an interdistance of 50 centimeters and acquired using the Georadar instrumentation of IDS – Engineering dei Sistemi S.p.a. – RIS MF HI-MOD model, equipped with a 200/600 MHz dual frequency antenna. The investigation depths were estimated considering an average electromagnetic wave propagation velocity of 0.1 m/ns. This average value was obtained from the slopes of the reflection hyperbolas present in the data. Each profile has been processed to eliminate coherent and inconsistent noise present in the original data. After processing the data with ReflexW software (Sandmeier, 2016) trying to eliminate both coherent and inconsistent noise, we proceeded with the analysis and interpretation in relation to the purposes envisaged by the study. For simplicity of graphic representation of the processed data, it was chosen to display the interpretative models of the investigated volume, in terms of normalized reflected amplitude. For each of the four areas investigated (central nave, side nave, portion in front of the Jubè, external area) a 3D model was built, using a code implemented in Matlab for the

construction of the data matrix and the Voxler application (Golden Software) for the graphic rendering. For the spatial interpolation the Inverse Distance Weighting algorithm (Shepard, 1968) was applied, which uses a weighted average based on the distance of the points from the observation point.

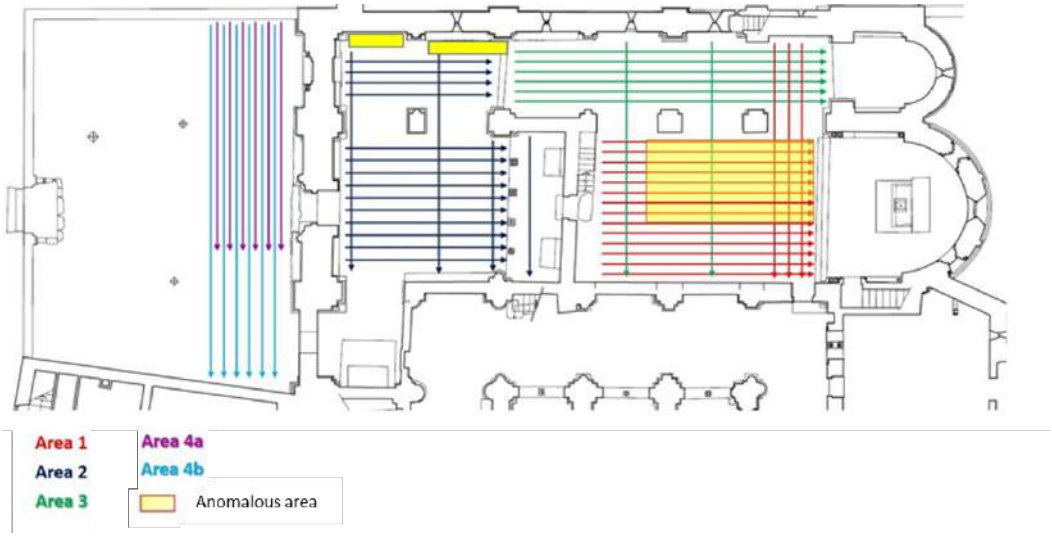

Fig. 1 – Location of the ground penetrating radar profiles.

All GPR profiles were carried out with an interdistance of 50 centimeters and acquired using the Georadar instrumentation of IDS – Engineering dei Sistemi S.p.a. – RIS MF HI-MOD model, equipped with a 200/600 MHz dual frequency antenna. The investigation depths were estimated considering an average electromagnetic wave propagation velocity of 0.1 m/ns. This average value was obtained from the slopes of the reflection hyperbolas present in the data. Each profile has been processed to eliminate coherent and inconsistent noise present in the original data. After processing the data with ReflexW software (Sandmeier, 2016) trying to eliminate both coherent and inconsistent noise, we proceeded with the analysis and interpretation in relation to the purposes envisaged by the study. For simplicity of graphic representation of the processed data, it was chosen to display the interpretative models of the investigated volume, in terms of normalized reflected amplitude. For each of the four areas investigated (central nave, side nave, portion in front of the Jubè, external area) a 3D model was built, using a code implemented in Matlab for the construction of the data matrix and the Voxler application (Golden Software) for the graphic rendering. For the spatial interpolation the Inverse Distance Weighting algorithm (Shepard, 1968) was applied, which uses a weighted average based on the distance of the points from the observation point.

The georadar survey carried out for a total of 54 profiles identified anomalies attributable to possible buried structures (fig. 2). In particular, some anomalies are compatible with the presence of crypts/burials in the central nave in the area near the main altar and, at greater depth (about 3 m) an anomaly in the initial part of the nave, near the Jubé. The latter is confirmed by another anomaly identified at the same depth on the opposite side of the arches. Some anomalies have also been identified in the side nave at a depth of approximately 2 m compatible with pre-existing architectural structures. As regards the external portion, the ground penetrating radar survey did

not reveal any other underground structures other than those already known from previous excavations (Crosetto, 2011).

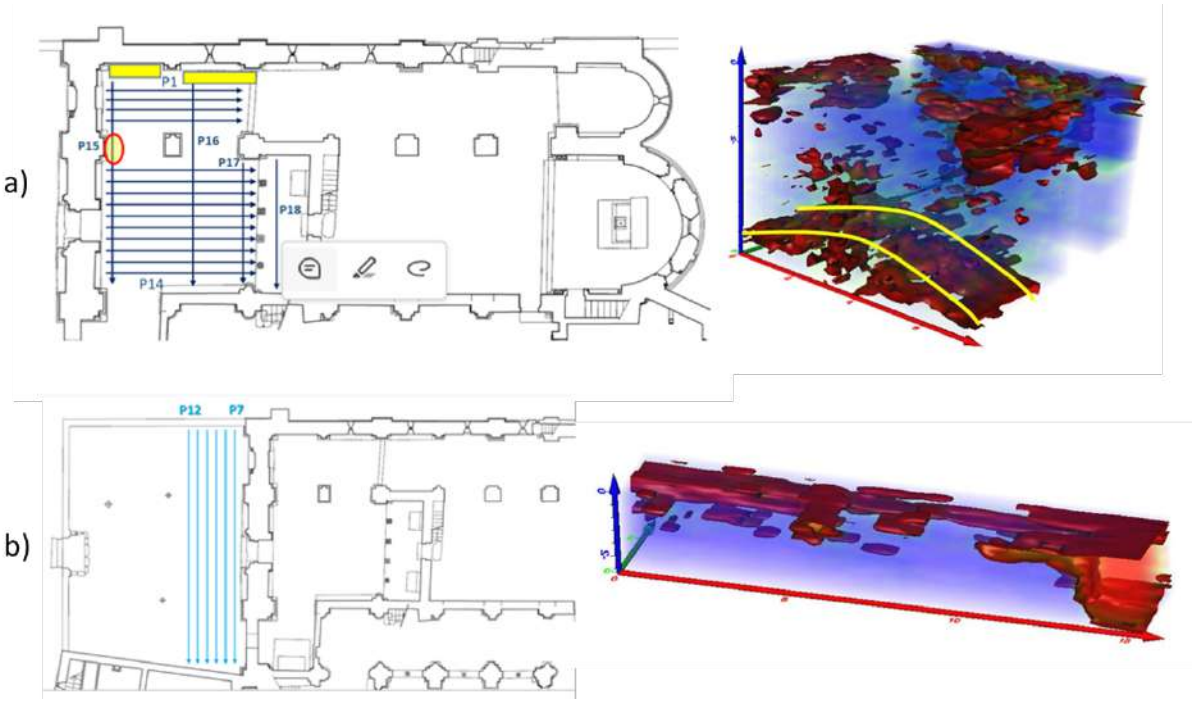

Fig. 2 – Partially GPR results for the area 2 (a) and the area 4b (b).

References

Capizzi P., Marrone M., Aleo Nero C., Bonfardeci A., Canzoneri A., Carollo A., Martorana R, Romano F. (2021) Georadar investigations in the Church of San Paolo (San Giacomo dei Militari, Palermo). Near Surface Geoscience 2021 – Bordeaux, France, 29 August – 2 September 2021, 1-5, https://doi.org/10.3997/2214-4609.202120203

Conyers LB, Leckebusch J (2010) Geophysical Archaeology Research Agendas for the Future: Some Ground penetrating Radar Examples. Archaeological Prospection, 17(2), 117-123. https://doi.org/10.1002/arp.379

Cozzolino, M., Di Giovanni, E., Gentile, V., Mauriello, P., Pizzano, N. (2020) Ground-Penetrating Radar Survey for the Study of the Church of Saint Cosma in Helerito (Tagliacozzo, L'Aquila, Italy). Geosciences, 10(6), 244. https://doi.org/10.3390/geosciences10060244

Crosetto, A., (2011) Santa Maria di Vezzolano: nuovi dati storici. In titolo volume Palazzo Carignano Torino.

Deiana R, Leucci G, Martorana R (2018) New Perspectives on Geophysics for Archaeology: A Special Issue. Surveys in Geophysics, 39(6), 1035–1038. https://doi.org/10.1007/s10712-018-9500-4

Goodman D, Piro S (2013) GPR Remote Sensing in Archaeology. Springer, 9. https://doi.org/10.1007/978-3-642-31857-3

Sandmeier, K.J. (2016) ReflexW Version 8.1. Program for Processing of Seismic, Acoustic or Electromagnetic Reflection, Refraction and Transmission Data. Software Manual, Karlsruhe, Germany.

Shepard, D. (1968) A two-dimensional interpolation function for irregularly-spaced data. Proc. 23rd National Conference ACM, ACM, 517-524.

Corresponding author: patrizia.capizzi@unipa.it

Identification of archaeological features using *Machine Learning* techniques applied to electromagnetic data

A. Capozzoli [1], E. Piegari [1], F. Cella [2], M. La Manna [1], V. Paoletti [1]

[1] Dipartimento di Scienze della Terra, dell'Ambiente e delle Risorse, Università degli Studi di Napoli Federico II, Naples, Italy

[2] Dipartimento di Scienze e Tecnologie, Università di Camerino, Camerino, Italy

Introduction

Over the past decades, geophysical investigations in the archaeological field have been recognized as an important tool for identifying target areas and planning dig works (e.g., Cella et al., 2015; Di Maio et al., 2016; El Qadi et al., 2019 and references therein). Indeed, they allow exploration of evermore extended surfaces with a significant reduction in costs associated with excavation campaigns. One of the geophysical prospecting methods with the highest values of the benefit-cost ratio is the frequency domain electromagnetic method (FDEM). This method allows obtaining quick information on both the electrical and magnetic properties of the investigated volumes from the measurements of the two components of the EM field. However, correlations between the maps of such components are commonly found only by visual inspection (e.g., Everett, 2013). The aim of the present study is to realize integrated maps of the two EM components in the attempt to obtain automatic identification of the target areas.

Material and methods

We analyze the electromagnetic (EM) data acquired in 2012 at the archaeological site of Torre Galli (Vibo Valentia, Calabria, Italy) where a magnetic study and two digs were previously conducted (Cella & Fedi, 2015). We apply the K-Means clustering algorithm to three FDEM dataset, one for each of the operating frequencies (5 kHz, 10 kHz and 15 kHz), in order to retrieve information about potential areas of interest at different depths. The K-means algorithm is an unsupervised Machine Learning technique grouping data with similar characteristics in a predefined number of clusters (e.g., Bhattacharya, 2021). We use two approaches to identify the optimal number of clusters for the specific problem. Specifically, we compute the Silhouette coefficient and apply the Elbow method to the partitions of data in the parameter space defined by the two components of the EM field. Then, we map in the real space the optimal clusters obtained for each analysed datasets and compare our results with the outcome of magnetic prospection.

Results

From the cluster analysis applied to the EM data for two operating frequencies (5 kHz, 10 kHz), it turns out that the Silhouette coefficient always identifies an optimal number of clusters, smaller than that from the Elbow method. In other words, optimal clusters validated by the Silhouette coefficient correspond to areas in the archaeological site that are much larger than those identified by the Elbow method. Looking at the clusters of major interest for archaeological studies, which are characterized by the highest values of magnetic susceptibility and electrical resistivity, it is found that groups from the Silhouette validation analysis can contain up to three of the optimal clusters identified by the Elbow method. However, in some cases the clusters from both the Elbow method and Silhouette coefficient agree in the identification of potential target areas, i.e., where the presence of a ditch is inferred. We stress that all the anomalous areas identified by the analysis of magnetic data fall within the areas of potential interest for the archaeological excavation operations identified by the present clustering analysis. Hence, the proposed approach shows that the application of unsupervised machine learning techniques to FDEM data is promising in improving the efficiency of this method making it more attractive for archaeological research.

References

Bhattacharya, S.; 2021: A Primer on Machine Learning in Subsurface Geosciences, 1, 1–172.

Cella, F., Fedi, M.; 2015: High-resolution geophysical 3D imaging for archaeology by magnetic and EM data: the case of the iron age settlement of Torre Galli, Southern Italy. Surveys in Geophysics, 36(6), 831-850.

Cella, F., Paoletti, V., Florio, G., Fedi, M.; 2015: Characterizing elements of urban planning in Magna Graecia using geophysical techniques: the case of Tirena (Southern Italy). Archaeological Prospection, 22(3), 207-219.

Di Maio, R., La Manna, M., Piegari, E.; 2016: 3D reconstruction of buried structures from magnetic, electromagnetic and ERT data: Example from the archaeological site of Phaistos (Crete, Greece). Archaeological Prospection, 23, 3-13.

El-Qady, G., Metwaly, M., Drahor, M. G.; 2019: Geophysical techniques applied in archaeology. Archaeogeophysics: State of the art and case studies, Springer, 1-25.

Everett, M.E.; 2013: Near-Surface Applied Geophysics. Pp.209.

Corresponding author: angelica.capozzoli@unina.it

A novel approach for the assessment of the deterioration of RC structures by means of non-invasive tests supported by numerical models

L. Capozzoli[1], G. De Martino[1], S. Imperatore[2], F. Nerilli[2], L. Telesca[1], E. Vasanelli[3]

[1] Institute of Methodologies for Environmental Analysis, National Research Council of Italy (IMAA CNR), C. da S. Loja—Zona Industriale, Tito Scalo, 85050 Potenza, Italy
[2] Department of Civil Engineering, "Niccolò Cusano" University of Rome, 00166, Italy
[3] Institute of Heritage Science, National Research Council (ISPC- CNR) via per Monteroni, 73100 Lecce (LE), Italy

Economic, political, and social implications related to the safety of reinforced concrete structures and infrastructures pose significant and unavoidable challenges. As regards only the economic aspect, the global non-destructive testing market is projected to grow from $6,80 billion in 2022 to $16.66 billion by 2029, at a CAGR of 13,66% [Report, online resource].

Deterioration phenomena affecting concrete and/or reinforcements cause physicochemical and mechanical variations, difficult to detect and localize by using conventional diagnostic tools and methods, which are often low-resolution, invasive, cost, and time-consuming. Moreover, numerical models can support the safety condition assessment of reinforced concrete structures but to date, there isn't a consolidated approach for deteriorated materials.

It is evident how coupled with semi-destructive and destructive tests and/or other well-known non-destructive tests, geophysical methodologies can play a fundamental role in RCS corroded RC structures inspecting and monitoring [Vasanelli et al.]. For this reason, the development of innovative strategies for corrosion diagnosis based on a combined and integrated use of geophysical and other NDT methodologies is strongly required [Maierhofer et al., 2010; Capozzoli and Rizzo, 2017; Capozzoli et al., 2021]. Nowadays, protocols for the diagnosis of deteriorated RCS are not fully established, as they depend on the specificity of the case studies under investigation. Moreover, the potentialities of geophysical methodologies, alone or integrated, are not fully unleashed.

From a structural point of view, a lot of efforts in performing experimental tests and in assessing theoretical models on corroded RC members are still needed, due to the amount of random parameters governing the physical problem and the chemical processes. In detail, a lack of well-established formulations to employ in FEM-based structural analyses of aged structures is emerged, even if some statistically assessed formulations are available [Coccia et al. 2016; Imperatore et al., 2017; Imperatore and Rinaldi, 2019; Benenato et al., 2022; Imperatore, 2022].

In this framework the two CNR Institutes ISPC (Institute of Heritage Science) and IMAA (Institute of Methodologies for Environmental Analyses) and UNICUSANO University are working on the two-year Research Project of National Relevance (PRIN-2022) ICARUS which aims at exploring the contribution that geophysical methodologies can give for detecting and monitoring the main degradation phenomena affecting RCS, considering both the concrete and the reinforcements deterioration.

ICARUS proposes the development of an innovative multiscale and multisensor geophysical methodology based on integrating empirical relationships between physical and mechanical parameters in different deterioration conditions. The project's objective will consist of developing an innovative strategy based on integrating geophysical analyses, conventional NDT and DT, and advanced statistical analyses to identify the material decay evolution and upgrade existing corrosion damage models. In addition, novel structural assessment approaches for deteriorated RCS will be proposed. At this aim, improved bond-slip and tension-stiffening laws will be developed to assess how corrosion affects the steel-to-concrete interaction at both local and global levels. The outcomes, coupled with empirical relationships based on geophysical measurements for cracked concrete and corroded reinforcements and proper finite element approaches, will allow the evaluation of the structural behaviour of deteriorated reinforced concrete structures.

ICARUS will try to accomplish mainly two goals:

1. Development of a non-invasive and multiscale approach for the geophysical characterization and monitoring of degradation, and development of damage empirical models, through the analysis of correlations between geophysical parameters and mechanical properties of concrete and RC elements with damage progression.

2. Modelling of the mechanical response of RCS at different damage levels due to deterioration phenomena. In detail, the attention will be focused on the decay of the mechanical properties of the concrete and the steel-to-concrete interaction using experimental, analytical, and numerical approaches.

In order to accomplish its mission, ICARUS will analyze the degradation mechanisms occurring in concrete and their simulation in small-scale samples with different geophysical methodologies, DT and NDTs will be applied to degraded samples, accurately selected on the basis of aging procedures and specimens' dimensions. The accuracy of each geophysical methodology in defining the degradation level will be step-by-step analyzed by laboratory measurements, at different damage levels starting from the sound conditions of the material. Microstructural, physical, chemical, and mechanical characterization tests at different stages of decay will support the tests.

Further, damage assessment of corroded RC members by means of destructive tests and geophysical methodologies will be accurately evaluated through a step-by-step laboratory procedure; then the variations of the geophysical response due to the artificial corrosion of rebars will be analyzed. The microstructural/physical properties of the corroded samples and their mechanical response will be examined to characterize the degradation phenomena. Artificial corrosion degradation of RC elements to obtain different crack patterns and/or corrosion levels will

be implemented for evaluating the mechanical performance of the corroded steel-concrete elements subjected to different corrosion levels.

Fig. 1 - The innovative multi-scale and multi-sensor based approach of ICARUS

The outcomes of ICARUS have economic potential as its activities may reduce the costs of restoration and rehabilitation interventions. Moreover, the approach is focused on the extension of the service life of structures by providing a more accurate diagnostic of the RC buildings and infrastructure conditions according to Cluster 5 of Horizon Europe 21-27 Program.

References

Benenato, A., Ferracuti, B., Imperatore, S., & Lignola, G. P. (2022). Corrosion level estimation by means of the surface crack width. Construction and Building Materials, 342, 128010.

Capozzoli L. and E. Rizzo, Combined NDT techniques in civil engineering applications: Laboratory and real tests, Constr Build Mat, 154, pp 1139-1150, 2017

Capozzoli L. et al., Multi-Sensors Geophysical Monitoring for Reinforced Concrete Engineering Structures: A Laboratory Test, Sensors, 21(16):5565, 2021

Coccia S. et al, Influence of corrosion on the bond strength of steel rebars in concrete. Mater Struct, 49(1), 537-551,2016

Imperatore S. and Z. Rinaldi, Experimental behavior and analytical modeling of corroded steel rebars under compression. Constr Build Mat, 226,126-138,2019

Imperatore S. et al., Degradation relationships for the mechanical properties of corroded steel rebars. Constr Build Mat, 148, 219-230,2017

Imperatore, S. (2022). Modelling Strategies for Reinforced Concrete Elements under Corrosion Degradation. Materials, 15(13), 4601.

Maierhofer C. et al., Non-Destructive Evaluation of Reinforced Concrete Structures: Non-Destructive Testing Method, Elsevier,2010

NDT and Inspection Market by Technique (Visual Testing, Magnetic Particle, Liquid Penetrant, Eddy-Current, Ultrasonic, Radiographic, Terahertz Imaging, Acoustic Emission), Method, Service, Application, Vertical and Region-Global Forecast, report, online resource, last access 2023

Vasanelli E. et al, Combining non-invasive techniques for reliable prediction of soft stone strength in historic masonries, Constr Build Mat, 146, 744-754,2017

corresponding author: luigi.capozzoli@cnr.it

A Dynamic and Multi-Source Hydrogeophysical Model to Remediate a Complex Hydrocarbon-Contaminated Site

P.Ciampi[1], G.Cassiani[2], G.P.Deidda[3], C.Esposito[1], G.Scarascia Mugnozza[1], M. Petrangeli Papini[4]

[1] Department of Earth Science, Sapienza University of Rome
[2] Department of Geosciences, University of Padua
[3] Department of Civil, Environmental Engineering and Architecture, University of Cagliari
[4] Department of Chemistry, Sapienza University of Rome

Contaminated sites pose intricate challenges in characterization and remediation planning due to the complex interplay of contaminants and hydrogeological properties, often resulting in under-sampling issues at the site-specific scale. This study introduces a dynamic multi-source approach to address the challenges of characterizing and remediating a hydrocarbon-contaminated site. A comprehensive dataset is compiled from diverse sources, including stratigraphic boreholes, laser-induced fluorescence surveys (LIF), electrical resistivity tomography (ERT), and groundwater hydrochemical monitoring. These data are integrated into an interactive big-data package, enabling real-time 3D modeling throughout the characterization and remediation phases. The study yields a comprehensive conceptual hydrogeophysical model that captures hydrogeological and geophysical structures, as well as the spatial and temporal dynamics of contamination. By combining knowledge from multiple sources, the multi-source hydrogeophysical clone provides qualitative-quantitative indicators to reduce uncertainties associated with subsurface interpretation by separating signatures of geologic material in the absence of light non-aqueous phase liquids (LNAPL) and the local increase in electrical conductivity associated with petroleum hydrocarbon biodegradation. It reveals the real characteristics of the pollutant, contamination mechanisms, and residual hydrocarbon sequestration influenced by hydrogeological dynamics and on-site remediation actions. The emerging hydrogeophysical conceptual site model (CSM) serves as a dynamic interface for designing enhanced remediation actions, specifically targeting LNAPL and involving reagent injections into the subsurface to stimulate the desorption and oxidation of residual hydrocarbons. Geophysical monitoring, utilizing ERT, reveals subsurface dynamics and variations in electrical conductivity during injection, extraction, and subsequent pumping activities. The study underscores the importance of collecting diverse data for a reliable and high-resolution reconstruction of the conceptual framework. The dynamic multi-source model explains contamination/decontamination dynamics based on the variation of electrical properties in space-time, also induced by the application of remediation processes at the field scale. Data-driven model discriminates geophysical evidence on the basis of lithologic characteristics and

contamination effects, providing considerable qualitative-quantitative insights into both the distribution of products in a highly heterogeneous medium and the hydraulic perturbations associated with the pumping operated by traditional physical extraction wells. This research enhances our understanding of contaminant remediation dynamics, emphasizing the need for integrated, multi-source approaches in addressing the complexities of heterogeneous geoenvironments.

References

Ciampi, P., Esposito, C., Cassiani, G., Deidda, G. P., Rizzetto, P., Petrangeli Papini, M. (2021): A field-scale remediation of residual light non-aqueous phase liquid (LNAPL): chemical enhancers for pump and treat. Environmental Science and Pollution Research, 28(26), 35286-35296. https://doi.org/10.1007/s11356-021-14558-2.

Ciampi, P., Esposito, C., Cassiani, G., Deidda, G. P., Flores-Orozco, A., Rizzetto, P., Chiappa, A., Bernabei, M., Gardon, A., Petrangeli Papini, M. (2022). Contamination presence and dynamics at a polluted site: Spatial analysis of integrated data and joint conceptual modeling approach. Journal of Contaminant Hydrology, 248, 104026. https://doi.org/10.1016/j.jconhyd.2022.104026.

Orozco, A.F., Ciampi, P., Katona, T., Censini, M., Petrangeli Papini, M., Deidda, G.P., Cassiani, G. (2021). Delineation of hydrocarbon contaminants with multi-frequency complex conductivity imaging. Science of the Total Environment, 768, 144997. https://doi.org/10.1016/j.scitotenv.2021.144997.

Corresponding author: paolo.ciampi@uniroma1.it

The audio and electrical monitoring of the Mefite area in ELF band

G. Cianchini[1], C. Fidani[1,2], A. Piscini[1], M. Soldani[1], A. De Santis[1], L. Perrone[1] , M. Orlando[1], D. Sabbagh[1]

[1] Istituto Nazionale di Geofisica e Vulcanologia, Roma, Italy
[2] Central Italy Electromagnetic Network, Fermo, Italy

A multi-parameter station came into operation last year near the Mefite site, a CO_2-rich vent located in Irpinia, province of Avellino, Campania Region. The aim of studying fluid migration in relation to tectonic activity at this particular site falls within the scope of the FURTHER (the role of FlUids in the pReparaTory pHase of EaRthquakes in Southern Apennines) project. In this station there are two magnetometers for continuous monitoring, two electrodes for electrical variations, a microphone, and occasionally other instruments for limited intervals of time. The Very Low Frequency band of the electric field sampled at Mefite in relation to moderate and strong seismic events in the Mediterranean region was previously reported (Cianchini et al., 2023). The Extremely Low Frequency band concerns both the electric and acoustic fields. Electric field in this band are monitored by an instrument of the Central Italy Electromagnetic Network, and near the earth's surface contains information about several phenomena both far and close to the electrode sensors (Fidani, 2011). They are natural and anthropogenic phenomena. Anthropogenic signatures of electric phenomena are regular shapes on spectrograms. For example, the horizontal lines of Figure 1 top represent the everywhere emission by the electrical power distribution network. The main frequency of this emission occurs at 50 Hz and a series of harmonics at multiple frequencies. Such anthropogenic emissions occur around the electrodes up to hundreds of m. Instead, the horizontal bands on the black background barely appearing in grey and blue of the spectrum under 50 Hz, are a natural phenomenon known as Schumann Resonances. These are eigenfrequencies of the cavity between the earth's surface and the ionosphere that behave like conductors. They are global phenomena of radiation sustained by lightning activity and selected by interference at 8, 14, 19, 25, 31 Hz, and more, that are little affected by small and local causes within 100 km. Spectrograms shown in Figure 1 are 147-minute records in the evening of December 22, 2022, with stable meteorological conditions indicated by a low density of vertical coloured lines, which are more evident at the low part of the spectra. Vertical lines are electrical discharges occurring in the atmosphere mainly generated by meteorological activity and partially generated by anthropogenic activity. Lightning can be detected at hundreds of km, as in this case, up to thousands of km. While anthropogenic switching of utilizers can be recorded up to one km from electrodes. Finally, a very evident local phenomenon is observed in the electrical ELF spectrogram (Top). It was appearing only on the E-W electrode, that is the electrode oriented towards the

Mefite lake. It appears as a well defined red-coloured band that develops irregularly in the central part of the recording between 50 and 200 Hz. It is a local oscillation of the electric field because it does not appear at both electrodes, and it was demonstrated to have a source not longer than some tenths of m large (Fidani and Martinelli, 2015). This is the phenomenon that we are searching to observe in connection with the fluid escaping from the ground to study some kind of link between them.

From the theoretical approach (Fidani and Martinelli, 2015; Fidani et al., 2020), this signal should be generated by charged oscillating clouds whose dimensions would be from tenths of cm to a few meters dimension. The charged cloud is a stable structure as the pressure force is supposed to balance the electric force. It was mathematically demonstrated that such a physical system is able to oscillate, and the charge magnitude balancing slight pressure holes was estimated to depend on the oscillation frequency. Charges from 10^{-4} to 10^{-5} Coulombs were associated with the measured frequencies. Being pressure variations hypothesized for this kind of electrical sources, a comparison was made between the most intense electric oscillation and acoustic recordings. searching for possible mechanical effects of oscillating cloud transduction in pressure waves or thinking of fluid emission changes possibly related to electric oscillation triggers. The comparison was made between respective spectrograms. Being the acoustic signal initially sampled at 27 kHz, the spectral overlap with the electric ELF (up to 2 kHz) spectra was problematic, also due to the logarithm scale for ELF with respect to the linear for audio. The acoustic recording is reported in Figure 1 bottom, for the same time interval on December 12, 2022. No connections appeared between intensities nor in shapes. Higher audio frequency recordings seem to be related to wind, whereas the corresponding frequencies of the electrical oscillation were restricted in the violet band of Figure 1 bottom. A reduction of audio sampled frequency was first decided to reduce the wind influence, and a plot in the logarithm scale was realized for a better comparison with the electric recording.

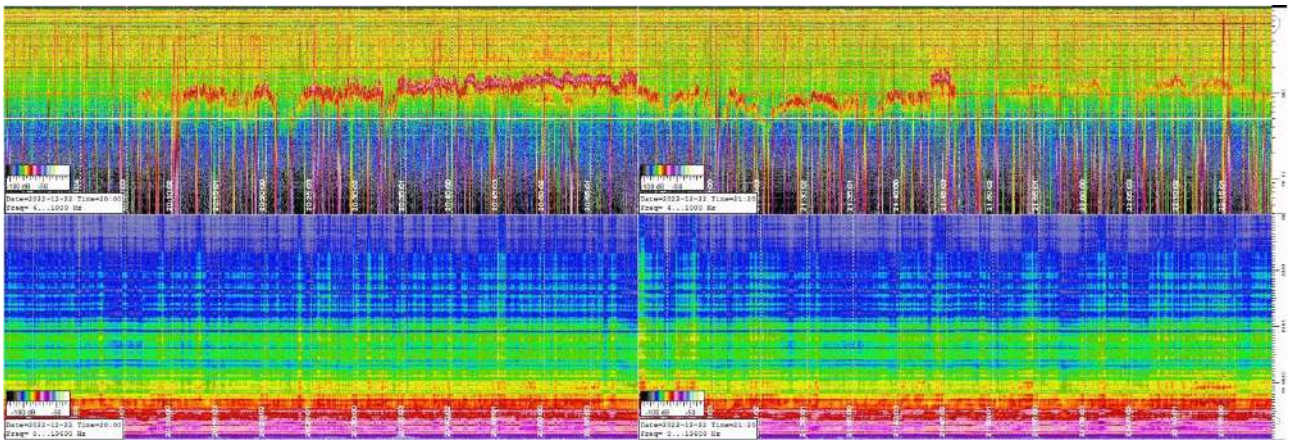

Fig. 1 – Spectrograms recorded on December 22, 2022, from 19:52 to 22:19 LT; the time is marked every 5 minutes by the vertical dotted lines. Frequency was reported in the logarithm scale on the y-axis and power of signals in dB by a colour legend. Two bands are related to the electrode E-W on the top, and to the microphone recording below. Labels on the left and in the middle referred to the power spectra intensities and times of the spectrograms.

From the beginning of April 2023 the audio sample frequency was reduced to 16 kHz, and the vertical frequency axis scale was set logarithmic covering the interval between 10 Hz and 8 kHz. In this way, spectrograms become comparable with the ELF ones for the electric field, and the spectral content in the lower part of the audio sound becomes more intelligible. During the Mefite station maintenance, it was possible to verify the good state of the microphone after several months of audio recording despite its continuous exposure to the corrosive emissions at Mefite. Indeed, the device was protected by a hood that was put on to shield it from gusts of wind for land audio recordings. While, the copper wires, although covered by sheath, were corroded perhaps due to small cracks in the sheath. Thus, a further comparison was momentarily not possible between electric and acoustic signals.

The spectral content of the lower part of the audio band, now visible by logarithmic scale, immediately evidenced a rich variety of eigenfrequencies. Furthermore, their amplitudes presented non-constant intensities both in a collective sense and in a singular sense. Some acoustic resonances appeared sporadically during the intense increase of the Mefite's blow. The Fourier analysis was particularly investigated at the time of small seismic events that occurred a few tenths of km away from the site. An example is shown in Figure 2, where more than 30 hours of audio recording have been reported starting from the day before the Mirabella M=2.1 earthquake occurred at the beginning of April 19, 2023. Hypocentre depth occurred at less than 10 km at a distance of around 20 km. The seismic event was preceded by a sensible noise increase that started about 11 hours before and was maintained for about 6 hours, then slowly faded over many hours. The noise increase was in turn preceded by two puff dampening lasting approximately one hour each, one immediately before the noise increase and the other around 4 hours before it. The earthquake time was indicated by a cyan vertical arrow and the colour legend permitted the evaluation of a noise increase of about 10 dB during the most intense emission, and audio suppressions of up to 10 dB during the dampening. Three sudden puffs with a 10 dB noise increase were evidenced. Moreover, the frequency band between 100 and more than 1000 Hz also showed an evident increase during the maximum noise manifestation.

The main eigenfrequencies of Figure 2 are at 45 and 65 Hz. They maintain constant intensity for a long time before the seismic event. Other less apparent horizontal bands occur at 103 Hz, and 125 Hz, other two bands at 300-400 Hz and 700-800 Hz, and many weak horizontal bands above 1000 Hz. More detailed observation of the power spectra in Figure 2 shows the entire series of 19, 45, 65, 103, 125, and 170 Hz, which appear more clearly during the damping hour preceding the significant increase of the audio noise of Figure 3 middle. Instead, longer periods of audio noise modulation whose durations were between 5 and 10 minutes are shown in Figure 3 left. Details of the third puff are shown in Figure 3 right, where a noise increase lasting two minutes between 10 and 40 Hz was accompanied by a well-defined audio note at 55-80 Hz with frequency increased in less than 2 minutes. It could be thought of as a resonance excitation of the final conduct due to the sudden intensification of the flux.

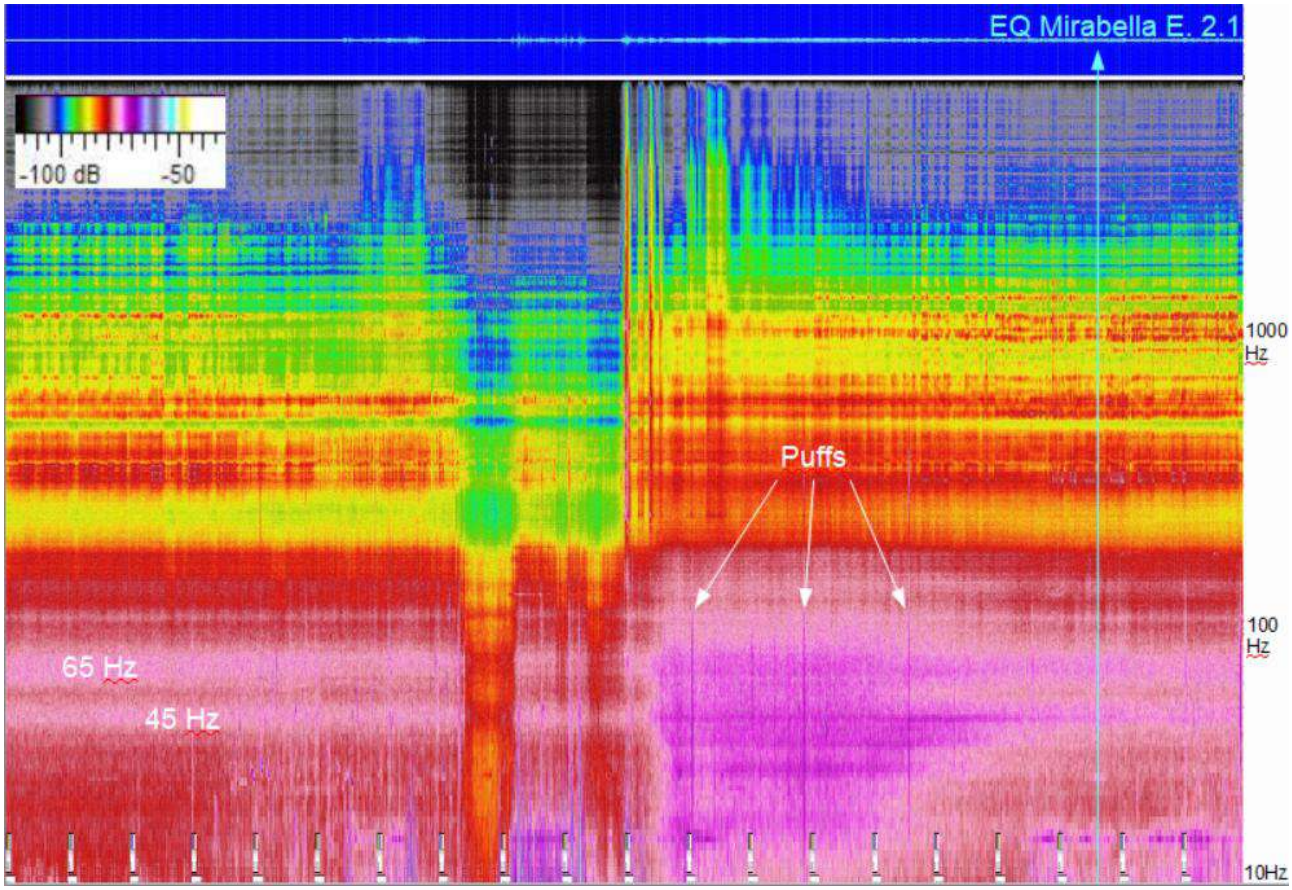

Fig. 2 – The acoustic spectrogram recorded on April 18 and the morning of 19, 2023, includes the moment of a small seismic event that occurred at Mirabella, M=2.1, about 20 km from Mefite. The Mirabella earthquake time is indicated by a vertical cyan arrow. Main eigenfrequencies and sudden puffs on the power spectra are indicated.

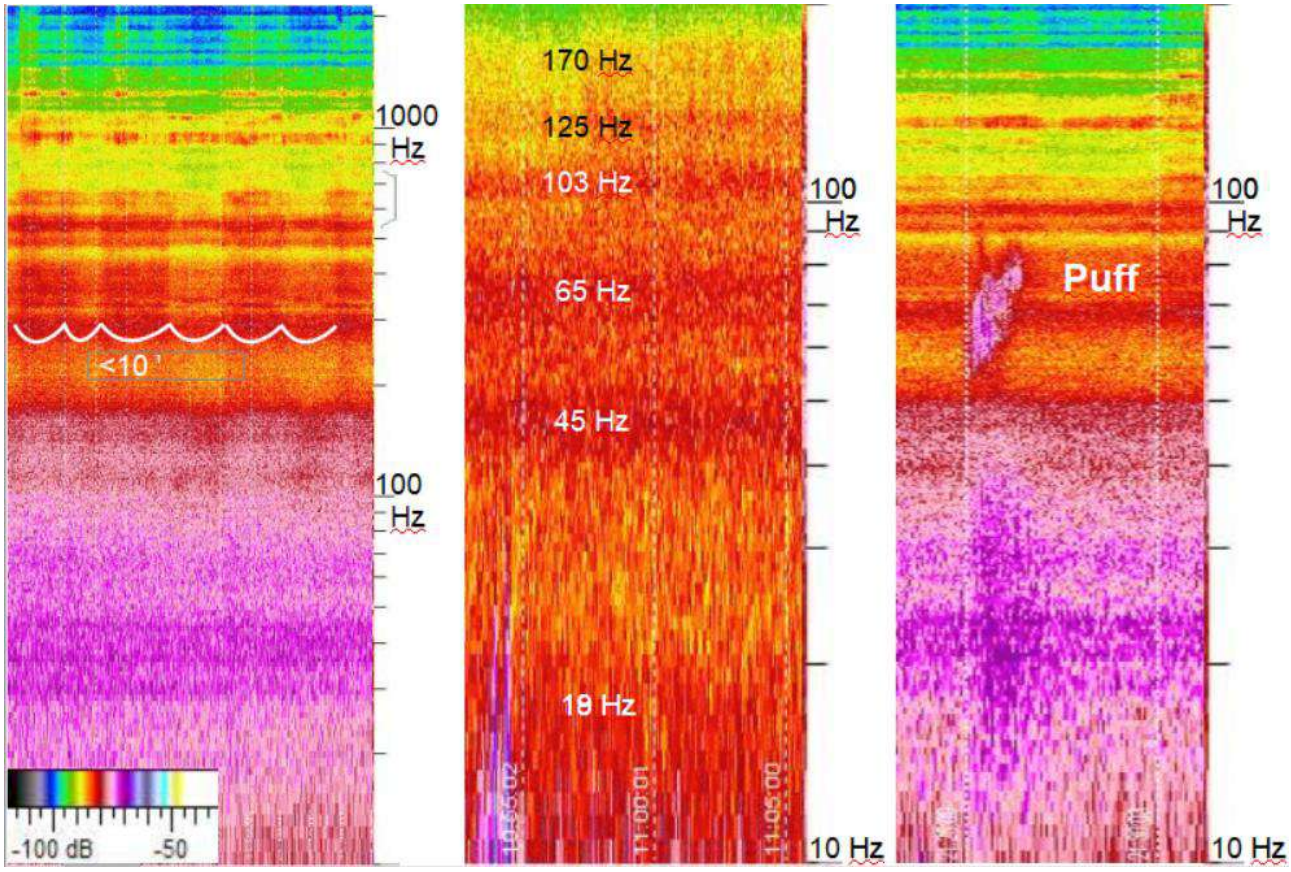

Fig. 3 – Details of the power spectrum relative to three moments (of less than 10 minutes to one hour) hours before the Mirabella M=2.1 earthquake. Periodic modulations of the noise of less than 10 minutes were evidenced between 200 and 800 Hz, on the left. The entire series of resonances from 19 to 170 Hz appeared during the damping interval at the centre. A detail of one of the three puffs is reported on the right where the sudden increase followed by a gradual fading that lasted two minutes is shown. The right plot also shows an unexpected growth of sound in a well-defined range between 55 and 80 Hz.

Acknowledgements

The authors thank the Limadou Scienza + (ASI), FURTHER (MUR) and Pianeta Dinamico (INGV-MUR) Projects for their financial support.

References

Cianchini G., et al.; 2023: A month of VLF detection at Mefite, Valle D'Ansanto, Italy. 41th GNGTS. February 7-9, Bologna.

Fidani C.; 2011: The Central Italy electromagnetic network and the 2009 L'Aquila earthquake: observed electric activity. Geosciences, 1 (1), 3–25.

Fidani C., and Martinelli G.; 2015: A possible explanation for electric perturbations recorded by the Italian CIEN stations before the 2012 Emilia earthquakes. Boll. Geofis. Teor. Appl. 56, 211–226.

Fidani C., et al.; 2020: Electric and Magnetic Recordings by Chieti CIEN Station During the Intense 2016–2017 Seismic Swarms in Central Italy. Front. Earth Sci., 8:536332.

Detecting fault geometries through electrical methods along some active faults of Mount Etna

F. D'Ajello Caracciolo[1], I. Nicolosi[1], V. Sapia[1], V. Materni[1], G. Tusa[1], M. Paratore[1], R. Azzaro[1]

[1] *Istituto Nazionale di Geofisica e Vulcanologia (INGV)*

Introduction

The Mt. Etna region is characterized by several active faults that play a significant role in local geodynamic processes (Azzaro et al., 2013a). Simultaneously, these faults exert a profound impact on the lives of local communities, strongly influencing land use across a substantial portion of the Etnean territory. The primary issue arising from the tectonic activity of these faults is related to seismic hazard, with many of them capable of generating strong earthquakes (Azzaro et al., 2013a). In the realm of earthquake geology, numerous studies have been conducted to map these active tectonic features and characterize their seismotectonic behavior (Azzaro et al., 2012).

Increasingly, local government authorities and professionals are considering the results of these research efforts for urban planning and infrastructure design, particularly in the aftermath of strong earthquakes causing significant damage to the building stock in the most densely populated areas of the volcano. This was evident in 2002 (Azzaro et al., 2010) following a flank eruption accompanied by an intense seismic crisis on the eastern flank of Etna. More recently, in 2018, a similar situation unfolded after the last eruption and a destructive earthquake (Azzaro et al., 2022).

In 2022, the regional Civil Protection Department initiated a new project for the seismic microzonation of 3rd level at Etna, with the aim of providing a detailed characterization of issues related to the interaction among active faults and urban planning. The goal is to improve and adapt to the Etnean territory, criteria and guidelines previously defined at a national level (Gruppo di lavoro MS, 2008). Currently, the scientific community involved in the project is focused on the characterization of the "active and capable faults" (hereinafter FAC), from both geological and geophysical points of view. Precise mapping and detection of active deformation lines by indirect methods, is the common target of all the participants.

In this framework, the INGV working group started a series of geophysical surveys in the eastern flank of Mount Etna in June 2023 (Fig.1). Specifically, electrical tomography and capacitive geoelectrical surveys were carried out along the Pernicana Fault, S. Leonardello Fault, and Fiandaca Fault. Geoelectrical methods, as demonstrated by Porreca et al. (2016), Civico et al.

(2017), Villani et al. (2015, 2017), have proven to be to be effective in revealing subsurface structures and fault geometries for this kind of applications.

Methods

Electrical tomography (ERT) is effectively employed in investigating geological horizons characterized by strong contrasts in electrical resistivity, often linked to lithological and structural variations. Measurements can be made using different arrays to maintain a good compromise between the vertical and horizontal shape of the recovered anomalies (Loke and Barker, 1996). An algorithm based on a least-squares deconvolution method is employed for the inversion of apparent resistivity, allowing 2D sections to be obtained through finite element calculation modules, also considering topographic corrections. A 10-channel, 72-electrode IRIS Syscal Pro was used for resistivity measurements, and the spatial coordinates of the electrodes were acquired through a Stonex S900 differential GPS with correction through the Italpos network.

This study focuses on the analysis and interpretation of two-dimensional electrical resistivity tomography profiles; each profile was primarily acquired using both Wenner and dipole-dipole (DD) electrode arrays. The electrical tomography profiles were acquired with a sampling interval of 1 m to achieve higher detail and, where possible, at 5 m intervals to reach greater depths of investigation.

Interpretative models are based on the inversion of a set of mixed apparent resistivity data from the two different arrays. To derive accurate true resistivity values from the measured apparent resistivity data, the smoothness-constrained least-squares method was employed. This method considers models with infinite perpendicular extension along the profile strike, as outlined in studies by Constable et al. (1987), deGroot-Headlin and Constable (1990), and Morelli and Labrecque (1996).

Preliminary results

The inversion models reveal the alternation of resistive and conductive layers, whose geometry and potential displacement highlight the presence of lateral discontinuities associated with recognized faults exposed at the surface. In a volcanic environment with volcanic and volcano-clastic products, electrical tomography reveals resistivity values ranging from medium-high to very high, consistently exceeding 300 Ohm/m. The dynamic range of resistivity values is characterized by the presence of more conductive layers with resistivity up to 1000 Ohm/m and more resistive layers with significantly higher values. These values align with the study area's characteristics, marked by lava flows and volcano-clastic products (Chiancone Formation).

In general, electrical tomography and capacitive geoelectrics reveal the presence of strong lateral discontinuities, whose geometry can be attributed to the existence of faults. Further studies, together with the integration of data from all the participants to the project, will provide indication for selecting the most suitable method/approach compared to different geological settings. The final goal is to compile guidelines for professionals, to be adopted as best-practise for future geophysical investigations.

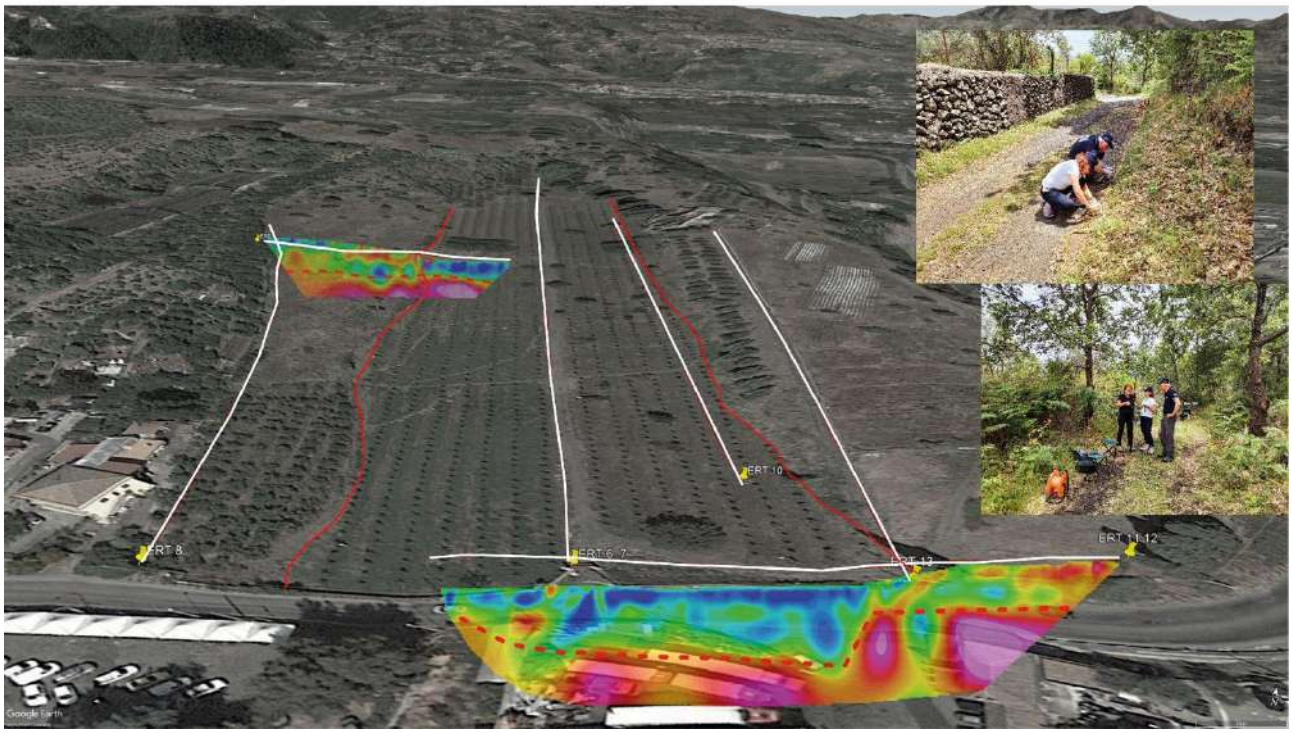

Figure 1: Perspective view of a measurement site along the S. Leonardello fault with traces of geoelectric profiles (in white), fault scarps (in red), and resulting 2D electrical tomography sections.

References

Azzaro R., Carocci C., Maugeri M. and Torrisi A. (Ed.); 2010: *Microzonazione sismica del versante orientale dell'Etna: studi di primo livello*. Regione Siciliana, Dipartimento della Protezione Civile, Le Nove Muse, Catania, 181 pp., 1 DVD-Rom, ISBN 978-88-87820-45-4.

Azzaro R., Branca S., Gwinner K. and Coltelli M.; 2012: *The volcano-tectonic map of Etna volcano, 1:100.000 scale: morphotectonic analysis from high-resolution DEM integrated with geologic, active faulting and seismotectonic data*. It. J. Geosciences (Boll. Soc. Geol. It.), 131 (1), 153-170.

Azzaro R., Bonforte A., Branca S. and Guglielmino F., 2013a: *Geometry and kinematics of the fault systems controlling the unstable flank of Etna volcano (Sicily)*. J. Volc. Geotherm. Res., 251, 5-15.

Azzaro R., D'Amico S., Peruzza L. and Tuvè, T.; 2013b: *Probabilistic seismic hazard at Mt. Etna (Italy): the contribution of local fault activity in mid-term assessment*. Journal of Volcanology and Geothermal Research, 251, 158-169.

Azzaro R., Pucci S., Villani F., Civico R., Branca S., Cantarero M., De Beni E., De Martini P.M., Cinti F.R., Caciagli M., Cucci L. and Pantosti D.; 2022: *Surface faulting of the 26 December 2018, Mw5 Mt. Etna earthquake (Italy): geological source model and implications for the seismic potential of the Fiandaca fault*. Tectonics, 41, DOI: 10.1029/2021TC007182.

Civico, R., Sapia, V., Di Giulio, G., Villani, F., Pucci, S., Baccheschi, P., et al. (2017). Geometry and evolution of a fault-controlled Quaternary basin by means of TDEM and single-station ambient

vibration surveys: The example of the 2009 L'Aquila earthquake area, central Italy. Journal of Geophysical Research: Solid Earth, 122, 2236–2259. doi.org/10.1002/2016JB013451.

Constable S.C., Parker R.L.and Constable C.G., (1987). Occams' inversion: A practical algorithm for generating smooth models from electromagnetic sounding data. Geophysics Vol. 52. N.3, 289-300.

De Groot-Hedlin, C., Constable, S., 1990. Occam's inversion to generate smooth, two dimensional models form magnetotelluric data. Geophysics 55, 1613-1624. doi.org/10.1190/1.1442813.

Gruppo di lavoro MS; 2008: *Indirizzi e criteri per la microzonazione sismica*. Conferenza delle Regioni e delle Provincie autonome – Dip. Della Protezione Civile, Roma, 3 vv. e DVD.

Loke, M.H., Barker, R.D., 1996. Rapid least-squares inversion of apparent resistivity pseudosections using a quasi-Newton method. Geophys. Prospect. 44, 131-152..

Morelli G. and Labrecque D., (1996). Advances in ERT inverse modeling European Journal of Environmental and Engineering Geophysics 1(2):171-186.

Porreca, M., Smedile A., Speranza F., Mochales T., D'Ajello Caracciolo F., Di Giulio G., Vassallo M., Villani F., Nicolosi I., Carluccio R., Amoroso S., Macrì P., Buratti N., Durante F., Tallini M. & Sagnotti L., (2016). Geological reconstruction in the area of maximum co-seismic subsidence during the 2009 Mw=6.1 L'Aquila earthquake using geophysical and borehole data, Italian Journal of Geosciences 135(2):1-33, doi:10.3301/IJG.2015.37.

Villani, F., Pucci, S., Civico, R., De Martini, P.M., Nicolosi, I., D'Ajello Caracciolo, F., Carluccio, R., Di Giulio, G., Vassallo, M., Smedile, A., Pantosti, D., 2015, Imaging the structural style of an active normal fault through multidisciplinary geophysical investigation: a case study from the Mw 6.1 L'Aquila earthquake region (central Italy). Geophys. J. Int. (2015) 200, 1676-1691.

Villani, F., & Sapia, V. (2017). The shallow structure of a surface-rupturing fault in unconsolidated deposits from multi-scale electrical resistivity data: The 30 October 2016 Mw 6.5 central Italy earthquake case study. Tectonophysics, 717(16), 628– 644. doi.org/10.1016/j.tecto.2017.08.00.

Corresponding author: francesca.caracciolo@ingv.it

Combining active and passive methods to understand the seismic velocity distribution in a thick Quaternary succession of the Po Plain. (Terre del Reno, Ferrara, Italy)

G. Di Giulio[1], L. Minarelli[1], M. Stefani[2], G. Milana[1], G. Tarabusi[1], M. Vassallo[1], S. Amoroso[1,3], A. Affatato[4], L. Baradello[4], L. Petronio[4]

1 Istituto Nazionale di Geofisica e Vulcanologia (Rome, Italy)

2 Università degli Studi di Ferrara (Ferrara, Italy)

3 Università degli Studi di Chieti-Pescara (Pescara, Italy)

4 Istituto Nazionale di Oceanografia e Geofisica Sperimentale – OGS (Trieste, Italy)

Introduction

To properly evaluate the local effects of earthquakes and improves the seismic profiles inversion, a good knowledge of the seismic velocity depth distribution is needed. Acquiring such a distribution is however a challenging issue in fast-subsiding alluvial sedimentary basins, with thick unlithified, low-velocity successions, and reduced seismic impedance contrasts, as in the Po Plain (Mascandola *et al*., 2021). Passive acquisition techniques, based on stand-alone stations and focused on the estimation of resonance frequency, can provide only raw information on the local velocity profile and are not particularly effective, by themselves, in areas as the lower Po Plain. Their proper interpretation needs independent stratigraphic data on the subsurface. Other passive techniques, based on array configurations of seismic stations, with varying geometries and apertures, increase the frequency band of analysis. Recent technology improvements and the advances in the array processing of three-component ambient-vibration recording further constrains the inversion process, generating a reliable shear-wave velocity profile, and supporting the extraction of the Rayleigh-wave ellipticity (Whatelet *et al*., 2018). HVSR and array methods however produce the most reliable results only in presence of sharp seismic contrasts, developed at a relatively shallow depth (approximately < 200 m), which is not the case of the study area. An effective approach to the reconstruction of deep velocity profiles, in similar sedimentary basins, consists in the combination of passive and active methods. Downhole and seismic reflection prospecting can provide reliable S and P velocity profiles. Petronio *et al*. (2023) shows an example of a successful application of such active methods in a case study from the Po Plain area, about 25 km west to our investigation site. The authors derived shear-wave (Vs) and compressional (Vp) velocity tomography models down to a depth of about 300 and 700 m respectively; Vs never exceed 600 m/s. Our study combines multiple geophysical techniques to define the seismic wave propagation model in a site at the south-west of Ferrara, near San Carlo (Fig. 1A), affected by the 2012 earthquakes. We acquired one of the deepest down-hole measurements so far available in the Po Plain, providing a rare opportunity to calibrate the velocity models produced by surface geophysical investigations. The Quaternary succession was drilled to the depth of almost 400 m,

cuttings were analysed, and a continuous spontaneous emission gamma log was measured. Accurate down-hole velocity measurements of both V_P and V_S were acquired, from the surface to the depth of 370 m, providing results in good match with a previous investigation, which was limited in depth (Minarelli *et al*. 2016). The down-hole recordings were compared with the results of the vertical seismic profile and of surface investigation we performed on site, consisting of a seismic reflection profile, passive seismic arrays, and single-station vibration measurements. The various sources of information were combined to generate a reliable Vs profile and an interdisciplinary image of the subsurface properties.

Geology and Stratigraphy Framework

The research region belongs to the external buried portion of the Apennines, dominated by active thrust-fold structures (Martelli *et al.*, 2017), developed through Plio-Pleistocene times (Ghielmi *et al*., 2013). The investigated site is placed on a broad syncline (Fig. 1A), part of the tectonic Ferrara Arc. The active faults generate a significant seismic activity, including that of May 2012. The strong synsedimentary deformation largely influenced the Plio-Quaternary stratigraphic architecture. The older unit involved in the research consists of Pliocene deep-marine terrigenous turbidites (P2, Fig. 3A). The interruption of the turbidite sedimentation in the study area (Porto Garibaldi Fm top) corresponds to the tectonic rising of submarine anticline bulges in western areas (e.g. Mirandola), preventing the currents from reaching eastern regions (Ghielmi *et al.* 2010, 2013). The following Marine Quaternary unit records the evolution from deep-water argillaceous deposits (QM2) to delta sediments (QM1). The combination of tectonics, eustasy, and climate fluctuations induced the unconformity surfaces supporting the subdivision of the following Quaternary successions into allostratigraphic units (Regione Emilia-Romagna *et al.*, 1998). A phase of deformation induced the unconformity base of the Emilia-Romagna Supersynthem, which is bipartite into the Lower (AEI) and Upper (AES) Emilia-Romagna Synthems by a surface associated with a gentler phase of structural reorganization and marine lowstand (Martelli, 2021). At the study site, the lowermost portion of AEI still records marine influences, associated with interglacial highstand phases. The upper part of AEI and in AES record purely continental conditions. The synthems in turn frame several subsynthems, each corresponding to an individual glacio-eustasy fluctuation, in the 100,000-year frequency band, as in the upper three Subsynthems (AES 6, 7, 8). The research well crossed the whole of the Emilia-Romagna Supersynthem and penetrated a large portion of QM1. The properties of the underlying units, down to the Pliocene turbidites (P2), were indirectly interpreted from the seismic investigation we performed.

Research methods and results

In the research site, multiple geophysical techniques were combined to achieve a reliable seismic wave propagation model. The site was selected because placed in the epicentral area of the 2012 seismic sequence, and because of the availability of an accessible deep well, where a previous down-hole investigation (Minarelli *et al.*, 2016) already measured both Vp and Vs velocities, to the depth of 265 m. We performed new accurate downhole measurements (Fig. 1B), to the depth of 370 m, together with passive and active seismic surveys at the surface. Active methods, performed by OGS authors, involved the data-acquisition, in the S-waves mode, by geophones and hydrophones in the deep borehole, using a Mini-Vibratory (MiniVib) as source. First-break arrivals and reflected waves were analysed to generate a 1D shear-wave velocity profile, analysed together with the reflection signals recorded by a linear pattern of horizontal geophones, placed at the surface. Passive methods were also applied, through a high-resolution frequency-wavenumber

beamforming (f-k) and spatial autocorrelation (SPAC) analysis (Hailemikael *et al.*, 2023), using a 2D array of seismic stations, with a maximum aperture of about 880 m (Fig. 1B). We computed the Rayleigh (R) and Love (L) dispersion curves (DC) from both (*i*) the linear array of geophones, using the f-k method, and the MiniVib as active source, and (*ii*) from the 2D array of seismic stations, using ambient vibration three-component data, though f-k and SPAC methods. The observed dispersion and H/V curves were jointly inverted with the Geopsy tool (Wathelet et al. 2020) to obtain the 1D shear-wave velocity (Vs) profiles (Fig. 2).

The main result of the work is a consistent mono-dimensional Vs profile, generated by the synthesis the active and passive methodologies, supporting the seismic stratigraphy interpretation of the subsurface to a depth of about 700 m (Fig. 3). The regional unconformity surfaces, supporting the stratigraphic subdivision of the Quaternary successions, are associated with discrete layers of sharp increase of the seismic velocity. The strongest velocity increase is associated with the top of the P2 turbidites, at about 680 m, in perfect match with the base of the Marine Quaternary (QM) illustrated by the Emilia-Romagna Region study, as visible in Fig. 3. The 1D seismic velocity model, developed at the study site, can be extrapolated to similar syncline areas in a wider Po basin area in the finality of seismic response analysis and microzonation analyses.

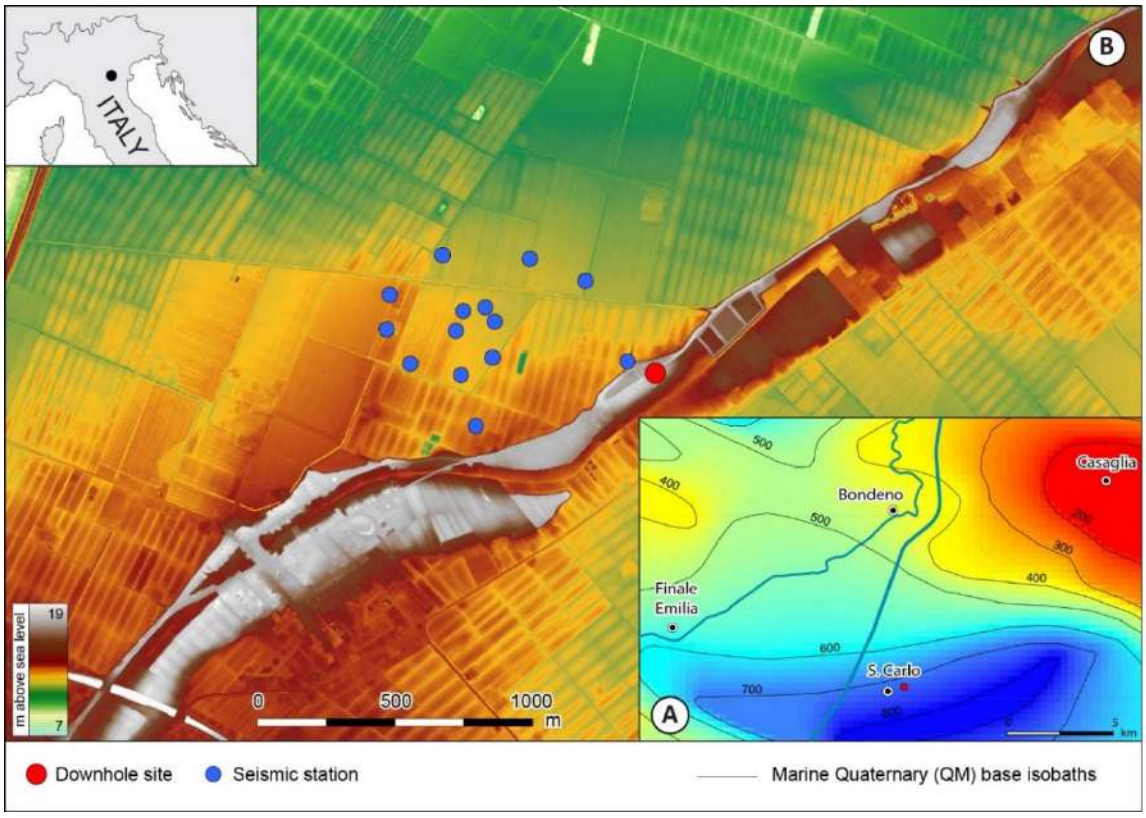

Fig. 1. (A) Depth of the Marine Quaternary top, which has been largely deformed by the ongoing compressional deformation (map produced by the Emilia-Romagna Region Geology Survey). The investigations site is placed on the syncline, at the south of the Casaglia High. (B) Location of the down-hole and of the array of seismic stations. A MiniVib as source was applied for the down-hole acquisition, whereas the seismic stations recorded ambient vibration data. The image background shows the Lidar generated elevation model, depicting the depositional fluvial ridge of the river Reno.

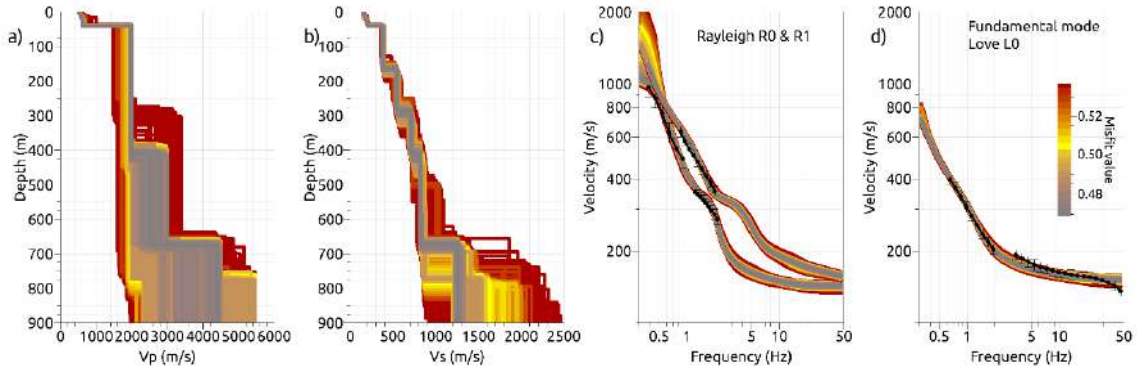

Fig. 2. Inversion results with the rainbow scale proportional to the misfit value. a) Vp models; b) Vs models; c) DCs of the fundamental Rayleigh (R0) and the first higher (R1) mode; d) DCs of the fundamental Love (L0) mode. The field DCs are overlaid in black.

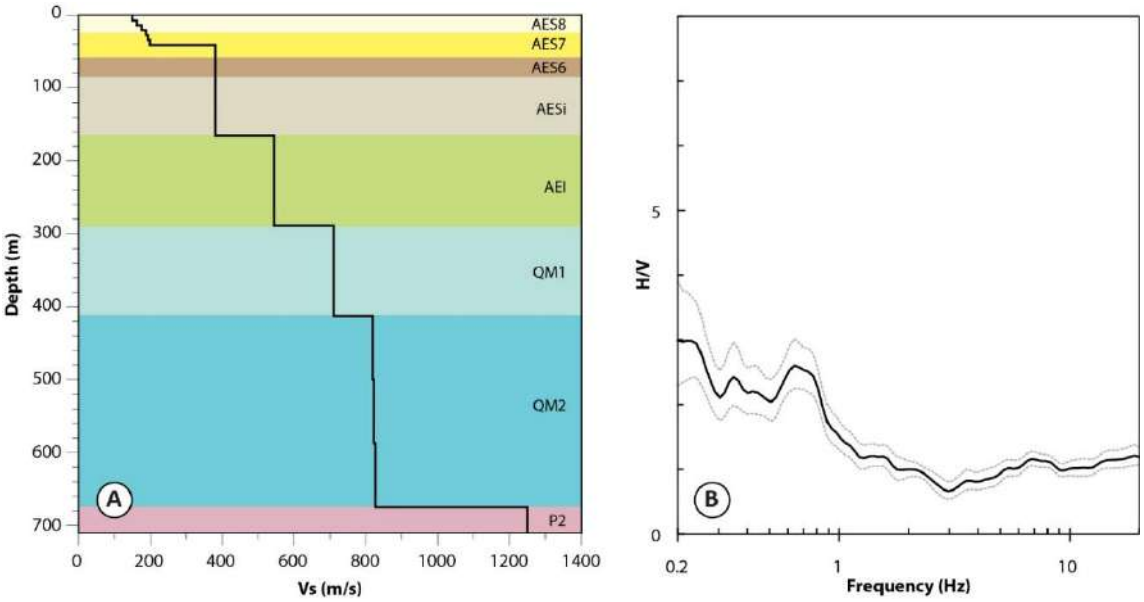

Fig. 3. (A) Average distribution of the S waves velocity with depth, generated by the synthesis of the active and passive methods data, correlated with the stratigraphic units described in the text. Sharp increases in velocity, of the best fitting model extracted from Fig. 2, are normally matched with the main discordance surfaces and stratigraphic boundaries. (B) H/V noise spectral ratios in proximity of the downhole site, derived from many hours of ambient vibration data acquired in November 2018.

Acknowledgements

This work is dedicated to and in memory of Lorenzo Petronio.

References

Ghielmi M., Minervini M., Nini C., Rogledi S. and Rossi M.; 2013: Late Miocene–Middle Pleistocene sequences in the Po Plain - Northern Adriatic Sea (Italy): The stratigraphic record of modification phases affecting a complex foreland basin. Mar. Pet. Geol., SI 42, 50–81.

Hailemikael S., Di Giulio G., Milana G., Vassallo M. and Bordoni P.; 2023: From ambient vibration data analysis to 1D ground-motion prediction of the Mj 5.9 and the Mj 6.5 Kumamoto earthquakes in the Kumamoto alluvial plain, Japan. Earth, Planets and Space, 75(1), p.105.

Mascandola C., Barani S., Massa M. and Albarello D.; 2021: New insights into long-period (> 1 s) seismic amplification effects in deep sedimentary basins: A case of the Po Plain basin of northern Italy. Bulletin of the Seismological Society of America, 111(4), pp.2071-2086.

Martelli L., Bonini M., Calabrese L., Corti G., Ercolessi G., Molinari F.C., Piccardi L., Pondrelli S., Sani F., Severi P.; 2017: Carta sismotettonica della Regione Emilia- Romagna e aree limitrofe, scala 1:250.000 (ed. 2016). Con note illustrative. Regione Emilia-Romagna, SGSS; CNR, IGG sez. FI; Università degli Studi di Firenze, DST; INGV sez. BO. D.R.E.AM. Italia.

Martelli L.; 2021: Assessment of Seismic Bedrock in Deep Alluvial Plains. Case Studies from the Emilia-Romagna Plain. Geosciences, 11(7), p.297.

Minarelli L., Amoroso S., Tarabusi G., Stefani M. and Pulelli G.; 2016: Down-hole geophysical characterization of middle-upper Quaternary sequences in the Apennine Foredeep, Mirabello, Italy. Annals of Geophysics, 59(5), p. S0543, https://doi.org/10.4401/ag-7114.

Petronio L., Baradello L., Poggi V., Minarelli L., Böhm G., Affatato A., Barbagallo A., Cristofano G., Sorgo D., Martelli L. and Lai C.G.; 2023: Combining SH-and P-wave seismic reflection survey to support seismic response analysis. A case study from Cavezzo (Italy) after the 2012 Emilia earthquake. Engineering Geology, 313, p.106916. https://doi.org/10.1016/j.enggeo.2022.106916.

Wathelet M., Guillier B., Roux P., Cornou C. and Ohrnberger M.; 2018: Rayleigh wave three-component beamforming: signed ellipticity assessment from high-resolution frequency-wavenumber processing of ambient vibration arrays. Geophysical Journal international, 215(1), pp.507-523.

Wathelet M., Chatelain J.L., Cornou C., Di Giulio G., Guillier B., Ohrnberger M. and Savvaidis A.; 2020: Geopsy: A user-friendly open-source tool set for ambient vibration processing. Seismological Research Letters, 91(3), pp.1878-1889.

Corresponding author: giuseppe.digiulio@ingv.it

Inductive Induced Polarization Effects: the Loupe EM synthetic case study

F. Dauti[1], A. Viezzoli[2], G. Fiandaca[1]

[1] The EEM Team for Hydro & eXploration, Dep. of Earth Sciences A. Desio, Università degli Studi di Milano, Milano (Italy)
[2] Emergo s.r.l., Cascina (Italy)

Introduction

The Loupe electromagnetic profiling system (Street et alii, 2018) is a two-operator, portable, time-domain electromagnetic system mounted on backpacks, designed to image electrical conductivity in the near-surface at high spatial and vertical resolution. This particular configuration (visible in *figure 1*), as well as drastically speed up the acquisition procedure, allows to acquire data where the topography and logistic are too complex for a standard EM loop. This extends the EM application to a great number of environments.

Figure 1. Loupe EM system configuration for an acquisition in the Val Sabbia (BS) mountainous area.

For the Loupe system, a quick transmitter waveform turn-off (10 μs) allows to get a good resolution in the near surface while the of 20 A of peak current and 13 turns in the coil allow to reach a good depth of investigation, exceeding 50 m.
With this work we aim to assess if and how the system is sensitive to Induced Polarization (IP) effects.
IP effects on EM data have been studied since the early '80s (e.g. Spies, 1980; Lee, 1981), and have re-gained attention in recent years thanks to the ability to invert for IP effects on EM data in terms of Cole-Cole models (e.g. Viezzoli et al., 2017; Lin et al, 2019; Couto et al., 2020; Grombacher et al., 2021). However, the importance of IP modelling in EM data is still often overlooked, and false structures (incorrect conductivity-thickness parameters) may be recovered when IP is not properly modelled (Viezzoli et al. 2017). In order to study the IP effect on the Loupe system, we focused on a simple but representative case: a two-layer model with a chargeable cover over a resistive bedrock. This case may represent targets suitable for the Loupe system: mine wastes; permafrost; weathered covers over bedrock on mountainous areas. The study is performed varying the electrical properties of the cover layer, and its thickness, in order to highlight quantitatively the significance of the IP effect.

Method

In order to define how the Induced Polarization affects the Loupe electromagnetic response, we compute the forward response (following Auken et al., 2015) from a large amount of two-layer models, consisting of a chargeable cover over a resistive bedrock. The model space is defined in terms of the Cole-Cole resistivity model, as defined by Pelton et al. (1978):

$$m_{IP} = \{\rho_j, m_{0_j}, c_j, thk_j\}, \quad j = 1,2 \qquad \text{(eq. 1)}$$

Table 1 contains the Cole-Cole parameters used for simulating the first chargeable layer, in all combinations. The second layer instead has been always considered a purely resistive layer at 1000 Ω*m. For each Cole-Cole two-layer model, we calculate a corresponding purely resistive two-layer model (using the DC resistivity value of the Cole-Cole model), and we compare the responses.

Chargeable first layer				
Rho [Ω*m]	**m0** [mV/V]	**Tau** [s]	**C**	**Thk** [m]
1	5	1e-04	0.5	5
2	8	3e-04		20
3	13	1e-03		
4	20	3e-03		
6	30	1e-02		
10	50	3e-01		

15	80	1e-01		
25	125	1		
40	199			
65	315			
100	500			

Table 1. Parameter values of the first layer.

The amount of distortion produced by IP for each forward response is computed as the mean absolute percentage difference over the entire response, as follows:

$$Distortion = \sum_{j=1}^{n} \frac{100}{n} \left\| \frac{fwr_{NOIP_j} - fwr_{IP_j}}{fwr_{NOIP_j}} \right\| \bullet \qquad \text{(eq.2)}$$

Where n represents the number of gates above the noise floor, set to 1e-12 V/Am^4 at 1 ms, in order to quantify only detectable IP effects; fwr_{NOIP_j} represents the jth gate of the forward response computed disregarding IP; fwr_{IP_j} is the jth forward response computed with IP.

Results

An example of comparison of forward responses with/without IP for the X and Z components of the Loupe system is shown in *figure 1*. The model, described in the textbox, represent a simplified but common geology, with a thin conductive, slightly chargeable cover that overlies a resistive second layer. As clearly evident, the transients affected by IP are heavily distorted, both for the X and for the Z component, culminating in the change of sign of the modelled signal.

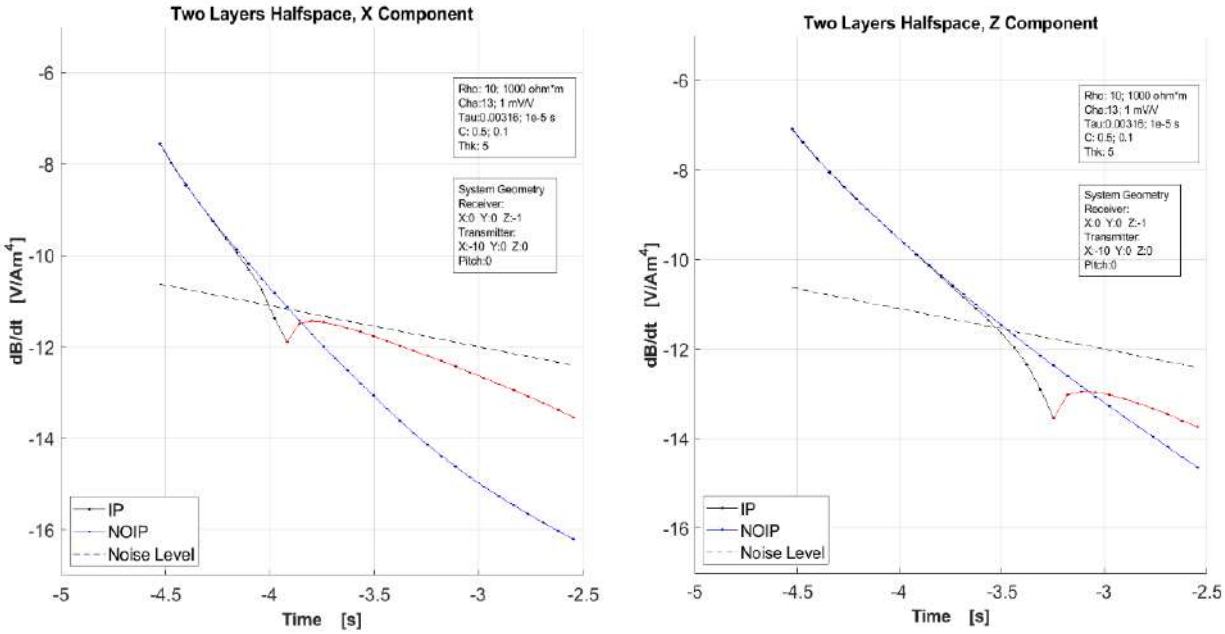

Below, *in figure 3*, follows an example of representation of the results in a 2D map, representing in color the distortion, as computed following equation 2, as a function of chargeability and resistivity of the first layer.

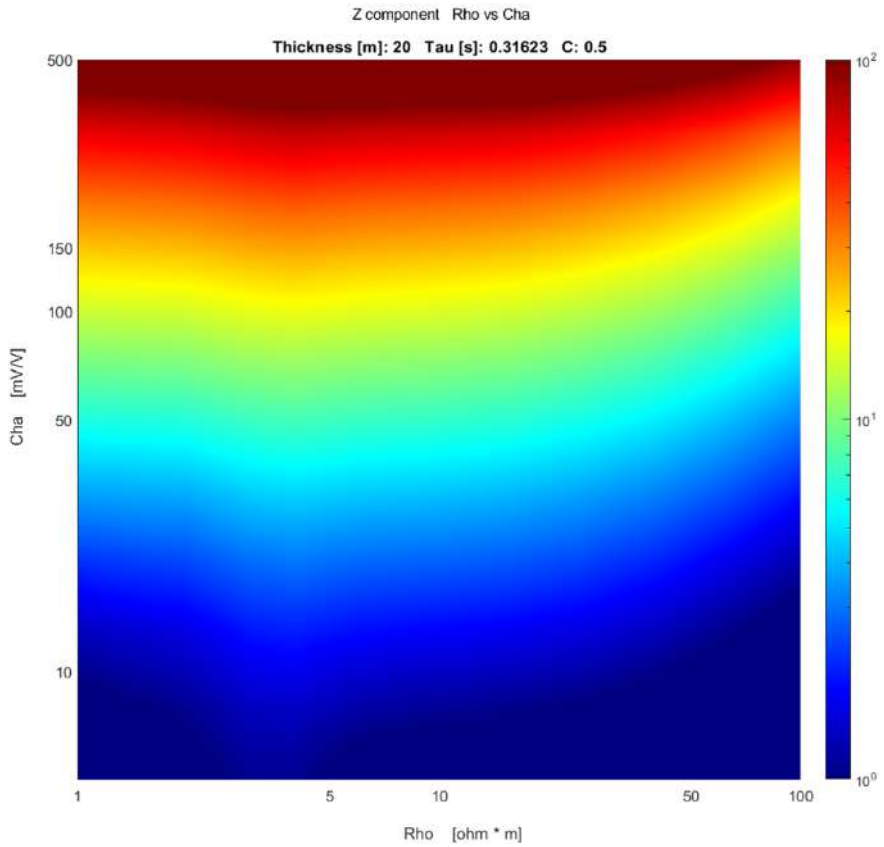

Figure 3. Representation of the IP Distortion (eq.2) for the Loupe Z component, for two layers models. The first layer thickness, Tau and C parameters are kept fixed in the title, while the Resistivity and Chargeability vary along the axes. The colorscale represents the difference, in percentage, between the IP affected halfspace and the purely resistive halfspace forward responses.

IP affects significantly the forward response even with low values for chargeability and high values for the time constant. The increase of the distortion follows the increase in chargeability, and already from 10 mV/V an error higher of 5% is reached. This spread of IP effects is linked to the two-layers configuration with resistive bedrock: the IP EM vortex currents, which flow in opposite direction of the eddy currents, propagate slowly in the second layer and dominate the current flow. In this configuration it is also interesting to see how even for a time constant of 0.3 ms it is possible to detect the IP effects above the noise level, also with a 75 Hz instrument.

Conclusions

The results presented in this study are surprising: in a two-layer environment with a chargeable cover over a resistive bedrock, even small chargeability values (e.g. 10 mV/V) creates significant effect in the responses measurable with the portable Loupe System, also with detectable data change of sign. Furthermore, these effects are not confined to low values of the time constant of the Cole-Cole model (e.g. below 1 ms), but persist also for tau values in the range of seconds. These results imply that the IP effect cannot be overlooked when operating with the Loupe system, for instance in surveys involving mine wastes, permafrost and weathered covers over bedrock on mountainous areas.

References

Auken E., Christiansen A.V., Kirkegaard C., Fiandaca G., Schamper C., Behroozmand A.A., Binley A., Nielsen E., Efferso F., Christensen N.B., Sorensen K., Foged N. & Vignoli G., 2015. An overview of a highly versatile forward and stable inverse algorithm for airborne, ground-based and borehole electromagnetic and electric data, Exploration Geophysics, 46, 223-235. 10.1071/eg13097

Couto Junior, M. A., Fiandaca, G., Maurya, P. K., Christiansen, A. V., Porsani, J. L., & Auken, E. (2020). AEMIP robust inversion using maximum phase angle Cole–Cole model re-parameterisation applied for HTEM survey over Lamego gold mine, Quadrilátero Ferrífero, MG, Brazil. Exploration Geophysics, 51(1), 170-183.

Grombacher, D., Auken, E., Foged, N., Bording, T., Foley, N., Doran, P. T., ... & Tulaczyk, S., 2021. Induced polarization effects in airborne transient electromagnetic data collected in the McMurdo Dry Valleys, Antarctica. Geophysical Journal International, 226(3), 1574-1583.

Lee, T., 1981. Transient electromagnetic response of a polarizable ground. Geophysics, 46,7, 1037-1041.

Lin, C., Fiandaca, G., Auken, E., Couto, M. A., & Christiansen, A. V., 2019. A discussion of 2D induced polarization effects in airborne electromagnetic and inversion with a robust 1D laterally constrained inversion scheme. Geophysics, 84(2), E75-E88.

Pelton, W. H., Rijo, L., & Swift Jr, C. M., 1978. Inversion of two-dimensional resistivity and induced-polarization data. Geophysics, 43(4), 788-803.

Spies, B.R., 1980. A field occurrence of sign reversals with the transient electromagnetic method. Geophysical Prospecting, 28, 620-632.

Street, G., Duncan, A., Fullagar, P., Tresidder, R., 2018. LOUPE – A Portable EM Profiling System. System, ASEG Extended Abstracts, 2018:1, 1-3, DOI: 10.1071/ASEG2018abW10_3G.

Viezzoli, A., Kaminski, V., Fiandaca, G., 2017. Modeling induced polarization effects in helicopter TEM data: Synthetic case studies. Geophysics, (82-2) E31-E50.

Reference Author: Francesco Dauti, francesco.dauti@unimi.it

Comparing various seismic equipment for H/V and dispersion measurements in three sites near Ferrara (Po Plain, Italy)

G. Di Giulio[1], L. Minarelli[1], G. Milana[1], M. Vassallo[1], G. Tarabusi[1], M. Stefani[2]

1 Istituto Nazionale di Geofisica e Vulcanologia (Rome, Italy)
2 Università degli Studi di Ferrara (Ferrara, Italy)

H/V spectral ratios and surface-wave analysis are very popular techniques in the engineering-seismology community to extract near-surface properties processing data of ambient seismic vibrations (Foti *et al*., 2018). The H/V ratios provide the fundamental resonance of a site (f0), the value of which is related to both the depth of the main impedance contrast and the shear-wave velocity (Vs) of the soft deposit (Molnar et al., 2022). Surface-wave analysis is largely used for the extraction of Rayleigh and Love dispersion curves, using several sensors, deployed in mono (1D) or bi-dimensional (2D) field geometry, for recording ambient vibrations (passive case). Surface-wave analysis computes dispersion curves for Rayleigh and Love waves (R and L, respectively), through frequency-wavenumber (f-k) and spatial autocorrelation (SPAC) methods (for methodology details see Hailemikael et al., 2023). Recent advances in the technology of seismic equipment make it possible to use many seismic sensors, different in properties and cost, for measurements the H/V and dispersion curves.

In this work, the research aim is to test the performance of different equipment in the estimation of the field curves (i.e. H/V and surface-wave dispersion). We show H/V and surface-wave curves (Rayleigh and Love), acquired with different sensors and field geometry, in three case studies from the Ferrara area, Po Plain (Italy). The Po sedimentary basin is the largest of Italy and is characterized by tick, soft terrigenous deposits and low-frequency resonance (Mascandola *et al*., 2021).

One of the selected sites is within the Ferrara city wall, near the Jewish cemetery, one in the village of Casaglia, about 9 km north-east of the city centre, one in the Pieve di Cento municipality, 20 km south-west of Ferrara town (Fig. 1). At each of the three sites, in October 2020, the following equipment for recording ambient vibrations was used: i) twelve seismic 24-bit dataloggers (Reftek 130) coupled with Lennartz three-components velocimeter (Le3D) with eigen-frequency of 0.2 Hz, ii) seven all-in-one three-components Terrabot stations produced by Sara Electronics, with an eigen-frequency of 4.5 Hz, iii) twenty-four vertical geophones with eigen-frequency of 4.5 Hz connected to a multi-channel station (Geode manufactured by Geometrics).

All the above equipment was deployed in 2D configuration, following nearly circular geometry, depending on the local logistic. Fig. 1 show an example of installation, at the Casaglia site. The Le3D and Terrabot velocimeters were arranged in the field with a maximum aperture varying from about 200 to 300 m (depending on site). The vertical geophones, which are constrained by cables, were deployed in a circular ring of 50 m of aperture. All the data were processed with similar parameters, using the Geopsy tool (Wathelet *et al*. 2020).

The comparison of the H/V curves (Fig. 2) shows that Le3D and Terrabot provide the same H/V spectral ratios, at the three selected sites, even if the f0 is well below the Terrabot eigen-frequency of 4.5 Hz. At the Casaglia site, the H/V curves show a consistent narrow and strong peak at 0.7 Hz, resulting from both Le3D and Terrabot instruments. The good agreement between Le3D and Terrabot is also verified at the Ferrara site, where the f0 is at about 0.2 Hz. A good fit is also observed for the last site at Pieve di Cento, where the H/V curves do not show a clear peak, but rather a bump between 0.2 and 0.3 Hz (Fig. 2).

Concerning the dispersion curves, we also observed a good fit between the three equipment typologies, taking into account the different geometry and number of receivers giving dispersion curves in different frequency bands. However, the resulting dispersion curves from Le3D, Terrabot and geophones show a good match in the nearly overlapping frequency band.

For the Casaglia site, corresponding to a structural high zone of the Po Plain (Tarabusi and Caputo, 2017), we also present a joint inversion of the dispersion and H/V curves (Fig. 3). The Vs profile shows a main interface at about 140 m deep, corresponding to the angular unconformity, erosive top of the marine Miocene marls. The overlying Quaternary succession largely consists of alluvial plain deposits, showing a downward Vs increase from 120 to 450 m/s.

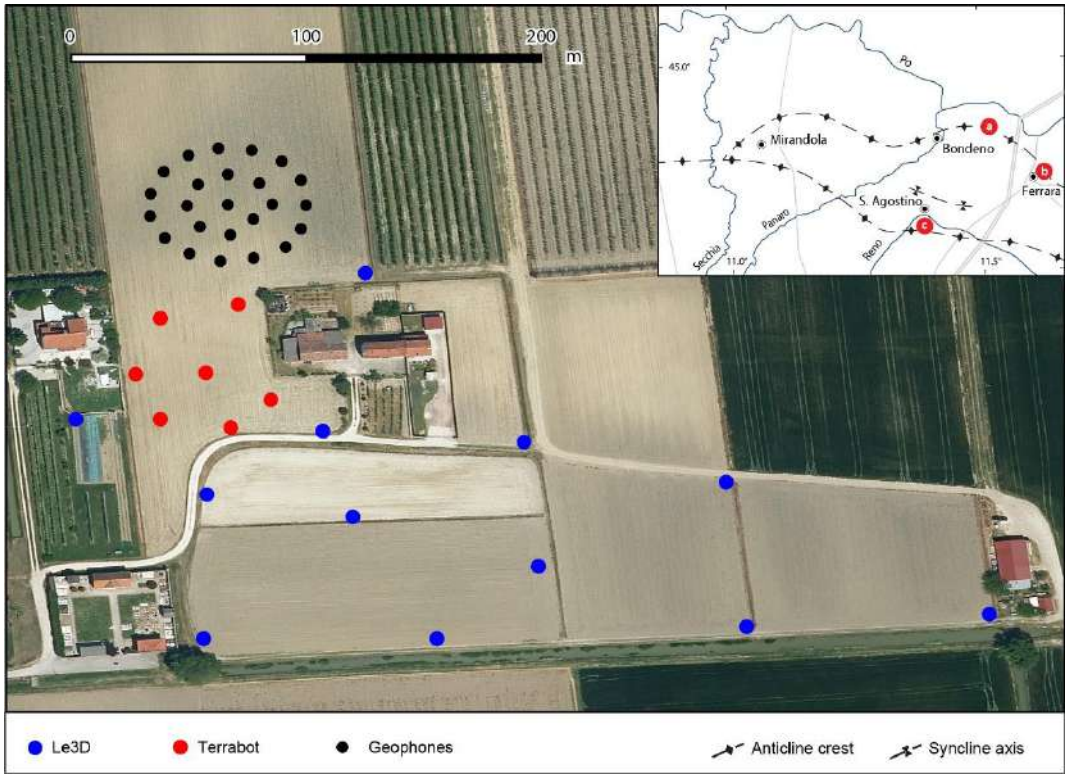

Fig. 1. Sensors array geometry for the Casaglia site. The seven Terrabot are shown as red dots (maximum aperture of 50 m), the twelve Le3D5s velocimeters are shown by blue colour (maximum aperture of about 300 m), the twenty-four vertical 4.5 Hz geophones are shown by black colour (maximum aperture of 60 m). The inset shows the position of the three investigated sites (Casaglia, Ferrara and Pieve di Cento).

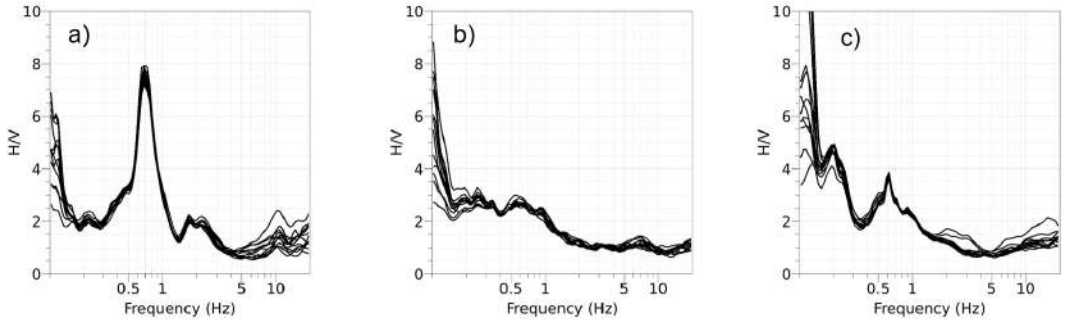

Fig. 2. H/V noise spectral ratios for Casaglia (a), Pieve di Cento (b), and for the northern sector of the city of Ferrara (c).

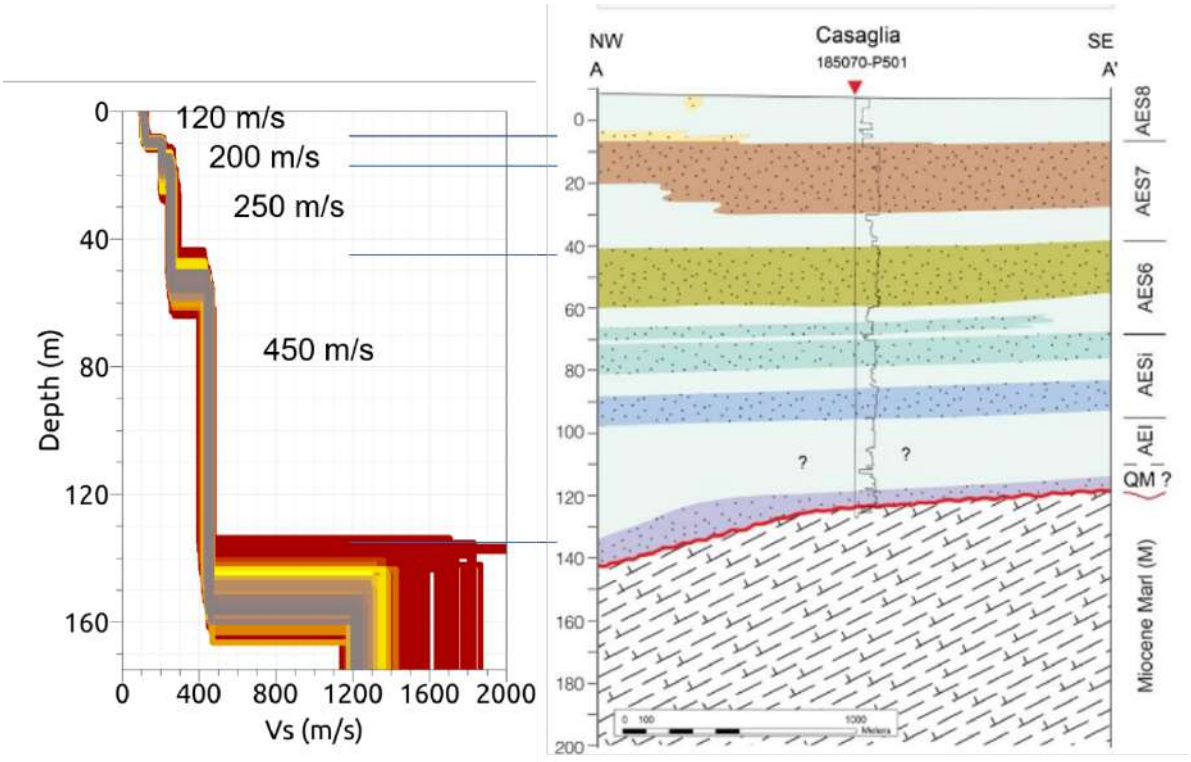

Fig. 3. Casaglia site. Shear-wave velocity profile derived from surface-wave inversion (the colour is proportional to the misfit value), together with stratigraphic interpretation of the Quaternary succession. The value of average Vs is also depicted in the profile.

References

Foti S., Hollender F., Garofalo F., Albarello D., Asten M., Bard P.Y., Comina C., Cornou C., Cox B., Di Giulio G. and Forbriger T.; 2018: Guidelines for the good practice of surface wave analysis: a product of the InterPACIFIC project. Bulletin of Earthquake Engineering, 16(6), pp.2367-2420

Molnar S., Sirohey A., Assaf J., Bard P.Y., Castellaro S., Cornou C., Cox B., Guillier B., Hassani B., Kawase H. and Matsushima S.; 2022: A review of the microtremor horizontal-to-vertical spectral ratio (MHVSR) method. Journal of Seismology, pp.1-33

Hailemikael S., Di Giulio G., Milana G., Vassallo M. and Bordoni P.; 2023: From ambient vibration data analysis to 1D ground-motion prediction of the Mj 5.9 and the Mj 6.5 Kumamoto earthquakes in the Kumamoto alluvial plain, Japan. Earth, Planets and Space, 75(1), p.105.

Mascandola C., Barani S., Massa M. and Albarello D.; 2021: New insights into long-period (> 1 s) seismic amplification effects in deep sedimentary basins: A case of the Po Plain basin of northern Italy. Bulletin of the Seismological Society of America, 111(4), pp.2071-2086.

Tarabusi G. and Caputo R.; 2017: The use of H/V measurements for investigating buried tectonic structures: The Mirandola anticline, Northern Italy, as a case study, Int. J. Earth. Sci. 106, no. 1, 341–353

Wathelet M., Chatelain J.L., Cornou C., Di Giulio G., Guillier B., Ohrnberger M. and Savvaidis A.; 2020: Geopsy: A user-friendly open-source tool set for ambient vibration processing. Seismological Research Letters, 91(3), pp.1878-1889.

Corresponding author: giuseppe.digiulio@ingv.it

Non-Destructive Testing for the conservation of a cultural heritage: GPR surveying on masonry walls at the Castellina Museum (Norcia, Italy).

M. Ercoli[1*], N. Cavalagli[2], M. Barchi[1], C. Pauselli[1], M. Porreca[1], R. Lupi[3].

1 Università degli Studi di Perugia, Dip. Fisica e Geologia, Italy.
2 Università degli Studi di Perugia, Dip. Ingegneria Civile ed Ambientale, Italy.
3 Università degli Studi di Perugia, Dip. di Scienze Politiche, Italy.

The conservation of historical masonry constructions represents one of the major challenges for scientific research, especially in the case of monumental buildings with high artistic and cultural values in areas characterized by high seismic hazard. Here, historical buildings are periodically shacked and damaged by strong earthquakes, and have been subjected to restorations and changes of their original configuration. By a mechanical point of view, in the last decades the research has been continuously involved in the development of advanced and effective methodologies, conventionally invasive, focused to derive a mechanical evaluation of their static and dynamic behaviour, as well as on the characterisation of masonry materials. At the same time, Non-Destructive Testing (NDT) techniques can be also very useful when the preservation of such cultural heritages needs to be ensured by reducing the invasive interventions (Santos-Assuncao et al., 2014). GPR is one of the non-invasive techniques providing high-resolution images of the subsurface, founding wide application in archaeological and civil engineering studies on ancient walls (Ercoli et al., 2016), as well as for masonry wall diagnostics (Lombardi et al., 2021; Negri and Aiello, 2021).

In this work, we have used a Ground Penetrating Radar (GPR) to obtain non-destructive information on the internal structure of a historic masonry wall of the Castellina Museum in Norcia city centre, which is currently unusable after the serious damaging caused by the long-lasting seismic sequence occurred in 2016-2017 (Norcia earthquake sequence, mainshock Mw=6.5, Porreca et al., 2018). We have investigated a wall located at the ground floor of the building, known to be part (the facade) of a previous edifice, the Palazzo del Podestà. On such a masonry wall, standard sonic tests (ST) have been formerly performed on localized areas to investigate the homogeneity degree of the masonry and, to identify the presence of possible voids, cracks and degraded areas. Such measures aimed to measure the propagation velocity of sonic waves on a regular grid, in order to obtain velocity maps able highlighting velocity variations, to be correlated with degraded areas.

Based on such pre-existing data, n°25 Common Offset GPR profiles have been collected across the same grid using high frequency antennas (1 GHz and 1.5 GHz), and later processed, aiming to

integrate and validate the existing data. Additionally, extensive profiling has been accomplished across a wider area, extending horizontally and vertically the initial grid. The first results show the internal structure of the wall, suggesting the presence of heterogenous material and possible internal issues, in agreement with ST maps. Such extensive GPR mapping also evidences the GPR signature sharply changing its reflectivity across the surveyed area, generally showing a significant decrease in reflectivity due to high signal attenuation (high electrical conductivity) particularly in the lower sectors but not without important lateral variations, possibly suggesting moisture variation and degraded sectors (Šťastný et al., 2021). Such behaviour needs further investigations using other NDT techniques (e.g. ERT, De Donno et al., 2017) and chemical analysis to verify the preliminary hypothesis and to assess the general state of conservation of the masonry, mandatory to program suitable remediation interventions in the near future.

References

De Donno, G., Di Giambattista L., Orlando L., 2017: High-resolution investigation of masonry samples through GPR and electrical resistivity tomography, Construction and Building Material, 154, 1234-1249.

Ercoli M., Brigante R., Radicioni F., Pauselli C., Mazzocca M., Centi G., Stoppini A., 2016: Inside the polygonal walls of Amelia (Central Italy): a multidisciplinary data integration, encompassing geodetic monitoring and geophysical prospections. J. Appl. Geophys., 127, 31-44.

Lombardi, F., Lualdi, M., Garavaglia, E., 2021: Masonry texture reconstruction for building seismic assessment: Practical evaluation and potentials of Ground Penetrating Radar methodology, Construction and Building Materials, 299, 124189.

Negri S., Aiello M.A., 2021: High-resolution GPR survey for masonry wall diagnostics, Journal of Building Engineering, 33, 101817.

Porreca, M., Minelli, G., Ercoli, M., Brobia, A., Mancinelli, P., Cruciani, F., Giorgetti, C., Carboni, C., Mirabella, F., Cavinato, G., Cannata, A., Pauselli, C., Barchi, M.R., 2018: Seismic reflection profiles and subsurface geology of the area interested by the 2016–2017 earthquake sequence (Central Italy). Tectonics 37, 1–22.

Santos-Assunçao S., Perez-Gracia V., Caselles O., Clapes J., Salinas V., 2014: Assessment of Complex Masonry Structures with GPR Compared to Other Non-Destructive Testing Studies. Remote Sens., 6, 8220-8237.

Šťastný P., Gašparík J., Makýš O.; 2021: Analysis of moisture and salinity of historical constructions before and after the application of REMEDIATIONS, Journal of Building Engineering, 41, 102785.

Acknowledgements

This project is founded by the Università degli Studi di Perugia, Finanziamento di Progetti di Ricerca di Ateneo Anno 2021, project “Un percorso di ricerca interdisciplinare nel Patrimonio Culturale materiale e immateriale: l’Umbria come laboratorio di indagine” (P.I. Prof.ssa Carla Falluomini), WP 2.4 - Conoscenza, valorizzazione e conservazione del patrimonio materiale e immateriale (Sottogruppo ‘‘Un’eredità fragile: per una rinascita dei patrimoni culturali in area sismica’’). The authors thanks the Municipality of Norcia for their kind support and collaboration.

*Corresponding author: maurizio.ercoli@unipg.it

Mapping surface/ground water interactions and embarkment composition along the Po river with transient electromagnetics

G. Fiandaca[1], A. Signora[1], S. Galli[1], J. Chen[1], C. Compostella[1], M. Gisolo[2], A. Viezzoli[3]

[1] The EEM Team for Hydro & eXploration, Department of Earth Sciences "Ardito Desio", Università degli Studi di Milano, Milano (Italy)
[2] A2A ciclo idrico s.p.a., Brescia (Italy)
[3] EMergo S.r.l. , Cascina (Italy)

In the last week of July 2023 the MapPo dimostrative survey has been carried out along the Po river and its embarkments with waterborne and ground-based electromagnetic methods, for more than 120 km of acquired data, as well as along 350 line km of airborne EM lines, across Lombardia, Veneto and Emilia Romagna (Fig. 1). The MapPo project aimed at mapping groundwater resources, and in particular, with its waterborne and ground-based acquisition, at studying the surface watwer/groundwater interaxctions and at mapping the internal composition of the embarkments.

The ground-based and waterborne acquisition have been carried out twith the tTEM (Auken et al., 2019) and FloaTEM (Maurya et al., 2022) systems, respectively (Fig. 2), while the airborne EM data have been acquired with the SkyTEM306HP system. Furthermore, 1.9 km of time-domain direct-current and induced polarization (DCIP) data have been measured, with the ABEM Terrameter LS2 instrument.

All data have been processed in EEMstudio, an opensource and freeware processing tool for electric and electromagnetic data (Sullivan et al., 2024; Fig. 1), and inverted with EEMverter (Fiandaca et al., 2024). Fig. 3 presents the tTEM and FloaTEM inversion models along 20 km of acquisitions, reaching more than 100 m of depth of investigation, together with the comparison of the DCIP inversion. The FloaTEM inversions allow to discriminate the interactions between river and groundwater, thanks to the ability to map the impermeable (conductive) areas below the river, whicle the tTEM inversions are able to image the thickness of the clays in the embarkment, evidencing the filtration areas mapped by the Po river basin authority. Furthermore, the presence of fossil saline water close to Ferrara, as well as sea water intrusion close to the Po di Goro are well imaged.

The tTEM and FloaTEM inversions are also well comparable with the airborne EM inversions, thank also to the possibility to invert both ground-based, waterborne and airborne EM data in a unique inversion kernel, i.e. EEMverter.

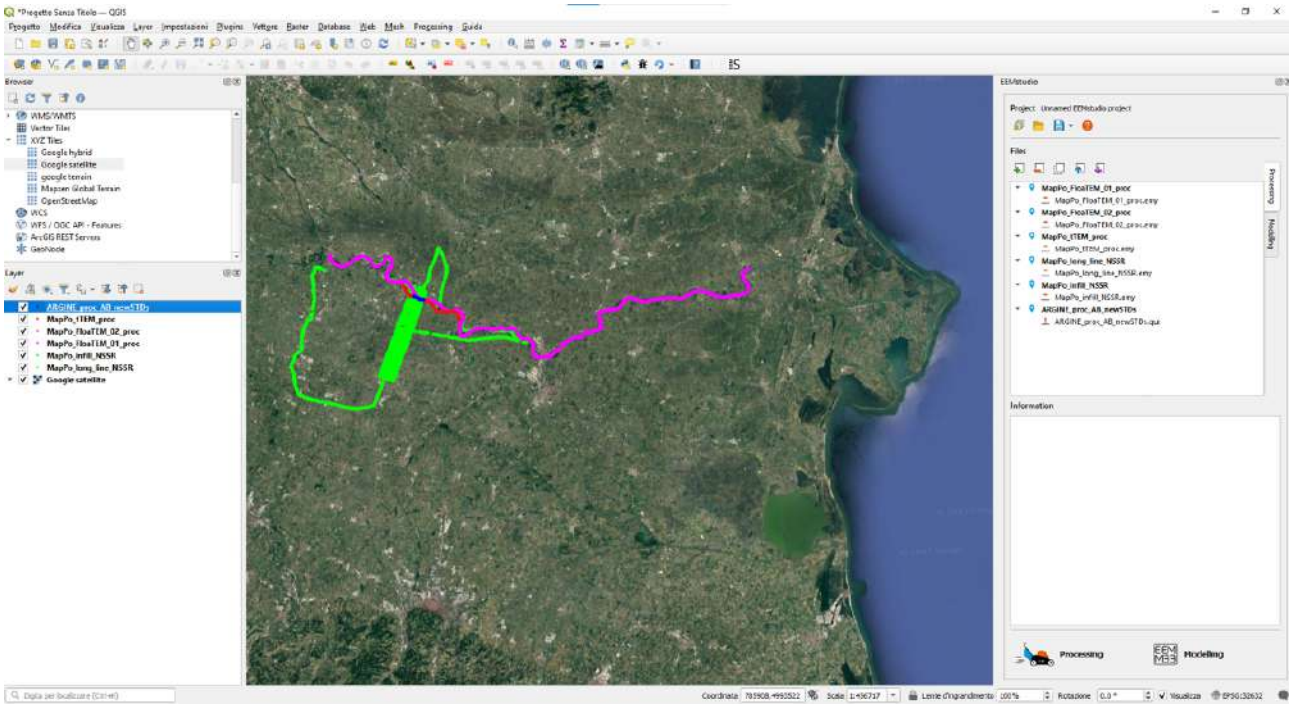

Figure 1. Acquisition lines of the MApPo project visualized in EEMstudio (Sullivan et al., 2024). Magenta line: FloaTEM acquisition. Red line: tTEM acquisition. Blue line: DCIP acquisition. Green lines: SkyTEM acquisition.

Figure 2. Images of the tTEM and FloaTEM acquisitions in the MapPo project.

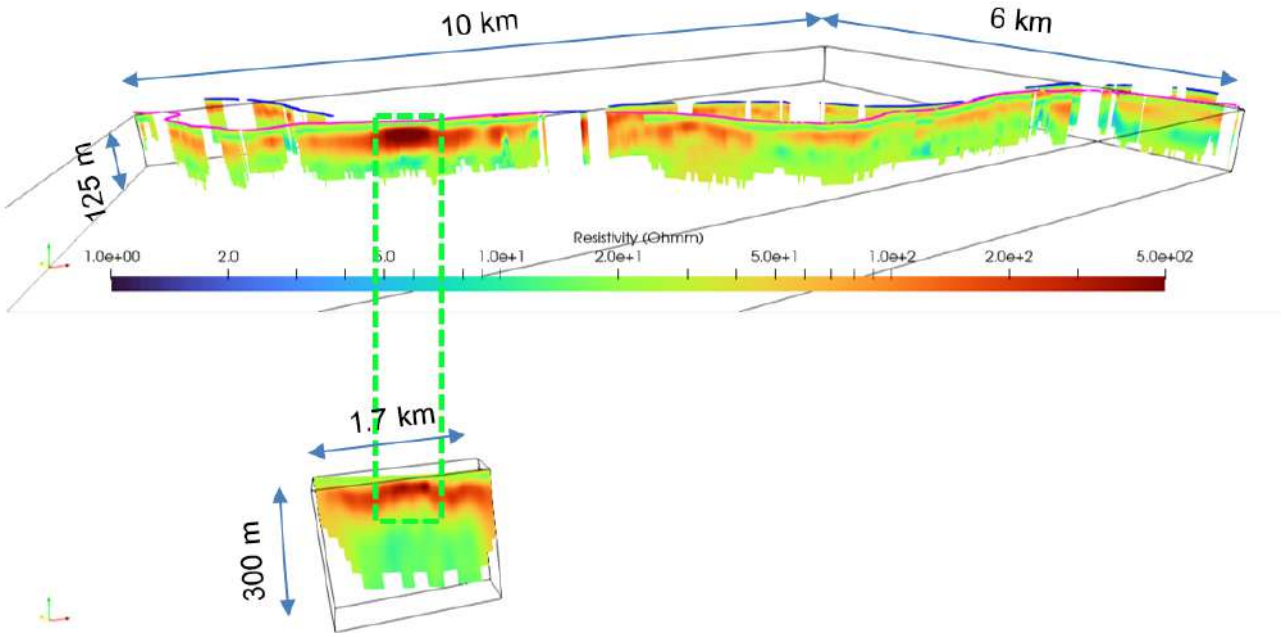

Figure 3. Inversion models of tTEM, FloaTEM and DCIP data along the Po river and its south embarkment. Dashed green line: filtration zone of the embarkment, mapped by adbpo.

Acknowledgments

This study has been funded by A2A ciclo idrico s.p.a., Emergo s.r.l. and The EEM Team for Hydro & eXploration.

References

Auken E., Foged N., Larsen J.J., Trøllund Lassen K.V., Maurya P.K., Dath S.M., Eiskjær T.T (2019). tTEM — A towed transient electromagnetic system for detailed 3D imaging of the top 70 m of the subsurface. Geophysics, 84 (1), E13-E22.

Fiandaca, G., Zhang, B., Chen, J., Signora, A., Dauti, F., Galli, S., Sullivan, N.A.L., Bollino, A., Viezzoli, A. (2024). EEMverter, a new 1D/2D/3D inversion tool for Electric and Electromagnetic data with focus on Induced Polarization. GNGTS 2024, 13-16 February 2024, Ferrara, Italy.

Maurya, Pradip Kumar, et al. "Efficient imaging of hydrological units below lakes and fjords with a floating, transient electromagnetic (FloaTEM) system." Hydrology and Earth System Sciences 26.11 (2022): 2813-2827.

Sullivan, N.A.L., Viezzoli, A., Fiandaca, G. (2024). EEMstudio: processing and modelling of electric and electromagnetic data in a QGIS plugin. GNGTS 2024, 13-16 February 2024, Ferrara, Italy.

Corresponding author: gianluca.fiandaca@unimi.it

Waterborne electromagnetics: two case studies

S. Galli[1], A. Signora[1], J. Chen[1], F. Schaars[2], M. Grohen[3], G. Fiandaca[1]

[1] The EEM Team for Hydro and eXploration, Dep. of Earth Sciences A. Desio, Università degli Studi di Milano, Milano (Italy)
[2] Artesia Water, Schoonhoven (The Netherlands)
[3] Wiertsema & partners, Tolbert (The Netherlands)

Introduction

Interactions between surface water and groundwater are the key for a good understanding of the hydrologic system (Harvey and Gooseff, 2015). In order to describe the hydrologic system, it's mandatory to have a good knowledge of hydrogeological settings below the water column of water. Non-invasive geophysical methods provide spatial information on subsurface properties, but on water bodies has always been difficult (Sheets and Dumouchelle, 2009) or impossible. Electrical and electromagnetic (EM) methods are among the most used geophysical techniques for hydrology (Christiansen et al., 2006; Siemon et al., 2009). Among the electrical methods, electrical resistivity tomography (ERT) has been used a lot for aquatic applications (Manheim et al., 2004). ERT surveys can be performed in many different configurations: with a towed floating cable, with still floating cables or with cables placed on the bottom of the water body. Transient electromagnetic (TEM) and frequency domain EM methods have been used too for hydrology (Ong et al., 2010) and exploration (Munk et al., 2016). Airborne methods have proved themselves reliable at mapping beneath water bodies (Fitterman and Deszcz-Pan, 1998), but they are expensive and have lower vertical and lateral resolution than ground-based methods (Hatch et al., 2010). The tTEM system (Auken et al., 2018), developed in Aarhus University, provided the necessary framework for adapting it to a floating EM system. The waterborne version of the tTEM system is referred to as FloaTEM (Maurya et al., 2022). In Lane et al. (2020) the FloaTEM system was used, in tTEM configuration without modifications, on rivers to characterize the hydrological systems. In this abstract, two applications of FloaTEM mapping carried out in freshwater lakes are presented, in very different geological environments: the southern shore of the Iseo lake in the Brescia province (Italy) and the artificial Ijsselmeer lake in the Netherlands.

Methods and results

For the data acquisition it was used a tTEM system adapted to work on water: the instrument is mounted on a boat made of plastic (to avoid spurious EM coupling in the measurements) that pulls other two smaller plastic boats carrying transmitter loop and receiver loop. To adapt the system for the waterborne survey, plastic supports were built to accommodate the instrumentation and to avoid cables to touch the propeller. Furthermore, an echo sounder synchronized with a GPS were

added in order to record bathymetry. Data were processed using an in-house developed open source and freeware QGIS plug-in, EEMstudio (Sullivan et al., 2024).

Figure 1 shows the acquisition layout and the inversion model of the data acquired in the southern shore of the Iseo lake and in the *Torbiere del Sebino* in the Brescia province (Italy).

In the Iseo lake area the goal is understanding the interactions between surface water and

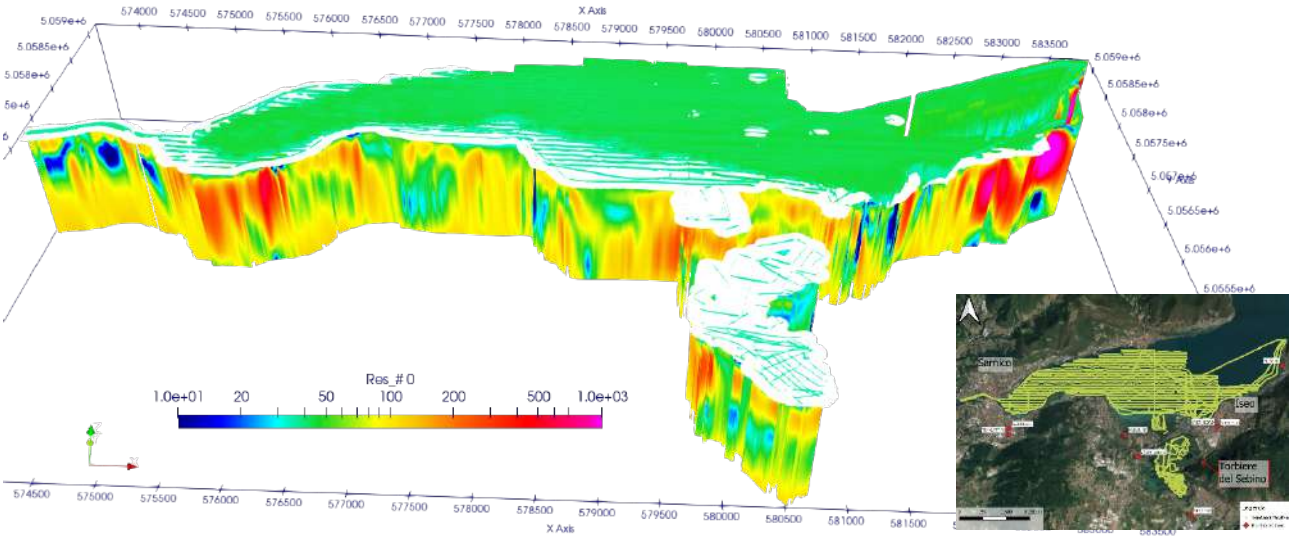

groundwater. In order to achieve this goal, over a five days campaign, 180 km of FloaTEM data were acquired in the Iseo lake and 20 km data were acquired in the Torbiere del Sebino, with a sounding every 5 meters.

The data were inverted in the EEMverter inversion suite (Fiandaca et al., 2024) using a 1D forward mesh interpolated to a 2D model mesh. Bathymetry was incorporated in the inversion breaking the vertical constraints at the bathymetric interface and forcing a narrower resistivity range in the water column (30-50 Ohm m).

Figure 2 shows a comparison between a standard inversion and the inversion that incorporates bathymetry: the bathymetry incorporation avoids overshooting/undershooting of resistivities in the shallowest layer.

Interesting features can be inferred from the inversion model presented in fig. 1: below the water column, in the eastern-most area, a very resistive anomaly (magenta) represents the mountain dipping directly in the lake. In the southern area, below the bottom of the lake, the discontinuous resistive anomaly represents the aquifer underlying the lake. These are the target bodies to understand how lacustrine water interacts with groundwater.

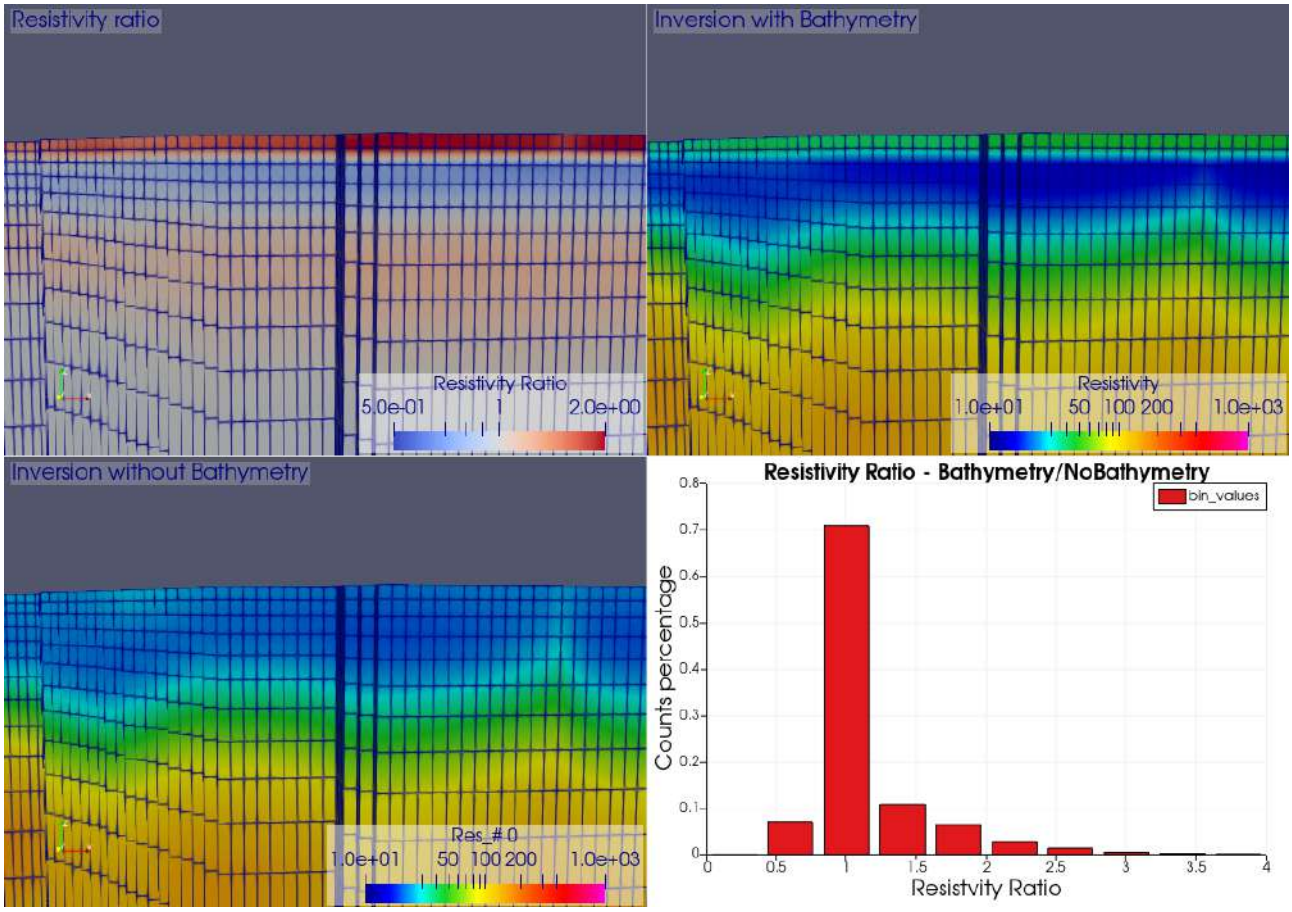

Figure 2: Comparison of standard inversion and bathymetric inversion of FloaTEM data. Top right: bathymetry incorporated in the inversion; Bottom left: standard inversion, without bathymetry incorporation; Top left: ratio between inversion with/without bathymetry incorporation; Bottom right: histogram of the ratio of the resistivity values of the two inversions.

In the Ijsselmeer survey (fig. 3) the geological setting was different and so was the goal: the IJsselmeer was part of the North Sea, but ì in 1932 a 32 km long damn was built, which separated the IJsselmeer from the North Sea; thus, the water gradually freshened, but salty water pockets remain below the lake, separated by a few meters thick discontinuous clay layer.

To map the clay layer and understand the interaction between saltwater and freshwater, over 65 km of FloaTEM data were acquired in a 3-day-long campaign in the western shore of the lake, close

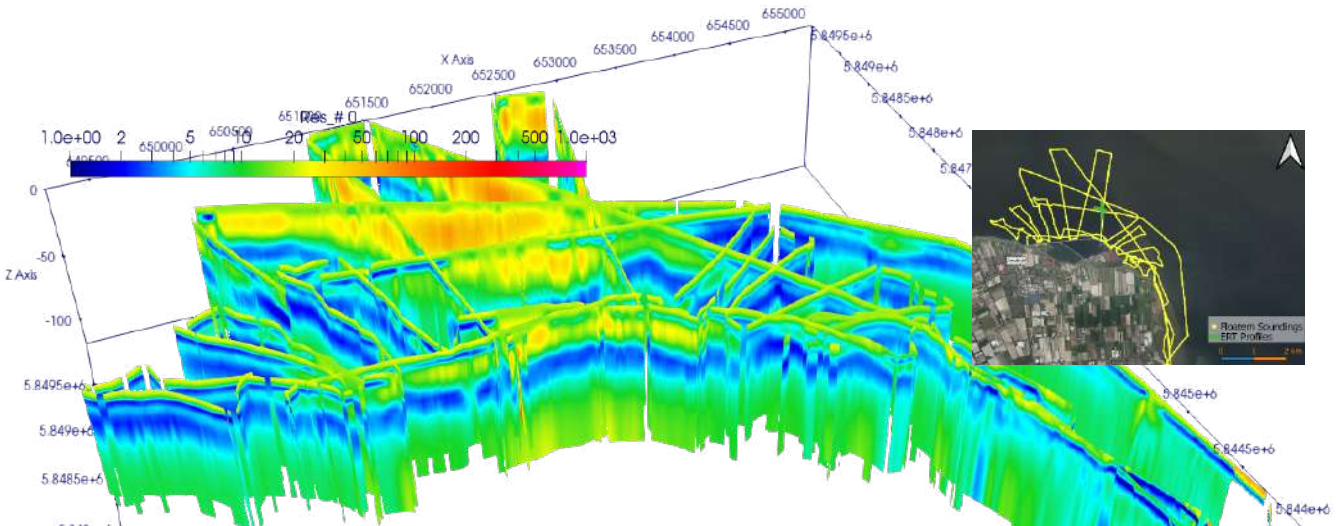

to PWN (a Dutch water management company) facilities in Andijk. Also, to validate data acquired in a new geological setting, a more established geophysical method was used: two underwater ERT profiles, 400 m long each, were acquired close to the FloaTEM soundings acquired in the previous days. The North-South profile was acquired with a Wenner array, the East-West was acquired with a Wenner-Schlumberger array. It was used one 400 m long cable with electrode spacing of 5 meters in the central 200 m and 10 meters on the sides, for a total of 61 electrodes.

Using this system, it was possible to identify areas where the continuity of the clay layer (more conductive) was interrupted and, therefore, it can be seen a freshwater bubble (more resistive) seeping downward from the lake.

Conclusions

Mapping geological heterogeneities below water bodies is mandatory to study interactions between surface waters and groundwater. The FloaTEM system can be a fast, reliable and efficent solution for acquiring data above rivers, lakes and other water bodies. This system offers a good lateral and vertical resolution that can help in mapping small-scale heterogeneities, crucial to correctly depict hydrologic frameworks. Furthermore, the FloaTEM results compare well with more established geophysical methods, such as ERT, but can be acquired with a much higher productivity. In this study the FloaTEM mapping was successfully used to identify interesting underground features in different hydrogeological environments, impossible to infer from ground-based data only.

References

Auken, E., Foged, N., Larsen, J., Lassen, K., Maurya, P., Dath, S., and Eiskjær, T.: tTEM – A towed transient electromagnetic system for detailed 3D imaging of the top 70 m of the subsurface, Geophysics, E13–E22, https://doi.org/10.1190/geo2018-0355.1, 2018.

Christiansen, A. V., Auken, E., and Sørensen, K. I.: The transient electromagnetic method, in: Groundwater Geophysics. A tool for hydrogeology, 1st Edn., edited by: Kirsch, R., Springer, 179–224, https://doi.org/10.1007/3-540-29387-6_6, 2006.

Danielsen, J. E., Auken, E., Jørgensen, F., Søndergaard, V., and Sørensen, K. I.: The application of the transient electromagnetic method in hydrogeophysical surveys, J. Appl. Geophys., 53, 181–198, 2003.

Fiandaca, G., Zhang, B., Chen, J., Signora, A., Dauti, F., Galli, S., Sullivan, N.A.L., Bollino, A., Viezzoli, A. (2024). EEMverter, a new 1D/2D/3D inversion tool for Electric and Electromagnetic data with focus on Induced Polarization. *GNGTS 2024, 13-16 February 2024, Ferrara, Italy.*

Fitterman, D. V. and Deszcz-Pan, M.: Helicopter EM mapping of saltwater intrusion in Everglades National Park, Florida, Explor. Geophys., 29, 240–243, https://doi.org/10.1071/EG998240, 1998.

Farquharson, C.G. & Oldenburg, D.W., (1998). Non-linear inversion using general measures of data misfit and model structure, Geophysics, 134, 213–227.

Harvey, J. and Gooseff, M.: River corridor science: Hydrologic exchange and ecological consequences from bedforms to basins, Water Resour. Res., 51, 6893–6922, https://doi.org/10.1002/2015WR017617, 2015.

Hatch, M., Munday, T., and Heinson, G.: A comparative study of in-river geophysical techniques to define variations in riverbed salt load and aid managing river salinization, 75, WA135–WA147, https://doi.org/10.1190/1.3475706, 2010.

Lane, J. W., Briggs, M. A., Maurya, P. K., White, E. A., Pedersen, J. B., Auken, E., Terry, N., Minsley, B., Kress, W., LeBlanc, D. R., Adams, R., and Johnson, C. D.: Characterizing the diverse hydrogeology underlying rivers and estuaries using new floating transient electromagnetic methodology, Sci. Total Environ., 740, 140074, https://doi.org/10.1016/j.scitotenv.2020.140074, 2020.

Manheim, F. T., Krantz, D. E., and Bratton, J. F.: Studying Ground Water Under Delmarva Coastal Bays Using Electrical Resistivity, Groundwater, 42, 1052–1068, https://doi.org/10.1111/j.1745-6584.2004.tb02643.x, 2004.

Maurya, P. K., Christensen, F. E., Kass, M. A., Pedersen, J. B., Frederiksen, R. R., Foged, N., Christiansen, A. V., and Auken, E.: Technical note: Efficient imaging of hydrological units below lakes and fjords with a floating, transient electromagnetic (FloaTEM) system, Hydrol. Earth Syst. Sci., 26, 2813–2827, https://doi.org/10.5194/hess-26-2813-2022, 2022.

Munk, L., Hynek, S., Bradley, D. C., Boutt, D., Labay, K. A., and Jochens, H.: Lithium brines: A global perspective: Chapter 14, Econ. Geol., 18, 339–365, https://doi.org/10.5382/Rev.18.14, 2016.

Ong, J. B., Lane, J. W., Zlotnik, V. A., Halihan, T., and White, E. A.: Combined use of frequency-domain electromagnetic and electrical resistivity surveys to delineate near-lake groundwater flow in the semi-arid Nebraska Sand Hills, USA, Hydrogeol. J., 18, 1539–1545, https://doi.org/10.1007/s10040-010-0617-x, 2010.

Pihlainen, S., Zandersen, M., Hyytiäinen, K., Andersen, H. E., Bartosova, A., Gustafsson, B., Jabloun, M., McCrackin, M., Meier, H. M., and Olesen, J. E.: Impacts of changing society and climate on nutrient loading to the Baltic Sea, Sci. Total Environ., 731, 138935, https://doi.org/10.1016/j.scitotenv.2020.138935, 2020.

Siemon, B., Christiansen, A. V., and Auken, E.: A review of helicopter-borne electromagnetic methods for groundwater exploration, Near Surf. Geophys., 7, 629–646, 2009.

Sullivan N. A. L., Viezzoli. A., Fiandaca, G.; 2024: EEMstudio: processing and modelling of electric and electromagnetic data in a QGIS plugin, *GNGTS 2024, 13-16 February 2024, Ferrara, Italy.*

Corresponding author: Stefano.galli2@unimi.it

Seismic noise surveys in the area of Etna volcano (southern Italy).

S. Hailemikael[1], D. Famiani[1], G. Milana[1], G. Tusa[2], M. Paratore[2], G. Brunelli[3], R. Azzaro[2]

[1] Istituto Nazionale di Geofisica e Vulcanologia, Rome, Italy.
[2] Istituto Nazionale di Geofisica e Vulcanologia, Catania, Italy.
[3] Istituto Nazionale di Geofisica e Vulcanologia, Milan, Italy.

In 2022 the regional Civil Protection Department started a new project for 3rd level seismic microzonation at Etna, coordinated under the umbrella of the Centro per la Microzonazione Sismica e le sue applicazioni (CentroMS). In the wide range of activities scheduled in the project, one of the targets is the dynamic characterization of the subsurface structure through seismic noise measurements. In this framework, a working group of the Istituto Nazionale di Geofisica e Vulcanologia (INGV) in July 2023 started a campaign of seismic acquisition in the eastern flank of the volcano, the most exposed in terms of seismic hazard due to a number of highly seismogenic faults crossing a very densely urbanised territory (Azzaro et al., 2012, 2013).

In general, the main scientific issue is to characterise subsurface structures related to very different geological and tectonic conditions. In fact, the volcanic environment is highly heterogeneous in terms of lithology for the presence of soft (pyroclastics) and hard (basalts) units determining strong lateral and vertical discontinuities. In addition, the tectonic activity contributes to complicate the geophysical interpretation, since the bedrock is extremely fractured near the fault zone. This also implies a significant role of subsurface fluids circulations.

The first surveys were carried out at 4 selected sites belonging to the national permanent seismic monitoring networks (Nicolosi-ENIC, Sant'Alfio-ESAL; Santa Venerina-EVRN and -SVN). Passive seismic surveys were also carried out at 3 additional sites to investigate the effect of active faults on the noise signals (polarization, see Di Giulio et al., 2009 and references herein).

For each investigated site (Fig. 1), noise data were recorded by nodal seismic sensors in array configuration adapting the experimental setup to environmental conditions. Each sensor is composed of a data recorder, which contains a battery, a 24-bit digitizer, 32 Gb solid-state memory, GPS and GLONASS receiver in a sealed case connected with a three-component geophone sensor with 4.5 Hz eigen-frequency.

In particular, the following parameters varied across sites:

i) number of sensors, ranging from 11 to 46;

ii) acquisition layout;

iii) maximum array aperture, ranging from 100 to 200 m;

iv) recording durations, ranging from 1.5 to 15 hours.

Single station data have been analysed by Horizontal-to-vertical spectral ratio method (H/V), considering also its azimuthal amplitude variation, while Rayleigh wave 3-component beamforming method (RTBF) has been adopted for array data processing.

Preliminary results obtained at seismic monitoring sites showed spatially consistent results across each array in terms of H/V functions, but only in the low frequency range, where low resonance frequency peaks ($f_0<2$ Hz) were often observed. Such resonance peaks displayed large amplitude variations, up to 50 %, as a function of the considered horizontal direction (Fig. 2). In the high frequency range ($f>2$ Hz), individual H/V functions across each array showed large differences in terms of amplitudes and secondary resonance frequencies (f_1), which suggests a large variability in the shallow elastic properties distribution within a short area.

In few cases, H/V functions calculated across active tectonic structures showed significant variations in terms of amplitude and shape, which are interpreted as correlated to the shallow sedimentary structure of the subsurface caused by such faults.

RTBF analysis performed on data acquired at seismic monitoring sites, showed clear dispersion curve (DC) images both for Rayleigh and Love wave, within a variable frequency range (2-10 Hz). While Love DC data appear dominated by the fundamental mode, Rayleigh-wave dispersion images showed a significant contribution of higher modes (Fig. 3), which support the idea of a complex subsurface model characterised by inverse dispersive properties with depth.

Such preliminary findings suggest a rather complex subsurface structure at the investigated sites on Etna volcano, whose reconstruction should be supported by advanced array processing and carefully considering all available geological information.

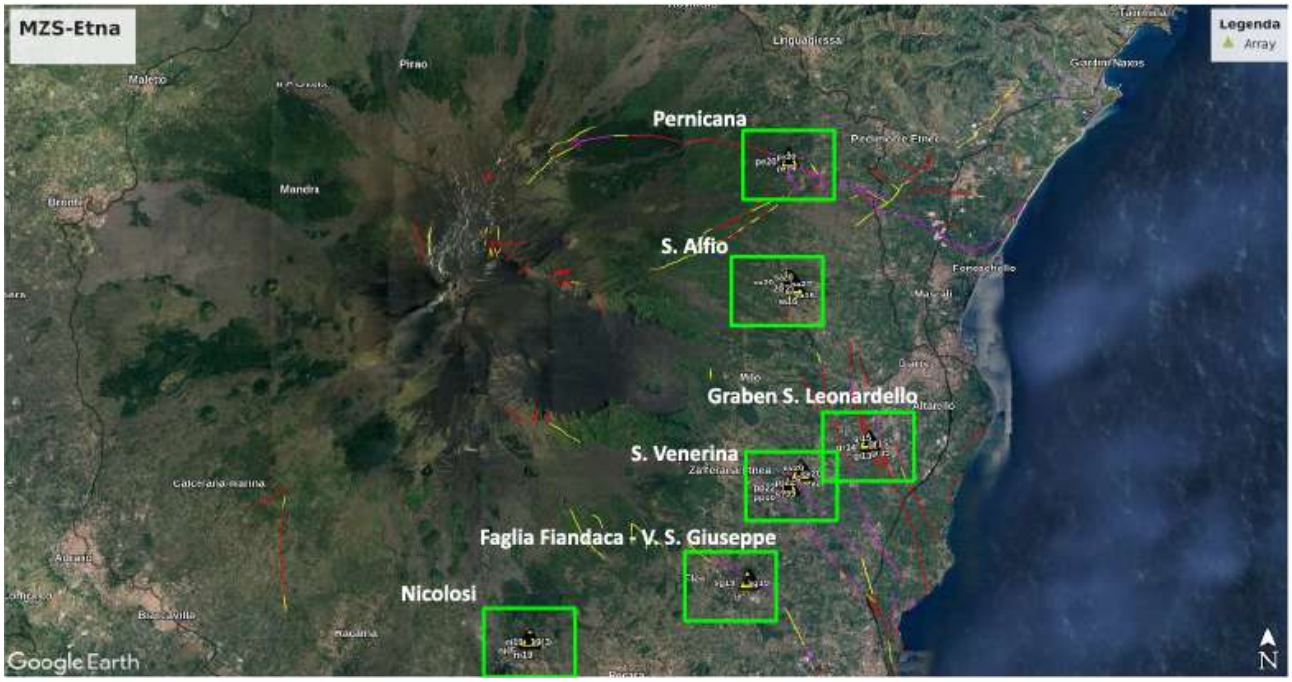

Fig. 1 Map of investigated sites

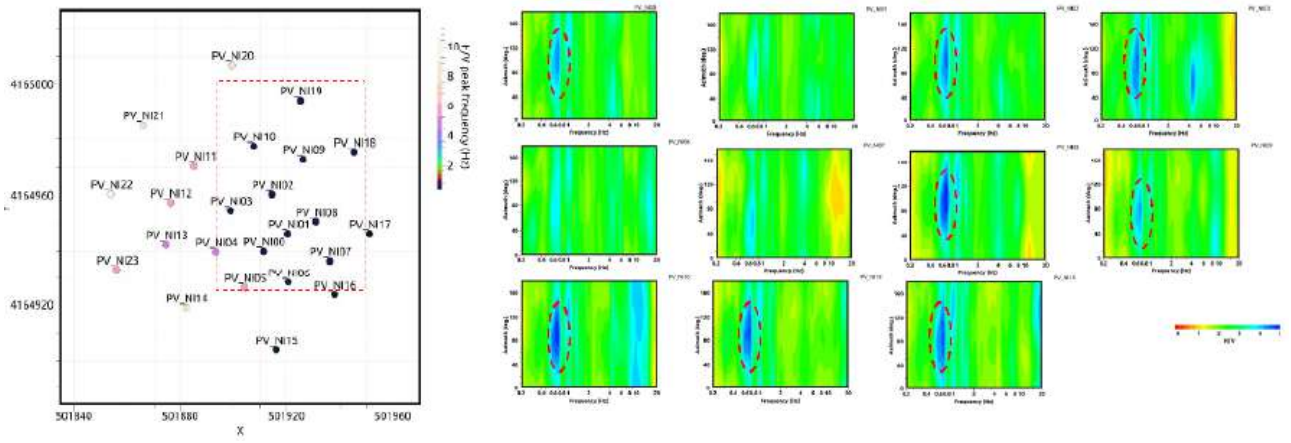

Fig. 2 Azimuthal variation of H/V functions at selected nodal stations of the passive array survey carried out at Nicolosi (ENIC) monitoring site.

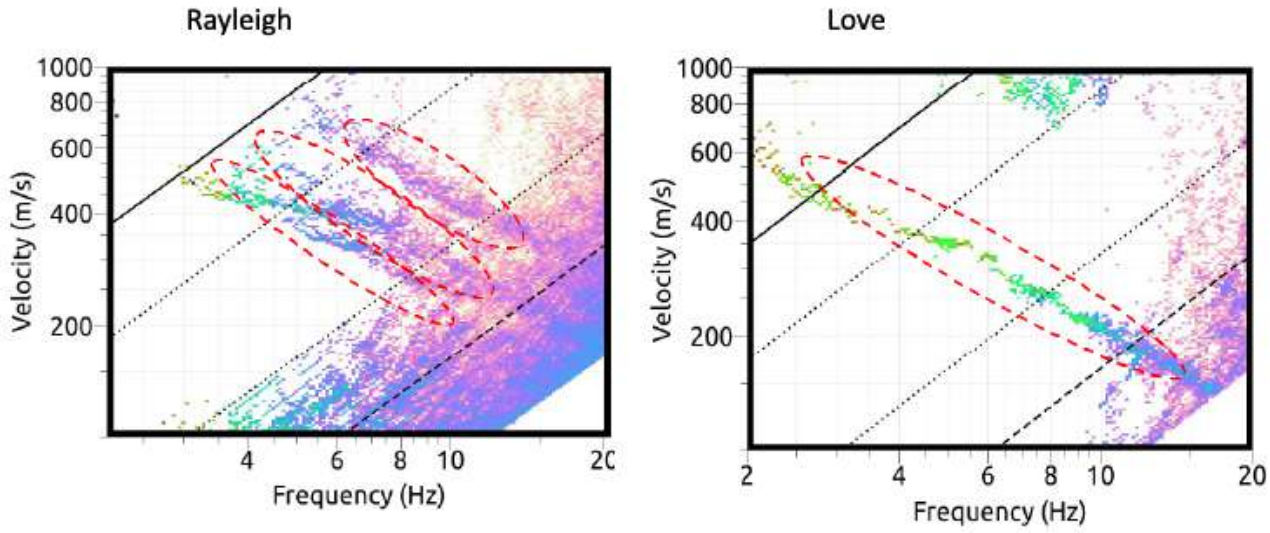

Fig. 3 Rayleigh and Love wave dispersion curves from RTBF analysis of the passive array data collected at Nicolosi (ENIC) seismic monitoring site.

References

Azzaro R., Branca S., Gwinner K. and Coltelli M.; 2012: The volcano-tectonic map of Etna volcano, 1:100.000 scale: morphotectonic analysis from high-resolution DEM integrated with geologic, active faulting and seismotectonic data. It. J. Geosciences (Boll. Soc. Geol. It.), 131 (1), 153-170.

Azzaro R., D'Amico S., Peruzza L. and Tuvè, T.; 2013: Probabilistic seismic hazard at Mt. Etna (Italy): the contribution of local fault activity in mid-term assessment. Journal of Volcanology and Geothermal Research, 251, 158-169.

Cultrera G., Cornou C., Di Giulio G., Bard P.Y.; 2021: Indicators for site characterization at seismic station: recommendation from a dedicated survey. Bull Earthquake Eng 19, 4171–4195.

Di Giulio G., Cara F., Rovelli A., Lombardo G., Rigano R.; 2009: Evidences for strong directional resonances in intensely deformed zones of the Pernicana fault, Mount Etna, Italy, J. Geophys. Res., 114, B10308, doi:10.1029/2009JB006393.

Di Giulio G., Cultrera G., Cornou C., Cornou C., Bard P.Y., Al Tfaily B.; 2021: Quality assessment for site characterization at seismic stations. Bull Earthquake Eng 19, 4643–4691.

Garofalo F., Foti S., Hollender F., Bard P.Y., Cornou C., Cox B.R., Ohrnberger M., Sicilia D., Asten M., Di Giulio G., Forbriger T., Guillier B., Hayashi K., Martin A., Matsushima S., Mercerat D., Poggi V., Yamanaka H.; 2016: InterPACIFIC project: comparison of invasive and non-invasive methods for seismic site characterization. Part I: Intra-comparison of surface wave methods. Soil Dyn Earthq Eng 82:222–240.

Molnar S., Cassidy J.F., Castellaro S. et al.; 2018: Application of Microtremor Horizontal-to-Vertical Spectral Ratio (MHVSR) Analysis for Site Characterization: State of the Art. Surv Geophys 39, 613–631.

Wathelet M., Guillier B., Roux P., Cornou C., Ohrnberger M., 2018: Rayleigh wave three-component beamforming: signed ellipticity assessment from high-resolution frequency-wavenumber processing of ambient vibration arrays. Geophysical Journal International 215 (1) 507–523.

Corresponding author: salomon.hailemikael@ingv.it

Geophysical surveys to detect buried archaeological remains in an area near the Dioscuri Temple (Valley of Temples, Agrigento, Italy)

S. Imposa[1], S. Grassi[1], G. Morreale[1], C. Pirrotta[1], L. Cavalier[2], A. Gilotti[3], D. Giuliano[4], E. Cayre[5], L.M. Caliò[6]

[1] Department of Biological, Geological and Environmental Sciences, University of Catania, Catania, Italy
[2] Unité mixte de Recherche Ausonius (UMR 5607), Université Bordeaux-Montaigne, Pessac, France
[3] Greensol S.R.L., Syracuse, Italy
[4] Department of Cultures and Society, University of Palermo, Palermo, Italy
[5] Post-doc researcher, Grand Programme de Recherche Human Past, Université de Bordeaux, Talence (France)
[6] Department of Human Science, University of Catania, Catania, Italy

Introduction

In the last few decades, geophysical prospections have been considered a fundamental tool for archaeological research due to their ability to expeditiously investigate large areas and identify buried targets in the subsoil without directly interacting with it (Witten, 2006; Grassi et al., 2021). These techniques enable more precise planning of excavation operations, enhancing their efficiency and cost-effectiveness, preserving the integrity of the subsoil and minimizing the risk of damaging potential discoveries (Cella et al., 2015). In this work, an extensive geophysical field survey was carried out, in which the Electromagnetic Method (EM) and Electrical Resistivity Tomography (ERT) were used in an unexplored area near the Dioscuri Temple (Valley of Temples, Agrigento, Sicily, Italy) (Fig. 1a,b). By integrating the data obtained from both geophysical methods, several underground anomalies attributable to buried structures were identified, due to their shape and physical attributes.
A preliminary archaeological dig carried out in one of the areas where the geophysical anomalies were located, revealed the existence of a wall built using local calcarenites blocks.
Subsequently, the wall was scanned using photogrammetric techniques to obtain a detailed 3D reconstruction. Preliminary analysis suggests that this wall is part of a building possibly dating to the Hellenistic or Classical period. This discovery probably represents only a very small portion of a larger and more complex structure. This structure may have played a key role in the religious topography of Akragas since it is located near the entrance to the sanctuary of the "circular altars".

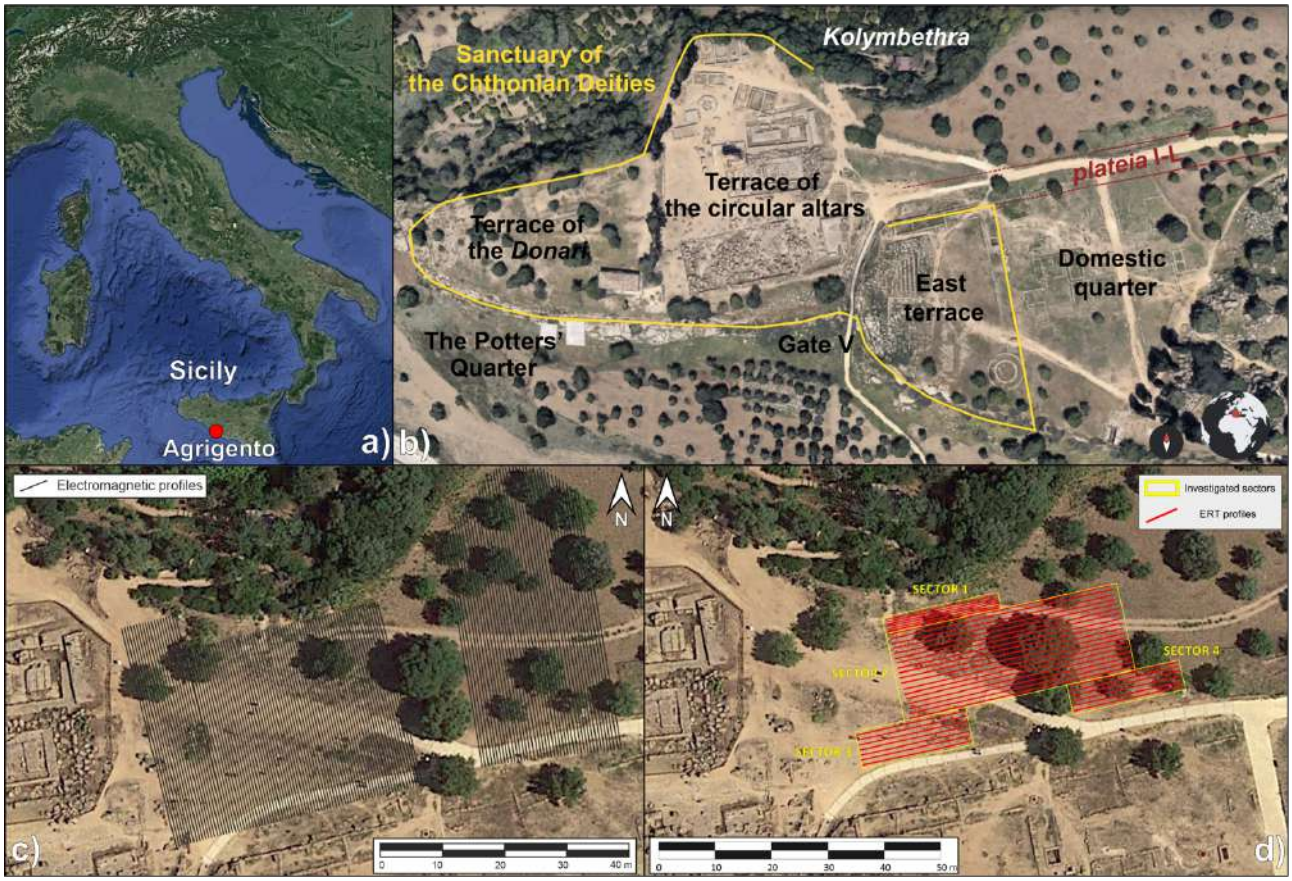

Fig. 1 – a) Location of the Valley of the Temples; b) aerial view of the Sanctuary of Chthonian deities; c) location of EM surveys and d) location of ERT surveys.

Methods and Data Collection

The electromagnetic survey method is one of the widely used techniques in archaeological research. It can identify the contrast of magnetic and electrical properties between buried structures and surrounding lithotypes (Bigman, 2012). This method is used to measure the electric currents produced in the subsurface by electromagnetic field induction using transmitting and receiving coils in the frequency domain (FDEM) (Di Maio et al. 2016).

The EM survey was performed on an area of about 3000 m², with an acquisition step of 0.5 m (Fig. 1c). Along each profile, the data were collected using a sampling step of 0.50 m. The equipment used is an AEMP14 multifrequency electromagnetometer, which consists of three coils: one transmitting and two receiving coils. The distance between the transmitting coil and the first receiving coil is 1.5 m, and the distance to the second receiving coil is 2.5 m. The device is capable to operate at 14 frequencies ranging from 2.5 kHz to 250 kHz.

Electrical resistivity tomography (ERT) is a geophysical method with a wide range of applicability. It allows to obtain 2D sections and 3D models showing the distribution of the resistivity in the subsoil (Tong and Yang, 1990; Sasaki, 1992). The investigated area was divided into 4 sectors, investigated by 38 ERT surveys spaced 0.50 m apart in sector 1, while the spacing increased to 1 m in sectors 2, 3 and 4 (Fig. 1d). The acquisitions were performed with two quadripolar configurations for each linear array: DD (Dipole-Dipole) and MGA (Multiple Gradient Array).

Results

For the data acquired by the EM method, the analysis focused on the quadrature component derived from the highest frequency antenna (250 kHz) to derive the trend of electrical resistivity. The resistivity map obtained reveals the presence of numerous electrical anomalies within the study area (Fig. 2a). These anomalies are characterized by high electrical resistivity values, ranging from 150 to 180 Ohm*m. The primary anomalous sector is characterized by a pronounced alignment of high electrical resistivity values. This sector extends into the central portion of the area, following an almost NNW-SSE direction. Another alignment is observed in the southern boundary of the study area, extends in E-W direction. Moreover, two minor alignments of outliers are observed in the northeastern and northwestern sectors, both of which follow a NW-SE direction.

Concerning ERT surveys, resistivity mapping was obtained for each sector. Low resistivity values, ranging from 1.25 to 1.95 log_Res (Ω*m), indicate the presence of loose or poorly consolidated sediments, suggesting the presence of overburden soils. On the other hand, high resistivity values above 1.95 log_Res (Ω*m) are indicative of more consolidated and cemented rock materials. Anomalies, mainly observed in sectors 1, 2 and 4 (Fig. 2b), consist of abrupt changes in resistivity values from low to high. Sector 3, on the other hand, does not show the presence of anomalies but is entirely characterized by high resistivity values, attributable to the geological characteristics of the site. All high resistive anomalies show a fairly regular pattern and shape. Based on these results, a preliminary archaeological excavation was performed, limited to the area highlighted in Figure 2b within the green circle (Sector 4).

Discussion and Conclusion

Electromagnetic (EM) surveys and ERT electrical resistivity tomographies, performed in the Temple Valley, show the presence of several portions characterized by high resistivity values, surrounded by areas with low resistivity values. The high resistivity anomalies suggest the existence of low conductivity bodies, which, considering the lithologies observed in the study area, are probably attributable to Pleistocene calcarenites. In contrast, areas characterized by higher conductivity values may indicate the presence of poorly consolidated filled soils resulting from the erosion process of blue-gray marly clays. Previous studies on archaeological sites, such as those by Di Maio et al. (2016), have shown that similar values of resistivity anomalies may be indicative of buried rock walls. Based on these evidences, along with the elongated and narrow shape of the alignment of anomalies, as well as their direction and location, it is plausible to assume that these anomalies represent remains of walls from buildings.

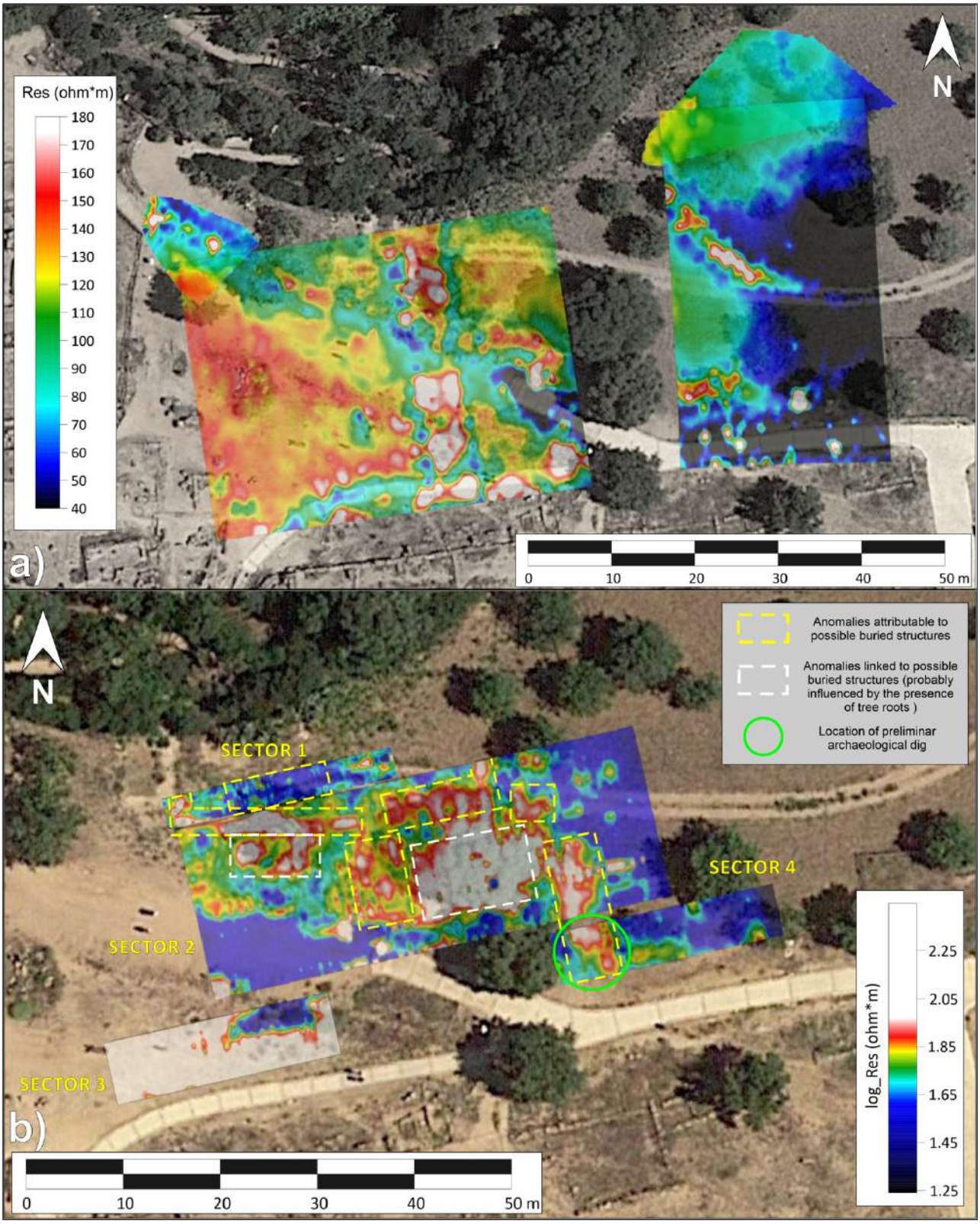

Fig. 2 – a) Electromagnetic resistivity map of the surveyed area and b) Electrical Resistivity map of the study area obtained from ERT surveys.

The archaeological dig performed where the geophysical surveys had identified anomalies revealed a 3.65-m-long wall section, SE-NW orientation, consisting of a single course of 5 preserved blocks of varying height (Fig. 3). The southernmost two blocks of this wall rest on fill, while the other 3 blocks rest partially on another, probably earlier wall with the same orientation,

it consists of large blocks (about 1.30 m long). The wall rests on a layer of clay in which flint fragments were found. The northern part of the wall was completed with coarse rubble mixed with soil. The pottery associated with these remains is currently being studied and should allow for an accurate dating and phase for the discovered building. This monument is located at the edge of the *plateia IL*, near the entrance to the sanctuary "of the circular altars." Given its properties and location, the significance of this monument is of crucial importance for the complete understanding of the religious topography of Akragas. Since the excavation is still in the early stages, further investigation is needed.

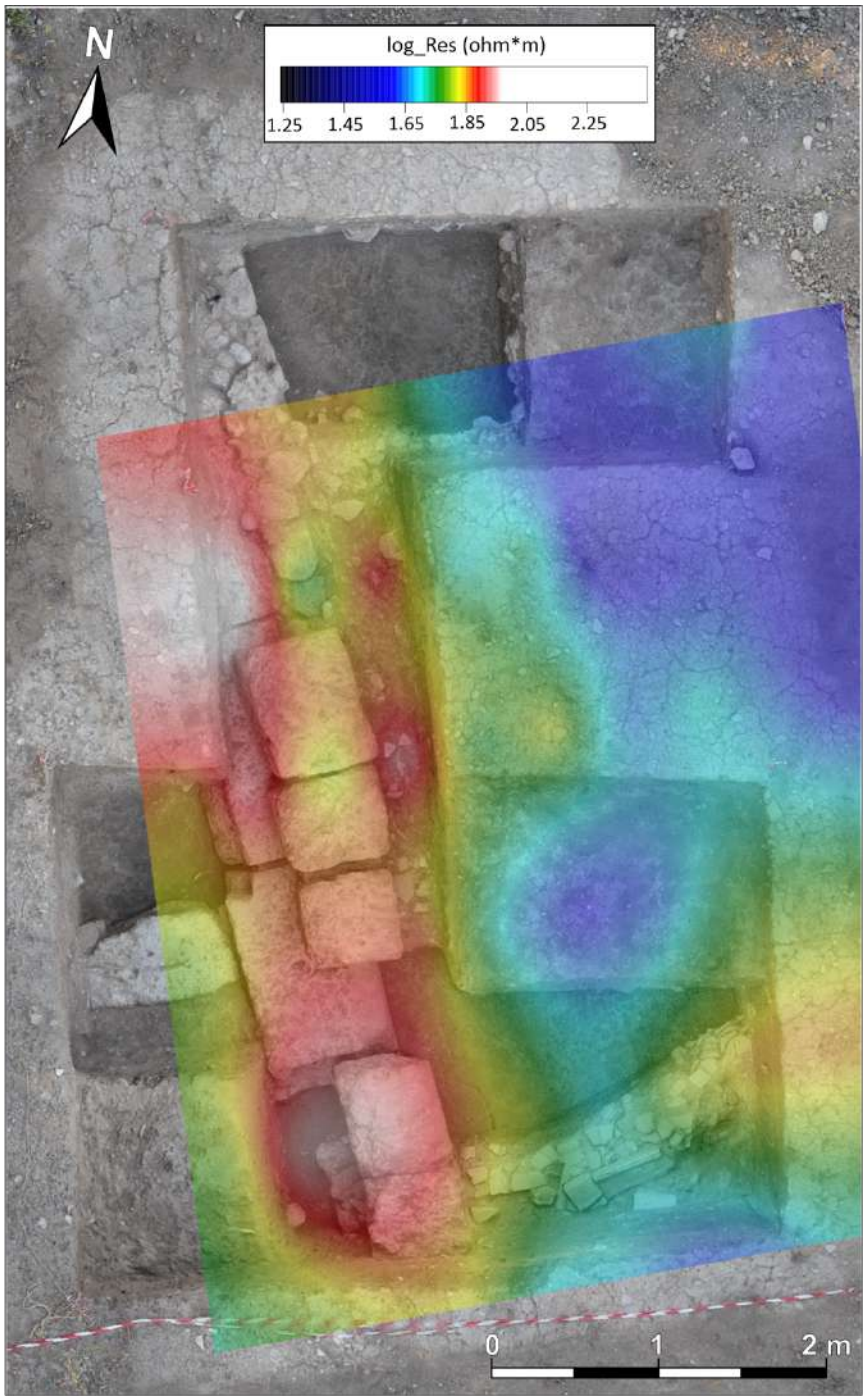

Fig. 3 - Resistivity map obtained from ERT data processing overlaid on the 3D reconstruction of the archaeological excavation.

EM and ERT techniques has proven to be an essential tool in guiding archaeological digs to discover buried remains, at the Akragas site. The processing of the data acquired have identified anomalies in the subsurface characterized by significant variations in physical parameters. Given their physical and geometrical characteristics, such anomalies were attributed to buried structures of anthropogenic origin. Based on the results obtained by ERT surveys, an initial test excavation was conducted in one of the areas identified by the geophysical surveys. Excavation revealed the presence of an unknown building of potentially crucial importance to the religious topography of the area under investigation.

The integration of geophysical techniques with traditional archaeological methods contributes to a more efficient, cost-effective, and informed approach to archaeological research and preservation.

References

Bigman D.P.; 2012: The use of electromagnetic induction in locating graves and mapping cemeteries: An example from Native North America. Archaeological Prospection. 19, 31–39. https://doi.org/10.1002/arp.1416.

Cella F., Fedi M. 2015: High-resolution geophysical 3D imaging for archaeology by magnetic and EM data: The case of the iron age settlement of Torre Galli, Southern Italy. Survey in Geophysics,36, 831–850.

Di Maio R., La Manna M., Piegari E.; 2016: 3D reconstruction of buried structures from magnetic, electromagnetic and ERT data: Example from the archaeological site of Phaistos (Crete, Greece). Archaeological Prospection. 23, 3–13. https://doi.org/10.1002/arp.1516.

Grassi S., Patti G., Tiralongo P., Imposa S., Aprile, D.; 2021: Applied geophysics to support the cultural heritage safeguard: A quick and non-invasive method to evaluate the dynamic response of a great historical interest building. Journal of Applied Geophysics. https://doi.org/10.1016/j.jappgeo.2021.104321

Sasaki Y.; 1992: Resolution of resistivity tomography inferred from numerical simulation 1. Geophysical Prospecting. 40(4):453–463

Tong L.T., Yang C. H.; 1990: Incorporation of topography into two-dimensional resistivity inversion. Geophysics, 55(3), 354-361.

Witten A.J.; 2006: Handbook of Geophysics and Archaeology, Equinox Pub: London, UK.

Corresponding author: gabriele.morreale@phd.unict.it

Characterizing groundwater springs in the Italian Alps: an integrated geological, geophysical, and hydrogeological approach

A. Lucchelli[1], A. Signora[1], F. Dauti[1], S. Galli[1], M. Gisolo[2], G. Fiandaca[1]

[1] The EEM Team for Hydro & eXploration, Department of Earth Sciences "Ardito Desio", Università degli Studi di Milano, Milano, Italy
[2] a2a Ciclo Idrico s.p.a., Brescia, Italy

Spring water is one of the major sources of drinking water for local communities throughout the Italian Alps and in mountain areas worldwide (ISTAT, 2020; United Nations, 2022). As water demand and pressure on groundwater resources increase in a context of fast-changing climate, there is a growing commitment to assess groundwater availability and develop sustainable water supply strategies.

The proper management of groundwater resources requires the characterization of the aquifer systems. In this regard, karst terrains pose unique challenges due to their complex and heterogeneous nature. This study focuses on the assessment of an aquifer system in a karst-fissured mountain environment, by employing an integrated approach based on three pillars: geology, geophysics, and hydrogeology. The study area, located in the Brescia Prealps (northern Italy), is characterized by a Lower-Middle Triassic succession with a fold-and-thrust architecture, typical of the Southern Alps domain, complicated by the presence of faults (Boni & Cassinis, 1973).

The geological pillar is based on a 3D geological-structural model developed using both bibliographic data and field observations. This model serves as the foundation for understanding the spatial distribution of geological formations and the major tectonic lineaments.

The geophysical pillar is built on both ground-based geophysics (classic electrical tomography, ERT, and innovative transient EM methods, i.e. Loupe TEM (Street et al., 2018)) and on densely-spaced airborne electromagnetics (AEM) (Fig. 1).

The hydrogeological pillar consists of spring discharge data, groundwater chemical analysis, and stable isotope analysis of Oxygen, Hydrogen, and Carbon (Fig. 1).

Where geological data is sparse, 3D geological modeling can be used to derive a homogeneous, realistic representation of geological features over the entire study area. In this study it was performed using the GeoModeller software by Intrepid Geophysics (Calcagno et al., 2008). Geophysical surveys, on the other hand, play a key role in capturing the subsurface heterogeneity and identifying preferential flow paths within the rock volumes. Together, these methods provide the information needed to understand aquifer architecture.

To model the electric and electromagnetic data the EEMverter inversion software has been used (Fiandaca et al., 2023). For the mutual calibration of geological and geophysical data, two rules

Fig. SEQ Figure * ARABIC 1 - Geophysical surveys tracks and location of the springs with their relative data.

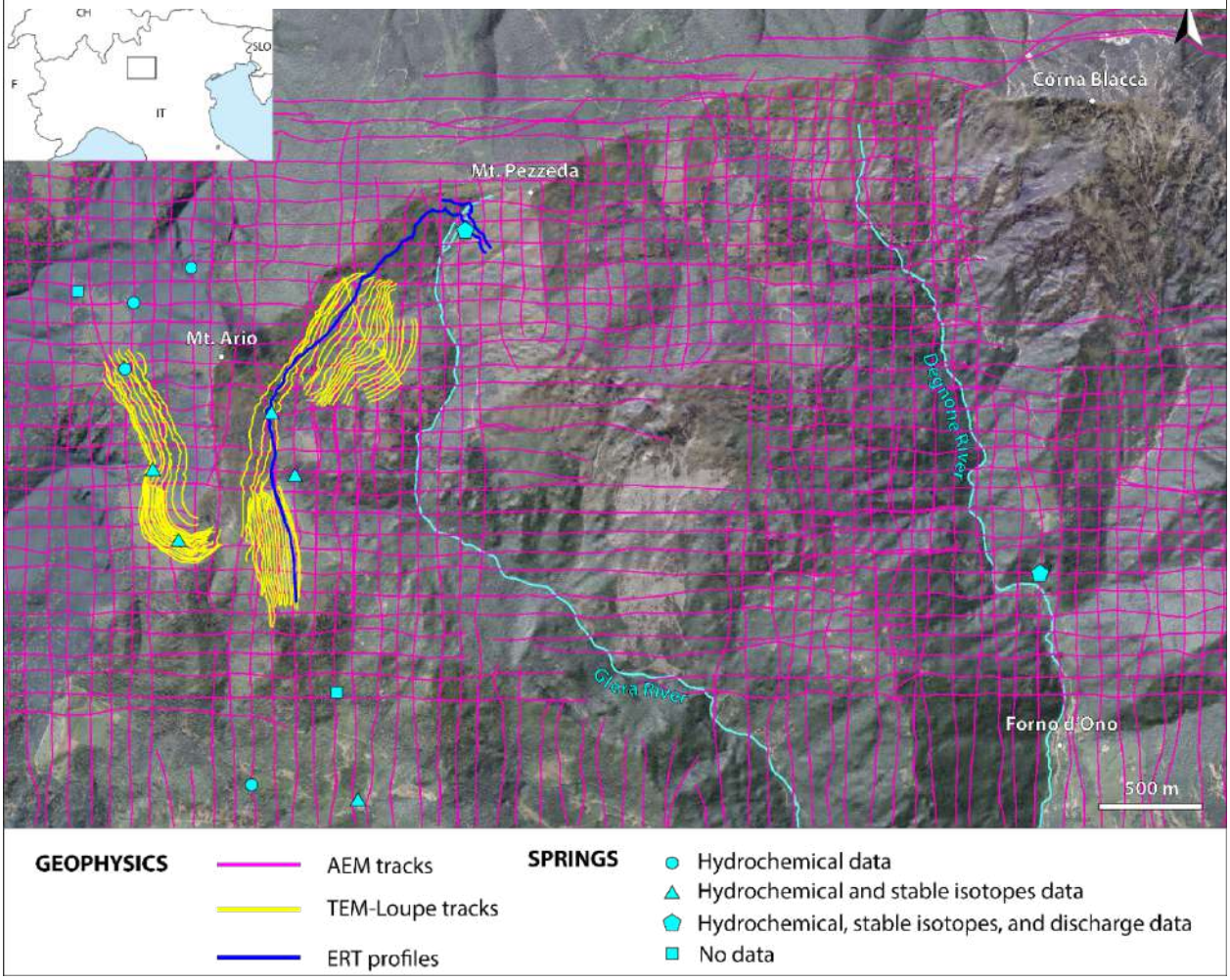

have been introduced in EEMverter. In the first rule, the basal boundaries of the geological formations are treated as barriers that separate different regions: the vertical constraints on the electrical resistivity parameter can be broken at these barriers. This rule accounts for the fact that adjacent geological formations can have significantly different electrical properties. The second rule takes allows to specify different resistivity ranges in each region.

The integration and mutual calibration of geophysical data with the 3D geological model allows for the refinement and validation of the model parameters, ensuring a more realistic representation of the aquifer system. This iterative process enhances the precision of the model and provides valuable insights into the hydrogeological characteristics of the investigated system (Fig. 2). Hydrogeology, and particularly the isotope analysis, helped to identify the origin of the groundwater and to determine an approximate elevation for the main recharge areas of the aquifer system (Longinelli & Selmo, 2003).

The results reveal the existence of different rock volumes with similar electrical behavior, within which heterogeneities in resistivity distribution are recognized. In addition, the integration of 3D geological modeling and geophysical surveys provides a comprehensive and accurate representation of subsurface structures (Fig. 3).

In conclusion, this research offers practical insights for the sustainable management of groundwater springs in complex geological settings and is the first step in the development of a

numerical flow model. This is essential for the assessment of groundwater availability as a function of climate change scenarios.

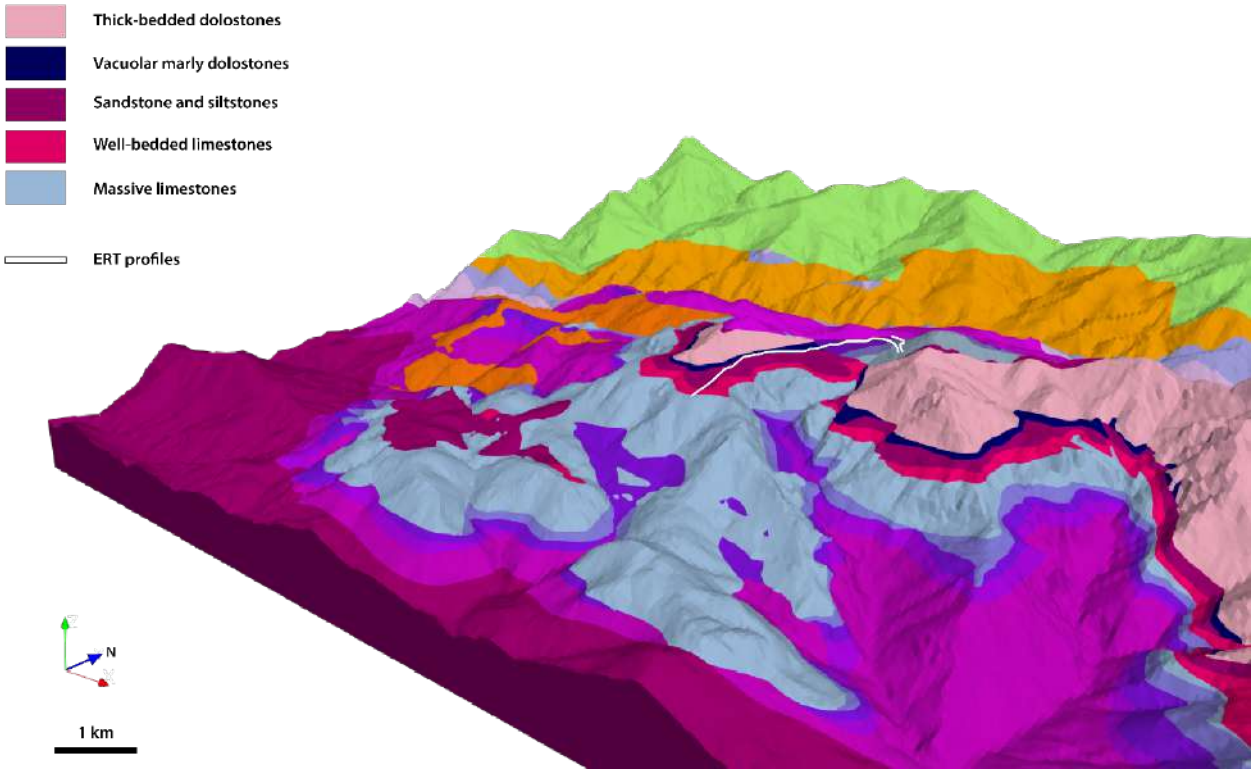

Fig. 2 – 3D geological model of the study area with the ERT track.

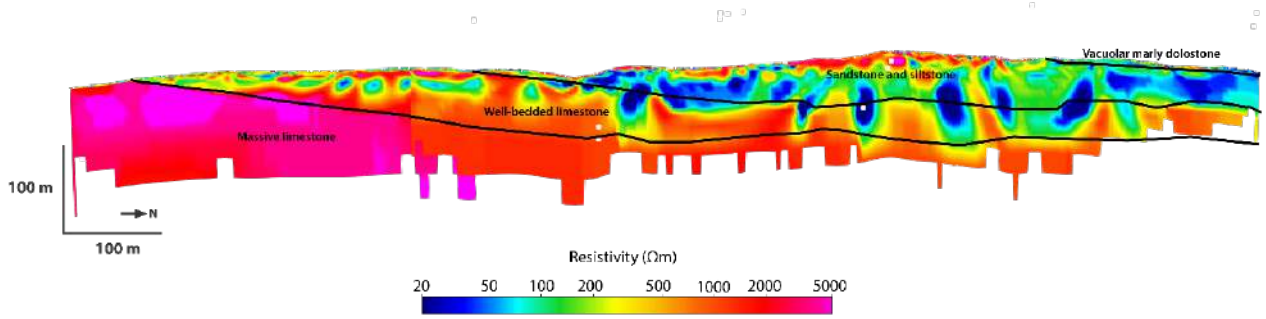

Fig. 3 – ERT profile integrated with geological boundaries exported directly from the 3D geological model.

Acknowledgments

This study has been carried out within the projects MountainHydro and HydroEEMaging, funded by a2a Ciclo Idrico S.p.A.

References

Boni A. & Cassinis G.; 1973: Carta geologica delle Prealpi Bresciane a sud dell'Adamello. Tipografia del libro.

Calcagno P., Chilès J.P., Courrioux G. & Guillen, A.; 2008: Geological modelling from field data and geological knowledge – Part I. Modelling method coupling 3D potential-field interpolation and geological rules. Physics of the Earth and Planetary Interiors 171, 147-157.

Fiandaca G., Zhang B., Chen J., Signora A., Dauti F., Galli S., Sullivan N.A.L., Bollino A., Viezzoli A.; 2023: Closing the gap between galvanic and inductive methods: EEMverter, a new 1D/2D/3D inversion tool for Electric and Electromagnetic data with focus on Induced Polarization. AEM2023 -8th International Airborne Electromagnetics Workshop.

ISTAT; 2022: Censimento delle acque per uso civile. https://www.istat.it/it/archivio/279363

Longinelli A., Selmo E.; 2003: Isotopic composition of precipitation in Italy: a first overall map. Journal of Hydrology 270, 75-88.

Street G., Duncan A., Fullagar P. & Tresidder R., 2018. Loupe – A portable EM profiling system. ASEG Extended Abstracts 1, 1-3.

United Nations; 2022: The United Nations World Water Development Report 2022 – Groundwater: Making the invisible visible. UNESCO, Paris.

Corresponding author: alice.lucchelli@unimi.it

Quantitative integration of geoelectrical data for mapping of leachate plumes: application to a MSW landfill in Central Italy

D. Melegari[1], G. De Donno[1], E. Piegari[2]

[1] DICEA (Sapienza - University of Rome, Rome, Italy)
[2] DISTAR (Federico II - University of Naples, Naples, Italy)

Introduction

Waste management is one of the main challenges for contemporary society, as highlighted by the United Nations SDGs (Target 12.4). Specifically, the uncontrolled accumulation of leachate in municipal solid waste (MSW) landfills represents a potential risk for the environment, since leachate is a liquid with a high pollutant content that can contaminate aquifers (Assamoi B., Lawryshyn Y.; 2012) and affect the stability of landfills. Therefore, mapping and monitoring the waste mass down to significant depths is required for an appropriate management of the landfill sites. Among the geophysical techniques, electrical resistivity tomography (ERT) and induced polarization (IP) methods are perfectly suited for this purpose given the electrical properties of leachate (highly conductive and chargeable) compared to the unsaturated waste mass (Soupios P., Ntarlagiannis D.; 2017).

In the present study we present an application of a machine learning-based approach for a quantitative integration of ERT and IP data for imaging of leachate levels in a MSW landfill located in Central Italy. The quantitative interpretation of resistivity, chargeability and normalized chargeability data is provided by using the Fuzzy C-means clustering algorithm which allows for the identification of the leachate accumulation zones and for assessing the reliability of the reconstruction by means of the membership value. The results of the cluster analysis are validated by the computation of the Silhoutte coefficient and supported by well data.

Study area, data acquisition and processing

The landfill is located in Central Italy on a steep slope, in which the leachate accumulation can trigger instability phenomena (Fig. 1a). We focused our investigation on four selected terraced steps with four electrical lines (L1-L4) 300 to 500 meters long (Fig. 1b), using a multi-parameter reconstruction through electrical resistivity tomography (ERT) and time-domain induced polarization (TDIP) methods. Experimental datasets were acquired through the Syscal Pro resistivity-meter (IRIS Instruments) with stainless steel electrodes spaced 5 m apart, using the dipole-dipole (DD) array and a roll-along configuration. For IP acquisition, we used a current

injection time of 2 s with 4 stacks, a time delay of 40 ms and a logarithmic sampling of the IP decay curve using 20 gates. We also logged leachate levels in five different piezometers along L2 and L3.

We inverted ERT/TDIP data for resistivity and integral chargeability using the VEMI software (De Donno G., Cardarelli E.; 2017), which employs the finite element method for solving the forward problem and a Gauss-Newton inversion algorithm, while the linear approach (Method I after Oldenburg D. W., Li Y.; 1994) is adopted for chargeability forward modelling. After inversion we added to the resistivity (ρ) and integral chargeability (M) models also the normalized chargeability (M_n) to emphasize the contribution of surface conductivity, derived by normalizing chargeability by the resistivity.

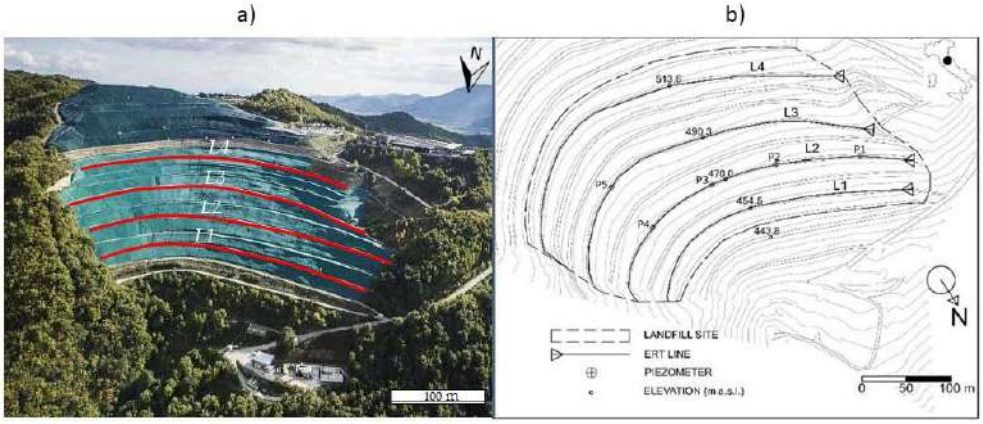

Fig. 1 – Aerial image (a) and plan (b) of the municipal solid waste landfill in Central Italy, with the location of the four investigated ERT/IP lines (L1-L4) and of the five piezometers (P1-P5)

To integrate information from electrical inverted models, we applied a machine learning-based approach (Piegari E. et al.; 2023), which is based on a cluster analysis in the parameter model space defined by the inverted values of ρ, M and M_n. However, instead of the widely-used K-means, we performed the cluster analysis by using the Fuzzy C-Means algorithm (Bezdek J. C.; 2013). This algorithm is a soft clustering approach, which allows data points to belong to multiple clusters with a degree of membership μ that is a function of the distance to the closest centroids. This makes the algorithm more robust to noise and outliers in the data compared to K-means and we can also have an assessment of the reliability of the clustered section by means of the degree of membership section. The optimal number of clusters was assessed by the Elbow method applied to the explained variance, while the quality of the results was finally evaluated by calculating the Silhouette value (Rousseeuw P. J.; 1987).

At the end of the clustering procedure, we achieved a single model that integrates all geoelectrical information providing an accurate identification of leachate accumulation zones through a color-based scale, where dark red color is associated to the fully saturated zones.

Results

The results are shown in Figure 2 for the L2 line, where is also available the direct information. The three inverted models resulting from inversion process (Fig 2a-c) are compared to the clustering models, with the leachate levels logged superimposed. The models from traditional approach (without clustering) show three main layers in agreement with the expected stratigraphy of a landfill: i) a shallow layer (thickness less than 10 m) showing high resistivity (ρ > 20 Ωm) and low chargeability (M < 2 mV/V), related to the presence of unsaturated waste and covering soil; ii) an intermediate layer with low resistivity (ρ < 20 Ωm) and high chargeability (M > 2 mV/V), which reflects the presence of leachate. This layer seems quite heterogeneous, with lateral changes due to a different degree of saturation inside the waste mass; iii) a deeper layer, extended down to the maximum depth of investigation (~ 50 m) with very high values of resistivity (ρ >> 20 Ωm) and low chargeability (M < 2 mV/V), associated to the presence of HDPE bottom liner, which does not allow current to flow outside the landfill. However, the electrical models still leave ambiguities on the identification of leachate accumulation zones, as confirmed by the mismatch between the high values of normalized chargeability and the leachate levels logged in P4.

The results of Fuzzy C-Means analysis are shown in terms of clustered (Fig. 2d) and membership sections (Fig. 2e), resulting from an optimal number of clusters equal to 8 computed by the Elbow method. The clustered section shows a less ambiguous and more accurate identification of the leachate accumulation, validated by direct information from P4, which is in good agreement with the cluster no. 8 (lowest ρ and highest M and M_n), while the other wells do not show significant leachate levels according to the clustering reconstruction. In addition, thanks to membership section we can evaluate the reliability of the reconstruction achieved by the clustering. Given the high values (μ > 0.75) displayed in the dark red cluster, we can validate the final reconstruction.

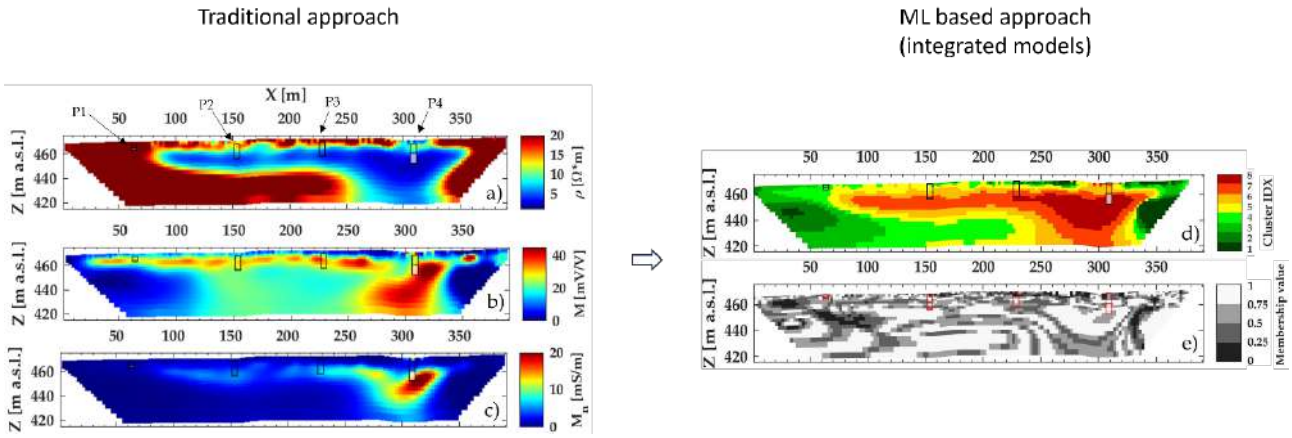

Fig. 2 – ERT/TDIP data inversion and clustering analysis on the L2 line: resistivity model (a), chargeability model (b), normalized chargeability model (c), clustered section (d) and membership section (e). The leachate levels logged in piezometers P1-P4 are marked with a white area.

Conclusions

In this work, we presented a machine-learning based approach to upgrade leachate identification in municipal solid waste landfill trough geoelectrical data. This approach supplies a promising method to reduce the residual ambiguities arising from ERT or TDIP standalone applications. We demonstrated two advantages: i) integrating ERT and IP data through clustering analysis can be effective for mapping the leachate accumulation zones with more accuracy compared to a traditional approach; ii) the membership section derived by using soft clustering can provide a quantitative validation of the final landfill clustered model, in addition to the available direct information. These development over the traditional approach represents an important step to improve landfill's drainage operations, particularly during the maintenance of MSW landfills. Future work will be focused on application of this method to other landfill sites in order to validate the parameters selected during the cluster analysis, especially with regard to the optimal number of clusters.

References

Assamoi B., Lawryshyn Y.; 2012: The environmental comparison of landfilling vs. incineration of MSW accounting for waste diversion. Waste management, 32(5), 1019-1030.

Bezdek J. C.; 2013: Pattern recognition with fuzzy objective function algorithms. Springer Science & Business Media.

De Donno G., Cardarelli E.; 2017: VEMI: a flexible interface for 3D tomographic inversion of time- and frequency-domain electrical data in EIDORS. Near Surface Geophysics, 15(1), 43-58.

Oldenburg D. W., Li Y.; 1994: Inversion of induced polarization data. Geophysics, 59(9), 1327-1341.

Piegari E., De Donno G., Melegari D. & Paoletti, V.; 2023: A machine learning-based approach for mapping leachate contamination using geoelectrical methods. Waste Management, 157, 121-129.

Rousseeuw P. J.; 1987: Silhouettes: a graphical aid to the interpretation and validation of cluster analysis. Journal of computational and applied mathematics, 20, 53-65.

Soupios P., Ntarlagiannis D.; 2017: Characterization and monitoring of solid waste disposal sites using geophysical methods: Current applications and novel trends. Modelling trends in solid and hazardous waste management, 75-103.

Corresponding author: davide.melegari@uniroma1.it

Mixed-dimensional forward-problem solver for the geoelectrical analysis of highly resistive liners in landfills

L. Panzeri[1,2], A. Fumagalli[2], L. Longoni[1], M. Papini[1], L. Zanzi[1], D. Arosio[3]

[1] Department of Civil and Environmental Engineering, Politecnico di Milano, Italy
[2] Department of Mathematics, Politecnico di Milano, Italy
[3] Dipartimento di Scienze Chimiche e Geologiche, Università degli studi di Modena e Reggio Emilia, Italy

To avoid the diffusion of the leachate in the subsoil and the possible contamination of aquifers, a thin liner of high-density polyethylene (HDPE) is placed underneath the waste in municipal solid waste landfills (MSWLFs). The conditions of the plastic membrane are of paramount relevance but, unfortunately, they are difficult to be assessed due to the location of the liner. A 3D code based on a mixed-dimensional mathematical model has been developed to simulate the flow of the current injected in the geoelectrical surveys to allow a non-destructive analysis of the highly resistive liner (Aguzzoli et al. 2020, Aguzzoli et al. 2021, Fumagalli et al., 2023, Panzeri et al., 2023)).

The peculiarity of our approach is to consider the problem as mixed-dimensional. This means that elements of different dimensions coexist in the same mesh (Fig.1). Due to their reduced dimension along x and y with respect to z, electrodes have been simulated as 1D elements (Peacemean 1978), while the liner is simulated as a 2D element because of its limited thickness (typically a few millimetres). The new code defines parallelepipedal boxes around the electrodes and exploits the finite volume Multipoint Flux Approximation method (MPFA). These conditions need to be mathematically expressed in the formulation of the forward problem also including the interface/ coupling conditions between the elements with different dimensions.

In this work, the results obtained with our Python code based on Porepy (Keilegavlen et al. 2021) have been compared, first, with two analytical solutions. One represents two horizontal layers with different conductivity (Sheriff et al., 1990), and the other is characterized by the presence of a conductive sphere in an infinite horizontal space (Aldridge and Oldenburg, 1989). After that, the results were compared with the outcomes of an open-source library for multi-method modelling and inversion in geophysics named pyGIMLi (Rücker et al. 2017). Finally, to further validate our modelling code, tests were performed with different settings in the laboratory on a homogeneous material (water) placed in a plastic box.

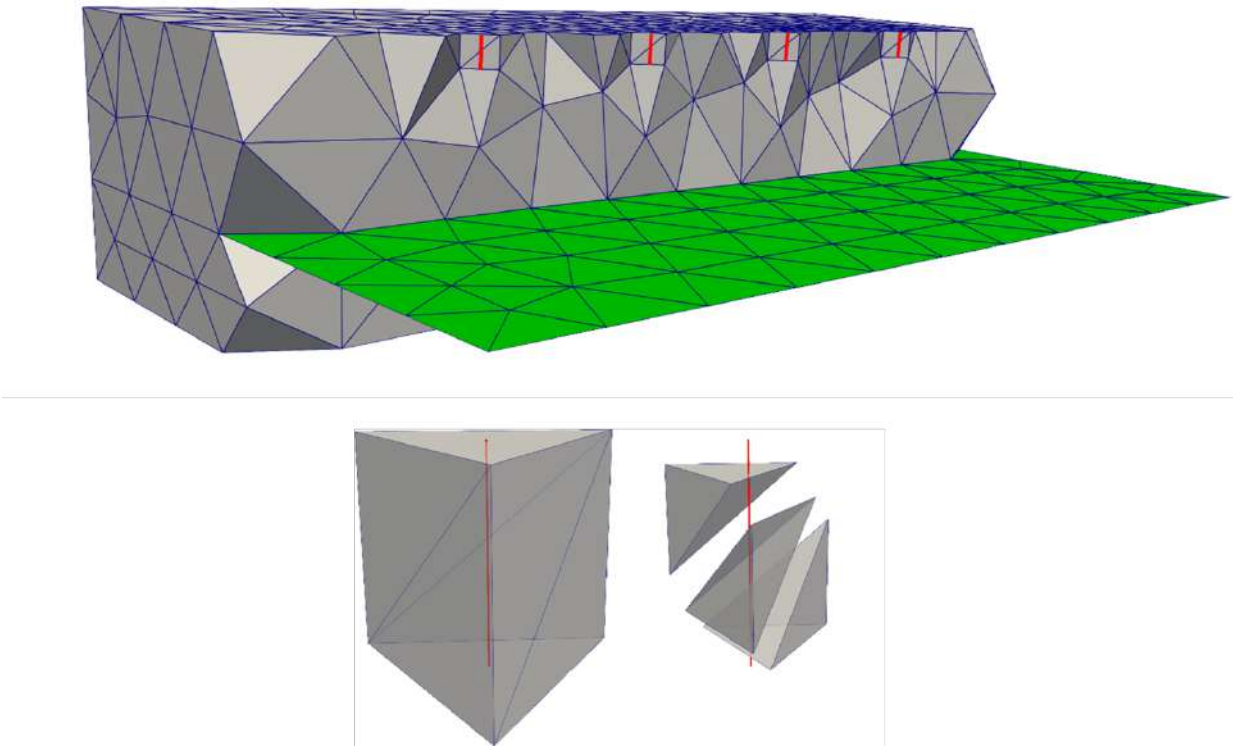

Fig. 1 – Mixed-dimensional mesh scheme. Graphical representation of the domain (grey), the liner in green and the electrodes in red. Below, a detail about the construction of cells around an electrode is shown (Fumagalli et al., 2023).

Particular attention has been given to mesh creation, which is very similar on one side, while on the other has a different structure due to the different approaches considered. In particular, pyGIMLi represents the electrodes as points and considers the nodes of the mesh as the degrees of freedom of the problem. This differs from the proposed approach in which the degrees of freedom are the elements of the mesh (tetrahedra). To make the results comparable, different meshes almost equal in terms of the number of nodes and elements have been created. Gmsh defines a characteristic length of the mesh which has been set equal to 0.5 cm in the region close to the electrodes and equal to 5 cm elsewhere. To have the same structure in pyGIMLi, a series of nodes with distances equal to 0.5 cm along the three dimensions have been defined in the area close to the electrodes.

Once the forward problem solver was validated, we were interested in the ability of our modelling code to obtain meaningful information about the liner in situ. A widespread issue for this type of analysis regards having satisfactory sensitivity far from the deployed electrodes. What types of arrays, how many measurements, and what electrode positions should we consider to best investigate the area where the membrane is located? To solve this problem, an analysis was performed with the aim of highlighting the areas with higher and lower sensitivity by paying special attention to the 2D elements of the membrane. The aim was to optimize the acquisition by following different strategies to reduce the number of measurements that would later be implemented in situ.

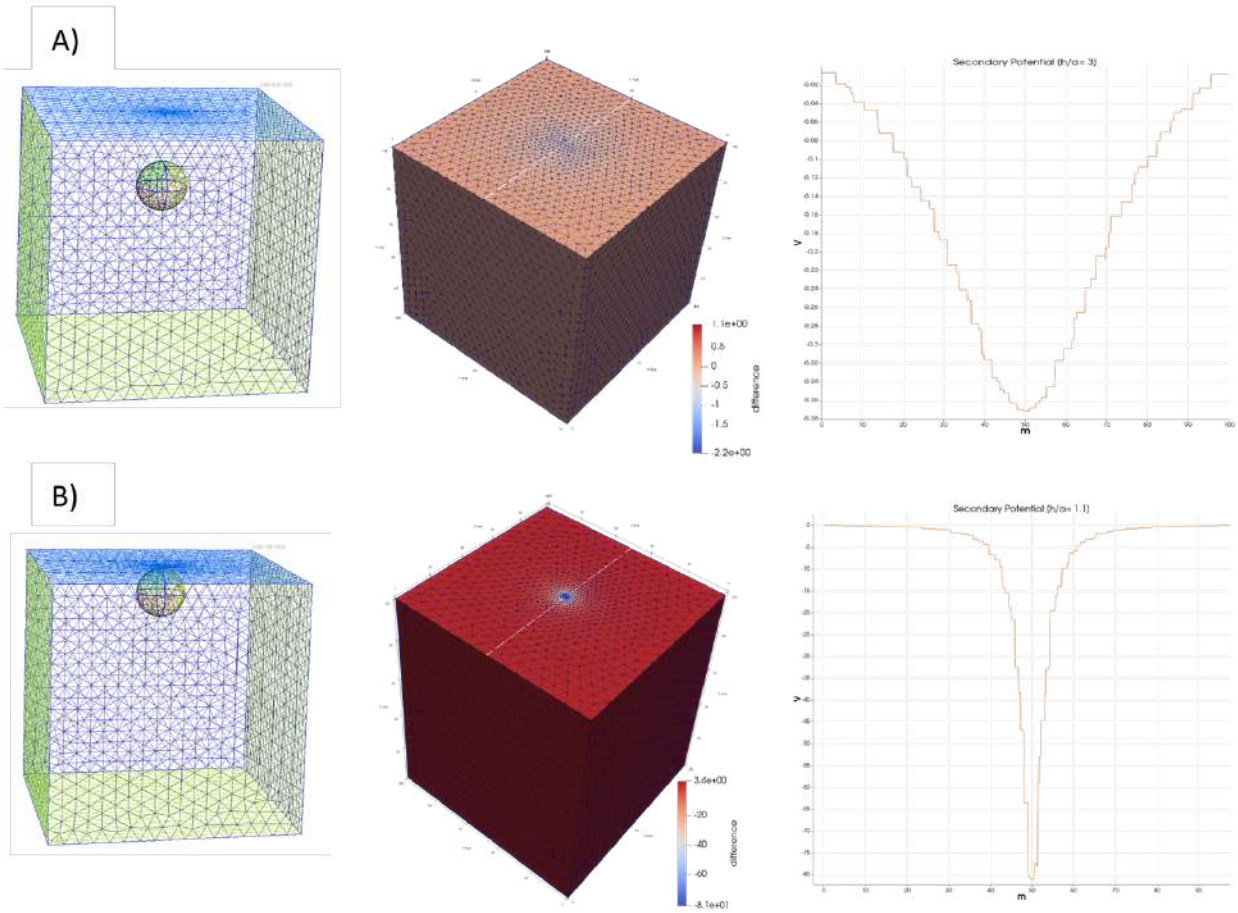

Fig. 2 – Simulation related to a conductive sphere (ρ2 = 10 Ωm) in a resistive background (ρ1= 1000 Ωm). A) Modelled mesh (left), computed secondary potential (centre) and computed secondary potential along a line of electrodes at the surface (right); the ratio between the depth of the sphere centre and its radius is 3 (depth = 30 m, radius = 10 m). B) same as A) with the ratio between the depth of the sphere centre and its radius equal to 1.1 (depth = 11 m, radius = 10 m).

References

Aguzzoli, A., Hojat A., Zanzi L., Arosio, D.;2020: Two Dimensional ERT Simulations to Check the Integrity of Geomembranes at the Base of Landfill Bodies. In 26th European Meeting of Environmental and Engineering Geophysics, 2020, p.1 – 5.

Aguzzoli, A., Fumagalli, A., Scotti, A., Zanzi, L., Arosio, D.;2021: Inversion of Synthetic and Measured 3D Geoelectrical Data to Study the Geomembrane below a Landfill. In 4th Asia Pacific Meeting on Near Surface Geoscience & Engineering, 2021, p.1 - 5.

Aldridge, D. F., & Oldenburg, D. W. ;1989: Direct current electric potential field associated with two spherical conductors in a whole-space 1. *Geophysical prospecting*, *37*(3), 311-330.

Fumagalli, A., Panzeri, L., Formaggia, L., Scotti, A., Arosio, D.; 2023: A mixed-dimensional model for direct current simulations in presence of a thin high-resistivity liner. *Journal for Numerical Methods in Engineering,* doi: 10.1002/NME.7407.

Keilegavlen, E., Berge, R., Fumagalli, A., Starnoni, M., Stefansson, I., Varela, J., and Berre, I.;2021: Porepy: An open-source software for simulation of multiphysics processes in fractured porous media. *Computational Geosciences*, *25*(1), 243-265.

Panzeri, L., Fumagalli, A., Aguzzoli, A., Zanzi, L., Longoni, L., Papini, M. Arosio, D.; 2023: Lab and modelling DC Resistivity Tests to Analyse the Response of a High Resistivity Liner. In 5th Asia Pacific Meeting on Near Surface Geoscience & Engineering, 2023, p.1 - 5.

Peaceman, D. W.; 1978: Interpretation of well-block pressures in numerical reservoir simulation (includes associated paper 6988). *Society of Petroleum Engineers Journal*, *18*(03), 183-194.

Rücker, C., Günther, T., & Wagner, F. M.;2017: pyGIMLi: An open-source library for modelling and inversion in geophysics. Computers & Geosciences, 109, 106-123.

Sheriff, R.E. Telford, W.M., Geldart, L.P.;1990: Applied Geophysics. Cambridge University Press, 2nd edition.

Corresponding author: lorenzo.panzeri@polimi.it

Application of conductive textile sachets as electrodes for electrical resistivity tomography measurements collected on debris and coarse-blocky surfaces

M. Pavoni [1], J. Boaga [1], A. Bast [2,3], Lichtenegger [2,3], J. Buckel [4]

[1]Department of Geosciences, University of Padova, Padova, Italy.
[2]WSL Institute for Snow and Avalanche Research SLF, Davos Dorf, Switzerland.
[3]Climate Change, Extremes and Natural Hazards in Alpine Regions Research Center CERC, Davos Dorf, Switzerland.
[4]Institute for Geophysics and Extraterrestrial Physics, Technische Universität Braunschweig, Braunschweig, Germany.

1. Abstract

Electrical resistivity tomography surveys are commonly applied in geophysical investigations performed in high mountain environments where debris and coarse-blocky surfaces can be found, e.g. landslide or rockfall deposits, blocky slopes and rock glaciers. In this harsh situation, obtaining acceptable contact resistances between the electrodes, usually composed of stainless-steel spikes, and the ground surface is challenging. The electrodes must be steadily coupled between the boulders (e.g. by hammering them) and, to improve the galvanic contact, sponges soaked in salt water are typically inserted among the spike and the rock surface (Hauck and Kneisel, 2008). Considering all this, it is clear that deploying ERT arrays in these environments is particularly time-consuming. To decrease this time effort, recently Buckel et al. (2023) applied conductive textile sachets as electrodes in ERT surveys performed on rock glaciers. To verify the reliability of this new electrodes approach, in this work we intensively tested the conductive textile sachets electrodes in different envinroments with debris and corse-blocky surfaces.

2. Introduction

It is well known in the geophysical community that collecting a high-quality ERT dataset requires a good galvanic contact between the electrodes and the ground surface (Day-Lewis, 2008). The parameter that represents the electrical contact area of two materials is defined as contact resistance. Low values of contact resistance allow to easily inject the electrical current and consequently to acquire ERT datasets with higher signal to noise ratio (Pavoni et al., 2022). This condition is particularly challenging to be achieved in envinroments with debris and corse-blocky surfaces. Coupling the electrodes with sponges soaked in salt-water is an efficient solution to minimize the contact resistance (Hauck and Kneisel, 2008). Despite this, the approach requires a significant amount of time to deploy the entire electrodes array, and a considerable amount of salt water to wet the sponges. Considering this, Buckel et al. (2023) proposed an alternative electrodes system to facilitate the preparation of ERT arrays in rock glacier envinroments. Instead of the traditional steel spikes, conductive textile sachets (wet with salt-water) are used as electrodes. In

this way, the electrodes don't need to be hammered between the boulders, but we can simply push them, and, compared to the sponges, we can use lower quantity of salt-water to wet them. To evaluate the performance of the conductive textile sachets, we compared the ERT measurements performed with this new electrode approach with the ERT measurements collected with the traditional steel spikes and sponges, considering common investigation lines. This comparative test has been carried out in three sites, which present different lithologies and size of the debris/boulders on the surface, and using different electrodes spacing. The collected datasets have been compered in terms of contact resistances, injected electrical current, measured apparent resistivities, reciprocal error, and inverted resistivity values.

3. Sites description

We tested the conductive textile sachets electrodes in three different envinroments that presents a debris and coarse-blocky surface: i) the Marocche di Drò landslide deposit, ii) the inactive rock glacier of Sadole, and iii) the active rock glacier of Flüelapass.

Marocche di Drò is a landslide deposit located in the lower part of Sarca Valley (Trento, Italy). Among the various landslide deposits in the area, we selected the Kas deposit, which is composed of calcareous debris, angular blocks, and limited vegetation cover (Martin et al., 2014). The comparative test was realized with 40 electrodes spaced 3 meters.

Sadole inactive rock glacier is located in the Sadole Valley (Trento, Italy). Steep rock walls and sharp crests, composed of magmatic ignimbrites rocks, surround the rooting area of the rock glacier. The rock glacier surface is composed of large size boulders, and widespread vegetation cover. The ERT survey line for the comparative test was realized with 43 electrodes spaced 5 meters, in a position with a coarse-blocky surface without vegetation, and where a discontinuos frozen layer was found in previous ERT investigations (Pavoni et al., 2023).

The Flüelapass active rock glacier is located in the eastern Swiss Alps (Engadin). The rooting area is surrounded by steep rock walls consisting of metamorphic amphibolite and paragneiss. Its surface is composed by a various granulometric size of debris and boulders, and isolated areas with finer sediment. The comparative test was carried out with an array of 48 electrodes spaced 2 meters.

4. Conductive textile sachets electrodes

Conductive textile sachets electrodes are realized with a commercial fabric (Holland Shielding Systems BV) made of polyester (65±5%) metallized with copper (20±2 %) and Nickel (15±2 %). Each sachet was realized with square pieces of 30 cm x 30 cm (the textile can be easily cut with sewing scissors), which were filled with 300 g of fine sand. The sachet is sealed with thin zip ties in such a way to leave a flake at the top where is possible to link the ERT cord clips. The cost to produce one conductive textile sachet electrode is about 15 euros, mainly due to the value of the metallic fabric, and the manufacturing of one sachet takes few minutes.

5. Data acquisition

In each test site, the ERT measurements have been collected with the same acquisition parameters and georesistivimeter (Syscal Pro, Iris Instruments). The datasets have been acquired with a dipole-dipole acquisition scheme with multiple dipole length, a stacking range between 3-6 (standard deviation threshold 5%), and with direct-reciprocal configuration to obtain a reliable estimation of the data error (Binley et al., 2015). Firstly, we collected the measurements with steel-spikes

electrodes hammered between the rocks and coupled with sponges soaked in salt water (e.g. Figure 1A). Subsequently, the same ERT array was measured using the conductive textile sachets electrodes pushed between the boulders and moistened with salt water (e.g. Figure 1B).

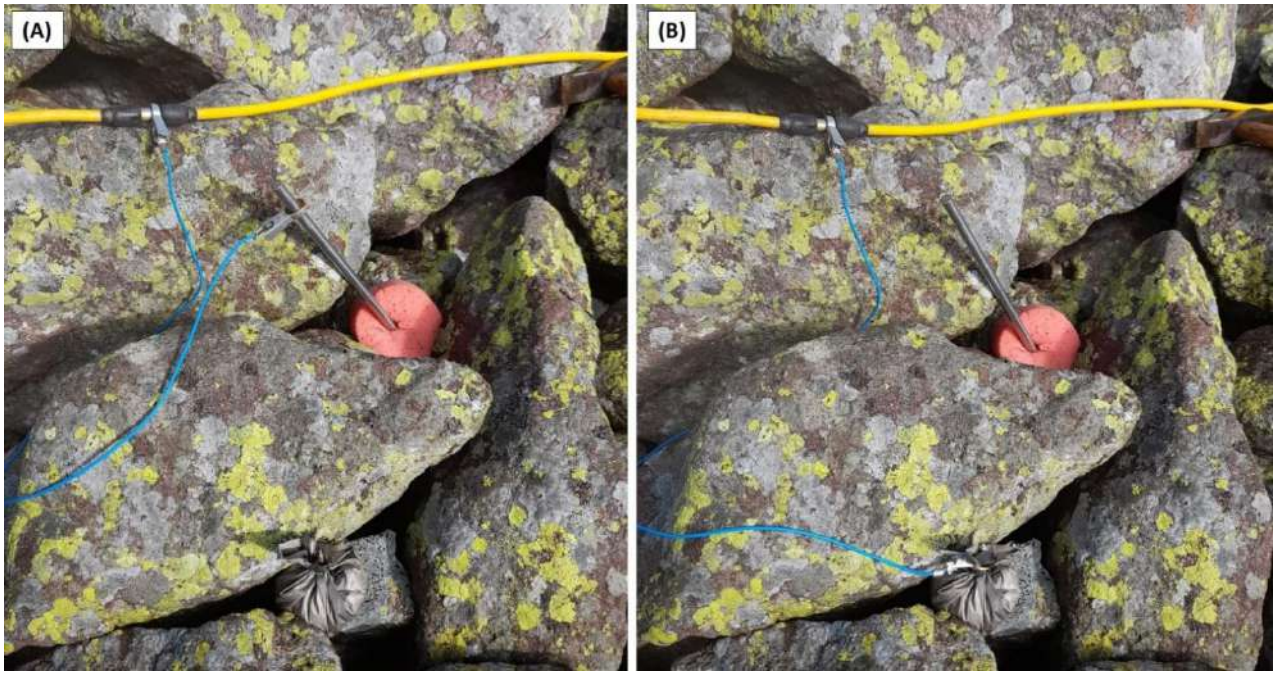

Figure 1. A) Example of measurements collected with steel-spike electrodes hammered between the boulders and coupled with sponges soaked in salt-water. B) Example of measurements collected with conductive textile sachets electrodes pushed between the boulders and wet with salt-water. Pictures realized during the comparative test performed on the inactive rock glacier of Sadole.

6. Data processing

To evaluate the reliability of the conductive textile sachets we compared the contact resistances, the injected electrical current, the measured apparent resistivities, the quadrupoles reciprocal error, and the inverted resistivity models obtained with the measurements collected with the different electrode's approaches. A statistical analysis was carried out following the approach proposed by Bast et al. (2015), using R (R-core-Team, 2022). Violin plots have been used for the data exploration, which include both the density distribution of the data and notched box plots. The robust Spearman correlation coefficient was calculated for each of the five variables.

To statistically compare the results obtained with steel-spikes electrodes and conductive textile sachets electrodes, for each site and variable, we fitted a robust linear regression model with an extended MM estimator (using the R package *robustbase* - Rousseeuw et al., 2009). Diagnostic regression plots were realized to verify that the model assumptions were met. Finally, the inverted resistivity models (inversion modelling performed with ResIPy – Blanchy et al. (2020)) are plotted and compared to evaluate the differences.

Discussion

The obtained results, which will be presented during the 42nd National Conference of the GNGTS 2024 in Ferrara (Italy), clearly demonstrate that conductive textile sachets electrodes can be successfully used to collect reliable ERT datasets in environments with debris and coarse-blocky surface, decreasing the time requested to deploy the investigation line. Consequently, applying this alternative electrode approach in future ERT measurements performed on rock glaciers, would allow to acquire measurements more rapidly, and the opportunity to collect more survey lines (e.g. realization of pseudo-3D geometries) extending the characterization of the investigated mountain permafrost area.

eferences

Bast, A., Wilcke, W., Graf, F., Lüscher, P., and Gärtner, H.; 2015: A simplified and rapid technique to determine an aggregate stability coefficient in coarse grained soils, CATENA, 127, 170-176, https://doi.org/10.1016/j.catena.2014.11.017.

Binley, A.; 2015: Tools and Techniques: Electrical Methods, in: Treatise on Geophysics (Second Edition), edited by: Schubert, G., Elsevier, Oxford, 233-259, https://doi.org/10.1016/B978-0-444-53802-4.00192-5.

Blanchy, G., Saneiyan, S., Boyd, J., McLachlan, P., and Binley, A.; 2020: ResIPy, an intuitive open source software for complex geoelectrical inversion/modeling, Computers & Geosciences, 137, 104423, https://doi.org/10.1016/j.cageo.2020.104423.

Buckel, J., Mudler, J., Gardeweg, R., Hauck, C., Hilbich, C., Frauenfelder, R., Kneisel, C., Buchelt, S., Blöthe, J. H., Hördt, A., and Bücker, M.; 2023: Identifying mountain permafrost degradation by repeating historical electrical resistivity tomography (ERT) measurements, The Cryosphere, 17, 2919–2940. https://doi.org/10.5194/tc-17-2919-2023.

Day-Lewis, F.D., Johnson, C.D., Singha, K., Lane, J.W.J.; 2008: Best practices in electrical resistivity imaging: Data collection and processing, and application to data from Corinna, Maine. In: An Administrative Report for the United States Environmental Protection Agency Region, p. 1.

Hauck, C. and Kneisel, C.; 2008: Applied Geophysics in Periglacial Environments, Cambridge University Press, ISBN 9780521889667.

Martin, S., Campedel, P., Ivy-Ochs, S., Viganò, A., Alfimov, V., Vockenhuber, C., ... & Rigo, M.; 2014: Lavini di Marco (Trentino, Italy): 36Cl exposure dating of a polyphase rock avalanche. Quaternary Geochronology, 19, 106-116.. https://doi.org/10.1016/j.quageo.2013.08.003.

Pavoni, M., Carrera, A., Boaga, J.; 2022: Improving the galvanic contact resistance for geoelectrical measurements in debris areas: a case study. Near Surf. Geophys. https://doi.org/10.1002/nsg.12192.

Pavoni, M., Boaga, J., Carrera, A., Zuecco, G., Carturan, L., & Zumiani, M.; 2023: Brief communication: Mountain permafrost acts as an aquitard during an infiltration experiment monitored with electrical resistivity tomography time-lapse measurements. The Cryosphere, 17(4), 1601-1607. https://doi.org/10.5194/tc-17-1601-2023.

Rousseeuw, P., Croux, C., Todorov, V., Ruckstuhl, A., Salibian-Barrera, M., Verbeke, T., Koller, M., and Maechler, M.; 2009: Robustbase: basic robust statistics, R package version 0.4-5, URL http:// CRAN. R-project. org/package= robustbase.

R-core-Team (2022): A Language and Environment for Statistical Computing, R Foundation for Statistical Computing. https://www.R-project.org (4.2.2) [code].

Corresponding author: mirko.pavoni@phd.unipd.it jacopo.boaga@unipd.it

Integrating cross-gradient joint inversion of ERT and SRT data and unsupervised machine learning on structured meshes incorporating topography

G. Penta de Peppo[1], M. Cercato[1], G. De Donno[1]

[1] *"Sapienza" University of Rome – DICEA*

Introduction

Among the geophysical methods applied for Civil and Environmental Engineering, the combined use of electrical resistivity tomography (ERT) and seismic refraction tomography (SRT) has shown to be effective for investigating the hydrogeological framework where civil structures and infrastructures are located, since these high-resolution methods are highly sensitive to different physical properties of the subsurface. Combining them in a coupled inversion scheme can significantly improve model reconstruction, so that the resulting subsurface models are more consistent and reliable than those obtained by comparing the results of individual inversions (Doetsch et al., 2010). During the last decades coupled inversions have become increasingly popular, in particular those involving one or more common additional terms in the objective function to be minimized, even though their practical implementation can be complex.

The structural gradient-based joint inversion approach is valid when changes in the geophysical properties are aligned, which is a reasonable assumption in a wide range of scenarios. The huge number of real-world case studies suggests that the cross-gradient joint inversion introduced by Gallardo and Meju (2004) is presently one of the most robust approaches. Currently, there are many applications of cross-gradient joint inversion on structured meshes with flat topography, but such algorithms are usually unable to manage non-flat surfaces. Jordi et al. (2020) developed a novel scheme on unstructured meshes, which can obviously adapt also to not-flat topographies, but for this purpose they modified the original cross-gradient method, which considers the direct neighbourhood of a single cell. We developed a new cross-gradient joint inversion routine in Python to process apparent resistivity and travel-time data incorporating topography, without modifying the original approach from Gallardo and Meju (2004) whose effectiveness is well demonstrated. In order to assess the impact of the coupled inversion scheme in both qualitative and quantitative terms a new standardization of the cross-gradient parameter is proposed ("Normalized cross-gradient", NCG). After the joint inversion procedure, an unsupervised machine learning algorithm is applied for improving the final interpretation by integrating the two output models into a single cross-section. Our approach is applied to both synthetic and field examples related to the application of ERT and SRT techniques to Civil and Environmental Engineering.

Individual inversions are carried out through the open-source pyGIMLi package (Rücker et al., 2017) properly adapted to work with the newly implemented structured mesh, and, for better comparison between separate and joint inversion results, the same inversion parameters, including regularization settings, initial model and forward modelling are used during each inversion step.

Method

Gallardo and Meju (2004) developed a structural procedure for two-dimensional simultaneous joint inversion in which the cross-gradient penalty function is applied to improve the resolution of common boundaries. This dimensionless function, which defines the geometrical similarity of two models as a distribution of gradients, is defined as:

$$t_{CG}(x,y,z) = m_r(x,y,z)m_v(x,y,z) \tag{1}$$

where $\mathbf{m}_r$ and $\mathbf{m}_v$ are resistivity and seismic velocity models, in our work variable in a two-dimensional space.

Adding the term in Eq.1 to the objective function, we obtain:

$$(m_r, m_v) = \left\| \frac{D_r\left(f(m_r) - d_r\right)}{D_v\left(f(m_v) - d_v\right)} \right\| + \frac{\lambda_r}{\lambda_v} \left\| \frac{C_r m_r}{C_v m_v} \right\| + \lambda_{CG} \left\| t_{CG}(m_r, m_v) \right\| \rightarrow min \tag{2}$$

In Eq.2 $\mathbf{D}_r$ and $\mathbf{D}_v$ are data weighting matrices, f($\mathbf{m}_r$) and f($\mathbf{m}_v$) the forward responses, $\mathbf{d}_r$ and $\mathbf{d}_v$ the observed data vectors, λ_r and λ_v weighting factors, $\mathbf{C}_r$ and $\mathbf{C}_v$ regularization matrices and λ_{CG} the cross-gradient weighting term. The objective function is nonlinear, since forward problems as well as the cross-gradient constraint are nonlinear, so to minimize it we used a first-order Taylor expansion (i.e. the Gauss-Newton method) and consequently solved the resulting system using the conjugate gradient algorithm.

The visual representation of the unchanged cross-gradient is rather complex, as it varies by several orders of magnitude and very differently from case to case, preventing a consistently accurate mode. Gallardo and Meju (2004) represented this quantity setting a minimum and maximum threshold. Observing that the unvaried cross-gradient always showed a Gaussian distribution, we defined a new standardization of it shown in Eq.3:

$$NCG = \frac{\left| t_{CG} \right|}{\left| t_{CG} \right|_{68}} \tag{3}$$

where $|t_{CG}|_{68}$ is the sixty-eighth percentile (a standard deviation threshold) of cross-gradient's absolute value distribution and the previous ratio is calculated for each cell of the mesh. This term, plotted between 0 and 10 compressing the variation between 1 and 10 showed the ability to well represent any case, overcoming the bottleneck of the unchanged cross-gradient visualization.

As an auxiliary tool we applied a fuzzy c-means (FCM) algorithm (Bezdek, 1981) to both individually and jointly inverted models yielding quantitative integrated cross-sections which resemble both models. FCM minimizes within-cluster variances (squared Euclidean distances) through an iterative process that assigns points to clusters in a probabilistic way (Paasche et al., 2010) reducing the objective function:

$$J = \sum_{i=1}^{c} \sum_{j=1}^{n} (u_{ij})^f \left\| d_j - v_i \right\|^2 \quad (4)$$

In Eq.4 n is the number of data points, c the number of clusters, u_{ij} the degree of membership of data point $\mathbf{d}_j$ to cluster i defined by its center $\mathbf{v}_i$ and f is the weighting exponent, set as 2. Finally, the output of fuzzy clustering is arranged in a unique plot developed by modifying the approach after Paasche et al. (2010), where primary colors denote different clusters while color saturation is proportional to the degree of membership to the assigned cluster.

Synthetic example

The synthetic example (Fig.1a) simulates a road embankment, in which a surface layer (ρ = 10 Ωm, v_P = 600 m/s) overlays an harder stabilising high-resistivity base (ρ = 1000 Ωm, v_P = 1800 m/s), both lying over a lower-resistivity and stiffer bedrock (ρ = 100 Ωm, v_P = 3000 m/s). Synthetic ERT dataset was generated by using 48 electrodes spaced 0.5 m apart in a dipole-dipole array with a maximum dipole length a_{max}=5 and a maximum dipole separation n_{max}=6. The resulting 945 apparent resistivity data points were contaminated with a zero-mean 3% Gaussian error. Analogously, for SRT geophones were located at the same electrode positions, simulating a shot every two geophones. A zero-mean Gaussian noise having a 0.1 ms standard deviation (median travel-time is about 5 ms) was added to the 1128 traveltime measurements. Results from separate inversions are shown in Fig.1b. The surface between superficial and intermediate layers, as well as the lateral extent of the latter are well defined in resistivity section, while the transition from the base to the bedrock is not well reproduced. Structural joint inversion (Fig.1c) highly improves the resistivity model, so that the base is properly placed where modelled with a significant upgrading in vertical reconstruction; jointly inverted velocity model exhibits an enhancement in a sharper transition from the superficial layer to the deeper ones. The NCG values (Fig.1d) from individual inversions are generally higher compared to those from the joint inversion, particularly in the area below the middle layer and in the transition between surface layer and bedrock. Finally, cluster analysis (Fig.1e) from jointly inverted models shows a better reconstruction, especially for the middle cluster (cluster no. 3) which is properly reconstructed within its real boundaries, and the bottom

layer (cluster no. 2) looks uniformed toned, improving the reconstruction compared to that achieved by individual inversion.

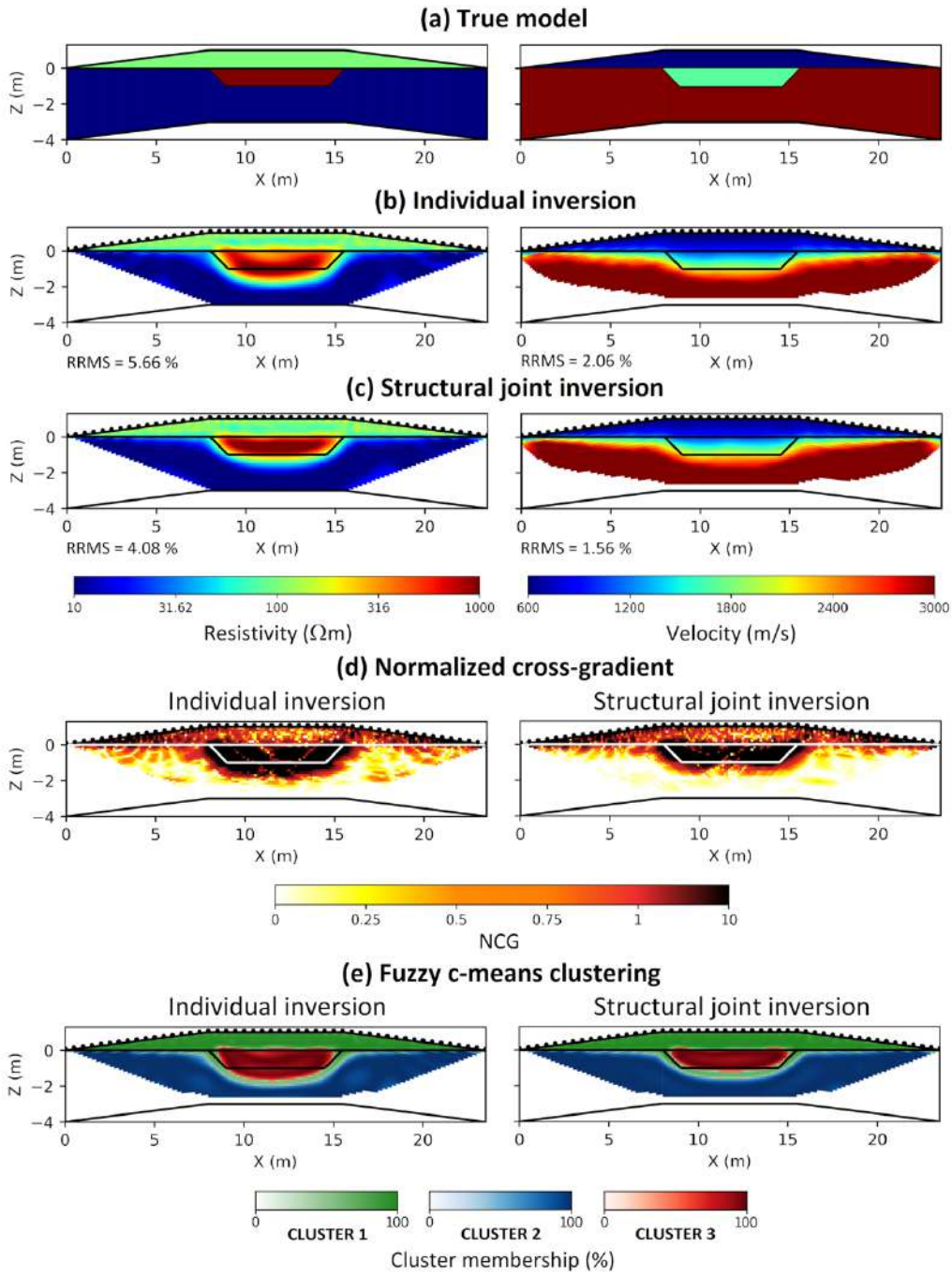

Figure 1. Synthetic example: (a) true model, (b) individual inversion, (c) cross-gradient joint inversion, (d) normalized cross-gradient, (e) fuzzy c-means clustering.

Field case study

The field case study is the Penne concrete dam located in central Italy (around 130 km east of Rome) and built in the second half of the sixties as a reservoir for irrigation (Fig. 2a). The hydro-geological layout of the site consists of Pliocene marly flysch having low permeability (hydraulic conductivity $K < 10^{-6}$ m/s), covered by Holocene ancient and recent alluvial deposits of the Tavo River. The alluvium is subdivided into a fine-grained shallower unit (clay and sandy silt) and a

coarse-grained high-permeable (K > 10^{-2} m/s) deeper one (sand and gravel). The dam was operating with a maximum water level well below the originally designed working conditions (256 m a.s.l.), since seepage phenomena occurring at the right abutment of the reservoir were confirmed by piezometric measurements that showed an increase of groundwater level downstream, which occurred when the reservoir level was higher than 250 m a.s.l. (Fig. 2b). Therefore, assessing the thickness and lateral extension of the coarse-graded highly permeable unit is pivotal for a correct design of the planned rehabilitation intervention (cut-off wall).

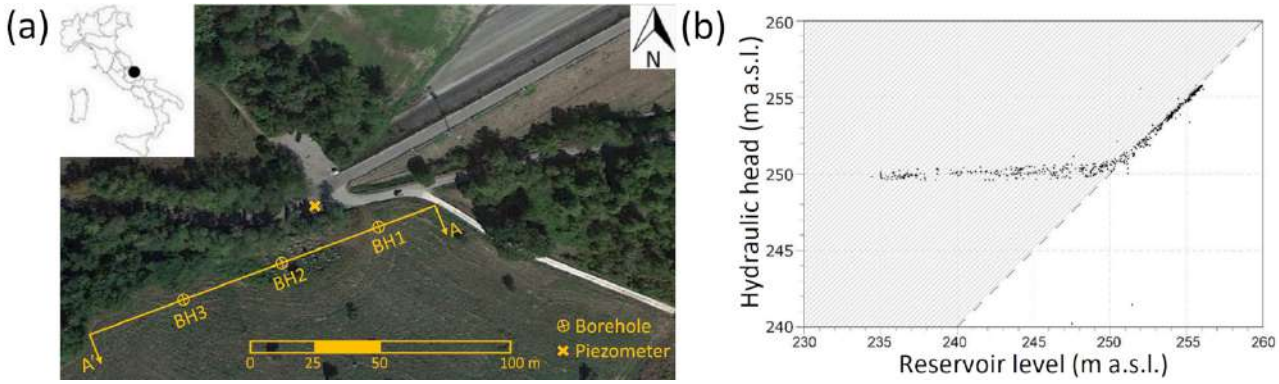

Figure 2. Penne case study (Central Italy): (a) aerial view with location of the ERT/SRT line and of the three boreholes; (b) hydraulic head logged as a function of the reservoir level (after Cardarelli, Cercato and De Donno, 2018).

Both ERT e SRT were performed along a 142 m alignment (Fig. 2a), with equally 2 m spaced sensor points (electrodes and geophones locations). ERT profile was acquired using the IRIS Instruments Syscal Pro resistivity-meter with 48 stainless steel electrodes in a pole-dipole array configuration, while P-wave seismic data were recorded employing a 48-channel system of 8 Hz vertical geophones by running a shot every two geophones using an 8-gauge Minibang shotgun. Three boreholes spaced 40 m apart along the geophysical line were drilled down the alignment for validating the geophysical surface investigations (Fig.2a). Results from individual inversion (Fig.3a) exhibit a three-layer geometry: low resistivity and P-wave velocity values (10-40 Ωm, 400-800 m/s) at shallow depths indicate the presence of the fine-grained alluvial deposits, followed by a less conductive formation (ρ = 100-300 Ωm, v_P = 1000-1800 m/s) that can be linked to the coarse-graded alluvial material and by a deep low-resistivity stiffer medium (ρ = 5-10 Ωm, v_P > 1800 m/s) revealing the presence of the flysch unit. Resistivity model clearly shows the thickness of the sand and gravel layer (about 7-10 m), but its lateral extent cannot be accurately determined in an area of lower resolution, even if it seems to vanish in the second part of section. Boreholes clarify the geometry of this layer: it has a thickness of 7 m (from 253 to 246 m a.s.l.) in BH1 (x = 23.5 m) and 8 m (at the same elevation) in BH2 (x = 63.5 m) confirming it has a sub-horizontal trend, but it was not detected in BH3 (x = 103.5 m), so we can deduce it ends between 63.5 and 103.5 m. The jointly inverted resistivity model (Fig.3b) displays a similar thickness of the coarse-graded material but its lateral extent is significantly reduced, ending around 80-85 m in good agreement with borehole data. Conversely, the P-wave velocity model remains nearly unchanged. The NCG index (Fig.3c) shows a decrease in the higher values at the central zone of the section, where the joint approach conspicuously impacts in better describing the termination of the sand and gravel unit. Finally, the quantitative integration of geophysical models through the results of cluster analysis is able to well

reconstruct the three main geological units of the study area (Fig.3d) and highlights the benefit of the joint approach, as cluster no. 3 ends abruptly at x = 81 m rather than extending endlessly towards last part of the section.

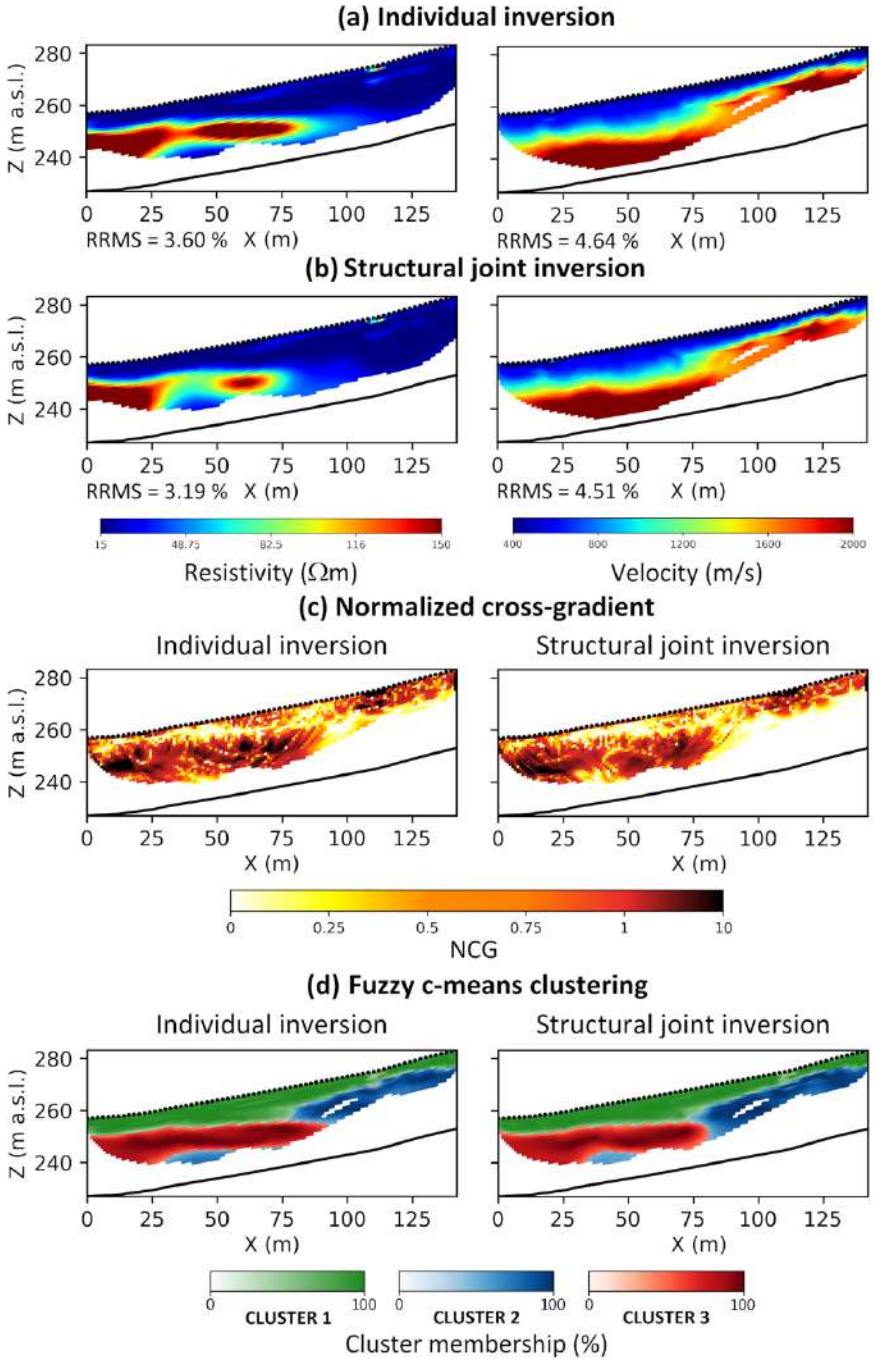

Figure 3. Field case study at the Penne dam (Central Italy): (a) individual inversion, (b) cross-gradient joint inversion, (c) normalized cross-gradient, (d) fuzzy c-means clustering.

Conclusions

A cross-gradient algorithm to jointly inverted ERT an SRT data on structured mesh incorporating topography was presented. The benefit of the proposed approach was quantitatively evaluated in terms of a new standardization of the cross-gradient parameter to assess the impact of the coupled scheme and a fuzzy c-means analysis to improve the final interpretation phase. A synthetic

example showed the reliability of the proposed algorithm for improving accuracy in model reconstruction in comparison to individual inversions. Then, the application to a field case study (investigation of the lateral abutment of a concrete dam) revealed the benefit of such an algorithm in a complex hydrogeological scenario, where the jointly inverted models are in better agreement with boreholes information, compared to individual inversions. The improvement provided by the coupled procedure with respect to single inversions is also strengthened by the lower root-mean-square errors and NCG values especially in the low-sensitivity deep zones and close to the interfaces between different layers. Finally, the fuzzy c-means analysis can allow for a final quantitative interpretation which resembles the effective layering of the case study, giving also an assessment of the reliability of the reconstruction by means of the membership values. Therefore, the proposed approach can be effective in improving the geophysical reconstruction for complex cases, where resistivity and P-wave velocities are expected to have sharp lateral and vertical changes.

References

Bezdek J. C.; 1981: Pattern recognition with fuzzy objective function algorithms. Plenum Press.

Cardarelli E., Cercato M. and De Donno G.; 2018: Surface and borehole geophysics for the rehabilitation of a concrete dam (Penne, Central Italy). Engineering Geology.

Doetsch J., Linde N., Coscia I., Greenhalgh S. A. and Green A. G.; 2010: Zonation for 3D aquifer characterization based on joint inversions of multimethod crosshole geophysical data. Geophysics.

Gallardo L. A. and Meju M. A.; 2004: Joint Two-Dimensional DC Resistivity and Seismic Travel Time Inversion with Cross-Gradients Constraints. Journal of Geophysical Research.

Jordi C., Doetsch J., Günther T., Schmelzbach C., Maurer H. and Robertsson J. O. A.; 2020: Structural joint inversion on irregular meshes. Geophysical Journal International.

Paasche H., Tronicke J. and Dietrich P.; 2010: Automated integration of partially colocated models: Subsurface zonation using a modified fuzzy c-means cluster analysis algorithm. Geophysics.

Rücker C., Günther T. and Wagner F. M.; 2017: pyGIMLi: An open-source library for modelling and inversion in geophysics. Computers and Geosciences.

Corresponding author: guido.pentadepeppo@uniroma1.it

In situ geophysical techniques for the hydrogeological hazard assessment in urban area: the Gorgoglione (Basilicata region, Southern Italy) case study

A. Perrone[1], J. Bellanova[1], G. Calamita[1], F. Falabella[2], M.R. Gallipoli[1], E. Gueguen[1], A. Pepe[2], S. Piscitelli[1], V. Serlenga[1], T.A. Stabile[1]

[1] Consiglio Nazionale delle Ricerche, Istituto di metodologie per l'analisi ambientale (IMAA) - Italy

[2] Consiglio Nazionale delle Ricerche, Istituto per il Rilevamento Elettromagnetico dell'Ambiente (IREA) - Italy

The geomorphological fragility of the Basilicata territory (southern Italy) and, in particular, the vulnerability to landslides can be considered the result of various causes such as the lithology of the outcropping terrain, the morphology of the reliefs, neotectonics, seismicity, climate and vegetation.

Since the 17th century, landslides have been recognized and recorded as a problem for the Lucanian territory (Boenzi, 1974; Stuart, 1993). In the 18th century, the changes in land use significantly increased the number of landslides. Subsequently other factors such as the experience of poorly designed and poorly constructed urban settlements, the defective disposal of water and wastewater, the limited consolidation against landslides and the progressive abandonment of land around inhabited centers territory, have contributed in accelerating the occurrence of landslides (Stuart, 1993; Vita-Finzi, 1969). Climate change and the incidence of extreme rainfall events in an already very fragile landscape have also played an important role in this acceleration into the 20th and 21st centuries.

Currently all 131 municipalities in Basilicata Region are involved by landslides (Inventory of Landslide Phenomena in Italy, IFFI Project 2020) and in 83 of them the landslides have affected the continuous and discontinuous urban fabric as well as industrial or commercial areas. In many cases, as for example in the Gorgoglione test site, the state of emergency has been declared with evacuation orders for residential buildings and commercial activities and, where necessary, also with the demolition of historic buildings (Perrone et al., 2021; Calamita et al., 2023).

Traditional direct techniques, such as geotechnical boreholes, offer point-specific information but can be highly invasive, leading to potential damage to economic and cultural resources such as archaeological sites and underground utilities, especially in the upper layers of the subsoil. In the

context of investigating landslides in urban areas, alternative approaches may be more suitable. A significant contribution can be achieved through the combined utilization of remote sensing and in situ geophysical techniques (Perrone et al., 2006; de Bari et al., 2011).

In this work, ground based SAR (GB-SAR) interferometry, electrical resistivity tomography (ERT) and passive seismic techniques have been integrated for investigating the phenomenon affecting the Gorgoglione urban area, located in the south-western part of Matera Province (Basilicata Region, southern Italy) on a hilly area at about 800 m a.s.l. (Fig.1). The GB-SAR results provided information on the activity status of the phenomenon. The ERT and the single-station seismic ambient noise measurements allowed the reconstruction of the subsoil geological setting, the identification of physical discontinuities correlated with lithological boundaries and sliding surfaces and the location of high water content areas.

This information was used to assess the landslide residual risk, to plan and implement the risk mitigation actions and to correctly design the remediation works.

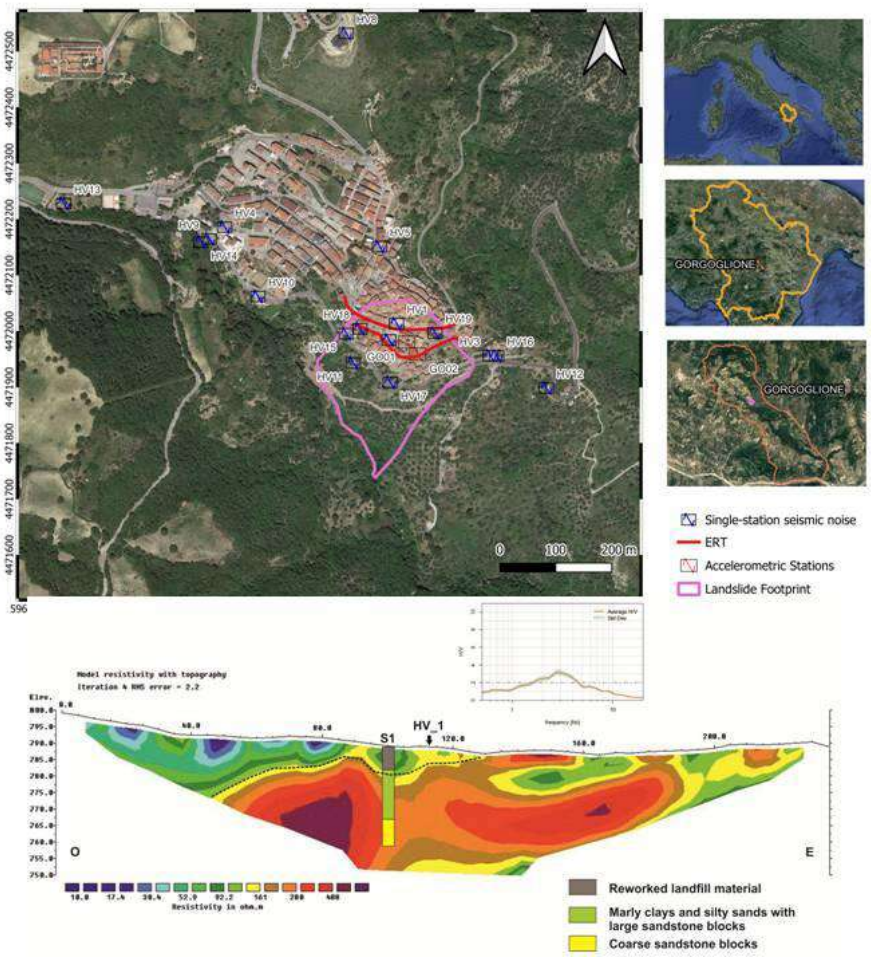

Fig. 1 – Map of Gorgoglione test site (Basilicata region, southern Italy) with location of the in-situ geophysical measurements carried out in the urban area.

References

Boenzi F.; 1974: Il dissesto idrogeologico in Basilicata dalla fine del 1600 ad oggi. Pages 23-28 in Atti del IV Simposio Nazionale sulla Conservazione della Natura, I, Bari.

Calamita G., Gallipoli M.R., Gueguen E., Sinisi R., Summa V., Vignola L., Stabile T.A., Bellanova J., Piscitelli S., Perrone A.; 2023: Integrated geophysical and geological surveys reveal new details of the large Montescaglioso (southern Italy) landslide of December 2013. Engineering geology 313 , pp. Art.n.106984-1–Art.n.106984-16.

de Bari C., Lapenna V., Perrone A., Puglisi C., Sdao F.; 2011: Digital photogrammetric analysis and electrical resistivity tomography for investigating the Picerno landslide (Basilicata region, southern Italy). Geomorphology 133, 34–46

IFFI Project (Inventario dei Fenomeni Franosi in Italia). ISPRA, Dipartimento Difesa del Suolo, Servizio Geologico d'Italia. Available online: http://www.progettoiffi.isprambiente.it/cartanetiffi/ (accessed on May 2020)

Perrone A., Canora F., Calamita G., Bellanova J., Serlenga V., Panebianco S., Tragni N., Piscitelli S., Vignola L., Doglioni A., Simeone V., Sdao F., Lapenna V.; 2020: A multidisciplinary approach for landslide residual risk assessment: the Pomarico landslide (Basilicata Region, Southern Italy) case study. Landslides 18, 353–365.

Perrone A., Zeni G., Piscitelli S., Pepe A., Loperte A., Lapenna V., Lanari R.; 2006: Joint analysis of SAR interferometry and electrical resistivity tomography surveys for investigating ground deformation: the case-study of Satriano di Lucania (Potenza, Italy). Engineering Geology 88, 260–273.

Stuart O.; 1993: 20-th century urban landslides in the Basilicata Region of Italy. Environmental Management 17 (4), 433-444.

Vita-Finzi C.; 1969: The Mediterranean valleys: geological changes in historical times. Cambridge University Press, Cambridge, UK

Corresponding author: angela.perrone@cnr.it

Geophysical-based approach for studying the submarine groundwater discharge: the SUBGEO Project

G. Romano[1], L. Capozzoli[2], V. Lapenna[2], M. Polemio[3]

[1] Department of Earth and Geo-Environmental Sciences, University of Bari Aldo Moro, Piazza Umberto I, 70121 Bari, Italy
[2] Institute of Methodologies for Environmental Analysis, National Research Council of Italy (IMAA CNR), C. da S. Loja—Zona Industriale, Tito Scalo, 85050 Potenza, Italy
[3] Research Institute for Hydrogeological Protection, National Research Council of Italy (IRPI CNR) 70126 Bari, Italy

The problem of water supply represents a priority for not only the Mediterranean Area but for the World if we consider the age-old problem of the drought exacerbated by the climate change events that are constantly seen [Jiao and Post, 2019]. Coastal aquifers are fundamental for water supply and innovative strategies are strongly required to detect and preserve water resources under increasing pressure. Developing new knowledge and innovative solutions for a systemic and inclusive approach of water management represents a big challenge for the scientific community.

Indeed, delineating coastal hydrogeologic structures, or hydrostratigraphy, is a crucial step for the characterization of groundwater flow and management of groundwater resources. Furthermore, hydrostratigraphic complexities play a fundamental role in the interactions occurring between coastal aquifers and marine ecosystems and influence the transport of solutes to coastal waters, and the response to climate change [Befus et al., 2014]. However, as coastal groundwater investigations are addressed to characterize and monitor the onshore resources and coastal fringe processes, the interactions between fresh groundwater within submarine aquifers remain poorly explored [Post et al., 2013; Knight et al., 2019]. The increasing water demand on the global scale because of per capita demand and population increases causes a strongly increasing exploitation of the available high-quality water resources, increasing the risk of salinization via mixing for seawater intrusion. These trends can be further worsened in large areas by the enduring effects of climate change. All these conditions are causing stress on the water resources of coastal aquifers. The management efforts require more knowledge of coastal springs and submarine groundwater discharge (SGD), to preserve residual fresh resources and to find the freshest possible groundwater for desalination [Polemio et al., 2020]. However, coastal areas, are challenging places for the application of geophysical methods due to their being highly dynamic and fragile systems and because they are constituted by two different operational conditions: land onshore and sea offshore. At present time, the relatively few surveys aimed to characterize the coastal areas are usually performed by joint together land and marine surveys. This practice, whereas of simple applications, has a relevant limit. The boundary area between the sea and the land, the area close

to the shore, remains poorly or not investigated either by the land surveyor by the marine one. Consequently, missing information on the area where seawater and groundwater start to interact, the reconstruction of the hydrogeological processes in the coastal area may be inaccurate or incomplete.

In this framework, the University of Bari (UNIBA) and the two CNR Institutes, IMAA and IRPI, have proposed the two-year Research Project of National Relevance (PRIN PNRR 2022) SUBGEO (Submarine groundwater discharge analysis with an innovative and integrated geophysical approach) addressed to develop and employ an innovative strategy based on the integrated multiscale and multiresolution geophysical investigation approach for the coastal underground freshwater reservoir non-invasive characterization.

SUBGEO aims to setup an innovative investigation strategy able to furnish continuous information from the land to the sea useful to define the water fluxes dynamics. A two-level strategy is proposed. In the first level, the investigations will provide an expeditious and not expensive overall characterization of the geophysical framework of the investigated area). The second investigation level will include a more complex integration of electrical and electromagnetic geophysical methodologies and will be more informative. The expected results will consist of a multiscale and multiresolution subsoil characterization from land to sea, that crossing the shoreline, will not have any spatial informational gap. The outcome of the second investigation level will support the creation of optimized hydrogeological models of the investigated area and can also be directly used by the decision-maker to implement sustainable water resources management strategies.

SUBGEO is addressed to gain useful tools for the optimal and sustainable management of the coastal areas and resources, operating on the largest Italian coastal aquifer, the Apulia region where the coastal aquifers fed the highest concentration of submarine springs and SGD [Polemio, 2016]. The project will develop an innovative geophysical approach based on the integrated use of aerial, land, land-marine and marine geophysical electric and electromagnetic techniques to provide spatially continuous and high-resolution information on the subsoil structure from the offshore areas, where the outward fluxes mix with the seawater, to the onshore ones. Finally, SUBGEO will be tuned by small-scale laboratory experiments and numerical simulations to define the best acquisition procedures and check the sensitivity of the strategy for different subsurface conditions.

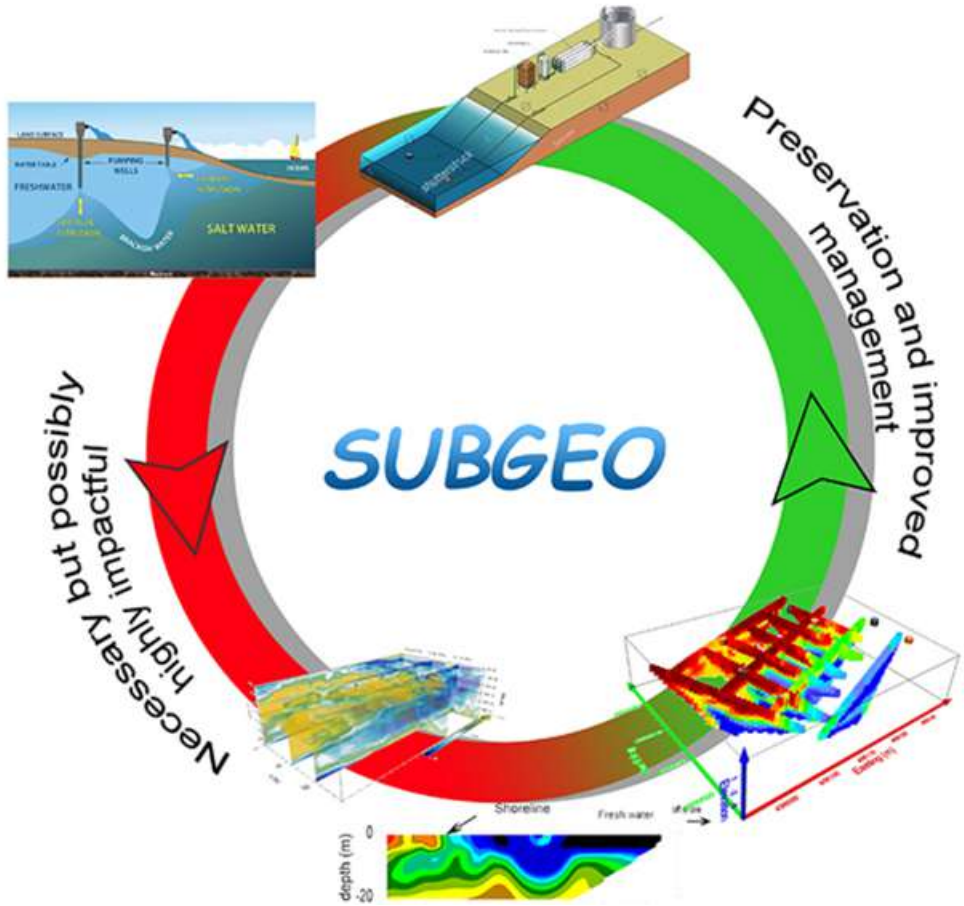

Fig. 1 - The proposed geophysical approach for characterizing coastal areas of SUBGEO

References

Befus et al., 2014, Geoelectrical signals of geologic and hydrologic processes in a fringing reef lagoon setting, J. Hydrol, 517, 10.1016/j.jhydrol.2014.05.070.

Jiao J., and V. Post, Coastal hydrogeology. Cambridge University Press, 2019.

Knight et al., 2019.Combined geophysical and analytical methods to estimate offshore freshwater extent, J. Hydrol, 576, 10.1016/j.jhydrol.2019.06.059

Polemio M., 2016, Monitoring and Management of Karstic Coastal Groundwater in a Changing Environment (Southern Italy) A Review of a Regional Experience. Water, 8, 10.3390/w8040148

Polemio, M. et al. 2020, Review of Utilization Management of Groundwater at Risk of Salinization. J. Water Resour. Plan. Manag, 146

Post et al., 2013, Offshore fresh groundwater reserves as a global phenomenon. Nature, 504, 10.1038/nature12858

Corresponding author: gerardo.romano@uniba.it

Integrated GPR and FDEM to detect brines pockets in Continental Antarctica

I. Santin[1], E. Forte[1], M. Guglielmin[2]

[1] Department of Mathematics, Informatics and Geosciences (University of Trieste, Italy)
[2] Department of Theoretical and Applied Science (University of Insubria, Italy)

Introduction

The extreme environmental condition of Antarctica and the presence of subcryospheric saline waters makes it one of the most relevant planetary analogues for Mars, especially since hypersaline brines were found on the red planet (*Martínez and Renno, 2013*). As a consequence, the interest on Antarctic brines have increased, especially to determine the lifeforms in these environments and their adaptability to extreme environmental conditions. From the geophysical point of view, brines are peculiar materials whose characteristics are strictly correlated with their salinity, density, temperature and pressure. Considering that, at liquid state, brines are hypersaline and therefore high-conductive solutions, electromagnetic (EM)-based methods, such as Ground Penetrating Radar (GPR) can be successfully exploited to detect and image brines pockets, although their EM signature on GPR data is not unequivocally defined (*Forte et al., 2020*). However, recently also Frequency-Domain Electromagnetic (FDEM) inductive methods are increasing their applications to glaciology, even though their effectiveness is not always fully demonstrated and, up to now, no applications to Antarctic brines detection have been reported.
We focus on Boulder Clay Glacier area (Victoria Land, East Antarctica), i.e. a coastal zone characterized by a glacier, its moraines and some perennially frozen lakes (*Guglielmin et al., 2009*). The area is located about 6 km SW from the Italian Antarctic Station (MZS in FIG.1A), close to the southern side of a gravel landing strip, built in 2019. Several boreholes have been dug both on the moraine, the glacier and some lakes, and at least three detected brines pockets have been sampled to study their prokaryotic (*Azzaro et al., 2021*) and fungal (*Sannino et al., 2020*) communities. In particular, Lake n.16 is neighbour with a CALM permafrost grid (FIG.1B), which is part of the CALM program aiming at the observation of the response of the active layer to climate change over multi-decadal time scales (*Guglielmin et al., 2009*). Such a grid has been relocated in its actual position in 2019 due to the landing strip building, and now it lies near a borehole discussed in *Sannino et al., 2020*. In this work, starting from the borehole dug in 2014 in which a liquid brine pocket was discovered, we proposed an integrated geophysical approach to define the EM signature of brine pockets, combining GPR and FDEM induction surveys. The geophysical characterization of brines pockets allows to deepen the investigation about the complex geomorphological settings of the area, providing a more constrained methodology to optimize the

position of future boreholes while developing and approach that can be exploited even in other geological, geomorphological, and glaciological situations.

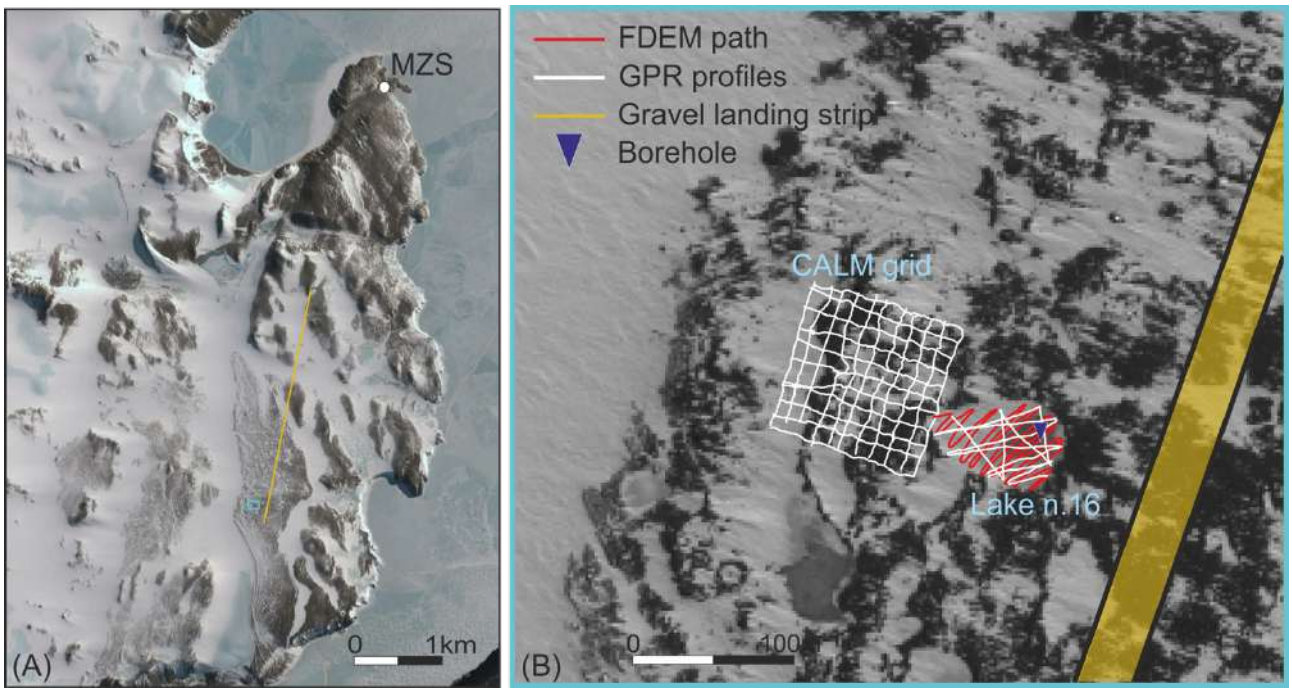

Fig. 1 – (A) Location map of CALM grid and Lake n.16 (light blue square) in Boulder Clay Glacier area (MZS: Mario Zucchelli Italian Station). (B) Ortophoto with superimposed the GPR profiles, in white, and the FDEM survey, in red. Yellow lines mark the position of the gravel landing strip.

Methods

During the XXXVIII Italian Expedition in Antarctica (November 2022), two GPR surveys were performed on the CALM grid and the neighbouring Lake n.16. On the latter, an FDEM survey was also collected. The 880 m-long FDEM dataset (red line in FIG.1B) was acquired with a CMD-2 probe (GF-Instruments), recording the mean conductivity value every 0.5 s, down to a maximum nominal depth of 2.5 m. The dataset is characterized by a high overall quality, with minimum and maximum values of 0.05 mS/m and 12 mS/m, respectively. The conductivity values were interpolated on a regular grid (2 m by 2 m) with a Kriging algorithm, obtaining the apparent conductivity map, shown in FIG.2. As far as the GPR surveys (white lines in FIG.1B), they were both performed with a ProEx GPR system (Malå Geoscience), equipped with 500 MHz shielded antennas. A basic processing flow was applied, including zero-time correction, band-pass filtering, amplitude recovery, depth conversion and topographic correction, considering a constant velocity of 0.17 m/ns (I.e. the typical value for pure clean glacial ice). To improve the EM characterization of brines pockets, the interpretation of CALM grid GPR dataset was supported by GPR attribute analysis, which already demonstrated their effectiveness in glacial environments (e.g. *Zhao et al., 2016*). We specifically focused on frequency-, phase- and texture-related attributes, integrating them during data interpretation.

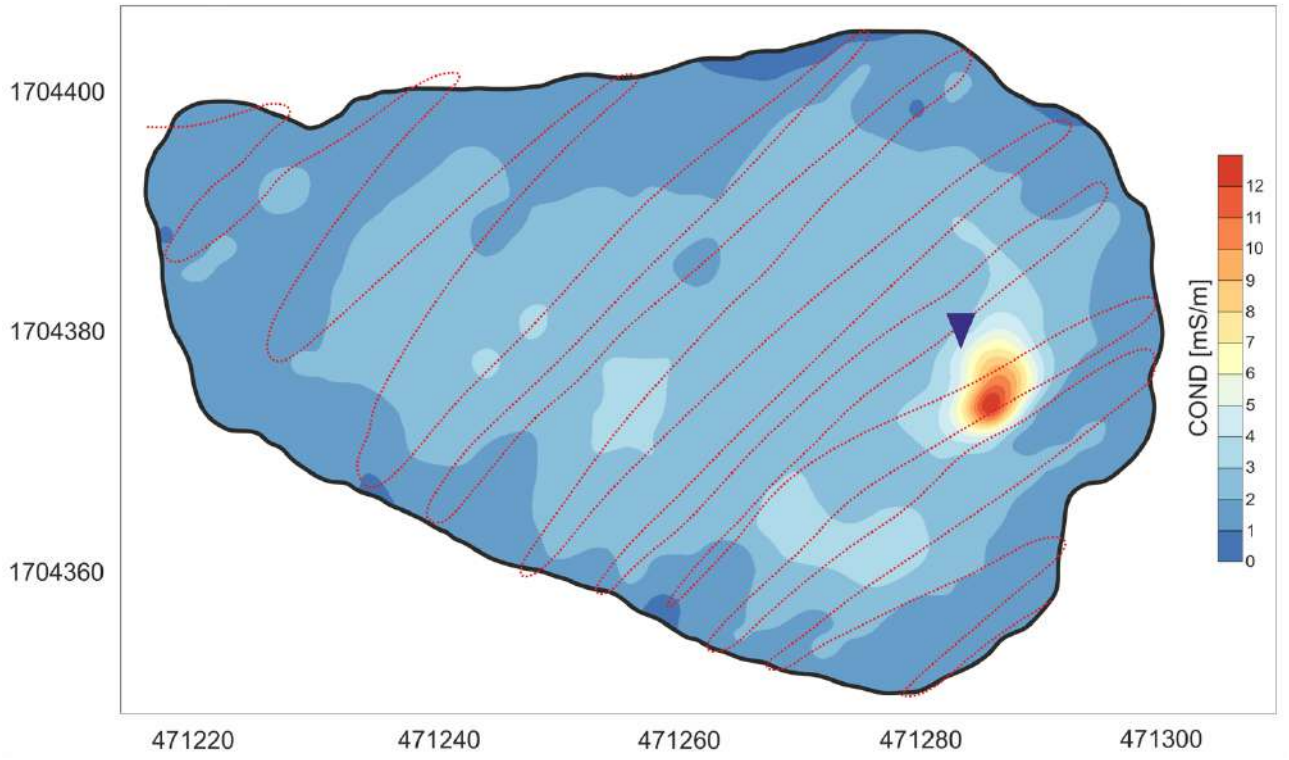

Fig. 2 – Apparent conductivity map down to a nominal depth of 2.5 m on Lake n.16. Red dotted line marks the path of the FDEM survey, while the blue triangle the location of borehole BC1 (taken from *Azzaro et al., 2021*).

Results and discussion

FIG.2 shows the mean apparent conductivity map of the Lake n.16 down to a maximum depth of about 2.5 m. It is characterized by a very low conductivity close to 0 mS/m, typical of the ice, however, a high conductivity spot is apparent, reaching a maximum value of more than 12 mS/m. In *Azzaro et al., 2021*, the borehole named BC1 whose location is marked in FIG.2 revealed the saltiest brines pocket of this lake at a depth of about 2.5 m; it is very close to the high conductivity spot highlighted by FDEM. It is interesting to note the accurate correlation between the information provided by the borehole and by the FDEM survey, both indicating the target depth at about 2.5 m, even considering the temporal interval of 8 years between the two surveys (2014 for the borehole and 2022 for the FDEM). GPR profiles in FIG.3A-3B cross close to the high conductivity spot and the borehole BC1 of *Azzaro et al., 2021.* On the two almost perpendicular GPR sections, it can be recognized the base of the lake as a high amplitude reflection at the bottom of the mainly transparent facies of the lake ice. However, the continuity of such horizon is interrupted near the BC1 borehole location, where the amplitude of the EM signal is strongly attenuated. Such extremely high attenuation is most likely produced by the high conductivity of the brines pocket, which limited the propagation of the EM signal. Such peculiar setting was found also on the GPR dataset of the neighbour CALM grid. FIG.3C shows the same high EM signal attenuation with the horizon interruption deepening, as described for Lake n.16. The spectral behaviour of the EM signal reveals a rapid decrease of frequency content, moving towards lower frequencies, corresponding to the transparent and high attenuated facies (red colour in FIG.3C'). In addition, the texture-related attributes highlight a more chaotic facies (FIG.3C''), possibly

suggesting fluids upwelling, while the phase-related attribute makes more evident the interruption of the continuity of all horizons across the highly attenuated facies.

It is remarkable to point that the GPR signature and response to the attributes analysis we performed on the GPR profiles of CALM grid, find a match with the outcomes described in *Forte et al., 2016* for other Antarctic coastal lakes. As a matter of fact, the accuracy of the match in terms of spectral behaviour and EM facies further validate the applicability of GPR as a low-time consuming method to identify hidden brines pockets. However, it is essential to point out that in some cases the signal is so attenuated that prevents the application of attributes analysis. Such situation occurs for instance on the GPR profiles of Lake n.16 where attributes analysis gave no remarkable results. Therefore, the integration of FDEM and GPR, allows to be more accurate and favourable about the presence of buried brines pockets.

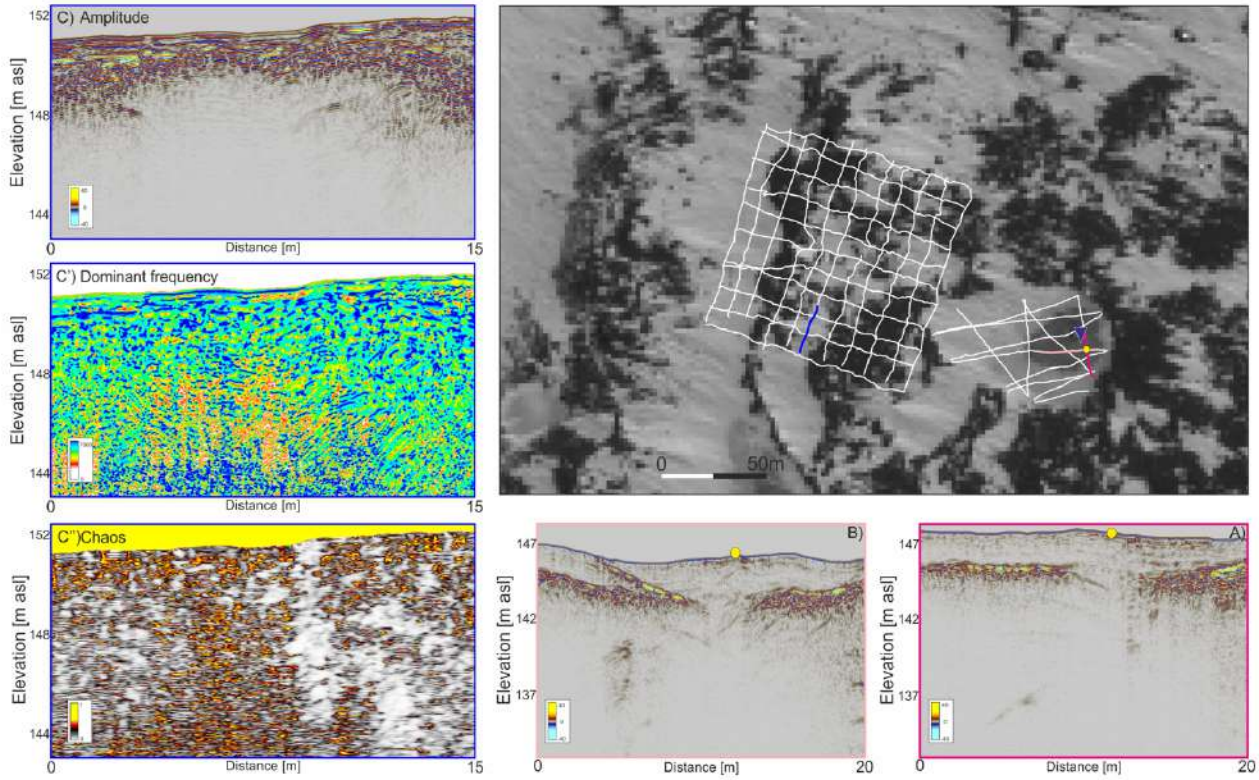

Fig. 3 – Exemplary GPR profiles on Lake n.16 (A, B) and on CALM grid (C, C', C''), both represented with white lines. C' and C'' display dominant frequency and chaos attributes, respectively, of profile C. Yellow dot marks the crossing point between A and B. Location of each GPR profile is highlighted by a coloured line: C, C', C'' with a blue line, while A and B with pink and magenta lines, respectively. Pink triangle marks the location of BC1.

Conclusion

We proposed a detailed analysis of the geophysical signature of Antarctic brines pockets, validated through boreholes. The integration of FDEM and GPR surveys allowed to characterize brines pockets in terms of high electrical conductivity and a peculiar EM facies, respectively. The high conductivity (up to more than 12 mS/m in the investigated area) related to the brines strongly affects the propagation of the EM wave generating an attenuated EM facies which is characterized, in addition to the low reflectivity, by a spectral shift to lower frequencies, horizons continuity

interruptions and an overall chaotic texture. The integrated peculiar and clear geophysical response of brines pockets can be exploited to effectively determine the presence of brines pockets and their approximated depth, thus resulting in a helpful strategy to map even large areas in which drill possible future boreholes for brines sampling.

Acknowledgements

This work was supported by grants CRYOVEG and IPECA from the National Antarctic Research Program (PNRA18_00288-D; PNRA18_00186-E). We gratefully acknowledge Schlumberger through the University of Trieste Petrel® interpretation package academic grant.

References

Azzaro M., Maimone G., La Ferla R., Cosenza A., Rappazzo A.C., Caruso G. et al.; 2021: The prokaryotic community in an extreme Antarctic environment: the brines of Boulder Clay lakes (Northern Victoria Land). Hydrobiologia, 848(8), 1837-1857. doi: 10.1007/s10750-021-04557-2

Forte, E., Dalle Fratte, M., Azzaro, M., Guglielmin, M.; 2016: Pressurized brines in continental Antarctica as a possible analogue of Mars. Scientific Reports, 6, 33158. doi: 10.1038/srep33158

Forte E., Dossi M., Guglielmin M.; 2020: The search for brines: GPR markers, proxies, and challenges. SEG Global Meeting Abstracts, 73-76. doi: 10.1190/gpr2020-020.1

Guglielmin M., Lewkowicz A.G., French H.M., Strini, A.; 2009: Lake-ice blisters, Terra Nova Bay area, Northern Victoria Land, Antarctica. Geografiska Annaler, 91, A(2), 99-111. doi: 10.1111/j.1468-0459.2009.00357.x

Martínez, G.M., Renno, N.O.; 2013: Water and Brines on Mars: Current Evidence and Implications for MSL. Space Science Reviews, 175, 29–51. doi: 10.1007/s11214-012-9956-3

Sannino C., Borruso L., Mezzasoma A., Battistel D., Zucconi L., Selbmann L. et al.; 2020. Intra- and inter-cores fungal diversity suggests interconnection of different habitats in an Antarctic frozen lake (Boulder Clay, Northern Victoria Land). Environmental Microbiology, 22(8), 3463-3477. doi: doi:10.1111/1462-2920.15117

Zhao W., Forte E., Colucci R.R., Pipan M.; 2016. High-resolution glacier imaging and characterization by means of GPR attribute analysis. Geophysical Journal International, 206(2), 1366–1374. doi: 10.1093/gji/ggw208

Seafloor morphology and very shallow stratigraphic information from acoustic data processing

C. Sauli and L. Baradello

Istituto Nazionale di Oceanografia e di Geofisica Sperimentale – OGS, Trieste.

Acoustic data acquired in Antarctica in 2006 and 2017 (PNRA projects Vild and Glevors) with the hull-mounted Chirp II DataSonics system aboard the N/R OGS Explora have been subjected to seismic processing to obtain a truly high-resolution data set, providing metric and sub-metric resolution, from which information on the very shallow stratigraphy can be obtained and increasing the possibility of correlation with sediment cores of the order of a few meters.

In particular, the processing of the 2006 data, originally stored in envelope mode (classical approach with Hilbert transform, Henkart, 2006), was possible after waveform recovery (Baradello et al., 2021), unlike the 2017 data, which were already stored in full-wave mode (only cross-correlation with the pilot sweep).

With the full-wave signal, the chirp data can be treated with traditional seismic processing, resulting in a significant improvement in signal-to-noise ratio (Quinn et al., 1997; Baradello, 2014) and an increase in lateral and vertical resolution. Ocean wave effects were attenuated by applying a non-surface-consistent static correction, while the true amplitude was recovered by applying the amplitude decay inversion function after spherical divergence. Predictive deconvolution (second zero of autocorrelation as gap length, 9 ms as operator length and 0.1 % white noise content) was applied for ripple attenuation.

The processing made the necessary changes to the sub-bottom profiles to overcome the noise problems due to the very rough sea during the recording phase and consequently improve the resolution and penetrability of the acoustic data. The possibility of visualizing with a certain continuity some internal reflectors in the first meters of the seabed, as well as the attempted correlation with the lithostratigraphic data derived from the core holes, allows us to analyze the geomorphology of some glacial landforms, even in the interior, and the acoustic facies.

Seafloor reflectivity mapping confirms the presence of some areas of greater hardness due to the possibly different lithology and physical/mechanical properties (i.e. greater compaction, dewatering) of glacial and glaciomarine sediments).

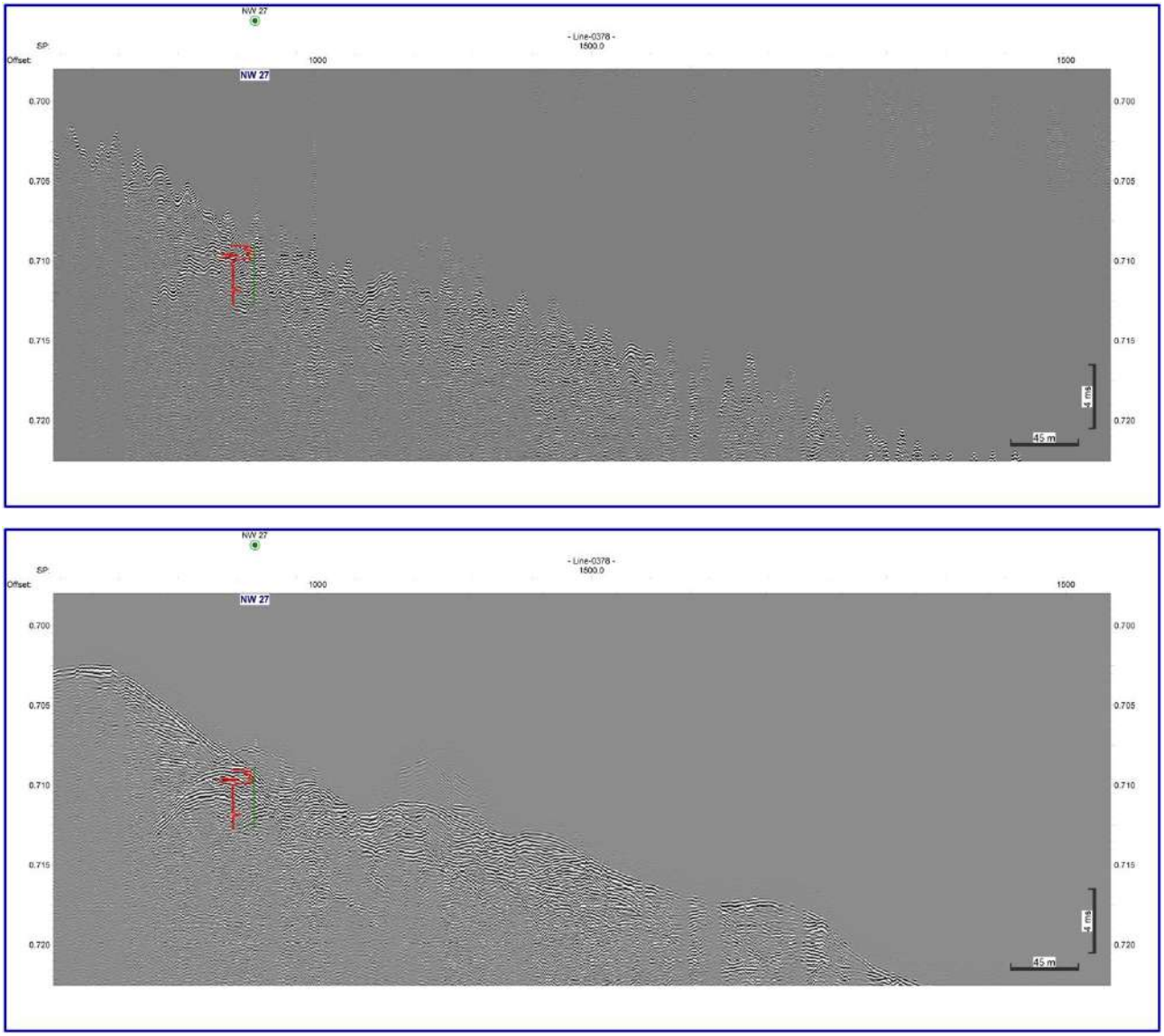

Fig.1 - Sub-bottom profile before(a) and after processing(b). Time/depth and susceptibility curve of a PNRA sediment core NW27, projected onto both profiles.

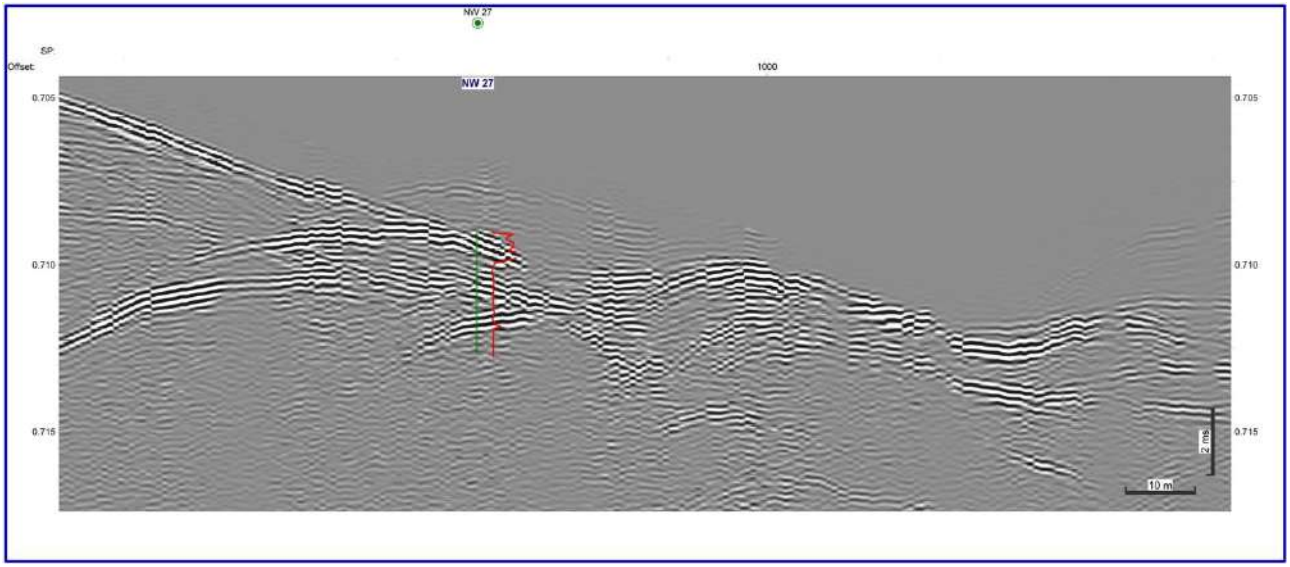

Fig.2 - Zoom section of the sub-bottom profile shown in Fig.1

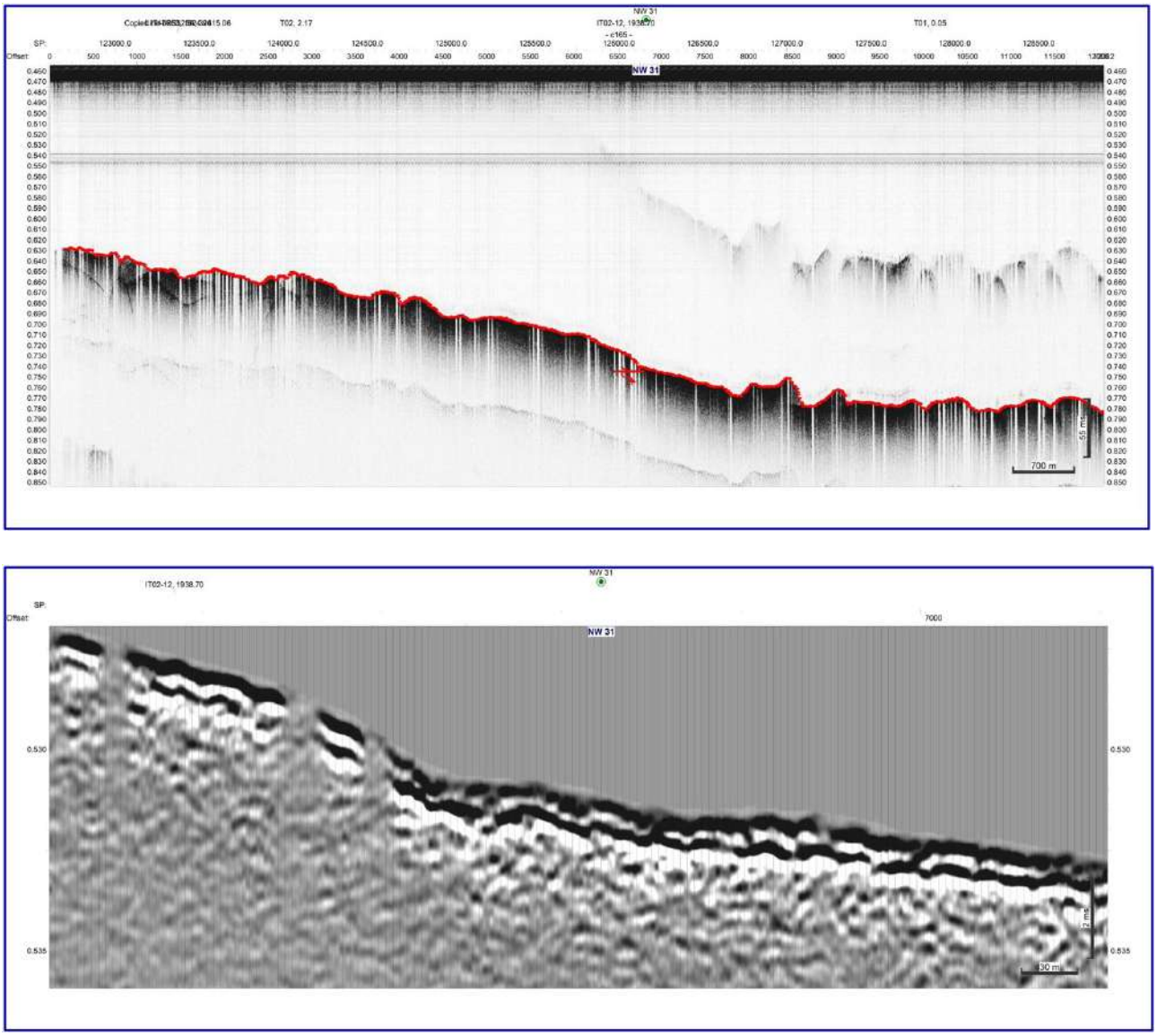

Fig. 3 - Sub-bottom profile originally stored in envelope mode(a) and below a zoom pseudo-seismic section(b) (Baradello et al. 2021) near the sediment core NW31 projection onto the profile.

References

Baradello L (2014) An improved processing sequence for uncorrelated Chirp sonar data. Marine Geophys Res 35(4):337–344

Baradello L., Battaglia F., Vesnaver A. (2021) Fast method to transform chirp envelope data into pseudo-seismic data. Marine Geophys Res 42:14 https://doi.org/10.1007/s11001-021-09436-y

Henkart P (2006) Chirp Sub-Bottom profiler processing – a review. Sea Technol 47(10):35–38

Quinn R, Bull JM, Dix JK (1998) Optimal processing of marine high resolution seismic reflection (Chirp) data. Marine Geophys Res. 20:13–20

Corresponding author: csauli@ogs.it

The Italian calibration and reference site for E & EM geophysical methods: The HydroGeosITe

A. Signora[1], S. Galli[1], F. Dauti[1], A. L. Sullivan[1], A. Lucchelli[1], M. Gisolo[2], G. Fiandaca[1]

[1] The EEM Team for Hydro & eXploration, Department Of Earth Sciences "Ardito Desio", Università degli Studi di Milano, Milano (Italy)
[2] A2A Ciclo Idrico S.p.a. , Brescia (Italy)

1. The HydroGeosITe project

From the spring of 2021 to July 2023 over 20000 line-km of airborne electromagnetic (AEM) data have been acquired for mapping and managing groundwater resources in the entire plain of Brescia province and a mountainous sector, over an area of approximately 1800 km^2 (Figure 1). Within this AEM campaign, the largest ever carried out in Italy for groundwater mapping and management, the water management company A2A Ciclo Idrico S.p.A. financed the HydroGeosITe project, which aims at establishing the first calibration and reference site for galvanic methods and for ground and airborne electromagnetic methods, for hydrogeological purposes. The need for calibration sites of EM systems derives by the sensitivity of EM data to system characteristics, such as receiver transfer function, transmitter current waveform, and transmitter-receiver synchronization and geometry, which if neglected lead to significant bias in the retrieval of the electrical properties (Christiansen et al., 2011). For instance, the Lyngby Danish reference site has been established for ensuring the calibration of both airborne and ground-based EM systems (Foged et al., 2013), while the Menindee Australian test range (Brodie and Cooper, 2018) focuses only on airborne systems, but covers a much longer stretch (more than 35 km). In both cases, calibrated systems are expected to retrieve satisfactory resistivity models, the eventual calibration consisting in adjusting the system characteristics until the inversion model compares well enough with the reference model.

Within the HydroGeosITe we have characterized the electrical properties of the subsurface with an unprecedented density of measurements, both in terms of conduction and polarization. This effort aims also to test a new inversion scheme where both inductive and galvanic (EM) and galvanic (DCIP) are incorporated into the same inversion framework. To validate the HydroGeosITe both in terms of calibration and reference, three boreholes are expected to be drilled, the first of which has been completed in December 2023, reaching the depth of 350 m from the surface. Accurate lithological description, along with future borehole-logging, is expected as well, likely positioning the HydroGeosITe as a key reference point in interpreting the future AEM campaign.

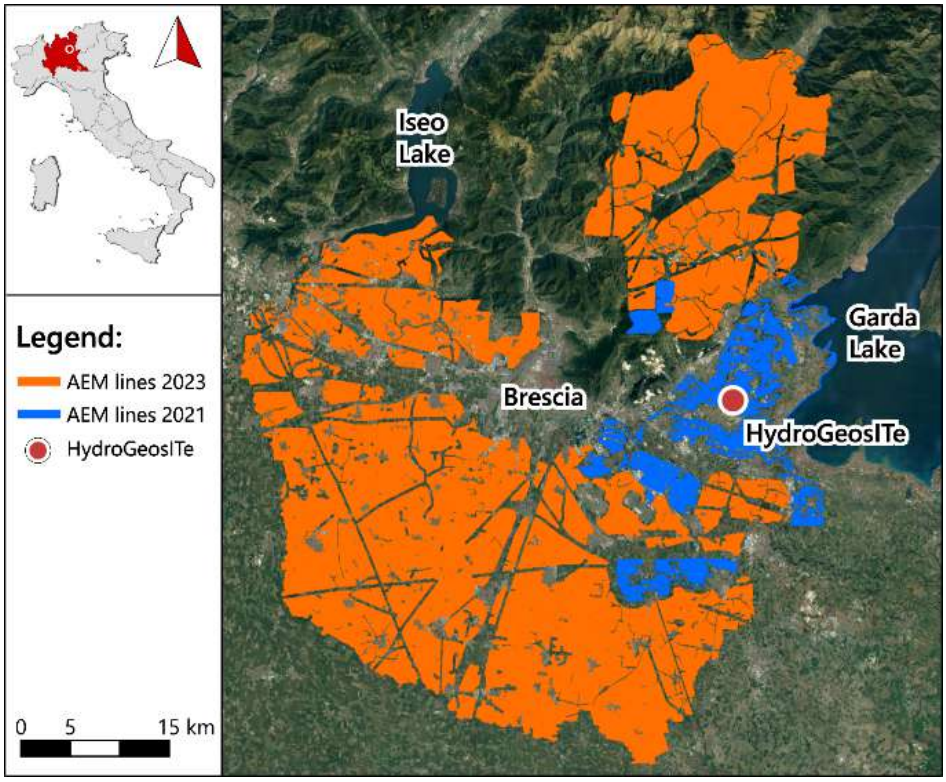

Figure 1 - Flight lines of 2021 and 2023 AEM campaigns in Brescia province. Blue lines represent the 2000 line-km of data flown in 2021; orange lines represent the 20000 line-km of the 2023 survey. The red dot shows the position of the HydroGeosITe.

2. Site characterization

The HydroGeosITe is located in northern Italy, close to the southern margin of the Italian Alpine chain (Fig. 1), within a fluvioglacial and glacial depositional environment which lays on bedrock, supposedly Pliocene marine bedrock. Therefore, the near surface deposits expect the complex superimposition and interdigitation of morain and fluvial deposits due to the repeated advance and retreat of the glacial system (Plesitocene) followed by the quaternary alluvial deposit of Chiese river's alluvial plain (Conti et al., 2009). The comprehensive geophysical measurements carried out to characterized this spot in such complex geological settings are presented in the following section and displayed in Figure 2. These involve both AEM acquisition and ground EM surveying with four different systems, along with galvanic acquisition of DCIP data.

2.2. AEM acquisitions

Concerning the AEM data (Fig. 2, bottom-left map), the SkyTEM312 system was employed in 2021 to survey the HydroGeosITe. The site has been surveyed again in summer 2023 using the new SkyTEM306HP. The 2023 AEM data were collected, overlapping with each other and with the geophysical ground measurements, at three different flight heights to ensure the absence of system bias, and with the aim of setting a quality standard for future AEM surveys.

2.3. Ground TEM acquisitions

Several ground transient electromagnetic (TEM) soundings have been measured with the ABEM WalkTEM 2 instrument in central-loop configuration, with two different transmitter units (TX-20 and TX-60, with 20 ampere and 60 ampere peak-to-peak maximum current, respectively) and three transmitter sizes (Fig. 2, top right map):

- Thirty 40x40 m^2 Tx-20 soundings, with 30 minutes of stacking time and 10 ms of acquisition time;
- Five 100x100 m^2 Tx-60 soundings, with 60 minutes of stacking time and 30 ms of acquisition time;
- One 200x200 m^2 Tx-60 sounding, with 100 minutes of stacking time and 30 ms of acquisition time.

All soundings were measured with two different receivers, RC5 and RC200, with 5 m^2 and 200 m^2 effective area, respectively. The 40x40 m^2 soundings reached approximately 300 m of depth of investigation (Christiansen and Auken, 2012), while the 100x100 m^2 went down to ≈400 m and the 200x200 m^2 down to ≈700 m.

2.4. tTEM and Loupe acquisitions

The tTEM system (Auken et al., 2019) has been employed to acquire more than 55 km of data (Fig. 2, bottom right) through a 3x3 m^2 transmitter with receiver in offset configuration. This system allows to carry out continuous TEM measurements when pulled by an ATV vehicle at the max speed of 20 km/h, to retrieve subsoil models up to ≈100 meters of depth. Almost the same area was surveyed with the Loupe portable system (Street & Duncan 2018) with 20 km of lines.

2.5. DCIP acquisitions

The DCIP data have been measured with the ABEM Terrameter LS2 system in 100% duty cycle (Olsson et al., 2015) with full waveform acquisition, and gated after harmonic denoising and drift removal following Olsson et al. (2016). As shown in Fig. 2, top right panel, approximately 4 km of data have been measured with 10 m electrode spacing, and another 4 km with 5 m electrode spacing. The gradient protocol has been used for acquisition, with 12 seconds of acquisition time and two stacks per quadrupole, with mean injected current of approximately 0.5 Amperes. The number of quadrupoles acquired among the different profiles ranges between 1400 and 2700 ca., depending on the profile length and the electrode spacing.

2.6.Drillings

Three boreholes few hundred meters deep (100 m, 190 m, 350 m) are being drilled, with lithological description and resistivity log; the 200 m deep borehole was completed in December 2023, while the other two will be completed within Spring 2024.

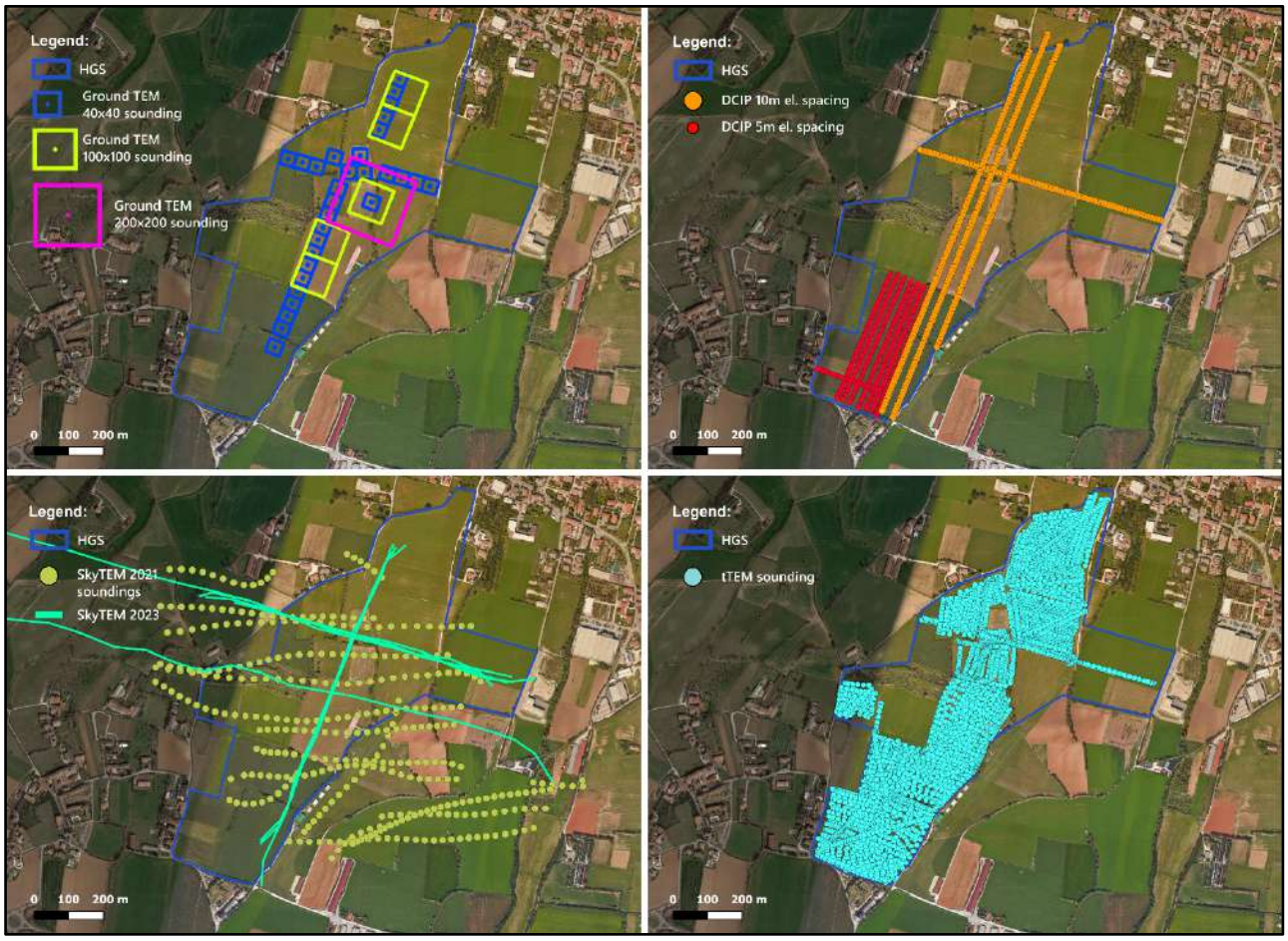

Figure 2 - Maps of the geophysical surveys carried out at the HydroGeosITe, with the perimeter of the area always accessible indicated in blue (HGS in the legend). Top left – Ground TEM soundings with 40x40 m² (blue squares) 100x100 m² (yellow) and 200x200 m² (magenta square) loop sizes. Top right – DCIP profiles with 10 m spacing (dotted orange lines, ≈ 4 km) and 5 m spacing. Bottom left – SkyTEM312 2021 soundings displayed by green-dots, while SkyTEM306HP 2023 soundings are displayed with marine-green lines for all the three different flight heights. Bottom right – tTEM soundings; approximately the same area has been covered with the Loupe system

3. Data Modelling and Joint inversion

Inductive and galvanic data give usually significantly different inversion models, due to their different sensitivity to the resistivity distribution. Often resistivity anisotropy is used to justify the lack of accordance between the two methods (e.g. Christiansen et al., 2007), even if recent publications have shown compatibility between AEM and galvanic data (Christensen, 2022), but without considering the induced polarization effect. However, Fiandaca et al. (2022) have shown that the IP phenomenon has a strong effect on inductive data also in environmental applications, with significant dependence of the effect on the system characteristics.

Following these findings, we propose first a comprehensive interpretation of the independent models, then the employment of joint inversion scheme to retrieve a unique model from both galvanic and inductive data taking into induced polarization. In particular, all the inversions are carried out following Fiandaca et al. (2024) with EEMverter, a software specifically designed for modelling IP in joint inductive/galvanic inversions. EM data are modelled in 1D, while the galvanic

DC and full-decay IP data are modelled in 2D (Fiandaca et al., 2013) in terms of the maximum phase angle (MPA) Cole-Cole re-parameterization (Fiandaca et al., 2018). The objective function of the inversion is defined as:

$$Q = \left[\frac{1}{N_d + N_r} \left(\sum_{i=1}^{N_d} \frac{\left(d_{obs} - d_{forward} \right)^2}{\sigma_{d_i}^2} \; ++ \; \sum_{i,j}^{N_r} \frac{\left(m_i - m_j \right)^2}{\sigma_{r_{i,j}}^2} \right) \right]^{\frac{1}{2}} \quad (1)$$

Where N_d and N_r are the numbers of data d_{obs} (both inductive and galvanic) and roughness constraints (on the unique joint model m), respectively, and the balance between inductive and galvanic data is achieved through their standard deviation σ_d^2. The independent inversions have been carried out with the same forward schemes of the joint inversion, but using only one data type at once. All data have been processed in EEMstudio (Sullivan et al., 2024) for culling outliers out before inversion. Both the geophysical galvanic and inductive models exhibit concordance with each other and display features likely consistent with the geological-stratigraphic characteristic of the area. The joint models derived from incorporating both E & EM data within a unified inversion framework, not only confirm the primary structures defined by the independent models but also significantly enhance the resistivity model resolution, as shown in Figure 3.

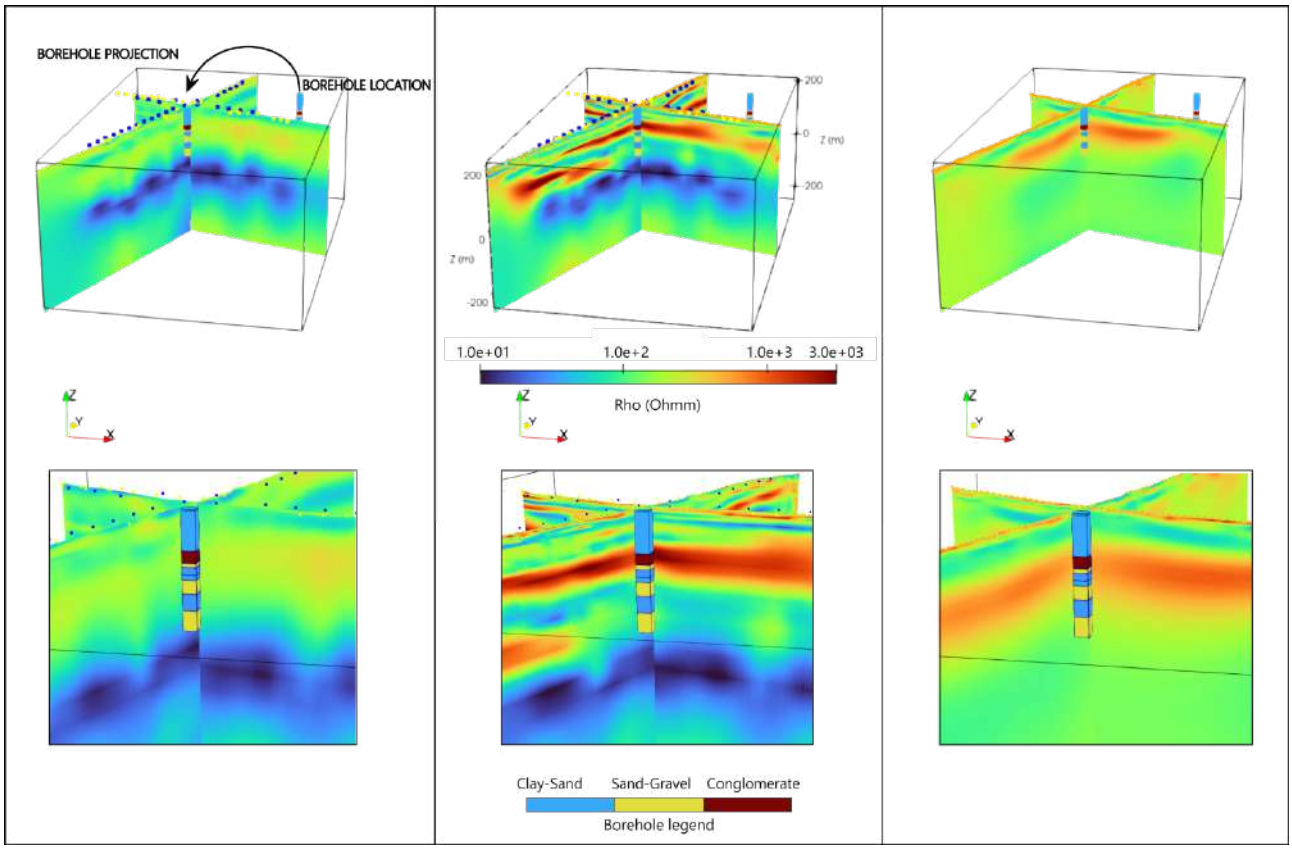

Figure 3: Inversion models of the crossing North-South and West-East profiles obtained through inductive-only AEM and ground TEM data (left), joint AEM-Ground EM-tTEM-DCIP data (center) and galvanic-only DCIP data (right), with full profile view in the top panels and zoom-in close to the crossing point in the bottom panels. The lithological description of a borehole near to the profiles is shown in color bars; for helping the comparison between borehole information and inversions, the borehole has been projected from its true position to the crossing point of the profiles. Ground EM, SkyTEM, tTEM sounding positions and electrodes are indicated with the same color coding of Figure 2

Acknowledgments

The HydroGeosITe project is funded by A2A Ciclo Idrico S.p.A. We acknowledge Emergo S.r.l for the support with AEM data.

References

Auken E., Foged N., Larsen J.J., Trøllund Lassen K.V., Maurya P.K., Dath S.M., Eiskjær T.T; 2019: tTEM — A towed transient electromagnetic system for detailed 3D imaging of the top 70 m of the subsurface. Geophysics, 84 (1), E13-E22.

Brodie R. C., Cooper, Y.; 2018: Spatially and conductivity Log constrained AEM inversion. AEGC2018 – 1st Australian Exploration Geoscience Conference, 18-21 February 2018, Sydney, Australia.

Christensen, N. B; 2022: Joint inversion of airborne TEM data and surface geoelectrical data. The Egebjerg case. Journal of Applied Geophysics, 196, 104511.

Christiansen, A. V., Auken, E., Foged, N., & Sørensen, K. I.; 2007: Mutually and laterally constrained inversion of CVES and TEM data: a case study. Near Surface Geophysics, 5(2), 115-123

Christiansen, A. V., Auken, E., & Viezzoli, A.; 2011: Quantification of modeling errors in airborne TEM caused by inaccurate system description. Geophysics, 76(1), F43-F52.

Christiansen, A.V. & Auken, E.; 2012: A global measure for depth of investigation. Geophysics, 77(4), WB171-WB177.

Conti M. and Conti A.; 2009: Tech. Rep. Comune di Bedizzole

Fiandaca, G., Ramm, J., Binley, A., Gazoty, A., Christiansen, A. V., & Auken, E;. 2013: Resolving spectral information from time domain induced polarization data through 2-D inversion. Geophysical Journal International, 192(2), 631–646.

Fiandaca, G., Madsen, L. M., & Maurya, P. K.; 2018: Re-parameterisations of the Cole–Cole model for improved spectral inversion of induced polarization data. Near Surface Geophysics, 16(4), 385-399.

Fiandaca, G. Dauti, F., Signora A.; 2022: Effect of induced plarization on galvanic and inductive data: where is it stronger? Near Surface Geoscience Conference, 18-22 September 2022, Belgrade, Serbia

Fiandaca, G., Zhang, B., Chen, J., Signora, A., Dauti, F., Galli, S., Sullivan, N.A.L., Viezzoli, A.; 2024: EEMverter, a new 1D/2D/3D inversion tool for Electric and Electromagnetic data with focus on Induced Polarization, GNGTS 2024, 13-16 February 2024, Ferrara, Italy.

Foged, N., Auken, E., Christiansen, A. V., & Sørensen, K. I.; 2013: Test-site calibration and validation of airborne and ground-based TEM systems. Geophysics, 78(2), E95-E106.

Olsson, P. I., Dahlin, T., Fiandaca, G., & Auken, E.; 2015: Measuring time-domain spectral induced polarization in the on-time: decreasing acquisition time and increasing signal-to-noise ratio. Journal of Applied Geophysics, 123, 316-321.

Olsson, P. I., Fiandaca, G., Larsen, J. J., Dahlin, T., & Auken, E.: 2016: Doubling the spectrum of time-domain induced polarization by harmonic de-noising, drift correction, spike removal, tapered gating and data uncertainty estimation. Geophysical Journal International, 207(2), 774–784.

Street, G., Duncan, A., Fullagar, P., & Tresidder, R.; 2018: Loupe-a portable EM profiling system. ASEG Extended Abstracts.

Sullivan N. A. L., Viezzoli. A., Fiandaca, G.; 2024: EEMstudio: processing and modelling of electric and electromagnetic data in a QGIS plugin, GNGTS 2024, 13-16 February 2024, Ferrara, Italy.

Corresponding author: alessandro.signora@unimi.it

EEMstudio: processing and modelling of electric and electromagnetic data in a QGIS plugin

N.A.L. Sullivan[1], A. Viezzoli[2], G. Fiandaca[1]

[1] The EEM Team for Hydro & eXploration, Department of Earth Sciences "Ardito Desio", Università degli Studi di Milano, Milano, Italy
[2] EMergo S.r.l., Cascina (PI), Italy

Introduction

In electric and electromagnetic (EM) methods, the typical workflow is acquisition, processing and modelling. The processing part is where we evaluate the data in order to exclude outliers from the inversion, and prevent the generation of artifacts in the models that do not reflect geology. EM and IP measurements are particularly affected by coupling with man-made metal structures and random noise, which alter the response of the ground, causing the presence of buried conductors in the model and spotted appearance (Viezzoli et al., 2013). It is therefore important to identify these interferences and remove these data from the dataset in order to obtain reliable models. Besides automatic processing, the preferred method for this refining is the manual culling of data, supported by a georeferenced map to remove coupling effects.

At the moment, many software and tools are available for the inversion of electric and electromagnetic data: for instance, there are AarhusInv (Auken et al., 2015), SimPEG (Cockett et al., 2015), the GA AEM programs (Brodie, 2016) and EMagPY (McLachlan et al., 2021) for inductive data and RES2DINV/RES3DINV (Loke, 2004), ResIPy (Blanchy et al., 2020) and pyGIMLi (Rücker et al., 2017) for galvanic data. However, focusing on data processing, the choice is restricted to less options. The most comprehensive one, with an integrated GIS for data georeferencing is the commercial software Aarhus Workbench (Auken et al., 2009), with AarhusInv for inversions (Auken et al., 2015).

EEMstudio is a QGIS plugin that allows to process electric and electromagnetic data, always keeping the link with the georeferenced map. It is freeware and open source, under license EUPL 1.2, and available for academic, teaching and professional use. It is going to be distributed together with EEMverter (Fiandaca et al., 2024), a modelling tool for electric and electromagnetic data with focus on induced polarization, which will be distributed freely as well for most of the ground-based applications.

In the following sections, all parts that constitute the plugin will be presented.

QGIS Widget

Locating the data and checking the acquisition surroundings during processing is essential to ensure a good quality analysis. Choosing QGIS as the base of EEMstudio means embedding a powerful Geographic Information System (GIS), the most widespread software available with this purpose, to the processing and modelling tools. This results in having just one workspace to work with and the possibility to use data files among other georeferenced layers.

EEMstudio plugin starts as a docked widget in the QGIS main window (Fig. 1). Here there is the possibility to organize data and modelling files, and open them for processing or visualization of the results, loading automatically the acquisition points.

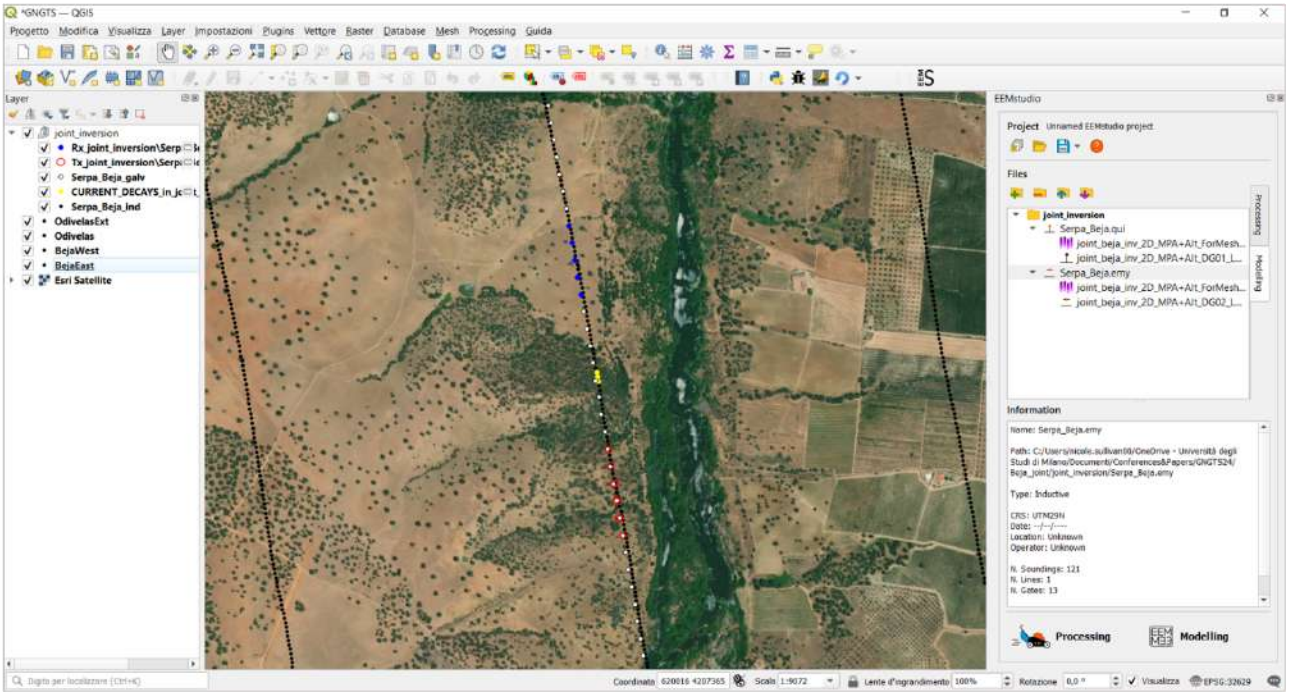

Fig. 1 – QGIS main window with EEMstudio widget on the right, used for management of processing and modelling files. Once uploaded, the coordinates of the acquisition points are automatically added to the QGIS layer, among eventual other layers in the QGIS project. In this figure, two types of data are shown: galvanic and inductive (airborne). White dots are the electrodes, red circles and blue points are the positions of the quadrupoles used in the soundings selected in the galvanic processing app (Figure 2a). Black dots are the inductive soundings and yellow points are the soundings highlighted in red in the inductive processing app (Figure 2b).

Processing

A separate window is dedicated to data processing and visualization of forward and model. Regarding processing, this graphic interface allows to select data to refine the dataset, to clean it from coupling effects and noise, using a vast range of shortcuts to optimize the process. Moreover, all the soundings that are shown and selected in this window are also plotted as georeferenced points in the QGIS map, to locate them instantly.

Two different types of this interface have been developed to fit various kinds of data: one for galvanic data and time-domain induced polarization (Fig. 2a) and one for transient EM data (airborne or ground-based, in Fig. 2b).

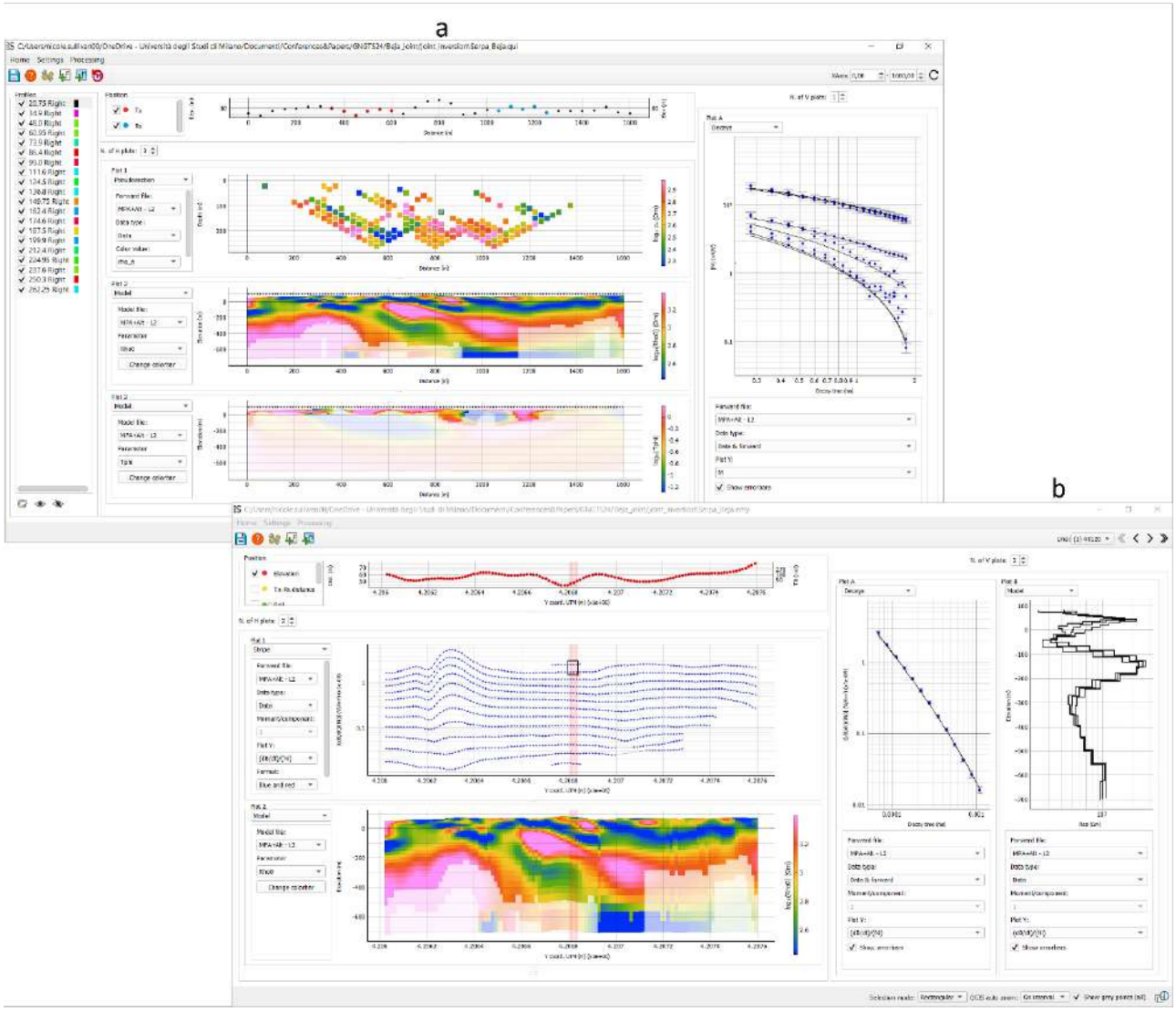

Fig.2 – Processing window supporting a) galvanic data visualization b) inductive data visualization. In galvanic window, first section: electrode position; second section: data pseudosection; third section: model of rho0; fourth section: model of phi; right panel: IP decay for the selected quadrupoles in the pseudosection. In inductive window, first section: flight altitude; second section: data (blue dots); third section: model of rho0; first left panel: decay in correspondence of the red highlights in the sections; models of rho0 in correspondence of the red highlights in the sections.

Both windows include many plots to show information of different nature, including pitch, roll and yaw for AEM data and electrode positions for galvanic data. As for measured data, for galvanic and IP data the user can choose between apparent resistivity and chargeability (gate by gate or integral chargeability in the pseudosection), as well as the full IP decay for selected quadrupoles, while for inductive data between apparent resistivity or every dB/dt normalization. It is also possible to

upload one or more forward models and model sections to compare easily data and results in a post-processing phase.

Modelling

Within EEMstudio it is also possible to manage easily modelling, with two different interfaces. The first one (Fig. 3a) has been developed to organize and prepare all necessary files with the desired configuration to launch 1D/2D/3D inversions, also in time-lapse and/or jointly among galvanic and inductive data using EEMverter (Fiandaca et al., 2024), the inversion kernel developed by the EEM Team for Hydro & eXploration, freeware for most ground-based applications. The other interface (Fig. 3b) has the purpose of building 1D/2D/3D synthetic models from scratch, which can be used as starting models or for forward computation.

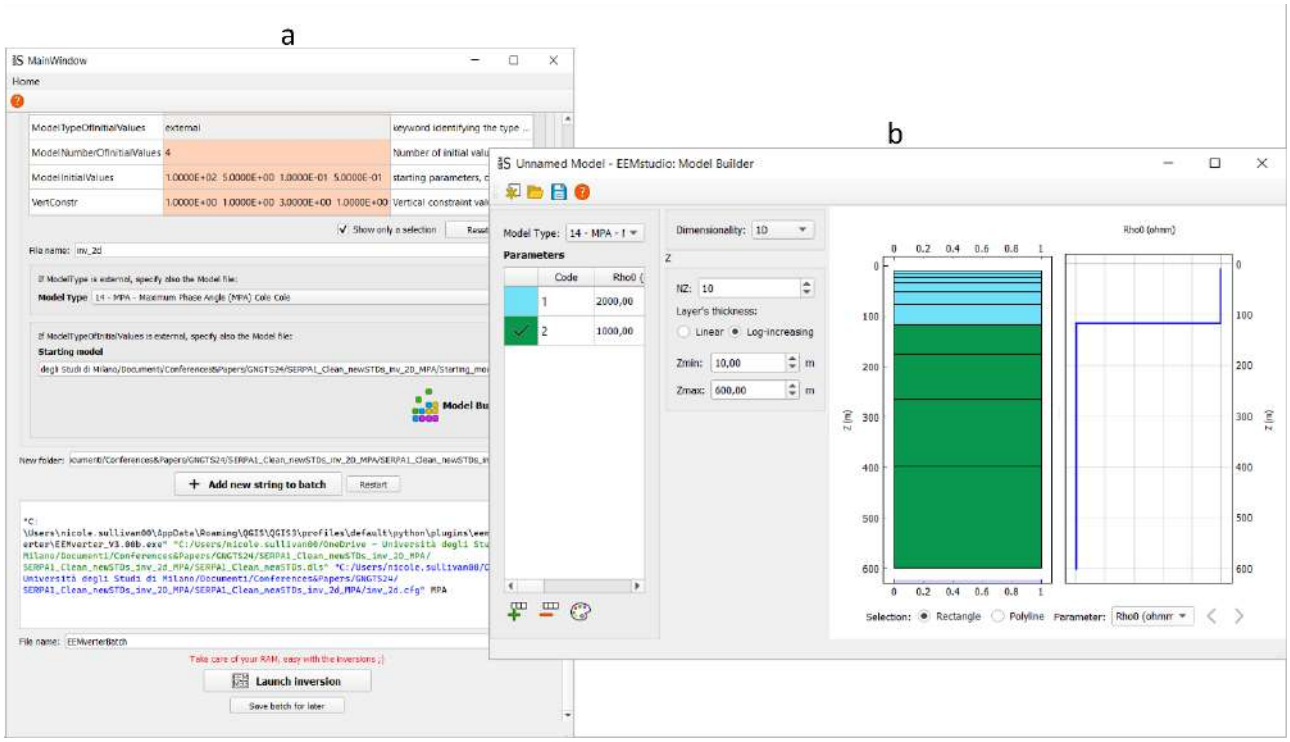

Fig3 – Modelling windows. a) Interface to gather all necessary files to launch easily inversions with EEMverter (Fiandaca et al. 2024). b) Model Builder, to build synthetic models. From left to right: table with the parameters and the associated colors, widgets to change the grid, grid where it's possible to select the cells and assign a color, 1D model of the row marked in blue on the bottom of the grid.

Conclusions

EEMstudio is a tool where it is possible to visualize, process and model electric and electromagnetic data, all within the QGIS environment, taking advantage of its potentiality. Moreover, QGIS is the most widespread open-source GIS software, used by geophysicists but especially by geologists, therefore having a common workspace to be confident with.

EEMstudio is also a freeware tool, available for everyone, from students to professionals, and have an open-source code, so that there is the possibility to modify and improve it to fit everyone necessity.

Acknowledgments

This study has been partially carried out within the Horizon Europe project SEMACRET.

References

Auken, E., Viezzoli, A., & Christensen, A. (2009). A single software for processing, inversion, and presentation of AEM data of different systems: The Aarhus Workbench. ASEG Extended Abstracts, 2009(1), 1-5.

Auken, E., Christiansen, A. V., Kirkegaard, C., Fiandaca, G., Schamper, C., Behroozmand, A. A., ... & Vignoli, G. (2015). An overview of a highly versatile forward and stable inverse algorithm for airborne, ground-based and borehole electromagnetic and electric data. Exploration Geophysics, 46(3), 223-235.

Blanchy, G., Saneiyan, S., Boyd, J., McLachlan, P., & Binley, A. (2020). ResIPy, an intuitive open source software for complex geoelectrical inversion/modeling. Computers & Geosciences, 137, 104423.

Brodie, R. C., 2016, User Manual for Geoscience Australia's Airborne Electromagnetic Inversion Software. Online: https://github.com/GeoscienceAustralia/ga-aem.git.

Cockett, R., Kang, S., Heagy, L. J., Pidlisecky, A., & Oldenburg, D. W. (2015). SimPEG: An open source framework for simulation and gradient based parameter estimation in geophysical applications. Computers & Geosciences, 85, 142- 154.

Fiandaca, G., Zhang, B., Chen, J., Signora, A., Dauti, F., Galli, S., Sullivan, N.A.L., Bollino, A., Viezzoli, A. (2024). EEMverter, a new 1D/2D/3D inversion tool for Electric and Electromagnetic data with focus on Induced Polarization.GNGTS 2024, 13-16 February 2024, Ferrara, Italy.

Loke, M. H. (2004). Tutorial: 2-D and 3-D electrical imaging surveys.

McLachlan, P., Blanchy, G., & Binley, A. (2021). EMagPy: Open-source standalone software for processing, forward modeling and inversion of electromagnetic induction data. Computers & Geosciences, 146, 104561.

Rücker, C., Günther, T., & Wagner, F. M. (2017). pyGIMLi: An open-source library for modelling and inversion in geophysics. Computers & Geosciences, 109, 106-123.

Viezzoli, A., Jørgensen, F., & Sørensen, C. (2013). Flawed processing of airborne EM data affecting hydrogeological interpretation, Groundwater, 51, 191–202.

Corresponding author: nicole.sullivan@unimi.it

Statistical analysis between the experimental and theoretical HVSR curves using different models.

Tanzini[1], E. Paolucci[2], D. Albarello[1,3]

[1]University of Siena, Italy
[2]University of Bologna, Italy
[3]CNR-IGAG, Montelibretti (Rome), Italy

Abstract
The ambient vibration Horizontal to Vertical Spectral Ratios (HVSR) (Nakamura, 1989) is a widely used technique to identify the seismic resonance phenomena induced by the presence of seismic impedance contrasts at depth. Moreover, the HVSR curve can be used to constrain the shear wave velocity (Vs) profile in numerical inversion procedures: to this purpose, different HVSR forward modeling were developed in the last decades, which differ from each other both for the basic theoretical assumptions related to the ambient vibration wavefield simulation and for the phases of the involved seismic waves. In order to explore if significant differences between these modeling exist, Paolucci et al. (2022) and Albarello et al. (2023) performed some comparisons using the results of large sets of numerical simulations obtained by considering realistic Vs profiles. These studies show that strong similarities between the resulting simulated curves exist.

In view of these conclusions, in this work, a comparison of the different theoretical HVSR modeling with experimental HVSR curves has been performed. HVSR measurements were carried out at test sites belonging to VEL (Valutazione Effetti Locali) down-hole database of the Tuscany Region (https://www.regione.toscana.it/-/banca-dati-vel).

Tanzini et al. (2023) described the procedure performed and information associated with the acquisition of experimental data, and the analyzed sites were implemented from 50 to 116 DHs. The experimental HVSR measurement obtained was compared with the various theoretical HVSR models used in Albarello et al. (2023). A minimum frequency threshold (MFT) was considered for each site, which corresponds to the maximum frequency that is reasonable to have with the Vs available from the DHs. The HVSR curves (experimental and theoretical) were therefore compared and a statistical analysis was performed, in particular the Pearson coefficient and the Goodness-of-fit Index S (GoF) proposed by Anderson (2004) were calculated taking into account consideration of the maximum peak of the curve in term of frequency (F_d) and amplitude (A_d). Finally, a global Similarity Index ($I_{\_Sim}$) was calculated to relate Pearson's coefficient and Index S (F_d and A_d) using different weights.

$$I_{\_Sim} = (\text{Pearson Coefficient}*0.2)+(F_d*0.5)+(A_d*0.3) \quad [1]$$

Out of 116 sites, only in 91 cases the numerical outcomes satisfactory reproduce the empirical HVSR curves. Moreover, the better agreement is not obtained by the same model. As concerns the remaining 25 cases, no correlation with the respective geological context or geographical position has been found. The same holds as concerns $V_{s,eq}$ or V_{s30} values, or the presence of anisotropy in the ambient vibration wavefield. Some inversion procedures were considered to evaluate at what extent unknown variable or possible experimental uncertainty relative to down-hole measurements. This analysis revealed that the lack of similarity cannot be explained by considering these aspects.

References

Albarello D., Herak M., Lunedei E., Paolucci E., Tanzini A.; 2023: Simulating H/V spectral ratios (HVSR) of ambient vibrations: a comparison among numerical models. Geophysical Journal International, Volume 234, Issue 2, August 2023, Pages 870–878, https://doi.org/10.1093/gji/ggad109

Anderson J.G.; 2004: Quantitative estimate of the goodness of fit synthetic seismogram. Proceedings of the 13thWorld Conference on Earthquake Engineering, B.B., Canada, August 1–6 2004, Paper n.243.

Nakamura Y.; 1989: A method for dynamic characteristics estimation of subsurface using microtremor on the ground surface. QR Railway Technical Research Institute, 30, 25 - 33.

Paolucci E., Tanzini A., Albarello D.; 2022: From HVSR to site SH response function: Potentiality and pitfalls inferred by 1D physical modelling. Soil Dynamics and Earthquake Engineering https://doi.org/10.1016/j.soildyn.2022.107703

Regione Toscana - VEL database: https://www.regione.toscana.it/-/banca-dati-vel

Tanzini A., Paolucci E., Albarello D.; 2023: Preliminary comparison between experimental and theoretical HVSR curves using different models. Gruppo Nazionale di Geofisica della Terra Solida, Atti del 41°Convegno nazionale, Trieste – sessione 2.2.

Corresponding author: Anna Tanzini tanzinianna@gmail.com

Imaging the buried Mirandola and Casaglia anticlines in the Po Plain, northern Italy, based on HVSR frequencies and amplitudes analysis

G. Tarabusi[1], G. Sgattoni[1], R. Caputo[2,3]

[1] Istituto Nazionale di Geofisica e Vulcanologia, Italy
[2] Dept. of Physics and Earth Sciences, Ferrara University, Italy
[3] CRUST, UR-UniFE, Italy

The Mirandola and Casaglia anticlines are two buried fault-propagation folds that started forming during Quaternary due to the seismogenic activity of blind segments belonging to the broader Ferrara Arc (Po Plain, Italy, Fig. 1). The last reactivation of segments of this Arc was during the May 2012 Emilia sequence (20 May, Mw 6.1 and 29 May, Mw 5.9 earthquakes, Pondrelli et al. 2012).

On top of these structures the thickness of the marine and continental deposits of the Po Plain foredeep is particularly reduced.

The results of a previous study carried out in correspondence of the Mirandola anticline area (Tarabusi and Caputo, 2017) represent the starting point of this research, in which we largely increased the dataset and extended the method to the area of the Casaglia anticline, where the stratigraphy and the relationships between the subsoil units are similar though partly different (Fig. 1). Indeed, in Casaglia, as in Mirandola, in correspondence with the structural culminations of the fault-propagation anticlines, the thickness of the continental Quaternary deposits is generally reduced and they directly overlay the Miocene units. As a consequence, a high impedance contrast occurs due to the abrupt increase of material density and hence of the seismic waves velocity.

For the purpose of the present research, numerous passive seismic measurements were carried out for obtaining the horizontal-to-vertical spectral ratios (HVSR) to identify resonance frequencies (Fig. 1). This approach has a twofold target: to supplement the existing data in the Mirandola region in order to enhance and extend the existing subsoil model, and to develop an analogous detailed subsoil model of the Casaglia area, which had not been explored previously.

A detailed image of the anticline structures was successfully obtained (Fig. 1), confirming the strong correlation between the HVSR outcomes, such as peak frequencies and amplitudes, and the available stratigraphic data primarily obtained from boreholes. We obtained high resolution resonance frequency and HVSR peak amplitude maps and a 3D reconstruction of both anticlines (Fig. 2).

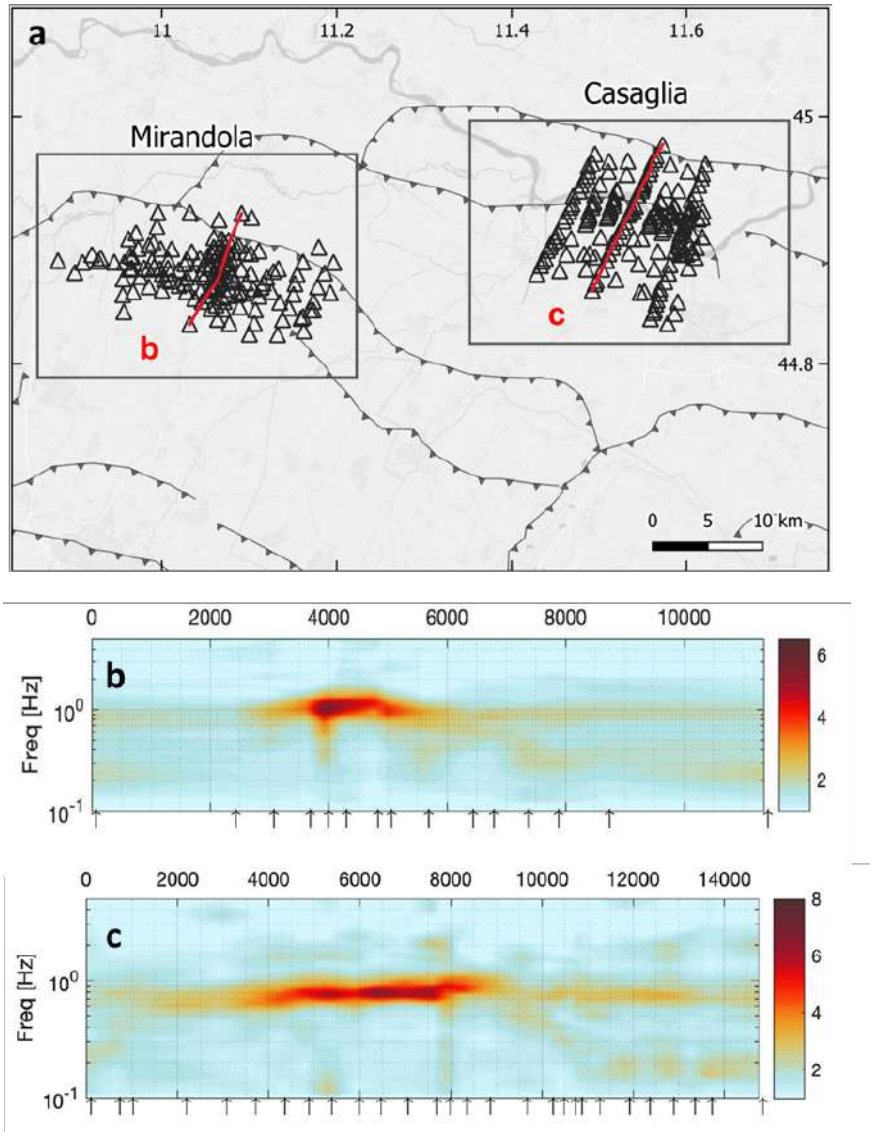

Fig. 1 - (a) Location of the HVSR measurements (triangles) within the two focus areas. Red lines indicate the traces of the transects represented in b) and c) showing absolute HVSR amplitudes.

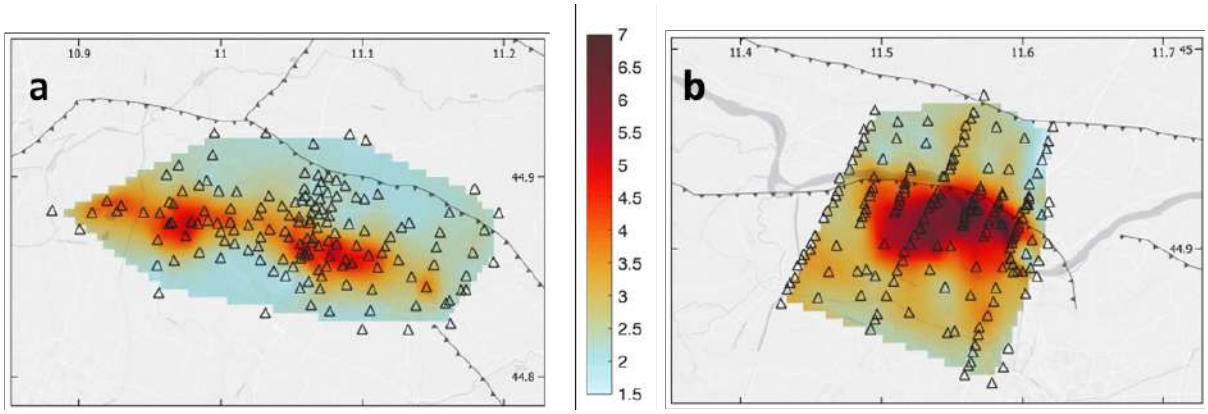

Fig. 2 - HVSR peak amplitude distributions at the Mirandola (a) and Casaglia (b) areas. The triangles are the single-station microtremor measurements used in the interpolation.

Furthermore, by assuming a power-law relation between Vs and depth, a peak frequency versus depth empirical relationship could be derived by fitting measured resonance frequencies with the

substrate depths identified in the nearby boreholes. This empirical relationship is valid for the shallow subsurface within the depth range used for the regression analysis (say, from -60 to -230 m), which allows the conversion from the frequency to the depth domain of the HVSR curves.

These results have several practical applications: firstly, they help identifying areas that are likely to experience greater ground motion amplification during an earthquake; secondly, they enable the development of empirical formulas for estimating the depth of the seismic bedrock based on HVSR outcomes (Martelli, 2021) with high accuracy; and thirdly, they highlight significant stratigraphic and structural differences between the Mirandola and Casaglia areas.

References

Martelli, L. (2021). Assessment of Seismic Bedrock in Deep Alluvial Plains. Case Studies from the Emilia-Romagna Plain. Geosciences 11(7):297. https://doi.org/10.3390/geosciences11070297

Pondrelli, S., Salimbeni, S., Perfetti, P., Danecek, P. (2012). Quick regional centroid moment tensor solutions for the Emilia 2012 (northern Italy) seismic sequence. Annals of Geophysics 55(4):615–621, doi: https://doi:10.4401/ag-6146

Tarabusi, G., Caputo, R. (2017). The use of HVSR measurements for investigating buried tectonic structures: the Mirandola anticline, Northern Italy, as a case study. International Journal of Earth Sciences 106(1), doi: https://doi.org/10.1007/s00531-016-1322-3.

Denser is better? Spatial sampling vs trace stacking in multichannel GPR data to improve sections and depth-slices readability for archaeological prospections.

A. Vergnano[1], C. Comina[1]

[1] *Università degli Studi di Torino, department of Earth Sciences; Torino, Italy*

Introduction

Among the geophysical indirect methods to preliminary assess the presence of underground structures for archaeological studies (and for many other applications), multichannel GPR systems have been under the spotlight for more than a decade (Corradini et al., 2022; Trinks et al., 2009; Viberg et al., 2020). Their peculiarity is to be composed of several radar antennas, both transmitter and receiver, placed one aside the other, in order to produce a spatially dense amount of data, which easily allows for full 3D surveys, with a logistical effort "similar" to that of a standard GPR single-channel system (Novo et al., 2012). This means that very high resolutions, usually of the order of few centimeters, can be easily achieved, making it possible to detect smaller targets (Linck et al., 2022), and making more reliable the interpolation process to produce horizontal depth-slices. Nevertheless, the data processing of multichannel GPR data can be significantly different (Trinks et al., 2018) and more time consuming, from traditional GPR systems, given the large amount of data created. Also, in some situations, the increased density of spatial sampling does not correspond to an increased quality of depth-slices given that small anomalies and wave scattering can disturb the data and reduce the visibility of more relevant targets of archaeological interest (i.e. walls or structures). Moreover, notwithstanding the benefits of new multichannel GPR systems, they are still subject to limitations intrinsic to the GPR wave propagation, for example the difficulty of penetrating for more than a few meters into the soil, and the data quality degradation in the presence of even small quantities of clay materials. This makes the data processing of multichannel GPR dataset an interesting research topic and various studies are available in recent literature, which include Principal Component Analysis (Linford, 2023), studies on the signal polarization and orientation (Lualdi and Lombardi, 2014), studies on various filters for artifact reduction (Verdonck et al., 2013), studies on positioning accuracy (Gabryś and Ortyl, 2020).
In this context, this work aims to assess the variation of depth-slices quality with the variation of between-channels resolution, and proposes an alternative processing step for noise reduction of GPR multichannel datasets. It focuses on two objectives connected one to each other:

• Which is the optimal resolution of multi-channel GPR data for archaeological applications, i.e. the minimum space sampling below which there is not a great improvement in the data?

• Can the data acquired by adjacent channels be stacked to improve the signal-to-noise ratio, and if so, in which cases this processing step can give substantial advantages?

Instrument and data processing

The GPR multichannel system used in this study is the Stream C manufactured by IDS and available at Officina della Ricerca e della Didattica of University of Torino. It has 34 antennas, 24 of which have the dipoles oriented vertically, and 10 horizontally, with respect to the acquisition direction. A total of 23 traces with both the transmitter and the receiver oriented vertically ("VV" with an horizontal separation of about 4 cm) and 9 horizontally ("HH" with an horizontal separation of about 10 cm) are therefore available for each acquisition (i.e. each swath). The central frequency band is 600 MHz; however, frequency distributions centered at about 250-300 MHz were observed in most test sites. This system was adopted in different case studies of archaeological interest in the past few years. Two example test sites are reported in the following to test the working objectives.

For both test sites the data were processed, using the Reflexw software, according to the following processing flow: 1. subtract-mean (dewow) filter with 4 ns timewindow; 2. automatic time-zero correction; 3. background removal; 4. energy decay (an automatic gain function); 5. meanfilter (a 1D moving average filter over a 10-sample window); 6. bandpass filter (100-1000 MHz); 7. subtracting average over 100 traces (= 5m); 8. fk migration with velocity estimated from hyperbola analysis; 9. energy decay; 10. Envelope; 11. normalize profiles (to better compare the depth-slices). Optionally, between step 3 and step 4, an additional processing step consisting in the stacking of an on purpose defined number of adjacent channels was adopted. After those processing steps, the 2D sections are combined to produce a 3D GPR data volume, which is then "cut horizontally" to produce depth-slices. The 3D GPR data volume was produced with a lateral resolution of 5 cm, and a interpolation distance of 50 cm (the interpolation was weighted on the squared distance between the data points and the output point).

First experiment: how the data quality of a GPR 3D data volume is dependent on the number of channels used.

The first dataset was acquired at the archaeological site of “Statio Ad Fines” in Malano in the municipality of Avigliana. Roman buildings and structures are attended at the test site. In this experiment, the 3D GPR data volume, and the consequent depth-slices, consider different subsets of the total 32 channels of the Stream C system. The results of this experiment, comparing the different subsets of channels, is reported in Fig. 1.

Looking at the upper panels of Fig. 1, one can notice the difference between VV and HH dipoles, which can detect different features of the subsoil: in particular, HH dipoles can "see" an elongated diagonal structure at the top of the picture, which VV dipoles struggle to detect. Conversely VV dipoles, can detect more clearly the rectangular features in the lower part of the area. This observation was expected, and it is in line with previous literature (Lualdi and Lombardi, 2014).

Moreover, looking at the HH and VV channels separately, the resulting images are clearer than the one with all the channels together.
Looking at the lower panels, one can appreciate the difference when using only a subset of the 32 VV dipoles: 8 dipoles (12 cm between-lines resolution), 4 dipoles (25 cm) and 2 dipoles (50 cm). In this test site, the 12-cm image and even the 25-cm one, do not differ too much from the all-VV (4cm) image. Instead, the 50-cm-resolution image, which have a resolution similar to surveys performed with single-antenna GPR systems, is much less clear, even if the major structures are still roughly detected.

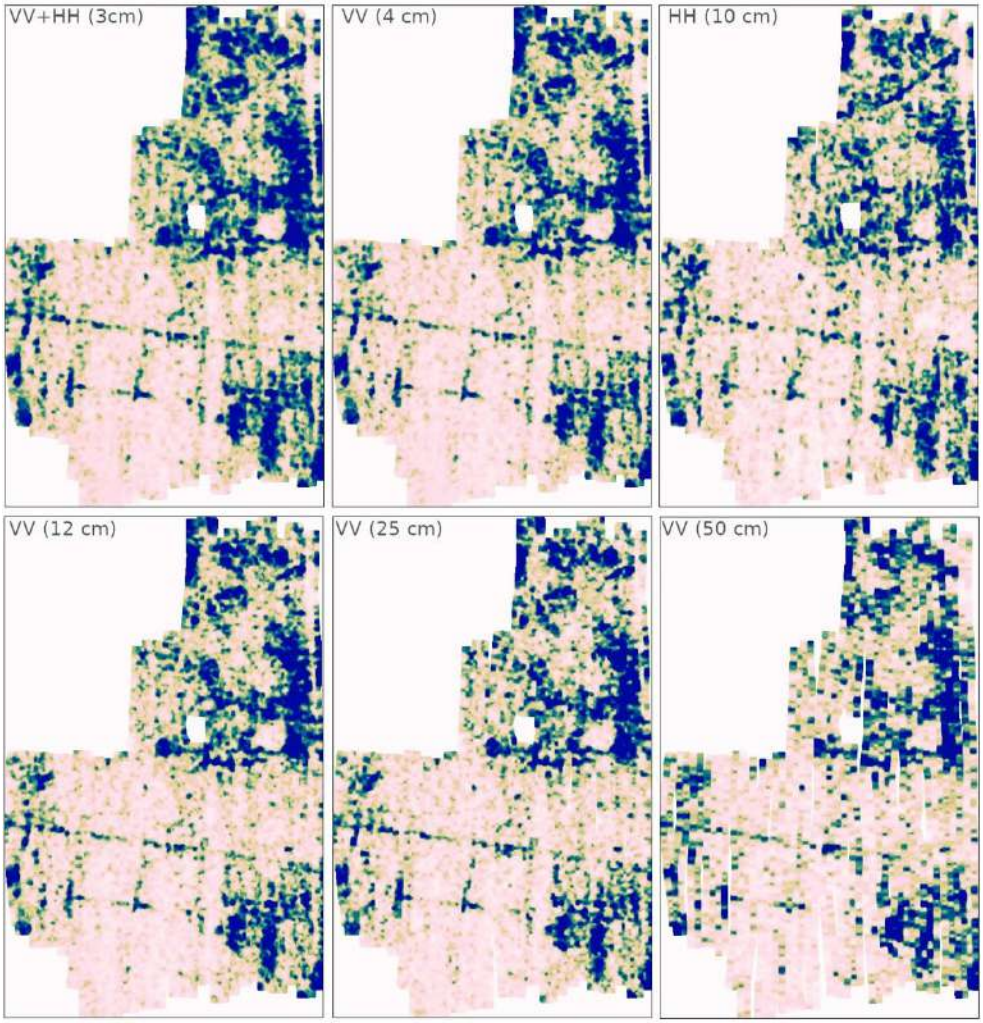

Fig. 1 – Comparison between 1.25 m depth-slices from 3D data volumes created using 6 different subsets of the total 32 channels of the Stream C: : upper panels) all the 32 channels, VV+HH (spacing about 3 cm), only the VV channels (spacing about 4 cm), only the HH channels (spacing about 10 cm); lower panels) different subsets of the VV channels with spacing of about 12, 25 and 50 cm respectively.

One can argue if the total amount of channels in the Stream C is really necessary to perform an archaeological investigation. Surely, the presence of both HH and VV dipoles seems important, and in the absence of both, the survey should be carried out in a grid shape, instead of a simpler boustrophedon path, to avoid missing some important targets. However, the depth-slice obtained using only 4 out of 23 channels is not much worse than the total one. Probably, lighter GPR multichannel systems including 4 VV channels and 4 HH channels could be an optimal compromise

between instrument cost and results. To fully review this statement, more test sites are expected to be analysed in such a way.

Second experiment: how the data quality of GPR 2D sections and 3D data volume may be improved by the stacking of adjacent channels.

The previous observations bring to the second experiment: since, in a typical test site, all the dipoles were not strictly necessary, an idea to make better use of them is to stack adjacent dipoles. This is meant to try to improve the signal-to-noise ratio, potentially useful at depth or when the data are noisy for various reasons. The second dataset was acquired at the archaeological park of Tindari in the municipality of Patti, Sicily, Italy. This site is recognized to be very challenging with respect to the GPR wave propagation given the high signal attenuation due to the presence of clay formations at the site (De Domenico et al., 2006).

Fig. 2 shows the improvement from non-stacked radargrams and radargrams obtained from the stacking of adjacent dipoles. The major improvements (red rectangles in Fig.2) were noticed in the 15-30 ns range, and this improvement is maintained in the 2D sections after the other processing steps (not shown here). The stacked 2D radargrams were then used to create 3D GPR data volumes, as in the first experiment.

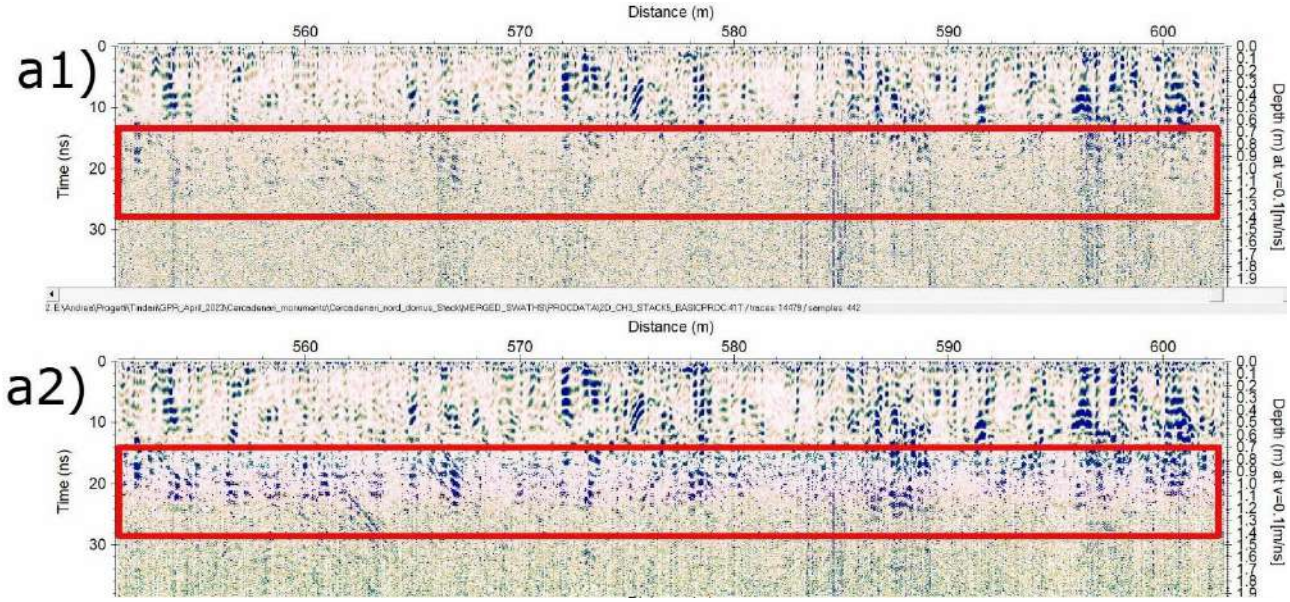

Fig. 2 – Comparison between GPR sections before and after stacking. **a1):** after dewow, move startime, and background removal. **a2)**: a1) + stacking of adjacent 5 channels. An energy decay gain filter was then applied to both sections to allow for meaningful visual readability.

In Fig. 3, the a-panels refer to a 60-cm depth-slice, while the b panels display a 40-cm depth slice. Looking at Fig. 3, it is possible to recognize that the stacking of adjacent radargrams can improve the overall quality of 3D data volumes, when sources of noise, or attenuation, or other problems, challenge the readability of depth-slices even at shallow depths. The noise gets reduced, which makes bigger features more visible.

In the data displayed and available, the improvement was still not able to clearly distinguish underground features which were not already visible without the stacking. In our opinion, the stacking of adjacent channels (or other processing steps based on this philosophy) is promising as

a tool to improve data readability in both 2D and 3D visualizations, but has still to be refined and tuned for different scenarios, and needs to be automatized in main GPR processing software. Moreover, while improving the signal-to-noise ratio at depth, it might affect the detection of smaller targets at shallow depths.

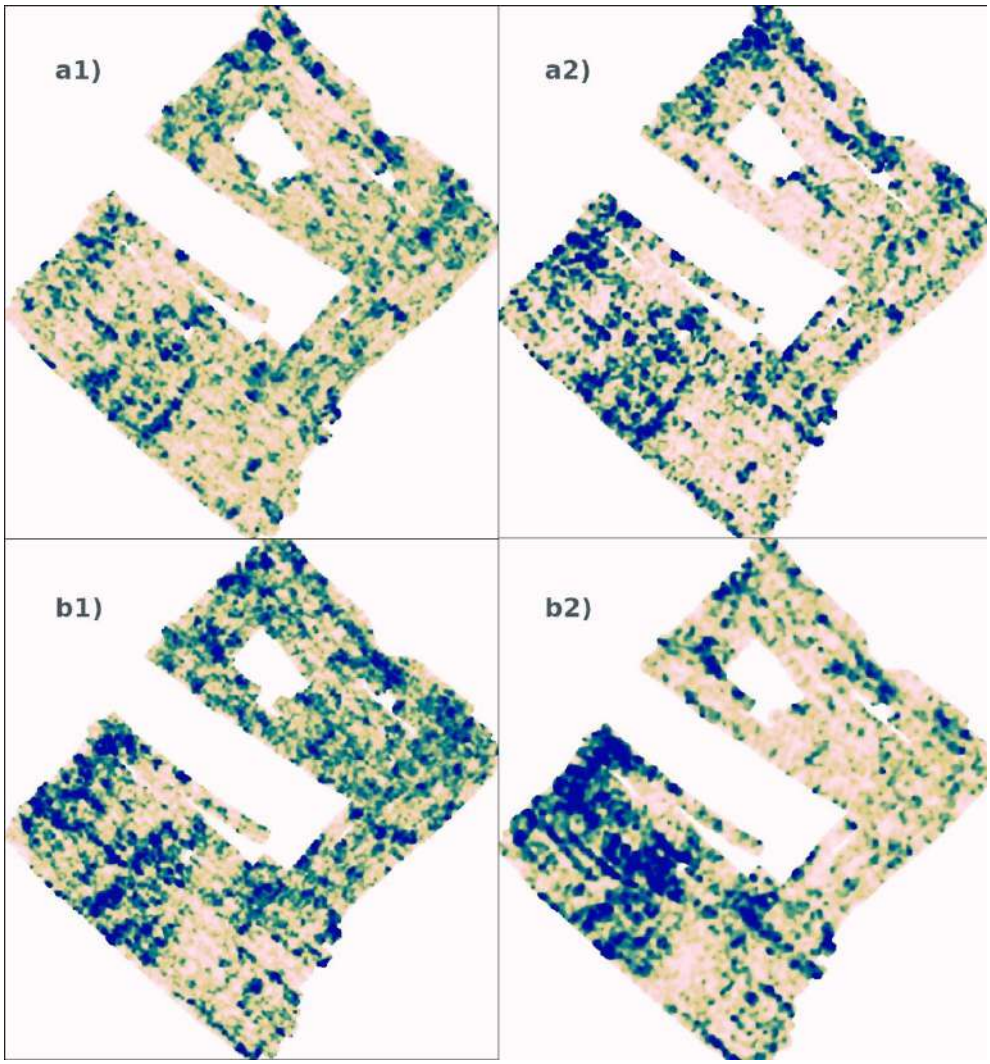

Fig. 3 – a) Comparison between a 60 cm depth-slice from Tindari test site, a1): non stacked, a2) stacked with 5 channels. b) as a), but at 40 cm depth.

Conclusions

The conclusion of this work is that denser is better if the data density is used in a proper way according to the exploration target. For simple explorative archaeological surveys, a multichannel GPR system that combines 4 VV and 4 HH channels could be sufficient in many situations. However, higher data densities allow performing the stacking of adjacent channels, which represents an interesting tool to improve the data quality at greater depths or in particularly challenging noisy sites.

Acknowledgements

Authors are indebted with Officina della Ricerca e della Didattica of University of Torino for the permission to use the GPR, with Prof. Rosina Leone of University of Torino and Parco Archeologico di Tindari for the work performed at the Tindari site and with Soprintendenza Archeologia Belle Arti e Paesaggio and A3 association for the work performed at the Malano site.

References

Corradini, E., Groß, D., Wunderlich, T., Lübke, H., Wilken, D., Erkul, E., Schmölcke, U., Rabbel, W., 2022. Finding Mesolithic Sites: A Multichannel Ground-Penetrating Radar (GPR) Investigation at the Ancient Lake Duvensee. Remote Sens. 14, 781. https://doi.org/10.3390/rs14030781

De Domenico, D., Giannino, F., Leucci, G., Bottari, C., 2006. Integrated geophysical surveys at the archaeological site of Tindari (Sicily, Italy). Journal of Archaeological Science 33 (2006) 961 – 970. https://doi.org/10.1016/j.jas.2005.11.004

Gabryś, M., Ortyl, Ł., 2020. Georeferencing of Multi-Channel GPR—Accuracy and Efficiency of Mapping of Underground Utility Networks. Remote Sens. 12, 2945. https://doi.org/10.3390/rs12182945

Linck, R., Stele, A., Schuler, H., 2022. Evaluation of the benefits for mapping faint archaeological features by using an ultra-dense ground-penetrating-radar antenna array. Archaeol. Prospect. 29, 637–643. https://doi.org/10.1002/arp.1870

Linford, N., 2023. Structure aware noise reduction of multi-channel ground penetrating radar data using Principal Component Analysis, in: Wunderlich, T., Hadler, H., Blankenfeldt, R. (Eds.), Advances in On- and Offshore Archaeological Prospection. Universitätsverlag Kiel | Kiel University Publishing, Kiel, pp. 427–429. https://doi.org/10.38072/978-3-928794-83-1/p87

Lualdi, M., Lombardi, F., 2014. Significance of GPR polarisation for improving target detection and characterisation. Nondestruct. Test. Eval. 29, 345–356. https://doi.org/10.1080/10589759.2014.949708

Novo, A., Dabas, M., Morelli, G., 2012. The STREAM X Multichannel GPR System: First Test at Vieil-Evreux (France) and Comparison with Other Geophysical Data. Archaeol. Prospect. 19, 179–189. https://doi.org/10.1002/arp.1426

Sandmeier, K.-J., 2021. Reflexw. Zipser Strasse 1, 76227 Karlsruhe, Germany. Available at: https://www.sandmeier-geo.de/index.html accessed on 6 December 2023.

Trinks, I., Gustafsson, J., Emilsson, J., Gustafsson, C., Johansson, B., Nissen, J., 2009. Efficient, large-scale archaeological prospection using a true 3D GPR array system. ArchéoSciences 367–370. https://doi.org/10.4000/archeosciences.1857

Trinks, I., Hinterleitner, A., Neubauer, W., Nau, E., Löcker, K., Wallner, M., Gabler, M., Filzwieser, R., Wilding, J., Schiel, H., Jansa, V., Schneidhofer, P., Trausmuth, T., Sandici, V., Ruß, D., Flöry, S., Kainz, J., Kucera, M., Vonkilch, A., Tencer, T., Gustavsen, L., Kristiansen, M., Bye-Johansen, L., Tonning, C., Zitz, T., Paasche, K., Gansum, T., Seren, S., 2018. Large-area high-resolution ground-penetrating radar measurements for archaeological prospection. Archaeol. Prospect. 25, 171–195. https://doi.org/10.1002/arp.1599

Verdonck, L., Vermeulen, F., Docter, R., Meyer, C., Kniess, R., 2013. 2D and 3D ground-penetrating radar surveys with a modular system: data processing strategies and results from archaeological field tests. Surf. Geophys. 11, 239–252. https://doi.org/10.3997/1873-0604.2013007

Viberg, A., Gustafsson, C., Andrén, A., 2020. Multi-Channel Ground-Penetrating Radar Array Surveys of the Iron Age and Medieval Ringfort Bårby on the Island of Öland, Sweden. Remote Sens. 12, 227. https://doi.org/10.3390/rs12020227

Corresponding Author: andrea.vergnano@unito.it

Session 3.3

Theoretical and methodological development in geophysics

GNGTS 2024

APPLIED GEOPHYSICS FOR ENERGY, ENVIRONMENT AND NEW TECHNOLOGIES

Session 3.3

Theoretical and methodological development in geophysics

Convenors of the session:
***Andrea Tognarelli* – andrea.tognarelli@unipi.it**
Luca Masnaghetti – LMasnaghetti@slb.com
***Gianluca Gola* – gianluca.gola@igg.cnr.it**

Contributions recommended for this session:

- **Theoretical Developments in Applied Geophysics**
- **New Technologies and Methods**
- **Geophysical Data Modelling and Inversion**
- **Novel Geophysical Acquisition and Processing Techniques**
- **Non Standard Applications in Geophysics**
- **Geophysical Data Integration and Interpretation**
- **Development and Application of Machine Learning Techniques and Data Analytics for Geophysical Data**
- **Geophysics for Sustainable Energy Development**

The session is focused on the theoretical and methodological development in geophysics. Novel approaches and new techniques related to digital data (seismic, electromagnetic, potential field) processing as well as the results of their application to specific case studies fit this session. Contributions that present innovative acquisition procedures (remote, superficial and in-situ), treatment, inversion and integration of geophysical data and multiphysics numerical modeling are accepted in this session. The session promotes multidisciplinarity and encourages the dissemination, comparison and technological transfer of innovative methods and technologies in the entire geophysical community.

Wavelet transform spectral analysis to estimate the depth of gravity and magnetic sources

M.A. Abbas[1,2], M. Milano[1], D.F. Barbolla[3], M. Fedi[1]

[1] University of Naples Federico II, Naples, Italy
[2] South Valley University, Qena, Egypt
[3] Institute of heritage Science - National Research Council, Lecce, Italy

Spectral analysis, which is based on the Fourier Transform, allows high-resolution analysis in the frequency domain but not in the space domain. Due to this lack of spatial resolution, well-known approaches such as Spector and Grant's method cannot provide information on the source positions. We propose to address these concerns by employing a scalogram analysis, which is achieved by study potential fields throughout the continuous wavelet transform. It allows detection and location of source contributions in the scalogram, with good resolution at both spatial and wavenumber level. As a new tool, we study here the depths to the top and bottom of the potential field sources locally on the 3D scalogram, along delimited sub-volumes, subareas, and scale-profiles. When such local spectral analysis is applied to synthetic data, the results are in good agreement with the information of the causative sources. We also apply the method to real aeromagnetic data of the Monte Vulture, Southern Italy.

Corresponding author: mahmoud.abbas@unina.it

PROBABILISTIC APPROACH TO FULL-WAVEFORM INVERSION OF SURFACE WAVES: A REAL DATA APPLICATION

S. Berti[1,2], M. Aleardi[1], E. Stucchi[1]

[1] Department of Earth Sciences (University of Pisa, Italy)
[2] Department of Earth Sciences (University of Florence, Italy)

Introduction

Surface waves play a crucial role in near-surface geophysics, offering a non-invasive way to determine the elastic properties of near-surface sediments: this turns out to be of fundamental importance, for example, for geotechnical site characterization. This analysis started with the spectral analysis of surface waves (SASW) and became increasingly popular after the introduction of the multichannel analysis of surface waves (MASW). The main limitation of these approaches is the reliance on a 1D layered model assumption, making them less effective in the presence of substantial lateral heterogeneity or when dealing with multimodal dispersion patterns in the context of low-velocity layers and strong velocity contrasts.

The advent of increased computational power in recent decades has made it possible the application of the full-waveform inversion (FWI) approach, which exploits the full information content of the recorded seismogram to infer high-resolution estimations of subsurface acoustic or elastic parameters. While acoustic FWI is commonly employed for imaging complex subsurface structures, it falls short in near-surface seismic studies due to the prevalence of surface waves. In this work, our focus shifts to multiparameter elastic FWI, aiming to construct P-wave and S-wave velocity models for near surface sediments. The inclusion of surface waves in the wavefields increases the nonlinearity of FWI, elevating the risk of the local approach getting stuck in some local minima of the usual L2 norm error function. In this context, the inversion outcomes become strongly dependent on the starting model. Although global optimization methods can mitigate this issue, they come at the cost of significantly increased computational demands (Lamuraglia et al. 2022).

Trying to overcome these issues, we propose a Bayesian inference framework for elastic FWI. Differently from the local approach, the proposed method provides a comprehensive evaluation of the uncertainty affecting the retrieved solution through the so-called posterior probability density function (PPD) in the model space. Based on the Bayes theorem, the PPD incorporates the information coming from both the prior knowledge on the model parameters and the recorded seismic data but, in case of nonlinear forward modelling, a sampling technique needs to be adopted to approximate this density function. In our case a Markov Chain Monte Carlo (MCMC) sampling strategy is used to numerically evaluate the statistical properties of the PPD. However, challenges arise in the form of the convergence rate dependency on the proposal distribution and the diminished sampling ability in high dimensional spaces, known as the curse of dimensionality.

To tackle these issues, we introduce a gradient-based Markov Chain Monte Carlo (GB-MCMC) method where the proposal distribution is constructed by the local gradient and the Hessian of the negative log posterior, and we also reduce the dimensionality of the problems making use of the

Discrete Cosine Transform (DCT) reparameterization. This approach is applied to a real dataset, acquired in the framework of the InterPACIFIC project at the test site of Grenoble (France, Garofalo et al. 2016).

Method

The method we employed is the same described in Berti et al. (2023) and applied to solve the acoustic FWI, but in the present study the method has been extended to the elastic case and validated on real data. For the sake of brevity, the theoretical description of the method is not included here, and we refer the reader to Berti et al. (2023) for more details. In essence, our implemented MCMC method defines the proposal distribution as a localized approximation of the PPD by leveraging information derived from the local gradient and Hessian of the negative log posterior computed around the current state of the chain. This significantly reduces the time requested by the algorithm to reach the steady state. The drawback of this procedure is that derivatives need to be evaluated for each sampled model, posing computational challenges when dealing with extensive model and data spaces. Therefore, a convenient strategy to reduce the computational complexity of this inverse problem is to compress the model and data spaces through appropriate reparameterization techniques, such as the DCT. The DCT of a signal reveals the energy distribution of the signal in the frequency domain spectrum. Typically, the majority of the signal's energy is expressed by low-order DCT coefficients and consequently, this mathematical transformation serves as a tool for model and data compression, achieved by setting the coefficients of the base function terms beyond a certain threshold equal to zero. The estimation of the optimal number of DCT coefficients needed to approximate the model and data spaces is a critical step of our inversion framework. For the seismic data, we have analyzed how the relative percentage error, calculated as the ratio between the L2 norm difference of the observed and compressed data and the L2 norm of the observed data, varies using different combinations of DCT coefficients; for the model space instead, we have used the available borehole data, investigating how the variability of the model, calculated as the ratio between the variance of the compressed and uncompressed models (Aleardi, 2021), changes with the number of retained DCT coefficients.

Results

To validate our proposed methodology, we applied the approach to a field dataset, acquired in Grenoble, France, as part of the InterPACIFIC project. Three in-line boreholes, spaced at 4.5m intervals, were drilled up to 50m depth. These available well-log data were used to validate the results obtained in our work. The dataset consists of three shot gathers, of which one is split-spread and two are off-ends, recorded by 48 vertical geophones with a spacing of 1 m and a natural frequency of 4.5 Hz. Pre-processing steps, including trace-by-trace amplitude normalization and a zero-phase band-pass filter (3-30Hz), were applied to enhance data quality. Then, a 3D to 2D correction is needed to compensate for the geometrical spreading between the real case point source and the 2D forward modelling where line sources are implicitly used in the simulations. For generating our predicted data, we have constructed a grid with a size of 276(nx_0) x 150(nz_0), where nx_0 and nz_0 are the number of grid points in the horizontal and vertical direction. The grid spacing is set to 0.25m in both directions, to avoid numerical dispersion in the finite difference modelling. The time sampling is 0.1ms for the forward modelling and the registration time is 0.5s. Both predicted and observed data were resampled to a 2ms time interval. The simulation of the shots is performed using SOFI2D (Bohlen, 2002), a viscoelastic forward modelling code that solves the pure elastic or viscoelastic wave equation by a finite difference scheme in the time domain. The model parameters to be estimated are the Vs and Vp values, and we are considering a homogeneous

constant model for the density. However, for brevity, only the Vs results will be discussed because this is notoriously the most informed model parameters when considering surface wave data. Parallelization of the calculation of the Jacobian matrix across different servers was employed to reduce computational costs.

The seismic data and velocity models must be projected onto the DCT space, where the MCMC sampling runs. For the data, we have noticed that 60x45=2700 retained coefficients resulted in a relative percentage error with respect to the observed data lower than 8%, reducing the the full 250x48x3=36000-D data space to a 60x45x3=8100-D domain (where are considering the same number of DCT coefficients for all the three shots). For the model space instead, 20 and 7 coefficients along the two DCT spatial dimensions explain more than 95% of variability of the model obtained extending the borehole data in the horizontal direction, reducing the 150x276x2=82800-D elastic space to an 20x7x2=280-D domain (i.e., we are considering the same number of DCT coefficients for both the Vp and Vs models). We need to point out that this compression not only reduces the dimensions of the vectors and matrices involved in the inversion procedure (such as the gradient and the Hessian), but also greatly reduces the number of forward evaluations needed to construct the Jacobian matrix and so, the overall computational cost of the algorithm.

The implementation used six cores on an Intel® Core™ i7-8700 CPU @ 3.20GHz. Each iteration, including computing the Jacobian, the gradient, the Hessian matrix and drawing a sample, takes approximately 8m wall clock time. A total of 4.000 iterations for a single chain required approximately 6 days. In our case we used five MCMC chains to sample the model space, which started from very simple two layered velocity models. Figures 1a and 1c show, respectively, one of the starting models of the chains used for the GB-MCMC inversion and the posterior mean model, computed considering all the chains. The prior information for the Bayesian inversion (prior mean vector and prior covariance matrix) are directly derived from the two layered model displayed in Figure 1a.

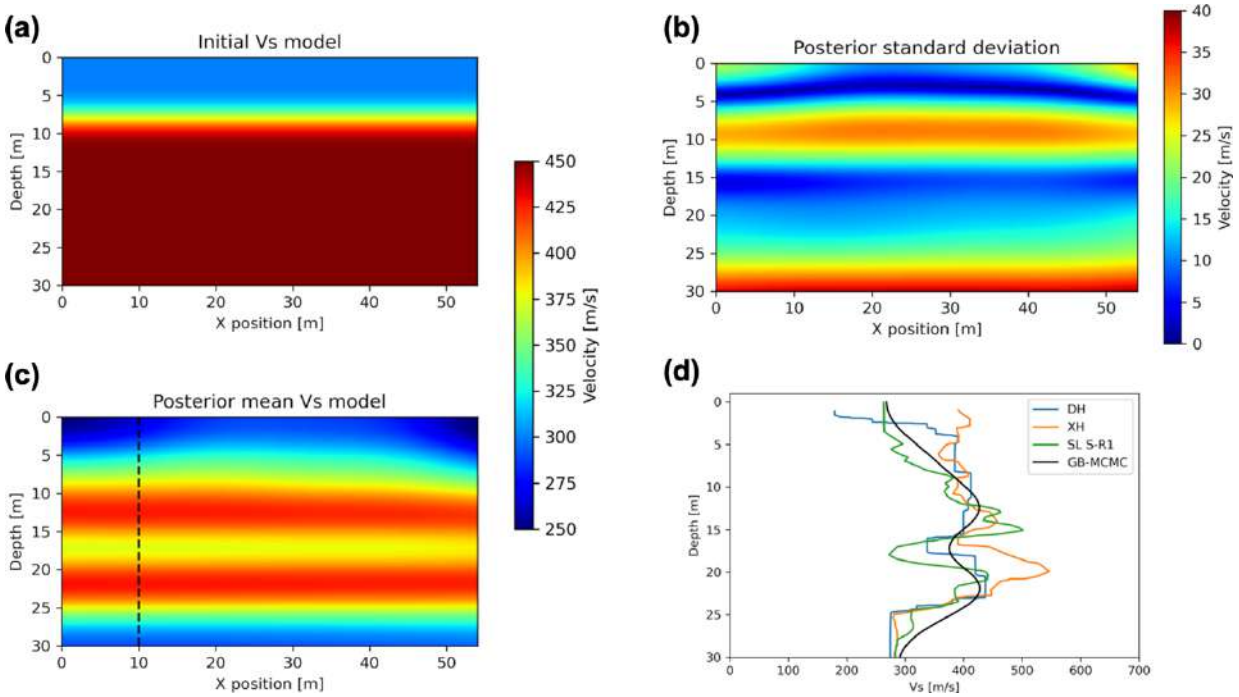

Fig. 1 (a) One of the starting models used for the GB-MCMC inversion; (b) Posterior standard deviation map; (c) Posterior mean Vs model considering the five chains; the dashed black line corresponds to the position of the available borehole data; (d) The borehole data together with the velocity profile of the predicted model at the horizontal position of 10m (black).

A comparison between the obtained results at the horizontal position of 10m and the available borehole data revealed an accurate reproduction of all the main velocity variations (Figure 1d). In particular, the two high velocity layers are clearly identified at depths 10-15m and 19-25 m with a Vs value around 430 m/s. In between, there is a very thin layer (around 3m of thickness) characterized by a lower Vs velocity, around 370 m/s. We are also able to observe the velocity inversion around 25m of depth, at the bottom edge of the model. As expected, this velocity layer is also characterized by the highest standard deviation values (Figure 1b), considering that it is below the high velocity layer and at the edge of the model. We need to consider that the standard deviation map suggests small uncertainties for all the velocity models (less than 40 m/s).
In Figure 2a we can see the evolution of the negative log-likelihood for all the chains, and we can notice that, after the end of the burn-in period, all the chains oscillate around the same values, meaning that we have reached the stationary regime. Figure 2b shows the acceptance ratio for the five chains, calculated as the ratio between the number of accepted models and the number of iterations. We can see that all the values are very high, compared to the ones usually achieved with standard gradient-free MCMC methods (around 20%), highlighting the superior efficiency of the proposed method. A comparison between the leftmost shot of the observed data (after pre-processing) and the data computed on the starting model of Figure 1a revealed significant cycle-skipping, indicating that any local approach would fail in locating the global minimum of the error function (Figure 3a). Differently, our approach finally provides a mean posterior model that is capable of successfully reproducing the observed seismic data (Figure 3b). This capability was emphasized by the close-ups of Figures 3c and 3d, in which we can appreciate the significant differences between the observed and initial data and how the cycle skips vanish when the data computed on the posterior mean model is considered. This means that the implemented approach could be also used to define an optimal starting model suitable for a subsequent step of local FWI.

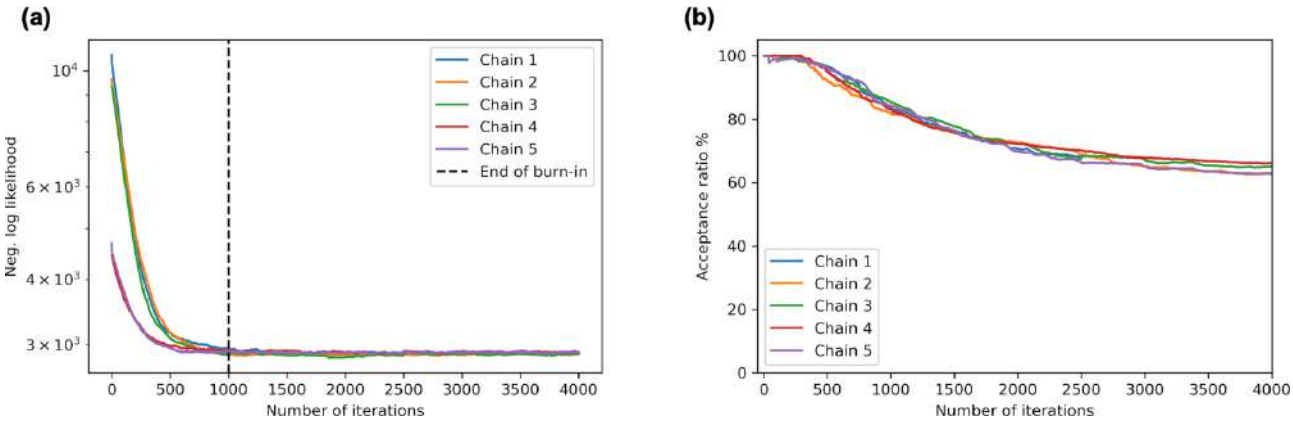

Fig. 2 (a) Evolution of the negative log-likelihood, which measures the misfit between observed and predicted data, for all the five chains and the end of the burn-in period (dashed black); (b) Acceptance ratio for all the five chains.

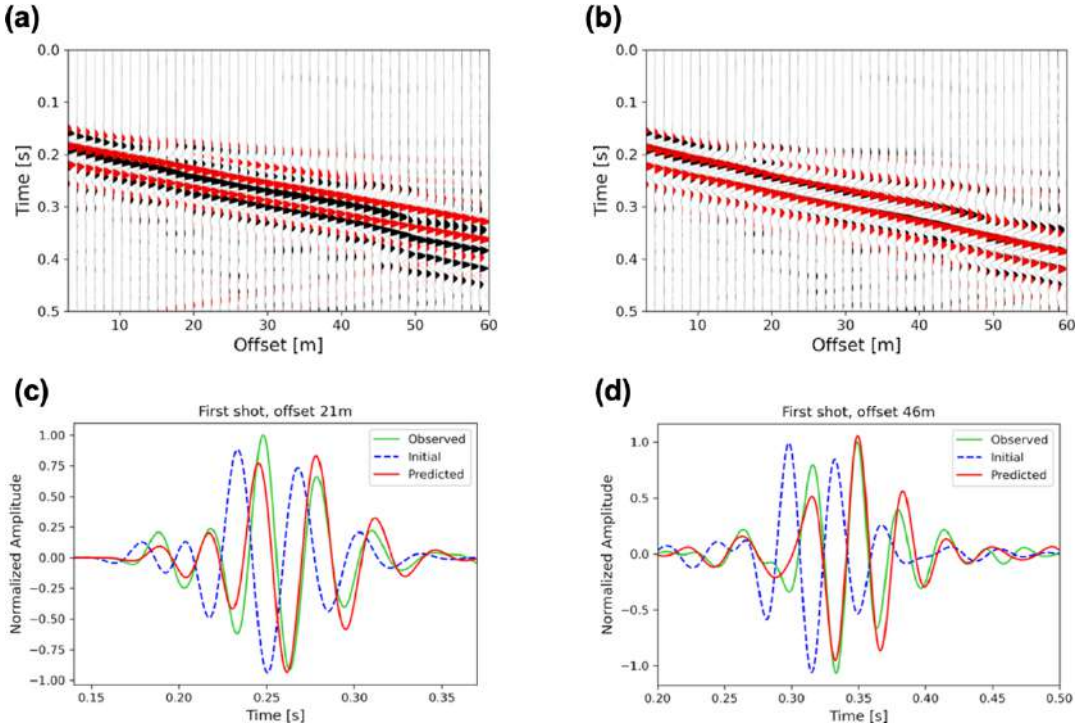

Fig. 3 (a) The leftmost shot of the observed data in black, compared against the data generated using one of the starting models (red); (b) Comparison between the same observed shot gathers (in black) and the data generated from the posterior mean model (in red); (c, d) Comparison of two seismic traces of the same shot of the observed data (green), the predicted data (red) and the initial data (dashed blue).

Conclusions

In this study we introduced a computationally efficient Bayesian elastic FWI, leveraging a GB-MCMC sampling technique along with a DCT compression applied to both the model and data spaces. The adopted MCMC strategy addresses the cycle-skipping problem affecting the local FWI approach, utilizing the local gradient and Hessian information of the posterior density to guide the sampling towards the most promising regions of the model space. This results in a significant reduction in computational burden of the probabilistic approach compared with standard gradient-free MCMC algorithms. We demonstrated the efficacy of the GB-MCMC elastic FWI applied to a field dataset, acquired in Grenoble. After pre-processing the seismic data in order to make it comparable with the data generated using the elastic forward modelling, five Markov chains were employed to numerically assess the PPD, each one starting from very simple initial models. The predicted posterior mean model accurately replicated all the vertical velocity variations evidenced by the available borehole data. In addition, our model prediction is also capable to closely match the observed seismic data, affirming the applicability and reliability of the proposed approach that can also be conveniently used to define a starting point for a subsequent step of local inversion, aimed at enhancing the velocity model's resolution and further minimize the difference between predicted and observed data. Our ongoing research focuses on optimizing the overall computational efficiency of our inversion procedure through the integration of deep learning techniques.

References

Aleardi, M.; 2021: A gradient-based Markov chain Monte Carlo algorithm for elastic pre-stack inversion with data and model space reduction. *Geophysical Prospecting*, 69(3).

Berti, S., Aleardi, M. and Stucchi, E.; 2023. A computationally efficient Bayesian approach to full-waveform inversion. *Geophysical Prospecting*, 1-24.

Bohlen, T.; 2002. Parallel 3D viscoelastic finite difference seismic modelling. *Computers and Geosciences*, 28, 887-899.

Garofalo, F., Foti, S., Hollender, F., Bard, P.Y., Cornou, C., Cox, B. et al.; 2016. InterPACIFIC project: comparison of invasive and non-invasive methods for seismic site characterization. Part I: Intra-comparison of surface wave methods. *Soil Dynamics and Earthquake Engineering*, 82, 222-240.

Lamuraglia, S., Stucchi, E. and Aleardi, M.; 2022. Application of a global-local full-waveform inversion of Rayleigh wave to estimate the near-surface shear wave velocity model. *Near Surface Geophysics*, 1-18.

Corresponding author: Sean Berti, sean.berti@unifi.it

Full-decay spectral modelling of time-domain induced polarization decoupling model and forward meshes with EEMverter

A.Bollino[1], G. Fiandaca[1]

[1] *The EEM Team for Hydro & eXploration, Department of Earth Sciences "Ardito Desio", Università degli Studi di Milano, Milano (Italy)*

Direct current (DC) resistivity and induced polarization (IP) geophysical methods are widely used in geophysical near-surface investigations, gaining information about subsurface conductivity structures by injecting electric currents into the ground and measuring electric voltages at different locations. The DC resistivity method provides information about the electrical conductive properties of the subsurface. In contrast, the IP method targets the capacitive characteristics offering additional insight into the physical and electrochemical nature of subsurface materials.
The IP phenomenon has been widely investigated both in time (TDIP) and frequency (FDIP) domains, in the laboratory, or through field studies. The TDIP has been used for many years for disseminated ores and mineral discrimination (e.g. Vanhala and Peltoniemi, 1992; Seigel et al., 1997, 2007). Over the last 20 years significant advancements in IP research have taken place, particularly with respect to the spectral content of the IP signal, which can be applied to engineering and environmental problems, such as the detection of contaminants and old landfills (e.g. Weller et al. 1999; Gazoty et al. 2012; Fiandaca et al., 2015; Johansson et al. 2015), and the derivation of grain size distribution parameters in unconsolidated sediments (e.g. Vanhala et al., 1992, Kemna et al., 2004, 2012).

In the frequency domain, IP phenomena can be represented as a complex conductivity $\sigma^*(\omega)$ that varies with frequency (ω), which can be expressed as:

$$\sigma^*(\omega) = |\sigma(\omega)| e^{i\varphi(\omega)} = \sigma'(\omega) + i\sigma''(\omega) \quad (1)$$

where * denotes a complex term, $|\sigma(\omega)|$ is the magnitude of conductivity, φ is the phase angle between injected current and measured voltage, $\sigma'(\omega)$ is the real component of conductivity, $\sigma''(\omega)$ is the imaginary component of conductivity, $\omega = 2\pi f$ is the angular frequency representation of frequency f, and $i = \sqrt{-1}$ (Binley, 2015). By neglecting electromagnetic (EM) effects, the complex potential $u^*(\omega) = u'(\omega) + iu''(\omega)$ is linked to the complex conductivity through Poisson's equation:

$$\nabla \cdot j_S^*(\omega, r) = \nabla \cdot \left[\sigma^*(\omega, r) E^*(\omega, r)\right] \quad (2)$$

where j_S^* is the applied source current density, $\boldsymbol{r}$ = (*x, y, z*) is the spatial location, and $E^*(\omega, r) = -\nabla u^*(\omega, r)$ is the complex electric field.

In the time domain, Poisson's equation is given as a convolution between the conductivity and the electric field as a function of the time *t* (e.g. Kemna, 2000):

$$\nabla \bullet j_s(t, r) = \nabla \cdot \left[\int_0^\infty \sigma(t', r) E(t - t', r) dt' \right] \tag{3}$$

where $\sigma(t)$ is the inverse Laplace transform of $\sigma^*(\omega)$ and $\boldsymbol{E}(t, \boldsymbol{r}) = -\nabla u(t, \boldsymbol{r})$.

As mentioned above, during the last two decades, significant advancements in induced polarization research have taken place, particularly with respect to spectral IP (SIP) and its increasing application in near-surface investigations even if surveys are usually modelled by taking into account only the integral chargeability, thus disregarding spectral content and neglecting the effect of the transmitted waveform, biasing inversion results. In this context, following Fiandaca et al. (2012, 2013)'s approach, EEMverter has been developed to model IP in electric and electromagnetic (EM) data within the same inversion framework and where the forward response is computed in the frequency domain for all dimensionalities, solving the full version of Poisson's equation, and then transformed into the time domain, thus avoiding the time-domain approximation (eq. 3). Here, we will focus only on the galvanic aspects in EEMverter modelling, while the other modelling features of EEMverter, such as EM modelling, time-lapse and joint inversion of galvanic and EM data are treated in Fiandaca a et al. (2024).

From a physical-mathematical point of view, resistivity and IP forward responses are modelled in the frequency domain for a range of frequencies using the finite element method. The responses are then transformed into the time domain for each quadrupole measurement and the transmitted current waveform is applied. In 2-D, the FD forward response assumes an isotropic 2-D distribution of the complex conductivity, neglecting electromagnetic induction. Considering the complex conductivity $\sigma^*(x, z, \omega)$ at a given frequency ω with a point source at the origin with (zero-phase) current *I,* the Poisson's equation can be defined as follow:

$$\frac{\partial}{\partial x}\left(\sigma^* \frac{\delta \sigma^*}{\delta x}\right) + \frac{\partial}{\partial z}\left(\sigma^* \frac{\partial \phi^*}{\partial z}\right) - \lambda^2 \phi^* \sigma^* = -I\delta(x)\delta(z) \tag{4}$$

where ϕ^* is the Fourier-transformed complex potential, λ is the Fourier transformation variable for the assumed strike (*y*) direction and δ represents the Dirac delta function.

Once the frequency domain potential ϕ^* is computed, the time domain computation is carried out through a cosine/sine transform, solved numerically in terms of Hankel transforms, expressed in terms of Bessel functions of order -1/2 and +1/2, respectively (Johansen and Sørensen, 1979):

$$\frac{1}{\pi} \int_0^\infty f(\omega) cos\ sin\ (\omega t) d\omega = \sqrt{r} \int_0^\infty f_1(\lambda) \lambda J_{\mp \frac{1}{2}}(\lambda r) d\lambda \tag{5}$$

Where $r = t\sqrt{2\pi}, \lambda = \frac{\omega}{\sqrt{2\pi}}$ and $f_1(\lambda) = \frac{1}{\sqrt{\lambda}} f\left(\frac{\lambda}{\sqrt{2\pi}}\right)$.

Finally, the time-domain IP decay is computed as the convolution of the impulse response with the current waveform $i(t)$ between the electrodes, solved as proposed by Fitterman and Anderson (1986) for piecewise linear current waveforms.

EEMverter is implemented in such a way that the inversion parameters are defined on the nodes of the model mesh and migrated to the forward mesh through interpolation (that can be chosen and selected by the user). The spatial decoupling between model and forward meshes allows for defining the model parameters, e.g., the Cole-Cole (Cole and Cole 1941; Pelton et al. 1978) ones, on several model meshes, one for each inversion parameter, for example.
For each dataset of the inversion process, a distinct forward mesh is defined. The interpolation from model parameters **M** into the values $\mathbf{m}_i$ is expressed through a matrix multiplication:

$$m_i = f_i(M) = F_i \bullet M \tag{6}$$

in which the matrix F_i holds the weights of the interpolation that depends only on the distances between model mesh nodes and the subdivisions of the ith forward mesh (Fiandaca et al., 2024).
As for the forward response, the Jacobian matrix is computed in the frequency domain and then transformed into the time domain. The time-domain Jacobian in the ith forward mesh is computed as:

$$J_{m_i,TD} = A \bullet T \bullet J_{m_i,FD} \tag{7}$$

where the matrix $\boldsymbol{T}$ holds the Hankel coefficients, the matrix $\boldsymbol{A}$ implements the effects of current waveform, gate integration and filters and the frequency-domain Jacobian $J_{m_i,FD}$ is calculated in 1-D through finite difference and in 2-D/3-D using the adjoint method and the chain rule as in Fiandaca et al. (2013) and Madsen et al. (2020), thus allowing to use any parameterization of the IP phenomenon in the inversion:

$$J_{m_i,FD} = J_{\sigma^*,i} \bullet \frac{\partial \sigma^*}{\partial_{m_i}} \tag{7}$$

where $J_{\sigma^*,i}$ is the Jacobian of the ith forward mesh with respect to the complex conductivity σ^* and $\frac{\partial \sigma^*}{\partial_{m_i}}$ is the partial derivative of the complex conductivity versus the model parameters (Fiandaca et al., 2024).
The Levenberg-Marquardt linearized approach is used for computing the inversion model:

$$M_{n+1,j} = M_{n,j} + \left[J_{M,j}^T C_d^{-1} J_{M,i} + R^T C_{R,}^{-1} R_j + \lambda I\right]^{-1} \bullet \left[J_{M,j}^T C_d^{-1} \bullet \left(d - f_{n,j}\right) + R^T C_{R,j}^{-1} R_j \bullet M_{n,j}\right] \tag{8}$$

where the subscript *j* indicates that the inversion process can be split in different inversion cycles: in each cycle *j* it is possible to change the forward computation for each dataset (e.g., from 1-D to 3-D), as well as to insert/remove data/constraints from the objective function (Fiandaca et al., 2023).

However, when using the resistivity and IP method to map subsurface geological structures with complex geometries, 1-D and 2-D inversion schemes are not always sufficient and 3-D modelling and inversion of the data are required. For this reason, EEMverter is also developed for 3-D inversion, following Madsen et al., (2020). To discretize the 3-D problem, a combined triple-grid inversion approach (presented by Günther et al. 2006) is adopted: a coarse tetrahedral mesh is used for the inversion (the model mesh) and two finer discretized tetrahedral meshes (one for the primary potential field and one for the secondary potential field) are used to compute the forward responses, balancing the modelling accuracy, the computational speed and memory usage. The results of the 2-D implementation on synthetic and field data, as well as the 3-D implementation under development, will be presented at the conference.

References

Binley, A. (2015). DC electrical methods.

Cole, K.S. & Cole, R.H., (1941). Dispersion and absorption in dielectrics I. Alternating current characteristics, *J. Chem. Phys.,* **9,** 341–351.

Fiandaca, G., Auken, E., Gazoty, A. & Christiansen, A.V., (2012). Time-domain induced polarization: full-decay forward modeling and 1D laterally constrained inversion of Cole-Cole parameters, *Geophysics,* **77,** E213–E225.

Fiandaca, G., Ramm, J., Binley, A., Gazoty, A., Christiansen, A. V., & Auken, E. (2013). Resolving spectral information from time domain induced polarization data through 2-D inversion. *Geophysical Journal International*, *192*(2), 631-646.

Fiandaca G., Christiansen A. and Auken E. (2015). Depth of investigation for multi-parameters inversions. Near Surface Geoscience 2015–21st European meeting of environmental and engineering geophysics.

Fiandaca, G., Madsen, L.M. & Maurya, P.K., (2018). Re-parameterisations of the Cole–Cole model for improved spectral inversion of induced polarization data, *Near Surf. Geophys.,* **16**(4), 385–399.

Fiandaca, G., Zhang, B., Chen, J., Signora, A., Dauti, F., Galli, S., Sullivan, N.A.L., Bollino, A., Viezzoli, A. (2024). EEMverter, a new 1D/2D/3D inversion tool for Electric and Electromagnetic data with focus on Induced Polarization. GNGTS 2024, 13-16 February 2024, Ferrara, Italy.

Fitterman, D. V., & Anderson, W. L. (1987). Effect of transmitter turn-off time on transient soundings. *Geoexploration*, *24*(2), 131-146.

Gazoty, A., Fiandaca, G., Pedersen, J., Auken, E., Christiansen, A.V. & Pedersen, J.K., (2012). Application of time domain induced polarization to the mapping of lithotypes in a landfill site, *Hydrol. Earth Syst. Sci.,* **16,** 1793–1804.

Günther, T., R¨ucker, C. & Spitzer, K., 2006. Three-dimensional modelling and inversion of dc resistivity data incorporating topography - II. Inversion, *Geophys. J. Int.,* **166,** 506–517.

Johansen, H.K. & Sørensen, K.I., (1979). Fast Hankel transforms, *Geophys.Prospect.,* **27,** 876–901.

Kemna, A, (2000). Tomographic inversion of complex resistivity: theory and application, *Thesis,* Der Andere Verlag, ISBN 3-934366-92-9.

Kemna, A., Binley, A., & Slater, L. (2004). Crosshole IP imaging for engineering and environmental applications. *Geophysics*, *69*(1), 97-107.

Kemna, A., Binley, A., Cassiani, G., Niederleithinger, E., Revil, A., Slater, L., ... & Zimmermann, E. (2012). An overview of the spectral induced polarization method for near-surface applications. *Near Surface Geophysics*, *10*(6), 453-468.

Madsen, L.M., Fiandaca, G., Auken, E. & Christiansen, A.V., (2017). Timedomain induced polarization - an analysis of Cole-Cole parameter resolution and correlation using Markov Chain MonteCarlo inversion, *Geophys. J. Int.,* **211**(2), 1341–1353.

Madsen, L. M., Fiandaca, G., & Auken, E. (2020). 3-D time-domain spectral inversion of resistivity and full-decay induced polarization data—full solution of Poisson's equation and modelling of the current waveform. *Geophysical Journal International*, *223*(3), 2101-2116.

Martin, T., Titov, K., Tarasov, A., & Weller, A. (2021). Spectral induced polarization: frequency domain versus time domain laboratory data. *Geophysical Journal International*, *225*(3), 1982-2000.

Pelton, W.H., Ward, S.H., Hallof, P.G., Sill, W.R. & Nelson, P.H., (1978). Mineral discrimination and removal of inductive coupling with multifrequency IP, *Geophysics,* **43,** 588–609.

Seigel H.O. (1959). Mathematical formulation and type curves for induced polarization. Geophysics 24(3), 547–565.

Seigel, H.O., Vanhala, H., Sheard, S.N., (1997). Some case histories of source discrimination using time-domain spectral IP. Geophysics

62, 1394– 1408.

Seigel, H., Nabighian,M., Parasnis, D.&Vozoff, K., (2007). The early history of the induced polarization method, *Leading Edge,* **26,** 312–321.

Tarasov, A. & Titov, K., (2007). Relaxation time distribution from time domain induced polarization measurements, Geophys. J. Int., 170, 31–43.

Vanhala, H., Peltoniemi, M., (1992). Spectral IP studies of Finnish ore prospects. Geophysics 57, 1545–1555.

Vanhala, H., Soininen, H., & Kukkonen, I. (1992). Detecting organic chemical contaminants by spectral-induced polarization method in glacial till environment. *Geophysics*, *57*(8), 1014-1017.

Weller, A., Frangos, W. & Seichter, M., (1999). Three-dimensional inversion of induced polarization data from simulated waste, *J. appl. Geophys.,* **41,** 31–47.

Corresponding author: arcangela.bollino@unimi.it

Differential arrival times for event location with DAS data

E. Bozzi [1], L. Gebraad [2],A. Fichtner [3], N. Piana Agostinetti [1], G. Saccorotti [4], T. Kiers [3], T. Nishimura [5]

[1] *University of Milano-Bicocca (Milan, Italy)*
[2] *Mondaic Ltd (Zurich, Switzerland)*
[3] *ETH Zurich, Institute of Geophysics (Zurich, Switzerland)*
[4] *Instituto Nazionale di Geofisica e Vulcanologia (Pisa, Italy)*
[5] *Tohoku University, Department of Geophysics (Tohoku, Japan)*

Standard seismic networks typically use absolute arrival times of specific seismic phases to estimate source locations. In this context, multiple sensors are positioned over a monitored area, aiming to minimize the azimuthal gap to known seismicity clusters. Distributed Acoustic Sensing (DAS) technology, which converts fiber optic cables (FOCs) into very dense seismic arrays, is nowadays used for similar purposes. DAS has the additional advantage of being able to exploit preexisting telecommunication FOCs (Telecom-FOCs). However, since the original installation purpose for Telecom-FOCs doesn't align with seismological needs, the spanned azimuthal directions can be limited. Hence, relying on absolute arrival times for event location might result in uncertain locations, given poor waveform moveouts and site-specific sources of noise in the data. Nevertheless, the intrinsic DAS channels' spatial density provide a good opportunity to test multi-channel cross-correlation techniques. Here, to assess the potential benefit from using differential arrival times for event location, we cross-correlate all possible DAS channel pairs and identify P-wave time delays. We focus on well-known test environments (i.e., known event locations) and use a Hamiltonian Monte Carlo algorithm to estimate hypocentral parameter uncertainties, considering both absolute and differential arrival times. We demonstrate how differential arrival times better constrain the events' azimuthal directions compared to absolute arrival times. However, computational costs are inevitably higher due to the significant increase in data points when considering all the P-wave delays. A mitigation to this issue is reached by selecting measurements based on thresholds for the minimum cross-correlation index and maximum interchannel distance. This work illustrates how to potentially alleviate DAS geometrical limitations on event location by exploiting selected differential arrival times.

Corresponding author: e.bozzi3@campus.unimib.it

A compact measuring system for UAV based magnetic anomalies surveys

R. Carluccio[1], I. Nicolosi[1], F. D'Ajello Caracciolo[1], L. Minelli[1]

[1] Istituto Nazionale di Geofisica e Vulcanologia (INGV)

One of the most commonly used applications of potential fields in geophysics is the measurement of field anomalies in order to produce regional maps. These anomalies are in fact due to anisotropies in terrain geology and can give indirect information on underground layers/structures. In the magnetic field case, anisotropies are mainly due to differences in magnetic susceptibility and to the presence of magnetised material (remanence) in the underlying structures.

Magnetic anomaly maps are usually realised scanning the area of interest with a sensible magnetometer, usually following a parallel, equally spaced lines pattern properly oriented with respect to North.

Areas of interest can generally scale over orders of magnitude ranging from regional (thousands of square kms) to hundreds of square meters. Up to recent years this kind of measure has mainly been done either with airborne measuring systems, airplanes or helicopters or by walking on the ground in small areas. With the advent of UAV systems a series of intermediate targets have become possible since low altitude, square kilometres orders surveys, even on impracticable (by man) wild areas could be easily managed in a fraction of time.

In the case of UAVs, however, there are some technical aspects that arise regarding the magnetic anomaly measure. The magnetometers required for these measurements are usually protons precession or optical pumping total field units, which are heavy and impractical as UAV payloads, weighing several kilograms. However, they are necessary because the anomalies being searched for can often be as low as a few nanotesla, which is five orders of magnitude less than the average Earth magnetic field. Fluxgate magnetometers are small and sensitive enough for this task, but they are difficult to use. Even if they can achieve the required sensitivity, they only measure the magnetic field component along their symmetry axis. In a moving frame, the only way to obtain a meaningful measurement is to mount three of them in an orthogonal frame (creating a tri-axial unit) and calculate the magnetic total field based on those readings. However, this procedure is affected by several factors, including: 1) the calibration of the three units in terms of their response function to the magnetic field and external temperature, 2) the orthogonality of their axes, and to a lesser extent, 3) the mutual interaction of the three sensors in space. It can be demonstrated that these factors can result in an error in the calculated total field that is much larger than the precision requirements mentioned earlier, unless a thorough and challenging calibration is performed for each individual unit.

Only in recent months however a new family of optical pumped miniaturised magnetometers have become available. They have furthermore characteristics comparable to their big-sized relatives.

On the basis of this new technology we have designed from scratch and realised a flying payload mounted in an aerodynamic “rocket-shape” towed assembly. Our system core is a new optically pumped micro magnetometer from QSPIN, the Total-Field Magnetometer (QTFM). Along with this sensor the system has GPS positioning system running at 10 Hz, 9- DOF IMU unit for attitude and heading reference, barometer and thermometer for indirect absolute altitude measuring, laser altimeter (up to 50 m) for direct terrain clearance (AGL) measure.

All of these data are acquired along with milliseconds onboard processor clock for post processing data resync. Data is read from sensors synchronous to the magnetic measure acting as master sync and stored on a local repository.

A bi-directional radio link has also been implemented in order to communicate to a ground based station through LORA (Long Range) signal modulation. It ensures radio connections over long ranges even with very low antenna RF power through the use of a redundant and compressed data modulation scheme. This is important to maximise efficiency with respect to onboard battery weight. The enhanced efficiency is however payd on data bandwidth: for our system setup a maximum of about 22 bytes/second are allowed for connection nominal distances of 5 kilometres and few mW in TX.

Over this link a binary compacted subset of survey measurements is transmitted to a base station: the subset ensures the issue of a magnetic data map rendered on a laptop for real time quality check of survey progression. Even if magnetic data is transmitted to the base station in a simplified-rounded way for bandwidth optimisation it can nonetheless act as data backup in the unlikely cases of on-board log failure.

It is also possible to remotely control the system through a handshake (ready to send status - acknowledge) protocol to change some survey parameters: measurements frequency (future feature), control of recording status and of recording parameters setup for differential barometric altitude measurement.

Fig. 1 shows the magnetometer rocket-shaped system (bird): all of the electronics are in the nose of the bird running around an arduino-like powerful 32 bit microcontroller. The actual sensor is instead put farthest from the electronics and from the battery in order to minimise unwanted magnetic noise: it is in the bird tail, inside the wooden ailerons holder. Apart from the electronic components, the bird is in fact entirely made of non-magnetic materials and during flight it is towed by the UAV with a 10 metres rope.

The system has been conceived to be independent from the AUV host platform. It is furthermore very light weighting about 1kg, battery included. It is very economical if compared with similar commercial systems. It is low energy consuming: a ~5000 mAh USB power pack gives 2-3 hours of autonomy. The actual implementation of the system has demonstrated to fly stable in moderate velocities even with some wind conditions. Future improvements foresee the implementation of an active stabilisation system to minimise bird pendulum-like oscillations for low velocity situations and/or caused by wind turbulence.

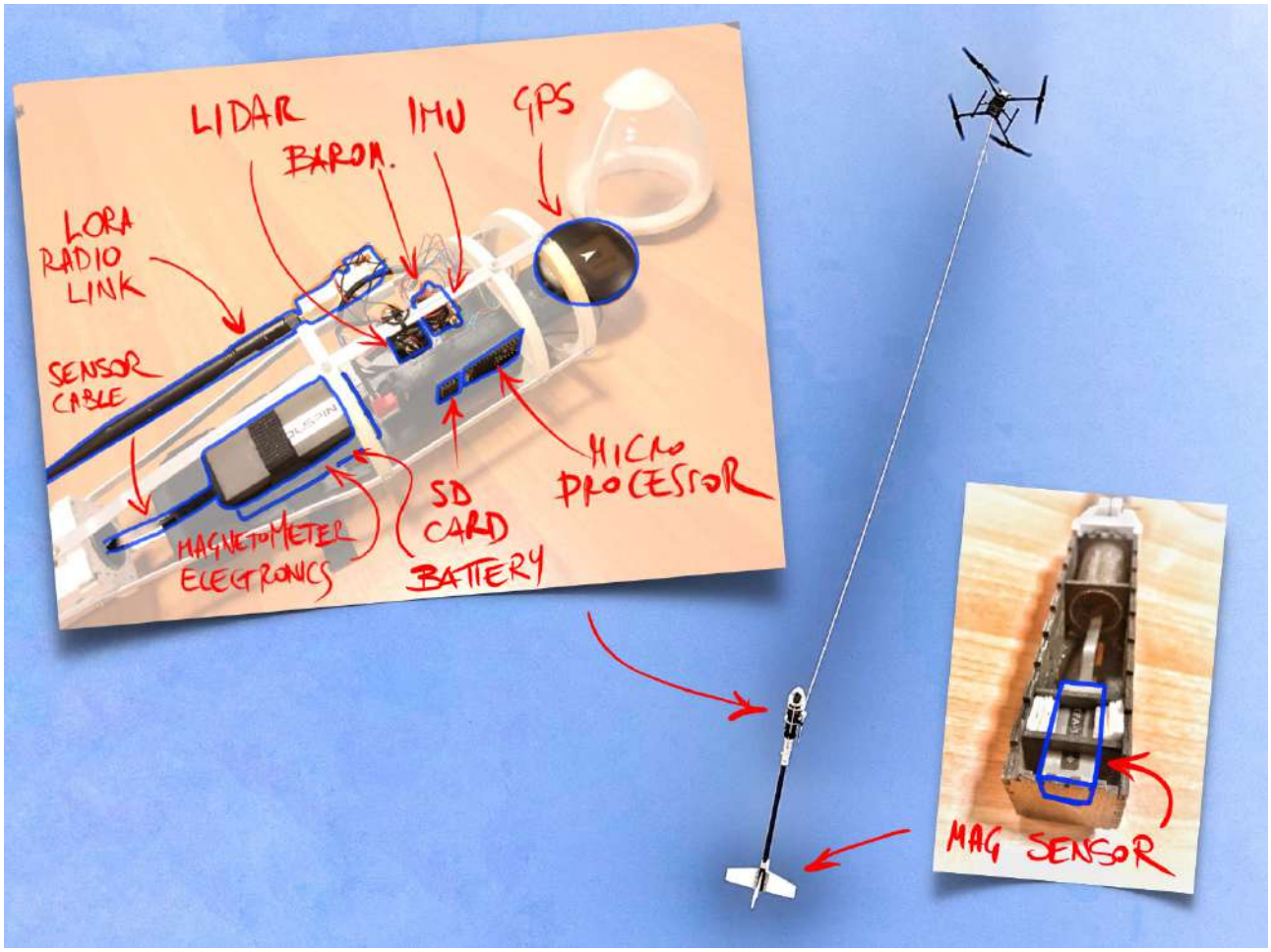

Fig. 1 – Bird towed by UAV with 10m cable with particular images showing operational parts and sensors.

.

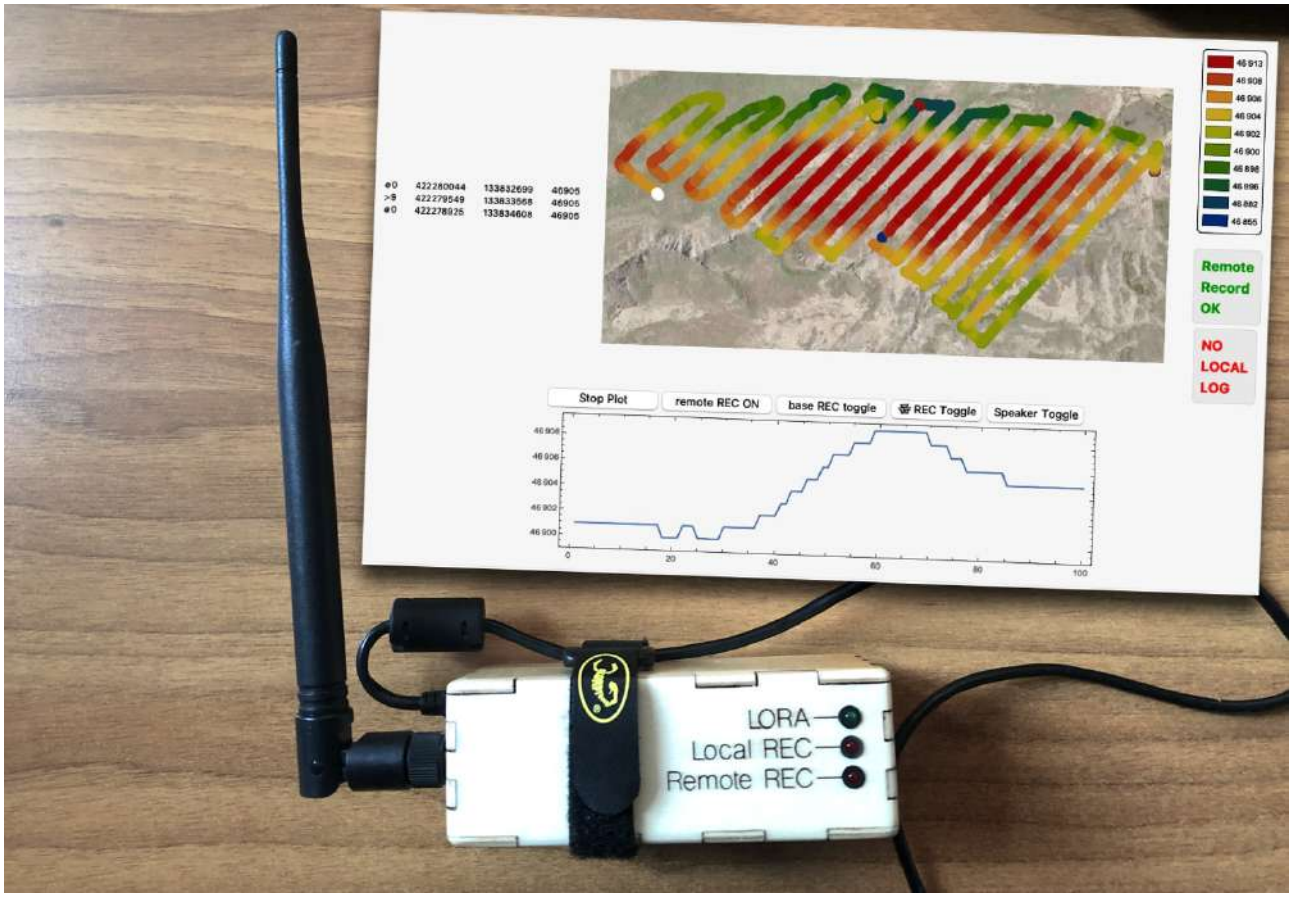

Fig. 2 – Base station LORA radio link together with a screengrab of the beta release of the real-time mapping software. Upper part of the software screen, from left to right: text dump of decoded data stream from the remote sensor, realtime geo-referenced map of survey raw data, adaptive and optimised real-time palette of magnetic field and messages flag signals. Lower part: moving chart of last 100 magnetic field measurements.

Fig. 2 is the base station system consisting of a LORA transceiver and binary packet demodulator USB connected to a laptop for real-time survey map rendering

Fig. 3 Shows processed a magnetic anomaly map of Campo Felice extensional basin, Abruzzo, central Italy, obtained from around 3-hour of UAV flight and a total profile length of 90 km. From post-flight analysis of measured data we have furthermore confirmed the reported sensor heading error to be less than 2 nanotesla.

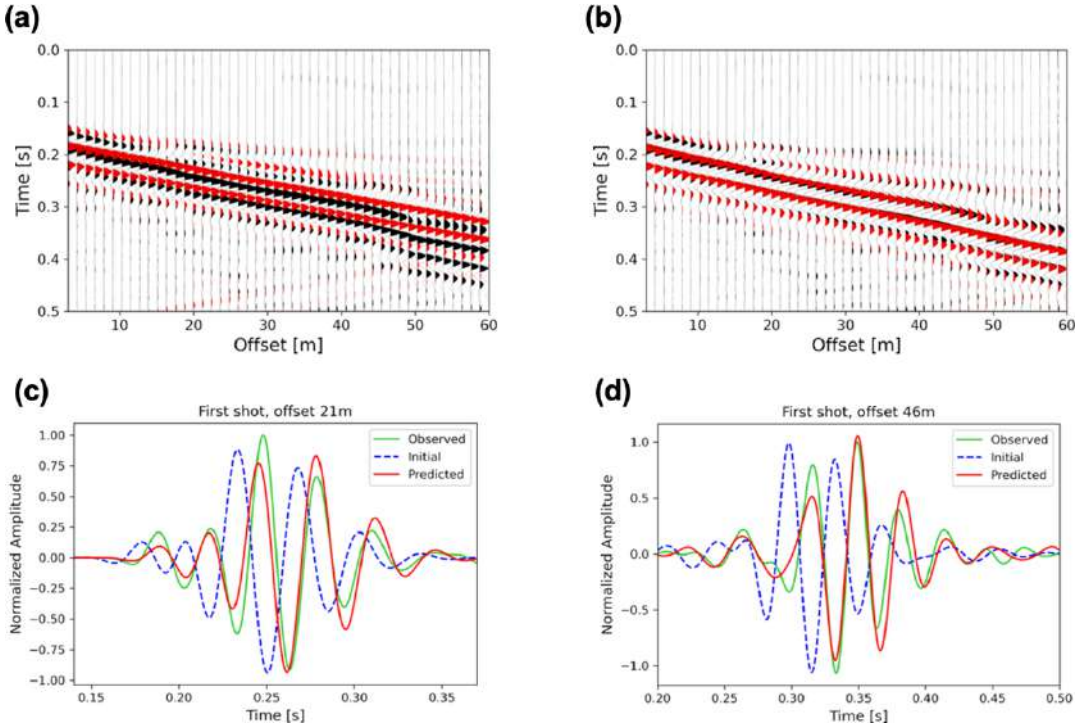

Fig. 3 – Reduced-To-the-Pole magnetic anomaly map of Campo Felice Plain displayed using a nonlinear intensity color scale and contour lines.

Conclusions

To recap, UAV-based surveys fill the gap between large-area airborne-based and ground-based magnetic surveys conducted by humans. In addition to the obvious advantage of being able to cover inaccessible areas, UAV surveys actually provide the highest resolution for geophysical surveys and open up new possibilities for local geological interpretation. They have advantages over ground-based surveys, which in theory could offer greater resolution but are hindered by their close proximity to superficial sources that can potentially produce a dominant signal and obscure geological features. Man-based surveys also suffer from terrain topography and sensor oscillations caused by walking, which introduce external noise. In contrast, UAVs can fly at an optimal minimum distance to maximise the spatial resolution of the geologic signal by following a smooth linear path that minimises external noise.

For example, we have successfully tested our system in different geological settings, such as intramontane Apenninic basins or mud volcanoes in Sicily, in order to characterise the subsurface geometry.

The QR code here reported points to the Youtube URL of a video showing one of the very first surveys conducted with the system that has been described.

Corresponding author: roberto.carluccio@ingv.it

Bayesian imaging method for towed transient electromagnetic data using probabilistic neural networks

J. Chen[1], G. Fiandaca[1]

[1]The EEM Team for Hydro & eXploration, Department of Earth Sciences "Ardito Desio", University of Milano, Milano (Italy).

Abstract

The towed transient electromagnetic (tTEM) can conduct efficient geological surveys on the near-surface of about 100 meters underground. Exploring fast and accurate on-site interpretation strategies for electromagnetic data is crucial for geoscientists and engineers to make high-quality decisions and further enhance the applicability of this technology. In this study, we designed a composite probabilistic neural network (cPNN) structure that can simultaneously provide deterministic imaging and Bayesian probabilistic imaging results, providing a comprehensive interpretation of the observed data and estimating its uncertainty. We verified this neural network with nearly 200 km tTEM survey data collected on the Iseo Lake in Italy. The results show that the cPNN network can effectively characterize the location of aquifers and underground clay layers, and the imaging results are consistent with conventional inversion and sonar bathymetry data. Furthermore, since the cPNN network can obtain the Gaussian distribution of underground resistivity, we can estimate the depth of investigation (DOI) of the imaging results and extract smooth models from the Gaussian distribution. The cPNN network can obtain approximate Bayesian inversion results for large tTEM dataset in only tens of seconds on a laptop, which has good practical value.

I Introduction

The towed transient electromagnetic (tTEM) is a new detection technology improved on the basis of the ground-based transient electromagnetic (TEM) method in recent years. This technology enables mobile geological surveys with all-terrain vehicles (Auken et al., 2019) or boats (Maurya et al., 2022), similar to the ground-based version of airborne transient electromagnetic (ATEM) technology (e.g. Silvestri et al., 2019). The survey speed of the tTEM system can reach nearly 20 kilometers per hour (Grombacher et al., 2021), and it can conduct efficient and low-cost geological surveys in large survey areas, with a typical depth of investigation (DOI) ranging from 80 to 100 meters.

At present, the tTEM has been successfully applied in various near-surface geological exploration fields such as agricultural ecological management, groundwater hydrology system mapping

(Grombacher et al., 2021), and groundwater vulnerability assessment (Sandersen et al., 2021). When carrying out large-scale exploration tasks, it is important for equipment operators to view the imaging interpretation results of the detection data, which is conducive to their on-site judgment of geological characteristics and instrument working status, so as to make high-quality decisions.

In recent years, a large number of studies have demonstrated the feasibility of deep learning algorithms in real-time imaging of TEM data (Colombo et al., 2021; Chen et al., 2022). These studies established a specific mapping between the exploration data and the resistivity parameter space based on deep neural network (DNN) frameworks. However, due to the ill-posedness and multi-solution nature of the geophysical electromagnetic inverse problem, the same exploration data can have multiple or infinite different geological model solutions. This one-to-many mapping relationship brings great training difficulty to the deep learning network and also affects the reliability of applying deep learning networks to interpret TEM data.

In this context, the development of probabilistic neural networks (PNN) has provided an effective solution to the nonlinear inversion problems in geophysics. The currently typical PNN structures include mixture density networks (MDN) and invertible neural networks (INN). MDN can learn to map a vector to an n-dimensional conditional probability distribution and parameterize it as a Gaussian mixture model (GMM) to learn arbitrary probability distributions (Mosher et al., 2021). INN can learn the bidirectional mapping between inputs and outputs, and it can estimate the posterior probability density function (PDF) by introducing additional latent variables on the output side. Both of these network structures can effectively simulate Bayesian posterior inference and have been successfully applied in geophysical inversion methods.

Inspired by the outstanding research mentioned above, we propose a composite probabilistic neural network (cPNN) structure that incorporates the LSTM autoencoder network with both DNN and MDN network structures. This design allows for simultaneous deterministic imaging and probabilistic estimation of tTEM data. Furthermore, we are able to evaluate the depth of investigation (DOI) through the resistivity Gaussian distribution output by the cPNN network.

II Bayesian imaging framework

As shown in Fig. 1, the Bayesian imaging framework based on the cPNN mainly includes three stages: data generation, network construction and training, and imaging result output. In the data generation stage, input data and label data for the entire network structure need to be prepared, including TEM response data and the corresponding theoretical resistivity model. In this study, considering the computational complexity caused by high-dimensional layer models and the superior shallow subsurface detection resolution of ground-based TEM compared to ATEM, the number of model layers is set to 30. We generated 30 depth interfaces within a range of 120 m underground using a log increasing with depth method. The last layer is assumed to be a semi-infinite half-space.

In the stage of imaging result output, the difference between MDN and conventional neural networks is that MDN outputs a conditional probability distribution, and it can learn arbitrary

probability distributions through Gaussian Mixture Models (GMMs). Taking TEM inversion as an example, suppose we have N training datasets $R=\{(\mathbf{d}_i, \mathbf{m}_i): i = 1, \ldots, N\}$, where **d** and **m** represent the input space of TEM data and the output space of resistivity model parameters, respectively. Given an input $\mathbf{d}_i$, if the trained resistivity model set $\mathbf{m}_i$ satisfies a prior probability density function distribution, the structure of a conventional neural network will output the corresponding $\mathbf{m}_i$ by minimizing the sum of squared errors on the set R. This output result will approximate the mean solution of the Bayesian posterior distribution $p(\mathbf{m}|\ \mathbf{d})$ (Earp et al., 2020). In contrast, MDN can directly output an estimate of the Bayesian posterior distribution $p(\mathbf{m}|\ \mathbf{d})$.

III cPNN network inversion results

The cPNN inversion has been tested on a FloaTEM survey carried out on the south shore of the Iseo lake to study the lake-groundwater interaction (Fig. 2), we carry out a waterborne tTEM (or FloatTEM) survey with a total survey line length of approximately 200 kilometers and a total of nearly 35,000 survey points (Galli et al., 2024). When carrying out measurements with the FloatTEM system, we installed a sonar sounding device on the boat to measure the bathymetry.

We compared the inversion results of the deep learning cPNN network with those based on the EEMverter (Fiandaca et al., 2024) modelling platform. The number of inversion layers and layer thickness are consistent with the deep learning training parameters. As shown in Fig. 3, both the DNN inversion results and the MDN inversion results output by the cPNN network similarly depict the hydrological characteristics under the Iseo lake, and its imaging results of the underground clay layer and underground aquifer are in good consistency with the inversion results of EEMverter. The gray grid in the figure is the bathymetry information of the lake water. It can be clearly seen that the imaging results of the cPNN network correspond well to the bathymetry information of the Sonar. The cPNN network takes about 35 seconds to invert Iseo data, while the EEMverter inversion based on the server platform takes approximately 6500 seconds.

IV Conclusions

In this study, we proposed a cPNN network structure that integrates DNN imaging-Net and MDN Bayesian-Net, which can directly convert the observed tTEM data into a resistivity model and estimate its uncertainty. The MDN Bayesian-Net captures the posterior PDF of the geological model, providing both maximum probability model and DOI as references, while the DNN imaging-Net provides an estimation of the posterior PDF mean solution. The two imaging results of cPNN complement each other and provide fast and comprehensive geological resistivity information.

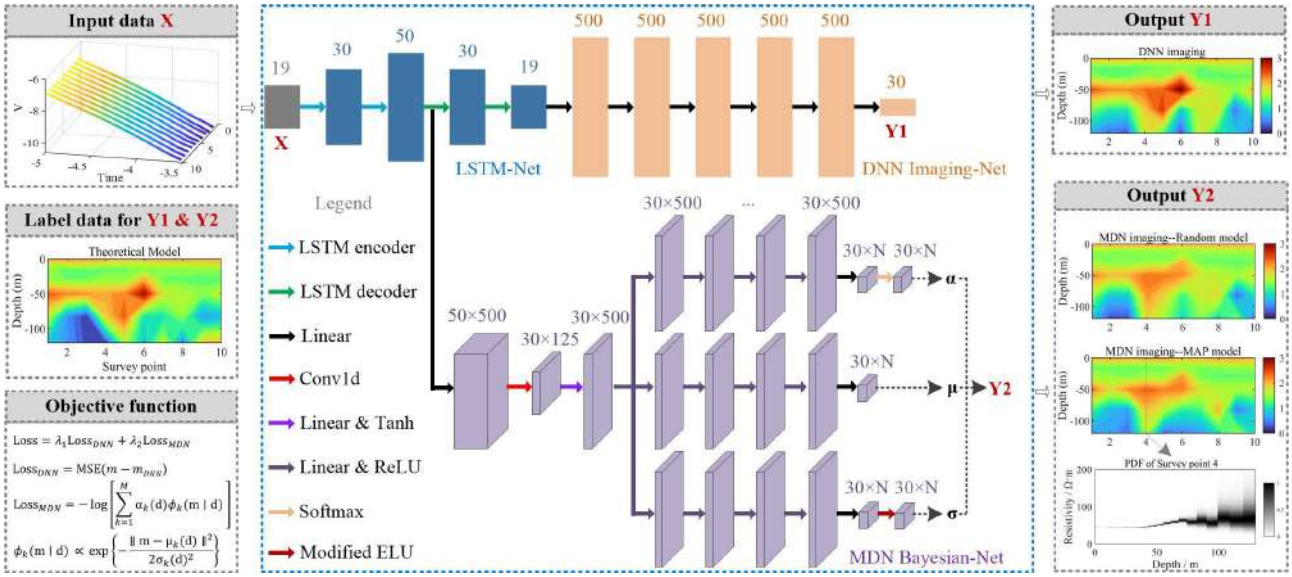

Fig. 1 The composite probabilistic neural network structure diagram. The input data of the cPNN network structure is TEM response data, and the label data is the corresponding theoretical resistivity models (Y1, Y2). The output data includes the DNN resistivity model and the MDN posterior probability distribution function. In this study, we set N=1.

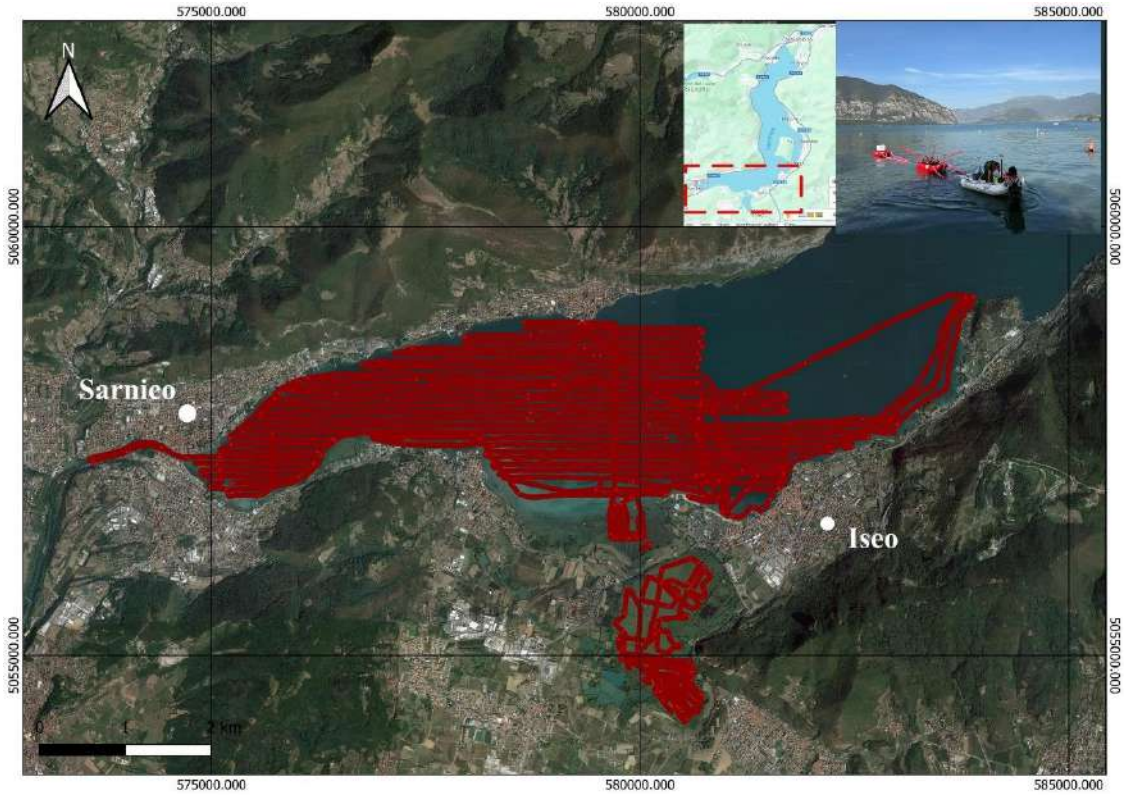

Fig. 2 The distribution of tTEM survey lines of the survey carried out on the south shore of the Iseo lake, together with an image of the acquisition and a map of the lake.

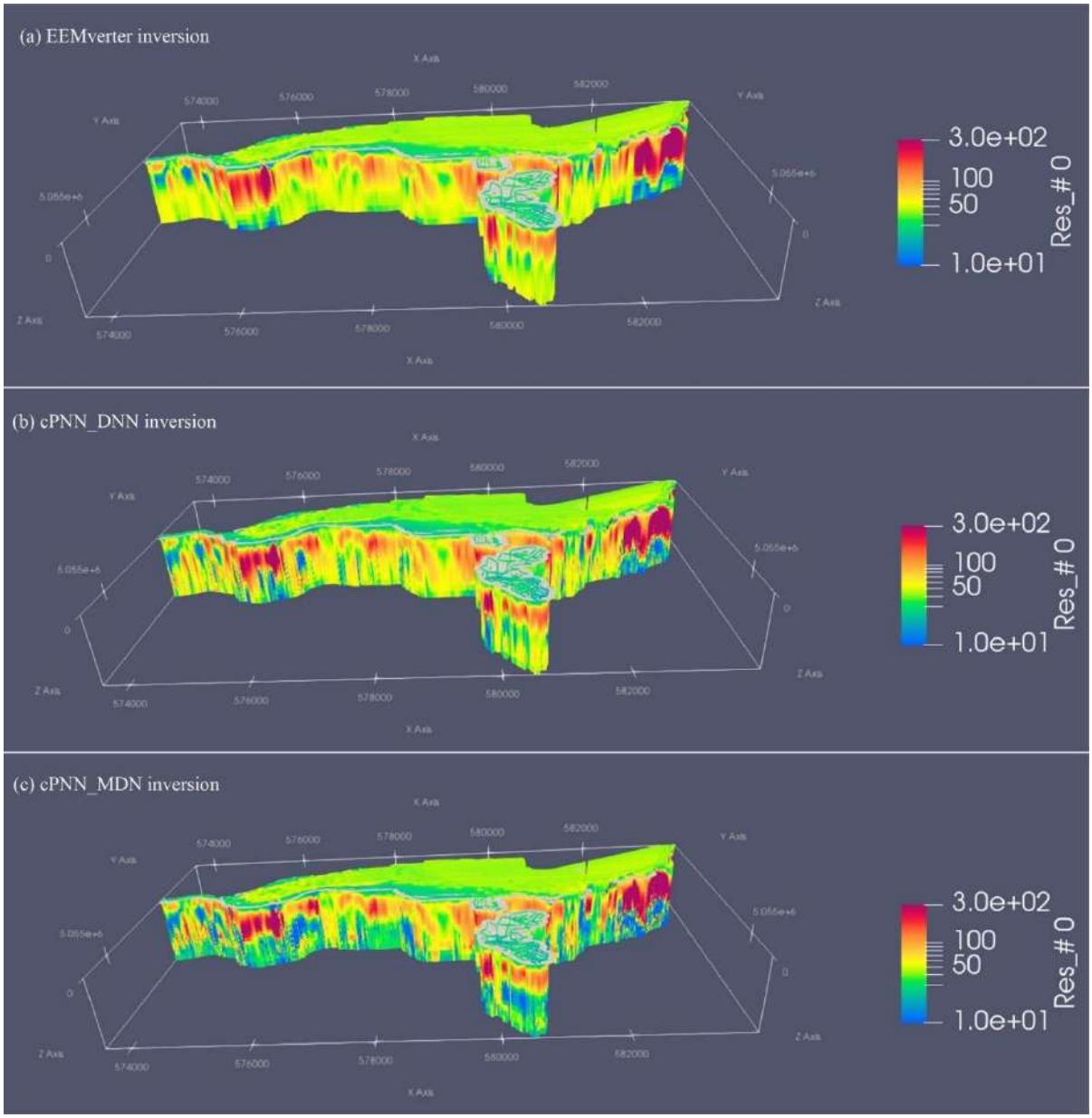

Fig. 3 Iseo lake tTEM data inversion results. From top to bottom: a) EEMverter deterministic inversion; b) Deep learning Neural Network (DNN) output of the cPNN network; c) mean value of the Mixture Density Network (MDN) output of the cPNN network.

Acknowledgments

This study has been carried out within the Horizon Europe project SEMACRET. The FloaTEM data have been acquired in the LakEMaging project, funded by Acque Bresciane.

References

Auken, E., Foged, N., Larsen, J. J., Lassen, K. V. T., Maurya, P. K., Dath, S. M., & Eiskjær, T. T. (2019). tTEM — A towed transient electromagnetic system for detailed 3D imaging of the top 70 m of the subsurface. *Geophysics*, *84*(1), E13–E22.

Colombo, D., Turkoglu, E., Li, W., Curiel, E. S., & Rovetta, D. (2021). Physics-driven deep-learning inversion with application to transient electromagnetics. *Geophysics*, *86*(3), E209–E224.

Chen, J., Zhang, Y., & Lin, T. T. (2022). Transient electromagnetic machine learning inversion based on pseudo wave field data. *IEEE Transactions on Geoscience & Remote Sensing*, *60*, 1–10.

Earp, S., Curtis, A., Zhang, X., & Hansteen, F. (2020). Probabilistic neural network tomography across Grane field (North Sea) from surface wave dispersion data. *Geophysical Journal International*, 223, 1741–1757.

Fiandaca, G., Zhang, B., Chen, J., Signora, A., Dauti, F., Galli, S., Sullivan, N.A.L., Bollino, A., Viezzoli, A. (2024). EEMverter, a new 1D/2D/3D inversion tool for Electric and Electromagnetic data with focus on Induced Polarization. *GNGTS 2024*, 13-16 February 2024, Ferrara, Italy.

Grombacher, D., Maurya, P. K., Lind, J. C., Lane, J., & Auken, E. (2021). Rapid mapping of hydrological systems in Tanzania using a towed transient electromagnetic system. *Groundwater*, 1–9.

Galli, S., Signara, A., Chen, J., Schaars, F., Grohen, M., Fiandaca, G. (2024). Waterborne electromagnetic: two case studies. *GNGTS 2024*, 13-16 February 2024, Ferrara, Italy.

Maurya, P. K., Christensen, F. E., Kass, M. A., Pedersen, J. B., Frederiksen, R. R., Foged, N., Christiansen, A. V., & Auken, E. (2022). Technical note: Efficient imaging of hydrological units below lakes and fjords with a floating, transient electromagnetic (FloaTEM) system. *Hydrology and Earth System Sciences*, *26*, 2813–2827.

Mosher, S. G., Eilon, Z., Janiszewski, H., & Audet, P. (2021). Probabilistic inversion of seafloor compliance for oceanic crustal shear velocity structure using mixture density neural networks. *Geophysical Journal International*, *227*, 1879–1892.

Neven, A., Maurya, P. K., Christiansen, A. V., Renard, P. (2021). tTEM20AAR: a benchmark geophysical data set for unconsolidated fluvioglacial sediments. *Earth System Science Data*, *13*, 2743–2752.

Prechelt, L. (1998). Early stopping — But when? *Neural networks: Tricks of the trade*, 55–69.

Silvestri, S., Christensen, C. W., Lysdahl, A. O. K., Anschütz, H., Pfaffhuber, A. A., & Viezzoli, A. (2019). Peatland volume mapping over resistive substrates with airborne electromagnetic technology. *Geophysical Research Letters*, *46*, 6459–6468.

Sandersen, P. B. E., Kallesøe, A. J., Mølle, I., Høyer, S., Jørgensen, F., Pedersen, J. B., & Christiansen, A. V. (2021). Utilizing the towed transient Electromagnetic method (tTEM) for achieving unprecedented near-surface detail in geological mapping. *Engineering Geology*, *288*, 106125.

Corresponding author: Jian.Chen@unimi.it

Dynamic Strain Transients Clustering Using an Unsupervised Machine Learning Strategy

B. Di Lieto[1], P. Romano[1], S. Scarpetta[2], A. Sangianantoni[1], G. Messuti[2]

[1] Istituto Nazionale di Geofisica e Vulcanologia, Osservatorio Vesuviano, Napoli, Italy;
[2]Università degli Studi di Salerno, Dipartimento di Fisica "E. R. Caianiello", Salerno, Italy.

In recent years, machine learning techniques have been exploited in volcanology in order to assess natural hazards, volcano dynamics changes and early warning information. Among all the other approaches followed so far, unsupervised algorithms have shown to be particularly reliable in dealing with huge datasets, thanks to their ability to exploit the underlying information carried by the dataset and classify data characteristics without the need to label the training dataset. Since assigning target labels to the training dataset may be hard and time-consuming in many cases, unsupervised strategies that exploit unlabelled data, have been successfully employed as a clustering and visualization tool in exploratory data analysis in a wide range of applications. Self-organized neural systems (SOM), specifically, have the intrinsic capability to analyze large sets of high-dimensional data and can be implemented in an online learning manner. A SOM algorithm was successfully applied to classify VLP events recorded from a borehole strainmeter at Stromboli volcano during the explosive sequence that occurred during the summer of 2019, when two distinct paroxysms, happened about a month and a half apart, violently shook the volcano. Stromboli is an active, open-conduit strato-volcano, characterized by moderately persistent volcanic activity with a paucity of deformation episodes, always a candidate as a natural laboratory for researchers investigating eruptive precursors on open-conduit volcanoes. Following recent research, data recorded from borehole strainmeters carry several pieces of information inherent the static and dynamic deformations, due to the intrinsic capability of the instrument of recording high precision data within a wide frequency range. The extension of the time period previously examined, from 2018 to 2020 (fig. 1), has led us to find other correlations between observed phenomenologies and VLP shape variations.

Valuable information is embedded in the data used in the current work, which could be used not only for scientific purposes but also from civil protection agencies. Such a variety of possible usage needs the setting of principles and legal arrangements to be implemented in order to ensure that data will be properly and ethically managed, used and accessed from the scientific community.

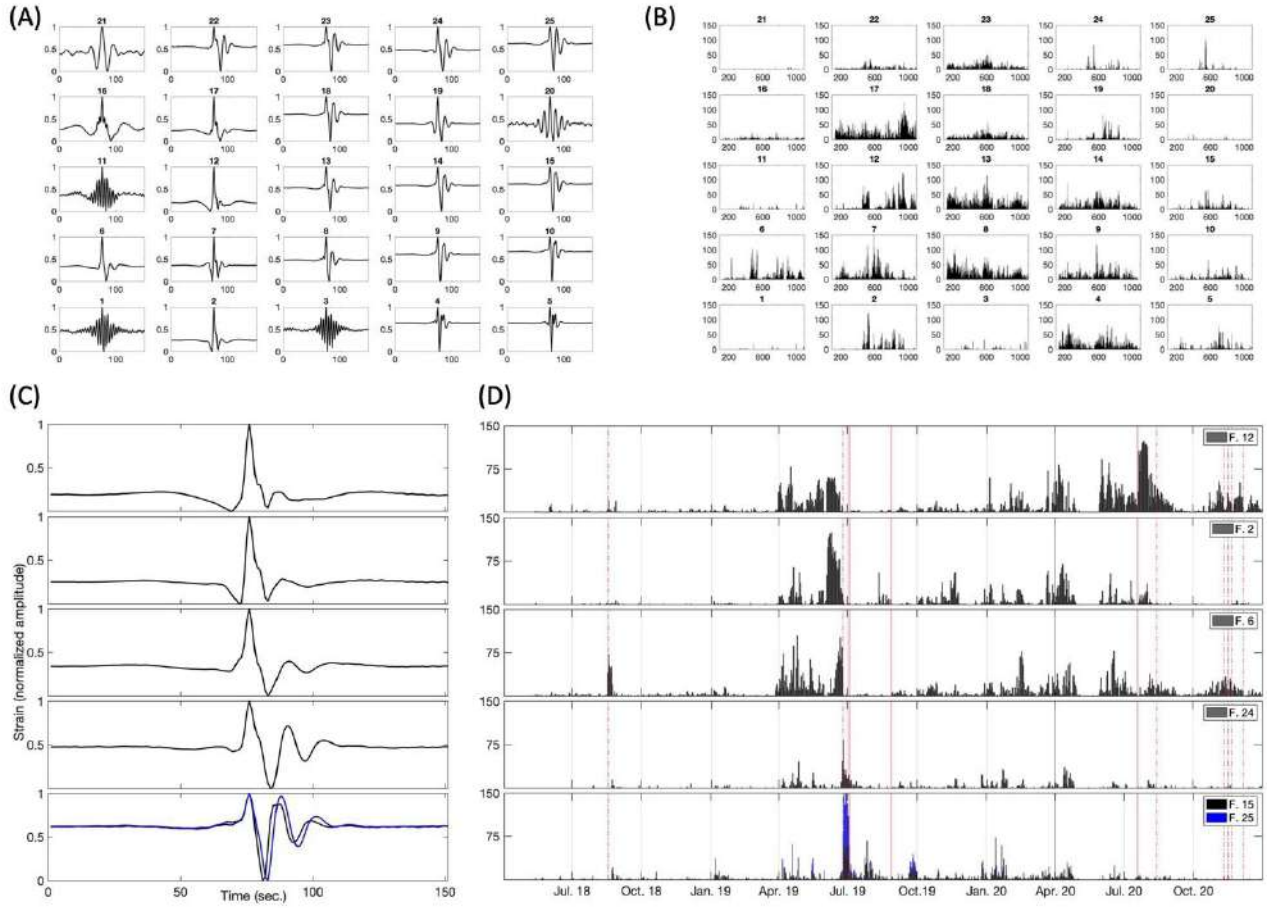

Fig. 1 – SOM cluster of families found in May 2018-December 2020 (A) Normalized stacked waveforms belonging to the i^{th} node of the SOM map (B) Temporal histograms of cumulative number of events per day belonging to the i^{th} node determined by the SOM algorithm (C,D) Normalized stacked waveforms and histograms of VLP data for noticeable families: black solid line marks the occurrence of the hybrid events on 31 March 2020; red dashed lines mark major explosions; the two red vertical solid lines mark the two paroxysmal events. (from Romano et al., 2022)

References

Romano P, Di Lieto B, Scarpetta S, Apicella I, Linde AT and Scarpa R; 2022: Dynamic strain anomalies detection at Stromboli before 2019 vulcanian explosions using machine learning. Front. Earth Sci. 10:862086. doi: 10.3389/feart.2022.862086

Corresponding author: bellina.dilieto@ingv.it

EEMverter, a new 1D/2D/3D inversion tool for Electric and Electromagnetic data with focus on Induced Polarization

G. Fiandaca[1], B. Zhang[2], J. Chen[1], A. Signora[1], F. Dauti[1], S. Galli[1], N.A.L. Sullivan[1], A. Bollino[1], A. Viezzoli[3]

[1] The EEM Team for Hydro & eXploration, Department of Earth Sciences "Ardito Desio", Università degli Studi di Milano, Milano (Italy)

[2] Institute of Earth exploration, Science and Technology, Jilin University, Changchun (China)

[3] EMergo S.r.l. , Cascina (Italy)

Introduction

The induced polarization (IP) phenomenon in airborne electromagnetic AEM data (AIP) presents a challenge to exploration in many parts of the world. It is a well-known phenomenon since Smith and Klein (1996) first demonstrated the presence of IP effects, which have been further discussed by several authors (e.g., Marchant *et al.*, 2014; Macnae, 2016; Viezzoli *et al.*, 2017). IP-affected AEM data are often interpreted in terms of the Cole-Cole model (e.g., Marchant et al., 2014; Viezzoli *et al.*, 2017; Lin *et al.*, 2019), but the inversion problem is particularly ill-posed: for a 1D inversion of a single sounding four parameters have to be retrieved for each model layer. Furthermore, AIP and ground IP modelling are usually carried out in different inversion frameworks, making a direct comparison of the results difficult. In this study we present a novel inversion software, EEMverter, specifically developed to model electric and electromagnetic data taking into account the IP phenomenon. Three distinctive features have been implemented in EEMverter: i) 1D, 2D and 3D forward modelling can be mixed sequentially or simultaneously in the iterative process within multiple inversion cycles, for diminishing the computational burden; ii) the joint inversion of AIP, ground EM-IP and ground galvanic IP data is fully supported with a common IP parameterization; iii) time-lapse inversions of AIP, EM and galvanic IP data is possible with both sequential and simultaneous approaches. In the following, the implementation of EEMverter is described, with examples of synthetic and field inversion results.

Method and results

In EEMverter the inversion parameters are defined on model meshes which do not coincide with the forward meshes used for data modelling: the link between model and forward meshes is obtained interpolating the model mesh parameters into the forward mesh discretization, as done for 1D AEM in Christensen et al. (2017), in 3D galvanic IP in Madsen et al. (2020) and in 3D EM in Zhang et al. (2021), Engebretsen et al. (2022) and Xiao et al. (2022a). This spatial decoupling allows

for defining the model parameters, e.g. the Cole-Cole ones, on several model meshes, for instance one for each inversion parameter. In this way, it is possible to define the spectral parameters, like the time constant and the frequency exponent in the Cole-Cole model, on meshes coarser than the resistivity and chargeability ones, vertically and/or horizontally, with a significant improvement in parameter resolution.

For each dataset of the inversion process, a distinct forward mesh is defined. The interpolation from the model parameters M defined on the model mesh nodes into the values m_i at the subdivisions of the ith forward mesh is expressed through a matrix multiplication, in which the matrix F_i holds the weights of the interpolation, which depends only on the distances between model mesh nodes and the subdivisions of the ith forward mesh:

$$m_i = f_i(M) = F_i \bullet M \qquad (1)$$

In EEMverter 1D, 2D and 3D forward & Jacobian computations have been implemented. In particular, Transient EM data are modelled in 1D following Effersø et al. (1999); in 3D the forward solution is carried out in frequency domain, with the finite element method, both with tetrahedral elements or with the octree approach, similarly to what has been done with the time-stepping time-domain approach in Zhang et al. (2021) and Xiao et al. (2022a). The finite element approach is used also for frequency-domain galvanic computations in 2D (Fiandaca et al., 2013) and 3D (Madsen et al., 2020). The transformation to time-domain is obtained through a fast Hankel transformation (as in Effersø et al., 1999) for both the forward response and the Jacobian.

The Jacobian of the model space J_M is computed summing the contributions of all forward meshes up (Christensen et al., 2017; Madsen et al., 2020, Zhang et al., 2021), using the domain decomposition with a forward mesh for each sounding in 3D EM computations (Cox et al., 2010; Zhang et al., 2021):

$$J_M = \sum_i J_{m_i} \bullet F_i^T \qquad (2)$$

The total Jacobian is used for computing the inversion model in a Levenberg-Marquardt linearized approach as follows:

$$M_{n+1,j} = M_{n,j} + \left[{J_{M,j}}^T {C_d}^{-1} J_{M,i} + R^T {C_{R,j}}^{-1} R_j + \lambda I \right]^{-1} \bullet \left[{J_{M,j}}^T {C_d}^{-1} \bullet \left(d - f_{n,j} \right) + R^T {C_{R,j}}^{-1} R_j \bullet M_{n,j} \right] \qquad (3)$$

In equation (3) the subscript j indicates that the inversion process can be split in several inversion cycles: in each cycle j it is possible to change the forward computation for each dataset (e.g. from 1D to 3D), as well as to insert/remove data/constraints from the objective function.

Fig. 1 presents the model and forward meshes for a joint inversion, in which 1D AEM and 1D ground EM computations are combined with 2D galvanic computations.

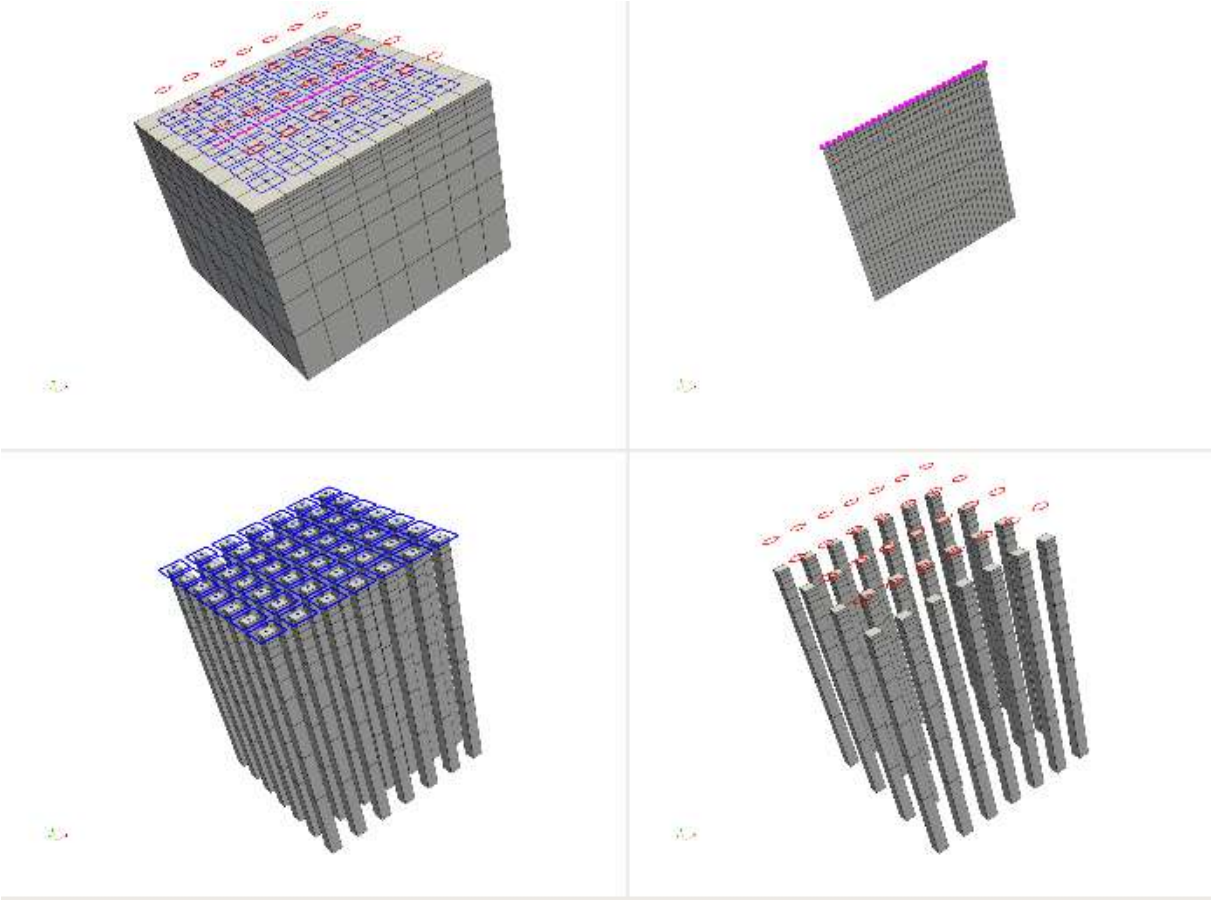

Figure 1. EEMverter multi-mesh inversion scheme for Joint inversion of inductive and galvanic data. Top left) Model mesh and data positions: red polygons for AEM frames; blue squares for ground TEM frames; magenta line for galvanic 2D profile. Top right) Galvanic 2D forward mesh. Bottom left) Ground TEM frames (blue squares) and corresponding 1D soundings (grey bars). Bottom right) AEM frames (red polygons) and corresponding 1D soundings (grey bars).

Fig. 2 presents the time-lapse approach of EEMverter, in which all the models of all the time steps can be inverted at once, without the need of relocating the model meshes when the positions of the acquisitions vary among the time steps, as in Xiao et al. (2022b).

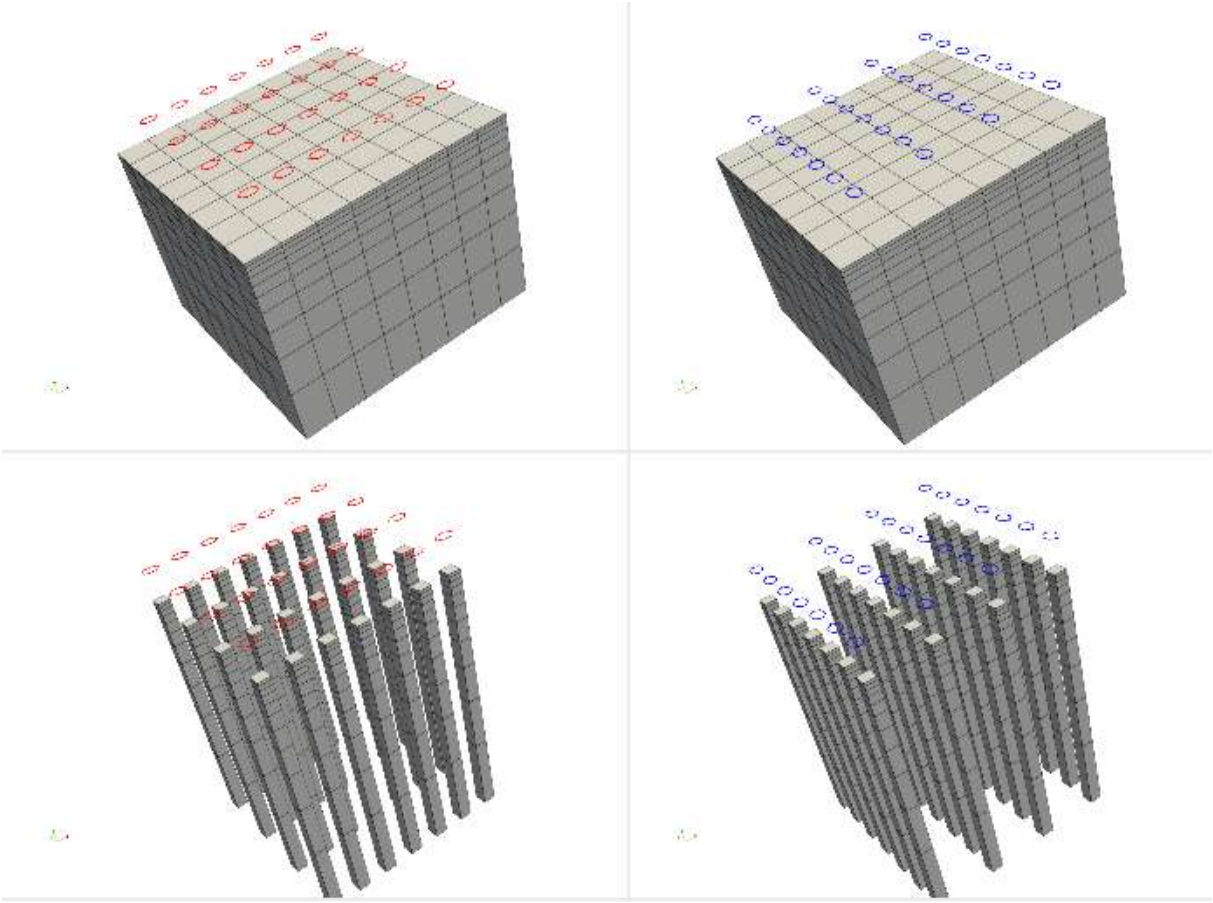

Figure 2. EEMverter multi-mesh inversion scheme for Time-Lapse inversion. Top left) Model mesh corresponding to the first Time-lapse acquisition (red polygons). Top right) Model mesh corresponding to the second Time-lapse acquisition (blue polygons), identical to the first model mesh despite of the different sounding positions. Bottom left) Forward meshes (grey bars) of the first acquisition (red frames). Bottom right) Forward meshes (grey bars) of the second acquisition (blue frames).

Fig. 3 presents the resistivity section of a synthetic model that mimics the electrical properties (both conduction and polarization) of sand, clay and consolidated formations, based on the petrophysical relations described in Weller et al. (2015), together with the inversion model of inductive and galvanic data. In particular, four different inversion results are presented: direct current and full-decay induced polarization (DCIP) galvanic data, with 10 m electrode spacing and 2D gradient sequence; AEM + ground EM data, with sounding distance of 40 m; AEM+ground EM + tTEM data (Auken et al., 2019), with tTEM soundings every 10 m; all data together in a joint inversion scheme.

The joint inversion presents much better resolution capability, with the inductive and galvanic data complementing each other in resolving both conductive and resistive layers. The same kind of improvement is found in Signora et al. (2024) with field data.

Another example of joint inversion of AEM and galvanic VES data in EEMverter, without IP modelling but with integration with resistivity logs is presented in Galli et al. (2024), where the asymmetric minimum support norm (Fiandaca et al., 2015) is used for an automated rejection of

conflicting borehole information. A similar approach is implemented in EEMverter also for automatic processing of AEM data (2021).

Examples of joint inversion of AEM, ground EM and galvanic IP data through EEMverter is presented in Dauti et al. (2024) in applications related to mineral exploration and in Signora et al. (2024) for the characterization of the HydroGeosITe, the Italian reference and calibration site for hydrogeophysical methods under development in Brescia, Italy.

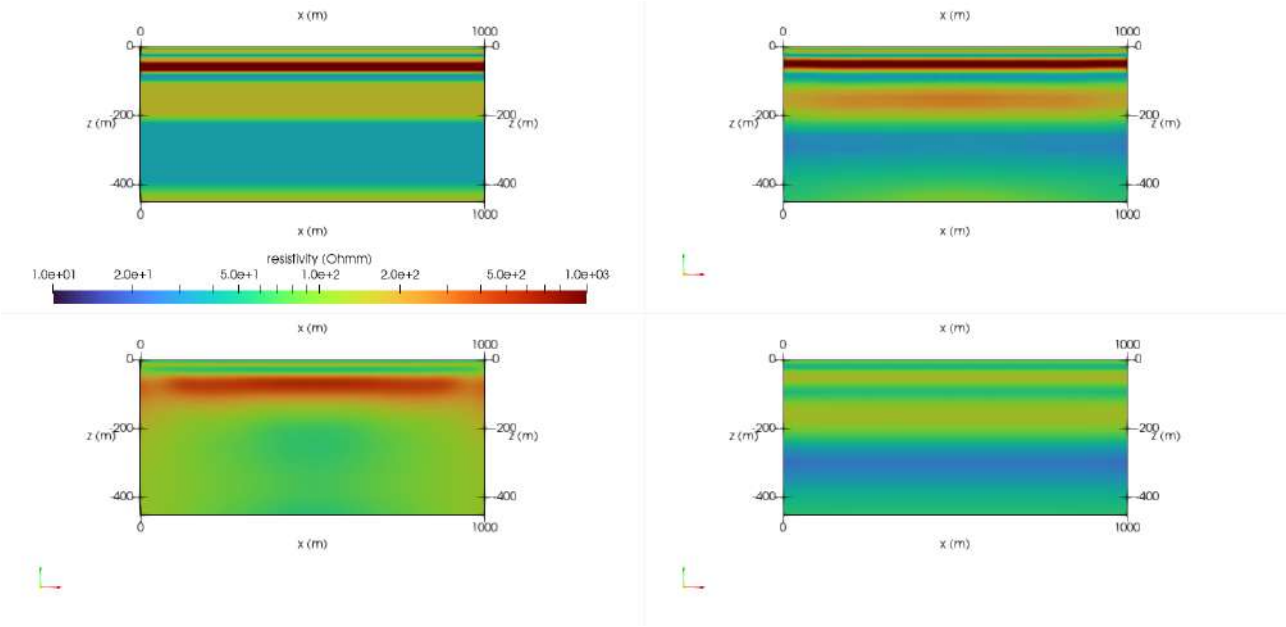

Figure 3. Synthetic model and inversion results. Top left) resistivity section of a MPA IP simulation of electrical properties; Bottom left) inversion model of DCIP data; Bottom right) inversion model of AEM+ground EM data; Top right) joint inversion of all inductive and galvanic data.

Conclusions

We presented EEMverter, a novel inversion software for electric and electromagnetic data with focus on induced polarization. Three distinctive features have been implemented in EEMverter: i) 1D, 2D and 3D forward modelling can be mixed sequentially or simultaneously in the iterative process within multiple inversion cycles, for diminishing the computational burden; ii) the joint inversion of AIP, ground EM-IP and ground galvanic IP data is fully supported with a common IP parameterization; iii) time-lapse inversions of AIP, EM and galvanic IP data is possible with both sequential and simultaneous approaches. We believe that EEMverter, with its common inversion environment for the IP inversion of inductive and galvanic data will help in closing the gap between electric and electromagnetic data in AEM applications.

Acknowledgments

This study has been partially carried out within the Horizon Europe project SEMACRET.

References

Auken E., Foged N., Larsen J.J., Trøllund Lassen K.V., Maurya P.K., Dath S.M., Eiskjær T.T (2019). tTEM — A towed transient electromagnetic system for detailed 3D imaging of the top 70 m of the subsurface. *Geophysics, 84 (1), E13-E22.*

Christensen, N. K., Ferre, T. P. A., Fiandaca, G., & Christensen, S. (2017). Voxel inversion of airborne electromagnetic data for improved groundwater model construction and prediction accuracy. *Hydrology and Earth System Sciences*, *21*(2), 1321-1337.

Christiansen, A. V., Auken, E., Foged, N., & Sørensen, K. I. (2007). Mutually and laterally constrained inversion of CVES and TEM data: a case study. *Near Surface Geophysics*, *5*(2), 115-123.

Cox, L. H., Wilson, G. A., & Zhdanov, M. S. (2010). 3D inversion of airborne electromagnetic data using a moving footprint. *Exploration Geophysics*, *41*(4), 250-259.

Dauti, F., Viezzoli, A., Fiandaca, G. (2024). Airborne and Ground IP: an integrated approach for exploration. *GNGTS 2024, 13-16 February 2024, Ferrara, Italy.*

Effersø, F., Auken, E., & Sørensen, K. I. (1999). Inversion of band-limited TEM responses*. Geophysical Prospecting,* 47(4), 551-564.

Engebretsen, K. W., Zhang, B., Fiandaca, G., Madsen, L. M., Auken, E., & Christiansen, A. V. (2022). Accelerated 2.5-D inversion of airborne transient electromagnetic data using reduced 3-D meshing. *Geophysical Journal International*, *230*(1), 643-653.

Fiandaca, G., Auken, E., Christiansen, A. V., & Gazoty, A. (2012). Time-domain-induced polarization: Full-decay forward modeling and 1D laterally constrained inversion of Cole-Cole parameters. *Geophysics*, *77*(3), E213-E225.

Fiandaca, G., Ramm, J., Binley, A., Gazoty, A., Christiansen, A. V., & Auken, E. (2013). Resolving spectral information from time domain induced polarization data through 2-D inversion. *Geophysical Journal International*, *192*(2), 631-646.

Fiandaca, G., Doetsch, J., Vignoli, G., & Auken, E. (2015). Generalized focusing of time-lapse changes with applications to direct current and time-domain induced polarization inversions. *Geophysical Journal International*, *203*(2), 1101-1112.

Fiandaca, G., Madsen, L. M., & Maurya, P. K. (2018). Re-parameterisations of the Cole–Cole model for improved spectral inversion of induced polarization data. *Near Surface Geophysics*, *16*(4), 385-399.

Fiandaca, G. (2021). Inversion-based automatic processing of AEM data. *Australasian Exploration Geoscience Conference AEGC2021, 13-17 September 2021, Virtual Conference.*

Galli, S., Shaars, F., Smits, F., Borst, L., Rapiti, A., Fiandaca G. (2024). Automated integration of AEM data, VES and borehole logs. *GNGTS 2024, 13-16 February 2024, Ferrara, Italy.*

Lin, C., Fiandaca, G., Auken, E., Couto, M. A., & Christiansen, A. V. (2019). A discussion of 2D induced polarization effects in airborne electromagnetic and inversion with a robust 1D laterally constrained inversion scheme. *Geophysics*, 84(2), E75-E88.

Haber, E., Oldenburg, D. W., & Shekhtman, R. (2007). Inversion of time domain three-dimensional electromagnetic data. *Geophysical Journal International*, *171*(2), 550-564.

Kang, S., Oldenburg, D. W., & Heagy, L. J. (2020). Detecting induced polarisation effects in time-domain data: a modelling study using stretched exponentials. *Exploration Geophysics*, *51*(1), 122-133.

Lin, C., Fiandaca, G., Auken, E., Couto, M. A., & Christiansen, A. V. (2019). A discussion of 2D induced polarization effects in airborne electromagnetic and inversion with a robust 1D laterally constrained inversion scheme. Geophysics, 84(2), E75-E88.

Marchant, D., E. Haber, and D. Oldenburg, 2014, Three-dimensional modeling of IP effects in time-domain electromagnetic data: Geophysics, 79, no. 6, E303–E314, doi: 10.1190/geo2014-0060.1.

Madsen, L. M., Fiandaca, G., & Auken, E. (2020). 3-D time-domain spectral inversion of resistivity and full-decay induced polarization data—full solution of Poisson's equation and modelling of the current waveform. *Geophysical Journal International*, *223*(3), 2101-2116.

Signora, A., Galli, S., Gisolo, M., Fiandaca, G. (2024). The Italian calibration and reference site for E & EM geophysical methods: The HydroGeosITe. *GNGTS 2024, 13-16 February 2024, Ferrara, Italy.*

Sullivan, N.A.L., Viezzoli, A., Fiandaca, G. (2024). EEMstudio: processing and modelling of electric and electromagnetic data in a QGIS plugin. *GNGTS 2024, 13-16 February 2024, Ferrara, Italy.*

Viezzoli, A., V. Kaminski, and G. Fiandaca, 2017, Modeling induced polarization effects in helicopter time domain electromagnetic data: Synthetic case studies. *Geophysics*, 82, no. 2, E31–E50.

Weller, A., Slater, L., Binley, A., Nordsiek, S., & Xu, S. (2015). Permeability prediction based on induced polarization: Insights from measurements on sandstone and unconsolidated samples spanning a wide permeability range. *Geophysics*, *80*(2), D161-D173.

Xiao, L., Fiandaca, G., Zhang, B., Auken, E., & Christiansen, A. V. (2022a). Fast 2.5 D and 3D inversion of transient electromagnetic surveys using the octree-based finite-element method. *Geophysics*, *87*(4), E267-E277.

Xiao, L., Fiandaca, G., Maurya, P. K., Christiansen, A. V., & Lévy, L. (2022b). Three-dimensional time-lapse inversion of transient electromagnetic data, with application at an Icelandic geothermal site. *Geophysical Journal International*, *231*(1), 584-596.

Zhang, B., Engebretsen, K. W., Fiandaca, G., Cai, H., & Auken, E. (2021). 3D inversion of time-domain electromagnetic data using finite elements and a triple mesh formulation. *Geophysics*, *86*(3), E257-E267.

Corresponding author: gianluca.fiandaca@unimi.it

Automated integration of AEM data, VES and borehole logs

S. Galli[1], F. Schaars[2], F. Smits[3,4], L. Borst[5], A. Rapiti[6], G. Fiandaca[1]

[1] The EEM Team for Hydro and eXploration, Dep. of Earth Sciences A. Desio, Università degli Studi di Milano, Milano (Italy)
[2] Artesia Water, 2871 BP Schoonhoven (The Netherlands)
[3] Waternet, 1096 AC Amsterdam (The Netherlands)
[4] Technical University of Delft, 2628 CD Delft (The Netherlands)
[5] PWN, 1991 AS Velserbroek, (The Netherlands)

Summary

Airborne electromagnetic (AEM) surveys are widely used for hydrogeological applications. Target areas for AEM campaigns may present a great deal of ancillary information (e.g., resistivity logs, lithology, etc.) and integrating them with AEM data is fundamental. Yet, using this information either as a-priori or a-posteriori may bring out conflicts between different datasets, preventing the fitting of all data. For instance, some borehole drillings may have been logged inaccurately, AEM data may present bias, or data may have been acquired at different times, with variations occurring in between.

In this study we present a way to integrate AEM data and other types of resistivity data (boreholes electrical logging and vertical electrical soundings, in this case), through an inversion scheme that identifies automatically conflicting data without preventing the general convergence of the process. In order to do so, we make use of a generalization of the minimum support norm, the asymmetric generalized minimum support (AGMS) norm, for defining the data misfit in the objective function of an iterative reweighted least squared (IRLS) gauss-newton inversion. The AGMS norm in the data misfit caps the weight of non-fitting data points, allowing for the inversion to focus on the data points that can be fitted. Outliers are identified after the AGMS inversion and excluded, in order to complete the inversion process with a classic L2 misfit.

We present an application of this method in the Netherlands, on a SkyTEM survey complemented with a vast and open-source database of ashore resistivity logs, as well as vertical electrical soundings (VES).

Introduction

In areas rich with ancillary data, their integration in the inversion is a must, for validation as well as for enhancing sensitivity. However, data integration can be a tricky process for many reasons: biased data, difference in supporting volume along with their location, or they may have been acquired in different periods, with variations occurring in between due, for instance, to the depletion of groundwater resources or seawater intrusion.
Conflicting data in an inversion process can easily prevent the proper convergence of the inversion, but culling too much data out might throw out important information. The removal of conflicting information is even more difficult when there is a significant amount of ancillary information, acquired over a long period of time.
To solve this challenge, we propose to use a generalization of the minimum support norm (Last and Kubik, 1983; Portniaquine and Zhdanov 1999), namely the asymmetric generalized minimum support AGMS norm (Fiandaca et al., 2015), for identifying outliers in a joint inversion of AEM data, vertical electrical soundings (VES) and borehole resistivity logs. We test the method on a synthetic example, mimicking a joint inversion of AEM data and borehole logs, with both correct and incorrect logging, as well as real data. The field case consists of a SkyTEM survey carried out in 2022, complemented with a vast and open-source database of ashore resistivity logs, as well as VES, acquired over many decades.

Method and results

The inversion of AEM, VES and borehole logs is carried out in EEMverter (Fiandaca et al., 2024), a new inversion algorithm in which different norms are applicable in the objective function for both data misfit and regularization through the iteratively reweighted least squared (IRLS) inversion scheme (Farquharson and Oldenburg, 1998).

In particular, the penalty of the data misfit x=d-f between data and forward response is expressed through the AGMS norm (Fiandaca et al., 2015) as:

$$\phi(x) = \alpha^{-1}\left[(1-\beta)\frac{\left(\frac{x^2}{\sigma^2}\right)^{p_1}}{1+\left(\frac{x^2}{\sigma^2}\right)^{p_1}} + \beta\frac{\left(\frac{x^2}{\sigma^2}\right)^{p_2}}{1+\left(\frac{x^2}{\sigma^2}\right)^{p_2}}\right] \quad (1)$$

where

$$\beta = \frac{\left(\frac{x^2}{\sigma^2}\right)^{(p_1,p_2)}}{1+\left(\frac{x^2}{\sigma^2}\right)^{(p_1,p_2)}}. \quad (2)$$

In (1) and (2), σ is the data standard deviation, p_1 and p_2 control the shape of the norm before and after x/σ=1 and α determines the total weight of the penalty.

With this choice of values for the norm settings the AGMS norm gives misfit 1 for x/σ=1 (i.e. the same value of the L2 norm), with similar penalty for low misfit (because of p_1=1) and a slow growth of the penalty when x/σ>1 (because of p_2=0.5). This slow growth allows for applying the AGMS norm in an iterative minimization process, because a decrease in x/σ gives a measurable penalty reduction.

This data norm is applied in a IRLS inversion composed of three inversion cycles (Fiandaca et al., 2024) with 1D forward/Jacobian computations:

1. a preliminary cycle which finds the best starting model without vertical variability of the parameters, through the use of a single-layer forward mesh;
2. a cycle where the AGMS norm is applied
3. the data norm is switched to the L2 norm, to reject the data with misfit above the set thresholds, and the inversion is carried out until the reach of the minimum misfit.

In all cycles, borehole logs are treated as data, with the forward response of the logs consisting in the interpolation of the model resistivity at the log locations (Fiandaca et al., 2024).

Fig. 1 presents a synthetic model of a fresh aquifer enclosed between an unsaturated sand dune and a brackish aquifer, and confined by clay layers. AEM data (Xcite system, New Resolution Geophysics) and three borehole logs are simulated and inverted with a classic L2 data norm and the AGMS norm, with three data scenarios:

1. only AEM data are available (Fig. 1D and 1G);
2. AEM data are complemented with the logs that bear correct information (Fig. 1E and 1H);
3. one log contains wrong resistivity values (Fig. 1F and 1I).

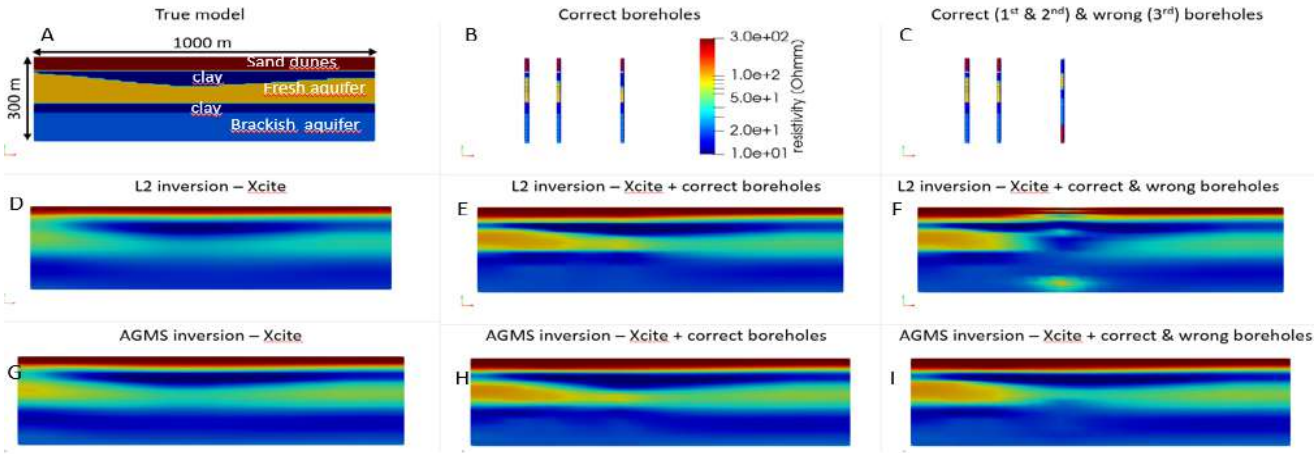

Figure 1. Conceptual model (A), boreholes information (all correct in B, one incorrect in C); model recovered by Xcite AEM data without drilling information using L2 norm (D) and AGMS norm (G); model recovered by Xcite with all correct drilling information using L2 norm (E) and AGMS norm (H); model recovered by Xcite with partially incorrect drilling information using L2 norm (F) and AGMS norm (I).

Both L2 and AGMS inversions improve the model retrieval when correct log information is added, but a very different behaviour occurs when wrong data are fed to the inversions: the L2 inversion shows a significant artifact at the location of the wrong resistivity log, while the AGMS inversion is almost insensitive to the outliers.

The same inversion procedure was used on a SkyTEM dataset acquired in the Netherlands in 2022, 25 kilometres west of Amsterdam (Fig. 2, top left inset), together with 94 borehole resistivity logs, 91 VES, acquired in the same area over a period ranging many decades, in which the volume of the fresh groundwater has changed considerably. Excessive water abstraction from deep wells between 1903 to 1957 caused depletion of fresh groundwater. In 1957 pumping stopped and infiltration with treated water from the river Rhine started. This enlarged the drinking water production capacity and restored the fresh water volume in the deep aquifer (Geelen et al., 2017; Olsthoorn and Mosch, 2020). The wells can still be used as a back-up system if the quality of the water in the river Rhine is not sufficient. That's why the integration of resistivity logs and VES with AEM data is difficult: data will conflict not necessarily because of their different support volume or sensitivity, but because they were acquired over different periods of time. Thus, with the AGMS inversion we aim at two distinct goals: improving the AEM inversion where borehole logs and VES information bring compatible information; identify the conflicting information, as a proxy of the variations that occurred on the fresh-sea water balance over the decades.

A 40 m x 80 m XY horizontal discretization and log-increasing depths from 5 to 400 m were used for the inversion, with the same three-cycle inversion scheme utilized for the synthetic case. Only borehole logs and VES data were rejected in the last cycle, the aim being to identify the information conflicting with the AEM data, which were carefully processed.

Fig. 2 presents the rejection rate for both log data and VES data with the AGMS joint inversion, in comparison with the rejection rate computed after an AEM-only inversion, in which log and VES data do not concur in the model definition. The rejection of log data is not applied to entire logs, but value by value along the borehole depth. So, the rejection rate indicates for each borehole log the fraction of values rejected. The overall rejection rates are presented also in Table 1.

Table 1: Comparison between rejection rates with AGMS joint inversion of AEM, VES and log data and with AEM-only inversion

	Total data	**Data rejected with AGMS**	**Rejection rate %**	**Data rejected with AEM-only**	**Rejection rate %**
Borehole logs	33646	4399	13	12646	38
VESs	1815	1159	64	1475	81

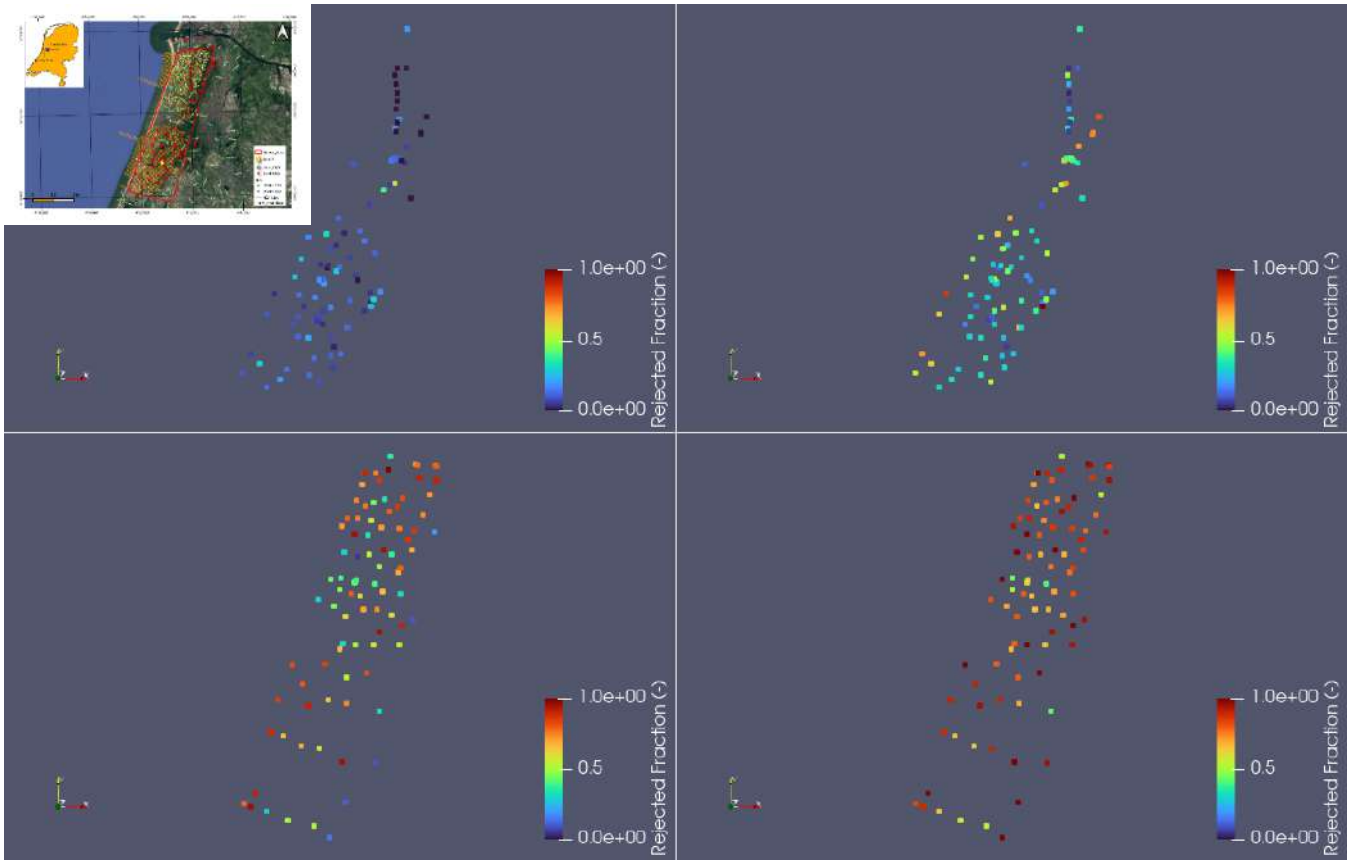

Figure 2. Plots of the fraction of rejected data with application of AGMS norm in joint inversion (left sections) and with AEM-only inversion (right sections); Top – rejections of log data; bottom – rejection of VES data. In the top right corner the surveyed area

As clearly shown by Fig. 2 and Table 1, the AGMS inversion has a much lower rejection rate, with very good compatibility between logs and AEM data, and poorer compatibility between the old VES data and the AEM ones. However, spatial patterns exist in the rejection fractions, which might be correlated with the variations occurred in the fresh-sea water interface. The AEM-only inversion has a much lower compatibility with the ancillary data, which is mostly due to equivalence problems instead of conflicting information.

Finally, Fig. 3 presents the comparison of the joint AGMS inversion and of the AEM-only inversion on an exemplary log, where AGMS inversion model fits much better the borehole information.

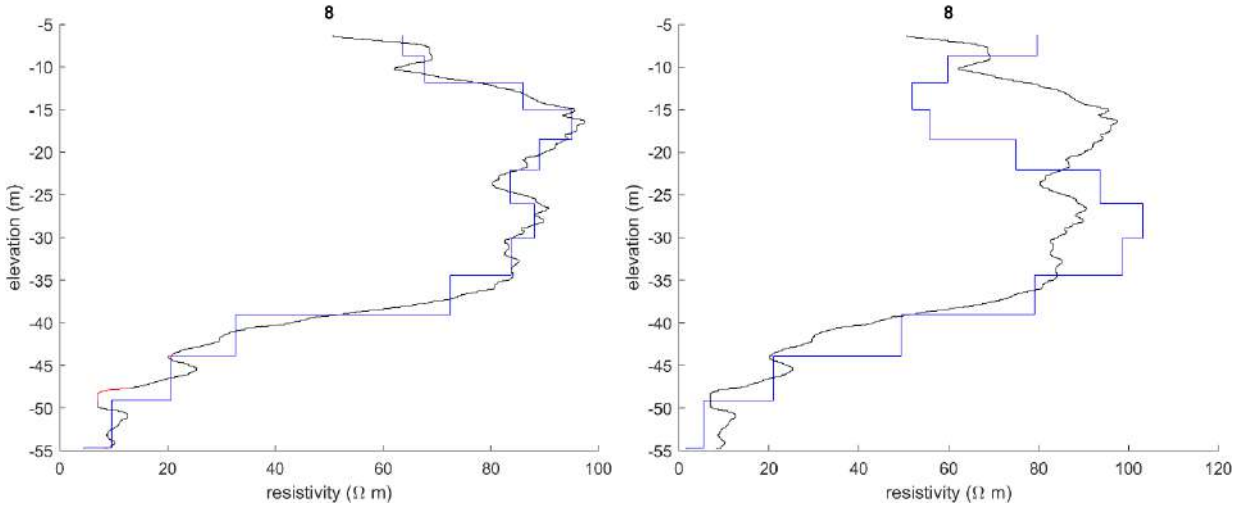

Figure 3. Comparison between Borehole#8 log (yellow star in Fig. 3) and inversion model. Left – AGMS joint inversion; right – AEM-only inversion. Blue lines – inversion model; black lines – resistivity logs; red lines – rejected data in resistivity log in the joint AGMS inversion.

Conclusions

The inversion scheme proposed in this study allows an automated integration of AEM data and resistivity logs, as well as ground-based galvanic VES measurements, even in presence of conflicting information. The AGMS data norm puts a cap at the misfit penalty of outliers, and grants convergence to the inversion without culling valuable information out.

This approach allows to integrate to AEM surveys a great amount of ancillary data, without the need of careful and time-consuming data vetting: the accurate inspection of ancillary information could be reserved only to the data rejected by the automated scheme, with the kept data readily usable for further integration and interpretation.

Furthermore, this automated integration scheme is fully general, and can be applied not only to AEM data, but to any geophysical problem simply using the appropriate forward modelling.

Acknowledgments

This work has been carried out within the project LakEMaging, funded by Acque Bresciane. The SkyTEM measurements are paid for by PWN, the municipality of Amsterdam, the waterboard Amstel, Gooi and Vecht, the Province of Noord-Holland and the Delta Programma Zoet Water (Delta Program for Fresh Water) of the Dutch Ministry of Infrastructure and Water Management.

References

Farquharson, C.G. & Oldenburg, D.W., (1998). Non-linear inversion using general measures of data misfit and model structure, Geophysics, 134, 213–227.

Fiandaca, G., Doetsch, J., Vignoli, G., & Auken, E. (2015). Generalized focusing of time-lapse changes with applications to direct current and time-domain induced polarization inversions. Geophysical Journal International, 203(2), 1101-1112.

Fiandaca, G., Viezzoli, A., Schaars, F. (2021). Advanced Automated Integration of Aem and drilling data, 48th IAH Congress, Brussels, Belgium, 6-10 september 2021.

Fiandaca, G., Zhang, B., Chen, J., Signora, A., Dauti, F., Galli, S., Sullivan, N.A.L., Bollino, A., Viezzoli, A. (2024). EEMverter, a new 1D/2D/3D inversion tool for Electric and Electromagnetic data with focus on Induced Polarization, GNGTS 2024, 13-16 February 2024, Ferrara, Italy.

Geelen, L. H. W. T., Kamps P. T. W. J., Olsthoorn T. N. (2017). "From overexploitation to sustainable use, an overview of 160 years of water extraction in the Amsterdam dunes, the Netherlands." Journal of coastal conservation 21.5: 657-668.

Last, B.J. & Kubik, K., 1983. Compact gravity inversion, Geophysics, 48, 713-721.

Olsthoorn, T. N., & Mosch, M. J. M. (2020). Fifty years artificial recharge in the Amsterdam dune area. In Management of Aquifer Recharge for Sustainability (pp. 29-33). CRC Press.

Portniaquine, O. & Zhdanov, M.S., 1999. Focusing geophysical inversion images, Geophysics, 64, 874-887.

Corresponding author: stefano.galli2@unimi.it

NUMERICAL PROBLEMS OF THE UNCERTAINTY ASSESSMENT OF THE SIBSON INTERPOLATION METHOD

M. Iurcev [1], F. Pettenati[1]

1 Istituto di Oceanografia e di Geofisica Sperimentale, OGS, Trieste

Introduction

In 2022 we presented a note (Iurcev et al. 2022) on the assessment of uncertainties for the Natural Neighbours – hereafter NN - interpolation method (Sibson 1980, 1981) with bidimensional scalar data. This non-parametric interpolation method uniquely determines the interpolated data and is therefore classified as a deterministic method. However, it is important to quantify the uncertainties due to the spatial distribution of the dataset to be interpolated. The implementation of this approach is now reported in Iurcev et al. 2023. This approach is based on a gradient method derived from the bivariate version of the Mean Value Theorem MVT (also known as the Lagrange Theorem) in $\mathbb{R}^2$, combined with Sibson's formula for interpolation (Iurcev et al. 2023).

This deterministic method, based on the MVT, raises two major issues. The first problem concerns gradient estimation. The second issue is the unknown location of the points ξ_i of MVT, along the line between the interpolation point and the i-th Natural Neighbour. The purpose of this note is to show how we have tried to solve these two issues.

Gradient estimation

In Iurcev et al. 2022, we presented an approach that is widely used in the literature. The approximation of the gradient using finite differences superimposed on a regular grid in which the function value is known or estimated. However, this method introduces an additional level of uncertainty as the function must be interpolated through the grid. The proposed approach is the Local Least Squares plane approximation of the unknown surface. The OLS (Ordinary Least Squares) approximation requires a subset of points $\boldsymbol{x}_i$, $f(\boldsymbol{x}_i)$ in the neighbourhood. If there are at least three non-colinear points in $\mathbb{R}^3$ space, the linear regression defines a plane whose slope is a possible gradient estimator. In this context, two different least squares strategies for computing the gradient for bivariate interpolation of surfaces are investigated by Belward et al. (2008). The two methods are based on the generalization of Moving Least Squares (MLS). The first method is the classical method based on a linear system of equations in which the gradient is derived by a second order truncated Taylor expansion. In the second method, the gradient is a consequence of the Finite Volume Method (FVM) solution which is used to solve a diffusion equation. Belward et

al. (2008) show that "the uniqueness of the gradient estimates, [using both methods], is not a result of the analytical properties of the approximation processes, it is a consequence of the method of linear least squares".

We studied some possibilities to compute the gradients by OLS, using the subset of points around a grid point. A method is an "n" estimate (based on NNs) and another using an "r" estimate (using the distance within a fixed radius). Of course, the choice of radius in the r-method is quite arbitrary, whereas the n-method is uniquely defined. If the radius is too small, the subset used for the OLS estimator may be for many interpolation points. If the radius is too large, the gradient estimate will be very poor. The best choice for the fixed radius depends on the local density of the dataset. As described in De Keyser et al. (2007), the method is only valid if the so-called spatial homogeneity condition is fulfilled.

To test the gradient, we used a random dataset of 500 points in the unitary square $[0,1]^2$ of Franke (1979) function. The Franke function is a differentiable function that is often used as a test function in literature. The main problem for the optimal radius depends strictly on the local spatial density of the dataset, instead. The NN bypasses this problem, but at the same time is not feasible if we approximate the points $\boldsymbol{\xi}_i$ with the relative NNs, since the vectorial expression becomes zero. The statistical tests performed so far suggest that OLS gradient estimation with a fixed radius can provide reasonable estimates. There are many ways to combine gradient estimation and our equations. Since the Franke function is known, it is also possible to obtain a "semi-exact estimator" using its exact gradient. The only problem is the true location of points $\boldsymbol{\xi}_i$, which must be approximated by the point of interpolation $\boldsymbol{x}^*$, the data points $\boldsymbol{x}_i$, the midpoint, or in some other way.

Although many interesting questions have been raised, the investigation is still ongoing and requires further analysis from both theoretical and experimental perspectives.

References

Belward J.A., Turner I.W., Ilić M.; 2008: *On derivative estimation and the solution of least squares problems*. J. Comp. and Appl. Math., 222, 511–523.

De Keyser J., Darrouzet F., Dunlop M.W., Décréau P.M.E.; 2007: *Least-squares gradient calculation from multi-point observations of scalar and vector fields: methodology and applications with Cluster in the plasmasphere*. Ann. Geophys., 25, 971–987, www.ann-geophys.net/25/971/2007/.

Franke R.; 1979: *A critical comparison of some methods for interpolation of scattered data*. Naval Postgraduate School, Monterey, CA, USA, Technical Report, NPS-53-79-003, <hdl.handle.net/10945/35052>.

Iurcev M., Majostorovic M., Pettenati F.; 2022: Introduction to Interpolation Uncertainty of the Natural Neighbors Method (Sibson). 40° Convegno Nazionale Gruppo Nazionale di Geofisica della Terra Solida GNGTS.Online, 27-29 Giugno. 2022, Trieste. Abstract, 504-506.

Iurcev M., Pettenati F.; 2023: *Exploring error estimation methods for natural neighbour interpolation: preliminary research and analysis.* Bull. Geoph. and Oceanog., 64, 4, 433-448, December 2023; doi 10.4430/bgo00423.

Sibson R.; 1980: *A vector identity for Dirichlet tessellation*. Math. Proc. Camb. Philos. Soc. 87, 151–155.

Sibson R.; 1981: *A brief description of natural neighbor interpolation*. Interpreting Multivariate Data, V. Barnett editor, Chichester, John Wiley, 21-36.

Corresponding author: miurcev@ogs.it

Ensemble-based Acoustic Full Waveform Inversion: A Synthetic Data Application

F. Macelloni[1], M. H. Altaf[1], M. Aleardi[1], E.M. Stucchi[1]

[1] Department of Earth Sciences, University of Pisa, Pisa, Italy

Introduction

Full Waveform Inversion (FWI) is one of the most powerful techniques to estimate the distribution of seismic wave velocity in the subsurface. The determination of the velocities from the recorded seismograms represents an inverse problem and FWI aims to solve it by exploiting the full information content of the data.

Despite the high resolution results that FWI is able to provide, there are some drawbacks we have to deal with when using this kind of optimization. One of them is the risk of being trapped in local minima of the objective function, which expresses the distance between observed and estimated data. This problem is mainly due to the lack of low frequencies in the data (cycle skipping issue) and to a starting model lying too far from the global minimum of the error function. To alleviate this problem, a global optimization approach could be adopted to replace the standard local, deterministic strategy, at the expense of a significant increase of the computational workload. Another limitation of the deterministic inversion is also the impossibility to assess the uncertainty affecting the estimated subsurface velocity model.

In this work we cast the FWI into a probabilistic framework. The aim of the work is twofold: making the FWI results less dependent from the starting model, while also estimating the uncertainty on the inversion outcomes. Therefore, our aim is not to estimate a single, best-fitting solution but providing as the final results the so called posterior probability density function from which extract significant statistical properties concerning the estimated model (i.e., mean model and the associated standard deviation).

In particular, we present an ensemble-based approach to FWI, using the Ensemble Smoother with Multiple Data Assimilation (ES-MDA) algorithm (Emerick et al., 2013). This method allows us to perform a Bayesian FWI by considering an ensemble of velocity models and iteratively updating each of these realizations. The underlying assumption is that data and model parameters follow a Gaussian distribution. MDA can be considered as an iterative version of the standard ES and, instead of a single and large correction, it performs multiple smaller updates, achieving good data predictions in less iterations. For additional details, see Thurin et al. (2019) and Aleardi et al. (2021b).

This kind of approach makes the inversion highly demanding from a computational point of view, so it is necessary to adopt some strategies to alleviate this effort: here we employ the Discrete Cosine Transform (DCT) to compress both data and model space. This technique reduces the number of unknown in the inversion and also the dimensions of the matrices and vectors involved in the ES-MDA approach. The DCT is a Fourier-related transform through which a signal can be expressed as sum of cosine functions. Since the DCT concentrates most of the energy of the signal in low order coefficients, it is possible to get an approximation of the original signal by discarding those that are very close to zero and retaining only the low order ones. Other information can be found in Britanak et al. (2010) and Aleardi et al. (2021a).

In this work we restrict the application of EB-FWI to a synthetic case, but its utilization to field data is being prepared. In fact, we processed a 2D seismic line from the FORGE (Frontier Observatory for Research in Geothermal Energy) geothermal experiment located in Utah, USA (Miller at al., 2018). Precisely for the purpose of applying a FWI to this dataset, we performed a dedicated processing, comprehensive of Migration Velocity Analysis (MVA), for improving the velocity field estimation.

Method

In this work we use an ensemble-based approach implementing the ES-MDA algorithm to cast the FWI in a Bayesian inference framework. The ensemble-based method represents a data assimilation algorithm in which the posterior distribution consists of a set, also called ensemble, of model realizations. It can be demonstrated that ES corresponds to a single Gauss-Newton step, but it usually requires many iterations to ensure a good data prediction when compared to MDA, which speeds up the convergence performing multiple assimilations (corrections) of the data.

The steps of MDA algorithm are the following: choice of the number of data assimilations (iterations); generation of the starting ensemble of models drawn from a Gaussian prior distribution; for each iteration and for each model of the ensemble, computation of the data associated to each member of the ensemble, perturbation of each data and update of the models. A schematic representation of the algorithm is shown in Fig.1. The perturbation of each data vector is made according to

$$\tilde{d_k} = d + \sqrt{\alpha_i} C_d^{\frac{1}{2}} \bullet n,$$

where: d is the observed data, $\tilde{d_k}$ is a random perturbation of the observed data, α is called inflation coefficient, C_d is the data covariance matrix and $n = N(0, Id)$, with $N(d, C_d)$ representing a Gaussian distribution and Id the identity matrix. The update of each model of the ensemble is defined as follows:

$$m_k^u = m_k^p + \tilde{K}\left(\tilde{d_k} - d_k^p\right),$$

with $k = 1, \ldots, N$, where N is the number of models in the ensemble, the superscripts u and p refers to variable computed at the current iteration (updated) and to the previous one,

respectively, and d_k^p is the data associated to the k-th model m_k^p. The matrix $K^{\sim}$ represents the so called Kalman gain, given by:

$$K^{\sim} = C_{md}^p \left(C_{dd}^p + \alpha C_d \right)^{-1}.$$

In the previous equation C_{md}^p is the cross-covariance matrix between the model m^p and the associated data d^p, whilst C_{dd}^p is the covariance matrix of the predicted data.

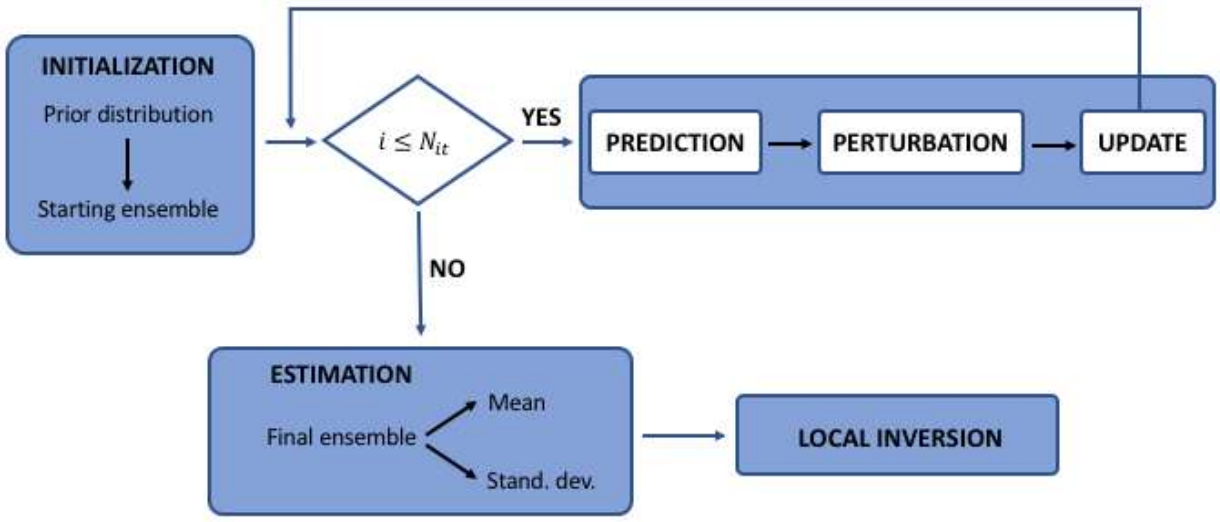

Fig. 1 – Schematic representation of the EB-FWI algorithm. This scheme also shows the possibility to apply a local FWI using as starting model the result of the global one. This step allows to improve the resolution of the result.

The velocity models forming the starting ensemble are drawn from a Gaussian prior distribution in which a Gaussian variogram has been included to impose the desired spatial variability on the velocity model.

The workload of the procedure can be alleviated by adopting a reparameterization technique able to considerably reduce the computational complexity of the problem. Among the possible methods, we choose the DCT for its compression ability, its linearity, the possibility to easily extend it to more than one dimension and because its application does not overload the inversion procedure with additional computational time. The compression power of this method relies on the fact that it is able to concentrate most of the information of the signal into the low order coefficients. As a consequence, the majority of these coefficients are very close to zero, and retaining only the low order ones is sufficient to approximate the original signal without losing relevant information. Furthermore, compressing data and model space, we considerably reduce the size of matrices and vectors involved in the computations. The DCT compression also mitigated the ensemble collapse issue, consisting in the fast convergence of the ensemble towards the mean and in the consequent underestimation of the posterior variance. The most common solution to

reduce this problem is to increase the ensemble size (Roe et al., 2016). The DCT, in this sense, helps in lowering the number of ensemble individuals needed to avoid collapse and, as a consequence, the number of forward modelling computations. We perform the compression through a 2D DCT, applying it in both horizontal and vertical directions. The choice of the number of DCT coefficients to retain in each direction is made through an analysis of the variability of the original signal that it is preserved after the compression. The variability is here defined as the ratio between the standard deviations of compressed and uncompressed signal (see Aleardi et al., 2021a).

Synthetic inversion

We applied the ES-MDA acoustic FWI to a portion of the synthetic Marmousi benchmark model. The considered model extends 4.3 km horizontally and 1.340 km in depth. This is the portion that has been inverted, and it lies below a water layer 0.260 km deep, considered when computing the synthetic seismograms. The inverted portion was discretized with a grid characterized by a spacing of 20 m in both horizontal and vertical direction. This results in 216 nodes along the horizontal direction and 68 on the vertical one. A Ricker wavelet with a central frequency of 5 Hz is considered as the source signature. We simulated 5 shots equally spaced along the horizontal axis, from the left to the right edge of the considered area and recorded by 200 receivers, with a constant receiver interval of 21.6 m. The time interval is 4 ms and the record length is 3 s. We added to the observed data uncorrelated Gaussian noise, with a standard deviation equal to 10% of the standard deviation of the noise-free data.

We observed that retaining 30 DCT coefficients along the first (horizontal) dimension and 15 along the second (vertical) one was enough to properly represent about 95% of the variability of the original V_p model. In this way, we can compress the model space from 68x216=14688-D to 15x30=450-D. A similar analysis on the seismic data led us to use 55 DCT coefficients along the horizontal and 65 along the vertical direction. Considering that we simulate 5 shots, the original 751x200x5=751000 parameters are reduced to 65x55x5=17875 in the compressed data space.

A test phase has been performed to assess the minimum number of models within an ensemble needed to obtain a good reproduction of the main features of the original velocity model. We noticed that a good compromise between the quality of the results and the computational time was possible considering ensembles of 10000 models. Increasing this number does not lead to a considerable improvement of the inversion result, whilst it highly affects the computational cost of the procedure. We further observed that 10 iterations of the algorithm are enough to reach convergence. The computational time required by the EB-FWI is approximately 8 days.

The acoustic forward modeling has been performed using Devito, a python package that implements a high performance finite difference partial differential equation solver (Louboutin et al., 2019). We run the serial code implementing the inversion on a server equipped with Intel® Xeon® Silver 4114 CPU @ 2.20 GHz.

Fig.2 shows the result of the inversion, comparing the original model, the corresponding model after the DCT compression, the model used as mean of the prior distribution and the mean of the

final ensemble. As a prior mean model we used a gradient model, with velocity values increasing from top to bottom and ranging from the minimum to the maximum value of the original model (Fig.2-c). We observe that the model obtained with the EB-FWI (Fig.2-d) contains all the main features visible in the DCT-compressed version of the original portion of the Marmousi model. The main differences are placed on the bottom and in lateral portions of the model, where the algorithm is sometimes not able to correct high or low wrong velocity values. Anyway, this happens in the less illuminated parts of the model, characterized by higher values of the standard deviation (Fig.2-e). A comparison of observed and predicted data is shown in Fig.3, along with their difference. The represented shot is the third of the five simulated, and its position corresponds to the center of the horizontal extension of the model. The represented seismograms show a good fit between observed and predicted data. Fig.3-b shows the shot gather computed on the gradient model, used as the mean of the prior distribution. Considering that this is the seismogram associated with the mean of the starting ensemble and comparing the observed data (Fig.3-a) with the seismogram corresponding to the mean of the last ensemble (Fig.3-c), we clearly see that the algorithm appears able to properly reproduce the main events in the data.

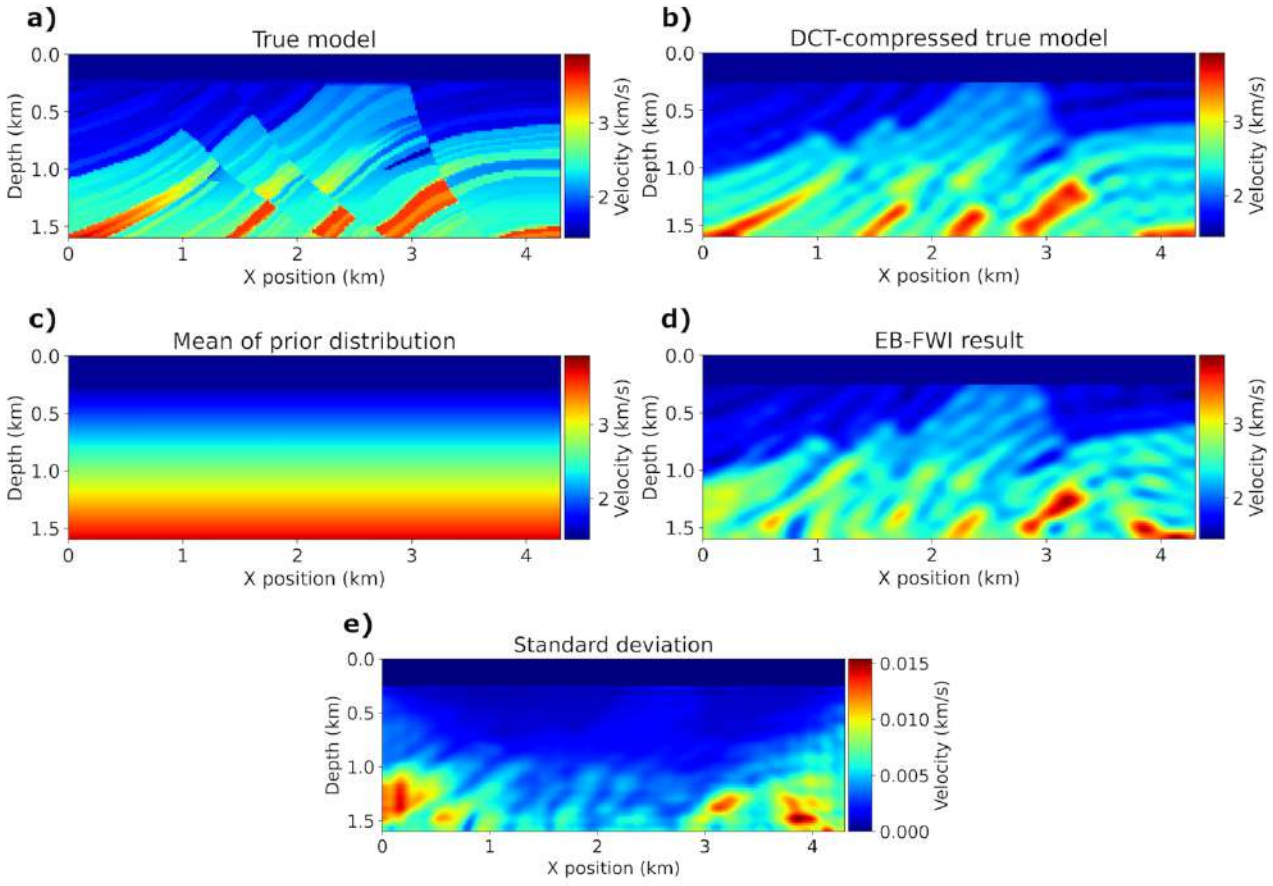

Fig. 2 – a) True model, portion of the synthetic Marmousi model; b) true model after the DCT compression; c) mean model of the prior distribution; d) final result of the EB-FWI; e) standard deviation associated to the inversion result.

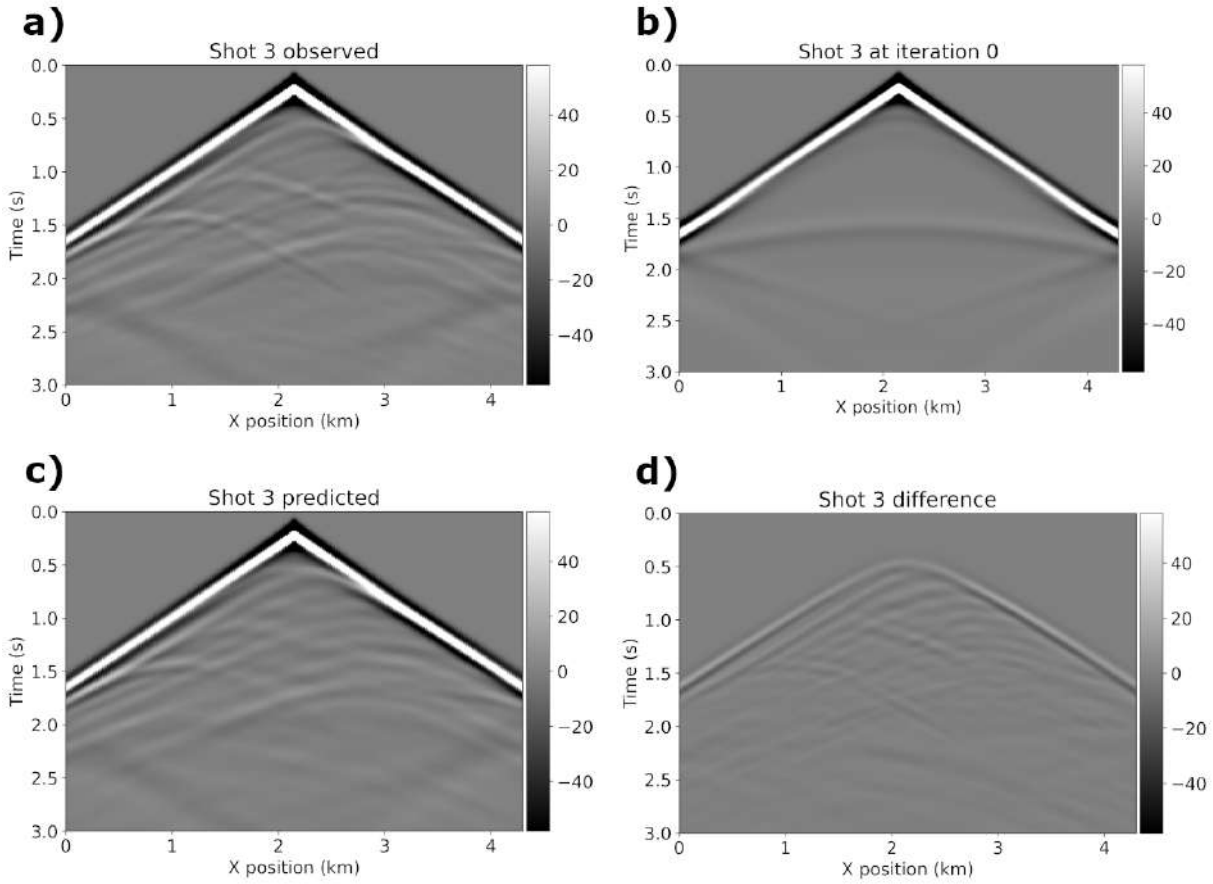

Fig. 3 – a) Observed seismogram; b) seismogram computed from the mean model of the prior distribution; c) predicted seismogram; d) difference between observed and predicted seismograms.

Conclusions

We presented an ensemble-based approach to FWI using the ES-MDA algorithm. To reduce the computational effort required by such an approach, we compress both data and model space through a 2D DCT. We applied the algorithm to a portion of the synthetic Marmousi model in the acoustic approximation. The results are satisfactory: the mean of the final ensemble contains all the main features of the original, DCT compressed, model showing the main differences on the deepest portion and on the edges. Even in data space we observe a good fit between observed and predicted data. The algorithm appears able to deal with the cycle skipping issue mitigating it: to this end, some tests, not shown here for the lack of space, have been performed.

Future steps of this research are further tests on the algorithm, with the aim of approaching the application to field data. The code will also be improved to run in parallel, to considerably reduce the overall computational time. Further investigations will be carried out to obtain a more reliable estimation of the uncertainties.

References

Aleardi M., Vinciguerra A. and Hojat A.; 2021a: A Convolutional Neural Network approach to Electrical Resistivity Tomography. Journal of Applied Geophysics, 193.

Aleardi, M., Vinciguerra, A., and Hojat, A.; 2021b: Ensemble-Based Electrical Resistivity Tomography with Data and Model Space Compression. Pure and Applied Geophysics, 178, 1781-1803.

Britanak, V., Yip, P.C., and Rao, K.R.; 2010: Discrete cosine and sine transforms: General properties, fast algorithms and integer approximations. Elsevier.

Emerick, A.A., and Reynolds, A.C.; 2013: Ensemble smoother with multiple data assimilation. Computers and Geosciences, 55, 3-15.

Louboutin, M., Lange, M., Luporini, F., Kukreja, N., Witte, P.A., Herrmann, F.J., Velesko, P., and Gorman, G.J.; 2019: Devito (v3.1.0): an embedded domain-specific language for finite differences and geophysical exploration. Geoscientific Model Development, 12(3), 1165-1187.

Miller, J., Allis, R., and Hardwick, C.; 2018: Seismic Reflection Profiling at the FORGE Utah EGS Site. GRC Transactions, vol. 42.

Roe, P., Almendral Vazquez, A., and Hanea, R.; 2016: Distinguishing Signal from Noise in History Matching – Analysis of Ensemble Collapse on a Synthetic Data Set. 15th European Conference on the Mathematics of Oil Recovery, 29 August – 1 September 2016, Amsterdam, Netherlands.

Thurin, J., Brossier, R., and Métivier, L.; 2019: Ensemble-based uncertainty estimation in full waveform inversion. Geophysical Journal International, 219(3), 1613-1635.

Fabio Macelloni, fabio.macelloni@phd.unipi.it

Greenland and Antarctica ice mass balance (2002-2017) through source decomposition in hypercompact atoms.

M. Maiolino[1], M. Fedi[1], G. Florio[1]

[1]University of Naples "Federico II" – DiSTAR, Dipartimento di Scienze della Terra dell'Ambiente e delle Risorse

We present a new estimation based on a novel approach named ECS (Extremely Compact Sources) of the ice-sheet total mass variation in Greenland and Antarctica using time varying NASA GRACE (Gravity recovery and climate experiment) Stoke's coefficient data in the time span 2002-2017. Over a 15-year period the NASA missions GRACE (Gravity Recovery and Climate Experiment) and the following GRACE-FO provided a unique opportunity to map the changes in Earth's gravitational field and gave to the scientific community a new vision of the major ice sheet dynamics. In the last years, it has become clear that the ice sheet total mass response to climate change is crucial for understanding the sea level rising phenomena related to grounded ice melting and to quantify the ice sheet front retreat in the polar regions. Even if an approximation of the total mass changes in the polar regions can be done with the standard methods, namely the conversion method (Wahr et al., 1998) or the point mass inversion (Baur et al., 2011), a major issue in the GRACE data interpretation comes from the leakage effect caused by the presence of outlying melting ice bodies which gravity effects interfere each other. Our estimation uses a novel approach that, exploiting the non-uniqueness of the gravity field, retrieves a hypercompact model of the sources by an iterative inversion. We will show that this approach solves the inherent leakage effects of the GRACE data and, thanks to the extreme compactness of the sources, allow us to do a quantification of the total mass loss in the study area with less ambiguity.

References

Baur, O., Sneeuw, N.; 2011: *Assessing Greenland ice mass loss by means of point-mass modeling: a viable methodology*. J Geod 85, 607–615. DOI https://doi.org/10.1007/s00190-011-0463-1.

Wahr, J., M. Molenaar, and F. Bryan.; 1998: *Time variability of the Earth's gravity field: Hydrological and oceanic effects and their possible detection using GRACE*. J. Geophys. *Res.*, 103(B12), 30205–30229, DOI:10.1029/98JB02844.

Offshore seismic monitoring: the Rospo seismic station as a pilot case study for the InSEA project.

A. Mantovani[a], A. Costanza[a], G. Fertitta[a], G. Tusa[a]

[a] *Istituto Nazionale di Geofisica e Vulcanologia, Osservatorio Etneo*

Introduction

Extending multiparameter monitoring, and in particular seismic one, to offshore areas represents a great challenge from many points of view. Nowadays it has become indispensable for a better understanding of the phenomena affecting the marine environment, as the oceans cover 70 percent of the Earth's surface, and also to provide a better localization of earthquakes along coastal and offshore sectors.

For many years, the Istituto Nazionale di Geofisica e Vulcanologia has been involved in the underwater multiparameter monitoring of the ocean floor (Beranzoli *et al*., 2000, 2015; D'Anna *et al*., 2009; Favali *et al*., 2006a, 2006b; Monna *et al*., 2005, 2013; Sgroi *et al*., 2006, 2007, 2019, 2021). Since 2005, the OBS Lab of Gibilmanna (Cefalù, Italy) has been dealing with the technological development of submarine systems, and the on-site specific operations for both deployment and recovery of the scientific instruments.

Recently the InSEA project (detailed description in De Santis *et al*., 2022), funded by the Italian Ministry of University and Research, aims to increase at national level the network of marine observation and monitoring systems in accordance with EMSO (European Multidisciplinary Seafloor and water column Observatory) ERIC (European Research Infrastructure Consortium) infrastructures in the less developed regions of Southern Italy. The project is developed according to six Objectives of Realization (ORs); in particular, among the activity belonging to the OR3, are listed the increase of the equipment for seafloor seismic monitoring (Ocean Bottom Seismometers - OBS) and the extent of the geophysical network between the Adriatic and Ionian Sea, by deploying submarine multi-parameter monitoring modules within the safety areas of five oil platforms (ca. 200 m away).

An opportunity to study the possible advantages and disadvantages of installing scientific instrumentation in such a prohibitive environmental context is represented by the Rospo seismic station. In May 2018, a Framework Agreement between the Ministry of Economic Development – General Department for the Safety of Mining and Energy (DGS-UNMIG), INGV and Assomineraria, was signed to start a scientific collaboration. Subsequently, DGS-UNMIG, INGV and EDISON Spa (as a member of Assomineraria) signed an Implementing Agreement for research purposes. As a first implementation of the Agreement, one of the conductor pipe (hereinafter c.p. D) of the Rospo Mare C oil platform (RSM-C, middle Adriatic Sea) has been made available for seismic and multiparameter monitoring. The installation of an OBS was concluded in January 2020 and, since February 2020, it belongs to the National Seismic Network (http://www.gm.ingv.it/index.php/rete-

sismica-nazionale), whose recorded data are transmitted in real time, through the EDISON network, to the INGV seismic monitoring centre.

The Rospo Mare C oil platform: arrangement and mechanical behaviour

The RSM-C oil platform (42° 14' 8,365" N, 14° 55' 54,682" E) is located offshore facing the city of Vasto and is part of a group of three platforms interconnected with each other by submarine pipelines. It is characterized by a four-legged reticular structure, about 100 m high from the seabed, while around 80 m are submerged. About 40 m of the c.p. D are buried within the soft sediments of the seafloor, while around 94 m between the seafloor and the sea surface, and other 10 m from the latter to the platform.

The offshore platforms are obviously subjected to several natural forces (winds, sea currents, waves) and anthropogenic ones (*e.g.* oil extraction processes), that excite the vibrational mode shapes of their structures. All these vibration fields can interfere with the seismic data acquisition system, in terms of quality of the recordings, reducing the Signal-to-Noise Ratio (SNR).

To calculate the natural frequencies of the c.p. D, we perform a finite element modal analysis, appropriately constrained, following the method described in Cammalleri and Costanza (2016). For the same purposes, the natural frequencies of other existing platforms, structurally similar to RSM-C, were collected from the literature (Jiammeepreecha *et al.*, 2008; Raheem *et al.*, 2012; Weldelassie, 2014). Furthermore, the frequencies of marine waves and those related to Von Karman's vortices (caused by sea currents flowing around the c.p. D) were considered. All those frequencies are listed in Tab. 1.

[Hz]					
	Nat. Freq. of platforms structurally similar to RSM-C				
Nat. Freq. C.p. D	[Jiammeepreecha]	[Raheem]	[Weldelassie, 2014]	Marine waves	Von Karman
0.3	0.8	1.1	0.25	0.005 – 0.15	0.03
0.8	0.8	1.1			0.06
1.5	2	1.4			0.12
2.5		3.6			0.15
3.7		3.6			

Tab 1. Vibration frequencies

Data acquisition system

The installation of an OBS at the base of the c.p. D of the RSM-C has been logistically possible, with the awareness of disturbances and relatively high noise levels between 0.1 and 10 Hz. As to minimize the influences of such disturbances, and also to ensure a good coupling, we developed a system which allows the sensor self-burying within the pelitic sediments of the seabed. As shown in Fig. 1, two conical caps are attached to the sensor and connected to a hydraulic circuit which conveys a flow of water from the top of the c.p. D to the seabed. A downward jet of water, coming out from below the sensor, digs a hole in the sediments, both ensuring an easier deployment and

recovery of the instrumentation. A dispersing nozzle was also designed to optimize the burying system.

The whole data acquisition system is composed of a broadband seismometer Nanometrics Trillium OBS 120 s and a Guralp DM24 digitizer inside the electronics vessel. A 150 m long marine cable, carrying data and power, connects the vessel to the surface unit. As it can be seen in Fig. 1 (a-c), a custom-made centering disc, made of polyethylene, guarantees the correct positioning of the bundle formed by the cables, rope and pipe above the sensor. It supports the electronic vessel and prevents the bundle from touching the walls of the c.p., as they may transmit mechanical noise to the sensor through the bundle.

The core of the surface unit is a Guralp EAM-U digital acquisition system, hosting a SEEDLink server. The server is accessible from the INGV seismic monitoring center, where a SEEDLink client will continuously receive the seismic data, available in near real-time.

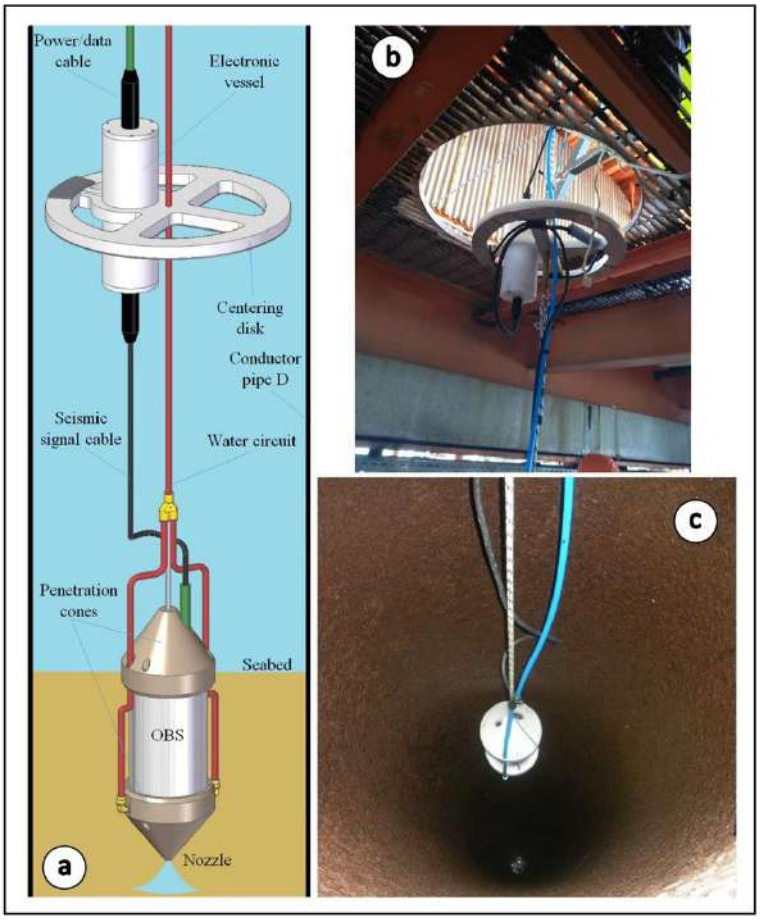

Fig. 1 – Schematic arrangement of the whole instrumentation deposited at the bottom of the c.p. D (a). In (b) and (c) a focus on the centering disc supporting the digitizer.

Quality evaluation of the recorded signals

As a first step, we collected the signals of the first week of each month, day by day, between March 2020 and October 2023 through the dedicated FDSN Web Services (https://www.fdsn.org).

Sample frequency is equal to 100 Hz so, as to investigate the whole range of frequencies of the sensor, we employ a signal windowing of 16.384 samples. We thus calculated the so-called Power Spectral Density (PSD, Fig. 2), the amplitude spectra and the spectral ratio (Nakamura, 1989) (Fig. 3d), as their temporal variability identifies the main noise sources at the recording sites, defines the noise levels of a station and assesses the earthquakes detection capability. Fig. 2 shows the PSDs calculated for the three components and the seasonal ones of the vertical component, for the whole period (308 days analysed). Comparing our results with the NLNM and NHNM reference curves (Peterson, 1993) we observed that the noise spectra levels are generally high and exceed the upper limit for period below 2 s and above 10-20 s. In the microseisms band (0.1-10 s), we observed the typical peaks, the so-called single (SF) and double frequency (DF), as a result of the interaction between atmosphere, sea surface, and seafloor (Webb, 1998).

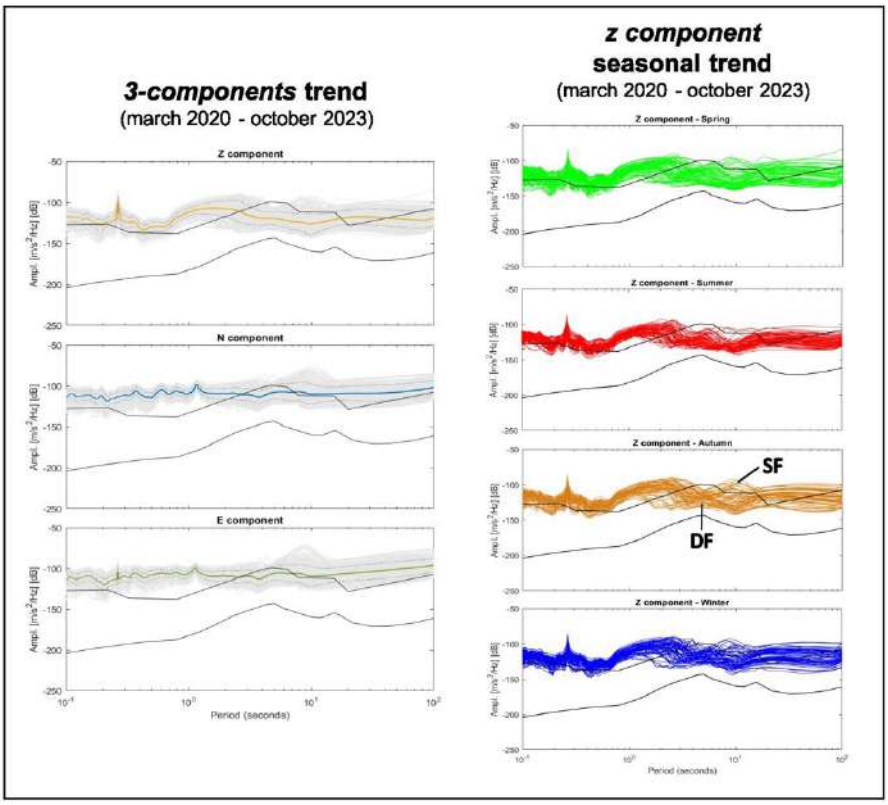

Fig. 2 – Seasonal and whole period PSD's for the three components. All the curves are reported in grey, while the mean one is color-coded. Peterson reference curves in black.

Because it is not always possible to check the arrangement of the instrumentation during the deployment, is fundamental the *a posteriori* establishment of the eventual correction to apply to the horizontal channels signals as to bring them to the conventional Cartesian reference. Among the several approaches known in the literature, we choose that proposed by Doran and Laske (2017) which is based on the measurement of the Rayleigh wave arrival angles. The result highlighted a deviation from north of 107°; therefore, by applying this correction we observed that the signal is almost constantly polarized towards SSE-NNW (Fig. 3c).

Nowadays this procedure has been automated in MATLAB by the development of an interface we called "*on demand*" (Fig. 3), which allows a qualitative inspections of the recorded signals in near real-time.

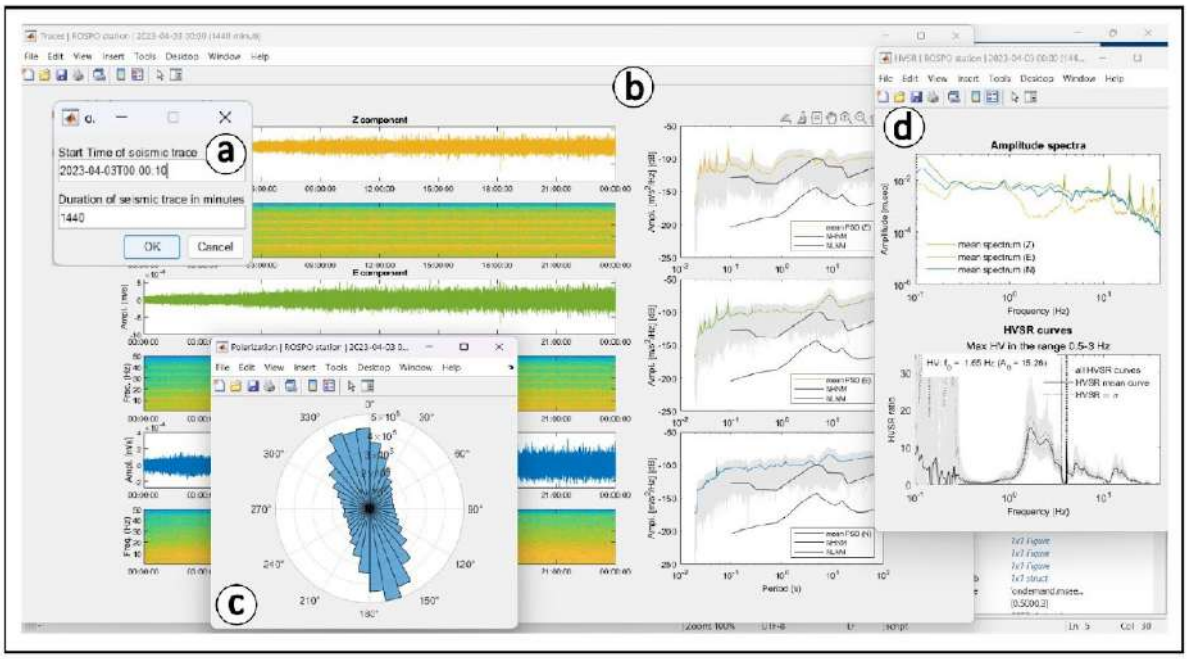

Fig. 3 – "On demand" interface. In (a) the dialog box. In (b) the spectrograms (on the left) and the Power Spectral Density (on the right) for the three components. In (c) the signal polarization polar histogram and in (d) the amplitude spectra (on the top) and the horizontal-to-vertical spectral ratio (on the bottom).

Conclusions

The OBS Lab of Gibilmanna performed the first installation of a broadband OBS at the bottom of one of the conductor pipes of the Rospo Mare C oil platform. For a preliminary analysis of the signals we developed a semi-automated MATLAB interface, which allow a fast qualitative evaluation. Notwithstanding our results highlighted that the site is noisy, compared to some land-stations, the system has been extensively tested and nowadays is fully functional. Hopefully, our experience and observations could help in exploring the opportunities that such structures may offer to extend the national seismic network to the marine environment, reducing the current seismic gap and thus improving earthquake's location.

References

Beranzoli L., Braun T., Calcara M., Calore D., Campaci R., Coudeville J.-M., De Santis A., Di Mauro D., Etiope G., Favali P., Frugoni F., Fuda J.-L., Gamberi F., Gasparoni F., Gerber H.W., Marani M., Marvaldi J., Millot C., Palangio P., Romeo G. and Smriglio G.; 2000. *GEOSTAR: the first European long term seafloor observatory*, EOS, Trans. Am. Geophys. Un., 81 (5), 45-49.

Beranzoli L., Ciafardini A., Cianchini G., De Caro M., De Santis A., Favali P., Frugoni F., Marinaro G., Monna S., Comntuori C., Qamili E and Sgroi T.; 2015. *A first insight into the Marsili volcanic seamount (Tyrrhenian Sea, Italy): Results from ORION-GEOSTAR3 experiment*. In: SEAFLOOR OBSERVATORIES. Springer Praxis Books. Springer, Berlin, Heidelberg.

Cammalleri M. and Costanza A.; 2016. *A closed-form solution for natural frequencies of thin-walled cylinders with clamped edges*. International Journal of Mechanical Sciences, 110, pp. 116-126.

D'Anna G., Mangano G., D'Alessandro A., D'Anna R., Passafiume G., Speciale S. and Amato A.; 2009. *The new INGV OBS/H.* Quaderni di Geofisica, 2009, N° 65.

Doran A. K. and Laske G.; 2017. *Ocean-Bottom Seismometer Instrument Orientations via Automated Rayleigh-Wave Arrival-Angle Measurements*. BSSA, Vol. 107, No. 2, pp. 691–708

De Santis A., Chiappini M., Marinaro G., Guardato S., Conversano F., D'Anna G., Di Mauro D., Cardin V., Carluccio R., Rende S.F., Giordano R., Rossi L., Simeone F., Giacomozzi E., Fertitta G., Costanza A., Donnarumma G.P., Riccio R., Siena G. and Civitarese G.; 2022. *InSEA Project: Initiatives in Supporting the Consolidation and Enhancement of the EMSO Infrastructure and Related Activities*. Front. Mar. Sci. 9:846701.

Favali P., Beranzoli L., D'Anna G., Gasparoni F., Marvaldi J., Clauss G., Gerber H.W., Nicot M., Marani M.P., Gamberi F., Millot C. and Flueh E.R.; 2006a. *A fleet of multiparameter observatories for geophysical and environmental monitoring at seafloor*, Ann. Geophys., 49, 2/3, 659-680.

Favali P., Beranzoli L., D'Anna G., Gasparoni F. and Gerber H.W.; 2006b. *NEMO-SN1 The 1st "Real-Time" Seafloor Observatory of ESONET*, Nuclear Instruments and Methods in Physics Research Section A: Accelerators, Spectrometers, Detectors and Associated Equipment, 567/2, 462-467.

Jiammeepreecha W., Chucheepsakul S. and Kantiyawichai K.; 2008. *Dynamic Analysis of Offshore Structures in the Gulf of Thailand by Using Abaqus Program*. In: Conference Paper, Conference: Proceedings of the 13th National Conference on Civil Engineering, At Chonburi, Thailand, May 2008.

Monna S., Frugoni F., Montuori C., Beranzoli L., Favali P.; 2005. *High quality seismological recordings from the SN-1 deep seafloor observatory in the Mt. Etna region*. Geophys. Res. Lett., 32, L07303.

Monna S., Sgroi T. and Dahm T.; 2013. *New insights on volcanic and tectonic structures of the southern Tyrrhenian (Italy) from marine and land seismic data*. Geochem. Geophys. Geosys., 14, 3703–3719.

Nakamura Y.; 1989. *A method for dynamic characteristics estimation of subsurface using microtremors on ground surface*. Quarterly report of Railway Technical Research of Institute of Japan, vol. 30, n. 1

Peterson J.; 1993. *Observation and Modeling of Seismic Background Noise*. US Geological Survey Open File Report; US Geological Survey: Albuquerque, NM, USA; pp. 96-322

Raheem A.S.E., Aal A.E. M.A., Shafy A.G.A. and Seed A.F.K.; 2012 *Nonlinear Analysis of Offshore Structures Under Wave Loadings*. In: Conference Paper, 15 WCEE, Lisbon.

Sgroi T., Braun T., Dahm, T. and Frugoni, F.; 2006. *An Improved Seismicity Picture of the Southern Tyrrhenian Area by the Use of OBS and Land-Based Network: the TYDE experiment*. Ann. Geophys. 49 (2-3), 801–817.

Sgroi T., Beranzoli L., Di Grazia G., Ursino A. and Favali P.; 2007. *New Observations of Local Seismicity by the SN-1 Seafloor Observatory in the Ionian Sea, Off-Shore Eastern Sicily (Italy)*. Geophys. J. Int. 169 (2), 490–501

Sgroi T., Di Grazia G., and Favali P.; 2019. *Volcanic Tremor of Mt. Etna (Italy) Recorded by NEMO-SN1 Seafloor Observatory: a New Perspective on Volcanic Eruptions Monitoring*. Geosciences 9 (3), 115.

Sgroi T., Polonia A., Beranzoli L., Billi A., Bosman A., Costanza A., Cuffaro M., D'Anna G., De Caro M., Di Nezza M., Fertitta G., Frugoni F., Gasperini L., Monna S., Montuori C., Petracchini L., Petricca P., Pinzi S., Ursino A. and Doglioni C.; 2021. *One Year of Seismicity Recorded Through Ocean Bottom Seismometers Illuminates Active Tectonic Structures in the Ionian Sea (Central Mediterranean)*. Front. Earth Sci. 9:661311.

Webb S. C.; 1998. *Broadband Seismology and Noise under the Ocean*. Rev Geophys. 36, 105-142.

Weldeslassie M.W.; 2014. *Investigation of Which Sea State Yield the Dominating Contribution to Fatigue Accumulation in Offshore Structures*. Master's Thesis.

Corresponding author: ambra.mantovani@ingv.it

ShellSet – Parallel dynamic neotectonic modelling

J. B. May[1], P. Bird[2,1], M. M. C. Carafa[1]

[1] Istituto Nazionale di Geofisica e Vulcanologia (INGV), Italy
[2] Department of Earth, Planetary, and Space Sciences, UCLA, U.S.A

Introduction

Recent decades have seen an almost continuous improvement in computing power and techniques; but the general scientific community too often misses out on these improvements. Research institutions, both academic and industrial (public and private), typically provide employees with personal machines for their work, with even the least powerful of these capable of simulations, in serial and parallel, that would have required much more expensive hardware only a decade previously. Unlocking this potential is key to accelerating scientific discovery in every field, particularly where modelling is concerned.

The calculations involved in forward modelling are often time-consuming, perhaps because of the number of calculations e.g., 3D models, or because the underlying model is very large, e.g., a global model. Reducing the time required for these models would improve program usability and lead to faster hypothesis testing. Simply relying on the relentless improvement of computing capabilities to increase program performance is sub-optimal and many existing programs would benefit from relatively small alterations to their source code to fully utilize these improvements.

Here, we present a hybrid parallel program called ShellSet (May et al. 2023). ShellSet improves upon well-known and robust software by simplifying the user interface, removing all prompted user input, and reducing the time to result by employing an MPI (message passing interface) framework to run multiple models in parallel.

Software

ShellSet (first presented in May et al., 2023) is a combination of three programs which are well known within sections of the geoscientific community, having been developed over recent decades, all of which are available from http://peterbird.name.

Briefly, OrbData calculates the crust and mantle-lithosphere thicknesses at each node of a given finite element grid, adding a “lithospheric density anomaly of chemical origin” at each node which is adjusted to achieve isostasy with other nodes. OrbScore calculates the scores for any/all of the six Shells predictions, for relative realism, against supplied real data. The six testable predictions

are: relative velocities of geodetic benchmarks (GV); most-compressive horizontal principal stress directions (SD); long-term fault heave and throw rates (FSR); rates of seafloor spreading (SSR); the distribution of seismicity on the map (SC); and fast-polarization directions of split SKS arrivals (SA).

Shells is where the main forward model calculations occur. Shells uses the thermal and compositional structure of thin spherical shells of planetary lithosphere, together with the physics of quasi-static creeping flow, to predict patterns of velocity, straining, and fault-slip on the surface of a planet. A primary goal of users has been to understand the balance of forces that move the plates while a secondary goal has been to predict fault slip rates and distributed strain rates for seismic hazard estimation.

Shells, OrbData and OrbScore are serial programs except for calls to Intel's Math Kernal Library (MKL) to solve generated linear systems. To improve these programs, we leverage the power of parallel computing to create a single program, ShellSet, which allows multiple models to be tested simultaneously. ShellSet, like Shells before it, uses MKL routines with OpenMP style threads to solve its system of linear equations. While the combination with OrbData and OrbScore moves inter-program interfaces from the user to the program - meaning a simplified user interface and further time savings.

ShellSet Vs an existing model

An example application of ShellSet is shown where we improve upon an existing global model (Earth5-049 in Bird et al., 2008).

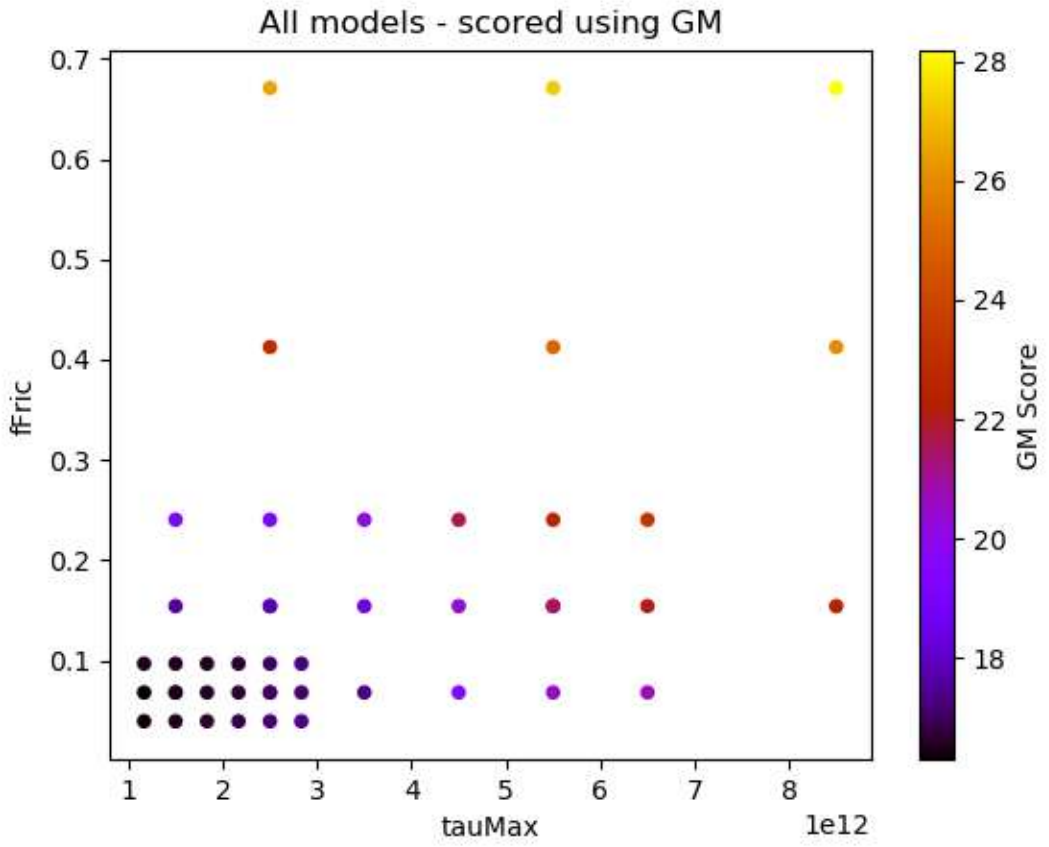

Figure 1: Complete 3-level grid search history of 2D parameter space generated by ShellSet.

We use ShellSet's grid search model generator to automatically search the defined 2D parameter space for an optimal model. The grid search contains 45 models, generated over 3 levels starting with 9 models before generating a further 9 within the cell of each of the best 2 models at the first and second levels, see Fig. 1.

Among the 45 models we find 8 models with an equal or improved (lower) geometric mean score. These 8 models can be seen in Tab. 1, along with the original score for the best model of Bird 2008 (Earth5-049) and a re-run to account for newer software accuracy (New Earth5-049).

Model ID	fFric	tauMax	Geometric Mean ($\sqrt[4]{SSR*GV*SD*SA}$)
Earth5-049	0.10	$2.00 * 10^{12}$	18.10
New Earth5-049	0.10	$2.00 * 10^{12}$	16.58
10	0.07	$1.50 * 10^{12}$	16.50
28	0.04	$1.17 * 10^{12}$	16.34
29	0.07	$1.17 * 10^{12}$	16.29
30	0.10	$1.17 * 10^{12}$	16.55
31	0.04	$1.50 * 10^{12}$	16.49
32	0.07	$1.50 * 10^{12}$	16.50
33	0.10	$1.50 * 10^{12}$	16.58
35	0.07	$1.83 * 10^{12}$	16.55
36	0.10	$1.83 * 10^{12}$	16.56

Table 1: Searched models with improved Geometric mean score when compared to Earth5-049.

ShellSet performance testing

The performance of ShellSet can be measured in 2 ways. Firstly, Tab. 2 proves that running multiple models in parallel can yield good performance improvement, even on a mid-level machine. It shows the time taken (mm:ss) for a given number of MPI processes to complete a set of models. The bracketed time is the speed up relative to the time taken by 1 process to complete the same number of models. This speed up is plotted in Fig. 2. It is trivial to state that larger machines would offer more significant improvements or the ability to test higher numbers of models and processes.

MPI Processes	Models						
	1	2	4	8	16	32	64
1	3:50	7:47	16:06	32:33	64:26	128:39	262:09
2	X	5:12 (1.50)	10:19 (1.56)	21:13 (1.52)	42:06 (1.53)	84:59 (1.51)	172:33 (1.52)
4	X	X	7:59 (2.02)	15:45 (2.05)	32:05 (2.01)	62:12 (2.07)	125:49 (2.08)
8	X	X	X	15:02 (2.15)	29:35 (2.18)	58:21 (2.21)	113:03 (2.32)
16	X	X	X	X	29:31 (2.18)	57:22 (2.24)	111:15 (2.36)

Table 2: Intel Core i9-12900 CPU at 2.4GHz desktop with 64GB RAM, 16 physical cores (8 performance, 8 efficient) and 24 threads.

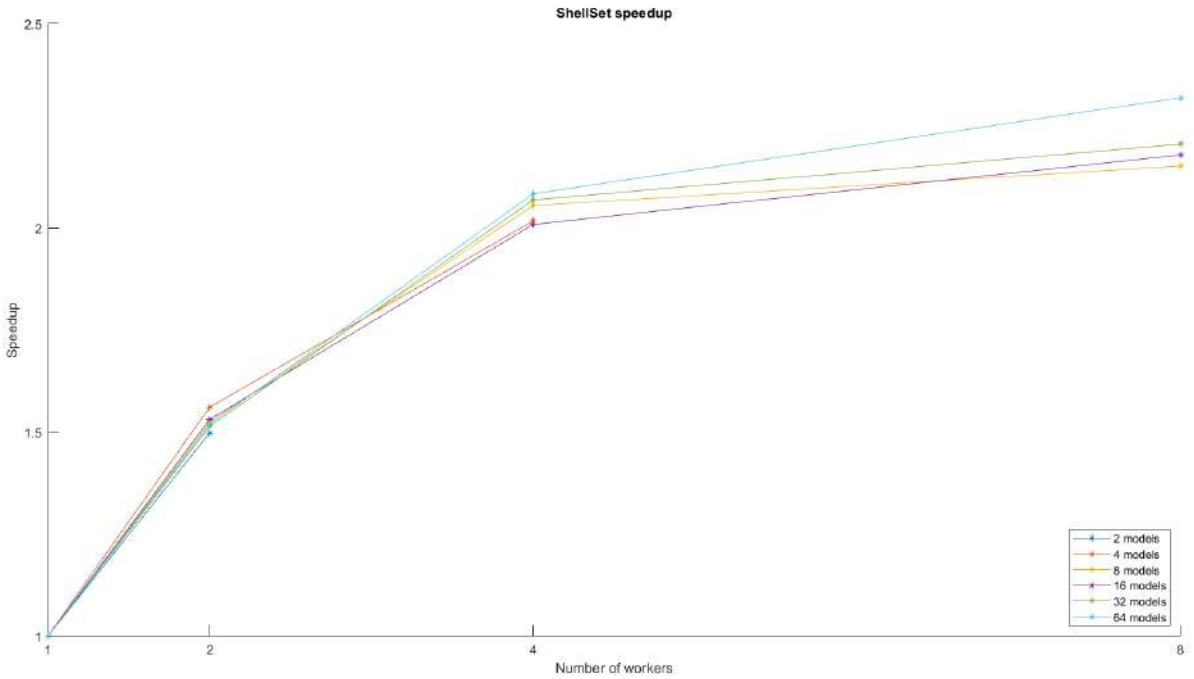

Figure 2: ShellSet speed up performance. The 16 worker speed up results are omitted as they are similar to 8.

Secondly, we know from experience that the simplified user interface and model input options greatly increase the program's performance. The original programs worked in serial (1 model at a time using parallel MKL routines) with the inter-program interfaces handled manually by the user, the newly optimized program removes this requirement on the user by automatically feeding information between the 3 constituent program parts. Not only do these automated connections offer a performance boost but they allow a "start and ignore" treatment of the program, meaning a user can simply begin a test and wait for the result with no further input required.

The ability to utilize parallel computing combined with a simplified user interface, ShellSet also includes a GUI to aid the user in setup, significantly widens the possible user base. This makes ShellSet accessible to anyone from seasoned researchers to master's or even bachelor's degree students whose research time may be limited.

References

Bird P., Liu Z., and Rucker W.K.; 2008: Stresses that drive the plates from below: Definitions, computational path, model optimization, and error analysis. Journal of Geophysical Research: Solid Earth, 113, B11.

May J.B., Bird P., and Carafa M.M.C.; 2023: ShellSet v1.1.0 - Parallel Dynamic Neotectonic Modelling: A case study using Earth5-049 (pre-print). EGUsphere, 1-21.

Corresponding author: jonbryan.may@ingv.it

An innovative machine learning algorithm for gravity modelling

C. Messina[1], L. Bianco[1], M. Fedi[1],

[1] *Department of Earth, Environment and Resources Sciences, University of Naples "Federico II", Naples, Italy*

We describe a Machine Learning algorithm for interpretation of gravity data generated by rather complex structures. We choose a Convolutional Neural Network (CNN) with a U-Net architecture. This architectural design of the network has been recently applied in gravity modelling scenarios, in which the training dataset was built introducing strong prior information about the source without obtaining a generalized training set. To overcome this limit we train the network through examples composed by labels constituted by simple elements, here called building blocks, with features being their corresponding gravimetric anomalies. Next to the training we test our method first analysing gravity anomalies produced by simple structures (e.g., prisms, horizontal cylinders), and then with those generated by increasingly complex sources with irregular shapes, such as salt diapirs. We show examples of 2D-3D of real cases. We assume that a gravimetric anomaly can be seen as composed of the constructive interference of anomalies generated by the edges of the source associated to building blocks. Moreover, this method streamlines decision-making and reduces computational efforts involved in assembling a suitable dataset.

Corresponding author: ciromessina631@yahoo.it

A data-driven supervised neural network approach for surface waves inversion: synthetic and field data applications

Felipe Rincón[1], Sean Berti[1,2], Mattia Aleardi[1], Eusebio Stucchi[1]

[1] University of Pisa, [2] University of Florence

Introduction

In near-surface applications, S-velocity models are commonly obtained through the analysis of the dispersion characteristic of the surface waves. One of the most popular approaches is the multichannel analysis of surface waves (MASW) which is a phase-velocity inversion method (Park et al., 1999). The forward operator involved in the computation of the dispersion curves presents two strong assumptions: a 1D layered model and plane-waves. These limitations strongly affect the capability of the method to account for lateral velocity variations. To overcome these limitations, it is imperative to employ more sophisticated methods such as Full Waveform Inversion (FWI). FWI is an inverse problem that exploits the full information content of the seismic waveforms. Traditionally it is solved through deterministic approaches which seek to find a single best-fit model that explains the observed data. Even though this approach is computationally efficient it heavily relies on a good starting model to reach convergence.

The rapid advancements in algorithms and computing present an unprecedented opportunity for significant progress in seismic inversion, enabling the solution of previously infeasible problems through data-driven approaches. A promising avenue of research involves establishing a direct inverse mapping from observed seismic waveforms to subsurface structures through the training of neural networks using paired data of seismic waveforms and corresponding velocity models (Wu et al., 2018). These approaches seek to leverage the power of deep learning to learn complex relationships between seismic data and subsurface properties, potentially revolutionizing the traditional FWI methodology. However, the efficacy of learning-based methods stems from their ability to leverage vast amounts of high-quality training data, a challenge for seismic methods due to their high costs and confidentiality concerns that limit the accessibility of seismic data. In this study we introduce a novel approach that combines a reparameterization of both the data and model parameters employing Discrete Cosine Transform (DCT) with neural networks to approximate the inverse operator. We tested our method in both synthetic and field data from the InterPACIFIC project (Garofalo et al., 2016). Our objective is to conduct time-effective training to generate S-velocity models from the data. The proposed model could serve as a starting point for a FWI frameworks, helping to mitigate the cycle skipping problem and reduce the number of iterations to reach convergence.

Methods

We performed our training in DCT-domain as a strategy to reduce the memory storage of the dataset, to enable a flexible matching relation between input and output second dimensions using a versatile number of coefficients, thereby facilitating the application of a reasonable number of geophones, and to reduce the number of model and data parameters during the learning process, leading to accelerate the training. The DCT is a linear orthogonal transformation that decomposes a signal into a combination of cosine functions oscillating at varying frequencies (Ahmed et al., 1974). To construct the Vs model dataset, we carefully selected a set of "base models" representing prevalent geological environments, including features like landslide, sinkholes, stratification, layer displacements, and landfills. Subsequently, we generated multivariate normal random models by utilizing the mean values of these base models and five distinct covariance matrices. To compute the seismograms, we utilized SOFI2D algorithm, an elastic forward solver proposed by Bohlen (2002). We kept fixed the hyperparameters of the forward computation guaranteeing that the CFL conditions were satisfied, and for all the computations we employed a Ricker wavelet of 15 Hz. In this way we generated 9500 Vs-model and data as the training dataset, with an additional of 500 for validation.

Figure 1a depicts a schematic representation of the neural network, showcasing the transformation of both input seismograms and the output velocity model into the DCT domain. The architecture comprises an encoding-decoding stage, employing max-pooling and transposed convolution, respectively. The number of channels progressively increases from 64 to 1024, with each stage duplicating its number until reaching a latent space, before decoding the information into the truncated DCT model dimension. Figure 1b displays the training and validation monitoring curves. Validation is conducted on 500 seismograms and velocity models pairs that were not utilized during the training process. The Mean Square Error (MSE) Loss function is utilized for monitoring the training (blue curve), alongside the L2-norm of the predicted data computed from the proposed model, serving as the validation metric (orange curve). Note that with an increase in the number of epochs, both the MSE and L2-norm decrease, indicating successful learning improvement by the network. However, after 1300 epochs (black-dashed curve), the loss function reached convergence, and the L2-norm becomes unstable, suggesting a potential occurrence of overfitting during training.

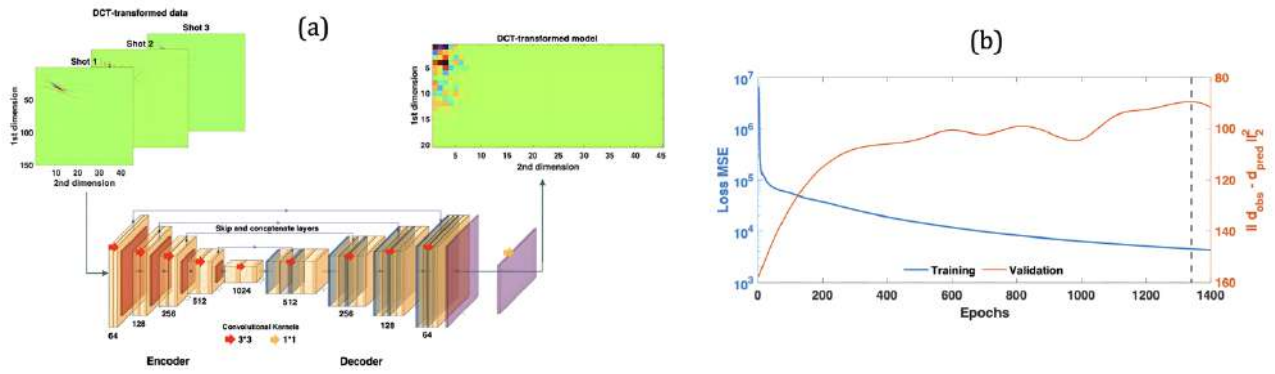

Fig. 1 – (a) Scheme of the network architecture for a 3-shots acquisition array. The input data and output velocity models are in DCT-domain. (b) Training and validation are represented by the blue and orange curves, respectively. The analysis is confined to the initial 1300 epochs, as indicated by the black-dashed curve, until which convergence is achieved.

Results

To illustrate the capability of the trained network to propose Vs-models, it is presented below an example for synthetic and field data. The field data was taken from the InterPACIFIC project which also includes Vs measurements in boreholes located at 10 m of the acquisition array. The borehole data was utilized to validate the obtained results. The synthetic data was constructed using the same array of the field data. The acquisition setting consists of 48 receivers separated 1 meter, and 3 sources (two off-end and one middle shots).

Synthetic data example: Figure 2 shows the network's prediction on the synthetic example. The data was created using the same Ricker wavelet as the training dataset. In Figure 2a it is shown the true and predicted velocity model. Note that the trained network accurately predicts both the main features and magnitudes of the true velocity model. In Figure 2b, a comparison between the observed and predicted data is presented. It is noteworthy that the data exhibit a perfect match and do not show any signs of cycle-skipping.

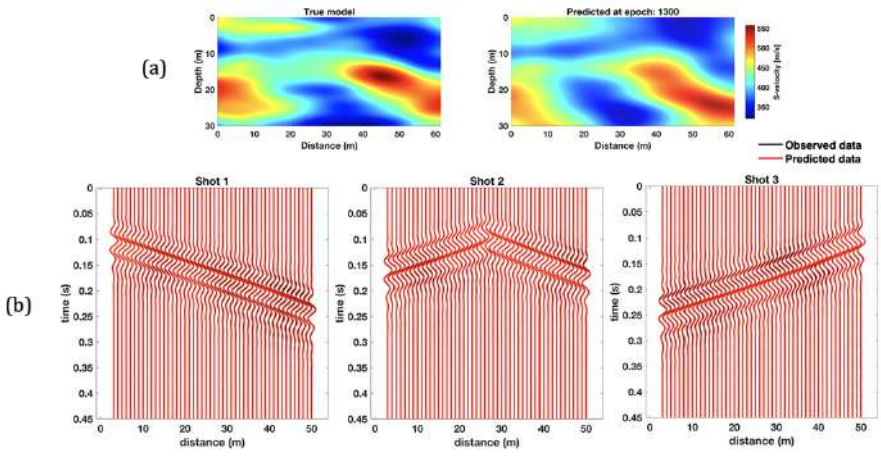

Fig. 2 – Synthetic example: (a) S-velocity model predicted using the NN at epoch 1300. (b) Observed and predicted data comparison.

InterPACIFIC data example: Figure 3 presents the network's prediction on a real dataset. To align the data with the training simulations, a low-pass filter with a cutoff frequency of 30 Hz was applied. The predicted data was computed using an estimated wavelet derived from the observed data after filtering. In Figure 3a, the predicted model is depicted alongside a mean 1D Vs-model profile (black curve) derived from multiple borehole measurements available from the InterPACIFIC project. Note that a significant high-low-high velocity contrast is observed in the borehole between 15-18 meters depth, aligning well with the corresponding features in the predicted model at that position. The network proposes a layered model with a velocity range consistent with those obtained from the borehole measurements. In Figure 3b it is shown the comparison between observed and predicted data. It is noteworthy that the data exhibits excellent agreement, except for traces located between the distances 30-40 meters. Despite this, the data does not present cycle-skipping, meaning that the predicted model is a very good starting model proposal for an FWI framework.

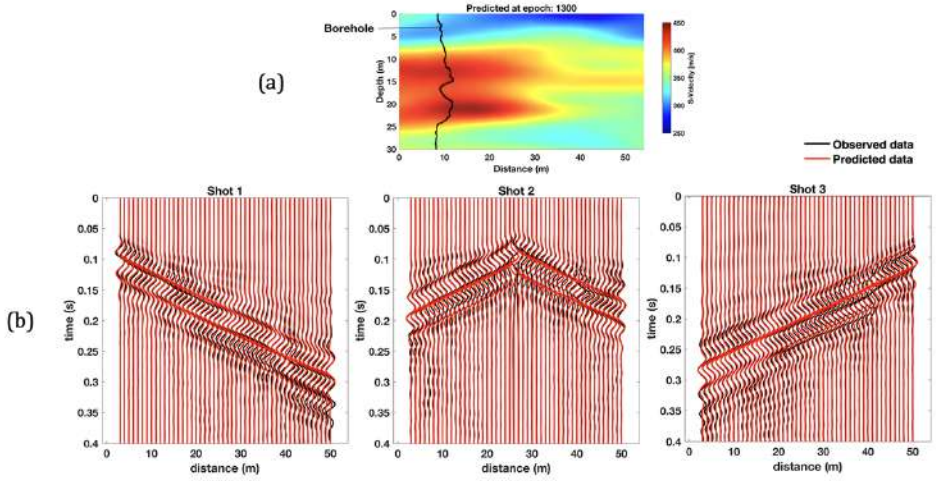

Fig. 3 – Field data example: (a) S-velocity model predicted using the NN at epoch 1300. (b) Observed and predicted data comparison.

Conclusions

We introduced a time-efficient neural network training in DCT-domain. The construction of the training and validation datasets was completed in parallel within 3.8 hours. The training process to reach epoch 1300 took 7.6 hours, and the required time to propose a model using the trained network and conduct the inverse DCT is 0.2 seconds. All these algorithms were performed in a computer system powered by a 12th Gen Intel(R) Core (TM) i9-12900KF equipped with NVIDIA GeForce RTX 3080 Ti graphics card and the system runs with CUDA Version: 11.8.

The use of DCT compression is an optimal strategy in neural network training, offering significant advantages. This approach notably reduces the memory requirement from 21 to 1.2 gigabytes, resulting in a 94% reduction in memory usage. Moreover, the computational cost during training is decreased by 74% with respect a full-domain training. Finally, the DCT compression enables

practical training with a reasonable number of geophones since the number of coefficients in the DCT can be readily adjusted to align with both the data and model requirements.

We demonstrated the trained network's capability in generating data-driven S-velocity model proposals with minimal data misfits between observed and predicted data. Modifications in array settings and source characteristics may necessitate retraining the network, which, under similar hyperparameters as presented in this work, requires approximately 11.4 effective hours. The proposed S-velocity model can serve as a starting model for FWI frameworks, offering the potential to reduce computational costs and address the cycle-skipping issue.

Acknowledgements

We express our gratitude to Nicola Bienati for providing valuable assistance and insightful comments that significantly enhanced the quality of this work.

References

Ahmed, N., Natarajan, T., & Rao, K. R. (1974). Discrete cosine transform. IEEE transactions on Computers, 100(1), 90-93.

Bohlen, T. (2002). Parallel 3-D viscoelastic finite difference seismic modelling. Computers & Geosciences, 28(8), 887-899.

Garofalo, F., Foti, S., Hollender, F., Bard, P. Y., Cornou, C., Cox, B. R., ... & Yamanaka, H. (2016). InterPACIFIC project: Comparison of invasive and non-invasive methods for seismic site characterization. Part I: Intra-comparison of surface wave methods. Soil Dynamics and Earthquake Engineering, 82, 222-240.

Moghadas, D., & Vrugt, J. A. (2019). The influence of geostatistical prior modeling on the solution of DCT-based Bayesian inversion: A case study from Chicken Creek catchment. Remote Sensing, 11(13), 1549.

Park, C. B., Miller, R. D., & Xia, J. (1999). Multichannel analysis of surface waves. Geophysics, 64(3), 800-808.

Wu, X., Shi, Y., Fomel, S., & Liang, L. (2018, October). Convolutional neural networks for fault interpretation in seismic images. In SEG International Exposition and Annual Meeting (pp. SEG-2018). SEG.

Corresponding author: felipe.rincon@phd.unipi.it

Filling active seismic null space with LSTM

G. Roncoroni[1] , I. Deiana[2] , E. Forte[1] , M. Pipan[1]

[1] *University of Trieste, Italy*
[2] *Stanford University, California, USA*

Introduction

Post-stack seismic data analysis plays a crucial role in understanding subsurface structures and petrophysical properties,often associated with a peculiar low or high frequency behaviour. Sinha et al. (2005) highlighted the presence of low-frequency shadows in association with hydrocarbon reservoirs, emphasising the significance of low-frequency information in post-stack seismic data for reservoir characterization. Moreover, the application of discrete wavelet transform-based multi-resolution analysis for spectral enhancement in post-stack seismic data was discussed by Camacho-Ramírez et al., 2016,which remarked on the role of frequency analysis in characterising heavy oil reservoirs. Reiser & Bird (2016) presented case studies of broadband quantitative interpretation, emphasising the utilisation of frequency-related information for improved target delineation and estimation of reservoir properties from post-stack seismic data. Additionally, Du et al. (2016) addressed the challenges of low signal-to-noise ratio and the importance of considering the main frequency and signal-to-noise ratio of seismic data for thin beds interpretation in post-stack seismic data. Furthermore, Karsli et al. (2006) discussed the application of complex-trace analysis for random-noise suppression and temporal resolution improvement in post-stack seismic data, emphasising the significance of frequency-related analysis for enhancing data quality, while Shi et al. (2009) addressed near-surface absorption compensation technology and its application in the Daqing Oilfields, stressing the importance of frequency-related compensation techniques for improving the resolution of post-stack seismic data. Moreover, Chopra et al. (2003) discussed high-frequency restoration of surface seismic data, indicating the relevance of frequency-related restoration techniques for enhancing the resolution of post-stack seismic data.Therefore, post-stack seismic data analysis encompasses various dedicated frequency-related analyses and methodologies, emphasising the significance of low and high-frequency information for reservoir characterization, attribute prediction, noise suppression, and resolution enhancement.

In fact, low and high-frequency extrapolation from active seismic data is essential for various applications such as imaging, reservoir characterization, and monitoring. Classical methods for low-frequency extrapolation involve techniques such as full-waveform inversion (FWI) and autoregressive (AR) spectral extrapolation. FWI with extrapolated low-frequency data has been proposed as an effective method for determining the low-wavenumber components of the model from extrapolated low frequencies (Sun & Demanet, 2020). Additionally, the autoregressive extrapolation method has been utilised to extend the spectral bandwidth of seismic data, enabling

the recovery of missing low and high frequencies for acoustic impedance inversion (Karsli, 2010; Karsli, 2006). In recent years, deep learning approaches have gained attention for low-frequency extrapolation from seismic data. Ovcharenko et al. (2019) and Li & Demanet (2016) have proposed application of deep learning - specifically convolutional neural networks - for low-frequency extrapolation, showing promising results in extrapolating low frequencies from multi-offset seismic data. Furthermore, machine-learning-based data recovery has been suggested for simultaneous deblending, trace reconstruction, and low-frequency extrapolation, indicating the potential of deep learning in addressing multiple challenges in seismic data processing (Nakayama & Blacquière, 2021). Multi-task learning has been proposed for addressing low-frequency extrapolation and elastic model building from seismic data, showing the potential of integrating classical physics-based methods with deep learning techniques (Ovcharenko et al., 2022). In addition to low-frequency extrapolation, high-frequency extrapolation from seismic data has also been a focus of research. Ovcharenko et al. (2020) emphasised the importance of low frequencies in high-frequency land seismic data due to the elastic nature of the Earth's subsurface, highlighting the significance of low-frequency extrapolation in addressing the challenges associated with high-frequency data inversion. Furthermore, a 1-D phase-tracking method has been proposed for extrapolating low-frequency data based on phases and amplitudes in the observed frequency band, indicating the significance of considering different dimensions for effective extrapolation (Li & Demanet, 2016).

Methods

We propose a novel 1-D approach based on LSTM (Long Short-Term Memory) Neural Networks (NN) to address the low- and high-frequency gap (i.e. null space) in reflection seismics. We trained two different NNs: one is trained to infer a lower frequency output from a higher frequency signal, from now on called low-frequency model, and another with switched input and output, from now on called high-frequency model, with both the input and output assumed to have maximum phase. The training dataset is generated using a convolutional approach. The data generation process involves creating synthetic noisy seismic traces for training, considering modifications to the classical seismic convolutional model to enhance its generalization to better mimic real seismic data. The NN is trained with a custom loss function that includes both amplitude and frequency components.

The method is easily scalable thanks to the fact that the NN operates without direct consideration of frequency, time length and sampling information, enabling the generation of desired frequency output just by adjusting how the input data is sampled. The NN will undergo the training based on a parameter known as Sample Duration (SD), representing the estimated duration of the source wavelet. We have the flexibility to resample each input signal provided to the network to align with the sample duration exploited in NN training. SD serves as the crucial parameter governing frequency content generation, enabling the network to produce new frequencies in accordance with it. Since it is not always easy to determine SD on field data, we use the second zero of the auto-correlation to make it easier to get and more objectivesuch a parameter. Once we have

trained the NN we can scale every signal to the trained SD and make the inference that will output a signal with half the frequency, for the Low-frequency model and one with a double central frequency, for the High-frequency model. Thanks to the constraints given by the custom loss function with the frequency counterpart taken into account, we are able to further generalize the results to other frequencies just by applying a Scaling Factor (SF), i.e. a factor applied to the SD therm that multiplies the number of samples in the output. This feature allows us to infer quite easily different frequency predictions. In Figure 1 we plot some of these predictions with varying SF: low-frequency model in Figure 1A where the input SD is divided by the SF and high-frequency model, in Figure 1B, where the SD is multiplied by the SF. The input in both of these results is a frequency filtered version of the Viking Graben Line 12 (Keys and Foster, 1998), filtered with a band-pass filter at 6-20Hz.

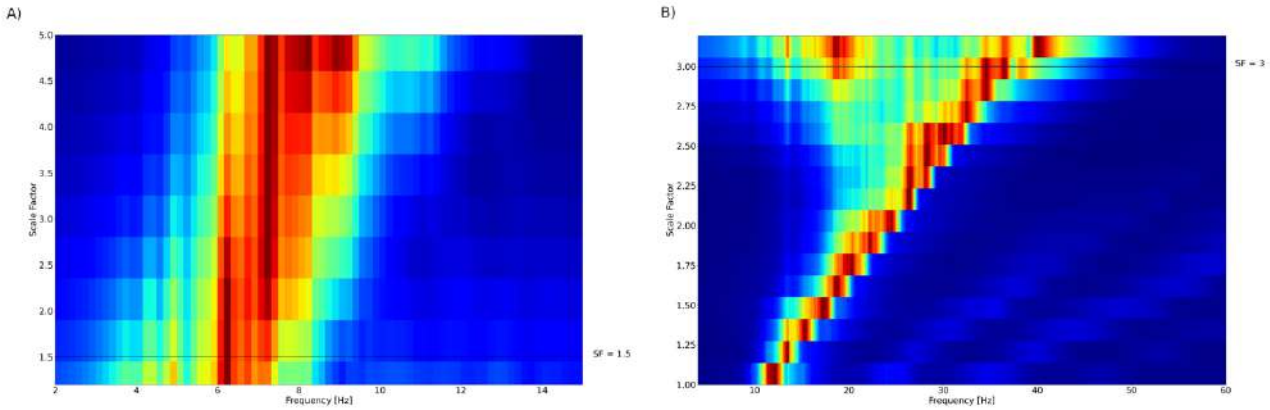

Figure 1: Low (A) and High (B) frequency inference of the Viking Graben Line 12 on the x-axis frequency, and on the y-axis the Scaling Factor. The solid line in A and B marks the chosen frequency that will be used in the next section.

Results and Discussion

Low Frequency inference

Results of the application of the methodology are shown in Figure 2. We moved the central frequency from 14Hz to 8Hz, as shown in the amplitude-frequency plot in Figure 2C. If we compare the input (Figure 2A) and the prediction (Figure 2B), it is clear that, as expected from the low frequency counterpart, more importance is given to main reflectors, e.g. horizontal reflector at 2s in the data. We can furthermore appreciate that amplitude is preserved as expected and interference is properly predicted, e.g. in the wedge around 1s in the first 750m .

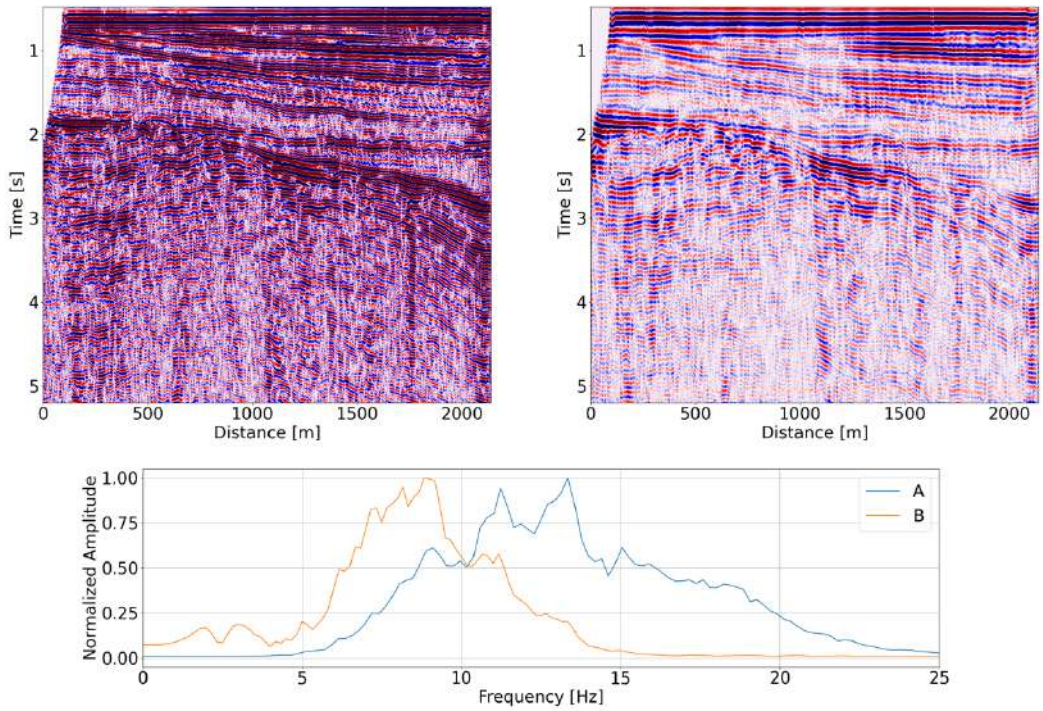

Figure 2: Low frequency inference on a section of the Viking Graben dataset: A represents the input data, B the low-frequency version and C the amplitude spectra of the seismic line depicted in A (blue)- and in B (orange).

High Frequency inference

For the High-Frequency model, the data shown in Figure 1B is depicted in Figure 3. Since the data had the predicted range of frequency in the raw data, we take now into account 2 different data: Figure 3A is the NN input with central frequency of 14Hz, as used in Figure 2, while in Figure 3C we show the reference data, i.e. the raw data after a 10-40Hz band-pass filter.

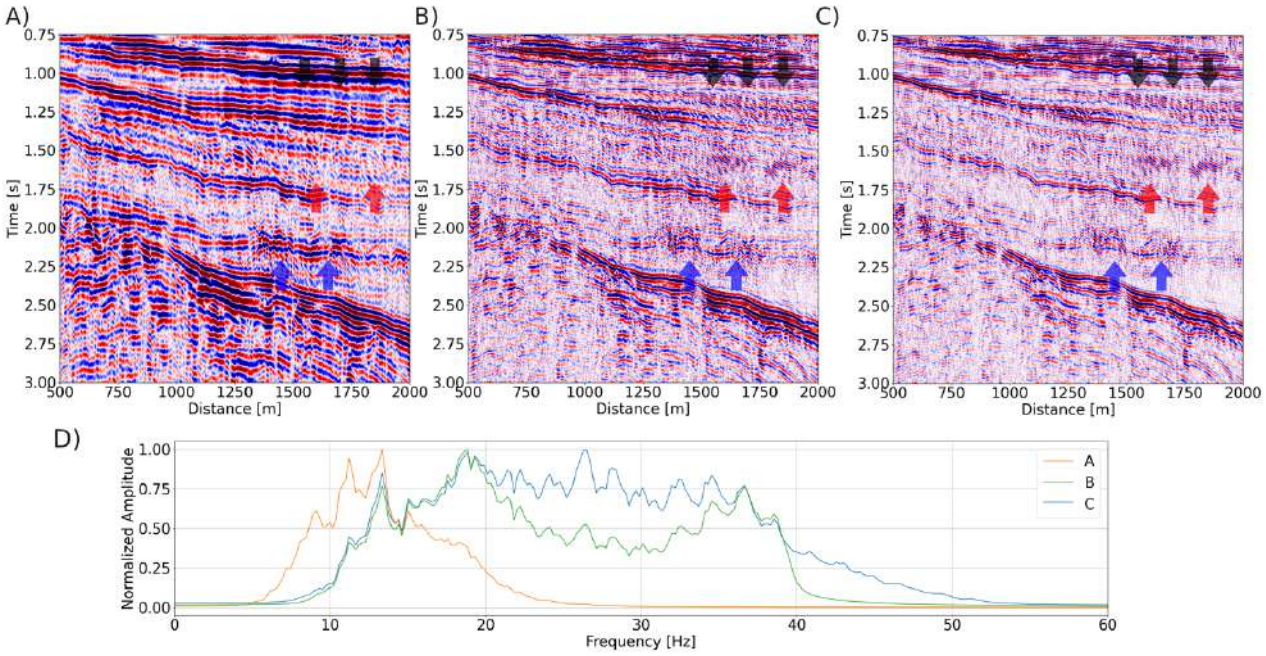

Figure 3: High frequency inference on a section of the Viking Graben dataset: A represents the low-filtered data, the same used in Figure 2A, B is the high frequency inference, and C represents the high frequency reference data. The amplitude spectra of the seismic line depicted in A (Orange), in B (Green), and C (Blue) are reported in D.

Thanks to this, we can make a proper comparison between the input (Figure 3A), the prediction (Figure 3B) and the reference data (Figure 3C). If we focus on the strongly dipping reflector marked with black and red arrows, we can see that while the prediction matches pretty well the reference, this feature was not visible (black arrow) or barely visible (red arrow) in the NN input. Further focus should be put on the diffraction patterns pointed out with the blue arrows: while the match is very good between NN predictions and reference data (i.e. Figure 3B and C), hyperbolas are difficult to be interpreted in the input lower frequency data (i.e. Figure 3A).

In order to further evaluate the results of the two models, we focus on the area from 120-1250m and from 0.6-1.3s (see e.g. Figure 2A). This area is very interesting because it images a typical wedge structure. In Figure 4 we present a wiggle plot of the input (Figure 4A) and the high-frequency inference (Figure 4B).

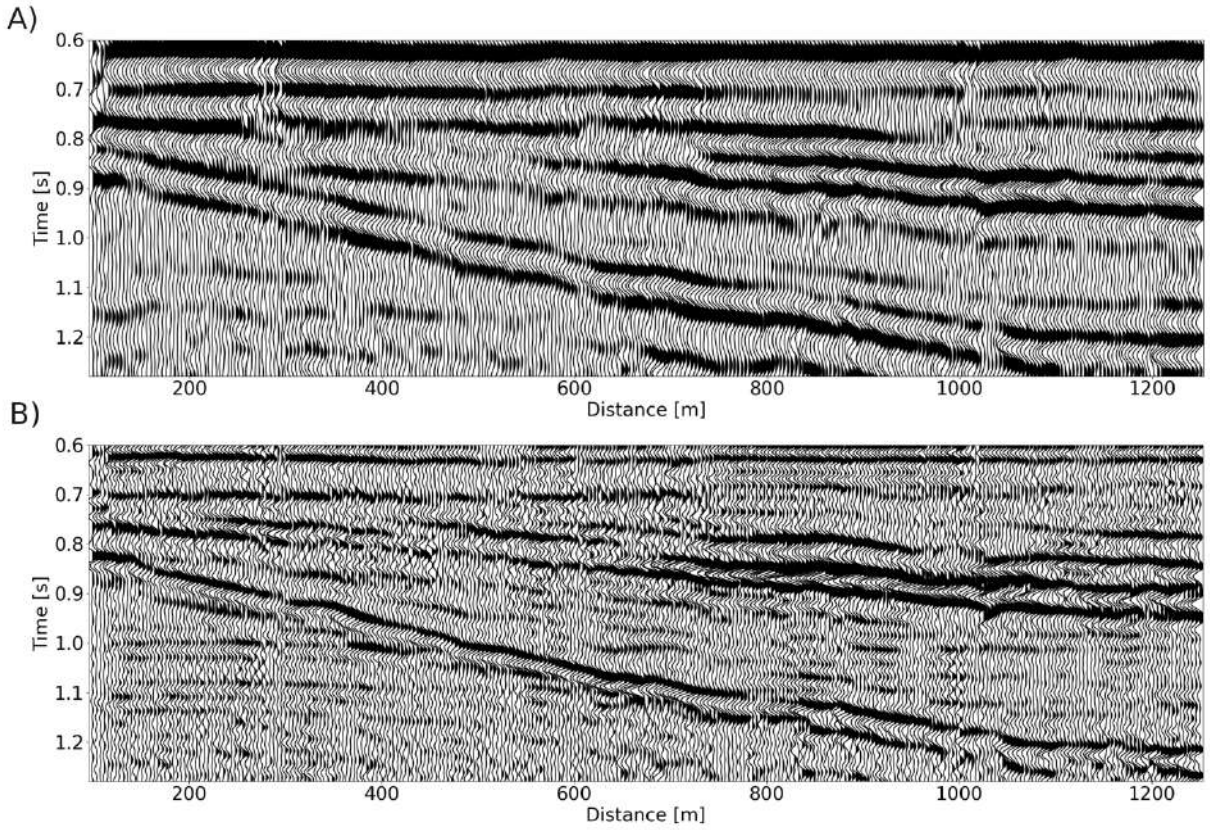

Figure 4: Wiggle plot of the area between 0.6s-1.3s and 120m-1250m of the Viking Graben dataset, focusing on a wedge structure. The input seismic line is shown in A, while the high frequency prediction of the same area is depicted in B.

In Figure 4B, the prompt detection of coherent signals is evident, notably horizontal reflectors beneath and within the wedge structure. Despite the limited leftward extent of the section, there is a remarkable improvement in vertical resolution, potentially enabling the identification of pinch-out structures.

Conclusions

We introduce a novel 1-D approach based on LSTM (Long Short-Term Memory) Neural Networks for addressing the low- and high-frequency gaps in seismic signal processing. The proposed method involves training two distinct neural networks: a low-frequency model, trained to infer lower frequency output from higher frequency signals, and a high-frequency model, trained with reversed input and output.

The method's scalability is assured thanks to its ability to operate without direct consideration of the frequency components, time length, and sampling information. The NN is trained with a custom loss function that incorporates both amplitude and frequency components. A crucial parameter known as Sample Duration (SD) governs the frequency content generation during training, providing flexibility for adjusting input data sampling and, consequently, the generated frequency output. The method's adaptability is demonstrated by rescaling signals to the trained

SD, allowing the inference of different frequencies through the application of a dedicated Scaling Factor (SF).

The results illustrate the effectiveness of the proposed approach in both low and high-frequency inferences using exemplary seismic data from the Viking Graben Line 12. The low-frequency model successfully shifts the central frequency from 14Hz to 8Hz while preserving amplitude and accurately predicting signal interference. The high-frequency model demonstrates reliable inference when compared to reference data the application of a band-pass filter between 10-40Hz, revealing a better detectability of different features, such as dipping reflectors and diffraction patterns, that were challenging to interpret in the lower frequency input data, while are confirmed by the reference data.

Overall, the proposed LSTM Neural Network-based approach proves to be a promising solution for addressing frequency gaps in seismic signal processing, offering high adaptability, scalability, and enhanced predictive capabilities for both low- and high-frequency components predictions.

References

Camacho-Ramírez, E., González-Flores, E., & Campos-Enriquez, J. (2016). Discrete wavelet transform-based multiresolution analysis and spectral enhancement to characterize heavy oil reservoirs in the southern gulf of mexico region. Interpretation, 4(4), T497-T505. https://doi.org/10.1190/int-2015-0184.1

Chopra, S., Alexeev, V., & Sudhakar, V. (2003). High-frequency restoration of surface seismic data. The Leading Edge, 22(8), 730-738. https://doi.org/10.1190/1.1605071

Du, W., Xin, P., Wang, P., & Sun, Y. (2016). Multiple-track ant body attribute extraction method improved.. https://doi.org/10.2991/iceeg-16.2016.72 Guo, J. and Wang, Y. (2004). Recovery of a target reflection underneath coal seams. Journal of Geophysics and Engineering, 1(1), 46-50. https://doi.org/10.1088/1742-2132/1/1/005

Karsli, H. (2006). Further improvement of temporal resolution of seismic data by autoregressive (ar) spectral extrapolation. Journal of Applied Geophysics, 59(4), 324-336. https://doi.org/10.1016/j.jappgeo.2005.11.001

Karsli, H. (2010). An application of the autoregressive extrapolation technique to enhance deconvolution results: a 2d marine data example. Geophysical Prospecting, 59(1), 56-65. https://doi.org/10.1111/j.1365-2478.2010.00895.x

Karsli, H., Dondurur, D., & Çifçi, G. (2006). Application of complex-trace analysis to seismic data for random-noise suppression and temporal resolution improvement. Geophysics, 71(3), V79-V86. https://doi.org/10.1190/1.2196875

Li, Y. and Demanet, L. (2016). Full-waveform inversion with extrapolated low-frequency data. Geophysics, 81(6), R339-R348. https://doi.org/10.1190/geo2016-0038.1

Nakayama, S. and Blacquière, G. (2021). Machine-learning-based data recovery and its contribution to seismic acquisition: simultaneous application of deblending, trace reconstruction, and low-frequency extrapolation. Geophysics, 86(2), P13-P24. https://doi.org/10.1190/geo2020-0303.1

Ovcharenko, O., Kazei, V., Alkhalifah, T., & Peter, D. (2022). Multi-task learning for low-frequency extrapolation and elastic model building from seismic data. Ieee Transactions on Geoscience and Remote Sensing, 60, 1-17. https://doi.org/10.1109/tgrs.2022.3185794

Ovcharenko, O., Kazei, V., Kalita, M., Peter, D., & Alkhalifah, T. (2019). Deep learning for low-frequency extrapolation from multioffset seismic data. Geophysics, 84(6), R989-R1001. https://doi.org/10.1190/geo2018-0884.1

Ovcharenko, O., Kazei, V., Plotnitskiy, P., Peter, D., Silvestrov, I., Bakulin, A., … & Alkhalifah, T. (2020). Extrapolating low-frequency prestack land data with deep learning.. https://doi.org/10.1190/segam2020-3427522.1

Reiser, C. and Bird, T. (2016). Advances in broadband quantitative interpretation.. https://doi.org/10.1190/segam2016-13818140.1

Shi, Z., Tian, G., Wang, B., & Chen, S. (2009). Near-surface absorption compensation technology and its application in the daqing oilfields. Applied Geophysics, 6(2), 184-191. https://doi.org/10.1007/s11770-009-0019-9

Sinha, S., Routh, P., Anno, P., & Castagna, J. (2005). Spectral decomposition of seismic data with continuous-wavelet transform. Geophysics, 70(6), P19-P25. https://doi.org/10.1190/1.2127113

Sun, H. and Demanet, L. (2020). Extrapolated full-waveform inversion with deep learning. Geophysics, 85(3), R275-R288. https://doi.org/10.1190/geo2019-0195.1

Robert G. Keys and Douglas J. Foster, (1998), "1. A Data Set for Evaluating and Comparing Seismic Inversion Methods," Open File Publications : 1-12. https://doi.org/10.1190/1.9781560802082.ch1

Corresponding author: groncoroni@units.it

Modelling temperature effect in time-lapse DC monitoring experiments through inversion of thermal diffusivity

A. Signora[1], G. Fiandaca[1]

[1] The EEM Team for Hydro & eXploration Dep. Of Earth Sciences A. Desio, Università degli Studi di Milano, Via Botticelli 23, Milano (Italy)

1. Motivation

In the recent years, time-lapse surveys have been performed widely to monitor, for instance, hydrogeological tracer experiments (Cassiani et al., 2006), groundwater watershed characterization (Miller et al., 2008; Deiana et al., 2018), seasonal variations (Hiblich et al., 2011; Musgrave and Binley 2011), landslide behaviour and evolution (Cassiani et al., 2009, Wilkinson et al., 2010), and so on. One of the main concerns, when resistivity surveys are performed, is to be sure to impute the variations to the right phenomena, distinguishing the electrical changes of interest from all the others, which are assumable as noise. Temperature variations might represent the main noise source in the time-lapse conductivity surveys since temperature has a strong impact on the resistivity parameters, hence the inversion results. For example, seasonal temperature trends could mask the conductivity variations, and thus lead to misleading interpretations, up to the depths from the surface that can be reached by external fluctuations. Haley et al. (2007; 2009; 2010) have pointed out the importance of considering the temperature variations in time-lapse geoelectrical surveys, including in the inversion procedure a correction for this effect. In this study we intend to disentangle the temperature effect from resistivity variations inverting for the thermal diffusivity of the medium in a simultaneous time-lapse inversion that does not require direct temperature measurements below ground, both on a synthetic dataset and on-field experiments.

2. Inversion scheme

The temperature effect on electrical resistivity is modelled through the equation proposed by Haley (2007):

$$\sigma_T = (1 + m(T - T_{25}))\sigma_{25} \tag{1}$$

where:

i) σ_T and T are effective electrical conductivity and temperature.

i) σ_{25} is the reference conductivity of the material at 25°degrees.

ii) T_{25} is the conventional temperature of 25 °C.

iii) m is the fractional change in electrical conductivity per degree Celsius.

The temperature is defined in the entire medium solving for the het equation:

$$\frac{\partial T}{\partial t} = k \frac{\partial^2 T}{\partial z^2} \tag{2}$$

Where, as depicted in Fig. 1, the temperature at the bottom of the model is considered constant, while the surface temperature varies seasonally. For any given thermal diffusivity k, the temperature can be estimated through the numerical solution of eq. 2 at each time instant and each depth.

Time-lapse 2D DC data are then inverted simultaneously in EEMverter (Fiandaca et al., 2024), using as model space the electrical resistivity at 25 °C in each inversion cell of all time-lapse models and a unique thermal diffusivity value k for the entire 2D profile. The sensitivity on the thermal diffusivity is retrieved enforcing time-lapse constraints between all time-lapse models, which favour the inversion models that minimize variations through the correct evaluation of the temperature effect. The asymmetric generalized minimum gradient support (AGMS) introduced by Fiandaca et al. (2015) has been used for time-lapse constraints.

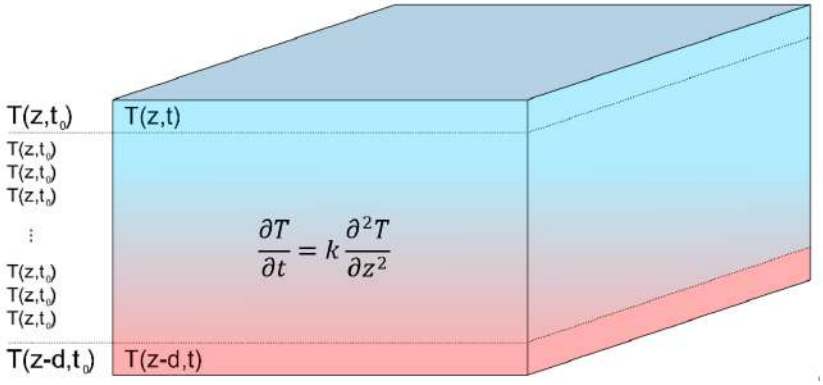

Figure 1. Schematization of the heat flux equation solved for the model discretization. Surface and bottom temperatures of the model need to be fixed as boundary condition within this inversion scheme.

3. Synthetic simulation and fieldwork case study

Synthetic simulations have been performed mimicking the seasonal variability of subsoil temperature caused by a homogeneous thermal diffusivity, constant temperature at depth and seasonal-varying surface temperature. On top of the temperature-induced changes in resistivity, a growing plume had been modelled, with 75-100 Ωm 25 °C resistivity in a homogeneous 150 Ωm halfspace. Nine time steps have been modelled, with 50 days of time difference, and all time-steps have been inverted simultaneously with AGMS time-lapse constraints.

Fig. 2 presents the comparison of the models obtained with: i) the standard resistivity inversion; ii) the simultaneous time-lapse inversion with temperature correction. Not only the time-lapse inversion retrieves the correct resistivity distribution, not altered by the temperature effect, but the simulated thermal diffusivity is retrieved correctly by the inversion.

As field example, a 730 days-long real experiment is analyzed. The temperature effect is clearly visible in data space, with apparent resistivity variations clearly correlated with surface temperature (Fig. 3). The survey has been carried out continuously on the rooftop of an MSW landfill, with stainless-steel electrodes whose position never changed for the whole duration of the study. The daily ERT (Electrical Resistivity Tomography) acquisitions were performed through 18 electrodes, spaced 5 meters from each other, with the Wenner-Alpha array configuration and 5 mA alternate currents injected with the frequency of 5 Hz. The result of this survey clearly shows a

sinusoidal fluctuation of the apparent resistivity values during the time and with decreasing magnitude with depth (Fig. 3, upper panels). This decreasing fluctuation points out the effect of the temperature variation on the external portions of the landfill, which vanish increasing the depth of analysis, as evident when comparing the apparent resistivity values and the temperature measured at the site (Fig 3, bottom panels). The deeper portions of the landfill, despite the presence of more noise measurements, show more stable apparent resistivity values through time, therefore less effect of the atmospheric temperature trends. Time-lapse inversions with modelling of temperture effect show much smaller resistivity variations throughout the entire monitoring, showing the improvement of the time-lapse scheme proposed in this study.

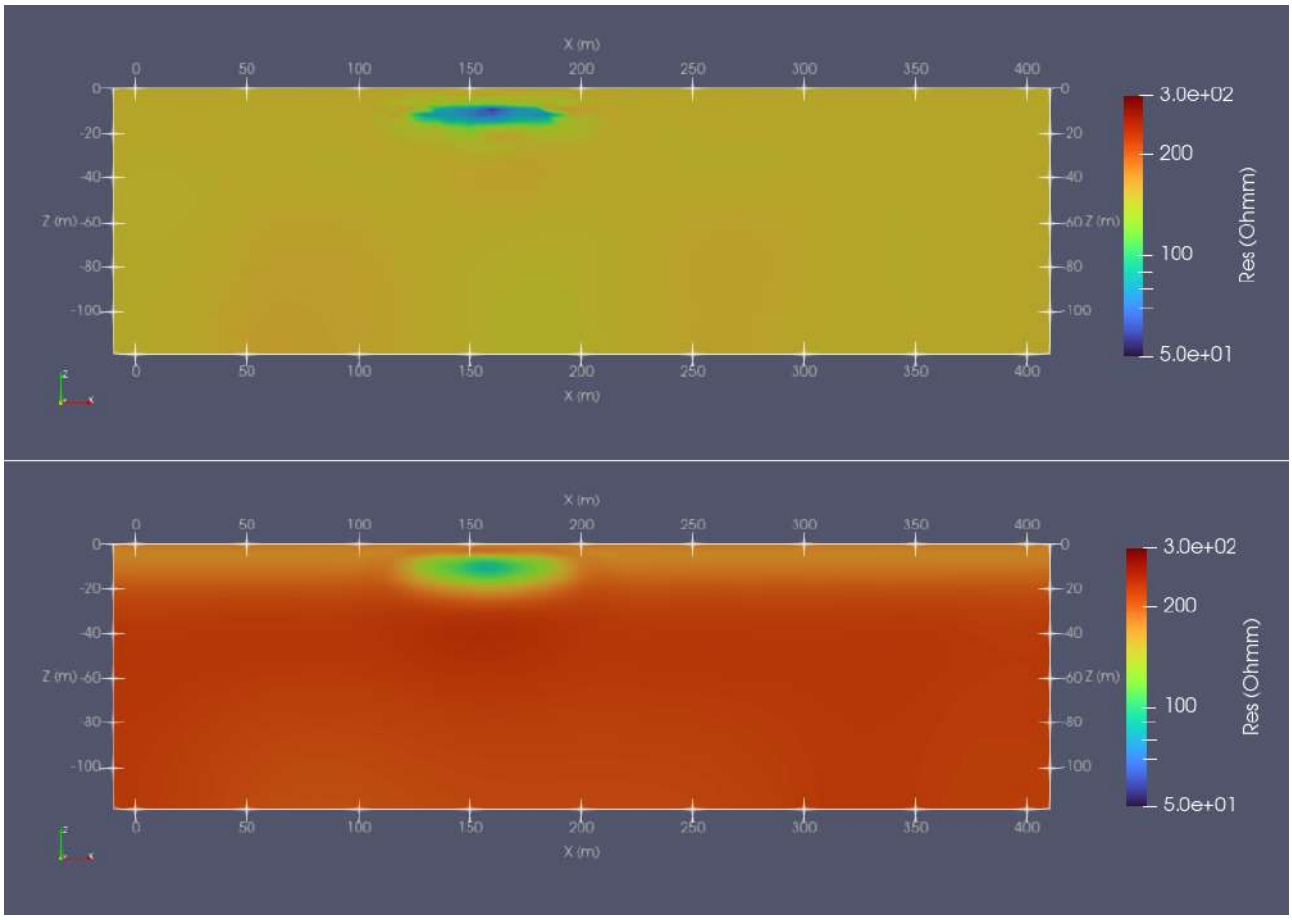

Figure 2. Comparison of standard resistivity inversion (bottom panel) and time-lapse inversion with modelling of thermal diffusivity (top panel).

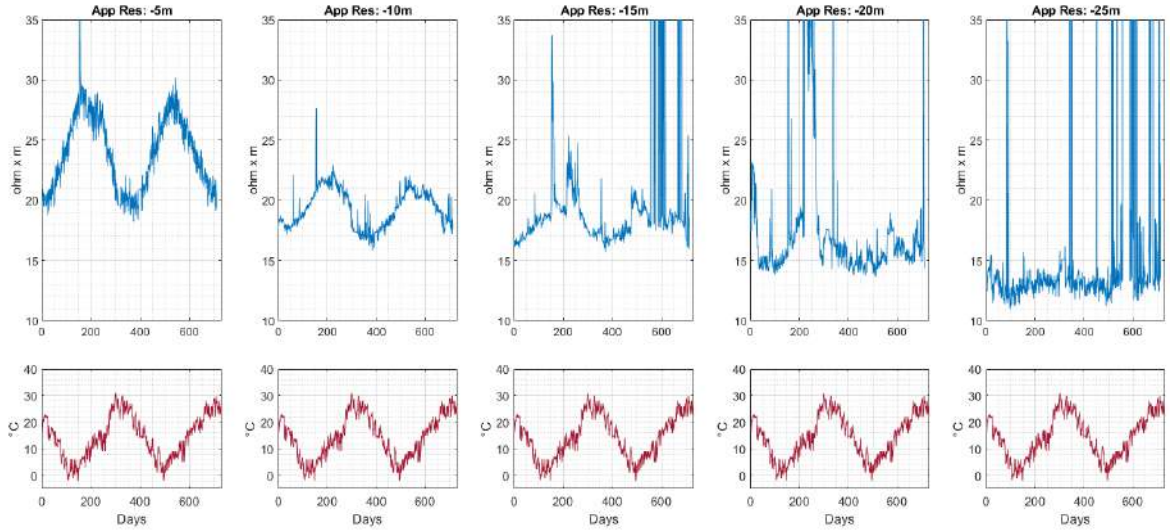

Figure 3. Fluctuation of apparent resistivity recorded within the body waste (blue lines) with different depths during the 740 day-long survey. The red lines in the below graphs represent the mean value of temperature for each survey day.

4. Conclusions

In this study a new time-lapse inversion scheme for modelling temperature effect in DC monitoring experiments is presented. The modelling scheme estimates the thermal diffusivity of the subsoil through the simultaneous inversion of time-lapse data, without the need of a direct measurement of the subsoil temperature. Both synthetic test and analysis of real data, acquired in a 730 days long monitoring experiment on an MSW landfill, show the potential of this new inversion scheme, which enable to disentangle temperature effects from resistivity variations induced by changes, for instance, of the groundwater coductivity.

Acknowledgments

We acknowledge Geo.Ti.La for the data provision. This study is funded by the project HydroGeosITe financed by A2A Ciclo Idrico.

References

Cassiani, G., 2009. Monitoring the hydrologic behaviour of a mountain slope via time-lapse electrical resistivity tomography. Near Surface Geophysics - NEAR SURF GEOPHYS.

Cassiani, G., Bruno, V., Villa, A., Fusi, N., Binley, A., 2006. A saline trace test monitored via time-lapse surface electrical resistivity tomography. Journal of Applied Geophysics 59, 244–259. https://doi.org/10.1016/j.jappgeo.2005.10.007

Deiana, R., Cassiani, G., Kemna, A., Villa, A., Bruno, V., Bagliani, A., 2007. An experiment of non-invasive characterization of the vadose zone via water injection and cross-hole time-lapse geophysical monitoring. Near Surface Geophysics.

Fiandaca, G., Doetsch, J., Vignoli, G., Auken, E., 2015. Generalized focusing of time-lapse changes with applications to direct current and time-domain induced polarization inversions. Geophys J Int 203, 1101–1112. https://doi.org/10.1093/gji/ggv350

Fiandaca, G., Zhang, B., Chen, J., Signora, A., Dauti, F., Galli, S., Sullivan, N.A.L., Bollino, A., Viezzoli, A., 2024. EEMverter, a new 1D/2D/3D inversion tool for Electric and Electromagnetic data with focus on Induced Polarization. GNGTS 2024, 13-16 February 2024, Ferrara, Italy.

Hayley, K., Bentley, L.R., Gharibi, M., 2009. Time-lapse electrical resistivity monitoring of salt-affected soil and groundwater. Water Resources Research 45. https://doi.org/10.1029/2008WR007616

Hayley, K., Bentley, L.R., Gharibi, M., Nightingale, M., 2007. Low temperature dependence of electrical resistivity: Implications for near surface geophysical monitoring. Geophysical research letters 34.

Hayley, K., Bentley, L.R., Pidlisecky, A., 2010. Compensating for temperature variations in time-lapse electrical resistivity difference imaging. GEOPHYSICS 75, WA51–WA59. https://doi.org/10.1190/1.3478208

LaBrecque, D. & Yang, X., 2001. Difference inversion of ERT data: a fast inversion method for 3-D in situ monitoring, J. Environ. Eng. Geophys., 6, 83–89.

Miller, C.R., Routh, P.S., Brosten, T.R., McNamara, J.P., 2008. Application of time-lapse ERT imaging to watershed characterization. GEOPHYSICS 73, G7–G17. https://doi.org/10.1190/1.2907156

Musgrave, H., Binley, A., 2011. Revealing the temporal dynamics of subsurface temperature in a wetland using time-lapse geophysics. Journal of Hydrology 396, 258–266. https://doi.org/10.1016/j.jhydrol.2010.11.008

Wilkinson, P.B., Chambers, J.E., Meldrum, P.I., Gunn, D.A., Ogilvy, R.D., Kuras, O., 2010. Predicting the movements of permanently installed electrodes on an active landslide using time-lapse geoelectrical resistivity data only. Geophysical Journal International 183, 543–556. https://doi.org/10.1111/j.1365-246X.2010.04760.x

Corresponding author: alessandro.signora@unimi.it

Amplitude and traveltime inversion for mono-channel Boomer surveys

A. Vesnaver, L. Baradello

Department of Geophysics, Istituto Nazionale di Oceanografia e Geofisica Sperimentale - OGS, Trieste, Italy

INTRODUCTION

Mono-channel recording systems with a Boomer seismic source are very cheap and can be easily deployed in sensitive environments such as lagoons or busy harbours (Zecchin et al. 2008). The price paid for these advantages is the lack of signal redundancy typical of multi-channel records, which makes it possible to estimate wave propagation velocity and angle-dependent reflectivity, and to improve the signal-to-noise ratio by stacking or migration. In this paper, we show that some of this information can be obtained by inverting the amplitudes and traveltimes of shallow primary reflections and their multiples, using a single offset in a Boomer survey.

Amplitudes and traveltimes can in principle be inverted separately, but doing so we do not use the information redundancy embedded in the velocity: it determines both the traveltimes along the ray paths and the amplitude of primaries and multiple reflections via the acoustic impedance contrasts at the layer interfaces. Therefore, the coupling of these two inversion algorithms can extract more information from our minimal data set. The possible ambiguities of one inversion can be limited by constraints coming from the other inversion, so improving the stability of both.

AMPLITUDE AND TRAVELTIME INVERSION

The simplest object function we can create for a joint inversion of amplitudes and traveltimes is the sum of the squared differences between measured and modeled data, minimizing it as a function of the Earth model parameters:

$$\mathbf{Object}(T_j, A_j, V, L, \rho) = \sum_j [T_j - t(V,L)]^2 + \sum_j [A_j - a(V,\rho)]^2 \quad , \qquad (1)$$

where T_j and A_j are the measured traveltimes and amplitudes of primaries and multiples in a single trace. We assume a 1D Earth model, with the data compensated for the geometrical spreading – (e.g., by a t^2 gain function). We note that the modeled traveltimes $t(V, L)$ depend on the layer velocity V and the layer thickness L, but not on the density ρ. Similarly, the modeled amplitudes $a(V, \rho)$ do not depend on the thickness L. Therefore, a separate inversion of amplitudes and traveltimes can avoid cross-talk between density and thickness. On the other hand, the velocity V influences both the amplitude (via the acoustic

impedance $I = \rho V$) and the transit time in a layer (via the ratio $LV = L / V$). Since the Earth model must be consistent with both data sets, the velocity value must be the same for both inversion solutions. Another condition for the two inversion algorithms is the stability of the acoustic impedance I and the transit time LV against random noise, which we found in several tests with synthetic data. Therefore, each of these values is a well-constrained part of the two separate solutions, and we imposed that they are kept constant, while we perturb the values of velocity, density and thickness.

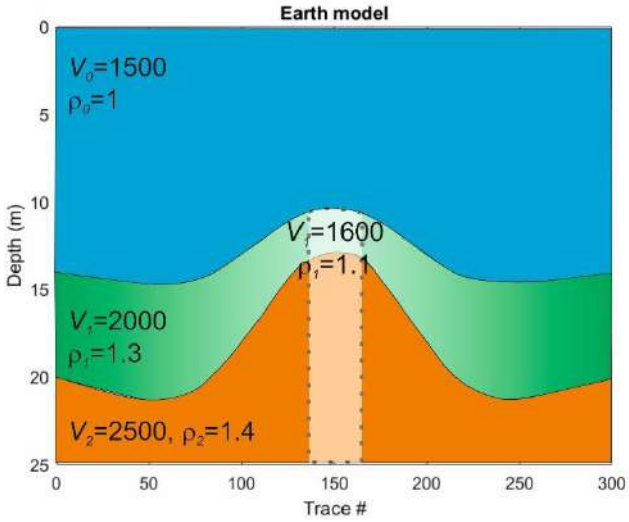

Fig.1 – Earth model simulating a mud volcano. Although the model is 2D, the simulation and inversion are carried out in 1D only, so assuming just slow lateral variations.

APPLICATION EXAMPLE

To test the stability of this coupled inversion, we built an Earth model (Figure 1) that mimics a mud volcano. Its cone makes the water depth variable, while the water density and velocity are constant and known (1500 m/s and 1 gr/cc, respectively). Our target is the first layer below the seafloor, which consists of sediments with P velocity and density that vary laterally and reach a minimum in the center of the volcano. The basement is again homogeneous. We simulated by ray tracing only primaries and multiples from the seafloor and the sediment layer base, with an offset of 10 m between source and receiver.

For the velocity inversion we need the two primaries of the latter ones, plus one or more multiples as peg-leg, intrabed or “simple” (Vesnaver and Baradello 2022a, b). The more, the better, because redundancy can reduce random noise due to picking errors and spurious events. For the amplitude inversion, we instead used only the primary and two reverberations between seafloor and sea surface to limit our solution space to the only two parameters we want to estimate, i.e., sediment velocity and density (Vesnaver and Baradello 2023). Including the amplitude of the other multiples is not so helpful: doing so, we would also have to calculate the velocity and density of the bedrock, leading to further unknowns and instabilities in our inversion.

Figure 2 shows the inversion results obtained by adding random noise of 0.1% to the amplitudes and traveltimes of 300 seismic traces, which corresponds to only a few samples.

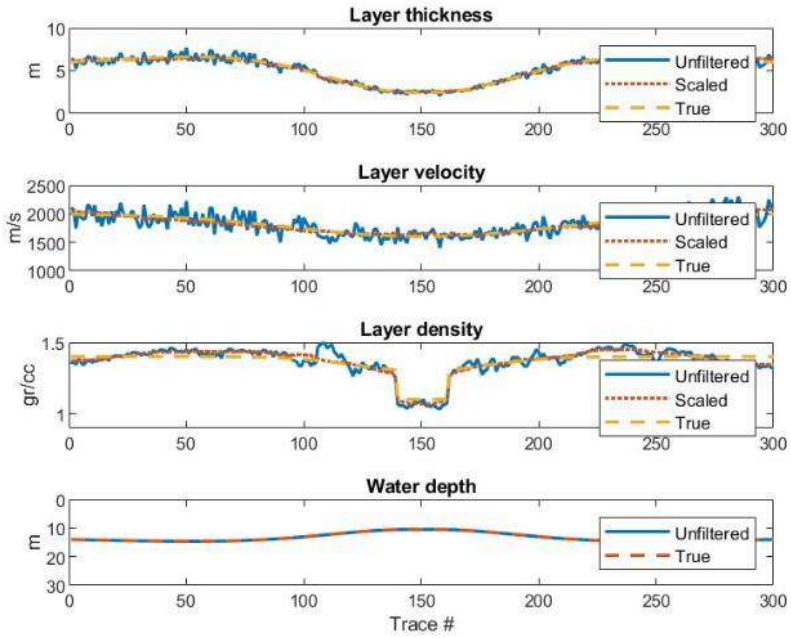

Fig.2 – Amplitude and traveltime inversion when a random noise percentage of 0.1% is added to the synthetic data. The smoothed, scaled estimate (dotted red line) fits well the true model (dashed yellow line).

To improve the stability of the inversion, we also introduced a lateral smoothing filter with a window length of 31 samples. The instability in the initial estimates (solid blue line) is completely removed by the smoothing and scaling (dotted red line), so that this curve practically matches that of the true model (dashed yellow line).

When the random noise increases to 0.5% (Figure 3), the estimated velocity is definitely unstable, but again the smoothed, scaled version (dotted red line) is not too far from the correct solution. The weakest estimate is that of density, which still correctly identifies a minimum value at the center of the mud volcano.

CONCLUSIONS

The lack of redundancy of a minimal survey, such as a mono-channel Boomer system, can be partially compensated for by interpreting and inverting the amplitudes and traveltimes of primaries and multiples. However, such an inversion requires a separate but coupled inversion of the dynamic and kinematic data to limit the crosstalk of physically independent variables.

The results obtained with different noise levels show that we can obtain an encouraging estimate even for density when the signal-to-noise ratio is very good. This information is important for offshore engineering and marine geology.

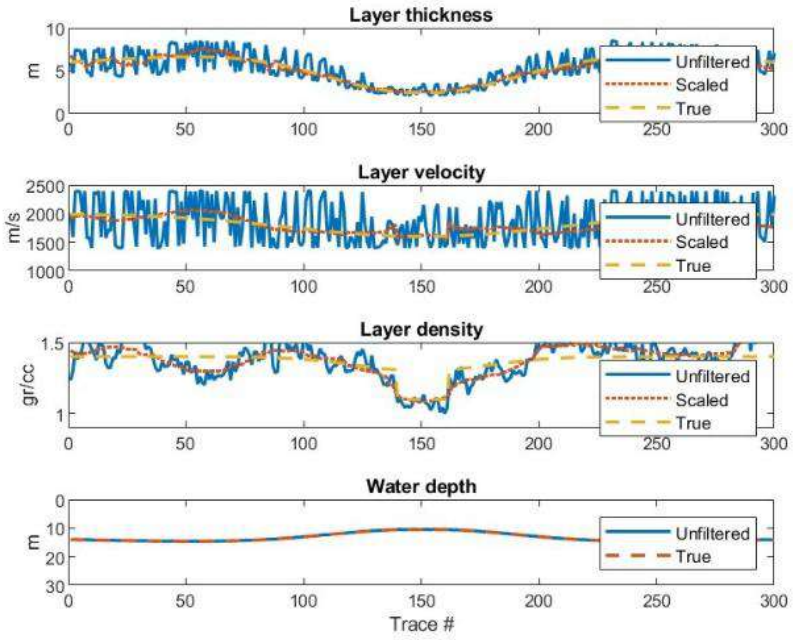

Fig.3 – Amplitude and traveltime inversion when a random noise percentage of 0.5% is added to the synthetic data. The unfiltered estimate (solid blue line) becomes unstable, especially for the velocity, but the smoothed, scaled version for all estimates (dotted red lines) remains fairly good.

References

Vesnaver A., Baradello L.; 2022a: *Shallow velocity estimation by multiples for monochannel Boomer surveys*. Applied Sciences, **12**, 3046. https://doi.org/10.3390/app12063046.

Vesnaver A., Baradello L.; 2022b: *Tomographic joint inversion of direct arrivals, primaries and multiples for monochannel marine surveys*. Geosciences, **12** (6), 219. https://doi.org/10.3390/geosciences12060219.

Vesnaver A., Baradello L.; 2023: *Sea floor characterization by multiples' amplitudes in monochannel surveys*. Journal of Marine Science and Engineering, **11**, 1662. https://doi.org/10.3390/jmse11091662.

Zecchin M., Baradello L., Brancolini G., Donda F., Rizzetto F., Tosi L.; 2008: *Sequence stratigraphy based on high-resolution seismic profiles in the late Pleistocene and Holocene deposits of the Venice area*. Marine Geology**, 253**, 3–4, 185-198. https://doi.org/10.1016/j.margeo.2008.05.010.

Corresponding author: aldo.l.vesnaver@gmail.com